

AD-A244 249

AGARD-CP-494

①



AGARD-CP-494

# AGARD

ADVISORY GROUP FOR AEROSPACE RESEARCH & DEVELOPMENT  
7 RUE ANCELLE 92200 NEUILLY SUR SEINE FRANCE

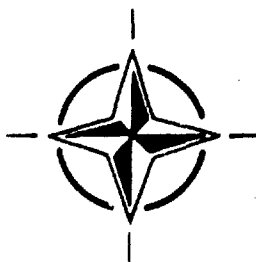
AGARD CONFERENCE PROCEEDINGS 494

## Vortex Flow Aerodynamics

(L'Aérodynamique des Ecoulements Tourbillonnaires)

DTIC  
ELECTRONIC  
S  
C

Best Available Copy



NORTH ATLANTIC TREATY ORGANIZATION

## The Mission of AGARD

According to its Charter, the mission of AGARD is to bring together the leading personalities of the NATO nations in the fields of science and technology relating to aerospace for the following purposes:

- Recommending effective ways for the member nations to use their research and development capabilities for the common benefit of the NATO community;
- Providing scientific and technical advice and assistance to the Military Committee in the field of aerospace research and development (with particular regard to its military application);
- Continuously stimulating advances in the aerospace sciences relevant to strengthening the common defence posture;
- Improving the co-operation among member nations in aerospace research and development;
- Exchange of scientific and technical information;
- Providing assistance to member nations for the purpose of increasing their scientific and technical potential;
- Rendering scientific and technical assistance, as requested, to other NATO bodies and to member nations in connection with research and development problems in the aerospace field

The highest authority within AGARD is the National Delegates Board consisting of officially appointed senior representatives from each member nation. The mission of AGARD is carried out through the Panels which are composed of experts appointed by the National Delegates, the Consultant and Exchange Programme and the Aerospace Applications Studies Programme. The results of AGARD work are reported to the member nations and the NATO Authorities through the AGARD series of publications of which this is one.

Participation in AGARD activities is by invitation only and is normally limited to citizens of the NATO nations.

The content of this publication has been reproduced directly from material supplied by AGARD or the authors

Published July 1991

Copyright © AGARD 1991  
All Rights Reserved

ISBN 92-835-0623-5



Printed by Specialised Printing Services Limited  
40 Chigwell Lane, Loughton, Essex IG10 3TZ



## **Recent Publications of the Fluid Dynamics Panel**

### **AGARDOGRAPHS (AG)**

**Experimental Techniques in the Field of Low Density Aerodynamics**  
AGARD AG-318 (E), April 1991

**Techniques Expérimentales Liées à l'Aérodynamique à Basse Densité**  
AGARD AG-318 (FR), April 1990

**A Survey of Measurements and Measuring Techniques in Rapidly Distorted Compressible Turbulent Boundary Layers**  
AGARD AG-315, May 1989

**Reynolds Number Effects in Transonic Flows**  
AGARD AG-303, December 1988

**Three Dimensional Grid Generation for Complex Configurations - Recent Progress**  
AGARD AG-309, March 1988

### **REPORTS (R)**

**Aircraft Dynamics at High Angles of Attack: Experiments and Modelling**  
AGARD R-776, Special Course Notes, March 1991

**Inverse Methods in Airfoil Design for Aeronautical and Turbomachinery Applications**  
AGARD R-780, Special Course Notes, November 1990

**Aerodynamics of Rotorcraft**  
AGARD R-781, Special Course Notes, November 1990

**Three-Dimensional Supersonic/Hypersonic Flows Including Separation**  
AGARD R-764, Special Course Notes, January 1990

**Advances in Cryogenic Wind Tunnel Technology**  
AGARD R-774, Special Course Notes, November 1989

### **ADVISORY REPORTS (AR)**

**Rotary-Balance Testing for Aircraft Dynamics**  
AGARD AR-265, Report of WG 11, December 1990

**Calculation of 3D Separated Turbulent Flows in Boundary Layer Limit**  
AGARD AR-255, Report of WG10, May 1990

**Adaptive Wind Tunnel Walls: Technology and Applications**  
AGARD AR-269, Report of WG12, April 1990

**Drag Prediction and Analysis from Computational Fluid Dynamics: State of the Art**  
AGARD AR-256, Technical Status Review, June 1989

### **CONFERENCE PROCEEDINGS (CP)**

**Vortex Flow Aerodynamics**  
AGARD CP-494, July 1991

**Missile Aerodynamics**  
AGARD CP-493, April 1990

**Aerodynamics of Combat Aircraft Controls and of Ground Effects**  
AGARD CP-465, October 1989

**Computational Methods for Aerodynamic Design (Inverse) and Optimization**  
AGARD CP-463, April 1989

**Applications of Mesh Generation to Complex 3-D Configurations**  
AGARD CP-464, April 1989

**Fluid Dynamics of Three-Dimensional Turbulent Shear Flows and Transition**  
AGARD CP-438, October 1988

**Validation of Computational Fluid Dynamics**  
AGARD CP-437, May 1988

**Aerodynamic Data Accuracy and Quality: Requirements and Capabilities in Wind Tunnel Testing**  
AGARD CP-429, October 1987

**Aerodynamics of Hypersonic Lifting Vehicles**  
AGARD CP-428, April 1987

**Aerodynamic and Related Hydrodynamic Studies Using Water Facilities**  
AGARD CP-413, October 1986

**Applications of Computational Fluid Dynamics in Aeronautics**  
AGARD CP-412, April 1986

**Store Airframe Aerodynamics**  
AGARD CP-389, October 1985

**Unsteady Aerodynamics — Fundamentals and Applications to Aircraft Dynamics**  
AGARD CP-386, May 1985

**Aerodynamics and Acoustics of Propellers**  
AGARD CP-366, October 1984

**Improvement of Aerodynamic Performance through Boundary Layer Control and High Lift Systems**  
AGARD CP-365, May 1984

**Wind Tunnels and Testing Techniques**  
AGARD CP-348, September 1983

**Aerodynamics of Vortical Type Flows in Three Dimensions**  
AGARD CP-342, April 1983

**Missile Aerodynamics**  
AGARD CP-336, September 1982

**Prediction of Aerodynamic Loads on Rotorcraft**  
AGARD CP-334, May 1982

**Wall Interference in Wind Tunnels**  
AGARD CP-335, May 1982

**Fluid Dynamics of Jets with Applications to V/STOL**  
AGARD CP-308, November 1981

**Aerodynamics of Power Plant Installation**  
AGARD CP-301, May 1981

**Computation of Viscous-Inviscid Interactions**  
AGARD CP-291, October 1980

**Subsonic/Transonic Configuration Aerodynamics**  
AGARD CP-285, May 1980

**Turbulent Boundary Layers Experiments, Theory and Modelling**  
AGARD CP-271, September 1979

**Aerodynamic Characteristics of Controls**  
AGARD CP-262, May 1979

**High Angle of Attack Aerodynamics**  
AGARD CP-247, October 1978

**Dynamic Stability Parameters**  
AGARD CP-235, May 1978

**Unsteady Aerodynamics**  
AGARD CP-227, September 1977

**Laminar-Turbulent Transition**  
AGARD CP-224, May 1977

## Foreword

Separation-induced vortex flows are an important part of the design and off-design performance of conventional fighter aircraft, and new or unconventional advanced fighter designs, missiles, and space plane concepts. A better understanding is needed in order to predict and control these vortex flows throughout the flight envelope at subsonic, transonic, and supersonic speeds, and especially during high lift operations for take-offs, landings, and sustained and instantaneous maneuvers.

The principal emphasis of the Symposium was on the understanding and prediction of vortex flows and their effects on vehicle performance, stability, control, and structural design loads. Topics of interest included vortex development and burst, modeling and validation of the full range of analytical methods, slender-body vortex flows at high angles-of-attack, vortex control and management, and unsteady vortex flow effects

J.F. Campbell/A.D. Young  
Co-Chairmen

## Avant-Propos

Les écoulements tourbillonnaires liés au décollage jouent un rôle important dans les performances normales et les performances hors normes des avions de combat conventionnels, ainsi que dans la conception des avions de combat modernes évolués ou expérimentaux, des missiles et des avions spatiaux.

Une meilleure compréhension de ces phénomènes permettrait de prédire et de maîtriser les écoulements tourbillonnaires dans tout le domaine de vol à des vitesses subsoniques, transsoniques et supersoniques, en particulier lors des opérations de sustentation au décollage, à l'atterrissage, et lors des manoeuvres soutenues et ponctuelles.

L'accent principal du symposium a été mis sur la compréhension et la prédiction des écoulements tourbillonnaires et leurs effets sur les performances, la stabilité, le pilotage, et les efforts structuraux d'étude des véhicules aériens. Parmi les sujets examinés on distingue: l'évolution et l'éclatement des tourbillons, la modélisation et la validation de l'intégralité des méthodes analytiques, les écoulements tourbillonnaires autour des corps effilés aux grands angles d'attaque, le contrôle et la maîtrise des tourbillons et les effets des écoulements tourbillonnaires instationnaires.

J.F. Campbell/A.D. Young  
Co-Présidents du Comité  
de Programme

## Fluid Dynamics Panel

**Chairman:** Dr W.J. McCroskey  
Senior Staff Scientist  
US Army Aero Flightdynamics Directorate  
Mail Stop N-258-1  
NASA Ames Research Center  
Moffett Field, CA 94035-1099  
United States

**Deputy Chairman:** Professor Ir J W Slooff  
National Aerospace Laboratory NLR  
Anthony Fokkerweg 2  
1006 BM Amsterdam  
The Netherlands

### PROGRAMME COMMITTEE

Dr J.F. Campbell (Co-Chairman)  
NASA Langley Research Center  
Transonic Aerodynamics Branch  
Mail Stop 301  
Hampton, VA 23665-5225  
United States

Prof. R. Decuyper  
Ecole Royale Militaire  
Chaire de Mécanique Appliquée  
Avenue de la Renaissance 30  
B-1040 Brussels, Belgium

Dr K.J. Orlik-Rückemann  
Institute for Aerospace Research  
NRC, Bldg M-10  
Montreal Road  
Ottawa K1A 0R6, Canada

Prof. A. Bonnet  
Department Aérodynamique  
Ecole Nationale Supérieure de  
l'Aéronautique et de l'Espace  
10 Avenue Edouard Belin, BP 4032  
31055 Toulouse Cedex, France

Prof. Dr Ing. K. Gersten  
Institut für Thermo- und Fluidodynamik  
Ruhr-Universität Bochum  
Postfach 10 21 48  
D-4630 Bochum 1, Germany

Prof. M. Onorato  
Dipartimento di Ingegneria  
Aeronautica e Spaziale  
Politecnico di Torino  
C. so Duca degli Abruzzi 24  
10129 Torino, Italy

Professor A.D. Young (Co-Chairman)  
70 Gilbert Road  
Cambridge, CB4 3PD  
United Kingdom

Ir A. Elsenaar  
National Aerospace Laboratory NLR  
Anthony Fokkerweg 2  
1059 CM Amsterdam  
The Netherlands

Professor A.F. de O. Falcao  
Depart. Engenharia Mecanica  
Instituto Superior Tecnico  
1096 Lisboa Codex  
Portugal

Professor J. Jimenez  
Escuela Tecnica Superior de  
Ingenieros Aeronauticos  
Dept. de Mecanica de Fluidos  
Plaza del Cardena Cisneros 3  
28040 Madrid, Spain

Dr U. Kaynak  
TUSAS  
Havacilik ve Uzay San. A.S.  
P.K. 18 Kavaklıdere  
06690 Ankara  
Turkey

Dr R.G. Bradley  
Director, Flight Sciences Dept  
Mail Zone 2888  
General Dynamics, Fort Worth Div.  
P.O. Box 748  
Fort Worth, TX 76101-748  
United States

### PANEL EXECUTIVE

Dr W. Goodrich

**Mail from Europe:**  
AGARD—OTAN  
Attn: FDP Executive  
7, rue Ancelle  
F-92200 Neuilly-sur-Seine  
France

**Mail from US and Canada:**  
AGARD—NATO  
Attn: FDP Executive  
APO New York 09777

Tel: 33 (1) 47 38 57 75    Telex: 610176F    Telefax: 33 (1) 47 38 57 99

# Contents

	Page
Recent Publications of the Fluid Dynamics Panel	iii
Foreword/Avant-Propos	v
Fluid Dynamics Panel	vi
<b>SESSION I — VORTEX COMPUTATIONAL TECHNIQUES — I</b>	Reference
Chairman: A. Bonnet	
Modeling and Numerical Simulation of Vortex Flow in Aerodynamics by H.W.M. Hoeijmakers	1
Comparison of Solution of Various Euler Solvers and One Navier-Stokes Solver for the Flow about a Sharp-Edged Cropped Delta Wing by B.R. Williams, W. Kordulla, M. Borsi and H.W.M. Hoeijmakers	2
Vortical Flow Simulation by Using Structured and Unstructured Grids by M. Borsi et al.	3
Analysis of Results of an Euler-Equation Method Applied to Leading-Edge Vortex Flow by J.I. van den Berg, H.W.M. Hoeijmakers and J.M.J.W. Jacobs	4
Experimental and Numerical Investigation of the Vortex Flow over a Delta Wing at Transonic Speed by E.M. Houtman and W.J. Bannink	5
<b>SESSION II — VORTEX COMPUTATIONAL TECHNIQUES — II</b>	
Chairman: R.G. Bradley	
Review of Vortex Computational Techniques by J.M. Luckring	6
On the Simulation of Compressible Turbulent Flows past Delta Wing, Delta Wing-Body and Delta Wing-Canard by A. Hilgenstock and H. Vollmers	7
Calculation of Hypersonic Leaside Vortices over Blunt Delta Wings by A. Rizzi, E.M. Murman, P. Eliasson and K.-M. Lee	8
On the Footprints of Three-Dimensional Separated Vortex Flows around Blunt Bodies by U. Dallmann, A. Hilgenstock, S. Riedelbauch, B. Schulte-Werning and H. Vollmers	9
Laminar-Flow Secondary Separation on a Slender Wing by K. Kirkköprü and N. Riley	10
Nonequilibrium Turbulence Modeling Effects on Transonic Vortical Flows about Delta Wings by U. Kaynak, E. Tu, M. Dindar and R. Barlas	11
<b>SESSION III — MEASUREMENTS AND VISUALIZATION</b>	
Chairman: M. Onorato	
Review of Aircraft Dynamic Loads Due to Flow Separation by D.G. Mabey	12
In-Flight Flow Visualization and Pressure Measurements at Low Speeds on the NASA F-18 High Alpha Research Vehicle by J.H. Del Frate, D.F. Fisher and F.A. Zuniga	13

	Reference
<b>Vortex Formation over a Close-Coupled Canard-Wing-Body Configuration in Unsymmetrical Flow</b> by A. Bergmann, D. Hummel and H.-Chr. Oelker	14
<b>An Experimental Study of the Flow over a Sharp-Edged Delta Wing at Subsonic and Transonic Speeds</b> by A. Elsenaar and H.W.M. Hoeijmakers	15
<b>Caractéristiques d'une Couche Limitée en Aval d'un Tourbillon de Bord d'Attaque</b> par G. Pailhas et J. Cousteix	16

**SESSION IV — SLENDER-BODY VORTEX FLOWS**  
Chairman: K. Gersten

<b>Ecoulement Tourbillonnaire sur Fuselage de Missile Etude Expérimentale et Modélisation</b> par P. Champigny et D. Baudin	17
<b>Asymmetric Vortex Flow over Circular Cones</b> by M. Pidd and J.H.B. Smith	18
<b>An Experimental Investigation of the Effect of Fineness Ratio on Lateral Force on a Pointed Slender Body of Revolution</b> by I.R.M. Moir	19

**SESSION V — VORTEX DEVELOPMENT AND BREAKDOWN**  
Chairman: A. Elsenaar

<b>Physique des Ecoulements Tourbillonnaires</b> par J. Delery	20
<b>Breaking Down the Delta Wing Vortex: The Role of Vorticity in the Breakdown Process</b> by R.C. Nelson and K.D. Visser	21
<b>Détermination de Critères d'Eclatement Tourbillonnaire par Résolution des Equations d'Euler et de Navier-Stokes</b> par T.H. Le, Ph. Mege et Y. Morchoisne	22
<b>Etudes Fondamentales sur l'Eclatement Tourbillonnaire et son Contrôle</b> par D. Pagan et P. Molton	23
<b>Investigation of Vortex Breakdown on a Delta Wing Using Euler and Navier-Stokes Equations</b> by S. Agrawal, R.M. Barnett and B.A. Robinson	24

**SESSION VI — VORTEX CONTROL**  
Chairman: A.D. Young

<b>Vortex Control — Further Encounters</b> by D.M. Rao	25
<b>On Aircraft Wake Properties and some Methods for Stimulating Decay and Breakdown of Tip Vortices</b> by R. Staufenbiel and T. Vitting	26
<b>Control of Forebody Vortices by Suction at the Nose of the RAE High Incidence Research Model</b> by A.J. Ross, E.B. Jefferies and G.F. Edwards	27
<b>An Experimental Investigation of Vortex Flaps on a Canard Combat-Aircraft Configuration</b> by D.A. Lovell	28

Reference

**SESSION VII -- UNSTEADY EFFECTS**

**Chairman: K.J. Orlik-Rückemann**

<b>Steady and Unsteady Aerodynamics of a Pitching Straked Wing Model at High Angles of Attack</b> by A.M. Cunningham Jr and R.G. den Boer	<b>29</b>
<b>Some Characteristics and Effects of the F/A-18 LEX Vortices</b> by D. Brown, B.H.K. Lee and F.C. Tang	<b>30</b>
<b>Multiple Roll Attractors of a Delta Wing at High Incidence</b> by E.S. Hanff and L.E. Ericsson	<b>31</b>
<b>Numerical Simulation of Vortex Street-Edge Interaction</b> by M.O. Kaya, C.R. Kaykayoglu, K.C. Bayar and J.M.R. Graham	<b>32</b>
<b>Numerical Simulation of Vortex Flows past Impulsively Started Wings</b> by A. Baron, M. Boffadossi and S. De Ponte	<b>33</b>
<b>Round Table Discussion</b>	<b>RTD</b>

# MODELING AND NUMERICAL SIMULATION OF VORTEX FLOW IN AERODYNAMICS

by

H.W.M. Hoeijmakers  
National Aerospace Laboratory NLR  
Anthony Fokkerweg 2, 1059 CM Amsterdam  
The Netherlands

## SUMMARY

A review is presented of mathematical models of different level of approximation for and their application to the numerical simulation of vortical type of flows occurring in subsonic and transonic aircraft aerodynamics. The paper covers computational methods for predicting the downstream development of vortex wakes as well as methods for simulating the detailed characteristics of configurations with leading-edge or body vortices. The emphasis is on the latter, strong-interaction, type of vortical flows. Promising new developments of the methods used at present are discussed in some detail. The possibilities, limitations and prospects of improvement of the methods are indicated and results of different methods are discussed. Also considered are some more fundamental aspects of the numerical simulation such as separation at sharp and round leading edges, separation at a smooth part of the surface, the structure of the leading-edge vortex and the merging of two vortices.

## 1. INTRODUCTION

In aircraft aerodynamics flows involving free shear (vortex) layers and vortex cores, generally termed vortex flows, play an important role (Küchemann, Ref. 1). At the high Reynolds numbers pertinent to aircraft aerodynamics free shear layers form whenever the flow encounters a sharp edge. The properties of the (thin) shear layer are determined by the conditions that at the edge (a geometrical singularity) the velocity remains finite and that vorticity is convected away from it, i.e. the Kutta condition. It should be realized that in the three-dimensional high-Reynolds-number flow of interest here the vorticity contents of the shear layer is primarily determined by the shear of the velocity vector (i.e. magnitude of the discontinuity in its direction) across the separation line, not by the vorticity within the viscous layers meeting at the separation line (Hirschel, Ref. 2).

Away from the edge the shear layer usually rolls up into one or more vortex cores which remain embedded within the shear layer and are continuously fed with vorticity from the shear layer. Sooner or later most of the vorticity generated at the edge will be concentrated in these regions with distributed vorticity. The resulting vortical flow structure is often well-ordered, steady and persistent.

On an aircraft configuration the flow may separate before a sharp edge is reached, i.e. at a smooth portion of the surface. In contrast to the separation at a sharp edge the location of the smooth-surface separation depends on Mach number, incidence, Reynolds number, state of the boundary layer, etc. and is not known a priori. In three-dimensional flow this type of separation (i.e. specifically the so-called "open" type of separation) may result in another well-defined and steady vortical flow structure, which itself is not very dependent on Reynolds number.

Other separations such as "closed" type of separations involve regions with recirculating flow. This type of vortex flow is largely dominated by viscous effects, often occurs at off-design conditions and has associated with it a usually unsteady and not-well-ordered vortical flow structure. The latter type of vortical flow is outside the scope of the present paper, which is primarily concerned with controllable and exploitable types of vortex flow.

Two types of vortex flow may be distinguished, vortex flow where there is a weak and vortex flow where there is a strong interaction between the vortical flow structures and the flow over the surface of the configuration.

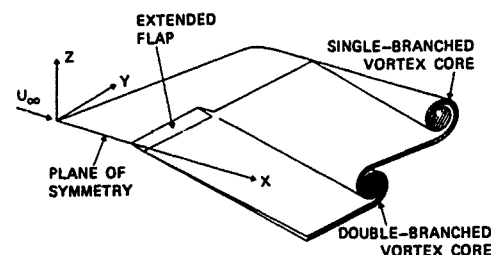


Fig. 1 Vortex wake; Weak-interaction vortex flow

The flow in the wake downstream of the trailing edge of a transport type of wing is usually a weak-interaction type of vortex flow. In this case the vorticity vector is in a direction approximately perpendicular to the separation line, i.e. in this case the trailing edge (Fig. 1). This means that the region with vortical flow is not in the close proximity of the configuration and that the influence of the vorticity on the velocity and pressure distribution on the surface of the configuration will be small. For weak-interaction vortex flow the lift increases approximately linearly with incidence, at least until viscous flow effects become significant.

Strong-interaction vortex flow can occur when the flow separates at the side edge of a low-aspect-ratio wing of low sweep or at the highly swept leading edge of a slender wing (Fig. 2) and also when the flow separates from the smooth surface of the forebody of a fighter aircraft or the elongated body of a missile configuration. In these cases the vorticity vector is approximately parallel to the separation line. A strong interaction also takes place when the vortex wake of one component of the configuration closely approaches other components of the aircraft. Examples are the interaction of the wake of the wing with the flow about the tail surfaces, the flow about a "close-coupled" canard-wing configuration and the flow about a strake-wing configuration. In the case of strong interaction the rotational flow region(s) are close to the surface of the configuration and often remain in the near proximity of the separation line. The local surface velocity and pressure distribution and the overall characteristics of



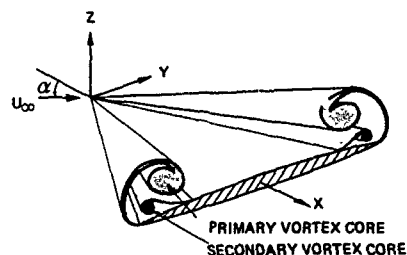


Fig. 2 Delta wing with leading-edge vortices; Strong-interaction vortex flow

the configuration are affected considerably, in some cases favourably in other cases unfavourably. For strong-interaction vortex flow typically the lift increases nonlinearly with incidence, up to higher incidences than without vortex flow. Ultimately a limit to the favourable effects is reached when large-scale vortex burst occurs above the configuration and eventually the steady and ordered vortex-flow pattern is destroyed.

Well-known are the favourable effects induced by the leading-edge vortices on highly swept wing and strake-wing configurations at high incidence, resulting in a substantial increase of their lift capability (e.g. Ref. 3). This is of great practical importance for configurations employing these wings with their, according to classical wing theory, relatively small lift slope ( $\partial C_L / \partial \alpha$ ). Other details of the vortex flow characteristics of fighter aircraft are still emerging, as demonstrated by Lamar et al. (Ref. 4), Campbell et al. (Ref. 5), Erickson et al. (Ref. 6) in several flow visualization investigations.

If the vortex lift capabilities of slender-wing, strake-wing, canard-wing and even more exotic configurations, that for their characteristics rely on ordered, controllable vortex flow, are to be fully utilized a detailed knowledge and adequate mathematical modeling of this type of flow is required.

It is in this area that computational methods can make a major contribution. The use of computational methods does not depend on the availability of experimental data and, at least in principle, it is possible to consider additional flight parameters and/or new configurations without much difficulty. This leads to a reduction of the number of candidate configurations to be considered for extensive wind-tunnel testing, or may even suggest improved designs. If the theoretical tools are capable of predicting not only the overall forces and moments, spanwise loadings, etc. but also the detailed surface velocity and pressure distribution they will be of great help to the aircraft designer. Furthermore the possibility to analyze in detail the complete flow field will help significantly in the analysis of the vortical flow structures.

It is the purpose of this paper to review computational methods for the simulation of the high-Reynolds-number flow about configurations featuring vortical flow structures. The characteristic feature of this type of flow is its strong nonlinearity. Due to the interaction of the vortical flow structures with the flow over the configuration the airloads vary nonlinearly with the direction of the free stream. A second nonlinear flow phenomenon appears as the free-stream Mach-number is increased from low-subsonic to transonic and supersonic, i.e. due to compressibility effects shock waves form. It is not uncommon that there is a strong coupling between the two types of nonlin-

earities (e.g. Refs. 7, 8 and 9). In the present paper methods that can be applied to cases where there is a coupled effect of the two nonlinearities will be considered. In this paper the emphasis will be on methods for the numerical simulation of inviscid flows. Methods for the numerical simulation of viscous flow applied to configurations with vortex flow are discussed in more detail in Paper 6 of this Symposium (Ref. 10).

Computational methods for unsteady flow or for the flow about oscillating configurations have not yet been developed to the same extent as the methods for steady flow. Although some of the steady flow methods discussed here have been extended (or can be applied) to the case of unsteady flow, here we will consider steady flow only.

Earlier reviews on vortical flow modeling and their computation can be found in Refs. 11, 12, 13, 14 and 15.

In the next sections we will start with a description of the main features of the physics of a number of vortex-dominated flows, followed by a discussion of the various mathematical models for the flow. In the subsequent sections examples are discussed of the application of these models to a number of, mostly generic, configurations. Ref. 10 provides examples of applications to more complete aircraft configurations.

## 2. DESCRIPTION OF ORDERED VORTEX FLOWS

In this section the physical features of a number of vortex flows are described. In all cases we will deal exclusively with flows that will be termed ordered vortex flows. Ordered vortex flows are flows with a topologically well-defined, steady and stable flow pattern, which is maintained within a sizable range of flight parameters (Mach number, incidence, sideslip, Reynolds number, etc.). This implies that most cases considered here are vortex flows associated with "controlled" flow separation, i.e. flow separating at "aerodynamically" sharp edges.

### 2.1. Vortex wakes - Weak interaction

At the trailing edge of a wing of finite span at incidence the velocity on the lower wing surface and the velocity on the upper wing surface differ in direction. Actually the static pressure should be continuous at the trailing edge, which for incompressible inviscid flow and for compressible inviscid flow without shocks results in the velocity vectors at the trailing edge being equal in magnitude but different in direction. This three-dimensional flow effect, caused by the air tending to flow around the wing tip from the lower ("pressure") side to the upper ("suction") side of the wing, results in the generation of vorticity and the formation of the vortex wake. In the vortex wake the vortex lines are approximately directed in free-stream direction, i.e. away from the trailing edge, and they are not located near the surface of the generating wing, resulting in a "weak interaction" between the vortex wake and the surface pressure distribution.

Since the Reynolds number is large, convection is much larger than diffusion and the vorticity remains within a thin free shear layer. Due to the velocity induced by the vorticity contained within the layer, the layer tends to roll up into vortex cores. This rolling-up may occur in various ways. The most well-known is the tip vortex: it is the single-branched vortex that forms at the free edge of a shear layer (Fig. 1). In case the trailing wake contains vorticity of both signs, vorticity of each sign will roll-up into separate vortices.

Examples of this are the wake of a highly swept wing and the wake of a wing with deployed part-span flaps. Such wakes contain both single-branched (at the edges) and double-branched vortex cores. Even if the shed vorticity is of one sign one or more double-branched vortices may be formed (see Fig. 1). Where these centers of roll-up develop is not always a priori evident. For a single straight trailing edge the local extrema of the trailing vorticity (inflection points in the spanwise loading) act often as a center of roll-up, but for more complex shapes the situation is less clear.

In downstream direction vorticity from the shear layer is continuously fed into the vortex core(s), resulting into a growth of the vortex core(s), both in strength and usually also in cross-sectional dimension. The stretching of the shear layer associated with the roll-up process counteracts the effect of viscous diffusion, so that quite often one observes that the shear layer remains relatively thin up to several spans downstream of the trailing edge.

Further downstream of the configuration the roll-up process will be completed, most of the vorticity residing within a limited number of vortex cores (e.g. the trailing vortex pair). The concentration of vorticity into these relatively compact regions of rotational flow is probably responsible for their surprisingly stable and persistent character. The strong and persistent trailing vortex system of large transport aircraft has proven to present a possible hazard for other air traffic, which has resulted in stringent rules imposed at present on air traffic involving large aircraft.

Still further downstream, cores with vorticity of the same or opposite sign, if close enough to each other, start to merge, accompanied by viscous diffusion and decay. Alternatively, complicated longitudinal instabilities may be triggered before the merging or decay process has started, resulting in a somewhat earlier break-up of the trailing vortex system.

In the present paper we will not consider the above type of weak-interaction vortex flow in much more detail but rather concentrate on strong-interaction vortex flow.

## 2.2. Delta-wing leading-edge vortex flow - Strong interaction

The low speed high-angle-of-attack flow about low-aspect-ratio highly swept wings with leading-edge vortex separation has been described extensively in the literature. Based primarily on experimental investigations by amongst others Legendre (Ref. 16), Earnshaw (Ref. 17), Wentz & McMahon (Ref. 18), Fink & Taylor (Ref. 19), Hummel (Ref. 20) and others the topology of the high-Reynolds number flow about these wings is well-established. At moderate to high angles of attack the flow separates at the leading edge, resulting in a free shear layer emanating from the edge (Fig. 2). Under influence of the vorticity contained within it, the free shear layer rolls up in a spiral fashion to form a relatively compact single-branched core with distributed vorticity, the so-called leading-edge vortex. The presence of this core in the proximity of the wing surface affects the pressure distribution on the wing to a large extent, the predominant effect being a low pressure region underneath the position of the vortex core. It is this suction peak that is mainly responsible for the increment in the lift due to the vortex flow, the so-called vortex lift. Depending on the leading-edge sweep a stable vortex-flow pattern can persist up to incidences as high as 25 to 35 deg.

It has also been observed in experiments that the adverse pressure gradient in the region just outboard of the lateral position of the center of the leading-edge vortex core causes a so-called secondary separation. The free shear layer emanating smoothly at the line of secondary separation rolls up in a vortex core also, its vorticity being of opposite sign compared to that of the vorticity within the leading-edge vortex core. The extent of the effect of secondary separation on the surface pressure distribution has been observed to depend strongly on whether the boundary layer is laminar or turbulent (Ref. 20). It appears that secondary separation effects are largest for the laminar case. Generally for both laminar and turbulent flow they become relatively more important for cases with narrower suction peaks, i.e. for wings at smaller incidences or for wings with lower leading-edge sweeps.

Viewed in downstream direction, the leading-edge vortex is continually being fed with vorticity generated at the leading edge which is transported through the free shear layer to the vortex core, so that the latter is increasing in strength as well as in cross-sectional dimension. Downstream of the trailing edge, i.e. in the wake, the free shear layer continues to feed vorticity into the leading-edge vortex core. In the wake the vorticity of sign opposite to that within the leading-edge vortex core, which is generated along almost all of the trailing edge between the plane of symmetry and the wing tip, starts to roll up in a double-branched, so-called trailing-edge vortex core. This two-vortex system, mushroom shaped, has first been observed experimentally by Maltby (Ref. 21) and more recently by Hummel (Ref. 20), Verhaagen (Refs. 22 and 23), Kjelgaard et al. (Ref. 24), Solignac et al. (Refs. 25, 26) and others. The latter few references also provide detailed surface and flow-field data.

A limit to the favourable effects induced by the vortex flow is reached when large-scale vortex breakdown occurs above the wing. Vortex breakdown manifests itself as an abrupt increase in the cross-sectional area of the vortex core, a decrease in the magnitude of axial and circumferential velocity components near the center of the vortex core and in an increase in the turbulence level in the vortex core. However, the global strong circulatory flow pattern does not disappear abruptly at the point where vortex breakdown occurs, it still persists. Upstream of this point the vortex is hardly affected. Vortex breakdown has first been identified in experimental investigations by e.g. Peckham (Refs. 27, 28), Elle (Ref. 29) and Lambourn & Bryer (Ref. 30) in the late fifties. The mechanism underlying vortex breakdown is still unclear, e.g. Hall (Ref. 31). However, vortex breakdown does appear to depend rather weakly on Reynolds number. The latter may suggest that in essence it is an inviscid flow phenomenon. It has been observed that with increasing angle of attack vortex breakdown progresses in upstream direction and that it occurs in regions where there is an increase in the pressure along the core, e.g. Erickson (Ref. 32). Part of the increase in core dimension may possibly be explained as the response of the inviscid outer part of the rotational core to a pressure rise. Further experimental investigations have been carried out by Kegelman & Roos (Refs. 33, 34 and 35) who measured at a low free-stream Mach number the flow field above 60- and 70-deg delta wings employing a Laser-Doppler-Velocimeter (LDV) and a 7-hole probe. In the case of vortex breakdown they found from the LDV measurements that on the vortex axis the axial component is about constant up to the breakdown location where the axial component of the velocity decreases abruptly and asymmetrically, but stays positive.

The probe measurement showed that in the vortex core the total-pressure loss is also about constant up to the breakdown location where it increases sharply. The portion of the vortex core with high losses in total pressure decreases up to the burst location, increases abruptly at the location of the burst and then starts to fill the entire vortex core. In this area the total-pressure losses start to decrease again. At the higher incidences vortex breakdown is often accompanied by an asymmetric flow pattern. For simple delta wings asymmetric flow patterns without vortex breakdown have been observed for leading-edge sweep angles in excess of 80 degrees.

Recently Gad-el-Hak & Blackwelder (Ref. 36), Payne et al. (Ref. 37) and Lowson (Ref. 38), have obtained results of low-speed experimental studies that indicate that the leading-edge shear layer is not really a smooth layer, but consists of a sequence of small vortices travelling along the layer towards the vortex core. Whether this thin shear-layer type of instability observed at low-Reynolds number and laminar flow conditions is a true characteristic of leading-edge vortex layers or possibly was induced by vibrations of the model or flow unsteadiness, is not yet completely clear. Recently Verhaagen & van Manen (Ref. 39) found that also at higher speeds the leading-edge shear layer might consist of small-scale vortical flow structures. It is not clear what effect the small-scale structures have on the time-averaged structure of the shear layer and on the formation of the vortex core. However, in the present study we will assume that the flow is steady and that free shear layers may be considered as steady regions with continuous rotational flow without small-scale sub-structures.

### 2.3 Strake-wing vortex flow - strong interaction

For wings with low or moderate leading-edge sweep favourable vortex flow effects can be invoked by adding a relatively small, highly swept leading-edge extension, commonly named "strake". The vortex flow above strake-wing configurations is more complex than the delta-wing vortex flow. Investigations by amongst others Wentz & McMahon (Ref. 18), Lamar & Luckring (Ref. 40), Brennenstuhl & Hummel (Refs. 41, 42) have provided valuable insight into the vortex layer structure above strake-wing configurations. Verhaagen (Ref. 23), employing a laser-light-sheet flow visualization technique, has acquired additional valuable topological information. Thompson (Ref. 43) has also provided such information from water-tunnel studies. From these investigations it follows that above a strake-wing configuration the (single-branched) leading-edge vortex, originating at the leading edge of the strake continues above the wing. The vortex modifies the wing flow field considerably inducing in addition to the favourable effects on the strake itself, favourable effects on the main wing as well. In case of sufficiently (depending on leading-edge sharpness, etc.) swept wing leading edges and at high angle of attack the flow separates also at the wing leading edge. This shear layer emanating from the wing leading edge constitutes the downstream continuation of the shear layer emanating from the strake leading edge (Fig. 3). In this single shear layer a double-branched vortex develops. This so-called wing vortex starts close to the kink in the leading edge and viewed in downstream direction, travels along the shear layer, looping around the (single-branched) strake vortex. At some point downstream of the kink the two cores (with distributed vorticity of the same sign) merge into one core. At smaller sweep angles and at lower incidences the flow does not separate at the wing leading edge. In this case the flow picture is not yet completely clear. Mostly it is assumed that the shear layer detaches (from the leading edge) at the kink

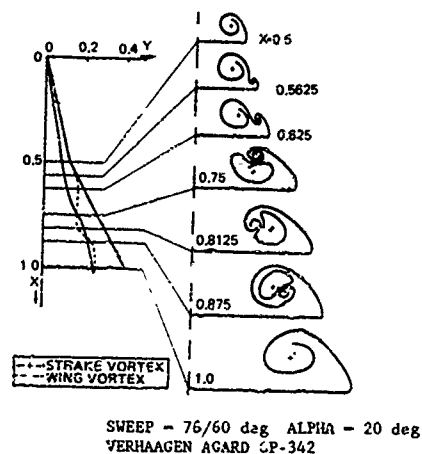


Fig. 3 Strake-wing configuration; Strong-interaction vortex flow

(as proposed by Küchemann, Ref. 1, p. 254). It might also be hypothesized that downstream of the kink the strake leading-edge shear layer continues as a shear layer that is attached to the wing upper surface, now emanating from some separation (?) line (see also the discussion in Smith, Ref. 44).

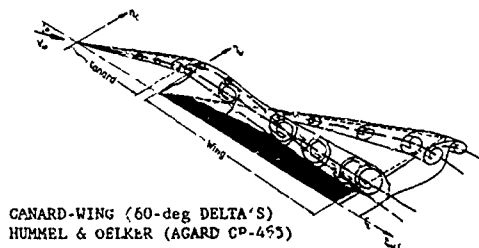
For the case of simple delta wings the angle of attack at which vortex breakdown reaches the trailing edge depends strongly on the sweep of the leading edge. For double-delta wings and strake-wing configurations such a simple correlation can not be obtained. Depending on the magnitude of the kink in the leading edge the wing vortex may burst long before the strake vortex breaks down.

### 2.4 Close-coupled canard-wing - Strong interaction

The close-coupled canard wing configuration is another example of a configuration exploiting vortex flow, which has been applied in advanced fighter concepts. The flow about a canard-wing combination is rather complex, especially in cases where both lifting surfaces have highly swept leading edges with leading-edge vortices. Fig. 4, from Hummel and Oelker (Refs. 45, 46), shows the flow structure at low speed and not too high incidence for a configuration consisting of two 60-deg swept delta wings. In the following a possible explanation is provided for the functioning of the canard-wing combination, this in terms of the modification of the flow structure about the wing in isolation at the same incidence.

On the part of the wing underneath the canard vortex wake the vortex wake from the canard causes a non-uniform downwash which will reduce the effective incidence on this part of the wing. This results in a delay of the formation of the wing leading-edge vortex and a reduction in the rate at which its strength builds up. This combined with the sidewash induced by the canard wake will cause the flow in the root-section region of the upper wing surface to be less susceptible to boundary-layer type of separations.

On the part of the wing outboard of the canard wake the effective incidence is increased by the induced upwash, but at the same time also the effective leading-edge sweep angle is increased by the induced sidewash. The rate at which vorticity is generated at the leading edge is increased by



CANARD-WING (60-deg DELTA'S)  
HUMMEL & OELIKER (AGARD CP-455)

Fig. 4 Canard-wing configuration; Strong-interaction vortex flow

the first but decreased by the second effect, the net influence of the two counteracting effects depending on the details of the lay-out of the configuration and the specific flow conditions.

Primarily because of the slower build-up of the strength of the wing leading-edge vortex along that part of the edge situated underneath the canard wake, the effect on wing vortex is that the wing vortex will be weaker when it encounters the adverse pressure gradient near the wing trailing edge. The result is that the occurrence of vortex breakdown above the wing, as well as stall, will be postponed to a higher incidence.

The wing induces an upwash on the canard thereby increasing its effective incidence. This implies that the effect on canard vortex is that the canard vortex will be stronger and consequently would experience vortex breakdown at a lower incidence than is the case for an isolated canard. However, in the case of a close-coupled canard, upon passing the canard trailing edge the canard vortex wake encounters a favourable pressure gradient due to the expansion of the flow over the forward part of the wing delaying and sometimes even re-structuring the canard vortex. At a given incidence, below the onset of vortex breakdown or boundary layer separations, the net effect of the interference is that the lift on the wing of the wing-canard configuration will be lower than for the case of the wing alone. It appears that usually this loss in lift is fully compensated by the lift on the canard, i.e. the lift of the wing-canard and the wing alone are almost equal. At the higher incidences the favourable effects of the interference prevail yielding an improved lift capability. In addition the canard also provides an additional trim and control-capability of the configuration. Ferretci & Salvatore (Ref. 47) provide detailed experimental information on the flow over a delta-canard configuration.

#### 2.5. Slender-body vortex flow - Strong interaction

The long slender nose of a modern fighter aircraft, operating at high incidence, experiences vortical type of flow separations on its lee side. The vortices resulting from these separations not only generate high local aerodynamic forces but also interfere with the flow about further downstream components of the aircraft such as wing and tail surfaces.

At low incidences the flow separates symmetrically, resulting in a symmetric flow pattern. At higher incidences the flow may still separate nearly symmetrically, or forced to do so, but the vortical flow about the forebody may become asymmetric and side forces of the same order of magnitude as the normal force may be induced. This results in large yawing moments which may be beyond the control capability of the aircraft. Furthermore the coupling between the forebody separated flow pattern and the motion of the aircraft can

cause self-induced coning, nose-slice motions while the interference with downstream lifting surface could cause dynamic stability problems such as excessive wing rock, e.g. Ericsson & Reding (Ref. 48).

The separation of the flow from the body depends on Mach number, incidence, on the state (laminar or turbulent) of the boundary layer and on Reynolds number. To illustrate this consider a slender body of revolution which is pitched from 0 to 90 deg angle of attack in subsonic flow. According to Chapman & Keener (Ref. 49) four flow categories can be distinguished (Fig. 5):

- (i) Fully attached flow;
- (ii) At moderate incidences (>10 deg) the cross-flow starts to separate over the rear end of the body at a point on its lee-ward side. This results in a symmetric lee-side vortex-flow pattern;
- (iii) At intermediate incidences (10< $\alpha$ <20 deg) the separation point gradually moves in upstream direction, while also the cross-flow separation point moves towards the shoulder of the body;
- (iv) At high angle of attack (>20 deg) the vortex flow pattern over the base region may become asymmetric, resulting in the body experiencing a side force and a yawing moment.

The factors that determine the onset of the asymmetric vortex flow pattern are angle of attack, Mach number, state of the boundary layer, Reynolds

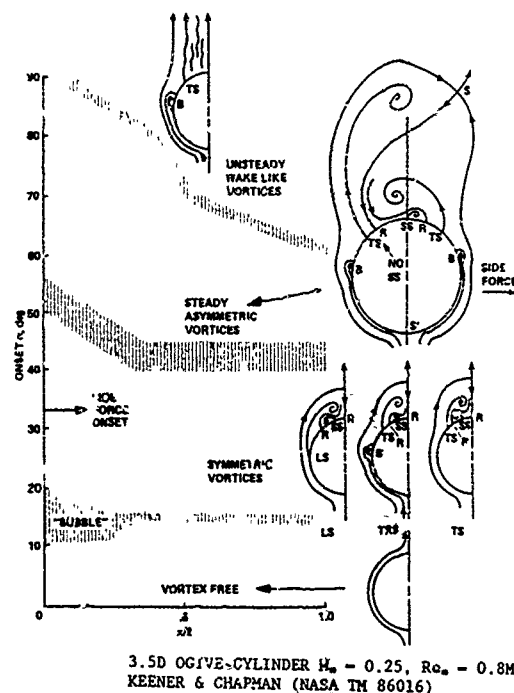


Fig. 5 Slender body; Strong interaction vortex flow

number, the shape of the body (forebody, after-body, cross-section). For instance increasing the Mach number at fixed incidence causes the separation lines on the body to move towards the windward side, which delays the onset of asymmetric flow. The critical Reynolds number boundary between laminar and transitional flow is almost independent of angle of attack, while the boundary between transitional and turbulent flow is affected by incidence, e.g. see Lamont (Ref. 50).

Other factors include nose bluntness (increasing the bluntness delays the onset of asymmetry). The reasons for an asymmetrical flow structure about a symmetrical body at symmetric free-stream conditions are:

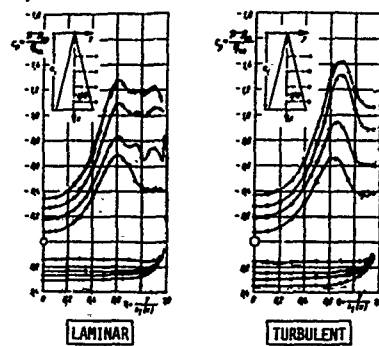
- asymmetries in the position of transition and separation lines, e.g. the ones on the starboard side starting closer to the nose than the ones on the port side, or differences in the location in the cross-flow plane;
- asymmetric solution for nominally symmetric conditions.

Especially the latter possibility of multiple (inviscid) solutions and their stability is an interesting feature of the nonlinear flow problem at hand.

## 2.6. Reynolds number effects

It appears that for a number of above discussed types of well-developed high-Reynolds-number vortex flows the influence of the Reynolds number on the flow structure is relatively small. For instance for the case of a sharp-edged delta wing it has been observed that for angles of attack not too close to the angle of attack for which the flow is still attached, the flow pattern depends only weakly on Reynolds number. The location of the secondary separation, just outboard of the suction peak induced by the leading-edge vortex, depends primarily on the state (laminar or turbulent) of the boundary layer on the upper surface of the wing. The latter has been demonstrated by for instance Hummel (Ref. 20) for a 76-deg swept delta wing at 20.5 deg incidence. In Fig. 6 Hummel's result is reproduced. It shows the surface pressure distribution at low speed for a Reynolds number of 0.9M for laminar and for turbulent flow. For laminar flow an early separation occurs at about 65% local semi-span, while for turbulent flow separation takes place much more outboard, i.e. at about 85% local semi-span, resulting in a much more pronounced leading-edge vortex induced suction peak.

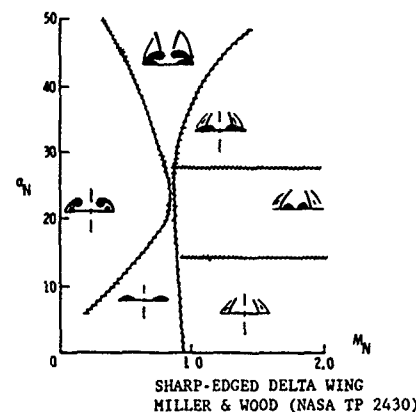
For delta-like wings with rounded leading edges, the flow does separate all along the leading edge merely when the incidence exceeds a certain threshold value.



76-deg DELTA WING ALPHA = 20.5 deg  
HUMMEL (AGARD CP-247)

Fig. 6 Sharp-edged delta wing; Effect of laminar or turbulent state of the boundary layer

hold value. For lower angles of attack the flow separates along part of the edge only, usually termed part-span leading-edge separation. At angles of attack just above the attached flow condition the flow separates close to the wing tip only. With increasing incidence the point on the leading edge where the primary separation and the formation of the leading-edge vortex starts moves in upstream direction from the wing tip towards the apex. The rate at which this process of part-span primary separation progresses does depend on the leading-edge radius and on Reynolds number.



SHARP-EDGED DELTA WING  
MILLER & WOOD (NASA TP 2430)  
Fig. 7 Sharp-edged delta wing; Effect of Mach number

## 2.7. Mach number effects

For thin slender wings at moderate incidence the influence of the Mach number on the characteristic features of the flow is small as long as  $M_\infty \cos \alpha$ , i.e. the Mach number normal to the leading edge, is less than about 0.7 and the incidence (in a plane normal to the leading edge) is not too high, see Fig. 7 taken from Miller & Wood (Ref. 8). At a given incidence for higher Mach numbers, or at a given Mach number higher incidences or for fixed Mach number and incidence for thicker wings, or for less slender wings, etc., nonlinear compressibility effects can become of dominating importance. This results in a wealth of possible flow patterns involving primary and secondary vortex cores, ("cross-flow" and "rear") shocks on the surface as well as in the flow field, regions with distributed vorticity produced downstream of shocks, shock-induced rather than pressure-gradient induced smooth-surface secondary separation, and all their mutual interactions, sometimes resulting in an abrupt rather than a gradually progressing vortex breakdown. Some of these flow patterns are discussed by Szodrach & Ganzer (Ref. 51), Miller & Wood (Ref. 8), Wood et al. (Ref. 52), Vorropoulos & Wendt (Ref. 9), Houtman & Bannink (Ref. 53), etc.

Schrader et al. (Ref. 54) report extensively on the influence of Mach and Reynolds number on delta-wing vortex flow. Ashill et al. (Ref. 55) report on a detailed investigation into the flow on swept wings at moderate to high incidences in transonic and supersonic flow.

An illustration of the effect of compressibility on primary separation is given in Fig. 8, taken from Boersen & Elsenaar (Ref. 56). It compares for a 65-deg cropped delta wing spanwise sections of the surface pressure distribution obtained for the case of a sharp with those obtained for the case of a round leading edge, and that for one subsonic ( $M_\infty = 0.4$ ,  $\alpha = 10$  deg,  $Re_\infty = 9M$ ) and one transonic ( $M_\infty = 0.85$ ,  $\alpha = 10$  deg,  $Re_\infty = 9M$ ) flow condition. For the sharp-edged wing the flow separates all along the leading edge, for both the subsonic and the transonic case. For the round-edged configuration the situation is rather different. Here the primary separation takes place along part of the leading edge, for the subsonic Mach number the flow remains attached along most of the leading edge, while for the transonic Mach number the flow is separated (shock-induced?) along most of the edge. Apparently the effect of the shape of the leading edge on the flow pattern decreases with increasing Mach number.

It must be realized that vortex flow with nonlinear compressibility effects are of utmost importance for the aerodynamics of aircraft capable of transonic maneuvering and supersonic speeds.

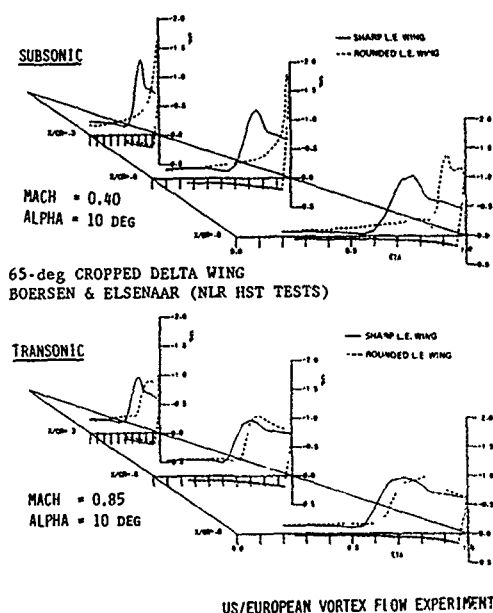


Fig. 8 Round- and sharp-edged 65-deg cropped delta wing; effect of compressibility

### 3. MATHEMATICAL MODELS

#### 3.1. Navier-Stokes equations

In aerodynamics the Navier-Stokes equations model essentially all relevant flow details such as separation and associated generation of vorticity, transport and stretching of vorticity, shock waves, transition from laminar to turbulent flow, etc.. For most applications the equations are solved on a body-fitted computational grid. If  $\bar{x} = \bar{x}(\xi)$  denotes the coordinate mapping, the equations for the conservation of mass, the three components of momentum and the total energy per unit volume of the continuous flow model of a gas in thermodynamic equilibrium, in the absence of body forces and external heat sources, generally designated as the Navier-Stokes equations, can be expressed as:

$$\frac{\partial \bar{U}}{\partial \tau} + \frac{\partial}{\partial \xi} (\bar{F} - \bar{F}_v) + \frac{\partial}{\partial \eta} (\bar{G} - \bar{G}_v) + \frac{\partial}{\partial \zeta} (\bar{H} - \bar{H}_v) = 0 \quad (1a)$$

In Eq. (1a)  $\bar{U}$  is the column vector containing the flow variables, expressed as:

$$\bar{U} = [\rho, \rho u, \rho v, \rho w, E]^T / J \quad (1b)$$

where  $J$  is the Jacobian  $J = \partial(\xi, \eta, \zeta) / \partial(x, y, z)$ . In Eq. (1a)  $\bar{F}$ ,  $\bar{G}$ , and  $\bar{H}$  are the components in the three coordinate directions of the inviscid flux vector, i.e.

$$\bar{F} = (\xi_x F + \xi_y G + \xi_z H) / J \quad (1c)$$

$$\bar{G} = (\eta_x F + \eta_y G + \eta_z H) / J \quad (1d)$$

$$\bar{H} = (\zeta_x F + \zeta_y G + \zeta_z H) / J \quad (1e)$$

while  $\bar{F}_v$ ,  $\bar{G}_v$ , and  $\bar{H}_v$  are the components of the viscous flux vector, i.e.

$$\bar{F}_v = (\xi_x F_v + \xi_y G_v + \xi_z H_v) / J \quad (1f)$$

$$\bar{G}_v = (\eta_x F_v + \eta_y G_v + \eta_z H_v) / J \quad (1g)$$

$$\bar{H}_v = (\zeta_x F_v + \zeta_y G_v + \zeta_z H_v) / J \quad (1h)$$

The components of the inviscid flux vector in terms of the Cartesian coordinate system follow from:

$$\bar{F} = [\rho u, \rho u^2 + p, \rho uv, \rho uw, (E + p)u]^T \quad (1i)$$

$$\bar{G} = [\rho v, \rho uv, \rho v^2 + p, \rho vw, (E + p)v]^T \quad (1j)$$

$$\bar{H} = [\rho w, \rho uw, \rho vw, \rho w^2 + p, (E + p)w]^T \quad (1k)$$

while the components of the viscous flux vector are:

$$F_v = [0, \tau_{xx}, \tau_{xy}, \tau_{xz}, u\tau_{xx} + v\tau_{xy} + w\tau_{xz} - Q_x]^T \quad (1l)$$

$$G_v = [0, \tau_{xy}, \tau_{yy}, \tau_{yz}, u\tau_{xy} + v\tau_{yy} + w\tau_{yz} - Q_y]^T \quad (1m)$$

$$H_v = [0, \tau_{xz}, \tau_{yz}, \tau_{zz}, u\tau_{xz} + v\tau_{yz} + w\tau_{zz} - Q_z]^T \quad (1n)$$

In above expressions  $\rho$  denotes the mass density,  $p$  the static pressure,  $\bar{u} = (u, v, w)^T$  the velocity vector,  $E = \rho(e + (u^2 + v^2 + w^2)/2)$  the total energy per unit volume,  $\bar{\tau}$  the shear stress tensor and  $\bar{Q} = (Q_x, Q_y, Q_z)^T$  the heat flux vector. The stress tensor  $\bar{\tau}$  is related to the rate of strain through Newton's law, while the heat-flux vector  $\bar{Q}$  is related to gradient of the temperature through Fourier's law, i.e.

$$\bar{\tau} = \mu(\nabla \bar{u} + (\nabla \bar{u})^T) + \lambda(\nabla \bar{u})^T \quad (1o)$$

$$\bar{Q} = -k \nabla T \quad (1p)$$

respectively. Here  $\mu$  is the molecular viscosity coefficient,  $\lambda$  is the bulk viscosity coefficient and  $k$  is the molecular thermal conductivity coefficient.

The above system of equations is supplemented by the equations of state. For the present type of flows the gas may be assumed to be an ideal perfect gas for which:

$$p = \rho RT \quad (1q)$$

$$e = c_v T \quad (1r)$$

where  $R = c_p - c_v$ . Here  $c_p$  and  $c_v$  are the specific heats which may be assumed to be constant. The bulk viscosity  $\lambda$  is related to the molecular viscosity  $\mu$  through Stoke's hypothesis, i.e.  $\lambda = -2\mu/3$ . The thermal conductivity  $k$  is also related to the molecular viscosity  $\mu$ , via the assumption of constant Prandtl number  $Pr$ , i.e.  $k = \mu c_p / Pr$ . For air the Prandtl number is  $Pr = 0.72$ . The molecular viscosity itself is a function of the temperature  $T$  only, as given by Sutherland's law (Ref. 57).

The boundary conditions are that at solid surfaces the velocity vanishes (no slip) and that solid surfaces are adiabatic or at a given constant temperature. At the far field distinction is to be made between inflow and outflow boundaries. For a well-posed problem five conditions are required at inflow and four at outflow boundaries.

#### 3.2. Reynolds-averaged Navier-Stokes equations

The Navier-Stokes equations as presented in Eq. (1) form the basis of methods for laminar flow. However, at Reynolds numbers typical of full-scale flight the flow becomes turbulent. The disparity of scales in a turbulent flow is very large and at the moment a direct numerical simulation of turbulent flows is quite impractical. The approach to overcome this difficulty is to split the flow quantities into a macroscopic part and a turbulent fluctuating part and use a statistical averaging procedure. Following Rubesin & Rose (Ref. 58) the density  $\rho$ , pressure  $p$ , shear stress tensor  $\bar{\tau}$  and heat flux vector  $\bar{Q}$  are decomposed in a time-averaged mean and a fluctuating part, e.g.  $\rho = \langle \rho \rangle + \rho'$ , the other flow quantities in a mass-weighted time-averaged and a fluctuating part, e.g.  $\bar{u} = \langle \bar{u} \rangle + \bar{u}'$ . Substitution into Eq. (1), followed by taking the time-average of the equations and neglecting some of the second-order correlations, yields the so-called Reynolds-averaged Navier-Stokes equations. This set of equations, for the time- or mass-weighted time-averaged values of the flow variables has exactly the same form as given in Eq. (1), but with the definition of the viscous stress tensor  $\bar{\tau}$  and the one of the heat-flux vector  $\bar{Q}$ , as given in Eqs. (1o) and (1p) respectively, replaced by:



$$\bar{T} = \mu(\bar{u} + (\bar{v}u)^2) + \lambda(\bar{v}u)I - \langle \rho u^2 u \rangle \quad (2a)$$

$$\bar{Q} = -k\bar{v}T + \langle \rho e^2 u \rangle \quad (2b)$$

where the flow quantities now denote the corresponding time-averaged quantities. While the full Navier-Stokes equations in general do not allow a steady-state solution the Reynolds-averaged equations do allow a steady state solution. Our interest is in steady solutions, but since a number of computational methods attain steady state as the limit for large time in a pseudo time-dependent approach, the time-dependence has been retained.

The Reynolds-averaged Navier-Stokes equations require a turbulence model for closure, i.e. one has to define appropriate constitutive relations for the "Reynolds stress-tensor"  $\langle \rho u^2 u \rangle$  and the "turbulent heat flux vector"  $\langle \rho e^2 u \rangle$ .

### 3.3. Turbulence modeling

A universally satisfactory turbulence model has not yet been formulated. It appears that for engineering applications a turbulence model, in which the Reynolds stress tensor and heat flux vector are expressed in terms of just mean-flow quantities rather than found from a set of additional transport equations for these quantities, derived from the equations for the fluctuations, performs as good as any other more sophisticated model, e.g. Marvin (Ref. 59). In the simpler of these models the Boussinesq assumption of effectively isotropic eddy viscosity and local equilibrium between production and dissipation of turbulent energy is made. This results into the so-called eddy-viscosity model in which the Reynolds-stress tensor and heat-flux vector are assumed to be proportional to the rate of strain and the temperature gradient, respectively, both of the mean-flow component. This leads to the situation in which  $\bar{T}$  and  $\bar{Q}$ , defined in Eqs. (2a) and (2b), can be expressed in the same form as is the case for laminar flow, i.e. as:

$$\bar{T} = (\mu + \mu_t)(\bar{u} + (\bar{v}u)^2) + (\lambda + \lambda_t)(\bar{v}u)I \quad (3a)$$

$$\bar{Q} = -(k + k_t)\bar{v}T \quad (3b)$$

In Eq. (3) the "turbulent diffusivities"  $\mu_t$  and  $\lambda_t$  are related to a characteristic length scale  $L$  and a characteristic velocity scale  $V$ , e.g.  $\mu_t = \rho LV$ . In the most simple, zero-equation, model  $L$  and  $V$  are correlated to the mean flow properties through algebraic laws. In more sophisticated eddy-viscosity models  $L$  and  $V$  are derived from quantities such as the turbulent kinetic energy and turbulent dissipation through partial differential equations. The algebraic model used most often in three-dimensional aerodynamics is the one due to Baldwin & Lomax (Ref. 60), which itself is based on the two-layer model reported by Cebeci et al. (Ref. 61). In the model different definitions of  $L$  and  $V$  are taken in the inner and outer part of the viscous shear layer. The "turbulent thermal conductivity"  $k_t$  follows, analogous to the molecular conductivity, from the assumption that the "turbulent Prandtl number"  $Pr_t$  is constant ( $\approx 0.9$ ), i.e.  $k_t = \mu_t c_p / Pr_t$ . The Baldwin & Lomax model is an equilibrium model that does not include any turbulence history effects, it depends on the local flow profile only and its basis is two-dimensional boundary-layer flow. However, Degani & Schiff (Refs. 62, 63) have showed that even in cases of massive cross-flow separation reasonable results can be obtained with a slightly modified model. They argue that the vortical lee-side flow can be viewed as consisting of attached boundary layers, primarily directed in streamwise direction, and a basically inviscid free shear layer which convects the vorticity generated within the

wall layers. In that case the length scale is based on the thickness of the wall layers, expressed in terms of the location of the maximum of some function involving the vorticity in the wall layer. If there is large-scale separation in streamwise direction the simple algebraic models become inadequate. Equilibrium models such as the above ones are not suited for separated flows for which the diffusion and convection of the turbulence are no longer negligible and introduce some imbalance between the production and dissipation of the turbulence. While retaining the eddy viscosity assumption these non-equilibrium effects can be taken into account by two-equation models e.g. the  $k - \epsilon$  model. However, despite its universality the two-equation models do not improve significantly and consistently the correlation with experimental data for separated flows.

The modeling of transition from laminar to turbulent flow or vice versa, which has a significant effect on the secondary separation on slender-wing configurations as well as the primary separation on slender bodies, is an even greater problem. At present it appears that most numerical simulations are carried out for all-laminar flow, all-turbulent flow or mixed flow with the transition locations specified empirically. It must be realized that in reality transition from laminar to turbulent flow does not occur at one discrete point but rather in a zone which length depends on amongst others the Reynolds number. However, for the high Reynolds numbers of interest here transition can be assumed to take place at a single curve on the surface. The location of the curve depends, in general, on Reynolds and Mach number, pressure gradient and streamline curvature (wing sweep), wall temperature, surface roughness, external disturbances, etc. A recent review on laminar-turbulent transition, the physics of turbulence, the modeling of turbulence, etc. has been presented by Landahl (Ref. 64).

### 3.4. Thin-layer Navier-Stokes equations

In cases where there is no large-scale streamwise flow separation the viscous terms in all directions but the one normal to the solid boundaries may be neglected. This results into the mathematical flow model governed by the "thin-layer Navier-Stokes equations" (TLNS). For a body-fitted coordinate system  $(\xi, \eta, \zeta)$  with  $\zeta$  approximately normal to the body surface the governing equation becomes, see Eq. (1a):

$$\frac{\partial \bar{U}}{\partial \xi} + \frac{\partial \bar{F}}{\partial \xi} + \frac{\partial \bar{G}}{\partial \eta} + \frac{\partial}{\partial \zeta}(\bar{H} - \bar{H}_v) = 0 \quad (4)$$

In the thin-layer assumption the viscous terms are simplified by assuming that all derivatives except those in the normal direction are small and/or not adequately resolvable on the grid used and thus dropped. So also in  $H_v$  only derivatives in  $\zeta$ -direction are retained. This mathematical model requires a fine grid in the direction normal to the body and that close to the body only, while in the directions along the body surface a much coarser mesh suffices. It will be clear that in the thin-layer approximation cases with strong adverse pressure gradients in streamwise direction cannot be handled.

### 3.5. Euler equations

For most of the high-Reynolds number flows of interest in vortex-flow aerodynamics viscous effects are confined to thin boundary layers, thin wakes and centers of vortex cores, i.e. the global flow features depend only weakly on Reynolds number. Neglecting in Eq. (1) the viscous and heat conduction terms altogether leads to the Euler equations for inviscid flow. This flow model allows the occurrence of shock waves, the generation of vorticity through shocks of varying strength as well as

through intersecting shocks and finally the convection and stretching of vorticity. Vorticity may occur in the form of distributed vorticity as well as in the form of vorticity concentrated in thin shear layers or vortex filaments. On a local scale, specifically at points where the flow separates from the surface, vorticity is generated and shed into the flow field, a model (Kutta-type of conditions) for viscous-flow dominated features will be required. The Euler equations follow from Eq. (1) as

$$\frac{\partial \bar{u}}{\partial t} + \frac{\partial \bar{F}}{\partial \xi} + \frac{\partial \bar{G}}{\partial \eta} + \frac{\partial \bar{H}}{\partial \zeta} = 0 \quad (5)$$

in differential form. The mathematical model based on the Euler equations requires explicitly the condition that the entropy is allowed to increase only, this to avoid the physically unrealistic expansion shocks. In the subsonic and transonic flow regime steady-state solutions are often obtained in a time-asymptotic fashion. The system of five equations, Eq. (5), is hyperbolic and the five eigenvalues corresponding to the characteristic velocities in each space direction, of the three Jacobian matrices are real. For subsonic flow four eigenvalues are positive, one is negative. Thus at the inflow boundary four conditions are specified from free stream quantities, one is obtained by extrapolation from the interior. At the outflow boundary one condition needs to be specified and the other four involve extrapolated quantities. At the solid surface the normal component of the velocity becomes zero ( $\bar{u} \cdot \bar{n} = 0$ ), but the tangential velocity is nonzero.

For the case of steady supersonic flow, it is often much more economical to solve the steady-flow equations using a space-marching technique. In this approach the solution is obtained by marching the (conical) solution obtained in the nose region to subsequent stations along the length of the configuration.

### 3.6. Potential flow

If there are no strong shocks and if the vorticity is confined to compact regions, the flow may be modeled as potential flow with embedded free vortex sheets and vortex cores (filaments). The governing equation is obtained from the Euler equations upon introduction of the velocity potential  $\Phi$  such that  $\bar{u} = \nabla \Phi$ , resulting in

$$\nabla \cdot (\rho \nabla \Phi) = 0 \quad (6a)$$

$$\rho = \rho_\infty \left[ 1 + \frac{\gamma-1}{2} M_\infty^2 (1 - |\nabla \Phi|^2 / U_\infty^2) \right]^{1/(\gamma-1)} \quad (6b)$$

The pressure coefficient then follows from the isentropic relation

$$C_p = (p - p_\infty) / \frac{1}{2} \rho_\infty U_\infty^2 = 2 \left[ \left( \frac{\rho}{\rho_\infty} \right)^{\gamma-1} - 1 \right] / \gamma M_\infty^2 \quad (6c)$$

The governing, so-called full-potential, equation is nonlinear, allows the occurrence of weak (isentropic) shocks, but requires that vortical flow regions are "fitted" explicitly into the solution. The latter in contrast with the above more complete models where they are "captured" implicitly as integral part of the solution. The boundary conditions are along with the usual far-field condition that the solid surfaces are stream surfaces ( $\bar{u} \cdot \bar{n} = 0$ ), that the vortex sheets are stream surfaces across which the static pressure is continuous while for vortex filaments various conditions are possible.

In the potential-flow formulation the problem reduces to solving for the velocity potential together with the position and strength of the vortex sheets and cores (wakes). The treatment of the wakes, free-floating in a fixed spatial grid around the configuration, poses considerable problems for computational methods solving the full-potential equation. Usually the position of the wakes are fixed and wake roll-up is not accounted for, limiting the application to low angles of attack.

In case shock waves are absent altogether and the perturbation to the free stream due to the presence of the configuration is small, the full-potential equation can be linearized, which leads to the Prandtl-Glauert equation. Writing the velocity as the sum of the free-stream and the gradient of the perturbation potential, i.e.  $\bar{u} = \bar{U}_\infty + \nabla \phi$ , the full-potential equation Eq. (6a) becomes

$$(1 - M_\infty^2) \frac{\partial^2 \phi}{\partial x^2} + \frac{\partial^2 \phi}{\partial y^2} + \frac{\partial^2 \phi}{\partial z^2} = 0 \quad (7)$$

For subsonic flow ( $M_\infty < 1$ ) the equation is elliptic, while for supersonic flow the equation is hyperbolic. The criterion on the magnitude of the allowable perturbations due to the presence of the geometry depends on the free-stream Mach number, the criterion being least strict for the lower Mach numbers. For incompressible flow ( $M_\infty = 0$ ) the small-perturbation assumption is no longer needed: both the Prandtl-Glauert and the full-potential equation then reduce to Laplace's equation.

The velocity potential and the position of the wakes can be solved for by using the boundary-integral type of approach. In this approach the velocity field can completely be expressed in terms of singularity distributions on the surface of the configuration and the wakes, hence a spatial grid is not required. The computational methods based on this formulation, the so-called panel methods, have proven to be a very effective tool for computing both the global and the local aerodynamic characteristics of the most complex aircraft configurations.

The main problem associated with the panel-method type of approach, aside from those associated with its relatively poor physical flow model for flows involving shocks, is the computation of the position of the rolling-up wakes through satisfying the nonlinear boundary conditions on the free vortex sheets. At lower incidences a rigid wake assumption often suffices, rendering the problem linear, but at the higher incidences one has to account more accurately for the interaction of the wakes with the flow on the nearby surfaces.

## 4. POTENTIAL-FLOW METHODS

### 4.1. Polhamus' suction analogy

The most widely used engineering method for predicting the characteristics of configurations employing leading-edge vortex flow is the so-called "Polhamus' suction analogy" (Polhamus, Ref. 65). The analogy is based on the empirical conjecture that the vortex lift effect can be predicted utilizing the edge suction forces of the attached-flow solution. In classical lifting-surface potential-flow theory the velocity tends to infinity at all edges except the (trailing) edges where the Kutta condition is imposed, resulting in a finite suction force at leading and side edges. This force acts normal to the leading edge and lies in the plane of the wing, (partly) counteracting the drag force. The magnitude of the suction force depends on the amplitude of the singularity in the loading at the edge. On a three-dimensional wing the normal force, found from integration of the distribution of the pressure difference across the lifting surface combines with the suction force to yield the correct lift, side force and induced drag of the wing. When the flow separates at the edge the Kutta condition is satisfied and the suction force is lost. In the "suction analogy" the



suction force is "recovered" as a force rotated through 90 deg to act in the direction normal to the wing surface. This implies that the aerodynamic forces and moments on configurations with vortex flow can be computed by utilizing any conventional linear attached flow method with rigid wakes attached to trailing edges, without the necessity of having to solve a complex nonlinear problem. The magnitude of the suction force then follows from the behaviour of the loading near the edge where in reality the flow is known to separate. The suction analogy has been applied to a variety of cases, both in subsonic and in supersonic flow. In general the correlation of computed forces, and to a lesser extent moments, with experimental data is surprisingly good. Thus far no theoretical explanation appears to have been given for the success of the suction analogy. However, the major drawback of the methods that use the suction analogy is that the pressure and velocity distribution cannot be predicted by the method and that more complex situations, e.g. the interaction of a canard vortex with a wing, strake-wing vortex flow, vortex breakdown, etc. require the development of new empirical concepts. With a vortex-lattice method as attached-flow solver Lamar and his co-workers (e.g. Lamar, Ref. 66) have developed the method towards a very useful engineering tool both for analysis and for design of quite general configurations, including strake-wing configurations.

#### 4.2. Fitted vortex-flow methods

The surface pressure distribution and the detailed flow field can be provided by methods based on the potential flow model with embedded ("fitted") vortex sheets and cores. Although some success has been booked incorporating free vortex sheets into the full-potential formulation (e.g. Refs. 67, 68, 69), here we will consider linearized potential flow, specifically incompressible flow, only (Fig. 9).

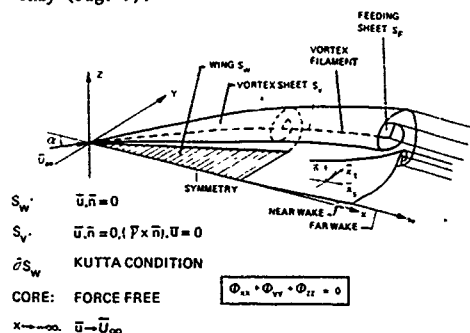


Fig. 9 Potential flow model of three-dimensional flow about slender wing

##### 4.2.1. Slender-body approximation

Configurations that develop leading-edge vortex flow are in general slender, in the sense that in the streamwise direction variations in geometry and in the flow quantities are much smaller than those in the cross-flow plane. In that case the full three-dimensional problem can be reduced to a sequence of quasi-two-dimensional problems in successive cross-flow planes. Within this framework the streamwise component of the perturbation velocity, required to compute the pressure, follows directly from the cross-flow plane solution. If in addition the geometry is conical, e.g. a delta wing, or a cone, the potential-flow solution is conical as well and only one cross-flow plane problem needs to be considered. The methods employing the slender-body approximation to conical configurations were the first to be applied with success to the computation of the flow about wings with

leading-edge vortex flow. In the early fifties, Legendre (Ref. 16) and Brown & Michael (Ref. 70), devised an approximate model in this framework in which all vorticity generated at the leading edge is assumed to be concentrated in one isolated vortex. The strength of the vortex, i.e. the total circulation of the vortex system is determined by applying the Kutta condition at the leading edge. In order to allow for the streamwise (here linear) growth in the strength of the vortex, the vortex is connected to the leading edge by a so-called "feeding sheet". This feeding sheet carries the cross-flow-plane component of the vorticity and to first approximation contributes to the streamwise velocity component only. The condition imposed on the isolated vortex/feeding sheet combination is that it sustains no net force.

The flow problem (for zero side-slip) is solved employing a conformal-mapping technique. This reduces the problem to having to determine the solution of a system of just three nonlinear algebraic equations for the strength and position of the vortex.

Later Mangler & Smith (Ref. 71) and Smith (Ref. 72) improved upon this early model by including a representation for the not rolled-up part of the leading-edge vortex sheet. This vortex sheet of finite extent, discretized by piecewise continuous constant-vorticity elements (panels), has a large effect on the Kutta condition. The model for the vortex core, i.e. the tightly rolled-up part of the vortex sheet (of infinite length), is Brown & Michael's model described above, but with the feeding sheet now connecting the vortex with the end of the vortex sheet. This vortex-core model provides a good description for the flow field away from the discrete vortex and its associated feeding sheet. In Smith's method the stream-surface boundary condition on the wing is satisfied using conformal mapping, while the vortex-sheet boundary conditions that a vortex sheet is a stream surface and that the pressure is continuous across it are imposed at discrete points (collocation). This results with the no-force condition on the vortex/feeding-sheet combination in a system of nonlinear algebraic equations for the strength and position of the vortex-sheet elements and of the vortex. Results of Smith's vortex sheet method compare quite satisfactorily with experimental (turbulent) flow data.

The above slender-body-approximation conical-flow methods have also been extended to the case of slender wings with curved leading edges or chordwise camber. Clark (Ref. 73) has extended Smith's method to non-conical planforms. He found that the method was unable to deal with cases where second centers of roll-up, i.e. double-branched vortices, began to develop. This is partly due to the difficulty of representing the details of tightly rolled-up parts of free vortex sheets using a continuous panel discretization. Discretizing vortex sheets by discrete vortices has a long history, primarily because of its simplicity and flexibility. Sacks et al. (Ref. 74) treated ring-body combinations employing a discrete-vortex representation for the leading-edge vortex sheet. Although the vortex sheet appears chaotic the predicted forces compare reasonably well with experimental data. Xieyuan (Ref. 75) applied Sacks' method to simulate the flow about straked (double-delta) wings, also showing disorderly arrangements of the discrete vortices, though the position of clusters of vortices agreed with the experimentally found positions of the strake and wing vortex. Ref. 76 gives more results of this method. In the discrete-vortex method several techniques can be used to delay the onset of chaos, e.g. rediscritization, amalgamation, re-discretization using sub-vortices, etc. Also the way in which the strength and position of

the vortex closest to the leading edge are determined can be improved upon. Peace (Ref. 77) developed an improved discrete-vortex method employing among other things the sub-vortex technique and a new vortex shedding model. The method has been applied to various slender wings, including strake-wing configurations; for the latter both the strake and the double-branched wing vortex were predicted. This demonstrated that discrete-vortex methods, though prone to numerical problems requiring careful tuning of the discretization, have the flexibility to cope with the vortex flow about more complex geometries, see also Maskev & Rao (Ref. 78), Nathman (Ref. 79), etc. A recent paper on application of a discrete-vortex method in the framework of a slender-body approximation is the one by Mendenhall and Lesieur (Ref. 80). The method is applied to a flattened fighter forebody with a sharp-edgedchine. The separation of the flow is fixed at the edge and the generation of vortex sheet at the edge is well-predicted. However, probably because the upstream influence of the wing is not accounted for in the method the correlation of computed and measured surface pressures is unsatisfactory. Further interesting applications of the slender-body discrete-vortex method are given by Cheng et al. (Ref. 81) who treat delta wings with leading-edge flaps, which for extreme flap deflections feature additional vortex systems, and compare predictions with data obtained from extensive flow visualization investigations.

In Ref. 82 a description is given of a slender-body-approximation method (VORSEBA), developed at NLR, in which the vortex sheet is discretized more accurately using curved panels and a model for single- and double-branched vortex cores. In the VORSEBA method the problem is solved in physical space rather than in some transformed space, which requires a discretization of the full cross-section of the configuration, but facilitates a more convenient application to configurations with complicated cross-sections. Some applications of this method are described later on in the present paper.

In the slender-body approximation applied to subsonic flow the upstream influence of the trailing edge, as well as the singularity at the apex, is not accounted for. Furthermore discontinuities such as occur at the kink in the leading edge of straked wings are not allowed in the strict sense of the slender-body approximation. Furthermore, it must be realized that in subsonic flow a conical geometry cannot invoke a conical velocity field and pressure distribution, although geometrically the streamline pattern, vortex flow topology, etc., observed in experiments on slender (nearly) conical configurations in subsonic flow have a strikingly conical appearance.

#### 4.2.2. Methods for three-dimensional flow

In the framework of three-dimensional flow the equivalent of the discrete-vortex method is the non-linear vortex-lattice method, which has attracted considerable attention, e.g. Belotserkovskii (Ref. 83), Reibach (Ref. 84), Kandil et al. (Ref. 85), Kim & Mook (Ref. 86), Rusak et al. (Ref. 87). In the non-linear vortex-lattice method the free vortex sheets from the leading and trailing edges are represented by discrete vortex filaments. These trailing line vortices are relaxed until their direction corresponds with the local flow direction. In regions of large variations, as usually occur in cases with vortex flow from leading and side edges, considerable numerical problems are encountered which become worse when more vortices are employed. Recent papers on the application of a vortex-lattice method to strake-delta and close-coupled wing-canard configurations have been presented by Rom (Ref. 88) and Gordon (Ref. 89). It is shown that the lift

and induced drag of such configurations can be predicted reasonably well, but that the pitching moment and also the detailed pressure distribution on the wing are in poor agreement with experimental data.

From a perusal of published results of nonlinear vortex-lattice methods, it must be concluded that, although forces and moments can be predicted reasonably well, representing a vortex sheet by discrete vortex filaments is apparently a too crude and too singularly behaved approximation, see also Luckring (Ref. 90) where a similar conclusion is reached.

In the panel-method approach such as developed by Johnson et al. (Ref. 91), vortex sheets are represented more accurately by a piecewise continuous doublet distribution on flat panels. The vortex sheet emanating from the leading edge is allowed to attain a position and strength such that the boundary conditions (zero normal velocity and continuous pressure) on the vortex sheet are satisfied. The rolled-up part of the leading-edge vortex sheet is modeled using the three-dimensional equivalent of Smith's discrete-vortex/feeding-sheet combination, i.e. a vortex-filament/feeding-sheet combination. The wake downstream of the trailing edge is taken as a surface that is a smooth continuation of the wing and leading-edge vortex sheet; i.e. the geometry of this vortex sheet is fixed. The doublet strength of the wake follows from imposing the condition that the pressure is continuous across the sheet, while the normal-velocity condition is not imposed. The main difficulty in the vortex-sheet method is that one has to solve for the strength and the position of the vortex sheet simultaneously, i.e. one imposes boundary conditions that are of mixed analysis (the normal velocity condition)/design (the pressure condition) type. Constructing a numerically stable scheme, i.e. expressing the panelwise representations for geometry and doublet distribution in terms of unknown parameters to be solved for, has proven to be difficult. Finally it was found that a scheme derived from a least-squares fit involving parameters associated with the representations on 16 neighbouring panels provided sufficient stability for most cases. In general the (mostly using a rather coarse paneling) computed forces and moments are in satisfactory agreement with experimental data, while pressure distributions are often unsufficiently resolved to reveal the details in the distribution in the region underneath the vortical flow region.

In Ref. 82 a panel method (VORSEP) is described, developed at NLR, for the three-dimensional flow problem. It is based on Johnson's formulation but has a near wake which is free to assume the position where both vortex-sheet boundary conditions are satisfied. Also the numerical approach differs from the one of Johnson's (LEV) method, e.g. curved panels instead of flat panels and a simpler scheme for the local representations of the doublet distribution and the geometry.

In the next section some applications of the panel methods VORSEP and VORSEBA to some incompressible flow cases are discussed in some detail.

#### 4.3. Solution for delta wings with leading-edge vortices

In this section the potential-flow solution is considered for three flat delta wings of different sweep angle ( $\Lambda = 65, 70$  and  $85$  deg) all inclined at an angle of  $20$  deg with respect to the oncoming flow. The solution from the VORSEP panel method is presented in Fig. 10. It shows for each of the three cases the spanwise pressure distribution at the chordwise sections  $x/c_a = 0.1(0.3)0.9$  and a three-dimensional view of the geometry of the wing, the leading-edge vortex sheet including the vortex-filament/feeding-sheet vortex-core model and the near-wake vortex sheet. The far wake,

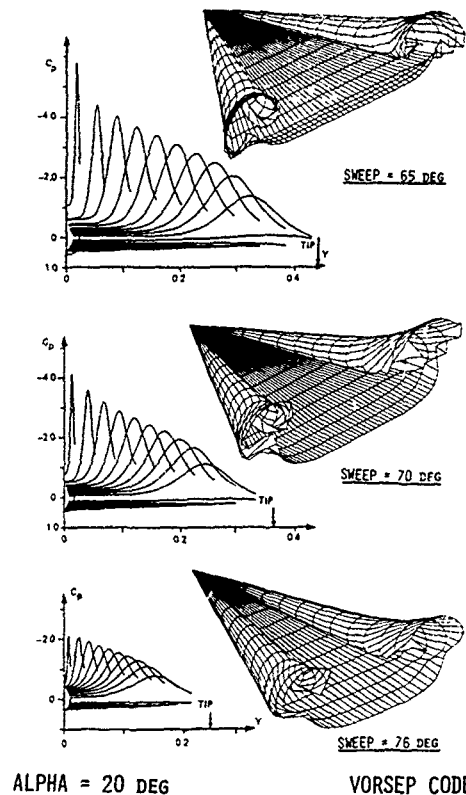


Fig. 10 Potential-flow solution of incompressible flow about thin delta wings

which consists of straight vortex lines attached to the last section of the near wake, is omitted from the figure. The solution is obtained assuming starboard/port-side symmetry with for half of the configuration 13 strips of 32, 34 and 27 panels for the 65-, 70- and 76-deg delta wing, respectively. The length of the leading-edge vortex sheet is chosen such that at least one complete turn of the sheet is taken into account. For the 70- and 76-deg delta wings the length of the three-strip near wake is 30%, for the 65-deg delta wing it is 10% root of the chord.

It is clear that the leading-edge vortex sheet has a conical appearance almost up to the trailing edge of the wing. It is evident from Fig. 10 that with increasing sweep angle the vortex system increases in cross-sectional dimension relative to the wing semi-span. In the VORSEP method the near-wake is fully relaxed, but the trailing-edge vortex is not modeled explicitly as another vortex-filament/feeding-sheet combination. However, the wrinkling showing up in the near wake vortex sheet forms the smoothed-out representation of the double-branched trailing-edge vortex that forms at precisely that location.

Analysis of the solutions has shown that at the trailing edge the magnitude of the circulation associated with the vorticity of sign opposite to that in the leading-edge vortex system is, in terms of the circulation of the leading-edge vortex system, larger for the lower than for the higher sweep angles. Since all of the negative vorticity eventually will end up in the trailing-edge vortex, the latter will be relatively stronger and more pronounced for wings with lower sweep angles, as is also evident from Fig. 10.

Fig. 10 also demonstrates that on the wing surface the pressure distribution is not conical (i.e. constant along lines  $y/x = \text{constant}$ ) at all: in chordwise direction the pressure coefficient increases monotonically from a region near the apex to the trailing edge. However, because of the geometrical conicity of the solution the position of the leading-edge vortex core and therefore the upper-surface suction peak is at about the same percentage local semi-span for most of the spanwise distributions shown. For the lower leading-edge sweep angles the rate at which vorticity is generated at the leading edge is largest, which at a given chordwise station results in the strongest vortex and in the highest level of the suction peak on the upper surface of the wing. On the other hand, at the higher sweep angles the level of the suction peak is lower but the influence of the leading-edge vortex is felt on a relatively larger part of the span of the wing.

Comparison of the computational results with experimental data demonstrates that the VORSEP method is capable of predicting the characteristics of vortex flow, see Fig. 11. In this figure the computed spanwise surface pressure distribution is compared with experimental data of Verhaagen (Ref. 92) and of Hummel (Ref. 20) for the case of the 76-deg (unit-aspect-ratio) delta wing at 20 deg incidence. Although agreement of computed (VORSEP) and measured pressure distributions is quite satisfactory, it also demonstrates one of the main difficulties of comparing computed (inviscid) and real-life vortex flow results, namely the occurrence of (smooth-surface) secondary separation on the upper surface of the wing. In Hummel's experiment the boundary layer was fully turbulent (trip wire), while in Verhaagen's experiment (natural) transition from laminar to turbulent flow took place at about 60% root chord. This corresponds with the secondary-separation effects being more pronounced in the latter experiment when compared with Hummel's test.

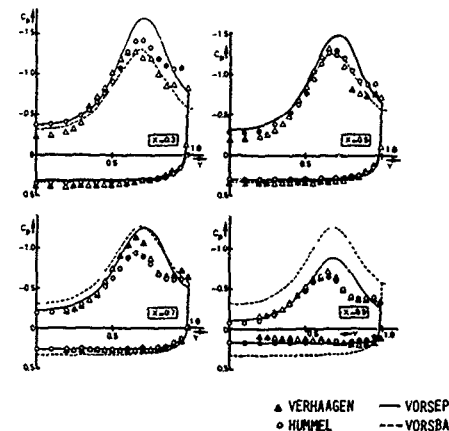


Fig. 11 Comparison of computed and measured surface pressure distribution for 76-deg delta wing at  $\alpha = 20$  deg

Further note that the method for three-dimensional flow (VORSEP) correctly predicts the increase of the pressure coefficient from apex towards trailing edge. It also appears that the VORSBA method, based on the slender-body approximation, provides a good prediction around 50% root chord. However, on the aft portion of the wing the upstream effect of the trailing edge becomes rapidly larger, invalidating the assumptions underlying the slender-body approximation.

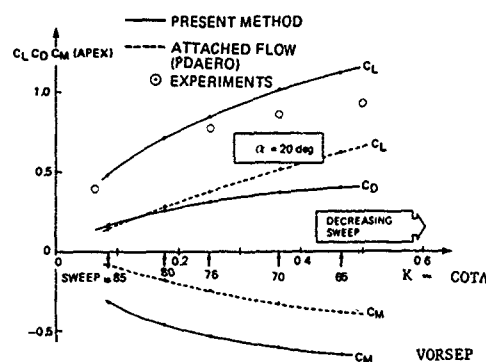


Fig. 12 Lift, drag and pitching-moment coefficient for delta wings at  $\alpha = 20$  deg

The effects of secondary separation become larger for lower incidence and lower sweep (more peaky upper-wing-surface pressure distributions) and are more severe for laminar flow compared to turbulent flow.

The lift, drag and pitching moment coefficients as a function of  $K = \cot\Lambda$  are plotted in Fig. 12. It shows that as the wing sweep decreases the lift increases, just like in attached flow. The relative amount of nonlinear lift decreases with decreasing sweep angle, as comparison with results of attached flow theory learns. Comparison with experimental data shows further that the lift coefficient is predicted quite well for sweep angles above 75 deg, but that at the lower sweep angles the present method tends to overpredict the lift. This is primarily due to the neglected secondary separation effects, which as remarked above are more severe for wings with lower sweep angles than for the more slender wings.

#### 4.4. An attempt to model secondary separation

As indicated above secondary separation can have a large effect on the pressure distribution on the upper surface of a delta wing. The position of secondary separation is determined by viscous-flow phenomena. In this section we study the effect on the inviscid solution of modeling the region of vortical flow due to the secondary separation by an additional vortex sheet that starts at some prescribed location on the upper wing surface and rolls up into a vortex core. Here it is assumed that the Reynolds number is high enough for the secondary separation vortex system to stand clear from the boundary layer on the wing. The test case chosen is the 65-deg delta wing at 20 deg incidence also discussed above, for which secondary separation effects are relatively severe. This choice of bears on the availability of experimental data from the International Vortex Flow Experiment for a similar wing (Ref. 56). For reasons of keeping the study as simple as possible the method based on the slender-body approximation (VORSBA) was used, which avoids some of the complexities of the three-dimensional problem while retaining the essential part of the problem. Furthermore the wing is considered to be infinitesimally thin and conical, while the configuration used in the experiment was a non-conical thickness distribution. The results of the investigation are presented in Fig. 13. It shows the case where there is no secondary separation and the cases where secondary separation (SS) is prescribed at 60(5)85 percent semi-span, respectively. In the experiment (Ref. 56) secondary separation was turbulent and took place at about 77.5 percent semi-span, as can be deduced from the measured pressure included in the figure. In the case of laminar flow on the wing surface the separation will be more inboard.

Fig. 13 shows that inclusion of the second vortex system has the qualitatively correct effect on the position of the primary vortex core, it moves inboard and upward. Furthermore, inspection showed that as the point of secondary separation moves outboard the magnitude of circulation within the primary vortex system and that within the secondary system both decrease, while the normal force is almost constant. The effect on the upper wing surface pressure distribution is that the height of the suction peak is reduced while its location is slightly more inboard. Just like in the experimental data a plateau of about constant pressure is formed just outboard of the secondary separation point. However, between this plateau and the leading edge the present computational model predicts a second suction peak. This suction peak, right underneath the vortex filament of the secondary vortex system, is much more pronounced than the one found in any experimental data, e.g. Refs 20, 56 and 92. In the numerical results the height of the secondary suction peak is directly associated with the presence of the vortex filament, representing the concentrated vorticity of the secondary vortex, in the near proximity of the wing surface. Including tertiary separation would probably reduce the height of the peak, but it may also be argued that in the real flow viscous effects will have a relatively large effect on the relatively weak secondary vortex, preventing the formation of a concentrated vortex core. Note that apart from the second suction peak the improvement of the correlation of computed and measured pressure distribution (with secondary separation at 77.5 percent semi span) is quite remarkable. At first sight the cross-sectional dimension of the secondary vortex system appears to be rather large, though similar large structures have been observed in LDV surveys by Schrader (Ref. 54) for a 63-deg sharp-edged delta wing and have been observed in water-vapour pictures for the rounded 65-deg delta-wing configuration (Ref. 93).

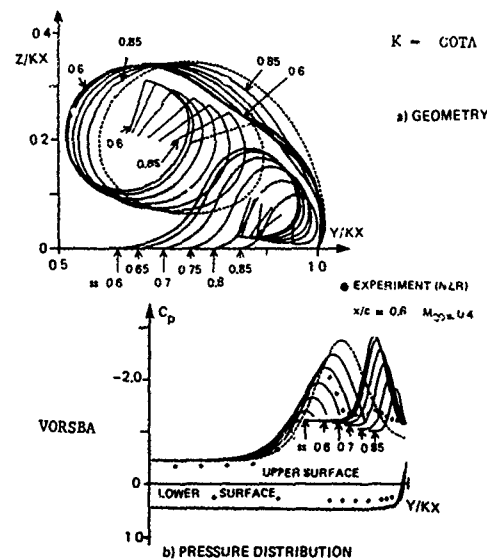


Fig. 13 Simulation of secondary separation for 65-deg delta wing at  $\alpha = 20$  deg

In an attempt to predict the secondary separation position it has been tried to match the assumed separation point with the separation point as follows from a boundary-layer calculation with as input the inviscid pressure distribution obtained in the presence of a primary and a secondary vortex

system, the latter emanating from the assumed secondary separation point (see de Bruin & Hoeijmakers, Ref. 94). This attempt was not successful, the laminar boundary layer always separated just downstream (outboard) of the primary suction peak, i.e. always upstream (inboard) of the assumed point of separation. This appears to be due to the singular behaviour of the inviscid solution at the assumed point of separation. The singular behavior is indicated in Fig. 14 where two quantities are plotted:

-  $A_s$ , the parameter in the expansion for the position of the secondary vortex sheet near the point of secondary separation  $y_{ss}$ , i.e.

$$z/Kx = A_s((y-y_{ss})/Kx)^{3/2} + \dots \quad (8a)$$

indicative for the magnitude of the singular behaviour in the curvature of the vortex sheet at  $y_{ss}$ , see F.T. Smith (Ref. 95).

-  $A_p$ , the parameter in the expansion for the pressure upstream of  $y_{ss}$ , i.e.

$$C_p = (C_p)_{ss} - A_p((y-y_{ss})/Kx)^{1/2} + \dots \quad (8b)$$

indicative for the singularity ( $\partial C_p / \partial y \rightarrow \infty$ ) in the pressure distribution as  $y \rightarrow y_{ss}$ .

The case of so-called "smooth separation" corresponds to the case of  $A_s$  (and  $A_p$ ) becoming zero. Due to inaccuracies in determining  $A_s$  and  $A_p$  from the discrete solution they do not become zero at exactly the same value of  $y_{ss}$ . For the present case smooth separation occurs at about 60 percent semi-span. Only in that case the singularity has disappeared and the boundary layer calculation could proceed up to  $y_{ss}$ . However, the so found location is much too far inboard when compared with experimental data.

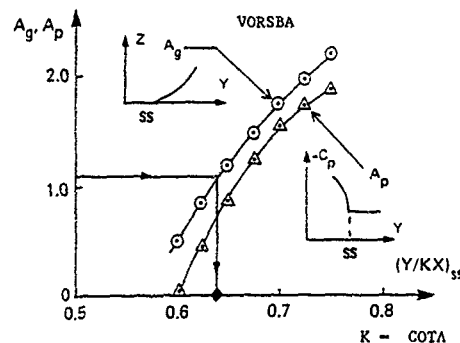


Fig. 14 Singularity at secondary separation in curvature and pressure distribution

The way to proceed is to allow for a strong interaction between the boundary layer and the inviscid flow field. In such an interaction the influence of the singularity due to the inviscid separation is spread in upstream direction which is not possible within classical boundary layer theory. This then induces a displacement effect of the boundary layer which weakens the adverse pressure gradient and enables the boundary layer to reach the assumed line of separation. For the case of separation from a slender cone Fiddes (Ref. 96) used the triple-deck formulation of Sychev and F.T. Smith, as extended to some special three-dimensional flow cases by F.T. Smith (Ref. 95), an asymptotic theory for large Reynolds numbers, to derive the permissible value of  $A_s$  as a function of the Reynolds number. The resulting expression involves, aside from the Reynolds number, certain boundary-layer quantities to be obtained from the case of "smooth separation".

From F. T. Smith's analysis and using quantities obtained from a three-dimensional boundary-layer calculation, it can be shown (see Ref. 82 for the details) that for a Reynolds number of 9M based on root chord:

$$A_s = 0.4506(Re_x)^{-1/18} \quad (8c)$$

where  $Re_x$  is the Reynolds number based on the chordwise distance along the root chord. It turns out that the so found permissible singularity in the curvature of the vortex sheet is quite small, shifting the position of the secondary separation by at most 2.5 percent semi-span, see Fig. 14. This shift is small, but presumably in line with F.T. Smith's asymptotic theory, and does not help much to arrive at a computed separation position that agrees more satisfactorily with experimental data.

This finding contrasts with the result of Fiddes (Ref. 96) where for the case of the (primary) smooth-surface separation from a 5-deg cone a much larger shift was found and correlation with experiment was remarkably good. Unfortunately subsequent inspection of the Fiddes' analysis revealed that a factor 4 is missing, reducing the shift by this same factor and destroying the earlier found excellent correlation with experiment. However, it brings the present result in line with the result for the primary separation from a slender cone.

In case of turbulent flow the "weak-interaction" model does not result in a satisfactory match between predicted and assumed locations of secondary separation either, see de Bruin & Hoeijmakers (Ref. 94). For the case of turbulent flow an asymptotic formulation has not yet been developed. As a matter of fact, carrying out a boundary-layer calculation with the measured pressure distribution as input, such as attempted by DeJarnette & Woodson (Ref. 97) and Houtman & Bannink (Ref. 98), also results in a separation just upstream of the measured location.

So in conclusion, predicting secondary separation location will require more elaborate models of the viscous-inviscid interaction than employed here.

#### 4.5. Solution within leading-edge vortex core

In the potential flow solution the vortex core is represented by a number of turns of the vortex sheet as far as its outer region is concerned and with the vortex-filament/feeding-sheet combination for its inner, tightly rolled-up part. The latter only serves as a means to account for the inner part in regions away from the center of the vortex core. In the potential-flow model the vorticity is concentrated in the turns of the vortex sheet and the direction of the velocity vector will be discontinuous across the sheet. In reality the vortex region will consist of distributed vorticity and the velocity will be continuous with at most steep gradients near the edge of the vortex core where some remains of the shear layer may still be discernible. In order to investigate the potential-flow vortex core a solution was obtained with a long (5 semi-spans) vortex sheet. The case considered is the (VORSBA) slender-body-approximation solution for the 76-deg delta wing at 20 deg incidence. The solution, presented in Fig. 15, has 20 wing panels and 112 panels on the vortex sheet. The panel scheme of the wing was uniform, that on the vortex sheet non-uniform, the panel width decreasing with increasing curvature. The vortex sheet loops 5 times around the vortex filament, with the last turns becoming nearly circular. The circulation contained in the vortex sheet amounts to 77.5 per cent of the total circulation in the vortex system. The strength of the vortex sheet, largest at the leading edge, decreases gradually along the vortex sheet. The local extrema in  $\gamma$  coincide with the local extrema

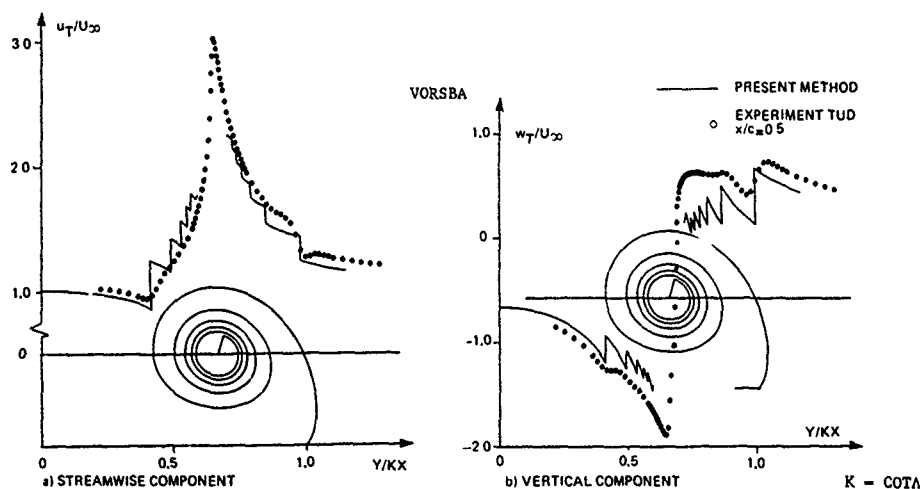


Fig. 15 Comparison of computed and measured velocity components on horizontal traverse through vortex core ( $\Lambda = 76$  deg,  $\alpha = 20$  deg)

in the curvature.

Included in Fig. 15 are the distribution of the streamwise (parallel to  $U_\infty$  - tunnel axis) and vertical component of the velocity along a horizontal traverse, in plane normal to  $U_\infty$ , through the center of the vortex core. The computed distributions show that towards the center of the vortex core the streamwise (axial) component increases stepwise in magnitude, reaching a value of about 2 times the free-stream velocity. Steps corresponds with passages through successive turns of the vortex sheet. The vertical (circumferential) component has the saw-tooth like distribution one would expect from a vortex-sheet core model. Note that the jumps in the velocity components become smaller as the center of the core is approached, corresponding with the decreasing strength of the vortex sheet as it spirals around the center. Since the spacing between successive turns becomes smaller the corresponding spatial vorticity distribution actually will increase in strength towards the center.

Comparison of the computed shape of the vortex sheet with the total pressure contours obtained by Verhaagen & Kruisbrink (Ref. 99) at the Delft University of Technology has shown that the location of the free shear layer and that of the computed vortex sheet agree quite well, while also the position of the vortex core is predicted satisfactorily.

Figs. 15a and 15b include a comparison of the computed velocity components (invariant with  $x$ ) with the measured (5-hole probe) components for a horizontal traverse through the vortex core at the midchord position, also from Ref. 99. For the streamwise velocity component the agreement between computed and measured distribution is remarkably good. For the vertical component theory and experiment still correlate qualitatively, but theory appears to underpredict the measured values of the circumferential velocity. Reasons for the discrepancy could be wind-tunnel wall interference which for the relatively large half-model employed are known to result in an effective incidence larger than the value of 20 deg used for the computations. Note that the first two full turns of the leading-edge vortex-sheet can be recognized in the experimental data, the remainder of the core may be considered as a region with distributed vorticity.

Luckring (Ref. 100) describes a method to incorporate a slender-body vortex core with distributed vorticity and a viscous sub-core into the solution of the three-dimensional-panel-method (LEV) of Johnson (Ref. 91), showing that in order to

have a good description of the flow field inside the core a short leading-edge vortex sheet suffices. However, predicting the onset of vortex breakdown with this hybrid model proved to be unsatisfactory.

A further experimental and numerical study into the flow inside the vortex core can be found in Verhaagen & van Ransbeeck (Ref. 101).

#### 4.6. Separated flow from a slender cone

In this section another interesting feature of the present nonlinear flow problem is considered: the possibility of multiple solutions.

For this consider the flow about a slender circular cone, with prescribed (primary) separation lines. The cone has a semi-vertex angle of 10 deg and is at 30 deg incidence with prescribed separation at  $\theta = \pm 130$  deg, where  $\theta = 0$  denotes the bottom of the cone (see Fig. 16). Geometrically this configuration is symmetric with respect to the vertical ( $y = 0$ ) plane, while also the uncoming free-stream is symmetric with respect to this plane. However, since asymmetric solutions are to be searched for no symmetry can be assumed in the computations and both starboard and port sides of the cone, each with their own vortex sheet, are to be considered. Here results will be presented from again the VORSBA slender-body-approximation panel method, applied directly in the physical plane. Similar results have been obtained by Fiddes & Smith (Ref. 102) using a succession of several conformal transformations followed by a panel-method type of approach to solve for the position and strength of the vortex sheets within the transformed plane.

Fig. 16 shows the VORSBA solutions found for 30 deg incidence, one symmetric and one asymmetric solution. The mirror-image of the latter solution is of course also a valid solution.

The symmetric solution was obtained by starting with short sheets and extending them panel by panel using one of the continuation procedures of the VORSBA method. The asymmetric solution gave more problems: The solution for short sheets was easily obtained by choosing the position of the vortex filaments in an asymmetric manner. However, extending the port-side sheet to a length such that it loops around the filament using a panel by panel extension was not successful: the last one or two panels of the vortex sheet had a strong tendency to curve inwards, i.e. to roll-up before winding around the vortex core. Ref. 82 describes in detail the procedure that did work for this case.



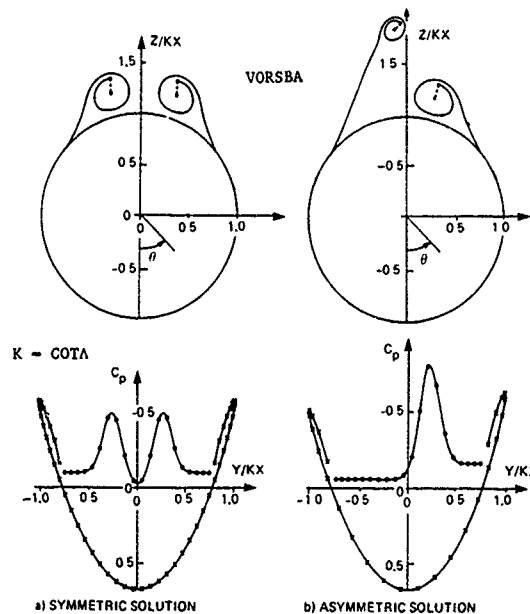


Fig. 16 Symmetric and asymmetric solution for 10-deg cone at  $\alpha = 30$  deg

Fig. 16 presents the final result of the computation, where the symmetric solution has 72 panels on the cone and 20 panels on each of the two vortex sheets, while the asymmetric solution has 46 panels on the cone, 30 panels on the starboard and 45 panels on the port side vortex sheet, respectively. There is a large difference between the two solutions, especially in the geometry of the port-side vortex sheets and the pressure distribution on the lee-side of the cone, i.e. underneath the vortex system. The pressure distribution on the windward side of the cone is not very much different for the symmetric and asymmetric case. Although the pressure distribution on the cone is so different for the two solutions the normal force is about the same, which for the asymmetric solution is produced almost entirely by the starboard vortex. The side force produced by the asymmetric solution amounts to about 20 percent of the normal force. Further analysis of the symmetric and asymmetric solution showed that the vortex sheet that moves away from the cone becomes weaker, while the one that stays near the cone becomes stronger.

The problems we encountered for the asymmetric solution with the port-side vortex sheet appear to be associated with the circumstance that the relatively long first part of this vortex sheet is almost straight (Fig. 16a) and of uniform strength which makes it susceptible to the Kelvin-Helmholtz instability. It also suggests that still another solution is possible, i.e. one in which a third (double-branched) vortex core is embedded within the port-side vortex sheet.

#### 4.7. Vortex-sheet stability

In general one may state that a vortex sheet is unstable to small perturbations, unless it is curved and/or stretching faster than some critical rate (e.g. Moore, Refs. 103, 104, 105). Both curvature and stretching are associated with a variation of the surface vorticity distribution. In fact, for a two-dimensional vortex sheet of constant strength it is rather catastrophic: the smaller the wave length of the perturbation, the faster is its linear rate of growth. Whether a local distortion of the vortex sheet, caused by this so-called Kelvin-Helmholtz instability grows into

a larger-scale flow structure (rolled-up vortex core) depends on its nonlinear growth behavior as allowed within the global flow pattern. However, vortex sheets employed here model free shear layers at high Reynolds numbers. These (thin) shear layers are also unstable, but not as dramatic: it appears that perturbations with wave lengths smaller than a few times the shear-layer thickness are damped (Rayleigh, Ref. 106).

In potential-flow methods with free vortex sheets, like the nonlinear panel methods discussed above, the numerical scheme necessarily implies some mechanism to damp the local vortex-sheet instability, though the important large-scale structures still evolve as part of the solution. For the panel method the parameter that implicitly controls the damping is the panel dimension. This has become evident in various applications of panel-method type of methods (Ref. 82). For instance in the case of the method for computing the evolution of two-dimensional vortex sheets (wake roll-up) the panel size actually determines the number of vortex cores developing.

As far as the slender-body-approximation method (VORSBA) for computing the flow about slender configurations with free vortex sheets is concerned the following can be remarked. Applying the method to a conical configuration means that the problem reduces to just one cross-flow-plane problem. This implies that any perturbations to the free vortex sheets will be constrained to be conical as well. It turns out that in this case the leading-edge vortex sheet, such as shown in Figs. 13, 15 and 16, is very stable. The latter has been investigated numerically by taking a specific portion of the vortex sheet and increasing the panel density for that portion by orders of magnitude. No instability whatsoever was observed, not even for cases for which in the literature (Payne et al., Ref. 37) experimental evidence for the formation of small-scale structures has been given, nor for cases for which vortex-breakdown has been reported. However as noted above, signs of instability modes have been experienced for the case of the asymmetric conical flow about the slender cone (Fig. 16). Furthermore, as is shown in Fig. 17, applying VORSBA to a slender double-delta configuration using a fine paneling in the cross-flow planes and a very small chordwise step to march from plane to plane in downstream direction, resulted in waves on the vortex sheet in the region downstream of the kink in the leading edge (Ref. 107). In this figure two waves are seen to travel along the vortex sheet, the first one starting at the kink, the second one further downstream. The first one is not amplified as it travels along the stretching vortex sheet. The

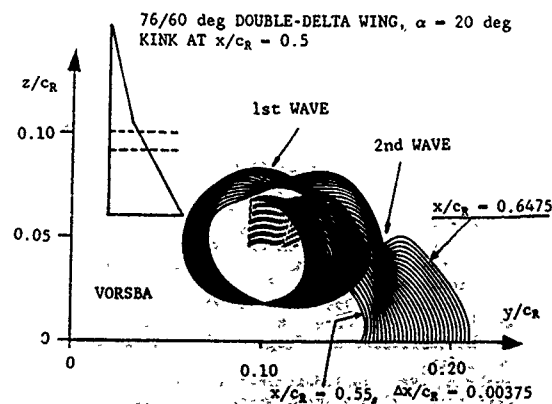


Fig. 17 Solution for 76/60-deg double-delta wing at 20-deg incidence

second one develops into a highly curved part of the vortex sheet suggesting the formation of a second center of roll-up, i.e. the wing vortex. Comparison with experimental data indeed shows that the second wave closely follows the path of the wing vortex.

For the case of three-dimensional leading-edge vortex sheets a possible instability may develop less constrained than for the quasi-two-dimensional cases considered above. However, in the applications carried out so far no "standing wave" type of small-scale structures have been encountered other than the one representing the trailing-edge vortex, see Fig. 10. Possibly the panel schemes employed so far were not fine enough to resolve these instabilities. Whether refining the paneling to a still higher levels will allow correspondingly finer scale structures to develop, or that the "standing-wave" type structures furnish sufficient stretching to stabilize the sheet, can only be speculated on. Also subject to speculation is whether at each level of refinement the global vortical flow structure as is predicted for the present level of panel densities, and which shows good agreement with high-Reynolds-number experimental data, remains the same.

## 5. EULER METHODS

### 5.1. Background

In the fitted-vortex-flow methods the topology of the vortical flow field must be known in advance, i.e. one must decide on the global structure of the vortex sheets and filaments (embedded vortex cores). Furthermore, most methods require some reasonable initial guess for the location of the vortex sheets and vortex filaments. For most slender-wing configurations at subcritical conditions this is not much of a problem, but for geometrically more complex configurations it is much more difficult to derive the topology of the vortical flow field in advance.

Computational methods solving the Euler equations have the advantage that regions with vorticity are "captured" rather than "fitted" as in the panel method approach, but one of the major drawbacks is that now an adequate spatial mesh is required. Also, just like is the case for the potential-flow methods the generation of vorticity, due to the separation of the flow from the solid surface whether at a sharp edge or at a smooth part of the geometry, must still be modeled since it is a process dominated by viscous forces. It should therefore be expected that in order to obtain physically relevant solutions of the Euler equations one or more additional conditions (i.e. Kutta conditions) have to be provided explicitly or are satisfied implicitly within the numerical scheme utilized to solve Euler's equations. On the other hand distributed vorticity generated at strong shocks is accounted for.

Historically seen the development of computational methods for solving Euler's equations has been motivated by the need to compute transonic flow involving strong (non-isentropic) shocks. Later it was realized that these methods allow for rotational flow effects and can be used to compute convection dominated separated flows. In this view the mathematical model based on Euler's equations, Eq. (5) admits "weak" solutions with both shock waves and vortex sheets. However, it should be noted here that there are some fundamental differences between shock waves and vortex sheets, which could have strong implications for their numerical treatment within Euler methods:

- (i) Across shock waves there is a convective mass transfer, across vortex sheets there is none;
- (ii) For shock waves uniqueness is provided by the entropy condition, for vortex sheets there appears to be no such condition;
- (iii) The strength of a shock wave is determined by its shape and the conditions on one side of the shock, for vortex sheets the jumps are arbitrary, except in the static pressure and the component of the velocity normal to the sheet which are continuous across the vortex sheet;
- (iv) Introduction of viscosity: The thickness of a shockwave is independent of the dissipation, while the vortex sheet discontinuity turns into a vortex layer which thickness does depend on the dissipation. Furthermore, depending on their stretching and curvature vortex sheets may be prone to Kelvin-Helmholtz type of instabilities, while the stability of a vortex layer depends on the stretching and curvature of the layer but also on the thickness of the layer, i.e. its stability decreases with decreasing thickness.

Specifically the latter implies that for Euler methods it will be much more difficult to accurately capture vortex sheet discontinuities than it is to capture shock wave discontinuities.

### 5.2. Types of computational methods

In the literature at least three different types of numerical approaches to solve the Euler equations can be found. Before describing some of the most used schemes a short description is given first.

a) Space-marching method. This type of method applies to steady supersonic flow only. In this case the disturbances propagate in downstream direction only and a marching procedure can be devised. Starting at some station near the nose of the configuration where the cross-flow-plane flow field is defined using a known solution for a cone, the solution is "marched" cross-flow-plane wise in downstream direction. Only the flow field between the surface of the configuration and the bow shock needs to be resolved. The latter is determined as part of the solution using a shock fitting procedure which exactly satisfies the Rankine-Hugoniot relations. In most methods the embedded shocks are captured. The spatial marching procedure is rather efficient and requires a computational mesh in the successive cross-flow planes rather than a fully three-dimensional (blocked) grid. For the space-marching Euler method to work it is required that the component in the marching direction of the local velocity is supersonic. In many cases of interest here this will not be the case and an alternative approach is needed.

b) Time-stepping method. In this approach the unsteady Euler equations are solved using a time-marching procedure to drive the solution, from some arbitrary initial state, to its time-asymptotic steady-state solution. Using such a pseudo-time dependent approach solutions have been obtained in the subsonic, transonic and low-supersonic flow regime. It is well-known that the convergence to steady state deteriorates badly for decreasing Mach numbers. For the often used multi-stage Runge-Kutta scheme the characteristic time-scale is of the order of  $L/(u + a)$ , where  $L$  is the length scale of the problem,  $u$  the magnitude of the local velocity and  $a$  the speed of sound. The characteristic time scale of the changes in physical flow-field features are of order  $L/u$ , which for the lower Mach numbers is much larger than the time-scale of the Runge-Kutta scheme, i.e. the Euler equations are stiff. In the computational Euler methods for low-subsonic or incompressible flow this difficulty is avoided by using the so-called artificial com-



compressibility concept (e.g. Rizzi, Ref. 108), also used for solving the Navier-Stokes equations for incompressible flows.

c) Vortical-particle method. This method, due to Rehbach (Rehbach, Ref. 109 and Morchoisne, Ref. 110) does not require the construction of a spatial mesh. In the (incompressible flow) method the velocity field is expressed as the contribution due to the "bound" wing surface vorticity (represented by the vortex-lattice method) and the contribution due to free floating "vorticity-carrying particles". The latter represent the spatial vorticity distribution. The approach followed is a time-dependent one; starting from rest, the vortical particles are traced. At each time step the strength of the "bound" vortices is determined by satisfying, for a given spatial vorticity distribution, the normal velocity boundary condition on the wing. Subsequently, from predetermined separation lines, here sharp edges, new vortical particles are shed into the flow field. The strength of the new vortices is derived from Kutta-condition type of considerations. The vortical particles already in the flow field are convected with the local velocity, while the rate of change of the total amount of vorticity contained in any particle is obtained from an integral form of the vorticity transport equation. In this grid-free method for solving Euler's equations for incompressible flow vorticity is produced at predetermined locations only, but the vortex shedding mechanism used in the numerical model may have a considerable effect on the computed flow. In this Lagrangian type of approach for solving the vorticity transport equation excessive spreading of vorticity is avoided, which can not always be said from finite-difference or finite-volume methods. A drawback of vortical-particle method is that in order to obtain a sufficiently detailed pressure distribution on the surface of the configuration the number of vortical particles has to be quite large, resulting in considerable computational cost.

5.3. Schemes for Euler and Navier-Stokes methods  
Before turning to specific methods a summary is given of a number of often used numerical schemes. The type of finite-difference and finite-volume schemes used to solve the Euler (and Navier-Stokes) equations have been central and upwind difference methods. The evolution of the methods has been from explicit finite-difference methods with central differencing to implicit finite-volume methods employing upwind difference schemes.

At present finite-volume methods are preferred over finite-difference methods, primarily because the former have shown to be particularly suited for solving the Euler equations. In the finite-volume method the flow equations are expressed in integral form, i.e. from Eq. (1):

$$\frac{d}{dt} \iiint_V U dV + \iint_{\partial V} [F - F_v, G - G_v, H - H_v]^T \cdot \vec{n} dS = 0 \quad (9)$$

which is applied to a large number of patched volumes  $V$ . Each control volume  $V$  consists of one cell of the computational grid (cell-centered methods) or parts of a number of neighboring cells of the computational grid (cell-vertex methods). In the finite-volume formulation the flow algorithm can be decoupled from the grid generation and therefore gives more flexibility with regard to geometry.

#### 5.3.1. Central-difference schemes

The most widely used scheme in earlier Euler and Navier-Stokes methods is the explicit predictor-corrector scheme of McCormack (Ref. 111). This two-level central difference scheme is stable and

second-order accurate. However, dissipative terms have to be added to eliminate oscillations in the vicinity of shocks. A problem associated with this scheme, if used in time-stepping procedures, is that the ultimate steady state reached depends on the time step.

An often used implicit central-difference method is the Beam & Warming (Ref. 112) scheme. In explicit methods the step size is limited for stability by the CFL condition. An implicit scheme may be unconditionally stable, at least in the sense of linear stability analysis, so that there is no theoretical limit to the allowable step size. However, because of the way in which the boundary conditions are implemented and most importantly because of the nonlinearity of the Euler and Navier-Stokes equations, too large time steps can still lead to instabilities and in addition can have an adverse effect on the solution accuracy. Furthermore, implicit schemes are more expensive per time step, more complex and difficult to vectorize. The well-known Flo-57 algorithm of Jameson (Ref. 113) employs a central-difference scheme for the time-dependent flow equations. It is based on an explicit multi-stage Runge-Kutta time discretization within a finite-volume formulation.

The Euler equations do not contain dissipation and the centered spatial difference schemes are not dissipative to lowest order. Artificial damping or viscosity is required to damp out high-frequency modes in the solution of the discrete equations and to capture shocks and contact discontinuities. To this purpose blended second and fourth difference dissipation terms are added to the discretized inviscid equations. The parameters controlling the precise blend of the added terms depend on the local pressure gradient and therefore adapt to the evolving solution. In some way the artificial dissipation mimics the effect of the true viscous terms in the Navier-Stokes equations by smoothing out steep gradients and damping oscillations. The order of magnitude of the added terms is of the order of the truncation error of the basic scheme, so that the added terms have little effect on the solution in smooth parts of the flow. Near steep gradients the solution is significantly changed, e.g. near a shock it eliminates pre- and post-shock oscillations but also smears out the shock. In conservative formulations usually the smoothing terms are designed such that they retain the conservation property of the algorithm.

A disadvantage of explicit methods is that they only slowly converge to steady state. To improve the rate of convergence most computational methods feature some or several acceleration techniques such as grid sequencing, local time stepping, residual averaging, enthalpy damping, multi-grid, etc.. It is also often found that the convergence rate is highly sensitive to the grid size, grid-point distribution, skewness of the grid, etc.. The dependence of the convergence properties of a method on the precise details of the grid is undesirable for any aerodynamic design and analysis code that has to be applied in practice.

Due to the relative simplicity of the explicit central-difference schemes they offer high computational efficiency on vector computers, which is one of the reasons these schemes are among those most commonly used in the numerical simulation of three-dimensional flows.

#### 5.3.2. Upwind-difference schemes

In recent years methods based on various upwind differencing techniques (e.g. Refs. 114, 115) have been developed for application to inviscid and viscous flow. The upwind methods aim at closely following the physical properties of the Euler equations. In most of the formulations positive and negative flux components are defined

based on the sign of the eigenvalues of the Jacobians. These components are then discretized with one-sided differences in the direction upwind of the direction of the characteristic propagation speed, often in some Total-Variation-Diminishing (TVD) formulation. Sometimes higher-order accuracy is attained by using so-called flux limiters near critical points such as stagnation, sonic and shock points.

The upwind schemes possess inherent dissipation and usually it is not necessary to explicitly add dissipative terms. Although user control of artificial dissipation may be a desirable option in some applications, it is not necessarily to be preferred and it does burden the application of the method with extra parameters to be tuned, sometimes on a case by case basis. The upwind formulations attempt to model the wave-like nature of the Euler equations, but the physical interpretation of this flux splitting technique is clear and unambiguous only for one-dimensional flows. Moreover, compared to central-difference schemes the amount of algebraic operations involved is large.

#### 5.4. Examples of Euler methods

##### 5.4.1. Space-marching methods

These methods are restricted to steady supersonic flow. Space-marching Euler methods are most extensively used for the prediction of the aerodynamics of missile configurations, including flow conditions at high angles of attack (e.g. Refs. 116, 117, 118, 119, 120, 121, 122).

In all cases it appears that in order to obtain consistent results a Kutta condition is required at sharp leading edges, of for example fins. Some of these methods also have the possibility to impose a Kutta condition at a point on a smooth part of the cross-sections of the elongated body of the configuration. This is utilized to provoke separation at empirically prescribed locations and to include in the numerical simulation the for missile aerodynamics often important interference of body vortices with downstream lifting surfaces. Wardlaw & Davies (Ref. 123) apply their upwind method space-marching Euler method (Ref. 121), without imposing any Kutta condition, to round and sharp-edged conical delta wings and demonstrate the importance of the mutual interaction of the cross-flow shock with the vortical-flow region associated with it and the influence of the numerical errors induced at the leading edge on this interaction.

##### 5.4.2. Time-stepping methods

One of the first applications of a finite-volume time-stepping method for solving Euler's equations to slender delta wings was reported by Eriksson & Rizzi (Ref. 124). It emerged that this method, comparable to Jameson's method (Ref. 113) generated a vortical flow without explicitly imposing a Kutta-type of condition at the sharp leading edge. Comparing the computed results with experimental data and also with results from panel method computations suggest that due to the relatively coarse mesh used in these early applications, the amount of vorticity contained in the vortical flow region is too small and the vorticity is spread over a too large area. As a result the computed upper surface suction peaks are lower than computed by a panel method; even lower than measured in experiment. A further anomaly is the appearance of a second, spike-like, suction peak right at the leading edge. This indicates that the flow turns around the edge before it separates at a location on the upper wing surface slightly inboard of the leading edge. In later applications (Hitzel & Schmidt, Ref. 125; and Rizzi, Ref. 126) the spike-like suction peak is not so dominantly present, while studies on the influence of mesh density (Rizzi, Ref. 126) reveal a rather large influence of mesh density and lay-out on computed pressure distributions.

The treatment of flow separation at "aerodynamically sharp" edges in methods solving Euler's equations is a major issue. When inviscid flow turns around the edge it will expand to the limit of vacuum pressure. However, viscous flow will separate at the edge before the inviscid expansion limit is reached. This suggests that truly simulating high-Reynolds number flow using Euler's equations requires some kind of modeling (Kutta conditions). This is common practice in Euler methods for supersonic flow employing a space-marching solution technique (see above), but not so in the more recent Euler methods that use a time-stepping solution technique.

Two reasons have been put forward for the inviscid separation phenomenon occurring in the latter type of methods:

(i) During the time stepping process, from rest to steady state, a transient shock wave appears at the leading-edge which produce vorticity due to the variation of its strength along the shock, resulting in the formation of the leading-edge vortex (Eriksson & Rizzi, Ref. 124; Hitzel & Schmidt, Ref. 125).

(ii) Separation occurs because of viscous-like terms due to (explicit and/or implicit) dissipative terms in the numerical scheme, e.g. shock-capturing algorithm, terms or procedures added for stability, surface boundary conditions, etc. (Raj, Refs. 127, 128; Newsome, Ref. 129; Kandil & Chuang, Ref. 130).

Raj (Ref. 128) reports that for the low Mach number cases he studied (using Jameson's FLO-57, Ref. 113) the flow near the sharp leading edge remained subcritical throughout the evolution to steady state and still a vortical type of flow emerged. It is also quite unlikely that in subsonic or transonic flow a leading-edge shock of varying strength would produce the amount of vorticity actually found in the numerical solutions. Usually it is observed that attached-flow Euler solutions for sharp-edged wings are obtained for very coarse meshes only.

Influence of mesh density is more conveniently being studied for conical flows, where just one cross-sectional quasi two-dimensional problem needs to be considered. In a careful study by Newsome (Ref. 129) for the case of supersonic conical flow about a delta wing with subsonic (not infinitely sharp) leading edges, using a central-difference scheme, two Euler solutions evolved, one for a relatively coarse mesh with and one for a fine mesh without leading-edge vortex separation. The latter solution, with the explicit dissipative terms turned off at the edge involves a cross-flow shock about 25% inboard of the leading edge, on its downstream side accompanied by a small region of distributed vorticity, similar to solutions found earlier using shock-fitting. Following the time-accurate transient solutions it was observed that the coarse-grid solution evolved from one with a cross-flow shock to one with leading-edge vortex separation. Using a similar configuration Kandil & Chuang (Ref. 130) confirmed these findings and also showed that increasing the artificial dissipation on one and the same grid could change an attached-flow solution to a separated-flow solution. Newsome & Thomas (Ref. 131) and Chakravarthy & Ota (Ref. 132), using upwind schemes, obtained attached coarse-mesh solutions for the above delta wing with round leading edges, suggesting that the up-wind schemes invoke less dissipation. For the sharp-edged wing an attached coarse-grid and a separated fine-mesh solution was obtained.

The above investigations strongly suggest that in the time-stepping Euler methods numerical dissipation is responsible for the flow separating "automatically", i.e. without explicitly having to impose a Kutta condition, at the sharp leading edge.

Micheltree et al. (Ref. 133) use an Euler code based on Jameson's formulation (Ref. 113) to compute the roll-up of the wake immediately downstream of a number of configurations. For this initial wake roll-up problem the Euler method is applied in a computational space encompassing the near wake region only, the inflow and initial conditions were provided by a conventional vortex-lattice method. The results of this study indicate that the Euler method gives vortex wake structures comparable to experimental data and other computational methods.

In the following we will concentrate on leading-edge vortex flow, i.e. the case of strongly interacting vortex flows.

In the literature many computational investigations report on predicting the steady vortex-dominated flow around delta wings, strake-delta wings and canard-wing configurations employing a time-stepping Euler method, addressing various aspects of the numerical simulation of this type of flow through Euler methods. Here we mention Rizzi (Refs. 134, 135, 136), Murman & Rizzi (Ref. 137), Powell et al. (Refs. 138, 139), Longo (Refs. 140, 141), Hitzel (Ref. 142, 143), O'Neill et al. (Ref. 144), Raj et al. (Refs. 145, 146), Sirbaugh (Ref. 147), Goodsell (Ref. 148), Marchbank (Ref. 149), etc..

In the following some results will be discussed obtained with the NLR Euler method for the three-dimensional inviscid flow about aircraft configurations.

#### 5.5. Application of NLR's Euler method

In this section some results obtained with the Euler method under development at NLR (Ref. 150) are presented for the flow about a 65-deg sharp-edged cropped delta wing at subsonic and transonic speed. The wing has a taper ratio of 0.15. The chordwise airfoil section is the NACA 64A005 airfoil which upstream of its point of maximum thickness (0.4 c) is smoothly blended into a biconvex shape. For this configuration, with an under-wing body, experimental data is available (Ref. 56) which was already used in the preceding chapter. For this same configuration more detailed information has recently become available, see Ref. 151. It is presumed that the presence of the under-wing body has only a small effect on the flow field away from the apex of the wing, so that the computational results for the wing-alone configuration can be compared with the measured data for the complete configuration. Further computational results on different aspects of the simulation have been reported in Refs. 152, 153 and 154.

The NLR Euler method (Ref. 150) solves the time-dependent Euler equations employing the fully-conservative, cell-centered scheme of Jameson et al. (Ref. 113). To obtain a steady-state solution, integration in time is carried out by a four-stage Runge-Kutta scheme, in which the dissipative terms are evaluated at the first step only. Convergence to a steady state is accelerated by using local time-stepping, enthalpy damping and residual averaging. For the conditions on the solid surface the method employs a linear extrapolation of the pressure from the flow field to the wall. The boundary conditions at the outer boundary of the computational domain are implemented using Riemann invariants.

At sharp edges nor at other positions can Kutta type of conditions be imposed.

The method can handle a grid with a patched multi-block structure. Since at internal block interfaces special boundary conditions can be imposed slope-discontinuous grid lines as well as jumps in cell size across the boundary are allowed, providing flexibility to facilitate application to complex configurations.

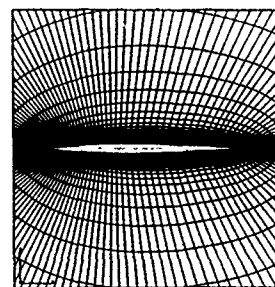
#### 5.5.1. Grids

For the results presented here two (8-block) grids of O-O topology have been used.

(i) A "fine" grid, which (for the starboard half of the wing) has grid dimensions  $288 \times 76 \times 56$  (1,225,728 cells), that is in chordwise direction 144 cells on both the wing upper and lower surface, in spanwise direction 76 cells and in normal direction 56 cells between the wing surface and the outer boundary of the computational domain.

(ii) A "medium" grid, obtained by combining groups of eight cells of the "fine" grid. This grid has dimensions  $144 \times 38 \times 28$  (153,216 cells).

PLANE OF SYMMETRY



WING SURFACE

72 x 38

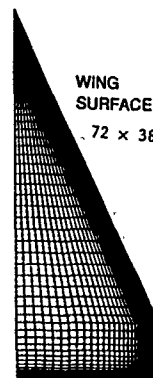


Fig. 18 Details of "medium" grid used in Euler calculations

Both grids are symmetric with respect to the horizontal plane of symmetry of the wing.

On the forward portion of the wing surface the grids are "conical" as is shown in Fig. 18 which presents details of the medium grid. The quasi-conical arrangement of the grid preserves the grid resolution near the apex. On the wing surface the grid lines are clustered near the apex, near the leading edge and near the trailing edge. In normal direction the cell stretching ratio is close to unity in the region where large gradients in the flow quantities are expected, specifically close to the wing surface.

The outer boundary of the computational domain is formed by the surface of a sphere with a radius of 5 root chords  $c_x$ , which has proven to be sufficient for the present applications.

The grid consists of eight patched blocks, the grid lines are continuous across block boundaries while the slope of the grid lines is very nearly continuous. The grid contains a singular line which starts at the apex and runs along the x-axis in upstream direction until it meets the outer boundary.

#### 5.5.2. Flow conditions

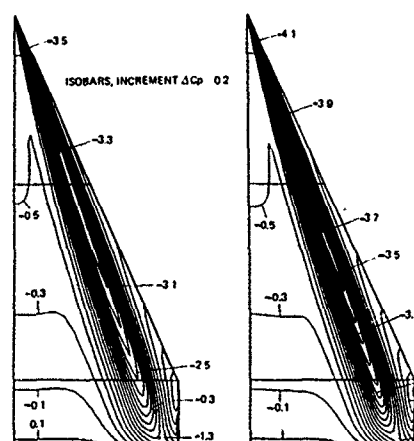
The flow around the cropped 65-deg sharp-edged delta wing at an incidence of 20 deg has been simulated in the subsonic flow regime for a free-stream Mach number of 0.5 and in the transonic flow regime for a free-stream Mach number of 0.85.

For the results of the computations presented the Euler method converged in 1500 to 2500 iterations, in which the root-mean-square norm of the time-like variation of the density dropped by four orders of magnitude, starting from the solution on the preceding grid level and from uniform free stream on the coarsest level.

Typical computing times, on the NEC SX-2 supercomputer installed at NLR, are one CPU hour for a complete computation on the "medium", five CPU hours for a complete computation on the "fine" grid.

### 5.5.3. Subsonic flow $M_\infty = 0.50$ , $\alpha = 20$ deg

For the calculation on the "medium" grid the second-order dissipative term was not used. The calculation on the "fine" grid was carried out with both the second- and the fourth-order dissipative terms switched on.



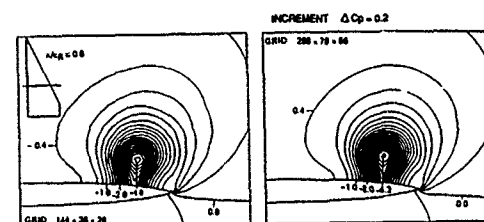
a) "MEDIUM" GRID 144x38x28 b) "FINE" GRID 288x76x56

Fig. 19 Isobars on wing upper surface  
 $M_\infty = 0.5$ ,  $\alpha = 20$  deg

The isobar pattern on the upper wing surface obtained from the computed results on the "medium" and "fine" grid are shown in Fig. 19a and 19b, respectively. For both grids the low-pressure region on the wing upper surface, forming the footprint of the leading-edge vortex, indicates that flow separation from the sharp leading-edge starts very close to the apex. As already observed for the potential-flow solutions of the preceding chapter the lowest values of the surface pressure coefficient are found near the apex underneath the vortex, typical for subsonic flow cases where there is a relatively large effect of the singularity at the apex as well as a relatively strong upstream influence of the trailing edge. For higher free-stream Mach numbers the region with lowest pressures moves to a more aft position on the wing, as will be shown later on.

Comparison of Figs. 19a and b shows that the Euler solution on the "medium" grid and the one on the "fine" grid do not differ in character. However, on the "fine" grid the pressures in the suction peak are substantially lower than those found in the result on the "medium" grid. For both grids the flow on the upper wing surface is supersonic in the low-pressure region, reaching Mach numbers above 1.5 on the "fine" grid.

In Fig. 20a the isobar patterns in the cross-flow plane  $x/c_R = 0.6$  are presented, as obtained from the solution on the "medium" and the one on the "fine" grid. These cross-flow-plane isobar pat-



a) "MEDIUM" GRID 144x38x28 b) "FINE" GRID 288x76x56

Fig. 20 Isobars in cross-flow plane  
 $M_\infty = 0.5$ ,  $\alpha = 20$  deg

terns clearly reveal the presence of a leading-edge vortex above the wing upper surface. The minimum value of the pressure, attained at the center of the vortex core, is lower for the solution on the "fine" grid than it is for the one on the "medium" grid. The position of minimum static pressure, i.e. the position of the center of the vortex core, is almost the same for the two grids. It turns out that the solution on the "fine" grid features a "cross-flow shock" underneath the vortex and just outboard of its center. In the cross-flow plane isobar pattern (Fig. 19b) the weak cross-flow shock is most clearly seen as a clustering of isobars at that location.

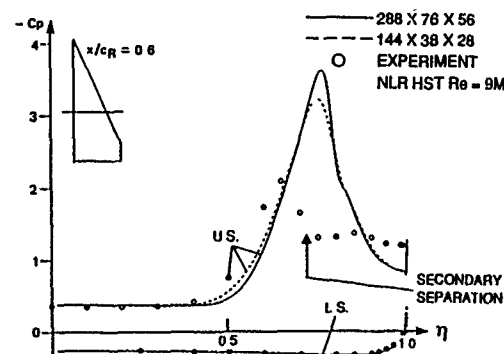
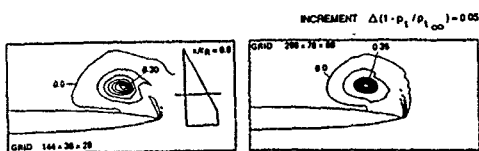


Fig. 21 Spanwise pressure distribution  
 $M_\infty = 0.5$ ,  $\alpha = 20$  deg

In Fig. 21 the spanwise pressure distribution as computed on the "medium" and the "fine" grid are compared with each other and with experimental data (Ref. 151) for the station  $x/c_R = 0.6$ . Comparison of the solution on the "fine" mesh with the "medium" one shows that when the grid is refined, the upper-wing surface pressure peak becomes steeper and higher while its position shifts slightly in outboard direction. There is an excellent agreement in the spanwise pressure distributions on the lower wing surface, as well as on the upper wing surface in the region close to the plane of symmetry and the region near the leading edge. The location of the cross-flow shock, in the "fine" grid result just outboard of the suction peak is recognized as the location where the spanwise pressure distribution steepens up. Comparison of the computed results with experimental data shows that for the lower wing surface the agreement is quite satisfactory. However, on the upper wing surface the Euler method grossly over-predicts the suction peak, also resulting in an overprediction of the lift coefficient by about 15 percent. This is primarily due to the circumstance that the Euler method lacks the ability to simulate flow separation from a smooth surface.

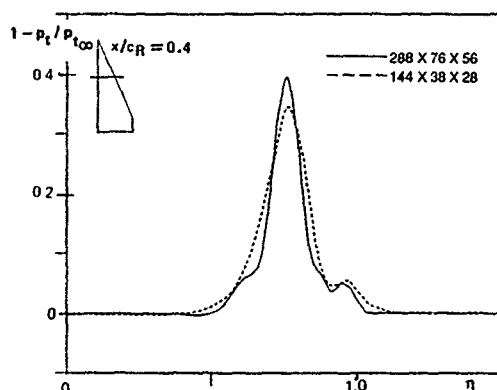
i.e. here the secondary separation, without explicitly incorporating some kind of a model for such viscosity dominated phenomenon. It might be expected that seen in the light of the findings of the study within the framework of potential-flow theory (see preceding chapter and Fig. 13), also within the framework of an Euler method the inclusion of a model for smooth-body separation will result in an improved correlation of predicted and measured surface pressure distributions.



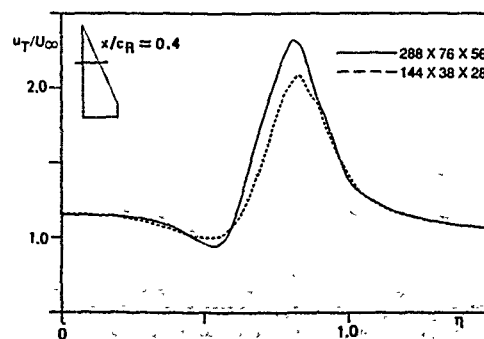
a) "MEDIUM" GRID 144x38x28 b) "FINE" GRID 288x76x56

Fig. 22 Contours of equal total-pressure loss in cross-flow plane.  $M_\infty = 0.5$ ,  $\alpha = 20$  deg

Figs. 22a and b show the cross-flow plane contours of equal total-pressure loss in the cross-flow plane at the station  $x/c_R = 0.6$  for the "medium" and "fine" grid, respectively. For inviscid flows without shocks the total pressure should be constant, equal to its free-stream value. In Euler methods errors are caused by the artificial dissipation introduced by the numerics. Primarily due to a fine grid resolution in the direction normal to the wing, the error in total pressure on the major part of the upper wing surface is small



a) TOTAL-PRESSURE LOSS



b) STREAMWISE VELOCITY COMPONENT

(less than 0.5% gain) for the solution obtained on both grids, with the "fine" having the smallest error. The error on the lower wing surface is due to the smaller gradients in the solution an order of magnitude smaller.

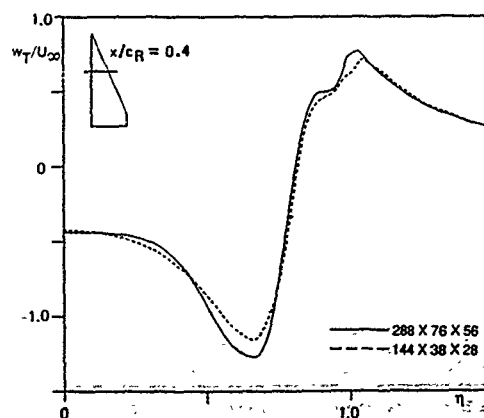
In the solution obtained on the "medium" as well as in one on the "fine" grid one observes that on the upper surface, at about 75% local semi-span, there is a sudden increase in total-pressure loss, to about 1% and 2% on the "medium" and "fine" grid, respectively. This increase is due to the occurrence of the (weak) cross-flow shock discussed above, which is strongest on the finer grid. Right at the leading edge, where the flow separates, without explicitly prescribing separation, total-pressure losses increase rather abruptly to values of about 10% of the free-stream value.

Figs. 22a and b clearly reveal that in the leading-edge vortex above the wing upper surface the total-pressure loss becomes largest, attaining values of 30 to 35%. The value of total-pressure loss at the center of the vortex core is higher in the "fine" grid solution than in the "medium" grid solution. However, on the "fine" grid the area in which there are significant total-pressure losses is smaller, i.e. it is more confined around the center of the vortex core. Apparently for the present subsonic case the reductions due to grid refinement of the errors in total pressure cause the area in which they occur to be reduced, but at the center of the core the reduction due to grid refinement cannot balance the increase of the errors associated with the improved resolution of steeper gradients.

Spanwise cross-sections taken at different chordwise stations of the wing indicate that there is very little variation with chordwise distance of the total-pressure loss, including the values at the center of the vortex core.

#### 5.5.4. Solution within leading-edge vortex core

As for the case of potential flow (see Fig. 15) the solution within the leading-edge vortex core is considered in more detail. Fig. 23 presents the "medium" and "fine" grid solution along a horizontal traverse through the center of the vortex core. The traverse is located in the plane  $x/c_R = 0.4$ . Fig. 23a shows the distribution of the total-pressure loss along the traverse. In this figure the effect of the fineness of the grid is clearly evident, namely the total-pressure loss decreases everywhere except near the center of the vortex core and in the leading-edge vortex "layer". In



c) VERTICAL VELOCITY COMPONENT

Fig. 23 Horizontal traverse through vortex core  
 $M_\infty = 0.5$ ,  $\alpha = 20$  deg



the "fine"-grid solution two passages of the layer through the traverse can be detected. Fig. 23b shows the distribution of the streamwise (parallel to the direction of  $\bar{U}_0$ ) velocity component of the velocity vector. At the center of the vortex core this component reaches values of about 2.3 times the free-stream value for the "fine" grid and about a 10% lower value on the "medium" grid. Crossings through the vortex layer appear as clearly steeper parts in the distribution. Fig. 23c displays the distribution of the vertical (circumferential) component of the velocity vector. Also here it is demonstrated that refining the mesh results in an improved resolution of steep gradients, i.e. the change in the direction of the velocity vector across the vortex layer is better represented on the "fine" grid.

It may be concluded that the computational results on the two grids are qualitatively the same, i.e. both solutions feature the same flow phenomena. Quantitatively there are some differences which can be understood in terms of differences in grid density. However, as far as the surface pressure distribution is concerned the differences between the results on the two grids are considerably smaller than the differences with experimental data.

In Ref. 155 it has been demonstrated that the differences between an incompressible Euler solution and a potential-flow panel-method solution are small.

#### 5.5.5. Total-pressure losses

As far as the total-pressure losses in the numerical solution is concerned it will be clear that they are largest in regions with the largest gradients in the flow field, such as occur in regions where vorticity is or becomes concentrated. For the present applications these regions are the center of the vortex core and the part of the leading-edge shear layer closest to the leading edge where it is strongest. It has been conjectured by amongst others Hirschel (Ref. 2) and Powell (Refs. 139, 156) that simulating numerically a shear layer employing an Euler method as the one used above implies total-pressure losses. Here it will be shown that this is not necessarily the case. Starting from Crocco's relation

$$\frac{\partial \bar{u}}{\partial t} + \bar{v}h = \tau \bar{S} + \bar{\omega} \bar{\omega} \quad (10a)$$

where  $h$  is the total enthalpy ( $h = E + p/\rho$ ),  $\bar{\omega}$  is the vorticity vector ( $\bar{\omega} = \nabla \times \bar{u}$ ) and  $S$  is the entropy. The latter can be related to the total pressure  $p_t$  through

$$p_t/p_\infty = \exp(-\Delta S/R) \quad (10b)$$

Since in unsteady inviscid flow it follows from the equation for the conservation of energy that  $h$  is constant, one finds from Eqs. (10a) and (10b) that in case  $\bar{u}$  and  $\bar{\omega}$  are parallel (so-called Beltrami flow) the total pressure will not change across the layer. Are there distributions of  $\bar{u}$  and  $\bar{\omega}$  that satisfy these conditions? Decomposing the velocity vector in terms of its component along the average of the velocity at the upper and the lower side of the layer and a component normal to this (see Fig. 24) as:

$$\bar{u} = U_0 (a(z)\bar{e}_1 + b(z)\bar{e}_2) \quad (10c)$$

it follows from the definition of the vorticity that:

$$\bar{\omega} = U_0 (b'(z)\bar{e}_1 + a'(z)\bar{e}_2) \quad (10d)$$

where  $z \in [-\delta, \delta]$ , i.e. within the layer. Setting then  $\bar{u} \times \bar{\omega} = \bar{0}$  yields:

$$a(z) = 1/\cosh f(z) \quad (10e)$$

$$b(z) = \tanh f(z) \quad (10f)$$

where  $f(-\delta) = -f(\delta)$ . It may be expected that these types of total-pressure conserving velocity profiles can be supported by a discrete Euler solution as long as locally the thickness of the layer is of the order of 3-5 cells of the grid. This is confirmed by the cross-flow iso-contour plots of the total pressure, such as Fig. 22, where the total-pressure losses in the leading-edge vortex layer rapidly diminish with distance from the leading edge where the vorticity is less high and the numerical dissipation has spread the layer to a sufficient degree.

Above kinematical arguments are quite similar to the ones used by Hirschel and Powell, but with the difference that in above analysis the component of the velocity along the average direction ( $\bar{e}_1$ ) is allowed to vary through the shear layer while it was held constant by Hirschel and Powell.

An additional important question to be posed is whether the total-pressure losses invoked by the numerics (i.e. errors of the numerical method used to solve the inviscid flow equations) in the insufficiently resolved thin shear layer near the leading edge remain local or convect somehow, subject to some diffusion, along the vortex layer towards the center of the vortex core. The present (subsonic) results strongly suggest that the errors have a local implication only, i.e. that the numerical total-pressure losses behave differently from the total-pressure losses encountered in the real viscous flow.

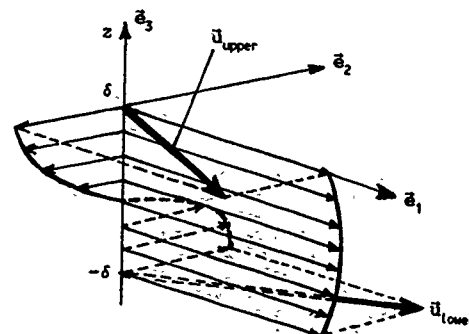


Fig. 24 Velocity distribution through finite-thickness shear layer

As far as the vortex core is concerned it can be remarked that Stewartson & Hall (Ref. 157) derived a constant-total-pressure Euler solution for the case of an isolated slender conical vortex core in incompressible flow, which can be extended to the slender but non-conical case (Ref. 82). The inviscid solution is valid up to the axis of the core where a singularity is present. By matching a viscous solution for the region very close to the core axis (the viscous subcore) to the inviscid solution for the outer parts of the core, the inviscid flow singularity could be removed. In this model total-pressure losses occur in the viscous subcore only, while in the real vortex the whole vortical flow region exhibits total-pressure losses. In spite of this the velocity and pressure distribution through the core agree satisfactorily with Earnshaw's (Ref. 17) experimental data. Brown (Ref. 158) considered the case of an isolated slender conical vortex core in inviscid compressible flow and also found an inviscid constant-total-pressure solution. In these two, in an ap-

proximate framework derived, but analytical, inviscid solutions singularities appear at the center of the core. The large gradients near the singularities will not be resolvable on a finite grid of a discrete solution leading to total-pressure losses in the vortex core. However, as the mesh is refined more and more the total-pressure losses in the numerical Euler solution will be confined to an region near the sharp leading edge and a region around the center of the vortex core and Beltrami flow will prevail everywhere else.

In Euler solutions on a finite grid it appears in general that for a given geometry at one specific free-stream condition ( $M_\infty, \alpha, \beta, \dots$ ) the total-pressure loss at the very center of the vortex core is rather insensitive to computational parameters, such as the coefficients in the explicitly added artificial dissipation terms, as well as the density of the grid, e.g. see Jacobs et al. (Ref. 152), or, but to a lesser extent, the numerical algorithm used to solve Euler's equations (Ref. 159). This insensitivity has been found especially for Euler solutions at transonic and supersonic free-stream Mach numbers (see also next section), and to a lesser extent at lower Mach numbers where for given incidence etc., the total pressure losses (in terms of  $p_{t0}$ ) are smaller. For conical flow about delta wings at supersonic free-stream Mach numbers Powell (Refs. 139, 156), Murman et al. (Refs. 137, 160) investigated (central-difference) Euler solutions and found them to be insensitive to computational parameters, implementation of boundary conditions, grid density, etc.. Furthermore, the level of the total-pressure loss at the center appears to agree with experimental data. However, it must be concluded that also at transonic and supersonic Mach numbers this is fortuitous and the total-pressure loss at the center of the core, just like in the rest of the core, is a purely spurious numerical artifact.

On the other hand, similar to the potential-flow solutions, the position of the vortex core, its vorticity contents, as well as the flow outside the core appear to be influenced only very little by exactly what occurs within the vortex core. However, it is to be expected that the characteristics, such as the onset of vortex breakdown, of the vortex core are affected by the numerically induced total-pressure losses within Euler solutions. Models for isolated axisymmetric conical vortex cores have been considered by Powell & Murman (Ref. 161) for incompressible viscous flow and by Mayer & Powell (Ref. 162) for both incompressible and compressible viscous flow. For incompressible flow it is shown that the total-pressure loss at the center of the core is only a function of the swirl (= circumferential / axial component of the velocity) at the edge of the vortex core, i.e. not of the Reynolds number. However, the radial distribution of the total-pressure loss does depend on Reynolds number, as does the location of the edge of the core. The latter is unfortunate, since the dimension of leading-edge vortices is almost independent of Reynolds number.

Some investigators have pursued total-pressure-loss free Euler solutions of the Euler equations. For conical supersonic steady flow Marconi (Ref. 163) used Moretti's "lambda scheme" based on characteristics, in which the bow shock is fitted and no artificial dissipation is required. The axial component of the velocity is obtained from the condition that the total enthalpy is constant and entropy is traced along streamlines. Crocco's relation, Eq. 10a, then yields that  $u \times \omega = 0$ . For the case with weak bow shock considered, i.e. a flat-plate 75-deg delta wing at  $M_\infty = 1.5$  and  $\alpha = 4$  deg, the flow indeed separates at the leading

edge without an explicit Kutta condition and a leading-edge vortex is formed. It has been checked numerically that  $\bar{v}_n$  and  $\bar{v}_s$  are at machine-zero levels. Indeed, it turns out that the magnitude of  $\bar{u} \times \bar{\omega}$  is acceptably small everywhere, except close to the leading edge and near the center of the vortex core where larger values are found. It also turned out that the cross-flow-plane velocity components and the static pressure are not much different from the ones found using a Jameson-type Euler solver, while the chordwise velocity component is affected somewhat. Kandil et al. (Ref. 164) found similar results. They investigated several non-standard sets of non-standard zero-total-pressure-loss Euler equations by replacing the energy equation by a homentropic or isentropic condition and/or the x-momentum or continuity equation by the condition that the total enthalpy is constant.

Finally the Eulerian/Lagrangian scheme proposed by Felici & Drela (Ref. 165) is to be mentioned. In this scheme numerical diffusion of the Euler solution in vortical flow regions is reduced by locally correcting the Euler solution employing a Lagrangian (vorticity and entropy) particle-tracking solution.

5.5.6. Transonic flow  $M_\infty = 0.85$ ,  $\alpha = 20$  deg  
The solutions on the "medium" and "fine" grids were obtained with the parameters controlling the dissipative terms set at their standard values for transonic flow, i.e. using both the second- and the fourth-difference dissipative terms.

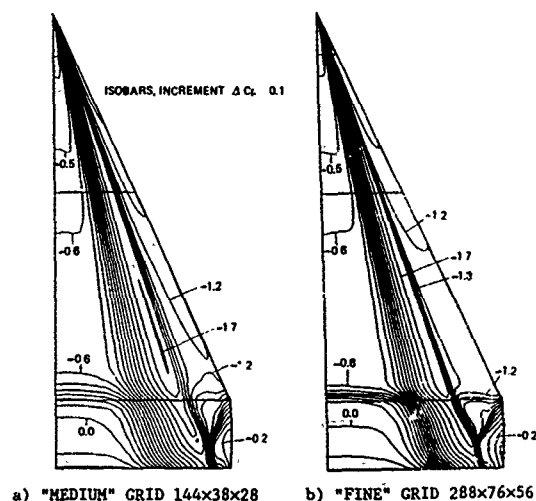
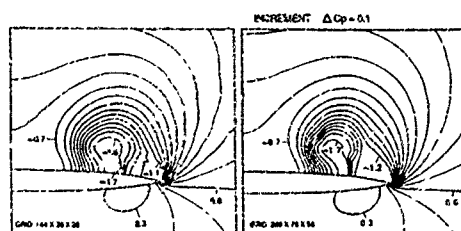


Fig. 25 Isobars on wing upper surface  
 $M_\infty = 0.85$ ,  $\alpha = 20$  deg

In Fig. 25a the upper wing surface isobar pattern is presented for the "medium" grid, in Fig. 25b for the "fine" grid. Both figures indicate that the formation of the vortex starts very close to the apex. Furthermore, in both pictures the closely-spaced isobars outboard of the pressure minimum indicate the presence of a "cross-flow shock", most clearly so on the rear part of the wing. On this part of the wing, outboard of the cross-flow shock a second shock appears. At about 93% root chord these two shocks merge and form a Y-shaped shock system, with as stem the strong cross-flow shock downstream of the 93% root chord station. On the central part of the wing at about 83% root chord a third shock appears, the so-called "rear shock". This weak shock is normal to the plane of symmetry and extends some distance in spanwise di-

rection. Comparison of the upper wing surface isobar pattern of the solution on the "fine" grid with the one on the "medium" mesh shows that on the "fine" grid the shocks are steeper, but more importantly, that no new flow features evolve. Compared to the pressure distribution at the lower Mach number the suction peaks are much reduced in height. The suction peak is now also in height about constant in chord-wise direction, i.e. at least on the forward part of the wing the surface pressure distribution is more conical.



a) "MEDIUM" GRID 144x38x28 b) "FINE" GRID 288x76x56

Fig. 26 Isobars in cross-flow plane.  
 $M_\infty = 0.85$ ,  $\alpha = 20$  deg

Fig. 26 presents the cross-flow-plane isobar pattern in the plane  $x/c_x = 0.6$  as obtained from the solution on the "medium" and the "fine" grid. For this case of compressible vortex flow the cross-flow shock is strong and clearly evident in the plot. The shock appears to bridge the gap between the wing upper surface and the vortical flow region. Outboard (i.e. downstream) of the cross-flow shock and underneath the shear layer emanating from the leading edge there exists a relative large region where the static and  $ac$  will be seen later on also the total pressure  $ac$  only slowly changing. Especially on the "fine" grid (Fig. 26a), where the shock is somewhat stronger, this is a rather extensive portion of the flow field. The "rear shock" is clearly visible in the isobar pattern in the plane of symmetry (Fig. 27), obtained from the solution on the "fine" grid. Although it is a weak (normal) shock it apparently extends quite some distance into the flow field.

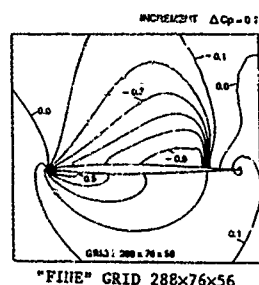


Fig. 27 Isobars in the plane of symmetry.  
 $M_\infty = 0.85$ ,  $\alpha = 20$  deg

In Fig. 28 (note change in vertical scale compared with Fig. 21) the spanwise surface pressure distribution at  $x/c_x = 0.6$  computed on the "medium" and the "fine" grid are compared with each other and with experimental data of the International Vortex Flow Experiment (Ref. 56). For the lower wing surface the agreement of computed and measured pressure distribution is excellent. For the upper wing surface it is shown that in the computed results the cross-flow shock is located between 70 and 75% local semi-span; in the measured data the much weaker cross-flow shock is situated further inboard, namely at about 60% local semi-span. The experimental data further indicate, as

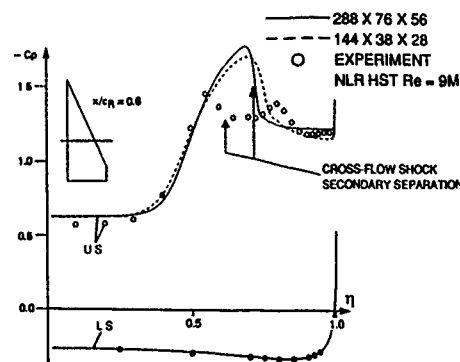


Fig. 28 Spanwise pressure distribution  
 $M_\infty = 0.85$ ,  $\alpha = 20$  deg

may be concluded from the pronounced second suction peak, that the cross-flow shock provokes an early secondary separation that results in a relatively strong secondary vortex. As for the case of subsonic vortex flow it is clear that in order to improve the correlation of the numerical simulation with experiments secondary separation effects must be included in the simulation. However, because of the less negative pressure coefficients for the higher Mach number, for the present case the effect of secondary separation is less severely felt in the integrated force and moment coefficients.

Fig. 29 presents the chordwise surface pressure distribution along the section situated in the plane of symmetry. Computed results are compared with experimental data from Ref. 151. It is seen that on the "fine" grid the "rear shock" is better resolved than on the "medium" grid, but also that it is at about the same position on both grids. There is a difference between the predicted and the measured position and strength of the "rear shock", presumably in part due to viscous effects. On the other hand, it may be expected that the position and strength of the leading edge vortex, the cross-flow shock and the rear shock are strongly interrelated. Improving the numerical simulation by including a secondary separation model will affect all three flow features. In terms of lift coefficient the Euler solutions result in values which are about 7.5% higher than the value found in the experimental investigation.

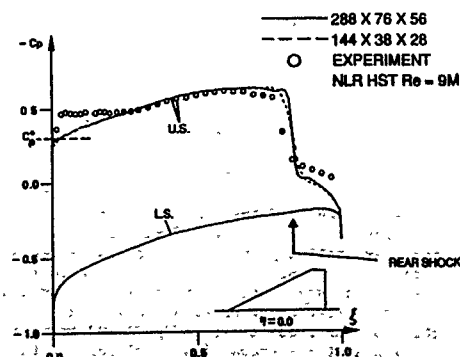
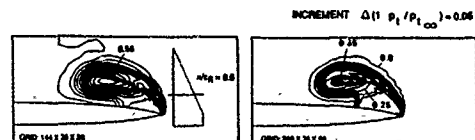


Fig. 29 Chordwise pressure distribution  
 $M_\infty = 0.85$ ,  $\alpha = 20$  deg



In summary it can be concluded that comparison of the results on the "medium" and on the "fine" grid indicates that for the surface pressure distribution increasing the grid density results in a steeper but also somewhat stronger "cross-flow shock" shifts the suction peak, i.e. the position of the vortex, slightly inboard steepens the "rear shock" has no effect on the lower wing surface pressure distribution.

Fig. 30a presents the cross-flow-plane pattern of contours of equal total-pressure loss in the plane  $x/c_x = 0.6$ , as obtained from the solution on the "medium" grid. Fig. 30b shows the corresponding plot for the "fine" grid. For this case of compressible vortex flow the cross-flow shock is strong and clearly shows up in plot. As the flow passes through the cross-flow shock the total pressure is reduced by 13-14% on the "medium" and by 23-24% of its free-stream value on the "fine" grid. For the latter grid the shock is stronger, which explains the larger loss in total pressure. On the wing surface away from the shock the errors in total pressure are smaller on the "fine" grid than those on the "medium" grid and comparable to those encountered at the lower Mach number. Outboard (i.e. downstream) of the cross-flow shock and underneath the shear layer emanating from the leading edge there exists a relative large region where the total pressure is about constant, equal to the lower value outboard of the shock. Across the shear layer from the leading edge the total pressure jumps again to its free-stream value. Fig. 30 shows that at the center of the vortex core the total pressure drops to 45 percent of its free stream value, both on the "medium" and on the "fine" grid, higher for transonic flow than for subsonic flow primarily because  $C_{p, \text{max}} + M_\infty^2$ . Further note that compressibility has a considerable effect on the shape of the vortex core. Increasing the Mach number results in a more flattened vortex core, which as a result of the interaction with the cross-flow shock is at a more inboard location. As for the lower Mach number the total-pressure loss at the center of the core does not vary very much with longitudinal distance along the vortex core.

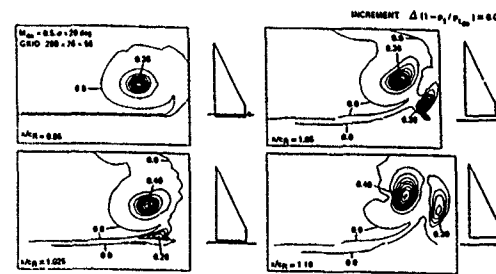


a) "MEDIUM" GRID 144x38x28 b) "FINE" GRID 288x76x56

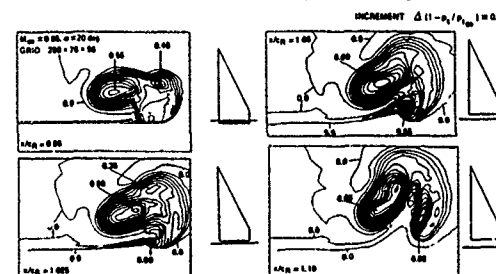
Fig. 30 Contours of equal total-pressure loss in cross-flow plane.  $M_\infty = 0.85$ ,  $\alpha = 20$  deg

Comparing the cross-flow-plane results obtained on the "medium" grid with those obtained on the "fine" grid it is observed that on the "fine" grid the region of the flow field with total-pressure losses has shrunk in dimension. However, the minimum total pressure, which occurs at the center of the vortex core, is about the same for both grids. It is hypothesized that as far as the total-pressure loss near the center of the core is concerned here also refining the mesh tends to decrease the discretization error and at the same time increases the gradients in the flow solution and thus the discretization error, now apparently such that, on the present type of grid and for this particular free-stream flow condition and this setting of the artificial dissipation parameters, the net effect is about the same loss in total pressure at the center of the core.

The overall conclusions that can be drawn for this flow condition are very similar to the ones drawn for the subsonic flow condition, namely that grid



a) SUBSONIC FLOW  $M_\infty = 0.5$ ,  $\alpha = 20$  deg



b) TRANSONIC FLOW  $M_\infty = 0.85$ ,  $\alpha = 20$  deg

Fig. 31 Contours of equal total-pressure loss in near-wake cross-flow plane ("fine" grid)

refinement does not result in new flow features and differences between computed and measured results, though considerably smaller here, are due to the Euler method not simulating secondary separation. In addition it is demonstrated that effects due to compressibility result in very significant changes in the flow solution, not unlike those found in the experimental investigation of for instance Bannink et al. (Ref. 166) for a similar 65-deg delta-wing configuration.

#### 5.5.7. Flow field in the near wake

The development of the flow in the near wake just downstream of the trailing edge is considered for both the subsonic and the transonic free-stream Mach number. This region of the flow field is of extreme importance for cases at somewhat higher incidences where the experiments (e.g. Refs. 56, 151 and 166) have shown that vortex breakdown occurs. For low subsonic flow Hummel's (Ref. 20) mushroom-shaped vortex wake consisting of the leading-edge vortex and the trailing-edge vortex is well known. It forms, even in inviscid flow, as has been demonstrated in the preceding chapter for the case of potential flow (Ref. 82). Fig. 31a shows for the subsonic case ( $M_\infty = 0.50$ ,  $\alpha = 20$  deg) the contours of equal total-pressure loss in four consecutive planes  $x/c_x = \text{constant}$ , namely  $x/c_x = 0.6, 1.0, 1.025$  and  $1.10$ , as obtained from the solution on the "fine" grid. This figure clearly indicates the formation of a mushroom-shaped wake with two regions of increased total-pressure losses, indicative for regions with vortical flow. In the near wake the leading-edge vortex can be identified as the continuation beyond the trailing edge of the region with significant total-pressure losses, such as shown in Fig. 22b and in the top figure of Fig. 31a for the plane  $x/c_x = 0.6$  and  $1.0$ , respectively. This vortex moves outboard and upward. Apparently because in the region considered the grid is still relatively fine and not yet stretching too much the vortex remains compact and is not diffused. The level of the total-pressure losses at the center of the core remains at the same level ( $\approx 35-40\%$ ).

The formation of the trailing-edge vortex starts right at the trailing edge ( $x/c_x = 1.0$ ) as evidenced by the local maximum (0.15) in the total-pressure loss at about 90% semi-span, caused by the high gradients in the solution in that region. Further downstream a vortex-like structure develops with increasing total-pressure losses at its center. Eventually, just like in low-speed flow a mushroom-shaped vortex wake, consisting of the leading-edge and the trailing-edge vortex evolves. For the transonic case ( $M_\infty = 0.85$ ,  $\alpha = 20$  deg) the contours of equal total-pressure are presented in Fig. 31b, for the same 4 cross-flow planes, again obtained from the solution on the "fine" grid. For the case of compressible vortex flow the situation is complicated by the presence of the strong cross-flow shock. It follows from Fig. 31b that downstream of the trailing edge the cross-flow shock disappears very rapidly (actually between  $x/c_x = 1.01$  and  $1.025$ ). As for the lower Mach number the leading-edge vortex continues downstream of the trailing edge, again without much diffusion, but now it does not appear to move upward and outboard that much. Furthermore, the formation of the trailing-edge vortex, by the roll-up of the wake, is now more vigorous resulting in higher total-pressure losses at its center. At  $x/c_x = 1.1$  the wake has again a mushroom-shaped structure but now occupying a larger area in the cross-flow plane than is the case for the lower Mach number. In the first two cutting planes presented in Fig. 31b an additional flow feature is observed, characterized by a local minimum in the total-pressure distribution. This feature can be traced back to the kink in the leading edge, i.e. to  $x/c_x = 0.85$ , and is termed the "tip vortex". Seen in consecutive cross-flow planes this vortex travels around the leading-edge vortex and at  $x/c_x = 1.05$  is so close to the core of the leading-edge vortex that it can no longer be distinguished and may be assumed to be fully merged with the latter.

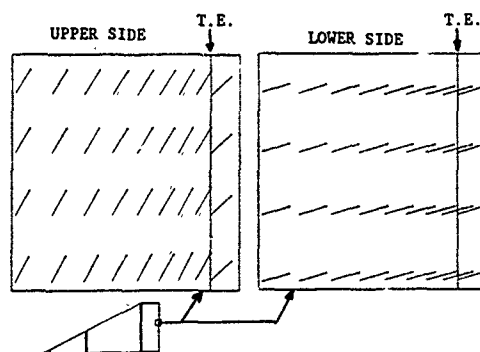


Fig. 32 Surface velocity vectors near the trailing edge,  $M_\infty = 0.85$ ,  $\alpha = 20$  deg ("fine" grid)

#### 5.5.8. Flow near the sharp edges

In the following the solution near the sharp trailing and leading edge is considered in some more detail for the transonic case ( $M_\infty = 0.85$ ,  $\alpha = 20$  deg). It has been verified that for the subsonic case the solution near the edges behaves qualitatively quite similar to the transonic case discussed below. Fig. 32 presents the velocity vectors (in the cell-face midpoints of the "fine" grid) on the upper and lower wing surface in a small region close to the trailing edge. The position chosen on the trailing edge is a location where the magnitude of the trailing vorticity with its main component perpendicular to the edge, is large. It is shown that at the trailing edge the velocity vector on the upper and the one on the lower surface are equal in magnitude but different in direction, resulting in a vorticity vector of negative sign. In truly inviscid (poten-

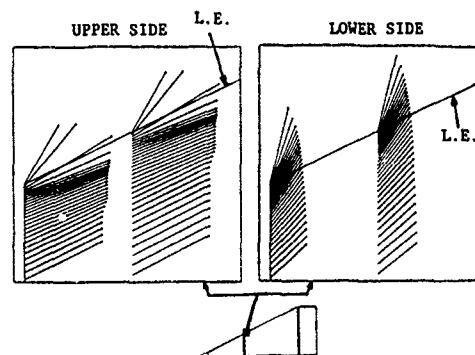


Fig. 33 Surface velocity vectors near the leading edge,  $M_\infty = 0.85$ ,  $\alpha = 20$  deg ("fine" grid)

tial) flow a vortex sheet will form which, because of the nonzero trailing-edge angle, will leave either the upper or the lower surface tangentially (e.g. Mangler & Smith, Ref. 167). For the present flow conditions this contact discontinuity will be tangential to the lower wing surface, implying that on the upper wing surface the velocity right at the edge (still being a weak singular point) has to be directed along the edge. On the upper side of the vortex sheet, just downstream of the trailing edge, the velocity vector will then to some extent turn back in chordwise direction. In the present discrete solution of the Euler method it appears that on the upper surface, 2 to three grid cells, upstream of the trailing edge the velocity vector already starts to turn in chordwise direction.

Fig. 33 presents the corresponding velocity vectors in a small region close to the leading edge at about the mid-chord position. Here the main component of the vorticity vector is along the edge. It is shown that at the leading edge the velocity vector on the upper and the one on the lower surface are equal in magnitude but different in direction, resulting in a vorticity vector of positive sign. In an inviscid (potential) flow model the leading-edge vortex sheet will be tangential to the lower wing surface, so that on the upper surface the velocity at the edge should be tangential directed along the edge, turning away from the edge on the (here strongly curved) vortex core. However, in the present discrete solution of Euler's equations the surface velocity vector starts to turn already 4 to 5 cells before the leading edge is reached.

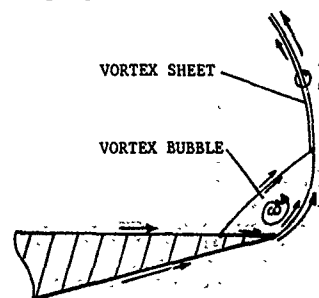


Fig. 34 Possible inviscid separation at a sharp edge

It might be conjectured that for the case of flows at high Reynolds numbers an inviscid model in which regions with distributed vorticity are allowed, like sketched in Fig. 34, forms an appropriate alternative model for the classical (potential-flow) sharp-edge separation model of Ref. 167. It concerns a model in which the separation at the sharp edge results in a bubble with distributed vorticity situated in the corner between

the vortex sheet and the wing upper surface. This greatly relieves the singularity at the edge, facilitating a more smoothly variation of the velocity field in the immediate neighborhood of the sharp edge. Above bubble-type model has been inspired by Küchemann's (Ref. 168) bubble-type separation model for the flow near the trailing-edge of an airfoil section.

#### 5.6. Application of Euler methods to more complex configurations

There have been already quite some attempts to apply time-stepping Euler methods to more complex configurations in subsonic and transonic speeds. An early example is given in Ref. 169, where an explicit finite-volume modified MacCormack predictor-corrector scheme is employed to solve the Euler equations on a grid with about 525K cells around the F-16. At the free-stream condition  $M_\infty = 0.9$ ,  $\alpha = 4.1$  deg convergence difficulties were reported while also comparison with experiment revealed some deficiencies. Argawal et al. (Ref. 170) use an Euler code based on Jameson's Flo57 (Ref. 113), enhanced with amongst others a TVD formulation, to simulate the flow about generic fighter consisting of a wing, body, horizontal and vertical tails and a faired-in inlet. The 269K-cell grid is still rather coarse, possibly for the higher incidences contributing to a less satisfactory correlation of predicted surface pressures with experimental data. Goodsell et al. (Refs. 171, 172) apply an Euler code also based on Jameson's Flo57 (Ref. 113) to the generic fighter configuration tested by Erickson (Ref. 6), i.e. a configuration with a sharp-edged 55-deg swept cropped delta wing, a fuselage with relatively long forebody with or without a (decoupled) chine and a bump as canopy. Computed results, obtained on a grid of about 425K cells, for subsonic and supersonic flow conditions are compared with experimental data. It appears that in case of the fuselage/wing configuration attached flow is predicted quite satisfactorily. At the higher incidences the flow is dominated by the smooth-surface separations on the forebody, precluding good correlation with results of an Euler method. For the fuselage/wing/chine combination the sharp-edged chine fixes the separations on the forebody and a much better correlation of theory and experiment is obtained. For flow conditions at which the experimental data show the occurrence of vortex breakdown, the Euler results become unstable and exhibit an oscillatory behavior. Application of a Flo-57 type of Euler method to a canard-wing-body and to a rather complete close-coupled wing-canard fighter configuration, the first one at  $M_\infty = 0.9$  on several grids with up to 500K points, the second one at  $M_\infty = 1.19$  employing a grid with about 375K points, has been reported by Raj et al. (Ref. 173) showing reasonable agreement of predicted and measured surface pressures, with some deviations occurring due to shock/boundary-layer interaction.

#### 5.7. Euler methods and vortex breakdown

It has been claimed that the finite-volume time-stepping methods for solving Euler's equations also simulate vortex breakdown. Experimental evidence indicates that vortex breakdown, at least its onset, depends only weakly on Reynolds number, so indeed, there may be some possibility that it can be modeled by Euler's equations. In experiments vortex breakdown, or burst, is characterized by a sudden expansion and a change in the coherent structure of the vortex core. Two types of breakdown have been identified, bubble-type and spiral-type, though some investigators argue that this distinction cannot really be made, while others find even more types. For the Reynolds numbers of interest here usually the spiral type of breakdown occurs. For both types the axial

component of the velocity decelerates and stagnates on the vortex axis and a region with reversed flow appears apparently with (bubble) or without (spiral) a zone with recirculating flow, i.e. in the vortex core the flow changes from a jet-like (as in Fig. 22c) to a wake-like type of flow. Downstream of the stagnation point the flow usually becomes unsteady and turbulent.

The process of leading-edge vortex breakdown is a three-dimensional unsteady and highly nonlinear problem and is not yet fully understood. Important ingredients appear to be

- (i) an in axial direction adverse external pressure gradient and
  - (ii) the strength (circulation) or rather the swirl ratio (circumferential / axial component of the velocity) at the edge of the core.
- If there is an adverse pressure gradient and the swirl ratio exceeds a critical value (slightly above 1.0) vortex breakdown will occur.

The role of the total-pressure losses at the center of the vortex core in the breakdown process is not clear. However, if these total-pressure losses play an important role (as conjectured by Lambourn & Bryer, Ref. 30) it might also be expected that viscosity and the Reynolds number would play an equally important role, precluding an inviscid model to be used for predicting vortex breakdown. This appears to be the case when (bubble-type) vortex breakdown is explained in terms of an analogy with boundary-layer separation, i.e. the flow with low total-pressure encountering an adverse external pressure gradient. However, also note that in the case of the boundary layer the pressure through the layer is constant and the velocity near the wall is low, while in case of the vortex core the pressure decreases rapidly towards the axis and the velocity is high although both quantities are lower than they would have been in an inviscid flow.

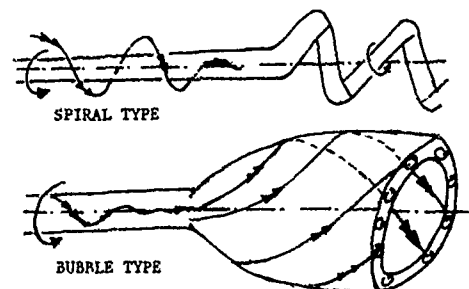


Fig. 35 Possible inviscid vortex breakdown

In the following a possible explanation of the spiral-type breakdown is given in terms of inviscid flow, derived from characteristics of vortex cores given in Ref. 82. In the vortex core, upstream of the breakdown point, the vortex lines (curves at each point tangent to the vorticity vector, i.e., if Crocco's relation is satisfied, curves identical to stream lines) spiral helicoidally inwards, from the edge towards the axis of the core (see sketch in Fig. 35). In this process the circumferential component of the vorticity is converted into an axial component and at the axis, where the vortex lines are directed along the axis, the vortex lines run closely together. This implies that near the axis the vorticity is highest. Associated directly with the axial component of the vorticity is the distribution of the circumferential velocity component, while the circumferential component of the vorticity induces the axial component of the velocity, i.e. the component that becomes large at the axis.

Upstream of vortex breakdown the axial component of the velocity near the axis of the core is retarded and even reversed in direction. In an inviscid flow model with distributed vorticity this implies that the circumferential component of the vorticity has to switch sign somewhere as it is convected from the edge of the core towards the center of the core. One possibility to accomplish this is that the region with highly concentrated vorticity near the center of the core (the "sub-core") is regarded as a vortex filament of small but finite cross-sectional dimension, embedded within the remainder of the rotational core. If curved such a filament may be subject to some torsional instability mode (e.g. Betchov, Ref. 174) and the core axis could start to meander in a spiral fashion, the direction of the spiral being opposite to the direction of the circulation of the filament. The tilting of the filament (that region of the core with the highest vorticity contents) then provides the large circumferential vorticity component in the sought for direction, and associated with it a large axial velocity component reducing abruptly the net velocity in upstream direction. Whether the spiralling vortex core is a standing wave and steady or a travelling wave and unsteady or breaks up rapidly is to be investigated. In this model the outer part of the vortex core has still the more or less coherent structure of the original vortex core, while closer to the axis the vortex lines spiralling around the meandering core center yield a less coherent picture. The internal structure of the vortex filament will be determined by viscosity, but its strength and position in space will be determined by the external, basically inviscid flow field.

An alternative to the meandering vortex filament, yielding a more continuous description of the vorticity and velocity distribution in the inner parts of the vortex core, is that the sub-core "opens up". In this model it is conjectured that the axial vortex lines close to the axis suddenly start to spiral (counter-circulation wise) around a central region, so forming a cigar-shaped shell of high vorticity (Fig. 35).

A possible further alternative explanation for the (inviscid) onset of vortex breakdown is that the outer turn of the leading-edge shear layer becomes unstable near the trailing edge and prevents the shear layer from rolling up into a tight vortex core. However it seems unlikely that this can result in a situation in which the circumferential component of the vorticity switches sign and a region with reversed flow is induced.

Quite some research on vortex breakdown (e.g. Pagan & Benay, Ref. 175; L  et al., Ref. 176), both experimental and theoretical, has concentrated on confined vortex flow inside a tube (see Hall, Ref. 31 and review by Leibovich, Ref. 177). It is not quite clear whether this type of vortex has exactly the same characteristics as a leading-edge vortex resulting from the roll-up of a free shear layer.

Experimental investigations including flow-field surveys on delta wings, above the incidence at which vortex breakdown starts, have been pursued, at low speed, by amongst others Kegelman & Roos (Refs. 33, 34, 35), Payne et al. (Refs. 37, 178) and Hawk et al. (Ref. 179). In some of these investigations the spiral type of instability has been observed.

In the applications of Euler methods to configurations with leading-edge vortex flow "vortex breakdown" has been reported on several occasions. Probably the first ones were Hitzel & Schmidt (Ref. 125) who reported, a presumably steady, "vortex breakdown" for a round-edged arrow wing at  $M_\infty = 0.5$  to be the cause of the lift beginning to

decrease at 35 deg incidence. Rizzi & Purcell (Ref. 135) report for a thin round-edged twisted and cambered cropped (55/45-deg) double-delta wing at  $M_\infty = 0.3$  and 10 deg incidence a grid sensitivity investigation. For the coarse (76,800) O-O type grid the Euler method converged, for the much finer (614,400) O-O grid a converged solution was obtained with about the same integrated forces and moments, but with smaller-scale features appearing in the free shear layer from the wing leading edge, which is conjectured to be the onset of the instability of the vortex core. Continuing this investigation Rizzi & Purcell (Ref. 180) (see also Murman & Rizzi, Ref. 137) report convergence on the coarse mesh also for higher incidences. On the fine mesh the situation is different, at 12.5 deg incidence the flow becomes unsteady while at 20 deg incidence the flow is steady but the vortex appears to be fully "burst" and the lift is lower than at 12.5 deg incidence. On the surface relatively large errors (total-pressure losses) occur. For this case of rather low sweep, experiments indicate vortex bursting at higher incidences than 10 deg, so the onset of "vortex breakdown" is predicted prematurely. Raj et al. (Ref. 145) found that the solution on a C-H type of grid with about 105,000 cells became unsteady, i.e. that the solution procedure did not converge, for a straked wing-body configuration at high incidence. For the strake-off case the critical incidence lowered from 30 to 18 deg. Pao (Ref. 181) used Raj's (Ref. 145) TEAM Euler code to investigate the flow about the F-1063 aircraft (60-deg round-edged thin delta wing) and reported for a C-H grid with about 80,000 cells failure of the solution to converge at 30 deg subsonically and at 19 deg transonically. In these two cases a region with reversed flow started to occur at 23 and 17 deg, respectively.

Hitzel (Refs. 142, 143) presents Euler solutions for the sharp-edged 65-deg delta wing considered earlier in this chapter. For  $M_\infty = 0.85$  and  $\alpha = 24$  deg experiments indicate that vortex breakdown occurs above the configuration. In the computed results complex flow structures appear which include shocks and regions with reversed flow. It is also indicated that in solutions for different grid densities rather different features may appear. Also for the subsonic case  $M_\infty = 0.4$ ,  $\alpha = 28.7$  deg results with reversed flow regions are given. Longo (Ref. 140) applies a cell-vortex Euler method to the same 65-deg delta wing employing an O-O type grid with about 110,000 points. He finds that reversed flow indicates the onset of "vortex breakdown". Furthermore it is found that while the total-pressure loss at the core axis is more or less independent on the parameters governing the explicitly added artificial dissipation terms, the location where reversed flow appears first is a function of these parameters. In Ref. 141 Longo shows that for the case of a canard/delta wing configuration the Euler method appears to simulate realistically the "bulging" of the canard vortex as it undergoes reversed flow and subsequent restructuring in the region between the canard and the main wing. Goodsell et al. (Ref. 172) report "vortex breakdown" to occur in their Euler solutions for a chine-delta configuration.

The Euler methods discussed above are all central-difference type of methods. O'Neil et al. (Ref. 144) present results of an upwind Euler method which also show "vortex breakdown" for sharp-edged 60 and 70-deg delta wings at low speed and higher incidences, i.e. slower convergence though almost always convergence is achieved for the integrated forces and moments. For their H-O type of grid with about 170,000 points they observe the spiral type of meandering of the vortex core. They argue that the onset of vortex breakdown can be deter-

mined employing an Euler code by using a so-called "shear-layer-collapse" criterion. This criterion considers, in cross-flow planes, the locus mapped out by the point at which the swirl ratio reaches its maximum on successive radial lines emanating from the vortex axis. For part of the circle the locus turns out to coincide with the shear layer from the leading edge, rather than to identify the edge of the vortex core. It is observed that "vortex breakdown" is preceded by the swirl ratio having its maximum at the axis and consequently a part of the locus (not the shear layer as they claim) collapses onto the axis. Actually this "collapse" occurs because at the axis of the core the axial component of the velocity becomes small and even zero yielding large values of the swirl ratio. It is shown that the locus obtained from computed results correlates reasonably well with the locus derived from measured data. Although the determination of the locus requires some criterion for finding the axis of the core, which may be a non-trivial matter for "burst" vortices, while also the notion of decomposing the velocity in an axial and a circumferential component is not really relevant for parts of the flow field not close to the vortex core, the locus provides some measure of the structural change of the vortex core near breakdown.

For all of above pseudo-time marching Euler methods the non-converged ("unsteady") solutions are physically meaningless and often large errors in total pressure (losses and gains) appear, not only in the flow field but also on the upper surface of the configuration. It appears also that as far as the onset of vortex breakdown in converged Euler solutions is concerned quite often observed similarities between experimental findings and computational results of Euler methods are spurious numerical effects associated with the particular discretization used. It is not uncommon that compared with experiments "vortex breakdown" occurs at too high an incidence on relatively coarse meshes and prematurely on fine meshes. This means that detailed studies of the influence on the Euler solution of grid characteristics such as lay-out, density, stretching, skewness and aspect ratio in the vortical flow region, is a prerequisite for further progress in the understanding of the phenomenon as well as in its prediction.

Also developing models for the viscous vortex cores (e.g. Powell et al., Refs. 161, 162) is of practical interest to help in unraveling the mechanisms involved. Similar to what Luckring (Ref. 100) did for a potential-flow method, it is worthwhile to investigate the feasibility to incorporate a viscous-core model into an Euler method. Lee & Brandt (Refs. 182, 183) have attempted to embed a simple viscous-core model in a Jameson-type Euler method. The viscous-core model is derived from the Navier-Stokes equations for steady, incompressible, axisymmetric and laminar flow in a slender vortex core. The solution in the core is formulated employing, in axial direction similar, velocity profiles for the axial and circumferential velocity components, allowing the equations to be integrated algebraically. The coupling is accomplished by adding a source of momentum, directed along the axis of the core, to the momentum and energy equations. During the iteration process the Euler solution in the core region is updated regularly. Results obtained for a number of delta wings at low speed on a rather coarse H-O type of grid with about 30,000 points show that without the viscous-core model the onset of "vortex breakdown" is predicted at a too high incidence while with the model the prediction of the upstream progress of the onset of "vortex breakdown" is predicted in remarkably accordance with experimental data.

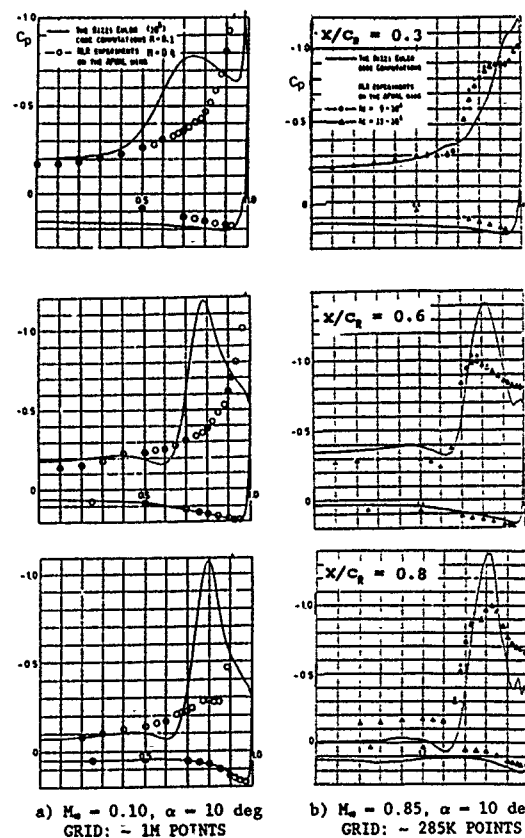


Fig. 36 Euler solution for 65-deg cropped delta wing  
Rizzi, Ref. 174

#### 5.8. Euler methods and smooth-surface separation

For highly-swept wings at incidence the primary source of the vorticity in the flow field is the shear of the velocity vector across the separation line, not the boundary layer approaching the separation line. However, the location of the separation line is determined by viscous effects. In the case of a sharp leading edge the geometrical singularity fixes the separation at the edge all along the leading edge, in reality as well as in the Euler solution. In the latter case through the numerical dissipation due to the explicitly added terms, the solution algorithm, grid characteristics, implementation of the boundary conditions, etc.. In the case of a round leading edge near the edge the gradients, and accordingly the numerical dissipation, in the Euler solution will be large, sometimes so large that the flow separates at or close to the edge. The resulting vortical flow pattern depends strongly on the location of the point at which the separation starts and the part-span vortex begins to build up in strength. This implies that separation from round leading edges may occur in Euler solutions but in a manner dependent on numerical dissipation and in general different from reality where separation is determined by the effects of the physical viscosity.

There have been several applications of Euler methods to round-edged highly swept wings at incidence, in general the measure of success dependent on the leading-edge radius and the grid characteristics. Especially at lower Mach numbers where the influence of the leading-edge radius on the part-span separation is large (e.g. see section 2.7 and Fig. 8) consistent correlation with experimental



data is not possible. As an example consider the result of Rizzi (Ref. 184) for the 65-deg round-edged cropped delta wing, which sharp-edged counterpart was considered in section 5.5, at a relatively low incidence of 10 deg. The comparison of computed and measured spanwise surface pressure distributions is reproduced in Fig. 36. The Euler solution shown in Fig. 36a is obtained for  $M_\infty = 0.1$  on a fine mesh with about one million grid points. Analysis of the computed and measured ( $M_\infty = 0.4$ ) pressure distributions reveals that in the experiment the primary flow separation occurs near the station at  $x/c_R = 0.8$ , while in the Euler solution the flow is already separated at the  $x/c_R = 0.3$  station, resulting in large discrepancies between theory and experiment. These cannot be explained in terms of the difference in the Mach number since at lower Mach numbers experiments generally show the primary separation to start at stations even further downstream. At higher Mach numbers where the flow separates earlier, the correlation might be better. This is demonstrated in Fig. 36b for  $M_\infty = 0.85$  and the same incidence of 10 deg. On the grid with about 285,000 points the flow separates just downstream of the  $x/c_R = 0.3$  station, in the experiment just upstream of this station.

As far as secondary separation is concerned it is noted that on the surface underneath the leading-edge vortex generally the gradients (along streamlines) in the flow quantities are much smaller than near the round leading edge. This implies that "secondary separation" usually does not occur in Euler solutions. This implies that, though typically integrated forces and moments are in satisfactory agreement with experimental data, predicted spanwise upper-surface pressure distributions have higher suction peaks too far inboard and no plateau region characteristic for secondary separation.

It has to be concluded that Euler methods are inadequate to capture consistently separation of the flow at geometrically smooth parts of the surface, in particular:

- secondary separation on sharp- or round-edged configurations, and
- primary (often part-span) separation on round-edged configurations.

It might be of practical importance to extend the capability of Euler methods by a model for these phenomena such that also the effects of smooth-surface separation are captured. For such a model incorporated in an Euler method, the location of the smooth-surface separation lines on the surface of the configuration have to be prescribed, i.e. have to be obtained from experiments, empirical correlations or otherwise. The primary objective is to obtain with such an augmented Euler method an aerodynamic tool with an improved modeling capability for which the computer requirements are affordable and the turn-around times practical enough for routine application in an design environment. Such a method bypasses the computational issues, typical for Navier-Stokes methods, which are associated with the small length-scales characteristic of viscous phenomena such as high-Reynolds-number boundary layers. However, because of the empiricism required as well as the assumptions that boundary and free-shear layers remain thin, no recirculating-flow regions occur, etc., the augmented method can be viewed upon as being complementary to, rather than as an alternative for, a Navier-Stokes method.

There have been attempts to incorporate smooth-surface separation models in Euler methods. Marconi (Ref. 185) presented a smooth-surface separation model, based on the work of Smith (Ref. 186), for secondary separation. In Ref. 163

Marconi applies the Kutta-type of conditions to a number of flat-plate delta wings with leading-edge separation in conical supersonic flow, demonstrating that vorticity is generated at the prescribed location and subsequently captured in the Euler solution as a free shear layer rolling up into a second vortex. Correlation with experiment is greatly improved. However, not unlike described for the attempt to model secondary separation in potential flow (see section 4.4 and Fig. 13), the surface pressure distribution underneath the secondary separation is higher than found in experiments. This discrepancy is attributed to viscous effects, such as in the boundary layer underneath the secondary vortex. In Ref. 187 this same model is used in a space-marching Euler method to predict the three-dimensional supersonic flow over simple missile-type bodies, now prescribing both primary and secondary separation lines. The results for the primary vortex are satisfactory, those for the secondary separation region are similar to above less satisfactory, again attributed to dominating viscous effects.

In the model of Smith and Marconi the conditions applied on the surface at the separation line are derived from the properties, i.e. the jumps in the flow variables, of a tangentially (in the case of isentropic flow) separating vortex sheet. Kwong & Myring (Ref. 188) propose a similar model for a finite-volume time-marching three-dimensional Euler method. Their model involves the choice of four parameters with which the direction of the velocity on either side of the separation line have to be specified. Applications so far for rather coarse meshes only show promising results, though having to specify four parameters, possibly varying along the separation line,  $m$ ,  $t$  introduce arbitrariness and turn out to be impractical.

Lee & Brandt (Refs. 163, 182), employing a Jameson-type of Euler method, account for the viscous boundary layer on the wing. Using simple formulae from the theory for incompressible turbulent flat-plate boundary layers, a shear stress directed along the surface velocity vector is added as a source term to the momentum and energy equations. The effect of the shear-layer thickness is simulated by modifying the usual way of extrapolation to find the surface pressure. Although no detailed comparison with experimental data is carried out it is suggested that for the 65-deg cropped delta wing with round leading edges improved results are obtained, including both primary and secondary separation.

## 6. NAVIER-STOKES METHODS

### 6.1. Background

An Euler method is not the suitable method for high-Reynolds-number flows with extensive regions of rotation originating from massive boundary-layer separation on smooth parts of the configuration surface. In these cases there exists a close coupling between the strength and the location of the leeward vortical flow and the position of the viscous layer separation lines on the surface of the configuration, which has precluded consistent, let alone accurate, predictions of the high-angle-of-attack flows with Euler methods. This is also the case when regions with recirculating flow and other "closed-type" of separation phenomena appear, possibly when vortex breakdown occurs and in general when frictional forces have to be accounted for.

Computational methods that take the true viscous terms into account, at least in principle, can simulate correctly all of above flow phenomena. In practice, flow simulation capability is limited by the grid resolution feasible on current computers.

and by the lack of adequate turbulence and transition models.

Navier-Stokes methods have been developed for three-dimensional flow as well as for conical flow. The latter case relates to the supersonic flow about a conical geometry. In inviscid flow the assumption that then the flow does not depend on the streamwise coordinate (i.e. is conical), is exact for supersonic flow, and approximate for subsonic flow about slender conical configurations. For viscous flow the streamwise coordinate cannot be eliminated from the viscous terms, which leads to the notion of "locally conically" flow in which the Reynolds number determines the location of the cross-flow plane (or intersection with a sphere centered at the apex). The assumption of conical similarity reduces the 3D problem to a 2D problem in the cross-flow plane. Note that in case of viscous flow the method does not properly account for the upstream influence of the flow, instead it is assumed that the flow at an infinitesimally small distance upstream is conically similar, which might be a valid approximation for viscous flows that vary slowly in streamwise direction. However, the computational expense of running a conical-flow method is a fraction of that of a fully 3D method. For solving the conical flow problem two ways can be followed. The first one is to introduce the conical similarity directly into the governing equations and boundary conditions and reformulate them in terms of cross-flow coordinates, resulting in source terms in the equations. The second possibility is to employ a 3D method on a single array of volumes obtained by linearly scaling a cross-flow plane grid towards a second cross-flow plane. At each iteration of the solution procedure the inflow conditions are updated with the results of the previous iteration, yielding a conical solution.

Especially for the high-speed flow about missile configurations there exists a rich history of numerical flow simulation employing some for this type of flow appropriate form of the Navier-Stokes equations (e.g. see Ref. 189 for a survey). Here the emphasis is on subsonic and transonic flow about wings and bodies. In the present paper the flow about relatively simple, generic, configurations is considered. Luckring (Ref. 56) paper includes a survey of Navier-Stokes computations for the flow about complex configurations.

#### 6.2. Leading-edge vortex flow

Several numerical simulations of leading-edge vortex flow using Navier-Stokes methods have been reported. Distinction can be made between implicit and explicit methods. The implicit methods to some extent avoid the CFL-condition time step restriction when fine grids are to be used to resolve the viscous layers. In the next sections results of a number of implicit and explicit methods will be discussed.

##### 6.2.1. Implicit methods

The method developed by Thomas, Newsome and others solves the thin-layer Navier-Stokes equations for unsteady, three-dimensional compressible laminar flow. It is a finite-volume method employing an upwind (first flux-vector, later flux-difference splitting) scheme for the convective fluxes, a central-difference scheme for the viscous terms and an implicit time integration with relaxation in streamwise and approximate factorization in cross-flow planes. Local time-stepping is used to speed up convergence to steady state. In the method artificial dissipation terms are not required. In Ref. 190 the method is applied to the conical as well as the 3D flow about a flat-plate-75-deg swept delta wing. For the case of  $M_\infty = 1.7$ ,  $Re_\infty = 3.5M$  and 8 deg incidence the conical solution on an O-type grid with 151 points circumferentially and 75 points normally features a well-

resolved primary and secondary vortex, very much resembling the vapour-screen visualization of Miller & Wood (Ref. 8). Also the computed spanwise surface pressure distribution is in good agreement with experimental data for a range of incidences. It is demonstrated that the results of the method run in conical mode and those of the method run in 3D mode on a grid with 20 planes of the same cross-flow-plane grid point density and distribution (~ 226K points in total) are in close agreement, up to 20 deg incidence. In Ref. 191 the conical flow computations are extended to other flow conditions and sweep angles. Furthermore the laminar flow results are compared with results of Powell's (Ref. 139) Jameson's type Euler method (on a different grid). It is demonstrated that the Navier-Stokes method captures both the primary and the secondary vortex, while the Euler method captures just the primary vortex. At the relatively high Mach number chosen (2.8) for the comparison the differences in the surface- $C_p$  distributions are only small. Also compared are results of the laminar thin-layer Navier-Stokes method with results of the method extended to solve the thin-layer Reynolds-averaged Navier-Stokes equations for turbulent flow employing the Baldwin & Lomax (Ref. 60) turbulence model as modified for extensive cross-flow separation by Degani & Schiff (Ref. 63). This comparison does show some significant differences in the flow field, not in the surface  $C_p$  distribution.

In Ref. 192 the method is used to investigate computationally the onset of primary separation on round-edged 65-deg delta wings for the case of supersonic ( $M_\infty = 1.6$ ) conical laminar and turbulent flow for incidences between 0 and 8 deg. Employing a O-type grid with 93 points in normal and 121 points along the cross-section it is shown that for turbulent flow increasing the leading-edge radius delays the primary separation. The effect of increasing the Reynolds number from 1 to 5 million has not much effect on the primary separation but moves secondary separation in outboard direction. For  $Re_\infty = 1M$  it is shown that for a given wing and fixed incidence the flow pattern may change from attached for turbulent flow to separated for laminar flow, while separated turbulent flow always corresponds with separated laminar flow. In general cases with attached flow converged better than cases with separated flow. For laminar separated flow "unsteadiness" in the solution could be eliminated by changing to a constant time step in the region encompassing the viscous layer, which also improved the convergence history dramatically. For turbulent separated flow much more severe "unsteadiness", in the region between the primary vortex and the leading edge, could not be eliminated and convergence is only marginal. It is conjectured that this problem is due to the interaction of secondary separation with the turbulence model, specifically the determination of the length scale in the region where the separating shear layer forms within the boundary layer. In Ref. 193 the method, with multi-grid implemented to speed up convergence, is applied to the low-speed laminar flow over the sharp-edged 76-deg delta wing of Hummel (Ref. 20). The solution obtained on a H-O type grid with ~ 545K points for  $M_\infty = 0.3$ ,  $Re_\infty = 0.95M$  and  $\alpha = 20.5$  deg reveals a well-developed primary vortex and a relatively large secondary vortex almost entirely embedded in a thick leading-edge shear layer (see Fig. 37, reproduced from Ref. 193). The computed surface pressure distribution is in reasonable agreement with experimental data, with some discrepancies in the secondary separation region close to the leading edge. Grid refinement studies indicated that the resolution in normal direction of the grid on the leeward side of the wing is of crucial importance. At 40 deg incidence a (presumably steady) bubble-type of vortex breakdown, with reversed axial flow, is evident in the results.



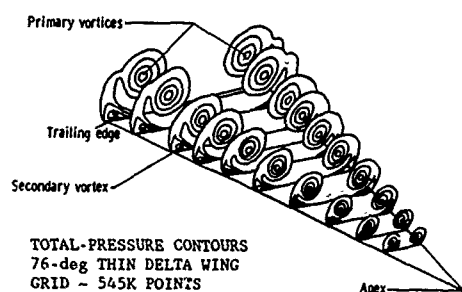


Fig. 37 Navier-Stokes solution, laminar flow,  
 $M_\infty = 0.3$ ,  $\alpha = 20.5$  deg,  $Re_\infty = 0.95M$   
 Thomas, Ref. 193

In Ref. 194 the method is applied to the low-speed laminar flow about a sharp-edged 75-deg delta wing, using a grid-embedding technique. In this technique the (structured) H-O type grid is enriched in those regions of the flow where large gradients are expected. The basis grid consists of 37 cross-flow planes, each with  $65 \times 65$  points. From the apex to the trailing edge the grid is doubled in all three directions in a region about 75% of the way circumferentially around the leading edge, with a second doubling in the two cross-flow-plane directions in the region around the vortex. The effective grid density amounts to a grid with nearly 5 million grid points. It is shown that for  $M_\infty = 0.3$ ,  $Re_\infty = 0.5M$  and  $\alpha = 20.5$  deg the solution in the leading edge vortex core improves considerably. The peak value of the streamwise velocity increases from 1.5 to 1.85 and 2.0 for successive grid enrichments, while in the experiment a peak value of 3.1 was measured.

The method developed by Hartwich, Hsu and Liu solves the Navier-Stokes equations, in artificial compressibility formulation, for three-dimensional, unsteady, incompressible laminar flow. The method employs an algorithm with an upwind TVD-like finite-difference scheme for the inviscid fluxes, central-differences for the viscous fluxes and an implicit time-integration procedure (with local-time stepping). In the method Approximate-Factorization (AF) is employed in cross-flow planes and Gauss-Seidel relaxation in chordwise direction. No artificial dissipation terms are required for numerical stability. Later the method was extended to solve the thin-layer (Reynolds-averaged) Navier-Stokes equations for laminar (turbulent) flow.

In Ref. 195 the method is applied to the sharp-edged 76/60-deg double-delta wing of Verhaagen (Ref. 23). The Reynolds number was 1.4M. Results obtained on a H-O type grid with ~ 531K points for the case 20 deg incidence indicate that the strake vortex is rather diffuse, the wing vortex is not resolved at all, upper-surface suction peaks are too low and too far outboard while the secondary separation is very shallow. This is thought to be due to a too coarse grid in the vortical flow region and the upwind scheme (at that time still first-order non-TVD) having too much numerical damping. Improving the upwind scheme to a higher-order TVD-like scheme improved the results substantially, though the secondary separation is still not resolved sufficiently and much too far outboard, indicating that the upwind scheme has still too much dissipation. This is also the case for Hummel's (Ref. 20) 76-deg sharp-edged delta wing at 20.5 deg incidence and  $Re_\infty = 0.9M$  considered in Ref. 196. This computation was carried out on an H-O type grid with ~ 370K points, apparently insufficient to obtain a sufficiently compact leading-edge vortex and associated with it a satisfactory height of the suction peaks and ac-

companying extensive secondary separation. Interestingly it is also shown that introduction of the thin-layer approximation gave almost identical results, albeit with a small (2%) saving in computing time. Computations at incidences up to 40 deg incidence resulted into steady-state solutions with for incidences above 32.5 deg a bubble-type of "vortex breakdown" with reversed flow. In Refs. 197 and 198 the investigation with the thin-layer approximation is continued using different grids, but with very similar results. Also including the Baldwin & Lomax (Ref. 60) turbulence model as modified for extensive cross-flow separation by Degani & Schiff (Ref. 63) in this formulation did not improve the correlation with experiment.

In Refs. 198 and 199 the method is applied to the thin round-edged 80/60-deg double-delta wing of Brennenstuhl (Refs. 41, 42). The Reynolds number was 1.3M. On the H-O type of grid with ~ 531K points the laminar-flow solution for 12 deg incidence does show the strake vortex, but not much of the wing vortex or the secondary separation. In Ref. 200 this case is considered for a range of incidences using a H-O type grid with ~ 850K grid points. Steady solutions could only be obtained for incidences below 25 deg. Although this grid is not refined in the vortical-flow region the merging process of the strake and the wing vortex is resolved more or less in accordance with experimental observation. However, details like the total-pressure loss at the center of the two vortex cores and the pressure suction peaks on the upper surface of the wing are predicted at lower levels than found in the experiment. These differences are attributed to too low grid density in the flow field and to laminar/turbulent transition effects not modeled in the numerical simulation. On a coarser mesh with ~ 225K points the solution remained "steady" and is reported to feature a bubble-type of "vortex breakdown" including a region with reversed axial flow. Further results for this case and for other planforms have been reported in Refs. 201 and 202.

Fujii, Kutler and Schiff developed a method that solves the thin-layer Navier-Stokes equations for three-dimensional unsteady compressible laminar flow. The algorithm employs central differences for both convective and viscous terms in combination with an implicit time-integration scheme with an LU-ADI factorization adaptation of the Beam-Warming (Ref. 112) method. A mix of nonlinear second- and fourth-order artificial dissipation terms is added to ensure stability. Fujii & Kutler (Ref. 203) simulate the laminar flow about thick rounded and blunted delta-wings as well as strake-wing configurations at  $M_\infty = 0.5$ . At the leading edge pressure spikes occur similar to those that show up in the results of finite-difference methods for solving Euler's equations. These again indicate that the flow is attached at the leading edge and separates a short distance inboard of the leading edge. In general this results in a weaker vortex than in case the flow separates at the edge. Although laminar flow was assumed, there is no sign of any secondary separation so dominantly present in laminar-flow experiments. In Ref. 204 the method is applied to the 80/60-deg round-edged thin double-delta discussed above. Using also a H-O type of grid, with ~ 853K points, the solution is obtained at  $M_\infty = 0.3$  for  $Re_\infty = 1.3M$  at a number of incidences. At the higher incidences flow unsteadiness was observed so that a constant time step was used in all computations. For 12 deg incidence the merging of the strake and the wing vortex is well simulated, although reportedly the upper-surface suction peaks are under-predicted and the secondary separation is too far outboard indicative for a too weak leading-edge vortex system. At 30 deg incidence bubble-type "vortex breakdown", with reversed

flow, occurs. Computations on much coarser grids revealed no vortex breakdown. At 35 deg incidence a spiral-type of vortex breakdown occurred with small regions with recirculating flow and increased unsteadiness. The same code but with the viscous terms switched off was also run on the same grid. This Euler solution showed for the present round-edged configuration much weaker vortical flow with, lift coefficients lower than those of the Navier-Stokes solution. In an attempt to improve the accuracy of the numerical simulation Ref. 205 considers a zonal method with overlapping zones of different grid densities. In Ref. 206 results of an upwind version of above method are presented, together with a comparison of results of the upwind and the central-difference method. This indicates that the upwind scheme is less dissipative than the central scheme.

Ekaterinaris & Schiff (Ref. 207) investigated several aspects of simulating the flow about the sharp-edged 75-deg delta wing of Kjølgaard & Sellers (Ref. 24) with the unsteady three-dimensional compressible laminar Navier-Stokes equations in the thin-layer approximation. Use is made of Fujii's (Ref. 204) central-difference implicit method and of Steger & Schiff's (e.g. Ref. 208) implicit partially upwind method in which for the inviscid fluxes flux-vector splitting is applied in chordwise and central differences in cross-flow planes. The viscous fluxes are centrally differenced. Artificial dissipation terms are added for numerical stability. Considered are an O-O and a H-O type of grid with ~ 823K points in single-block as well in multi-block ("zonal") mode. Also the Chimera scheme of overlapping ("embedded") grids was used to preserve the grid resolution in the leeward vortical flow structure but to reduce the number of grid points in less critical areas. Results were obtained for  $M_\infty = 0.3$ ,  $Re_\infty = 1M$  and incidences of 20.5, 32 and 40 deg. At 20.5 deg a good agreement with experimental data is obtained using the upwind method on the single-block fine grid, though there are discrepancies in the secondary-separation region. For this condition the effect of grid density, grid topology, zonal and embedded grids as well as numerical scheme were investigated. The study into the effect of the grid density emphasized the need for adequate resolution in the direction normal to the wing upper surface. Grid topology had a slight, multi-blocking had little, and grid reduction through embedding had some effect on the solution. As far as the numerical algorithm is concerned it appeared that the central-difference method resulted in a smaller secondary separation located further outboard. At the higher incidences of 32.5 and 40 deg steady solutions were obtained with a bubble-type of vortex breakdown with reversed flow. Further study in Ref. 209 using the upwind method with the Baldwin & Lomax (Ref. 60) turbulence model as modified by Degani & Schiff (Ref. 63) showed no major influence of the turbulence at 20.5 deg angle of attack: an unexpectedly slight shift of the secondary separation in outboard direction and not much of an increase in the height of the upper surface suction peak. As far as the solutions at higher incidences is concerned there appears to be an effect of the inclusion of the turbulence modeling on the location and extent of the vortex breakdown region. Above 50 deg incidence vortex breakdown changes from bubble- into a spiral-type and the solution becomes unsteady. Also considered is the influence of the sweep angle on the solution by considering the thin sharp-edged wing of Schrader et al. (Ref. 54).

In Refs. 210 and 211 Webster & Shang discuss several aspects of the application of (approximately-factorized implicit Beam-Warming (Ref. 112) algorithm, central-difference) Navier-Stokes methods to the supersonic flow around a thin sharp-edged 75-deg delta wing with subsonic leading edges. For  $M_\infty = 1.95$  and  $Re_\infty = 4.48M$  the flow is considered at 10, 20 and 30 deg incidence. Most comparisons were carried out for the 20 deg case on a H-H type grid with 512K points. It turned out that there are only minor differences between results of the thin-layer laminar method, those of the thin-layer turbulent (Baldwin & Lomax) method, as well as those of the full Navier-Stokes method. Also doubling the number of grid points to ~ 1M did not result in essential differences. For the case of 30 deg incidence the laminar solution of both the thin-layer and the full Navier-Stokes method revealed an embedded reverse flow region, surprisingly not in the primary vortex core but in the region of the secondary vortex core. Per iteration and time step the full Navier-Stokes method is about 30% more expensive in CPU time than the thin-layer method. In Ref. 212 the above laminar full Navier-Stokes method is applied to the low-speed ( $M_\infty = 0.2$ ,  $Re_\infty = 0.9M$ ) flow about the sharp-edged 75-deg delta wing of Hummel (Ref. 20) at 20.5 deg incidence. On an H-H type of grid with ~ 435K points the solution is steady but shows only fair agreement with experiment, especially in the secondary separation region. For the same type of grid with increased resolution in normal and spanwise direction and a total of ~ 1M points the (temporal inaccurate) solution did not reach a steady state. The resulting flow field features a leading-edge shear-layer with small-scale structures conjectured to be due to a Kelvin-Helmholtz type of instability. However, the small-scale structures appear close to the leading edge, i.e. in that part of the shear layer that is most changing in strength (stretching) and most curved, and not in the least curved part of the shear layer like observed experimentally by Payne et al. (Ref. 37).

#### 6.2.2. Explicit methods

As early as 1983 Krause, Shi & Hartwich (Ref. 213) reported on results of an explicit finite-difference Navier-Stokes method for three-dimensional incompressible flow, formulated in terms of Cartesian coordinates. It concerned a flat-plate delta wing of unit aspect ratio at 15 deg incidence. It was found that in the numerical simulation the influence of the Reynolds number on the development of the leading-edge vortex is negligible. It is also indicated that the effect of the truncation errors associated with the finite-difference scheme for inviscid flow already introduce an (artificial) vorticity production term in otherwise irrotational flow. However, on the relatively coarse grids used a secondary vortex did not develop.

Rizetta & Shang (Ref. 214) compare results of an Euler and a Reynolds-averaged Navier-Stokes method based on McCormack's (Ref. 111) time-dependent, explicit, two-step predictor-corrector, central-difference scheme. The methods are applied to a sharp-edged 75-deg delta wing with subsonic leading edges in three-dimensional supersonic flow ( $M_\infty = 1.95$ ,  $\alpha = 10$  deg) on one and the same H-H type of grid with just ~ 51K points. Comparison of the Euler and the (laminar) Navier-Stokes results indicates the occurrence of secondary separation, embedded within the viscous layer, in the Navier-Stokes solution. It is also shown that the size and the location of the primary vortex is not affected much by the inclusion of the viscous terms, while the effect on the surface pressure distribution is as expected. However, for the coarse grid used definitive conclusions could not be drawn.

Müller & Rizzi extended Rizzi's Euler method (explicit Runge-Kutta with local time-stepping, central-difference finite-volume, added artificial dissipation terms) to a method solving the time-dependent laminar Navier-Stokes equations. In Ref. 215 the method is applied to the round-edged 65-deg cropped delta wing for the flow condition  $M_\infty = 0.85$ ,  $\alpha = 10$  deg,  $Re_\infty = 2.38M$  for which experiments indicate primary separation along almost the whole span. Employing an O-O type grid with only ~ 53K points, the numerical solution also appears to feature primary separation along most of the leading edge, but the suction peak underneath the resulting primary vortex is too low and the secondary separation is absent or very shallow. In Refs. 216 and 217 the same case is considered on a much finer (~ 410K point) grid, for which convergence is degraded remarkably but which gives a much better resolution of the primary vortex and of the secondary separation. Compared to an earlier Euler solution (on grid with 1M points) correlation of computed and measured surface pressure distributions is also much improved, but there remain relatively large discrepancies in the region of the secondary separation where further vortices appear in the numerical simulation. Comparison of the Navier-Stokes solution with an Euler solution on a similar (~ 300K point) grid with about the same density along the surface but coarser in normal direction can be found in Ref. 218.

Development of a Navier-Stokes method starting from an Euler method has been carried out at several other places. For instance Raj et al. (Ref. 173) developed a method for three-dimensional viscous flow starting from their on Jameson's time-explicit, spatial central-difference finite-volume scheme based TEAM code. This method can solve for laminar flow or for turbulent flow. In the latter case the Reynolds-averaged Navier-Stokes equations are solved with the usual Baldwin & Lomax turbulence model or with some other more sophisticated models.

Sicilari et al. (Ref. 219) describe a (cell-vertex) finite-volume method for solving both the time-dependent Euler and (laminar) Navier-Stokes equations for conical flow. The scheme used employs explicit Runge-Kutta time integration and central differences to spatially discretize the inviscid and the viscous fluxes. The usual artificial dissipation terms are added for stability. Multigrid is used to speed up convergence. Also Kandil et al. (Ref. 164) report on the development of a Jameson type explicit, central-difference Euler and (laminar) Navier-Stokes method for conical as well as three-dimensional flow.

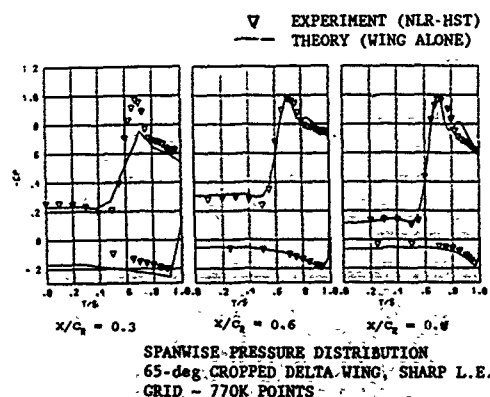
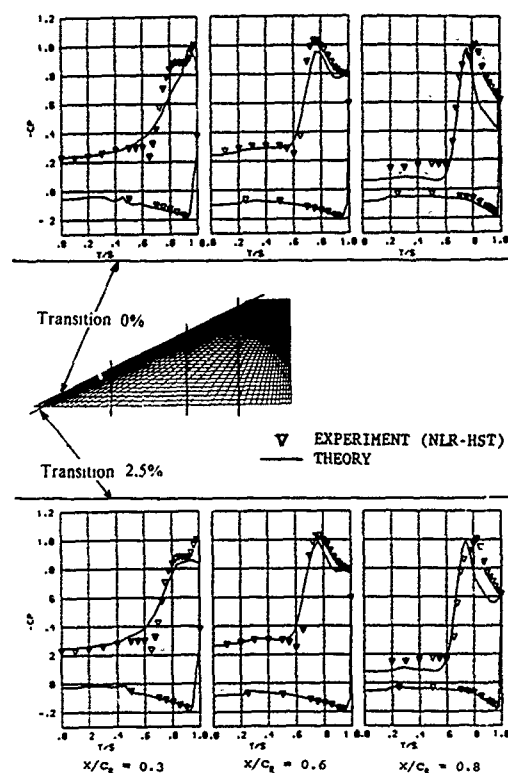


Fig. 38 Navier-Stokes solution, turbulent flow,  $M_\infty = 0.85$ ,  $\alpha = 10$  deg,  $Re_\infty = 9M$  Hilgenstock, Ref. 220



INFLUENCE OF TRANSITION LOCATION  
65-deg CROPPED DELTA-WING/BODY CONFIGURATION, ROUND L.E.  
GRID ~ 2M POINTS

Fig. 39 Navier-Stokes solution, laminar/turbulent flow,  $M_\infty = 0.85$ ,  $\alpha = 10$  deg,  $Re_\infty = 9M$  Hilgenstock, Ref. 220

In the (full) Reynolds-averaged Navier-Stokes method of Hilgenstock (Ref. 220) a finite-volume cell-centered central-difference scheme is used together with a four-stage Runge-Kutta procedure for time integration. The multi-block method employs an algebraic turbulence model based on that of Baldwin and Lomax (Ref. 60) and includes the modifications for separated flow proposed by Degani and Schiff (Ref. 63). The method is applied to the 65-deg cropped delta wing configuration of the "International Vortex Flow Experiment" (Ref. 56) for the flow condition  $M_\infty = 0.85$ ,  $\alpha = 10$  deg. For the case of the sharp leading edge, employing a H-H type of multi-block grid with ~ 770K points, the computed surface pressure distribution for turbulent flow at  $Re_\infty = 9M$  correlates satisfactorily with the measured data (Fig. 38, reproduced from Ref. 220). The discrepancies on the lower surface are due to the omission of the underwing fuselage/sting in this computation. The in spanwise direction H-type of grid is near the apex too coarse to resolve the flow accurately on the forward part of the upper wing surface (see  $x/c_2 = 0.3$ ). On the aft part of the wing both the position and height of the (primary, most inboard) suction peak is predicted very well. However, in the results of the numerical simulation the location of the secondary separation is slightly too far inboard, resulting in a stronger secondary vortex than in reality as evidenced by the somewhat more pronounced second suction peak. For the case of round leading edges the complete configuration has been considered. The multi-block grid used for this case is of C-H type with about 2M points. For this more demanding case it turned

out that for a given user-specified location of the transition location the solution for  $Re_\infty = 4.5M$  is almost identical to the one for  $Re_\infty = 9M$ . However, the solution proved to be rather sensitive to the choice of the transition location, as is shown in Fig. 39 for  $Re_\infty = 9M$ , also reproduced from Ref. 220. Unfortunately for the present flow condition the precise transition location has not been recorded in the experiment. Apparently the best computational results are obtained for the case in which the primary separation is laminar. For the latter case the agreement of theory and experiment is excellent on the lower wing surface but requires still some improvement on the upper wing surface.

### 6.3. Slender-body vortex flow

The flow about slender smooth bodies like cones and ogival bodies is dominated by flow separation at some separation line along part of its length, in the cross-sections located near the shoulder of the body. Besides the primary separation and the vortical flow pattern associated with it, is it the possible occurrence at higher incidences of asymmetric flow patterns that has attracted much attention. Though the latter may be inviscid in nature, as has been indicated in the preceding chapters, primary separation is a viscous process which simulation requires Navier-Stokes methods.

Siclari & Marconi (Ref. 221) present results of their explicit, central-difference method (Ref. 219) for solving the Navier-Stokes equations for the supersonic laminar flow about a slender 5-deg semi-vertex angle circular cone. The free-stream condition chosen is  $M_\infty = 1.8$  and  $Re_\infty = 0.1M$ , the

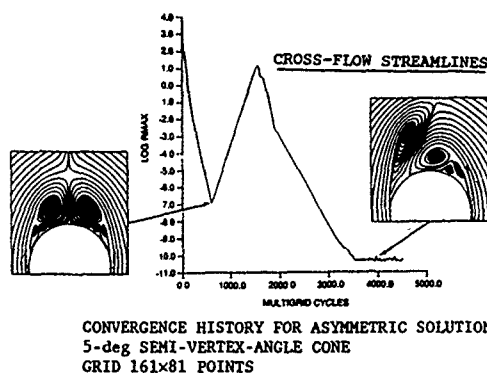


Fig. 40 Navier-Stokes solution, laminar conical flow,  $M_\infty = 1.8$ ,  $\alpha = 20$  deg,  $Re_\infty = 0.1M$  Marconi & Siclari, Ref. 221

grid contains 81 points in normal direction and 81 points on the half-circle in circumferential direction. It is shown that half-plane solutions with symmetry forced at the vertical plane feature primary separation for incidences over 10 deg. On the full-plane grid without symmetry invoked the solution remained symmetric up to about 12.5 deg incidence and becomes asymmetric above this critical value. Fig. 40 reproduces the result for 20 deg incidence. For this case the solution started out symmetric but after a substantial reduction of the residual asymmetry creeps into the solution and following an increase in the residual the iteration process converges towards an asymmetric solution. The latter is a truly converged solution with a residual which could be held at "machine-zero" for any number of further iterations. The convergence history suggests that above the critical incidence the symmetric solution is unstable, while the asymmetric solution is stable.

Uniqueness is assessed by starting the solution procedure with the free stream at a slight (2 deg) side slip, returning to zero side-slip after a number of iterations, which as reported results in the same asymmetric solution but at lower computational expense.

Although, as shown in Fig. 40, the vortical structure in the near field is rather asymmetric the location of the starboard and port-side primary separation points is almost symmetric. This contributes to the conjecture that the asymmetry may be an inviscid-flow feature and provides prospects for the inviscid flow computations with user-specified separation lines (e.g. see Fig. 16 for the VORSBA potential-flow solution for the case  $\alpha/\delta = 3$ ). In the symmetric solution shown in Fig. 40 (for  $\alpha/\delta = 4$ ) three centers of roll-up appear in each half plane: the primary vortex, the counter-rotating secondary vortex and a third co-rotating vortex within the primary vortex layer. In the asymmetric solution one of the vortex systems has the above described topology, the other one features just the primary vortex which has moved away from the cone. This contradicts the findings from the VORSBA computations. There it was conjectured that possibly the relatively long free shear layer of the second vortex system might become unstable and a co-rotating embedded vortex was expected to form.

At incidences above 25 deg the asymmetry of the still steady solution is reduced and symmetry is recovered, which is also observed in experiment, though there the flow then becomes unsteady. In Ref. 222 the investigation into asymmetric solutions is extended to other Mach numbers as well as to other cone angles and other cross-sectional shapes. At higher Mach numbers the asymmetry is reduced, conjectured to be due to diminished communication between starboard and port side vortex systems associated with the cross flow becoming supersonic. Also in accordance with experimental evidence it is demonstrated that thinning the circular cone to a cone with an elliptic cross-section reduces the asymmetry, while adding a small sharp-edged strake completely eliminated the asymmetry. It is also reported that the upwind implicit method of Thomas (Ref. 193), run in conical mode on a similar grid, produced the same steady asymmetric solutions. However, in order to reduce the residual to "machine-zero" the flux limiters had to be turned off.

Finally three-dimensional flow computations are reported on for the case of the flow about a cone-ogive-cylinder configuration. Taking the asymmetric conical solution as the solution at the starting station, results are obtained of an implicit marching (parabolized) Navier-Stokes method with both cross-flow viscous terms retained. These results indicate that the solution, computed on 26 cross-flow planes with a  $191 \times 95$  grid, remains asymmetric and on the cylindrical part of the configuration evolves into a vortex-street type of vortical flow pattern.

Results similar to Siclari's have been reported by Kandil et al. (Refs. 223, 224 and 225) using various implicit methods for laminar flow including thin-layer, double-layer and full Navier-Stokes methods employing upwind and central difference schemes. However, for the cases at higher incidences unsteady asymmetric solutions are reported.

Vatsa & Thomas (Ref. 226) compare results of two thin-layer Navier-Stokes methods, both using Baldwin & Lomax's turbulence model, applied to the low-speed ( $M_\infty = 0.4$  in the calculations) turbulent flow over a 6:1 prolate spheroid (extensively measured by Meier at DLR) at high incidence. One method is Vatsa's Jameson type explicit central-difference method extended to the Navier-Stokes equations, the second method is Thomas' implicit upwind flux-difference splitting method. The com-

parison is carried out for a range of Reynolds numbers and incidences. For the C-0 type grid with ~ 175k points it appears that the two approaches give qualitatively similar results; often the difference between the two methods being smaller than the difference between the experimental data and either of the two computational methods.

Hartwich applies his implicit upwind flux-difference splitting scheme (Ref. 198) for solving the thin-layer Navier-Stokes equations to the flow about the 3.5 calibre tangent-ogive forebody configuration tested by Keener & Chapman (Ref. 49, see also Fig. 5). The incompressible three-dimensional turbulent flow at  $Re_\infty = 0.8M$  is simulated using the Baldwin & Lomax turbulence model with Degani & Schiff's modification and also modified slightly different in the region of primary separation. Steady-state solutions are obtained on C-0 type grids with for the half-space calculations (Ref. 227) about 190K points with a refinement to 353K points, for the full-space calculations (Ref. 228) about 375K points in some cases refined to a grid of ~ 535K points. Solutions are obtained for a variety of flow conditions, including cases with transitional flow. The numerical results show a satisfactory agreement with experimental data. For 20 deg incidence the solution is symmetric, for both 30 and 40 deg the solution is asymmetric. Modification of the axisymmetric geometry by deforming the nose into an elliptic shape demonstrated that with this imperfection the symmetric solution remained symmetric while the asymmetric solution could be biased to yield either positive or negative side force, i.e. the flow could be controlled, by rolling the configuration. It is further reported that for the case of laminar flow the solution also becomes asymmetric above 20 deg incidence, but then is unsteady.

Also Degani, Schiff et al. study the simulation of viscous flow about slender smooth bodies. The flow is simulated solving the thin-layer Navier-Stokes equations for three-dimensional laminar or turbulent time-dependent compressible flow using Steger & Schiff's (Ref. 208) implicit, in streamwise direction upwind and in cross-flow planes central-difference scheme. Several aspects of the solutions were considered; such as the influence of gridding, the effect of different turbulence models, etc. (see Refs. 229 and 230). As far as the influence of the turbulence model is concerned it is shown that for the low-speed flow about Meier's 6:1 prolate spheroid the Baldwin & Lomax model with Degani & Schiff's modification performs best or comparable with more sophisticated models, especially in capturing primary and secondary smooth-surface separation. In Ref. 231 Degani numerically investigated the three-dimensional compressible flow about the same 3.5 calibre tangent-ogive as considered above by Hartwich for the case of incompressible flow, but this at a lower Reynolds number ( $Re_\infty = 0.2M$ ) and for laminar flow. Time-accurate solutions were obtained for  $M_\infty = 0.2$  on a full-space C-0 type grid has ~ 354K points. Near the nose of the body a space-fixed time-invariant geometrical disturbance could be added. For 20 deg incidence the solution is steady and symmetric, irrespective of the presence of a nose disturbance. For 40 deg incidence the solution is steady and symmetric for the unperturbed nose, steady and asymmetric for the perturbed nose. In the latter case the level of asymmetry was found to be dependent on the size and the location of the perturbation, with the asymmetry disappearing completely upon the removal of the imperfection. This finding is in contrast with the results of some of the conical and three-dimensional flow computations discussed above, but in accordance with the results of earlier three-dimensional flow computations with the same method

where a the disturbance due to a jet could turn the asymmetry on or off. This leads Degani and Schiff to the conjecture that in their numerical solution procedure the asymmetry is caused by a convective type of instability growing in space only, rather than an absolute type of instability growing both in space and time. For incidences exceeding 40 deg the flow around the cylindrical part becomes unsteady and vortex shedding develops as soon as for some finite time a small temporal disturbance is introduced.

#### 6.4. Vortex breakdown

Employing viscous flow methods vortex cores in isolation or in tubes have been studied rather intensively, e.g. Hafez & Ahmad (Ref. 232), Liu & Menne (Ref. 233), Spall & Gatski (Ref. 234) and Krause & Liu (Ref. 235). In these numerical simulations of viscous flow both bubble- and spiral-types of vortex breakdown have been found. However, it is not very clear how tube vortex flow is related to the flow in a three-dimensional leading-edge vortex.

The discussion in section 6.2 of results of Navier-Stokes methods for leading-edge vortex flow already included cases with vortex breakdown. Here it is to be noted that though the mathematical model used is more complete than the one of the Euler methods, the grid densities used in the vertical flow region for calculations with Navier-Stokes methods is usually not much different from the grid densities used for Euler computations. This implies that in the vortex core the flow features captured by a Navier-Stokes method will not differ much from the ones captured by an Euler method. Resolution of viscous-flow dominated features (if any) of importance for the process of (the onset of) vortex breakdown will require much finer grids, both in the cross-flow plane and in axial direction near the breakdown point, than hitherto used. Also of importance in this respect is the way in which turbulence models are to be implemented in vortex cores, a subject that has not received much attention at all.

## 7. ASSESSMENTS

### 7.1. Potential-flow methods

The main limitation of the potential-flow methods (i.e. panel methods) considered in the present survey is that they are based on a limited mathematical model of the physics, i.e. the model governed by the Prandtl-Glauert equation for linearized sub-critical compressible potential flow, or Laplace's equation for incompressible flows. The methods can handle flows with vorticity by means of free vortex sheets and vortex filaments fitted into the otherwise potential flow, but cannot accommodate shocks. A practical drawback of potential-flow methods applied to configurations with strong-interaction vortex flow is that for complex geometries vortex-sheet fitting becomes too complex for routine application. An advantage of the relatively low-cost method is that it can give a good insight in some of the fundamental aspects of low-speed well-ordered vortex flows. This because the method treats thin free shear layers as vortex sheets rather than layers smeared out by numerical effects.

### 7.2. Euler methods

The Euler methods allow rotational flow as well as shocks everywhere within the flow field and convection and stretching of vorticity is accounted for without having to deal explicitly with discontinuity surfaces. Solutions to the Euler equations permit generation of vorticity, inviscidly, through shocks of varying strength or the intersection of shocks. However, Euler's equations do not account for vorticity generated through vis-



cous processes such as boundary-layer separation. In three-dimensional flow fields such as on the lee-side of a smooth slender body at incidence, at round leading edges, or on the configuration surface underneath a primary vortex, open type of boundary-layer separation is outside the viscous layer accompanied by a shear in the velocity vector across the separation line. This shear in the velocity acts as the source of the flow field vorticity. To simulate these flows the effects of viscosity have to be modeled employing Kutta type conditions at user-specified separation lines. As is the case for the potential-flow methods above the position of these lines is obtained empirically or possibly through a (strong-interaction) boundary-layer computation. In pseudo-unsteady methods to solve the discretized Euler equations the Kutta condition at sharp subsonic edges is, or appears to be, enforced implicitly by the numerical dissipation invoked by the numerical scheme. Since the separation point is determined by the geometry its position is insensitive to the magnitude of both physical and numerical viscosity, at least for the high Reynolds numbers of interest. For separation from smooth parts of the surface smooth-surface separation models have to be applied at user-specified separation lines. Utilization of such models could enhance the use of Euler methods as an aerodynamic tool with for an industrial design environment affordable computer requirements and practical turn-around times.

In numerical flow simulations using the Euler equations vorticity may be generated by numerical error, while on the other hand the numerical schemes are dissipative and even without the explicit addition of artificial dissipation will diffuse vorticity. This counteracts the concentration of vorticity into strong vortices in a manner that may not be similar to what occurs in the real (viscous) flow. Since the degree of diffusion depends on the grid quality and in particular the grid point density it means that grids should be fine not only near the surface of the configuration but also in the vortical-flow regions. Also in order to accurately predict the strong interaction of "long-living" vortical flow structures, due to separation from a forebody or from canard surfaces, with the flow about the rest of the configuration will require a large number of grid points.

As far as vortex breakdown is concerned the situation is not yet clear. Euler methods do seem to indicate a transition of the vortex core structure from a compact filament type of core to a spiral or bubble type of structure. More research is needed in this area to sort out the sensitivity of the computed "vortex breakdown" to grid topology, grid point density, artificial dissipation, etc., as well as into the fundamental physics of the vortex breakdown phenomenon.

### 7.3. Navier-Stokes methods

The advent of supercomputers and mini-supercomputers has brought the application of Euler codes within reach of the airframe designer. The computational requirements for a Navier-Stokes method are an order of magnitude higher than those for an Euler method. This because additional terms in the flow equations have to be evaluated and specifically because the grid must be substantially finer in order to resolve adequately the viscous layers. The introduction of supercomputers such as the CRAY 2 and CRAY YMP has permitted a quantum jump in the size of computational grids. Central memory of these computers is so large that the size of the memory no longer sets the practical limit of the number of cells and hence the spatial resolution.

It is now possible, at least in principle, to treat high-angle-of-attack flows over bodies and aircraft components with methods based on the Reynolds-averaged Navier-Stokes equations with sufficient grid resolution to resolve the main features of the three-dimensional separated flow field. The practical limit is set by the time required for convergence of the calculations and by the cost of these large-scale computations. The CPU requirement for a Reynolds-averaged Navier-Stokes method for steady flow is typically of the order of 50  $\mu$ sec per grid point per iteration. The number of grid points is of the order of  $10^6$  and more, the number of iterations may be several thousands, which leads then to run times exceeding 35 hours. These computer-time requirements are such that a frequent application within a design environment is not feasible.

Navier-Stokes methods have demonstrated their capability to simulate viscosity-dominated features in vortex flow aerodynamics. However, the current status of turbulence and transition modeling is not such that reliable predictions based on the Reynolds-averaged Navier-Stokes equations are possible for those flow situations where they are most needed: high angle-of-attack transitional or turbulent flows with shocks and separated vortex flow.

In most applications of Navier-Stokes methods the grid is refined adequately near the solid surfaces, this to resolve the viscous surface flow and secondary separation. For the simulation of vortical flow the grid should also be refined in the vortical flow regions, i.e. the grid should be fine enough to resolve the convection-dominated free-floating shear-layers and vortex cores. For cases with vortex breakdown, though presumably not a viscous-dominated process, the grid should be still fine enough to capture the small-scale details of the flow near the point where the bubble and/or spiral forms within the leading-edge vortex. This implies that in the numerical simulation it has to be made sure that the inviscid (Euler) terms in the equations will behave consistent and in the appropriate manner.

### 7.4. Asymmetric vortex flows

The vortical flow about configurations at high incidence constitutes a nonlinear flow problem. Even for the case of linearized potential flow the problem is nonlinear, namely through the boundary conditions on the free vortex sheets. The nonlinearity of the problem allows multiple solutions to exist. The intriguing grossly asymmetric vortex flow patterns at nominally symmetric free-stream conditions, observed in experimental investigations on slender bodies, have also been found in numerical simulations by potential-flow methods within the frame-work of slender-body theory as well as by Euler and Navier-Stokes methods for conical and for three-dimensional flow. The origin of the asymmetry as well as the stability of both the symmetric and the asymmetric solutions needs to be further investigated.

### 7.5. Grid sensitivity of solution

In the literature there are not too many examples of investigations into the sensitivity of the Euler and Navier-Stokes solutions to grid-point density and grid-point distribution. It appears that the resolution of the grid has a large influence on the way in which vorticity is concentrated into vortex cores. This has a direct influence on the induced low pressure regions on nearby configuration surfaces and on secondary separation phenomena caused by the primary vortical flow structure.

A more fundamental matter concerns the solution of the Euler equations for increasingly finer meshes. In the limit of zero mesh size the free-shear-layers, captured within the solution, tend to free-vortex-sheets. The latter however, may be prone to Kelvin-Helmholtz instabilities which, in a time-stepping method, will become evident as "unsteadiness" in the numerical solution. In this respect it is quite useful to compare solutions of different methods, such as a Navier-Stokes solution, an Euler solution and a free-vortex-sheet panel method solution.

#### 7.6. Grid generation

To obtain the numerical solution of the flow field other than with a panel method, i.e. using an Euler or a Navier-Stokes method, the flow domain must be discretized first. The basic requirement for an accurate and efficient numerical simulation of the flow field about a 3D configuration is a computational grid possessing the for the specific CFD method required level of smoothness and orthogonality. The generation of such a grid which in addition has an adequate density in those regions, often of disparate length scale, where large gradients are expected while still having an acceptable number of points is a task that requires much expertise and a substantial number of manhours.

A description of the various approaches to grid generation and developments aimed at obtaining more flexibility in the grid generation process is beyond the scope of the present paper. However, it is generally recognized that especially for Navier-Stokes methods some form of grid adaptation is required in order to increase accuracy and resolution for a given level of cost. As far as computational vortex flow is concerned there have been promising developments for structured grids (e.g. Powell et al., Ref. 236) as well as for unstructured grids (e.g. Batina, Ref. 237), both for conical flow computations. Three-dimensional solution-adaptive grid methods are not yet far enough developed to be used in practical applications.

#### 8. CONCLUDING REMARKS

Considerable progress has been booked in the modeling, the numerical simulation and the understanding of aerodynamic vortex flows at subsonic and transonic speeds. Euler and Navier-Stokes methods have demonstrated their potential capability to simulate the details of the flow nonlinearities due to compressibility and vortical flow, as well as of the interaction of shocks and vortices.

Before the more advanced CFD methods will play a significant role in the prediction of the aerodynamics of complex configurations in that part of the flight envelope where it is most needed, much more work needs to be done on algorithm development, efficient grid generation, adaptive grid techniques, assessing the sensitivity of solutions to numerically parameters, controlling the influence of artificial dissipation, turbulence modeling for shock-induced separation and large-scale separated flow, modeling of transition etc. Much effort is required to validate and integrate various techniques into an effective aerodynamic tool that indeed can treat arbitrary configurations and complex flows.

Methods based on the inviscid-flow approximation, with nonlinear compressibility and rotational flow effects (convection and stretching of vorticity, possibly as well as generation of vorticity through some model for smooth-surface separation) included, will play an increasingly more important role in the prediction of vortex flow aerodynamics.

Viscous flow methods have demonstrated their promising potential capability, but much research is required to reduce their computational costs and to improve their turbulent-flow capability.

Verification of computational methods requires the detailed comparison of results produced by computational methods based on different mathematical models as well as produced by methods based on the same mathematical model but using a different numerical scheme. Furthermore verification requires the comparison of predicted results with well-understood, clearly documented experimental data. The experimental data must be of the proper type and in sufficient detail to accurately describe the physics of the flow field. Only a few systematic experimental/theoretical programs on obtaining detailed tailor-made data for CFD verification have been carried out to date.

Vortex flow aerodynamics has many interesting facets on a more fundamental level. This includes the behaviour of evolving wakes, the formation of vortex cores, the interaction of vortices with solid surfaces, the interaction of vortices and shock waves, the stability and dynamics of vortex systems, multiple solutions and their stability, the generation of vorticity, vortex breakdown, etc. Computational methods are indispensable in the analysis leading to a further insight into and eventually exploitation of these flow phenomena.

#### REFERENCES

1. Küchemann, D.: The Aerodynamic Design of Aircraft. Pergamon Press (1978).
2. Hirschel, E.H., Rizzi, A.: The Mechanism of Vorticity Creation in Euler Solutions for Lifting Wings. In: Proceedings of Symposium on "International Vortex Flow Experiment on Euler Code Validation", ed. by A. Elsasser and G. Eriksson. FFA, Stockholm, October 1-3 1986, pp. 127-161 (1986).
3. Polhamus, E.C.: Applying Slender Wing Benefits to Military Aircraft. J. of Aircraft, Vol. 21, No. 8, pp. 545-559 (1984).
4. Lamar, J.E., Bruce, R.A., Pride, J.D., Smith, R.H., Brown, P.W., Johnson, T.D.: In-Flight Flow Visualization of F-106B Leading-Edge Vortex Using the Vapor-Screen Technique. AIAA Paper 86-9785 (1986).
5. Campbell, J.F., Chambers, J.R., Rumsey, C.L.: Observations of Airplane Flow Fields by Natural Condensation Effects. AIAA Paper 88-0191 (1988).
6. Erickson, G.E., Schreiner, J.A., Rogers, L.W.: Multiple Vortex and Shock Interactions at Subsonic, Transonic and Supersonic Speeds. AIAA Paper 90-3023 (1990).
7. Stanbrook, A., Squire, L.C.: Possible Types of Flow at Swept Leading Edges. Aeron. Quarterly Vol. 15, pp. 72-82 (1964).
8. Miller, D.S., Wood, R.M.: An Investigation of Wing Leading-Edge Vortices at Supersonic Speeds. AIAA Paper 83-1816 (1983). See also J. of Aircraft Vol. 21, No. 9, pp. 680-686 (1984) and NASA TP 2430 (1985).
9. Vorropoulos, G., Wandt, J.F.: Laser Velocimeter Study of Compressibility Effects on the Flow Field of a Delta Wing. AGARD-CP-342, Paper 9 (1983).
10. Lückring, J.M.: Review of Vortex Computational Techniques. This FDR Symposium, AGARD-CP-342, Paper 6 (1990).



11. Hoeijmakers, H.W.M.: Computational Vortex Flow Aerodynamics. AGARD CP-342, Paper 18; see also NLR MP 83017 U (1983).
12. Smith, J.H.B.: Vortex Flows in Aerodynamics. Ann. Rev. Fluid Mech. Vol. 18, pp. 221-242 (1986).
13. Newsome, R.W., Kandil, O.A.: Vortical Flow Aerodynamics - Physical Aspects and Numerical Simulation. AIAA Paper 87-0205 (1987).
14. Hoeijmakers, H.W.M.: Methods for Numerical Simulation of Leading-Edge Vortex Flow. In: "Studies of Vortex Dominated Flows", Ed. M.Y. Hussaini and M.D. Salas, Springer Verlag, pp. 221-269 (1987). See also NLR MP 85052 (1985).
15. Raj, P.: Recent Developments in the Computational Solutions of Euler Equations. Paper presented at 3rd Int. Congr. of Fluid Mech., Cairo, Egypt, Jan. 2-4 (1990).
16. Legendre, R.: Écoulement au Voisinage de la Pointe Avant d'une Aile à Forte Flèche aux Incidences Moyennes. La Rech. Aeron. Vol. 30, pp. 3-8; Vol. 31, pp. 3-6; Vol. 35, pp. 7-8 (1952).
17. Earnshaw, P.B.: An Experimental Investigation of the Structure of a Leading-Edge Vortex. ARC R&M No. 3281 (1962).
18. Wentz, W.H., McMahon, M.C.: An Experimental Investigation of the Flow Fields about Delta and Double-Delta Wings at Low Speeds. NASA CR 521 (1966).
19. Fink, P.T., Taylor, J.: Some Early Experiments on Vortex Separation. ARC R&M No. 3489 (1967).
20. Hummel, D.: On the Vortex Formation Over a Slender Wing at Large Incidence. AGARD CP-247, Paper 15 (1979).
21. Maltby, R.L.: Flow Visualization in Wind Tunnels Using Indicators. AGARDograph No. 70 (1962).
22. Verhaagen, N.G.: An Experimental Investigation of the Vortex Flow over Delta and Double-Delta Wings at Low Speeds. AGARD CP-342, Paper 7 (1983).
23. Verhaagen, N.G., Naarding, S.H.J.: Experimental and Numerical Investigation of the Vortex Flow Over a Yawed Delta Wing. AIAA Paper 88-2563 (1988). See also J. of Aircraft, Vol. 26, No. 11, pp. 971-978 (1989).
24. Kjelgaard, S.O., Sellers III, W.L., Weston, R.P.: The Flow Field over a 75 Degree Swept Delta Wing at 20.5 Degrees Angle of Attack. AIAA Paper 86-1775 (1986).
25. Carcaillet, R., Manie, F., Pagan, D., Solignac, J.L.: Leading-edge Vortex Flow over a 75 Degree-Swept Delta Wing - Experimental and Computational Results. ICAS Paper 86-1.5.1 (1986).
26. Solignac, J.-L., Pagan, D., Molton, P.: Experimental Study of Incompressible Flow on the Upper Surface of a Delta Wing. Rech. Aérosp. No. 1989-6, pp. 47-65 (1989).
27. Peckham, D.H., Atkinson, S.A.: Preliminary Results of Low Speed Wind Tunnel Tests on a Gothic Wing of Aspect Ratio 1.0. ARC Rep. CP-508 (1957).
28. Peckham, D.H.: Low Speed Wind Tunnel Tests on a Series of Uncambered Slender Pointed Wings with Sharp Edges. ARC Rep. R&M No. 3186 (1958).
29. Elle, B.J.: An Investigation at Low Speed of the Flow Near the Apex of Thin Delta Wings with Sharp Leading Edges. ARC Rep. R&M No. 3176 (1958).
30. Lambourne, N.C., Bryer, D.W.: The Bursting of Leading-Edge Vortices - Some Observations and Discussion of the Phenomenon. ARC Rep. R&M No. 3282 (1961).
31. Hall, M.G.: Vortex Breakdown. An. Rev. of Fl. Dyn., Vol. 4, pp. 195-218 (1972).
32. Erickson, G.E.: Water-Tunnel Studies of Leading-Edge Vortices. J. of Aircraft, vol. 19, No. 6, pp. 442-448 (1982).
33. Kegelman, J.T., Roos, F.W.: Effects of Leading-Edge Shape and Vortex Burst on the Flowfield of a 70-degree-sweep Delta Wing. AIAA Paper 89-0086 (1989).
34. Kegelman, J.T., Roos, F.W.: The Flowfields of Bursting Vortices over Moderately Swept Delta Wings. AIAA Paper 90-0599 (1990).
35. Roos, F.W., Kegelman, J.T.: An Experimental Investigation of Sweep-Angle Influence on Delta Wing Flows. AIAA Paper 90-0383 (1990).
36. Gad-el-Hak, M., Blackwelder, R.F.: The Discrete Vortices From a Delta Wing. AIAA J., Vol. 23, No. 6, pp. 961-962 (1985).
37. Payne, F.M., Ng, T.T., Nelson, R.C., Schiff, L.B.: Visualization and Flow Surveys of the Leading-Edge Vortex Structure on Delta-Wing Planforms. AIAA Paper 86-0330 (1986). See also AIAA J. Vol. 26, No. 2, pp. 137-143 (1988).
38. Lowson, M.V.: The Three-Dimensional Vortex Sheet Structure on Delta Wings. AGARD CP-438, Paper 11 (1988).
39. Verhaagen, N.G., Manen, R. van: A Laser-Light-Sheet Investigation of the Leading-Edge Vortex Layer. Unpubl. Work, Fac. Aerosp. Eng., Technical University Delft (1987).
40. Luckring, J.M.: Aerodynamics of Strake-Wing Interactions. J. of Aircraft, Vol. 16, No. 11, pp. 756-762 (1979).
41. Brennenstuhl, U., Hummel, D.: Vortex Formation over Double-Delta Wings. ICAS Paper 82-6.6.3 (1982).
42. Brennenstuhl, U., Hummel, D.: Experimentelle und Theoretische Untersuchungen über die Wirbelbildung an Doppeldeltaflügeln. ZFW, Vol. 11, pp. 37-49 (1987).
43. Thompson, D.H.: A Visualization Study of the Vortex Flow Around Double-Delta Wings. ARL-AERO-R-165 (1985).
44. Smith, J.H.B.: Theoretical Modelling of Three-dimensional Vortex Flows in Aerodynamics. AGARD CP-342, Paper 17 (1983). See also Aeron. J., April 1984, pp. 101-116 (1984).
45. Hummel, D., Oelker, H.-Chr.: Effects of Canard Position on the Aerodynamic Characteristics of a Close-Coupled Canard Configuration at Low Speed. AGARD CP-465, Paper 7 (1989).
46. Oelker, H.-Chr., Hummel, D.: Investigations on the Vorticity Sheets of a Close-Coupled Delta-Canard Configuration. ICAS Paper 88-3.11.R1 (1988). See also J. of Aircraft, Vol. 26, No. 7, pp. 657-666 (1989).
47. Ferretti, A., Salvatore, A.: Aerodynamic Analysis of the Flow Characteristics of a Delta-Canard Configuration. ICAS Paper 90-3.9.2 (1990).

48. Ericsson, L.E., Reding, J.P.: Steady and Unsteady Vortex-Induced Asymmetric Loads on Slender Vehicles. *J. of Spacecraft*, Vol. 18, pp. 97-109 (1981).
49. Chapman, G.T., Keener, E.R.: The Aerodynamics of Bodies of Revolution at Angles of Attack to 90°. *AIAA Paper 79-0023* (1979), see also NASA TM 86016 (1986).
50. Lamont, P.J.: Pressure Around an Inclined O-give Cylinder with Laminar, Transitional or Turbulent Separation. *AIAA J.* Vol. 20, No. 11, pp. 1482-1499 (1982).
51. Szodruch, J., Ganzer, U.: On the Lee-Side Flow for Slender Delta Wings at High Angle of Attack. *AGARD CP-247 Paper 21* (1979).
52. Wood, R., Bauer, S., Byrd, J., McGrath, B., Wesselmann, G.: Influence of Wing Geometry on Leading-Edge Vortices and Vortex-Induced Aerodynamics at Supersonic Speeds. *AIAA paper 89-0085* (1989).
53. Houtman, E.M., Bannink, W.J.: Experimental Investigation of the Transonic Flow at the Leeward Side of a Delta Wing at High Incidence. Report LR-518, Faculty of Aerospace Engineering, Delft University of Technology (1987).
54. Schrader, K.F., Reynolds, G.A., Novak, C.J.: Effects on Mach Number and Reynolds Number on Leading-Edge Vortices at High Angles-of-Attack. *AIAA Paper 88-0122* (1988).
55. Ashill, P.R., Fulker, J.L., Simmons, M.J., Betts, C.J.: Flow Features of Highly-Swept Wings at Subsonic and Supersonic Speeds. *ICAS Paper 90-3.9.1* (1990).
56. Boersen, S.J., Elsenaar, A.: Tests on the AFVAL 65° Delta Wing at NLR: A Study of Vortex Flow Development between Mach = .4 and 4. In: Proceedings of Symposium on "International Vortex Flow Experiment on Euler Code Validation", ed. by A. Elsenaar and G. Eriksson. FFA, Stockholm, October 1-3 1986, pp. 23-36 (1986).
57. Liepmann, H.W., Roshko, A.: Elements of Gasdynamics. John Wiley & Sons, New York (1957).
58. Rubesin, M.W., Rose, W.C.: The Turbulent Mean-Flow, Reynolds-Stress, and Heat-Flux Equations in Mass-Averaged Dependent Variables. *NASA TM-X-62248* (1973).
59. Marvin, J.C.: Turbulence Modeling for Computational Aerodynamics. *AIAA J.* Vol. 21, No. 7 (1983), pp. 941-955.
60. Baldwin, B.S., Lomax, H.: Thin Layer Approximation and Algebraic Model for Separated Turbulent Flows. *AIAA Paper 78-257* (1978).
61. Cebeci, T., Smith, A.M.O., Mosinkis, G.: Calculation of Compressible Adiabatic, Turbulent Boundary layers. *AIAA J.* Vol. 8, pp. 1974-1982 (1970).
62. Degani, D., Schiff, L.B.: Computation of Supersonic Viscous Flows Around Pointed Bodies at Large Incidence. *AIAA Paper 83-0034* (1983).
63. Degani, D., Schiff, L.B.: Computation of Turbulent Supersonic Flows Around Pointed Bodies Having Cross-Flow Separation. *J. of Comp. Physics*, Vol. 66, pp. 173-196 (1986).
64. Landahl, M.T.: CFD and Turbulence. *ICAS Paper 90-0.1* (1990).
65. Polhamus, E.C.: A Concept of the Vortex Lift of Sharp-Edge Delta Wings Based on a Leading-Edge Suction Analogy. *NASA TN D-3767* (1966).
66. Lamar, J.E.: Analysis and Design of Strake-Wing Configurations. *J. of Aircraft*, Vol. 17, No. 1, pp. 20-27 (1980).
67. Murman, E.M., Stremel, P.M.: A Vortex Wake Capturing Method for Potential Flow Calculations. *AIAA Paper 82-0947* (1982).
68. Steinhof, J., Suryanarayanan, K.: The Treatment of Vortex Sheets in Compressible Potential Flows. *AIAA Paper 83-1881* (1983).
69. Steinhof, J., Senge, H., Decker, F.: Application of Vortex Embedding to Aircraft Flows. *AIAA Paper 90-1626* (1990).
70. Brown, C.E., Michael, W.H.: Effect of Leading-Edge Separation on the Lift of a Delta Wing. *J. of Aeron. Sciences*, Vol. 21, pp. 690-694 (1954).
71. Mangler, K.W., Smith, J.H.B.: A Theory of the Flow Past a Slender Delta Wing with Leading-Edge Separation. *Proc. Roy. Soc. A*, Vol. 251, pp. 200-217 (1959).
72. Smith, J.H.B.: Improved Calculations of Leading-Edge Separation from Slender, Thin, Delta Wings. *Proc. Roy. Soc. London*, Vol. A 306, pp. 67-90; see also RAE TR 66070 (1968).
73. Clark, R.W.: Non-Conical Flow past Slender Wings with Leading-Edge Vortex Sheets. *RAE TR 76037* (1976).
74. Sacks, A.H., Lundberg, R.E., Hanson, Ch.W.: A Theoretical Investigation of the Aerodynamics of Slender Wing-Body Combinations Exhibiting Leading-Edge Separation. *NASA CR-719* (1967).
75. Xie-yuan, Y.: Roll-Up of Strake/Trailing-Edge Vortex Sheets for Double-Delta Wings. *J. of Aircraft*, Vol. 22, No. 1, pp. 87-89 (1985).
76. Xie-yuan, Y., Nan, X., Guo-hua, D.: Numerical Simulation of Rolling Up of Leading/Trailing-Edge Vortex Sheets for Slender Wings. *AIAA J.*, Vol. 27, No. 10, pp. 1313-1318 (1989).
77. Peace, A.J.: A Multi-Vortex Model of Leading-Edge Vortex Flows. *Int. J. Num. Meth. in Fluids*, Vol. 3, pp. 543-565 (1983).
78. Maskew, B., Rao, B.M.: Calculation of Vortex Flows on Complex Configurations. *ICAS Paper 82-6.2.3* (1982).
79. Nathman, J.K.: Estimation of Wake Roll-Up over Swept Wings. *AIAA Paper 84-2174* (1984).
80. Mendenhall, M.R., Lesieur, D.J.: Prediction of Vortex Shedding from Forebodies with Chines. *ICAS Paper 90-3.5.2* (1990).
81. Cheng, H.K., Edwards, R.H., Jia, Z.X., Lee, C.J.: Vortex-Dominated Slender-Wing Problems. Studies by a Point-Vortex Method. *AIAA Paper 88-3744* (1988).
82. Hoelmakers, H.W.M.: Computational Aerodynamics of Ordered Vortex Flows. *NLR Report TR 88088 U* (1989).
83. Belotserkovskii, S.M.: Calculation of the Flow about Wings of Arbitrary Planform at a Wide Range of Angles of Attack. *RAE Lib. Transl. 1433* (1968).
84. Rehbach, C.: Numerical Calculation of Three-Dimensional Unsteady Flow with Vortex Sheets. *AIAA Paper 78-111* (1978).

85. Kandil, O.A., Mook, D.T., Nayfeh, A.H.: Non-linear Prediction of Aerodynamic Loads on Lifting Surfaces. *J. of Aircraft*, Vol. 13, No. 1, pp.22-28 (1976).
86. Kim, M., Mook, D.: Application of Continuous Vorticity Panels in Three-Dimensional Lifting Flows with Partial Separation. *AIAA Paper 89-0117* (1989).
87. Rusak, Z., Wasserstrom, E., Seginer, A.: Numerical Calculation of Nonlinear Aerodynamics of Wing-Body Configurations. *AIAA Journal*, Vol. 21, No. 7, pp. 929-936 (1983).
88. Rom, J., Melamed, B., Almoshnino, D.: Comparison of Experimental Results with the Non-Linear Vortex Lattice Method Calculations for Various Wing-Canard Configurations. *ICAS Paper 90-3.3.4* (1990).
89. Gordon, R. Numerical Simulation of Vortical Flows over a Strake-Delta Wing and a Close-Coupled Delta-Canard Configuration. *AIAA Paper 90-3002* (1990).
90. Luckring, J.M.: Comment on "Convergence Characteristics of a Vortex-Lattice Method for Nonlinear Configuration Aerodynamics". *J. of Aircraft*, Vol. 23, No. 10, pp. 798-799 (1986).
91. Johnson, F.T., Tinoco, E.N., Lu, P., Epton, M.A.: Three-Dimensional Flow over Wings with Leading-Edge Vortex Separation. *AIAA J.*, Vol. 18, No. 4, pp. 367-380 (1980).
92. Verhaagen, N.G.: Measurement of the Pressure Distribution on a Biconvex Delta Wing of Aspect Ratio 1. Unpubl. Rep. Fac. Aerosp. Eng., Delft University of Technology (1979).
93. Kelm, R., Ganzer, U.: Laser-Messungen in Transsonischen Wirbelströmungen. *DGLR Jahrbuch 1990*, pp. 335-344 (1990).
94. Bruin, A.C. de, Hoeijmakers, H.W.M.: Computation of Three-Dimensional Boundary Layer Transition and Separation on a 65 Deg Swept Delta Wing at 20 Deg Angle of Attack. *NLR MP 86075 U* (1986).
95. Smith, F.T.: Three-Dimensional Viscous and Inviscid Separation of a Vortex Sheet from a Smooth Non-slender Body. *RAE TR 78095* (1978).
96. Fiddes, S.P.: A Theory for the Separated Flow Past a Slender Elliptic Cone at Incidence. *AGARD CP-291*, Paper 30 (1980).
97. DeJarnette, F.R., Woodson, S.H.: Numerical and Experimental Determination of Secondary Separation on Delta Wings in Subsonic Flow. *J. of Aircraft*, Vol. 22, No. 7, pp. 602-608 (1985).
98. Houtman, E.M., Bannink, W.J.: Numerical and Experimental Determination of Secondary Separation at the Leeward Side of a Delta Wing in Compressible Flow. *ICAS Paper 88-5.4.3* (1988).
99. Verhaagen, N.G., Kruisbrink, A.C.H.: The Entrainment Effect of a Leading-Edge Vortex. *AIAA Paper 85-1584* (1985). See also *AIAA J.*, Vol. 25, No. 8, pp. 1025-1032 (1987).
100. Luckring, J.M.: A Theory for the Core of a Three-Dimensional Leading-Edge Vortex. *AIAA Paper 85-0108* (1985). See also Luckring's North-Carolina-State-University PhD thesis "A Method for Computing the Core Flow in Three-Dimensional Leading-Edge Vortices" (1985).
101. Verhaagen, N.G., van Ransbeeck, P.: Experimental and Numerical Investigation of the Flow in the Core of a Leading Edge Vortex. *AIAA Paper 90-0384* (1990).
102. Fiddes, S.P., Smith, J.H.B.: Calculations of Asymmetric Separated Flow Past Circular Cones at Large Angles of Incidence. *AGARD CP-336*, Paper 14 (1982).
103. Moore, D.W., Griffith-Jones, R.: The Stability of an Expanding Circular Vortex Sheet. *Mathematika*, Vol. 21, pp. 128-133 (1974).
104. Moore, D.W.: The Stability of an Evolving Two-Dimensional Vortex Sheet. *Mathematika*, Vol. 23, pp. 35-44 (1976).
105. Moore, D.W.: The Spontaneous Appearance of a Singularity in the Shape of an Evolving Vortex Sheet. *Proc. Roy. Soc. Lond., Series A*, Vol. 365, pp. 105-119 (1979).
106. Rayleigh, J.W.S. Lord.: The Theory of Sound. Dover Publications, New York, 2nd edition, Vol. II, 1945, pp. 392-394 (1896).
107. Maseland, J.E.J.: Experimental and Numerical Investigation of the Vortex Flow over a 76°/60° Double-Delta Wing at 20° Incidence. Unpublished Report, Faculty of Aerospace Engineering, Delft University of Technology (1990).
108. Rizzi, A.: Computation of Inviscid Incompressible Flow with Rotation. *JFM*, Vol. 153, pp. 275-312 (1985).
109. Rehbach, C.: Numerical Calculation of Three-Dimensional Unsteady Flow with Vortex Sheets. *AIAA Paper 78-111* (1978).
110. Morchoisne, Y.: Calcul D'écoulements Instationnaires par la Méthode des Tourbillons Ponctuels. Paper presented at AGARD-FDP-RTD, Aix-en-Provence, France, April 10, 1986 (1986).
111. MacCormack, R.W.: The Effect of Viscosity in Hypervelocity Impact Cratering. *AIAA Paper 69-354* (1969).
112. Beam, R.M., Warming, R.F.: An Implicit Finite Difference Algorithm for Hyperbolic System in Conservation Form. *JCP*, Vol. 23, pp. 87-110 (1976).
113. Jameson, A., Schmidt, W., Turkel, E.: Numerical Solutions of the Euler Equations by Finite Volume Methods using Runge-Kutta Time-Stepping Scheme. *AIAA Paper 81-1259* (1981).
114. Thomas, J.L., van Leer, B., Walters, R.W.: Implicit Flux-Split Schemes for the Euler Equations. *AIAA Paper 85-1680* (1985).
115. Yee, H.C.: Upwind and Symmetric Shock-Capturing Schemes. *NASA TM-89464* (1987).
116. Klopfer, G.H., Nielsen, J.N.: Euler Solutions for Wing and Wing-Body Combinations at Supersonic Speed with Leading Edge Separation. *AIAA Paper 80-0126* (1980).
117. Klopfer, G.H., Kuhn, G.D., Nielsen, J.N.: Euler Solutions of Supersonic Wing-Body Interference at High Incidence Including Vortex Effects. *AIAA Paper 83-0460* (1983).
118. Weiland, C.: Vortex Simulations Past Wings Using the Euler Equations. *AGARD CP-342*, Paper 19 (1983).
119. Hensch, M.J., Nielsen, J.N., (eds.): Tactical Missile Aerodynamics: Progress in Astronautics and Aeronautics, Vol. 104 (1986).

120. Guillen, P., Lordon, J.: Numerical Simulation of Separated Supersonic Flows Around Tactical Missiles. In AGARD-CP-437 (1988).
121. Wardlaw Jr., A.B., Davies, S.F.: A Second-Order Godunov Method for Tactical Missiles. AGARD CP-412, Paper 12 (1986).
122. Priolo, F.J. Wardlaw Jr., A.B.: Supersonic Non-Circular Missile Computations. AIAA Paper 88-0278 (1988).
123. Wardlaw Jr., A.B., Davies, S.F.: Euler Solutions for Delta Wings. AIAA Paper 89-3398 (1989).
124. Eriksson, L.E., Rizzi, A.: Computation of Vortex Flow Around Wings Using the Euler Equations. Proc. 4th GAMM Conf. on Num. Meth. in Fl. Mech., Ed. H. Viviani, Vieweg Verlag, pp. 87-105 (1981).
125. Hitzel, S.M., Schmidt, W.: Slender Wings with Leading-Edge Vortex Separation: A Challenge for Panel Methods and Euler Solvers. AIAA Paper 83-0562 (1983). See also J. of Aircraft, Vol. 21, No. 10, pp. 751-759 (1984).
126. Rizzi, A.: Euler Solutions of Transonic Flows Around the Dillner Wing - Compared and Analyzed. AIAA Paper 84-2142 (1984). See also J. of Aircraft, Vol. 22, No. 4, pp. 325-328 (1985).
127. Raj, P., Sikora, J.S.: Free-Vortex Flows: Recent Encounters with an Euler Code. AIAA Paper 84-0135 (1984).
128. Raj, P.: Computational Simulation of Free Vortex Flows Using an Euler Code. ICAS Paper 84-1.3.1 (1984).
129. Newsome, R.W.: A Comparison of Euler and Navier-Stokes Solutions for Supersonic Flow over a Conical Delta Wing. AIAA Paper 85-0111 (1985). See also AIAA J. Vol. 24, No. 4, pp. 552-561 (1986).
130. Kandil, O.A., Chuang, A.: Influence of Numerical Dissipation on Computing Supersonic Vortex-Dominated Flows. AIAA Paper 86-1073 (1986). See also AIAA J., Vol. 25, No. 11, pp. 1426-1434 (1987).
131. Newsome, R.W., Thomas, J.L.: Computation of Leading-Edge Vortex Flow. NASA CP 2416, pp. 305-330 (1985).
132. Chakravarthy, S.R., Ota, D.K.: Numerical Issues in Computing Inviscid Supersonic Flow Over Conical Delta Wings. AIAA Paper 86-0440 (1986).
133. Micheltree, R.A., Hassan, H.A., Margason, R.J.: Euler Equation Analysis of the Initial Roll-Up of Aircraft Wakes. AIAA Paper 86-0078 (1988). See also J. of Aircraft, Vol. 23, No. 8, pp. 650-655 (1986).
134. Rizzi, A., Eriksson, L.-E., Schmidt, W., Hitzel, S.M.: Simulating Vortex Flows Around Wings. AGARD CP-432 Paper 21 (1983).
135. Rizzi, A., Purcell, C.J.: Numerical Experiment with Inviscid Vortex-Stretched Flow Around a Cranked Delta Wing: Subsonic Flow. AIAA Paper 85-4080 (1985).
136. Rizzi, A.: Three-Dimensional Solutions to Euler Equations with One-Million Grid Points. AIAA J., Vol. 23, No. 12, pp. 1986-1987 (1985).
137. Murman, E.M., Rizzi, A.: Applications of Euler Equations to Sharp-Edge Delta Wings with Leading Edge Vortices. AGARD CP-412, Paper 15 (1986).
138. Powell, K.G., Murman, E.M., Miller, D.S., Wood, R.M.: A Comparison of Experimental and Numerical Results for Delta Wings with Vortex Flaps. AIAA Paper 86-1840 (1986).
139. Powell, K.G.: Vortical Solutions of the Conical Euler Equations. MIT Report CFDL-TR-87-8 (1987).
140. Longo, J.M.A.: The Role of the Numerical Dissipation on the Computational Euler-Equations Solutions for Vortical Flows. AIAA Paper 89-2232 (1989).
141. Longo, J.M.A., Das, A.: Numerical Simulation of Vortical Flows over Close-Coupled Canard-Wing Configurations. AIAA Paper 90-3003 (1990).
142. Hitzel, S.M.: Wing Vortex-Flows up into Vortex Breakdown. A Numerical Simulation. AIAA Paper 88-2518 (1988).
143. Hitzel, S.: Low and High Speed, High Angle-of-Attack Flow Around a Delta-Wing by an Euler-Simulation. RAeS Conference "The Prediction and Exploitation of Separated Flow", London, April 18-20 1989, Paper 24 (1989).
144. O'Neill, P.J., Barnett, R.M., Louie, C.M.: Numerical Simulation of Leading-Edge Vortex Breakdown Using an Euler Code. AIAA Paper 89-2189 (1989).
145. Raj, P., Sikora, J.S., Keen, J.M.: Free-Vortex Flow Simulation using a Three-Dimensional Euler Aerodynamic Method. ICAS Paper 86-1.5.2 (1986). See also J. of Aircraft, Vol. 25, No. 2, pp. 128-134 (1988).
146. Raj, P., Keen, J.M., Singer, S.W.: Applications of an Euler Aerodynamic Method to Free-Vortex Flow Simulation. AIAA Paper 88-2517 (1988).
147. Sirbaugh, J.R.: Euler Analysis of the AFWAL 65° Delta Wing. AIAA Paper 87-2272 (1987).
148. Goodsell, A.M.: 3-D Euler Calculations of Vortex Flows over Delta Wings. MIT Rep. CFDL-TR-87-6 (1987).
149. Marchbank, W.R.: Numerical Investigation into Vortex Sheet Capture Using an Euler Code. RAeS Conference "The Prediction and Exploitation of Separated Flow", London, April 18-20 1989, Paper 23 (1989).
150. Boerstoeel, J.W.: Progress Report of the Development of a System for the Numerical Simulation of Euler Flows, with Results of Preliminary 3D Propeller-Slipstream/Exhaust-Jet Calculations. NLR TR 88008 U (1988).
151. Elsenaar, A., Hoeijmakers, H.W.M.: An Experimental Study of the Flow Over a Sharp-Edged Delta Wing at Subsonic, Transonic and Supersonic Speeds. Paper presented this Symposium (1990).
152. Jacobs, J.M.J.W., Hoeijmakers, H.W.M., van den Berg, J.I., Boerstoeel, J.W.: Numerical Simulation of the Flow about a Wing with Leading-Edge Vortex Flow. Paper presented at 11th Int. Conf. on Num. Methods in Fluid Dyn., June 1988, Williamsburg, USA. Also NLR MP 88041 U (1988).
153. Jacobs, J.M.J.W., Hoeijmakers, H.W.M.: Aspects of the Application of an Euler-Equation Method to the Simulation of Leading-Edge Vortex Flow. In Proceedings of 8th GAMM Conference on Numerical Methods in Fluid Mechanics, Sept. 1989, Delft, The Netherlands. Also NLR MP 89272 U (1989).

154. Hoeijmakers, H.W.M., Jacobs, J.M.J.W., van den Berg, J.I.: Numerical Simulation of Vortical Flow over a Delta Wing at Subsonic and Transonic Speeds. ICAS Paper 90-3.3.3. Also NLR TP 90029 (1990).
155. Hoeijmakers, H.W.M., Rizzi, A.: Vortex-Fitted Potential Solution Compared with Vortex-Captured Euler Solution for Delta Wing with Leading-Edge Vortex Separation. AIAA Paper 84-2144 (1984). See also AIAA J. Vol. 23, No. 12, 1985, pp. 1983-1985 (1985).
156. Powell, K.G., Murman, E.M., Perez, E.S., Baron, J.S.: Total Pressure Loss in Vortical Solutions of the Conical Euler Equations. AIAA Paper 85-1701 (1985). See also AIAA J., Vol. 25, No. 3, pp. 360-368 (1987).
157. Stewartson, K., Hall, M.G.: The Inner Viscous Solution for the Core of a Leading-Edge Vortex. JFM, Vol. 15, pp. 306-318 (1963).
158. Brown, S.: The Compressible Inviscid Leading-Edge Vortex. JFM, Vol. 22, pp. 17-32 (1965).
159. Williams, B.R., Kordulla, W., Borsi, M., Hoeijmakers, H.W.M.: Comparison of Solutions of Various Euler Solvers and One Navier-Stokes Solver for the Flow About a Sharp-Edged Cropped Delta Wing. This FDP Symposium, AGARD CP- , Paper 2 (1990).
160. Murman, E.M., Powell, K.G., Goodsell, A.M., Landahl, M.: Leading-Edge Vortex Solutions with Large Total Pressure Losses. AIAA Paper 87-0039 (1987).
161. Powell, K.G., Murman, E.M.: A Model for the Core of a Slender Viscous Vortex. AIAA Paper 88-0503 (1988).
162. Mayer, E.W., Powell, K.G.: Similarity Models for Viscous Vortex Cores. AIAA Paper 90-0592 (1990).
163. Marconi, F.: Flat Plate Delta Wing Separated Flows with Zero Total Pressure Losses. AIAA Paper 87-0038 (1987).
164. Kandil, O.A., Chuang, A., Shifflette, J.M.: Finite Volume Euler and Navier-Stokes Solvers for Three-Dimensional and Conical Vortex Flows over Delta Wings. AIAA Paper 87-0041 (1987).
165. Felici, H.M., Drela, M.: Eulerian/Lagrangian Solution of 3-D Rotational Flows. AIAA Paper 90-1631 (1990).
166. Bannink, W.J., Houtman, E.M., Ottochian, S.P.: Investigation of the Vortex Flow over a Sharp-Edged Delta Wing in the Transonic Speed Regime. Report LR-594, Faculty of Aerospace Engineering, Delft University of Technology (1989).
167. Mangler, K.W., Smith, J.H.B.: Behaviour of the Vortex Sheet at the Trailing Edge of a Lifting Wing. RAE TR 69049 (1969).
168. Küchemann, D.: Inviscid Shear Flow Near the Trailing-Edge of an Aerofoil. ZFW, Vol. 15, Heft 8/9, pp. 292-294 (1967).
169. Karmen Jr., S.L., Steinbrenner, J.P., Kisilewski, K.M.: Analysis of the F-16 Flow Field by a Block Grid Euler Approach. AGARD CP-432, Paper 18 (1986).
170. Argawal, R.K., Deese, J.E., Johnson, J., Steinhoff, J.: Euler Calculations of Flow Over a Complete Fighter Aircraft. AIAA Paper 89-2221 (1989).
171. Goodsell, A.M., Madson, M.D., Melton, J.E.: TranAir and Euler Computations of a Generic Fighter Including Comparisons with Experimental Data. AIAA Paper 89-0263 (1989).
172. Goodsell, A.M., Melton, J.E., Madson, M.D.: A Transonic/Supersonic CFD Analysis of a Generic Fighter. ICAS Paper 90-6.4.2 (1990).
173. Raj, P., Olling, C.R., Singer, S.W.: Application of Multizone Euler/Navier-Stokes Aerodynamic Methods to Aircraft Configurations. ICAS Paper 90-6.4.4 (1990).
174. Betchov, R.: On the Curvature and Torsion of an Isolated Vortex Filament. JFM, Vol. 22, Part 3, pp. 471-479 (1965).
175. Pagan, D., Benay, R.: Vortex Breakdown Induced by an Adverse Pressure Gradient: Experimental and Numerical Approaches. AIAA Paper 87-2487 (1987).
176. Lê, T.H., Mège, P., Morchoisne, Y.: Simulation Numérique de L'éclatement Tourbillonnaire par Résolution des Equations D'Euler en Fluide Incompressible. Rech. Aérosp., No. 1989-5, pp. 45-49 (1989).
177. Leibovich, S.: Vortex Stability and Breakdown. AGARD CP-342, Paper 23 (1983). See also AIAA J. Vol. 22, No. 9, pp. 1192-1206 (1984).
178. Payne, F.M., Ng, T.T., Nelson, R.C.: Experimental Study of the Velocity Field on a Delta Wing. AIAA Paper 87-1231 (1987).
179. Hawk, J.D., Barnett, R.M., O'Neill, P.J., Walters, M.M.: Investigation of High Angle of Attack Vortical Flows over Delta Wings. AIAA Paper 90-0101 (1990).
180. Rizzi, A., Purcell, C.J.: Disordered Vortex Flow Computed Around a Cranked Delta Wing at Subsonic Speed and High Incidence. ICAS Paper 86-1.4.1 (1986).
181. Pao, J.L.: Vortical Flow Analysis for F-106B Configuration. AIAA Paper 88-3745 (1988). See also J. of Aircraft, Vol. 27, No. 2, pp. 185-187 (1990).
182. Lee, K.D., Brandt, S.A.: Modeling of Vortex Dominated Flowfields in the Euler Formulation. ICAS Paper 88-5.9.3 (1988).
183. Lee, K.D., Brandt, S.A.: An Inviscid/Viscous Coupling Approach for Vortex Flowfield Calculations. AIAA Paper 89-1961 (1989).
184. Rizzi, A., Drouge, G., Purcell, C.J.: Euler Simulation of Shed Vortex Flows Over the 65 Degree Delta Wing. In Proceedings of Symposium on "International Vortex Flow Experiment on Euler Code Validation", ed. by A. Elsenaar and G. Eriksson. FFA, Stockholm, October 1-3 1986, pp. 289-343 (1986).
185. Marconi, F.: On the Prediction of Highly Vortical Flow Using an Euler Equation Model. In "Studies of Vortex Dominated Flows", Ed. M.Y. Hussaini and M.D. Salas, Springer-Verlag, pp. 311-364 (1987).
186. Smith, J.H.B.: Behavior of a Vortex Sheet Separating from a Smooth Surface. RAE TR 77058 (1977).
187. Marconi, F.: Fully Three-Dimensional Separated Flows Computed with the Euler Equations. AIAA Paper 87-0451 (1987).

188. Kwong, C.M., Myring D.F.: Fusiform-Body Separated Flow Field Calculation using Euler and Boundary Layer Methods. RAES Conference "The Prediction and Exploitation of Separated Flow", London, April 18-20 1989, Paper 27 (1989).
189. Hoefjmakers, H.W.M.: The Role of Computational Fluid Dynamics in Missile Aerodynamics. Paper 7 of Proceedings of NEAR Conference "Missile Aerodynamics", Monterey, Calif., Nov. 1988. Also NLR MP 88072 (1988).
190. Thomas, J.L., Newsome, R.W.: Navier-Stokes Computations of Lee-Side Flows over Delta Wings. AIAA Paper 86-1049 (1986).
191. McMillin, S.N., Thomas, J.L., Murman, E.M.: Euler and Navier-Stokes Solutions for the Leeward Flow over Delta Wings at Supersonic Speeds. AIAA Paper 87-2270 (1987).
192. McMillin, S.N., Pittman, J.L., Thomas, J.L.: A Computational Study of the Incipient Leading-Edge Separation on a 65° Delta Wing at  $M = 1.60$ . AIAA Paper 90-3029 (1990).
193. Thomas, J.L., Taylor, S.L., Anderson, W.K.: Navier-Stokes Computations of Vortical Flows over Low Aspect Ratio Wings. AIAA paper 87-0207 (1987). See also AIAA J., Vol. 28, No. 2, pp. 205-212 (1990).
194. Krist, S.L., Thomas, J.L., Sellers III, W.L., Kjølgaard, S.O.: An Embedded Grid Formulation Applied to a Delta Wing. AIAA Paper 90-0429 (1990).
195. Hsu, C.-H., Hartwich, P.-M., Liu, C.H.: Incompressible Navier-Stokes Solutions for a Sharp-Edged Double Delta Wing. AIAA Paper 87-0206 (1987). See also J. of Aircraft, Vol. 25, No. 4, pp. 442-447 (1988).
196. Hartwich, P.-M., Hsu, C.-H.: High-Resolution Upwind Schemes for the Three-Dimensional Incompressible Navier-Stokes Equations. AIAA Paper 87-0547 (1987). See also AIAA J., Vol. 26, No. 11 pp. 1321-1328 (1988).
197. Hartwich, P.-M., Hsu, C.-H., Luckring, J.M., Liu, C.H.: Numerical Study of the Vortex Burst Phenomenon for Delta Wings. AIAA Paper 88-0505 (1988).
198. Hartwich, P.-M., Hsu, C.-H., Luckring, J.M., Liu, C.H.: Aerodynamic Applications of an Efficient Incompressible Navier-Stokes Solver. ICAS Paper 88-5.9.1 (1988).
199. Hsu, C.-H., Hartwich, P.-M., Liu, C.H.: Incompressible Navier-Stokes Computations of Vortical Flows Over Double-Delta Wings. AIAA Paper 87-1341 (1987). See also J. of Aircraft, Vol. 25, No. 8, pp. 675-676 (1988).
200. Hsu, C.-H., Liu, C.H.: Navier-Stokes Computation of Flow Around a Round-Edged Double-Delta Wing. AIAA Paper 88-2560 (1988). See also AIAA J. Vol. 28, No. 6, pp. 961-968 (1990).
201. Hsu, C.-H., Liu, C.H.: Upwind Navier-Stokes Solutions for Leading-Edge Vortex Flows. AIAA Paper 89-0265 (1989).
202. Hsu, C.-H., Chen, Y.-M., Liu, C.H.: Preconditioned Upwind Methods to Solve 3-D Incompressible Navier-Stokes Equations for Viscous Flows. AIAA Paper 90-1496 (1990).
203. Fujii, K., Kutler, P.: Numerical Simulation of the Leading-Edge Separation Vortex for a Wing and Strake-Wing Configuration. AIAA Paper 83-1908 (1983); see also AIAA Paper 84-1550 (1984).
204. Fujii, K., Schiff, L.B.: Numerical Simulation of Vortical Flows Over a Strake-Delta Wing. AIAA Paper 87-1229 (1987). See also AIAA J. Vol. 27, No. 9, pp. 1153-1162 (1989).
205. Fujii, K.: A Method to Increase the Accuracy of Vortical Flow Simulations. AIAA Paper 88-2562 (1988).
206. Fujii, K., Obayashi, S.: Use of High-Resolution Upwind Scheme for Vortical Flow Simulations. AIAA Paper 89-1955 (1989). See also J. of Aircraft, Vol. 26, No. 12, pp. 1123-1129 (1989).
207. Ekaterinaris, J.A., Schiff, L.B.: Vortical Flow over Delta Wings and Numerical Prediction of Vortex Breakdown. AIAA Paper 90-0102.
208. Ying, S.X., Steger, J.L., Schiff, L.B., Bagannoff, D.: Numerical Simulation of Unsteady, Viscous High-Angle-of-Attack Flows Using a Partially Flux-Split Algorithm. AIAA Paper 86-2179 (1986).
209. Ekaterinaris, J.A., Schiff, L.B.: Numerical Simulation of the Effects of Variation of Angle of Attack and Sweep Angle on Vortex Breakdown over Delta Wings. AIAA Paper 90-3000 (1990).
210. Webster, W.P., Shang, J.S.: Numerical Simulation of Reversed Flow over a Supersonic Delta Wing at High Angle of Attack. AIAA Paper 89-1802 (1989).
211. Webster, W.P., Shang, J.S.: Comparison Between Thin Layer and Full Navier-Stokes Simulations Over a Supersonic Delta Wing. AIAA Paper 90-0589 (1990).
212. Gordnier, R.E., Visbal, M.R.: Unsteady Navier-Stokes Solutions for a Low Aspect Ratio Delta Wing. AIAA Paper 90-1538 (1990).
213. Krause, F., Shi, X.G., Hartwich, P.M.: Computation of Leading-Edge Vortices. AIAA Paper 83-1907 (1983).
214. Rizetta, D.P., Shang, J.S.: Numerical Simulation of Leading-Edge Vortex Flow. AIAA Paper 84-1544 (1984). See also AIAA J., Vol. 24, No. 2, pp. 237-245 (1986).
215. Müller, B., Rizzi, A.: Navier-Stokes Simulation of Laminar Flow Over the 65 Deg Round Leading Edge Delta Wing at  $M_\infty = 0.85$  and  $\alpha = 10$  Deg. In: Proceedings of Symposium on "International Vortex Flow Experiment on Euler Code Validation", ed. by A. Elsenaar and G. Eriksson. FFA, Stockholm, October 1-3 1986, pp. 269-280 (1986).
216. Müller, B., Rizzi, A.: Navier-Stokes Computation of Transonic Vortices Over a Round Leading Edge Delta Wing. AIAA Paper 87-1227 (1987). See also Int. J. for Num. Meth. in Fluids, Vol. 9, pp. 943-962 (1989).
217. Rizzi, A., Müller, B.: Large-Scale Viscous Simulation of Laminar Vortex Flow Over a Delta Wing. AIAA J., Vol. 27, No. 7, pp. 833-840 (1989).
218. Rizzi, A., Müller, B., Purcell, C.J.: Comparison of Euler and Navier-Stokes Solutions for Vortex Flow Over a Delta Wing. AIAA Paper 87-2347 (1987). See also Aeron. J., April 1988, pp. 145-153 (1988).
219. Siclari, M.J., DelGuidice, P., Jameson, A.: A Multigrid Finite Volume Method for Solving the Euler and Navier-Stokes Equations for High Speed Flows. AIAA Paper 89-0283 (1989).



220. Hilgenstock, A.: Ein Beitrag zur numerischen Simulation der transsonischen Strömung um einem Deltaflügel durch Lösung der Navier-Stokes'schen Bewegungsgleichungen. DLR-FB 90-13 (1990). See also Paper 7 of this FDP Symposium.

221. Siclari, M.J., Marconi, F.: The Computation of Navier-Stokes Solutions Exhibiting Asymmetric Vortices. AIAA Paper 89-1817 (1989).

222. Siclari, M.J.: Asymmetric Separated Flows at Supersonic Speeds. AIAA Paper 90-0595 (1990).

223. Kandil, O.A., Wong, T.-C., Liu, C.H.: Navier-Stokes Computations of Symmetric and Asymmetric Vortex Shedding Around Slender Bodies. AIAA Paper 89-3397 (1989).

224. Kandil, O.A., Wong, T.-C., Liu, C.H.: Prediction of Steady and Unsteady Asymmetric Vortical Flow Around Cones. AIAA Paper 90-0598 (1990).

225. Kandil, O.A., Wong, T.C., Kandil, H.A.: Computation and Control of Asymmetric Vortex Flow Around Circular Cones Using Navier-Stokes Equations. ICAS Paper 90-3.5.3 (1990).

226. Vatsa, V.N., Thomas, J.L., Wedan, B.W.: Navier-Stokes Computations of a Prolate Spheroid at Angle of Attack. AIAA Paper 87-2627 (1987). See also J. of Aircraft, Vol. 26, No. 11, pp. 986-993 (1989).

227. Hartwich, P.-M., Hall, R.M.: Navier-Stokes Solutions for Vortical Flows over a Tangent-Ogive Cylinder. AIAA Paper 89-0337 (1989).

228. Hartwich, P.-M., Hall, R.M., Hensch, M.J.: Navier-Stokes Computations of Vortex Asymmetries Controlled by Small Surface Imperfections. AIAA Paper 90-0385 (1990).

229. Schiff, L.B., Degani, D., Cummings, R.M.: Numerical Simulation of Separated and Vortical Flows on Bodies at Large Angles of Attack. Proceedings of 4th Symposium on Numerical and Physical Aspects of Aerodynamic Flows, Long Beach, Jan. 16-19 1989.

230. Gee, K., Cummings, R.M., Schiff, L.B.: The Effect of Turbulence Models on the Numerical Prediction of the Flow Field about a Prolate Spheroid at High Angle of Attack. AIAA Paper 90-3106 (1990).

231. Degani, D.: Numerical Investigation of the Origin of Vortex Asymmetry of Flows over Bodies at Large Angle of Attack. ICAS Paper 90-6.6.1 (1990). See also AIAA Paper 90-0593 (1990).

232. Hafez, M., Ahmad, J.: Vortex Breakdown Simulation, Part III: Compressibility Effects. Proceedings of 4th Symposium on Numerical and Physical Aspects of Aerodynamic Flows, Long Beach, Jan. 16-19 1989.

233. Liu, C.H., Menne, S.: Simulation of a Three-Dimensional Vortex Breakdown. AIAA Paper 89-1806 (1989).

234. Spall, R., Gatski, T.: A Computational Study of the Taxonomy of Vortex Breakdown. AIAA Paper 90-1624 (1990).

235. Krause, E., Liu, C.H.: Numerical Studies of Incompressible Flow Around Delta and Double-Delta Wings. ZFW, Vol. 13, pp. 291-301 (1989).

236. Powell, K.G., Beer, M.A., Law, G.W.: An Adaptive Embedded Mesh Procedure for Leading-Edge Vortex Flows. AIAA Paper 89-0080 (1989).

237. Batina, J.T.: Vortex-Dominated Conical-Flow Computations Using Unstructured Adaptively-Refined Meshes. AIAA Paper 89-1816 (1989).



COMPARISON OF SOLUTION OF VARIOUS EULER SOLVERS AND ONE NAVIER-STOKES SOLVER  
FOR THE FLOW ABOUT A SHARP-EDGED CROPPED DELTA WING<sup>\*)</sup>

by

B.R. Williams - RAE, Farnborough, UK  
W. Kordulla - DLR, Göttingen, West Germany  
M. Borsi - Aeritalia, Turin, Italy  
H.W.M. Hoeijmakers - NLR, Amsterdam, The Netherlands

#### SUMMARY

For the flow about a sharp-edged cropped 65-deg delta wing numerical solutions obtained with different Euler methods are compared with each other, with the numerical solution of a Reynolds-averaged Navier-Stokes method and with experimental data. At the selected free-stream Mach number of 0.85 and angle of attack of 10 deg the flow features a leading-edge vortex, is transonic but contains weak shocks only. The results of the Euler methods have been obtained on one and the same C-H type of grid with close to 300,000 cells. This investigation, carried out within the frame work of a four-nation collaborative program, indicates that for the test case considered there are, from a theoretical point of view, significant differences between results from different Euler methods, even if artificial dissipation is minimized. However, the correlation of the Euler solutions with experimental data shows much larger differences due to the failure to represent secondary separation in the Euler methods and is therefore unsatisfactory. The results of the Reynolds-averaged Navier-Stokes method demonstrate an improved correlation of theory and experiment.

#### INTRODUCTION

Vortical flow plays a critical role in the high-angle-of-attack aerodynamics of contemporary fighter aircraft. Improving the performance of these aircraft and of designs of the next generation of fighters requires advances in the knowledge of the physics of vortical flow, improvements in wind-tunnel techniques and assessment of the capabilities of numerical flow simulation methods.

To aid the development of computational methods for simulating the vortical flow about fighter aircraft a collaborative program is carried out under the auspices of the Independent European Programme Group (IEPG), Panel III Sub-Group 6. Four nations (United Kingdom, Germany, Italy and the Netherlands) participate in this 5-year program, designated Technical Area 15 (TA15) "Computational Methods in Aerodynamics". The program started in June 1987.

One of the first cases considered for assessing the capability of Euler and Navier-Stokes computational methods is the flow about the isolated sharp-edged wing of the configuration considered in Ref. 1. It concerns a cropped 65-deg delta wing of taper ratio 0.15. The chordwise section is the NACA 64A005 airfoil which at its point of maximum thickness is smoothly blended into the bi-convex shaped nose. During the early stage of the collaborative program flow solutions were obtained by all participants with different Euler solvers on different grids for the transonic condition of  $M_\infty = 0.85$  and  $\alpha = 10$  deg.

The main conclusion that could be drawn from the comparison of these numerical results was that for this sharp-edged wing the differences which existed between the Euler solutions obtained by the various methods appear to arise more from differences between the grids than from differences between the solution algorithms.

To confirm this conclusion a so-called "common exercise" was set up. It involved each participant using its own Euler solver to produce a flow solution on one and the same high-quality grid. The free-stream condition to be considered was once again  $M_\infty = 0.85$ ,  $\alpha = 10$  deg. For this condition the flow features a full-span leading-edge vortex, is transonic but contains weak shocks only. At the incidence selected vortex breakdown has not to be accounted for, because for this configuration vortex breakdown occurs above the wing for angles of attack in excess of 20-22 deg.

Any solution algorithm for numerically solving the Euler equations introduces implicitly or explicitly artificial dissipation into the solution, which affects the accuracy of the solution of the Euler equations. It was decided that, as far as the explicitly added dissipation is concerned, all solutions to be generated should have the minimum amount of artificial dissipation commensurate with obtaining a converged solution.

The purpose of the present paper is to present the results of the comparison of the "minimum-dissipation" Euler solutions with each other. It concerns seven solutions, namely the ones obtained with Euler solvers available at:

- British Aerospace Warton (BAe) (United Kingdom),
- MBB-München (MBB) (West-Germany),
- Dornier-Friedrichshafen (DOR) (West-Germany),
- DLR-Braunschweig (DLB) (West-Germany),
- Aeritalia-Turin (AIT) (Italy),
- Aermacchi (AEM) (Italy),
- NLR (Netherlands).

Euler methods are capable of simulating flow separation from sharp leading (and trailing) edges: it appears that at sharp edges sufficient artificial viscosity is introduced to model faithfully the effects of the true viscosity (Ref. 2). Secondary separation, which occurs in a smooth region of the upper surface of the wing, just outboard of the vortex induced suction peak, is not modeled automatically in the Euler methods. Like any other separation from a smooth part of the surface it has to be simulated through a viscous-flow method. To address the influence of secondary separation the results of the Euler methods are compared with results of the Reynolds-averaged Navier-Stokes method of DLR-Göttingen, for the same case but obtained on a different grid, as well as with available experimental data (Refs. 1, 3).

<sup>\*)</sup> This investigation has been carried out within the framework of IEPG-TA15, under contract with: (i) for UK, the UK the Ministry of Defence (Procurement Executive); (ii) for West-Germany, the German Ministry of Defence (BMVg); (iii) for Italy, the Italian Ministry of Defence; (iv) for the Netherlands, the Netherlands Agency for Aerospace Programs (NIVR) for the Ministry of Defence.

## OUTLINE OF THE METHODS USED

The Euler methods of British Aerospace, Dornier, Aeritalia, Aeromacchi and NLR are quite similar. All five methods are based upon the finite-volume central-difference cell-centered scheme of Jameson et al (Ref. 4). Discretization of the five time-dependent nonlinear equations for the conservation of mass, momentum and energy, expressed in integral form, proceeds in two steps, spatial and temporal. These two steps are not independent since the stability of the temporal integration depends on the type of the spatial discretization. The central difference scheme (here with the flow variables located at the cell centers) for the spatial discretization allows odd-even decoupling of the flow variables at adjacent cells. Due to aliasing errors this decoupling may inhibit convergence of the temporal integration of the nonlinear semi-discrete equations. Furthermore, discontinuities in the flow field may cause divergence of the time-integration procedure. Therefore the following artificial dissipative terms are added to the semi-discrete equations. Fourth-difference terms to provide the background dissipation for suppressing point-to-point oscillations. Second-difference terms, to provide damping for stabilizing the integration in regions with large pressure gradients such as near shocks. The steady-state solution is obtained using a four-stage or five-stage (AEM) Runge-Kutta procedure to integrate the discretized equations in time. In this procedure the dissipative terms are evaluated at the first stage or a few selected stages only, this to reduce the computational cost. Convergence is accelerated employing local time-stepping, implicit residual averaging, enthalpy damping and multi-grid, not necessarily implemented in each of the five Euler solvers considered here. For the conditions on the solid surface the methods employ an extrapolation of the pressure to the wall. The conditions on the far-field boundary of the computational domain are implemented using Riemann invariants.

Since Euler solutions with minimum dissipation are the interest of this paper the explicitly added artificial dissipation terms are described in more detail. Added to the right-hand-side of the discretized equations, written as

$$V_{ijk} \frac{d}{dt} \vec{w}_{ijk} = - \vec{Q}_{ijk}$$

with  $\vec{w}_{ijk}$  the vector with the 5 flow variables at

the center of cell  $ijk$ ,  $\vec{Q}_{ijk}$  the net convective

flux out of cell  $ijk$  and  $V_{ijk}$  the volume of cell

$ijk$ , is the net dissipative flux  $\vec{D}_{ijk}$

$$\vec{D}_{i,j,k} = \vec{d}_{i+1,j,k} - \vec{d}_{i-1,j,k} + \vec{d}_{i,j+1,k} - \vec{d}_{i,j-1,k} + \vec{d}_{i,j,k+1} - \vec{d}_{i,j,k-1}$$

with for example

$$\vec{d}_{i+1,j,k} = \frac{h_{i+1,j,k}}{\Delta t} \{ \epsilon_{i+1,j,k}^{(2)} (\vec{w}_{i+1,j,k} - \vec{w}_{i,j,k}) - \epsilon_{i+1,j,k}^{(4)} (\vec{w}_{i+2,j,k} - 3\vec{w}_{i+1,j,k} + 3\vec{w}_{i,j,k} - \vec{w}_{i-1,j,k}) \}$$

and  $\frac{1}{\Delta t} h_{i+1,j,k}$  a non-linear scaling factor

depending on cell dimensions, the velocity and the speed of sound. With the pressure sensor defined as

$$u_{i,j,k} = \frac{|p_{i+1,j,k} - 2p_{i,j,k} + p_{i-1,j,k}|}{|p_{i+1,j,k} + 2p_{i,j,k} + p_{i-1,j,k}|}$$

the factors  $\epsilon^{(2)}$  and  $\epsilon^{(4)}$  are defined as

$$\begin{aligned} \epsilon_{i+1,j,k}^{(2)} &= K^{(2)} u_{i+1,j,k} && \text{BAe} \\ &= \text{Min}(\frac{1}{2}, K^{(2)} u_{i+1,j,k}) && \text{DOR, AIT, NLR} \\ &= K^{(2)} \text{Min}(\frac{1}{2}, u_{i+1,j,k}) && \text{AEM} \end{aligned}$$

and

$$\begin{aligned} \epsilon_{i+1,j,k}^{(4)} &= \text{Max}(0, K^{(4)} - \epsilon_{i+1,j,k}^{(2)}) && \text{BAe, AEM} \\ &= \text{Max}(0, K^{(4)} - \delta u_{i+1,j,k}) && \text{DOR, AIT} \\ &= K^{(4)} \text{Max}(0, \frac{1}{64} - \delta u_{i+1,j,k}) && \text{NLR} \end{aligned}$$

respectively, with  $u_{i+1,j,k} = \text{Max}(u_{i+1,j,k}, u_{i,j,k})$

and  $\delta$  is a switching parameter.

The Euler-equation method of DLR-Braunschweig (Ref. 5) uses a finite-volume central-difference scheme in which the flow variables are located at the cell vertices. A 5-stage Runge-Kutta procedure is used for time integration. The distribution formula for the cell fluxes is as proposed by Hall (Ref. 6). Second- and fourth-order artificial dissipative terms identical to the BAe ones above, are added for stability. In the code several convergence accelerating techniques are implemented.

The Euler-equations method of MBB uses a Godunov type averaging procedure based on an eigenvalue analysis of the unsteady inviscid equations by means of which the fluxes are evaluated at the faces of the finite volume, with separate sets of constant flow variables on either side of the face (the flow variables are defined at the cell centers). The sum of the flux differences is approximated by a third-order spatial characteristic flux extrapolation scheme. Sensor functions are used to detect non-monotonous behaviour of the flow variables. At locations where such behaviour is detected, e.g. at shocks, the scheme reduces to a first-order accurate scheme. Dissipation is inherently provided in the upwind formulation and in this method no explicitly added artificial dissipative terms are required. To obtain a steady-state solution, an explicit time relaxation technique is used. For a more extensive description of the method, see Ref. 7.

The (full) Reynolds-averaged Navier-Stokes method of DLR-Göttingen uses a finite-volume central-difference (flow variables located at cell centers) approach with a four-stage Runge-Kutta procedure for time integration. The code can be run on a multi-blocked grid. In turbulent flow calculations a modified algebraic turbulence model based on that of Baldwin and Lomax is employed. A more extensive description of the method can be found in Ref. 8.

## GRIDS

The seven Euler solutions were computed on the so-called BAe-A grid, generated by British Aerospace Warton. Since it may be assumed that the flow is symmetric, only the solution in the starboard half space is considered. The grid is generated as a one-block grid, with C-H type of topology, which for some of the codes was sub-divided into a multi-block grid. There are 192 cells in chordwise direction, 32 cells in the direction normal to the wing and 48 cells in spanwise direction, a total of 294,912 cells. On the wing upper surface, there are 72 cells in chordwise and 34 cells in spanwise direction.

For the plane  $z = 0$ , the outer boundary, the wing planform and the outline of the "tip extension" are presented in Fig. 1a. For the plane of symmetry the outer boundary, the wing, the wake cut and the grid line intersecting the wing trailing edge are shown in Fig. 1b. The upstream farfield boundary is more than 10, the downstream one more than 4 root chords away from the wing. In lateral direction the outer boundary is at 5 semi-spans from the plane of symmetry. The grid on the wing surface consists of curves of about constant percentage chord and about constant fraction of the semi-span, see Fig. 1c. The mesh is dense near the leading edge and near the wing tip, with mild stretching ratios everywhere. Fig. 1d shows part of the grid in the plane of symmetry. Close-ups of the grid near the apex and near the trailing edge are presented in Figs. 1e and 1f, respectively.

The Euler code of DLR Braunschweig was run on the grid described above with two grid surfaces near the trailing edge deleted, i.e. such that in chordwise direction the grid immediately upstream of the trailing edge is coarser. The Euler solver of Aermacchi was run on the grid with one grid surface near the wing tip deleted, i.e. such that in spanwise direction the grid inboard of the tip is coarser.

The Reynolds-averaged Navier-Stokes solution was obtained on a different grid. This multi-block grid is of H-R type of topology with about a total of 2 million cells. On the wing upper and lower surfaces the grid has 40x40 cells each, see Fig. 2a. In order to resolve the boundary layer, the grid density in the direction normal to wing near the wing surface is much higher than for the BAe-A grid used for the Euler calculations, see Fig. 2b.

#### COMPARISON OF RESULTS OF EULER METHODS

The following characteristics are compared:

- pressure and total-pressure distributions
- lift, drag, pitching moment, root-bending moment, number of supersonic points
- position of and total-pressure loss at the center of the leading-edge vortex.

Before presenting the results of the comparison, the setting of the parameters of the explicit artificial dissipation terms is discussed and the general features of the Euler solutions are described.

#### Numerical Dissipation

Each of the seven Euler-equation methods has demonstrated to be able to compute a fully-converged solution on the BAe-A grid. For the Euler-equation methods with explicitly added artificial dissipation terms, the minimum values of the parameters in the expressions for the artificial dissipation required to obtain a converged steady-state "minimum dissipation" solution were:

	$K^{(2)}$	$K^{(4)}$	$\delta$	$\epsilon^{(2)}$	$\epsilon^{(4)}$
BAe	0.0	1/64	-	0	1/64
DOR	0.0	1/32	2	0	[0, 1/32]
AIT	0.15	1/125	0	[0, 1]	1/125
AEM	0.0	1/64	-	0	1/64
NLR	0.0	1.75	0	0	7/256
DLB	0.25	1/256	-	$\frac{1}{2}u_{ijk}$	[0, 1/256]

It turns out that because the flow is very nearly shock free the second-difference dissipation term can be switched off in most Euler codes. A more precise comparison of the amount of artificial dissipation used in the various codes is not possible because it also depends on the scaling factor, see above expression for  $d_{ijk}$ , which appears to be different for each code. Also other sources of numerical dissipation implicit in the solution

algorithm such as the non-uniformity of the grid, the implementation of the far-field boundary conditions and especially the boundary conditions at the wing surface, play a different role in each of the Euler codes considered.

#### DESCRIPTION OF EULER SOLUTIONS

The solutions obtained on the BAe-A grid by the various Euler codes are qualitatively very similar. Before discussing the quantitative differences in detail the global characteristics of a representative solution are described. Fig. 3 shows the solution computed with the NLR Euler method. Presented are the isobar pattern on the upper wing surface of the wing, the isobar pattern in three consecutive planes perpendicular to the wing planform and the contours of equal total-pressure loss in the same three planes.

The low-pressure region on the wing upper surface, which is the foot print of the leading-edge vortex, indicates that flow separation starts very close to the apex. The lowest values of the pressure coefficient are found on the aft part of the wing, which is typical for the higher free-stream Mach numbers. In the cross-flow plane isobar patterns the center of the leading-edge vortex is located at a point of minimum pressure. Although the flow is supersonic over a large portion of the wing upper surface, judging from the isobar patterns, shocks are absent in the flow field, except possibly close to the trailing edge where a weak cross-flow shock develops just out-board of the position of the vortex.

For the wing in steady inviscid flow without shocks the total pressure should be constant, equal to its free-stream value. For such a flow Euler methods introduce variations in total pressure by the discretization, the explicit artificial dissipation terms, boundary conditions, etc. Due to the fine grid with low stretching rates close to the wing the error in total pressure is small on the upper and lower surface of the wing. Right at the sharp leading-edge, where the flow separates, there is a spike in the total pressure loss. Also in the flow field the high gradients in the free shear layer and in the leading-edge vortex cause significant losses in total pressure, up to about 40% at the center of the core. Therefore contours of equal total pressure are instrumental in outlining the structure of the vortex system.

#### SPANWISE DISTRIBUTIONS OF STATIC AND TOTAL PRESSURE

Fig. 4a presents spanwise sections of the pressure distribution on the upper and lower surface of the wing. In each plot the results of the seven Euler methods are identified by different symbols connected by straight-line segments, solid ones for the upper surface, dashed ones for the lower surface of the wing. All plots are at the same scale, facilitating easy assessment of the correlations.

The results indicate the following:

(i) The pressure distributions on the lower wing surface are almost identical ( $\Delta C_p < 0.02$ ), except near the apex and near the trailing edge where the differences are one order of magnitude larger.

(ii) The pressure distribution on the upper surface of the wing indicates that all solutions feature a concentrated leading-edge vortex. The height of the suction peak underneath the vortex shows differences in  $C_p$  of the order of 0.15 over most parts of the wing, somewhat larger values near the apex and the trailing edge. The spreading in the lateral position of the suction peak is of the order of 5% local semi-span.

(iii) The solutions fall into two groups:  
 A) Those from the Euler methods of BAe, Dornier, Aeritalia, Aermacchi and NLR; these are the central-difference (flow variables at cell centers) methods based on Jameson's approach. The solution of AIT's method is quite similar to the other four but with a somewhat lower suction peak, giving evidence of the higher levels of numerical dissipation.  
 B) Those from the Euler methods of DLR and MBB, a central-difference (flow variables at cell vertices) and upwind method, respectively.

(iv) The suction peak of the second group is higher and narrower than that of the first group of solutions.

(v) The differences in the results of the seven Euler codes, despite strong similarities in the formulations of five of them, are most apparent at the apex, the leading edge and the trailing edge. However, from a practical point of view, the differences between the various results are acceptably small.

(vi) In most results the pressure distribution on the upper surface of the wing shows a spike, or a spike and a wiggle at the leading edge.

Fig. 4b shows spanwise sections of the total pressure (loss) on the upper and lower surface of the wing for the same five stations considered in Fig. 4a. It is observed that:

(i) On the lower surface the total pressure losses are rather small, with losses of the order of 0.01 of the free-stream value near the plane of symmetry.

(ii) Total pressure losses (or gains) on the upper surface are larger, and are quite different for each solution, but considering characteristic features of the distributions the same classification (groups A and B) of the solutions can be made.

(iii) In all solutions the largest values of total pressure losses are attained at the apex, at the leading edge and near the suction peak, i.e. at locations with large gradients in the solution. The highest values exceed 10% of the free-stream value. Away from these regions the errors fall below 5%, with the method of BAe having the lowest and the upwind method of MBB having the highest losses.

(iv) Over some part of the upper surface of the wing the solutions of group A exhibit a gain in total pressure, a feature most pronounced in the solution of NLR (about 3% of the free-stream value).

The comparison of the local Mach number distribution (not shown here) has indicated that this quantity is more susceptible to differences in the methods than the static pressure distribution. This suggests that in Bernoulli's equation the loss in total pressure is converted in changes in velocity rather than in static pressure. Notably on the wing upper surface the Mach number distribution between the plane of symmetry and the suction peak shows a considerable spreading ( $\Delta M \approx 0.06$ ). In this same region the differences in the static pressure are relatively much smaller. The differences in the peak values (1.7 underneath the vortex) of the local Mach number are of the order of 0.15 at most.

#### CHORDWISE DISTRIBUTION OF STATIC AND TOTAL PRESSURE

In Fig. 5a a chordwise section of the surface pressure distribution is given for  $y/s = 0.0, 0.5$  and  $0.9$ , where  $s$  denotes the local semi-span. In the figures the same identification is used as in the previous sections. In the plane of symmetry ( $y/s=0.0$ ) the solutions are close together. At the trailing edge the Kutta condition appears to be satisfied. At the apex the solutions show a sharp peak, negative  $C_p$  on the upper, positive  $C_p$  on the lower wing surface, indicative of the singularity in the solution at that point?

Fig. 5a confirms what was observed in the spanwise sections of the pressure distribution, i.e. the solutions fall into two groups with acceptably small differences between the solutions of the two groups. Near the wing tip ( $y/s > 0.9$ ) the pressure distributions on the upper wing surface show larger differences (up to 0.5 in  $C_p$ ), probably due to the large gradients in the solution provoking a different behaviour of the artificial dissipative terms in that region.

In Fig. 5b chordwise sections of the total pressure distribution on the surface of wing are compared. Except in the plane of symmetry and right at the tip the total pressure losses on the wing lower surface are small. On the wing upper surface the total pressure coefficient (losses or gains) differs from method to method, though the character of the distributions is quite similar for the Euler methods of NLR, BAe, Dornier, Aeritalia and Aermacchi (group A). The result produced by the NLR code has total pressure production over relatively the largest part of the upper surface. Group B of Euler methods apparently features somewhat more numerical dissipation at the wing surface than the methods of group A. In MBB's result wiggles are apparent which appear to travel in downstream direction, i.e. in a direction away from the leading edge. In the results of each participant wiggles appear near the trailing edge.

#### FORCES, MOMENTS, NUMBER OF SUPERSONIC POINTS

Using the surface pressure distributions from the Euler solutions the lift, drag, pitching moment (with apex as moment center) and root-bending moment coefficients were computed. Arbitrariness was eliminated by using the same numerical integration procedure.

The result is given below reference area = 0.2279 reference length = 1.0):

	$C_L$	$C_D$	$C_{M_y}(\text{apex})$	$C_{M_x}$	NSUP
NLR	0.538	0.0882	-0.337	0.1034	32,705
BAe	0.530	0.0868	-0.332	0.1015	30,600
DOR	0.522	0.0857	-0.327	0.0997	29,853
MBB	0.515	0.0842	-0.319	0.0969	21,761
DLB	0.518	0.0841	-0.322	0.0978	19,867
AIT	0.526	0.0861	-0.328	0.1002	28,872
AEM	0.530	0.0869	-0.334	0.1022	30,564
Delta	0.023	0.0041	0.018	0.0065	
Exp.	0.457	0.0846	-0.271	n.a.	n.a.

where  $C_L$  and  $C_D$  are the lift and drag coefficient,  $C_{M_y}$  is the pitching moment about the apex and  $C_{M_x}$  is the root-bending moment. The table includes the values from the "International Vortex Flow Experiment" (Ref. 1) for the same Mach number and incidence and at a Reynolds number of 9 million. Note that the measured data were obtained for a wing-(under-wing)body combination while the computations were carried out for the isolated wing.

The predicted lift coefficients vary between 0.515 and 0.538, the measured one equals 0.457, i.e. the lift coefficient is over-predicted primarily due to the neglect of the secondary separation in the Euler computations. The drag coefficients vary between 0.0841 and 0.0822, the experimental value is 0.0846. The pitching moment coefficient (referenced to the apex) has been predicted in the range -0.319 to -0.337, the experimental value is considerably less nose down, namely -0.271. The predicted root-bending moment coefficient has a spreading of 10% with values between 0.0969 and 0.1034.

The table also lists the number of supersonic points found in the computation. It is clear that there is some scatter in this global flow characteristic, with the solutions grouping together as found before for the pressure distributions.

#### POSITION OF THE CENTER OF THE VORTEX CORE

The position of the minimum of the total pressure in subsequent cross-flow planes is often presumed to indicate the trajectory of the "center of the vortex core". This trajectory and the magnitude of the total-pressure loss along the trajectory are presented in Fig. 6. The "center of the vortex" follows a path which more or less lies along a ray from the apex. The differences in the lateral position of the center of the vortex computed by the various codes are of the order of 5 percent of the local semi-span. It appears that the vertical positions of the vortex center predicted by most Euler methods are close together. The magnitude of the total pressure loss at the "center of the vortex" shows that the loss is of the order of 40% of the free-stream value, with near the trailing edge larger values for the solutions of DLR and MBB. The MBB solution shows a linear increase in total pressure loss, starting with 25% at the apex and increasing to 55% at the trailing edge, while the other solutions exhibit an almost constant total pressure loss along most of the vortex axis.

#### COMPARISON OF RESULTS OF EULER AND NAVIER-STOKES METHODS AND EXPERIMENTAL DATA

Fig. 7 shows the isobar pattern on the upper surface of the wing as obtained from the results of an Euler method (NLR), the one obtained from the (turbulent flow) results of the (full) Reynolds-averaged Navier-Stokes method of DLR-Göttingen and the one obtained from experimental data (Ref. 3). It should be remarked here again that the wind-tunnel model has a body attached to the lower surface of the wing. The body extends in the upstream direction almost up to the apex and fairs smoothly into the sting downstream of the trailing edge. It is presumed that on the major part of the upper surface of the wing the influence of the body on the pressure distribution is small. For the case considered here it is estimated that downstream of the 25% root chord station the body influence is negligible.

The three isobar patterns of Fig. 7 show qualitatively the same dominating feature, i.e. the region with low pressure underneath the leading-edge vortex. However, quantitatively there are substantial differences. This is exemplified in Figs. 8a and 8b which present four spanwise and three chordwise sections of the pressure distributions, respectively. To indicate differences in the results of the Euler methods both the results of the NLR and of the BAE Euler code are included. The following is observed:

(i) Comparison of the results from the Euler methods with the experimental data shows that the Euler methods predict an upper surface pressure distribution with a suction peak which is too high and too far outboard and without a plateau region between the suction peak and the leading edge. These differences are primarily due to the failure of the Euler methods to predict secondary separation and associated secondary vortical flow region.

(ii) Comparing the results of the Euler methods with the one of the Reynolds-averaged Navier-Stokes method shows that correlation of computed results with experimental data is much better for the Navier-Stokes method. However, note that on the forward part of the wing ( $x/c_r < 0.4$ ) the resolution of the Navier-Stokes grid on the wing surface is rather too coarse (Fig. 2a) to yield useful results.

(iii) On the upper surface of the wing, secondary separation is observed at about 78, 81, 83 and 92 percent local semi-span at  $x/c_r = 0.3, 0.6, 0.8$  and  $0.967$  respectively, while it is predicted by the Reynolds-averaged Navier-Stokes method at about 80, 78, 78 and 88% at the corresponding stations. Anyway, the predicted location at  $x/c_r = 0.3$  will not be very accurate because of the low resolution of the grid on the forward part of the wing. So it appears that the secondary separation occurs too early in the computation with the Reynolds-averaged Navier-Stokes method. Furthermore, the clearly visible second suction peak in the computed results, which is not that pronounced in the measured data, suggests that the predicted secondary vortex is stronger than the real one. It is suggested that the main reason for the discrepancy is the lack of adequate turbulence modeling, i.e. the algebraic model employed is not entirely suited to simulate turbulent secondary separation correctly.

(iv) There are also discrepancies between the results of the Navier-Stokes method and experimental data in the tip region and near the plane of symmetry close to the trailing edge. In the latter region the influence of the sting, not represented in the computation, is probably the reason for the less satisfactory correlation.

(v) On the lower surface the result of the Reynolds-averaged Navier-Stokes method is in close agreement with the result of the Euler methods. Correlation with experimental data is also satisfactory, taking into account the effect on the flow of the underwing body of the wind-tunnel model.

(vi) The lift and drag coefficients predicted by the Navier-Stokes method is in better agreement with experimental data of Ref. 1 than those predicted by the Euler methods, as is indicated in the table below:

	$C_L$	$C_D$
EULER-MAX.	0.538	0.0882
EULER-MIN.	0.515	0.0841
NAVIER-STOKES	0.461	0.0855
EXP. (REF. 1)	0.457	0.0846

## CONCLUDING REMARKS

Results of seven Euler solvers have been compared for the test case ( $M_\infty = 0.85$ ,  $\alpha = 10^\circ$ ) of the flow about a 65-deg swept sharp-edged cropped delta wing. The results have been obtained on one and the same grid (BAE-A) with about 300,000 grid points. It appears that if artificial dissipation is minimized as much as possible similar solutions are obtained from the central-difference (flow variables located at cell centers) methods of NLR, British Aerospace, Dornier, Aeritalia and Aeromacchi.

A second group of solutions by DLR with a central-difference (flow variables defined at cell vertices) scheme and MBB with an upwind scheme, tend to a similar solution which is different from the one of the first group. The most pronounced difference between the two groups of solutions is that for the latter group of two methods the upper-surface suction peak is somewhat narrower, higher and at a more outboard location.

Locally near the apex, leading edge, tip and trailing edge the solutions can be quite different, but practically speaking the results show a sufficient degree of agreement.

Comparison of the results of the Euler methods with experimental data emphasizes the necessity to include some modeling of the effects of secondary separation in these methods.

The results of the Reynolds-averaged Navier-Stokes method demonstrate, compared with the results of the Euler methods, an improved correlation of computation and experiment, primarily resulting from a simulation of the secondary separation.

## ACKNOWLEDGEMENT

The authors drafted this paper for the Technical Coordination Group (TCG) of IEPC-TA15 and thank the participants in the TCG for the synergistic collaboration within the program. The "minimum-dissipation" Euler solutions were provided by W.R. Marchbank (British Aerospace, Warton, U.K.), J.M.A. Longo (DLR-Braunschweig, Germany), W. Schwarz (MBB, Ottobrunn, Germany), S.M. Hitzel (Dornier, Friedrichshafen, Germany), M. Borsi (Aeritalia, Turin, Italy), E. Malfa (Aeromacchi, Varese, Italy) and J.M.J.W. Jacobs (NLR, Amsterdam, The Netherlands). The Navier-Stokes solution was provided by A. Hilgenstock (DLR, Göttingen, Germany). The paper was produced at NLR.

## REFERENCES

1. Elsenaar, A., Eriksson, G.: Proceedings of the Symposium on "International Vortex Flow Experiment and Euler Code Validation", Stockholm, Oct. 1-3, 1986.
2. Murman, E.M., Rizzi, A.: Applications of Euler Equations to Sharp-Edged Delta Wings with Leading-Edge Vortices. AGARD CP412, Paper 15 (1986).
3. Elsenaar, A., Hoeijmakers, H.W.M.: An Experimental Study of the Flow Over a Sharp-Edged Delta Wing at Subsonic, Transonic and Supersonic Speeds. Paper 15 of this Symposium.
4. Jameson, A., Schmidt, W., Turkel, E.: Numerical Solution of Euler Equations by Finite Volume Methods Using Runge-Kutta Time-Stepping Scheme. AIAA Paper 81-1259 (1981).
5. Rossow, C.: Comparison of Cell-Centered and Cell-Vertex Finite Volume Schemes. Proceedings of the 7th GAMM Conference on Numerical Methods in Fluid Mechanics, Notes on Numerical Fluid Mechanics, Vol. 20, pp. 327-334 (1987).
6. Hall, M.G.: Cell-Vertex Multi-Grid Scheme for Solution of the Euler Equations. In Proceedings of Conference on Numerical Methods for Fluid Dynamics, Reading, U.K. (1985).
7. Eberle, A.: Characteristic Flux Averaging Approach to the Solution of Euler's Equations. VKI Lecture Series 1987-04 (1987).
8. Hilgenstock, A.: Ein Beitrag zur numerischen Simulation der transsonischen Strömung um einen Deltaflügel durch Lösung der Navier-Stokes'schen Bewegungsgleichungen. Dr.-Ing Dissertation, Universität Karlsruhe, February 1990. Also report DLR-FB 90-13. See also Paper 7 of this Symposium.

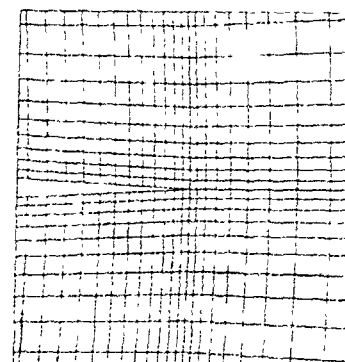
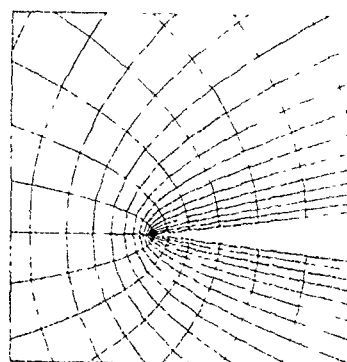
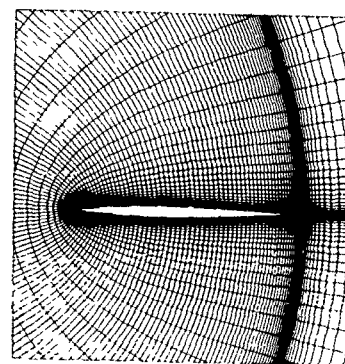
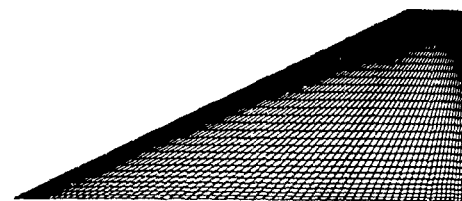
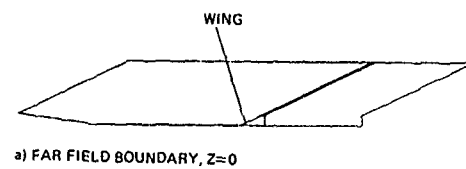


Fig. 1 BAe-A grid used for the seven Euler solutions ( $192 \times 48 \times 32$ )

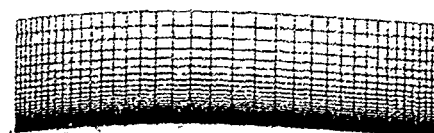
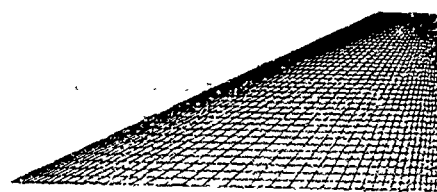


Fig. 2 Grid used for the Navier-Stokes solution (28 cells)



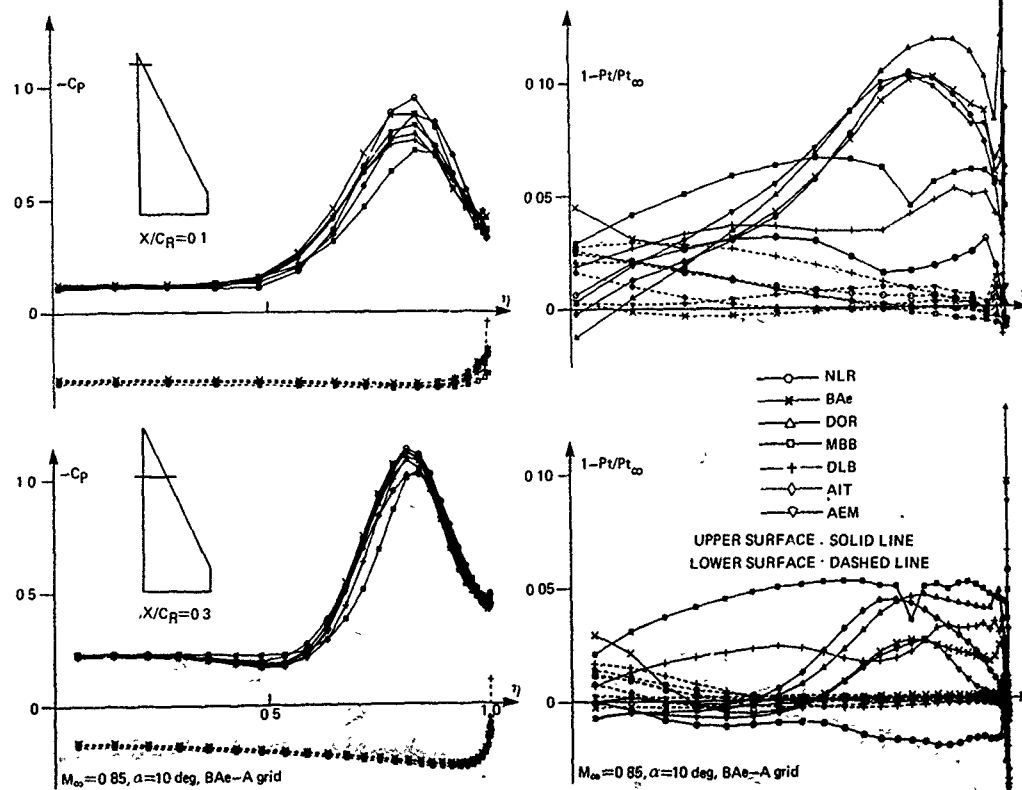
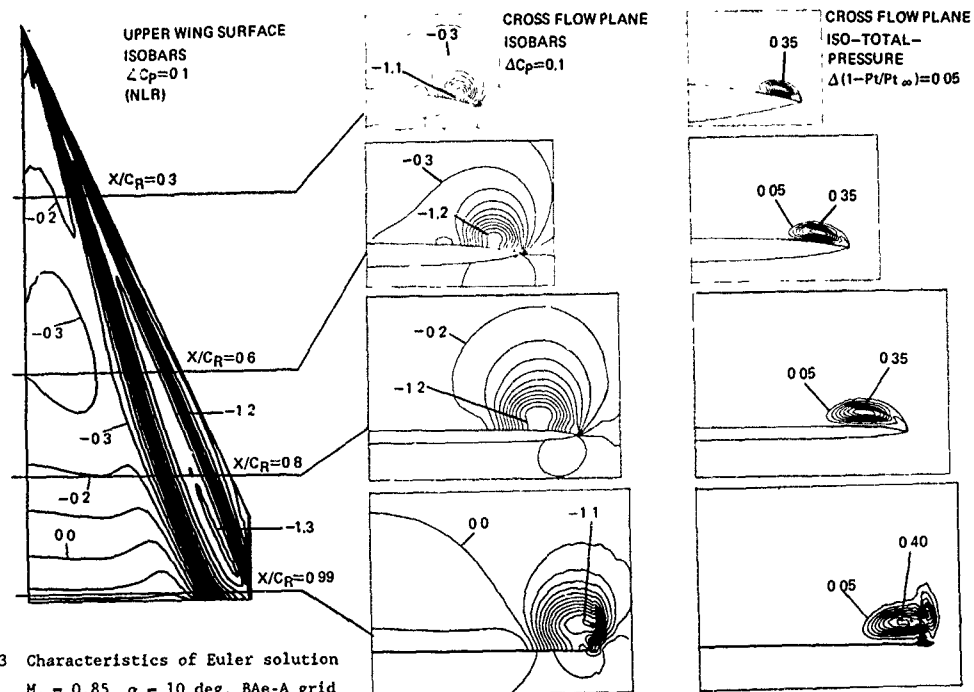
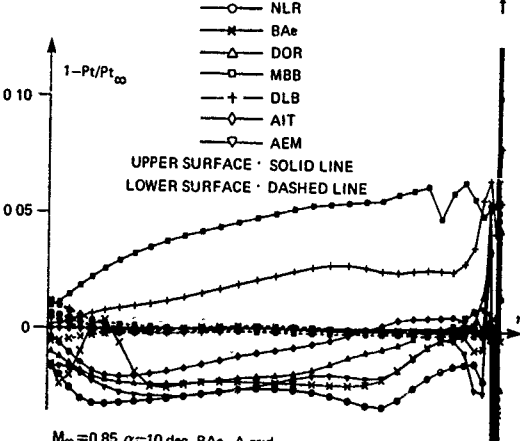
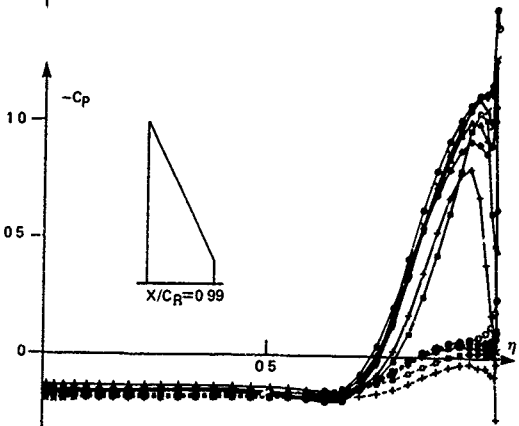
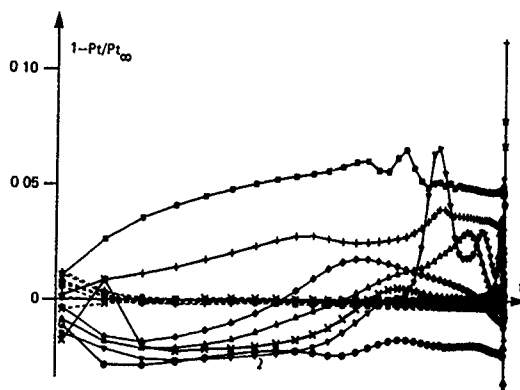
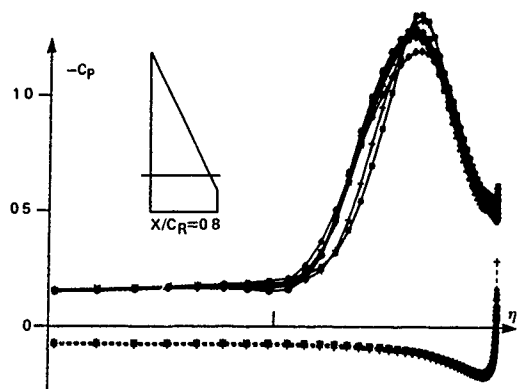
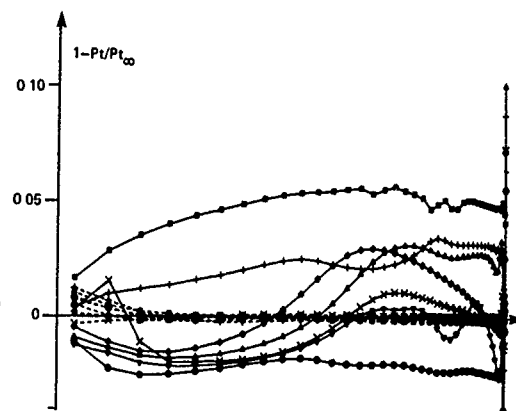
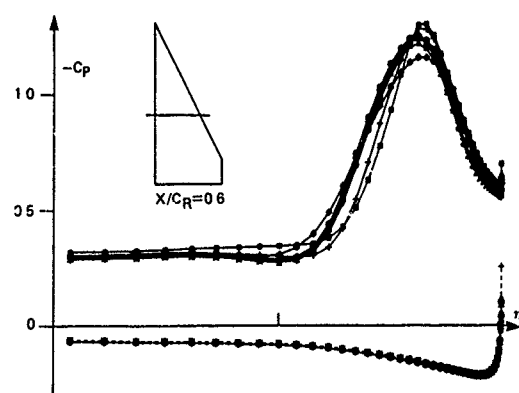


Fig. 4a Spanwise pressure distribution, Euler methods (continued)

Fig. 4b Spanwise distribution of total pressure, Euler methods (continued)



○ NLR  
 × BAe  
 △ DOR  
 □ MBB  
 + DLB  
 ◇ AIT  
 ▽ AEM

UPPER SURFACE · SOLID LINE  
 LOWER SURFACE · DASHED LINE

$M_\infty = 0.85, \alpha = 10^\circ$ , BAe-A grid

$M_\infty = 0.85, \alpha = 10^\circ$ , BAe-A grid

Fig. 4a Spanwise pressure distribution,  
Euler methods

Fig. 4b Spanwise distribution of total pressure,  
Euler methods

2-10

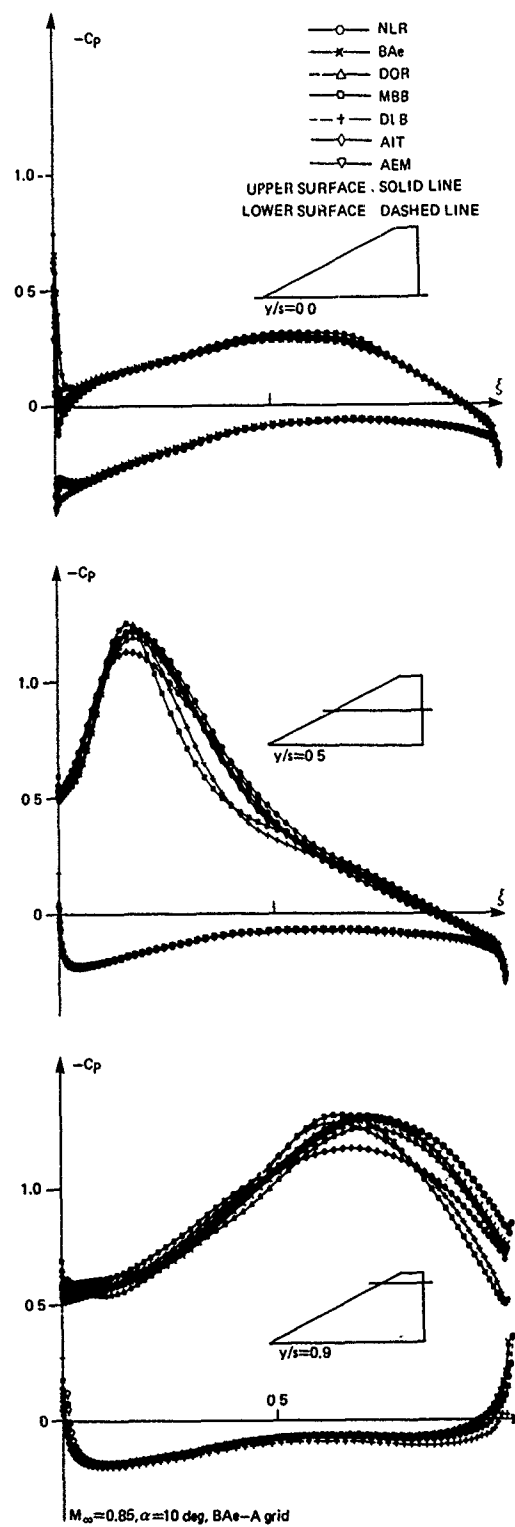


Fig. 5a Chordwise pressure distribution  
Euler methods

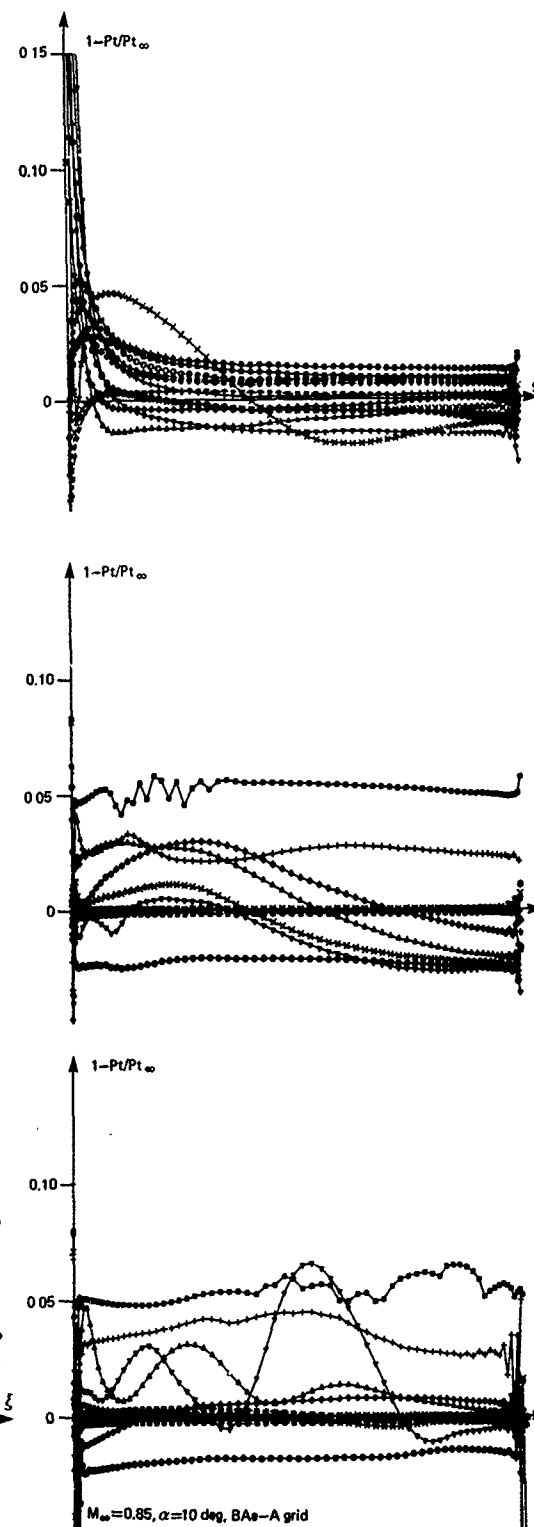


Fig. 5b Chordwise distribution of total pressure  
Euler methods

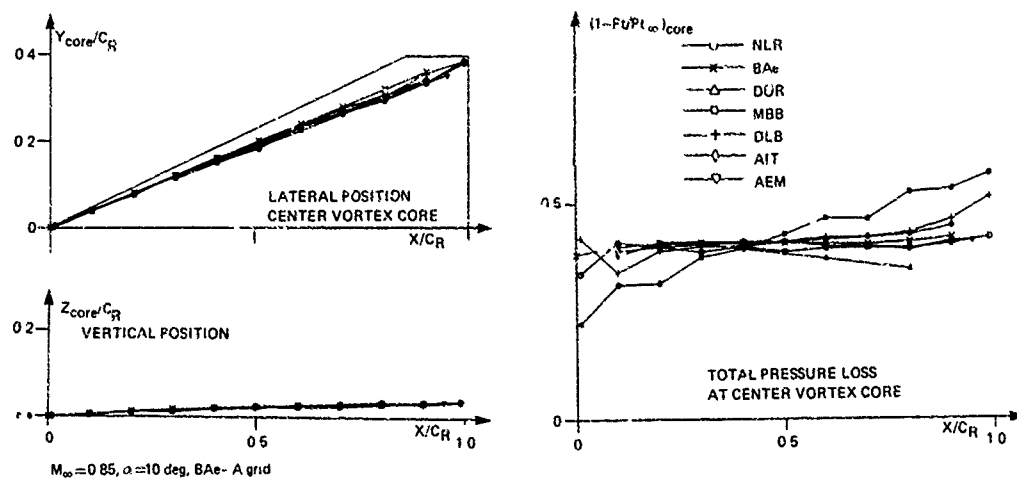


Fig. 6 Trajectory of center of leading-edge vortex and value of total pressure loss at vortex core center

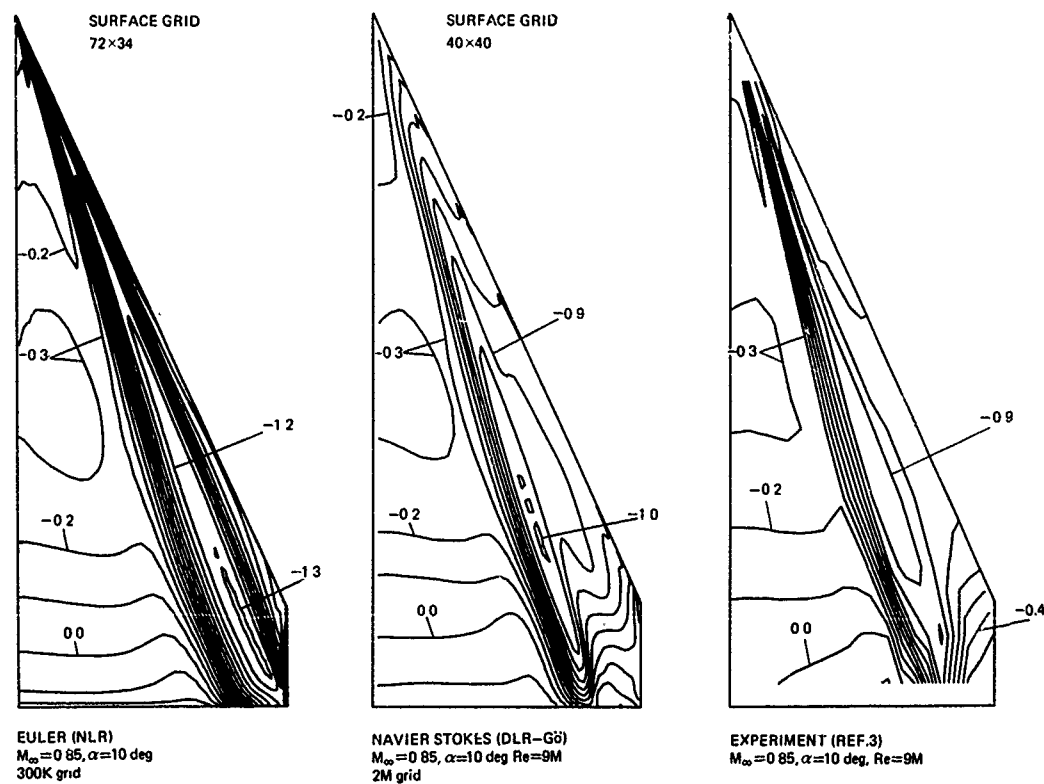
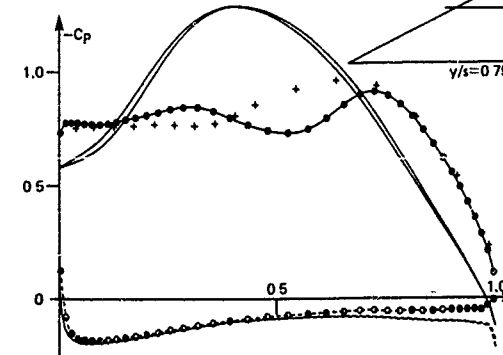
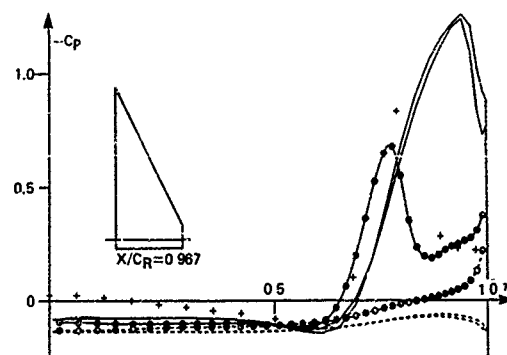
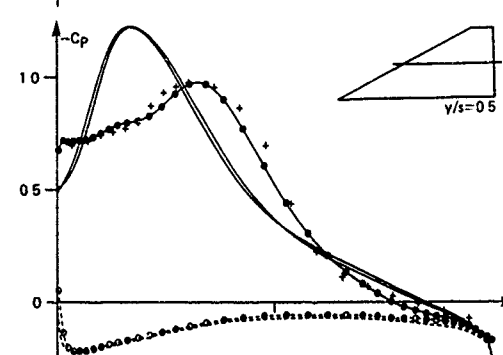
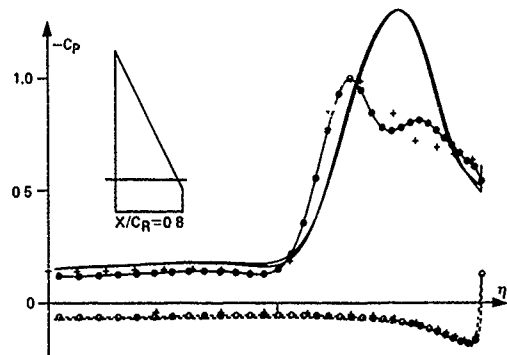
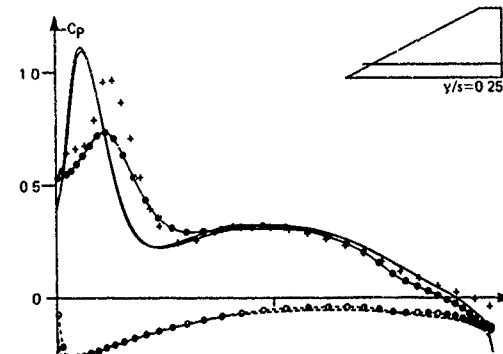
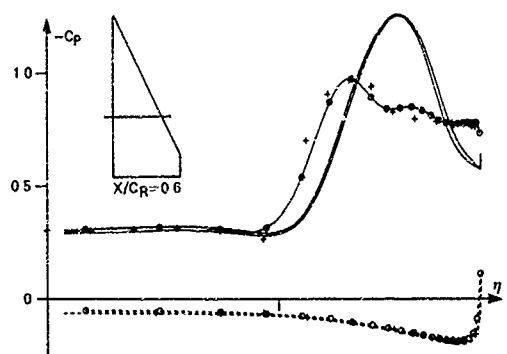
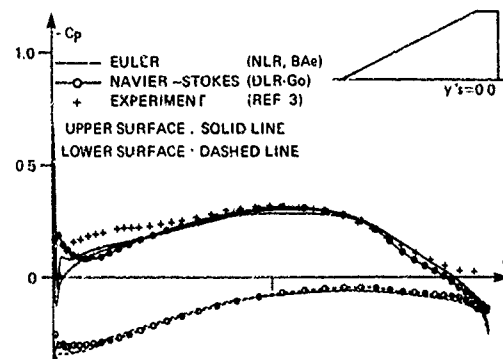
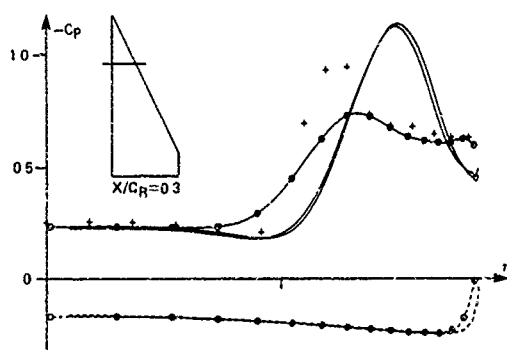


Fig. 7 Comparison of isobar pattern on upper wing surface, Euler method, Navier-Stokes method, experiment ( $\Delta C_p = 0.1$ )



$M_\infty = 0.85, \alpha = 10^\circ, (Re = 9M)$

$M_\infty = 0.85, \alpha = 10^\circ, (Re = 9M)$

Fig. 8a Comparison of spanwise pressure distribution, Euler method, Navier-Stokes method, experiment.

Fig. 8b Comparison of chordwise pressure distribution, Euler method, Navier-Stokes method, experiment.

## Vortical Flow Simulation by Using Structured and Unstructured Grids

M. Borsi, L. Formaggia, E. Hettner, S. Santillan, V. Selmin, S. Tarditi

AERITALIA G.A.D.  
TEVT — Computational Fluid Dynamics  
C.so Marche 41, 10146 TORINO, ITALY

### Abstract

Two Euler equation solvers based on finite volume formulations on structured and unstructured grids are applied to the simulation of transonic vortical flow around a delta wing-body configuration. The description of the mesh generation techniques, some details on the flow solvers and a comparison between the methods are presented.

### Introduction

In this work we will present numerical results for a vortex flow on a wing-body configuration obtained by employing both structured grids of hexahedra cells and unstructured tetrahedral meshes. The reason of using both strategies is twofold. Firstly, we believe that the level of maturity reached nowadays by unstructured grid generators and solvers, which is testified by several works [2,3,4,5,6], makes this approach liable to belong with full rank among the tools used for computational fluid dynamics in an industrial environment. Secondly, we wanted to assess the capabilities of the unstructured grid generator and solver developed at Aeritalia G.A.D. versus a more traditional structured grid approach. In fact, the nature of the flow problem one wish to solve may tip the balance in favour of the use of one or the other methodology. We then feel it is appropriate to have the ability of using effectively both strategies. We will here briefly recall what are, in our opinion, the pros and cons of the two approaches.

#### Unstructured grids

##### • Pros:

- High geometrical flexibility, no need to use multiblock strategies even with complex 3D configurations.
- Possibility of localised refinement.
- Relatively straightforward implementation of adaptive procedures.

##### • Cons:

- Grid generation and solution time may be greater on relatively simple geometries.
- Less experience on solvers and grid generation algorithms.
- More difficulties in visualising meshes and solutions.
- Higher memory requirement per grid point.

Its geometrical flexibility makes the approach particularly suited for complex 3D geometries and for grid adaptation [5,6]. In particular, the possibility of having highly localised refinements, thanks to the lack of structure in the grid, may allow to place points exactly where needed, thus resulting in a better control on the global number of mesh points.

#### Structured Grids

##### • Pros:

- Fast generation and solution on simple grids
- Relative easy visualisation of meshes and solutions.
- More experience on the numerical schemes.

##### • Cons:

- Difficult handling of complex geometries, with necessary implementation of multiblock strategies.
- Requires an highly experienced user to generate good quality meshes.
- In an adaptive refinement procedure there is a risk of gross overmeshing, due to the requirement of maintaining the grid structure.
- More constraints on grid density control.

It seems that the two approaches somehow balance each other. Moreover, they must not be thought necessarily as alternatives. Some authors are investigating



the possibility of combining the two methodologies, see for instance [7,8].

In the present work a 65-deg. sharp edged cropped delta wing-body configuration described in Ref. [1] has been studied. A sketch of the configuration is illustrated in Fig. 1.

### Unstructured mesh generation algorithm

The algorithm adopted for the generation of unstructured 3D meshes is based on the front advancing technique [5,9]. The approach may be divided into two steps: surface discretisation and domain triangulation. In the first step triangular meshes are generated over the surface elements which define the boundary of the computational domain. This triangulation forms the boundary discretisation. The geometry of each surface element is normally defined by means of surface splines passing through an array of points (knots). Fig. 2 shows the surface definition and corresponding triangulation of 4 of the 10 surface elements which define the wing body configuration of Fig.1. The surfaces defining the exterior limits of the domain are illustrated in Fig. 3. In order to generate a mesh with the desired density distribution, a measure of the local spacings required inside the domain must be provided. The dimensions of a typical tetrahedron are defined by means of three spacing parameters  $s_1, s_2, s_3$ , and associate directions  $\alpha_1, \alpha_2, \alpha_3$  [9]. The specification of the value of those parameters over the computational domain provides an effective tool for the control of the mesh density and skewness. For a uniform mesh only one parameter is required, which represents the desired spacing throughout the domain. Fig. 4 shows the surface mesh obtained by two different spacing distributions. In the second mesh an higher mesh density has been provided in the vortex region.

In the second stage of the generation process a mesh of tetrahedra is built inside the domain. The information about the assembly of triangular boundary facets is set up to form the initial front. The front is a data structure which keeps track of the information about the set of triangular facets still available for the generation process. The assembly of those facets forms the boundary between the part of the domain which has been triangulated and the part which has not yet. The front must be updated every time a new element is formed and it becomes empty at the end of the triangulation process. The generation proceeds by choosing a triangle in the front as a base for a new tetrahedron. The triangle will be joined either with an existing node or with a new one in order to form an element whose dimension is as near as possible to the prescribed one.

### Structured mesh generation algorithm

The structured grid generator is based on the multi-block approach [12,14,17] implemented without constraints on the mesh topology, but with the restriction of block continuity across faces (i.e. one face can be shared by at most two blocks and there must be grid line continuity across faces).

The first step necessary to handle a new grid is the choice of its overall topology. The H-O topology has been selected for the 65 degree wing sweep configuration in order to obtain a quasi-conical mesh that seems to be more appropriate to resolve the expected vortical flow. The far field is a cylinder oriented along the longitudinal axis. Its elliptical sections have the major axis aligned with the span direction.

The second step is the generation of suitable surface meshes on both the body and the far field. The grid can be generated with algebraic techniques [13] that allow a good control of the grid points distribution with few parameters.

The block decomposition of the flow domain follows. The body and far field surfaces are subdivided in order to create blocks consistent with the adopted topology. Blocks with degenerated edges and/or faces are allowed and, in our case, a singular line on all the blocks in contact with the wing apex was generated. Inner and outer boundaries are connected with lines whose shapes are properly chosen in order to control some grid properties such as orthogonality and smoothness.

The grid generation process is carried out working first on edges then on faces and finally on blocks and once an element subdivision has been established it will be kept fixed in the next step.

The mesh generation on block faces is performed by algebraic techniques. The point distribution depends on the shape of the face edges, on their subdivision and on the type of interpolation function used to blend an edge with the opposite one [15,17]. The direction of grid lines can be controlled also by imposing additional constraints like surface parametric derivatives on the boundaries in order to obtain the desired mesh characteristics. Care must be taken, in this case, to avoid mesh overlapping.

Finally grid generation inside blocks is carried out. The same technique developed for the faces is used also in this case, so the previous considerations can be applied again.

### Euler solver

Steady solutions to the Euler equations are captured by pseudo-time integration of the usual conservation

laws:

$$\frac{\partial W}{\partial t} + \frac{\partial F(W)}{\partial x} + \frac{\partial G(W)}{\partial y} + \frac{\partial H(W)}{\partial z} = 0. \quad (1)$$

Eq. (1) is a locally differential version of a more general conservation principle

$$\frac{\partial}{\partial t} \int_{\Omega} W d\Omega + \int_{\Gamma} \vec{F} \cdot \vec{\nu} d\sigma = 0, \quad (2)$$

which expresses that the rate of change of the quantity  $W$  in a volume  $\Omega$  is equal to the balance of the fluxes  $\vec{F}$  of this quantity through the boundary  $\Gamma$  of  $\Omega$ . Namely, it expresses the conservation of mass, momentum and total energy for an inviscid flow.

Spatial discretisation is performed by computing the integral form of the Euler equations on a finite control volume  $C_i$ , illustrated in Figs. 5 and 6, and assuming a constant value for  $W$  over the control volume. The flux balance is evaluated by splitting the control volume boundary into panels  $\partial S_{ij}$ , so that each panel is shared by a pair of cells  $C_i$  and  $C_j$ . Thus, the flux balance reduces to the sum of the contributions due to each panel over which we assume that the fluxes are constant. The following integrated normal can be computed:

$$\vec{\eta}_{ij} \equiv (\eta_{ij}^x, \eta_{ij}^y, \eta_{ij}^z) = \int_{\partial S_{ij}} \vec{\nu} d\sigma. \quad (3)$$

The discrete equation can then be written as it follows

$$\text{area}(C_i) \frac{dW_i}{dt} + \sum_{j \in K(i)} \Phi(W_i, W_j, \vec{\eta}_{ij}) = 0, \quad (4)$$

where  $K(i)$  represents the set of indices of neighbouring cells of  $C_i$ . The numerical flux  $\Phi$  is a function of the quantity  $W$  at the cells  $C_i$  and  $C_j$ , and of the integrated normal. This formula is general and the property of the scheme will depend only on the choice for the numerical flux, which is required to be consistent with the physical one:

$$\Phi(W, W, \vec{\eta}) = \mathcal{F}(W, \vec{\eta}) \equiv F\eta^x + G\eta^y + H\eta^z \quad (5)$$

A second order spatial approximation can be obtained by setting:

$$\begin{aligned} \Phi(W_i, W_j, \vec{\eta}_{ij}) &= \frac{F(W_i) + F(W_j)}{2} \eta_{ij}^x \\ &+ \frac{G(W_i) + G(W_j)}{2} \eta_{ij}^y \\ &+ \frac{H(W_i) + H(W_j)}{2} \eta_{ij}^z. \end{aligned} \quad (6)$$

This approximation does not allow a clean capture of flow discontinuities without undesirable spurious oscillations that could induce numerical instabilities, therefore, we need to add some artificial dissipative terms.

We describe now a way to construct such artificial dissipative terms both for structured cell centered and for unstructured node centered schemes.

#### Structured cell centered scheme:

In a structured mesh, we can associate to each cell  $C_i$  a triplet of indices  $i, j, k$ . The dissipative operator can be written as

$$\begin{aligned} D_{i,j,k}(W) &= d_{i+\frac{1}{2},j,k} - d_{i-\frac{1}{2},j,k} \\ &+ d_{i,j+\frac{1}{2},k} - d_{i,j-\frac{1}{2},k} \\ &+ d_{i,j,k+\frac{1}{2}} - d_{i,j,k-\frac{1}{2}}, \end{aligned} \quad (7)$$

where the dissipative flux  $d_{i+\frac{1}{2},j,k}$  is defined by the usual formula [10]

$$\begin{aligned} d_{i+\frac{1}{2},j,k} &= \\ &\frac{\lambda_{i+\frac{1}{2},j,k}}{2} \left( \epsilon_{i+\frac{1}{2},j,k}^{(2)} (W_{i+1,j,k} - W_{i,j,k}) \right. \\ &\quad \left. - \epsilon_{i+\frac{1}{2},j,k}^{(4)} (W_{i+2,j,k} - 3W_{i+1,j,k} \right. \\ &\quad \left. + 3W_{i,j,k} - W_{i-1,j,k}) \right). \end{aligned} \quad (8)$$

#### Unstructured node centered scheme:

In a similar manner, the dissipative operator for the unstructured grid solver is written as

$$D_i(W) = \sum_{j \in K(i)} D_{ij}, \quad (9)$$

where the dissipative flux  $D_{ij}$  is defined by

$$D_{ij} = \frac{\lambda_{ij}}{2} \left( \epsilon_{ij}^{(2)} (W_j - W_i) - \epsilon_{ij}^{(4)} (\nabla W_j - \nabla W_i) \right) \quad (10)$$

where  $\nabla W$  is a discretized version of an undivided Laplacian operator.

For the two schemes, the scaling factor  $\lambda$  represents the local value of the spectral radius of the Jacobian matrix  $\partial \mathcal{F} / \partial W$ . Shock capturing is controlled by the coefficient  $\epsilon^{(2)} (\leq 1)$ , which is made proportional to a non-dimensional shock sensor; typically, the normalised second difference of the pressure. The coefficient  $\epsilon^{(4)}$  provides the background dissipation in smooth parts of the flow and can be used to improve the ability of the scheme to damp high frequency modes. In the neighborhood of shock waves,  $\epsilon^{(4)}$  is put equal to zero to cut off the fourth difference operator which could otherwise cause oscillations. More details about the unstructured solver can be found in [11].

The multiblock flow solver used for this calculation has been developed with the main goal of treating grid blocks independently from the overall mesh topology. Two layers of halo cells are needed to compute the second and fourth order terms in the artificial viscosity model. These cells are placed on each contact faces between two blocks and the variable values are taken from the adjacent block. The scheme does not require

any special treatment of degenerated edges or faces. Boundary conditions at the symmetry plane are imposed by simply mirroring the variables, at solid walls linear pressure extrapolation from the inner values in the flow field is assumed, while at the far field a flux splitting procedure is used.

The unstructured solver does not require any special technique for symmetry and wall boundary conditions, as it is a node centered scheme. At far field, it uses the same procedure as the structured solver.

An explicit multistage Runge-Kutta time stepping scheme is used to integrate the equation in time. Convergence to steady state is improved by the use of acceleration techniques such as local time stepping, residual smoothing and enthalpy damping

### Numerical experiments

We have investigated transonic vortical flow over the previously described wing-body configuration at  $M_\infty = 0.85$  with a 10 degrees angle of attack.

#### Structured grid:

Using the technique described above a mesh composed by 12 blocks with a total of 309760 cells was generated. The final result is shown in Figs. 7-9. The block structure is reported in Fig. 7. The symmetry plane and the body surface are shown in Fig. 8, while Fig. 9 illustrates three I-constant surfaces to give an idea of the mesh resolution in the flow field.

A vortex over the wing upper side has been captured by our calculation. Fig. 10 shows that it seems to originate quite close to the configuration apex, while Fig. 11 depicts its development in the flow field in terms of pressure. The vortex core is detectable by the analysis of the total pressure losses distribution. Isoplots of this variable, shown in Fig. 12, are used to trace it in the flow field and indicate that vorticity is generated at the wing apex and is fed also from the sharp leading edge. Finally, the surface pressure in correspondence of three cuts on the body is presented in Fig. 13.

#### Unstructured grid:

Firstly, an experiment with a coarse mesh (30256 nodes) was made in order to get an initial solution which would indicate the trends of the flow structure. Fig. 14 shows the body surface discretisation, which consist approximately of 12000 triangular facets. This initial result shows a vortex on the wing leeward side.

In order to improve the solution, we have used a mesh refinement technique. A first problem appears: where shall we refine?

The quantity of major interest is the pressure distribution on the wing body. As a consequence, one may think that the best way to refine the mesh is just to put more points on the body surface. But, a closer analysis of the flowfield showed us that the pressure distribution

on the wing, in this kind of vortical flow, is strongly related to the resolution of the vortex, whose core is located over the body surface. Therefore, a better resolution of the vortex will induce a better resolution of the pressure distribution on the body surface without needing to create more points on it.

The criterion used for the mesh refinement procedure is based on an entropy deviation sensor, which best identify the vortex location. A refined mesh of 55722 nodes was generated by splitting the mesh sides where the value of the sensor exceeded a prescribed limit.

The new solution indicates that the pressure in the suction peak is substantially lower than the one found in the results on the coarse level grid as shown in Fig. 15. Figs. 16 to 18 illustrate the effect of mesh refinement on the solution. Isoplots of the pressure are shown in Fig. 19. Finally, the surface pressure in correspondence of three cuts on the body is presented in Fig. 20.

#### Comparison between the two approaches:

Figs. 21 to 23 present comparisons of the solution obtained by the two methods. The results appear to be quite similar in the flow field. The vortex in the unstructured grid solution is well resolved, thanks to the adaptive strategy, even if the number of nodes is much lower than the one used in the structured grid. Comparison in terms of pressure coefficients on the body surface indicates some discrepancies in the vortex region, but in our experience we think that they could depend from different mesh resolution in critical areas where vorticity is generated. Further investigations are still necessary to better understand the effects of mesh density on the solution.

### Conclusions

Solutions of vortex flows around a wing-body configuration obtained with structured and unstructured grids have been presented. Comparable results have been obtained which confirm the suitability of the unstructured approach also for transonic vortical flow simulation. We have found that the mesh density in the vortex core largely influence the accuracy of the solution, making the use of adaptive strategy quite attractive. However, we believe that additional studies on the effects of mesh density in the vortex region and at sharp leading edges are needed, together with further research on adaptive strategies.

### References

- [1] *Proceedings of the Symposium on International Vortex Flow Experiment and Euler Code Validation*, Stockholm, Oct. 1-3 1986, ed. by A. Elsenaar and G. Eriksson.

- [2] A. Jameson, T.J. Baker (1987): "Improvements to the Aircraft Euler Method", AIAA Paper 87-0452.
- [3] T.J. Baker (1987): "Three Dimensional Mesh Generation by Triangulation of Arbitrary Point Sets", AIAA Paper 87-1124.
- [4] B. Stoufflet, J. Périaux, I. Fezoui, A. Dervieux (1987): "Numerical Simulation of Three Dimensional Hypersonic Euler Flows around Space Vehicles Using Adapted Finite Elements", AIAA Paper 87-0560.
- [5] J. Peraire, J. Peiro, L. Formaggia, K. Morgan, O.C. Zienkiewicz (1988): "Finite Element Euler Computations in Three Dimensions", *Int. J. Numer. Methods Eng.*, 26, 2135-2159.
- [6] J. Peraire, K. Morgan, J. Peiro (1990): "Unstructured Finite Element Mesh Generation and Adaptive Procedures for CFD", in *Application of Mesh Generation to Complex 3D Configurations*, AGARD-CP-464, (NATO, Brussels) Paper 18.
- [7] N.P. Weatherill (1988): "A Strategy for the Use of Hybrid Structured-Unstructured Meshes in CFD", in *Numerical Methods for Fluid Dynamics*, ed. by K.W. Morton and M.J. Baines, (Oxford University Press, Oxford).
- [8] A.J. Bocci (1990): "Recent Developments in CFD at ARA", in *Proceedings of 17<sup>th</sup> ICAS Congress*, Stockholm, ICAS-90-6.8.3, pp. 1569-1585.
- [9] J. Peraire, K. Morgan, J. Peiro (1990): "Unstructured Meshes for CFD", VKI Lecture Series 1990-06 on Numerical Grid Generation, June 11-15, Brussels.
- [10] A. Jameson (1985): "Numerical Solution of the Euler equation for Compressible Inviscid Fluids", in *Numerical Methods for the Euler Equations of fluid Dynamics*, ed. by F. Angrand, A. Dervieux, J.A. Desideri and R. Glowinski (SIAM, Philadelphia), pp. 199-245.
- [11] V. Selmin (1989): "A Multistage Method for the Solution of the Euler Equations on Unstructured Grids", in *Proceedings of the fifth International Symposium on Numerical Methods in Engineering*, Vol. 2, ed. by R. Gruber, J. Périaux and R.P. Shaw (Springer-Verlag, Berlin, Heidelberg), pp. 449-454.
- [12] J. Thomson, Z.U.A. Warsi, C.W. Mastin (1985): "Numerical Grid Generation", (North-Holland, New York).
- [13] J.D. Foley, A. Van Dam (1984): "Fundamentals of Interactive Computer Graphics", (Addison Wesley, Reading, Mass.).
- [14] S. Sengupta, J. Hauser, P.R. Eiseman, J.F. Thompson (Editors) (1988): "Numerical Grid Generation in Computational Fluid Mechanics '88", (Pineridge Press Ltd, Swansea).
- [15] L.E. Eriksson (1982): "Generation of Boundary-Conforming Grids Around Wing-Body Configurations Using Transfinite Interpolation", *AIAA J.* 20, No 10, pp. 1313-1320.
- [16] A. Jameson, W. Schmidt, E. Turkel (1981): "Numerical Solutions of the Euler Equations by Finite Volume Methods using Runge-Kutta time-stepping schemes", AIAA Paper 81-1259.
- [17] "Applications of Mesh Generation to Complex 3-D Configurations", AGARD CP-464 (NATO, Bruxelles).
- [18] A. Rizzi, G. Drougge, B. Müller (1989): "Navier-Sokes and Euler Solutions for Vortex Flow over a Delta Wing", in *Symposium Transonicum III, II-TAM Symposium Göttingen*, ed. by J. Zierep and H. Oertel, (Springer-Verlag, Berlin, Heidelberg), pp.305-316.

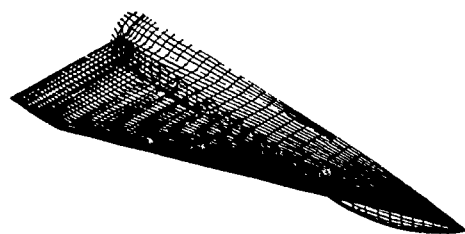


Fig.1 Surface definition of the wing-body configuration.

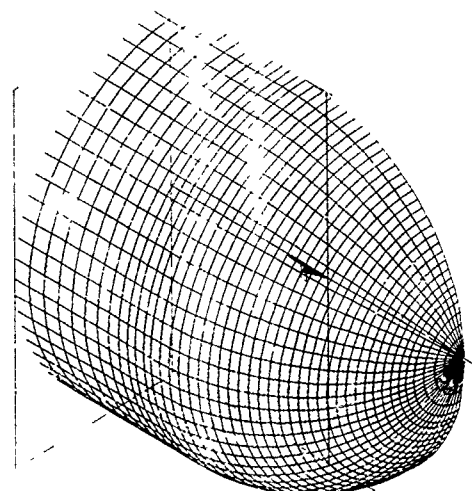


Fig.3 Definition of outer boundary and symmetry (unstructured case).

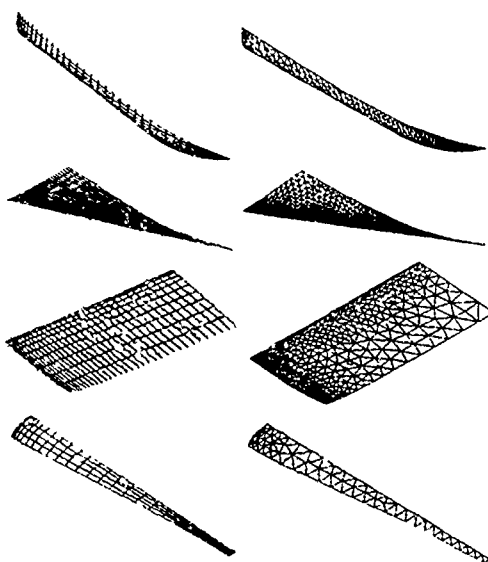


Fig.2 Definition and corresponding triangulation of four surfaces of the wing-body.

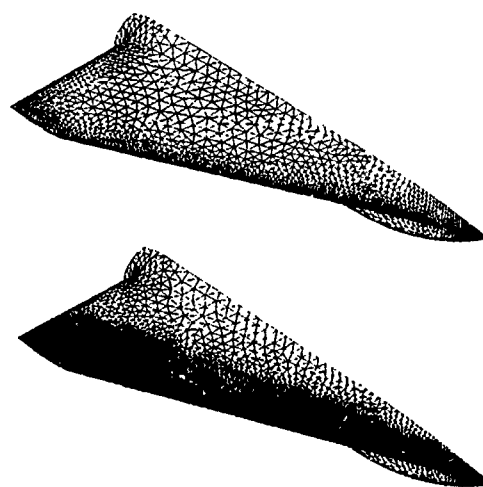


Fig.4 Surface triangulation for two different spacing distribution.

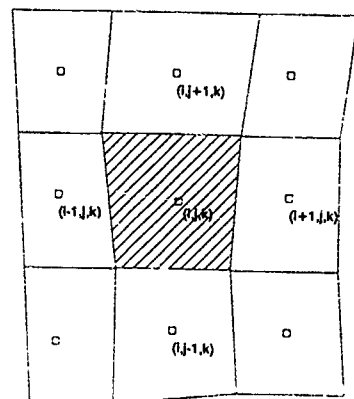


Fig. 5 Sketch of the structured control volume lattice.

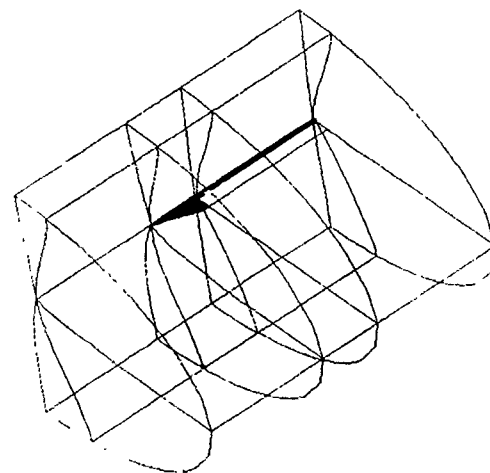


Fig. 7 Block structure of the structured mesh.

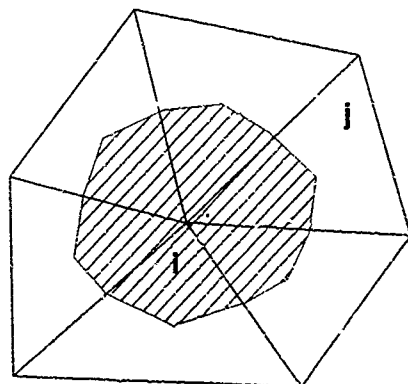


Fig. 6 Sketch of an unstructured control volume.

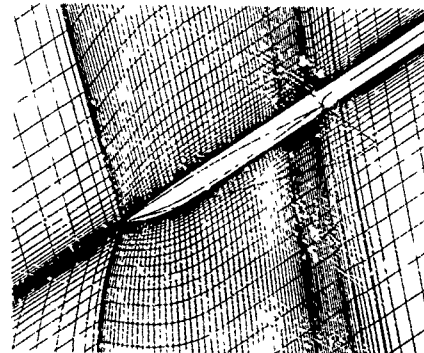


Fig. 8 Symmetry plane discretisation.



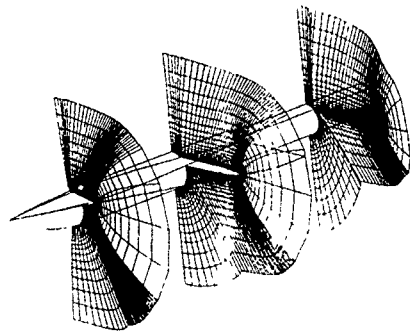


Fig.9 Three surface cuts at constant  $I$  of the structured grid.

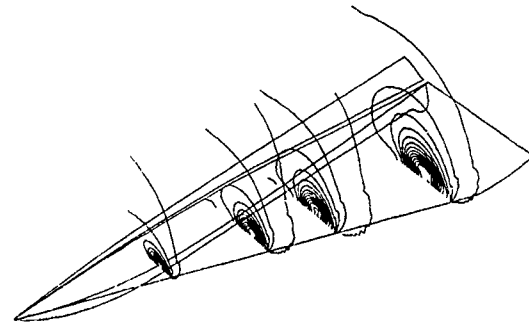


Fig.11 Pressure coefficients contours at several cuts in the structured grid.

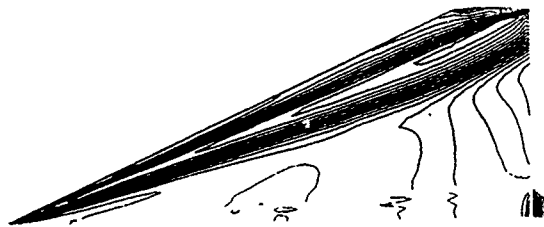


Fig.10 Pressure coefficient contours on the upper surface.

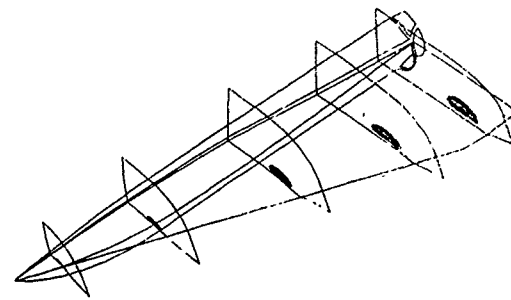


Fig.12 Total pressure loss contours at several cuts in the structured grid.

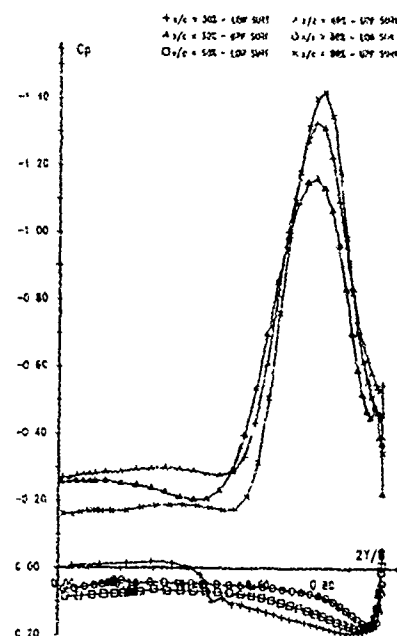


Fig.13 Pressure coefficient distribution on the body surface in correspondance of 30%,60% and 80% of the root chord.

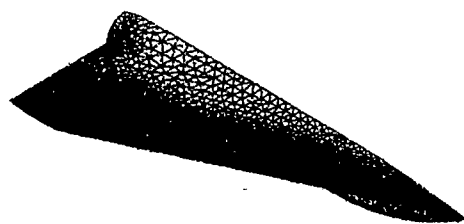


Fig.14 Surface discretisation of the coarse unstructured grid.

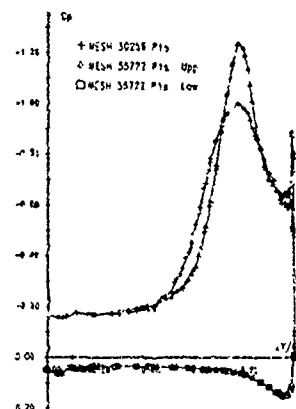


Fig.15 Comparison of pressure coefficient for the coarse and adapted unstructured grid at 80% of the root chord.

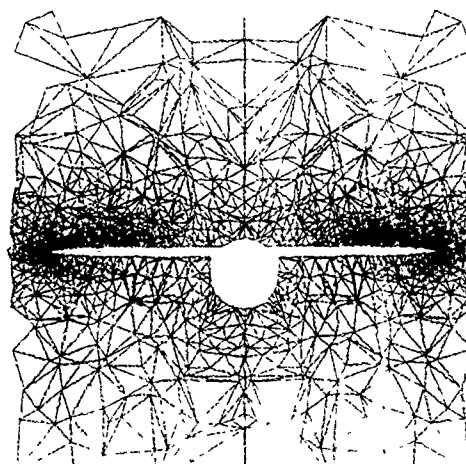


Fig.16 Two cuts showing the better resolution in the vortex region for the adapted grid (right).

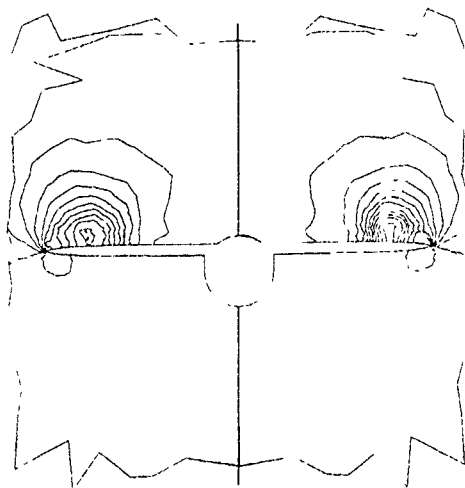


Fig.17 Pressure coefficients for the initial (left) and adapted (right) grid.

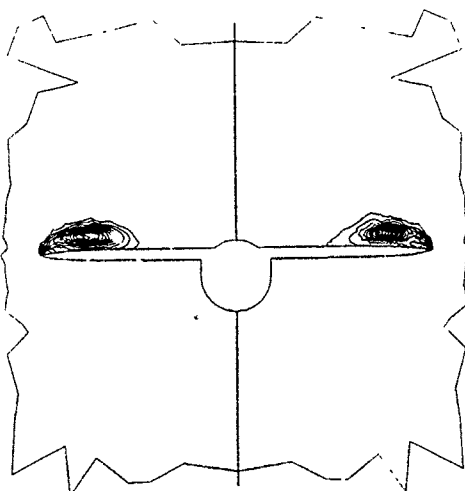


Fig.18 Entropy deviation for the initial (left) and adapted (right) grid.

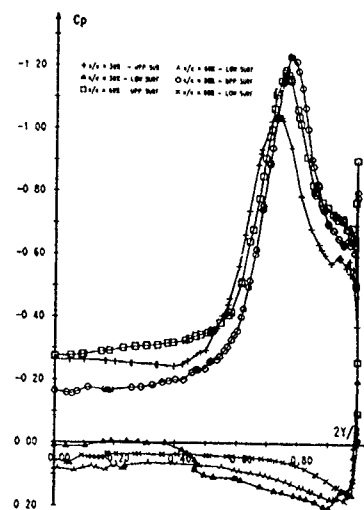


Fig.19 Body pressure coefficient curves in correspondence of three cuts in the unstructured grid.

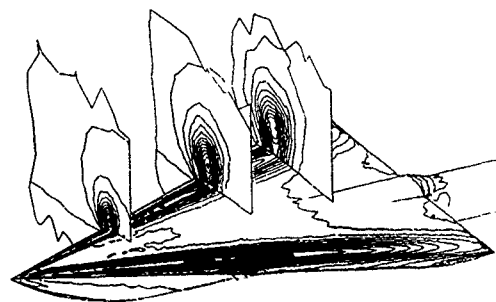


Fig.20 Pressure coefficient contours in correspondence of three cuts in the unstructured grid.

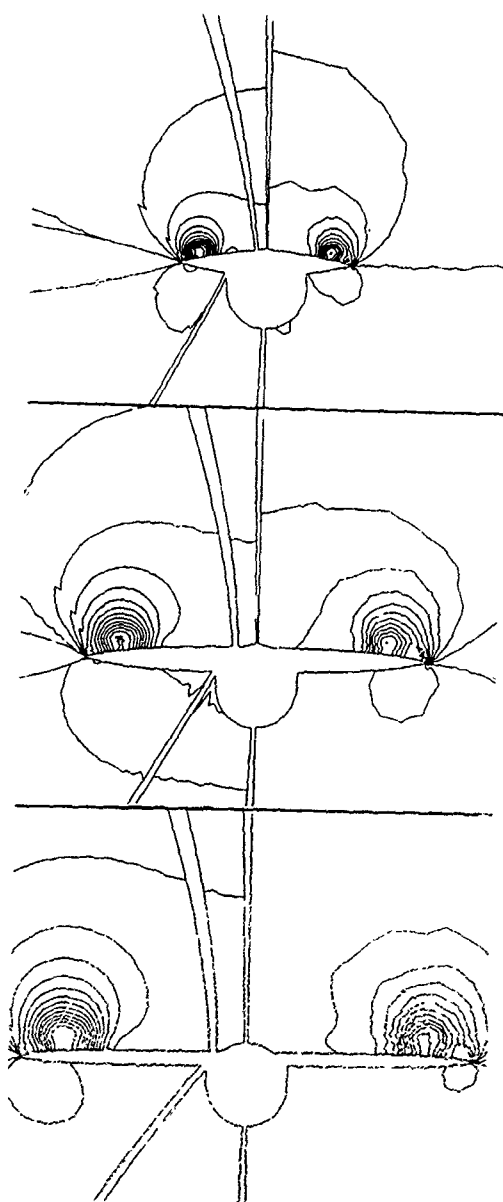


Fig.21 The pressure coefficients for the structured grid (left) are compared with the unstructured result (right) at 30%,60% and 80% of root chord.

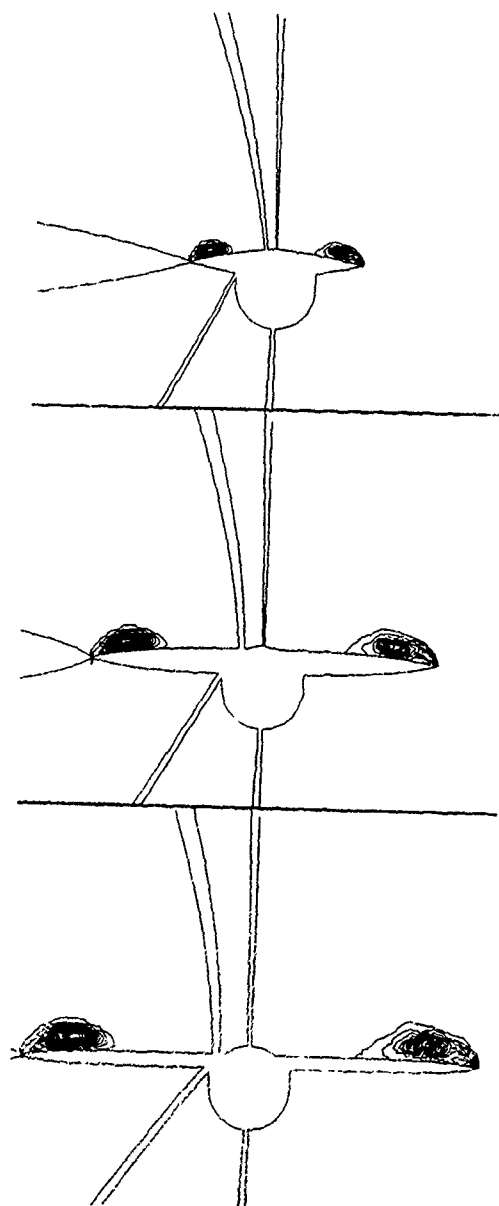


Fig.22 The entropy deviation for the structured grid (left) are compared with the unstructured result (right) at 30%,60% and 80% of root chord.

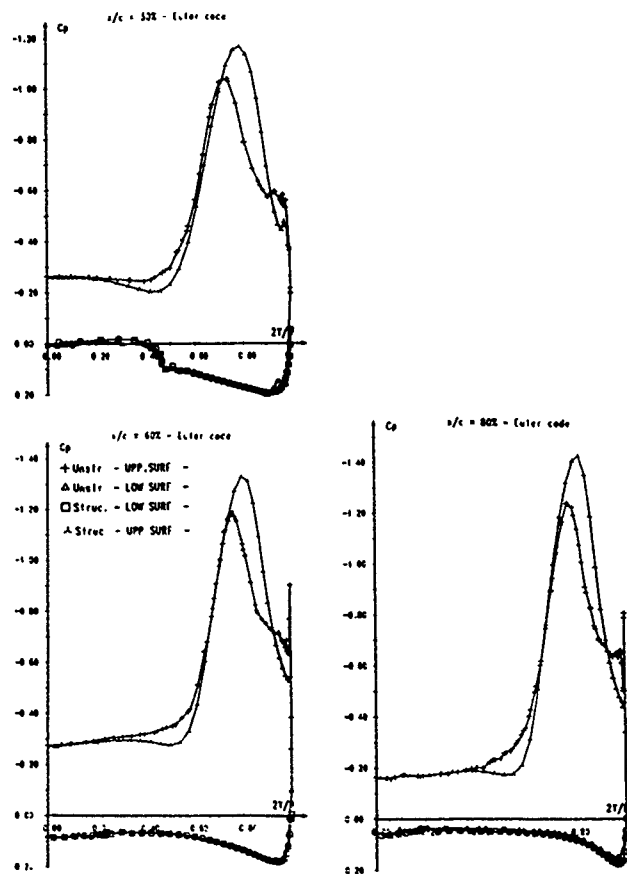


Fig.23 Body pressure coefficient distribution for the structured and unstructured grid at 30%,60% and 80% of root chord.

# ANALYSIS OF RESULTS OF AN EULER-EQUATION METHOD APPLIED TO LEADING-EDGE VORTEX FLOW<sup>\*)</sup>

by

J.I. van den Berg, H.W.M. Hoeijmakers and J.M.J.W. Jacobs  
National Aerospace Laboratory NLR  
P.O. Box 90502, 1006 BM Amsterdam  
The Netherlands

## SUMMARY

The flow about a 65-deg sharp-edged cropped delta wing with and without an under-wing body is simulated by solving the Euler equations. Results are presented for the wing-body configuration at a transonic free-stream Mach number at incidences ranging from 10 to 20 deg for which in the flow field above the wing a strong vortex develops as well as shocks for the high incidence of 20 deg. Results for subsonic to transonic free-stream Mach numbers at high incidence are obtained for the wing-alone configuration for which in the presence of a strong vortex, at transonic free-stream Mach number shocks appear in the solution. For the wing-body configuration, the computational results are compared with experimental data, and the solution in the near wake is investigated.

## INTRODUCTION

Vortical flow due to separation from sharp leading edges plays an important role in the aerodynamics of high-performance fighter aircraft and missiles operating at high incidence. The formation of the leading-edge vortex above the upper surface of the wing as a result of the rolling-up of the free shear layer which forms at the sharp leading edge, as well as the influence of the vortex on the flow over the upper surface of the wing, is only slightly dependent on Reynolds number. This implies that this type of high-Reynolds-number flow can be simulated by inviscid flow models.

Potential-flow methods have been applied successfully to the sub-critical flow about delta-like wing configurations (Ref. 1). In these methods the vortical flow is modelled by "fitting" vortex sheets and vortex filaments into the potential flow field. Although their position and strength is determined as part of the solution, the topology of the flow must be well-defined and known in advance.

The mathematical model based on the Euler equations allows for rotational flow everywhere in the flow field. Computational methods based on this flow model "capture" vortical flow regions along with (strong) shocks as part of the discrete flow solution. This implies that computational methods based on this mathematical model are rather attractive for cases with vortical flow, shocks and the mutual interaction of these two non-linear flow phenomena. At transonic speed the latter type of flow occurs for the case of highly-swept wing configurations at high incidence. The computer resources required for an Euler method can be met by the presently available supercomputers. Application of Euler methods to vortex flow have already demonstrated their potential for utilization in the aerodynamic analysis of fighter-like aircraft and missiles.

Many investigations have been carried out to study the prediction of steady-state, vortex-dominated flow by methods based on the Euler equations (Refs. 2-7), addressing various aspects of the numerical simulation of this type of flow.

In the model based on the Euler equations viscous effects are neglected. However, these effects are known to be responsible for the occurrence of secondary separation underneath the leading-edge vortex (see Fig. 1). The secondary vortex which results from this smooth-surface flow separation, affects the position and strength of the primary vortex. To take these effects into account more elaborate models of the flow must be used. In the literature several investigations into numerical boundary conditions to prescribe this secondary separation within an inviscid flow model can be found (Refs. 8-10). Furthermore several investigations have already been made to extend the flow model based on Euler's equations to a flow model based on the Navier-Stokes equations (Refs. 11-13). However, compared to Euler methods, Navier-Stokes methods require relatively fine grids to resolve the small-scale viscous effects, leading to computer time requirements too large for applications in a design environment.

In the present paper the Euler method under development at NLR is applied to the subsonic and transonic flow about a 65-deg sharp-edged cropped delta wing with and without an under-wing body.

The delta wing has a taper ratio of 0.15. The chordwise airfoil section is the NACA 64A005 airfoil which upstream of its point of maximum thickness (0.4 c) is smoothly blended into a biconvex shape. Attached to the lower wing surface is a body which starts at the apex of the wing, has an ogival type of nose ( $x/c_a \leq 0.35$ ) and smoothly blends into a cylindrical body. Downstream of the trailing edge, the body is attached to a sting of circular cylindrical shape. The diameter of the sting is substantially smaller than the maximum width of the body.

For the wing-body configuration detailed experimental data is available up to high incidences and the structure of the vortical flow field is reasonably well known (Refs. 14-15).

The purpose of the present investigation is to assess the capability of the Euler method to simulate accurately the details of the flow around the generic fighter-like configurations considered.

For these configurations the flow is dominated by a strong vortex resulting from flow separation at the sharp leading edge. At transonic speed there is, in addition, the interaction of this vortex with shocks resulting in a rather complex flow pattern. The present computational study is mainly concerned with the following:

<sup>\*)</sup> This investigation has been carried out under contract with the Netherlands Agency for Aerospace Programs (NIVR) for the Netherlands Ministry of Defence.



- comparison of computational results with experimental data for the wing-body configuration;
- analysis of fundamental aspects of the flow in the near wake of the wing-body configuration;
- evolution of the solution with increasing incidence for the wing-body configuration at fixed Mach-number;
- evolution of the solution with increasing Mach number at fixed incidence for the wing-alone configuration.

In Ref. 16 earlier computational results have been presented for the flow about the wing-alone configuration.

#### OUTLINE OF METHODS USED

The Euler simulation system under development at NLR consists of subsystems for geometry processing, grid generation, flow calculation, flow visualization and data processing (Ref. 17-19).

The computational meshes for the wing-alone and the wing-body configuration have been obtained using the NLR grid-generator (Ref. 17). With this grid generator, multi-blocked surface-fitted grids are produced. The grids are initialized through transfinite interpolation, and tuned through a method based on elliptic partial differential equations with interactively controlled weight functions. The grid lines are continuous but may be slope-discontinuous across block boundaries.

The Euler method (Ref. 18) used solves the time-dependent Euler equations employing the fully conservative algorithm of Jameson et al. (Ref. 20). The five equations for the conservation of mass, momentum in each of the three space directions and energy are discretized using a cell-centered central-difference scheme. Second- and fourth-order artificial dissipation terms are added to the discretized equations. The fourth-order dissipative term provides the back-ground dissipation required to suppress the tendency for odd-even point decoupling of the solution. In regions with large gradients, e.g. near shocks, the second-order dissipative term is required to damp pre- and post-shock oscillations. A switch function, dependent on the second derivative of the pressure, is used as sensor to detect the locations where the second-order dissipative term is switched on and the fourth-order term is switched off.

To obtain steady-state solutions, integration in time is carried out by a four-stage Runge-Kutta scheme in which the dissipative terms are evaluated at the first step only. Convergence to steady state is accelerated by applying local time-stepping, enthalpy-damping and residual-averaging.

At the solid wall the boundary condition of zero normal velocity is applied, combined with a second-order extrapolation of the pressure from the flow field towards the solid-wall. The boundary conditions at the outer boundary of the computational domain are based on one-dimensional Riemann invariants.

The NLR Euler method can handle multi-blocked grids. At the internal block interfaces a special boundary condition is implemented which accommodates slope-discontinuous grid lines as well as jumps in cell size across block boundaries. It is permitted to have a grid with degenerated cells, i.e. cells with faces and/or edges collapsed into a line or a point. Presently the blocks are patched one-to-one, in the near future this severe constraint in constructing a multi-block grid will be relaxed.

Visualization and inspection of the solutions is carried out on graphical workstations using in-house developed software (Ref. 19). The methods are developed and implemented on the NLR computer network consisting of a NEC-SX2 supercomputer, a Cyber 962 mainframe supplemented by graphic workstations for visualization, a file-transfer and a terminal network.

#### GRIDS

For the wing-body configuration a 16-block C-O type grid is used to discretize the starboard half of the computational domain. In chordwise direction the grid is of C-type, in spanwise direction of O-type topology. The grid has dimensions  $108 \times 82 \times 28$  (247,968 cells), that is in chordwise direction 108 cells (80 from the apex towards the trailing edge, 28 from the trailing edge towards the downstream outer boundary), 82 cells in spanwise direction (38 on the upper wing surface, 44 on the lower wing-body surface) and 28 cells in the direction from the configuration surface towards the outer boundary. On the forward part of the upper surface of the wing the grid is "conical" (see in Fig. 2). Grid lines are clustered near the apex, near the leading edge and near the trailing edge. Adjacent to the solid surface, where the gradients in the flow are expected to be large, the cell-stretching ratio in the direction normal to the solid surface is close to unity. The grid has a singular line running from the apex in upstream direction towards the outer boundary. The outer boundary is  $4.5c_x$  from the apex in upstream direction,  $5c_x$  from the trailing edge in downstream direction,  $3c_x$  from the leading edge in spanwise direction and  $5c_x$  from the configuration surface in normal direction, where  $c_x$  is the root chord.

For the wing-alone configuration an 8-block grid has been generated with an O-O type topology. The grid has dimensions  $144 \times 38 \times 28$  (153,126 cells), that is in chordwise direction 144 cells on both the wing upper and lower surface, 38 cells in spanwise direction and 28 cells between the wing surface and the outer boundary of the computational domain. This grid is symmetric with respect to the horizontal plane of symmetry of the wing. On the wing upper surface the grid characteristics are comparable to those of the grid of the wing-body configuration. The grid is quasi-conical, cells are clustered near the apex, leading- and trailing-edges. Also in normal direction the cell stretching ratio near the wing has been kept close to unity. The grid has also a singular line which runs from the apex in upstream direction towards the outer boundary. The outer boundary of the computational domain is formed by the surface of a sphere with center at  $\xi = x/c_x = 0.7$ ,  $\eta = y/s = 0.0$ ,  $\zeta = z/s = 0.0$  and radius of  $5c_x$ , where  $s$  denotes the local semi-span.

#### FLOW CONDITIONS

With the Euler method the flow around the wing-body configuration has been simulated in the transonic flow regime for a fixed free-stream Mach number of 0.85 and angles of attack of 10, 15 and 20 degrees.

The flow around the wing-alone configuration has been computed for both the subsonic and transonic flow regime. Results will be presented for free-stream Mach-numbers of 0.15, 0.50 and 0.85 for a fixed incidence of 20 deg.

All calculations have converged in 1500 to 2500 iterations, in which the root-mean-square norm of the time-like variation of the density reduces by four orders of magnitude, starting from the solution on the preceding grid level and from uniform free-stream flow on the coarsest level. On the NEC-SX2 supercomputer typical computing times are one to two CPU hours for a complete computation on the grids described.

#### ANALYSIS OF COMPUTATIONAL RESULTS

##### Main features of transonic flow solution

For the transonic free stream Mach number of 0.85, 20 deg incidence, the numerical solution on the wing-body configuration is compared with experimental data obtained in the NLR HST wind tunnel at a Reynolds number of 9 million for nominally the same configuration (Ref. 15). The most important difference between the geometry used in the computation and that of the wind-tunnel model is that for the first, the body starts at the apex of the wing, while for the latter the body starts somewhat downstream of the apex of the wing. The solution was obtained with the parameters controlling the artificial dissipative terms set at their standard values for transonic flow, i.e. with the fourth-difference term switched on, the second-difference term taking over at locations with large gradients.

Fig. 3 shows the isobar pattern on the upper surface of the wing-body configuration obtained from the Euler solution and the one obtained from the measured pressure distribution. The low-pressure region on the upper surface, forming the foot print of the leading-edge vortex, indicates that flow separation from the leading edge starts very close to the apex. On the forward part of the wing the pressure distribution is more or less conical. In the computed result the closely spaced isobars outboard of the pressure minimum indicates the presence of a "cross-flow shock" underneath the vortex core. On the rear part of the configuration upper surface, a second shock appears in the computed result. At  $x/c_R = 0.95$  this shock, which starts near the kink in the leading edge, merges with the cross-flow shock into a Y-shaped shock system, with as stem the strong cross-flow shock. On the central part of the wing a so called "rear shock" appears, normal to the plane of symmetry. This shock is due to the upstream effects of the trailing edge, where the Kutta condition must be satisfied.

In the isobar pattern of the measured data the rear shock shows up, as does the cross-flow shock. However, the Y-shaped shock system is not present. For this the following explanation is given. In the experiment a cross-flow shock is formed just downstream (outboard) of the suction peak underneath the leading-edge vortex. Viscous effects will cause the flow to separate immediately downstream (outboard) of the cross-flow shock. The secondary vortex that is subsequently formed, causes the leading-edge vortex as well as the cross-flow shock to move to a more inboard location and simultaneously will lower the suction peak due to the primary vortex. In the final equilibrium situation the cross-flow shock is at a much more inboard position than formed in the inviscid flow solution without secondary separation and a Y-shaped shock system does not form.

In Fig. 4, showing the calculated isobar pattern in the plane of symmetry ( $y/s = 0.0$ ), the rear shock is clearly visible. The extent of the region with supersonic flow can be determined easily since the  $C_p = -0.3$  isobar corresponds with the critical value of the pressure coefficient. Also a

second (weak) shock appears at the junction of the wing and the sting. Here the flow first accelerates sharply over the discontinuity, followed immediately by a compression through a shock. Experimental data is not available that close to the trailing-edge, but it may be expected that viscous effects cause local flow separation which will smooth out the local suction peak.

Fig. 5 presents the pressure distribution in a cross-flow plane perpendicular to the configuration at  $x/c_R = 0.6$ . Due to the clearly visible cross-flow shock and other compressibility effects, the vortical flow region in transonic flow has a flatter shape than in case of subsonic flow. This cross-flow shock causes the isobars to lean backwards towards the plane of symmetry. Outboard of the cross-flow shock and underneath the shear layer from the leading edge there is a relatively large region where the variations in the pressure are small.

In Fig. 6 the computed surface pressure distribution at the spanwise section  $x/c_R = 0.6$  is compared with NLR experimental data (Ref. 15). On the lower surface the agreement of computed and measured data is excellent. For the upper surface the situation is less satisfactory. In the Euler solutions the cross-flow shock is located at about 75% local semi-span, while in the experiment the (weaker) cross-flow shock is located much further inboard at 60% local semi-span. The experimental data further indicate, as may be concluded from the pronounced second suction peak, that the cross-flow shock provokes an early secondary separation that results in a relatively strong secondary vortex.

Fig. 7, which compares the computed and measured surface pressure distribution along the chordwise section in the plane of symmetry, in general shows a satisfactory correlation. The rear shock shows up clearly in the Euler solution. However, in the computation, it is situated at a slightly more downstream location than in the measurement, probably due to the neglect of viscous effects in the numerical simulation. At the trailing edge the steep expansion and subsequent shock associated with the flow over the junction of the wing and the sting, appears to be rather pronounced. Viscous effects probably will modify this feature considerably. Finally note that at the apex there are relatively large differences between theory and experiment. These are presumably due to differences in the geometry as well as to viscous effects.

##### Flow solution in the near wake

In this section the development of the flow field just upstream and just downstream of the trailing edge in the near wake is analyzed in detail. The case considered is again the transonic flow about the wing-body configuration at a free-stream Mach number of 0.85 and 20 deg incidence. Since experiments have indicated onset of vortex breakdown for higher incidences than the one considered, we don't have to consider this complex and not yet fully understood flow phenomenon. Hummel (Ref. 21) showed that, at least for subsonic flow conditions, a complex vortex structure develops in the near wake. The constitutive elements of this mushroom-shaped vortex structure, are the leading-edge vortex and the so-called trailing-edge vortex. The latter vortex contains

vorticity of sign opposite to that contained in the leading-edge vortex and forms immediately downstream of the trailing edge. Although the sign (negative) of the vorticity in the trailing-edge vortex is the same as that in the vortex resulting from the smooth-surface secondary separation underneath the leading-edge vortex, it is a different vortex. This has been confirmed in inviscid flow simulations (Refs. 16,22). It forms as a consequence of the wake at the trailing edge ( $x/c_R = 1.0$ ) containing vorticity of both signs, i.e. negative in the shear layer between the plane of symmetry and some lateral location near that of the leading-edge vortex, positive in the remainder of the shear layer from the trailing edge, in the shear layer from the tip and in the leading-edge vortex itself (Ref. 22).

In inviscid flow simulations total-pressure losses should occur in shock waves only. However, in results of Euler codes total-pressure losses also occur due to discretization errors, implementation of approximate boundary conditions etc., as well as due to the explicitly added artificial viscosity terms of the numerical algorithm. For the present type of applications, these numerically induced total-pressure losses are largest in regions with large gradients, specifically in regions with concentrated vorticity such as, free shear layers and in particular vortex cores.

Fig. 8 shows the distribution of the losses in total pressure in five consecutive planes  $x/c_R = \text{constant}$ , namely  $x/c_R = 0.95, 1.0, 1.025, 1.05$  and  $1.10$ . In the planes  $x/c_R = 0.95$  and  $1.0$ , the leading-edge vortex can be identified by the region with significant total-pressure losses, up to a loss of 60% of the free-stream value at the center of the vortex core. The closely-spaced isolines perpendicular to the surface underneath the vortex core indicate the cross-flow shock which gives rise to a loss of 15% of the free-stream value. That the total-pressure losses due to the cross-flow shock are that high, can be explained in terms of the local Mach number upstream of the shock having a value in the order of 2. It follows from Fig. 8 that the leading-edge vortex continues downstream of the trailing edge, as a region with total-pressure losses of about the same magnitude, gradually changing its shape in response to the changing flow field. Downstream of

the trailing edge a second region with significant total-pressure losses (up to 45% of the free-stream value) develops rapidly. It is the "trailing-edge vortex" which results from the roll-up of the negative vorticity contained in the wake. The leading-edge and the trailing-edge vortex interact with each other and at the section  $x/c_R = 1.10$ , a mushroom-shaped vortex system results, just as found in subsonic flow. Also note that downstream of the trailing edge the cross-flow shock has disappeared.

Another feature can be detected in the sections at  $x/c_R = 0.95, 1.0, 1.025$ , namely a distortion in the isobar pattern signifying a third region with concentrated vorticity. This feature has associated with it a loss in total pressure of 30-35% of the free-stream value and can be traced back to the kink in the leading edge, i.e. to  $x/c_R = 0.85$ . It is termed the "tip vortex". Because this tip vortex leaves the leading edge at a relatively large angle with respect to the surface, it has little effect on the surface pressure distribution. From the contours in the consecutive cross-flow planes it can be seen that the tip vortex travels around the leading-edge vortex. At  $x/c_R = 1.10$  it is so close to the core of the leading-edge vortex that it can no longer be distinguished and may be assumed to be fully merged with the latter.

#### Evolution of Euler solution with incidence

In this section the evolution with incidence of the Euler solution around the wing-body configuration at the transonic free-stream Mach number of 0.85 is discussed. Computational results are presented for incidences of 10, 15 and 20 deg. Fig. 9 shows the isobar pattern on the upper surface of the configuration for these three incidences. Judging from the region with low pressures it is seen that with increasing incidence the leading-edge vortex becomes stronger and shifts to a more inboard position. For all cases the leading-edge flow separation and the vortex formation starts at the apex. At 10 deg incidence the flow is still nearly shock free, with only a cross-flow shock near the wing tip. For the incidences of 15 and 20 deg the cross-flow shock develops on the remainder of the wing, moving in inboard direction with increasing incidence. On the rear part a Y-shaped shock system evolves, resulting from the process in which a second shock develops on the aft part of the wing near the wing tip, which subsequently merges with the cross-flow shock. As far as the "rear shock" is concerned it is seen that it starts to develop at 15 deg incidence and is well-developed at 20 deg incidence.

In Fig. 10a the isobar pattern in the cross-flow plane  $x/c_R = 0.6$  are presented for the three incidences. With increasing incidence the region on the upper surface influenced by the leading-edge vortex becomes larger, while the center of the vortex moves more inboard and upward. In the flow field above the upper surface, the cross-flow shock develops accompanied by a gradually more backward leaning of the isobars around the center of the vortex core. In the vortex core itself, the static pressure decreases with increasing incidence, indicating that the vortex becomes stronger. Also note that downstream (-outboard) of the cross-flow shock the region where the static pressure is about constant increases in area. Fig. 10b shows the corresponding cross-flow plane isolines of total-pressure losses. It indicates that at low incidence the vortical flow region is rather close to the surface while with increasing incidence, the region with vortical flow increases in cross-sectional area. The maximum total-pressure loss occurs at the center of the vortex core and its magnitude increases with incidence from 35% at 10 deg to 60% of the free-stream value at 20 deg incidence. Across the cross flow shock the total-pressure losses amount from 5% at 15 deg incidence to 15% at 20 deg incidence. In each of the three cases considered in Fig 10b, the shear layer from the leading edge is clearly outlined as a region with significant total-pressure losses.

Fig. 11 shows the development with incidence of the distribution of the surface pressure coefficient at the spanwise section  $x/c_R = 0.6$ . Again it shows that the height of the suction peak and therefore the strength of the vortex, increases with increasing incidence. The suction peak grows both in height and in width and moves in inboard direction, while on its outboard flank the cross-flow shock develops. The upper-surface attachment point, indicated by a local maximum in the pressure coefficient inboard of the leading-edge vortex, rapidly moves towards the plane of symmetry with increasing incidence. At 20 deg incidence it has reached the plane of symmetry. The primary attachment point on the lower wing surface, which at 10 deg incidence is still very close to the leading edge, gradually moves away from the leading edge with increasing incidence. The distribution of the surface pressure coefficient along the chordwise section in the plane of symmetry, presented in Fig. 12, clearly shows the

development of the rear shock with incidence. As incidence increases, shock strength increases and its location moves to a more aft position. Furthermore note that with increasing incidence a suction peak on the upper surface develops near the wing apex. It is assumed that this is due to the singularity in the inviscid transonic solution at the apex which will also include the influence of the body. Also shown is the development of the suction peak and shock at the junction of the wing and the sting.

#### Evolution of Euler solution with Mach number

In this section we investigate the effect of increasing the Mach number at a fixed incidence of 20 deg from a low subsonic (0.15) to a subsonic (0.50) and a transonic (0.85) free-stream Mach number. For this study the wing-alone configuration is considered. It is assumed that at the high incidence of 20 deg the influence of the underwing body of the wind-tunnel model on the flow field above the upper surface of the wing will be so small, that we can consider the wing-alone configuration instead.

Fig. 13 shows the isobar pattern on the upper surface of the wing for the three Mach numbers. The patterns show that in each case a region with low pressure develops on the upper surface indicative for the presence of a strong leading-edge vortex. On the forward part of the wing the lowest values of the surface pressure coefficient are obtained for the lowest free-stream Mach number. This is typical for subsonic Mach numbers where there is a relatively large effect of the singularity at the apex as well as a strong upstream influence of the trailing edge, and for which in addition the vacuum pressure coefficient (which varies like  $1/M_\infty^2$ ) is lowest. With increasing Mach number the height of the suction peak decreases rapidly and the region with the lowest pressures moves to a more aft position on the wing, resulting in a more conical pattern. Simultaneously the location of the suction peak moves to a more inboard position and a shock-wave pattern evolves.

It should be realized that apart from the circumstance that the flow is still not fully supersonic the flow pattern cannot become exactly conical because the wing-body nor the wing-alone configuration have a conical geometry.

The effect of the presence of the under-wing body on the upper-surface pressure distribution can be assessed by comparing those isobar patterns in Figs. 9 and 13 that were computed for the same condition ( $M_\infty = 0.85$ ,  $\alpha = 20$  deg). It indeed confirms that for the wing-body (Fig. 9) and for the wing-alone (Fig. 13), a pattern is obtained with strong similarities in the shape of the region with low pressure, the location of the cross-flow shock, the occurrence of the Y-shaped shock structure on the aft part of the configuration, the location of the rear shock, etc. Some more significant differences are found near the junction of the wing and the sting. Smaller differences may be attributed to differences in grid topology and grid density.

In Fig. 14a the isobars in the cross-flow plane at  $x/c_x = 0.6$  are presented for the three Mach numbers considered. With increasing Mach number the center of the vortex core (= the point of minimum static pressure) moves inboard and downward. Also, with increasing Mach number the pressure coefficient in the core increases rapidly. For the transonic Mach number the contours near the center become less circular in appearance indicating a vortex core of a flatter shape. Furthermore at  $M_\infty = 0.85$  the

cross-flow shock appears and associated with it a region with about equal static pressure. In Fig. 14b the corresponding cross-flow plane patterns of isolines of total-pressure loss are presented. It confirms that at the transonic free-stream Mach number the region with vortical flow is much flatter than at subsonic free-stream Mach numbers. The maximum total-pressure loss, occurring at the center of the vortex core increases rapidly with increasing Mach number.

Comparison of the patterns for  $M_\infty = 0.85$ ,  $\alpha = 20$  deg in Figs. 10 and 14, for the wing-body and the wing-alone configuration respectively, confirm that at  $x/c_x = 0.6$  for this flow condition the effect of the presence of the body on the flow above the upper surface of the configuration is small.

In Fig. 15 the spanwise surface pressure distribution is presented at  $x/c_x = 0.6$ . On the lower surface the pressure coefficient is not affected very much by compressibility effects. On the upper surface the effect of the Mach number on the distribution of the pressure coefficient is very large. At the section at  $x/c_x = 0.6$ , increasing the Mach number from 0.15 to 0.50 increases the height of the suction peak somewhat, reduces its width slightly and moves it to a more inboard position. Increasing the Mach number to 0.85 reduces the height of the suction peak dramatically and moves its position still further inboard, while also one sees the development of the cross-flow shock.

The chordwise surface pressure distribution along the section in the plane of symmetry (Fig. 16), indicates the effects of compressibility on the flow. Increasing the Mach number results in a distribution that is more conical, at least on the forward part of the wing. On the aft part of the wing the rear shock is required to increase the pressure discontinuously in order to enable fulfillment of the Kutta condition at the trailing edge. Comparison for  $M_\infty = 0.85$ ,  $\alpha = 20$  deg of the result in Fig. 12 for the wing-body configuration with the one in Fig. 16 for the wing-alone configuration shows, naturally, large differences for the lower side of the configuration and near the apex and wing-sting junction for the upper surface.

#### CONCLUDING REMARKS

Results of an Euler method have been obtained for the transonic ( $M_\infty = 0.85$ ) flow around a wing-body configuration consisting of a 65-deg sharp-edged cropped delta wing and an under-wing body for incidences of 10, 15 and 20 deg. For the wing-alone configuration results have been obtained for subsonic ( $M_\infty = 0.15, 0.50$ ) and transonic ( $M_\infty = 0.85$ ) flow at 20 deg incidence. For the wing-body configuration the calculations were carried out on a grid of C-O topology with 240K cells. For the wing-alone configuration a comparable grid of O-O topology with 150K cells is used.

For the wing-body configuration at  $M_\infty = 0.85$  and  $\alpha = 20$  deg computed results were compared with experimental data available for this configuration. The differences in the height and the position of the suction peak in the pressure distribution on the upper surface of the configuration as obtained from the Euler method and these found in the experiment are primarily attributed to the effect of secondary separation, which is not modeled in the present numerical simulation. To obtain a better agreement between theory and experiment it is deemed necessary to include some kind of explicit modeling of the effect of secondary separation in the Euler method.

It is shown that the Euler method is capable of simulating the mushroom-shaped vortex structure formed by the leading-edge vortex and the trailing-edge vortex in the near wake of the wing. This investigation has also revealed the occurrence, at transonic speed, of a third vortex, termed the "tip-vortex".

The investigation into the evolution of the flow field about the wing-body configuration with increasing incidence has shown that there is a strong influence of compressibility on the flow solution. Increasing the incidence leads to the formation of a strong "cross-flow" shock underneath the leading-edge vortex, while on the aft part of the configuration a "Y-shaped" shock system evolves. On the aft part of the configuration in addition a "rear shock" appears. It is shown that these shocks develop quite gradually for the incidence increasing from 10 to 20 deg (still below the onset of vortex breakdown observed in experimental investigations).

Compressibility effects have also been assessed by considering, for the wing-alone configuration, the evolution of the Euler solution at fixed incidence but increasing free-stream Mach number. It is shown that at low Mach numbers, the lowest values of the surface pressure coefficients are attained on the upper surface near the apex. With increasing Mach number the height of the suction peak on the upper surface decreases rapidly on the forward part of the configuration and less so on the aft part of the configuration, resulting in a more conical appearance of the isobar pattern.

#### REFERENCES

- Hoeijmakers, H.W.M.: Methods for Numerical Simulation of Leading-Edge Vortex Flow. In *Studies of Vortex Dominated Flows*, ed. M.Y. Hussaini and M.D. Salas, Springer Verlag, pp. 223-267 (1987). Also NLR MP 85052 U.
- Murman, E.M., Rizzi, A.: Applications of Euler Equations to Sharp-Edged Delta Wings with Leading Edge Vortices. AGARD CP412, Paper 15 (1986).
- Longo, J.M.A.: The Role of the Numerical Dissipation on the Computational Euler-Equations-Solutions for Vortical Flows. AIAA Paper 89-2232 (1989).
- Hitzel, S.M.: Wing Vortex-Flows up into Vortex Breakdown. A Numerical Simulation. AIAA Paper 89-2232 (1989).
- O'Neill, P.J., Barnett, R.M., Louie, C.M.: Numerical Simulation of Leading-Edge Vortex Breakdown using an Euler Code. AIAA Paper 89-2189 (1989).
- Raj, P., Sikora, J.S., Keen, J.M.: Free-Vortex Flow Simulation using a Three-Dimensional Euler Aerodynamic Method. *J. of Aircraft*, Vol. 25, No. 2 (1988).
- Wardlaw Jr, A.B., Davies, S.F.: Euler Solutions for Delta Wings. AIAA Paper 89-3398 (1989).
- Smith, J.H.B.: Behaviour of a Vortex Sheet Separating from a Smooth Surface. RAE TR 77058 (1977).
- Marconi, F.: On the Prediction of Highly Vortical Flows using an Euler Equation Model. In *Studies of Vortex-Dominated Flows*, M.Y. Hussaini and M.D. Salas, Springer Verlag ed., pp. 311-364 (1987).
- Kwong, C.M., Myring, D.F.: Fusiform Body Separated Flow Field Calculation Using Euler and Boundary Layer Methods. Paper 27, Proceedings of the Royal Aeronautical Society Conference on "The Prediction and Exploitation of Separated Flow", London, (1989).
- Chaffari, F., Luckring, J.M., Thomas, J.L., Bates, B.L.: Navier-Stokes Solutions about the F/A-18 Forebody-LEX Configuration. AIAA Paper 89-0338 (1989).
- Fujii, K., Obayashi, S.: High-Resolution Upwind Scheme for Vortical Flow Computations. *J. of Aircraft*, Vol. 26, No. 12, pp. 1123-1129 (1989).
- Hsu, C.-H., Liu, C.H.: Upwind Navier-Stokes Solutions for Leading-Edge Vortex Flows. AIAA Paper 89-0265 (1989).
- Elsenaar, A., Eriksson, G.: Proceedings of the Symposium on "International Vortex Flow Experiment and Euler Code Validation" FFA, Stockholm, 1-3 Oct. (1986).
- Elsenaar, A., Hoeijmakers, H.W.M.: An Experimental Study of the Flow Over a Sharp-Edged Delta Wing at Subsonic, Transonic and Supersonic Speeds. Paper presented at the AGARD FDP Symposium "Vortex Flow Aerodynamics", Oct. 1990.
- Hoeijmakers, H.W.M., Jacobs, J.M.J.W., Berg, J.I. van den: Numerical Simulation of Vortical Flow Over a Delta Wing at Subsonic and Transonic Speeds. ICAS Paper 90-3.3.3 (1990).
- Boerstoel, J.W. et al: Design and Testing of a Multiblock Grid-Generation Procedure for Aircraft Design and Research. NLR TP 89146 U (1989).
- Boerstoel, J.W.: Progress Report of the Development of a System for the Numerical Simulation of Euler flows, with Results of Preliminary 3D propeller-Slipstream/Exhaust-Jet Calculations. NLR TR 88008 U (1988).
- Buysen, F.A.: Flow Visualisation at NLR: VISU3D. NLR TP 89317 (1989).
- Jameson, A., Schmidt, W., Turkel, E.: Numerical Solution of Euler Equations by Finite Volume Methods Using Runge-Kutta Time-Stepping Scheme. AIAA Paper 81-1259 (1981).
- Hummel, D.: On the vortex Formation over a Slender Wing at Large Angles of Incidence. AGARD CP247, Paper 15 (1979).
- Hoeijmakers, H.W.M.: Computational Aerodynamics of Ordered Vortex Flows. NLR TR 88088 U (1989).

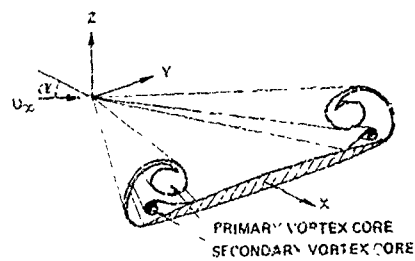
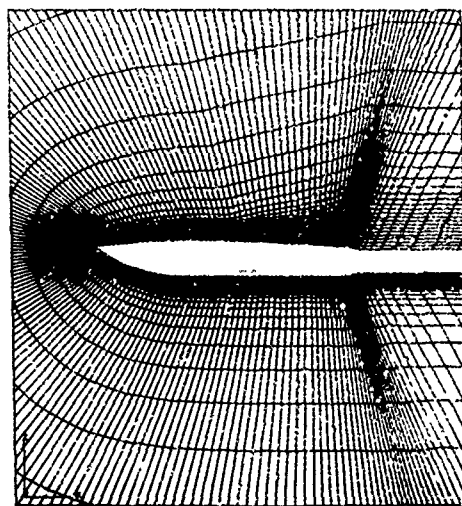


Fig 1 Vortex flow about a delta wing



a. Plane of symmetry



b. Wing-body surface

Fig 2 CO grid around the wing-body configuration

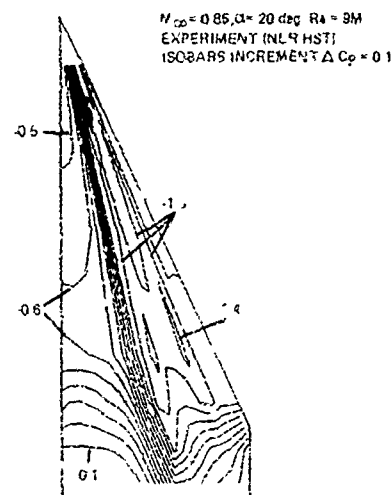
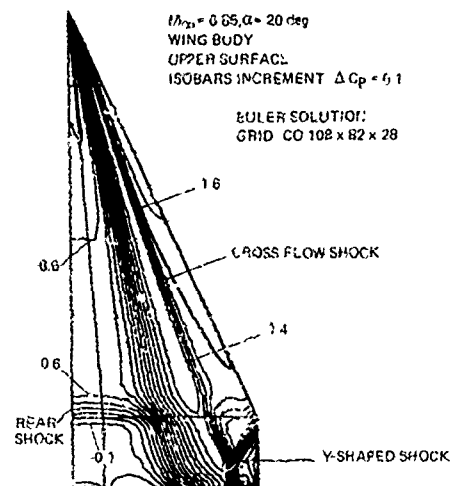


Fig 3 Isobar pattern on the upper surface of the wing-body configuration.

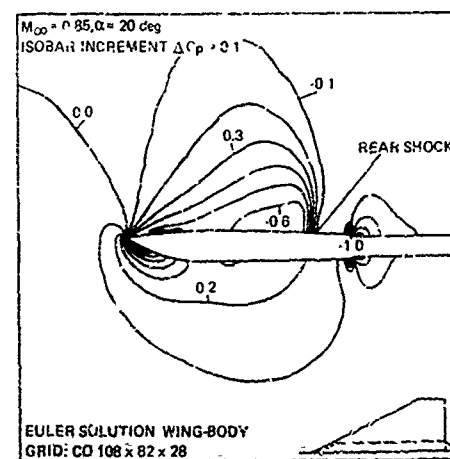
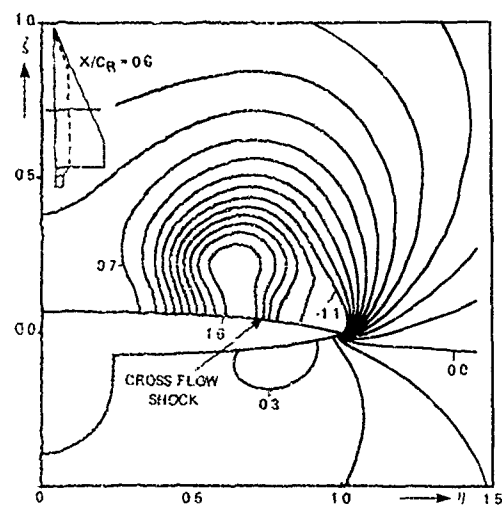


Fig 4 Isobar pattern in plane of symmetry





$M_\infty = 0.85, \alpha = 20 \text{ deg}$   
 ISOBARS INCREMENT  $\Delta C_p = 0.1$   
 EULER SOLUTION  
 GRID: CO 106 x 82 x 28

Fig. 5 Isobar pattern in plane  $x/c_R = 0.6$

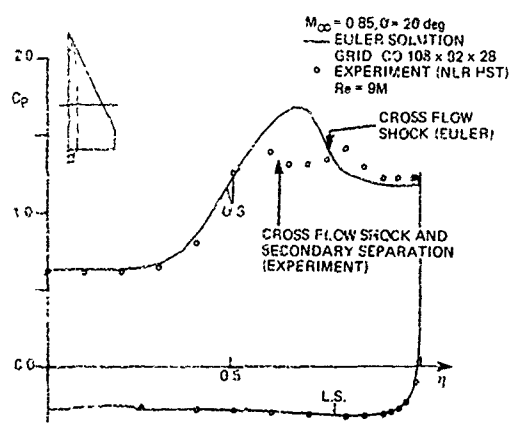


Fig. 6 Comparison of calculated and measured spanwise surface pressure distribution.

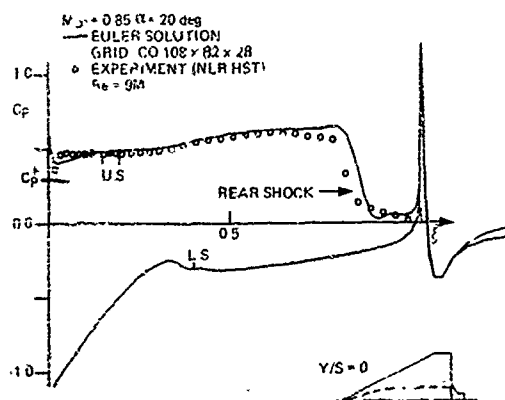
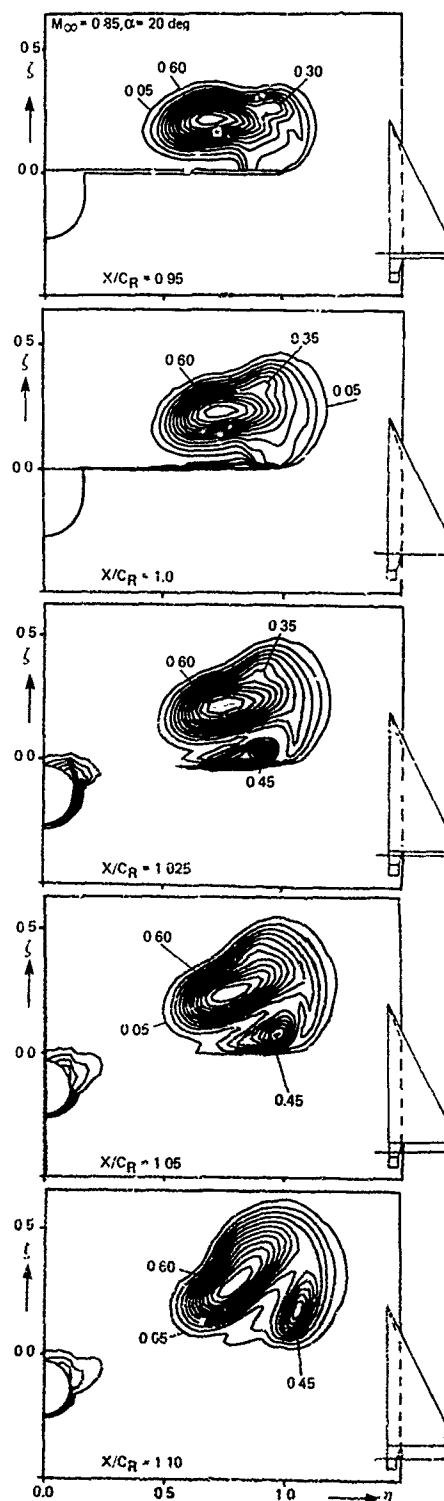


Fig. 7 Comparison of calculated and measured chordwise surface pressure distribution.



INCREMENT  $\Delta(P_t/P_{t\infty}) = 0.05$   
 EULER SOLUTION  
 GRID: CO 128 x 82 x 28

Fig. 8 Contours of equal total pressure-loss in planes  $x/c_R = \text{constant}$

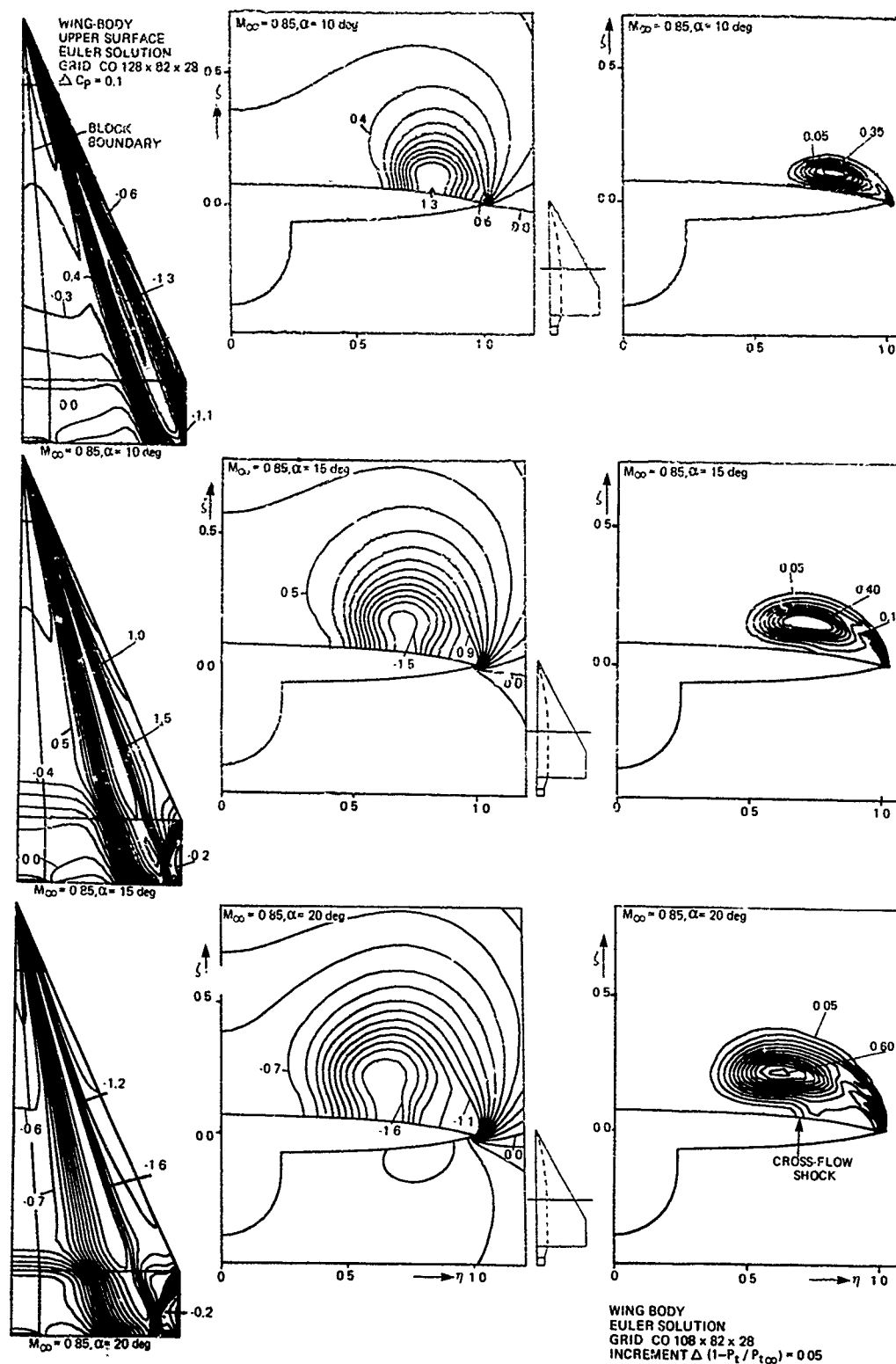


Fig. 9 Isobar pattern on upper surface for three angles of attack

Fig. 10a Isobar pattern in plane  $x/c_p = 0.6$  for three angles of attack

Fig. 10b Contours of equal total pressure loss in plane  $x/c_p = 0.6$  for three angles of attack

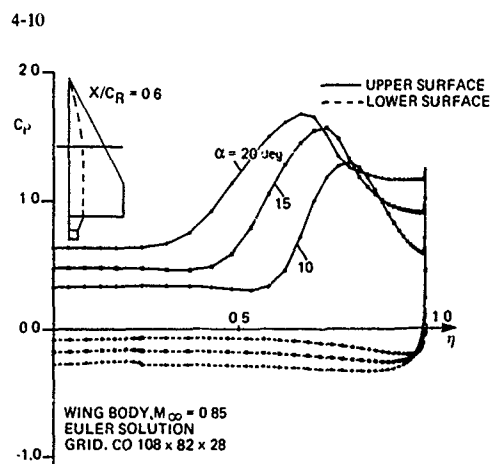


Fig. 11 Spanwise surface pressure distribution for three angles-of-attack at  $x/c_R = 0.6$

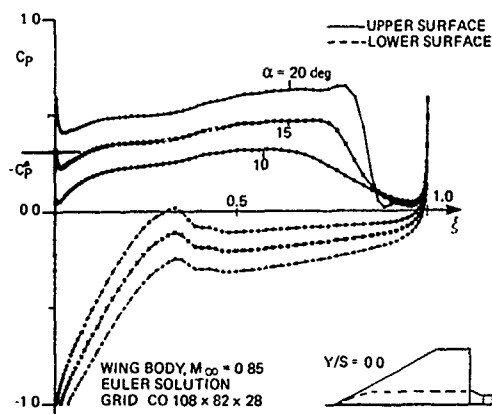


Fig. 12 Chordwise surface pressure distribution for three angles of attack at  $y/s = 0.0$

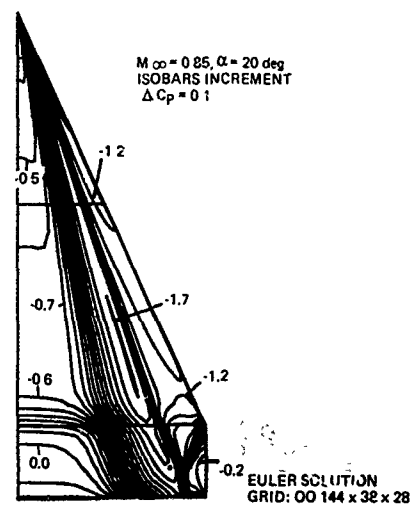
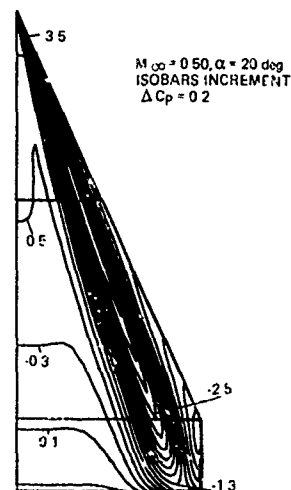
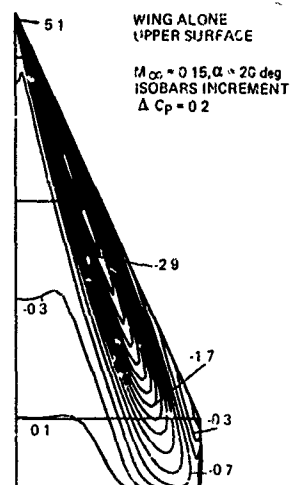
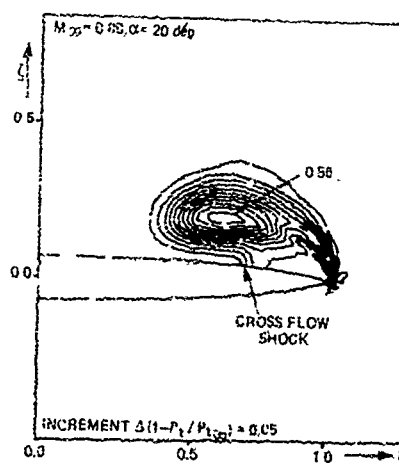
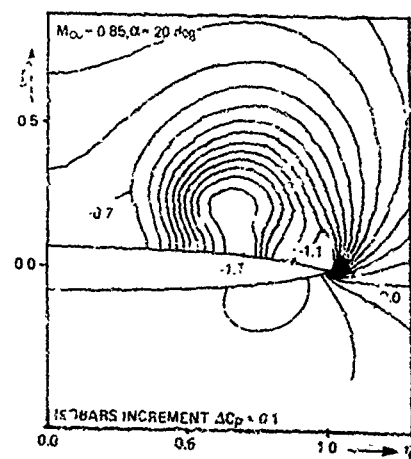
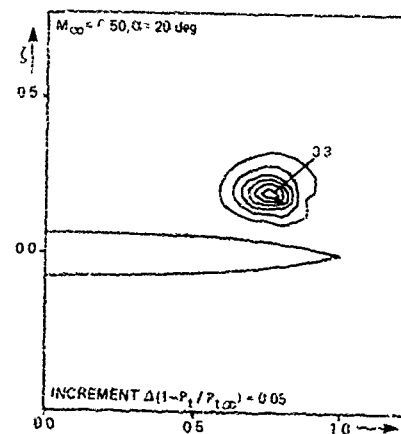
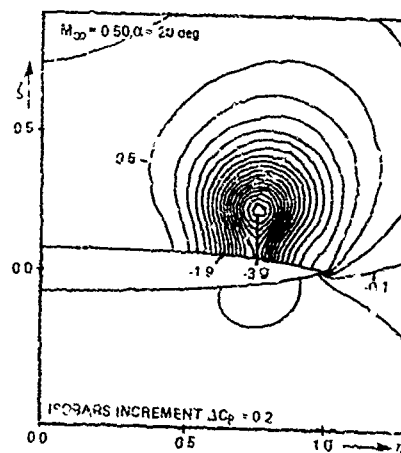
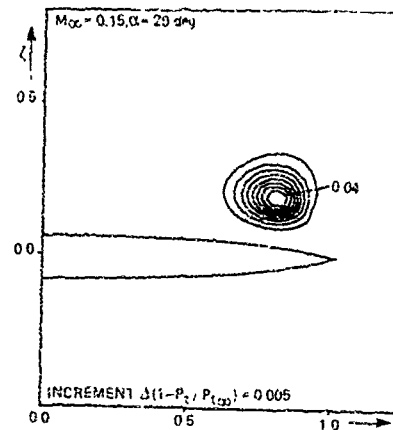
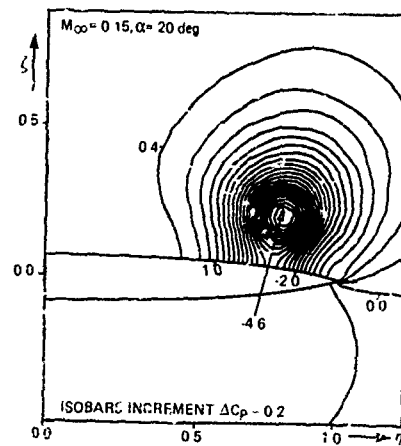


Fig. 13 Wing surface isobar pattern for three Mach numbers



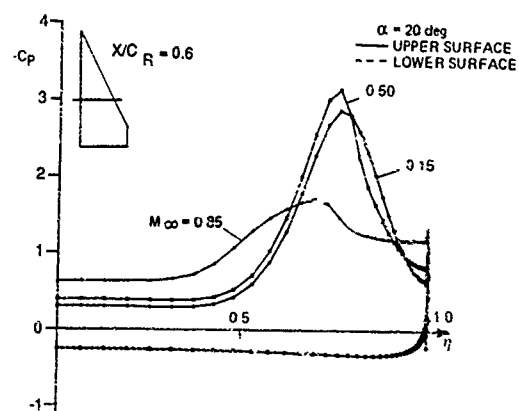
WING ALONE  
EULER SOLUTION  
GRID: 144 x 38 x 28

WING ALONE  
EULER SOLUTION  
GRID: 144 x 39 x 28

Fig. 14a Isobar pattern in plane  $x/c_R = 0.6$  for three Mach numbers

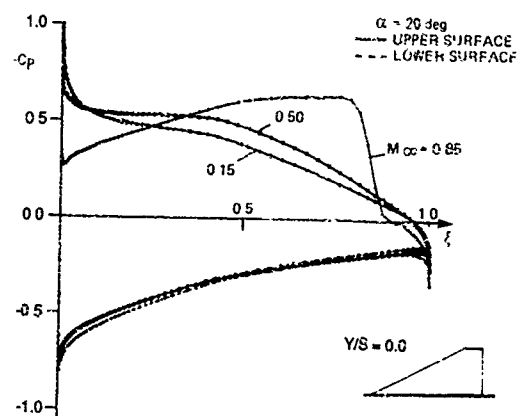
Fig. 14b Contours of equal total pressure loss in plane  $x/c_R = 0.6$  for three Mach numbers

4-12



WING ALONE  
EULER SOLUTION  
GRID OO 144 x 38 x 28

Fig. 15 Spanwise surface pressure distribution for three Mach numbers at  $x/c_R = 0.6$



WING ALONE  
EULER SOLUTION  
GRID OO 144 x 38 x 28

Fig. 16 Chordwise surface pressure distribution for three Mach numbers for  $y/s = 0.0$

# EXPERIMENTAL AND NUMERICAL INVESTIGATION OF THE VORTEX FLOW OVER A DELTA WING AT TRANSONIC SPEED

E.M. Houtman, W.J. Baarsink  
University of Technology Delft,  
Faculty of Aerospace Engineering,  
P.O. Box 5058, 2600 GB Delft  
The Netherlands

## SUMMARY

The flow around a sharp-edged delta wing with 65° sweep and a flat upper surface is investigated experimentally as well as numerically. The experimental program contains surface pressure measurements, oil flow visualization and flow field explorations at the Mach numbers 0.60 and 0.85 and angles of attack up to 20°. The results show a transonic leeward flow structure with several shock waves. At a Mach number of 0.85 and 20° angle of attack vortex breakdown is observed. The vortex breakdown goes along with a double shock system in the symmetry plane region. In the numerical program a 3D Euler code is used with two upwind schemes; one of the flux-splitting type and one of the flux-difference-splitting type. The results show significant differences between the two discretization schemes, in particular in the region of the vortex. Between computations and experiments large differences are observed due to the absence of secondary separation, and, at the higher angles of attack, due to the absence of vortex breakdown in the computations

flow field may be very complex and difficult to predict by computational methods.

Computational methods based on the Euler equations are able to capture strong shock waves and vortical flow regions as integral part of the discrete solution. For the case of aerodynamically sharp leading edges the formation of leading edge vortex flow due to separation is only slightly dependent on the Reynolds number. This implies that such a flow can be simulated by an inviscid flow model. The opposite, however, is true for secondary- and even tertiary vortices, shed off from the smooth upper surface. These category of vortices is of an entirely viscous nature, since they are generated at those locations where the boundary layer can no longer sustain an adverse pressure gradient and will separate. These vortices have a large influence on the pressure distribution on the surface, and also on the strength and location of the primary vortex. The consequence is that Euler methods usually overestimate the expansion due to the primary vortex.

## LIST OF SYMBOLS

$A_1$	primary attachment line
$c_r$	rootchord
$E$	total energy per unit mass
$e$	internal energy per unit mass
$f, g, h$	flux vectors
$f_R$	numerical flux function (approximate Riemann solver)
$H$	total enthalpy
$h_i$	characteristic mesh size
$M$	Mach number
$n$	outward unit normal vector on control volume
$p$	static pressure
$p_t$	total pressure
$q$	state vector of conserved variables
$S_2$	secondary separation line
$t$	time
$u, v, w$	velocity components in Cartesian coordinate system
$x, y, z$	Cartesian coordinate system
$\alpha$	angle of attack
$\theta$	angle between unit normal and x-axis
$\rho$	density
$\phi$	angle of unit normal in y-z plane with y-axis
$\Omega$	control volume
$\Omega_{ijk}$	finite volume
$\partial\Omega$	boundary of control volume
$\omega$	damping parameter in Defect Correction Iteration

## subscripts:

$i, j, k$	indices in computational domain
$le$	leading edge
$\infty$	free stream value

## INTRODUCTION

The vortical flow field of a delta wing in the high speed range has been the subject of intensive study during the last decade. The development of numerical codes based on the Euler- or Navier-Stokes equations, which are able to predict complex vortical flows, gave rise to the demand for experimental data to validate the numerical results. In the high speed range the flow above a delta wing is characterized by strong vortices and embedded shock waves. Even in the case of a simple geometry like a flat triangular wing, the

In 1983 a joined experimental and theoretical program, known as 'The International Vortex Flow Experiment on Euler Code Validation' [1,2], was started up. The purpose was to obtain an experimental data base for a 65° delta wing in the high speed regime, to validate computational results. This program contained not only experiments to get integral data such as forces and surface pressures, but also detailed flow field explorations, in order to be able to make a more complete comparison and to get a better insight in the physics of the flow field. The analysis of the experimental and computational data was concentrated on some topics, two of which are mentioned. First there is the formation of different types of shock waves. Globally two different types of shock waves can be distinguished: embedded shock waves of a conical nature between the primary vortex and the upper surface and the so-called rear shock waves in the symmetryplane region. Another topic is the structure and mechanism of vortex breakdown. Especially in the transonic region there is a complicated interaction between the rear shock and the vortex breakdown. Although a large amount of data is available, the topics are as yet far from understood.

Within the scope of the International Vortex Flow Experiment some investigations were done at the Delft University of Technology on a 65° delta wing with flat upper surface and cropped wing tips [1,3]. This model was based on an early design concept of the model proposed by the International Vortex Flow Experiment Group. These investigations included oil flow visualization, Schlieren pictures and flow field explorations by a 5-hole probe. A rather good insight in the topological flow structure was obtained, but the existence of embedded shock waves could only be suggested. After the Int. Vortex Flow Exp. Test series, a new, somewhat different, model was manufactured with pressure orifices, in order to obtain a more complete set of experiments [4].

Beside the experimental program, a numerical experiment was accomplished with a 3D-Euler code. This code is developed by the first author as an extension of a 2D-code developed at the Centre of Mathematics and Computer Science (CWI) in Amsterdam by Koren and Spekreijse [5],[6]. The 3D-code uses three different types of upwind schemes based on the Riemann problem for 1D-flows, the flux-splitting scheme of van Leer [7] and the flux-difference-splitting schemes of Osher [8] and Roe [9]. For the solution procedure a nonlinear Gauss-Seidel relaxation, accelerated by multigrid, is used. The investigation of the behaviour of these upwind schemes in the simulation of vortical flows was the object of this numerical program.

## EXPERIMENTAL EQUIPMENT

The experiments have been performed in the TST-27 transonic-supersonic windtunnel of the Laboratory of High Speed Aerodynamics, Department of Aerospace Engineering at the Delft University of Technology. The windtunnel is of the blow-down type, with a test section of 26cm x 27cm and with a slotted upper- and lower wall. Two identical models with a flat upper surface and a leading edge sweep angle of 65° were used, the rootchord of the models was 120mm (fig. 1a,b). One of the models is provided with 43 pressure taps, the other one (without pressure taps) was used for oilflow visualization tests and flow field measurements. The tests have been performed at angles of attack from 5° to 20° and at free stream Mach numbers of 0.6, 0.7, 0.75, 0.8, 0.85 and 0.90, with emphasis on 0.85; this Mach number was a target in most tests within the framework of the International Vortex Flow Experiment. The Reynolds number based on the root chord varied from 3.0 to 3.6 million.

Furthermore some flow field investigations were made with a 5-hole hemispherical head probe. The probe has been calibrated at Mach numbers from 0.55 to 1.8 and up to angles of attack of 60°, which covers the region of Mach numbers and flow angles to be expected in the flow field above a delta wing in transonic flow. Due to the time consuming character of the flow field tests have been performed at only one Mach number (0.85) and at two angles of attack (10° and 15°). The measurements were made in cross-flow planes normal to the free stream direction, by traversing the probe in spanwise direction at constant heights above the surface. The flow field in the symmetry plane was investigated by making traverses in upward direction (away from the surface).

## NUMERICAL METHOD

## A. Discretization

The governing equations are the Euler equations, expressing the conservation of mass, momentum and energy for an inviscid, non-heatconducting perfect gas in the absence of external forces. The equations in integral form are given by:

$$\iint_{\partial\Omega} \frac{\partial q}{\partial t} dv + \iint_{\partial\Omega} (f(q) \cdot n_x + g(q) \cdot n_y + h(q) \cdot n_z) ds = 0$$

where  $\partial\Omega$  is the boundary of a control volume  $\Omega$ ,  $(n_x, n_y, n_z)^T$  is the outward unit normal on  $\partial\Omega$ ,  $q$  is the vector of conserved variables:

$$q = (\rho, \rho u, \rho v, \rho w, \rho E)^T$$

Here  $\rho$  is the density,  $u, v, w$  are the velocity components in the  $x, y, z$  directions respectively;  $E$  is the total energy given by  $E = e + \frac{1}{2}(u^2 + v^2 + w^2)$ , in which  $e$  is the internal energy per unit mass. The internal energy  $e$  may be expressed in terms of the pressure  $p$  and the density  $\rho$  with the ratio of specific heats  $\gamma$  as  $e = p/(\gamma - 1)\rho$ .

$f(q), g(q)$  and  $h(q)$  are the flux vectors:

$$f(q) = (\rho u, \rho u^2 + p, \rho uv, \rho uw, \rho uH)^T$$

$$g(q) = (\rho v, \rho uv, \rho v^2 + p, \rho vw, \rho vH)^T$$

$$h(q) = (\rho w, \rho uw, \rho vw, \rho w^2 + p, \rho wH)^T$$

where  $H$  is the total enthalpy defined as  $H = E + \frac{p}{\rho}$ . This equation may be simplified by the use of the property that the Euler equations are rotationally invariant:

$$f(q) \cdot n_x + g(q) \cdot n_y + h(q) \cdot n_z = T^{-1} \cdot f(T \cdot q)$$

where  $T$  is a rotation matrix defined as:

$$T = \begin{bmatrix} 1 & 0 & 0 & 0 & 0 \\ 0 & \cos\theta & \sin\theta\cos\phi & \sin\theta\sin\phi & 0 \\ 0 & -\sin\theta & \cos\theta\cos\phi & \cos\theta\sin\phi & 0 \\ 0 & 0 & -\sin\phi & \cos\phi & 0 \\ 0 & 0 & 0 & 0 & 1 \end{bmatrix}$$

The angles  $\theta$  and  $\phi$  define the unit normal:  $(n_x, n_y, n_z)^T = (\cos\theta, \sin\theta\cos\phi, \sin\theta\sin\phi)^T$ .

A straightforward and simple discretization of the steady equations is obtained by subdividing  $\Omega$  into disjoint hexahedral cells  $\Omega_{ijk}$  (finite volumes) and then requiring that for each volume  $\Omega_{ijk}$  separately:

$$\iint_{\partial\Omega_{ijk}} T^{-1} \cdot f(T \cdot q) ds = 0$$

For practical reasons the physical domain is subdivided into a structured grid, where  $\Omega_{i+1,j,k}$ ,  $\Omega_{i,j+1,k}$  and  $\Omega_{i,j,k+1}$  are the neighbouring cells of  $\Omega_{ijk}$ . Assuming constant states within the cells and constant flux vectors at the cell interfaces, the finite volume discretization may thus be written:

$$f_{i+\frac{1}{2},jk} - f_{i-\frac{1}{2},jk} + f_{i,j+\frac{1}{2},k} - f_{i,j-\frac{1}{2},k} + f_{i,j,k+\frac{1}{2}} - f_{i,j,k-\frac{1}{2}} = 0$$

with  $f_{i+\frac{1}{2},jk} = T_{i+\frac{1}{2},jk}^{-1} \cdot f(T_{i+\frac{1}{2},jk} \cdot q)$ ,  $s_{i+\frac{1}{2},jk}$  and similar expressions for  $f_{i-\frac{1}{2},jk}$ ,  $f_{i,j+\frac{1}{2},k}$  and  $f_{i,j-\frac{1}{2},k}$ ;  $s_{i+\frac{1}{2},jk}$  is the surface of the cell interface.

The flux vectors  $f(T_{i+\frac{1}{2},jk} \cdot q)$  have to be calculated by a numerical flux function. For this purpose three different upwind schemes may be used: the flux-splitting scheme of van Leer [7] and the flux-difference-splitting schemes of Osher [8] and Roe [9]. These schemes need no additional dissipation terms. Advantage of the flux-difference-splitting schemes over the van Leer scheme is that contact discontinuities (shear layers) are maintained in a better way. On the other hand the computational costs are higher. An upwind scheme may be written as:

$$f_{i+\frac{1}{2},jk} = T_{i+\frac{1}{2},jk}^{-1} \cdot f_R \left( T_{i+\frac{1}{2},jk} \cdot q_{i-\frac{1}{2},jk}^*, T_{i+\frac{1}{2},jk} \cdot q_{i+\frac{1}{2},jk}^* \right)$$

where  $f_R$  is the numerical flux function and  $q^*$  and  $q^+$  are the state vectors at either side of the cell interface in negative and positive  $i$ -direction, respectively. The spatial accuracy is determined by the way in which the states  $q^*$  and  $q^+$  are specified. A scheme with first order spatial accuracy is achieved by assuming constant states within the cells:  $q_{i-\frac{1}{2},jk}^* = q_{ijk}$ ;  $q_{i+\frac{1}{2},jk}^* = q_{i+1,jk}$ . First order accuracy is

too low for practical application, and discontinuities not aligned with grid lines are smeared out disastrously. A second order accurate scheme is obtained by applying an interpolation of the states in adjacent finite volumes with the  $\kappa$ -scheme, using the Van Albada limiter [10], which has the property of second order accuracy in the smooth part of the flow field and of steepening discontinuities, without introducing non-monotonicity (wiggles). The interpolation formulae are:

$$q_{i-\frac{1}{2},jk}^* = q_{ijk} + \frac{s_i}{4} [(1-\kappa s_i)(q_{ijk} - q_{i-1,jk}) + (1+\kappa s_i)(q_{i+1,jk} - q_{ijk})]$$

$$q_{i+\frac{1}{2},jk}^* = q_{i+1,jk} + \frac{s_i}{4} [(1-\kappa s_i)(q_{i+1,jk} - q_{ijk}) + (1+\kappa s_i)(q_{ijk} - q_{i-1,jk})]$$

where:

$$s_i = \frac{2(q_{ijk} - q_{i-1,jk})(q_{i+1,jk} - q_{ijk}) + \epsilon}{(q_{i-1,jk} - q_{ijk})^2 + (q_{ijk} - q_{i+1,jk})^2 + \epsilon}$$

in which  $\epsilon$  is a small number ( $\approx 10^{-7}$ ) to avoid dividing by zero. The computations shown in this paper are performed with  $\kappa = 0$  (Fromm scheme).



The treatment of the boundary conditions is very consistent with the numerical flux calculations at the internal cell faces following the Osher scheme. If the boundary conditions are not completely specified, the unknown components are determined by means of the Riemann invariants [5].

#### B. Solution Procedure

The system of nonlinear discretized equations is solved by a multigrid technique. Within this multigrid a nonlinear variant of the Collective Gauss-Seidel relaxation is applied to the first-order accurate discretized equations. In the relaxation method one or more Newton steps are used for the collective update of the five state vector components in each finite volume. The relaxation sweeps start from alternating corner points in the computational domain in order to improve the robustness of the method. In order to permit vectorization and parallelization on a modern supercomputer, the relaxation sweeps are performed in diagonal planes of the computational domain; finite volumes in such a plane can be updated simultaneously without any recursion. For the second-order accurate discretized system of equations, however, no robust relaxation method is available. In that case an Iterative Defect Correction (IDeC) process is used to find an approximate solution of the second order accurate discretized equations [6]. The nonlinear multigrid is preceded by a nested iteration, which consists of a number of nonlinear multigrid iterations on successive finer grids.

A nested sequence of grids  $\Omega_m$  ( $m = 1, 2, \dots, n$ ) is developed, with corresponding mesh sizes  $h_1 > h_2 > \dots > h_n$ . Hence  $\Omega_1$  is the coarsest grid and  $\Omega_n$  is the finest grid. A coarse grid is created by skipping every other point in the three directions on the finer grid, so that a finite volume on a given grid is the union of  $2 \times 2 \times 2$  finite volumes on the next finer grid. Let  $F_m^1(q_m) = r_m$  and  $F_m^2(q_m) = r_m$  denote the nonlinear systems of first- and second-order accurate discretized equations on  $\Omega_m$ , with  $r_m$  a possible non-zero right-hand side. Then the nonlinear multigrid (NMG) is defined in the following way:

- improve  $q_m$  by a number of (pre-)relaxation iterations to  $F_m^1(q_m) = r_m$
- compute the defect  $d_m = r_m - F_m^1(q_m)$
- calculate an approximate  $q_{m-1}$  on the next coarser grid:  $q_{m-1} = I_m^{n-1} q_m$ , where  $I_m^{n-1}$  is a restriction operator; here the average of the values at the eight cells at the finer grid is used to set the value on the coarser grid
- calculate a right-hand side  $r_{m-1} = F_{m-1}^1(q_{m-1}) + I_m^{n-1} d_m$ , where  $I_m^{n-1}$  is a restriction operator for the defect; the defect on the coarser grid is the sum of the defects in the corresponding eight finer grid cells
- improve the solution of  $F_{m-1}^1(q_{m-1}) = r_{m-1}$  by a number of NMG-iterations; the result is called  $q_{m-1}$
- correct the approximation  $q_m$  by:  $q_m^{new} = q_m^{old} + I_{m-1}^n (q_{m-1} - q_{m-1})$  where  $I_{m-1}^n$  is a prolongation operator; the correction to the coarse grid cell is given to the corresponding eight finer grid cells
- improve  $q_m$  by a number of (post-)relaxation iterations to  $F_m^1(q_m) = r_m$

The Iterative Defect Correction for the solution of the second order accurate system of equations can be written as:

$$F_m^1(q_m^{i+1}) = F_m^1(q_m^i) + \omega \cdot (r_m - F_m^2(q_m^i)) \quad i = 0, 1, 2, \dots$$

where  $q_m^0$  is the solution on the finest grid obtained by the nested iteration followed by a number (normally 1) nonlinear multigrid iterations to the first order accurate system of equations, and  $\omega$  is a damping parameter. In the first part of the solution procedure (about 10 IDeC iterations) the process had to be damped ( $\omega = 0.5$ ); later on no damping ( $\omega = 1.0$ ) was necessary. A schematic view of the solution procedure is given in fig. 2. The total amount of IDeC iterations was about 50. The computations are performed on a Convex C-240 mini-supercomputer.

The first- and second order operators do not need the use of the same numerical flux function. For reasons of computational costs the van Leer scheme is preferred, in particular in the time-consuming relaxation procedure. For the second order operator the more sophisticated Osher or Roe scheme may be used, without a substantial growth of computing costs, since the IDeC method requires only one evaluation per cycle.

#### C. Grid

For the computations a grid of a C-O topology is used. This grid consists of 5-levels; at the lowest level it consists of  $4 \times 4 \times 2$  cells and at the highest level  $64 \times 64 \times 32$  cells. This means in chordwise direction 64 cells (C-type) with 48 cells on the wing, in spanwise direction 64 cells (O-type) covering a half wing and 32 cells between the wing surface and the outer boundary. Views of the grid can be seen in fig. 3a where the grid in the symmetry plane and on the surface is shown and in fig. 3b where the grid in a wing cross-section is shown. On the surface the grid is conical, which preserves a good resolution near the apex. The grid lines are clustered both near the apex and the trailing edge.

### RESULTS

#### A. Experiments

The pressure distributions at the surface for the lowest Mach number ( $M_\infty = 0.6$ ), shown in fig. 4 and 5, are typical for conditions at which no phenomena like embedded shock waves and vortex breakdown occur. The suction peak induced by the primary vortex increases with increasing angle of attack and moves towards the wing symmetry line. A second much less pronounced suction peak appears outboard of the primary one at higher angles of attack ( $15^\circ$  and  $20^\circ$ ), which is caused by secondary separation. The pressure distribution along the rootchord (fig. 5) shows that the flow is not conical; at all angles of attack a compression towards the trailing edge is found.

Some results of the oil flow visualization study are shown in fig. 6 and 7 ( $\alpha = 10^\circ$  and  $20^\circ$ , respectively). At angles of attack up to  $18^\circ$  a well known flow pattern is found, which is almost independent of the free stream Mach number. Apart from regions in the vicinity of the wing apex and the trailing edge a rather regular surface streamline pattern is found, which seems to have a conical similarity; this in contrast to the pressure measurements. In the oil flow picture for  $\alpha = 10^\circ$  (fig. 6) a primary attachment line can be distinguished. The place of the attachment line may also be recovered from the spanwise pressure distribution, where a local pressure maximum appears. The flow in between the two lines is approximately parallel to the wing symmetry line. For angles of attack of  $15^\circ$  and higher the primary attachment line coincides with the wing symmetry line. In the secondary separation lines an outboard shift at approximately 40% rootchord position can be observed. This is caused by transition from a laminar boundary layer upstream to a turbulent boundary layer downstream, since a turbulent boundary layer can sustain an adverse pressure gradient over a longer distance than a laminar boundary layer.

At an angle of attack of  $20^\circ$  (fig. 7) the flow pattern reveals a breakdown of the starboard vortex. At that side the secondary- and tertiary separation lines run into each other at 60% rootchord position and from that position on only one line continues at a further outboard position.

Increasing the Mach number to 0.85 introduces some drastic changes in the flow field. For angles of attack up to  $15^\circ$  rather regular pressure distributions are measured (fig. 8), except that there appear large supersonic zones in the flow field. At an angle of attack of  $20^\circ$  an 'irregular' behaviour appears in the pressure distribution. The suction peak in spanwise direction has collapsed, apparently due to breakdown of both vortices, which can be observed in the oil flow pattern (fig. 10). The leading edge vortex becomes disorganized causing a smaller amount of circular motion. Also the rootchord pressure distribution has changed drastically (fig. 9). There is a

strong compression in the 30% - 65% rootchord region, followed by a substantial expansion downstream of 65% rootchord. At 80% position again a compression towards the trailing edge is recognized. The expansion may be explained from the size of the burst vortex, which is always larger than that of a non-burst vortex. Due to this obstacle a sort of converging streamtube of chordwise flow develops near the symmetry plane, with an acceleration of the flow. The rootchord pressure distribution allows two shock waves to be implemented, one between 50% and 65% rootchord and the other at 82.5% rootchord. The resolution of the pressure orifices upstream of 65% rootchord is too low to illustrate this. These possible shock locations are however confirmed by Schlieren pictures (fig. 11). Following the change of the pressure distribution and observing the Schlieren pictures at the angles of attack below vortex breakdown to values at breakdown, one observes that the upstream shock already exists before vortex breakdown occurs. Therefore a tentative conclusion would be that the downstream shock is generated by the vortex breakdown, and not the reverse.

A compilation of the spanwise and rootchord pressure distributions at an angle of attack of  $20^\circ$  for various Mach numbers is given in figs. 12 and 13. The pressure distributions for the Mach numbers 0.75 and 0.80 show the same (but less pronounced) behaviour as in the case of  $M_\infty = 0.85$ , but in these cases no pressures less than the critical value are measured (no supersonic zone). Also in the Schlieren pictures no shocks have been observed. The conclusion could be that the shocks occurring at the high subsonic free stream Mach numbers do not have a large influence on the vortex breakdown position.

Next, some results of the flow field explorations will be considered. These explorations have only been performed at angles of attack of  $10^\circ$  and  $15^\circ$ . For an angle of attack of  $20^\circ$  the flow field is dominated by vortex breakdown and shock waves. Some explorations with the probe in this flow field showed drastic changes in the Schlieren picture while traversing the probe, indicating that no reliable measurements could be obtained.

The directional flow field in a plane normal to the free stream direction is shown in fig. 14. The flow field is drawn according to a conical representation, since the oil flow visualization study gave an indication of at least a 'geometrical' conical flow. By 'geometrical' conical we mean that certain phenomena like attachment lines, separation lines etc. occur along straight lines through the apex. The positions of the primary attachment line (A1) and the secondary separation line (S2) have been obtained from the corresponding oil flow picture. The directional flow field suggests an attachment line at almost the same position. The lines of constant total pressure at the same cross-section have been drawn in fig. 15, which shows the great influence of the shear flow of the leading edge vortex. A total pressure loss of 43.4% with respect to its free stream value is measured.

#### B. Numerical Results

For the present configuration calculations have been performed for the Mach number 0.60 and 0.85. First the subsonic flow at  $M_\infty = 0.60$  and  $\alpha = 10^\circ$  will be considered.

The pressure distributions at the rootchord station  $x/c_r = 0.70$  and along the rootchord are drawn in figs. 17 and 18, respectively. The results of the computations with the van Leer- and the Roe scheme are compared with the experimental results. Along the rootchord the agreement of both numerical solutions with the experiments is rather good. Major differences between both numerical solutions and experiments are observed in the spanwise pressure distribution in the region of the flow affected by the primary vortex. The pressure distribution from the Roe-scheme result is in better agreement with the experiment than the van Leer-scheme result. An explanation for this could be the fact that the Roe-scheme models contact discontinuities (shear layers) in a better way than the van Leer-scheme. The pressure peak in the Roe-scheme result is of the same magnitude as that of the experiments. This is in contrast with the usual experience that Euler

computations overestimate the pressure peak, due to the absence of the secondary separation. Noteworthy is also the existence of a local pressure maximum in the Roe-scheme result at the position of primary attachment in contrast to the van Leer-scheme result. This local pressure maximum is in agreement with the experimental result and with the theory for conical stagnation points.

Next, a transonic flow at a Mach number of 0.85 is considered. In fig. 19 the pressure distribution at the rootchord station  $x/c_r = 0.70$  and in fig. 20 the pressure distribution along the rootchord are drawn. For this case also the Roe-scheme result is in better agreement with the experimental result than the van-Leer scheme result. The local pressure maximum at the position of the attachment line is recovered better, and the pressure increase towards the trailing edge is more realistic. For both computational results no effects of secondary separation are encountered.

The existence of the primary attachment line can also be observed in the directional field following a conical representation, in the plane  $x/c_r = 0.70$  (fig. 21). In this picture also the line  $p_t/p_{t,\infty} = 0.98$  is drawn, enclosing a region of flow with total pressure losses caused by the primary vortex. The value of total pressure loss is 45.1% at the centre of the vortex, which is comparable to that of the experimental result (fig. 15).

At an angle of attack of  $20^\circ$  some shock waves appear in the flow field. In the pressure distribution at the station  $x/c_r = 0.70$  (fig. 22) a steep pressure gradient can be observed at about 77% local span, which is clearly a cross-flow shock. For both schemes the shock consists of only one interior point. The suction peak for the van Leer-scheme result is less than that for the Roe-scheme result. The second shock (the so-called rear shock) can be observed in the pressure distribution along the rootchord (fig. 23) at about 77% position, also consisting of only one interior shock point for both schemes. The agreement with the experiments is bad, because of the absence of vortex breakdown in the computational results.

The shape of the two shocks on the upper surface is visible in the isobar pattern (fig. 24). The cross-flow shock, which has a conical shape, is present over practically the complete wing length. The rear shock in the symmetry plane region extends some distance in the direction of the leading edge vortex.

The conical directional field in the cross-plane normal to the wing surface at 70% rootchord is drawn in fig. 25, together with the line  $p_t/p_{t,\infty} = 0.98$ , enclosing a region of total pressure losses. The length of the arrows is proportional to the conical Mach number, i.e. the velocity component normal to a line through the wing apex divided by the speed of sound. At the position of the cross-flow shock the length of the arrows changes abruptly. Fig. 26 presents the isobars in the cross-plane  $x/c_r = 0.70$ . The cross-flow shock shows up in the clustering of the isobars. It appears to extend up to the vortical flow region.

The contours of total pressure are drawn in the figs. 27 and 28 for the solutions with the Roe-scheme and the van Leer-scheme respectively. The result for the van Leer-scheme gives a slightly larger total pressure loss in the vortex core than the result for the Roe-scheme, 67.6% and 65.7%, respectively. Furthermore the region of flow with a loss of total pressure for the van Leer-scheme result is larger than that for the Roe-scheme result. As has been noted before, this may be written on the account of the better modelling of shear-layers by the Roe-scheme. For this result also the cross-flow shock can be recovered better in the lines of constant total pressure.

#### CONCLUDING REMARKS

Experimental and computational results have been obtained for a delta wing with  $65^\circ$  sweep angle in subsonic ( $M_\infty = 0.60$ ) and transonic flow ( $M_\infty = 0.85$ ). From the measurements of surface pressures, Schlieren pictures, oil flow visualizations and 5-hole probe explorations the following conclusions may be drawn.

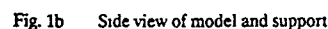
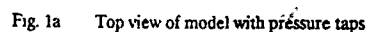
- The differences between computational- and experimental results are primarily due to the effect of secondary separation, which is not modelled in the numerical method. Secondly differences are observed at conditions where vortex breakdown occurs in the experiments. This phenomenon has not been observed in the numerical results.

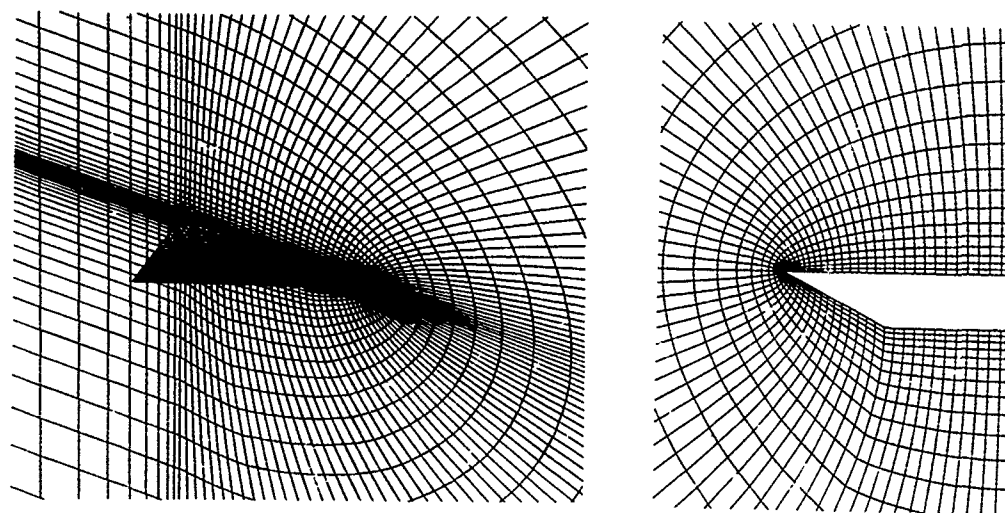
- At transonic speed ( $M_\infty = 0.85$ ) and high angle of attack ( $\alpha = 20^\circ$ ) a cross-flow shock of almost conical shape develops on practically the complete wing length and a rear shock on the aft part of the wing.
- The flux-difference-splitting scheme of Roe leads to a better simulation of the flow field outside the vortical flow region (primary attachment line, rootchord pressure distribution) than the flux-splitting scheme of van Leer. Furthermore the region of flow with loss of total pressure is smaller.

1 A. Elsenaar, G. Eriksson : "Proceedings of the Symposium on the International Vortex Flow Experiment on Euler Code Validation", Stockholm, October 1-3, 1986

- 2 A. Elsenaar, L. Hjelmborg, K. Butefisch, W.J. Bannink : "The International Vortex Flow Experiment", in: Validation of Computational Fluid Dynamics, AGARD CP-437, 1988
- 3 E.M. Houtman, W.J. Bannink : "Experimental Investigation of the Transonic Flow at the Leeward Side of a Delta Wing at High Incidence", Report LR-518, Delft University of Technology, 1987
- 4 W.J. Bannink, E.M. Houtman, S.P. Ottochian : "Investigation of the Vortex Flow over a Sharp-edged Delta Wing in the Transonic Speed Regime", Report LR-594, University of Technology Delft, 1989
- 5 S.P. Spekreijse : "Multigrid Solution of the Steady Euler Equations", Doctoral Thesis, Delft, 1987
- 6 B. Koren : "Defect Correction and Multigrid for an efficient and accurate computation of airflow flows", Journal of Computational Physics 77, pp. 183-206, 1986
- 7 B. van Leer : "Flux-vector splitting for the Euler Equations", Lecture Notes in Physics 170, pp. 507-512, 1982
- 8 S. Osher, S. Chakravarthy : "Upwind Schemes and Boundary Conditions with applications to Euler equations in general geometries", Journal of Computational Physics 50, pp. 447-481, 1981
- 9 P.L. Roe : "Approximate Riemann Solvers, parameter vectors and difference schemes", Journal of Computational Physics 43, pp. 357-372, 1982
- 10 G.D. Van Albada, B. van Leer, W.W. Roberts : "A comparative study of computational methods in cosmic gas dynamics", Astron. Astrophys. 108, pp 76-84, 1982

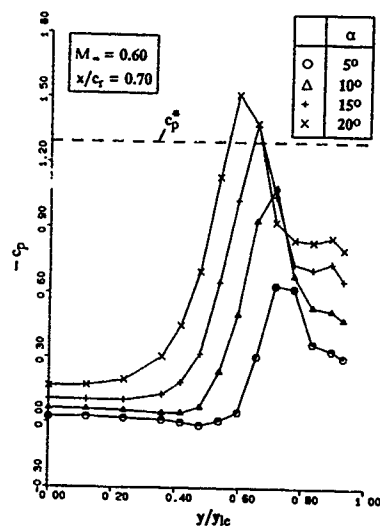
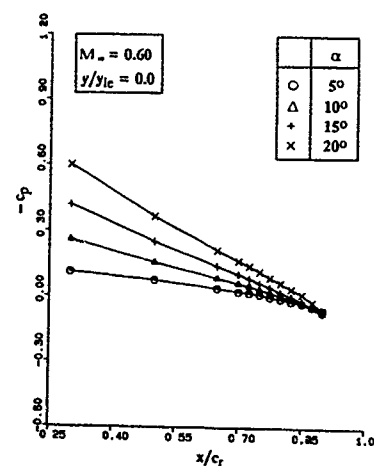
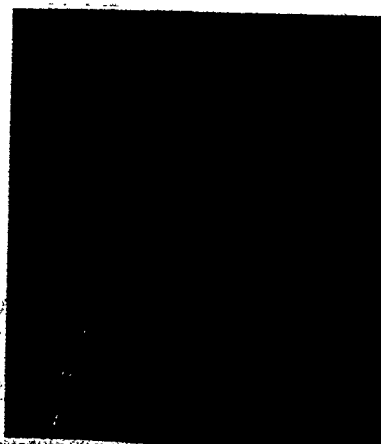
The authors would like to thank mr. S.P. Ottochian and mr. F. Vossen who contributed to the experimental investigations in partial fulfilment for their final engineering degree.

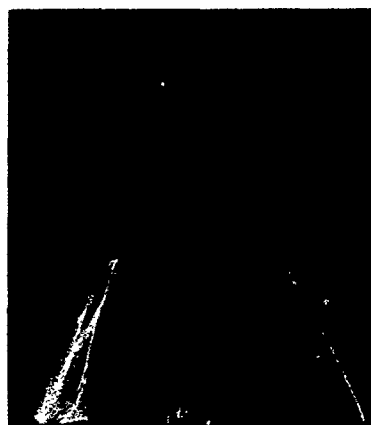
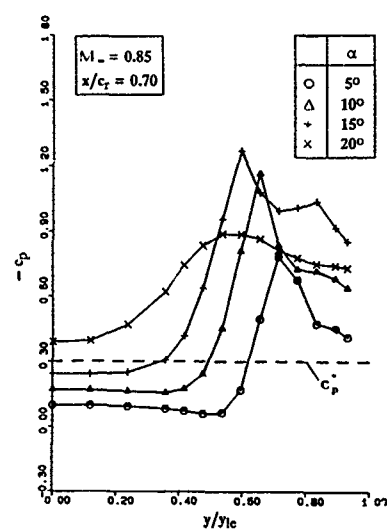
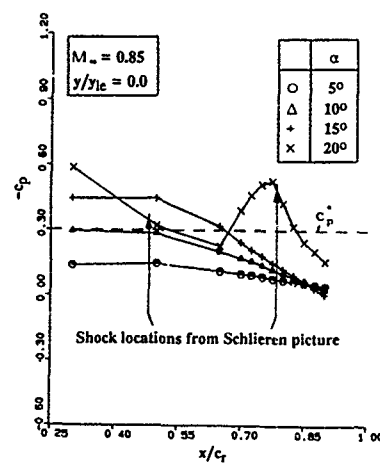
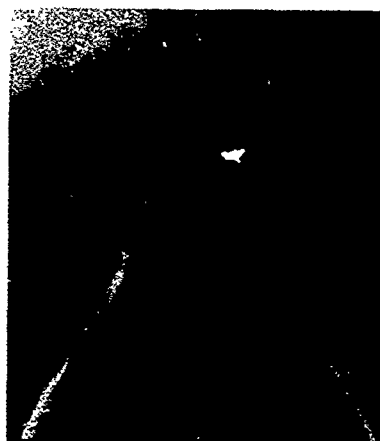
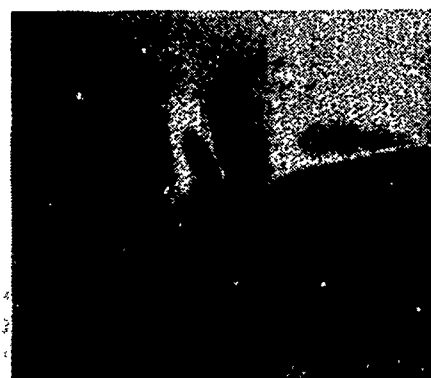


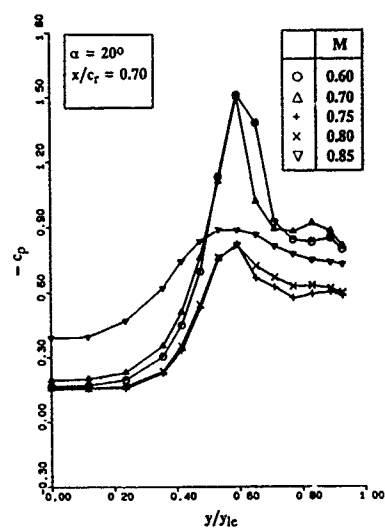
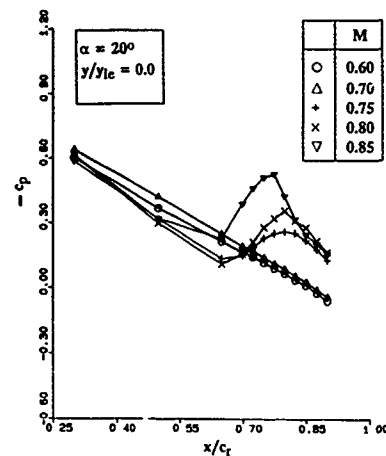
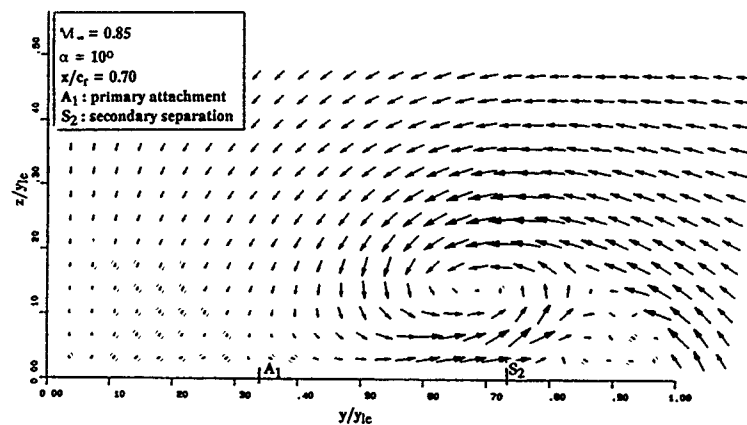
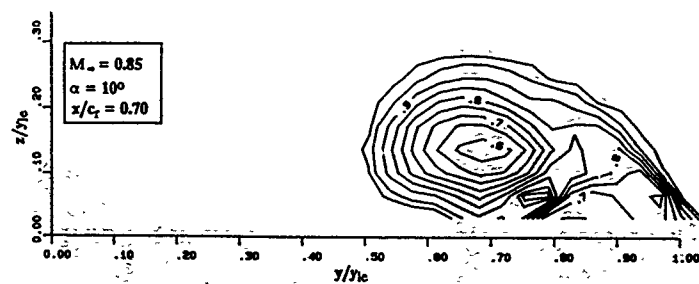


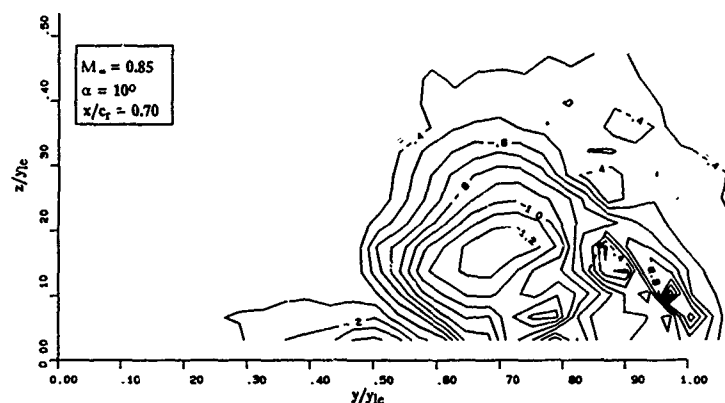
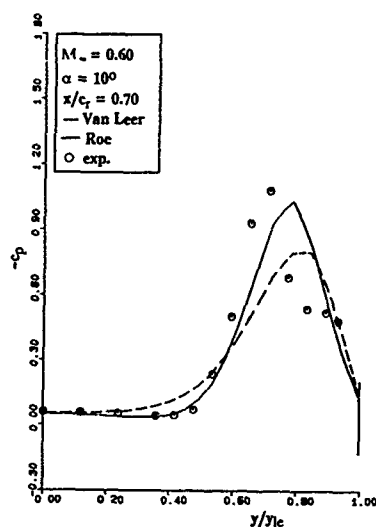
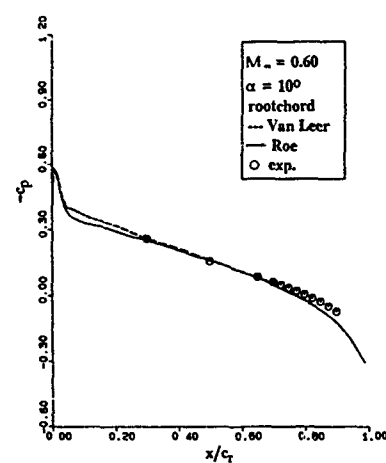
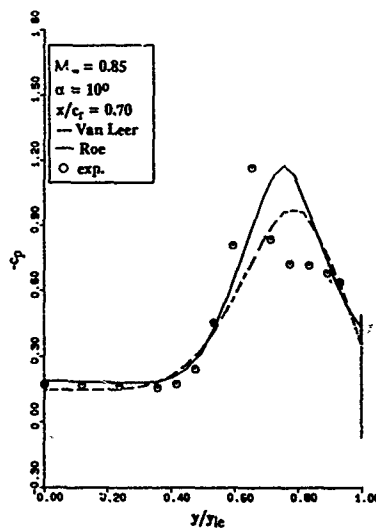
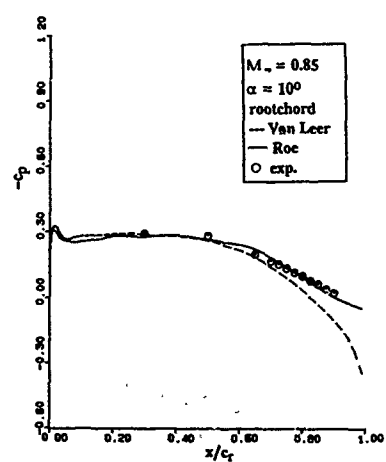
a) Perspective view on symmetry plane and wing surface

b) Cross-sectional view

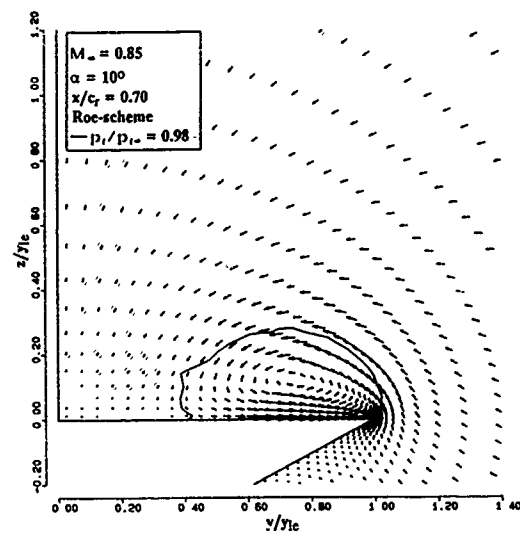
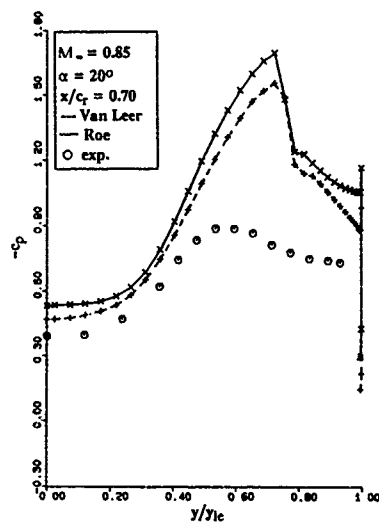
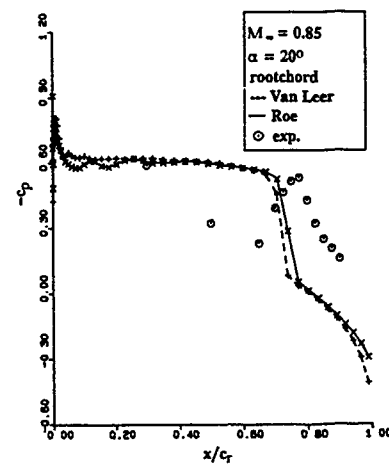
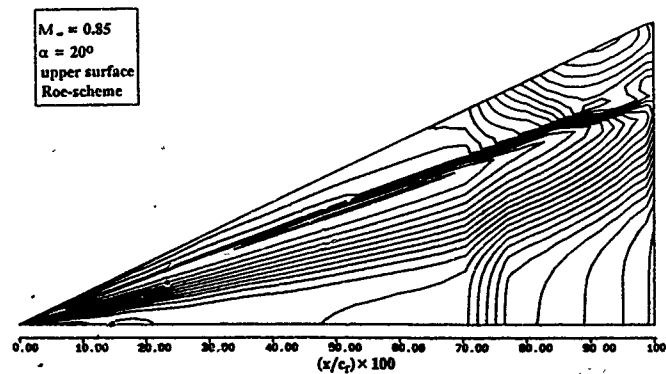
Fig. 3 Computational grid ( $64 \times 64 \times 32$ )Fig. 4 Experimental spanwise pressures at  $M_\infty = 0.60$ Fig. 5 Experimental pressures along rootchord at  $M_\infty = 0.60$ Fig. 6 Oil flow visualization at  $M_\infty = 0.60$ ,  $\alpha = 10^\circ$

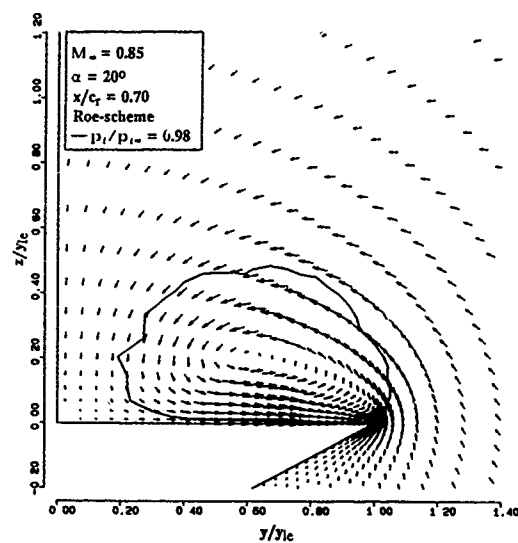
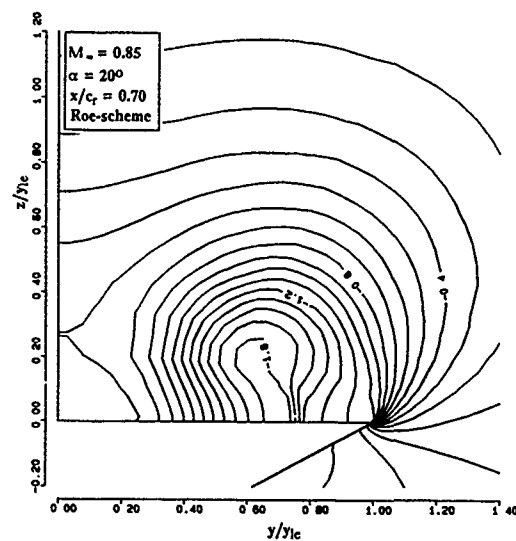
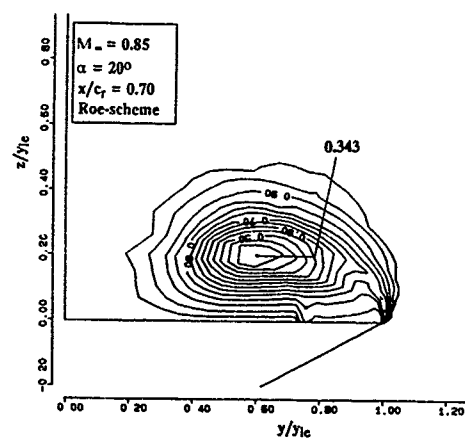
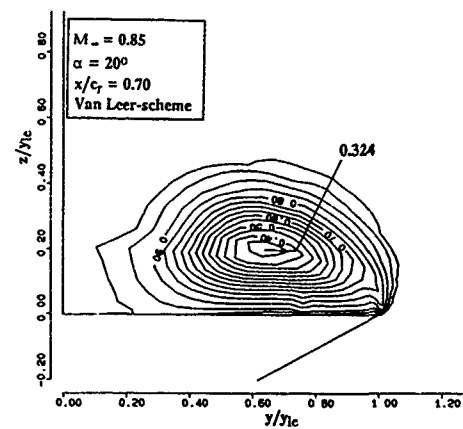
Fig. 7 Oil flow visualization at  $M_\infty = 0.60$ ,  $\alpha = 20^\circ$ Fig. 8 Experimental spanwise pressures at  $M_\infty = 0.85$ Fig. 9 Experimental pressures along rootchord at  $M_\infty = 0.85$ Fig. 10 Oil flow visualization at  $M_\infty = 0.85$ ,  $\alpha = 20^\circ$ Fig. 11 Schlieren picture at  $M_\infty = 0.85$  and  $\alpha = 19^\circ$  showing two shocks

Fig. 12 Experimental spanwise pressures at  $\alpha = 20^\circ$ Fig. 13 Experimental pressures along rootchord at  $\alpha = 20^\circ$ Fig. 14 Experimental cross-flow directions at  $M_\infty = 0.85$  and  $\alpha = 10^\circ$ Fig. 15 Experimental lines of constant total pressure at  $M_\infty = 0.85$  and  $\alpha = 10^\circ$

Fig. 16 Experimental lines of constant static pressure at  $M_\infty = 0.85$  and  $\alpha = 10^\circ$ Fig. 17 Computational and experimental spanwise pressures at  $M_\infty = 0.60$  and  $\alpha = 10^\circ$ Fig. 18 Computational and experimental pressures along rootchord at  $M_\infty = 0.60$  and  $\alpha = 10^\circ$ Fig. 19 Computational and experimental spanwise pressures at  $M_\infty = 0.85$  and  $\alpha = 10^\circ$ Fig. 20 Computational and experimental pressures along rootchord at  $M_\infty = 0.85$  and  $\alpha = 10^\circ$



Fig. 21 Computed cross-flow directions using the Roe scheme;  $M_\infty = 0.85$ ,  $\alpha = 10^\circ$ Fig. 22 Computational and experimental spanwise pressures at  $M_\infty = 0.85$  and  $\alpha = 20^\circ$ Fig. 23 Computational and experimental pressures along rootchord at  $M_\infty = 0.85$  and  $\alpha = 20^\circ$ Fig. 24 Isobars at upper surface of the delta wing computed with the Roe scheme at  $M_\infty = 0.85$  and  $\alpha = 20^\circ$

Fig 25 Computed cross-flow directions;  $M_\infty = 0.85$ ,  $\alpha = 20^\circ$ Fig 26 Computed isobars using the Roe scheme,  
 $M_\infty = 0.85$ ,  $\alpha = 20^\circ$ Fig 27 Computed lines of constant total pressure at  
 $M_\infty = 0.85$  and  $\alpha = 20^\circ$  using the Roe schemeFig 28 Computed lines of constant total pressure at  
 $M_\infty = 0.85$  and  $\alpha = 20^\circ$  using the van Leer scheme

# RECENT PROGRESS IN COMPUTATIONAL VORTEX-FLOW AERODYNAMICS

James M. Luckring  
NASA-Langley Research Center  
Hampton, VA, 23665-5225, USA

## SUMMARY

A review of recent progress in computational vortex-flow aerodynamics at the Langley Research Center is presented. Emphasis is placed on Navier-Stokes methodology, both for compressible and incompressible flows, and results are presented from central and upwind-biased schemes for fully laminar, transitional, and fully turbulent flows. In addition, results are presented from selected potential-based methods to address the hierarchy of formulations presently available for the computational analysis of aerodynamic vortex flows. Some comparisons among this hierarchy of methods are shown.

## NOMENCLATURE

$C_A$	axial coefficient, Axial Force/ $q_\infty S_{ref}$
$C_D$	drag coefficient, Drag/ $q_\infty S_{ref}$
$C_{D,0}$	drag coefficient at zero lift
$\Delta C_D$	$C_D - C_{D,0}$
$C_f$	skin friction coefficient, Skin Friction/ $q_\infty S_{ref}$
$C_L$	lift coefficient, Lift/ $q_\infty S_{ref}$
$C_{L,v}$	vortex-lift coefficient
$C_m$	pitching-moment coefficient, Pitching Moment/ $q_\infty S_{ref} \bar{c}$
$C_p$	pressure coefficient, $(p - p_\infty)/q_\infty$
$C_s$	suction coefficient, Suction/ $q_\infty S_{ref}$
$c_p$	specific heat at constant pressure
$c_v$	specific heat at constant volume
$c_y$	section side-force coefficient, Section Side Force/ $q_\infty d$
$\bar{c}$	mean aerodynamic chord
$D$	body base diameter
$d$	local body diameter
$E_0$	total energy per unit volume
$\vec{F}, \vec{G}, \vec{H}$	flux vectors
$F_{BL}$	Baldwin-Lomax function
$h_0$	total enthalpy, $(E_0 + p)/\rho$
$J$	Jacobian of coordinate transformation
$k$	conductivity
$\ell$	reference body length
$M_\infty$	freestream Mach number
$Pr$	Prandtl number
$\vec{Q}$	state vector
$q$	total velocity
$q_\infty$	freestream dynamic pressure
$Re, R_D, R_\ell$	Reynolds number based on $\bar{c}, D, \ell$
$r_n$	nose radius
$S_{ref}$	area of reference wing planform, extended to configuration centerline
$u, v, w$	body-axis Cartesian velocity components

$v^*$	wall-friction velocity, $\sqrt{\tau_w/\rho}$
$y/s$	fraction of semispan. Also, fraction of LEX exposed semispan.
$y^+$	inner-law variable, $yv^*/\nu$
$\alpha$	angle of attack, degrees
$\alpha_b$	$\alpha$ for incipient vortex breakdown
$\beta$	angle of sideslip, degrees. Also, incompressible coupling parameter.
$\gamma$	ratio of specific heats, $c_p/c_v$
$\mu$	viscosity
$\nu$	kinematic viscosity, $\mu/\rho$
$\theta$	circumferential angle
$\theta_b$	boat-tail angle
$\theta_c$	cone angle
$\Lambda$	sweep angle, degrees
$\phi$	Perturbation velocity potential. Also, roll angle, degrees
$\xi, \eta, \zeta$	body-fitted coordinates
$\rho$	density
$\tau_w$	wall shear stress

## Subscripts

$le$	leading edge
$l$	laminar
$max$	maximum
$t$	turbulent
$te$	trailing edge
$v$	viscous

## 1.0 INTRODUCTION

Vortex flows have long intrigued scientists and engineers from both a fundamental fluid mechanics as well as an applied aerodynamics perspective. They occur at all aerodynamic scales (e.g., boundary layer, wing, trailing wake) and, more broadly, also occur on geophysical scales in the form of tornados, hurricanes, and large scale ocean structures. To this day vortices continue to be a very challenging and important flow to measure, compute, and use effectively. Along with shock waves and boundary layers, vortices complete a triad of extensively studied fluid entities in aerodynamics and fluid mechanics.

The focus of this paper is on separation-induced vortex flows such as those which emanate from forebodies or swept-wing leading edges. The concept of this type of vortex flow appears to have been originally put forth by Wilson and Lovell (1947) to explain large vortex-lift increments obtained on a DM-1 glider model being tested in the Langley 30 x 60

foot full-scale wind tunnel. They postulated the occurrence of a cross-flow separation near the leading edge which, when superimposed with the longitudinal flow on the slender delta wing, would cause a vortex to form inboard of the leading edges and above the wing. It is from their origin in a cross flow separation that these vortex flows are referred to as "separation-induced" vortex flows, as contrasted with, for example, the vortices which form in the wake of a three-dimensional lifting surface due to the spanwise variation of lift. The primary length scales of these vortices is larger than typical viscous length scales, thus distinguishing the separation-induced vortex from other vortices which arise within viscous layers (e.g., Görtler vortices, juncture vortices, etc.)

Efforts to computationally simulate separation-induced vortex flows for aerodynamic applications go back at least to Legendre (1953) for delta wings and, more classically, to Riabouchinski (1922). Most recently, significant strides in numerical algorithm development coupled with advanced computer technology have resulted in practical formulations capable of simulating the subject flow with the Euler equations or the thin-layer form of the Navier-Stokes equations in three dimensions for elliptic problems.

Navier-Stokes predictions of viscous separation-induced vortex flows are emphasized in this paper. Potential-based methods have also been included due to their speed and accuracy in estimating force and moment properties. This class of technology plays an important role in preliminary design. All methodology selected for this paper has been developed at the Langley Research Center; it is indicative of present state of the art techniques in use at other institutions as well.

Three Navier-Stokes methods which have proven to be both accurate as well as efficient have been selected. They are i) CFL3D, an upwind-biased, finite-volume formulation for compressible flow, ii) TLNS3D, a central-difference, finite-volume formulation for compressible flow, and iii) FMC1, a high-resolution finite-difference formulation for incompressible flow. (See figure 1.) Both of the finite-volume formulations are cell-centered schemes. All of these methods provide for laminar, transitional, or turbulent flow and can also model inviscid Euler flow. They have all been developed for structured grids.

Two potential flow formulations which have continued to be extended and used have also been selected. They are i) FVS, a free-vortex-sheet "fitting" higher-order panel method based on the Prandtl-Glauert equation with nonlinear boundary conditions, and ii) the Suction Analogy, a conservation principle most often coupled with linear techniques such as lower-order panel methods. (See figure 2.)

Salient attributes of the Navier-Stokes and potential methods are presented first, followed by a variety of applications demonstrating present capabilities and including comparisons among the meth-

ods employed. Some details of the Navier-Stokes formulations are included in the appendices to clarify differences among them.

## 2.0 METHODOLOGY

Consider first the governing equations cast in an integral finite-volume form

$$\frac{\partial}{\partial t} \int \int \int \hat{Q} dV + \int \int \hat{f} \cdot \hat{n} dS = 0 \quad (1)$$

Here the time rate of change of the state vector  $\hat{Q}$  within a cell is balanced by the net flux  $\hat{f}$  across the cell surface. Discretization of the governing equations results in a consistent approximation to the integral form of the conservation laws

$$\hat{Q}_t + (\hat{F} - \hat{F}_v)_{,\xi} + (\hat{G} - \hat{G}_v)_{,\eta} + (\hat{H} - \hat{H}_v)_{,\zeta} = 0 \quad (2)$$

cast in general curvilinear coordinates.

### 2.1 Compressible, Upwind Difference

The upwind method CFL3D has been developed by Thomas (1985b-1987) for the three-dimensional, Reynolds-averaged, Navier-Stokes equations. The state vector is taken as

$$\hat{Q} = J^{-1} [\rho, \rho u, \rho v, \rho w, E_0]^T \quad (3)$$

The equations are typically solved in their thin-layer form

$$\hat{F}_v = \hat{G}_v = 0 \quad (4)$$

thus accounting for viscous flux terms only in the  $\zeta$  direction (normal to the body) and the various flux terms of equation 2 are presented in Appendix 5.1 for the thin layer approximation. With the ideal gas assumption, the pressure and total enthalpy are expressed as

$$p = (\gamma - 1)(E_0 - \frac{1}{2}\rho q^2) ; \quad h_0 = \frac{\gamma}{\gamma - 1} \frac{p}{\rho} + \frac{1}{2} q^2 \quad (5; 6)$$

Turbulence effects are accounted for through the notion of an eddy viscosity and eddy conductivity.

$$\mu = \mu_t + \mu_l = \mu_l (1 + \mu_t/\mu_l) \quad (7)$$

$$k = k_t + k_l = k_l (1 + k_t/k_l) \quad (8)$$

and  $k = \mu c_p / Pr$  for laminar or turbulent flow. Turbulence effects are modeled with the two-layer algebraic eddy-viscosity model developed by Baldwin and Lomax (1978). For regions with separation induced vortex flow, the vorticity function constructed by Baldwin and Lomax,  $F_{BL}(\zeta)$ , will exhibit two relative extrema, the first of which is associated with the attached boundary layer eddy viscosity. The second (and larger) maxima is due to the vorticity associated with the separation-induced vortex flow. The notions of Degani and Schiff (1983) are drawn upon

to differentiate between these extrema and thus determine proper turbulence length scales. The search for  $F_{BL,max}$  is terminated when local values of  $F_{BL}$  have diminished to approximately 90% of the first relative extrema found searching away from the wall.

The inviscid fluxes can be evaluated with either of two upwind approaches, the flux-difference splitting approach of Roe (1986) or the flux-vector splitting approach of van Leer (1982). Viscous flux terms are evaluated with central differences. Characteristic far-field boundary conditions are used as described by Thomas and Salas (1985). Typical surface boundary conditions are employed which include options for adiabatic wall or specified wall temperature.

The flow is advanced in time with the conditionally stable three-factor approximate factorization scheme as described by Anderson (1988). On the NASA-Langley Cray-2S *Voyager* the algorithm requires approximately 22  $\mu$ -seconds/cycle/grid point for the Roe scheme and approximately 45  $\mu$ -seconds/cycle/grid point for the van Leer scheme.

The method allows for all classes of structured grid topologies. Most recently the Ramshaw (1985) approach was implemented by Thomas (1989) to extend this method for blocked-grid applications.

## 2.2 Compressible, Central Difference

The central-difference scheme, TLNS3D, has been developed by Vatsa (1986) for solving the three-dimensional, Reynolds-averaged, Navier-Stokes equations. This development was done in close collaboration with Swanson and Turkel (1986) who developed TLNS2D, a related two-dimensional method. Both methods are extensions to the Euler methodology developed by Jameson (1981, 1983). The basic governing equations and fluxes are the same as described for CFL3D. Turbulence quantities can be evaluated either with the Baldwin Lomax (1978) algebraic model or with the Johnson-King (1985) closure model.

The numerical evaluation of the fluxes is performed with central differences. Dissipation terms are minimized in TLNS3D, principally through a local Mach number scaling as discussed by Swanson and Turkel (1987) and employed by Kaynak and Flores (1987). Characteristic far-field boundary conditions are used along with conventional surface boundary conditions.

The flow is advanced in time with an explicit four-stage Runge Kutta technique, and the method makes extensive use of multi-grid and mesh sequencing along with other convergence acceleration techniques. The algorithm requires approximately 50  $\mu$ -seconds/cycle/grid point of Cray-2S time.

The method allows for most classes of structured grid topologies and is presently restricted to single block applications.

## 2.3 Incompressible, High Resolution

This high-resolution scheme, FMC1, has been

developed by Hartwich (1986-1989) for the incompressible three-dimensional, Reynolds-averaged, Navier-Stokes equations. The state vector is expressed as

$$\hat{Q} = J^{-1} [p, u, v, w]^T \quad (9)$$

This draws on the artificial compressibility concept of Chorin (1967) and the coupling parameter  $\beta$  can be found in the appropriate flux terms of appendix 5.2. In most cases this parameter is set to unity.

Turbulence effects are again represented with the algebraic Baldwin Lomax (1978) model. In addition to the Degani-Schiff (1983) model for massively separated flows, Hartwich has developed a model for determining proper length scales in the case of massively separated flows from a smooth surface such as a forebody or a missile. This model has been used for transitional flow computations about a 3.5 caliber tangent-ogive model.

Inviscid fluxes are determined with second-order discretization based upon Total Variation Diminishing (TVD) principles as described by Hartwich (1988b). Viscous fluxes are evaluated with central differences. Hartwich refers to his approach as a high-resolution scheme since spurious oscillations are suppressed but not eliminated, as would be the case for a TVD scheme, when applied to one-dimensional nonlinear hyperbolic conservation laws and linear systems.

Far-field boundary conditions are treated explicitly by imposing free stream conditions on all boundaries except for the outflow boundary where first-order extrapolation is used in conjunction with free-stream pressure. No-slip surface conditions are used along with pressure extrapolation from the limiting boundary layer form of the Navier-Stokes equations.

The solution is advanced in time with a hybrid algorithm comprised of approximate factorization in cross-flow planes with symmetric planar Gauss-Seidel relaxation in the third dimension. The algorithm requires approximately 55  $\mu$ -seconds/cycle/grid point of Cray-2S time.

The method allows for all classes of structured grid topologies and is restricted to single block applications.

## 2.4 Potential Formulations

Consider now the case of a subsonic or supersonic flow with small perturbations. This flow is governed by the linear Prandtl-Glauert equation

$$(1 - M_\infty^2)\phi_{,xx} + \phi_{,yy} + \phi_{,zz} = 0 \quad (10)$$

subject to appropriate boundary conditions. When the vortex is directly simulated or "fitted", the associated boundary conditions render the overall problem to be nonlinear. The free-vortex-sheet method was developed to solve this problem with higher-order panel technology by Brune (1975) and subsequently improved by Johnson (1980) and Luckring (1986). The method has also been extended

by Luckring (1985) to model details of the vortex core flow by coupling the asymptotic Stewartson and Hall (1963) solution along with Hall's (1961) parabolized Navier-Stokes vortex core model to the three-dimensional free vortex sheet for estimating incipient vortex breakdown (figure 3).

When the vortex is not directly simulated, its effects on forces and moments can be represented through the Polhamus suction analogy (1966). This is a concept of conservation of leading or side-edge suction. It has historically been coupled with simple linear-theory panel methods to achieve rapid and accurate estimates of the nonlinear force and moment properties associated with the vortex flow. For subsonic applications, Lamar and Gloes (1975) coupled the suction analogy with the vortex-lattice method of Margason and Lamar (1971) and this method is used for the subsonic results presented in this paper.

For supersonic applications Carlson (1979, 1980) developed an approach to evaluate attainable leading-edge suction by accounting for various limiting factors (such as vacuum pressure) in the suction computation. The approach has been effective even for relatively complex configurations (Carlson, 1990).

### 3.0 RESULTS

Results are organized to wing-dominated separation followed by forebody-dominated separation. Finally, recent applications to the F/A-18 aircraft are presented which embrace both wing and forebody separated vortex flows.

#### 3.1 Wing-Dominated Separation

Subsonic force and moment properties can be estimated quite accurately for isolated vortices at subcritical conditions with the potential methods. More recently, estimates of the vortex state (coherent, burst, or asymmetric) have been obtained as well. An example for predicting the vortex breakdown boundary is presented in figure 4a. Results from the coupled FVS viscous-vortex-core model (Luckring, 1985) predict the experimental trends (Wentz and Kohlman, 1968) due to leading and trailing edge sweep variations quite well. The leading-edge trend is repeated in figure 4b along with the predicted vortex asymmetry boundary from consideration of a diverging core criterion of Polhamus (1986). Also shown are data for vortex asymmetry from Fox and Lamar (1974) as well as vortex bursting as determined from buffet onset by Boyden and Johnson (1981).

Lift estimates from the free vortex sheet as well as the suction analogy are compared to the experimental results of Wentz and Kohlman (1968) in figure 5 for two delta wings of differing leading-edge sweep. For the 70° wing, both methods provide a good estimate of the lift up to the point where vortex breakdown is manifested in the experiment. However, for the 80° wing the free vortex sheet provides a better estimate than does the suction anal-

ogy from approximately 20 degrees angle of attack to the point where breakdown is once again manifested experimentally. The suction analogy has traditionally been viewed as providing a conservative upper bound for vortex lift increments and the decrement between it and the free vortex sheet is due to vortex curvature and crowding effects implicitly represented in the free vortex sheet. (This decrement can also be viewed as a lack of full suction recovery.) Also shown is the theoretical condition of incipient vortex breakdown (labeled critical swirl) along with the theoretical condition of incipient vortex asymmetry (labeled diverging cores). These correlate well with the appropriate breaks in the experimental data.

Force and moment estimates for the unit-aspect-ratio Hummel (1979) delta wing are presented in figure 6. The free vortex sheet provides accurate estimates of lift, drag, and pitching moment, including the camber effects, up to the angle of attack where vortex breakdown occurs at the trailing edge. Although not shown on the figure, Navier-Stokes solutions from CFL3D (Thomas and Newsome, 1986) and FMC1 (Hartwich, 1988) also predict the lift well. Hartwich has also shown good predictions for the pitching moment from FMC1. Both methods provide a reasonable approximation of the aerodynamics associated with vortex breakdown.

Predictions of the spanwise turbulent pressure distributions are shown in figure 7 for the free-vortex-sheet method. Differences on the upper surface are primarily due to secondary vortex effects not modeled in the inviscid theory. These computations are viewed as an upper bound which the experiment would approach if viscous flow effects were to diminish.

Predictions of the spanwise laminar surface pressure distributions are shown in figure 8 for the Navier-Stokes methods CFL3D and FMC1. Both methods predict the flow quite well. Both methods differ from experiment in a very consistent manner. Most notably, they both predict a more negative suction peak for the secondary vortex at the aft two stations and they both predict more negative lower surface pressures at the aft most station shown. A comparison of the laminar surface flow pattern between FMC1 and experiment is presented in figure 9 and shows good correlation. Similar predictions of the surface flow pattern have been obtained with CFL3D.

Force and moment properties of fairly complex configurations can be estimated through the suction analogy approach with considerable accuracy. An example for a generic high-speed configuration (Luckring, 1988) of figure 10 is presented in figures 11 and 12 for low-speed aerodynamic properties. These computations were performed with full vortex lift estimates. For configurations where attainable leading edge thrust is a factor, Carlson's approach also provides quite reasonable estimates. See figures 13 and 14.

At supersonic speeds the leading-edge vortex flow becomes more complex due to shock interactions. A useful parametric data base for delta wings was developed by Miller and Wood (1985). They extended the Stanbrook and Squire (1964) classifications to account for a variety of shock, vortex, and shock-vortex flow regimes in terms of the angle of attack and Mach number normal to the leading edge. A limited number of computations by Thomas and Newsome (1986) with CFL3D showed good prediction of shocked, vortex, and shock-vortex flows, both in terms of surface pressure distributions as well as off-body flow structure. A more detailed analysis of these flows has recently been completed by McMillin (1990) with CFL3D. The McMillin results led to a refinement in the flow classification.

### 3.2 Forebody-Dominated Separation

**Tangent Ogive** - Computations for the symmetric flow about a 3.5 caliber tangent-ogive cylinder have been performed by Hartwich and Hall (1989) with the incompressible solver FMC1 for  $\alpha = 20^\circ, 30^\circ$  and  $R_D = 0.2, 0.8, 3.0 \times 10^6$ . As with many forebody flows, transition effects and blunt shear-layer separation details can play an important role in both the local as well as the overall aerodynamic properties. Hartwich addressed these features with a variety of techniques.

A longitudinal transition location of the attached flow was extracted from the data base<sup>†</sup> for one set of flow conditions. The variation of this location with angle of attack and Reynolds number was approximated with an Esch factor (1975) as described by Polhamus (1984). Laminar cross-flow separation was modeled until the scale of the separation exceeded an empirical boundary-layer thickness. At this point the turbulence model is invoked, thereby representing a flow with laminar separation followed by transitional shear layer.

C-O topology grids were generated with an elliptic solver of Hartwich (1986) and the baseline grid was comprised of  $40 \times 73 \times 65$  points in the longitudinal, circumferential, and normal directions respectively. Grid sensitivity studies showed no appreciable effect of varying the far-field location from 7 to 28 body diameters or of varying the longitudinal discretization from 40 to 105 stations. Cross flow grid sensitivity demonstrated second order convergence of normal-force coefficient to the experimentally determined value. These solutions require approximately 400 cycles to converge which, for the baseline grid, correspond to about 1.2 hours of Cray-2S time.

<sup>†</sup> The data included in Hartwich's publications were obtained by Dr. P. J. Lamont while at the NASA Ames Research Center; access to these otherwise unpublished data was provided by Dr. L. B. Schiff, also of NASA Ames.

Results from this formulation are presented for  $R_D = 0.2 \times 10^6$  and  $\alpha = 20^\circ$  in figure 15 and for  $R_D = 0.8 \times 10^6$  and  $\alpha = 30^\circ$  in figure 16. At the forward stations the flow is laminar, and either the fully laminar or transitional flow computations predict the data well. Further downstream the flow transitions and the transitional flow computation provides good estimates of the surface pressure distributions. There is apparently little upstream influence of transition on the laminar flow on the forward portion of the configuration. Good predictions of Reynolds number effects were also shown by Hartwich (1989).

The data at  $\alpha = 30^\circ$  (figure 16) indicate the flow to be slightly asymmetric. It is well known that roll orientation of the model can play a major role in the extent of asymmetry (see, for example, Keener, 1977) and the data selected for figure 16 correspond to the minimum asymmetry condition. In addition to laminar flow results, transitional flow results are also presented not only for Hartwich's model (labeled method A) but also for a variation on that model (labeled method B) where turbulence effects are patterned more closely after the Degani-Schiff extensions to the Baldwin-Lomax model. Either formulation provides reasonable estimates of the data.

Computations allowing for flow asymmetry were performed by Hartwich (1990) for  $\alpha = 20^\circ, 30^\circ, 40^\circ$  at  $R_D = 0.8 \times 10^6$ . At higher angles of attack the flow continues to become more asymmetric, and Hartwich showed that the data at  $\alpha = 40^\circ$  exhibited a bi-stable state. The flow exhibited two "equal but opposite" states which occurred with every  $90^\circ$  of roll angle; the flow repeated itself with  $180^\circ$  of roll.

Hartwich deduced that a small out of roundness of the forebody apex could be a causative agent for this observed flow behavior. For asymmetric computations the tangent-ogive geometry was modified by linearly increasing the cross-sectional ellipticity over the first 3.6% of the forebody from unity to a value of 2 at the apex (where the geometry itself is singular). The grid was comprised of  $40 \times 145 \times 65$  points and incorporated increased longitudinal clustering to resolve elliptic apex effects as well as increased radial stretching for improved laminar sublayer resolution. The circumferential branch-cut orientation and boundary condition formulation had no effect on the results.

The general character of the asymmetric flow is shown in figure 17 and a periodic vortex shedding is observed. The condition of maximum or minimum asymmetry in the local flow pattern was found to correspond to a maximum or minimum sectional sideforce, in absolute value, respectively.

Results for  $\alpha = 40^\circ$  are shown in figure 18. For figure 18(a) the elliptic nose was rolled  $45^\circ$  and the comparison is presented against Lamont's data for one of the bi-stable states which occurred experimentally for  $\phi = 0^\circ$ . For figure 18(b) results are shown for both experiment and computational model having been rolled by  $90^\circ$ . In both cases, the correlation



is quite good. Other computations for  $\alpha = 20^\circ$  with the asymmetric geometry yielded essentially symmetric flow solutions, as was observed experimentally. The conjecture of an apex out-of-roundness triggering the stable asymmetric flow patterns seems to be substantiated by these results. Integration of the surface pressures in the side-force direction is consistent with the observed flow patterns and correlates with experiment well, figure 19.

**Prolate Spheroid** - Computations for the symmetric flow about a 6:1 prolate spheroid have been performed by Vatsa (1987) for  $\alpha = 10^\circ, 30^\circ$  and  $R_L = 1.6, 7.2, 7.7 \times 10^6$ . These Reynolds numbers correspond to  $R_D = .27, 1.2, 1.28 \times 10^6$  which are within the range investigated by Hartwich for the 3.5 tangent-ogive configuration. This work included a detailed comparison of the upwind solver CFL3D and the central-difference solver TLNS3D.

C-O topology grids were generated with an algebraic method based upon the principles of transfinite interpolation (Smith, 1982, Eriksson, 1984). The baseline grid was comprised of  $73 \times 49 \times 49$  points. Grid sensitivity studies showed expected trends in solution properties with the baseline grid producing a faithful rendition of the flow. Solutions from TLNS3D required approximately 3500 cycles to converge the flow which corresponded to about 7 hours of Cray-2 time. (Extensions to the algorithm since the prolate spheroid study have resulted in many solutions being obtained in nominally 300 cycles.) Approximately 3500 cycles were required for CFL3D solutions which corresponded to 3.5 Cray-2 hours. Results were computed for  $M_\infty = 0.4$  whereas the experimental results were obtained at  $M_\infty = 0.1$ . Numerical studies showed little change in computed solution properties for  $0.4 \geq M_\infty \geq 0.1$  although convergence for these compressible flow solvers degraded as  $M_\infty$  decreased.

Typical results are presented in figure 20 for a transitional flow simulation. Both formulations predicted similar surface flow patterns, and the agreement between theory and experiment is excellent. (Discussion of the experimental findings may be found in the papers by Kreplin (1982) and by Meier (1984, 1985).) Laminar flow results were similar except for skin friction results at the rear of the model which were underpredicted. At the higher angle of attack and Reynolds number condition the structure of the off-body flow field is comparably predicted between the two formulations, figure 21. The central difference method is slightly more dissipative and most of the differences between the two formulations is consistent with this feature.

### 3.3 Aircraft Application

Computations about aircraft geometries with Navier-Stokes formulations have recently begun to appear in the literature. A considerable effort has

been directed towards the F/A-18 aircraft in association with the High Alpha Research Program (HARP) being conducted by NASA. Computations about the forebody-LEX portion of the aircraft have been performed by Ghaffari (1989) with an extended version of CFL3D for longitudinally blocked grids by Thomas (1989). The computations have been performed matching recent wind-tunnel test and flight-test conditions. Some of these computations will be summarized in this section.

H-O topology grids were generated using established transfinite interpolation techniques with the method (Richardson, 1987) applicable to slender shapes. A baseline grid (of approximately 185,000 points) was established with sufficient normal clustering near the surface to adequately resolve the laminar sublayer for the turbulent boundary layer flow for the selected wind-tunnel freestream conditions ( $M_\infty = 0.6$ ,  $R_L = 0.8 \times 10^6$ , and  $\alpha = 20^\circ$ ). This grid produced an average normal cell size next to the wall of approximately  $10^{-4}c$  which corresponds to  $y^+ \approx 2$  for the turbulent computations; a laminar sublayer generally extends out to  $y^+ \approx 8.5$ . The same grid was used for the laminar computations as well. At the flight freestream conditions ( $M_\infty = 0.34$ ,  $R_L = 13.5 \times 10^6$ , and  $\alpha = 19^\circ$ ) the baseline grid produced  $y^+ \approx 8$ . Converged results required approximately 2.5 hours of Cray-2 computer time.

**Wind-Tunnel Computations** - The computed total pressure contours and surface streamline patterns are shown in figures 22 and 23 for fully laminar as well as fully turbulent flow, respectively. These solutions are obtained at  $M_\infty = 0.6$ ,  $R_L = 0.8 \times 10^6$ , and  $\alpha = 20^\circ$ . The cross flow total pressure contours for the laminar computations (figure 22(a)) clearly show the LEX primary and the secondary vortex systems. Furthermore, there exists a clear primary separation line (as indicated by the converging surface streamlines) on the forebody along with a secondary separation line on the leeward side of the aft forebody. These are fairly flat bubble-type separations which, in general, occur on the order of a boundary layer thickness.

A closeup view of the LEX-body laminar flow structure is shown in figure 22(b). This result shows a very complex separated flow that exists under the LEX. Figure 22(b) also provides a close view of the surface flow in the vicinity of the longitudinal grid-patching station (i.e., the LEX apex station). Note that the flow properties are very smooth across this interfacing patch between the two blocks of grid. The laminar LEX upper surface pattern (figure 22(c)) clearly shows the secondary separation line with the subsequent reattachment line (indicated by the diverging surface streamlines) between the secondary separation line and the leading edge. A tertiary vortex is also indicated outboard of the secondary reattachment line.

The turbulent flow computations demonstrate

a drastically different flow structure as shown in figure 23. For example, it appears that the primary and the secondary forebody separations are completely eliminated in the turbulent case, figure 23(a). In addition, the separated flow pattern beneath the LEX (figure 23(b)) has been reduced in scale and simplified in the turbulent case. Compared to the laminar flow results, the turbulent flow pattern on the LEX upper surface (figure 23(c)) shows an outboard movement of the secondary separation line, as expected, and reduced evidence of the tertiary flow

A comparison of the computed surface pressure coefficients for both laminar and turbulent flow are shown in figures 24 and 25 for six stations located at  $x/\bar{c} = 0.334, 0.587, 0.891, 1.390, 1.701, \text{ and } 2.143$ . For reference, the nose is located at  $x/\bar{c} = 0$ , the LEX apex is located at  $x/\bar{c} = 1.006$  and the LEX-wing juncture at  $x/\bar{c} = 2.482$ . The experimental data obtained by Erickson (1988) are also shown for both the starboard and port sides of the model to assess flow symmetry. Figure 24 shows the variation of the surface pressure coefficients as a function of azimuthal angle  $\theta$  on the forebody. (The windward and leeward sides of the forebody correspond to  $\theta = 0^\circ$  and  $180^\circ$ , respectively.) Differences between the laminar and turbulent solutions occur in the range  $130^\circ \leq \theta \leq 165^\circ$  in association with flow separation which occurs for laminar case. In general, a good correlation with experiment is achieved. Most differences between theory and experiment can be attributed to grid resolution effects.

The LEX computed surface pressure coefficients are shown in figure 25 along with the experimental data as a function of LEX exposed semispan,  $y/s$ . (In this way,  $y/s = 0$  corresponds to the LEX-body juncture and  $y/s = 1$  corresponds to the LEX leading edge.) Figure 25(a) reveals a good agreement between the experimental data and the turbulent flow computation; the laminar flow under predicts the primary vortex suction peak. The correlation between theory and experiment begins to degrade at station 5 and continues to do so at station 6. This trend is consistent with differences between the computational and experimental geometries (i.e., forebody-LEX vs. complete aircraft), particularly as regards wing and inlet induced effects. None the less, it is noteworthy that the forebody pressures as well as the pressures on the forward portion of the LEX can be accurately predicted with the turbulent computations on the isolated forebody-LEX geometry.

**Flight-Test Computations** - Flight-test solutions were obtained at  $M_\infty = 0.34$ ,  $R_\tau = 13.5 \times 10^6$ , and  $\alpha = 19^\circ$ . Grid sensitivity effects in the normal direction were assessed for various flow parameters (e.g., Mach contours, density contours, surface flow patterns, surface pressure contours, etc.) and no major differences were found.

A side view of the computed surface flow streamlines on the forebody at flight condition is

shown in figure 26(a). This figure also shows part of the LEX geometry. The surface flow pattern obtained in flight as reported by Fisher (1988) is shown in figure 26(b) from a similar vantage point. The body separation line under the LEX is well predicted by the theory. Furthermore, the overall surface flow pattern around the forebody agree well, qualitatively, with the flight test results. A good correlation is also achieved on the windward side (of the front part) of the forebody as shown in figure 27.

Results from Thomas (1989) are presented in figures 28 and 29 for  $\alpha = 30^\circ$  and comparable Reynolds and Mach numbers to the results of figures 27 and 28. At these conditions the forebody flow is separated and the correlation between theory and experiment is still quite good.

#### 4.0 CONCLUDING REMARKS

A review of some recent aerodynamic computations for cases dominated by separation-induced vortex flows has been presented. The results demonstrate that a wide range of computational methodology exists for analyzing these flows. The simplified methods included in this overview are based upon potential flow assumptions. They typically provide good force and moment estimates for a range of configurations including fairly complex geometries.

Advanced computational methods presently solve the Navier-Stokes equations in the thin-layer form. These methods have also been successfully applied to a variety of configuration geometries ranging from simple delta wings and forebodies to the forebody-LEX portion of the F/A-18 aircraft. As part of these results, the Navier-Stokes methods have been demonstrated to provide good predictions for both sharp-edged wing separation as well as blunt forebody separation. In addition, successful computations have been achieved for laminar, turbulent and transitional flows.

#### 5.0 APPENDICES

Basic features of the governing equations used for the results presented in this paper are provided below. Additional details may be found among the references.

##### 5.1 Compressible Governing Equations

The inviscid flux terms from the governing equation are defined as follows:

$$\hat{Q} = \frac{1}{J} \begin{Bmatrix} \rho \\ \rho u \\ \rho v \\ \rho w \\ E_0 \end{Bmatrix}; \quad \hat{F} = \frac{1}{J} \begin{Bmatrix} \rho U \\ \rho U u + \xi_x p \\ \rho U v + \xi_y p \\ \rho U w + \xi_z p \\ (E_0 + p)U \end{Bmatrix}$$

$$\hat{G} = \frac{1}{J} \begin{Bmatrix} \rho V \\ \rho V u + \eta_x p \\ \rho V v + \eta_y p \\ \rho V w + \eta_z p \\ (E_0 + p)V \end{Bmatrix}; \quad \hat{H} = \frac{1}{J} \begin{Bmatrix} \rho W \\ \rho W u + \zeta_x p \\ \rho W v + \zeta_y p \\ \rho W w + \zeta_z p \\ (E_0 + p)W \end{Bmatrix}$$

The contravariant velocity components in these equations are given by:

$$\begin{Bmatrix} U \\ V \\ W \end{Bmatrix} = \begin{Bmatrix} \xi_x u + \xi_y v + \xi_z w \\ \eta_x u + \eta_y v + \eta_z w \\ \zeta_x u + \zeta_y v + \zeta_z w \end{Bmatrix}$$

The viscous flux terms from the governing equation are defined as follows:

$$\hat{H}_v = \frac{M_\infty \mu}{R_\varepsilon J} \begin{Bmatrix} 0 \\ u_{,\zeta} \phi_{\zeta 1} + \zeta_x \phi_{\zeta 2} \\ v_{,\zeta} \phi_{\zeta 1} + \zeta_y \phi_{\zeta 2} \\ w_{,\zeta} \phi_{\zeta 1} + \zeta_z \phi_{\zeta 2} \\ ((\frac{\varepsilon^2}{2})_{,\zeta} + \frac{T_{,\zeta}}{Pr(\gamma-1)}) \phi_{\zeta 1} + W \phi_{\zeta 2} \end{Bmatrix}$$

where

$$\begin{Bmatrix} \phi_{\xi 1} \\ \phi_{\eta 1} \\ \phi_{\zeta 1} \end{Bmatrix} = \begin{Bmatrix} (\xi_x)^2 + (\xi_y)^2 + (\xi_z)^2 \\ (\eta_x)^2 + (\eta_y)^2 + (\eta_z)^2 \\ (\zeta_x)^2 + (\zeta_y)^2 + (\zeta_z)^2 \end{Bmatrix}$$

$$\begin{Bmatrix} \phi_{\xi 2} \\ \phi_{\eta 2} \\ \phi_{\zeta 2} \end{Bmatrix} = \frac{1}{3} \begin{Bmatrix} u_{,\xi} \xi_x + v_{,\xi} \xi_y + w_{,\xi} \xi_z \\ u_{,\eta} \eta_x + v_{,\eta} \eta_y + w_{,\eta} \eta_z \\ u_{,\zeta} \zeta_x + v_{,\zeta} \zeta_y + w_{,\zeta} \zeta_z \end{Bmatrix}$$

The transformation metrics are:

$$\begin{bmatrix} \xi_x & \eta_x & \zeta_x \\ \xi_y & \eta_y & \zeta_y \\ \xi_z & \eta_z & \zeta_z \end{bmatrix} =$$

$$J \begin{bmatrix} y_{,\eta} z_{,\zeta} - z_{,\eta} y_{,\zeta} & z_{,\xi} y_{,\zeta} - y_{,\xi} z_{,\zeta} & y_{,\xi} z_{,\eta} - z_{,\xi} y_{,\eta} \\ z_{,\eta} x_{,\zeta} - x_{,\eta} z_{,\zeta} & x_{,\xi} z_{,\zeta} - z_{,\xi} x_{,\zeta} & z_{,\xi} x_{,\eta} - x_{,\xi} z_{,\eta} \\ x_{,\eta} y_{,\zeta} - y_{,\eta} x_{,\zeta} & y_{,\xi} x_{,\zeta} - x_{,\xi} y_{,\zeta} & x_{,\xi} y_{,\eta} - y_{,\xi} x_{,\eta} \end{bmatrix}$$

and the Jacobian of the transformation is given by:

$$J^{-1} = x_{,\xi}(y_{,\eta} z_{,\zeta} - z_{,\eta} y_{,\zeta}) - y_{,\xi}(x_{,\eta} z_{,\zeta} - z_{,\eta} x_{,\zeta}) + z_{,\xi}(x_{,\eta} y_{,\zeta} - y_{,\eta} x_{,\zeta})$$

## 5.2 Incompressible Governing Equations

The inviscid flux terms from the governing equation are defined as follows:

$$\hat{Q} = \frac{1}{J} \begin{Bmatrix} p \\ u \\ v \\ w \end{Bmatrix}; \quad \hat{F} = \frac{1}{J} \begin{Bmatrix} \beta U \\ Uu + \xi_x p \\ Uv + \xi_y p \\ Uw + \xi_z p \end{Bmatrix}$$

$$\hat{G} = \frac{1}{J} \begin{Bmatrix} \beta V \\ Vu + \eta_x p \\ Vv + \eta_y p \\ Vw + \eta_z p \end{Bmatrix}; \quad \hat{H} = \frac{1}{J} \begin{Bmatrix} \beta W \\ Wu + \zeta_x p \\ Wv + \zeta_y p \\ Ww + \zeta_z p \end{Bmatrix}$$

Here  $\beta$  is an artificial compressibility coupling parameter which is typically set to unity. The contravariant velocity components in these equations are the same as stated in appendix 5.1.

The viscous flux terms from the governing equation are defined as follows:

$$\hat{H}_v = \frac{1}{R_\varepsilon J} \begin{Bmatrix} 0 \\ u_{,\zeta} \phi_{\zeta 1} + \zeta_x \phi_{\zeta 2} \\ v_{,\zeta} \phi_{\zeta 1} + \zeta_y \phi_{\zeta 2} \\ w_{,\zeta} \phi_{\zeta 1} + \zeta_z \phi_{\zeta 2} \\ ((\frac{\varepsilon^2}{2})_{,\zeta} + \frac{T_{,\zeta}}{Pr(\gamma-1)}) \phi_{\zeta 1} + W \phi_{\zeta 2} \end{Bmatrix}$$

and  $\phi_{\zeta 1}$  and  $\phi_{\zeta 2}$  are given by the expressions in appendix 5.1.

## 6.0 REFERENCES

- Anderson, W. K.; Thomas, J. L.; and Whitfield, D. L. (1988): Three-Dimensional Multigrid Algorithms for the Flux-Split Euler Equations. NASA TP-2829.
- Baldwin, B. S.; and Lomax, H. (1978): Thin Layer Approximation and Algebraic Model for Separated Turbulent Flows. AIAA Paper No. 78-257.
- Boyden, R. P.; and Johnson, W. G., Jr. (1981): Preliminary Results of Buffet Tests in a Cryogenic Wind Tunnel. NASA TM-81923.
- Brune, G. W.; Weber, J. A.; Johnson, F. T.; Lu, P.; and Rubbert, P. E. (1975): A Three-Dimensional Solution of Flows Over Wings with Leading-Edge Vortex Separation. Part 1 - Engineering Document. NASA CR-132709.
- Carlson, H. W.; Mack, R. J.; and Barger, R. L. (1979): Estimation of Attainable Leading-Edge Thrust for Wings at Subsonic and Supersonic Speeds. NASA TP-1500.
- Carlson, H. W.; and Mack, R. J. (1980): Studies of Leading-Edge Thrust Phenomena. AIAA Journal of Aircraft, Vol. 17, No. 12.
- Carlson, H. W.; Darden, C. M.; and Mann, M. J. (1990): Validation of a Computer Code for Analysis of Subsonic Aerodynamic Performance of Wings with Flaps in Combination with a Canard or Horizontal Tail and an Application to Optimization. NASA TP-2961.
- Chorin, A. J. (1967): A Numerical Method for Solving Incompressible Viscous Flow Problems. Journal of Computational Physics, Vol. 2, No. 1.
- Degani, D.; and Schiff, L. B. (1983): Computation of Supersonic Viscous Flows Around Pointed Bodies at Large Incidence. AIAA Paper No. 83-0034.
- Erickson, G. E. (1988): Experimental Study of the F/A-18 Vortex Flows at Subsonic and Transonic Speeds Using a Laser Vapor Screen Technique. SAE Paper No. 881421.
- Eriksson, L. E. (1984): Practical Three-Dimensional Mesh Generation Using Transfinite Interpolation. Journal of Fluid Mechanics, Vol. 148, pp. 45-78.
- Esch, H. (1975): The Influence of Reynolds Number on the Normal-Force Characteristics of Slender Cylindrical Bodies. ESA TT-170.
- Fisher, D. F.; Richwine, D. M.; and Banks, D. W. (1988): Surface Flow Visualization of Separated

Flows on the Forebody of an F-18 Aircraft and Wind-Tunnel Model. NASA TM 100436.

Fox, C. H., Jr.; and Lamar, J. E. (1974): Theoretical and Experimental Longitudinal Aerodynamic Characteristics of an Aspect Ratio 0.25 Sharp-Edge Delta Wing at Subsonic, Transonic, Supersonic, and Hypersonic Speeds. NASA TN D-7651.

Ghaffari, F.; Luckring, J. M.; Thomas, J. L.; and Bates, B. L. (1989): Navier-Stokes Solutions about the F/A-18 Forebody-LEX Configuration. AIAA Paper No. 89-0338.

Hall, M. G. (1961): A Theory for the Core of a Leading-Edge Vortex. *Journal of Fluid Mechanics*, Vol. 11.

Hartwich, P. M. (1986): Three-Dimensional Grids as Solutions of Elliptic Systems. AIAA Paper No. 86-0430.

Hartwich, P. M.; and Hsu, C. H. (1986): An Implicit Flux-Difference Splitting Scheme for Three-Dimensional, Incompressible Navier-Stokes Solutions to Leading Edge Vortex Flows. AIAA Paper No. 86-1839-CP.

Hartwich, P. M.; Hsu, C. H.; Luckring, J. M.; and Liu, C. H. (1988): Numerical Study of the Vortex Burst Phenomenon for Delta Wings. AIAA Paper No. 88-0505.

Hartwich, P. M.; and Hsu, C. H. (1988b): High Resolution Upwind Schemes for the Three-Dimensional Incompressible Navier-Stokes Equations. AIAA Journal, Vol. 26, No. 11, pp. 1321-1328. See also AIAA Paper No. 87-0547, 1987.

Hartwich, P. M.; and Hall, R. M. (1989): Navier-Stokes Solutions for Vortical Flows over a Tangent-Ogive Cylinder. AIAA Paper No. 89-0337.

Hartwich, P. M.; Hall, R. M.; and Hensch, M. J. (1990): Navier-Stokes Computations of Vortex Asymmetries Controlled by Small Surface Imperfections. AIAA Paper No. 90-0385.

Hummel, D. (1979): On the Vortex Formation Over a Slender Wing at Large Angles of Incidence. AGARD CP-247, Paper No. 15.

Jameson, A.; Schmidt, W.; and Turkel, A. (1981): Numerical Solutions to the Euler Equations by Finite Volume Methods Using Runge-Kutta Time-Stepping Schemes. AIAA Paper No. 81-1259.

Jameson, A.; and Baker, T. J. (1983): Solution of the Euler Equations for Complex Configurations. AIAA Paper No. 83-1929.

Johnson, D. A.; and King, L. S. (1985): A Mathematically Simple Turbulence Closure Model for Attached and Separated Turbulent Boundary Layers. AIAA Journal, Vol. 23, No. 11.

Johnson, F. T.; Lu, P.; Tinoco, E. N.; and Epton, M. A. (1980): An Improved Panel Method for the Solution of Three-Dimensional Leading-Edge Vortex Flows. Volume I - Theory Document. NASA CR-3278.

Kaynak, U.; and Flores, J. (1987): Advances in the Computation of Transonic Separated Flows over Finite Wings. AIAA Paper No. 87-1195.

Kreplin, H. P., Vollmers, H.; and Meier, H. U. (1982): Measurements of the Wall Shear Stress on an Inclined Prolate Spheroid. *Zeitschrift für Flugwissenschaft und Weltraumforschung*, Vol. 6, pp. 248-252.

Lamar, J. E.; and Gloss, B. B. (1975): Subsonic Aerodynamic Characteristics of Interacting Lifting Surfaces with Sharp Edges Predicted by a Vortex-Lattice Method. NASA TN D-7921.

Legendre, R. (1953): Écoulement au voisinage de la pointe avant d'une aile à forte flèche aux incidences moyennes. *Recherches Aeronautiques (ONERA)*, No. 35, pp. 7-8.

Luckring, J. M. (1985): A Theory for the Core of a Three-Dimensional Leading Edge Vortex. AIAA Paper No. 85-108.

Luckring, J. M.; Hoffler, K. D.; and Grantz, A. C. (1986): Recent Extensions to the Free-Vortex-Sheet Theory for Expanded Convergence Capability. NASA CP-2416, paper no. 4.

Luckring, J. M.; Fox, C. H., Jr.; and Cundiff, J. S. (1988): Reynolds Number Effects on the Subsonic Aerodynamics of a Generic Accelerator Configuration. Fourth National Aero-Space Plane Technology Symposium, Paper No. 82.

Margason, R. J.; and Lamar, J. E. (1971): Vortex-Lattice Fortran Program for Estimating Subsonic Aerodynamic Characteristics of Complex Planforms. NASA TN D-6142.

McMillin, S. N.; Thomas, J. L.; and Murman, E. M. (1990): Navier-Stokes and Euler Solutions for Leeward Flows over Supersonic Delta Wings. NASA TP-3035.

Meier, H. U.; Kreplin, H. P.; Landhauber, A.; and Baumgarten, D. (1984): Mean Velocity Distributions in Three-Dimensional Boundary Layers, Developing on a 1:6 Prolate Spheroid with Artificial Transition. DFVLR IB 222-84A11, March.

Meier, H. U.; and Cebici, T. (1985): Flow Characteristics of a Body of Revolution at Incidence. Third Symposium on Numerical and Physical Aspects of Aerodynamic Flows.

Miller, D. S.; and Wood, R. M. (1985): Lee-Side Flow Over Delta Wings at Supersonic Speeds. NASA TP-2430.

Polhamus, E. C. (1966): A Concept of the Vortex Lift of Sharp-Edged Delta Wings Based on a Leading-Edge-Suction Analogy. NASA TN D-3767.

Polhamus, E. C. (1984): A Review of Some Reynolds Number Effects Related to Bodies at High Angles of Attack. NASA CR-3809, August.

Polhamus, E. C. (1986): Vortex Lift Research: Early Contributions and Current Challenges. NASA CP-2416, Paper No. 1.

- Ramshaw, J. D. (1985): Conservative Rezoning Algorithms for Generalized Two-Dimensional Meshes. *Journal of Computational Physics*, Vol. 59, pp 193-199.
- Riabouchinski, D. (1922): Sur Les Equations du Mouvement a Deux Dimensions de Solides Dans un Liquide Avec Tourbillons. *Comptes Rendus*, CLXXV, pp. 442-445.
- Richardson, P. F.; and Morrison, J. H. (1987): Displacement Surface Calculations for a Hypersonic Aircraft. AIAA Paper No. 87-1190.
- Roe, P. L. (1986): Characteristic Based Schemes for the Euler Equations. *Annual Review of Fluid Mechanics*, pp. 337-365.
- Smith, R. E. (1982): Algebraic Grid Generation. *Numerical Grid Generation*, Elsevier, New York, pp. 137-168.
- Stanbrook, A.; and Squire, L. C. (1964): Possible Types of Flow at Swept Leading Edges. *Aeronautical Quarterly*, Vol. 15, pp. 72-82.
- Stewartson, K.; and Hall, M. G. (1963): The Inner Viscous Solution for the Core of a Leading Edge Vortex. *Journal of Fluid Mechanics*, Vol. 15.
- Swanson, R. C.; and Turkel, E. (1986): A Multi-stage Time-Stepping Scheme for the Navier-Stokes Equations. AIAA Paper No. 86-0035.
- Swanson, R. C.; and Turkel, E. (1987): Artificial Dissipation and Central Difference Scheme for the Euler and Navier-Stokes Equations. AIAA Paper No. 87-1107-CP.
- Thomas, J. L.; and Salas, M. D. (1985): Far-Field Boundary Conditions for Transonic Lifting Solutions to the Euler Equations. AIAA Paper No. 85-0020.
- Thomas, J. L.; and Walters, R. W. (1985b): Upwind Relaxation Algorithms for the Navier-Stokes Equations. AIAA Paper No. 85-1501.
- Thomas, J. L.; van Leer, B.; and Walters, R. W. (1985c): Implicit Flux-Split Schemes for the Euler Equations. AIAA Paper No. 85-1680.
- Thomas, J. L.; and Newsome, R. W. (1986): Navier-Stokes Computations of Lee-Side Flows over Delta Wings. AIAA Paper No. 86-1049.
- Thomas, J. L.; Taylor, S. L.; and Anderson, W. K. (1987): Navier-Stokes Computations of Vortical Flows Over Low Aspect Ratio Wings. AIAA Paper No. 87-0207.
- Thomas, J. L.; Walters, R. W.; Ghaffari, F.; Weston, R. P.; and Luckring, J. M. (1989): A Patched Grid Algorithm for Complex Configurations Directed Towards the F-18 Aircraft. AIAA Paper No. 89-0121.
- van Leer, B. (1982): Flux-Vector Splitting for the Euler Equations. ICASE Report No. 82-30, Sep.
- Vatsa, V. N. (1986): Accurate Solutions for Transonic Viscous Flow Over Finite Wings. AIAA Paper No. 86-1052.
- Vatsa, V. N.; Thomas, J. L., and Wedan, B. W. (1987): Navier-Stokes Computations of Prolate Spheroids at Angle of Attack. AIAA Paper No. 87-2627-CP.
- Wentz, W. H., Jr.; and Kohlman, D. L. (1968): Wind-Tunnel Investigation of Vortex Breakdown on Slender Sharp-Edged Delta Wings. NASA CR-98737.
- Wilson, H. A., Jr.; and Lovell, J. C. (1947): Full-Scale Investigation of the Maximum Lift and Flow Characteristics of an Airplane Having Approximately Triangular Planform. NACA RM-L6K20. (Declassified July, 1950.)

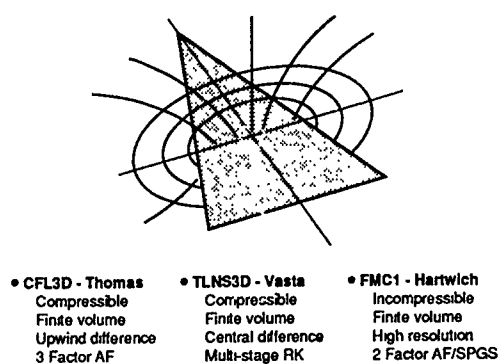
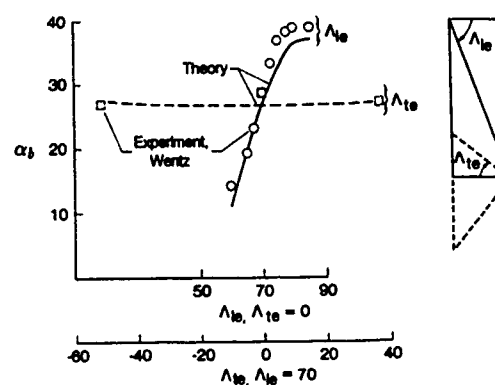


Figure 1.- Navier-Stokes formulations.



(a) Vortex breakdown boundaries. (From Luckring, 1985.)

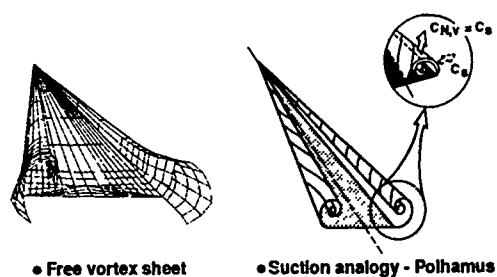
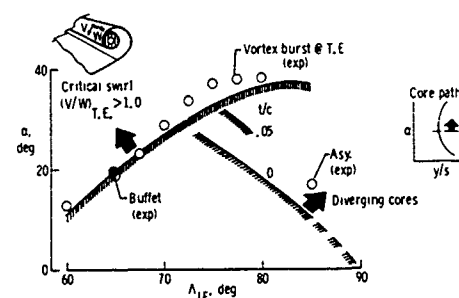


Figure 2.- Potential-based formulations.



(b) Breakdown and Asymmetry. (From Polhamus, 1986.)

Figure 4.- Prediction of vortex flow regimes.

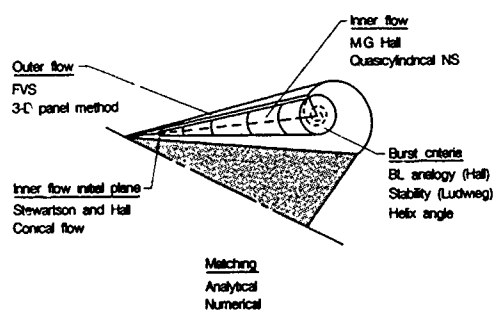


Figure 3.- Coupled vortex core and free vortex sheet. (From Luckring, 1985.)

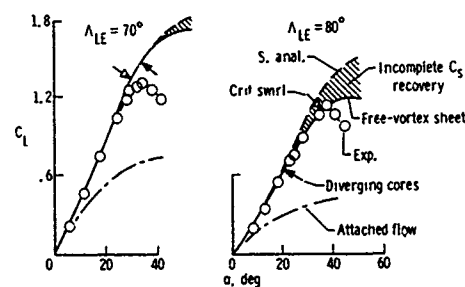
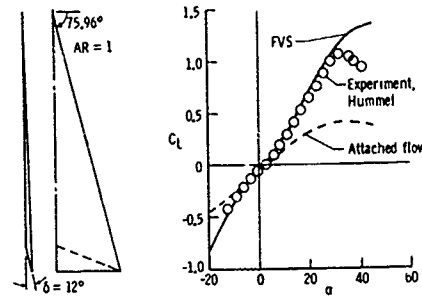
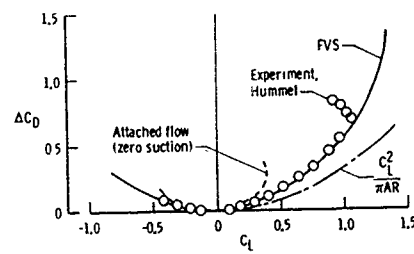


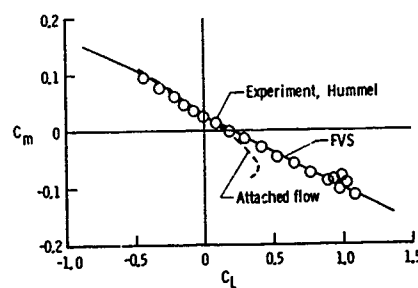
Figure 5.- Some predictions of vortex lift effects.



(a) Lift.



(b) Drag.



(c) Pitching moment.

Figure 6.- Force and moment correlation, Hummel delta wing.

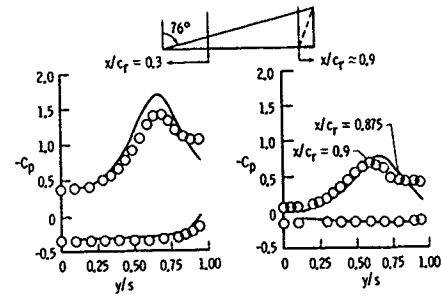
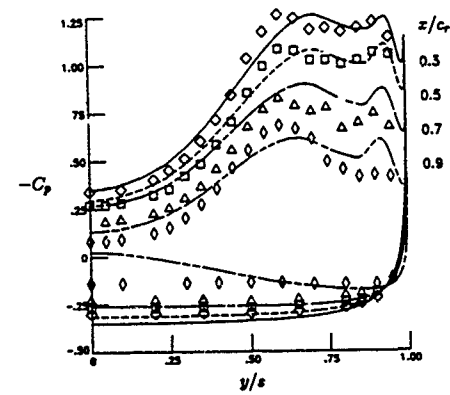
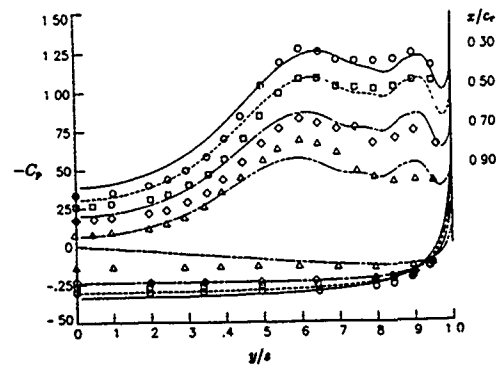


Figure 7.- Pressure correlation, Hummel delta wing. Inviscid FVS, turbulent experiment.



(a) Incompressible. (From Hartwich, 1987.)



(b) Compressible, Upwind. (From Thomas, 1987.)

Figure 8.- Pressure correlation, Hummel delta wing. Laminar CFD, laminar experiment.



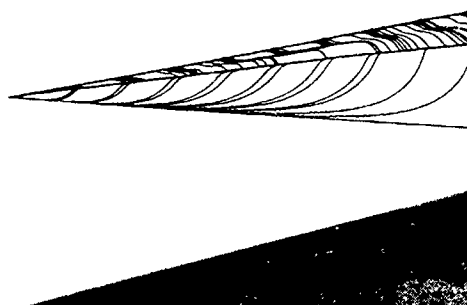


Figure 9.- Upper surface flow patterns, Hummel delta wing. Laminar FMC1, laminar experiment.

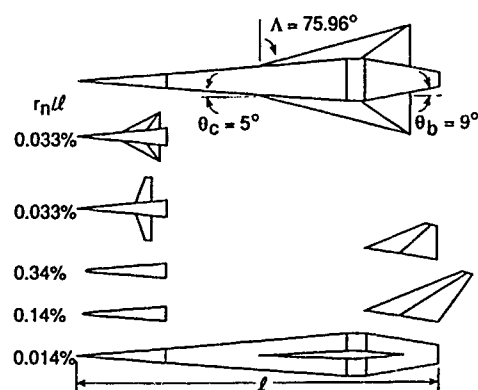
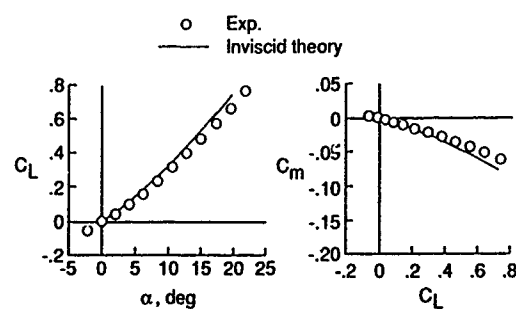
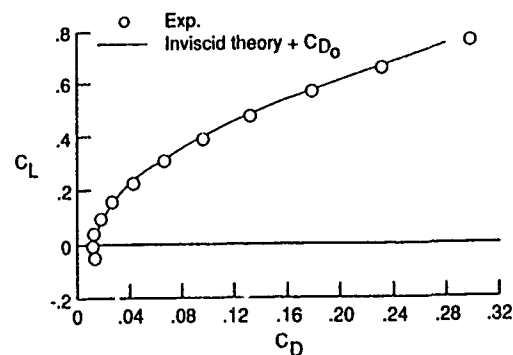


Figure 10.- Generic high-speed configuration. (From Luckring, 1988)

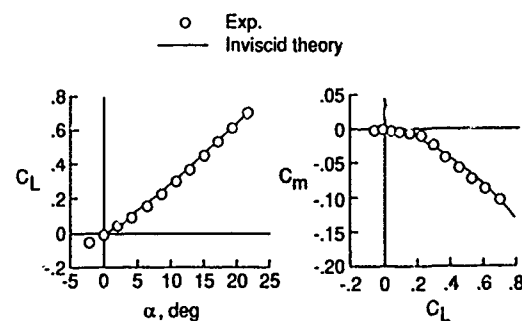


(a) Lift and pitching moment.

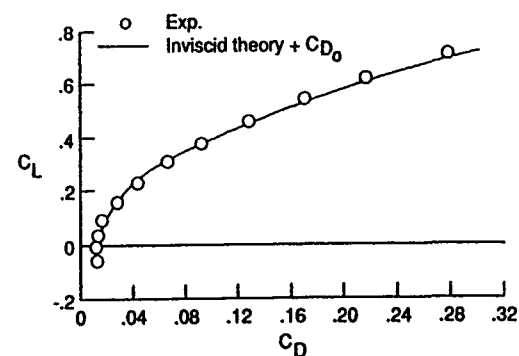


(b) Drag-due-to-lift estimate.

Figure 11.- Estimates for low  $AR$  canard configuration.  $M_\infty = 0.3$ ,  $R_L = 18 \times 10^6$ . (From Luckring, 1988)

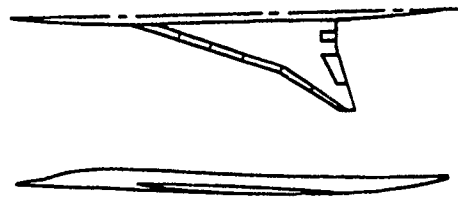


(a) Lift and pitching moment.

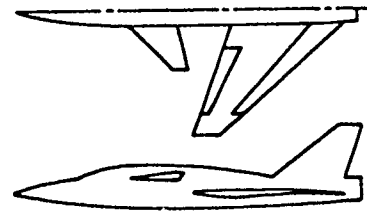


(b) Drag-due-to-lift estimate.

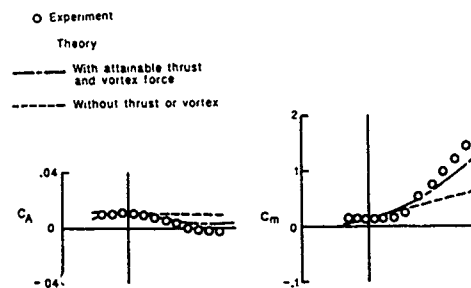
Figure 12.- Estimates for high  $AR$  canard configuration.  $M_\infty = 0.3$ ,  $R_L = 18 \times 10^6$ . (From Luckring, 1988)



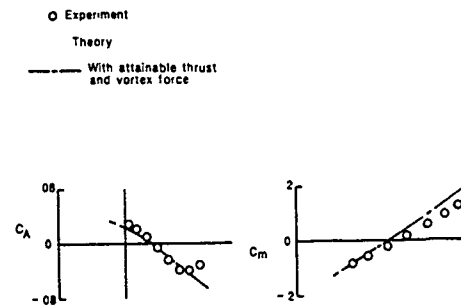
(a) Arrow-wing configuration.



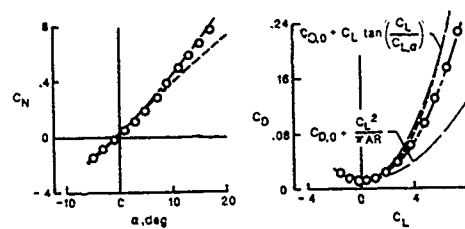
(a) Forward-swept configuration.



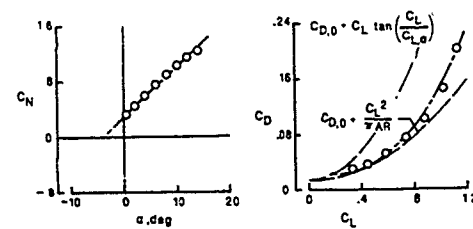
(b) Axial force and pitching moment.



(b) Axial force and pitching moment.



(c) Normal and drag force.



(c) Normal and drag force.

Figure 13.- Estimates for arrow-wing supersonic transport.  $M_\infty = 0.09$ ,  $R_\tau = 4.2 \times 10^6$ . (From Carlson, 1990)

Figure 14.- Estimates for forward swept configuration.  $M_\infty = 0.6$ ,  $R_\tau = 2.5 \times 10^6$ . (From Carlson, 1990)

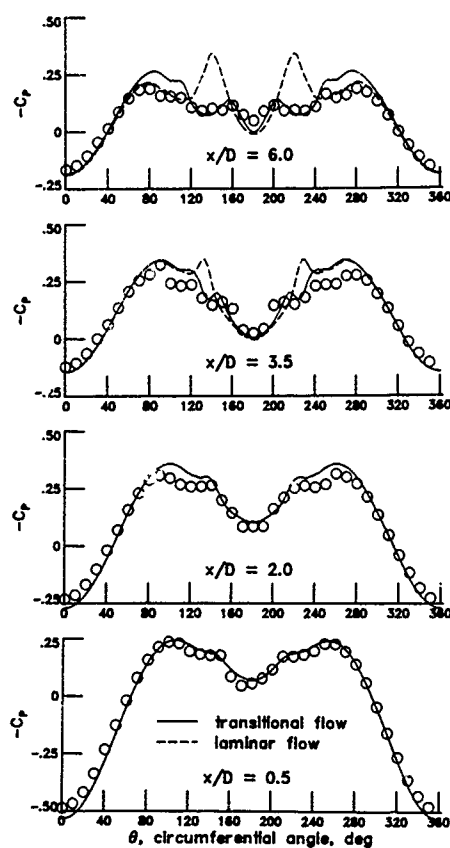


Figure 15.- Circumferential pressures for a 3.5 caliber tangent-ogive cylinder.  $\alpha = 20^\circ$ ,  $R_D = 0.2 \times 10^6$ . (From Hartwich, 1989)

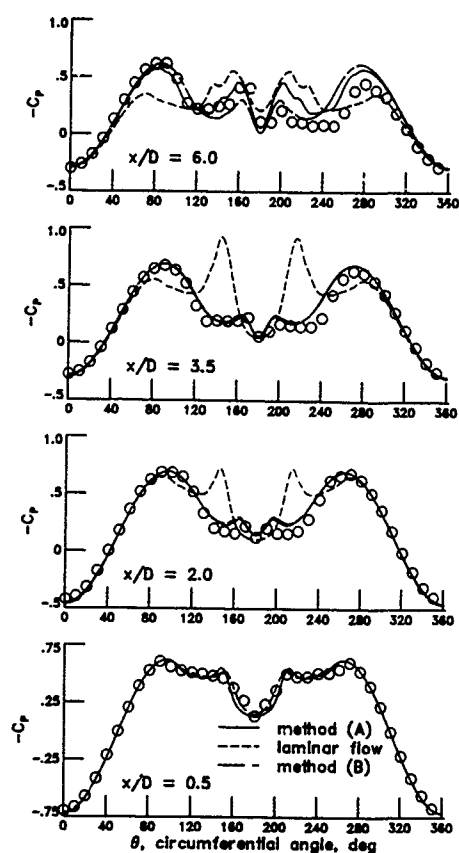
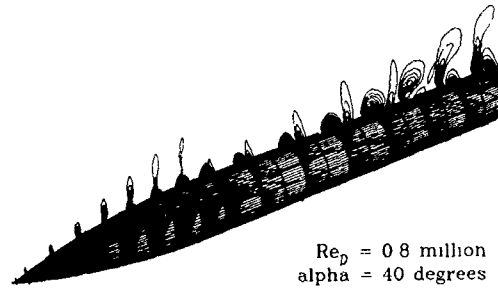
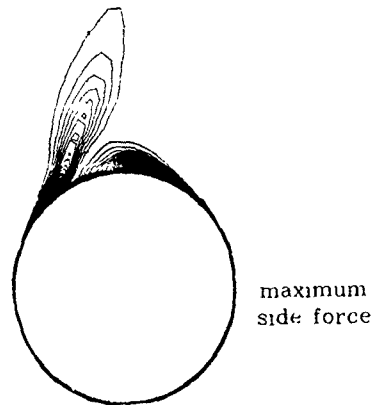
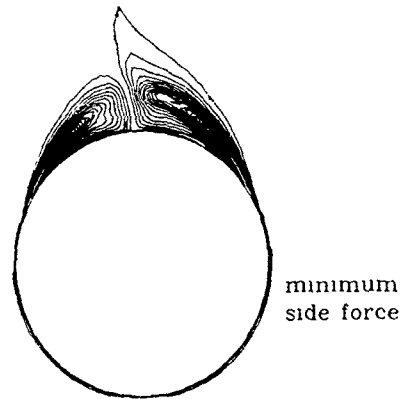
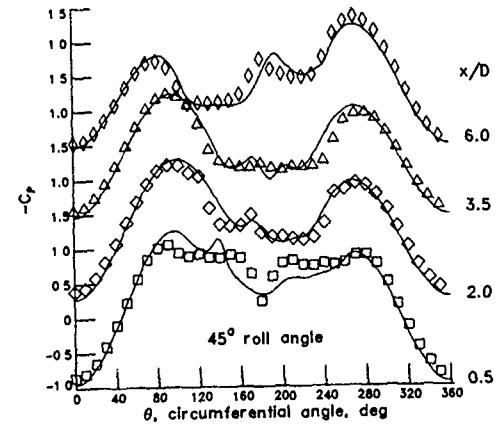
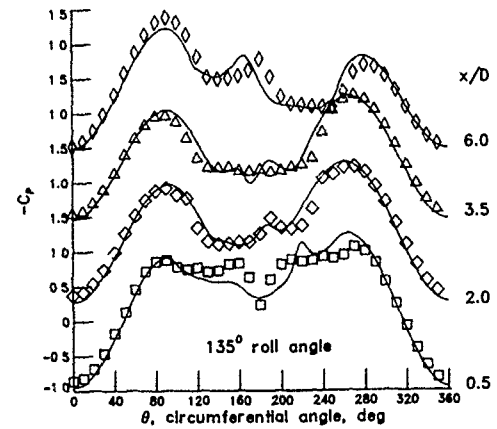
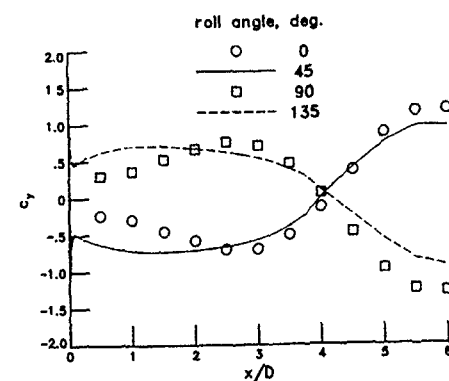
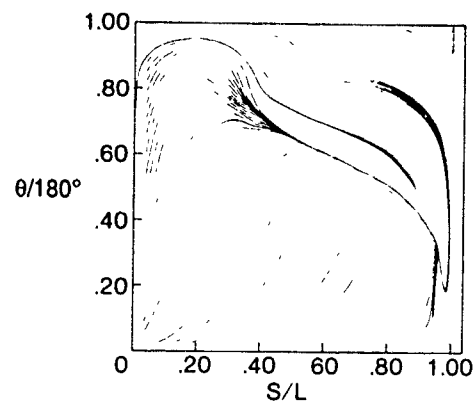


Figure 16.- Circumferential pressures for a 3.5 caliber tangent-ogive cylinder.  $\alpha = 30^\circ$ ,  $R_D = 0.8 \times 10^6$ . (From Hartwich, 1989)

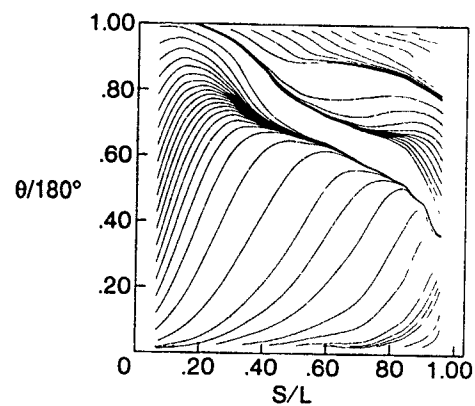


(a) Surface flow with crossplane helicity density.

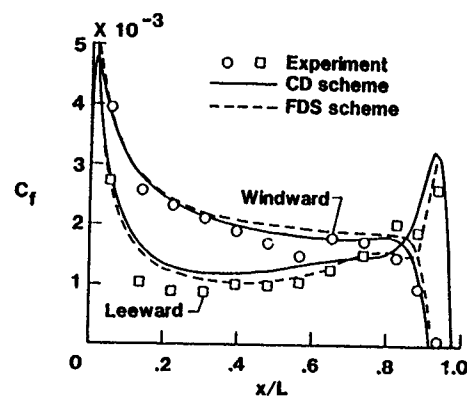
(b) Crossplane helicity density,  $x/D = 1.75$ (c) Crossplane helicity density,  $x/D = 4.0$ Figure 17.- Asymmetric flow solution.  $\alpha = 40^\circ$ ,  $R_D = 0.8 \times 10^6$ . (From Hartwich, 1990.)(a)  $\phi = 45^\circ$ .(b)  $\phi = 135^\circ$ .Figure 18.- Circumferential pressures.  $\alpha = 40^\circ$ ,  $R_D = 0.8 \times 10^6$ . (From Hartwich, 1990.)Figure 19.- Sectional side force.  $\alpha = 40^\circ$ ,  $R_D = 0.8 \times 10^6$ . (From Hartwich, 1990.)



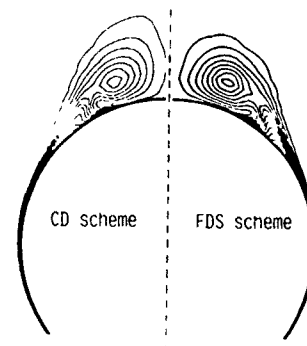
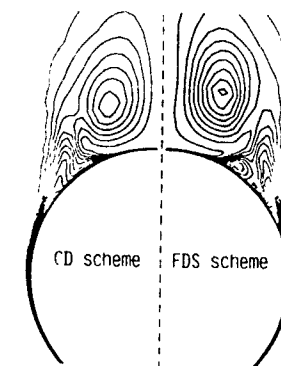
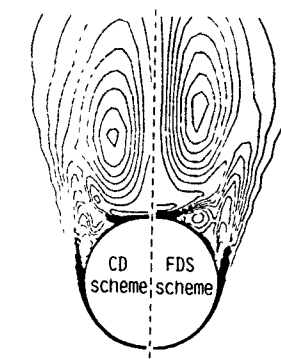
(a) Surface flow, upwind.

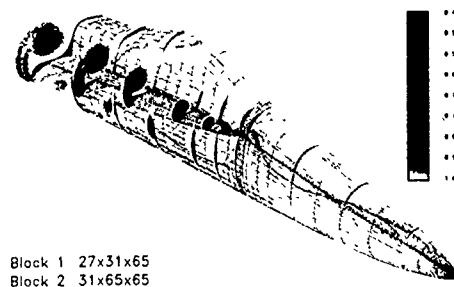


(b) Surface flow, experiment.

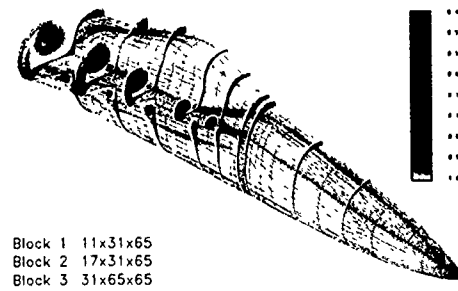


(c) Skin friction.

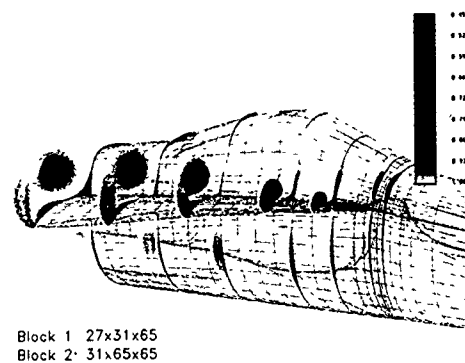
Figure 20.- Prolate spheroid results, transitional flow.  $\alpha = 10^\circ$ ,  $R_D = 1.6 \times 10^6$ . (From Vatsa, 1987.)(a)  $x/\ell = 0.50$ .(b)  $x/\ell = 0.75$ .(c)  $x/\ell = 0.95$ .Figure 21.- Prolate spheroid results, turbulent flow.  $\alpha = 30^\circ$ ,  $R_D = 7.2 \times 10^6$ . (From Vatsa, 1987.)



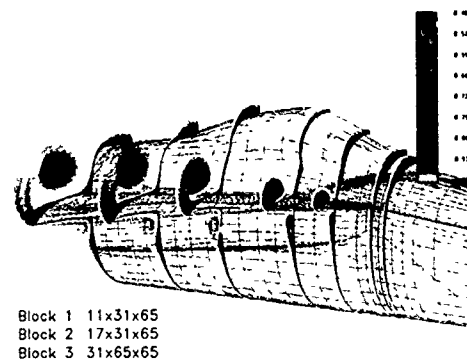
(a) Forebody-LEX.



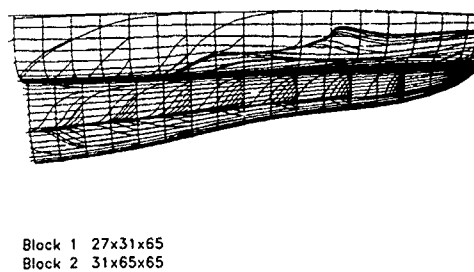
(a) Forebody-LEX.



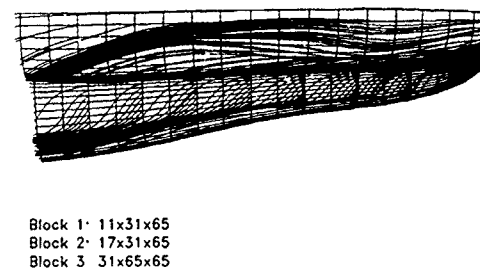
(b) Body detail.



(b) Body detail.



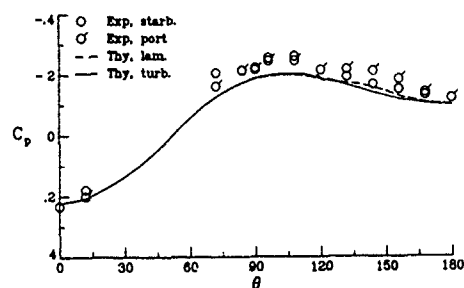
(c) LEX upper surface.



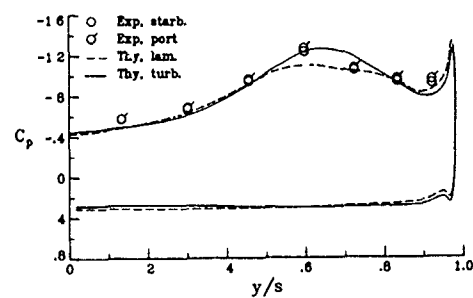
(c) LEX upper surface.

Figure 22.- Total pressure contours with surface flow pattern. Laminar flow,  $M_\infty = 0.6$ ,  $R_\tau = 0.8 \times 10^6$ ,  $\alpha = 20^\circ$ . (From Ghaffari, 1989.)

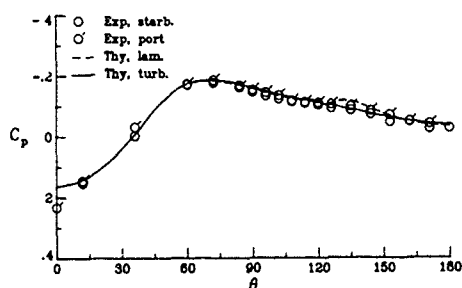
Figure 23.- Total pressure contours with surface flow pattern. Turbulent flow,  $M_\infty = 0.6$ ,  $R_\tau = 0.8 \times 10^6$ ,  $\alpha = 20^\circ$ . (From Ghaffari, 1989.)



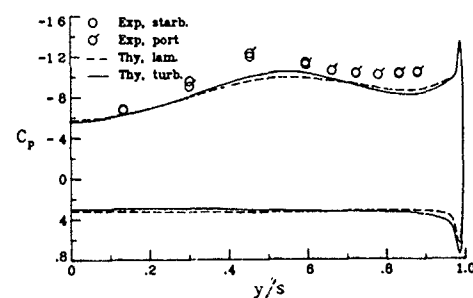
(a) Station 1



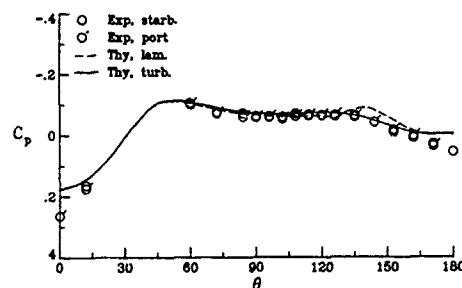
(a) Station 4



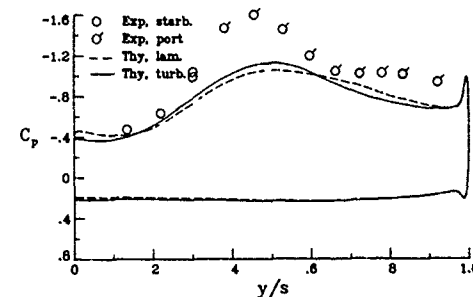
(b) Station 2



(b) Station 5



(c) Station 3



(c) Station 6

Figure 24.- Correlation between theory and experiment - Forebody surface  $C_p$ .  $M_\infty = 0.6$ ,  $R_x = 0.8 \times 10^6$ ,  $\alpha = 20^\circ$ . (From Ghaffari, 1989.)

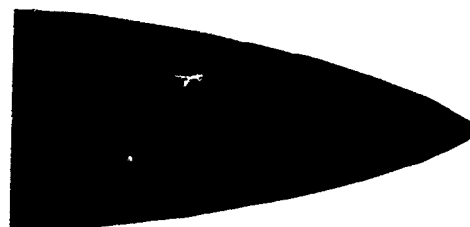
Figure 25.- Correlation between theory and experiment - LEX surface  $C_p$ .  $M_\infty = 0.6$ ,  $R_x = 0.8 \times 10^6$ ,  $\alpha = 20^\circ$ . (From Ghaffari, 1989.)





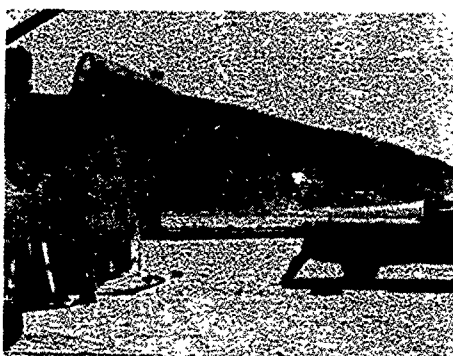
Block 1 11x31x65  
Block 2 17x31x65  
Block 3 31x65x65

(a) Computation.



Block 1. 11x31x65  
Block 2. 17x31x65  
Block 3 31x65x65

(a) Computation.



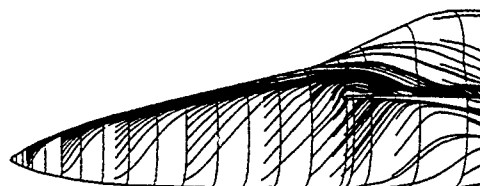
(b) Experiment.

Figure 26.- Comparison of computed turbulent surface streamlines with flight test. Bottom view,  $M_\infty = 0.34$ ,  $R_\tau = 13.5 \times 10^6$ ,  $\alpha = 19^\circ$ . (From Ghaffari, 1989.)

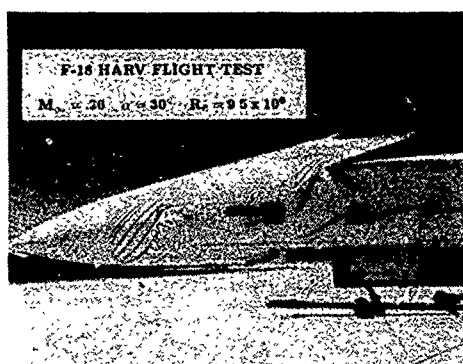


(b) Experiment.

Figure 27.- Comparison of computed turbulent surface streamlines with flight test. Bottom view,  $M_\infty = 0.34$ ,  $R_\tau = 13.5 \times 10^6$ ,  $\alpha = 19^\circ$ . (From Ghaffari, 1989.)

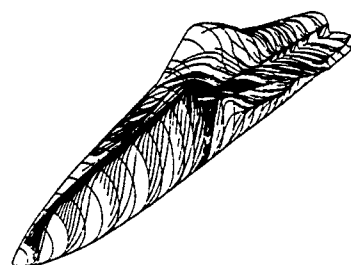


(a) Computation.



(b) Experiment.

Figure 28.- Comparison of computed turbulent surface streamlines with flight test. Side view,  $M_\infty \approx 0.3$ ,  $R_\epsilon \approx 10 \times 10^6$ ,  $\alpha = 30^\circ$ . (From Thomas, 1989.)



(a) Computation.



(b) Experiment.

Figure 29.- Comparison of computed turbulent surface streamlines with flight test. 3/4 front view,  $M_\infty \approx 0.3$ ,  $R_\epsilon \approx 10 \times 10^6$ ,  $\alpha = 30^\circ$ . (From Thomas, 1989.)

**On the Simulation of Compressible Turbulent  
Flows Past Delta Wing, Delta Wing-Body  
and Delta Wing-Canard**

A Hilgenstock, H. Vollmers  
DLR SM-TS, Bunsenstr. 10,  
D-3400 Göttingen

**ABSTRACT**

The turbulent flow around a delta wing at incidence is simulated numerically using a finite-volume Navier-Stokes method. The numerical simulation makes use of a simple algebraic turbulence model. Using a sharp leading edge delta wing, the influence of grid refinement is investigated. The realistic wing-body configuration with round leading edge is used to discuss the influence of the position of the transition line. Experimental and numerical data are compared to validate the numerical method. The topological structure of the flow is discussed. An explanation is given for the low particle density area close to the primary vortex as it is visualized by laser light sheet technique. First results for a closed coupled delta-wing-canard configuration are discussed also.

**INTRODUCTION**

Within the IEPG-TA15 program a reference Navier-Stokes solution is generated to be compared with the results of Euler solutions and with experiments. The comparison with the Euler solution is described in [1]. This paper covers the comparison of experimental and numerical data, generated by the solution of full Navier-Stokes equations. The grid generation technique and the numerical method as well as additional results are reported in [2].

The delta wing has a leading edge sweep of  $65^\circ$  (Figure 1) and interchangeable leading edges: a sharp leading edge and a rounded one. For the sharp-edged wing the primary separation is due to the geometrical singularity at the leading edge and is not depending on viscous effects. So this geometry can also be considered as a proper test case for Euler methods. For the round edge, the primary separation depends for small angles of incidence on viscous effects, so that Euler methods fail and Navier-Stokes methods have to be considered. For the selected free-stream conditions:

- free-stream mach number  $M_\infty = 0,85$
- angle of incidence  $\alpha = 10^\circ$
- yaw angle  $\beta = 0^\circ$
- Reynolds numbers for turbulent flows  
 $Re_\infty = 4,5 \cdot 10^6$  as well as  $Re_\infty = 9,0 \cdot 10^6$

the location of the onset of primary separation for two different types of leading edges is also sketched in Figure 1. The separation of the sharp-edged wing is sketched on the starboard side of the wing, the separation at the round-edged wing is shown on the portside. Here the primary separation starts not at the apex of the wing but outside the plane of symmetry on the upper wing surface.

A typical flow situation for the sharp-edged wing is shown in Figure 2. The primary vortex separates at the apex of the wing along the entire leading edge and attaches at the primary attachment line on the wing

upper surface. Inside the vortex core a distinct area of low pressure can be found. The "footprint" of the vortex is measured by pressure taps in the experiment. A typical spanwise pressure distribution is shown on the left (portside) side of the wing. The pressure is nearly constant between the plane of symmetry and the attachment line of the primary vortex. Then the pressure decreases rapidly to its lowest value below the vortex core. Going further to the leading edge, the pressure increases again decelerating the flow and yielding a smaller counter rotating secondary vortex below the primary one. The secondary vortex displaces the primary vortex inboard and upward. The secondary separation line is also shown in the sketch.

**GRID SENSITIVITY STUDY FOR THE WING WITH A SHARP LEADING EDGE**

As mentioned for the sharp-edged delta wing the primary separation is due to the geometry and not primarily dominated by viscous effects. As the separation is fixed, this leading edge case is selected to investigate the grid dependency of the numerical solution.

The mesh is divided into 10 blocks with H-H and O-H topology (Figure 3). The reference mesh has nearly 770,000 node points. The upper wing surface is represented by  $40 \times 40$  points and 40 points are distributed in the wing normal direction. The mesh density is increased close to the wing to resolve the boundary layer. The first cell above the wing has a mesh size of the order of  $C \cdot 10^{-4}$  to resolve the viscous sublayer.  $C$  is the local chord length in spanwise direction. The mesh topology as well as the spacing of the first cell and the farfield boundary is kept constant throughout the mesh variation.

For the second mesh the number of points in spanwise direction is increased from 40 to 70 node points while for the third mesh the number of points in the wing normal direction is increased to 70. The refined meshes have approximately 1,400,000 node points. The mesh variation is shown in table 1 for block 3 (in Figure 3).

The comparison of experimental pressure measurements and numerical data is shown for three different stations and for each of the three different meshes. In Figure 4 for the reference grid, in Figure 5 for the second grid and in Figure 6 for the third grid. The experimental data are represented by triangles, the numerical results by lines.

Looking first at the results for the reference mesh (Figure 4), the spanwise location of the suction peak is well predicted. At 30% root chord the numerical result below the vortex core on the upper wing surface is not in good agreement with the experimental data. The same is valid at the lower wing side. In the experiments a fuselage was mounted on the lower side on the wing, extending up to the apex of the wing. At 30% root chord the body diameter is half the wing span, i.e. the influ-

	wing chord	span	normal to the wing
1 grid (reference)	40	40	40
2 grid	40	70	40
3 grid	40	40	70

Table 1. Number of grid points in block 3 (Figure 3)

ence of the body on the flow may not be neglected. This may even influence the flow on the upper wing surface where the flow is probably accelerated due to the displacement effect of the fuselage. At 60% root chord the body influence is negligible and the agreement between experimental and numerical results is much better. Only the pressure decrease between the primary attachment line and the vortex core is not as strong as in the experiment. The same is true at 80% root chord. At this station additionally the secondary separation is not well predicted.

The second mesh is refined in spanwise direction. The suction peak at 30% root chord is slightly better predicted (Figure 5). This is due to the better spanwise resolution of the primary vortex. As the H-H-type mesh topology creates a rather coarse mesh in the front part of the wing a more conical mesh type may be better to resolve the vortex in this area. At 60% and 80% root chord the results are nearly the same as in Figure 4 for the reference mesh.

The third mesh is refined only in the wing normal direction. The results are shown in Figure 6. Although the mesh density is increased, the numerical results at the 30% station are comparable to the reference mesh. In this area the primary vortex is that close to the surface in the already highly resolved boundary layer that a further increase of mesh points is not necessary. At 60% and 80%, however, the pressure decrease between the attachment line and the vortex core is now in better agreement with experimental data. The vortex at the rear part of the wing is outside the highly dense mesh of the boundary layer. So the increase of mesh points in the normal direction will result in a better resolution of the main vortex. The secondary vortex separates too early in spanwise direction and the suction peak is too strong. This indicates that the flow in the experiment is more turbulent (higher viscosity delays the secondary separation) than in the numerical simulation.

The agreement at the lower wing surface at 30% root chord can be increased by simulating the body below the wing. The grid sensitivity study shows that the numerical solution is very close to the experimental data if the vortex area is highly resolved. To avoid wasting of mesh points outside the boundary layer in areas where no vortical flow occurs, some grid adaption technique should be used to optimize the mesh and improve the numerical results.

#### COMPARISON WITH EXPERIMENTAL DATA FOR THE WING-BODY CONFIGURATION WITH ROUNDED LEADING EDGE

Most of the experiments have been performed on the delta wing with the rounded leading edge. For this leading edge type the primary separation is highly dependent on viscous effects and not as much on the geometry as it is the case for the sharp-edged wing. Figure 7 shows the surface mesh used and the mesh in the plane of symmetry for the wing-body configuration. The total number of grid points is reduced to 1,000,000

by selecting a C-H mesh topology, keeping the mesh resolution constant compared to the sharp leading edge case. The wing upper surface is resolved by 50°58 points and 65 points are used in the surface normal direction. The total number of blocks is 15. The blocks around the wing have C-H mesh topology, behind the wing a H-H topology is used to simulate the turbulent wake flow with the Baldwin/Lomax turbulence model. Beside the wing tip two blocks with O-H type meshes are introduced to model the flat cut-off tip of the wing correctly (Figure 7).

Experiments for the selected free-stream conditions were carried out at NLR [3] with a Reynolds number based on the root chord length of  $9 \cdot 10^6$  and at DLR [4] with the Reynolds number  $4.5 \cdot 10^6$ . The first step is to compare the two experimental surface pressure measurements in Figure 8. At 60% and 80% root chord the agreement between the two wind tunnel results is excellent, but at 30% root chord a major difference appears. The NLR results show a distinct primary vortex (the pressure minimum is inboard the wing), whereas the DLR results indicate just an onset of primary separation with the suction peak right at the leading edge. This suggests that the difference in the experimental results are due to the differences in the Reynolds numbers. In order to check this, both Reynolds numbers were simulated numerically and the results are shown in Figure 9 for the high and in Figure 10 for the low Reynolds number together with the related experimental data. Differences between the two numerical simulations cannot be found. This indicates that there is another reason that forces the different onset of primary separation in the two wind tunnel results.

The numerical simulations were carried out with the assumption of fully turbulent flow on the entire wing, because experiments with an artificial transition strip at 10% root chord and free transition did not result in differences in the experimental data. Earlier laminar numerical simulations indicate strong dependence of the onset of primary separation on the local flow conditions, i.e. whether the flow is turbulent or not. To check this assumption, the transition position in the numerical simulation is changed from the former leading edge position to 2.5% and 10% local chord. The transition position at 2.5% local chord shows good agreement concerning the pressure distribution at the 30% root chord location (Figure 11) except that the slope of the pressure decrease between the primary attachment line and the vortex core cannot be resolved properly due to the low spanwise mesh density in this area. At 60% root chord the agreement between experimental data and numerical simulation is good but with the restriction that the secondary separation is too dominant. The secondary separation starts too early because of inadequate turbulence modelling and lifts the primary vortex off the wing. This reduces the suction peak calculated on the wing surface. The same applies to the 80% root chord station.

Another possibility to compare experimental data with the numerical solution is the interpretation of oil

flow pictures and skin friction lines as is done in Figure 12. The oil flow picture on the portside of the wing was taken after the tunnel run. The skin friction lines on the starboard side are numerically integrated with a computer graphic system called comadi[9]. To compare both results one has to look at the spanwise position of the primary attachment line and the secondary separation line. These lines are marked with arrows at the 60 % root chord position. For this root chord position the general agreement between the experimental and numerical pressure distribution is excellent with respect to the spanwise position of the attachment and separation line (Figure 11). The spanwise positions are listed in the following table 2:

	attachment line primary vortex	vortex core primary vortex	separation line secondary vortex
$c_p$ -distribution (exp.) [4]	60%	75%	90%
skin friction line (num.)	54%	-	86%
oil flow visualisation (exp.) [5]	78%	-	97%

Table 2. Spanwise position of primary attachment and secondary separation line at 60% root chord.

The first line in the table shows the spanwise position for the experimental data resulting from the pressure measurements, the second line represents the results of the numerically simulated skin friction lines and the third line represents the data figured out from the oil flow picture. Especially the spanwise position of the primary attachment line determined by the oil flow picture deviates from both other results, the experimental pressure distribution and the numerical skin friction lines. The oil flow picture suggests a primary vortex much smaller than in the numerical simulation and the experimental surface pressure result. The reason for this may be found in the oil flow visualisation technique itself. To obtain an oil flow picture, the model surface is covered with some fluid during the wind tunnel is set off. Then the tunnel is turned on and the flow is accelerated to the desired free-stream conditions. To reach these conditions will take a finite time during that the oil flow is moving on the wing surface. If the oil flow dries up before the selected free-stream Mach number in the tunnel is reached, the oil flow picture will show a smaller primary vortex because of lower flow speed.

The numerical simulation of the skin friction lines also indicates that the secondary separation is not adequately modeled. Due to the lack of correct turbulence modelling the secondary separation will be too dominant. So the secondary separation occurs too early (at 86% span at 60% root chord). This will, of course, displace the primary vortex too much inboard (54% span instead of 60% as in the experiment).

The comparison between the oil flow picture and the numerical results indicates that the experimental result represents not the selected free-stream condition. This statement is supported by the fact that both experimental results (oil flow picture and pressure distribution) are inconsistent with each other concerning the spanwise position of primary attachment and secondary separation line.

Figure 13 shows another experimental result for the delta wing with the round leading edge [7]. Here a

three-component laser-doppler anemometer is used to measure the velocity vectors in an plane at 80% root chord. The cross flow above the vortex and a "hole" in the area of the primary vortex are clearly identified. The "hole" indicates a region where no experimental LDA data could be received within an acceptable sampling time. The reason for this will be discussed in the next chapter. Figure 14 presents the numerical result where the loci of the velocity vectors are the same as in the experiment, such that in the ideal case the vectors should be aligned.

Comparing Figure 13 and Figure 14 the velocity vectors above the vortex look the same. Below the vor-

tex close to the wing upper surface, the numerical simulation indicates a high cross flow velocity which is not present in the experimental data. In this area close to the surface the LDA method experiences difficulties. The high cross flow velocity vectors are also found in a FFA experiment (Figure 15, [6]), where the velocity vectors are determined using a 5-hole probe. This experiment validates the numerical simulation.

#### PHYSICAL INTERPRETATION OF THE NUMERICAL DATA FOR THE WING WITH ROUND LEADING EDGE

Figure 13 shows that inside the primary vortex area no velocity vectors could be measured because of low fluid particle density inside the vortical area. These fluid particles are essential necessary for the LDA technique. Another technique to visualize the particle distribution inside a plane is the laser light sheet technique. In this case the wind tunnel is filled with disco smoke ahead of the test section. The smoke is transported with the flow and eliminated by laser light in the plane of interest. Figure 16 from [8] shows the experimental laser light sheet at around 50% root chord. The smokeless hole is clearly identified in the area of the primary vortex. This is an indication that in this area the LDA technique can not be used with the employed seeding to determine the velocity vectors. Two questions arise:

- what is the reason for the "hole" in the laser light sheet, and
- how is it possible to avoid the "hole"?

The numerical simulation will give the answer to these questions.

The creation of a numerical solution for the three dimensional Navier-Stokes equations will result in a huge amount of data of the order of  $8 \cdot 10^6$  words. The only possibility to interpret this data base is to use high ended computer graphics. Used for the results presented in this paper is a graphic system called comadi[9]. Within this program, besides standard graphics like isofrings, solid surfaces etc., more

sophisticated graphics can be employed for the analysis of the data. One can, for example, find vortices automatically. Not only well known vortical structures like primary and secondary vortex can be found but also vortical structures unknown in advance are identified by the program. The technique to do this is described in the appendix.

The information given by the oil flow technique in the experiment which shows the primary attachment line or the secondary separation line can also be extracted from the numerical results (Figure 17). In Figure 18 the global information is reduced to the important lines. The primary attachment line starts at about 10% root chord for the selected free-stream conditions. Streamlines starting ahead do not pass under the primary vortex and remain between the plane of symmetry and the primary attachment line. At about 25% root chord the primary separation line can be identified. Only skin friction lines starting in this very small area between 10% and 25% root chord are passing below the main vortex. At about 60% root chord the open secondary separation takes place. Again the secondary separation line is formed only by skin friction lines starting between 10% and 25% root chord.

Figure 19 shows the streamlines of the primary and secondary vortex as well as an additional vortex close to the plane of symmetry. This additional vortex was earlier found by applying the laser light sheet technique ([8]). The streamlines are plotted with a hidden-line technique which allows a detailed insight of the vortex formation. The core of the vortex is displayed by black lines only, the outer part is represented by gray (coloured in the original plot) lines. It is clearly seen, that the outer-part streamlines do not move towards the center of the vortex. They do not mix up with streamlines representing the vortex core.

Figure 20 shows a sketch of relevant selected streamlines. The area of the core is marked with number one. The streamlines marked with the number two separate at the primary separation line (number four) on the front part of the wing, turn around the vortex core and separate again at the primary separation line coming from the plane of symmetry. The same is valid for the streamlines marked with number three, except that these streamlines will form the secondary vortex because of the positive pressure gradient below the primary vortex core and the leading edge of the wing.

After looking at the skin friction lines and the streamlines the question of the "hole" of the vortex in the laser light-sheet picture is considered. Figure 21 is a perspective view from the rear of the vortex in the direction of the origin of the vortex. The streamline number two in Figure 20 moves around the leading edge, separates at the primary separation line number two in Figure 21, turns around the vortex core towards the primary attachment line (number three), separates at the secondary separation line (number four) and reattaches close to line number five.

For the laser light sheet technique the area ahead of the wing is homogeneously filled with smoke. Moving downstream the smoke is also in the small ribbon (left white in Figure 21) below the wing. The particle density in this ribbon is of course the same as in front of the wing. Moving downstream this ribbon will be extended over the whole vortex area so that the particle density will be reduced, resulting in the "hole" in the vortex area.

To verify the above statement the laser light

sheet technique was simulated numerically. Start points for streamline integration were homogeneously distributed in front of the wing to simulate the smoke at the inlet plane of the wind tunnel test section (Figure 22). The integration of the streamlines is then performed for the whole area. Like the laser light sheet illuminates only a small slice out of the flow field, the graphic program cuts a plane with finite depth out of the streamlines (Poincaré cut). The result for this simulation is shown in Figure 23 together with the experimental laser light sheet picture. The numerical result shows the same topology as the experiment. The area of the vortex core is not filled with smoke (particles).

For the LDA measurement technique it would be necessary to feed disco smoke into the primary vortex very close to its origin, that is directly off the surface and between 10% and 25% root chord. The other possibility is to eject smoke out of the wing directly into the vortex. This is of course a problem because the origin of the vortex is unknown in advance. Additionally, changes in the flow conditions will result in changes of the position of the onset of the primary vortex.

#### DELTA WING-CANARD CONFIGURATION

The investigated delta wing-canard configuration consists of two sharp-edged wings with cut-off wing tips. The leading edge sweep of the canard is 60°, the trailing edge sweep is 35°. The main wing geometry is the same as for the wing alone configuration. The surface mesh used for the numerical simulation is shown in Figure 24. Because of the sharp-edged wings the H-H-type mesh topology is used, although it is well known that this type of mesh is not very efficient away from the wing. The total number of mesh points is 2,000,000, that is twice the number of points used for the C-H-mesh for the wing alone configuration, although the mesh resolution is not increased. For simplicity the numerical simulation is performed with the assumption of laminar flow. Note that turbulence modelling with scalar approach is rather difficult. Typical results for the selected free-stream conditions:

- free-stream mach number  $M_\infty = 0,85$
- angle of incidence  $\alpha = 10^\circ$
- yaw angle  $\beta = 0^\circ$
- Reynolds numbers  $Re_\infty = 4,5 \cdot 10^6$

are shown in the following Figures.

Figure 25 shows the surface pressure distribution on the canard and the wing. The canard vortex separates at the apex of the wing very similar to the flow for the wing alone case. A small secondary vortex is also formed below the main canard vortex. At the rear part of the canard a strong pressure gradient in the plane of symmetry is visualized indicating a shock. The primary separation on the main wing is very different from the wing alone configuration. The onset of primary separation is now delayed due to the interaction between the canard vortex and the main wing primary vortex. The separation of the main wing primary vortex starts not at the apex of the wing as it was the case for the wing alone configuration. Below this vortex again a secondary vortex can be found.

A comparison of experimental ([3]) and numerical pressure distribution is shown in Figure 26. At the 30% wing root chord station the agreement between the experimental data and the numerical simulation is good on the upper wing surface. On the lower wing surface the disagreement is due to the influence of the

fuselage which is not modeled in the numerical simulation. At 60% and 80% wing root chord the spanwise position of the primary vortex is well predicted but the suction peak below the vortex core is not well simulated. The reason for this is the strong influence of the secondary vortex. Due to the laminar flow assumption this vortex is enlarged, and separates too early in spanwise direction. So the main vortex is lifted off the wing increasing the surface pressure on the wing upper surface. At the lower wing surface the influence of the fuselage can be neglected as in the wing alone case. The spanwise position of the vortex core is well predicted.

Figure 27 shows the total pressure loss distribution in spanwise direction for 13 different cuts, starting at -10% wing root chord on the canard. The maximum total pressure losses are more or less related to the vortex core area. The canard primary vortex forces the wing primary vortex to separate not at the wing apex but at about 30% root chord. Both vortex systems remain uncoupled. The canard primary vortex as well as the wing primary vortex are accompanied by the two trailing edge counter rotating vortices.

Figure 28 shows the streamlines of the canard vortex, the canard trailing edge vortices and the wing primary- and secondary vortex. It is clearly seen, that the canard and the wing vortex remain separated, that the canard vortex is above the wing vortex and that the wing vortex originates far outboard beside the canard vortex. The canard vortex is highly accelerated over the main wing. This reduces the cross flow velocity relative to the axial velocity resulting in a smaller "swirl" of the canard vortex.

#### CONCLUSIONS

The paper discussed the validation of the numerical method. The first step was the sensitivity study concerning mesh dependency of the solution for the sharp-edged delta wing. The comparison with experimental data indicates that the agreement is improved if the mesh is adapted to the vortical flow solution, yielding a very fine mesh in the vortex region. If the mesh is sufficiently fine the numerical solution shows excellent agreement with the experimental data.

More extensive investigations were performed for the delta wing with the round leading edge. Here the influence of the transition from laminar to turbulent flow conditions were found to be very important for the onset of primary separation. The location where the transition takes place is not known in advance and has to be determined by careful comparison with experimental data. Once the transition position is found, the agreement between experimental and numerical results is good. Considering other experimental data like oil flow pictures or LDA measured velocity vectors the numerical simulation gives some hints, where the experiments require special care. Examples are the velocity distribution below the primary vortex or the attachment line of the primary vortex in the oil flow picture.

On the other hand the comparison indicates that the numerical simulation is strongly dependent on the turbulence model used. This turbulence model is not adequate to simulate separated flows well. The primary separation is well simulated because of some modifications of the turbulence model, but especially the secondary separation is predicted much too early resulting in a slight falsification of the entire flow solution.

Topological flow considerations (or numerical

flow field visualisations) allow an explanation for the "hole" in the laser light sheet photograph. The streamlines, that is for stationary flow the smoke particle traces, do not swirl into the vortex core so that no smoke particle will be transported into the core area. Here the used computer graphic system was extremely helpful for understanding the flow phenomena. A short introduction to this graphic system will be presented in the appendix of this paper.

The results for the delta wing-canard configuration show that the two vortex systems remain uncoupled. The main wing primary vortex separation is delayed due to the interaction with the canard primary vortex. Comparison with experimental pressure distribution shows that the spanwise position of the vortex is well predicted, but the pressure minimum is not in good agreement with experimental values due to the laminar flow assumption.

#### APPENDIX

The development of post processing systems for CFD results are going on in almost every institution treating fluid flow fields. There are three main reasons for this. One is the visualization of the huge amount of data because the eyes are the broadest channel of information to a human being. The second is the application of tools to reveal the physics of a flow field. New diagnostic tools have been suggested for the classification and description of the physics in order to reduce the huge amount of information, e.g. by capturing the topology of the flow field. The third reason is closely related to the second. The validation of the CFD results is mainly achieved by comparison to other numerical results or to experimental data. While for other CFD results the same tools may be applied, the experimentalists are considerably restricted in their tools. Thus comparisons can only be made by simulating the experimental tools, e.g. light sheets, schlieren and shadow pictures. Comparisons of oil flow pictures and lines of skin friction as well as particle traces and streamlines have been extensively applied, though there are shortcomings due to the finite mass and volume of particles in experiment.

The immense number of tools for the investigation of data and ways of graphical representation of data require an arrangement of these possibilities in a system that

- leads to a good synopsis for the user,
- makes selections transparent to the user,
- allows enhanced control by the user,
- allows easy implementation of innovations.

The analysis and graphics system *comadi* has been developed along these lines. As the understanding of geometrical entities as grid fields, surfaces built up from polygons, lines, etc is common, they are introduced to the system as data. The system is considered as a set of *data transformations* from and to these entities:

- *Reading / Writing:* Transformation (conversion) of file data to system data and vice versa
- *Making:* Transformation of system data into other system data. The transformations may be described by physical laws (evaluation of Mach number, pressure loss) or by geometrical operation (contours, integration of lines, plane-cuts)
- *Displaying:* Transformation of system data into an image. The creation of start points using mouse



position may be considered as an inverse of this transformation.

A geometrical illustration of this idea is given in Figure 29. The kinds of data are the entries of a chessboard, while the transformations are arranged in the third dimension. Though the display to the screen and the input/output operations and the functions may be treated in the same abstract way as data transformations, they are distinguished in order to have a better understanding for the user and to emphasize their roles as shown in Figure 30. The name *comadi* is derived from this construction: data compile make & display [9].

The interactive user interface is mouse controlled and uses menu and button techniques. A window with editing facilities is supplied for input and output of control strings like file names. The repeatability of creation and drawing of data without interactive intervention as well as the creation of movie pictures is furnished.

Currently the following kinds of data have been introduced:

- *Grid Field 3d* and *Grid Field 2d* are considered as the usual output of computer programs for flow simulation. These results may be stored in the system up to four dimensions. The values of coordinates of vectors or values of scalars are stored on each node of the grid. For reasons of storage saving a subspace of the grid nodes may be read in. The information of the original grid is saved during data transformations. Grid Fields are also the result of data transformation, e.g. evaluation of Mach number, enthalpy, norm of vector. The information contained in Grid Fields may be displayed in several ways, e.g. the grid edges in different manners, as a shaded surface using some given direction of light, or with colours corresponding to intervals of a scalar function (colour coding).
- *Surface of Polygons* and *Surface of Polygons with Scalar* are used for displaying generally shaped surface, which might be created as the contour surface of some function being constant, e.g. Mach number. They can have a further information (scalar value) at each node that may be used for shading the surface. Thus it may nearly be displayed as grids.
- *Line* and *Line with Scalar* are e.g. the result of integrations on fields of directions (stream lines) or of contours of constant values of some function on a given surface (isobars). They can have a further information (scalar value) at each point that may be used for shading the line.
- *Start Points* are used to describe the initial conditions of lines in direction fields. They may be created from other kinds e.g. by discriminating an interval of scalar values.
- *Points* and *Points with Scalar* may be applied for displaying experimental data for comparison. They can have a further information (scalar value) that may be used for colouring the point. Further applications are the representation of time lines which simulate the bubble method in water tunnels and singular points extracted from a vector field.
- *Information on Block Connections* are used for controlling the integration of direction fields being stored in several sets (blocks) of grid fields.
- *Pixrects* may be applied for storage and display of

images of any size from or to the screen or of images from experiments, e.g. laser light sheets, shadow graphs, schlieren photos, oil flow patterns

- *Text & Layout* may be applied for storage and display of texts.
- *GINO Simulation Data* are used for simulation of calls to several subroutines of the GINO plotting system using constant parameters
- *Axis Parameter* may be applied for storage and display of scaling axis of rather general nature, e.g. curved

The memory for the storage of these data is allocated dynamically. Thus the machine memory is optimally used.

#### Detection of Vortices

As mentioned in the text above the graphic system is able to detect vortices automatically. For this *comadi* evaluates the discriminant for complex eigenvalues of the gradient tensor of the velocity field, i.e. in cartesian coordinates (x,y,z)

$$\begin{pmatrix} u_x & v_x & w_x \\ u_y & v_y & w_y \\ u_z & v_z & w_z \end{pmatrix}$$

where (u,v,w) are the cartesian components of the velocity vector and  $u_x$ , etc are the respective partial derivatives. If the discriminant indicates complex eigenvalues there exist locally a generic vortex in a gaussian frame, where the local velocity is at rest [10]

In order to have the more accustomed two-dimensional view the tensor may be projected on a plane being perpendicular to the local direction of velocity. In this case the regimes of the flow field may be classified as shown in Figure 31. As this may be evaluated at every point it may also be used to indicate volumes with vortices. A more convenient and uniform scaling of the discriminant is achieved when it is locally divided by the norm of the velocity. Typical results are shown in paper No. 9 of this report [11].

#### 1. Bibliography

- [1] Williams, B.R., Kordulla, W., Borsi, M., Hoeijmakers, H.W.M.: *Comparison of Solution of Various Euler Solvers and One Navier-Stokes Solver for the Flow About a Sharp-Edged Delta Wing*. Paper 2 of this Symposium
- [2] Hilgenstock, A.: *Ein Beitrag zur numerischen Simulation der transsonischen Strömung um einen Deltaflügel durch Lösung der Navier-Stokeschen Bewegungsgleichungen*. Dissertation Universität Karlsruhe (TH), DLR-FB 90-13, 1990
- [3] Hirdes, R.H.C.M.: *US/EUROPEAN VORTEX FLOW EXPERIMENT. Test Report of Wind Tunnel Measurements on the 65 deg. Wing in the NLR High Speed Wind Tunnel HST*. NLR TR 85046 L, May 1985.
- [4] Hartmann, K.: *Force and Pressure Measurements Including Surface Flow Visualization on a Cropped Delta Wing*. in Proceedings on the "International Vortex Flow Experiment on Euler Code Validation", Stockholm, October 1-3, 1986 (published by FFA), p. 63-88.
- [5] Hartmann, K., Bötefisch, K.A.: *private communication*. 1989.

- [6] Rizzi, A., Müller, B.: *Large-Scale viscous Simulation of Laminar Vortex Flow Over a Delta Wing* AIAA Journal, vol 27, No. 7, p 833ff, 1989
- [7] Bötetfisch, K.A., Paltek, D., Sauerland, K.-H.: *Three Component LDA Measurements on a 65 Deg Delta Wing* DFVLR-IB 222-87 A34, 1987
- [8] Bötetfisch, K.A., Hartmann, K.: *Flow Field Visualisation Study on a 65 Degree Delta Wing at  $M_\infty = 0.85$*  Strömung mit Ablösung, S 159-168, DGLR-Bericht 88-05, 1988.
- [9] Vollmers, H.: *A Concise Introduction to COMADI* DLR-IB 222 - 89 A22, 1989.
- [10] Vollmers, H., Kreplin, H.-P., Meier, H.U.: *Separation and Vortical-Type Flow around a Prolate Spheroid - Evaluation of Relevant Parameters* AGARD CP 342, April 1983, Rotterdam, Netherlands
- [11] Dallmann, U., Hilgenstock, A., Riedelbauch, St., Schulte-Werning, B., Vollmers, H.: *On the Footprints of Three-Dimensional Separated Vortex Flows About Blunt Bodies*. Paper 9 of this Symposium

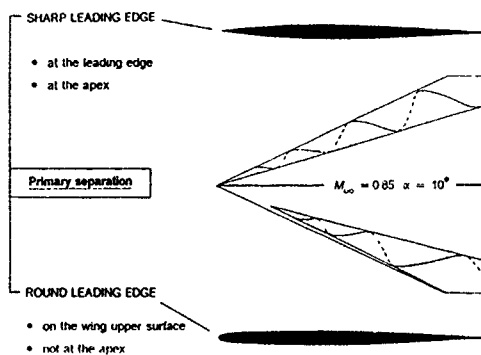


Figure 1. Geometry of the delta wing as well as primary separation for different types of leading edges.

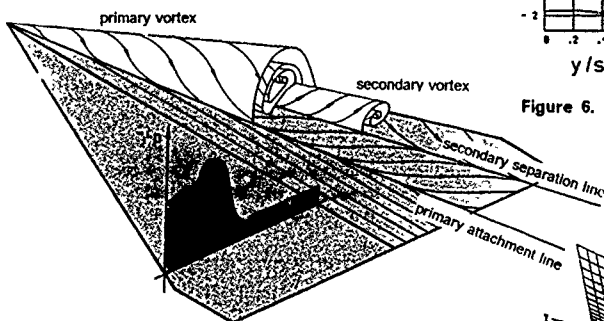


Figure 2. Vortical flow over a sharp edged delta wing.

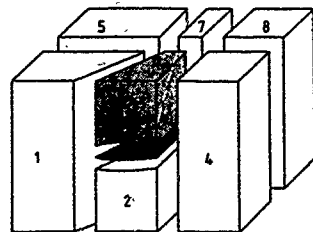


Figure 3. Block structure for the sharp edged delta wing.

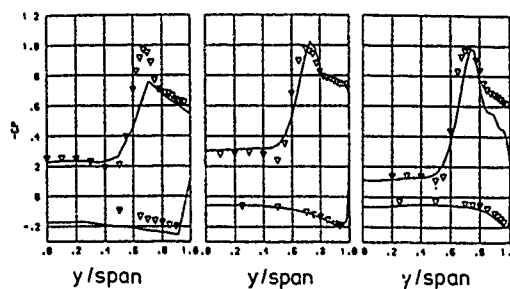


Figure 4.  $c_p$ -distribution at  $x/cr = 0.3$  (left),  $0.6$  (middle) and  $0.8$  (right), (reference grid,  $40^*40^*40$ ,  $M_\infty = 0.85$ ,  $\alpha = 10^\circ$ ).

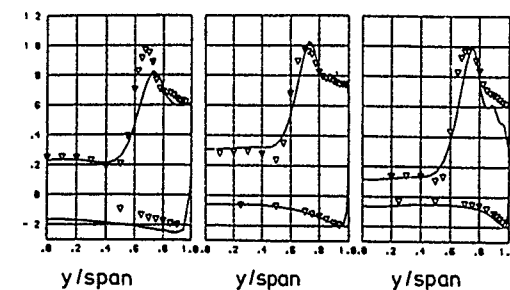


Figure 5.  $c_p$ -distribution at  $x/cr = 0.3$  (left),  $0.6$  (middle) and  $0.8$  (right), (grid refinement in spanwise direction,  $40^*70^*40$ ,  $M_\infty = 0.85$ ,  $\alpha = 10^\circ$ ).

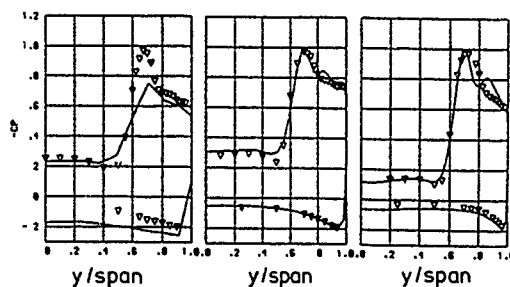


Figure 6.  $c_p$ -distribution at  $x/cr = 0.3$  (left),  $0.6$  (middle) and  $0.8$  (right), (grid refinement in wing normal direction,  $40^*40^*70$ ,  $M_\infty = 0.85$ ,  $\alpha = 10^\circ$ ).

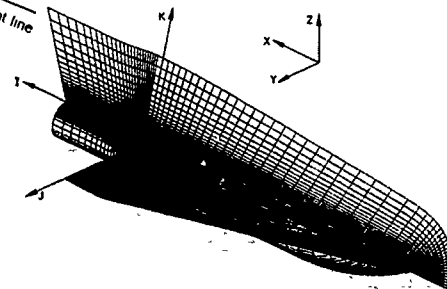


Figure 7. Wing-body configuration: surface mesh and mesh in the plane of symmetry, with C-H, H-H, and O-H mesh topologies, blocktopology on the right.

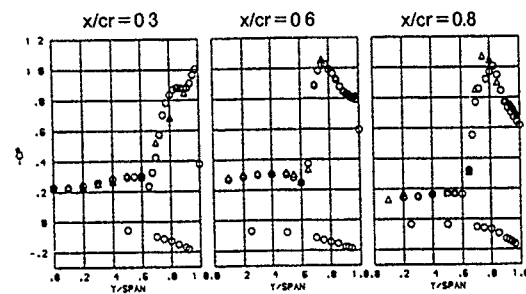


Figure 8 Comparison of surface pressure distribution for two wind tunnels, triangles = NLR, circles = DLR-measurements ( $M_\infty = 0.85$ ,  $\alpha = 10^\circ$ )

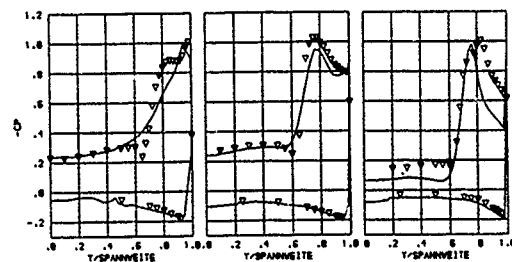


Figure 9.  $C_p$ -distribution at  $x/cr = 0.3$  (left),  $0.6$  (middle) and  $0.8$  (right), transition at  $0\%$ , measurement (NLR): triangles,  $Re = 9,000,000$ ,  $M_\infty = 0.85$ ,  $\alpha = 10^\circ$ .

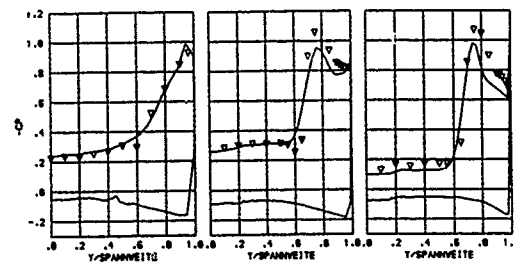


Figure 10.  $C_p$ -distribution at  $x/cr = 0.3$  (left),  $0.6$  (middle) and  $0.8$  (right), transition at  $0\%$ , measurement (DLR): triangles,  $Re = 4,500,000$ ,  $M_\infty = 0.85$ ,  $\alpha = 10^\circ$ .

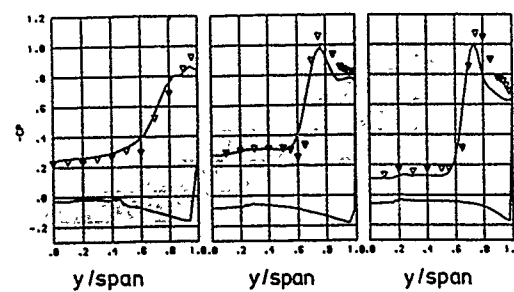


Figure 11.  $C_p$ -distribution at  $x/cr = 0.3$  (left),  $0.6$  (middle) and  $0.8$  (right), ( $Re = 4,500,000$ ; transition at  $2.5\%$ ,  $M_\infty = 0.85$ ,  $\alpha = 10^\circ$ ).

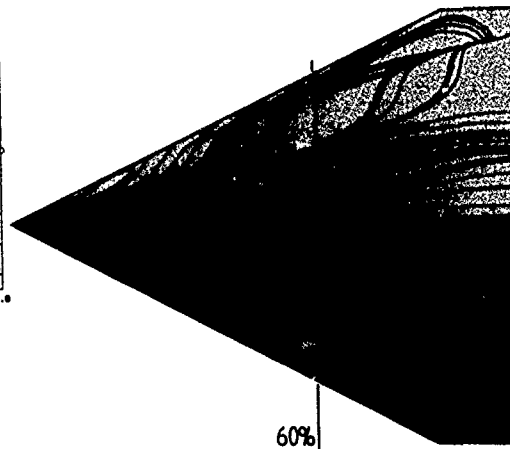


Figure 12. Comparison between oil flow picture (bottom) and skin friction line (top) at  $x/cr = 0.6$  ( $M_\infty = 0.85$ ,  $\alpha = 10^\circ$ ).

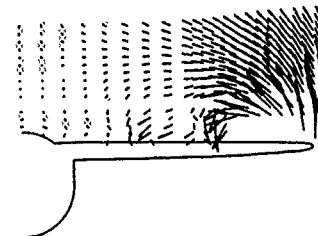


Figure 13. Velocity vectors at  $x/cr = 80\%$  (LDA-technique,  $M_\infty = 0.85$ ,  $\alpha = 10^\circ$ ).

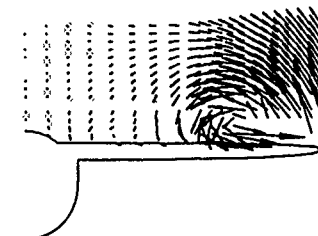


Figure 14. Velocity vectors at  $x/cr = 80\%$  (numerical results at the same location as the experimental data,  $M_\infty = 0.85$ ,  $\alpha = 10^\circ$ ).

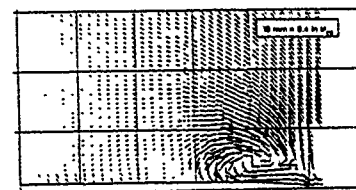


Figure 15. Velocity vectors at  $x/cr = 80\%$  (five hole probe measurements of FFA-Schweden,  $M_\infty = 0.85$ ,  $\alpha = 10^\circ$ , [6]).

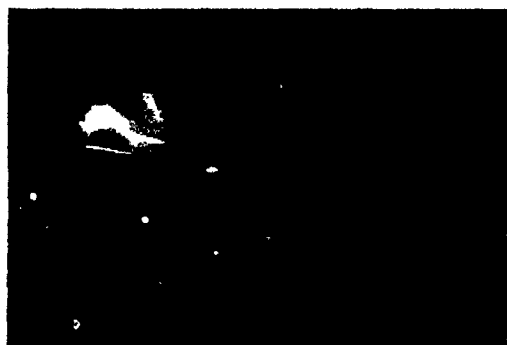
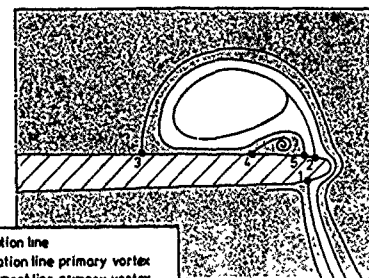


Figure 16. Laser light sheet orthogonal to the plane of symmetry ( $M_\infty = 0.85$ ,  $\alpha = 10^\circ$  [8]).



- 1 stagnation line
- 2 separation line primary vortex
- 3 attachment line primary vortex
- 4 separation line secondary vortex
- 5 attachment line secondary vortex

Figure 21. Streamline sketch (three dimensional drawing, looking inside the vortex core from the rear of the wing).

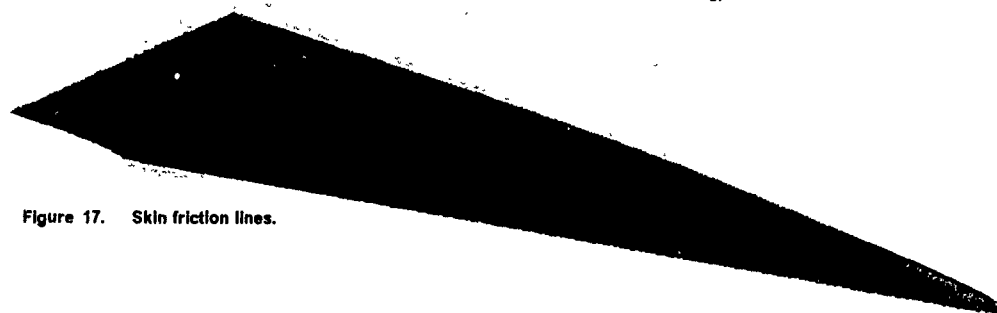


Figure 17. Skin friction lines.

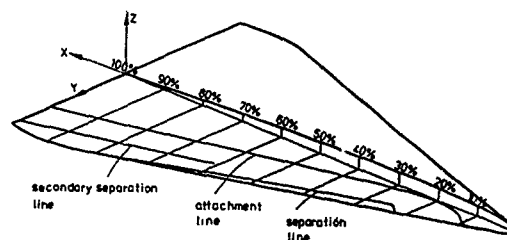


Figure 18. Skin friction lines with primary separation line, primary attachment line and secondary separation line (sketch).

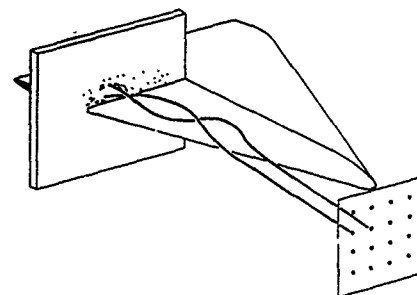


Figure 22. Numerical laser light sheet simulation (sketch).

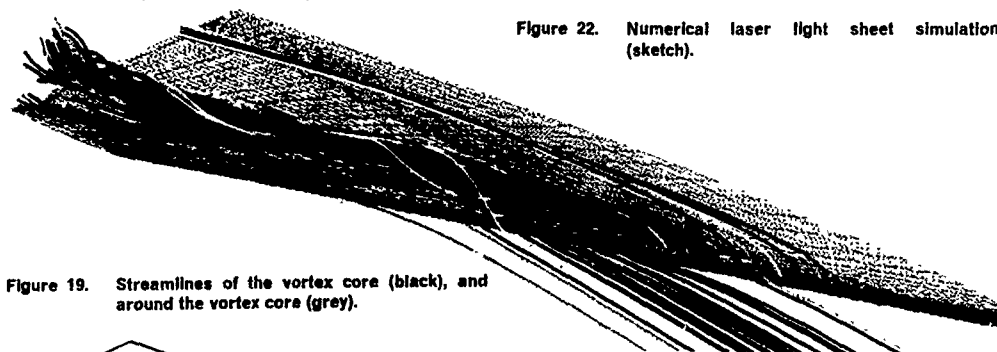
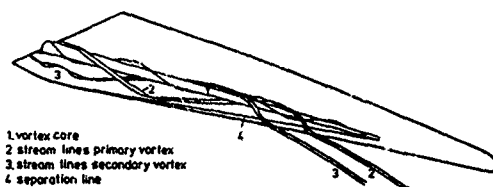


Figure 19. Streamlines of the vortex core (black), and around the vortex core (grey).



- 1 vortex core
- 2 stream lines primary vortex
- 3 stream lines secondary vortex
- 4 separation line

Figure 20. Sketch of selected streamribbons around the vortex core.



Figure 23. Numerical laser light sheet simulation and comparison with experimental result.

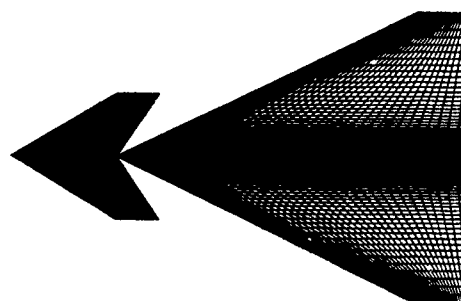


Figure 24. Surface grid for the delta wing-canard configuration. Canard grid:  $50^\circ 40'$ , wing grid:  $50^\circ 40'$ .

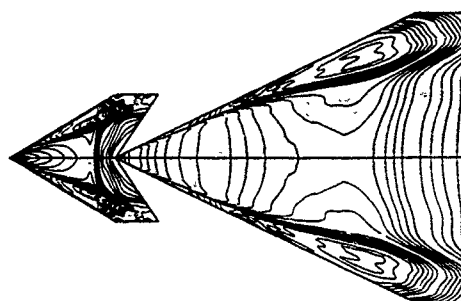


Figure 25. Surface pressure distribution for the delta wing-canard configuration.

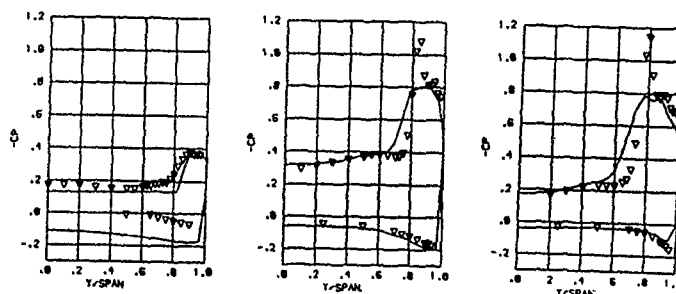


Figure 26.  $c_p$ -distribution at  $x/cr=0.3$  (left),  $0.6$  (middle) and  $0.8$  (right), (WC1-SLE,  $M_\infty = 0.85$ ,  $\alpha = 10^\circ$ ).

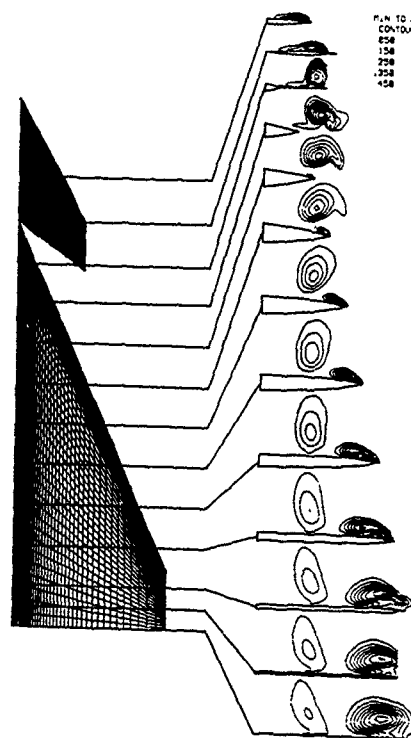


Figure 27. Total pressure loss at  $x/cr = -0.1, 0, 0.1, 0.2, \dots, 0.8, 0.9, 1.0$  and  $0.95$  wing root chord (WC1-SLE,  $M_\infty = 0.85$ ,  $\alpha = 10^\circ$ ).

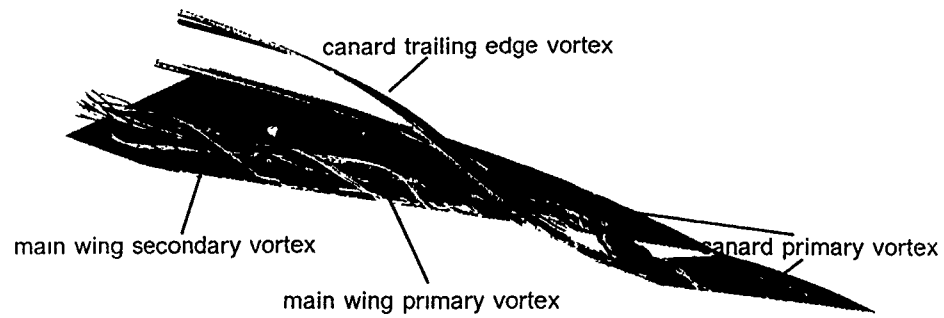


Figure 28. Streamlines of canard-vortex, canard trailing edge vortex and main wing primary and secondary vortex (WC1-SLE,  $M_\infty = 0.85$ ,  $\alpha = 10^\circ$ ).

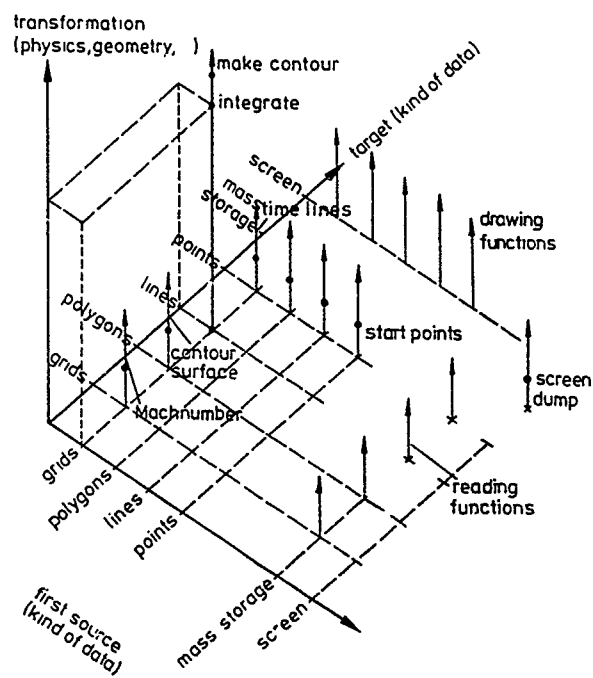
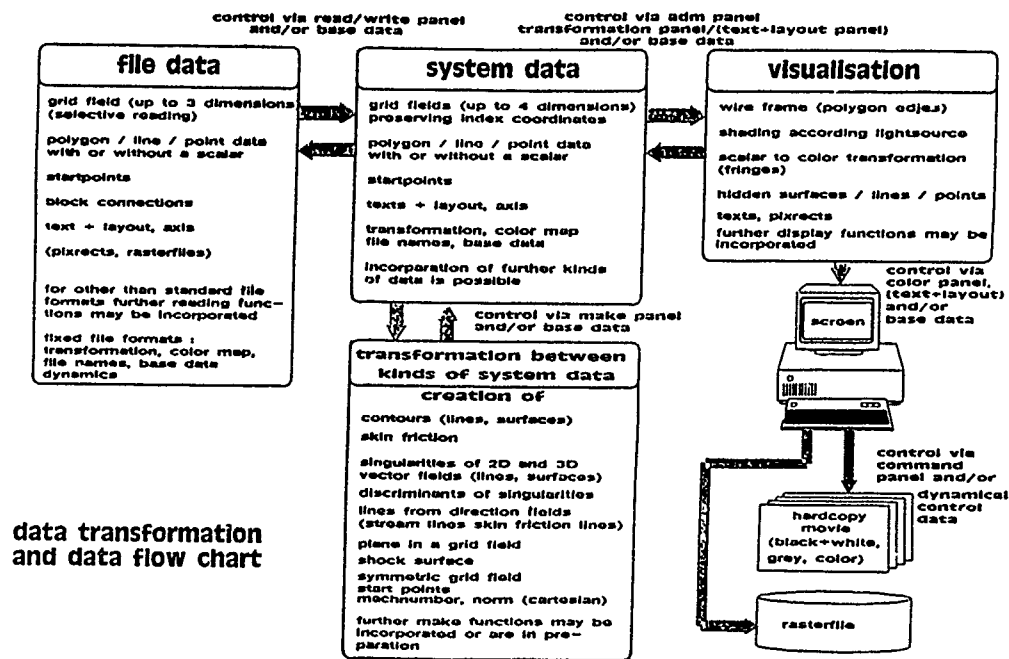


Figure 29. Data transformation model of COMADI.





data transformation  
and data flow chart

Figure 30. Data flow chart of COMADI.

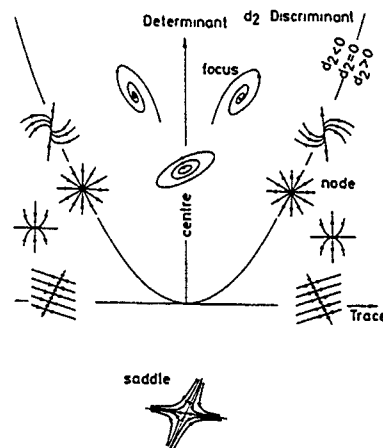


Figure 31. Behaviour of autonomous ordinary differential equations of two degrees of freedom in different regions.

## Calculation of Hypersonic Leaside Vortices Over Blunt Delta Wings

Arthur Rizzi

FFA, The Aeronautical Research Institute of Sweden  
S-16111 Bromma, Sweden

Earl M. Murman

Department of Aeronautics & Astronautics  
Massachusetts Institute of Technology  
Cambridge, MA 02139, USA

Peter Eliasson

KTH, The Royal Institute of Technology  
S 10044 Stockholm, Sweden

Kuok-Ming Lee

Department of Aeronautics & Astronautics  
Massachusetts Institute of Technology  
Cambridge, MA 02139, USA

### Abstract

We investigate hypersonic vortical flow on the leaside of a blunt delta wing by solving both the Euler equations and the Navier-Stokes equations with two different and independent numerical methods in order to evaluate the inviscid and viscous mechanisms of leaside vortex formation. The emphasis of the paper is on the analysis of the results, which includes a very detailed and side-by-side comparisons of Euler versus Navier-Stokes results from the same method as well as comparisons of results from the two different methods. The intent is to reach a reasonable understanding of the computed flow structures, including flow separation, shear layers, vortices, shock waves, entropy losses. We have found that instead of the concentrated vortex usually found over a delta wing in transonic speed, the flow in hypersonic speed is dominated by a shear layer that separates just past the blunt leading edge and forms a more distributed vortical region over the wing. However, the flow predicted by Euler is quite different from Navier-Stokes, also distinct from the transonic case. The Navier-Stokes results agree qualitatively with the sparse experimental data that we have, but not quantitatively. The quantitative details of the solutions, but not the overall flow structure, show some sensitivity to mesh resolution. The windside features like the bow shock agree well in all the numerical solutions. But there are substantial discrepancies in the prediction of the Stanton number on the wing surface.

### Introduction

Current interest in developing advanced space planes like the NASP, HERMES, and the superConcorde has brought forth the problem of understanding the leaside vortical flow over these vehicles when they travel at hypersonic speeds. Unlike the subsonic and transonic speed regimes, these vortical flows have little effect on the lift performance and the

effectiveness of control surfaces since the leaside pressures are near vacuum. They are however characterized by shock waves, separated flow, and shear layers, and these may have important consequences on heating and local effects like a shock wave or shear layer impinging on a configuration detail, e.g. a flap or other protuberance. What is of interest then are the flow features of this low-pressure region, what its structure is, and what interactions take place. It is here that our current knowledge is incomplete.

### Features of Hypersonic Wing Flow

The way we approach the problem is to study the simpler but typical case of hypersonic flow over a wing. Current understanding follows from classical analysis based on flow past a flat thin delta wing of zero thickness. Squire [1] and later Miller and Wood [2] among others have studied the various types of structures that may occur (Fig 1). At moderate supersonic speed the bow shock is detached, and the flow attaches on the windward side inboard of the leading edge. It cannot expand smoothly around the sharp leading edge but separates and develops into a vortex. At higher speed the attachment point shifts outboard to the leading edge. Now the flow can deflect smoothly around the leading edge through a Prandtl-Meyer expansion fan. But at some inboard point on the leeward side it must turn in the freestream direction through a cross-flow shock. This shock may cause the boundary layer to separate. In an Euler simulation it may be strong enough to create sufficient vorticity and thus vortex flow. At still higher speeds the bow shock attaches at the leading edge, but the expansion and crossflow shock remain as at lower speed.

There are, however, limits to each of the above processes. For example Fig 2 presents the usual classical analysis of flow normal to the leading edge. The flow expands around the leading edge until it is parallel to the upper surface, i.e. it remains attached. But if the freestream Mach number is great enough, it can happen that the flow expands

to vacuum before it becomes parallel to the upper surface. Another situation occurs on the upper surface. The leading edge influences the flow only inside the Mach cone shown in Fig. 2. Outside of it the flow is in the freestream direction, and the crossflow shock appears where these two regions meet. Again, if the speed is great enough, the trace of the Mach cone can move to the left of the centerline. Nonlinear effects must be important and the exact flow pattern is not known. Figure 2 summarizes the limits of shock detachment and expansion to vacuum [L. Squire, private communication]. For a 70° swept delta wing, vacuum is reached in the flow at  $M_\infty = 7$  and  $\alpha = 40^\circ$ . The conclusions from this analysis lose precision when the wing has a round leading edge and thickness. The analysis must then be carried out by numerical solution.

An important issue is the creation of vorticity in the numerical solution of an inviscid flow. At high supersonic Mach numbers and angles of attack, the entropy loss through the bow shock can vary considerably from windward to leeward side. From Crocco's theorem, this can introduce significant vorticity. These features are generally well understood for cone flow [3] of circular cross-section where a vortical layer forms on the cone surface which is wetted by streamlines passing through various points on the shock, and a vortical singularity emerges on the leeward side symmetry point. The corresponding pattern which develops as the cone is continuously distorted into thinner elliptical delta wings is not known (at least to the present authors), but it is possible that the vorticity generated by the bow shock could concentrate into a leeward vortex. The same conclusion holds for the crossflow shocks.

#### Outline of Paper

The subject of the paper is the numerical simulation of a hypersonic vortical flow on the leeward side of a blunt delta wing. The primary results to be presented are for flow at  $M_\infty = 7.15$  and  $30^\circ$  incidence past a thick delta wing of  $70^\circ$  sweep and constant leading edge radius; a non-conical wing. We study this flow by solving both the Euler equations and the Navier-Stokes equations with two different and independent numerical methods in order to evaluate the inviscid and viscous mechanisms of leeward vortex formation. Both methods are cell-centered finite-volume techniques, but they differ in a number of ways, and the computer codes have been written completely independently. The first [4,5] is denoted KTH, and the second [6,7] MIT. Some experimental measurements are available for comparison. The emphasis of the paper is on the analysis of the results, which includes a very detailed and side-by-side comparisons of Euler versus Navier-Stokes results from the same method as well as comparisons of results from the two different methods. The intent here is to reach a sound description and reasonable understanding of the computed flow structures, including flow separation, shear layers, vortices, shock waves, and entropy losses. Surface pressure and heat transfer results are also presented.

#### Numerical Method

We describe only briefly the two finite-volume approaches [4-7] we take to solve the Navier-Stokes equations written in Cartesian coordinates over a control volume  $V$  with boundary  $\partial V$

$$\frac{\partial}{\partial t} \iiint_V u dV + \iint_{\partial V} \mathcal{H}(u) \cdot n dS = 0 \quad (1)$$

where the vector of state variables  $u = (\rho \quad \rho u \quad \rho v \quad \rho w \quad \rho E)^T$  contains density  $\rho$ ,  $x$ ,  $y$ , and  $z$  components of velocity  $u$ ,  $v$ , and  $w$ , and energy per unit mass  $E$ . The  $x$  direction is aligned with the body axis. The flux tensor  $\mathcal{H}$  is composed of inviscid and viscous parts

$$\mathcal{H} = (F_I - F_V)e_x + (G_I - G_V)e_y + (H_I - H_V)e_z \quad (2)$$

in the  $x$ ,  $y$ , and  $z$  coordinate directions, respectively.

The inviscid fluxes are given by

$$F_I = \begin{pmatrix} \rho u \\ \rho u^2 + p \\ \rho uv \\ \rho uw \\ \rho uH \end{pmatrix}, \quad G_I = \begin{pmatrix} \rho v \\ \rho uv \\ \rho v^2 + p \\ \rho vw \\ \rho vH \end{pmatrix}, \quad (3)$$

$$H_I = \begin{pmatrix} \rho w \\ \rho uw \\ \rho vw \\ \rho w^2 + p \\ \rho wH \end{pmatrix},$$

and the viscous fluxes given by

$$F_V = \begin{pmatrix} 0 \\ \tau_{xx} \\ \tau_{xy} \\ \tau_{xz} \\ u\tau_{xx} + v\tau_{yx} + w\tau_{zx} - q_x \end{pmatrix}, \quad G_V = \begin{pmatrix} 0 \\ \tau_{yx} \\ \tau_{yy} \\ \tau_{yz} \\ u\tau_{xy} + v\tau_{yy} + w\tau_{zy} - q_y \end{pmatrix}, \quad (4)$$

$$H_V = \begin{pmatrix} 0 \\ \tau_{zx} \\ \tau_{zy} \\ \tau_{zz} \\ u\tau_{xz} + v\tau_{yz} + w\tau_{zz} - q_z \end{pmatrix}.$$

$H$  is the stagnation enthalpy,  $H = E + p/\rho$ , and  $p$  is the static pressure.

Components of the viscous stress tensor are,

$$\begin{aligned}\tau_{xx} &= \frac{2}{3}\mu \left( 2\frac{\partial u}{\partial x} - \frac{\partial v}{\partial y} - \frac{\partial w}{\partial z} \right) & \tau_{xy} = \tau_{yx} &= \mu \left( \frac{\partial u}{\partial y} + \frac{\partial v}{\partial x} \right) \\ \tau_{yy} &= \frac{2}{3}\mu \left( 2\frac{\partial v}{\partial y} - \frac{\partial u}{\partial x} - \frac{\partial w}{\partial z} \right) & \tau_{yz} = \tau_{zy} &= \mu \left( \frac{\partial v}{\partial z} + \frac{\partial w}{\partial y} \right) \\ \tau_{zz} &= \frac{2}{3}\mu \left( 2\frac{\partial w}{\partial z} - \frac{\partial u}{\partial x} - \frac{\partial v}{\partial y} \right) & \tau_{zx} = \tau_{xz} &= \mu \left( \frac{\partial w}{\partial x} + \frac{\partial u}{\partial z} \right)\end{aligned}\quad (5)$$

The heat flux terms are

$$q_x = -k \frac{\partial T}{\partial x} \quad q_y = -k \frac{\partial T}{\partial y} \quad q_z = -k \frac{\partial T}{\partial z}, \quad (6)$$

or, using the perfect gas relation  $H = C_p T + .5(u^2 + v^2 + w^2)$  to eliminate the temperature  $T$ , and introducing the Prandtl number  $Pr = \frac{\mu C_p}{k}$ ,

$$\begin{aligned}q_x &= -\frac{\mu}{Pr} \left( \frac{\partial H}{\partial x} - v \frac{\partial u}{\partial x} - u \frac{\partial v}{\partial x} - w \frac{\partial w}{\partial x} \right), \\ q_y &= -\frac{\mu}{Pr} \left( \frac{\partial H}{\partial y} - u \frac{\partial u}{\partial y} - v \frac{\partial v}{\partial y} - w \frac{\partial w}{\partial y} \right), \\ q_z &= -\frac{\mu}{Pr} \left( \frac{\partial H}{\partial z} - u \frac{\partial u}{\partial z} - v \frac{\partial v}{\partial z} - w \frac{\partial w}{\partial z} \right).\end{aligned}\quad (7)$$

The value of the Prandtl number  $Pr$  was taken as a constant 0.72 for the laminar flow solutions presented in this paper. The Sutherland formula relates the coefficient of viscosity to the local temperature (or enthalpy) and closes the system of equations.

We make the usual finite-volume approximation to Eq.(1) for a hexahedra cell of volume  $V$  (Fig. 3)

$$\begin{aligned}\frac{d}{dt} u_V &= -\frac{1}{V} \iint_{\partial V} \mathcal{H}(u) \cdot n dS \\ &= -\frac{1}{V} \sum_{f=1}^6 \mathcal{H}(u)_f \cdot S_f = \sum_{f=1}^6 F(u)_f\end{aligned}\quad (8)$$

#### Space Discretization: Inviscid Terms

The scheme for the inviscid terms is the same in both codes. It is a cell-centered finite volume discretisation in space that is fully conservative (at steady state with local time stepping). The flux at a cell face is computed as the flux of the average of the two state variables to the left and right of the face. An artificial smoothing term that is a nonlinear blend of second and fourth differences stabilizes this discretisation. The semidiscrete form of the scheme applied to Eq.(8) in one space dimension illustrates these points

$$\frac{d}{dt} u_j = \delta F_j = F_{j+1/2} - F_{j-1/2} \quad (9)$$

where

$$\begin{aligned}F_{j+1/2} &= F\left(\frac{u_j + u_{j+1}}{2}\right) \\ &\quad + \alpha_{j+1/2} \delta u_{j+1/2} - \beta_{j+1/2} \delta^3 u_{j+1/2}\end{aligned}\quad (10)$$

and

$$\alpha_{j+1/2} = \frac{1}{2} \epsilon_2 \left( \frac{1}{\Delta t_j} + \frac{1}{\Delta t_{j+1}} \right) \max(dp_j, dp_{j+1}) \quad (11)$$

$$dp_j = \frac{|p_{j+1} - 2p_j + p_{j-1}|}{|p_{j+1} + 2p_j + p_{j-1}|} \quad (12)$$

$$\beta_{j+1/2} = \max\left(\frac{1}{2} \epsilon_4 \left( \frac{1}{\Delta t_j} + \frac{1}{\Delta t_{j+1}} \right) - \alpha_{j+1/2}, 0\right) \quad (13)$$

It must be pointed out that the numerical smoothing terms have to be treated correctly near boundaries in order to maintain good convergence and to keep the variations in entropy small [8]. The condition for pressure on the wing surface is set by second-order extrapolation from the field values.

#### Space Discretization: Viscous Terms

The usual boundary conditions are enforced on the wing, which is isothermal  $T_w = 288K$ . The farfield is assumed to be inviscid and is treated by either setting or extrapolating the locally one dimensional Riemann invariants. But the viscous terms are treated differently in the two codes.

#### Cell-Vertex Method (KTH)

In the KTH code the viscous terms are computed by a 3-point cell-vertex scheme using an auxiliary staggered grid. The vertices  $S$  of the staggered grid are given by the cell centers of the main grid where the state variables are located (Fig. 4). The vertices of the main grid  $N$  are then taken as the cell centers of the staggered grid. Derivatives at the vertices, say  $N1$ , are computed from the gradient theorem applied to the cell defined by the surrounding staggered-grid points,  $S1$  to  $S4$ . The viscous tensor can then be obtained, and the viscous and thermal fluxes computed at the vertices  $N$ . They are averaged over the cell face to give the numerical flux at the center of the face for use in Eq.(8).

#### Thin Layer Approximation (MIT)

The viscous terms in the governing equations can be simplified if one assumes that gradients of viscous stress and heat flux in directions parallel to the body are negligible compared to those gradients in the direction normal to the body. All viscous terms that contain derivatives parallel to the body surface can then be eliminated, giving the thin-layer form of the Navier-Stokes equations. In a real flow this assumption holds only in attached, high Reynolds number regimes. However, in a numerical solution the assumption is consistent with the full equations when the computational grid does not adequately resolve gradients of viscous stress and heat flux in the streamwise or cross stream directions. The terms then are discretized by centered differences in the normal direction.

#### Time Integration

After space discretization Eq.(8) becomes

$$\frac{d}{dt}u_{ijk} = \sum_{f=1}^4 F(u)_f = \delta F_{ijk} = (\delta_i + \delta_j + \delta_k)F_{ijk} \quad (14)$$

where Eqs.(9)-(13) imply the meaning of the difference operators. The resulting semidiscrete system of ordinary differential equations (14) is solved in either of two ways with local time steps. The first is a standard explicit four stage Runge-Kutta time integration (KTH). The second is a novel semi-implicit solver (MIT) which is implicit in the direction normal to the wing and explicit in the two directions tangential to it. This approach enhances stability and convergence.

The standard four-stage scheme applied to Eq.(14) is

$$\begin{aligned} u_{ijk}^{(1)} &= u_{ijk}^n + \alpha_1 \Delta t \delta F_{ijk}^n \\ u_{ijk}^{(2)} &= u_{ijk}^{(1)} + \alpha_2 \Delta t \delta F_{ijk}^{(1)} \\ u_{ijk}^{(3)} &= u_{ijk}^{(2)} + \alpha_3 \Delta t \delta F_{ijk}^{(2)} \\ u_{ijk}^{n+1} &= u_{ijk}^{(3)} + \alpha_4 \Delta t \delta F_{ijk}^{(3)} \end{aligned} \quad (15)$$

where the superscripts identify the temporal level and the multistage coefficients are  $\alpha_1 = 1/4$ ,  $\alpha_2 = 1/3$ ,  $\alpha_3 = 1/2$ , and  $\alpha_4 = 1$ . The local time step is used.

The semi-implicit scheme of MIT leads to a linear tridiagonal matrix multiplying the left-hand side of each stage of Eqs.(15). See Ref. [7] for further details.

## Computed Results

To investigate the suitability of these techniques for hypersonic flow simulation, INRIA and GAMNI organized a workshop on "Hypersonic Flows for Reentry Problems" in Jan 1990. Calculations of laminar flow over a 70° swept blunt delta wing at 30° angle of attack, Mach number of 7.15,  $Re$  of  $5.85 \times 10^6$ , wall temperature of 288K and freestream temperature of 74K have been carried out as part of the workshop and are presented here.

Three different types of grids, H-O (MIT), O-O, and C-O (KTH), are used with point densities ranging from 150 to over 400 thousand, and they allow us to study the effect of grid topology as well as grid resolution in the MIT and KTH solutions to the Euler and Navier Stokes equations.

## Euler Equations

Figure 5 displays the grids used in the KTH and MIT results. The KTH mesh is an O-O type where the trailing edge is rounded, as is the trailing-edge tip because of the presence of the parabolic singular line there. Streamlines integrated in the KTH Euler (and NS) results (Fig. 6) show that a vortex does in fact develop in the solutions, and it may be generated by the cross-flow shock in the Euler case. Surface streamlines in Fig. 7 indicate that the flow does indeed separate at the shock. The comparison in Fig. 7 between the KTH and the MIT results show that

the shock and the separation occur in different locations in the two solutions.

Figure 8 compares the isoMach contours and the total pressure coefficient  $C_{p_i} = 1 - \frac{p_i}{p_{i\infty}}$  in the 50% chord plane. On the windward side there is a strong bow shock (normal Mach number of 4.5) with a large total pressure loss (90%, which is consistent with the normal Mach number). The flow expands rapidly about the leading edge but remains attached. Curiously, there is additional total pressure loss through this expansion which may be numerical in origin or which may be related to the entropy layer and vortical singularity in flow over a circular cone (more about this below).

What is most surprising about this comparison is that the two solutions are so different (cf Mach contours). On the leeward side at about mid-span the flow separates from the surface in the MIT results, and an oblique crossflow shock of short extent occurs. A shear layer is evident which travels inboard and upward until it meets a crossflow shock that turns the flow downstream. A vortical flow is trapped between the shear layer and the wing surface. The KTH results on the other hand show a crossflow shock that bubbles out at its foot and the resulting vortical flow region is more confined. We have here a case of two quite different Euler solutions, and we must ask ourselves why. One probable answer is that the problem is nonunique. We are solving the inviscid equations for flow over a very blunt and smooth body which does not invoke a Kutta condition for the flow to separate at a specific location. This situation contrasts to the usual situation in transonic delta wing flow where the leading edge is very thin and often sharp. In the absence of a geometric Kutta condition to fix separation, one has to expect nonuniqueness because now even small differences in artificial dissipation, which plays a role in inviscid separation, can lead to very large differences in the solution. The plots of the total pressure loss  $C_{p_i}$  on the surface (Fig. 8) suggest that this may indeed be the case. Through the bow shock both solutions lose over 90% of its total pressure, then an additional loss occurs around the leading edge. Small differences here may be responsible for large differences in the point of separation, and consequently lead to the two different leeward flow patterns.

In any case the flow patterns in these two solutions are quite different from that expected in the classical thin-wing analysis, and also different from circular cone flow. Presumably the vortex results from the vorticity created in the cross-flow shock. But the reason for the entropy gain around the leading edge is still unclear. This local feature may be related to the vortical singularity found in circular-cone flow where streamlines possessing different entropy levels converge. In our case a very strong entropy gradient may exist around the leading edge because of the confluence of streamlines with different levels of entropy since they have passed through different parts of the bow shock.

Let us investigate this matter further. Figure 9 presents four streamlines, the first with label 1 passes closest to the leading edge and the fourth (label 4) closest to the bow shock. The total pressure coefficient  $C_{p_i}$  is plotted versus distance along these streamlines. As said earlier after passing through the bow shock, the value starts at about 90%, but we now see that the loss around the leading edge is

greatest for the streamline closest to the leading edge. Another increase occurs further downstream where the trace passes through the trailing edge shock. We conjecture that the loss around the leading edge is due either: 1) entirely to truncation error, or 2) to a physical entropy layer that is strongest nearest the wing surface, and that gets smeared out across streamlines in the numerical solution.

#### Navier-Stokes

The MIT-NS grid has 32 cells in the streamwise direction, 96 in the circumferential and 96 in the body normal directions, and the KTH-NS grid has 32, 96, and 128, respectively (Fig. 10). The C-O mesh used for the KTH-NS solution has a polar singular line at the apex that caused insurmountable problems for the NS solver. We overcame these by rounding off the first 2% of the apex. Since the results with this rounding were no different than those obtained with a 5% rounding, we conclude that the rounding has very little effect overall. The trailing edge and its tip are thick with sharp corners. Here, and in the MIT results, all variables in the computation are extrapolated at the outflow boundary, which in effect makes the wing infinitely long. No problems were encountered with this type of boundary condition.

Figure 11 compares the KTH Euler and NS Mach contours in the symmetry plane, and shows the bow shock. The windward flow is quite similar in the two flows, but the leeward flow pattern is a little different. The Mach contours nearest the upper surface and ahead of the trailing edge are not as dense in Euler as they are in NS. The same remark applies to the isobars plotted only on the leeward in the range  $-0.028 < C_p < -0.020$  with increments 0.0005. We interpret this pattern to be the indication of a small shock (cf Fig 12).

Figure 12 presents isoMach contours of the flowfield at the 50% chord and compares KTH-NS with MIT-NS, and KTH-NS with KTH-Euler. It is reassuring to see that the two NS solutions agree rather closely in their overall features, and an indication that the problem is uniquely posed. On the leeward the Euler and NS solutions are quite different. The Euler flow displays a crossflow shock that bubbles out at its foot, causes the flow to separate, and a vortical region to develop behind it (Fig 12). The NS flow on the other hand separates just past the maximum expansion at the leading edge. The shear layer extends inboard to where it meets the crossflow shock over the wing, it then turns downward towards the wing surface where a small embedded shock (cf Fig 11) turns it once again outboard towards the leading edge. It finally rolls up to form a vortical layer. Between the wing and the shear layer a secondary vortex develops from the boundary layer separating from the wing (Fig. 13). The direction of the flow motion in this plane is given by velocity vectors (Fig 13a) and their integrated path lines (Fig 13b), i.e. in-plane streamlines. In each case the vortex is clearly identified.

#### Upper Surface

While both NS solutions have the same qualitative features, namely one primary separation and one secondary

separation, Fig. 14 shows that the locations of these two separations are different in the two solutions. Figure 14 also indicates that there are substantial differences in the computed Stanton number  $St$  but not in the skin friction component  $C_{fy}$ . It is disappointing to see that the two solutions cannot predict heat transfer to the windward surface more closely than they do. However they do agree very well on the peak heating at the leading edge (windward attachment line). The peak value is about 3.1 times larger in magnitude than that at the windward symmetry plane. It is noteworthy that this factor agrees well with the value 3.2 given by the infinite yawed-cylinder analysis of Reshotko and Beckwith [9]. Agreement between the two solutions is better on the upper surface, except near the symmetry plane where the shear layer hits the upper surface. Here the MIT results predict a substantially higher surface heating than do the KTH results.

Lastly Fig. 15 shows that the pressure distribution under the vortex is quite different in the Euler and NS results of KTH. The pressure on the upper surface is extremely low. It is lower in Euler than in NS, but Euler shows a typical vortex signature in  $C_p$  near the symmetry line. Vacuum occurs at  $C_p = -0.028$  and the Euler solution very nearly reaches it. Figure 16 shows this pocket of near-vacuum flow over the wing in KTH-Euler and KTH-NS solutions. Notice that in Euler the pocket touches the wing surface, but in NS it does not.

#### Mesh Refinement

In order to ascertain how dependent these features are on the mesh resolution, we present here a comparison of two NS- KTH results, one on the fine mesh (discussed above) and the other on a medium mesh with half the number of points in each direction of the fine mesh. The skin friction lines in Fig. 17a show that the general flow structure (one primary and one secondary separation) remains unchanged, but that their locations are grid dependent. On the other hand Fig. 17b indicates that the flow structure in the mid-chord section is relatively insensitive to the grid.

#### Boundary and Shear Layer Structure

The variation in flow properties along the vertical line  $L$  above the wing in the 50% section are plotted in Fig 18. The Mach number varies continuously from 0 to over 6. Almost all of the total pressure is lost in the boundary layer, and there is a temperature gradient right at the wall because it is cooler than the surrounding flow, but the temperature drops off rapidly in the outer layer. There is substantial shear in the layer because the spanwise velocity  $v$  swings from positive to negative

#### Comparison with Experiments

The oil flow pattern in Fig. 19 confirms the flow structure of one primary and one secondary separation on the upper surface of the wing, but it also shows a very substantial trailing edge effect on the boundary layer that extends almost up to midchord. The reasons for this are still unclear, but it may be due to 1) upstream influence through

the boundary layer, or 2) vortex breakdown, or 3) nitrogen liquefaction effects in the tunnel. In any case the abrupt kink in the secondary separation line suggests that laminar to turbulent transition has taken place. Since our calculations are purely laminar, we have to expect differences in the comparisons.

Four pressure taps are located at the mid-chord station, just ahead of the separation bubble. Figure 20 presents their comparison with the KTH-NS and MIT-NS surface  $C_p$  values. Although there is a shift in the levels of the two sets of results, the trend to a higher pressure at the symmetry plane, where the shear layer meets the wing, is similar in each result. The data is rather sparse, but what little there is seems to confirm our picture of a shear-layer dominated vortical flow structure.

Lastly, Fig. 21 compares the KTH-NS computed flow direction and Mach numbers in the midchord section with measurements made with a Pitot tube. Unfortunately the pressure level in the vortical region was too low for the tube to make reliable readings, so we cannot obtain confirmation of this feature here. However, there is good agreement in some regions, while there are one or two marked discrepancies.

### Conclusions

We have found that instead of the concentrated vortex usually found over a delta wing in transonic speed, the flow in hypersonic speed is dominated by a shear layer that separates just past the blunt leading edge and forms a more distributed vortical region over the wing (Fig 22).

However, the flow predicted by Euler is quite different from Navier Stokes, also distinct from the transonic case. This may be due primarily to the very blunt leading edge.

The Navier Stokes results agree qualitatively with the sparse experimental data that we have, but not quantitatively. We have seen some sensitivity to mesh resolution in regards to the quantitative details of the solutions, but not to the overall flow structure. The windside features like the bow shock agree well in all the numerical solutions. But there are substantial discrepancies in the prediction of the Stanton number on the upper surface.

### Acknowledgments

Two people have been very instrumental in the making of this paper. Dave Darmofal at MIT has done a yeoman's job of mounting all the solutions in the visualization system VISUAL3 and has spent many hours analysing the results and discussing them with us. Shiva Scrinivasan at FFA has played a pivotal role in helping us to get the KTH-NS solution on the CRAY-XMP. We are extremely grateful to both of them.

### References

1. Squire, L.C., "Regimes Over Delta Wings at Supersonic and Hypersonic Speeds", *Aero Quart*, Feb 1976, pp 1-14

2. Miller, D.S. and Wood, R.M., "Lee-Side Flow Over Delta Wings at Supersonic Speeds", NASA TP 2430, June 1985
3. Sears, W.R. (editor), *General Theory of High Speed Aerodynamics*, Vol 6, High Speed Aerodynamics and Jet Propulsion, Princeton University Press, 1954
4. Müller, B. and Rizzi, A., "Navier-Stokes Calculations of Transonic Vortices over a Round Leading Edge Delta Wing", *Intl J. Numerical Methods Fluid Mechanics*, Vol 9, 1989, pp 943-962.
5. Eliasson, P. and Rizzi, A.: Hypersonic Leeside Flow Computations Using Centered Schemes for Euler Equations, *Proc 8th GAMM Conf Num Meth Fluid Mech*, (ed) P. Wesseling, NNFM 29, Vieweg, Braunschweig, 1990.
6. Lee, K.M., "Numerical Simulation of Hypersonic Flow Over a Blunt Leading Edge Delta Wing", MIT SM Thesis, October 1989. Also MIT CFDL-TR-89-9.
7. Loyd, B., Lee, K.M. and Murman, E.M. "Semi- Implicit Navier Stokes Solver (SINSS) Calculations of Separated Flow about Blunt Delta Wings", AIAA Paper 90-0590, January 1990.
8. Olsson, P.: Flow Calculations Using Explicit Methods on a Data Parallel Computer, Rep. No.117, Uppsala Univ. 1989
9. Reshotko, E. and Beckwith, I.E.: Compressible Laminar Boundary Layer Over a Yawed Infinite Cylinder with Heat Transfer and Arbitrary Prandtl Number, NACA Report 1379, 1958, p.15.

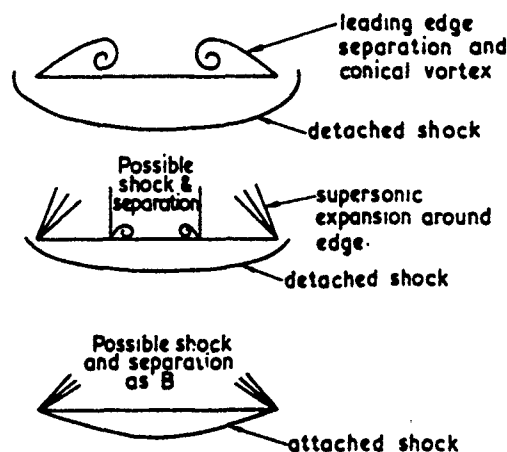


Fig 1 Types of flow on thin delta wing at hypersonic speed.



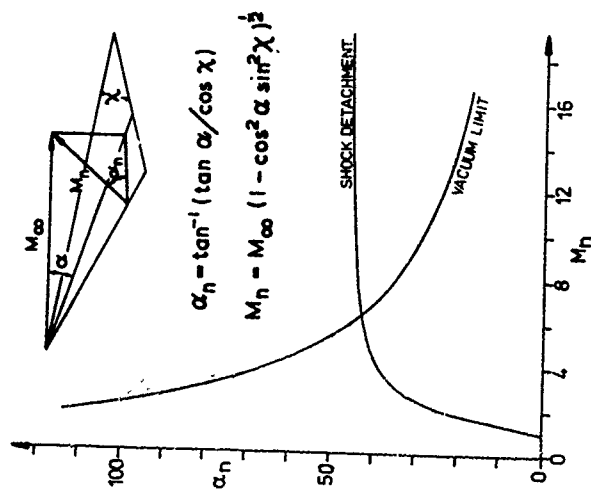
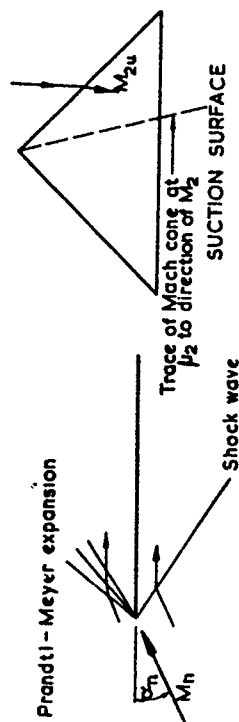


Fig 2 Analysis of flow normal to the leading edge: a) Prandtl-Meyer expansion b) limits for attached shock and expansion to vacuum (I. Squire, private communication)

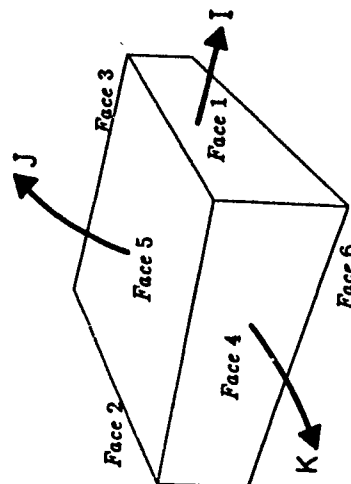


Fig 3 Six faces of computational hexahedron.

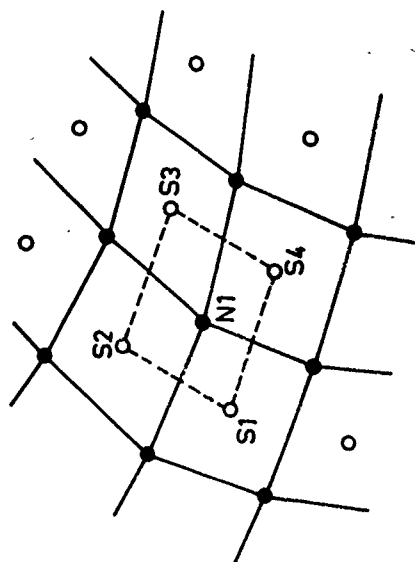


Fig 4 Staggered mesh for viscous flux calculation.

8-8

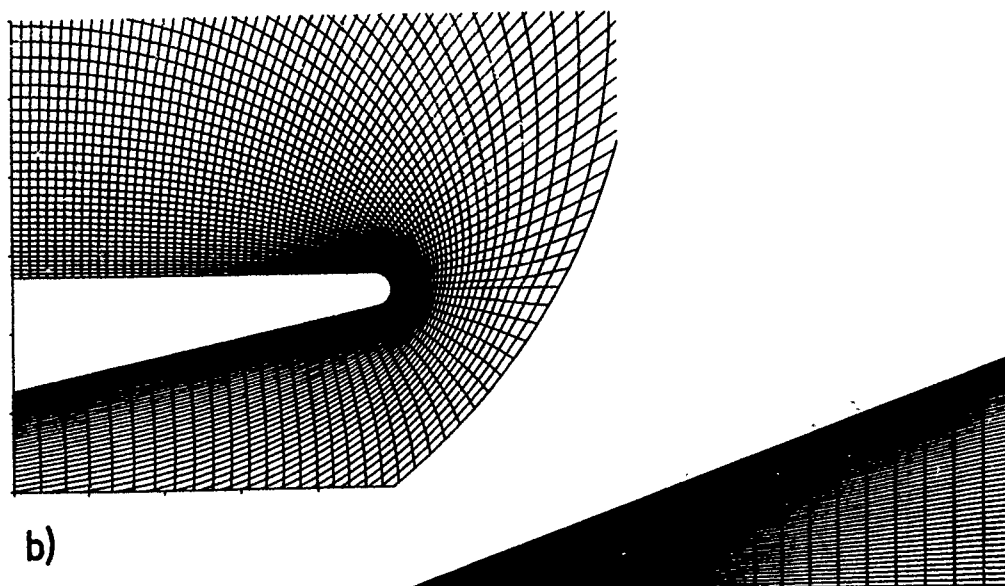
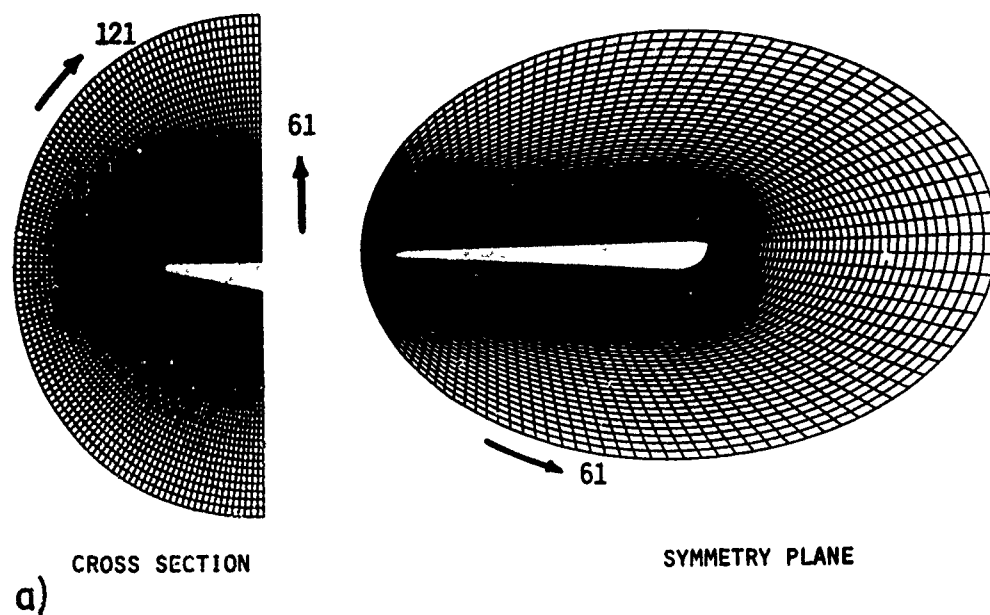


Fig. 5 Mesh for Euler solutions: a) KTH 0-0 type 61x61x121  
b) MIT H-0 type 33x49x97

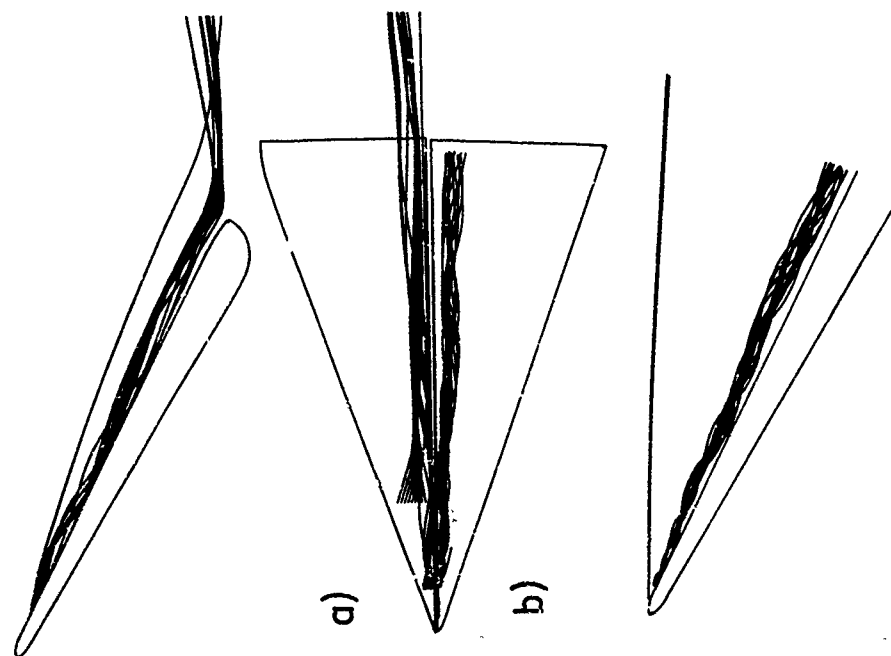


Fig. 6 Vortex streamlines in  
a) KTH-Euler and b) KTH-NS

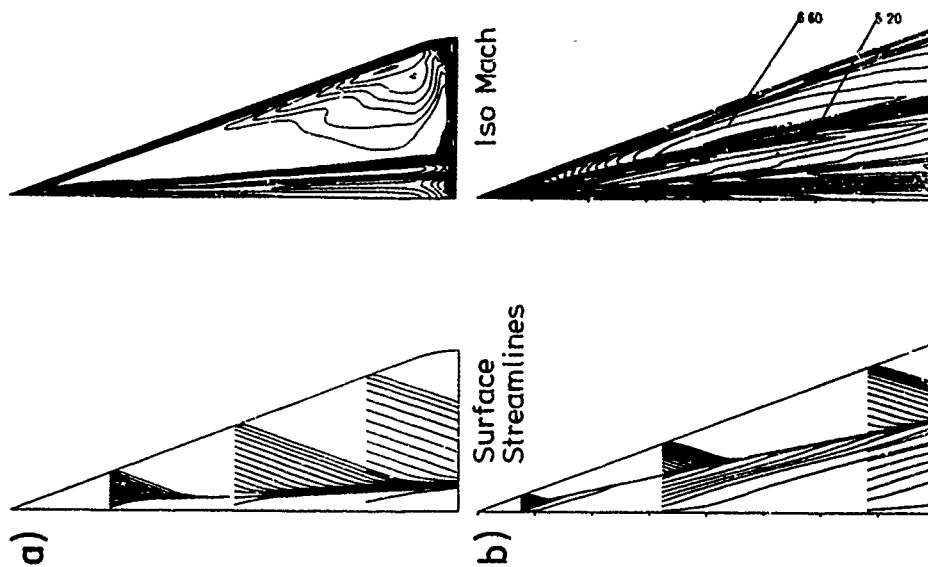


Fig. 7 Comparing a) KTH and b) MIT  
Euler results upper surface

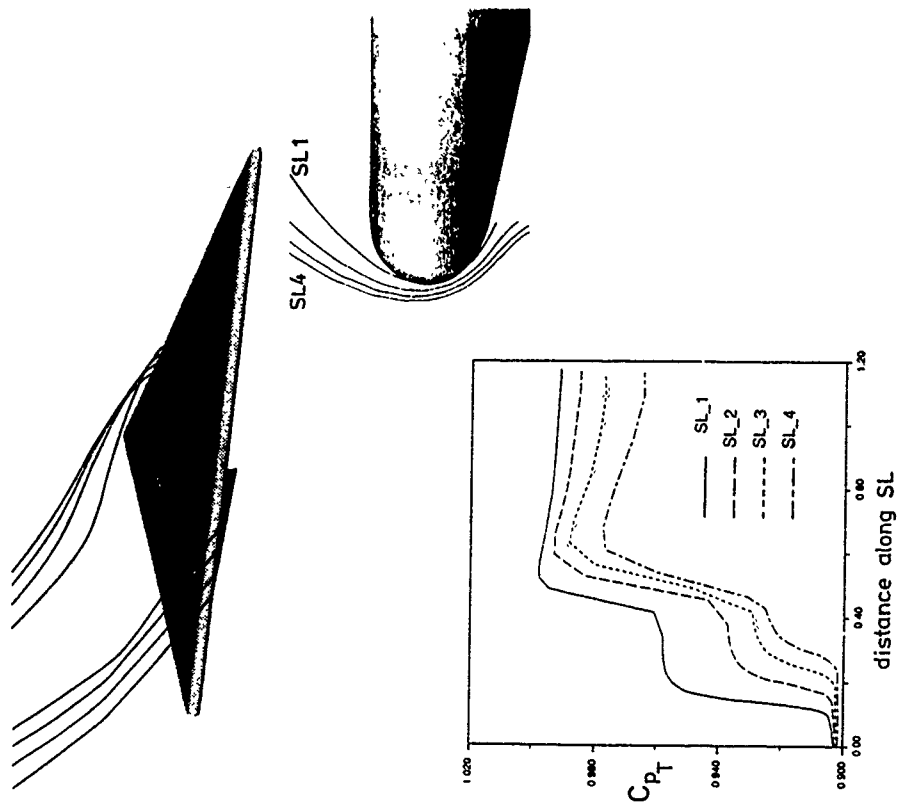


Fig. 9 Total pressure loss  $C_{pT}$  along streamlines around leading edge. KTH-Euler.

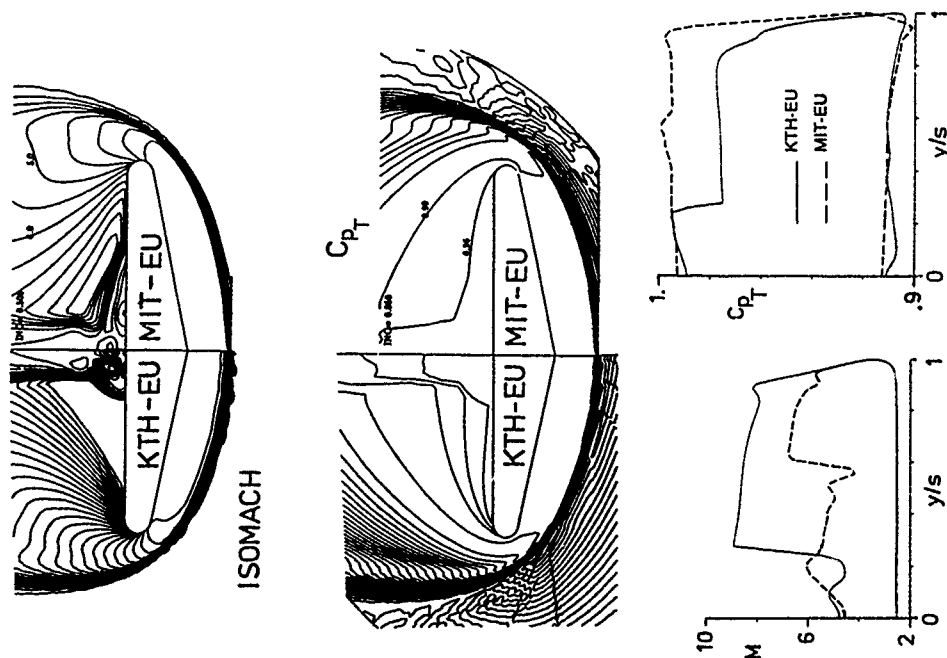


Fig. 8 Comparing KTH and MIT Euler results 50% section

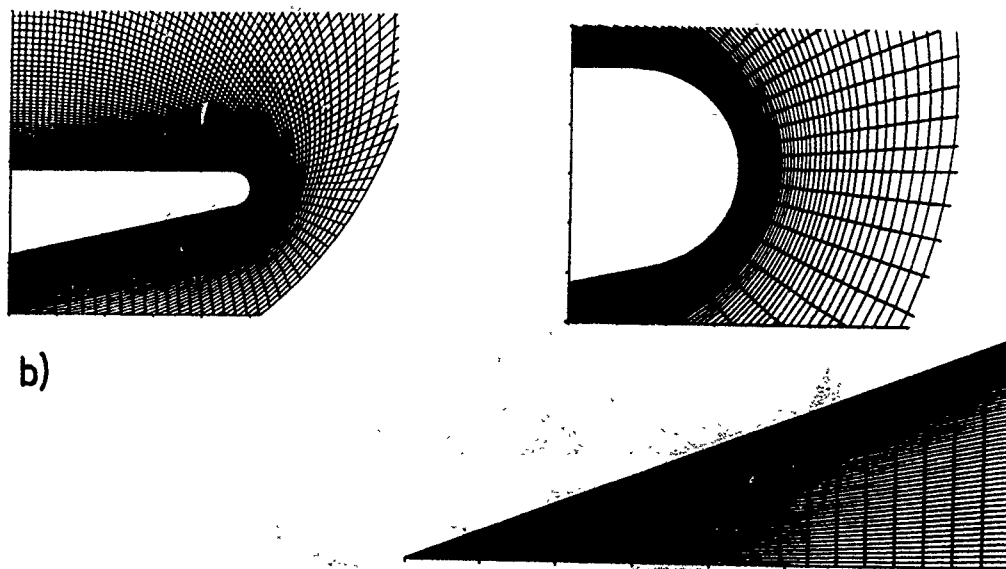
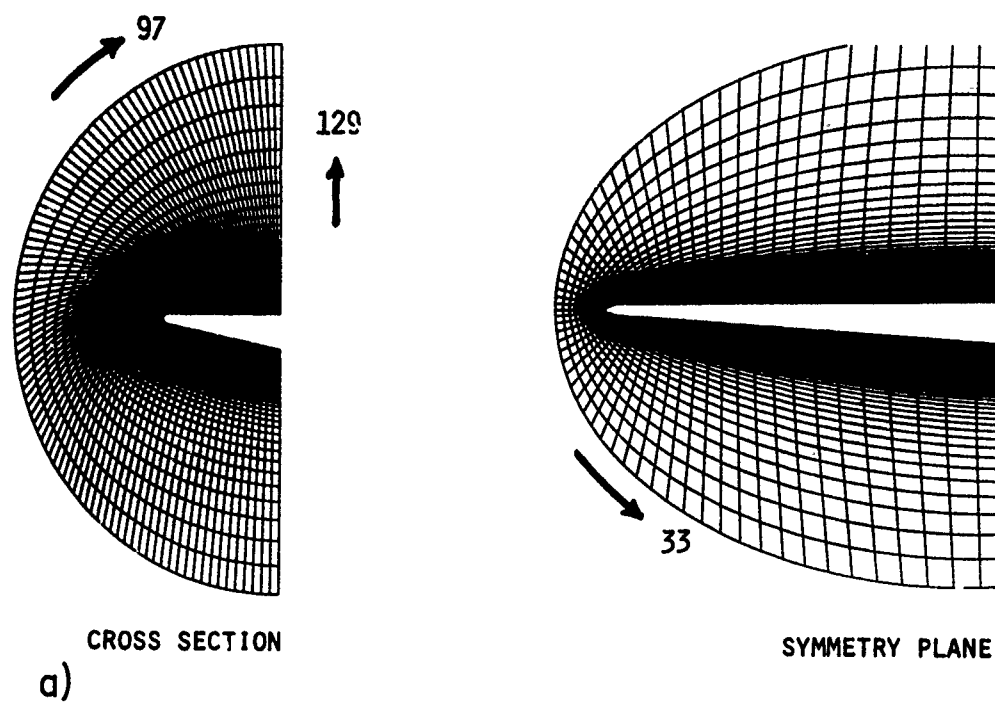


Fig. 10 Meshes for NS solutions: a) KTH C-0 type 33x129x97  
b) MIT H-0 type 33x97x97

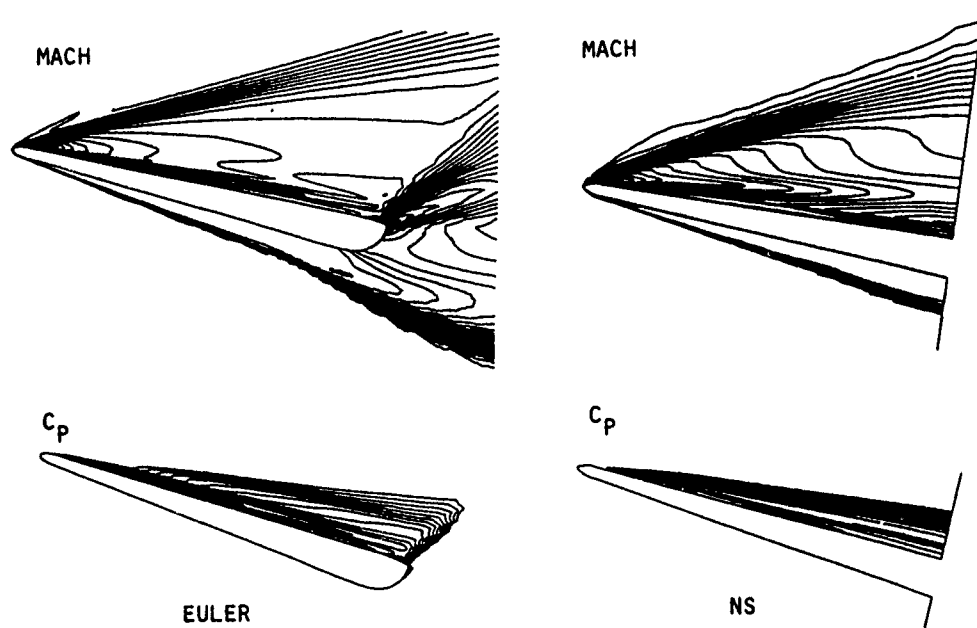


Fig. 11 Comparing KTH-EU and KTH-NS solutions in symmetry plane  $y = 0$

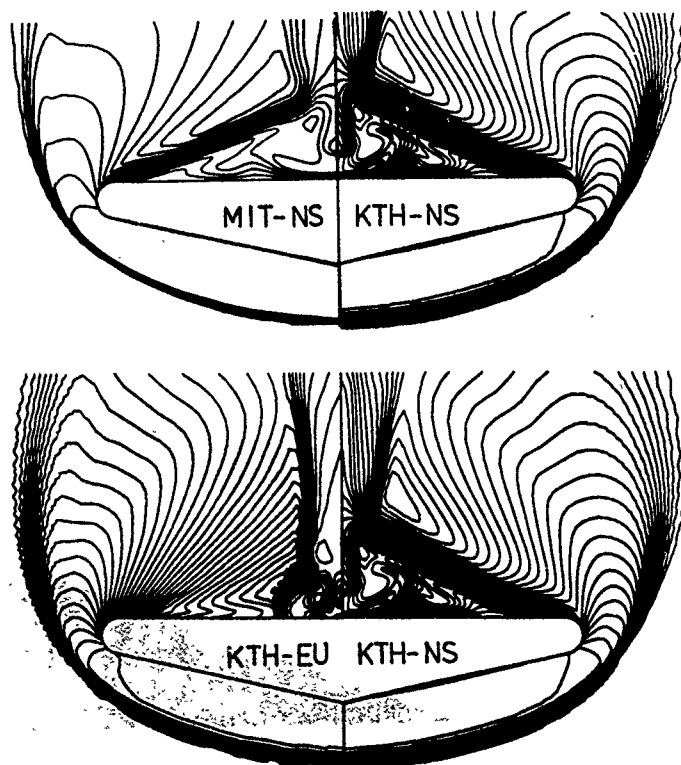


Fig. 12 Comparing isoMach contours in 50% section:  
KTH-NS, MIT-NS and KTH-EU

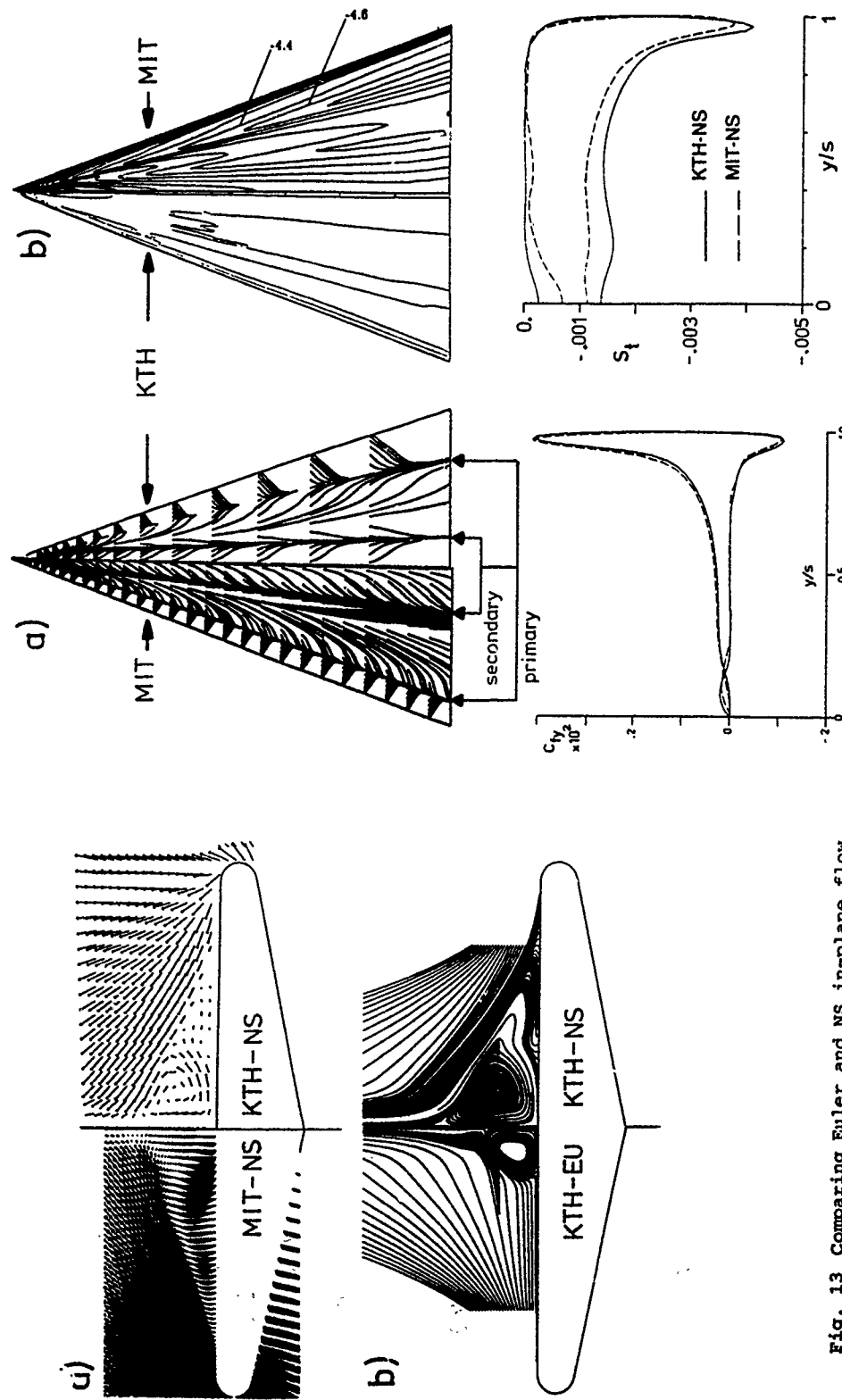


Fig. 13 Comparing Euler and NS in-plane flow directions  
 a) velocity vectors  
 b) streamlines 50% section

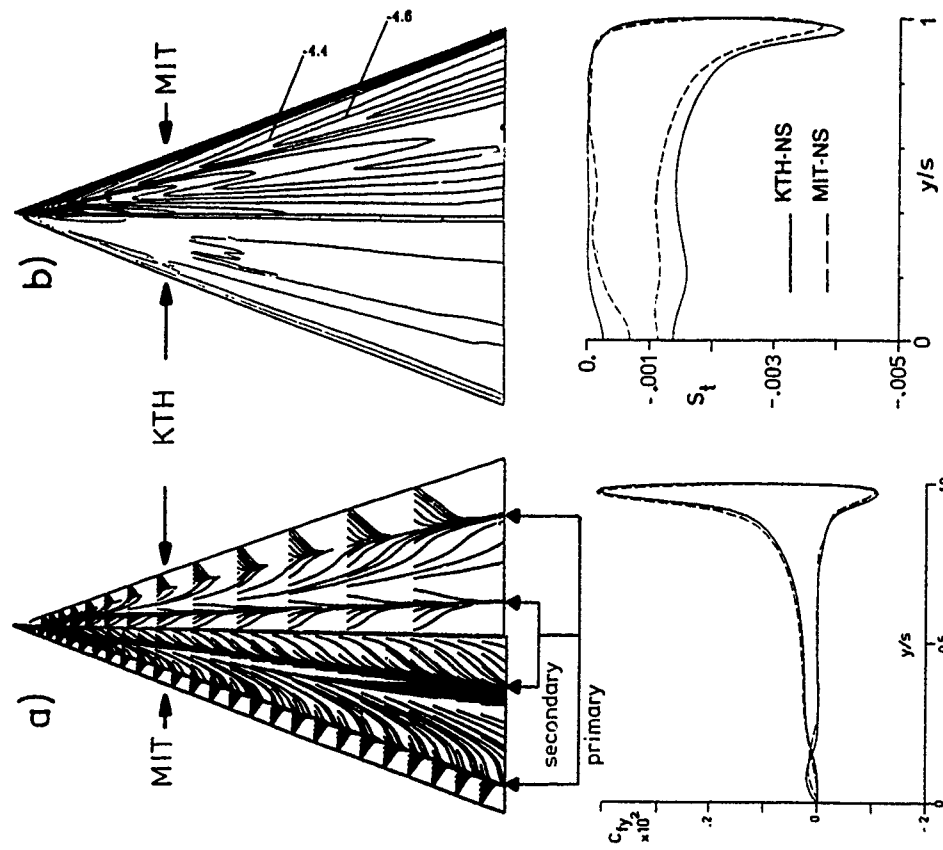


Fig. 14 Comparing KTH and MIT lines and Stanton number  $S_t$   
 a) skin friction  
 b) Stanton number  $S_t$



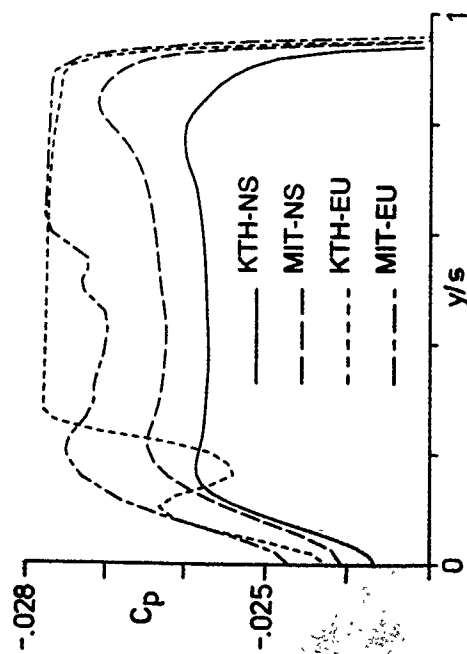
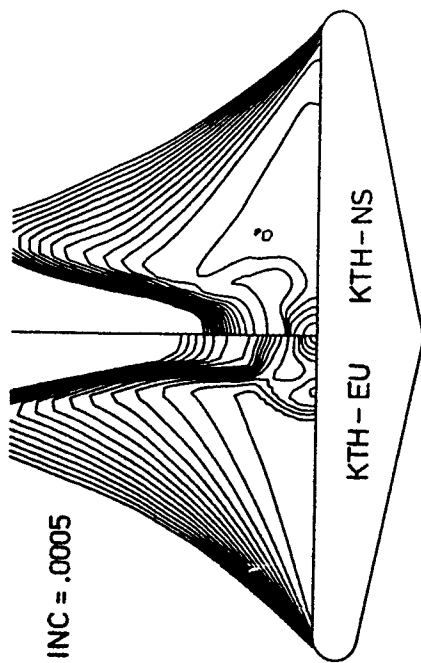


Fig. 15 Comparing NS and Euler  $C_p$  values over and on wing. 50% section.

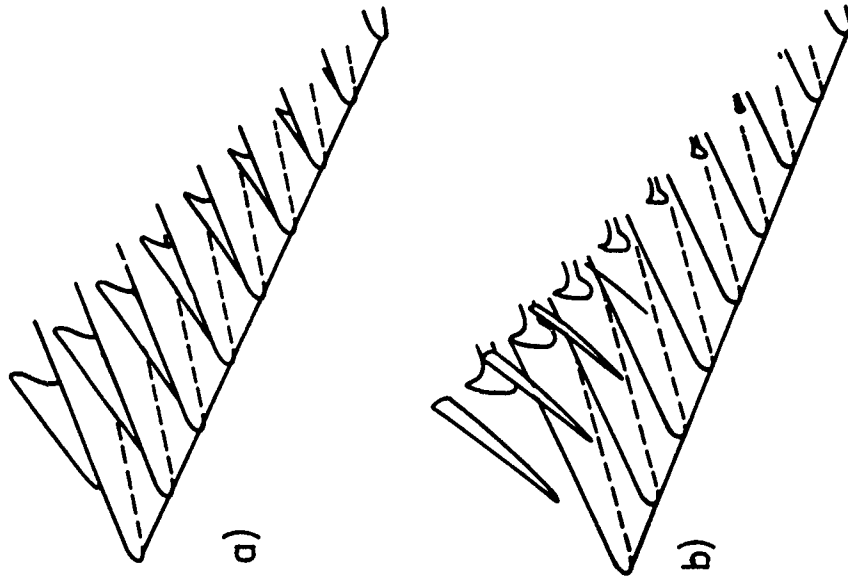


Fig. 16 Near-vacuum IsoC surface  
a) KTH-EU  $C_p = -0.0276$   
b) KTH-NS  $C_p = -0.0265$

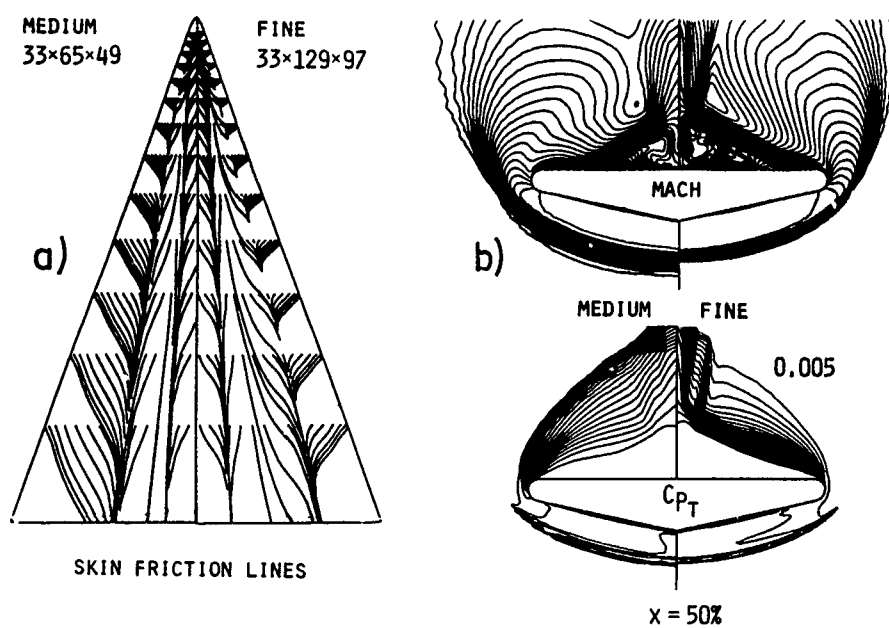


Fig. 17 Mesh refinement effects KTH-NS a) skin friction lines  
b) isoMach and  $C_{pT}$  50% section

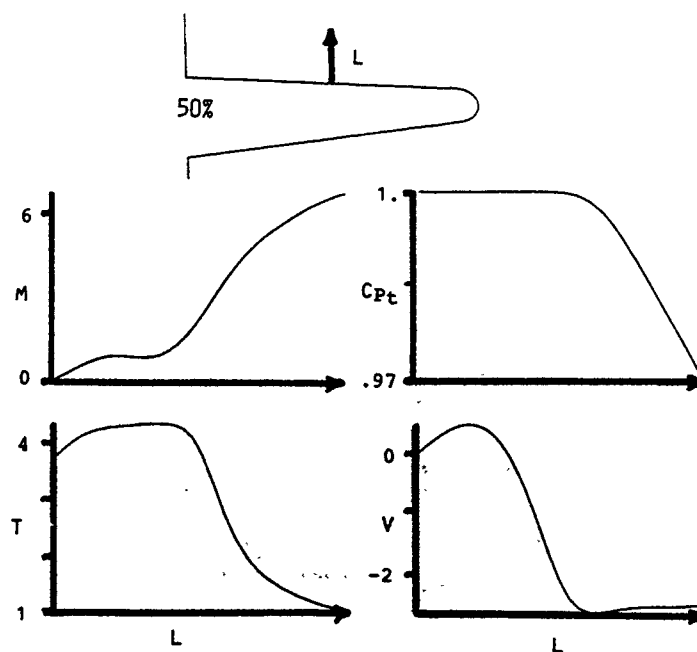


Fig. 18 Boundary and shear layer profiles along line L  
KTH-NS 50% section

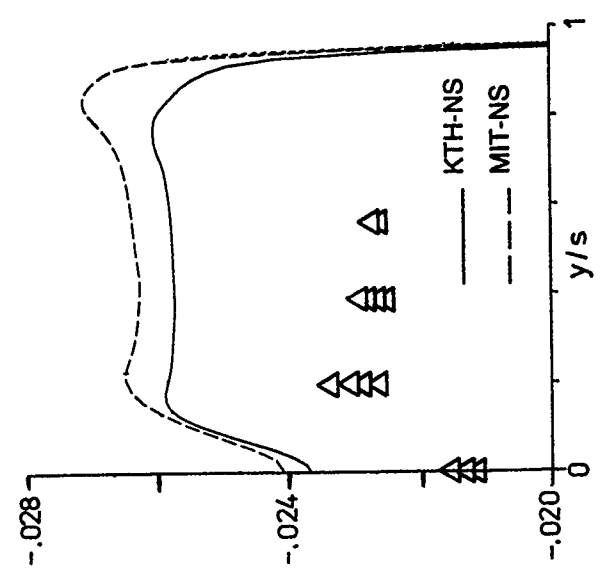
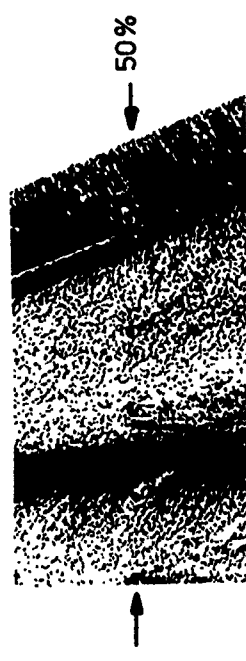


Fig. 20 Comparison of KTH-NS and MIT-NS surface  $C_p$  with measured  $C_p$  50% section

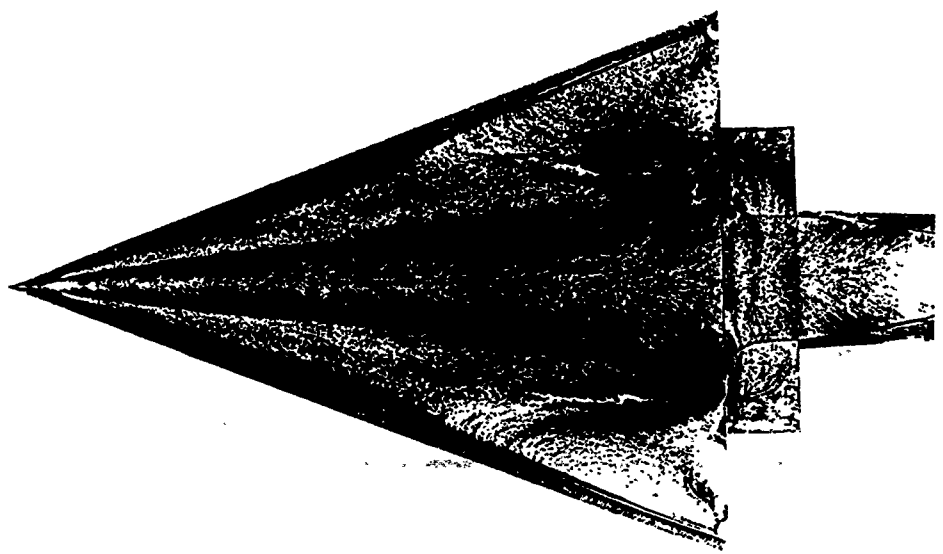


Fig. 19 Oil flow Experiment

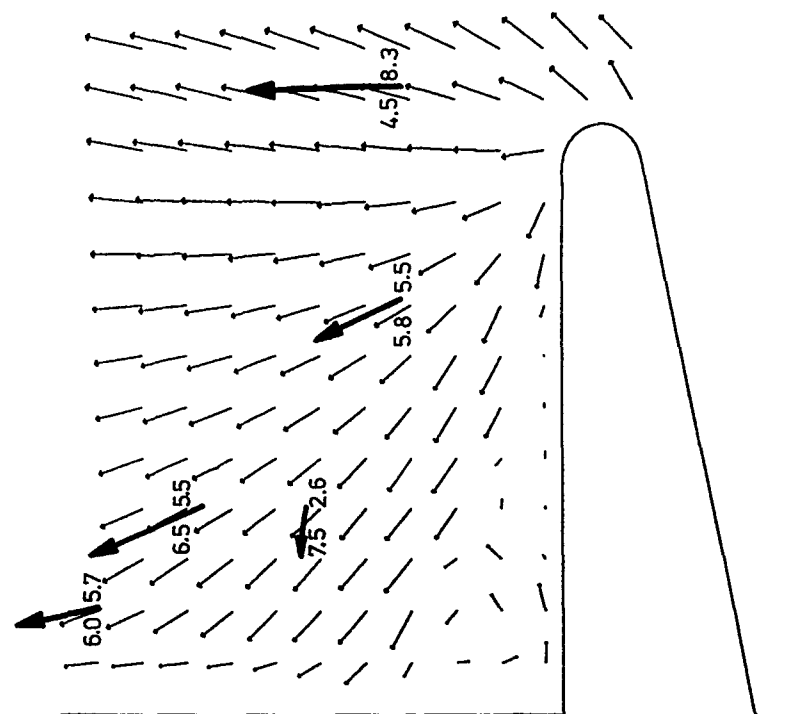


Fig. 21 Comparison computed (KTH-NS) and measured flow direction and Mach number. Bold arrows are measured. Value to left is computed, value to right is measured Mach number. 50% section

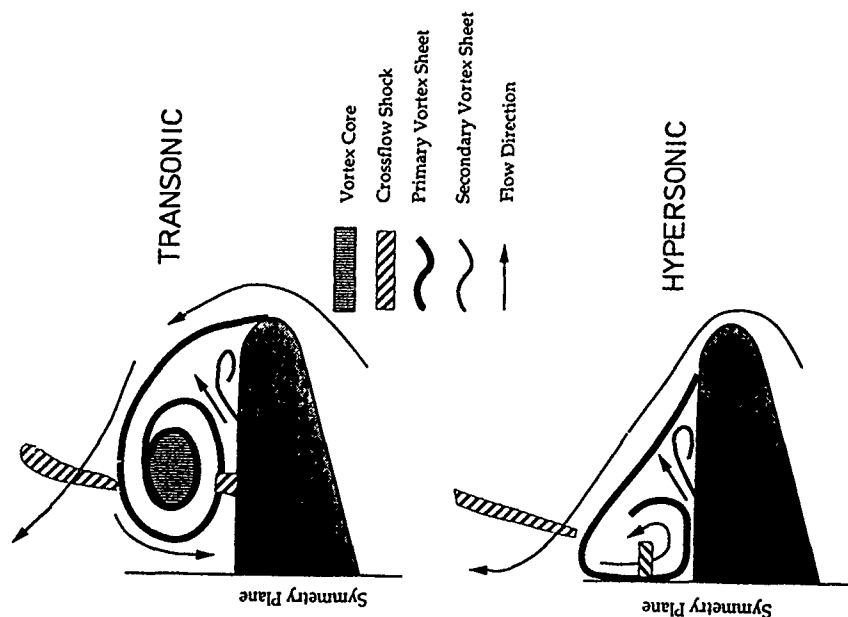


Fig. 22 Differences in transonic and hypersonic vortex flow. Schematic

## ON THE FOOTPRINTS OF THREE-DIMENSIONAL SEPARATED VORTEX FLOWS AROUND BLUNT BODIES

### Attempts of defining and analyzing complex flow structures

Uwe Dallmann, Achim Hilgenstock, Stefan Riedelbauch,  
Burkhard Schulte-Werning, Heinrich Vollmers

DLR Institute for Theoretical Fluid Mechanics,  
Bunsenstrasse 10, D-3400 Göttingen, FR Germany

#### Abstract

This paper summarizes an analysis of vortex flows around different configurations in very different ( $Ma$ ,  $Re$ )-regimes. Subsonic, transonic and hypersonic separated vortex flows are considered. The common interest was to study the relationships between the topologies of steady or unsteady, two-dimensional or three-dimensional separated vortex flow structures and their "footprints" which they leave on the boundaries (walls) or within any sections across the flow field. From this point of view we analyze numerical Navier-Stokes simulations in the following respect:

Topological changes of the instantaneous sectional streamlines and the skin-friction patterns of incompressible flows are considered during vortex shedding and during onset of three-dimensionality of the flow. Two-dimensional separation bubbles, separation from a cylinder in crossflow and separation from a sphere are analyzed.

The formation of vortex cores and their relationship to so called open or closed flow separation, wall vorticity, wall pressure, wall heat flux and various sectional flow data are investigated in compressible flows such as the transonic transitional flow around a round edged delta wing and the hypersonic laminar flow around a double ellipsoid.

#### Introduction

Apart from the common interest in calculating drag, lift, Strouhal numbers and several other quantities of flows around complex configurations, there are complex vortex flow phenomena under the most simple boundary conditions which lack even a qualitative understanding. As a matter of fact, little is known about

- a) the formation of three-dimensional vortex flows although the boundaries are either two-dimensional (cylindrical) or axisymmetric or even spherical,
- b) the bifurcation from a steady separation bubble to unsteady vortex shedding,
- c) the mechanisms which lead to the creation of stable, three-dimensional (often steady) vortex configurations with the formation of multiple vortex cores around or in the wake of simple shaped bodies like prolate spheroids, hemisphere-cylinder configurations, etc., and
- d) the relationships between the topologies of different flow quantities in a given incompressible or compressible vortex flow.

The last topic raises the question whether the local formation of the onset of a vortex flow feature - (namely the creation of a swirling flow region in mid-air) - can be assigned to a topological change of physical quantities: From an applicational point of view any quantity which leaves a unique measurable "footprint" on the

wall (body surface) would be preferred. However, it will not be necessary that all such changes will be seen in the velocity field. The topological structure of a flow consists of topological properties of, at least, all of the dependent variables. Dallmann & Schulte-Werning [1] raised the following question: "What are the necessary and sufficient topological (rather than analytical) informations about a flow that have to be equivalent and have to be compared in any two simulations such that any further topological properties of any other quantity (variables or invariants) will be preserved in these two simulations?" The answer is not known, and we concentrate the present investigation on qualitative changes which occur in velocity fields and a few parts of a more complete analysis.

A precise definition of unsteady separation structures or unsteady vortex motion is still lacking (Lugt [2]). A description of topological changes in a sequence of instantaneous streamline patterns is, necessarily, dependent on the frame of reference and therefore calls for other, additional and, if possible, invariant topological properties to be analyzed. However, in a frame fixed either to the body (for the purpose of analyzing flow separation from that body) or fixed to a certain convection speed of moving vortex structures (for the purpose of analyzing physical properties of vortex motion like entrainment, vortex pairing, etc.) the topological analysis of instantaneous velocity fields has been proven to be a useful investigation tool. It allows to restrict the discussion of huge data fields to an analysis of topological changes and their dependence on numerical or physical perturbations or parametric variations.

It is quite surprising that no general picture exists on the topological sequence of instantaneous streamlines during the temporal evolution of two-dimensional vortex shedding. How stationary can separation and attachment points be in unsteady separation bubbles or during von Kármán-vortex shedding?

It is often stated that during the vortex shedding process the instantaneous separation and attachment lines move on the body and annihilate each other at the very instant when a vortex is shed. However, this picture does not fit to those observations in surface flow visualizations where sharp almost stationary separation lines but oscillating or blurred attachment lines are seen (Dallmann & Schewe [3], Stücker [4]).

Many papers have been published in recent years on topics of experimental or numerical visualizations of three-dimensional separating flows around blunt or pointed bodies. Qualitative changes in the observed surface flows were recognized to occur due to changes in parameters like Reynolds number, Mach number, angle of attack, body shape, etc. A description of surface flow topology turned out to be a useful means to

reduce the qualitative information provided by the surface flow data (or visualizations) to give a precise description of flow changes in terms of topological changes. However, surface flow trajectories, especially wall shear stress informations are never - even in two-dimensional flow - sufficient to conjecture qualitative features within the outer (mid-air) flow field. Hence, for the formation of a vortex core - (even when a precise definition would allow to locate or define it in mid-air) - a wall shear stress topology in general cannot provide sufficient conditions for a vortex existence. The so called open separation is one such striking example. Although the surface flow topology in terms of the wall shear stress pattern on the delta wing considered in this paper or on a prolate spheroid, does not change in a wide range of angles of attack, separated vortices are observed on the leeward side of the bodies (We remind the reader that any, arbitrarily weak or strong convergence of neighbouring wall shear stress trajectories does not cause any topological change of that surface flow).

It should be well known that any connections of the locations of extremum values of quantities measured within sectional planes across a flow do not provide an information which is invariant under changes of the sections' orientations. For instance, the locus of maximum values of iso-vorticity sectional plots or helicity density, etc., is not an invariant trace of a "vortex core" within a general three-dimensional flow. Therefore, an invariant definition of a vortex core is required and will be used here and such well-defined vortices can then be considered with respect to open or closed separation lines, wall-pressure and wall-heat flux topology, sectional plane data etc.

The problem of thermal loads on reusable space vehicles requires an accurate prediction of the body surface heat-flux or temperature distribution. It is well known, that high heat-fluxes are present in the stagnation region and on the windward side of blunt bodies. But, increased heating can be also observed on the leeward side caused by the separated flow. Therefore, the present investigation also tries to throw some light on the relationship between the qualitative changes of the structure of thermal flow quantities and the outer vortex flow structure. For that purpose the numerically simulated flow fields past a double-ellipsoid are analyzed.

The interpretation of the resulting huge data bases of the numerical simulations presented in this paper is done on SUN-graphics workstations with the graphic program COMADI by Vollmers [5].

#### **Topological description of unsteady separation and vortex shedding**

In the following we reconsider earlier conjectured structural changes of instantaneous flows associated with unsteady two-dimensional vortex motion and flow separation.

##### **Unsteady wakes behind cylinders**

Perry et al. [6] examined the properties of the instantaneous streamline and streakline patterns behind a circular cylinder for incompressible low Reynolds number flow during the process of vortex shedding. The instantaneous flow topology had been deduced from a movie of Prandtl's water tunnel experiment. They proposed a simple model for the vortex shedding sequence (fig. 2a) indicating instantaneous "vortex" motion when the observer is moving with the cylinder. Sun et al. [7] numerically simulated the cylinder flow for  $Re = 1500$  and  $Ma = 0.3$ . After analyzing the topological structures, and the structural changes extracted from their paper we obtain a sequence shown

in fig. 2b which is different to fig. 2a. The difference lies in the incipient formation process of a vortex behind the body before it starts growing and will be shed downstream. The sequence of fig. 2a leads to an annihilation of separation and attachment lines during each cycle of vortex shedding, while the sequence of fig. 2b creates a vortex without annihilation of instantaneous separation and attachment lines and hence avoids large amplitude oscillations of those (primary) separation lines of zero skin friction. This is in agreement with the oil-flow visualizations shown in Dallmann & Schewe [3] and with Stucke's laser visualizations [4]. Sharp and almost stationary separation lines are observed on cylinders during vortex shedding! In addition we remark that the first vortex which is shed from a cylinder results from the sequence shown in fig. 1. The separated recirculation zones become at first asymmetric before a global bifurcation (break-up of separatrices) leads to the first shed vortex. Hence, the sequence of fig. 2b exhibits identical global bifurcations of all the vortices which are shed, while the sequence of fig. 2a does not. Although the secondary separations ("secondary eddies") in the higher Reynolds number cases of Braza et al. [8] complicate the topological analysis considerably the basic vortex shedding sequence is of the type shown in fig. 2b.

##### **Unsteady separation bubbles**

Fig. 3a shows one commonly considered possibility how the instantaneous streamline topology could (from a kinematical point of view) change during unsteady flow separation associated with vortex shedding from single separation bubble. One recognizes the annihilation of separation and attachment lines during every cycle of vortex shedding. A different model has been proposed by Dallmann [9] and a sketch is given in fig. 3b. It shows how a single separation bubble splits into (at least) three instantaneous vortices and that a global structural flow bifurcation (reconnection of separatrices) leads to the downstream shedding of initially two vortices before the remaining bubble starts growing again with an almost spatially fixed primary separation line. Of course, the instantaneous streamline pattern may change after the global flow bifurcation has released the vortices and the pattern will depend on the actual vorticity fields. The numerical simulations of Gruber [10] and Pauley et al. [11] are consistent with the model proposed in fig. 3b. This topological model allows to understand how unsteady flows may show (almost) stationary, well identifiable separation lines while two-dimensional attachment lines are blurred in most flow visualizations. The choice between sequence 3a or 3b could be due to different Reynolds numbers. No experiment to clarify this point is known to the authors.

At this point we may introduce a Galileian invariant definition of a vortex. An instantaneous, "swirling motion", which we may call a "vortex" within an arbitrary Galileian frame of reference, certainly exists where the local velocity gradient tensor exhibits complex eigenvalues. Hence, a necessary condition for incipient or local vortex formation is the change of sign of the local Jacobian determinant, and a sufficient criterion is fulfilled by having those complex eigenvalues (Dallmann [12], Vollmers [13]).

##### **Three-dimensional wake formation behind spheres**

Three-dimensional wakes develop around spheres or around axisymmetric bodies even at zero angle of attack. A symmetry break of the axisymmetric flow to a three-dimensional near wake flow necessarily precedes the onset of unsteady vortex shedding from a sphere. No unsteady, axisymmetric vortex shedding is observed. This is one difference between vortex shed-

ding from cylinders in crossflow and from spheres as one increases the Reynolds number. We want to check whether the primary separation on a sphere remains stationary during vortex shedding cycles.

The present analysis is based on solutions of the complete, time-dependent viscous equations of motion for a thermal and caloric perfect gas. The dimensionless parameters governing the flow field ( $Re$ ,  $Ma$ ,  $Pr$ ) are defined in the usual way where the sphere diameter is the characteristic length. The free stream Mach number is set to  $Ma = 0.4$ . As initial condition the impulsively started body is employed where the initialization is done with the freestream quantities.

To solve the equations of motion numerically, implicit finite-difference schemes of Beam and Warming type are employed which are second order accurate in space. The axisymmetric flow is computed by a fully implicit scheme with second order accuracy in time (Müller [14]), the three-dimensional flow is computed by a hybrid implicit/explicit method with first order accuracy in time, which was initially developed by Riedelbauch & Müller [15] and extended to a fully implicit scheme with second order accuracy by Schulte-Werning [16]. Fourth-order damping terms are added explicitly to damp high frequency oscillations, second-order damping terms are added implicitly to extend the stability range of the algorithm. For the axisymmetric calculations an O-type grid with  $111 \times 111$  grid points is used, while the three-dimensional calculations shown in this paper are performed on a spherical grid system with  $71 \times 71 \times 71$  points. For a better resolution of the physical situation the grid points are exponentially clustered in the boundary layer (at  $Re = 500$  there are approximately 15 points within the boundary layer) and near the rear symmetry line.

In fig. 4a we show the steady flow structure at separation as a result of an unsteady simulation of axisymmetric flows for  $Re = 300, 600$  and  $1000$ . Flow separation at the rear stagnation point starts at  $Re \geq 10$  and the now appearing closed axisymmetric separation line moves upstream. Above  $Re = 500$  secondary separation (fig. 4b) takes place which leads, due to another bifurcation in the flow field, into multiple structured recirculation zones.

Fig. 5a shows the non-axisymmetric and steady skin-friction patterns of the three-dimensional flow around the sphere as seen by an upstream view onto the rear for  $Re = 200, 300$  and  $400$ . A plane of flow symmetry forms which is not imposed by the numerics. Sectional streamlines in a plane of symmetry which is seen in fig. 5b,c are shown in fig. 5d for  $Re = 400$ . Even for  $Re = 100$  a pure axisymmetric solution (which is topologically unstable against three-dimensional perturbations) at the separation line is not obtained but small inherent perturbations of the numerical algorithm caused a bifurcation to the corresponding topologically stable three-dimensional flow behaviour with a small overlying swirl near the separation line. For increasing  $Re$  this line moves upstream approximately to the equator of the sphere. During this movement a spatial symmetry break occurs, which was not imposed in the boundary conditions but may be regarded as a second answer of an unstable flow behaviour to numerical perturbations. A similar behaviour will lead to three-dimensional wakes in experiments. The now visible flow pattern on the wall indicates that a three-dimensional flow has formed and exhibits instantaneous saddle-node-saddle and node-saddle-node bifurcations along the almost circular and almost stationary (!) separation line and within the "separated" flow region, while the rear stagnation point moves off the geometrical axis. It is of interest that the boundary layer in the attached flow region upstream of the separation line remains fairly axisymmetric.

We are finally interested in finding out if and how topological changes in the wall-flow pattern are related to the wake flow unsteadiness. Fig. 6 shows a time-sequence of calculated skin-friction patterns. Analyzing the associated topology at each time level leads to a minimum Strouhal number based on the topological changes of the wall vorticity distribution (skin-friction pattern) of  $St \approx 0.038$ . This value is much smaller than the experimental value based on force measurements or wake flow visualizations (see Clift et al. [17], page 107) which is about  $St \approx 0.2$ . Hence, in order to get this experimental value in agreement with the simulation, the sequence of topological changes shown in fig. 6 has to appear on a time-interval of  $\Delta T = St^{-1} = 5$  which is shorter than the interval chosen for two successive plots in fig. 6.

We would like to emphasize, that the stationarity of the primary separation line, the three-dimensionality which precedes unsteadiness and the topological (rather than quantitative) changes of the skin-friction pattern have to be in agreement with experiments at first, before quantitative agreements can be achieved. We should mention, that recent incompressible calculations of Shirayama & Kuwahara [18] on a  $200 \times 100 \times 81$  O-type grid had an effect on the Strouhal number. At  $Re = 500$  two modes with  $St_1 = 0.125$  and  $St_2 = 0.204$  were identified, while for a  $50 \times 50 \times 81$  grid they resolved a Strouhal number  $St = 0.133$  based on lift force data. Results for  $Re = 750$  are given by Schulte-Werning in [16] (see also [19] [20]) where, according to the axisymmetric flow calculations shown in fig. 4b, three-dimensional secondary separations arise and a considerable spatial-temporal complexity of the flow is recognized in the separated flow region only.

Fig. 7 is attempt to indicate that the near wake flow behind a sphere becomes three-dimensional before vortex shedding sets in. As soon as the so called singular streamsurface which initially trapped the near-wake bubble breaks up due to instability above a certain Reynolds number, the resulting horseshoe-type vortices will exhibit streamwise vorticity. This behaviour, seen in experiments, has been visualized via vortex-line integration by Shirayama & Kuwahara [18] [21] as well as by Schulte-Werning & Dallmann [16] [1] (fig. 8a) where also vortex line reconnection in the near wake has been observed. The streamwise oriented vorticity in the wake induces two streamwise oriented vortices, i.e. helically swirling motions in the velocity field. Fig. 8b helps to identify these vortices by plotting regions of complex eigenvalues of the velocity gradient tensor. This definition of a vortex will be considered in more detail next.

#### Open separation and vortex core formation in a flow around a delta wing

We are interested in the determination of three-dimensional vortices and vortex cores caused by so called open flow separation from a round edged delta wing.

The following discussion is based on a numerical simulation of the compressible transitional flow around a round edged delta wing at a Reynolds number  $Re = 4.5 \times 10^6$ , a Mach number  $M_\infty = 0.85$  and an angle of attack  $\alpha = 10^\circ$  in a Newtonian fluid. (See also the paper of Hilgenstock & Vollmers [22]).

For the freestream conditions described, the flow around a delta wing is dominated by a primary vortex separating close to the leading edge of the wing. Because of the spanwise pressure gradient a secondary vortex is generated below the primary vortex.



It turned out that for quantitative comparisons between the different experiments as well as between experimental and numerical simulations a precise determination of the transition location is crucial. The transition location for the present investigation is kept at 2.5% local chord of the delta wing.

The complete Navier-Stokes equations are integrated with a finite volume four-stage Runge-Kutta method. Extrem clustering of grid points near the leading edge is chosen in order to avoid possible vorticity generation due to numerical (resolution) errors. The boundary layer along the plane of symmetry is resolved by up to 30 node points. The turbulent flow calculations are based on an algebraic turbulence model. For details see [22] [23].

A perspective view of the wing and of the leeward vortices is shown in fig. 9. The skin-friction pattern displayed in fig. 10 delivers first informations in order to detect flow separation. A so called open separation line forms at about 25% root chord on the upper side of the wing surface very close to the leading edge. Skin friction lines which reach the leeward side turning around the leading edge between 0% and 10% root chord do not enter the region below the primary vortex. They stay between the plane of symmetry and a so called primary attachment line. Only the skin friction lines which enter the leeward side between 10% and 25% root chord will be trapped below the primary vortex. Fig. 10 also shows that the wall-pressure minimum is not at all in the region of separation line formation. For the rounded leading edge, however, the primary separation is not fixed at the leading edge, and depends strongly on the geometry of the leading edge, the sweep angle, the transition from laminar to turbulent flow and so forth.

Let us now display the vortex core above the wing. Figs. 11a-d show especially selected streamlines within the primary and secondary vortex cores. How can we define the location of such "vortex cores" when open flow separation takes place? We make use of an analytical definition of a vortex already mentioned above. Dallmann [12] and Vollmers [13] have suggested to locate vortices in regions where the velocity gradient tensor  $\text{grad } \vec{v}$  exhibits complex eigenvalues and the only one existing real eigenvector defines the local axis of rotation of the fluid as seen by an observer moving with the flow. Fig. 11a shows this region for the flow in the vortex core above a round edged delta wing. The findings of Vollmers [13], the studies of Shirayama [24] and Levy et al. [25] as well as the basic considerations of vortex structures and vorticity field topology by Dallmann [26] suggest that vortex cores also exhibit regions of strong vortex stretching, by locally increasing the parallel alignment of local velocity vector and vorticity vector and maximizing helicity density.

After having identified "vortices" other flow quantities like local Mach number, static pressure and total pressure loss, etc., are now considered in selected planes normal to the plane of symmetry. Also the core streamlines are displayed to relate the vortex to local minima and maxima of the above quantities. As mentioned in the introduction a trace connecting such extremum values within sectional planes in general cannot serve to locate a "vortex core". However, in the special case of a delta wing flow the gradients of the above mentioned quantities within cross-sections are much larger than along the vortex core (defined by the region of complex eigenvalues of the velocity gradient tensor). Hence, only in such a case the non-invariant sectional data analysis turns out to be useful after having identified the vortex cores by invariant means. Looking at any sectional data or sectional streamlines without additional information about the location of core streamlines might be misleading.

Fig. 11b shows the total pressure loss in several planes between 50% and 90% root chord. The maximum total pressure loss is very much aligned with the primary vortex core. Fig. 11c shows that the vortex core is not related to the maximum of the local Mach number, but is rather accompanied by a local saddle point between two maximum values. The maximum Mach number value located above the vortex core is due to high mainflow velocity, the maximum below is due to high cross-flow velocity. Further analysis of the data (not displayed) in planes between 10% and 90% root chord shows that the vortex core is aligned with a local static pressure minimum and a density minimum. A maximum entropy increase is also approximately aligned with the vortex core (fig. 11d).

As fig. 9 indicates, the steady streamlines roll up around a vortex core. However, they do not converge towards an axis within the vortex core. On the other hand, the experimental findings of Engler [27] for subsonic flow clearly indicate that the vorticity is concentrating in a sheet which rolls up until it winds around a core. Successive windings have been identified by use of an ultrasonic laser measuring system. Shirayama [24] has integrated the vorticity lines of a numerical incompressible Navier-Stokes simulation of the laminar flow around a sharp edged delta wing at  $Re = 10000$ ,  $\alpha = 30^\circ$ . The flow turned out to be unsteady, while the results presented here show a steady, transitional, transonic flow. We wanted to find out how the vorticity behaves in our flow field. Fig. 12a indicates that  $|\text{curl } \vec{v}|$  plotted in five sections across the wing gradually "separates" out of the boundary layer near the leading edge. A local extremum value of vorticity is squeezed off downstream of about 45% root chord location. Further downstream this maximum develops a plateau of vorticity which is closely aligned with the vortex core defined above. No roll-up of a vortex sheet is recognized in our transitional, steady, transonic flow simulation. Fig. 12b shows that helicity density maximizes at the same location as vorticity does.

Our delta wing has a round leading edge and the separation lines are neither fixed to certain critical points in the skin-friction pattern nor do they leave from the wing tip. By the help of fig. 13 we intend to show the following. If there were critical points, like those shown in fig. 14 (bottom case) we would follow the so called singular streamsurface defined by the special set of streamlines leaving or reaching the critical points. Of course, the local axis of the developing vortex would start at a focus on the wall (or at a globally winding node). However, a local axis of the vortex leaving the focus or node does not necessarily follow the single streamline that leaves the focus!

The singular streamsurface SS2 may fold, unfold, it may show so called focal windings [12] [26] with streamsurface singularities. Its behaviour is a result of the vorticity field induction. The nodal-point / saddle-point combination ( $F - S$ ) on the wall may also annihilate. No critical points are then left on the wall (see fig. 14 two middle cases). However, separated vortices are still present and the difficulty arises how to trap vortices and vortex cores by proper streamline integration. The same problem arises for vortex-line integration. At the time being no topologically defined "skeleton" of a vortex caused by open flow separation can be given other than the vortex core definition by complex eigenvalue as discussed above. Fig. 13 also indicates that there may be regions (for instance the vortex core region) where streamlines are fed in via a narrow gap of initial points only. This is an important issue for flow visualizations. (See the paper of Hilgenstock & Vollmers [22]).

Thermal "footprints" on a wall of separating vortices, with interactions of closed and open separations (Wang et al. [28]), are considered next.

**Separated vortices and wall heat fluxes  
in hypersonic flows past a double ellipsoid  
at various angles of attack**

The hypersonic flow past a double-ellipsoid is experimentally investigated at CEAT and numerically simulated for comparison and validation purposes of both numerics and experiments. This geometry was a testcase for the *Workshop on Hypersonic Flows for Reentry Problems*, too. The comparison of experimentally and numerically determined flow field data agrees well. This is also true for the heat flux in the symmetry plane being a very sensitive quantity. (No other locations of quantitative values of the heat flux are available so far from the experimentalists). The assumption of laminar flow is in accordance with the experiments. The windtunnel conditions are: Mach number  $M_\infty = 8.15$ , freestream stagnation temperature  $T_0 = 800\text{ K}$ , isothermal wall  $T_w/T_0 \approx 0.37$ , Reynolds number  $Re_\infty = 960000$  with the characteristic length  $L$  equal to the large half axis of the base ellipsoid and a ratio of the specific heats  $\gamma = 1.4$ . Flow field solutions are obtained for angles of incidence  $\alpha = 0^\circ, 20^\circ, 25^\circ, 30^\circ, 35^\circ, 40^\circ$ .

The basic equations under consideration are the unsteady Navier-Stokes equations in thin-layer approximation. An unsteady approach is necessary for the double-ellipsoid simulations since the flow field contains a subsonic area in the stagnation region of the base ellipsoid besides the subsonic part of the boundary layer. In this case the governing equations exhibit an elliptic behaviour requiring a time marching solution procedure. The use of a constant time-step in the whole flow field allows the computation of an unsteady flow behaviour. Otherwise, the time-stepping approach (usually) converges the flow field to a steady state.

The equations are solved numerically via a finite difference scheme on a surface oriented grid system. The bow shock is considered to be one boundary of the computational space, where a shock-fitting procedure is applied. Thus, one result of the solution is the location of the bow shock. On the other hand the shock-fitting approach requires a reliable updating of the entire mesh after each time step. This is done in an algebraic manner. Details of the numerical procedure are given in [29].

So far, we are not interested in flow field simulations with an angle of yaw. Thus, a symmetry plane has been introduced to reduce the computational effort. A simple extrapolation formula  $\partial^2 q / \partial \xi^2 = 0$  is chosen at the outflow boundary in the supersonic region modelling the outgoing signal propagation. This is also done in the subsonic part of the boundary layer where the steady flow is assumed to be governed by parabolic equations. Thus, the present solutions do not include the base flow and the wake probably being unsteady. The number of grid points for zero angle of incidence is 392000 and for all the other cases it is 315000. For  $\alpha = 0^\circ$  the distribution of the points in near wall normal direction is chosen such that the boundary layer and the slip surface downstream of the shock bow shock interaction are resolved. For the other angles of incidence no fine mesh near the bow shock is used because the bow shock is not longer interacting with the embedded shock.

The flow field is characterized by a separated flow region as well as an embedded shock caused by the second ellipsoid (canopy). The strength of this canopy shock varies due to the different angles of incidence. This variation also causes changes of the footprints of the flow which are investigated in the following.

Fig. 14a displays the structure of the skin-friction lines calculated for various angles of incidence  $\alpha = 0^\circ$ ,

$25^\circ, 30^\circ$  and  $40^\circ$ . Superimposed we have plotted the local wall heat fluxes by mapping it onto a gray scale where maximum values appear bright. Strong local maximum values of wall heat-fluxes appear in the front stagnation region at every angle of incidence. Increased heating appears in regions of flow attachment on the canopy at  $\alpha = 0^\circ$ .

Fig. 14b shows selected streamlines of the solutions which, according to the behaviour of the numerical residuum have converged to a steady state. At  $\alpha = 0^\circ$  a horseshoe-type vortex flow separation is indicated by the skin-friction behaviour in front of the canopy; it is clearly a closed type of flow separation. A second vortex flow develops on top of the canopy according to fig. 14b for increasing  $\alpha$  which is of the open type according fig. 14a. No critical points of separation can be identified along skin-friction lines D. At  $\alpha = 0^\circ$  two further open type separations may be conjectured from local wall shear stress convergence at B and C.

The flow topology changes between  $\alpha = 0^\circ$  and  $\alpha = 40^\circ$  where we recognize that the former closed separation line of the horseshoe vortex has changed into an open type. In order to describe the correct outer flow topology it is necessary to identify all the critical points within the flow field. Wall-flow analysis is not sufficient (see Dallmann [12] and Kordulla et al [30], see also Chong et al [32] where "deformation tensor" has to be replaced by "velocity gradient tensor").

Hence, we locate the other critical points in the velocity field. They appear in the plane of flow symmetry in front of the canopy (fig. 15). It is seen that classical types of horseshoe-vortex "footprints" appear in this section: Footprints of three vortices are seen at  $\alpha = 0^\circ$  and  $30^\circ$  (perhaps there are additional smaller ones right in the corner, possibly due to insufficient numerical resolution). At  $\alpha = 40^\circ$  only one vortex is indicated. We recognize that there is local flow attachment (instead of flow separation!) in front of the canopy on the bottom ellipsoid. Based on these observations we make use of the elementary topological structures developed in Dallmann [26] in order to define a skeleton of the complex vortex flow. The sketched parts of fig. 15 are an attempt to show how the horseshoe-type vortices associated with closed-type separation lines and other open-type flow separations interact and change. One recognizes that, due to vortex-vortex interaction away from the wall via Biot-Savart induction, vortices caused by open-type separation (no critical points involved) are trapped by the singular stream-surfaces defined by closed-type flow separations (ensembles of critical points involved). However, this is just a lucky event because the closed-type horseshoe vortices are present in our case due to the canopy. Otherwise we are left with the same problems of detecting vortex cores and proper streamline integration as stated in the last section. Fig. 16 gives an impressive sequence of oil-flow visualizations, where due to different nose configurations closed- and open-type primary and secondary separations appear simultaneously and combine with each other.

In fig. 17 we have plotted regions of complex eigenvalues of the velocity gradient tensor again in order to locate vortex cores. Here the in-plane swirling motion has been excluded in such a way that only the streamwise vortical, swirling motion within sections normal to each streamline is considered.

We are finally interested in the relationship between the structure of the vortex flow (defined on the basis of the steady velocity field) and the thermal loads on the body. In fig. 18 we show for  $\alpha = 40^\circ$  plots of skin-friction patterns and wall-parallel gradients of the heat flux across the isothermal boundary (in fig. 18b,c,d,g superimposed on skin-friction pattern). Based on figs. 14, 18 we identify two special features: First we recog-

nize that the maximum heat fluxes may appear considerable distances away from stagnation points (fig. 18d,e) and that it is not correct to assume that maximum heat-flux values are always associated with stagnation points in three-dimensional flows! As a matter of fact, there are two local minimum heat-flux regions on starboard and port in front of the canopy in regions (fig. 18e) where, according to fig. 14b and 18a the external velocity field is directed towards the base ellipsoid in a swirling motion. The last feature is not observed at the low angles of incidence. In conclusion we find that both, oil-flow visualizations and heat-flux visualizations, are required simultaneously and one information does not allow to conjecture the other.

#### Conclusions

1. The sequence of topologies of instantaneous velocity fields of unsteady wakes behind cylinders has been studied. We recognize that numerical simulations of the flow around a cylinder at  $Re = 1500$ ,  $Ma = 0.3$  [7] show a sequence which is essentially different to one deduced [6] from Prandtl's experiment. There is no annihilation of instantaneous separation and attachment points during a vortex shedding cycle.
2. A topological model is proposed which allows that separation lines may be (almost) stationary although unsteady vortex shedding from separation bubbles occurs.
3. The numerical simulations of the flow around a sphere exhibit a stationary separation line. This line is almost circular, the attached flow remains almost axisymmetric while the separated flow region and the wake become three-dimensional prior to the onset of vortex shedding. Periodic topological changes of the instantaneous skin-friction patterns are observed within the separated flow region.
4. "Vortex cores" as well as "vortices" in general swirling flows can be located by identifying regions where the velocity gradient tensor exhibits complex eigenvalues. The laminar wake behind a sphere in subsonic flow, the transitional transonic flow around a round-edged delta wing and the laminar hypersonic flow past a double-ellipsoid served as examples.
5. Maximum values of the heat flux across the wall in general compressible flows do not appear at stagnation points of the velocity field topology, although they may occur nearby. The wall shear stress topology and the wall heat flux topology do not have coinciding critical points in general.

#### Acknowledgement

Th. Herberg kindly assisted in plotting several delta wing data.

#### References

- [1] Dallmann, U. & Schulte-Werning, B.: Topological changes of axisymmetric and non-axisymmetric vortex flows. In: Topological Fluid Mechanics, Proc. of the IUTAM Symp., Cambridge, 1989, (H.K. Moffatt, A. Tsinobori, eds.) Cambridge Univ. Press, 1990, 372-383.
- [2] Lugt, H.J.: The Dilemma of Defining a Vortex. In: Theoretical and Experimental Fluid Mechanics, Eds.: U. Möller, K.G. Roesner, B. Schmidt, Springer Verlag Berlin - Heidelberg - New York, 1979.
- [3] Dallmann, U. & Schewe, G.: On Topological Changes of Separating Flow Structures at Transition Reynolds Numbers. AIAA 87-1266-CP.
- [4] Stöckle, P.: Über die Ablösung der Strömung am querangeströmten Kreiszylinder. Dissertation Universität Hannover, 1990.
- [5] Vollmers, H.: A Concise Introduction to COMADI. Report DLR-IB 221-89 A 22, 1989.
- [6] Perry, A.E., Chong, M.S. & Lim, T.T.: The vortex-shedding process behind two-dimensional bluff bodies. J. Fluid Mech. 116, 1982.
- [7] Sun, Y.C.; Shen, S.F. & Zhu, Z.: A Numerical Simulation of the Flow Development Behind a Circular Cylinder Started from Rest and a Criterion for Investigating Unsteady Separating Flows. Acta Mechanica 71 (1988).
- [8] Braza, M.; Chassaing, P. & Ha Minh, H.: Numerical Study and Physical Analysis of the Pressure and Velocity Fields in the Near Wake of a Circular Cylinder. J. Fluid Mech., Vol.165 (1986).
- [9] Dallmann, U.: On the Formation of Three-Dimensional Vortex Flow Structures. DFVLR-IB 221-85 A 13 (1985).
- [10] Gruber, K.: Numerische Untersuchungen zum Problem der Grenzschichtablösung. Fortschritt-Berichte VDI, Reihe 7, Nr. 146 (1987), VDI-Verlag, Düsseldorf.
- [11] Pauley, L. Main, P. & Reynolds, W.: On the Structure of Two- and Three-Dimensional Unsteady Separation. AIAA 89-0287-CP.
- [12] Dallmann, U.: Topological structures of three-dimensional flow separations. DFVLR-IB 221-82 A 07, 1982.
- [13] Vollmers, H., Kreplin, H.-P., Meier, H.U.: Separation and vortical-type flow around a prolate spheroid - Evaluation of relevant parameters. AGARD-CP-342, 1983.
- [14] Müller, B.: Navier-Stokes solution for hypersonic flow over an intended nosetip. AIAA Paper 85-1504.
- [15] Riedelbauch, S., Müller, B.: The simulation of three-dimensional viscous supersonic flow past blunt bodies with a hybrid implicit/explicit finite-difference method. DFVLR-FB 87-32 (1987).
- [16] Schulte-Werning, B.: Numerische Simulation und topologische Analyse der abgelösten Strömung an einer Kugel. Dissertation Univ. Munich, 1990; DLR-FB 90-43.
- [17] Clift, R., Grace, J.R. & Weber, M.E.: Bubbles, Drops and Particles. Academic 1978.
- [18] Shirayama, S., Kuwahara, K.: Flow past a sphere topological transitions of the vorticity field. AIAA 90-3105, 1990.
- [19] Dallmann, U.: Analysis of simulations of topologically changing three-dimensional separated flows. Proc. IUTAM Symposium on Separated Flows and Jets, Novosibirsk, UdSSR, July 9-13, 1990, Springer, to appear.
- [20] Schulte-Werning, B., Dallmann, U.: Numerical simulation of vortex chain formation by vorticity shedding from a sphere into the wake. Proc. IUTAM Symposium on Separated Flows and Jets, Novosibirsk, UdSSR, July 9-13, 1990, Springer, to appear.
- [21] Shirayama, S. & Kuwahara, K.: Patterns of Three-Dimensional Boundary Layer Separation. AIAA-87-0461.
- [22] Hilgenstock, A., Vollmers, H.: On the simulation of compressible turbulent flows past delta wing, delta wing body and delta wing-canard. 67th AGARD Fluid Dynamics Panel Symp., The Hague, 1990.
- [23] Hilgenstock, A.: Ein Beitrag zur numerischen Simulation der transsonischen Strömung um einen Deltaflügel durch Lösung der Navier-Stokes'schen Bewegungsgleichungen. Dissertation Universität Karlsruhe (TH). DLR-FB 90-13, 1990.
- [24] Shirayama, S.: A structure of leading-edge and tip vortices at a delta wing. AIAA 89-1803-CP.
- [25] Levy, Y., Segner, A.: Graphical representation of three-dimensional vortical flows by means of helicity density and normalized helicity. AIAA 88-2598-CP, p.687-699.
- [26] Dallmann, U.: Three-Dimensional Vortex Structures and Vorticity Topology. Proc. IUTAM Symposium on Fundamental Aspects of Vortex Motion, 31.8.-4.9.1987, Tokyo, Japan, (H. Hasimoto and T. Kambe, eds.), North-Holland Amsterdam, 1988, pp.183-189.
- [27] Engler, R.H.: Vortex breakdown - investigations by using the ultrasonic-laser method and laser-sheet technique. ICAS-88-3.11.3, 1988, 1731-1737.
- [28] Wang, K.C., Zhou, H.C., Hu, C.H. & Harrington, S.: Three-dimensional separated flow structure over prolate spheroids. Proc. R. Soc., A 421, 73-90, 1990.
- [29] Riedelbauch, S., Brenner, G., Möller, B. & Kordulla, W.: Numerical simulation of laminar hypersonic flow past a double-ellipsoid. AIAA-89-1840, 1989.
- [30] Kordulla, W., Vollmers, H., Dallmann, U.: Simulation of three-dimensional transonic flow with separation past a hemisphere-cylinder configuration. AGARD Meeting, Aix-en-Provence, 1986. AGARD-CP-412, 31-1 - 31-15.
- [31] Chong, M.S., Perry, A.D., Cantwell, B.J.: A general classification of three-dimensional flow fields. Phys. Fluids A, Vol.2 (5), 1990, 765-777.

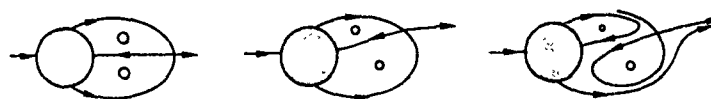


Fig. 1 Topological change leading from a steady, symmetrical near wake bubble via an asymmetric flow to unsteady vortex shedding (global bifurcation)

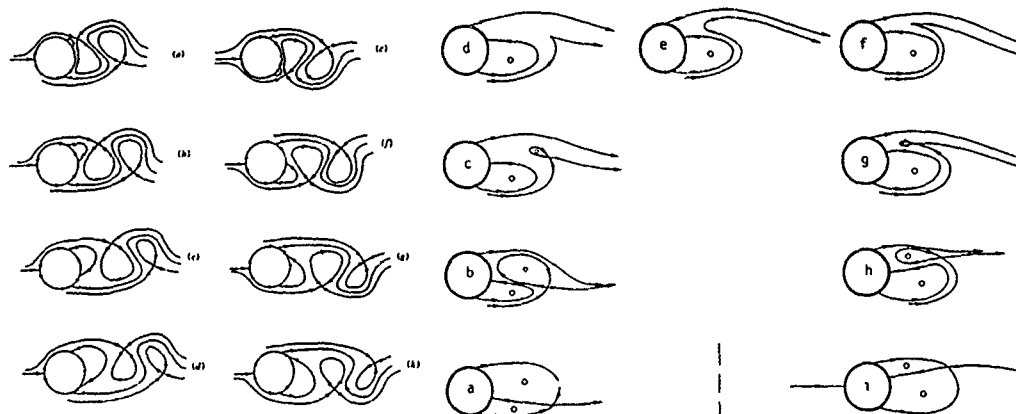


Fig. 2a Simple model for steady incompressible vortex shedding at low Reynolds numbers proposed by Perry et al. [6]. Observer moving with the cylinder

Fig. 2b Sequence of topological changes of instantaneous streamline patterns based on the simulations of Sun et al [7]. Half a shedding period is sketched  $Re = 1500$ ,  $Ma = 0.3$ .

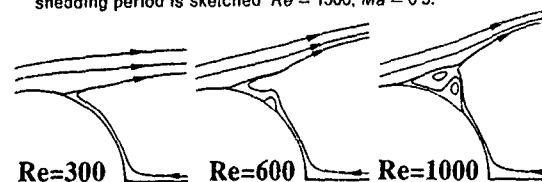


Fig. 4a Streamlines in the flow separation region on the sphere

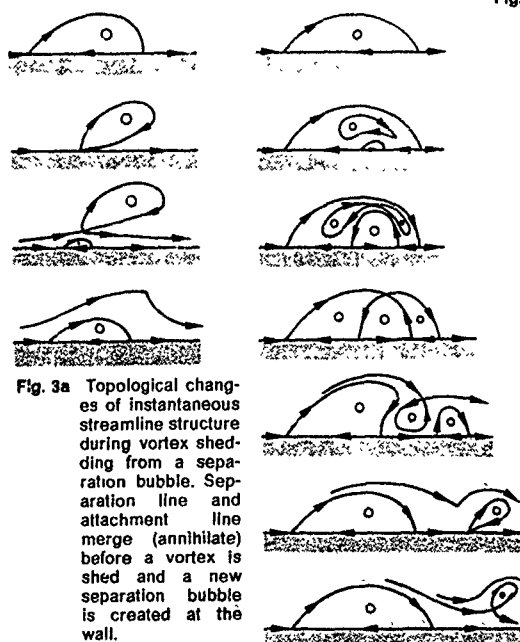


Fig. 3a Topological changes of instantaneous streamline structure during vortex shedding from a separation bubble. Separation line and attachment line merge (annihilate) before a vortex is shed and a new separation bubble is created at the wall.

Fig. 3b Unsteady separation and vortex shedding: Due to the formation of multiple connected recirculation zones no annihilation of separation and attachment lines is required during the process of vortex shedding.

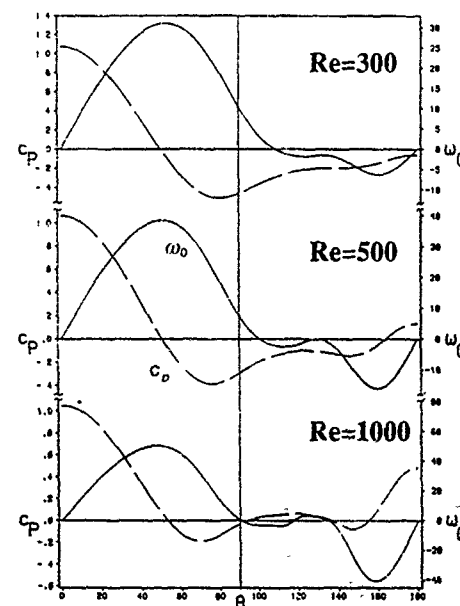


Fig. 4b

Pressure  $c_p$  and vorticity  $\omega_0$  on the sphere, indicating incipient secondary separation at  $Re = 500$  in axisymmetric flow.

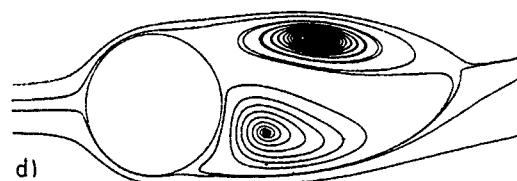
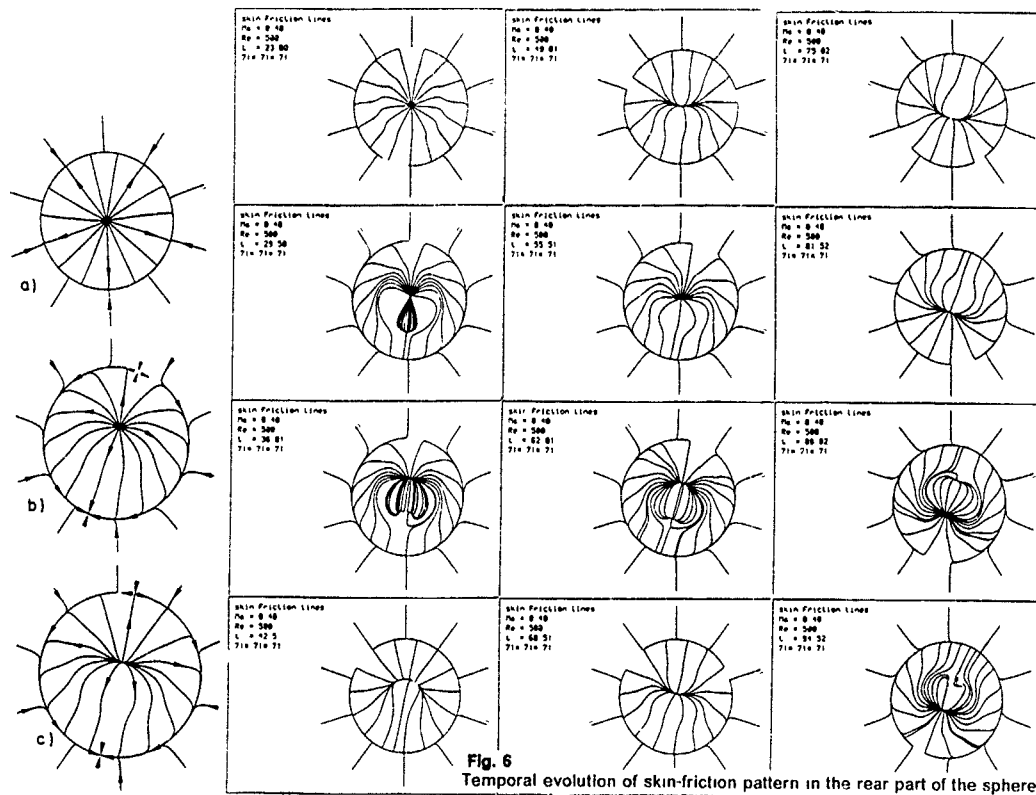


Fig. 5 Stationary skin friction lines on the sphere for  $Re = 200$  (a),  $300$  (b),  $400$  (c). Sectional streamlines (d) in a plane of wake flow symmetry based on fig. 5c,  $Re = 400$

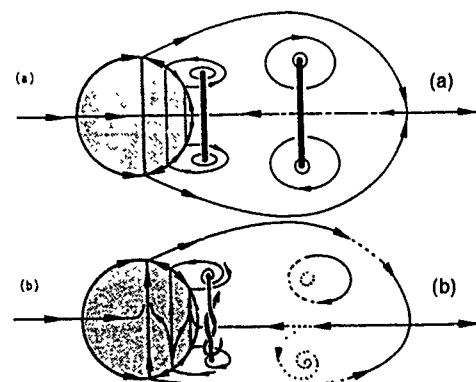


Fig. 7 Topological structure of (a) two-dimensional or axisymmetric separated flow with secondary separation and (b) onset of three-dimensional separation. Torus-like vortex rings (c) break up, azimuthal flow develops and horseshoe-type vortices (d) form.

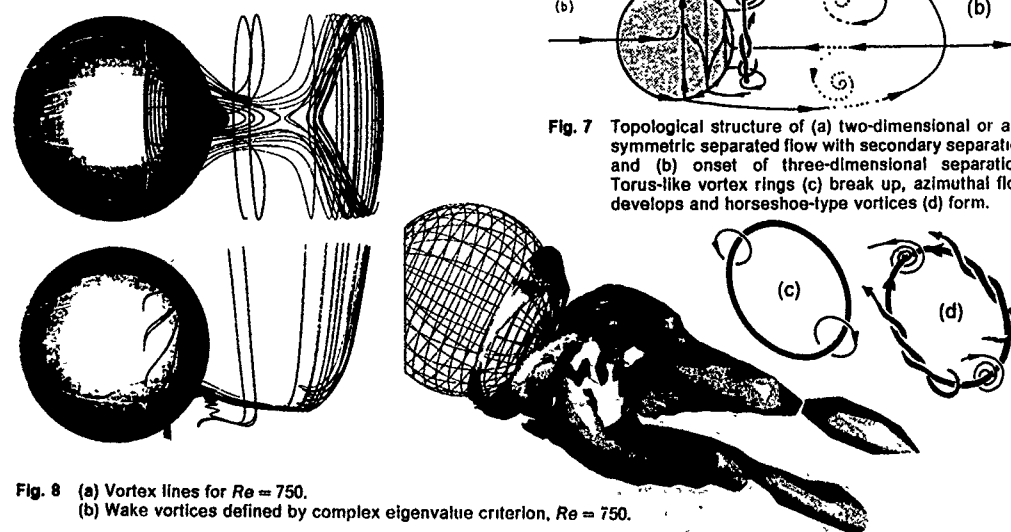


Fig. 8 (a) Vortex lines for  $Re = 750$ . (b) Wake vortices defined by complex eigenvalue criterion,  $Re = 750$ .

Fig. 9 Vortex flow around a round edged delta wing.

Fig. 10 Skin-friction lines (black) and iso-wall pressure contours (white) in the vortex formation region.

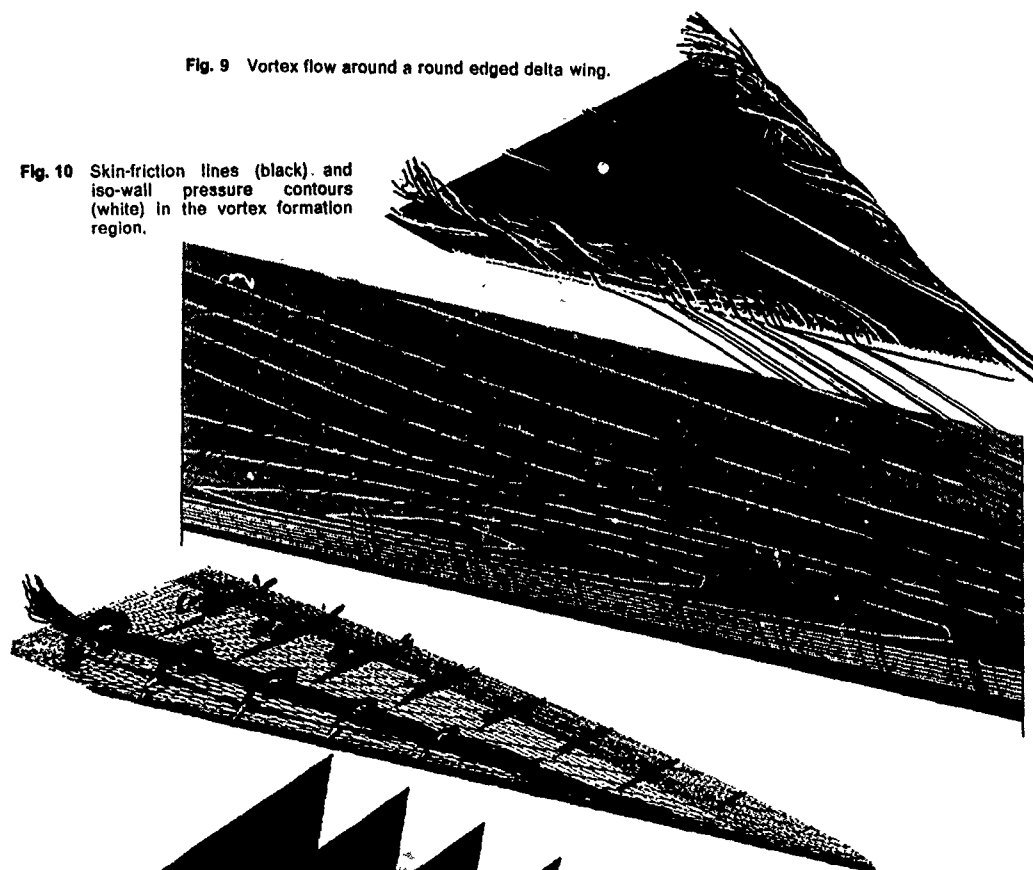


Fig. 11a Vortex core identified by regions of complex eigenvalues of the velocity gradient tensor.

Fig. 11b Total pressure loss contours and core streamlines.

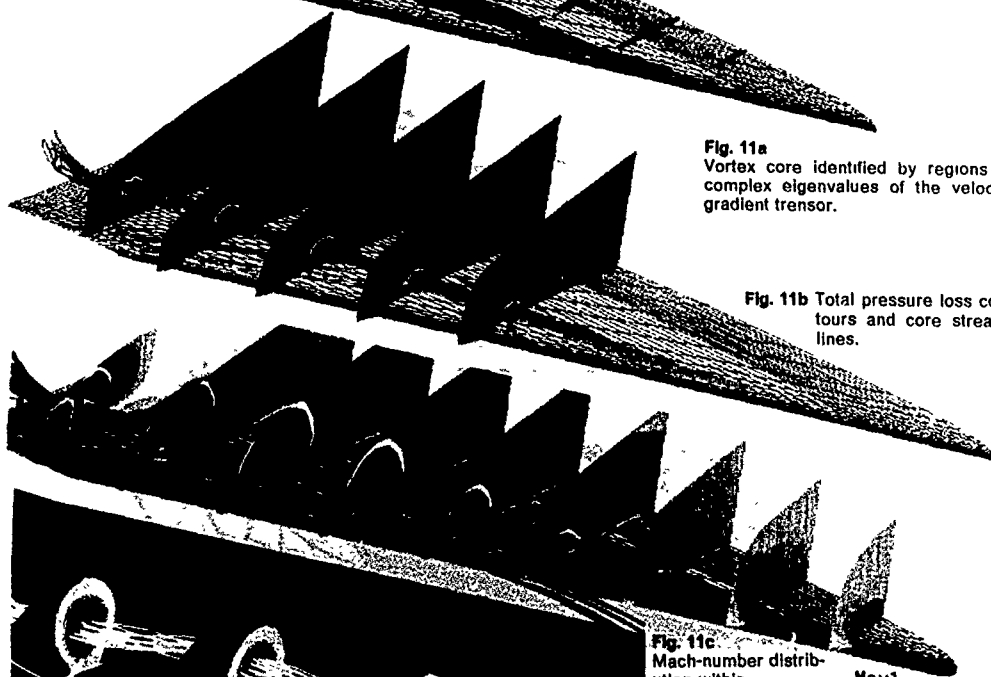


Fig. 11c Mach-number distribution within selected planes and core streamlines.

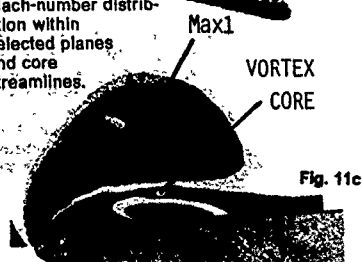
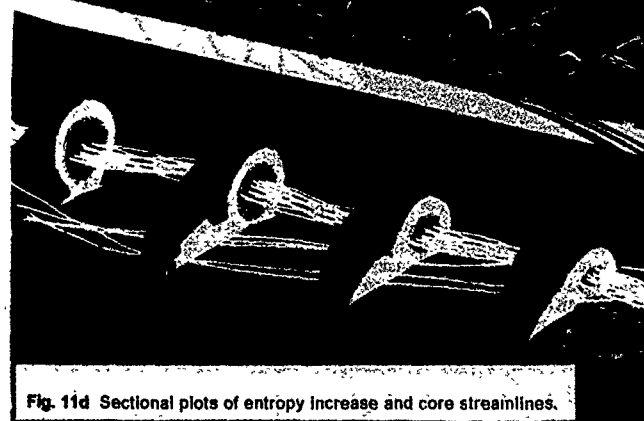


Fig. 11d Sectional plots of entropy increase and core streamlines.



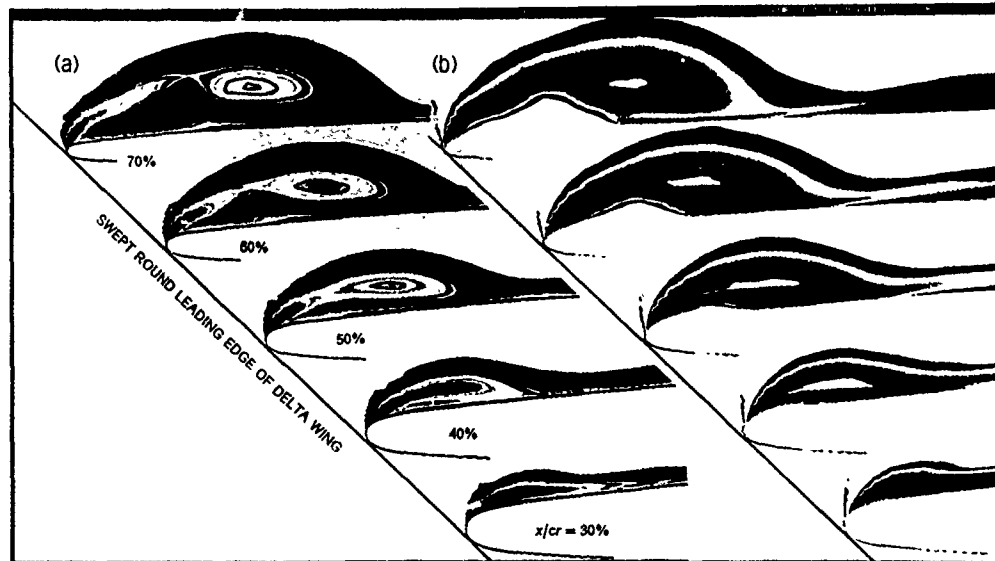


Fig. 12 Sectional plots of iso-vorticity (a) and iso-helicity density (b) on transonic delta wing.

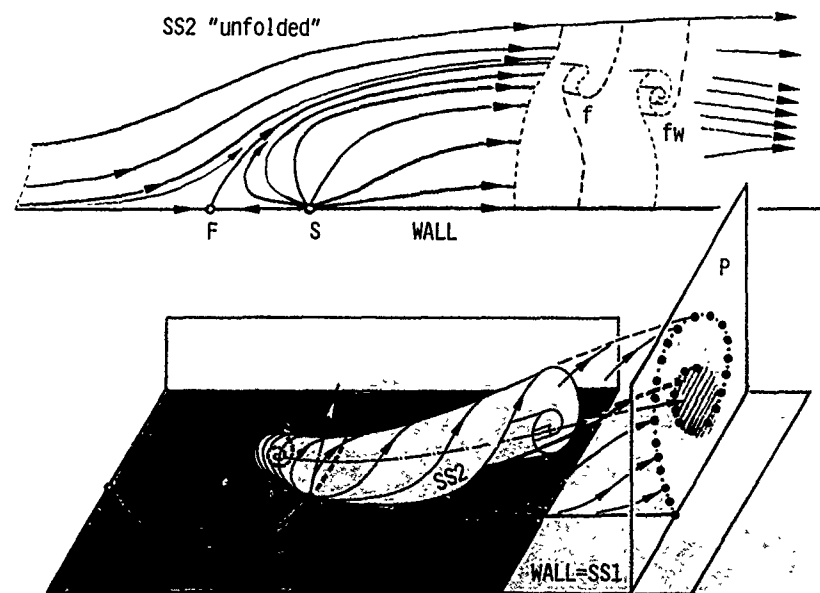


Fig. 13 Sketch indicating singular streamsheets  $WALL = SS1$  and  $SS2$  and "Poincaré section"  $P$ . A sectional streamline pattern in  $P$  would provide a very different information. Only smoke or dye ejected close to  $S$  and  $F$  will provide the correct sectional information in  $P$  (dots, non-uniform smoke or dye intensity in laser light sheet visualization). The "unfolded", singular streamsurface ( $SS2$ ) is shown on top.  $SS2$  may develop a vortex core by a fold or a focal winding. Streamlines converge to the focus  $F$  at the wall; a vortex-core axis does not stay aligned with the streamline leaving the focus. The dashed area may even occur dark in light visualizations due to conical core streamline divergence.  $F$  and  $S$  may annihilate; then  $SS2$  is not a singular streamsurface anymore and the vortex formation is due to open separation.





Fig. 14a Skin-friction pattern and wall heat-flux (gray scale) on double ellipsoid

Fig. 14b Selected streamlines running into and out of vortex cores.

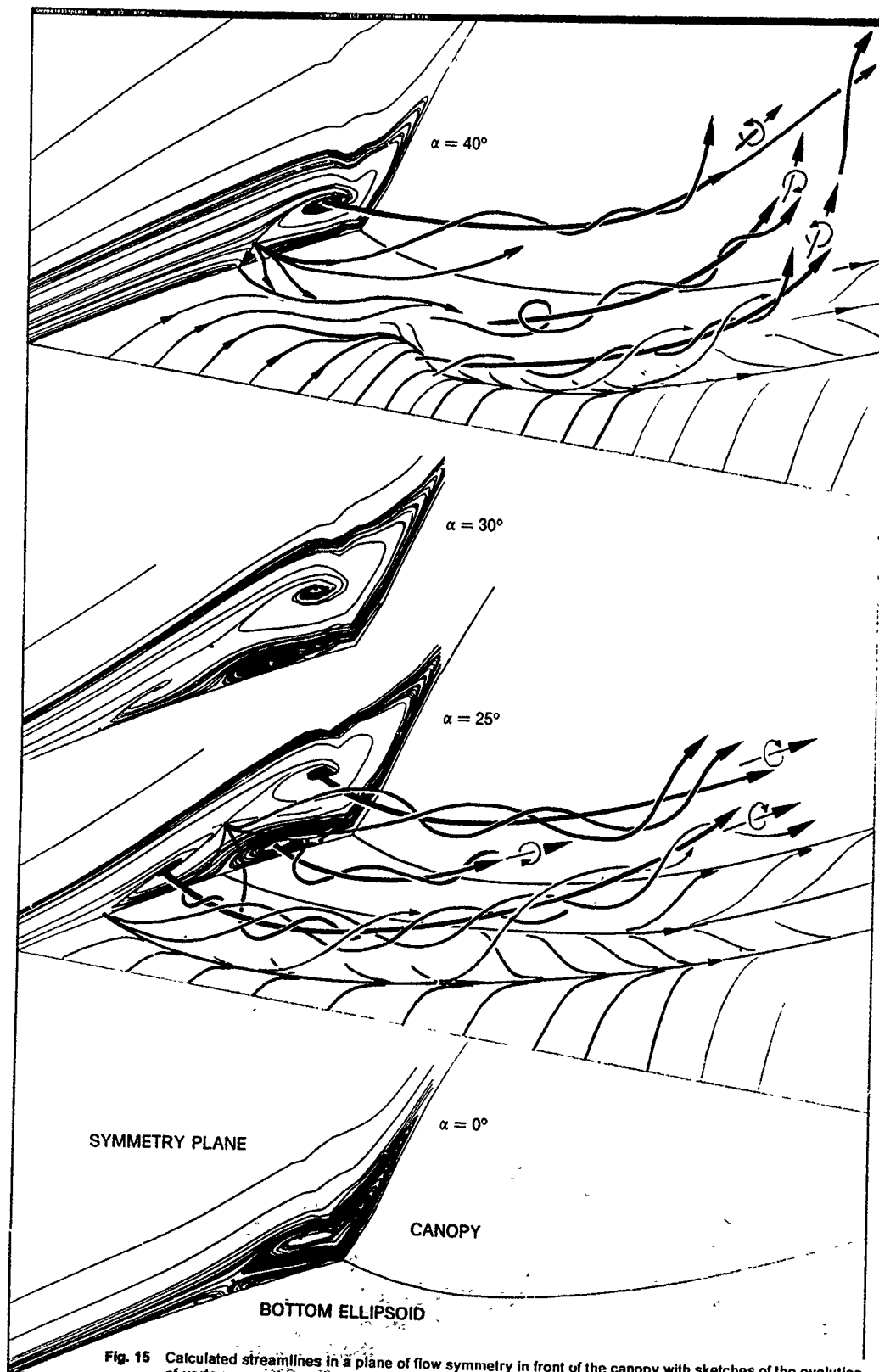


Fig. 15 Calculated streamlines in a plane of flow symmetry in front of the canopy with sketches of the evolution of vortex cores, horseshoe vortices, vortices caused by open and closed separations.



Fig. 16 Oil-flow visualizations on different bodies at  $Re = 7.7 - 8 \times 10^5$ ,  $\alpha = 30^\circ - 40^\circ$   
[by courtesy of H.U.Meier, experiments done at DLR Göttingen]

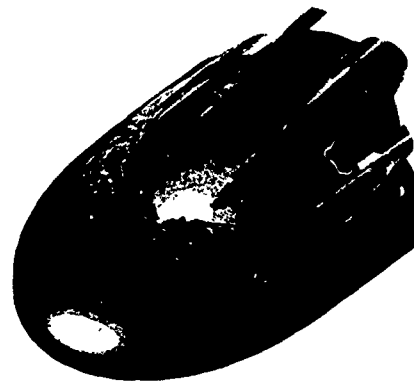


Fig. 17 Regions of complex eigenvalues of velocity gradient tensor.

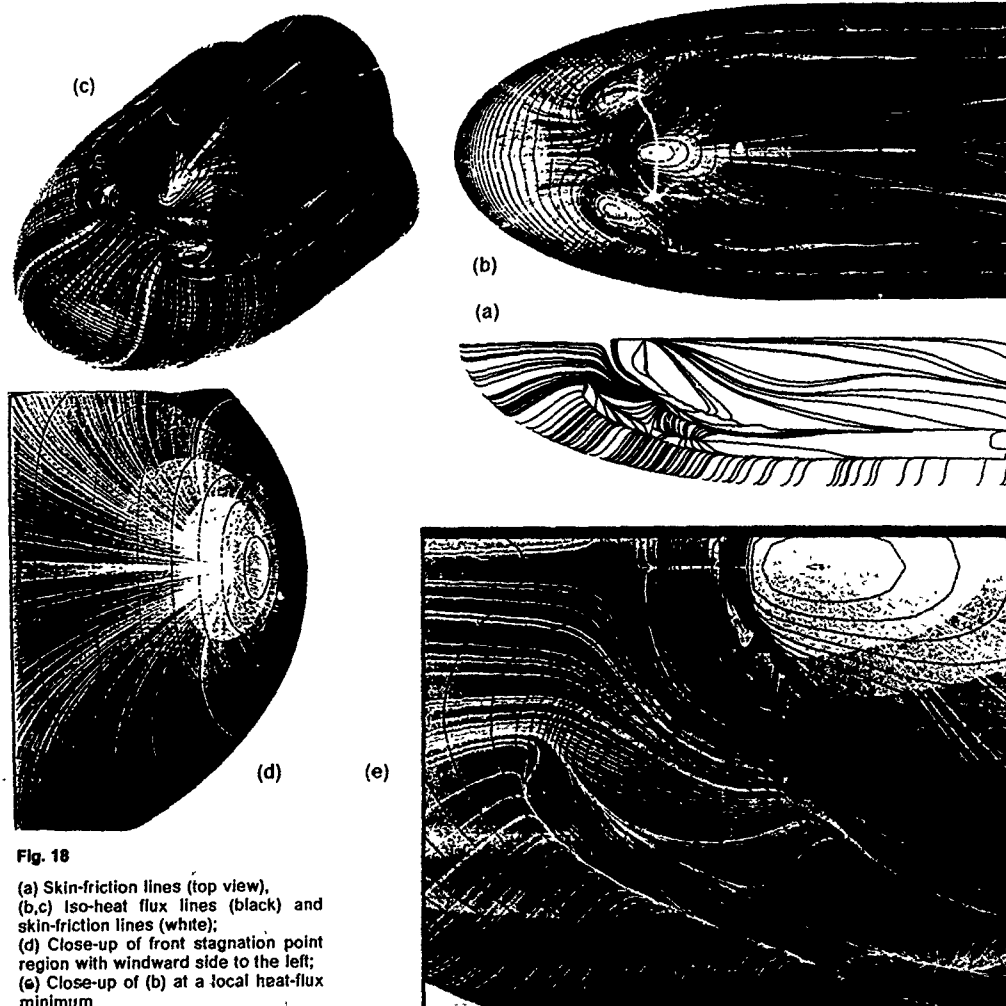


Fig. 18

(a) Skin-friction lines (top view),  
(b,c) Iso-heat flux lines (black) and  
skin-friction lines (white);  
(d) Close-up of front stagnation point  
region with windward side to the left;  
(e) Close-up of (b) at a local heat-flux  
minimum

## LAMINAR-FLOW SECONDARY SEPARATION ON A SLENDER WING

by

K. Kirkköprü and N. Riley

School of Mathematics, University of East Anglia  
Norwich NR4 7TJ  
United Kingdom

## SUMMARY

High Reynolds number laminar flow of an incompressible fluid past a slender delta wing at incidence is considered. An interactive viscous-inviscid calculation is carried out to determine the secondary-separation flow properties on the wing. The overall interactive procedure includes a modification to the leading-edge vortex-sheet configuration which represents the primary separation. Encouraging comparisons are made with experiment.

## 1. INTRODUCTION

In this paper we are concerned with the secondary separation which occurs on the upper surface of a thin slender delta wing placed at incidence in a uniform stream. The fluid is assumed to be incompressible, the flow laminar. Our starting point is the inviscid, conical flow solution for primary separation, in which spiral vortices roll up from the leading edge of the wing, based on the model of Smith (Ref. 1). With the pressure field and surface velocities given from this configuration, we solve the interactive boundary-layer equations over the wing surface and along the leading-edge vortex sheet. Although the interactive equations are multi-structured we treat them in the manner set out by Veldman (Ref. 2) for two-dimensional flows. This means that the main viscous layer, and much thinner sub-layer are accommodated within the classical boundary-layer thickness. Riley (Ref. 3) has shown that at high Reynolds numbers, the interaction in the situation under consideration is largely two-dimensional in nature. This is reflected in the form the interaction law takes. The transverse component of slip velocity at the wing surface, that is the component perpendicular to the separation line, is modified in the interaction. The corresponding modification to the radial component is based upon the conical flow assumption for the outer inviscid flow. The viscous displacement velocity is represented, for the outer inviscid flow, as a source distribution along the wing and the sheet. This source distribution modifies the outer inviscid flow, which is re-calculated to give new positions and strengths for the leading-edge vortex configuration. We now have a new inviscid flow-field with which to carry out the interactive calculation. This process is repeated until a converged solution is achieved.

Earlier models of the secondary separation phenomenon include the inviscid models of Nutter (Ref. 4) and Bruin and Hoeijmakers (Ref. 5). In these models the secondary separation is represented by a spiral vortex sheet that leaves the wing surface smoothly, with the inviscid secondary separation line fixed arbitrarily on it. The solutions presented by these authors differ to the extent that they appear to belong to different solution branches. And in this respect we note that Nutter did find dual solutions for his isolated vortex models of secondary separation. Nutter combined his inviscid model with a boundary-layer calculation which is used to fix the position of flow separation by varying the position of the inviscid separation line until the boundary layer, developing in the given inviscid flow field, separates at the line of inviscid flow separation. In Ref. 5 solutions are presented for varying position of the inviscid separation line, including that for

'smooth' separation which is equivalent to Nutter's solution. There is some experimental evidence, in the water tunnel experiments of Thompson (Ref. 6), which is in favour of the inviscid flow models. However the pressure distributions which result from them are quite different from any that have been observed in practice.

Experiments by, for example, Marsden *et al* (Ref. 7), Hummel (Ref. 8), clearly show the secondary separation phenomenon, and in particular that the full pressure recovery beyond separation, of the inviscid models, is not achieved. The results we have obtained show qualitative agreement with the measured pressure distributions over the wing. Thus the suction rises to a peak value beneath the vortex core and after only a small pressure recovery, to the point where secondary separation takes place, there is a pressure plateau up to the leading edge. Over the Reynolds number range for which we have obtained solutions our pressure distributions display a conical character which is not a feature of the experimentally obtained results. For example, the experimental pressure measurements of Hummel cannot be said to exhibit any conical features. Pressure levels increase monotonically from the apex to the trailing edge. Our predicted pressures are higher than the experimental values over the forward part of the wing, and lower than those over the rear portion. By contrast, geometric features of the real flows do exhibit conical flow properties, and our estimates of the positions of the secondary separation line and the vortex cores show good agreement with experiment. We may conclude that our model of the secondary separation phenomenon is a significant improvement upon earlier models, and displays the main flow features that we attribute to secondary separation.

## 2. MATHEMATICAL TREATMENT

The problem we address is that of high Reynolds number, steady, laminar flow of an incompressible fluid past a slender, thin delta wing, of semi-apex angle  $\gamma$ , at incidence  $\alpha$  to a uniform stream, speed  $U$ . It is assumed that  $\alpha - \alpha/\gamma = O(1)$ . A consequence of the high Reynolds number assumption is that we may expect viscous effects to be confined to the neighbourhood of the wing and shear layers in the flow. Vorticity is generated in the boundary layers and is convected into the free shear layers which originate at, and roll up from, the leading edges of the wing to form the coherent leading-edge vortex structures. The flow outside the shear layers may be treated as inviscid and irrotational. The slenderness approximation allows us to eliminate streamwise derivatives, in favour of cross-stream derivatives, in the full potential equation. However, whilst that allows us to solve for the potential flow in a cross-flow plane, it precludes streamwise influence between one cross-flow plane and another. In particular it does not allow us to take account of the upstream influence from the trailing edge of the wing. The satisfaction of a Kutta condition at the trailing edge has a marked influence on the pressure distribution over the wing surface, a point to which we shall return later when discussing our results. In addition to the assumptions made above we also assume that the outer inviscid flow is conical. The conical flow assumption is effectively a similarity assumption under which the solution need be found in only one cross-flow plane, the solution in other

planes follows by simple scaling. The conical flow assumption also proves to be advantageous in our treatment of the thin viscous layers.

As implied above our approach to this problem is to seek a solution in an outer inviscid region and match this with a solution which is valid in the thin viscous layers at the wing surface and free shear layers. However, we should emphasize that our procedures, described below, are not strictly hierarchical in the sense that the inviscid and viscous calculations are completely separate. It is well-known that a classical boundary-layer development in an adverse pressure gradient, such as is encountered on the outboard part of the wing in the present situation, terminates in a singularity. Our treatment of the viscous layers overcomes this difficulty by incorporating an interaction with the outer inviscid flow. This interaction is a local one, and the role of the outer solution procedure is to adjust the position and strength of the leading-edge vortex configuration to the displacement effects associated with the thin viscous layers. It proves convenient to discuss the inviscid and viscous parts of our treatment of the problem separately.

Consider first the inviscid-flow problem, and refer to Fig. 1(a,b) for a sketch of the physical configuration, and appropriate co-ordinate systems. We introduce dimensionless variables for which the free stream speed  $U$  is a velocity scale, the wing semi-span  $s$  as a length scale for the cross-flow co-ordinates,  $s/K$ , where  $K = \tan \alpha$ , as a length scale for the streamwise co-ordinate, and  $KU$  as a scale for the disturbance velocity potential. The fluid velocity  $\vec{V}$  may then be represented as

$$\vec{V} = \nabla(\phi + \psi), \quad (1)$$

where, within our slender treatment,  $\phi$  satisfies the two-dimensional potential equation

$$\phi_{yy} + \phi_{zz} = 0, \quad (2)$$

and a subscript denotes a derivative. In Fig. 1(a) dimensional co-ordinates are denoted by a prime. With the potential  $\phi$  as the real part of a complex potential  $W(Z)$ ,  $Z = y + iz$ , our task now is to construct a complex analytic function that satisfies all the appropriate boundary conditions. The condition at infinity requires

$$W + iaZ \rightarrow 0 \text{ as } Z \rightarrow \infty, \quad (3)$$

whilst at the wing surface  $|y| \leq 1$ ,  $z = 0$ , we require

$$\text{Im} \left\{ \frac{dW}{dZ} \right\} = -v_N \quad (4)$$

The quantity  $v_N$  is a 'transpiration' velocity due to the viscous displacement effect of the boundary layer on the wing surface. The remaining boundary conditions are to be satisfied on the vortex sheets which originate from the leading edge, and at the leading edge itself where a Kutta condition is to be satisfied such that

$$\frac{dW}{dZ} \text{ is finite at } y = \pm 1, z = 0. \quad (5)$$

On the sheet, as on the wing surface, we take account of the viscous displacement effect, which is significant due to flow separation on the upper surface of the wing. Thus, if  $\Delta$  is the difference operator across the sheet (inside minus outside), and  $\hat{n}$  is the unit inward normal to the trace of the sheet in the cross-flow plane, then

$$\Delta \phi_n = v_N.$$

If we take the outer surface of the sheet as a

stream surface then, following Smith (Ref. 1), we have

$$\phi_n = -r \sin \theta \quad (6a)$$

with the corresponding condition on the inner surface of the sheet

$$\phi_n = -r \sin \theta + v_N \quad (6b)$$

The remaining condition on the sheet is that the pressure jump across it  $\Delta C_p = 0$  where

$$C_p/K^2 = -2\phi_x - (\phi_y^2 + \phi_z^2) + a^2$$

Within the framework of our conical flow assumption the pressure condition may be written as

$$\Delta \phi = \Delta \phi_\sigma (r \cos \theta - \phi_{\sigma m}) - \frac{1}{2} v_N^2, \quad (7)$$

where the suffix  $m$  denotes the mean value of a quantity across the sheet. The vortex sheets are of infinite extent; for computational convenience only a finite part of the sheet is retained. The inner spiral which represents the vortex core is replaced by a concentrated vortex which is joined to the free end of the finite part of the sheet by a cut. This cut not only renders the potential single-valued but also allows vorticity to be fed to the core from the sheet. Since the isolated vortex will not, in general, be aligned with the flow it will experience a force. This force we balance by the force on the cut so that, globally, the fluid is force free. This force-free condition is, on the starboard isolated vortex,

$$\lim_{Z \rightarrow Z_v} \left[ \frac{dW}{dZ} - \frac{\Gamma}{2\pi i} \frac{1}{Z - Z_v} \right] = 2\bar{Z}_v - \bar{Z}_E, \quad (8)$$

where  $\Gamma$  is the circulation of the starboard isolated vortex. To construct the complex potential it proves convenient to introduce the conformal transformation

$$Z^{*2} = Z^2 - 1, \quad Z^* = y^* + iz^* \quad (9)$$

Our vortex configuration in a cross-flow section of the  $Z^*$ -plane is shown in Fig. 1(c), where the cross-section of the wing has now been transformed to the slit  $y^* = 0$ ,  $|z^*| \leq 1$ .

The complex velocity in the transformed plane may now be constructed as

$$\begin{aligned} \frac{dW}{dZ^*} = & -ia + \frac{\Gamma}{2\pi i} \left[ \frac{1}{Z^* - Z_v^*} - \frac{1}{Z^* + \bar{Z}_v^*} \right] + \frac{1}{2\pi i} \int_0^{\sigma_M^*} g^*(\sigma^*) \times \\ & \left[ \frac{1}{Z^* - Z^*(\sigma^*)} - \frac{1}{Z^* + \bar{Z}^*(\sigma^*)} \right] d\sigma^* + \frac{1}{\pi i} \int_0^1 \frac{v_N}{Z^* - t^*} \left| \frac{dt}{dt^*} \right| dt^* \\ & + \frac{1}{2\pi i} \int_0^{\sigma_M^*} v_N \left| \frac{dZ}{dZ^*} \right| \left[ \frac{1}{Z^* - Z^*(\sigma^*)} + \frac{1}{Z^* + \bar{Z}^*(\sigma^*)} \right] d\sigma^*, \end{aligned} \quad (10)$$

where  $\sigma_M^*$  represents the length of the finite part of the vortex sheet in the cross-flow plane. In (10) the first term represents the free stream whilst the second and third terms are contributions from the isolated vortices, and distributed vorticity, strength  $g^*(\sigma^*) = -\Delta \phi / d\sigma^*$ , along the finite parts of the vortex sheets, respectively. The remaining terms represent distributed sources on the upper surface of the wing, and along the vortex sheets, due to the viscous displacement effect of the boundary layer and the free shear

layers. The presence of this source distribution means that the sheets are more correctly referred to as source-vortex sheets. The conditions (3), (4) are automatically satisfied by (10). The remaining conditions, namely (5), which becomes  $dW/dZ^* = 0$  at  $Z^* = 0$ , (6), (7) and (8) serve to determine the unknowns which are the strength  $\Gamma$  and position  $Z_v$  of the isolated vortices, and the strength  $g^*$  and position of the finite parts of the vortex sheets. The source strength is treated as a known quantity, with  $v_N$  given from the viscous calculation.

Our solution procedure follows that of Barsby (Ref. 10), and we introduce intrinsic co-ordinates (see Fig. 1(c))  $(\sigma^*, \psi^*)$  in the transformed plane such that

$$Z^*(\sigma^*) = \int_0^{\sigma^*} e^{i\psi^*(s)} ds \quad (11)$$

To perform the necessary numerical integrations around the sheet, it is divided into  $2n$  equal steps of length  $h$  in arc length  $\sigma^*$ . This defines  $2n+1$  pivotal points in terms of the angle  $\psi^*$  at these points, the first of which coincides with the leading edge at which  $\psi^*(0) = g^*(0) = 0$ . We next introduce intermediate points midway between each pivotal point at which we denote the unknown quantities by  $\psi_i^*, g_i^*, i = 1, 2, \dots, n$ . It is these quantities we calculate, and together with  $Z_v^*$  and  $\Gamma$  they constitute a set of  $4n+3$  unknowns. These are determined from the force and Kutta conditions, which constitute three equations, and the sheet conditions (6a, b), (7), combined to give

$$-g^*(\sigma^*)e^{i\psi^*} \left| \frac{dZ^*}{d\sigma^*} \right|^2 \left[ \bar{Z} \frac{dZ^*}{d\sigma^*} - \frac{dW}{d\sigma^*} \right] + i g^*(\sigma^*) \left| \frac{dZ^*}{d\sigma^*} \right| v_N - i v_N^2 = \Gamma + \int_{\sigma^*}^{\sigma_N^*} g^*(s) ds \quad (12)$$

which, when evaluated at the  $2n$  intermediate points, yield a further  $4n$  conditions. The conditions to be satisfied involve an evaluation of  $dW/dZ^*$  in (10). For points on the sheet the singular integrals are interpreted as Cauchy Principal Values and the singularity is extracted in a standard manner. All remaining integrals are evaluated using high-order integration formulae. The resulting  $4n+3$  nonlinear algebraic equations are solved using a multi-dimensional Newton scheme. With the values of  $\psi_i^*, g_i^*$  determined at the intermediate points the values of  $\psi^*, g^*$  at the pivotal points are then obtained by 4-point Lagrangian interpolation. For the results described in Section 4 we have worked with nine pivotal points, so that  $n=4$ , which we find gives a good representation of the vortex configuration as compared, for example, with the results of Smith (Ref. 1).

We turn next to the thin viscous boundary layers on the wing surface and viscous shear layers at the vortex sheets. Central to our study are the classical laminar-flow boundary-layer equations which we present in the form used by Brown (Ref. 10) for conical flow. We work with the cylindrical polar co-ordinates  $(r, \theta, z)$  of Fig. (1a), where a length  $\ell$  has been used to make lengths dimensionless. For the velocity  $(u, v, w)$  the free-stream speed  $U$  is again used as a scale. With the Reynolds number  $Re = U\ell/\nu$ , we introduce the scaled variables

$$\xi = z\ell^{-1}Re^{1/2}, \quad \bar{w} = w\ell^{-1}Re^{1/2} \quad (13)$$

and then the further simplification

$$\bar{w} = \bar{w} + i f u \quad (14)$$

leads to, in the high-Reynolds number limit,

$$v u_\theta + \bar{w} u_r - v^2 - u_r^2 = v_e(u_{e\theta} - v_e) \quad (15a)$$

$$v v_\theta + \bar{w} v_r + u v - v_r^2 = v_e(v_{e\theta} + u_e) \quad (15b)$$

$$\frac{3}{2}u + v_\theta + \bar{w}_r = 0 \quad (15c)$$

For the viscous shear layers on the sheets we ignore curvature effects in the boundary-layer equations, as if the sheets had been 'unrolled' onto the plane  $z = 0$ , so that (15) are still appropriate. The quantities  $u_e, v_e$  are the external velocity components with which the boundary layer solution must match. We denote the inviscid slip velocities calculated from the potential flow solution described above as  $(u_{ep}, v_{ep})$ . Additional conditions to be satisfied are that the solution is given at the line of attachment  $\theta = \theta_a$ , obtained by a standard expansion procedure, and that the no-slip condition is satisfied on the wing. On the sheet we have adopted a condition of no shear, so that  $\bar{w} = u_r = v_r = 0$  at  $\xi = 0$ . This latter condition is an approximation, but is found to have a negligible effect on the overall flow properties which are dominated by the secondary separation on the upper surface of the wing.

Note that for conical flow all quantities are independent of  $\bar{r}$ , and the calculation of the three-dimensional boundary layer reduces to solving for the radial and transverse velocity components at one cross-flow station; the solutions at other stations follow from a simple scaling. Consistent with this, the right-hand side of (15a) should be set to zero, representing as it does  $-\partial p / \partial \bar{r}$ . It is retained at present for reasons that become clear below.

The adverse transverse pressure gradient, which arises from  $v_{ep}$ , may be expected to terminate the resolution of the boundary-layer equations (15) in a singularity at the point of separation. Such singular behaviour has been confirmed by Nutter (Ref. 4). The singular behaviour is removed if the pressure is allowed to adjust to local flow conditions, and the work of Sychev (Ref. 11) and Smith (Ref. 12) shows that a triple-deck structure, centred upon the point of separation, is crucial for an interactive coupling between the boundary layer and the potential-flow region. Veldman's approach (Ref. 2) to the problem, which incorporates the main features of the asymptotic solution for  $Re \gg 1$ , is one in which a composite equation, rather than composite solution, is employed. It is this approach that we adopt.

The two-dimensional asymptotic theory (Refs 11,12) has been adapted by Riley (Ref. 3) for slender conical flows of the type under consideration here. Our aim is to ensure that the dominant features of that theory are retained in our present treatment. The main deck of the triple-deck structure has thickness  $O(\ell Re^{-1/2})$ , a scaling on which our equations (15) are based. The lower deck, of thickness  $O(\ell Re^{-5/8})$  is embedded within this. Thus if at a large, but finite, Reynolds number sufficient numerical resolution is available (15) will encompass both the lower and main decks. In the region outside the main deck the perturbation to the inviscid potential flow is 'driven' by the viscous displacement velocity  $\bar{w}_d$ . The asymptotic theory (Ref. 3) shows that since the changes which take place normal to the separation line in this slender conical flow are very rapid, compared with those parallel to it, the flow structure exhibits many of the features of a two-dimensional flow. If therefore we write  $\xi = \bar{r}\ell$ ,  $\eta = z$  and scale the perturbation potential by  $U\ell$ , denoting it by  $\phi$ , then we have

$$\phi_{\xi\xi} + \phi_{\eta\eta} = 0 \quad (16)$$

The solution of (16) is to vanish as  $\xi^2 + \eta^2 \rightarrow \infty$ , and on  $\eta = 0$ ,  $\tilde{\phi}_\eta = (r\text{Re})^{-1/2} \tilde{w}_d$ . The solution for  $\tilde{\phi}$  yields a perturbation to the slip velocity  $v_e$  such that

$$v_e = v_{ep} + (r\text{Re}r^2)^{-1/2} \int_{\xi-\xi'}^{\xi} \frac{\tilde{w}_d}{\xi-\xi'} d\xi' \quad (17a)$$

$$= v_{ep} + (\text{Re}_r r^2)^{-1/2} \int_{\xi-\xi'}^{\xi} \frac{\tilde{w}_d}{\xi-\xi'} d\xi', \quad (17b)$$

where we have set  $\hat{r} = r$ ,  $\hat{r}'$  is dimensional radial distance measured from the apex of the wing, and  $\text{Re}_r = U\hat{r}'/\nu$ , so that we now have a representation of the flow which is locally conical. In (17) the integration extends over the interaction region which encompasses both the separation and re-attachment points. For the displacement velocity  $\tilde{w}_d$ , we again invoke the two-dimensional nature of the flow in the interaction region, which is indicated by the asymptotic theory, so that

$$\tilde{w}_d = \frac{\partial}{\partial \theta} \int_0^\infty (v_e - v) d\xi'. \quad (18)$$

The numerical solution of the boundary-layer equations (15) is carried out using the Keller box method (Ref. 13) in a form which allows us to exploit Veldman's quasi-simultaneous interactive procedure (Ref. 2). The discretised forms of (15), in which  $u_e$  is assumed known, and (17) yield a system of nonlinear algebraic equations for the unknowns  $u, v, w, v_e$  and  $\tilde{w}_d$ . Newton's method is again employed to linearise these equations resulting in a matrix of coefficients which is of  $5 \times 5$  block tridiagonal form with an additional column of  $5 \times 5$  matrices. The equations are solved by the block elimination method, for which further details may be found in Ref. 14.

Numerical solution of the boundary-layer equations commences with the attachment line profiles. Initially the solution is advanced using the classical boundary-layer equations only. A switch to the interactive scheme is made when the region of strong interaction is encountered. In this region, where the pressure gradient is initially adverse, flow separation and concomitant flow reversal is encountered. In order to continue the forward integration it has been found necessary to employ the FLARE approximation in the momentum equations (15a, b). In this approximation the transverse convective terms are set to zero when  $v < 0$ ; a justification for this approximation is that when  $v < 0$ ,  $|w| \ll 1$ . Also, because of the elliptic character of our interactive equations, implied by the interactive law (17), it is necessary to make several sweeps along the boundary layer to obtain a converged solution.

In our calculations we have adopted a wing of semi-apex angle  $\gamma = 10^\circ$  with 51 grid points on the wing surface corresponding to  $\delta\theta = 0.2^\circ = 3.491 \times 10^{-3}$  radians. The number of similarly spaced points on the vortex sheet varies with incidence parameter  $\alpha$ , and the calculation on the sheet extends to the point at which  $\tilde{w}_d$  is effectively zero. There are, for example, 32 such grid points on the sheet for  $\alpha = 1$ . The extent of the computational domain normal to the wing surface is dependent upon the Reynolds number, and increases as the Reynolds number increases. We have taken advantage of the box method to use a variable mesh size, typically with  $\delta\xi = 0.025$  close to the boundary and  $\delta\xi = 0.5$  at the outer edge of the boundary layer which, again typically, is at  $\xi_\infty = 0(10^2)$ .

### 3. SOLUTION STRATEGY

The solution strategy we have adopted for the highly nonlinear problem outlined above involves several iterative processes. We outline here our overall strategy.

Our first task is to obtain the initial inviscid solution with  $v_N = 0$ ; such solutions have been obtained previously by Smith (Ref. 1). From this potential flow solution we have the 'slip' velocity components  $u_{ep}, v_{ep}$ , and we are then in a position to study the viscous boundary layers and shear layers. To avoid the singular behaviour at separation we use the interactive approach outlined in Section 2, and allow the pressure to adjust as the step-by-step integration of (15) is carried out. In practice this leads to a continuous adjustment of the external velocity component  $v_e$ , at a fixed  $\text{Re}_r$ , as in equation (17b). Beyond the position of secondary separation it has been found necessary to employ the FLARE approximation in the region of reversed flow. Beyond the leading edge the boundary layers from the upper and lower wing surfaces merge. Since we do not calculate the boundary layer on the lower wing surface, we replace the condition that the upper and lower boundary layers merge smoothly, by the condition that  $\tilde{w} = u_T = v_T = 0$  at  $\xi = 0$  on the vortex sheet. We are satisfied that our solution is not sensitive to this condition, dominated as it is by the separated flow on the upper surface of the wing. The elliptic nature of our viscous calculation which is reflected in the expression (17) means that one sweep is not sufficient to complete the calculation. Further sweeps are necessary with  $v_{ep}$  in (17) fixed. At the commencement of each sweep  $u_e$  is changed. Initially it takes the value  $u_{ep}$ , but is updated at the commencement of each sweep from the equation  $du_e/d\theta = v_e$  in order to maintain local conicality.

When the above iterative procedure is deemed to have converged, and as many as 30 to 40 sweeps may be required to achieve convergence, we may update the outer inviscid solution. The changes to this are brought about by the displacement effect of the wing boundary layers, and the shear layers. With  $\tilde{w}_d$  as in (18) we have  $v_N = \tilde{w}_d/K\text{Re}_r^{1/2}$  to represent the displacement effect in the inviscid solution. The inviscid solution is now recalculated to provide new values of the slip velocity ( $u_{ep}, v_{ep}$ ). The viscous solution is then completed as before, but with one slight modification. Since the displacement effect is now included in the inviscid solution, as well as in (17), we modify (17) such that

$$v_e = v_{ep} + (\text{Re}_r r^2)^{-1/2} \int_{\xi-\xi'}^{\xi} \frac{\tilde{w} - \tilde{w}_{dp}}{\xi-\xi'} d\xi'. \quad (19)$$

In (19)  $\tilde{w}_{dp}$  is the displacement velocity obtained in the previous viscous calculation, and the displacement effect is not now duplicated.

The overall iterative procedure outlined above is continued until convergence, according to some pre-set criteria, has been achieved. In the converged solution we have  $\tilde{w}_d = \tilde{w}_{dp}$ , the right-hand side of (15a) is zero, and the velocities  $v_N, \tilde{w}_d$ , which represent the displacement effect in the inviscid and viscous solutions respectively, are self-consistent.

We discuss the results obtained by the above procedures in the next section.

### 4. RESULTS AND DISCUSSION

As we have already indicated, the starting point for our solutions is the inviscid-flow model in which the primary separation is represented by a vortex sheet springing from the leading edge. For the case  $\alpha = 1$  we show, in Fig. 2(a), the distribution of  $v_{ep}$  from the initial inviscid solution for which, of course,  $\tilde{w}_d = 0$  in (10). Figs 2(b,c,d) show the immediate succession to this in our solution procedure. Thus, Fig. 2(b) shows the distribution of  $v_e$  from the first interactive boundary-layer calculation and Fig. 2(c) the



corresponding viscous displacement velocity  $\bar{w}_d$ . The latter is responsible for the modification to the outer inviscid solution, and in Fig. 2(d) we show the first change to  $v_{ep}$  brought about by the displacement effect. The results shown in Figs 2(b,d) represent one global iteration. In Figs 2(e,f) we show the converged solution after ten global iterations. There is a small irregularity at the leading edge in the inviscid solution which we have been unable to eliminate or explain. We remark that after six global iterations we have introduced under-relaxation such that  $v_{ep} = \frac{1}{2}(v_e + v_{ep})$ . However, a point of interest is that after the fifth global iteration the distribution of  $v_e$  from the viscous part of the calculation is virtually unchanged. Indeed on the wing itself  $v_e$  and  $v_{ep}$  coincide after these five global iterations. The reason that the rate of convergence of  $v_{ep}$  is lower than that of  $v_e$  may be attributed to the changes which take place in the source and vortex strengths on the vortex sheet during each global iteration. These are small enough not to affect the result of the viscous-inviscid interactive calculation, but not sufficiently small that changes in flow properties calculated from the inviscid solution, particularly in the neighbourhood of the sheet, may be ignored. The implication of this is that important features of the flow, such as wing surface pressures, may be determined before there is complete convergence on the sheet itself.

The vortex sheet shape itself changes from that of the primary inviscid flow, as is illustrated in Fig. 3 where the results from the initial inviscid solution, and after one and ten global iterations are compared. The observed displacement is in accord with experiment as we discuss later. In Fig. 4 we compare the pressure distribution with the initial inviscid solution. We see that the suction peak is lower and, as may be expected when there is a region of separated flow, there is not a full pressure recovery beyond separation. For this case flow separation occurs when  $\theta/\gamma = 0.679$ . This may be compared with the values of  $\theta/\gamma = 0.761, 0.607$  obtained by Nutter (Ref. 4) from his boundary-layer calculation, and inviscid secondary separation model respectively. However, neither the pressure distributions predicted by Nutter, nor those from a similar model in Ref. 5 resemble in any way those predicted by the present method, or experimentally observed distributions. The displacement effect associated with the flow separation is well illustrated by the displacement function

$$\delta(\theta) = \int_0^\infty \left(1 - \frac{v}{v_e}\right) d\tau \quad (20)$$

In Fig. 5 we show velocity profiles  $v(\theta, \tau)$  through the separated region of flow. In this figure we also include the curve  $v = 0$ , thus delineating the reversed-flow region, and the displacement function  $\delta(\theta)$ .

With the incidence parameter maintained at  $a = 1$  we have also obtained solutions for  $5 \times 10^3 < Re_r < 2 \times 10^5$ . Pressure distributions in this range are shown in Fig. 6. We remark that for  $Re_r \geq 10^4$ , in this range, the pressure distributions are virtually identical. Only towards the lower end of the range does the separation line begin to move outboard from the value  $\theta/\gamma = 0.679$ . Eventually, of course, the region of separated flow disappears altogether. Similarly the position of the isolated vortex core is relatively unaffected by variations of Reynolds number in this range. Table 1 shows the position of the separation line and isolated vortex as functions of  $Re_r$ . The displacement function  $\delta(\theta)$ , (20), does increase dramatically with  $Re_r$ , but when scaled with  $Re_r^{-1/2}$  it, too, is virtually insensitive to variations with Reynolds number in this range.

Table 1

Position of the separation line  $\theta_s/\gamma$ , and isolated vortex core as functions of  $Re_r$ ;  $a = 1$ .

$Re_r$	$\theta_s/\gamma$	$Z_v$
$5 \times 10^3$	0.778	$0.636 + 0.284i$
$5 \times 10^4$	0.679	$0.637 + 0.280i$
$2 \times 10^5$	0.652	$0.636 + 0.278i$

The above results imply that for  $Re_r \geq 10^4$  the main flow properties behave in a conical fashion in the range of  $Re_r$  under consideration. In spite of our procedures this is not a result that can have been guaranteed. The conical nature of the displacement function has implications for the inviscid model of secondary separation considered by Nutter. The vortex, springing from the wing surface, which represents the secondary separation phenomenon in Nutter's model, would be subsumed by the thick separated viscous layer that we have described above. Our results suggest that this region does not decrease in thickness as  $Re_r$  increases. This suggests in turn that Nutter's inviscid model can never be the appropriate limiting flow at high Reynolds number. To be sure, this particular criticism does not apply to the secondary vortex of Bruin and Hoeijmakers (Ref. 5) which appears to be from a different solution branch from Nutter's. However their solution appears to bear no more resemblance to reality than Nutter's.

We have extended the range of solutions obtained by considering the effects of incidence variation at  $Re_r = 5 \times 10^4$ . In particular we have obtained solutions for the four values of the incidence parameter  $a = 0.5(0.5)2.0$ .

Results which we have obtained by varying  $a$  are shown in Figs 7,8. The pressure variations over the wing surface are shown in Fig. 7. As with the case  $a = 1$  the characteristic features of these are that the suction peak is reduced, when compared with the inviscid flow solutions in the absence of secondary separation, and that beyond the suction peak there is only a minimal pressure recovery. The position of the separation line itself is shown in Table 2. The sheet shapes for this range of the incidence parameter are shown in Fig. 8.

Table 2

Position of the separation line  $\theta_s/\gamma$  as a function of the incidence parameter  $a$ ;  $Re_r = 5 \times 10^4$

$a$	$\theta_s/\gamma$
0.5	0.730
1.0	0.679
1.5	0.657
2.0	0.651

Some of the flow features we have presented above may be compared with experiment. Detailed spanwise pressure distributions have been presented by Fink *et al* (Ref. (15)), Hummel (Ref. 8) and Marsden *et al* (Ref. 7). We make a comparison between the experimental results of Ref. 15, for which  $Re_r = 4 \times 10^5$ , the inviscid results of Smith (Ref. 1) and our present results, in Fig. 9. Our results exhibit features similar to those observed in experiments, in the sense that as we move outboard from the position of peak suction there is not the significant pressure recovery predicted by a purely inviscid theory. In some of the experimental observations there is evidence of a turbulent reattachment of the flow. In our model, which is based upon a laminar flow, the separated flow region extends beyond the leading edge. The experimental pressure distributions in Fig. 9 show higher suction values than our present model predicts. However the extent to which the experi-

mental pressure distributions exhibit conical features is open to question. This is clear from the streamwise surface pressures shown in Fig 10, adapted from Hummel (Ref. 8) where  $Re = 9 \times 10^5$  based on chord. The suction at  $\theta/\gamma = 0.6$  is approximately a maximum. Over the forward part of the wing the suction values are higher than we predict, and fall in the streamwise direction to the trailing edge where they are lower than we predict. Figure 11, which is an adaptation of Smith's Fig. 37 (Ref. 1), shows the normal force coefficient as predicted by the inviscid theory, and as obtained from the pressure measurements of Refs 7,15 assuming the flow to be conical. To this we have added the normal force coefficient from our present work which, on the whole, shows good agreement with experiment.

Although measured pressure distributions along the wing surface are not conical, geometric features of the real flows, which include the separation line, the vortex sheet and the vortex core are remarkably conical. For  $\alpha = 1.5$  Hummel (Ref. 8) finds  $\theta_s/\gamma = 0.67$  whilst for  $0.5 < \alpha < 0.75$  Marsden et al (Ref. 7) measure  $\theta_s/\gamma = 0.66$ . These values may be compared with our calculated values in Table 2. Lowson (Ref. 16) has provided a useful correlation of vortex core positions from no fewer than ten investigations, which include both laminar and turbulent flow. Our Fig. 12 is adapted from his Fig. 2, which shows the experimental results in more detail. There is general agreement that the effect of the secondary separation is to move the vortex core both upward and inboard. That our results are consistent with this may be seen from Fig. 12.

We may conclude that our model of the secondary separation phenomenon, based as it is upon a fully interactive viscous-inviscid flow, is superior to those which rely upon inviscid vortex sheet models of the type discussed in Refs 4,5. However, whilst geometric features of the flow, such as the position of the separation line and vortex-core positions, are predicted satisfactorily, we can record only qualitative agreement between the measured and calculated pressure distributions.

#### ACKNOWLEDGEMENT

This work was carried out with the support of the Procurement Executive, MoD.

#### REFERENCES

1. J.H.B. Smith, Improved calculations of leading-edge separation from slender delta wings, *Proc. R. Soc. A* 306 pp67-90 (1968).
2. A.E.P. Veldman, A numerical method for the calculation of laminar, incompressible boundary layers with strong viscous-inviscid interaction, *NLR TR 79023U* 48pp (1979).
3. N. Riley, Separation from a smooth surface in a slender conical flow, *J. engg Math.* 13 pp75-91 (1979).
4. J. Nutter, *PhD Thesis*, University of East Anglia (1979).
5. A.C. de Bruin and H.W.M. Hoeijmakers, Computation of three-dimensional boundary layer transition and separation on a  $65^\circ$  swept delta wing at  $20^\circ$  angle of attack, *NLR MP 86075U* 12pp (1986).
6. D.H. Thompson, Visualization of separated flows in a water tunnel, Australian Defence Scientific Service, Tech. Memo ARL/A.266 (1971).
7. J.E. Marsden, R.W. Simpson and W.J. Rainbird, An investigation into the flow over delta wings at low speeds with leading edge separation, *C.O. Ae., Cranfield Rept. No 114* 43pp (1958).
8. D. Hummel, Experimentelle Untersuchung dreidimensionaler laminarer Grenzschichten an einem schlanken Deltaflügel, *Zeits. Flug. Welt* 10 pp133-145 (1986).
9. J.E. Barsby, Calculations of the effects of blowing from the leading edges of a cambered delta wing, *ARC R & M 3800* 51pp (1978).
10. S.N. Brown, Singularities associated with separating boundary layers, *Phil. Trans. R. Soc. A* 257 pp409-444 (1965).
11. V.V. Sychev, On laminar separation, *Mekhanika Zhidosti i Gaza* 3 pp47-59 (1972).
12. F.T. Smith, The laminar separation of an incompressible fluid streaming past a smooth surface, *Proc. R. Soc. A* 356 pp443-463 (1977).
13. H.B. Keller, A new difference scheme for parabolic problems, in *Numerical Solution of Partial Differential Equations* (ed. J. Bramble) Academic, New York 1970.
14. K. Kirkkopru and N. Riley, Secondary separation from a slender delta wing, *J. engg Math.* (submitted).
15. P.T. Fink and J. Taylor, Some low speed experiments with  $20^\circ$  delta wings, Imperial College, Dept. of Aeronautics, A.R.C. 17854 (1955).
16. M.V. Lowson, Visualization measurements of vortex flows, *AIAA Paper-89-0191* (27th Aerospace Sciences Meeting, Reno) 10pp (1989).

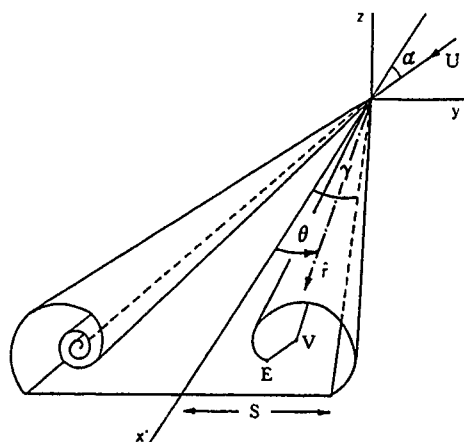


Fig. 1(a) The wing, vortex sheets and co-ordinate system

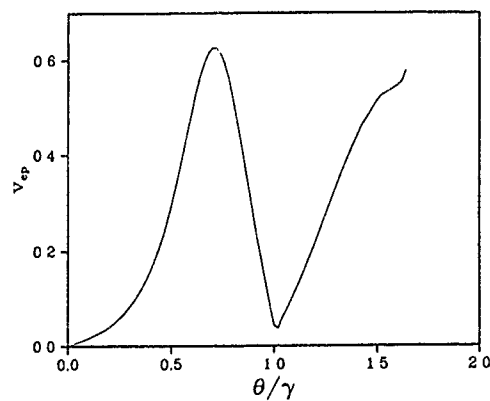


Fig. 2(a) Slip velocity  $v$  from the inviscid flow model with  $ep_a = 1$ ,  $w_d = 0$ .

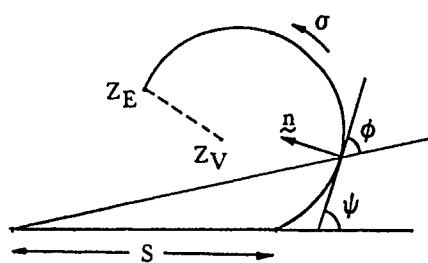


Fig. 1(b) Axes and co-ordinates in the cross-flow plane

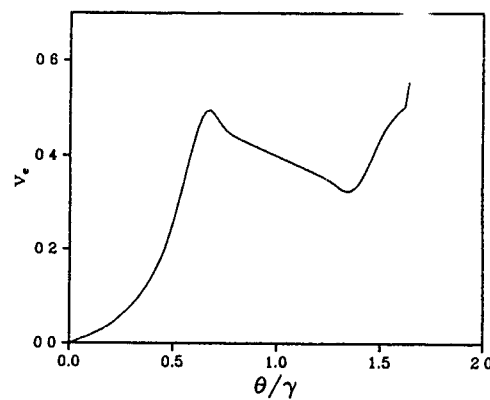


Fig. 2(b)  $v_e$  from the first interactive calculation with  $a = 1$ ,  $Re_x = 5 \times 10^4$

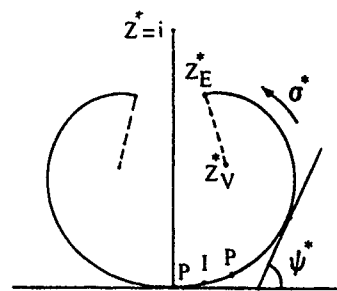


Fig. 1(c) The transformed plane.  
P pivotal, I intermediate point

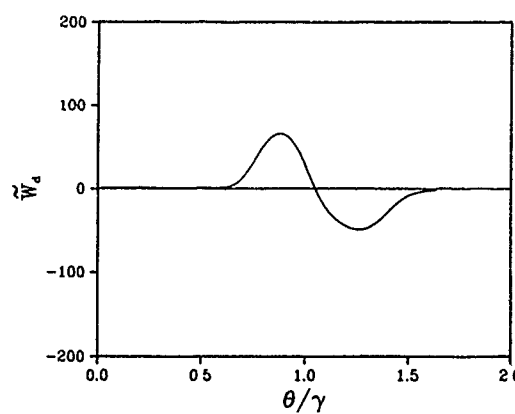


Fig. 2(c)  $w_d$  from the first interactive calculation with  $a = 1$ ,  $Re_x = 5 \times 10^4$

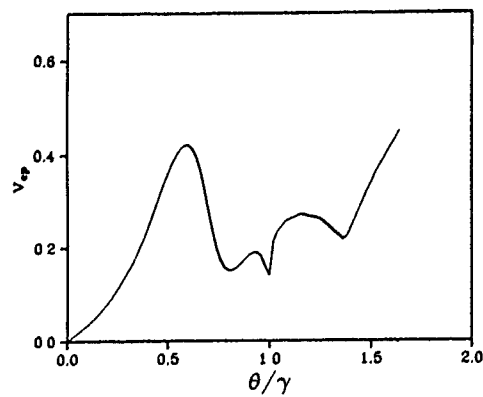


Fig. 2(d)  $v_{ep}$  from the inviscid flow solution with  $a = 1$  and  $\tilde{w}_d$  as in Fig. 2(c)

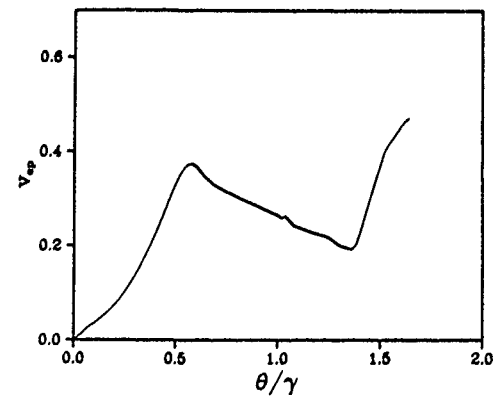


Fig. 2(f)  $v_{ep}$  from the tenth global iteration with  $a = 1$ ,  $Re_\tau = 5 \times 10^4$

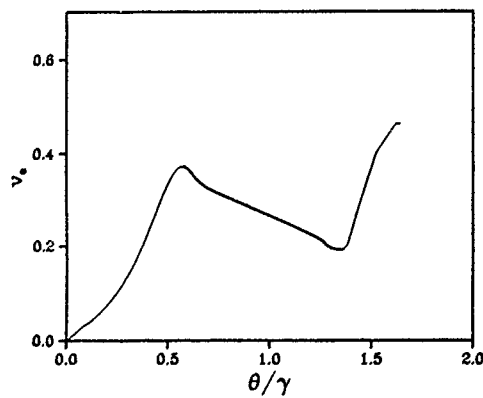


Fig. 2(e)  $v_e$  from the tenth interactive calculation with  $a = 1$ ,  $Re_\tau = 5 \times 10^4$

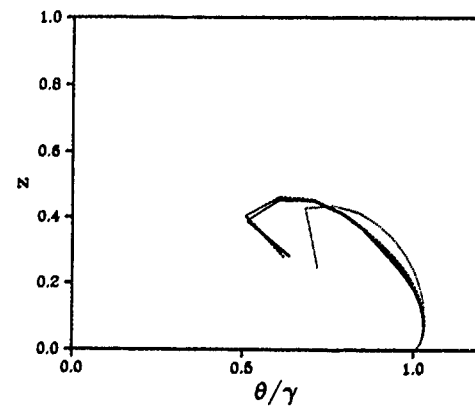


Fig. 3 Vortex sheet shape. (.....) initial inviscid solution, (-----), (—) one and ten global iterations.  $a = 1$ ,  $Re_\tau = 5 \times 10^4$

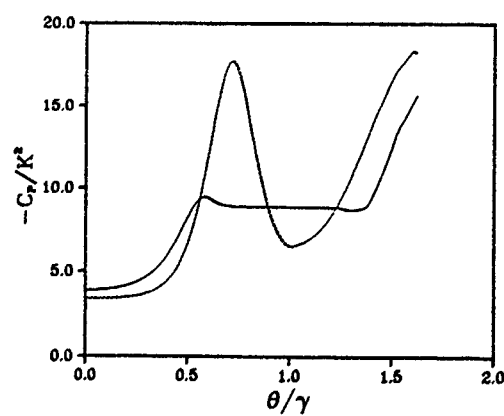


Fig. 4 Comparison of pressure distributions on the upper surface. (—) initial inviscid solution, (-----) interactive solution,  $a = 1$ ,  $Re_\tau = 5 \times 10^4$

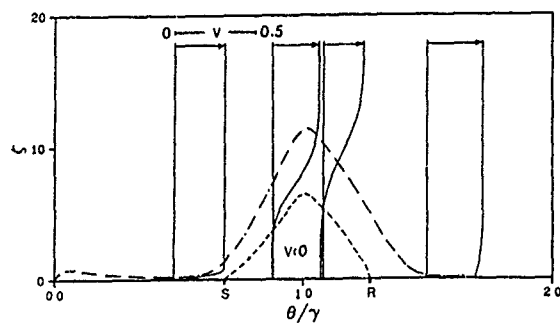


Fig. 5 Velocity profiles and the separated flow region. Separation S, reattachment R. (-----)  $v = 0$ , (-----) displacement function  $\delta$

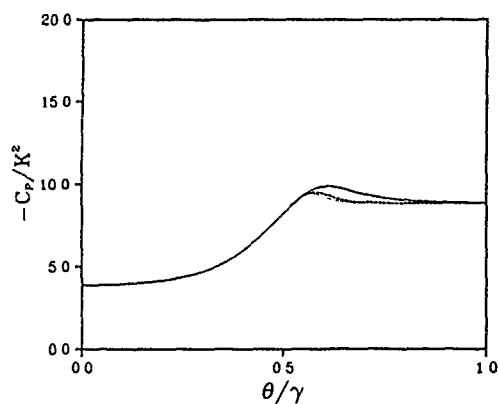


Fig. 6 Pressure on upper surface,  $a = 1$ . (—)  $Re_\tau = 5 \times 10^3$ , (---)  $5 \times 10^4$ , (....)  $2 \times 10^5$

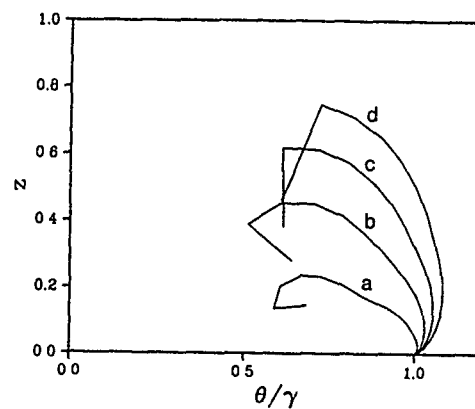


Fig. 8 Sheet shapes,  $Re_\tau = 5 \times 10^4$ . Notation as Fig. 7

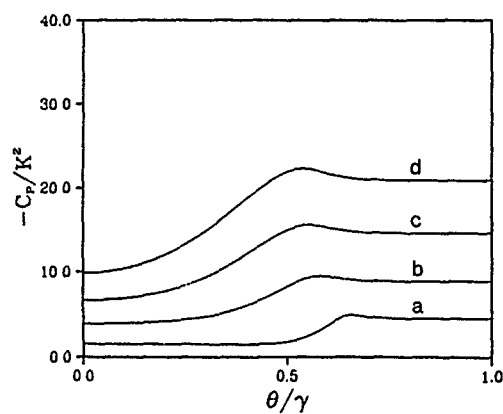


Fig. 7 Pressure on upper surface  $Re_\tau = 5 \times 10^4$  (a)  $a = 0.5$ , (b)  $a = 1.0$ , (c)  $a = 1.5$ , (d)  $a = 2.0$

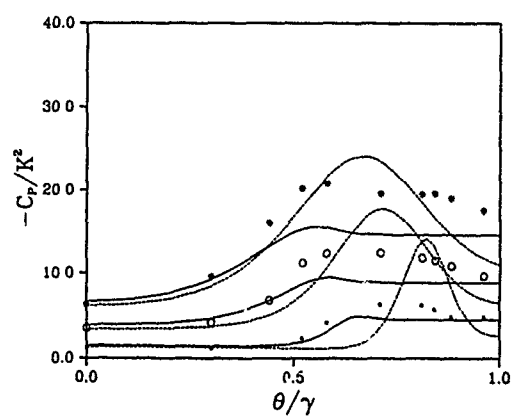


Fig. 9 The pressure distributions of Fig. 7 (—) compared with the inviscid solution (Ref. 1) (---) and experiment (symbols) (Ref. 15)

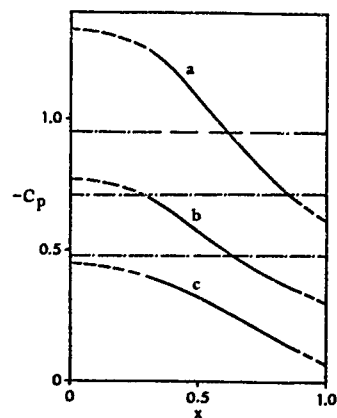


Fig. 10 Experimental pressure plots (Ref. 8) (—) and extrapolation (---) compared with present results (---) (a)  $y = 0.6$ , (b)  $y = 0.4$ , (c)  $y = 0.2$

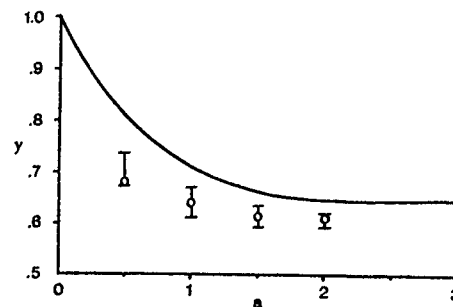


Fig. 12(a) Vortex core lateral position. (—) Ref. 1, O present calculations. I denotes range of experimental results (Ref. 16) for  $10^4 \leq Re_T \leq 7 \times 10^4$

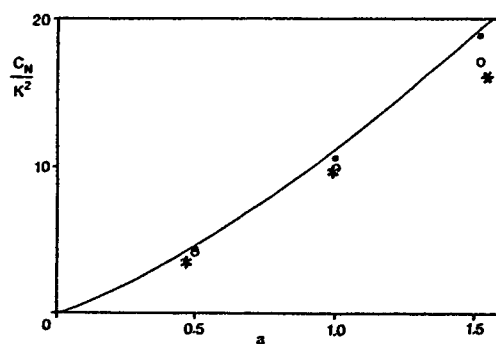


Fig. 11 Normal force coefficient, (—) Ref. 1, O Ref. 15, \* Ref. 7, O present

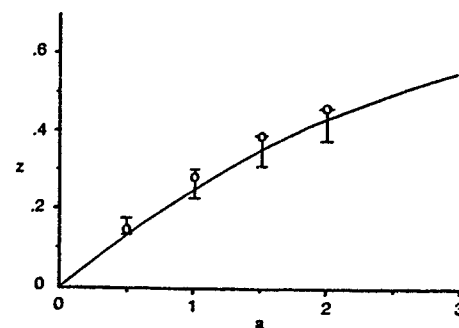


Fig. 12(b) As 12(a) but for the height of the vortex

# NONEQUILIBRIUM TURBULENCE MODELING EFFECTS ON TRANSONIC VORTICAL FLOWS ABOUT DELTA WINGS

Unver Kaynak\*

TUSAŞ Aerospace Industries, P.K. 18, 06690, Kavaklıdere, Ankara, TURKEY

Eugene Tu\*

NASA Ames Research Center, Moffett Field, CA 94035, U.S.A.

Mustafa Dindar† and Remzi Barlas†

TUSAŞ Aerospace Industries, P.K. 18, 06690, Kavaklıdere, Ankara, TURKEY

## SUMMARY

The Johnson-King turbulence model that has proved to be a viable method for calculating two-dimensional transonic separated flows has been extended into three-dimensions. The implementation was done for Navier-Stokes flow solvers written in general curvilinear coordinates. The present approach used in turbulence modeling is based on streamwise integration of an ordinary differential equation (o.d.e.) that governs the maximum Reynolds shear stress behaviour. Streamwise integration of the o.d.e. approach was found to offer great mathematical simplicity and economy for three-dimensional Navier-Stokes methods. Thus, the new method is quick, simple and very cheap. The new method was first checked against the data of a well-known transonic axisymmetric bump experiment, and a good agreement was obtained. Later, the new method was used to compute the flow around a low aspect ratio wing in a transonic wind tunnel. Finally it was employed to study the nonequilibrium turbulence effects on the transonic vortical flows about a 65° sweep round leading-edge delta wing.

## 1. INTRODUCTION

The aerodynamic characteristics of aircraft in transonic regime are very sensitive to viscous effects, and selection of the turbulence model in numerical codes largely determines the level of success for capturing these effects. One well known aspect of turbulence is that it is slow to respond to changes in the mean strain field. The so-called equilibrium models that are widely used in Navier-Stokes computations fail to adequately model this aspect of the turbulence, and exaggerate the turbulent boundary layer's ability to produce the Reynolds shear stresses in regions of adverse pressure gradient. As a consequence, too little momentum loss within the boundary layer is predicted in the region of the shock wave along the aft part of the aerodynamic body. This in turn causes the equilibrium models to predict shock waves too far aft of the experiment.

Recently, a "nonequilibrium" algebraic turbulence model was formulated<sup>1,2</sup> which attempts to capture the aforementioned important aspect of turbulence, that is the slow response of the turbulence to rapid changes in the mean strain field. This "non-equilibrium" algebraic model (i.e., the Johnson-King model<sup>3</sup>) employs an ordinary differential equation (o.d.e.) that is de-

rived from the turbulent kinetic energy (t.k.e.) equation. The performance of this turbulence model relative to popular "equilibrium" models was measured for three airfoil test cases of the 1987 AIAA Viscous Transonic Airfoil Workshop, Reno, Nevada. It was observed that the Johnson-King model exhibited impressive improvements for the prediction of the transonic separated airfoil flows. Since then, this model was further improved to account for some deficiencies in the original model<sup>4</sup>.

Although, a direct extension into three-dimensions doesn't seem to be straightforward, some researchers have attempted to develop forms of this "non-equilibrium" turbulence model in three-dimensions in which similar improvements in predictive quality were realized. Among these were Abid<sup>5</sup> who made a simple extension of this model for an inverse three-dimensional boundary layer method, and Kavasoglu et al.<sup>6</sup> for a direct three-dimensional boundary layer method with significant improvements for the selected test cases. As for the Navier-Stokes applications, there are two cases that are known to the authors: the simplest extension of the model using a stripwise o.d.e. for a wing calculation as reported by Yoshizawa<sup>7</sup> and a p.d.e. approach used by Abid et al.<sup>8</sup>. The latter has shown significant advancements in simulating the transonic separated flow around the ONERA M6 wing.

The proposed method here for three-dimensions models most relevant physics while maintaining mathematical simplicity by solving the governing o.d.e. on a mean streamline that passes through the point at which the Reynolds shear stress attains its maximum. This idea was provoked by the fact that the turbulent kinetic energy equation on which the present o.d.e. was derived, describes the time rate of change of the turbulent kinetic energy following a fluid particle. Therefore, it sounds reasonable to integrate the o.d.e. on a mean streamline at the max shear stress point, thereby describing the downstream development of the shear stress. Solving an o.d.e. instead of a p.d.e. also offers great mathematical simplicity and economy for three-dimensional Navier-Stokes methods.

The present work specifically targets the flow simulation of generic fighter wings (high sweep/low aspect ratio wings and/or delta wings) that has been an area of continuous improvement since the first transonic separated finite wing simulation of Mansour<sup>9</sup>. The transonic flow predictions for the same wing geometry (WING C) were further perfected by Kaynak et al.<sup>10</sup> using a zonal Navier-Stokes approach.<sup>10</sup> Another

\* Research Scientist  
† Research Assistant



significant work in this area was by Vatsa<sup>11</sup> for the simulation of the ONERA M6 wing. Application of a simple simple relaxation (nonequilibrium) turbulence model for a finite wing in a transonic wind tunnel was first realized by Kaynak and Flores<sup>12</sup>. In their work, computed surface skin-friction lines for the wing upper surface very closely resembled the experimental oil-flow picture that shows a mushroom type separation. In the present work, the degree of the accuracy of the new model will be first measured by comparing the calculations against a well-known transonic axisymmetric bump experiment. Later, a low aspect ratio finite wing with a NACA0012 cross-section mounted in a transonic wind tunnel will be simulated. Finally, the Johnson-King model will be used to study the nonequilibrium phenomenon on a delta wing in transonic flow. The subject of the numerical simulation is the so-called AFWAL wing that is a 65° sweep round leading-edge delta wing of the International Vortex Flow Experiment.<sup>13</sup> This model was the subject of various earlier studies<sup>14,15</sup> using Euler and/or Navier-Stokes flow solvers in laminar and turbulent flow regimes. It was reported<sup>14</sup> that the effect of viscosity and turbulence modeling of these flows was not yet fully understood. Furthermore, transonic flows around delta wings create complex shock patterns in which crossflow and streamwise shocks are known to exist. Such a complex shock system is bound to induce some nonequilibrium effects on the flow field. Thus, it is hoped that implementation of the Johnson-King model will possibly help us to better understand the viscosity and nonequilibrium turbulence effects on transonic vortical flows.

## 2. NUMERICAL METHOD

The strong conservation form of the Navier-Stokes equations is used for shock capturing purposes. To enhance numerical accuracy and efficiency, and to handle boundary conditions more easily, the governing equations are transformed from the cartesian coordinates  $(x, y, z, t)$  to general time-dependent curvilinear coordinates  $(\tau = t, \xi = \xi(x, y, z, t), \eta = \eta(x, y, z, t), \zeta = \zeta(x, y, z, t))$ . In high Reynolds number flows, the viscous effects are confined to thin layers near rigid boundaries. Furthermore, one generally does not have enough grid points to resolve the streamwise viscous gradients. Hence, for many Navier-Stokes computations the viscous derivatives along the body can be dropped. This leads to the thin-layer (Reynolds-Averaged) Navier-Stokes equations that read

$$\partial_t \bar{Q} + \partial_\xi \bar{E} + \partial_\eta \bar{F} + \partial_\zeta \bar{G} = Re^{-1} \partial_\xi \bar{S} \quad (1a)$$

where  $\bar{Q} = J^{-1}[\rho, \rho u, \rho v, \rho w]$  is the vector of the dependent variables,  $J$  is the Jacobian of the transformation,  $Re$  is the Reynolds number,  $\bar{E}$ ,  $\bar{F}$  and  $\bar{G}$  are the inviscid flux vectors, and  $\bar{S}$  is the (thin-layer) viscous flux vector. Complete description of the thin-layer equations is documented in Ref. 16. In this study, the NASA-Ames ARC3D<sup>17</sup> program and multi-zone TNS<sup>18</sup> program were used to solve the thin-layer equations. These programs use implicit approximate factorization algorithms of the Beam and Warming<sup>19</sup> for time-accurate calculations, and a diagonal version of this algorithm by Pulliam and Chaussee<sup>20</sup> for steady-state or first-order time-accurate calculations. Just for a reminder, the latter algorithm is given below:

$$T_\Delta(I + \Delta t A_\Delta) \hat{N}(I + \Delta t A_N) \times \hat{P}(I + \Delta t A_P) T_\Delta^{-1} \Delta \bar{Q} = \hat{R} \quad (1b)$$

Here,  $\Delta$ 's are the diagonal matrices,  $T$ ,  $\hat{N}$  etc. are the similarity transformation matrices,  $\Delta t$  is the time step,  $\Delta \bar{Q}$  is the change in the vector of the dependent variables, and  $\hat{R}$  is the residual vector. For more details, please see the relevant papers.<sup>14,16</sup>

## 3. TURBULENCE MODELING

The simplest three-dimensional turbulence models are the direct extensions of two-dimensional models. This is done by assuming an isotropic turbulence structure in which the eddy-viscosity is the same for all directions. Thus, the turbulent shear stresses in streamwise ( $x$ ) and spanwise ( $y$ ) directions read

$$\tau_x = \rho(-\overline{u'v'}) = \rho \nu_t \frac{\partial u}{\partial y} \quad (2a)$$

$$\tau_y = \rho(-\overline{v'u'}) = \rho \nu_t \frac{\partial v}{\partial x} \quad (2b)$$

However, this assumption is scarcely correct. The experimental data of Van den Berg and Elsenaar<sup>21</sup> and of Bradshaw and Pontikos<sup>22</sup> show that three-dimensionality of the flow affects the turbulence structure. As the three-dimensionality develops, the experimental results show that the outer level of the mixing-length reduces and the ratio of the shear stress to turbulence kinetic energy decreases. Therefore, there is a significant decrease in the magnitude of the shear stress compared with an equivalent two-dimensional boundary layer. In addition to this, the direction of the shear stress vector lags behind the velocity gradient vector components. All this certainly shows that the eddy viscosity is not isotropic, and direct extension of 2-D models into 3-D models is in fact not straightforward.

Furthermore, the calculation methods that assume a unique relationship between the shear stress and the mean velocity profile are not realistic for boundary layers in arbitrary pressure gradients, because the past turbulence history is also important for the shear stress, not just the local conditions. It was argued by Bradshaw et al.<sup>23</sup> that the shear stress is closely related to the turbulent kinetic energy. Thus, models aiming at including history effects by using an equation governing the streamwise shear stress development, as derived from the turbulent kinetic energy equation (t.k.e.) have shown successes in the past.<sup>4,24</sup> In this work, both the Baldwin-Lomax<sup>25</sup> and Cebeci-Smith<sup>26</sup> models are used as equilibrium models, and the Johnson-King<sup>1</sup> model is used to study the nonequilibrium effects. In the following lines, the latter two models are presented.

### The Cebeci-Smith Model

In this formulation, the boundary layer is a composite two-layer structure consisting of inner and outer layers. In the inner layer, the eddy-viscosity is described by

$$\nu_t = (D \kappa \epsilon)^{1/2} \quad (2c)$$

where  $\omega$  is the magnitude of the vorticity,  $\epsilon$  is the normal distance from the wall and  $\kappa = 0.41$  is the Karman's constant. The near-wall damping term  $D$  is given by

$$D = 1 - \exp[-\epsilon/\nu_t A^+ ] \quad (2d)$$

with  $A^+ = 26$ , and the wall friction velocity  $u_* = (\tau_w/\rho_w)^{1/2}$ . In the outer layer, a Clauser formulation for the eddy viscosity is used

$$\nu_e = 0.0168 g_* \delta_*^2 \gamma \quad (2e)$$

where  $g_*$  is the magnitude of the boundary layer edge velocity,  $\delta_*$  is the incompressible (total) displacement thickness given by

$$\delta_* = \int_0^{\delta} (1 - \frac{u}{u_e}) dy \quad (2f)$$

where the magnitude of the mean velocity is  $q = (u^2 + v^2 + w^2)^{1/2}$ . The boundary-layer edge was simply determined by taking the  $\delta_*$ -location at which the total pressure attains a value that is equal to

$$p_t = C(p_t)_{max} + (1 - C)(p_t)_{wall} \quad (2g)$$

where  $C$  is a constant in 3 to 5 percent range. A recent method<sup>24</sup> for predicting the boundary-layer edge using the Coles' profile family may also be used for some class of problems. In this method, the boundary-layer edge is found by using a relation that reads

$$\delta = 1.936 \ell_{z,max} \quad (2h)$$

where  $\ell_{z,max}$  is the normal distance at which the moment of vorticity

$$f(z) = \ell_z \omega \quad (2i)$$

takes on its maximum value. In the outer formulation, the Klebanoff intermittency factor is given by

$$\gamma = [1 + 5.5 (\frac{z}{\delta})^2]^{-1} \quad (2j)$$

Finally, the eddy-viscosity distribution is found from

$$\nu_t = \min(\nu_i, \nu_e) \quad (2k)$$

### The Johnson-King Model

The Johnson-King model accounts for the convection and diffusion effects by solving an o.d.e. governing the streamwise development of the maximum shear stress derived from the turbulent kinetic energy (t.k.e.) equation. An eddy-viscosity distribution is assumed across the boundary layer that is functionally dependent on the maximum Reynolds shear stress. Using an isotropic turbulence assumption, the total Reynolds shear stress at a point may be assumed to be in the following form:

$$\tau = \nu_t \omega \quad (3a)$$

Here,  $\nu_t$  and  $\omega$  are the eddy-viscosity and vorticity at a point. Note that the total Reynolds shear stress  $\tau$  as defined above is in fact  $\tau/\rho$ , but the above definition is used here for convenience. The following blending formula for the inner and outer layer eddy-viscosity formulations is used to set the eddy viscosity:

$$\nu_t = \nu_w [1 - \exp(-\nu_w/\nu_e)] \quad (3b)$$

which behaves like the inner and outer formulas for small and large  $\ell_z$  values respectively, and smoothly blends the inner and outer regions. It also makes  $\nu_t$  functionally dependent on  $\nu_w$  across the boundary layer. The inner formula is given by

$$\nu_w = D^2 \kappa \ell_z \tau_w^{1/2}$$

where  $\tau_w$  is the maximum value of the shear stress to be found by solving an o.d.e. as will be explained below. The damping function  $D$  is given by

$$D = 1 - \exp(-\ell_z \tau_w / \nu_w A^+) \quad (3d)$$

However, the constant  $A^+$  is taken to be as 17 as opposed to 26, to account for the different wall distance dependencies of the two formulations. The outer eddy viscosity is given by

$$\nu_e = \sigma(s) 0.0168 g_* \delta_*^2 \gamma \quad (3e)$$

The parameter  $\sigma(s)$  provides the link between the assumed eddy-viscosity distribution, and the o.d.e. that governs the streamwise development of the maximum Reynolds shear stress.

The rate equation in the form of an o.d.e. could be obtained from the turbulent kinetic energy ( $k = \frac{1}{2}(\overline{u'^2} + \overline{v'^2} + \overline{w'^2})$ ) equation by making an assumption similar to Bradshaw et al.<sup>25</sup> that the ratio of the maximum shear stress  $\tau_m$  to maximum t.k.e.  $k_m$  is constant. Under this assumption, the total Reynolds shear stress equation in cartesian coordinates that is evaluated at the maximum shear stress point ( $m$ ) reads

$$\begin{aligned} \frac{\partial \tau_m}{\partial t} + u_m \frac{\partial \tau_m}{\partial x} + v_m \frac{\partial \tau_m}{\partial y} + w_m \frac{\partial \tau_m}{\partial z} \\ = \frac{e_1}{L_m} (r_m^2 / \rho - \tau_m^2 / \rho) - e_1 D_m \end{aligned} \quad (3f)$$

The shear stress can be obtained by solving the p.d.e. as was done in Ref. 7. However, an equivalent and cheaper way is available for solving this equation. Notice that the left hand side of the above equation is the material derivative of  $\tau_m$  following a fluid particle. From vector analysis, by making a steady flow assumption, this is equal to the directional derivative of  $\tau_m$  in the mean velocity vector direction  $q_m = q_m(u_m, v_m, w_m)$ . Therefore, the above equation reduces to an o.d.e.

$$q_m \frac{d\tau_m}{ds} = \frac{e_1}{L_m} (r_m^2 / \rho - \tau_m^2 / \rho) - e_1 D_m \quad (3g)$$

Here,  $ds = ds(dx, dy, dz)$  is in the direction of the mean velocity vector passing through the point at which  $\tau$  is at its maximum. In Eqs. (3f) and (3g) the subscript ( $m$ ) denotes the equilibrium value corresponding to  $\sigma(s) = 1$ , subscript ( $m$ ) denotes the value evaluated at maximum shear point,  $q_m$  is the magnitude of the mean velocity, and  $D_m$  is the diffusion term at  $\tau = \tau_m$  (see Johnson and King<sup>7</sup> for its modeling). Furthermore, the modeling constant  $e_1$  and the dissipation length scale  $L_m$  are given by

$$e_1 = \frac{\tau_m}{k_m}, \quad L_m = \frac{r_m^2 / \rho}{e_m} \quad (3h)$$

where  $e_1$  is taken as 0.25, and  $e_m$  is the dissipation. The dissipation length scale  $L_m$  is assumed to scale with  $\ell_z$  in the inner part of the boundary layer, and with the boundary-layer thickness  $\delta$  in the outer part of the boundary-layer (see Ref. 1 for the functional form). The diffusion term is modeled as

$$D_m = \frac{C_{M1} \tau_m^{3/2}}{e_1 [0.7 - (\ell_z/\delta)_m]} [1 - \sigma(s)^{1/2}] \quad (3i)$$

where  $C_{M1}$  is a modeling constant taken as 0.5. The above o.d.e. (Eq. 3g) could be solved easily by using a standard technique such as the backward (implicit) Euler method. Making the change of variable  $g = 1/\tau_m^{1/2}$  and implementing the backward Euler method on Eq. 3g at a location

$(j, k)$  result in

$$g_{j,k} = \frac{g_{m,n} + \Delta s C_{j,k}(1 + D_{j,k})}{1 + \Delta s C_{j,k}/g_{m,n}} \quad (3j)$$

where

$$C_{j,k} = \frac{a_1}{2\tau_m L_m}, \quad D_{j,k} = \frac{G_{Mf} L_m [1 - \sigma(s)^{1/2}]}{a_1 \delta [0.7 - (L_s/\delta)_m]} \quad (3k)$$

Solution of Eq. (3j) necessitates the downstream value of  $g$  (i.e.  $g_{m,n}$ ) at a certain location, and this is obtained by performing the extrapolation as shown in Fig. 1. The extrapolation could be achieved in the following way: At grid point  $(j, k)$ , first the maximum shear stress point  $m$  is found in the normal direction and the direction of the local mean flow velocity vector is determined. Then  $g_{m,n}$  is extrapolated from the downstream cells, and also the spatial step  $\Delta s$  is determined to compute  $g$  at point  $(j, k)$ . Once  $g_{j,k}$  is found,  $\tau_m$  is computed and the link parameter  $\sigma(s)$  is established according to the following scheme

$$\sigma(s)^{n+1} = \sigma(s)^n \frac{\tau_m}{(\nu_1 \omega)_m} \quad (3l)$$

where  $n$  denotes the iteration level of the time-marching scheme. The initial conditions for integrating this o.d.e. may be obtained by assuming that the flow is in equilibrium at the start of the calculations, i.e.  $\nu_1 = \nu_{1,eq}$  and  $\tau_m = \tau_{m,eq}$ . The latter can be obtained from the experiment or from the Cebeci-Smith model. Alternatively, the wall shear velocity  $u_\tau$  as determined from the experiments or calculations could be used.

#### 4. RESULTS AND DISCUSSION

In this section, results of three different configurations using the new turbulence model will be given. First, detailed comparisons will be done for a transonic axisymmetric separated bump flow. Second, a low aspect ratio wing of NACA0012 cross-section mounted in a transonic wind tunnel will be simulated. Finally, transonic vortical flows around a 65 deg. sweep round leading edge delta wing will be studied.

##### Validation. Transonic Axisymmetric Bump Flow:

In order to validate the new turbulence model, preliminary calculations were done for a flow case that has a good experimental data base and that has been numerically studied by other investigators<sup>1,20</sup> previously. In general, validation should include detailed comparisons including the shear stress, boundary layer parameters and velocity profiles. For this purpose, the axisymmetric bump experiment of Bachalo and Johnson<sup>20</sup> was chosen. In this experiment, a thin walled cylinder (15.2 cm outer diam.), with an axisymmetric circular-arc bump attached 61 cm from the cylinder leading edge. The bump has a thickness of 1.9 cm and a chord length of 20.3 cm. This flow model was specifically designed to simulate the type of viscous-inviscid interactions that can develop on airfoil sections at transonic conditions. The model was tested in Ames 2-by-2 foot transonic wind tunnel and 6-by-6 foot supersonic wind tunnel for a range of Mach and Reynolds numbers.

The new turbulence model was included in the NASA-Ames ARC3D<sup>17</sup> and TNS<sup>18</sup> Navier-Stokes flow solvers and the ARC3D program was first run at IBM 3090 150E scalar computer installed at TUSAS Aerospace Industries (TAI), Inc. using coarse grids. Later, the calculations

were repeated at NASA-Ames Research Center for fine grids using the Cray-YMP supercomputer. One such algebraically generated finite-difference grid is shown in Fig. 2. The grid has dimensions  $136 \times 7 \times 46$  in the streamwise, circumferential and normal directions respectively. Exponential stretching is used in the normal direction. Since the experiment was axisymmetric, only 5 to 7 planes were used in the circumferential direction in a 90 deg. pie. The first grid point off the body is  $2 \times 10^{-3}$ , and the streamwise grid resolution is 1% of the chord between  $x/c = 0.50$  and  $x/c = 1.00$ . The Mach number is 0.875 and the Reynolds number is  $13.6 \times 10^6/m$ .

The results of the bump calculations are shown in Figs. 3-8. In Fig. 3, surface pressure coefficients using the equilibrium turbulence models of Baldwin and Lomax<sup>16</sup> (B-L) and Cebeci and Smith<sup>21</sup> (C-S) and the nonequilibrium model of Johnson and King<sup>1</sup> (J-K) are compared with the experiment.<sup>20</sup> As shown in the figure, whereas the equilibrium models (B-L and C-S) predict the shock too aft of the experiment, the J-K model predicts the shock wave location and the resulting pressure plateau very well. Note that the equilibrium models are quite similar to each other and the pressure plateau is just nonexistent in these models.

The behaviour of the Reynolds shear stress and viscous layer growth are very intimately related with the surface pressure. Fig. 4 shows the maximum Reynolds shear stress ( $\tau_m$ ) distributions of the C-S and J-K models. The equilibrium model of C-S exhibits a very sharp peak in the vicinity of the shock and a very rapid decay in downstream. On the other hand, the J-K model yields a softer increase near the shock and more persistent level downstream in result of the solution of the Eq. 3g. Too much increase of the shear stress in the equilibrium models also causes the lateral shear stress gradient  $\partial\tau/\partial s$  to be larger than those observed in the experiment. As a result, the boundary layer displacement thickness will be less and the pressure recovery will be higher. On the other hand, lesser increase of the shear stress associated with the nonequilibrium J-K model will reduce the amount of the eddy viscosity. As a consequence, the inner part of the boundary layer will lose more momentum in the shock, and its ability to withstand adverse pressure gradients will be reduced. This will produce a larger viscous layer growth. In Fig. 5, the displacement thickness calculated by the C-S and J-K models are compared with the experiment. In concert with the better shear stress prediction in the boundary layer, the J-K model agrees with the experiment quite well.

The mean velocity profiles are compared with the experiment in Fig. 6. In Ref. 2 the computed velocity profiles were offset by 3% relative to the experiment due to approximately that much difference in the shock wave locations. The results of this paper were also offset by the same amount. Strictly speaking, there is not as much strong justification to follow Ref. 2 in our case, but still some percentage of this offset may be attributed to the present difference in shock locations and some percent, may be to experimental uncertainties. One thing that may be added to the discussion is that the present solution, although not given here, does not give as much shock curvature as the shadowgraph picture of the experimental shock. The differences in the shock

curvatures rather than the shock locations may support to justify the present offset of 3%. As shown in Fig. 6, the J-K model qualitatively predicts the boundary-layer profiles quite well, superior to the profiles produced by the B-L and C-S models. This is especially visible around the separated regions in which the curvature of the equilibrium profiles are of opposite sign to that observed in the experiment and that predicted by the J-K model. In result of this, the separation and reattachment points for the J-K model ( $0.73 \leq x/c \leq 1.10$ ) was in closer agreement with the experiment ( $0.70 \leq x/c \leq 1.15$ ) than, say, the C-S model ( $0.76 \leq x/c \leq 1.07$ ). The mean velocity profiles indicate that the equilibrium models are not good in the inner layer producing curvature of the opposite sign. Also, it is obvious that the nonequilibrium model needs improvements in the recovery region downstream of the reattachment.

Figure 7 shows the nonequilibrium state of the flow, that is the streamwise variation of the link parameter  $\sigma(s)$  which may be regarded as the ratio of the production to dissipation. This quantity attains high values at the recovery region downstream of the reattachment and therefore is limited to a value of, say, 2 in this region without any adverse impact in the  $C_p$ -predictions following Ref. 2. Some experimental values are also put on the figure that shows a pretty good agreement with the computation. Finally, the convergence rate of the B-L and J-K models are compared in Fig. 8. First of all, since only an o.d.e. is solved as opposed to the p.d.e. for the maximum shear stress, extra cost of computation in the nonequilibrium model is negligible. There is only added cost of the interpolation routine for calculating the downstream value of  $\tau_w$ . Also, as shown in Fig. 8, extra stiffness associated with the nonequilibrium added to the equations does not cause a significant slow down in the convergence rate, and quite comparable speeds were obtained. As a result, the new method is comparable to a p.d.e. approach in terms of accuracy, and furthermore it is simple, cheap and efficient.

#### Low-Aspect-Ratio Wing in a Wind Tunnel:

Transonic flow around the low-aspect-ratio wing of Lockman and Seegmiller<sup>27</sup> was simulated using the four-block version of the Transonic Navier Stokes (TNS)<sup>10</sup> program. In this program, the flow field around a wing is divided into four zones (Fig. 9), and the Euler and Navier-Stokes equations are solved. For this, an H-H type base coarse grid is generated and then subdivided into zones. Zone 1 is the base grid with some points removed around the wing. Zone 2 is constructed by doubling the number of grid points by using the base grid closer to the wing, again leaving a hole near the wing. There is one or two cells of overlap between the zones. Finally, Zones 3 and 4 are generated by filling the space between the wing and Zone 2 by clustering points near the wing. In Zones 1 and 2, the Euler equations are solved, and in Zones 3 and 4 the (Reynolds-Averaged) Navier-Stokes equations are solved. This provides a flexibility in grid generation for complicated geometries and efficiency in the flow solutions. For more information, the reader is referred to Ref. 10.

A finite difference grid for simulating the flow around the wing mounted in NASA-Ames High

Reynolds Number Channel-I is shown in Fig. 10. The present grid has a total of 231,006 grid points. The individual grid point breakdown for the zones are the following: Zone 1 has  $69 \times 27 \times 22$  points, Zone 2 has  $73 \times 35 \times 24$  points and Zone 3 and 4 have  $65 \times 33 \times 30$  points each. In the present grid the points are not clustered near the side walls, so no attempt was made to model viscous flow near the walls. The wing has an aspect ratio of 1.5, a taper ratio of 1, a sweep of  $20^\circ$  and no camber, and consists of a NACA0012 cross-section. The flow conditions were  $M_\infty = 0.836$ ,  $\alpha = 2^\circ$  and  $Re_c = 8 \times 10^6$ . Previous studies are available for this wing by the first author<sup>11</sup> and by Vatsa and Wedan<sup>28</sup> for slightly lower Mach number. Also, there is accumulated evidence with regards to the effects of grid resolution, tunnel exit boundary conditions, artificial dissipation, turbulence modeling and tunnel side walls on the accuracy of the simulations. Use of these previous studies<sup>11,28</sup> will be made for interpreting the present results.

The experimental oil-flow photograph and computational skin-friction lines are shown in Fig. 11. Fig. 11a is taken from Ref. 27 and shows the so-called mushroom type separation. The strong shock wave in the experiment separates the wing upper surface flow and brings about two counter-rotating vortices. Figs. 11b, 11c and 11d are belong to the calculations using the B-L, C-S and J-K models respectively. First of all, in all these numerical simulations, the strong shock wave separates the flow all the way to the side wall. Lack of viscous flow simulation at the wall have a very negative effect on the simulations. It is known that viscous layer displacement effects tend to reduce the strength of the shock wave towards the wall.<sup>29</sup> As shown in Fig. 11d, only the J-K model produces at least one of the vortices of the mushroom. The inboard vortex could not be captured by any of the models, and lack of the viscous layer modeling near the side wall is probably the leading cause for this. Despite the inability to capture the inboard vortex, the J-K model gives the best result subject to the present limitations.

The comparison of the surface pressure coefficients for the C-S and J-K models are shown at three span stations (50%, 77% and 90%) in Fig. 12. As shown, whereas the comparison is quite well at two outboard stations (77% and 90%) for the J-K model, the inboard station of 50% is not as good (in fact, the B-L prediction is rather luckily right on the data). But, as was already explained above, the sidewall boundary conditions are probably the primary cause for this. Also, the J-K model was run only on the upper surface, and the C-S model was used on the lower surface. The effect of the exit plane boundary conditions are also important as was documented in Refs. 11 and 28. Hence, before making conclusive statements, more work needs to be done for this case. It should, however, be remembered that some iterations are necessary to correctly assess the right level of the downstream pressure boundary condition. Because, as that condition changes, the location and the strength of the shock wave will change and Eq. 3g will produce different nonequilibrium states as it responds to the shock jump. In other words, lowering the downstream pressure will suck the shock downstream but the nonequilibrium effects will push it back forward by thickening the boundary layer. Of course this will interact with

the side wall conditions which will tend to lessen the strength of the shock if viscosity is included. The final solution should match the experimental value of the incoming Mach number, the side and upper and lower wall pressures correctly, so that one may more conclusively comment on the turbulence closure model's performance.

#### Transonic Vortical Flow About the AFWAL Wing

The flow over a swept delta wing is characterized by a primary vortex separating from the leading edge and a counter-rotating secondary vortex separating from the leeward side inboard of the leading edge. Since the nonlinear lift induced by these vortices is very important for fighter aircraft manoeuvrability, there are ongoing efforts to study and predict such flows. The International Vortex Flow Symposium<sup>14</sup> which was held in Stockholm, October 1-3, 1986, was the result of a joint U.S./European effort to experimentally and numerically study the transonic vortical flows about delta wings. The model geometry was a round or sharp leading edge cropped delta wing with a modified NACA 64A005 profile with zero twist and camber, and with sweep angles of 55° or 65°. In order to check the performance of the new turbulence model, and to illuminate the effect of turbulence modeling on the flow field, the 65° sweep angle delta wing model that was manufactured by AFWAL was chosen.

The C-H type finite difference grid for this delta configuration with total number of 354,246 grid points is shown in Fig. 13. The number of grid points is 151 × 51 × 48 in streamwise, spanwise and normal directions respectively. The wing surface has 111 × 30 points in the streamwise and spanwise directions, and the grid resolution in the leading and trailing edges were 0.001 and 0.005 chord respectively. The wake has 20 points and the normal grid resolution off the body is  $2 \times 10^{-3}$  chord. The outer boundary is 4 to 5 chord lengths away from the body. In the grid generation, a hyperbolic type grid generation technique was used for each 2-D streamwise cross-sections, then those planes were stacked together to obtain the final 3-D grid. The grid at the tip is defined by the revolution of the airfoil at that location. The flow conditions were  $M_\infty = 0.55$ ,  $\alpha = 10^\circ$  and  $Re_{\text{model}} = 9 \times 10^6$ . The transition was fixed at the 11% of the root chord. The Baldwin-Lomax and Johnson-King turbulence models were used to study this flow field. Both models converged more than three orders of magnitude in the L2 norm of the residual in about 3000 iterations on the Cray-2 supercomputer installed at the NASA-Ames Research Center. It took 10.01 and 11.67 seconds per iteration for the B-L and J-K models respectively. However, the overhead in the computer time is largely due to the yet unvectorized version of the J-K model, and the real overhead should drop to a perhaps a few percent after the vectorization. In the calculations, the wing was modeled as a clean wing contrary to the experiment that has a support on the lower side.

Figure 14 shows the calculated surface pressure coefficients as compared with the experiment at the streamwise stations of 30%, 60% and 80% of the root chord. First of all, both turbulence models (B-L and J-K) predict almost identical results for the pressure. The compar-

isons are quite good at the 60% and 80% stations for both models. However, the numerical predictions are rather poor at the 30% station due probably largely to the poor grid resolution at the leading edge. Note that despite the lack of modeling of the body support under the wing, the lower surface pressure comparisons are surprisingly very good. The calculations predict double suction peak at the 80% station that is not very clear in the experiment. These suction peaks are because of the primary and secondary separations as shown in Fig. 15. In this figure, both models find a primary separation very close to the leading edge and a strong secondary separation more inboard of the wing. Similar secondary separation was also predicted by the laminar simulation of Müller and Rizzi<sup>15</sup> for the same round leading edge wing. A perspective view of the primary vortex shed from the leading edge computed by the J-K model is given in Fig. 16.

Since almost identical results were obtained by both B-L and J-K models, the nonequilibrium effects should be insignificant for this flow case. This is demonstrated in Fig. 17 in which the nonequilibrium state  $\sigma(s)$  of the flow is given at  $s/c = 0.30, 0.60, 0.80$ . Here,  $\sigma(s)$  generally stays above the value of 1.0 which does not induce a significant change in the overall flow field. Note that the pressure suction of the vortices are sensed by  $\sigma(s)$ . It appears that this flow is largely convection dominated. At this point, some comments about the turbulence models are warranted: The Baldwin-Lomax model that is very popular for the Navier-Stokes computations have a difficulty of distinguishing the proper peak among the several peaks occurring in the moment of vorticity,  $F(s)$  for predicting the outer layer eddy viscosity. The tendency is that the model picks the second peak induced by the vortex sheet. This in turn falsely results in much too high viscosity that wipes out many flow features. Special techniques such as one given in Ref. 29 is necessary to select the proper peak. Since the present implementation of the J-K model uses the Clauser formulation (Eq. 2e) for the outer eddy viscosity, such a problem does not occur.

#### CONCLUSION

The Johnson-King model that has shown successes for two-dimensional separated flows has been extended into three-dimensions using an streamwise o.d.e. approach. The new method is equivalent to a p.d.e. approach in accuracy, computationally cheap, and convergence rate is comparable to an equilibrium model. The new model was compared against three test cases. First, the accuracy was validated against the transonic axisymmetric bump experiment and very satisfactory results were obtained, including a fast convergence rate despite the stiffness induced by the nonequilibrium effects. Second, the flow around a low aspect ratio wing mounted in a transonic wind tunnel was simulated, and some vortical flow structure that is nonexistent for the equilibrium models was captured. Finally, a transonic vortical flow around a 65° sweep delta wing was simulated, and it was found that the flow is convection dominated and nonequilibrium effects do not take a significant part in this flow. As a result, the new method is a viable one for three-dimensional Navier-Stokes methods with increased accuracy without significantly increasing the computational cost.

# Acknowledgments:

This research has been made possible under the NATO-AGARD Support to Southern Flank Countries Program, Project No. T-57, "Numerical Study of Transonic Separated Wing Flows." Support of the NASA-Ames Research Center in use of supercomputers is also gratefully acknowledged.

## REFERENCES

- [1] Johnson, D.A. and King, L. S., "A Mathematically Simple Turbulence Closure Model for Attached and Separated Turbulent Boundary Layers," *AIAA Journal*, Vol. 23, No.11, Nov.1985, pp.1684-1692.
- [2] Johnson, D.A. "Transonic Separated Flow Predictions with an Eddy-Viscosity Reynolds-Shear-Stress Closure Model," *AIAA Journal*, Vol. 25, No.2, Feb.1987, pp.252,259.
- [3] Johnson, D.A. and Coakley, T.J., "Improvements to a Nonequilibrium Turbulence Model," *AIAA Tech. Note* (to be published).
- [4] Abid, R., "Extension of the Johnson-King Turbulence Model to the 3-D Flows," *AIAA Paper 88-0223*, Jan. 1988.
- [5] Kavsoglu, M.S., Kaynak, U. and Vandalsem, W.R., "Three-Dimensional Application of the Johnson-King Turbulence Model for a Boundary-Layer Direct Method," *IS-CFD*, Nagoya, Japan, Aug. 1989.
- [6] Yoshiara, Hideo, "Problem Areas in Applied Computational Fluid Dynamics," *IS-CFD*, Nagoya, Japan, Aug. 1989.
- [7] Abid, R., Vatsa, V.N., Johnson, D.A. and Wedan, B.W., "Prediction of Separated Transonic Wing Flows with a Non-Equilibrium Algebraic Model," *AIAA Paper 89-0558*, Jan. 1989.
- [8] Mansour, N.N., "Numerical Simulation of the Tip Vortex Off a Low Aspect-Ratio Wing at Transonic Speed," *NASA TM 85932*, April 1984.
- [9] Kaynak, U., Holst, T.L., Cantwell, B.J., and Sorenson, R.L., "Numerical Simulation of Transonic Separated Flows over Low Aspect Ratio Wings," *AIAA Paper 86-0508*, Jan. 1986.
- [10] Holst, T.L., Kaynak, U., Gundy, K.L., Thomas, S.D. and Chaderjian, N., "Numerical Solution of Transonic Wing Flows Using an Euler/Navier-Stokes Zonal Approach," *Journal of Aircraft*, Vol. 24, No. 1, Jan. 1987, p. 17.
- [11] Vatsa, V.N., "Accurate Solutions for Transonic Wing Flows over Finite Wings," *AIAA Paper 86-1052*, May 1986.
- [12] Kaynak, U. and Flores, J., "Advances in the Computation of Transonic Separated Flows over Finite Wings," *AIAA Paper 87-1195*, June 1987.
- [13] *Proceedings of the International Vortex Flow Experiment on Euler Code Validation*, Stockholm, Sweden, ed. A. Elsenaar, NLR, 1986.
- [14] Eberle, A., "3-D Euler Calculations Using Characteristic Flux Extrapolation," *AIAA Paper 85-0119*, 1985.
- [15] Schmatz, M. A., Brenneis, A., and Eberle, A., "Verification of an Implicit Relaxation Method for Steady and Unsteady Viscous and Inviscid Flow Problems," *AGARD FDP Symposium on Validation of Computational Fluid Dynamics*, Lisbon, May 1988.
- [16] Baldwin, B.S. and Lomax, H., "Thin-Layer Approximation and Algebraic Model for Separated Turbulent Flows," *AIAA Paper 78-257*, Jan. 1978.
- [17] Pulliam, T.H. and Steger, J.L., "Implicit Finite Difference Simulations of Three-Dimensional Compressible Flow," *AIAA Journal*, Vol. 18, 1980, pp. 159-167.
- [18] Beam, R.W. and Warming, R.F., "An Implicit Finite-Difference Algorithm for Hyperbolic Systems in Conservation Form," *Journal of Comp. Physics*, Vol. 23, 1976, pp. 87-110.
- [19] Pulliam, T.H. and Chaussee, D.S., "A Diagonal Form of an Implicit Approximate Factorization Algorithm," *Journal of Comp. Physics*, Vol. 39, 1981, pp. 347-363.
- [20] Van der Berg, B. and Elsenaar, A., "Measurements in a Three Dimensional Incompressible Turbulent Boundary Layer in an Adverse Pressure Gradient Under Infinite Swept Wing Conditions," *NLR-TR-72092U*, Netherlands, 1972.
- [21] Bradshaw, P. and Pontikos, N.S., "Measurements in the Turbulent Boundary Layer on an 'Infinite' Swept Wing," *Journal of Fluid Mechanics*, Vol. 159, pp. 105-130 (1985).
- [22] Bradshaw, P., Ferriss, D.H. and Atwell, N.P., "Calculation of Boundary-Layer Development Using the Turbulent Energy Equation," *Journal of Fluid Mechanics*, Vol. 28, Part 3, pp. 593-616 (1967).
- [23] Cebeci, T. and Smith, A.M.O., "Analysis of Turbulent Boundary Layers," Academic Press, 1974.
- [24] Stock, H.W. and Haase, W., "The Determination of Turbulent Length Scales in Algebraic Turbulence Models for Attached and Slightly Separated Flows Using Navier-Stokes Methods," *AIAA Paper 87-1302*, June 1987.
- [25] Viegas, J.R., Rubesin, M.W. and Horstmann, C.C., "On the Use of Wall Functions as Boundary Conditions for Two-Dimensional Separated Compressible Flows," *AIAA Paper 85-0180*, Jan. 1985.
- [26] Bachalo, W.D. and Johnson, D.A., "An Investigation of Transonic Turbulent Boundary Layer Separation Generated on an Axisymmetric Flow Model," *AIAA Paper 79-1479*, 1979.
- [27] Lockman, W.K. and Seegmiller, H.L., "An Experimental Investigation of the Subcritical and Supercritical Flow About a Swept Semispan Wing," *NASA TM-84367*, June 1983.
- [28] Vatsa, V. and Wedan, B.W., "Navier-Stokes Solutions For Transonic Flow Over a Wing Mounted in a Wind Tunnel," *AIAA Paper 88-0102*, Jan. 1988.
- [29] Degani, D. and Schiff, L.B., "Computation of Turbulent Supersonic Flows Around Pointed Bodies Having Cross-Flow Separation," *Journal of Computational Physics*, Vol. 66 (1986), pp. 173-196.



## FIGURES

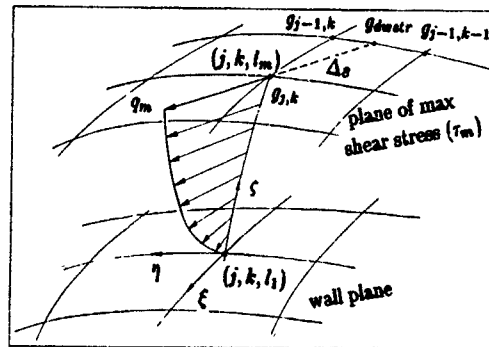


Fig. 1 Extrapolation of maximum shear stress ( $\tau_m$ ) from the downstream cells.

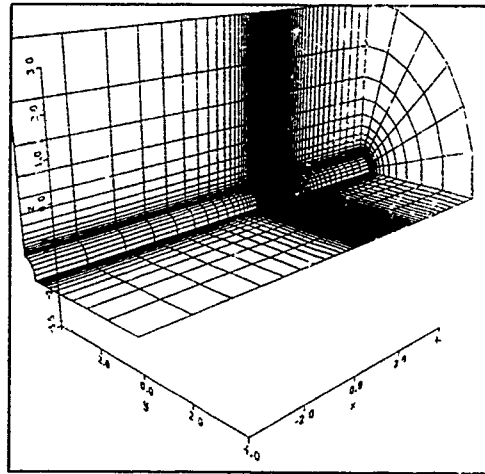


Fig. 2 Algebraic axisymmetric bump grid (136 x 7 x 45).

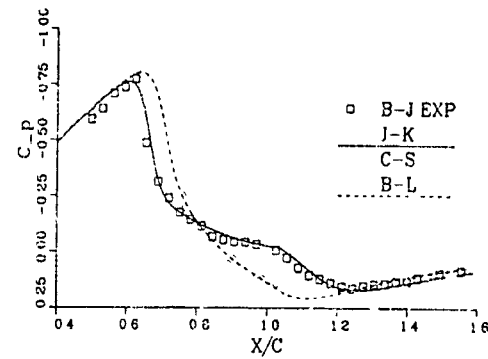


Fig. 3 Comparison of predicted and experimental surface pressure coefficient distributions on axisymmetric bump,  $M_\infty = 0.875$ ,  $Re = 13.6 \times 10^6/m$ , B-L, C-S and J-K turbulence models, B-J experiment.

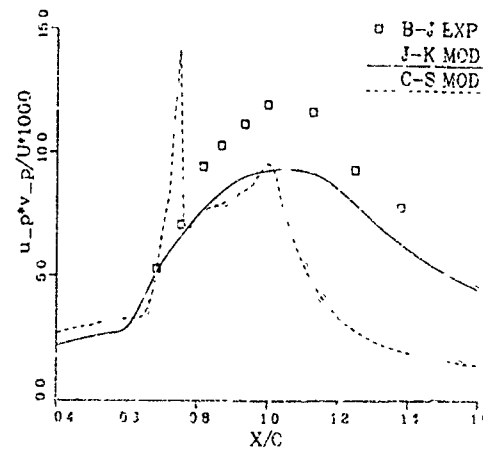


Fig. 4 Maximum Reynolds shear stress distribution on the axisymmetric bump,  $M_\infty = 0.875$ ,  $Re = 13.6 \times 10^6/m$ , C-S and J-K turbulence models.

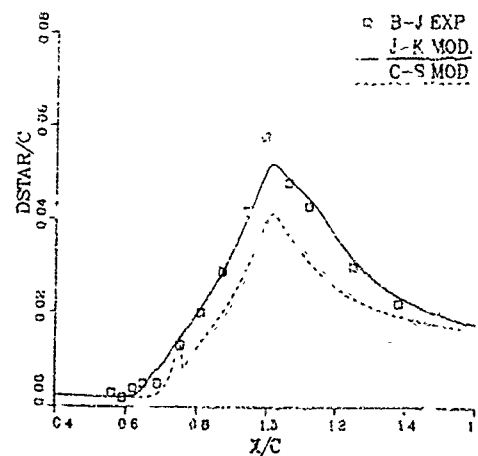


Fig. 5 Displacement thickness distribution on the axisymmetric bump,  $M_\infty = 0.875$ ,  $Re = 13.6 \times 10^6/m$ , C-S and J-K turbulence models.

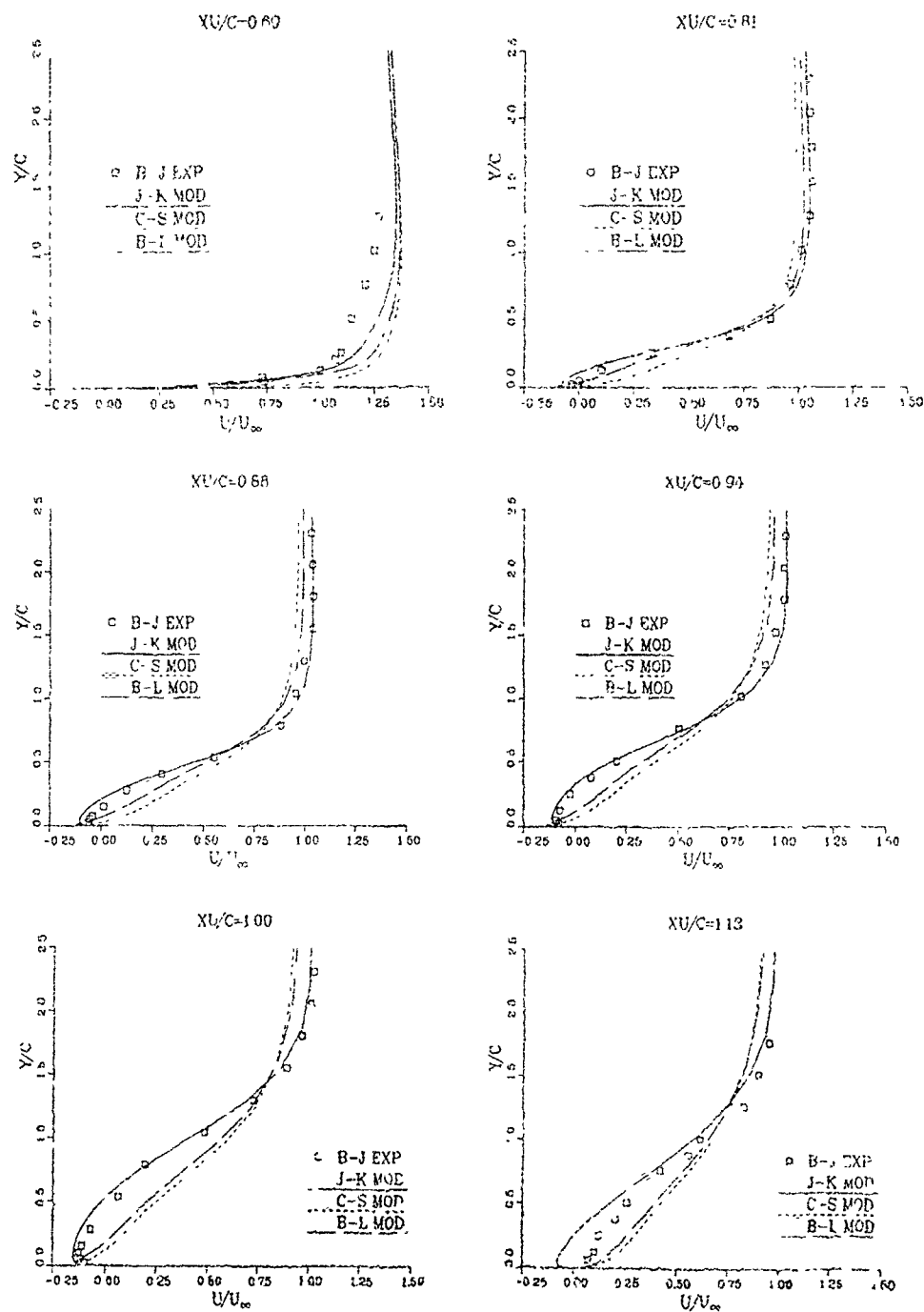


Fig. 4 Computed and experimental mean velocity profiles on axisymmetric bump,  $M_\infty = 0.375$ ,  $Re = 12.6 \times 10^6/m$ , B-L, C-S and J-K turbulence models.



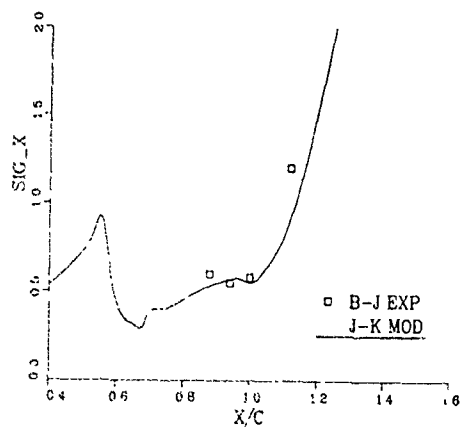


Fig. 7 The streamwise variation of  $\sigma(\epsilon)$  of the nonequilibrium state of the flow.

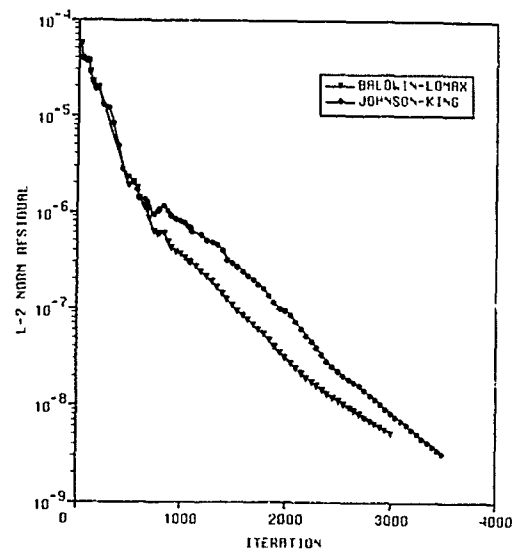


Fig. 8 Comparison of convergence rates for B-L and J-K turbulence models.

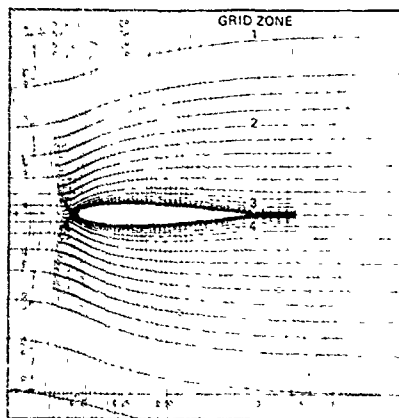


Fig. 9 Expanded view of the embedded grid near the wing geometry showing the four zones.

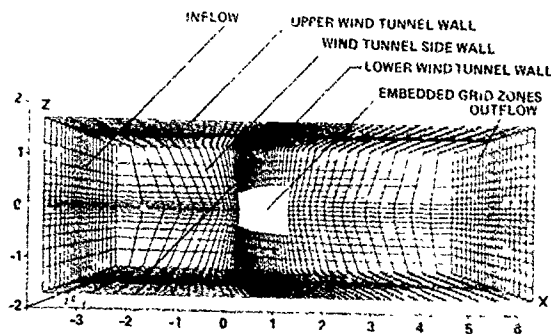
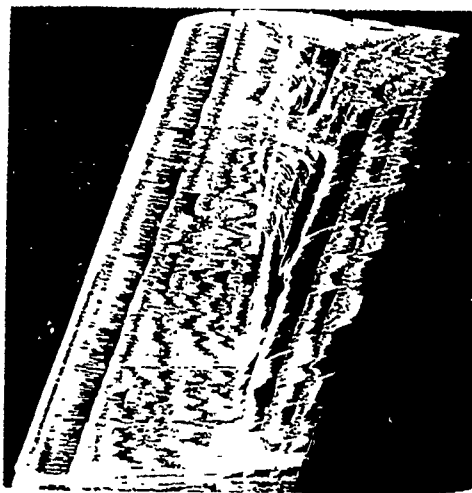
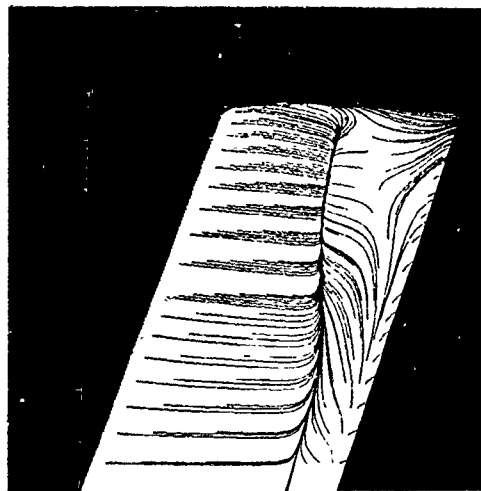


Fig. 10 Global finite-difference grid showing detail wind tunnel walls (NASA-Ames High Reynolds Number Channel-I)

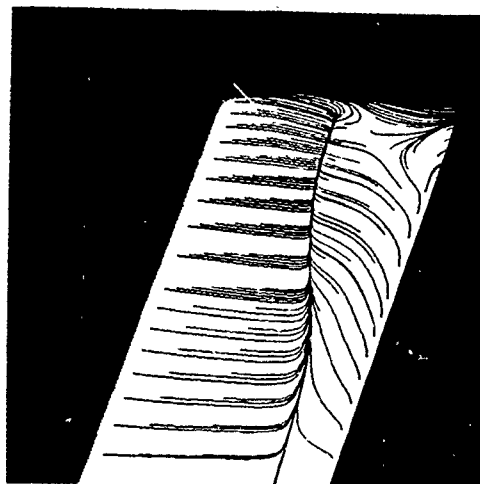
a) Oil-Flow



b) Baldwin-Lomax



c) Cebeci-Smith



d) Johnson-King

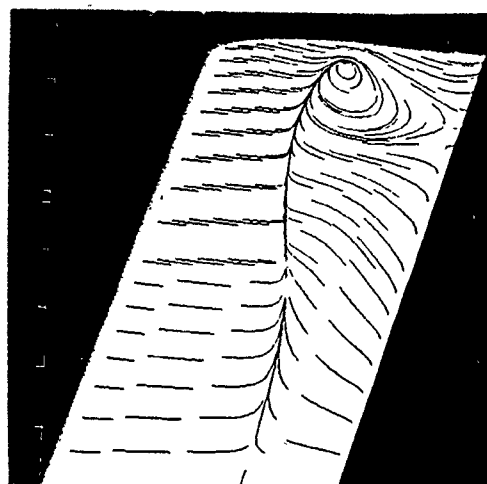


Fig. 11 Comparison of the experimental oil-flow photograph and computed skin-friction lines, NACA0012 airfoil section,  $AR = 3$ ,  $\Lambda = 20^\circ$ ,  $M_\infty = 0.828$ ,  $\alpha = 2^\circ$ ,  $Re = 8 \times 10^6$ , B-L, C-S, and J-K turbulence models.

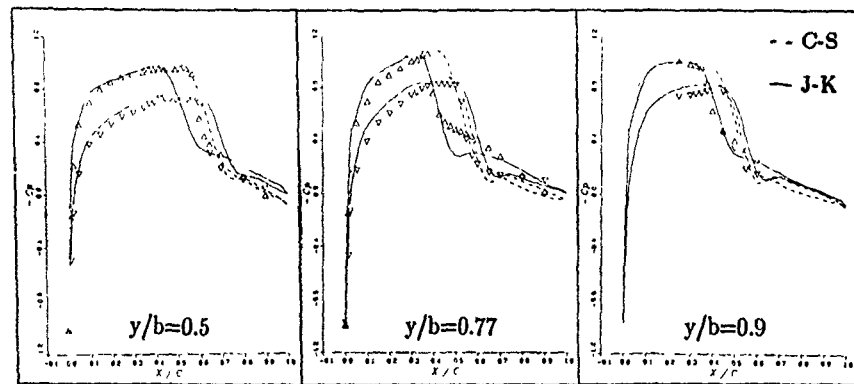


Fig. 12 Comparison of experimental and predicted pressure coefficients, NACA0012 airfoil section,  $AR=3$ ,  $\Lambda=20^\circ$ ,  $M_\infty=0.828$ ,  $\alpha=2^\circ$ ,  $Re=8 \times 10^6$ , C-S, and J-K turbulence models.

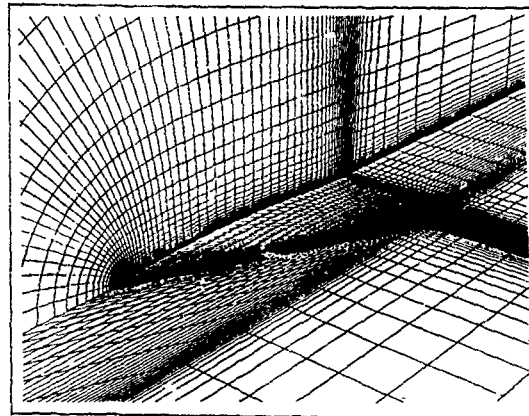


Fig. 13 C-H type hyperbolic grid around  $65^\circ$  sweep delta wing ( $151 \times 61 \times 46$ ).

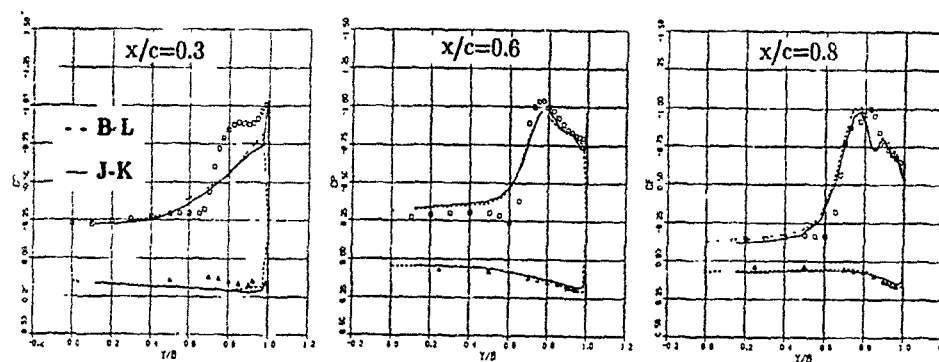
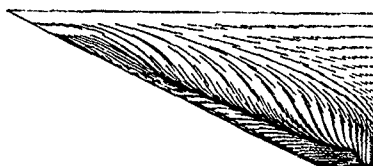


Fig. 14 Computed and experimental surface pressure coefficients on  $65^\circ$  sweep delta wing,  $M_\infty=0.85$ ,  $\alpha=10^\circ$ ,  $Re=9 \times 10^6$ , B-L and J-K turbulence models.

B-L Model



J-K Model

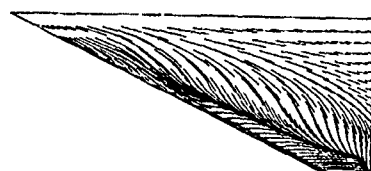


Fig. 15 Computed skin friction lines on 65° sweep delta wing showing both primary and secondary separations,  $M_\infty = 0.85$ ,  $\alpha = 10^\circ$ ,  $Re = 9 \times 10^6$ , B-L and J-K turbulence models.

J-K Model, Primary Vortex



Fig. 16 A perspective view of the primary vortex shedding from the leading edge of the 65° delta wing,  $M_\infty = 0.85$ ,  $\alpha = 10^\circ$ ,  $Re = 9 \times 10^6$ , J-K turbulence model.

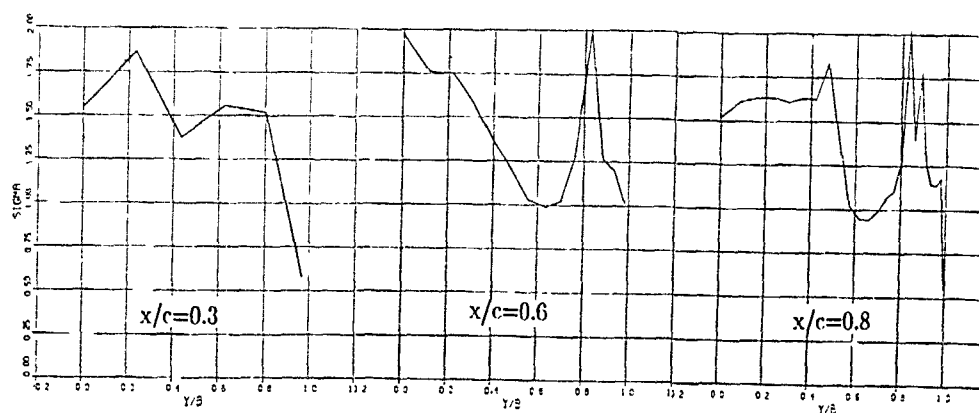


Fig. 17 Variation of  $\sigma(s)$  of the nonequilibrium state at constant streamwise locations,  $M_\infty = 0.85$ ,  $\alpha = 10^\circ$ ,  $Re = 9 \times 10^6$ , J-K turbulence model.

# REVIEW OF AIRCRAFT DYNAMIC LOADS DUE TO FLOW SEPARATION

by

D.G. Mabey  
Royal Aerospace Establishment  
Bedford MK41 6AE  
United Kingdom

## SUMMARY

This paper presents a detailed review of the 70th meeting of the AGARD Structures and Materials Panel, prepared for the AGARD Fluid Dynamics Panel. Accordingly emphasis is placed on the Aerodynamic information presented, rather than on the Structural Aspects.

Experimental results and computations are described for flows with bubble and vortex separations. Some conclusions are drawn and recommendations are made for further research. In particular, the review suggests that much greater attention should be given to establishing the magnitude of possible scale effects (both in experiments and calculations) and to the prediction of fin buffeting.

## 1 INTRODUCTION

The 70th meeting of the AGARD Structures and Materials Panel included a specialists' meeting on "Aircraft Dynamic Loads due to Flow Separation". The problems to be considered had been defined by a pilot paper<sup>1</sup>, which also recommended a uniform notation. Sixteen papers were included in the programme<sup>2-17</sup> and these have been published<sup>18</sup>. The current interest in this specialised topic was indicated by the attendance of about 130 scientists at this meeting.

The objective of the present review paper is to summarize aerodynamic results which are of interest to the AGARD Fluid Dynamic Panel when discussing the problems of "Vortex Flow Aerodynamics". However, some reference to structural problems is inevitable.

Sections 2.1 and 2.2 respectively review the experimental and computational results. Section 3 highlights major achievements and shortcomings, while Section 4 offers some conclusions and recommendations. The views expressed are solely those of the author.

## 2 REVIEW OF PAPERS

### 2.1 Experimental Results

#### 2.1.1 Bubble flows

Two interesting papers describe shock oscillations at transonic speeds caused by bubbles on supercritical aerofoils. The first paper<sup>2</sup> discusses measurements of normal force fluctuations  $C_N$ , on a 16% thick supercritical aerofoil (Fig 1) provided with a trailing-edge flap. For every flap setting, shock oscillations at a discrete frequency occur over a wide range of Mach number and angle of incidence (cf Fig 1 for a flap setting,  $\delta = -4^\circ$ ).

Somewhat surprisingly, for a fixed Mach number the shock oscillation frequency does not change significantly with the angle of incidence. This is inconsistent with observations on another supercritical aerofoil described in the second paper<sup>3</sup>.

Here the prime objective is to measure the buffet onset on a typical supercritical aerofoil (the CAST 7) and to see how this changes as Reynolds number is varied over a wide range (about  $2.5 \times 10^6$  to  $25 \times 10^6$ ). Most of the measurements were made with free transition but a few comparative measurements were made with fixed transition. Shock oscillations were observed after buffet onset, driven by the interaction of the complex flow at the foot of the shock (ie the bubble) and at the trailing-edge. The variation of both the shock height and the boundary layer thickness at the trailing edge is cyclic (Fig 2). With free transition the shock frequency decreased with increasing Reynolds number (Fig 3). Full comparative measurements with fixed transition are not available but would have been of great interest. In these experiments the shock oscillation frequency varies with the angle of incidence, in contrast to the measurements of Ref 2.

Refs 4, 5, and 6 relate primarily to investigations of the buffet and buffeting on a low aspect ratio, trapezoidal wing, which has a swept bubble separation from the sharp leading edge. The half model has an NACA 64-A-005 section and was tested both with and without a strake. Interest was centred mainly on flows separated from the sharp leading edge at high angles of incidence, and hence no roughness was applied to fix transition, although for these low speed tests the Reynolds number was only  $2.4 \times 10^6$ . The model was intended to be stiff but was provided with freedom to move in pitch or roll. Even without the strake the wing flow is highly three-dimensional (Fig 4) yet despite this, the overall forces and the buffeting (Fig 5) are the same in character as those observed on aerofoils with a sharp leading edge. Fig 5 shows that because of the high level of unsteadiness in the open jet tunnel, the model has a significant response even under attached flow conditions. Analysis of the measurements shows that the aerodynamic forcing associated with the separated flow is unaffected by the relatively small amplitudes of model motion. However, the motion dependent aerodynamic forces (which generate aerodynamic damping) are affected strongly by flow separations (Fig 6). Hence these variations in aerodynamic damping need to be scaled carefully from model to flight tests, as demonstrated previously<sup>19</sup>.

Ref 7 provides a simple description of a forward mounted spoiler as a source of buffet excitation on a wing at low speeds. The spoiler creates a bubble which is almost two-dimensional so that the steady and fluctuating pressures agree well with those observed previously<sup>20</sup>, the rms pressures peaking just upstream of the mean reattachment position (Fig 7). No large change in steady lift occurs until the bubble reattachment point reaches the trailing edge of the wing.

Ref 8 provides a summary of what must surely be the most comprehensive flight-tunnel comparison of buffet and buffeting ever made<sup>21</sup> - that on the TACT-F 1-11. For this relatively stiff aircraft, the effects of static and dynamic aeroelastic distortion are small, and scale effects are also small. The buffet excitation was judged independent of the wing motion, both in flight and the wind tunnel, consistent with other research<sup>6,19</sup>. In flight an LCO occurred in the wing torsional mode which did not occur on the wind tunnel model. A full explanation for this apparent anomaly has been given by quasi-steady theory<sup>21</sup>.

Ref 9 describes the effect of varying aspect ratio and sweep on buffeting at low speeds with well separated flows. The wing sections were of constant chord, with a chamfered leading edge. This unusual section was to ensure a fixed separation position at the low Reynolds number of the tests, followed by a long separation bubble. The wing aspect ratios varied from 8-4, with sweep angles of 0°, 20° and -20°. For the frequency parameters,  $n = fc/U > 0.1$  typical of wing bending at low speeds, the buffet excitation parameter in the first wing bending mode is about  $\sqrt{nG(n)} = 0.003$  to  $0.004$  consistent with previous measurements in wind tunnels and in flight on wings with more practical sections. For frequency parameters much lower (which would normally be inappropriate for the bending mode) the levels of  $\sqrt{nG(n)}$  were appreciably higher. Increases in excitation at such low frequency parameters could be important for rigid body motions at high angles of incidence.

#### 2.1.2 Vortex flows

Two papers were specially related with vortex flows.

Ref 10 relates to a wind tunnel and flight investigation of tail buffet and buffeting on the CF-18 aircraft (the Canadian version of the F-18). Measurements are presented of overall forces, fluctuating pressures (buffet excitation) and structural responses (buffeting). A significant feature of the wind tunnel tests was the careful choice of roughness used to fix transition<sup>22</sup> to ensure that flow separations on the model develop in the same way as in flight. An interesting feature of the flight buffeting is that the bending response of the fins is "in-phase" (Ref 10, Fig 43). The LEX fence provides a significant reduction in buffet (Fig 8) and buffeting (Figs 9 and 10). However the

paper gives no indication as to how the position and size of the LEX were determined. Ref 23 states many hundreds of different fixes were attempted before this particular fence was developed. It also gives many complementary observations on the flow about the aircraft.

Ref 11 also relates to a directly comparable investigation of fin buffeting on the F-18 aircraft. The authors suggest that fin buffeting may be predicted from either a simple analogue model (representing the principal modes of interest - first and second bending for the F-18) or by integrating the unsteady pressures measured on a rigid fin. However, the authors make no discussion of the difficulty of establishing the aerodynamic damping in the modes. For the analogue model, it is assumed (though not stated explicitly) that the correct aerodynamic damping can be achieved by representing the correct ratio of aerodynamic/structure stiffness as well as the frequency parameter. The rigid fin provides no estimate of aerodynamic damping. Levels appropriate to attached flow have been assumed when predicting the response (again this is not stated explicitly). This is unlikely to be a good assumption because of the tremendous variations in the vortex field (cf Fig 12 of Ref 14).

Using the measurements presented in Fig 3 of Ref 11, the present author has calculated the rms level of pressure fluctuations,  $p/q$ , for a typical point on the fin and plotted these against the angle of incidence (Fig 11). A rapid increase in  $p/q$  occurs above  $\alpha = 18^\circ$ , and a maximum value of about 0.32 is reached at  $\alpha = 36^\circ$ . Using the measurements in Fig 6 of Ref 11, Fig 12 shows the corresponding rms pressure fluctuation spectra ( $\sqrt{nG(n)}$ ) according to the AGARD definition plotted against a frequency parameter based on an arbitrary reference length. Results are shown for  $\alpha = 24^\circ, 32^\circ, 36^\circ$  and  $52^\circ$ . It is important to notice the sharp peak in the spectrum, which moves to lower frequency parameters as the angle of incidence increases from  $\alpha = 24^\circ$  to  $36^\circ$ . [For this configuration the bursting of the LEX Vortex is thought to determine the peak in the excitation spectra]. In contrast, for  $\alpha = 52^\circ$  the buffet excitation is much lower and the spectrum is much flatter, resembling the usual situation.

#### 2.1.3 Aerodynamics of controls

Ref 12 shows how the interaction between the canard and wing flows on a model of a typical combat aircraft is controlled by the canard effective incidence,  $\alpha_c$ . The measurements include overall forces, steady and fluctuating pressures, canard buffeting and wing buffeting. All these measurements can be related with  $\alpha_c$ .

Previous experience suggests that scale effects will be significant on the canard whenever  $\alpha_c$  is close to the values required for buffet onset ( $\alpha_c = +12^\circ$  and  $-12^\circ$  corresponding with separation on the upper and lower surfaces of the

uncambered canard of Ref 12). In addition scale effects will be significant on the wing close to buffet onset (about  $\alpha = +12^\circ$  and  $-2.6^\circ$  for this cambered wing). Hence large scale effects can be expected at the four points in the  $\alpha$ ,  $\alpha_c$ , domain indicated in Fig 13.

Ref 13 discusses the problems of predicting the buffeting forces on the wings of a transport aircraft. High Reynolds numbers are required, and  $12 \times 10^6$  can be achieved at reasonable kinetic pressures on large half models when tested in the ONERA S-1 Tunnel at Modane. Hence the effects of static aeroelastic distortion are of reasonable magnitudes and can be estimated. Ref 13 makes 3 important observations:

- (1) For a transport aircraft wing buffeting can be reduced by Active Control Technology if a control can be placed in a region where the flow is still attached after buffet onset.
- (11) When exciting a transport wing in pitch, very large oscillations can develop at transonic speeds, immediately after the onset of flow separation (Ref 13, Fig 14).
- (111) Great care is needed to establish 'buffet-onset' on a transport aircraft because what is prescribed in the air-worthiness regulations is a particular level of response at a particular point - normally the pilot's seat. In contrast, in a wind tunnel test buffet onset is normally synonymous with incipient separation. A very different 'buffet onset' might be obtained from the buffeting response, of say, an engine nacelle.

## 2.2 Computational results

Edwards provided a comprehensive review<sup>14</sup> of the capability of predicting unsteady airloads due to separated flows. Periodic aerodynamic shock oscillations at transonic speeds on rigid aerofoils can be predicted successfully (Fig 14), as can transonic aileron buzz (Fig 15). Unfortunately similar success has not been achieved in predicting the large Limit Cycle Oscillation (LCO) in the first bending mode observed at transonic speeds on a flexible high aspect ratio wing with a supercritical section. The extensive measurements on this three-dimensional configuration (Fig 16) constitute a serious challenge to Computational Mechanics, as well as providing a warning to designers of advanced transport aircraft. Further details of this important experiment (which might facilitate further analysis) are given elsewhere<sup>14</sup>.

Edwards discussed also the successful computation of the highly three-dimensional flow round the forebody of the F-18 aircraft at  $M = 0.30$ ,  $\alpha = 30^\circ$  both for laminar flow at  $R = 0.2 \times 10^6$  (Fig 17a) and for turbulent flow at  $R = 10 \times 10^6$  (Fig 17b). Edwards also addressed the much more difficult problems of what computer

time might be required to compute the buffet excitation about the fins of an F-15 model (Fig 18); this would require accurate calculation of the vorticity convection. Subject to a number of assumptions, Edwards concluded that the total time required for one condition would be 138 hours for an Euler Code and 950 hours for a thin-layer Navier-Stokes Code (Ref 14, Table 1). Edwards gives additional evidence for these conclusions elsewhere<sup>15</sup> and these considerations are relevant to the discussion of vortex flows in Section 2.1.2. Possibly these computation times could be reduced if the principal feature of the separated flow which causes the peak in the excitation spectra (cf Fig 12) could be established.

Costes and Petot provided a comparison between a semi-empirical prediction method and measurements of the aerodynamic forces due to unsteady separation on a high aspect ratio wing oscillating at large amplitude. Comparisons were presented for sweep angles,  $\Lambda$ , of  $0^\circ$ ,  $+20^\circ$  and  $-20^\circ$  and were relevant to the performance of helicopter rotors. The results were generally good for  $\Lambda = 0^\circ$  but poor for  $\Lambda = +20^\circ$  and  $-20^\circ$ , particularly for sections near the tip.

Meyer and Zwaan<sup>16</sup> presented a quasi-steady theory to predict LCO in fighter type aircraft (Fig 19) at transonic speeds from steady pressure measurements (or predictions). The prediction method explains the LCO observed in flight and stresses that the motion is determined by the flow at the wing-tip, rather than at the wing-root (cf Figs 20 & 21). In principle this method could be adopted to predict LCO.

## 3 DISCUSSION

It is convenient to discuss the findings of this meeting under 3 general headings: experimental results, theoretical results and discussion of some general shortcomings.

With regard to the experimental results, a wide range of problems was addressed including variations in wing aspect ratio, sweep, section, Mach number and angle of incidence; fin buffeting at high angles of incidence and canard/wing interaction. However, although there were many interesting new measurements, some presentations gave an impression which can only be expressed adequately by the French phrase 'deja vu'. With respect to the very important question of fin buffeting, it was alarming to learn that "some fins fail after only 300 hours flying time". In the author's view such a low life is unlikely to be indicative of random scatter in fatigue testing, as one structural engineer suggested. It is more likely to be indicative of a very sensitive flow on the aircraft which has been adversely affected by some minor imperfection, eg a small misalignment of the fuselage nose. This important aspect of fin buffeting was not addressed, but the effect of the small LEX fence on the F-18 is significant<sup>10</sup>. For the F-18 the bursting of the LEX vortex is

thought to determine the peak in the excitation spectra. However on other combat aircraft the separations may be radically different, and yet the excitation spectra may still contain a sharp peak. This would mean that each configuration will have to be the subject of special tests.

With regard to the theoretical results, the most impressive advance since the publication of the pilot paper<sup>1</sup> has been the prediction of LCO, for which 2, rather similar quasi-steady methods are now available<sup>16,22</sup>. However an early attempt to predict the LCO oscillation in bending of the NASA Wing with an inviscid transonic small perturbation code was unsuccessful<sup>14</sup>. Perhaps the quasi-steady method might be applied here? The meeting has also confirmed that the linear model for the prediction of buffeting works well as long as the modal aerodynamic damping appropriate to the separated flow can be measured. The aerodynamic damping can be measured either on an ordinary, nominally rigid wind tunnel model (made of aluminium in preference to steel to give larger motion) or by oscillating a nominally rigid wing (as in the experiments cited<sup>4,5,6</sup>). However Edwards showed<sup>14</sup> that CFD techniques cannot yet be used to predict either the aerodynamic damping or the buffet excitation.

Ref 1 issued 2 specific challenges to the CFD community. The first, the prediction of shock oscillations on bi-convex wings - is well established. However, despite this success with thin-layer Navier Stokes codes, this method has not been applied as a matter of routine to more realistic supercritical aerofoils or NACA or RAE aerofoils. It would have been particularly interesting to have predicted oscillation frequencies for the supercritical aerofoils of Refs 2 and 3. However, these calculations were not made nor was the type of shock motion specified, as recommended in a previous AGARD paper<sup>27</sup>. [The shock motions in both Refs 2 and 3 appear to be Tijdeman type A<sup>28</sup>]. The second challenge to the CFD community was the prediction of the buffet excitation caused by a bubble (represented at this meeting by Ref 7). No author attempted the computation of this relatively simple flow.

Opinions are likely to differ with regard to the shortcomings of the meeting. One was the failure to use the consistent and logical notation specified<sup>1</sup>. The prediction of aircraft dynamic loads due to flow separation is an extremely difficult problem. Why make it more difficult by not presenting results in non-dimensional form? For example, it would have been invaluable to compare the independent measurements on virtually the same aircraft in Refs 10 and 11 in terms of the buffet excitation parameter, but this was not done. AGARD has had a consistent notation for measurements of pressure fluctuations<sup>29</sup> since 1958 and for the buffet excitation parameter since 1988.

Similarly there was often a marked reluctance to present results in terms of a frequency parameter. Of course, in many problems there is uncertainty about the best choice for the reference length for the problem in question. This is a particularly interesting and difficult question for fin buffeting (both in experiments and in prediction attempts). For aerofoils the chord is generally used whereas for a bubble the local bubble length can be used, even for a swept bubble<sup>12</sup>. Taking an aerofoil as a simple example, it is much better to have a frequency parameter.

$$n = \frac{fc}{U}, \quad (1)$$

or

$$v = \frac{2\pi fc}{U}, \quad (2)$$

or

$$k = \frac{\pi fc}{U}, \quad (3)$$

than a frequency,  $f$ , in Hz. This may mean a great deal to a pilot's comfort or to the fatigue life of the structure, but it is of little interest to an aerodynamicist striving to establish the physics of the problem.

Another common shortcoming was a general failure to address the question "How sensitive will this flow be to variations in Reynolds number?" Fig 3 of Ref 3 for the CAST 10 aerofoil suggests that even with fixed transition large scale effects can persist at Reynolds numbers up to  $25 \times 10^6$ . Hence it could be dangerous to suggest (as in Ref 13) that there is a universal, minimum test Reynolds number which will ensure full scale results. It follows that much more attention should be given to the ways in which transition is fixed, and to careful comparisons with transition free measurements (where appropriate). This was illustrated in Ref 3 and advocated in the AGARD Manual on this topic<sup>30</sup>. Ideally wind tunnel tests and CFD computations should include some variation in Reynolds number. Often the CFD specialist rests content at successfully predicting an incipient flow separation on an aerofoil at, say  $M = 0.85$ ,  $R = 1.5 \times 10^6$ . The aeronautical engineer would like him to make the calculations also at  $R = 15 \times 10^6$  and  $150 \times 10^6$ . This philosophy will become particularly important with respect to the prediction of the aerodynamic characteristics of hypersonic vehicles. In an attempt to clarify the controversial question of the simulation of scale effects, Ref 1 suggested that the meeting should include a special session devoted entirely to unsteady measurements in cryogenic wind tunnels, which allow scale effects and the effects of aeroelastic distortion to be distinguished<sup>31</sup>. Unfortunately not one paper was submitted on this area. No papers were submitted on flap or cavity buffeting.



It is interesting to note that one paper addressed a question which arose out of a previous AGARD meeting on Unsteady Aerodynamics<sup>27</sup>. The question was "What are the reasons behind the constancy of the buffet excitation parameter at the heavy buffeting limit for wings of widely varying planform". Ref 9 gives no answer, but confirms previous observations for unswept and swept back wings. In addition, it shows that the same limit applies for wings swept forward 20°. These observations thus still present a challenge to experimental aerodynamicists and the CFD community.

In summary, the main achievement is the prediction of Limit Cycle Oscillations (LCO) and the presentation of some interesting new experiments. The main failures are the reluctance to adopt a common notation, to identify the type of shock motions and to take an adequate account of scale effects, both in experiments and computations.

#### 4 CONCLUSIONS AND RECOMMENDATIONS

This review suggests 4 main conclusions and 6 recommendations.

The conclusions are:

- (1) Useful progress has been made in the prediction of Limit Cycle Oscillations.
- (2) The linear model for the prediction of buffeting has been verified carefully in both wind tunnels and flight tests.
- (3) Aerodynamic damping in separated flows depends on the mode shape, frequency parameter, Mach number and angle of incidence. It cannot currently be predicted theoretically but it can be derived from experiments.
- (4) On combat aircraft at high angles of incidence, severe fin buffeting may occur, even at zero sideslip.

The recommendations are:

- (1) The AGARD notation for buffet excitation and buffeting response should be adopted, so that aerodynamicists can acquire a better understanding of the separated flows giving dynamic loads.
- (2) Much greater attention should be given to establishing the magnitude of possible scale effects, both in experiments and calculations.
- (3) Special tests in cryogenic wind tunnels should be made to distinguish between genuine scale effects and the effects of aeroelastic distortion. Such measurements would be of equal interest for landing configurations (say at  $M = 0.2$ ) or cruise configurations (say at  $M = 0.85$ ).

- (4) Wherever possible, the type of transonic shock motion should be identified in both theoretical studies and time-dependent experiments.
- (5) For fin buffet at high angles of incidences, a careful study should be made to establish what feature of the separated flow determines the peak in the excitation spectra.
- (6) Researchers should be careful to assess and remove any tare effects of flow unsteadiness in wind tunnels which will not occur in flight.

#### SYMBOLS

$c$	chord
$\bar{C}_N$	rms normal force coefficient
$k = \pi fc/U$	frequency parameter (eqn 3)
$M$	Mach number
$\sqrt{nF(n)}$	rms level of excitation (AGARD notation - Ref 29)
$n = fc/U$	frequency parameter (eqn 1)
$Re$	Reynolds number
$\bar{p}$	rms pressure fluctuations
$q$	kinetic pressure
$x$	streamwise co-ordinate
$\alpha$	angle of incidence
$\delta$	flap setting
$\delta_{TE}$	boundary layer thickness at trailing edge
$\Lambda$	sweep angle
$v = 2\pi fc/U$	frequency parameter (eqn 2)

#### REFERENCES

- 1 D.G. Mabey, Some aspects of aircraft dynamic loads due to flow separation. AGARD R-750 (1988)
- 2 B.H.K. Lee, Effects of trailing-edge flap on buffet characteristics of a supercritical aerofoil.
- 3 E. Stanewsky, Experimental investigation of buffet onset and penetration on a supercritical aerofoil at transonic speeds.
- 4 P. Bublitz, H. Zingel, Experimental investigation of buffet excitation forces on a low aspect ratio trapezoidal half-wing in incompressible flow.

## REFERENCES (concluded)

- |    |   |    |  |
|----|---|----|--|
| 5  | H. Zingel, Experimental investigation and semi-empirical prediction of the dynamic response of a low aspect ratio trapezoidal wing due to flow separation.                        | 20 | D.G. Mabey, Analysis and correlation of data on pressure fluctuations in separated flow. AIAA J. Aircraft 9 (9), pp 642-645 (1972)   |
| 6  | H. Forsching, Motion-induced unsteady airloads in separated flow.   | 21 | C.F. Coe; A.M. Cunningham, Predictions of F 1-11 TACT aircraft response and correlations of fluctuating pressures measured on aluminium and steel models and the aircraft. NASA CR 4069 (1987) |
| 7  | P.G. Myers, D.L. Birdsall, The forward mounted spoiler as a source of buffet excitation.  | 22 | A.M. Cunningham, Practical problems - airplanes. Chapter 3 of Unsteady Transonic Aerodynamics, Vol 120, Progress in Astronautics and Aeronautics (published by AIAA) pp 75-132 (1989)          |
| 8  | A. Cunningham,  | 23 | G.E. Erickson et al, Experimental investigation of the F/A-18 Vortex flows at subsonic through transonic speeds. AIAA 89-2222 (1989)   |
| 9  | D.J. Maull, S.Z. Zan, The effect of wing planform on low speed buffeting.   | 24 | C.V. Eckstrom, D.A. Seidel, M.C. Sandford, Unsteady pressure and structural response measurements on an elastic supercritical wing. AIAA J. Aircraft, Vol 27, No 1 p 75-80, (1990)             |
| 10 | B.H.K. Lee, D. Brown, M.B. Zgela, D.C. Poirel, Wind tunnel and flight tests of tail buffet on the CP-18 aircraft.   | 25 | J.W. Edwards, Assessment of computational prediction of tail buffeting. NASA TM 101613 (1990)  |
| 11 | M.A. Ferman, S.R. Patel, N.H. Zimmerman, G. Gesternkorn, A unified approach to buffet response of a fighter empennage.  | 26 | D.G. Mabey, Aeroelastic oscillations caused by transitional boundary layers and their attenuation. AIAA J. Aircraft Vol 24, 7, pp 463-469  |
| 12 | D.G. Mabey, B.L. Welsh, C.R. Pyne, Interaction between the canard and wing flows on a model of a typical combat aircraft.   | 27 | D.G. Mabey, J.R. Chambers, Technical Evaluation Report on Unsteady Aerodynamics - Fundamentals and applications to aircraft dynamics. AGARD AR 222, (1986)                                     |
| 13 | R. Destuynder, New method to determine buffeting forces in a wind tunnel.   | 28 | H. Tijdeman, Investigation of the transonic flow around oscillating aerofoils. NLR 77-090U (1977)  |
| 14 | J.W. Edwards, Unsteady airloads due to separated flow on aerofoils and wings.   | 29 | T.B. Owen, Techniques of pressure fluctuation measurements employed in RAE low speed wind tunnels AGARD Report R 172 (1958)  |
| 15 | J.J. Costes, D. Petot, Coupled aerodynamic forces due to unsteady stall on a high aspect ratio wing oscillating at high amplitude.  | 30 | AGARD Fluid Dynamics Panel, Boundary layer simulation and control in wind tunnels. AGARD AR 224 (1988)   |
| 16 | J.J. Meijer, R.J. Zwaan, Investigation of a semi-empirical method to predict limit cycle oscillations on a modern fighter aircraft.   | 31 | D.G. Mabey, Some remarks on dynamic aeroelastic model tests in cryogenic wind tunnels NASA CR 145029 (1975)  |
| 17 | L.E. Ericsson, Unsteady separated flow phenomena causing self excited structural oscillations.  |    |  |
| 18 | Anon, Aircraft dynamic loads due to flow separation AGARD CP 483, (1990)  |    |  |
| 19 | G.F. Butler, J.G. Jones, The prediction of buffeting response in flight from wind-tunnel measurements on a model of conventional construction. RAE Technical Report 84-045 (1984) |    |  |

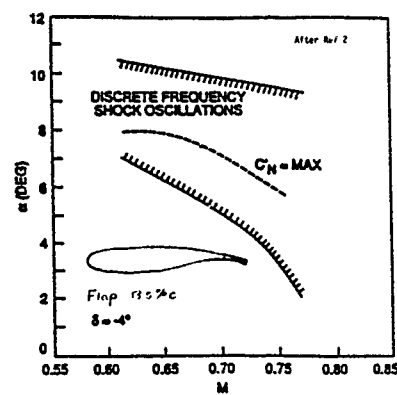


Fig 1 Region of discrete frequency shock oscillations at  $\delta = -4^\circ$

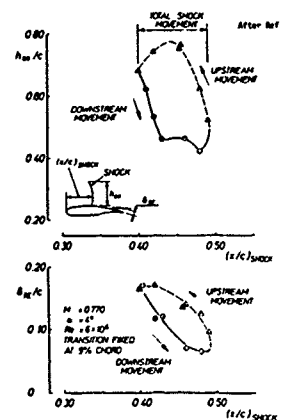


Fig 2 Shock movement and trailing-edge boundary layer thickness

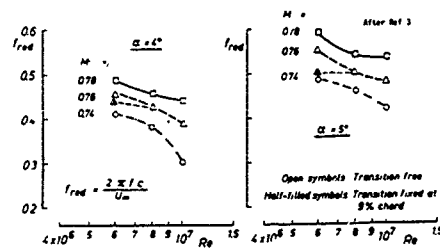


Fig 3 Dependence of reduced shock oscillation frequency on Reynolds number

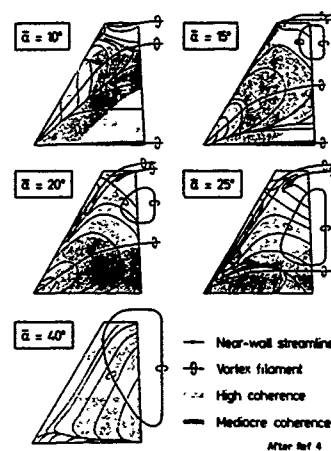


Fig 4 Flow on wing for  $Re = 2.4 \cdot 10^6$

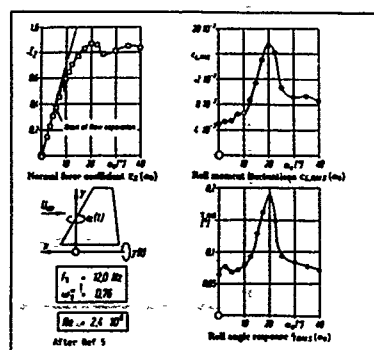


Fig 5 Dynamic response due to flow separation (buffeting)

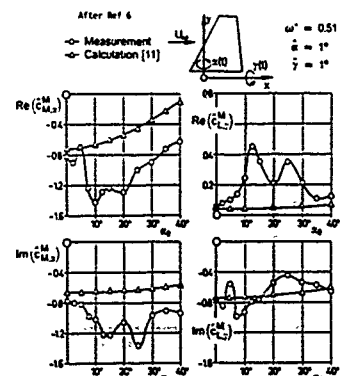


Fig 6 Measured and calculated amplitudes of motion induced pitching moment and rolling moment coefficients at various steady mean incidences

12-8

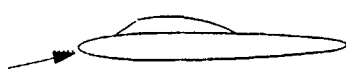
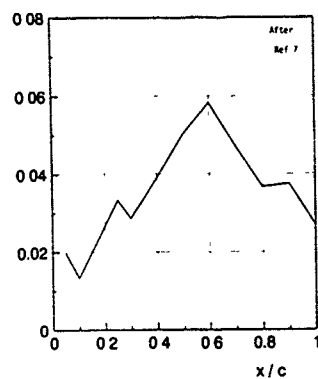
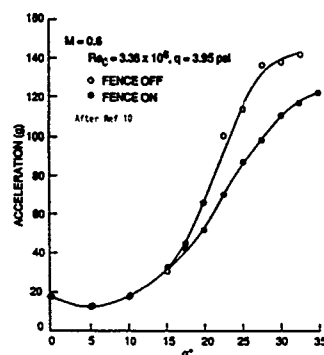
Variation of  $\bar{p}/q$ Fig 7 Short bubble:  $\alpha = 4^\circ, 5 = 20^\circ$ 

Fig 9 Variation of fin acceleration with incidence

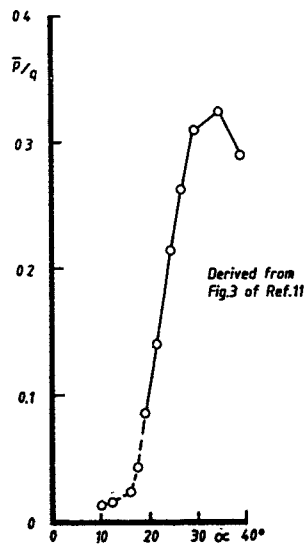


Fig 11 Variation of rms pressure fluctuations on fin with angle of incidence

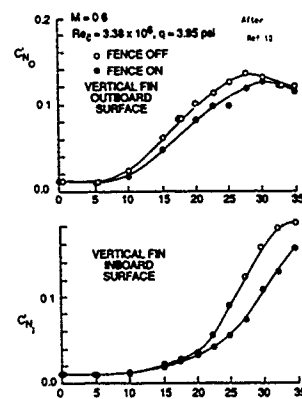


Fig 8 rms normal force coefficient on fin outboard and inboard surfaces

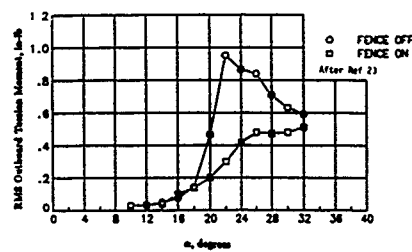


Fig 10 Effect of LEX fence on fin second mode torsional response

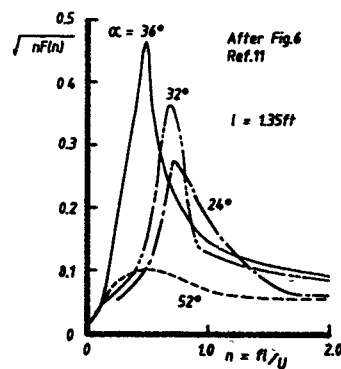


Fig 12 Variation of typical pressure fluctuation spectra on wing with angle of incidence

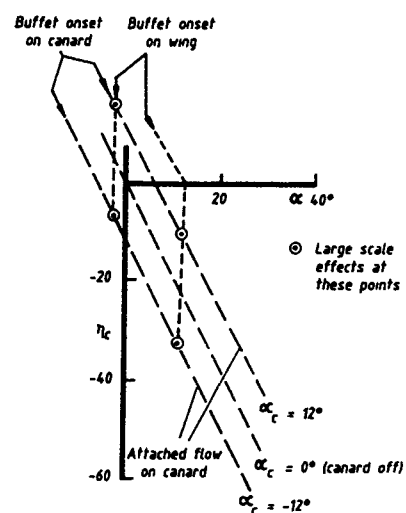


Fig 13 Interaction between canard flow and wing buffeting in  $\alpha$ ,  $\eta_c$  domain

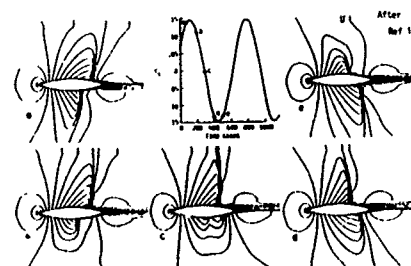


Fig 14 Calculated shock oscillation for 18% biconvex aerofoil using Navier-Stokes code  $M = 0.78$ ,  $Re = 11 \times 10^6$

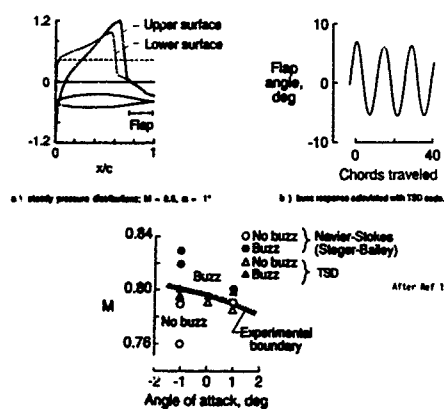


Fig 15 Experimental and calculated aileron buzz conditions

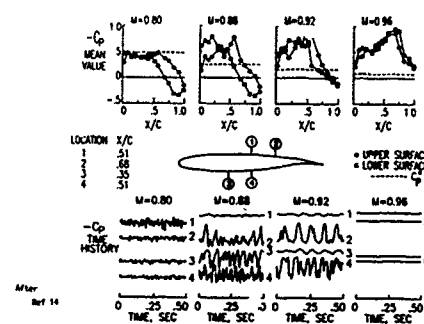


Fig 16 Mean chordwise pressure distributions and sample pressure histories at  $\eta = 0.87$  on a supercritical wing

12-10

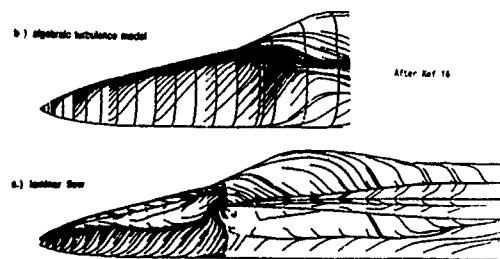


Fig 17 Effect of turbulence modeling on forebody flow on an F-18 for  $M = 0.3$ ,  $Re = 2 \times 10^5$ ,  $\alpha = 30^\circ$

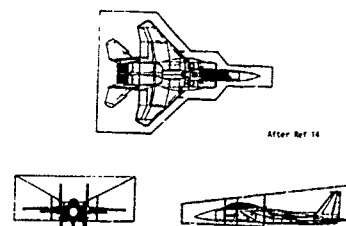


Fig 18 Near field volume for the F-15 aircraft requiring grid density sufficient for accurate vorticity convection calculations

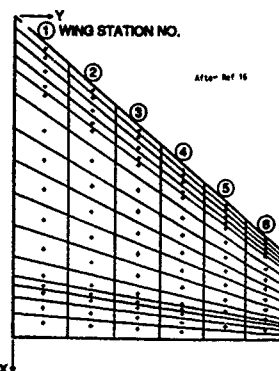


Fig 19 F-16 wing planform with pressure orifices and panels

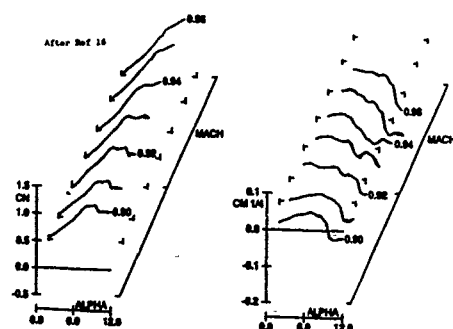


Fig 20 Steady lift and moment coefficients for the tip section as functions of Mach number and incidence

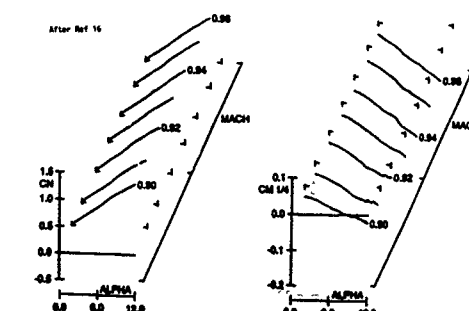


Fig 21 Steady lift and moment coefficients for the root section as functions of Mach number and incidence

## In-Flight Flow Visualization and Pressure Measurements at Low Speeds on the NASA F-18 High Alpha Research Vehicle

John H. Del Frate, David F. Fisher, and Fanny A. Zuniga

NASA Ames Research Center  
Dryden Flight Research Facility  
P.O. Box 273  
Edwards, CA 93523-0273

### 1 ABSTRACT

In-flight results from surface and off-surface flow visualizations and from extensive pressure distributions document the vortical flow on the leading-edge extensions (LEXs) and forebody of the NASA F-18 high alpha research vehicle (HARV) for low speeds and angles of attack up to  $50^\circ$ . Surface flow visualization data, obtained using the emitted fluid technique, were used to define separation lines and laminar separation bubbles (LSB). Off-surface flow visualization data, obtained by smoke injection, were used to document both the path of the vortex cores and the location of vortex core breakdown. The location of vortex core breakdown correlated well with the loss of suction pressure on the LEX and with the flow visualization results from ground facilities. Surface flow separation lines on the LEX and forebody corresponded well with the end of pressure recovery under the vortical flows. Correlation of the pressures with wind-tunnel results show fair to good correlation.

### 2 INTRODUCTION

In recent years, more emphasis has been placed on expanding the envelope of fighter aircraft to include controlled flight at high angle of attack exceeding the maximum lift coefficient ( $C_{L_{max}}$ ). Fighters such as the F-18 and F-16 use leading-edge extensions (LEXs) or wing body strakes which provide additional lift caused by the vortical flow these devices develop at moderate to high angles of attack (ref. 1). However, the prediction and control of this vortical flow and the mutual interactions of the vortices are not well understood. The combined effect of the LEX and the forebody vortices on the vehicle aerody-

namics must be understood to avoid any adverse effects such as buffet or a loss of stability and control, and to take full advantage of the benefits that can be derived for fighter aircraft.

Vortical flow interactions on scale models in wind tunnels are not well understood at this time. Experimental data from different scale wind-tunnel F-18 models have shown conflicting results even when tested at the same Reynolds number (ref. 2). For example, the interaction of the forebody and LEX vortices on 6- and 7-percent scale F-18 models typically resulted in apparent lateral stability for all angles of attack, including stall and post stall regions. However, airplane flight data and wind-tunnel results for the large scale (16 percent) model at low Reynolds numbers indicated a region of lateral instability near maximum lift. This apparent scale effect is still being investigated. Understanding such scale effects is essential for successful design of future fighters intended to operate at high angles of attack.

NASA is currently conducting a High Alpha Technology Program (HATP) to (1) increase the understanding of the high angle of attack aerodynamics, (2) improve prediction techniques, (3) provide design guidelines, and (4) investigate new concepts for vortex control on advanced highly maneuverable aircraft.

This program uses the F-18 configuration as a validation and demonstration tool. The HATP incorporates wind-tunnel tests of subscale, (refs. 3 and 4), and full-scale models and components, calibration and validation information for computational fluid dynamics (CFD) codes, (refs. 5-9), piloted simulations and full-scale flight testing (refs. 10-17).

As part of this program, the Ames-Dryden Flight Research Facility has been conducting extensive flow visualization and pressure distribution studies on the NASA F-18 high alpha research vehicle (HARV) to document the characteristics of the forebody and the LEX vortices. Surface and off-surface flow visualization results have been reported in references 10 through 16. The off-surface flow visualization results presented were performed using smoke injection and are correlated to wind- and water-tunnel results. The surface flow visualization was performed using the emitted fluid technique. Pressure distribution results have been reported for the flight case in reference 16. The surface pressure measurements were made at five forebody stations and at three LEX stations on the aircraft and are correlated with similar data from a 6-percent wind-tunnel model and selected flow visualization data from flight.

This paper presents a selection of results from both the flow visualization and the pressure measurement studies conducted at low speeds and for angles of attack up to 50°.

### 3 NOMENCLATURE

b	aircraft span, ft	$\ell$	length of aircraft from nose apex to engine exhaust plane, 54.4 ft
BART	Basic Aerodynamics Research Tunnel, NASA Langley Research Center	LEX	leading-edge extension
$C_L$	lift coefficient	LSB	laminar separation bubble
$C_p$	pressure coefficient	LSWT	low-speed wind tunnel, McDonnell Aircraft Company
$C_p^*$	pressure coefficient corresponding to local speed of sound, $C_p^* = \left( \frac{2}{\gamma M_\infty^2} \right) \left\{ \left( \frac{(\gamma-1)M_\infty^2 + 2}{\gamma+1} \right)^{3/5} - 1 \right\}$	$M_\infty$	free stream Mach number
d	diameter of fuselage forebody, in.	m.a.c.	mean aerodynamic chord, 11.525 ft
DTRC	David Taylor Research Center 7 × 10 transonic wind tunnel	R	reattachment line location
ECM	electronic counter measures	$R_1$	primary reattachment line location
F.S.	fuselage station, in. (nose apex at 59.82 in.)	$R_2$	secondary reattachment line location
FVF	Flow Visualization Facility water tunnel, NASA Ames-Dryden	$R_3$	tertiary reattachment line location
HARV	high alpha research vehicle	$Re_\ell$	Reynolds number based on mean aerodynamic chord
HATP	High Alpha Technology Program	$Re_d$	Reynolds number based on diameter
		$Re_\ell$	Reynolds number based on local maximum fuselage diameter, corrected for angle of attack using the method of reference 18.
		s	local span distance from LEX-fuselage junction to LEX leading edge, in.
		$S_1$	primary separation line location
		$S_2$	secondary separation line location
		$S_3$	tertiary separation line location
		x	measured location along aircraft longitudinal axis, positive measured aft from nose, ft
		Y	measured location along aircraft lateral axis, positive measured from center line out left wing, ft
		y	distance along LEX local semispan, positive measured out left wing, in.
		$\alpha$	aircraft angle of attack, right wingtip angle-of-attack vane corrected for upwash and angular rates, deg
		$\alpha'$	angle of attack used in the determination of $Re_\ell$ , deg. At F.S. 70, 85, and 107, $\alpha' = \alpha - 5.6^\circ$ because the nosecone is depressed from the aircraft waterline $5.6^\circ$ . At F.S. 142 and 184, $\alpha' = \alpha$



- $\beta$  aircraft angle of sideslip, average of left and right wingtip sideslip vanes corrected for angle of attack, positive nose left, deg
- $\gamma$  ratio for specific heats of air, 1.4
- $\theta$  forebody cross section circumferential angle ( $0^\circ$  is bottom centerline, positive is clockwise as seen from a front view,  $0^\circ$  to  $360^\circ$ ), deg

#### 4 VEHICLE DESCRIPTION

The NASA HARV (fig. 1) is a single-place preproduction F-18 aircraft built by McDonnell Douglas and Northrop and is powered by two General Electric F404-GE-400 afterburning turbofan engines. The aircraft features a mid-wing with leading- and trailing-edge flaps which operate on a schedule that is a function of angle of attack and Mach number. For  $M_\infty \leq 0.76$  and  $\alpha \geq 26^\circ$ , the leading-edge flap is down  $33^\circ$  (maximum) and the trailing-edge flap is at zero. The LEXs are mounted on each side of the fuselage from the wing roots to just forward of the canopy. The aircraft has twin vertical stabilizers canted out  $20^\circ$  from the vertical and differential all-moving horizontal tails. The NASA F-18 HARV, with the current flight control computers and control laws (8.3.3 programmed read only memory (PROM) set), is flown by NASA in the fighter escort configuration without stores. The aircraft carries no missiles and the wingtip missile launch racks have been replaced with special camera pods and wingtip airdata booms. The flight-test nose-boom has been removed from the aircraft. The aircraft has an unrestricted angle-of-attack flight envelope in this configuration with the center of gravity between 17-percent and 25-percent mean aerodynamic chord (m.a.c.) as defined by the Naval Air Training and Operating Procedures Standardization (NATOPS) manual.

#### 5 TEST TECHNIQUES, HARDWARE, AND INSTRUMENTATION

##### 5.1 Off-Surface Flow Visualization Technique

The vortex cores were visualized using smoke as the tracer material as described in references 11 through 15 and similar to that described in reference 19. Smoke was

introduced into the flow field through flush ports on the forebody at approximately 28 in. aft of the nose apex and circumferential angles ( $\theta$ s) of  $80^\circ$  and  $280^\circ$ . On the LEX, the smoke was routed to ducts which exhaust slightly below and approximately 4 in. aft of the LEX apex.

At the desired test conditions, the smoke was entrained in the flow field vortices which were videotaped and photographed with onboard cameras (fig. 1) or from chase aircraft (ref. 15). Smoke duration was normally 30 sec. The upper surfaces of the airplane were painted black to enhance visualization of the smoke traces.

##### 5.2 Surface Flow Visualization Technique

The surface flow visualization technique used on the F-18 HARV consists of emitting liquid dye from flush orifices on the forebody and the LEX upper surface as shown in figure 2. These orifices, which were also used to gather pressure data, will be discussed in the next section. The hardware for the surface flow visualization system is described in detail in references 10 and 12 and is similar to that described in reference 20. The liquid dye used for this program consisted of a mixture of propylene glycol monomethyl ether (PGME) and a red toluene-based dye. The dye is emitted from orifices on the forebody and the LEX upper surface while the aircraft is at the desired flight condition. Upon evaporation of the solvents within the mixture, the dye is left on the surface of the aircraft and traces the surface flow streamlines as can be seen in figure 3. Photos are taken on the ground after the flight to document the surface flow streamlines.

##### 5.3 Static Pressure Orifice Locations

Pressure measurements were made on both the forebody and the LEXs of the F-18 HARV (ref. 16) at fuselage locations selected to correspond with orifice locations on both the 0.06- and 0.16-scale wind-tunnel models (refs. 3 and 4).

Five rings of static pressure orifices were installed on the forebody forward of the canopy as shown in figure 2. At the first two rows, fuselage station (F.S.) 70 ( $x/l = 0.015$ ) and F.S. 85 ( $x/l = 0.038$ ), 32 static pressure orifices were spaced about the forebody. While at the last three rows, F.S. 107 ( $x/l = 0.071$ ), F.S. 142 ( $x/l = 0.126$ ) and F.S. 184 ( $x/l = 0.190$ ), 64 orifices were spaced about

the forebody. For all the rows, the majority of the pressure orifices were placed on the upper surface where the greatest pressure gradients were expected.

Both the left and right LEXs were instrumented with three rows of pressure orifices located at F.S. 253 ( $x/\ell = 0.295$ ), F.S. 296 ( $x/\ell = 0.361$ ) and F.S. 357 ( $x/\ell = 0.454$ ). The number of orifices installed at each station on the upper surface of each LEX varied from 13 to 20 and from 4 to 5 at each station on the lower surface.

Typical cross sections of the forebody and LEX orifice stations and the orientation of the orifices are given in figure 4. The view is looking aft on the aircraft with the bottom fuselage centerline at  $0^\circ$  and the top centerline fuselage at  $180^\circ$ . At the LEX stations,  $y/s = 0.0$  is defined as the LEX fuselage junction while  $y/s = 1.0$  is the leading edge of the LEX,  $+1.0$  for the left LEX leading edge and  $-1.0$  for the right LEX leading edge.

Several protrusions on the forebody should be noted. Two small, elliptical shaped electronic counter measures (ECM) antenna covers (fig. 4) were located on the sides of the fuselage centered at F.S. 134,  $\theta = 85^\circ$  and  $275^\circ$  and were approximately 9.5-in. long, 4-in. wide and protruded approximately 1.7 in. Also, two aircraft production pitot-static probes (fig. 4) were located on the lower fuselage at F.S. 164 to 177 and  $\theta = 35^\circ$  and  $325^\circ$ . The LEX was virtually free of significant protrusions forward of the orifice rows.

#### 5.4 Airdata System

Airspeed, altitude, angle of attack ( $\alpha$ ), and angle of sideslip ( $\beta$ ) were measured using airspeed booms shown in figure 5, mounted on specially designed wingtip photo pods as shown in figure 1. On the right wingtip a standard NACA noseboom (ref. 21), (fig. 5(a)), was installed with the tip mounted 7.3 ft forward of the wingtip leading edge. On the left wingtip, a swiveling probe (ref. 16), (fig. 5(b)), was similarly located. It is estimated that  $\alpha$  and  $\beta$  were accurate to  $\pm 0.5^\circ$  for  $\alpha$  up to  $40^\circ$ , and  $\pm 1^\circ$  for  $\alpha$  up to  $50^\circ$ . It is also estimated that  $M_\infty$  is accurate to  $\pm 0.005$  at  $\alpha = 50^\circ$ , and  $\pm 0.003$  for  $\alpha < 30^\circ$  (ref. 16).

### 6 FLIGHT-TEST PROCEDURES

The off-surface flow visualization data reported herein were obtained during 1-g flight conditions. The nominal altitudes were between 20,000 and 30,000 ft and the

Mach numbers varied from approximately 0.2 to 0.4. Angles of attack ranged from  $10^\circ$  to approximately  $54^\circ$  over the course of this flight-test program, however, this report only presents results for  $\alpha = 15.8^\circ$  to  $47.7^\circ$ . Sideslip angles ranged from  $7.5^\circ$  to  $-4.8^\circ$  for the data in this report.

The on-surface flow visualization data were also obtained in 1-g stabilized flight. When the aircraft was at the desired angle of attack, the PGME dye was emitted through the flush orifices. The flight condition was held for approximately 75 sec to allow the PGME-dye mixture to set. One surface flow visualization test point was obtained for each flight with this method (ref. 10). Results are presented for  $\alpha \sim 30^\circ$  and  $47^\circ$ .

Surface pressure data presented were obtained in quasi-stabilized, 1-g flight maneuvers. Data were obtained at nominal altitudes of 20,000 and 45,000 ft. At the higher angles of attack, constant altitude could not be maintained during the 1-g maneuvers and data were obtained in a descent. Time segments of 0.4-sec duration were used for data analysis purposes. The data presented are for angles of attack from  $10^\circ$  to  $50^\circ$  with sideslip angle  $0^\circ$ .

A ground augmented guidance system similar to that described in reference 22 was implemented on the heads up display in the aircraft cockpit and used to assist the pilot to fly the desired flight conditions precisely.

## 7 RESULTS AND DISCUSSION

### 7.1 Description of F-18 Flow Field

The F-18's flow field is substantially dominated by vortices as seen in an example from a water-tunnel test shown in figure 6 at  $\alpha = 30^\circ$ . The vortex cores noted on the figure are generated by flow which separates at moderate to high angles of attack from the forebody surface and at the sharp leading edge of each LEX. The LEX vortex cores are tightly wound and extend downstream until experiencing vortex core breakdown. Visible evidence of vortex core breakdown is a stagnation of flow in the core with a sudden expansion in the core diameter. Similarly, the forebody vortex cores extend downstream where they can interact with the LEX vortices. Interaction results in the forebody vortex cores being pulled beneath the LEX vortices and then redirected outboard.

## 8 EFFECT OF ANGLE OF ATTACK ON LEX VORTICES

### 8.1 Off-Surface Flow Visualization

The occurrence of vortex core breakdown has been reported to be particularly sensitive to an adverse pressure gradient along the vortex (ref. 23). It follows then that as angle of attack increases, thus moving the onset of the adverse pressure gradient forward, the vortex core breakdown location will move nearer the LEX apex. Examples of this trend are shown in figures 7(a-f). These wingtip still photos show the path of the LEX vortex core and its breakdown as photographed from the right wingtip camera at  $\alpha = 15.8^\circ$ ,  $20^\circ$ ,  $24.2^\circ$ ,  $29.9^\circ$ ,  $35^\circ$ , and  $42.5^\circ$  with approximately  $0^\circ$ -sideslip.

At  $\alpha = 15.8^\circ$ , (fig. 7(a)), the LEX vortex is already well developed with the core maintaining inboard and close to the surface extending over the LEX and breaking down aft of the wing trailing edge (not seen in photo). As the angle of attack increases from  $20^\circ$  to  $35^\circ$ , (figs. 7(b-e)), the LEX vortex breakdown, which was defined previously as the location where a stagnation of flow in the core occurs accompanied by a sudden expansion in the core diameter, moves forward from just in front of the vertical stabilizers to near the aft end of the canopy. At  $\alpha = 42.5^\circ$ , (fig. 7(f)), the vortex core was not observed and it is believed that the breakdown has moved all the way to very near the LEX apex.

The LEX vortex core breakdown location showed fore and aft fluctuations at steady-state flight conditions. Average longitudinal LEX vortex core breakdown locations were determined from onboard video cameras and are plotted as a function of angle of attack in figure 8. For angles of attack between  $20^\circ$  and  $40^\circ$ , the LEX vortex core breakdown position moved forward nearly linear with increasing angle of attack. On average, a  $5^\circ$ -change in angle of attack changes the longitudinal location 10 percent of the fuselage length.

The vortex core breakdown location was observed to fluctuate fore and aft more at longitudinal locations aft of  $x/\ell = .43$ . Due to the fore and aft fluctuations of the vortex core breakdown, the flight results are approximate to within  $\pm .04 x/\ell$ .

In addition to the F-18 HARV flight results, figure 8 also includes results obtained with subscale models in

water tunnel (ref. 15) and several wind-tunnel studies (refs. 4, 15). Even though there is a wide variation in model scale and Reynolds number and different fluid mediums, the plot shows reasonable agreement between data from the different sources.

### 8.2 Surface Flow Visualization

Presented in figures 9 and 10 are photographs of surface flow visualization on the LEX of the HARV using the emitted fluid technique for  $\alpha \sim 30^\circ$  and  $47^\circ$ , respectively. The fluid emitted from the orifices marks the surface streamlines. Where the streamlines merge, lines of separation are defined and conversely, where the streamlines diverge, lines of reattachment are defined. Observed in both figures 9 and 10, the secondary vortex line of separation ( $S_2$ ) is defined by the inboard edge of the wide band of dye while the tertiary vortex line of separation ( $S_3$ ) is defined by the outboard edge of the band. A schematic of the flow is shown in cross section in the inset of figure 9.

Although shown by the surface flow visualization technique, the secondary and tertiary vortices as shown in the schematic were not observed using smoke flow visualization. This was probably because of their relative weakness and small size as compared to the primary vortex and the location of the smoke injection.

In comparing the surface flow visualization data at  $\alpha \sim 30^\circ$  and  $47^\circ$ , the separation lines are observed to be farther outboard for the  $\alpha \sim 47^\circ$  case, especially at F.S. 357. As noted in the previous section, at  $\alpha \sim 47^\circ$ , vortex core breakdown is very near the LEX apex. Even though vortex breakdown has already occurred, the secondary and tertiary lines of separation are still evident in the surface flow. While the flow appears highly unorganized, it is in fact structured, though extremely turbulent.

### 8.3 Measured Pressures

The effects of angle of attack on the LEX surface static pressure distribution are presented in figure 11 for angles of attack from  $10^\circ$  to  $50^\circ$  at the low speed ( $0.2 < M_\infty < 0.4$ ), 1-g flight conditions. Pressure coefficients are plotted from the LEX as a function of LEX span,  $y$  and  $s$  as defined previously in figure 4. As the aircraft angle of attack increases from  $10.0^\circ$  to  $25.8^\circ$ , (figs. 11(a)

and (b)), the LEX maximum suction pressure peaks increase in magnitude and move inboard. At F.S. 357,  $\alpha \sim 30^\circ$  and above (figs. 11(b) and (c)) the effect of the LEX vortex core breakdown on the pressure distribution can be seen. As shown in figure 8, at  $\alpha = 30^\circ$ , vortex core breakdown occurs very near F.S. 357 ( $x/\ell = 0.454$ ) and moves forward as angle of attack is increased further. This causes a decrease in the maximum suction pressure and a flattening of the pressure distributions when vortex core breakdown occurs at and moves forward of the measurement station. Similar trends are noted at F.S. 296 and F.S. 253 for  $\alpha = 39.3^\circ$  and  $45.4^\circ$ , respectively. At the highest angles of attack, (fig. 11(c)), the flow becomes less symmetrical, particularly at F.S. 253.

#### 8.4 Correlation of LEX Pressure Distributions with Flow Visualization

Surface flow features from the surface flow visualization results previously presented in figures 9 and 10 for  $\alpha \sim 30^\circ$  and  $47^\circ$  have been correlated in figure 12 with the pressure distributions obtained on the LEX at  $\alpha = 30.0^\circ$  and  $48.1^\circ$ . Surface flow visualization was obtained only on the left LEX, however, the separation line locations are shown on both sides for comparison with the pressure distributions because they were obtained at near zero sideslip. At  $\alpha \sim 30^\circ$ , (fig. 12(a)), the secondary separation lines,  $S_2$ , correspond well with the end of pressure recovery outboard of the maximum suction pressure peaks. The tertiary separation lines,  $S_3$ , seem to correspond with the end of pressure recovery inboard of the secondary suction peak near the LEX leading edge.

The lateral location of the primary vortex core on the F-18 HARV was determined with smoke visualization for  $\alpha \sim 30^\circ$  (refs. 15 and 16). The locations shown in figure 12(a) at F.S. 296 and 357 are just inboard of the maximum suction pressure peaks. This agrees well with the lateral position of vortex cores on a sharp delta wing suggested by Hummel and Redeker in reference 24 and verified by Seshadri and Büetefisch in reference 25, which showed the lateral position of the vortex core coincided closely with the maximum suction peak.

At  $\alpha = 48.1^\circ$ , (fig. 12(b)), the LEX primary vortex core breakdown occurred forward of F.S. 253 and all three stations experienced turbulent, buffeting vortical flow while the aircraft was in a mild wing rock. At F.S. 296 and 357 the pressure distributions were essentially flat

and did not have distinct suction pressure peaks. At F.S. 253, the pressure distribution was slightly asymmetrical and the end of pressure recovery did not correspond as well with the separation lines caused in part by the unsteadiness of the flow and the difficulty in locating the separation lines at this condition.

#### 8.5 Correlation of Flight and Wind-Tunnel Pressure Distributions on LEX

The LEX pressure distribution results from a 6-percent scale F-18 model (ref. 4) are correlated with flight data at  $\alpha \sim 30^\circ$  at  $M_\infty \sim 0.3$  and at  $\alpha = 50^\circ$  at  $M_\infty \sim 0.2$  in figure 13. Wind-tunnel data was available from only the upper surface of the LEX. At  $\alpha \sim 30^\circ$ , (fig. 13(a)), the wind tunnel tends to underpredict slightly the suction pressures at F.S. 253 and 296. The suction pressure peaks are predicted better at F.S. 357. Both the flight and wind-tunnel results indicate some asymmetry in the LEX pressure distributions at  $\alpha = 50^\circ$ , (fig. 13(b)).

### 9 EFFECT OF ANGLE OF ATTACK ON FOREBODY VORTICES

#### 9.1 Off-Surface Flow Visualization

Two photographs of smoke entrained in the right forebody vortex core, taken from the right wingtip camera, are shown in figures 14(a and b) for  $\alpha = 29.5^\circ$  and  $47.7^\circ$ , and  $\beta \sim 0^\circ$ . At both angles of attack, the right forebody vortex core is well defined. At  $29.5^\circ$ , (fig. 14(a)), the forebody vortex stays very close to the aircraft surface as it moves over the top of the canopy and aft over the fuselage. In contrast, the forebody vortex core at  $\alpha = 47.7^\circ$ , (fig. 14(b)), lies farther away from the surface of the aircraft from its point of origin and continues to a location aft of the canopy where it appears to be drawn down into the region directly above the LEX. Additionally, the forebody vortex core at  $47.7^\circ$  appears to have a larger diameter.

The forebody vortices do not appear to be as strong as the LEX vortices because of the lack of persistence and uniformity in the core definition. In fact, over the course of the 100-flight series, natural flow visualization of the forebody vortices caused by condensation was observed by the pilot only once whereas the LEX vortices were observed frequently.

## 9.2 Surface Flow Visualization

Surface flow visualization on the forebody of the HARV using the emitted fluid technique is presented in the photos of figures 15 and 16 for  $\alpha \sim 30^\circ$  and  $47^\circ$ , respectively. Noted in the figures are the primary vortex separation lines ( $S_1$ ), secondary separation lines ( $S_2$ ), the lines of reattachment (R), and the laminar separation bubbles (LSBs). A cross section view of the flow about the forebody is shown in the inset (fig. 15). Again, the separation and reattachment lines are defined as they were for the LEX. An LSB was observed on the forebody, appearing as a kink in the surface flow streamlines. This is confirmed by noting that this only occurred near the nose apex and that at  $\alpha \sim 47^\circ$ , (fig. 16(b)), the turbulent boundary layer from the screwheads shown on the forebody do not create a kink in the surface streamlines.

A comparison of the forebody surface flow visualization at  $\alpha \sim 30^\circ$  with that obtained at  $47^\circ$  shows that the separation lines at  $\alpha \sim 47^\circ$  have moved much nearer the nose apex. This indicates a stronger, more fully developed vortex system at  $\alpha \sim 47^\circ$ . In both cases, the separation lines appear to be nearly symmetrical for  $\beta \sim 0^\circ$ .

## 9.3 Measured Pressures

The effects of angle of attack on the forebody pressure distribution are presented in figure 17 for angles of attack from  $10^\circ$  to  $50^\circ$  at low speed, 1-g flight conditions. Pressure coefficients are presented as a function of circumferential angle,  $\theta$ , and for each of the five forebody stations. Note the change in scale from the LEX results. The maximum suction pressures are much greater in magnitude for the LEX (fig. 11) than for the forebody at the same angle of attack (fig. 17).

At F.S. 70, F.S. 85 and F.S. 107, and starting at  $\alpha = 19.7^\circ$ , (fig. 17(a)), the flow accelerating around the forebody induces a pair of maximum suction pressure peaks on the sides of the fuselage at  $\theta \sim 100^\circ$  to  $120^\circ$  and  $240^\circ$  to  $260^\circ$ . As the angle of attack was increased, these maximum suction peaks became much more pronounced, (figs. 17(b) and (c)). At F.S. 85 and 107, the forebody primary vortex pair footprints (ref. 4), indicated by suction pressure peaks at  $\theta = 168^\circ$  and  $192^\circ$ , first become evident at  $\alpha = 34.3^\circ$  (fig. 17(b)). As the angle of attack is

increased, these footprints become more negative and indicate the presence of the primary vortex cores above the surface (ref. 26). It should be noted that at these fuselage stations the pressure distributions in all cases are symmetrical about  $\theta = 180^\circ$  for  $\beta \sim 0$  for angles of attack up to  $50^\circ$ .

At F.S. 142, sharp peaks at  $\theta = 90^\circ$  and  $270^\circ$  in the pressure coefficient curve starting at  $\alpha = 19.7^\circ$  (fig. 17(a)), are the result of local separation behind the two small, elliptical shaped ECM antenna covers described previously under Experiment Description. As the angle of attack is increased to  $50^\circ$  (fig. 17(c)), these peaks move up around the fuselage to  $\theta = 108^\circ$  and  $252^\circ$ .

At F.S. 142, the forebody cross section has become elliptical in shape. The magnitude of the maximum suction pressure peaks at this location have become somewhat diminished above  $\alpha \sim 25^\circ$  or  $30^\circ$ , (figs. 17(b) and (c)), compared to the three forward stations. Distinct footprints of the primary vortex are present near  $\theta \sim 160^\circ$  and  $200^\circ$  beginning around  $\alpha = 25^\circ$  (fig. 17(b)). These footprint peaks are less distinct at  $\theta \sim 160^\circ$  than at  $\theta \sim 200^\circ$  because this area of the aircraft contains the doors for the in-flight refueling probe and is not as smooth and flush as the left side where there are no doors, joints, or other discontinuities. These footprints have a maximum magnitude at  $\alpha = 45^\circ$  diminishing significantly at  $\alpha = 50^\circ$ , probably indicating that the vortices have begun to lift from the surface. Again, the pressure distributions are generally symmetrical about  $\theta = 180^\circ$  with the differences accounted for by local protuberances or discontinuities.

At F.S. 184, the maximum suction pressure peaks have moved up to  $\theta \sim 120^\circ$  and  $240^\circ$ , (figs. 17(b) and (c)), caused by the local influence of the LEX. At this station, the apex of the LEXs is only 13 in. aft, (fig. 4), and is located at  $\theta \sim 123^\circ$  and  $237^\circ$ . As can be seen in figure 4, the surface flow visualization shows the streamlines pulled up and over the LEX for  $\alpha \sim 26^\circ$ . The maximum suction peaks for  $\alpha > 25^\circ$  are further reduced in magnitude compared to F.S. 142 because the primary vortices are lifted farther from the surface. The primary vortex footprints at  $\theta \sim 165^\circ$  and  $195^\circ$  can still be observed at  $\alpha > 25^\circ$ , (figs. 17(b) and (c)), but are more diminished in magnitude compared to those at F.S. 142. For  $\alpha = 34.3^\circ$  and greater, the peaks in the pressure coefficient curves at  $\theta \sim 48^\circ$  to  $60^\circ$  and  $300^\circ$  to  $312^\circ$  are due to local separation caused by the aircraft production

pitot-static probes mentioned previously. Again, at this location, the pressure distributions are nearly symmetrical about  $\theta = 180^\circ$  with only small differences in the primary vortex footprint due to discontinuities caused by the refueling probe doors.

The general trend in the data from the forebody is for the maximum suction pressure peaks to first appear at  $\alpha \sim 20^\circ$  and increase in magnitude as angle of attack is increased. In addition, the footprints of the primary vortex first appear at  $\alpha \sim 25^\circ$  at F.S. 142 and F.S. 184 and progress forward toward the nose apex as the angle of attack is increased.

#### 9.4 Correlation of Forebody Pressure and Flow Visualization Results

Surface flow visualization results for  $\alpha \sim 30^\circ$  and  $47^\circ$  (figs. 15 and 16) are correlated with forebody flight pressure distributions at  $\alpha = 30.0^\circ$  and  $48.1^\circ$  in figure 18. The surface flow visualization and the forebody pressure measurements were obtained on separate flights. Some differences in the results can therefore be expected because of slightly different test conditions and test techniques.

In figure 18(a) at F.S. 70 and for  $\alpha \sim 30^\circ$ , and in figure 18(b) at F.S. 70, F.S. 85, and F.S. 107 and for  $\alpha \sim 47^\circ$ , LSBs were identified in the surface flow visualization (ref. 13). Laminar separation bubbles are more closely identified with the critical Reynolds number range ( $2 \times 10^5 < Re_d < 4 \times 10^5$ ) than the supercritical range ( $4 \times 10^5 < Re_d < 6 \times 10^6$ ) (ref. 24). The  $Re_d$  values for the flight data are given in the figures. At F.S. 107, (fig. 18(b)), the LSB located by the surface flow visualization at  $\theta = 113^\circ$  and  $247^\circ$  correlates well with the kinks in the pressure distribution at  $\theta = 108^\circ$  to  $114^\circ$  and  $246^\circ$  to  $252^\circ$ . This is consistent with the discussion in reference 27 where the kink or flattening in the pressure distribution was correlated with an LSB for a tangent-ogive cylinder. Laminar separation kinks in the pressure distribution are also noted for the data at  $\alpha = 30^\circ$  at F.S. 107, (fig. 18(a)), though laminar separation was only noted in the surface flow visualization near F.S. 70. Unfortunately, the orifices were not dense enough to define the kinks in the pressure distribution caused by the LSB at F.S. 70 and F.S. 85. The kinks on the windward side of the maximum suction pressure peaks at F.S. 107 for  $\theta = 84^\circ$  to  $90^\circ$  and  $270^\circ$  to  $276^\circ$  are not explained at this time. No

deviation in the surface streamlines was detected in the flow visualization at these circumferential locations.

The peaks in the pressure distributions for F.S. 142 at  $\theta \sim 95^\circ$  and  $265^\circ$ , (fig. 18(a)), are caused by the ECM antenna covers as noted earlier.

The primary separation lines,  $S_1$ , as identified by the surface flow visualization in figures 15 and 16, correlated well with the end of pressure recovery on the lee side of the forebody. This can be seen most clearly in figure 18(b) at F.S. 85 to 184 and in figure 18(a) at F.S. 142 and 184. This correlation also agrees well with the data of references 26 and 27 for a cone and an ogive. Also shown in figure 18, the secondary vortex separation line,  $S_2$ , occurs slightly outboard of the footprints of the primary vortex pairs at F.S. 142 and F.S. 184 in figure 18(a) and at F.S. 107 to 184 in figure 18(b).

#### 9.5 Correlation of Flight and Wind-Tunnel Pressure Distributions on Forebody

Forebody pressure distribution results from a 6-percent scale F-18 model (ref. 4) are correlated with flight data at  $\alpha \sim 30^\circ$  at  $M_\infty \sim 0.3$  and at  $\alpha = 50^\circ$  at  $M_\infty \sim 0.2$  in figure 19. Wind-tunnel data were available at only three forebody fuselage stations, F.S. 107, 142, and 184.

In figure 19(a), flight and wind-tunnel data are presented for  $\alpha = 30.0^\circ$  and  $M_\infty \sim 0.3$ . At these conditions, the comparisons are good with the exception at F.S. 142 where the wind-tunnel data does not indicate the footprints of the primary vortex pair at  $\theta \sim 160^\circ$  and  $200^\circ$ . The wind-tunnel model did not simulate the protuberances caused by the ECM antenna covers, the production probes, and the refueling doors and hence, these effects are not present. At F.S. 107, there appears to be a kink in the wind-tunnel pressure distribution caused by an LSB at  $\theta \sim 120^\circ$  to  $132^\circ$ , which is slightly more leeward than the flight values. The model and flight Reynolds numbers,  $Re_d$ , for all three stations are all in the supercritical range though the flight values are almost an order of magnitude greater.

Results from flight and wind-tunnel data at  $\alpha = 50.0^\circ$  and  $M_\infty \sim 0.2$  are presented in figure 19(b). At these conditions, the comparison of the results is mixed. The model Reynolds numbers,  $Re_d$ , in this case are critical whereas the flight values are supercritical. The footprints

of the primary vortex are evident for both the flight and wind-tunnel data. At F.S. 107, the wind-tunnel maximum suction pressure coefficients are approximately 0.2 lower in magnitude than the flight values, however the location of the LSBs and the pressure distributions at the primary vortex footprints agree well. At F.S. 142 the data at the maximum suction pressure peaks compare well but the comparison is not as good at the primary vortex footprints. At F.S. 184, there appears to be an asymmetry in the wind-tunnel pressure distribution that does not appear in the flight data.

## 10 FOREBODY-LEX VORTEX ASYMMETRIES AND INTERACTIONS

The effects of angle of attack on the LEX and forebody flows have been shown in the previous sections using both off-surface and surface flow visualization techniques as well as surface pressure measurements. In this section, the effect of sideslip and the forebody-LEX vortex interactions will be discussed using only the off-surface flow visualization technique.

### 10.1 Effect of Sideslip on LEX Vortices

The effect of angle of sideslip on the vortex core breakdown position is illustrated in figures 20(a-c) as photographed from the right wingtip camera during a wings level sideslip maneuver at  $\alpha \sim 25^\circ$ . The right LEX vortex core breakdown position can be seen moving aft as sideslip angle is decreased from  $4.5^\circ$  (right LEX vortex on windward side) to  $-3.4^\circ$  (right LEX vortex on leeward side) where positive angle of sideslip is flow from the right or nose left as viewed by the pilot.

The following trends were observed from studying the onboard video data as well as from the wingtip still photos. With sideslip, the windward vortex core moves inboard and down closer to the surface with breakdown occurring much farther forward than at  $0^\circ$  sideslip. Conversely, the leeward vortex core was observed to move outboard and away from the surface with the vortex core breaking down farther aft than at  $0^\circ$  sideslip.

The breakdown location was determined using onboard video data, and plotted in figure 21 for  $\alpha \sim 20^\circ$ ,  $25^\circ$ , and  $30^\circ$ . In this figure, the lateral location of the vortex core breakdown was plotted against longitudinal

location of the vortex core breakdown for positive, negative, and  $0^\circ$ -sideslip conditions.

Figure 21 shows that at  $\alpha \sim 20^\circ$ , for the small sideslip angles of this study, the vortex breakdown moves more along the longitudinal direction than in the lateral direction, however, this effect is reduced as angle of attack increases.

## 10.2 Forebody-LEX Vortex Interactions

### 10.2.1 Angle of Attack Effects

Shown in figures 22(a-c) is a series of photos of the right forebody vortex taken with the right wingtip camera for  $\alpha = 29.5^\circ$  to  $42.5^\circ$  at  $\sim 0^\circ$ -sideslip. In the photos it can be observed that an interaction between the forebody and LEX vortex cores exists (inset sketches which have been reconstructed from other flight data are shown for clarity). At  $\alpha = 29.5^\circ$  (fig. 22(a)), the forebody vortex core is pulled down beneath the LEX vortex just aft of the LEX/wing leading-edge flap hinge junction. As the angle of attack increases, (figs. 22(b-c)), the location of this interaction moves forward. The longitudinal location of this interaction is plotted in figure 23 as a function of angle of attack. Accuracy of the data is  $\pm 0.04$ .

Also plotted in figure 23 is the location of the LEX vortex core breakdown taken from figure 8. It should be noted that the forebody-LEX vortex interaction, for the presented  $\alpha$  in  $0^\circ$ -sideslip cases, occurs aft of the LEX vortex core breakdown position. Since the diameter of the LEX vortex structure increases significantly after breakdown as seen previously from wingtip photographs, it is not surprising that the forebody vortex core might be pulled under the LEX vortex core because of the downward action of the LEX vortex which is now closer to it because of its suddenly increased diameter.

The forebody-LEX interaction locations gathered from a water-tunnel test on a 3-percent scale F-18 model (ref. 15) are also plotted on figure 23. Good correlation between the flight and the model data is found in spite of a large difference in Reynolds number and fluid medium.

### 10.2.2 Sideslip Effects

Sideslip has a significant effect on the forebody vortices. Forward of the canopy, the two forebody vortices



are nearly symmetrical at  $\beta \sim 0^\circ$ , for the angles of attack presented. With sideslip, these vortices are rotated about the forebody to an asymmetrical location similar to the schematic of figure 24. The rotation of the forebody vortices due to sideslip was also illustrated in a report by Erickson (ref. 12) where F/A-18 water-tunnel flow visualization photos showed the leeward primary separation line rotated down and that of the windward side rotated up.

At the higher angles of attack, the effect of sideslip causes the windward forebody vortex to travel up and over the top of the canopy. In some cases, this windward forebody vortex core has been observed to cross the aircraft centerline and interact with the leeward LEX vortex near the vertical tails. At the same time, the leeward forebody vortex moves along the side of the canopy to interact and merge with the leeward LEX vortex near the canopy. The location of this forebody-LEX interaction as determined from onboard video and still photos is shown in figure 25 as a function of sideslip for an  $\alpha \sim 33^\circ$ .

From figure 25 it can be seen that as the aircraft experiences greater sideslip angles, the interaction of the leeward forebody vortex core with the LEX vortex core occurs farther forward, and the windward forebody vortex core does so farther aft. This appears to be caused by the location of the forebody vortices as affected by angle of sideslip. With sideslip, the windward forebody vortex is moved up and over toward the top of the canopy and away from the corresponding LEX vortex. Conversely, at the same time, the leeward forebody vortex is moved down along the side of the canopy and closer to the corresponding LEX vortex.

Upon comparing the effect of sideslip on the longitudinal movement of the forebody-LEX vortex core interaction and the longitudinal movement of the LEX vortex cores, it was noted that the trends opposed each other. As sideslip increased, the breakdown location of the windward LEX vortex core moved forward while the location of the windward forebody-LEX vortex interaction moved aft. The inverse was true on the leeward side.

## 11 CONCLUDING REMARKS

A low-speed correlation of in-flight flow visualization, surface pressure measurements, water-tunnel, and

wind-tunnel results for the vortical flows on the forebody and leading-edge extensions of an F-18 aircraft have been reported for angles of attack up to  $50^\circ$ . Both off-surface flow visualization using smoke injection and surface flow visualization using the emitted liquid dye technique were used to obtain photographic data from flight. In-flight surface pressure measurements were made at five forebody stations and at three LEX stations on the aircraft and were correlated with similar data from a 6-percent scale wind-tunnel model.

The off-surface flow visualization showed a strong vortical field above the LEX and that the LEX vortex core breakdown location moved forward with increasing angle of attack. The LEX vortex core breakdown from wind-tunnel and water-tunnel tests correlated reasonably well with the flight results. In general, as angle of attack increased, the LEX pressure distributions experienced an increase in the magnitude of the maximum suction pressure peaks as the vortex core breakdown approached them and then a decrease and the general flattening of the pressure distribution as the vortex core breakdown progressed forward of them. The LEX secondary separation, as determined from surface flow visualization, corresponded well with the end of pressure recovery outboard of the maximum suction pressure peaks. The wind-tunnel data tended to underpredict the suction pressures at some locations at  $\alpha = 30^\circ$ . Both flight and wind-tunnel results showed asymmetries at  $\alpha = 50^\circ$ .

Vortical flow was also observed on the forebody using flow visualization starting at  $\alpha \sim 25^\circ$ . The general trend for the forebody pressure distributions was for the maximum suction pressure peaks to first appear at  $\alpha \sim 19^\circ$  and increase in magnitude as the angle of attack was increased. Footprints of the primary vortex pairs first appeared at  $\alpha \sim 25^\circ$  on the aft portion of the forebody and progressed forward as the angle of attack increased. The forebody primary separation lines, as identified by surface flow visualization, correlated well with the end of pressure recovery leeward of the maximum suction peak. Both the surface pressure  $C_p$  levels and the off-surface flow visualization indicated that the forebody vortex system is weaker than the LEX vortex system. At  $\alpha = 30^\circ$ , the comparison of the flight and wind-tunnel pressure distributions were in general, good, but the wind-tunnel data did not show the presence of the vortex footprints and also exhibited some asymmetry not present in the flight data.



Interactions were observed between the forebody and LEX vortical flow fields. These interactions were both a function of angle of attack and sideslip. The effect of angle of sideslip was to cause asymmetrical forebody-LEX interactions as well as asymmetrical LEX vortex core breakdown.

## 12 REFERENCES

1. Skow, A.M., G.E. Erickson, "Modern Fighter Aircraft Design for High-Angle-of-Attack Maneuvering," AGARD LS-121, Paper No. 4, 1982.
2. Erickson, Gary E., *Water Tunnel Flow Visualization and Wind Tunnel Data Analysis of the F/A-18*, NASA CR-165859, 1982.
3. Banks, Daniel W., "Wind-Tunnel Investigation of the Forebody Aerodynamics of a Vortex-Lift Fighter Configuration at High Angles of Attack," SAE Paper 881419, Oct. 1988.
4. Erickson, G.E., R.M. Hall, D.W. Banks, J.H. Del Frate, J.A. Schreiner, R.J. Hanley, and C.T. Pulley, "Experimental Investigation of the F/A-18 Vortex Flows at Subsonic Through Transonic Speeds, Invited Paper," AIAA 89-2222, 1989.
5. Thomas, James L., Robert W. Walters, Taekyu Reu, Farhad Ghaffari, Robert P. Weston, and James M. Luckring, "A Patched-Grid Algorithm for Complex Configurations Directed Toward the F/A-18 Aircraft," AIAA 89-0121, Jan. 1989.
6. Ghaffari, F., J.M. Luckring, J.L. Thomas, and B.L. Bates, "Navier-Stokes Solutions about the F/A-18 Forebody-LEX Configuration," AIAA 89-0338, Jan. 1989.
7. Schiff, Lewis B., Russell M. Cummings, Reese L. Sorenson, and Yehia M. Rizk, "Numerical Simulation of High-Incidence Flow over the F-18 Fuselage Forebody," AIAA 89-0339, Jan. 1989.
8. Schiff, Lewis B., Russell M. Cummings, Reese L. Sorenson, and Yehia M. Rizk, *Numerical Simulation of F-18 Fuselage Forebody Flow at High Angles of Attack*, NASA CP-10038, vol. 1, 1989, pp. 345-359.
9. Cummings, Russell M., Yehia M. Rizk, Lewis B. Schiff, and Neal M. Chaderjian, "Navier-Stokes Predictions of the Flowfield Around the F-18 (HARV) Wing and Fuselage at Large Incidence," AIAA 90-0099, Jan. 1990.
10. Fisher, David F., David M. Richwine, and Daniel W. Banks, *Surface Flow Visualization of Separated Flows on the Forebody of an F-18 Aircraft and Wind-Tunnel Model*, NASA TM-100436, 1988. Also AIAA 88-2112.
11. Curry, Robert E., and David M. Richwine, "An Airborne System for Vortex Flow Visualization on the F-18 High-Alpha Research Vehicle," AIAA 88-4671, Sept. 1988.
12. Fisher, David F., and Robert R. Meyer, Jr., *Flow Visualization Techniques for Flight Research*, NASA TM-100455, 1988. Also in "Flight Test Techniques," AGARD CP 452, paper no. 20.
13. Fisher, David F., John H. Del Frate, and David M. Richwine, "In-Flight Flow Visualization Characteristics of the NASA F-18 High Alpha Research Vehicle at High Angles of Attack," SAE Paper 892222, Sept. 1989.
14. Schneider, Edward T., and Robert R. Meyer, Jr., "F-18 High Alpha Research Vehicle: Description, Results and Plans," SETP 33rd Symposium Proceedings, Sept. 1989.
15. Del Frate, John H. and Fanny A. Zuniga, "In-Flight Flow Field Analysis on the NASA F-18 High Alpha Research Vehicle With Comparisons to Ground Facility Data," AIAA 90-0231, Jan. 1990.
16. Fisher, David F., Daniel W. Banks, and David M. Richwine, "F-18 High Alpha Research Vehicle Surface Pressures: Initial In-Flight Results and Correlation with Flow Visualization and Wind-Tunnel Data," AIAA 90-3018, Aug. 1990.
17. Whitmore, Stephen A., Timothy R. Moes, and Terry J. Larson, *Preliminary Results From a Subsonic High Angle-of-Attack Flush Airdata Sensing (HI-FADS) System: Design, Calibration, and Flight Test Evaluation*, NASA TM-101713, 1990.
18. Polhamus, Edward C., *A Review of Some Reynolds Number Effects Related to Bodies at High Angles of Attack*, NASA CR-3809, 1984.

19. Fennell, L.J., "Vortex Breakdown—Some Observations in Flight on the HP115 Aircraft," Reports and Memoranda No. 3805, Sept. 1971. (Replaces R.A.E. Technical Report 71177 - A.R.C. 34 400).
20. Bisgood, P.L., "The Application of a Surface Flow-Visualisation Technique in Flight," Reports and Memoranda No. 3769, Feb. 1974. (Replaces R.A.E. Technical Report 74022 - A.R.C. 35 554).
21. Richardson, Norman R., and Albin O. Pearson, *Wind-Tunnel Calibrations of a Combined Pitot-Static Tube, Vane-Type Flow-Direction Transmitter, and Stagnation-Temperature Element at Mach Numbers From 0.60 to 2.87*, NASA TN D-122, 1959.
22. Meyer, Robert R., Jr., and Cdr. Edward T. Schneider, *Real-Time Pilot Guidance System for Improved Flight Test Maneuvers*, AIAA 83-2747, Nov. 1983. See also NASA TM-84922, 1984.
23. Payne, Francis M., "The Structure of Leading Edge Vortex Flows Including Vortex Breakdown," A Dissertation from the Aerodynamics Laboratory, Department of Aerospace and Mechanical Engineering, University of Notre Dame, IN, May 1987.
24. Hummel, D. and G. Redeker, *Experimental Determination of Bound Vortex Lines and Flow in the Vicinity of the Trailing Edge of a Slender Delta Wing*, NASA Technical Translation, NASA TT F-15,012, 1973.
25. Seshadri, S.N. and Karl-Aloys Büetefisch, "Evaluation of LDA 3-Component Velocity Data on a 65° Delta Wing at  $M = 0.85$  and First Results of an Analysis," DFVLR-FB 89-19, 1989.
26. Peake, D.J., D.F. Fisher, and D.S. McRae, "Flight, Wind Tunnel, and Numerical Experiments with a Slender Cone at Incidence," AIAA Journal, Vol 20, No. 10, p. 1338, Oct. 1982.
27. Hall, Robert M., "Influence of Reynolds Number on Forebody Side Forces for 3.5-Diameter Tangent-Ogive Bodies," AIAA 87-2274, Aug. 1987.

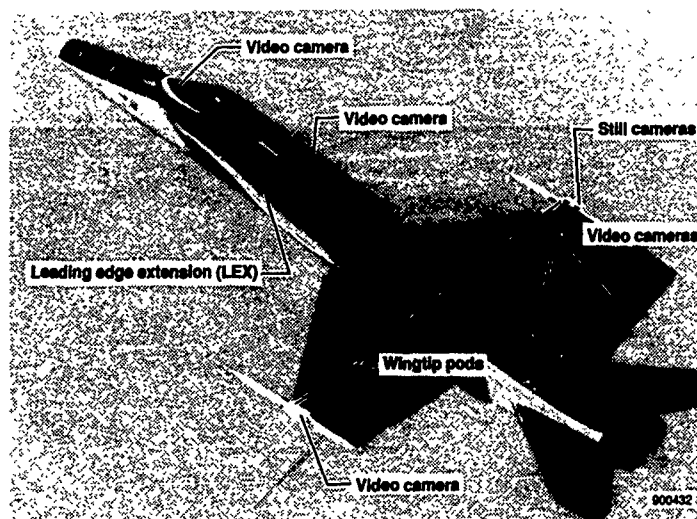


Figure 1. The F-18 HARV.

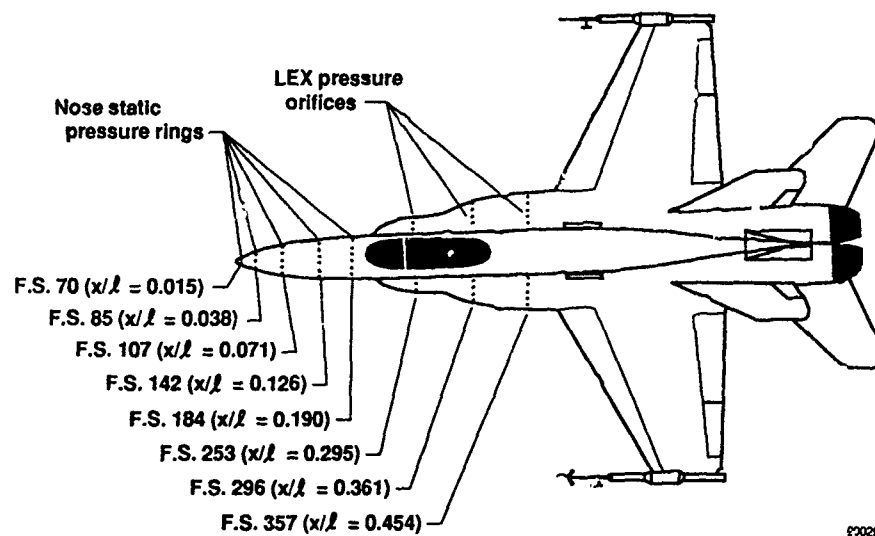


Figure 2. Forebody and LEX pressure measurement stations.

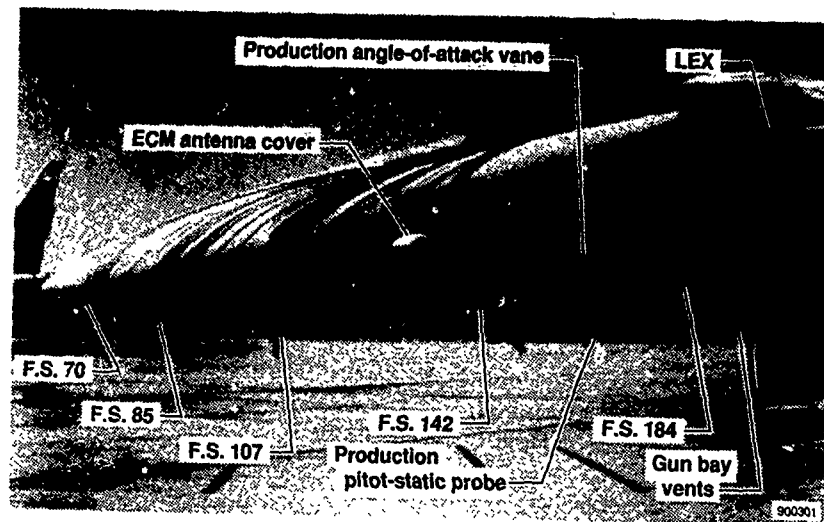
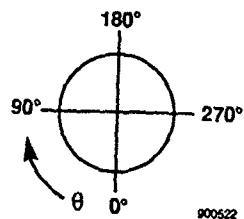
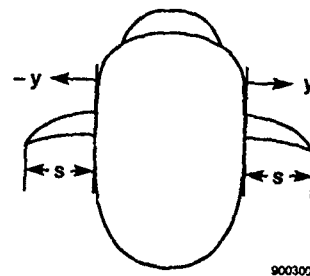


Figure 3. Locations of protrusions near forebody pressure measurement stations. Surface flow streamlines marked using emitted fluid techniques (shown for  $\alpha = 26^\circ$ ).

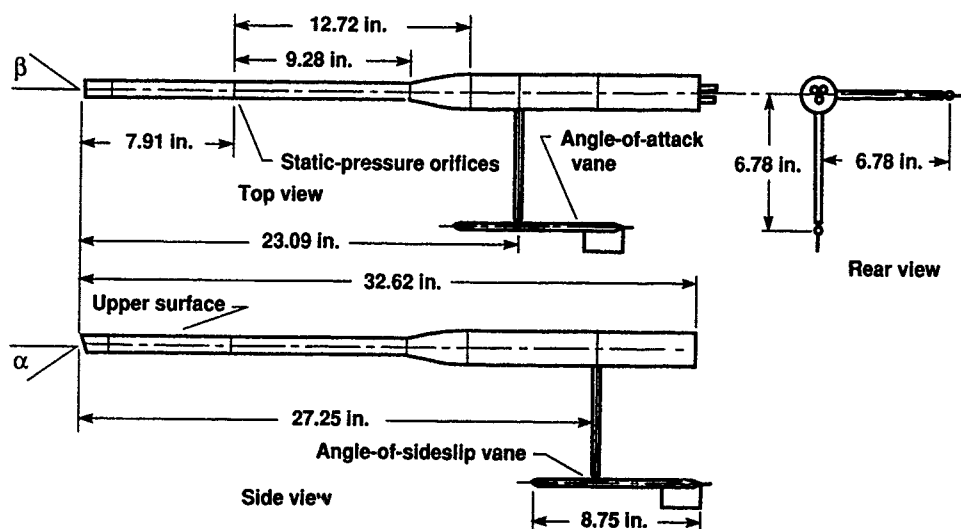


(a) Forebody circumferential angle.



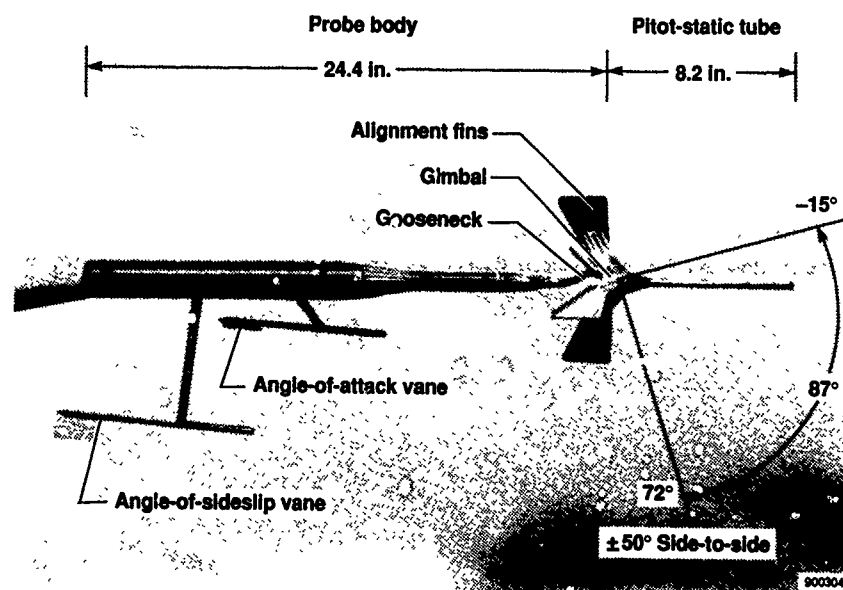
(b) LEX spanwise position.

Figure 4. Typical cross sections of pressure measurement stations and orifice orientation, looking aft.



(a) NACA airdata probe, right wingtip, (ref. 21).

900443



(b) Swiveling-head airdata probe, left wingtip.

Figure 5. Airdata probes mounted on F-18 HARV wingtips.

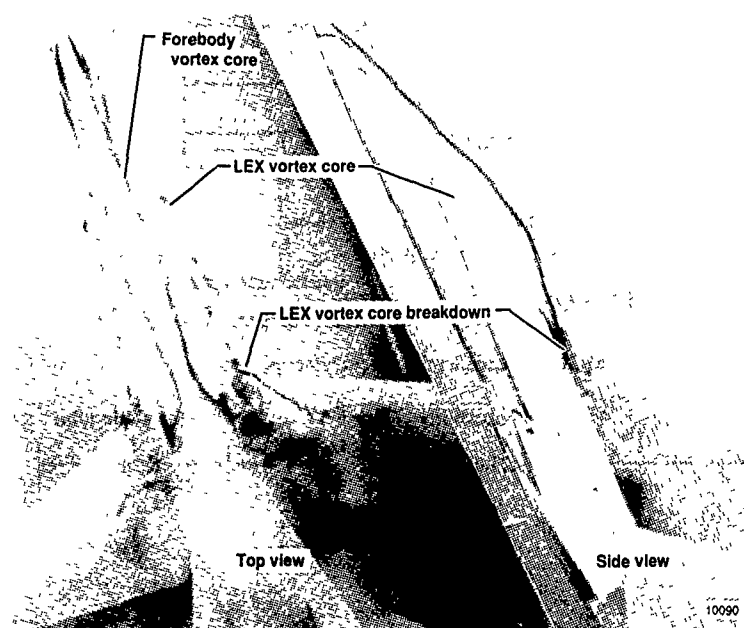
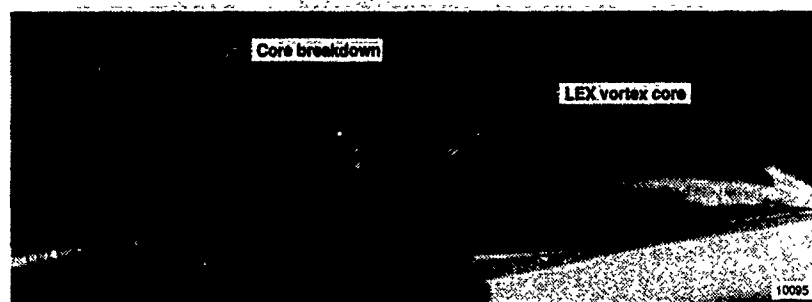


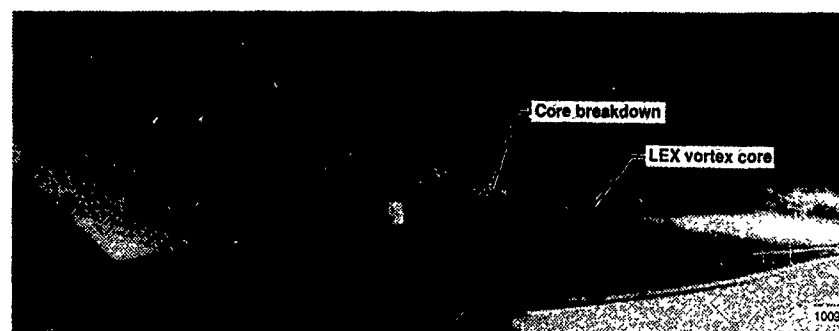
Figure 6. Vortex flow on a 3-percent model of the F-18 airplane in a water tunnel,  $\alpha = 30^\circ$ ,  $\beta = 0^\circ$ , (ref. 15).



(a)  $\alpha = 15.8^\circ$  and  $\beta = 0.2^\circ$ .

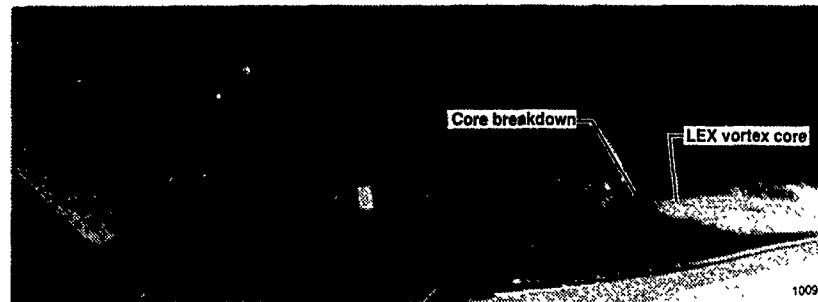


(b)  $\alpha = 20^\circ$  and  $\beta = 0^\circ$ .



(c)  $\alpha = 24.2^\circ$  and  $\beta = -0.8^\circ$ .

Figure 7. Right wingtip view showing effects of increased angle of attack on LEX vortex core and breakdown point



(d)  $\alpha = 29.9^\circ$  and  $\beta = 0.3^\circ$ .



(e)  $\alpha = 35^\circ$  and  $\beta = 1.8^\circ$ .

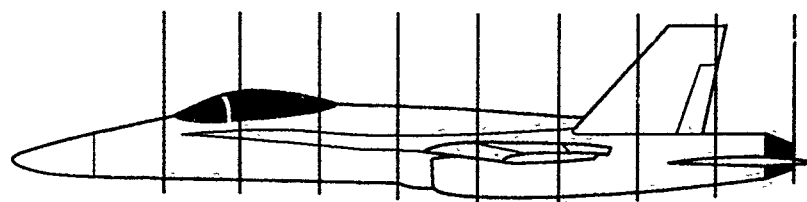
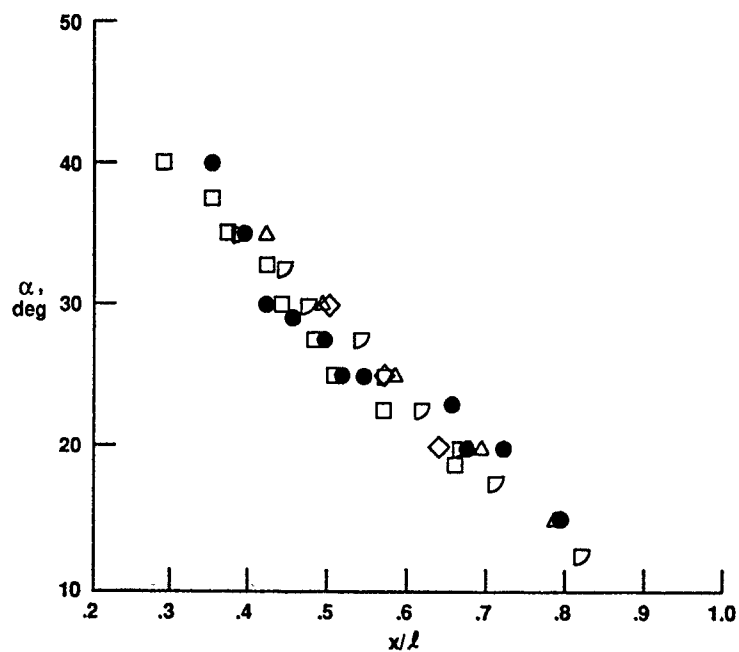


(f)  $\alpha = 42.5^\circ$  and  $\beta = 0.9^\circ$ .

Figure 7. Concluded.



	$Re_{\bar{c}}$	Model scale, percent	Fluid medium	Ref.
● Flight	8 to $13 \times 10^6$	—	Air	15
□ DTRC	$1.75 \times 10^6$	6	Air	4,15
◇ BART	$1.60 \times 10^5$	3	Air	15
△ LSWT	$3.60 \times 10^5$	12	Air	15
▽ FVF	$1.26 \times 10^4$	3	Water	15



900434

Figure 8. Comparison of F-18 LEX vortex core breakdown between flight and ground facilities.

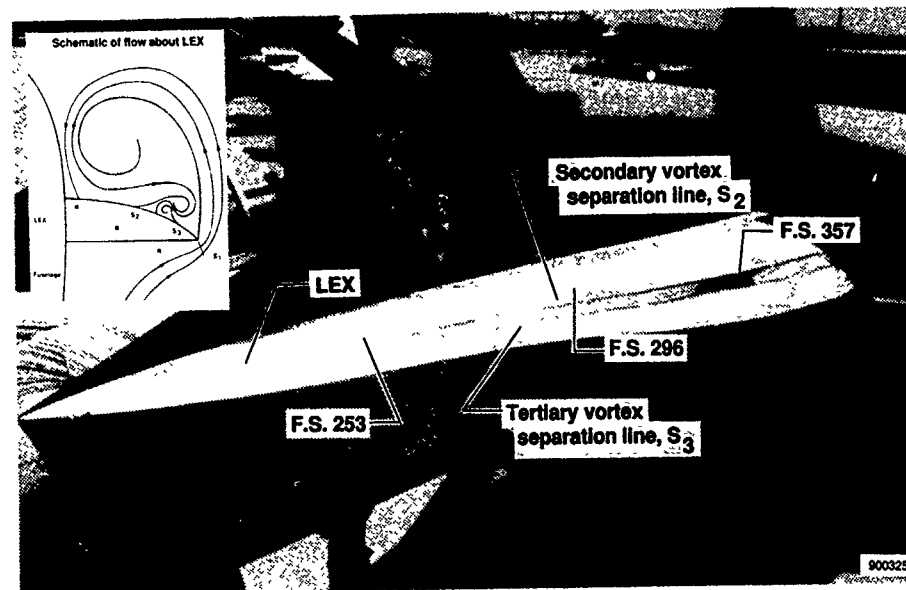


Figure 9. Surface flow visualization on left LEX of F-18 HARV for  $\alpha \sim 30^\circ$ .

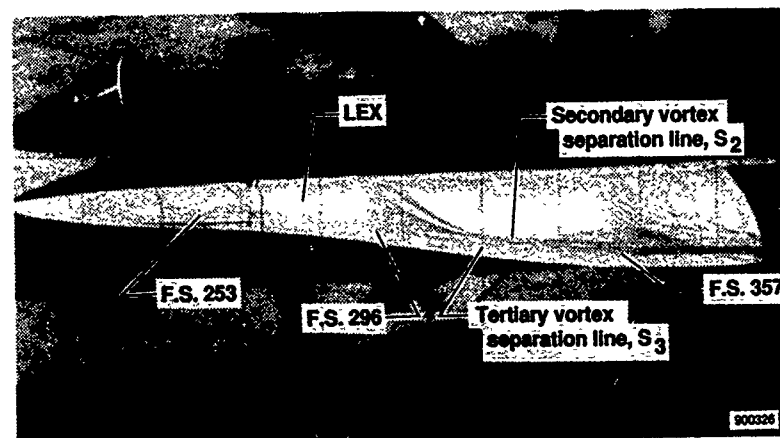
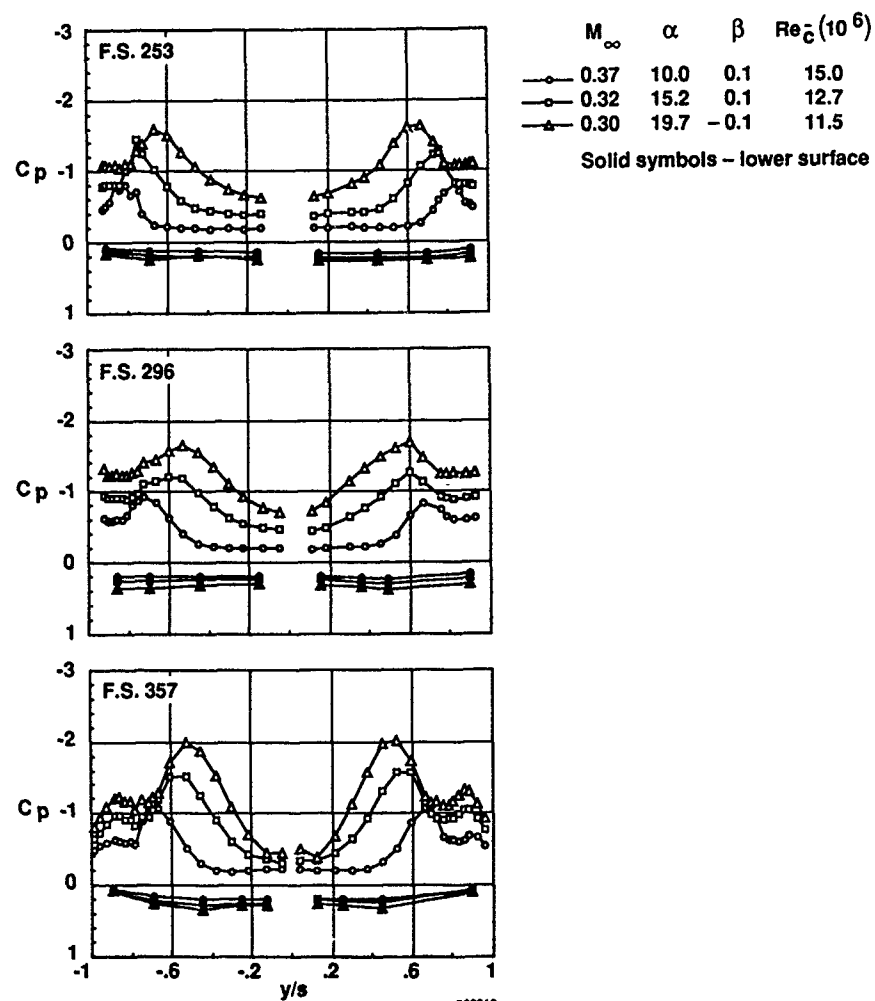
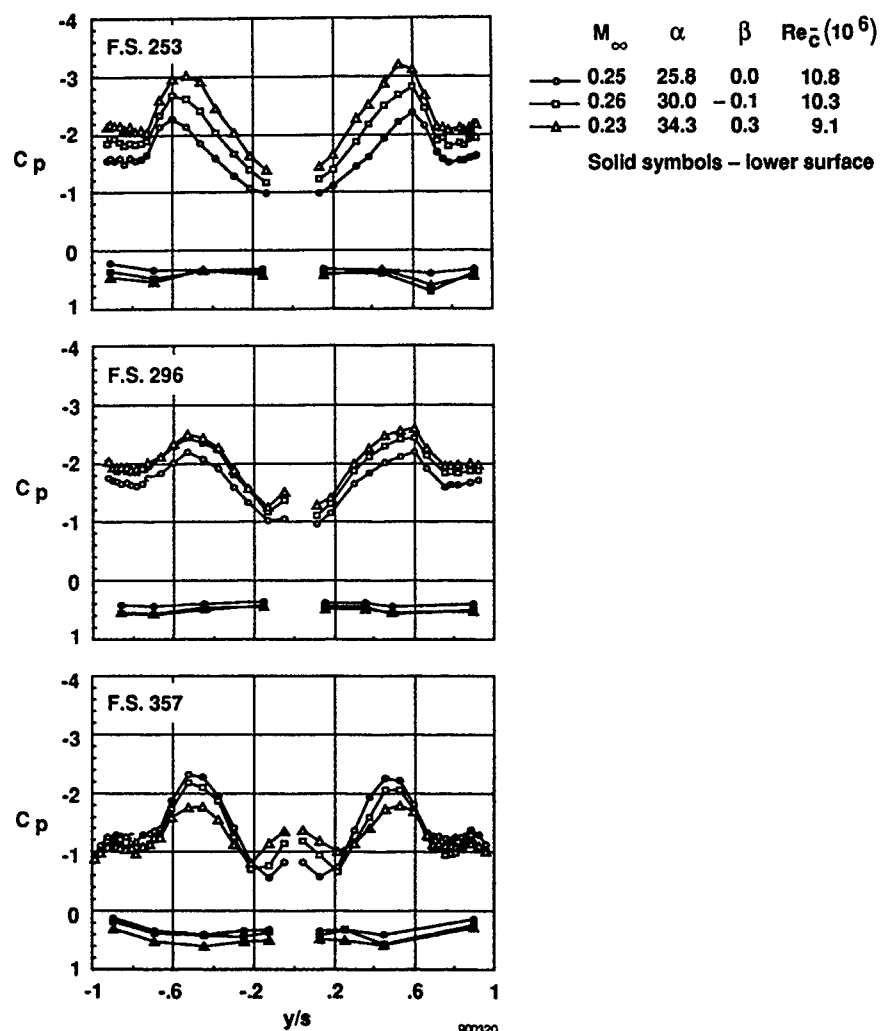


Figure 10. Surface flow visualization on left LEX of F-18 HARV for  $\alpha \sim 47^\circ$ .



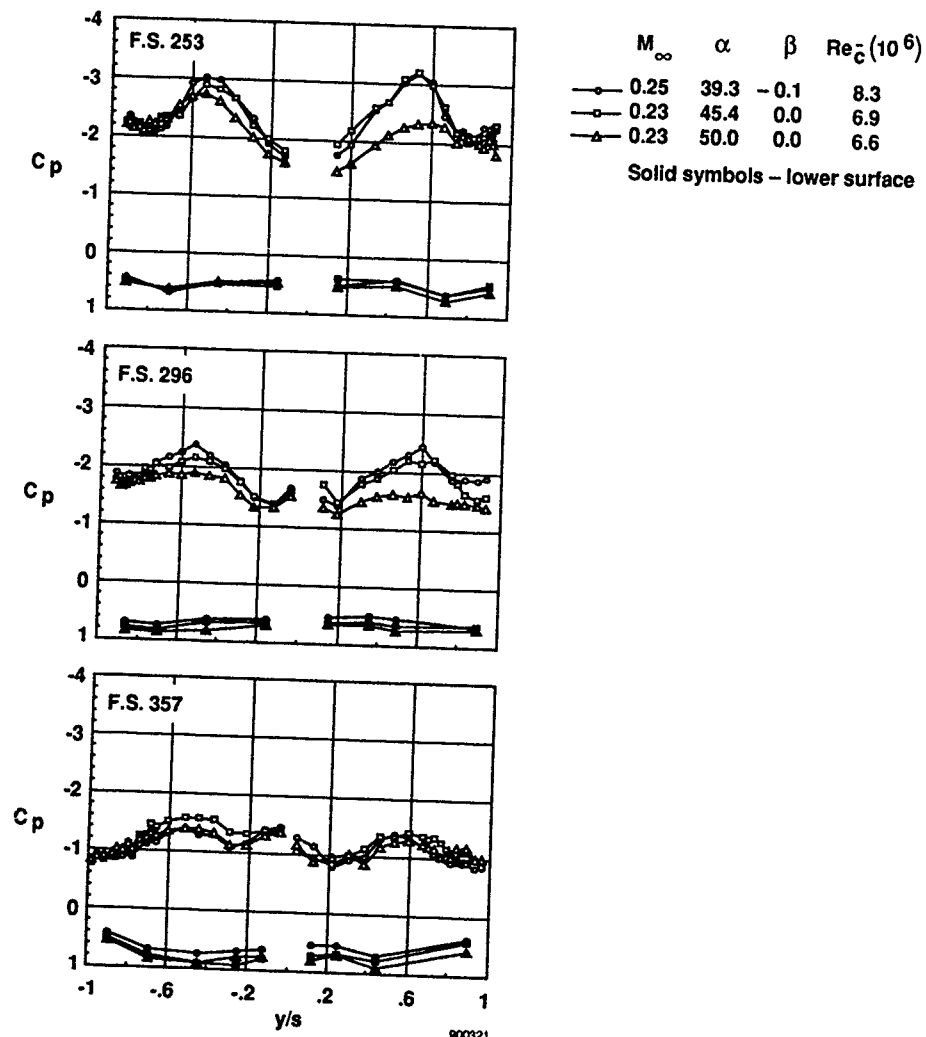
(a)  $\alpha = 10.0^\circ, 15.2^\circ$ , and  $19.7^\circ$ ;  $M_\infty \sim 0.35$ .

Figure 11. Effect of angle of attack on LEX surface static pressure coefficients on the F-18 HARV at low speed.



(b)  $\alpha = 25.8^\circ, 30.0^\circ$ , and  $34.3^\circ$ ;  $M_\infty \sim 0.25$ .

Figure 11. Continued.



(c)  $\alpha = 39.4^\circ, 45.4^\circ$ , and  $50.0^\circ$ ;  $M_\infty \sim 0.25$ .

Figure 11. Concluded.

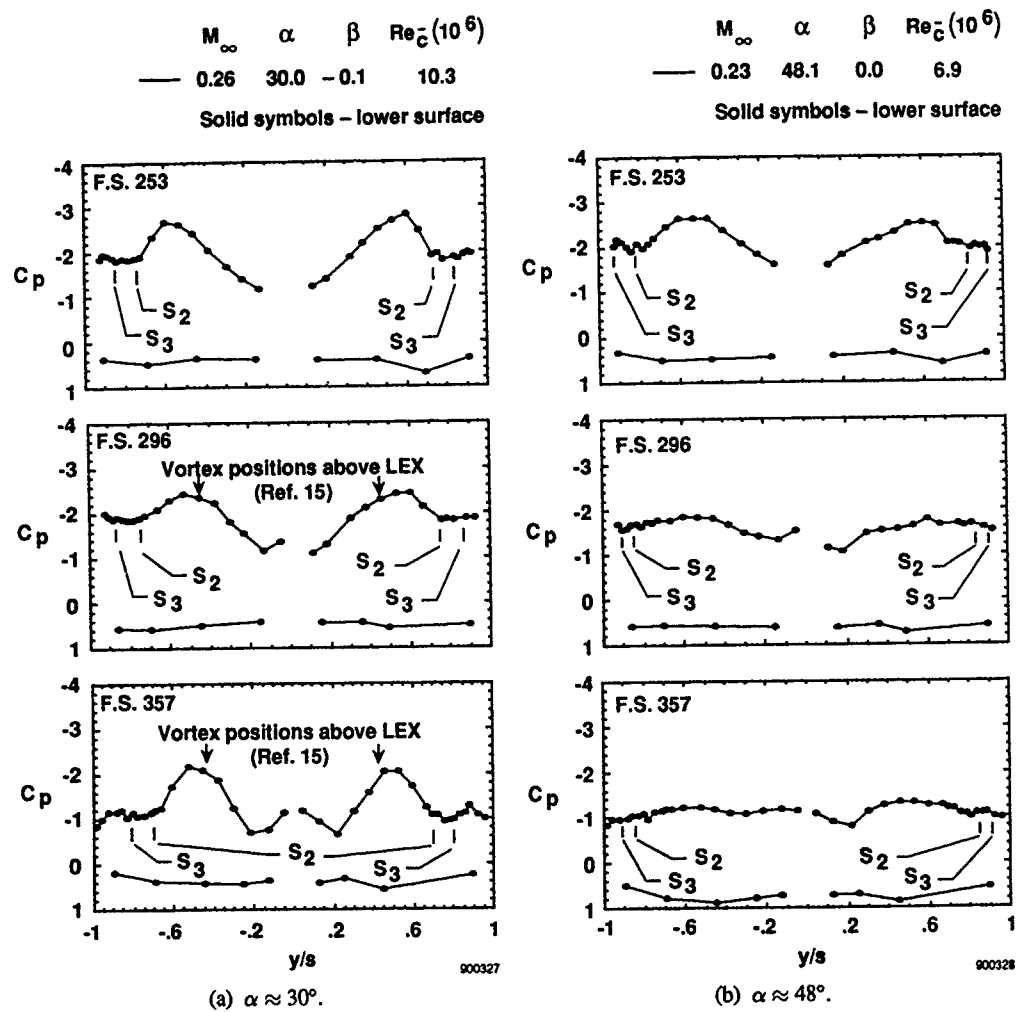


Figure 12. Comparison of LEX surface static pressure coefficients with flow visualization results on the F-18 HARV.

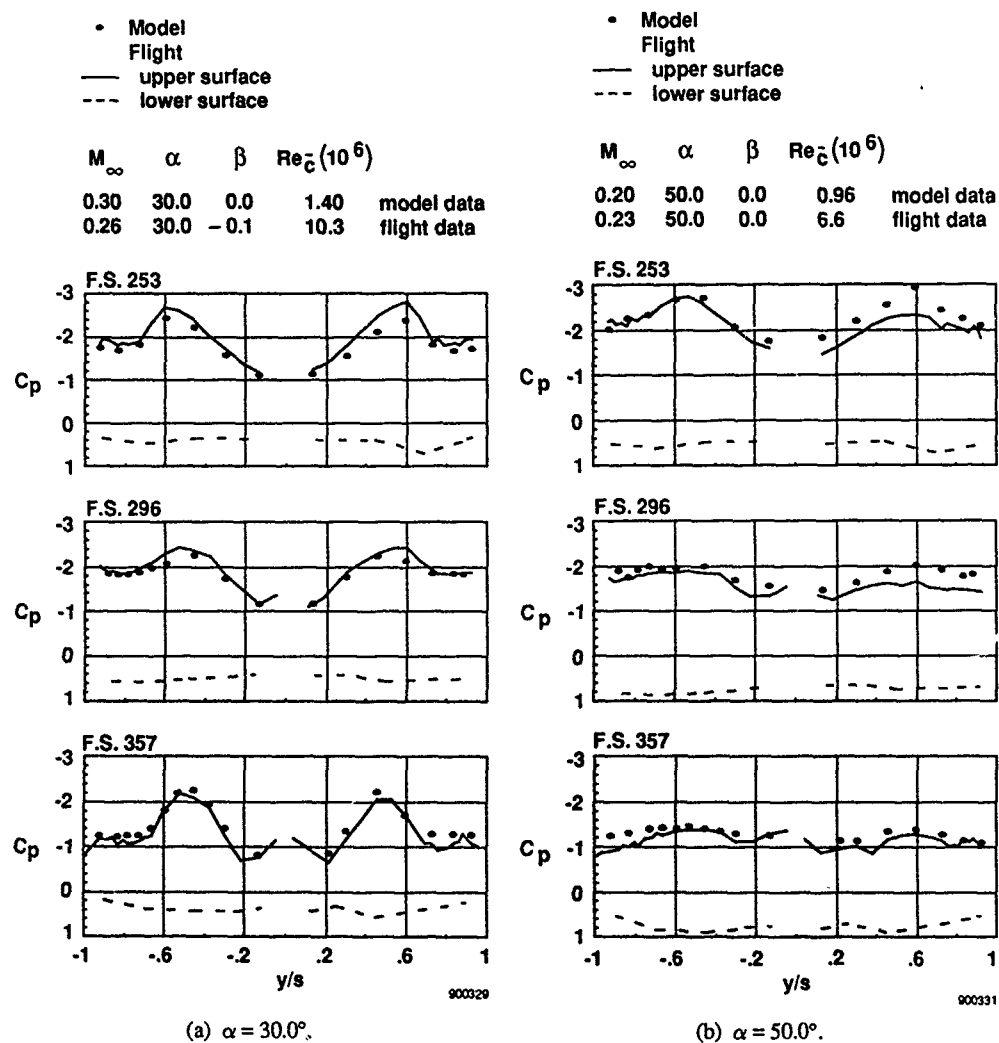
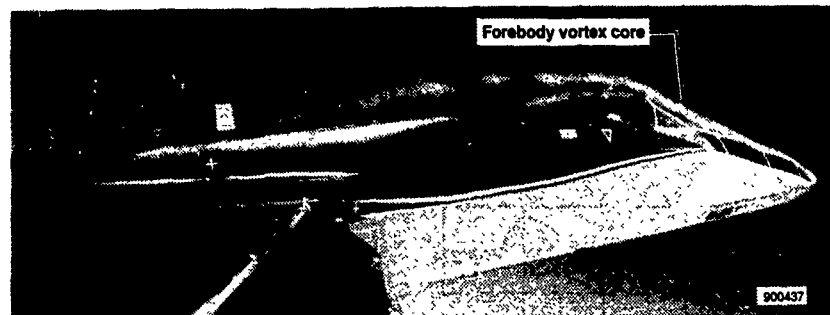


Figure 13. Comparison of flight- and wind-tunnel measured LEX surface static pressure coefficients on the F-18 HARV.



(a)  $\alpha = 29.5^\circ, \beta = 0.4^\circ$ .



(b)  $\alpha = 47.7^\circ, \beta = 0.7^\circ$ .

Figure 14. Photographs from wingtip cameras of smoke entrained in forebody vortex core at two angles of attack.



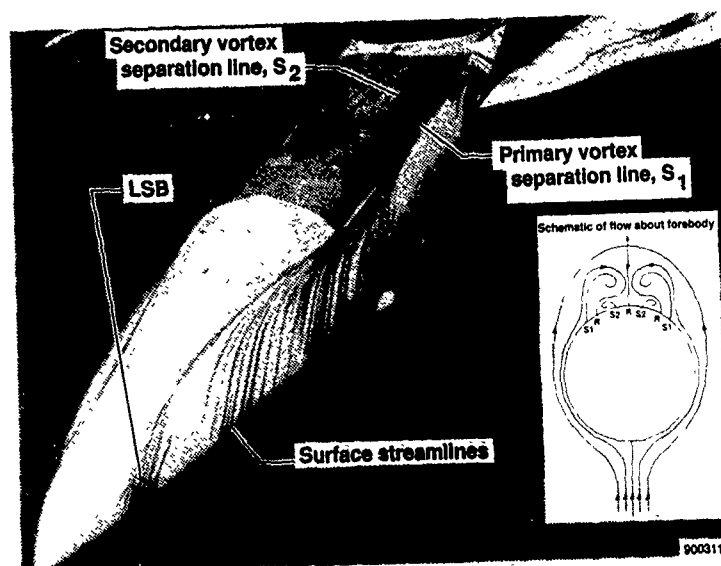
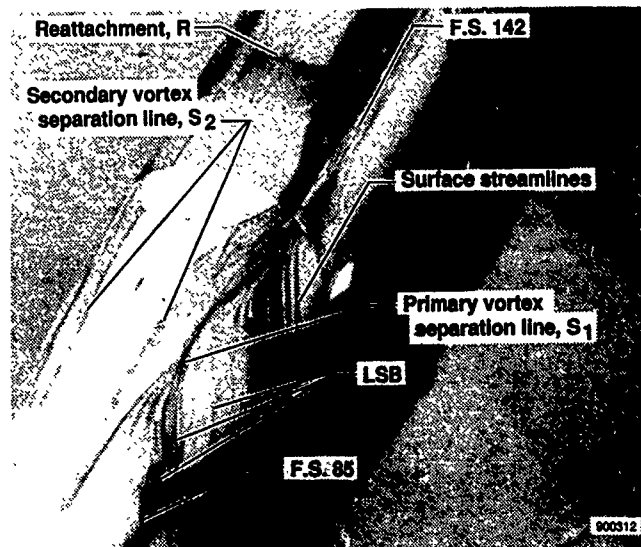
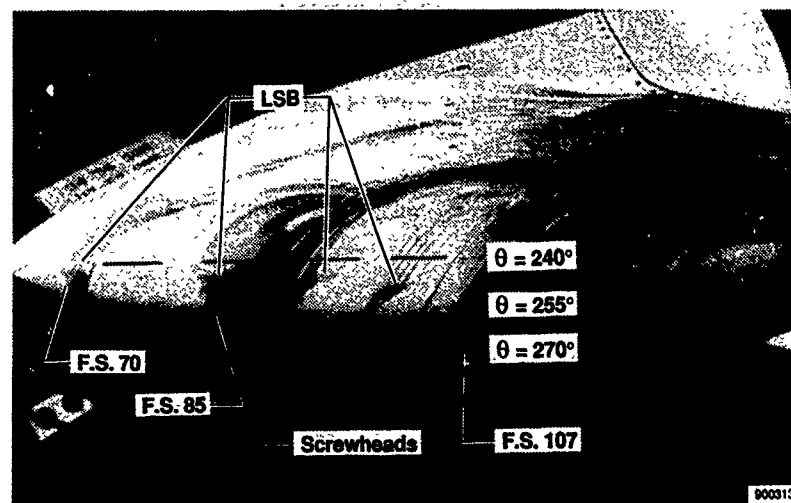


Figure 15. Surface flow visualization of F-18 HARV forebody for  $\alpha \sim 30^\circ$ .



(a) 1/4 view.



(b) Closeup of nosecone.

Figure 16. Surface flow visualization on F-18 HARV forebody for  $\alpha \sim 47^\circ$ .

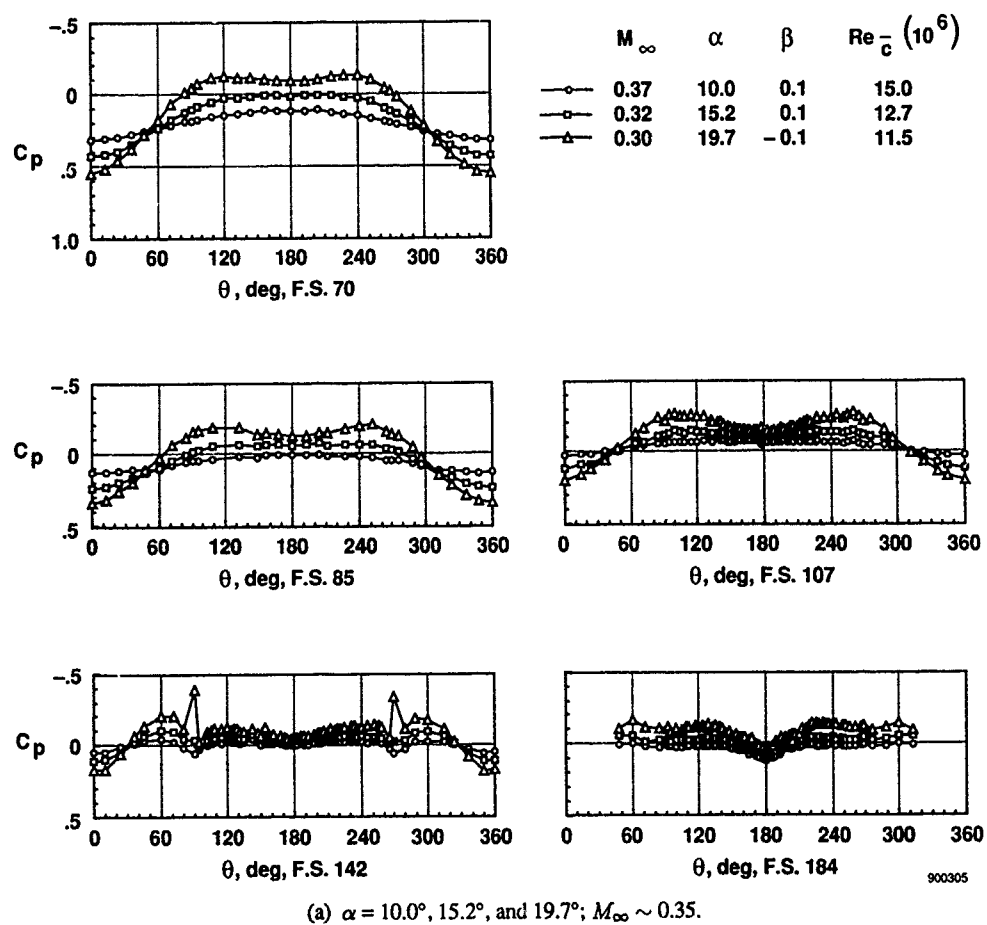
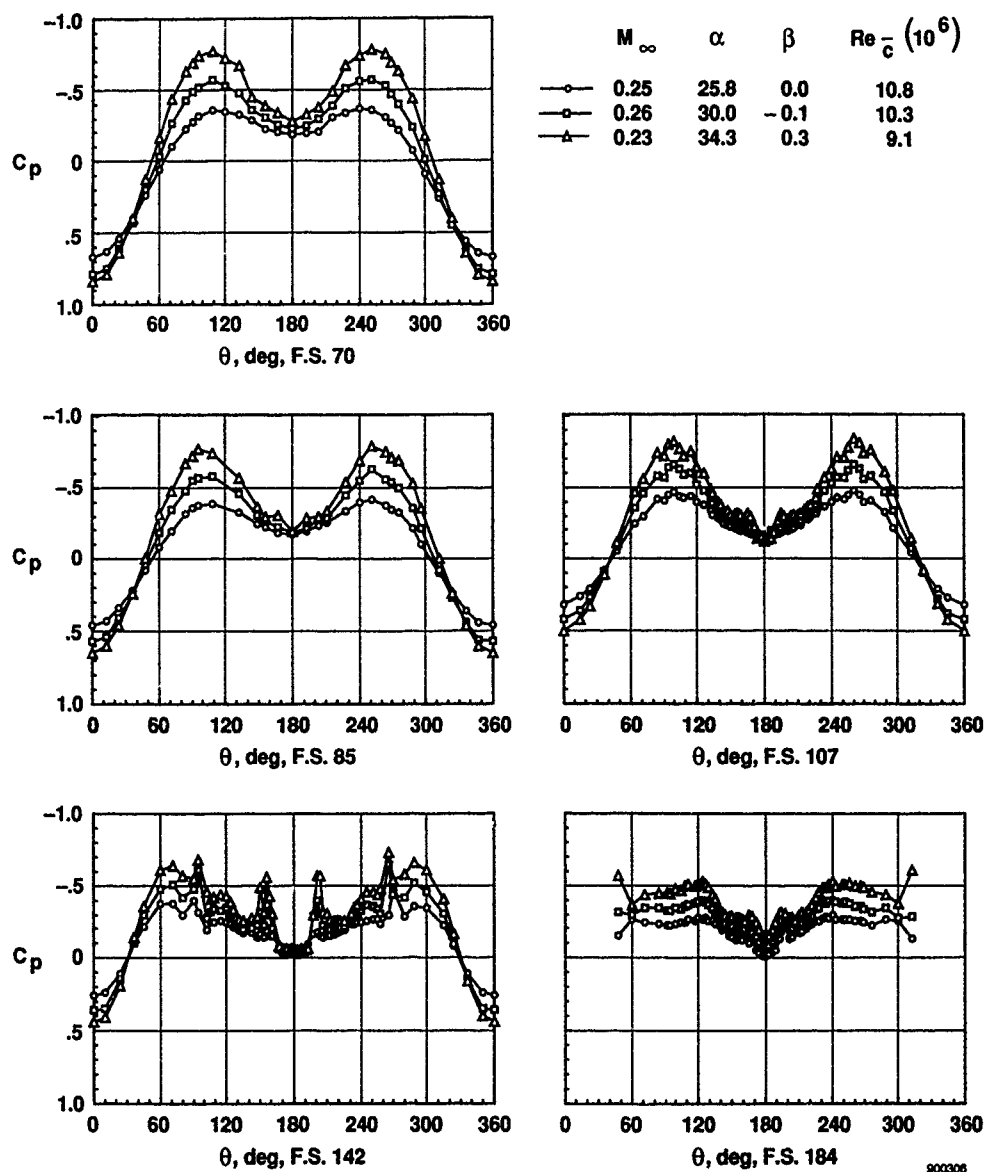
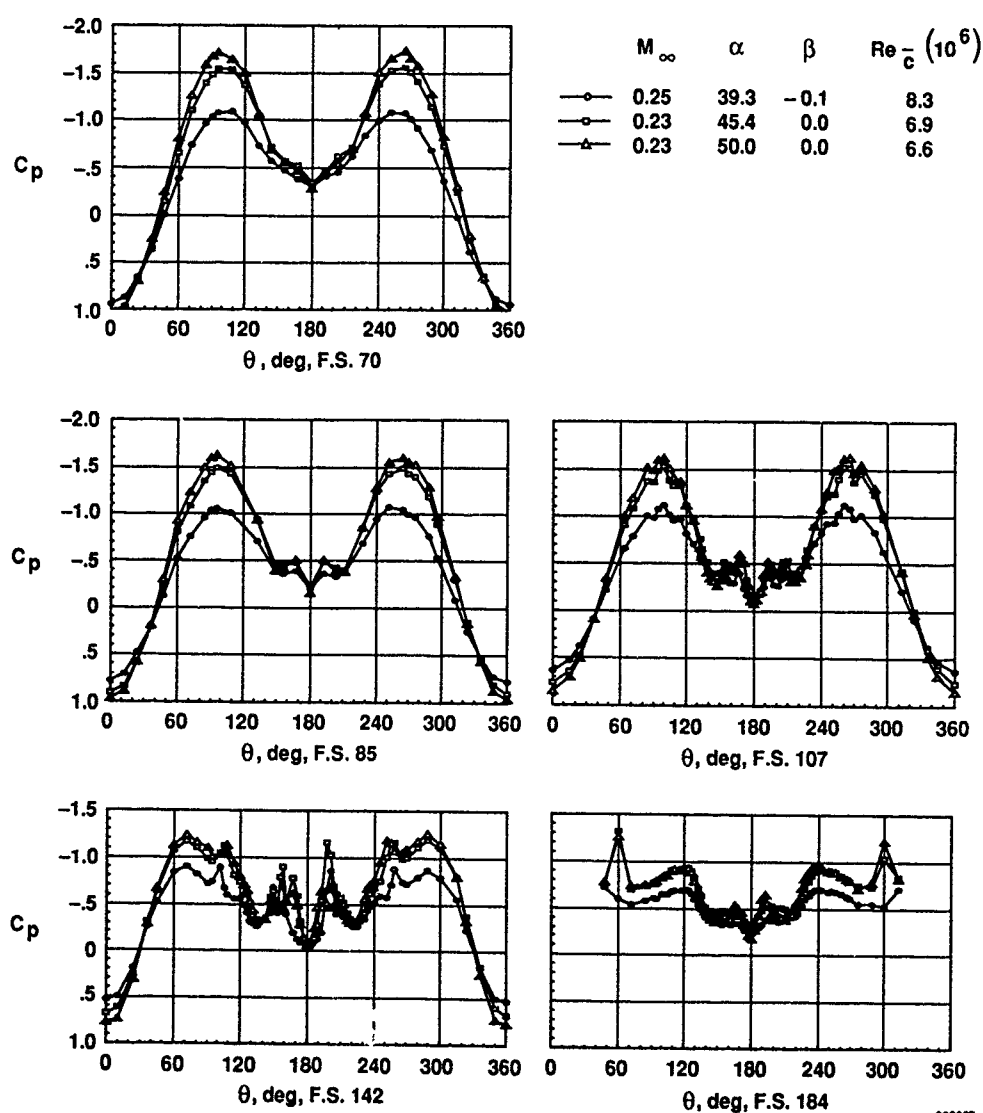


Figure 17. Effect of angle of attack on forebody surface static pressure coefficient on the F-18 HARV at low speed.



(b)  $\alpha = 25.8^\circ, 30.0^\circ$ , and  $34.3^\circ$ ;  $M_\infty \sim 0.25$ .

Figure 17. Continued.



(c)  $\alpha = 39.3^\circ, 45.4^\circ$ , and  $50.0^\circ$ ;  $M_\infty \sim 0.25$ .

Figure 17. Concluded.

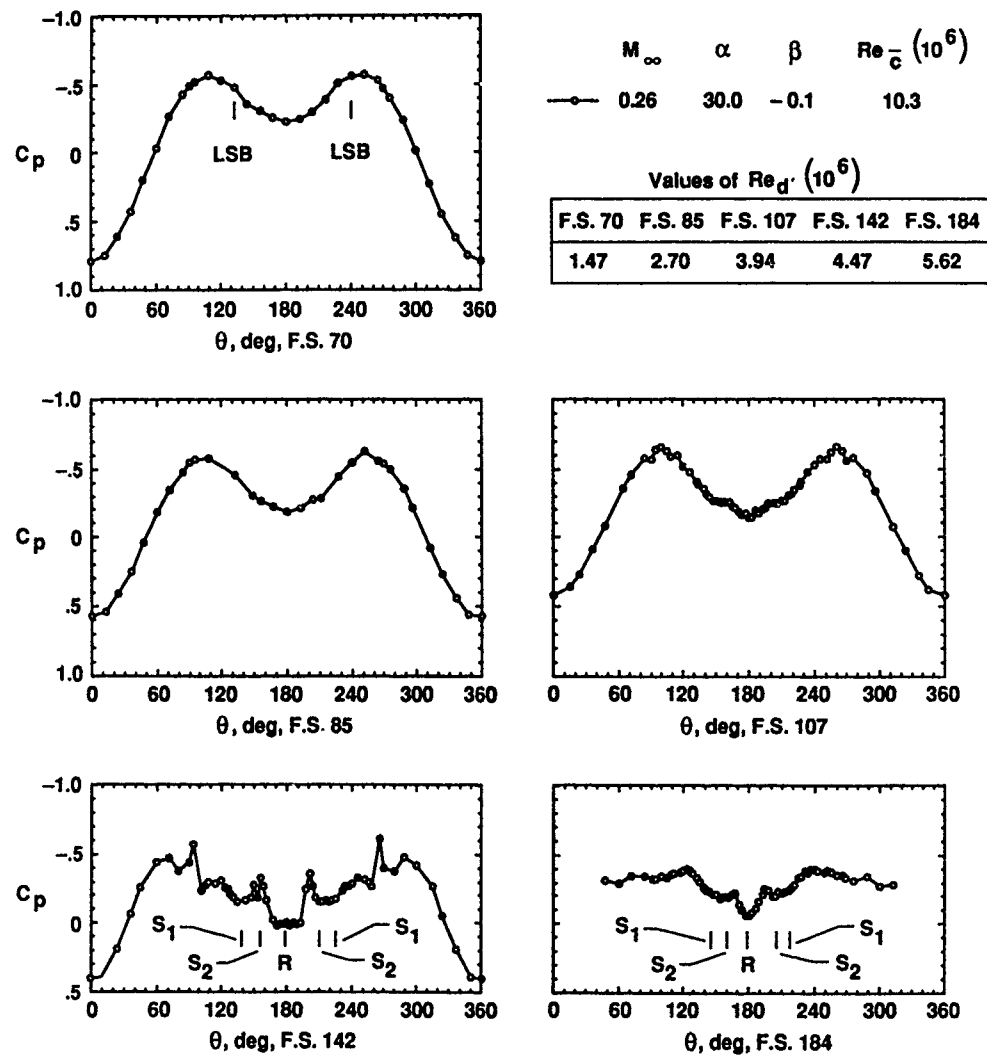
(a)  $\alpha \approx 30.0^\circ$ .

Figure 18. Comparison of forebody surface static pressure coefficients with flow visualization results on the F-18 HARV.

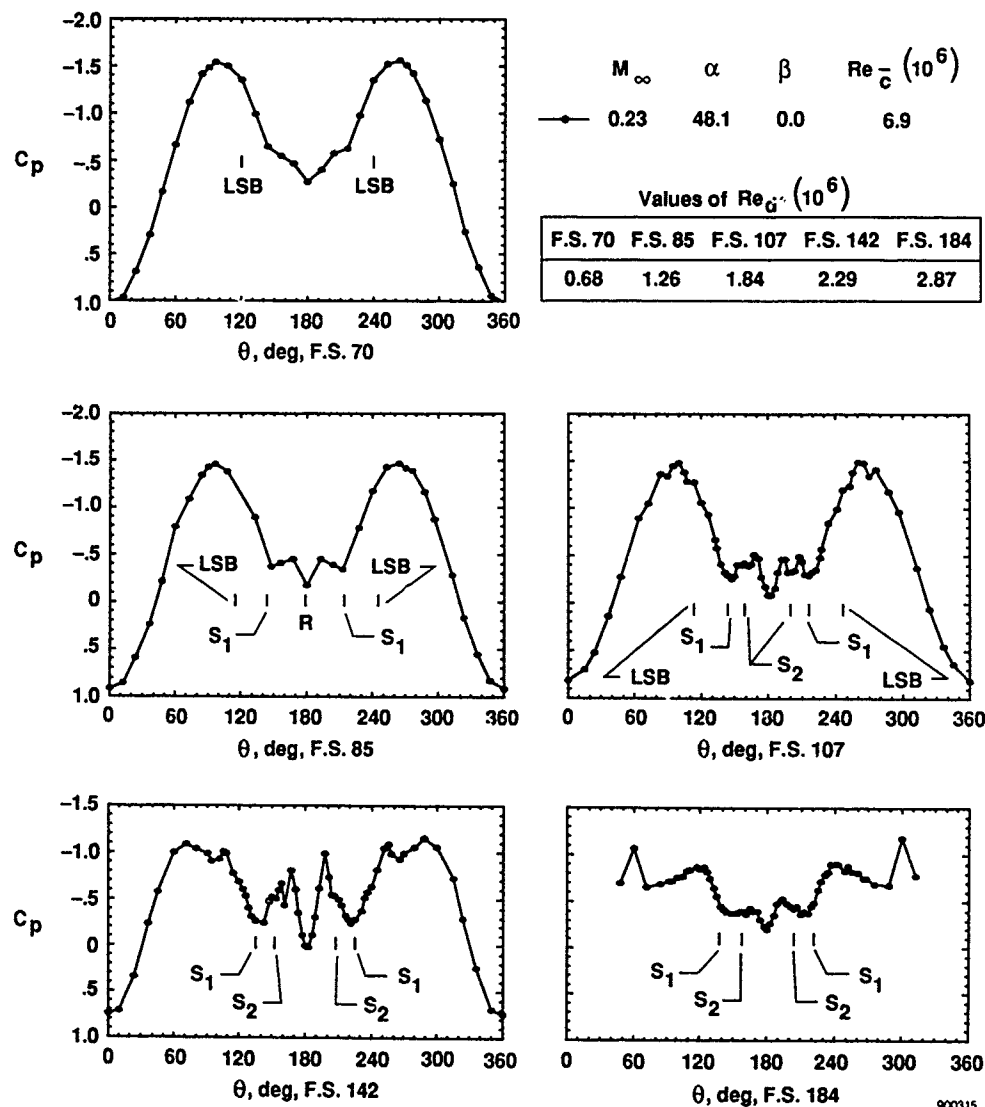
(b)  $\alpha \approx 48^\circ$ .

Figure 18. Concluded.

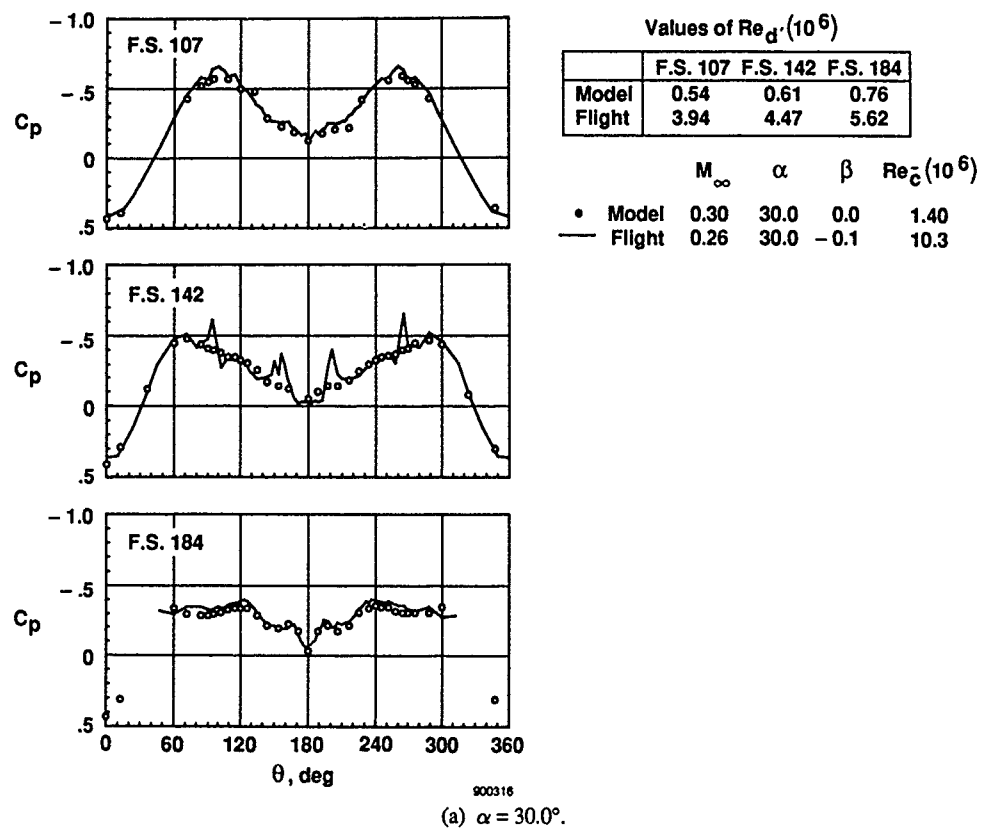


Figure 19. Comparison of flight- and wind-tunnel measured surface static pressure coefficients on the F-18 HARV forebody.



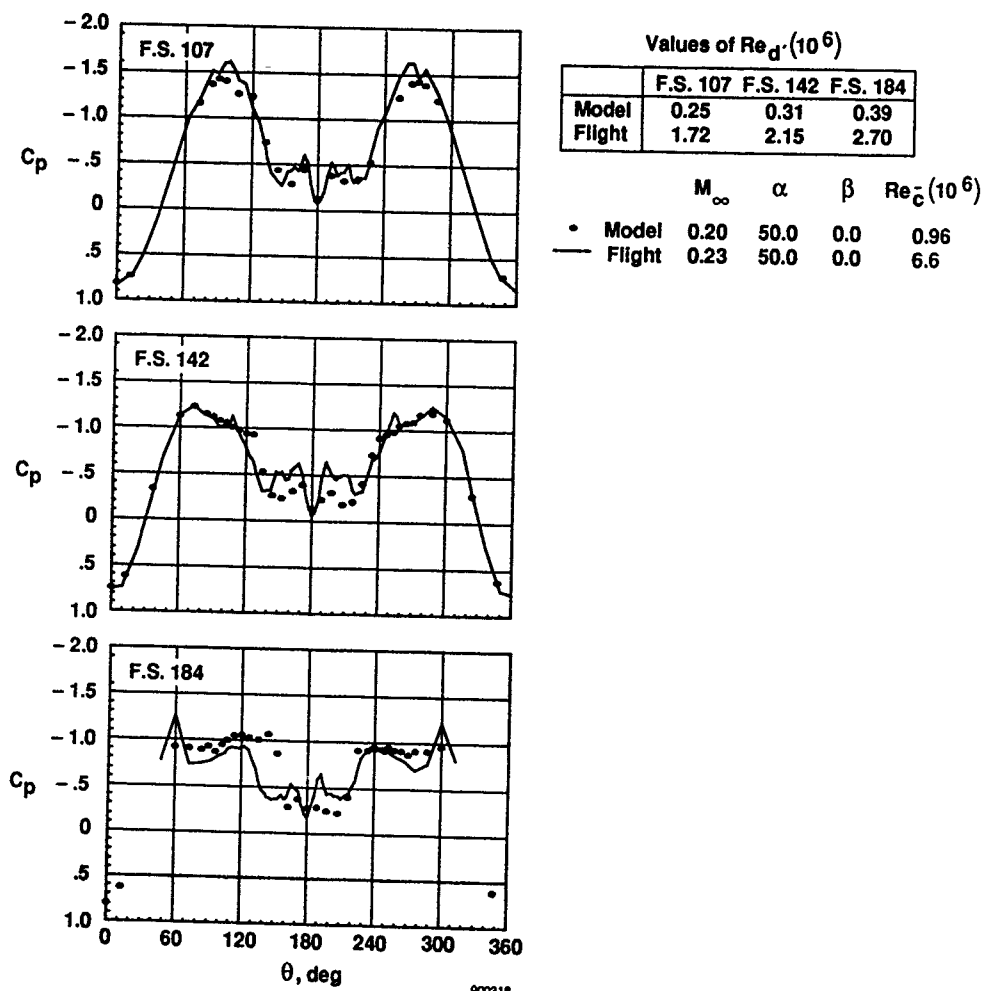
(b)  $\alpha \approx 50.0^\circ$ .

Figure 19. Concluded.

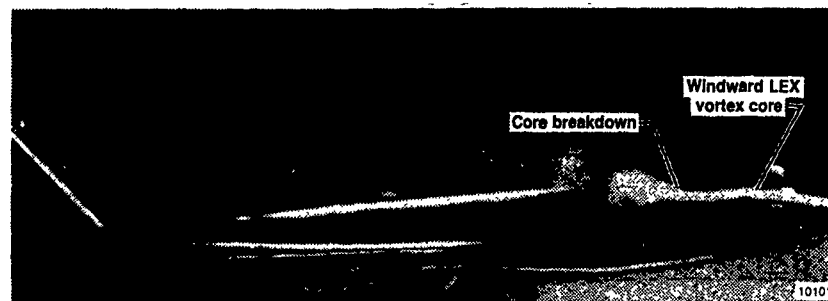
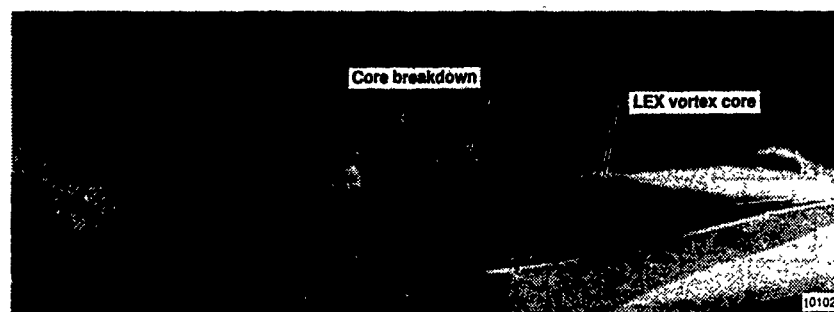
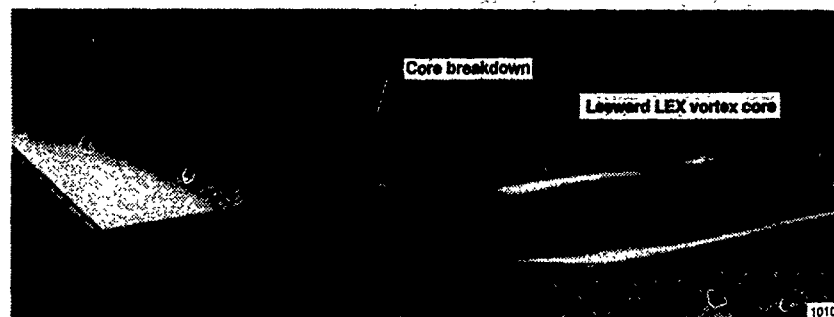
(a)  $\alpha = 26^\circ$  and  $\beta = 4.52^\circ$ .(b)  $\alpha = 25^\circ$  and  $\beta = 1^\circ$ .(c)  $\alpha = 24.7^\circ$  and  $\beta = -3.4^\circ$ .

Figure 20. Right wingtip view showing effects of increased angle of sideslip on LEX vortex core and breakdown point.

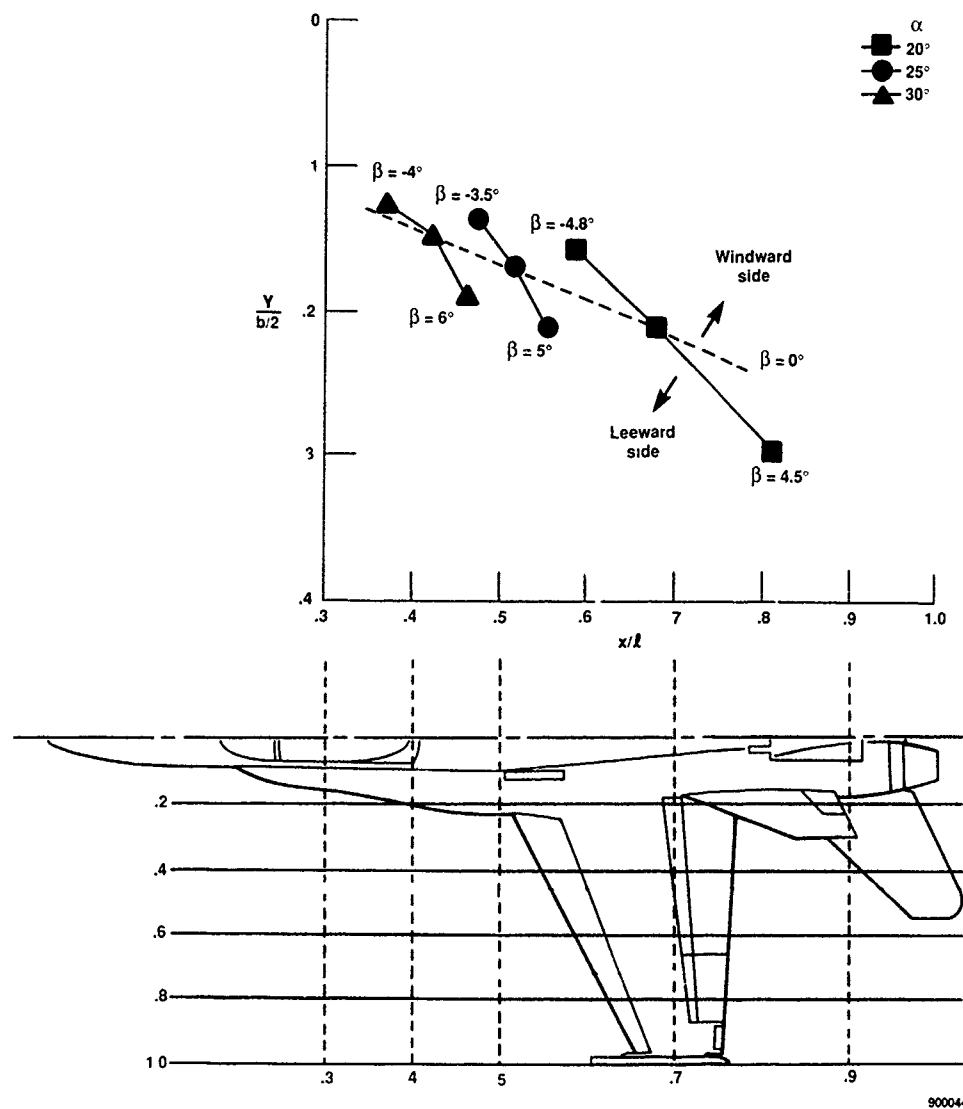
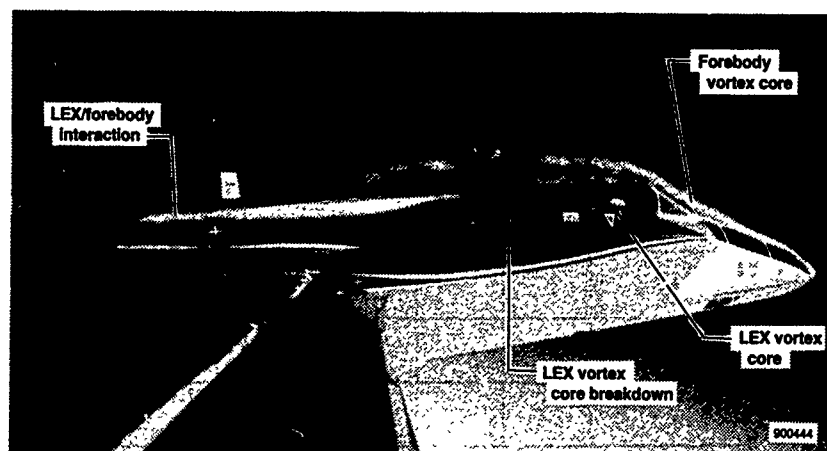
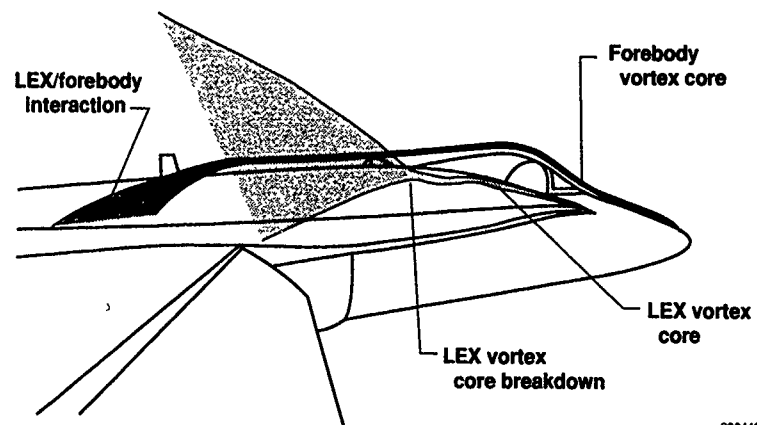
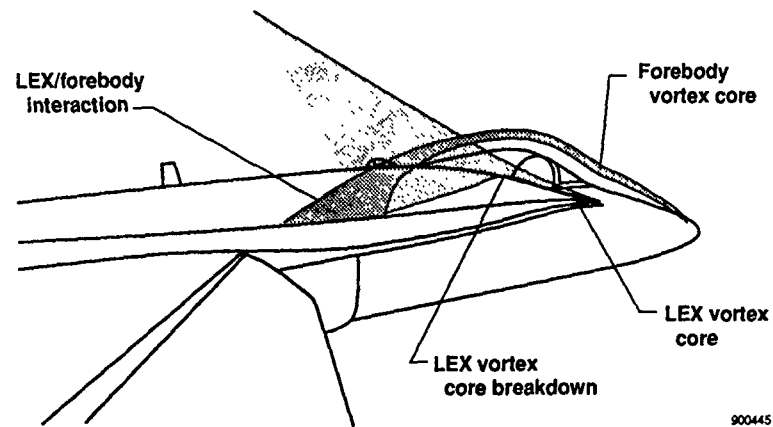


Figure 21. Comparison of left F-18 LEX vortex core breakdown location for a range of angle of sideslip and angle of attack.



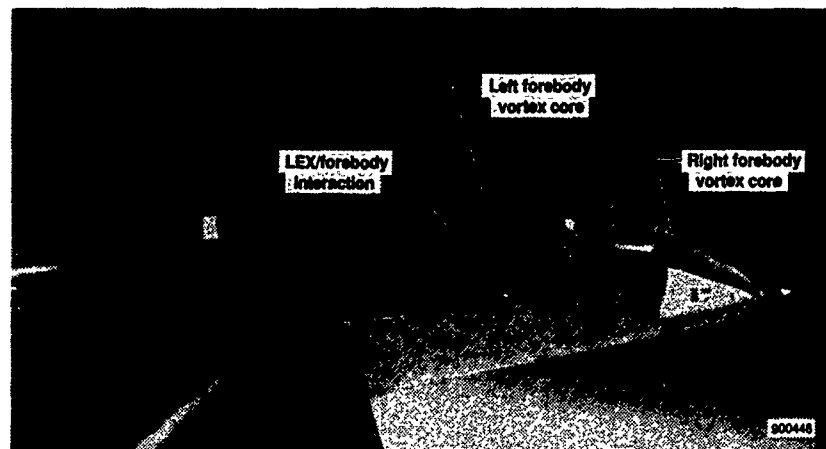
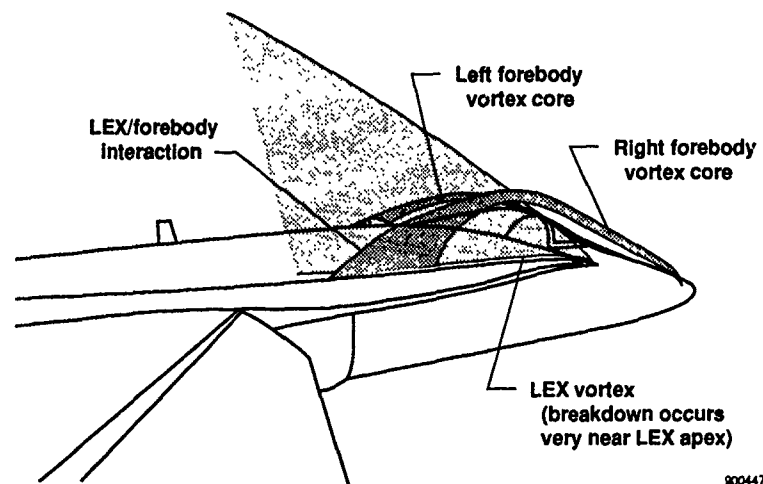
(a)  $\alpha = 29.5^\circ$  and  $\beta = 0.4^\circ$ .

Figure 22. Wingtip view of forebody vortex system.



(b)  $\alpha = 38.7^\circ$  and  $\beta = 0^\circ$ .

Figure 22. Continued.



(c)  $\alpha = 42.5^\circ$  and  $\beta = -0.5^\circ$ .

Figure 22. Concluded.

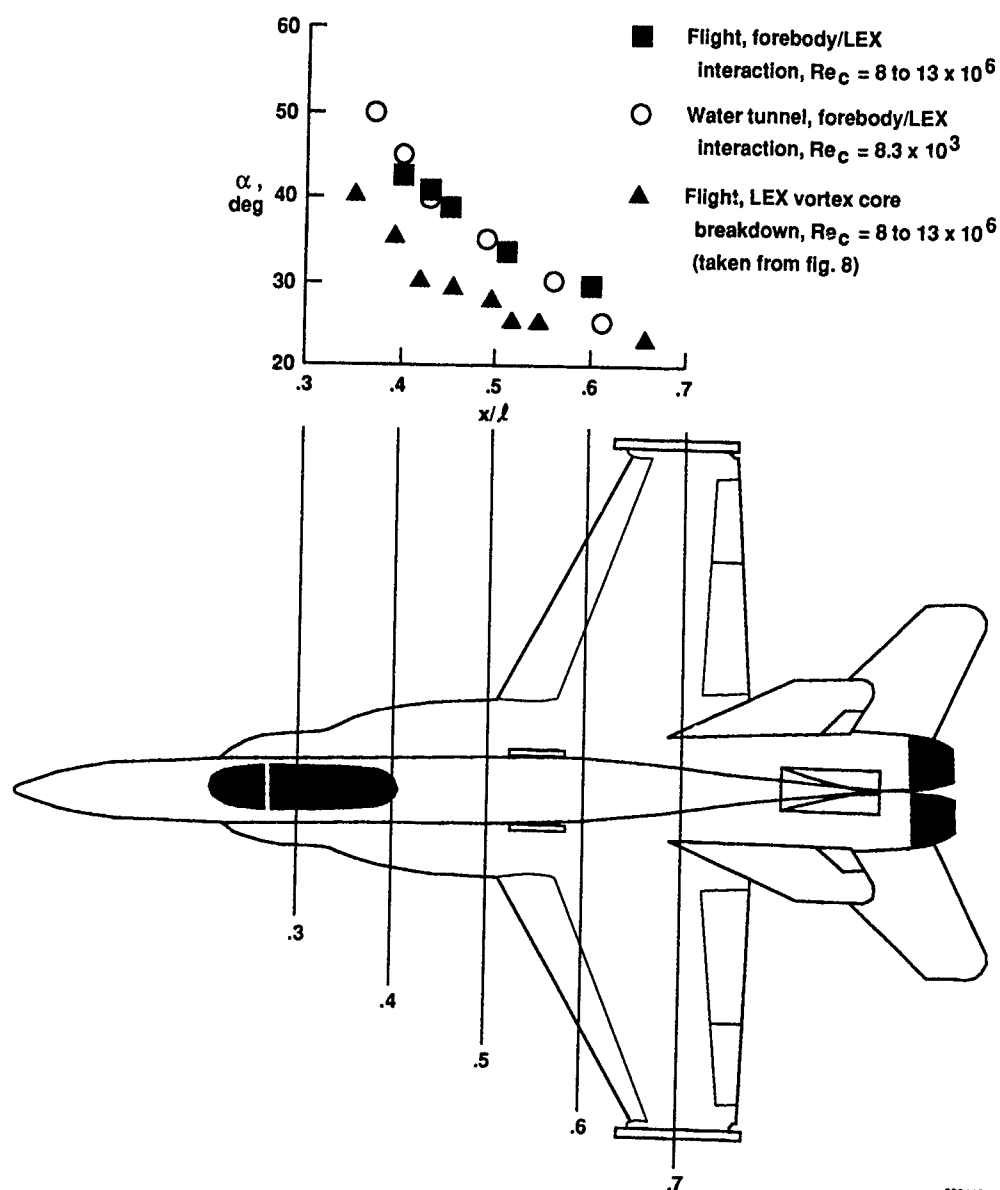


Figure 23. Longitudinal location of LEX vortex core breakdown and of forebody and LEX vortex interaction for various angles of attack,  $\beta = 0^\circ$ .

900449

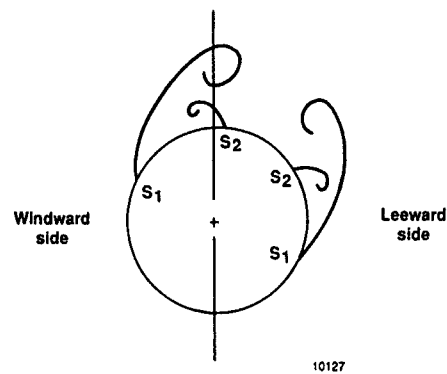
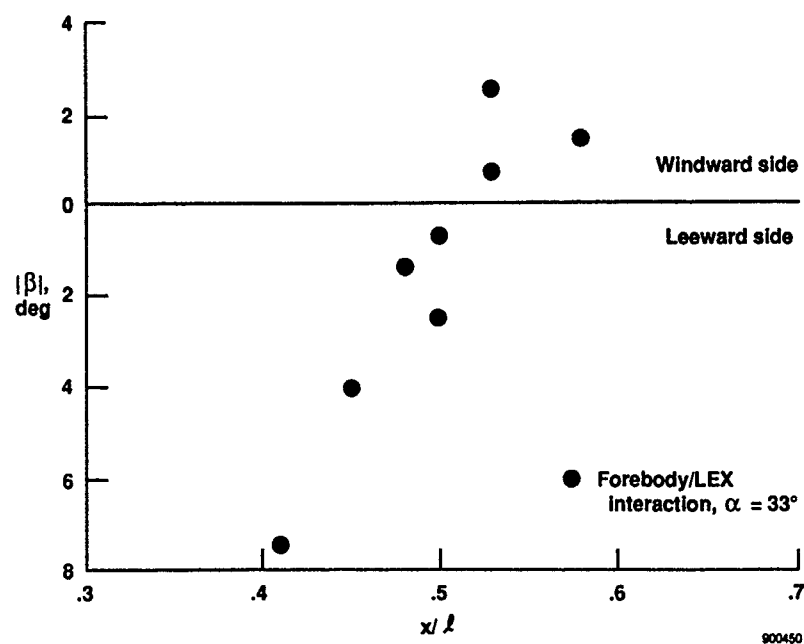


Figure 24. Cross sectional view of forebody vortex system at sideslip.

Figure 25. Flight measured location of forebody/LEX vortex interaction as a function of sideslip,  $\alpha = 33^\circ$ .



VORTEX FORMATION OVER A CLOSE-COUPLED  
CANARD-WING-BODY CONFIGURATION  
IN UNSYMMETRICAL FLOW<sup>\*)</sup>

by

A. Bergmann, D. Hummel  
Institut für Strömungsmechanik, TU Braunschweig  
Bienroder Weg 3, D - 3300 Braunschweig

and

H.-Chr. Oelker  
Dornier Luftfahrt GmbH  
Postfach 1303, D - 7990 Friedrichshafen

SUMMARY

A close-coupled canard-wing-body combination has been investigated in unsymmetrical flow. The configuration consisted of a delta canard and a delta wing ( $A_C = A_W = 2.3$ ) and a body of revolution as fuselage. Six-component and surface pressure distribution measurements as well as flow visualizations by means of the laser-lightsheet technique have been carried out at Reynoldsnumbers (based on wing inner chord) of  $Re = (1.1)1.4 \cdot 10^6$  for the canard-off and the canard-on configuration.

For large angles of attack distinct jumps of the aerodynamic coefficients have been detected in unsymmetrical flow which are due to sudden changes of the flow structure. On the canard-off configuration they are caused by the collapse of the vortex-type flow on the windward side of the configuration into a deadwater-type flow which takes place when the vortex breakdown position within the wing vortices reaches the wing apex. On the canard-on configuration the sensitive and favourable interference between canard and wing is suddenly disturbed. Apart from a small region in the vicinity of the symmetrical flow in which a vortical flow at the canard can be maintained up to extremely large angles of attack, in unsymmetrical flow at high angles of attack the flow over the windward side of the canard collapses from a vortex-type flow to a deadwater-type flow due to a sudden loss of favourable interference, and this causes the jumps in the slope of the aerodynamic coefficients.

LIST OF SYMBOLS

Geometric Quantities

		$S'$	Area of canard or wing which is not shrouded by the fuselage (marked in Fig. 2 by hatching)
$A = b^2/S$	Aspect ratio of canard or wing	$b = 2s$	Span of canard or wing
$N_{25}$	Geometric neutral point of canard or wing (original planform: Leading-edge extended to $y_C = y_W = 0$ according to Fig. 2)	$c(y)$	Local chord of canard or wing
		$c_i = c(y = 0)$	Inner chord of canard or wing
$N_{25}$	Geometric neutral point of those parts of canard or wing which are not shrouded by the fuselage (marked in Fig. 2 by hatching)	$c_r = c(y = r_F)$	Root chord of canard or wing
$R = r/c_{1W}$	Relative forward position of the canard	$\bar{c} = \frac{1}{S_W} \int_{-S_W}^{+S_W} c_W^2 dy_W$	Mean aerodynamic chord of the original wing
$S$	Area of canard or wing (original planform: Leading-edge extended to $y_C = y_W = 0$ according to Fig. 2)	$d_F = 2r_F$	Diameter of the cylindrical portion of the fuselage
		$l_F$	Length of the fuselage

<sup>\*)</sup> This work was partly supported by Deutsche Forschungsgemeinschaft under contract DFG Hu 254/8.

$l_F$	Length of the fuselage	$c_n = N/q_\infty S_H$	Yawing moment coefficient (Reference axis and sign according to Fig. 4)
$l_{1F}, l_{2F}, l_{3F}$	Length of front, cylindrical and rear part of the fuselage	$c_p = (p - p_\infty)/q_\infty$	Static pressure coefficient
$r_F$	Radius of the cylindrical portion of the fuselage	$p$	Static pressure
$\bar{r}$	Horizontal distance between the geometric neutral points of canard and wing ( $\bar{r} = \Delta x_{N25C} - \Delta x_{N25W} = \Delta x'_{N25C} - \Delta x'_{N25W}$ )	$q_\infty$	Free stream dynamic pressure
$s$	Half span of canard or wing	$\alpha$	Angle of attack (Angle between the free stream velocity component $V_\infty \cos \beta$ and the wing plane, see Fig. 4)
$s_1$	Local half span of canard or wing	$\beta$	Angle of sideslip (Angle between the free stream velocity and the symmetry plane $y = 0$ of the configuration, see Fig. 4)
$t$	Maximum thickness of canard or wing	$\nu$	Kinematic viscosity
$x, y, z$	Body-fixed coordinates, origin on the axis of the fuselage at the intersection of leading-edge and fuselage contour ( $y = r_F$ ) for canard or wing	Subscripts	
$\Delta x_{N25}$	Distance of the geometric neutral point $N_{25}$ of canard or wing from the trailing-edge of the wing (or from the rear end of the cylindrical portion of the fuselage)	C	Canard
$\Delta x'_{N25}$	Distance of the geometric neutral point $N'_{25}$ of canard or wing from the trailing-edge of the wing (or from the rear end of the cylindrical portion of the fuselage)	F	Fuselage
		W	Wing
		$\infty$	Free stream conditions
$\xi = x/c_r$	Dimensionless body-fixed longitudinal coordinate for canard or wing	1. INTRODUCTION	
$\eta = \frac{y - r_F}{s_1 - r_F}$	Dimensionless local lateral coordinate for canard or wing.	Canard configurations have been investigated for a long time and there exists a large number of publications of experimental and theoretical work on this topic. It is known since H. Behrbohm [1] in 1965 that close-coupled canard configurations with canard and wing of small aspect ratios in the range of $1 \leq A \leq 3$ have substantial advantages: The maximum lift coefficient $c_{Lmax}$ and the corresponding angle of attack $\alpha(c_{Lmax})$ can be increased considerably by adding a delta canard to a delta wing. The advantage is due to favourable interference between the vortex systems of canard and wing. Therefore, today a close-coupled canard configuration is a characteristic feature of modern fighter aircraft.	
$\varphi$	Leading-edge sweep of canard or wing		

## Aerodynamic Quantities

$Re = V_\infty \cdot c_{iw} / \nu$	Reynoldnumber
$V_\infty$	Free stream velocity
$c_L = L/q_\infty S_H$	Lift coefficient
$c_D = D/q_\infty S_H$	Drag coefficient
$c_m = M/q_\infty S_H \bar{c}$	Pitching moment coefficient (Reference point $N_{25W}$ , nose-up positive, see Fig. 4)
$c_Y = Y/q_\infty S_H$	Side force coefficient
$c_l = L/q_\infty S_H s$	Rolling moment coefficient (Reference axis and sign according to Fig. 4)

Canard configurations have been investigated for a long time and there exists a large number of publications of experimental and theoretical work on this topic. It is known since H. Behrbohm [1] in 1965 that close-coupled canard configurations with canard and wing of small aspect ratios in the range of  $1 \leq A \leq 3$  have substantial advantages: The maximum lift coefficient  $c_{Lmax}$  and the corresponding angle of attack  $\alpha(c_{Lmax})$  can be increased considerably by adding a delta canard to a delta wing. The advantage is due to favourable interference between the vortex systems of canard and wing. Therefore, today a close-coupled canard configuration is a characteristic feature of modern fighter aircraft.

Short-coupled canard configurations have been studied extensively in series of measurements at Naval Ship Research and Development Center (NSRDC) [2 - 5] and at NASA [6 - 13]. These experimental investigations were mainly aimed at finding practicable solutions. The trimming capabilities of close-coupled canard configurations in comparison with conventional configurations have been investigated by R. B. Eberle et al. [14] and S. E. Goldstein, C. P. Combs [15] and the aerodynamics of such configurations beyond stall have been considered by H. John, W. Kraus [16] and W. Kraus [17].

More recently new activities related to short-coupled canard configurations have been started by J. Er-EI, A. Seginer [18] as well as within the "Inter-

national Vortex Flow Experiment" (VFE) by G. Drougge [19]. These investigations were aimed at an understanding of the physics of the vortex formation over such configurations and a proper calculation of such flows by means of Euler- and Navier-Stokes-codes. The investigations were mainly concerned with symmetrical flow around a short-coupled canard configuration described in Ref. [19]. Although much effort was devoted to the canard-off configuration, some results for the canard-on configuration are available and summarized by A. Elsenaar et al. [20]. Force and pressure distribution measurements as well as a detailed study of the incompressible flow around this configuration have been carried out by H.-Chr. Oelker [21].

In close relation to the Vortex Flow Experiment at Institut für Strömungsmechanik of Technische Universität Braunschweig a comprehensive research program has been performed on a second close-coupled canard configuration with a delta wing and a delta canard ( $A_w = A_c = 2.31$ ). Force and pressure distribution measurements, flow visualizations and flow field measurements have been carried out by D. Hummel and H.-Chr. Oelker [22 - 26]. From these investigations the mechanisms of interference between canard and wing may be regarded as well understood for this configuration in symmetrical flow. Fig. 1 summarizes the flow pattern. At the canard a primary vortex is formed which is accompanied by a secondary vortex (not shown in Fig. 1) and by a counter-rotating trailing-edge vortex downstream of the canard's trailing-edge. This vortex formation is the same as for a single delta wing according to D. Hummel [27]. Over the wing the canard vortex system remains separate from the wing vortex system. In the inner portion of the wing the canard's trailing vortex sheet merges with the upper surface boundary layer of the wing. The flow separation at the leading-edge of the wing is suppressed in the front part of the wing due to downwash effects caused by the canard's vortex system. Therefore the wing vortices are formed with some delay. They are again accompanied by a secondary vortex (not shown in Fig. 1) and by a counter-rotating trailing-edge vortex downstream of the wing. With increasing angle of attack this flowfield remains virtually unchanged. Vortex breakdown takes

place neither in the canard's nor in the wing's vortex system. This is due to favourable interference effects: In the canard's vortex system a strong tendency towards vortex breakdown is present downstream of the canard's trailing-edge, but the acceleration of the flow over the leading-edge of the wing keeps vortex breakdown away from the canard vortices apart from some vortex stretching between canard and wing [22]. Due to the downwash of the canard the wing operates at lower effective angles of attack and therefore vortex breakdown is also delayed in the wing's vortex system. Due to these favourable effects the lift of a close-coupled canard configuration is larger than that of the wing alone. At very large angles of attack, the sensitive interference is no longer able to avoid vortex breakdown and a sudden lift loss is caused by vortex breakdown within the canard vortices first and then also within the wing vortices.

Short-coupled canard configurations have also been investigated in unsymmetrical flow and some publications, e. g. Refs. [8], [9], [11], [16], [17], present lateral aerodynamic characteristics. The aim of these investigations were considerations of lateral stability and control of such configurations but details of unsymmetrical flowfields have not yet been studied. For this purpose the  $A = 2.31$  delta canard wind tunnel model of the Institut für Strömungsmechanik at Technische Universität Braunschweig has been equipped with a body of revolution as fuselage. This extended version of the configuration has been tested in unsymmetrical flow by means of force and pressure distribution measurements and the flowfield has been studied using the laser-lightsheet technique. The first results of these investigations will be presented subsequently.

## 2 EXPERIMENTAL SET-UP AND TEST PROGRAM

The experimental investigations have been carried out in the 1.3 m wind-tunnel of the Institut für Strömungsmechanik of Technische Universität Braunschweig.

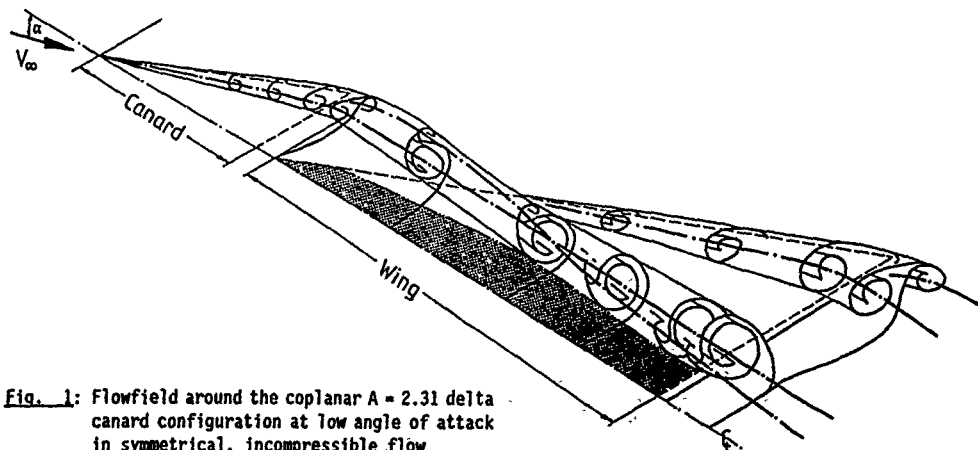


Fig. 1: Flowfield around the coplanar  $A = 2.31$  delta canard configuration at low angle of attack in symmetrical, incompressible flow

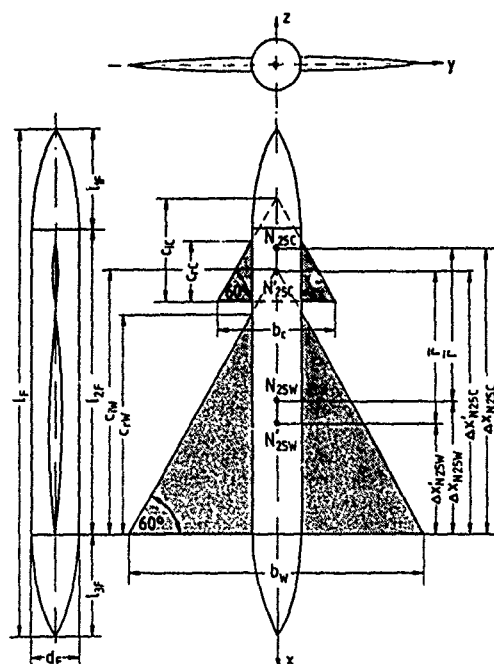


Fig. 2: Canard-wing-fuselage configuration

## 2.1 WIND-TUNNEL MODEL

The investigations have been performed for a canard-wing-body configuration, which is shown in Fig. 2. The geometric data may be taken from Tab. 1. Canard and wing have delta planforms of aspect ratio  $A_C = A_W = 2.31$  and a corresponding leading-edge sweep of  $\psi_C = \psi_W = 60^\circ$ . In both cases symmetric parabolic arc airfoils for the inner section ( $y_C = y_W = 0$ ) and parabolic contours in spanwise direction have been used. For canard and wing the thickness at the leading-edge was 1 mm. In relation to the sizes of canard ( $b_C = 240$  mm) and wing ( $b_W = 600$  mm) these leading-edges may be regarded as sharp. The fuselage is a body of revolution which consists of a cylindrical portion of length  $l_{2F} = 6.05 d_F$  and attached are front and rear parts of length  $l_{1F} = l_{3F} = 2.00 d_F$ . Their shape has been taken as a polynomial of fourth order which meets the cylindrical part continuously with respect to slope and curvature. Canard, wing and fuselage are equipped with a tube system underneath the surface and with pressure holes in order to measure the surface pressure distribution. The arrangement of the sections 1 to 30 and the positions of the pressure holes are shown in Fig. 3. In the sections 1 to 5 and 14, 15 the pressure distribution could be measured on the fuselage only, and in the sections 6 and 7 on the canard only a reduced number of pressure holes was available.

The geometric data of the combinations wing-fuselage and canard-wing are also collected in Tab. 1. The wing was added to the fuselage in such a way, that the trailing-edge of the wing coincided with the rear end of the cylindrical part of the fuselage. A mid-wing configuration was chosen and the setting

Tab. 1: Geometric data of the configuration

Canard	Aspect ratio	$A_C = 2.31$
	Leading-edge sweep	$\psi_C = 60^\circ$
	Thickness ratio	$(t/c_1)_C = 0.05$
Wing	Aspect ratio	$A_W = 2.31$
	Leading-edge sweep	$\psi_W = 60^\circ$
	Thickness ratio	$(t/c_1)_W = 0.05$
Fuselage: Body of revolution	Thickness ratio	$d_F/l_F = 1/10.05$
	Cylindrical section	$d_F/l_{2F} = 1/6.05$
	Front and rear part	$d_F/l_{1F} = d_F/l_{3F}$
		$= 1/2.00$
Combination Wing-Fuselage:		
	Relative fuselage width	$d_F/b_W = 1/6$
	Position of $N_{25W}$	$\Delta x_{N_{25W}/b_W} = 0.433$
	Position of $N_{25W}$	$\Delta x_{N_{25W}/b_W} = 0.361$
	Mid-wing position	
Combination Canard-Wing:		
	Relative canard size	$b_C/b_W = 0.4$
	Position of $N_{25C}$	$\Delta x_{N_{25C}/b_W} = 0.931$
	Position of $N_{25C}$	$\Delta x_{N_{25C}/b_W} = 0.859$
	Forward position of canard	$R = \bar{r}/c_{1W} = 0.575$
	Coplanar	

angle between the wing plane and the fuselage axis was  $\epsilon_W = 0^\circ$ . Concerning the canard-wing combination the span ratio is  $b_C/b_W = 0.4$  corresponding to an area ratio of  $S_C/S_W = 0.16$ . The ratio of the areas of canard and wing not shrouded by the fuselage is  $S_C'/S_W' = 0.078$  which may be regarded as a reasonable value related to practical application. The longitudinal position of the canard in relation to the wing is fixed. However the wind tunnel model allows some variation of the canard's vertical location and setting angle. In the present investigations the special case of a coplanar mid-wing configuration has been studied.

## 2.2 DESCRIPTION OF THE TESTS

The wind tunnel investigations have been carried out at free stream velocities of  $V_\infty = 34$  m/s and  $V_\infty = 40$  m/s, which correspond to Reynoldsnumbers of  $Re = 1.1 \cdot 10^6$  and  $Re = 1.4 \cdot 10^6$ .

Six-component measurements have been carried out for  $-5^\circ \leq \alpha \leq 40^\circ$  with  $\Delta \alpha = 2.5^\circ$  and the angle of sideslip has been varied in the range  $-10^\circ \leq \beta \leq 26^\circ$  with  $\Delta \beta = 2^\circ$ . The aerodynamic coefficients have been evaluated from the measurements using the experimental coordinate system and the reference point shown in Fig. 4. These measurements have been carried out for the wing alone, the canard-off wing-body combination as well as for the canard-wing-body configuration.

Pressure distribution measurements have been carried out for 8 selected angles of attack and for a few angles of sideslip. The test program for the canard-off and the canard-on configuration may be taken from Tab. 2.

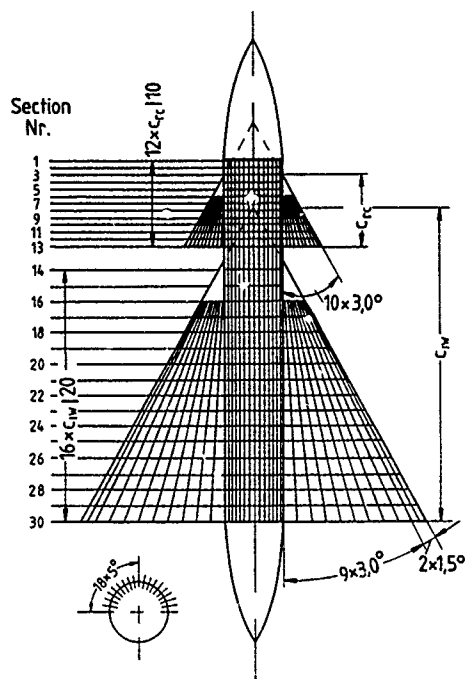


Fig. 3: Positions of the pressure holes on canard, wing and fuselage

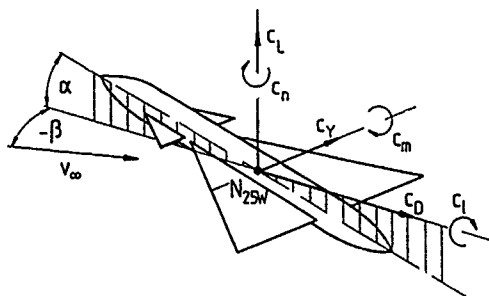


Fig. 4: Experimental coordinate system for wind tunnel data reduction

Tab 2: Test program for the suction side pressure distribution measurements on the canard-off and the canard-on configuration

$\alpha$ [°]	$\beta$ [°]	Remarks
8.7	0	10 20
14.5	0	
19.3	0	6 10 20
24.2	0	10 20 <sup>+</sup>
26.6	0	10 20
29.1	0	
34.1	0	
39.1	0	

+ pressure side also  
canard-on only

In addition the flowfield has been visualized by means of the laser-lightsheet technique. For each position of the wind-tunnel model the lightsheet was adjusted perpendicular to the free stream and moved downstream from the apex of the fuselage to its rear end. The corresponding flow pattern was documented by a video camera on a video tape.

### 3 RESULTS

#### 3.1 VORTEX FORMATION OVER THE CANARD-OFF CONFIGURATION

##### 3.1.1 SIX-COMPONENT MEASUREMENTS

Results of the balance measurements for symmetrical flow  $\beta = 0^\circ$  are shown in Fig. 5. The canard-off wing-fuselage configuration reaches slightly lower lift coefficients compared to the wing alone [21] which represents the well-known interference effect. The wing-fuselage configuration shows larger nose-up pitching moments than the wing alone due to Munk's

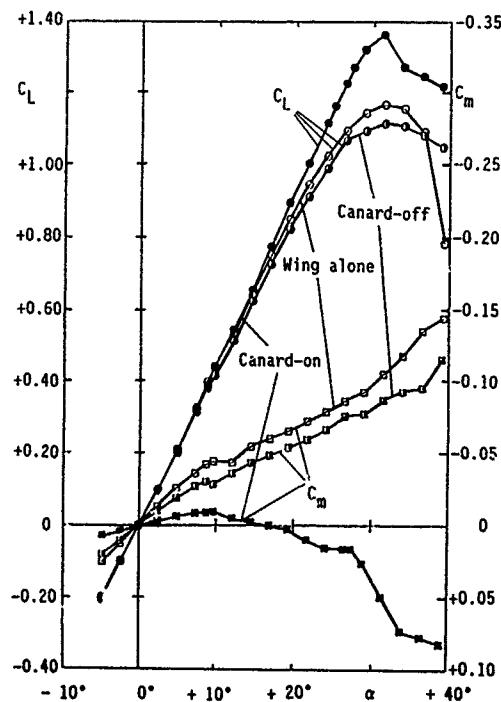
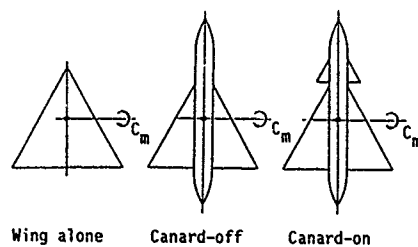


Fig. 5: Results of three-component measurements for wing alone (O □), canard-off (● □) and canard-on (● ■) configuration at  $Re = 1.1 \cdot 10^6$

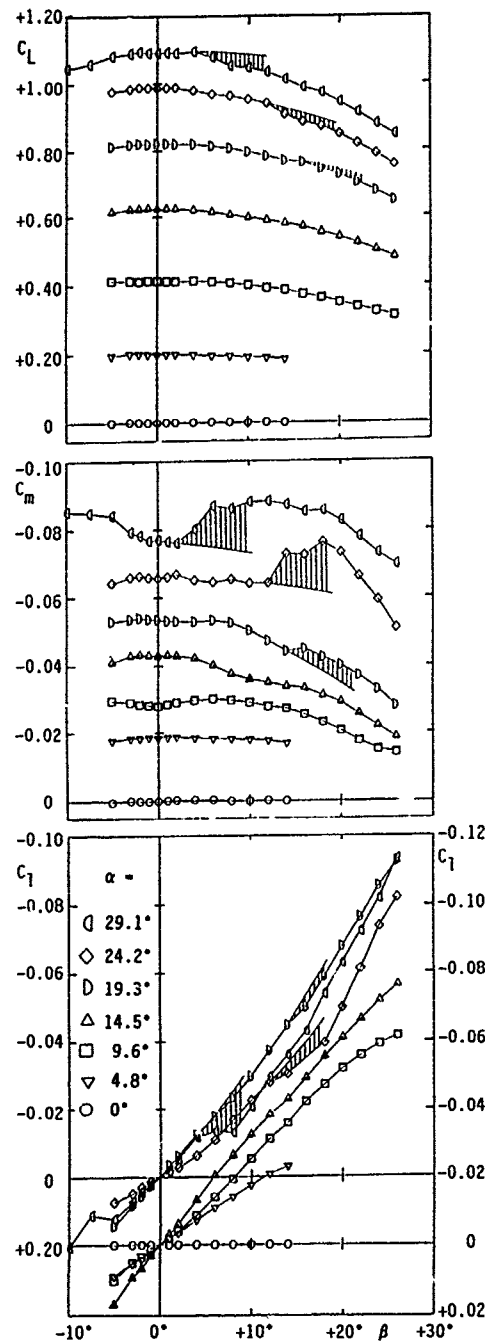


Fig. 6: Results of six-component measurements for the canard-off configuration at  $Re = 1.1 \cdot 10^6$

moment of the fuselage. The slight reductions of lift and nose-down pitching moment slope for  $\alpha > 10^\circ$  indicate the occurrence of vortex breakdown over the wing. The results for the canard-on configuration will be discussed in section 3.2.

Some results of the six-component measurements on the canard-off configuration are plotted in Fig. 6. At low angles of attack lift and pitching moment depend only slightly on the angle of sideslip and the unsymmetry of the flow causes a rolling moment. The drag is closely related to the lift characteristic and side force and yawing moment correspond to the rolling moment characteristic; they are not shown for simplicity. In symmetrical flow vortex breakdown is present over the wing for  $\alpha > 10^\circ$  and in unsymmetrical flow vortex breakdown takes place over the windward side of the wing at even lower angles of attack. The effects of vortex breakdown are not distinctly marked in the aerodynamic characteristics plotted in Fig. 6. This is due to the well known fact, see e. g. D. Hummel, G. Redeker [28], that for a delta wing of aspect ratio  $A = 2.31$  the vortices are relatively weak and the nonlinear effects in the aerodynamic characteristics are small. At larger angles of attack, however, considerable kinks occur in the slopes of the aerodynamic characteristics which are marked in Fig. 6 by hatching. These sudden changes of the aerodynamic coefficients are caused by corresponding changes in the structure of the vortical flow over the configuration which will be analyzed in more detail subsequently.

### 3.1.2 FLOW STRUCTURE IN SYMMETRICAL FLOW

A first sequence of pressure distributions measured on the suction side of the canard-off configuration is shown in Fig. 7 for symmetrical flow  $\beta = 0^\circ$  and angles of attack  $\alpha = 19.3^\circ, 29.1^\circ, 34.1^\circ$  and  $39.1^\circ$ . This series is completed by Fig. 8a for  $\alpha = 8.7^\circ$  and by Fig. 9a for  $\alpha = 24.2^\circ$ . In these pressure distributions the positions of the wing vortices are clearly indicated by distinct suction peaks. At low angles of attack, see e. g. Fig. 8a, no vortex breakdown is present over the wing. The vortex breakdown position crosses the wing trailing-edge for  $\alpha = 10^\circ$  and moves upstream with increasing angle of attack. The vortex breakdown locations given in Figs. 7, 8 and 9 have been determined from the flow visualizations by means of the laser-lightsheet technique. They can also be identified by the characteristic shape of the pressure distributions. Upstream of the breakdown position in the region of a regular vortex formation a very steep suction peak is present. On the other hand downstream of the breakdown position in the region where a deadwater-type flow in the vortex center is surrounded by an ordinarily structured flow, the suction is reduced and the pressure distribution is flattened in spanwise direction. Nevertheless downstream of the breakdown position considerable variation of the suction in spanwise direction is present and the pressure distribution is far away from a deadwater-type structure with constant pressure.

At an angle of attack  $\alpha = 34.1^\circ$  vortex breakdown within the wing vortices occurs very close to the wing apex. For angles of attack  $\alpha > 34.1^\circ$  at the very beginning of a flow around the wing leading-edge the regularly structured front part of the vortex disappears. Consequently downstream of the vortex breakdown position the vortex-type flow in which the deadwater-type flow was embedded so far disappears.

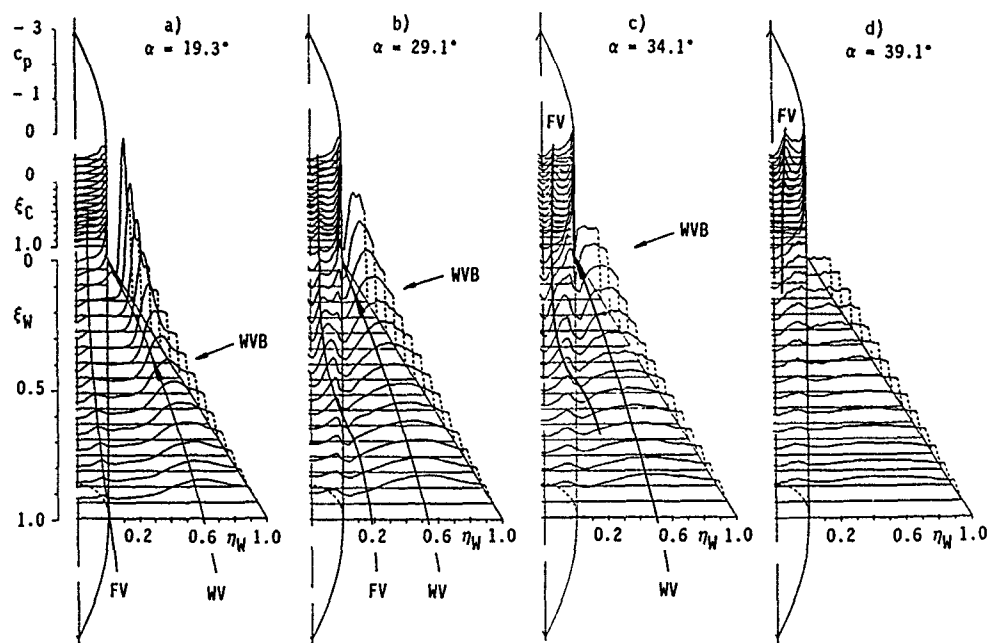


Fig. 7: Suction side pressure distribution for the canard-off configuration in symmetrical flow  $\beta = 0^\circ$  for various angles of attack  $\alpha$ ,  $Re = 1.4 \cdot 10^6$  (WV Wing vortex, FV Fuselage vortex, B Breakdown)

also. This means that a vortex formation along the leading-edge of the wing does no longer exist. At  $\alpha > 34.1^\circ$  the flow structure changes from a vortex-type flow with vortex breakdown to a deadwater-type flow over the wing. For  $\alpha = 39.1^\circ$  the pressure distribution on the upper surface of the wing becomes more or less constant in spanwise and chordwise direction. The change of the flow structure over the wing leads to a reduction of lift and to a certain increase of nose-down pitching moment which can be taken from Fig. 5. No abrupt variations of the aerodynamic coefficients in the region of maximum lift take place. This might be due to some favourable interference effects which will be discussed subsequently.

At low angles of attack, see e. g. Fig. 8a, no fuselage vortices could be detected neither from the flow visualizations nor from the measured pressure distributions. At  $\alpha = 19.3^\circ$  fuselage vortices are definitely formed over the body in front of the wing and their traces can be detected from local suction in the fuselage pressure distribution. A tendency towards merging of the fuselage vortex system into the wing vortex system can easily be recognized from Fig. 7a. With increasing angle of attack the fuselage vortices increase in strength and the tendency towards merging with the corresponding wing vortex increases as well. One has to bear in mind, however, that within the wing vortices vortex breakdown takes place close to the apex of the wing. Therefore the fuselage vortices interfere with wing vortices which are already destroyed by vortex breakdown to a large extent. Details of this kind of interference have not yet been studied. Fig. 7 shows that the traces of the fuselage vortices get lost over the wing for  $\alpha > 30^\circ$ . In this case the fuselage vortices may influence the

deadwater-type flow downstream of the breakdown point in such a way that some flow structures are created there which delay the collapse of vortical flow over the wing. This kind of interference might be responsible for the smooth slope of the aerodynamic coefficients in the region of maximum lift.

### 3.1.3 FLOW STRUCTURE IN UNSYMMETRICAL FLOW

A second sequence of pressure distributions measured on the suction side of the canard-off configuration is shown in Fig. 8 for a low angle of attack  $\alpha = 8.7^\circ$  and various angles of sideslip  $\beta$ . In symmetrical flow  $\beta = 0^\circ$  no vortex breakdown is present over the wing, but the breakdown position is located close to the trailing-edge downstream of the wing. With increasing angle of sideslip the wing vortex on the windward side moves inboard and the wing vortex on the leeward side moves outboard. In the wing vortex on the windward side the vortex breakdown position moves upstream with increasing angle of sideslip. This behaviour is well known for delta wings, see e. g. D. Hummel, G. Redeker [28]. Up to an angle of sideslip of  $\beta = 10^\circ$  no fuselage vortex could be detected from the pressure distributions as well as from the flow visualizations. For  $\beta = 20^\circ > \alpha$  a small fuselage vortex can be recognized from some suction in the fuselage pressure distribution. This vortex passes downstream to the leeward side and causes suction on the wing and on the fuselage in the region of the wing body junction. A corresponding counter-rotating fuselage vortex from the leeside is located on the lower side of the configuration. The fuselage vortex system remains separate from the wing

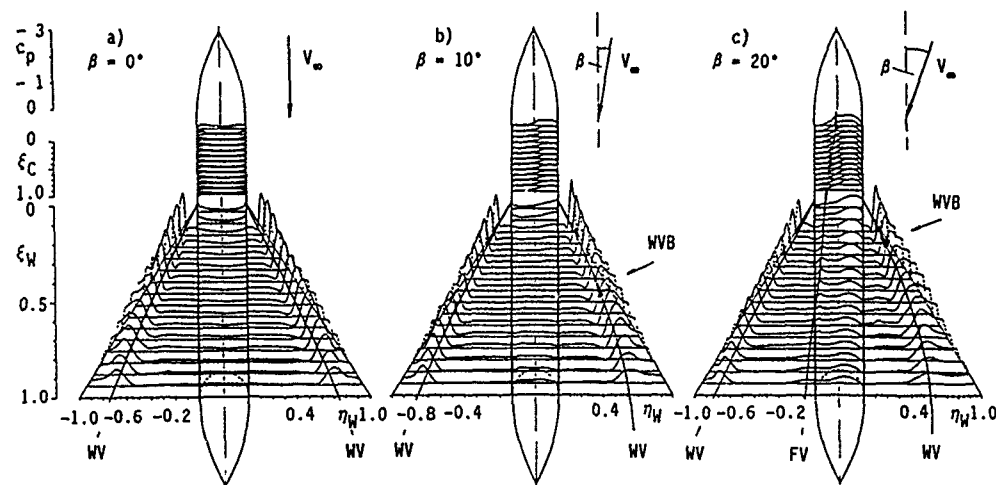


Fig. 8: Suction side pressure distributions for the canard-off configuration at angle of attack  $\alpha = 8.7^\circ$  and different angles of sideslip  $\beta$ ,  $Re = 1.4 \cdot 10^6$  (WV Wing vortex, FV Fuselage vortex, B Breakdown)

vortex system. Its effect on the pressure distribution and the aerodynamic coefficients is very small.

Another sequence of pressure distributions measured on the suction side of the canard-off configuration is shown in Fig. 9 for a moderate angle of attack  $\alpha = 24.2^\circ$  and various angles of sideslip  $\beta$ . In this case vortex breakdown takes place far upstream over the wing even in symmetrical flow  $\beta = 0^\circ$ . The steep and pointed pressure distributions upstream and the flattened distributions downstream of the breakdown position are clearly indicated. With increasing angle of sideslip the whole vortex system moves towards the leeward side of the configuration. Vortex breakdown within the wing vortices moves downstream on the

leeward side and upstream on the windward side. At an angle of sideslip of  $\beta = 10^\circ$  vortex breakdown on the windward side of the wing reaches the wing apex. In this situation the same change of the flow structure as described for  $\alpha = 34.1^\circ$  in symmetrical flow now takes place on the windward side of the wing. At the very beginning of a flow around the leading-edge the regularly structured front part of the vortex disappears. Consequently downstream of the vortex breakdown position the vortex-type flow in which the dead-water-type flow was embedded so far disappears also. This means that a vortex formation along the windward leading-edge of the wing does no longer exist. A sudden change of the flow structure from a vortex-

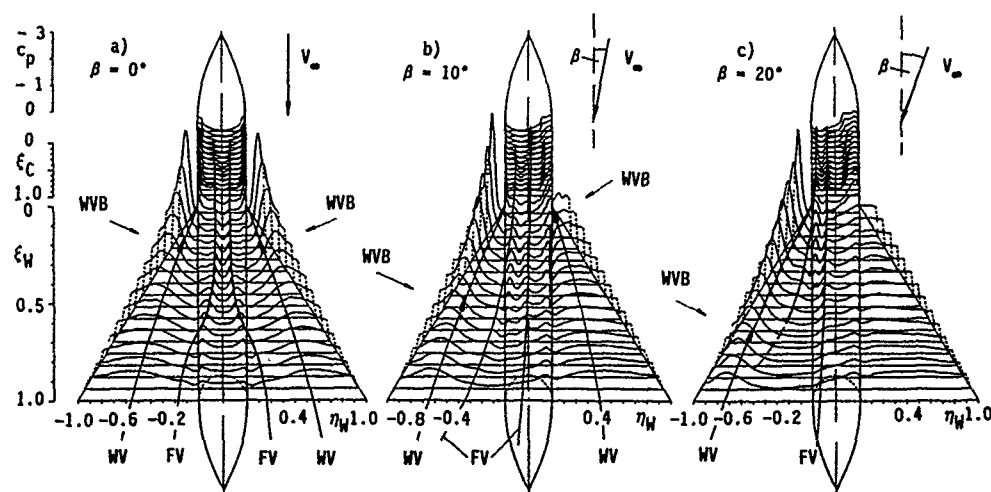


Fig. 9: Suction side pressure distributions for the canard-off configuration at angle of attack  $\alpha = 24.2^\circ$  and different angles of sideslip  $\beta$ ,  $Re = 1.4 \cdot 10^6$  (WV Wing vortex, FV Fuselage vortex, B Breakdown)



type flow with vortex breakdown to a deadwater-type flow takes place. The pressure distribution becomes constant in spanwise and chordwise direction over the whole windward side of the wing and this indicates that a deadwater-type flow is present over this part of the configuration. The sudden change of the flow structure and of the corresponding pressure distribution on the windward side of the wing leads to losses in lift and to additional positive rolling moments as well as to a considerable increase of the nose-down pitching moment. These modifications of the aerodynamic coefficients are clearly marked in Fig. 6. However, this change of the flow structure leads in symmetrical flow at high angles of attack to a smooth variation of the aerodynamic coefficients whereas in unsymmetrical flow at moderate angles of attack abrupt changes in the aerodynamic characteristics occur. The reason for this difference might be the influence of the fuselage vortices. At high angles of attack in symmetrical flow a considerable effect of the fuselage vortices on the deadwater-type flow of the wing is present. In unsymmetrical flow at moderate angles of attack, however, the windward fuselage vortex remains always separate from the wing vortex. In Figs. 9b and 9c this vortex passes even to the leeward side of the fuselage. Therefore the fuselage vortex of the windward side does not influence the windward wing flow. The result is a sudden collapse from vortex-type flow to deadwater-type flow on the windward side of the wing and this sudden change of the flow structure leads to the abrupt modifications of the aerodynamic coefficients.

The flow structure at the canard-off configuration for different angles of attack  $\alpha$  and various angles of sideslip  $\beta$  is documented in Fig. 10 for the right-hand half of the wing. For  $\beta > 0$  this half represents the windward side and for  $\beta < 0$  the leeward side. The lower border marks the occurrence of vortex breakdown at the trailing-edge of the wing. It is not distinctly recognized in the results of the six-component measurements, since the nonlinearities are small for a wing of aspect ratio  $A = 2.31$ . The upper border is related to the collapse of vortical-type flow over the wing and to the establishment of a deadwater-type flow over the wing. This collapse is distinctly marked in the six-component measurements. With

decreasing angle of attack the changes in the aerodynamic derivatives at increasing angles of sideslip occur more and more abruptly.

### 3.2 VORTEX FORMATION OVER THE CANARD-ON CONFIGURATION

#### 3.2.1 SIX-COMPONENT MEASUREMENTS

The results of the balance measurements for symmetrical flow are shown in Fig. 5 already. Adding the canard to the wing-fuselage configuration leads to a considerable increase of lift and to a reduction of nose-down pitching moment. This behaviour is well known from the previous investigations of D. Hummel, H.-Chr. Oelker [22 - 26] and H.-Chr. Oelker [21], but one has to bear in mind that although the same canard and the same wing have been used the configurations were different. Due to the thick fuselage in the present investigations the ratio of the unshrouded areas  $S_C^*/S_W^*$  of canard and wing is much smaller than in the previous investigations with an extremely thin fuselage. Nevertheless the interference mechanisms are obviously quite similar. The additional lift at the canard is mostly compensated by lift losses at the wing through downwash effects. Thus lift is shifted towards the canard which leads to additional nose-up pitching moments. The increase of lift at higher angles of attack is due to favourable interference effects [21], [22] by which vortex breakdown within the vortices of canard and wing is suppressed simultaneously. The effective angle of attack of the wing is reduced by the downwash of the canard and this leads to a delay of wing vortex breakdown. By adding the canard to the wing-fuselage configuration vortex breakdown over the wing is shifted from  $\alpha > 10^\circ$  for the canard-off configuration to  $\alpha > 17^\circ$  for the canard-on configuration. On the other hand the wing vortex system induces an acceleration of the flow mainly in the region of the canard's trailing-edge and therefore vortex breakdown does not take place within the canard vortices over the canard up to very large angles of attack.

Results of the six-component measurements on the canard-on configuration are plotted in Fig. 11. At a first glance they are very similar to those for the canard-off configuration according to Fig. 6. In symmetrical flow  $\beta = 0^\circ$  the vortex breakdown position traverses the wing trailing-edge at  $\alpha = 17^\circ$  and in unsymmetrical flow vortex breakdown takes place over the windward side of the wing at even lower angles of attack. Again the effects of vortex breakdown are not distinctly marked in the aerodynamic characteristics according to Fig. 11 since the nonlinear effects are relatively small. At larger angles of attack  $\alpha > 24^\circ$  sudden changes in the aerodynamic characteristics similar to those on the canard-off configuration take place. However the losses of lift and of negative rolling moment as well as the additional nose-down pitching moments are much larger for the canard-on configuration than for the canard-off configuration. The corresponding changes in the structure of the flow will be analyzed in detail subsequently.

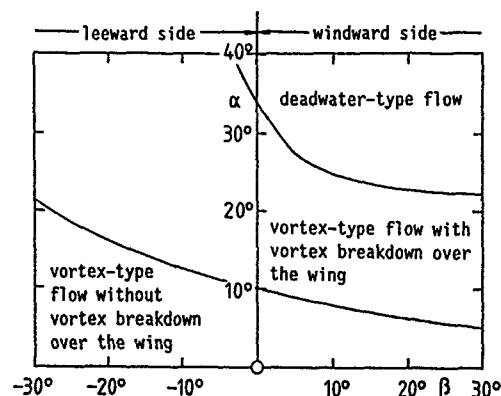


Fig. 10: Flow structure on the canard-off configuration for different angles of attack  $\alpha$  and various angles of sideslip  $\beta$  (Flow state is documented for the right-hand half wing)

#### 3.2.2 FLOW STRUCTURE IN SYMMETRICAL FLOW

A series of pressure distributions measured on the suction side of the canard-on configuration is shown

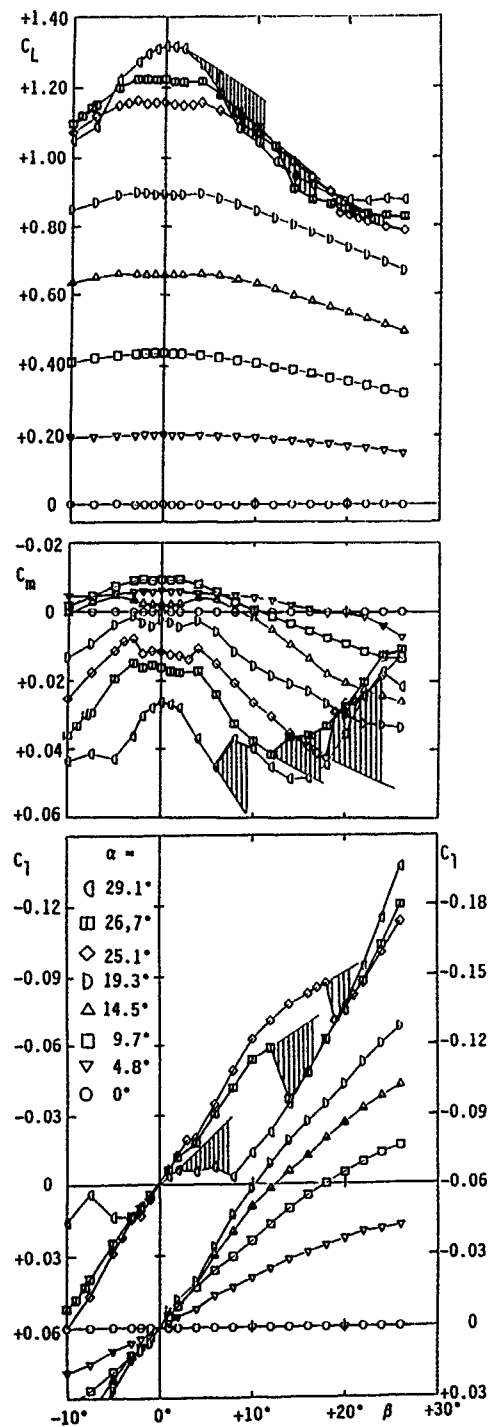


Fig. 11: Results of six-component measurements for the canard-on configuration at  $Re = 1.1 \cdot 10^6$

in Fig. 12 for symmetrical flow  $\beta = 0^\circ$  and angles of attack  $\alpha = 19.3^\circ$ ,  $29.1^\circ$ ,  $34.1^\circ$  and  $39.1^\circ$ . This sequence is completed by Fig. 13a for  $\alpha = 24.1^\circ$ . At

low angles of attack  $\alpha < 20^\circ$  the vortex systems of wing and canard remain separate from each other over the whole configuration, but a tendency towards merging of the two vortex systems is clearly indicated. With increasing angle of attack the canard vortices move downwards and outwards over the rear part of the configuration. The traces of the canard vortices are marked in the pressure distributions by some local suction in the wing's pressure distribution. For  $\alpha > 28^\circ$  the merging process of the two vortex systems takes place over the wing. This behaviour is quite different from that found in the previous investigations by D. Hummel, H.-Chr. Oelker [22 - 26] and H.-Chr. Oelker [21] in which separate vortex systems have been detected. The difference in the flow structure is due to the fact that although the same canard and the same wing have been used the unshrouded areas of canard and wing were different for the two fuselage widths. This means that the interference between canard and wing depends sensitively on the relative positions of the interacting vortex systems.

The fuselage vortices on the canard-on configuration are difficult to detect from the pressure distributions according to Figs. 12a and 13a as well as from the flow visualizations. Some suction in the pressure distribution on the fuselage in the region of the canard indicates the existence of fuselage vortices. They are much weaker than at the canard-off configuration according to Fig. 7 since for the canard-on configuration the free-floating nose of the fuselage is considerably shorter. The relatively large suction on the fuselage close to the junction with the wing should not be mis-interpreted as generated by fuselage vortices. These low pressures are caused by the nearby canard vortices in the case of the canard-on configuration (Fig. 12) and by the wing vortices in the case of the canard-off configuration (Fig. 9b). This suction on the fuselage contour must be regarded as a thickness effect. Fig. 12 indicates that with increasing angle of attack a tendency for merging of the fuselage vortices into the canard-wing-vortex system is present. This means that at very high angles of attack  $\alpha > 28^\circ$  in symmetrical flow  $\beta = 0^\circ$  a merged vortex system exists over the configuration which consists of the vortices from wing, canard and fuselage.

The process of vortex merging over the rear part of the configuration causes considerable effects related to the pressure distributions according to Fig. 12 and to the aerodynamic coefficients according to Fig. 5. For the canard-on configuration the upstream movement of the breakdown position in the wing vortices with increasing angle of attack is extremely reduced. This important fact is quite obvious from a comparison of Figs. 7 and 12. Furthermore the favourable upstream influence of the wing vortex flow on the canard is large and due to this effect vortex breakdown does not occur within the canard vortices up to very large angles of attack. To maintain a vortex-type flow on the canard at these high angles of attack is only possible through the interference effects from the wing.

At very high angles of attack this interference is very complicated due to the fact that the canard vortices show a bubble-type flow structure in the region between canard and wing. This phenomenon has been demonstrated by D. Hummel, H.-Chr. Oelker [21], [22], but it is not yet fully understood. Downstream

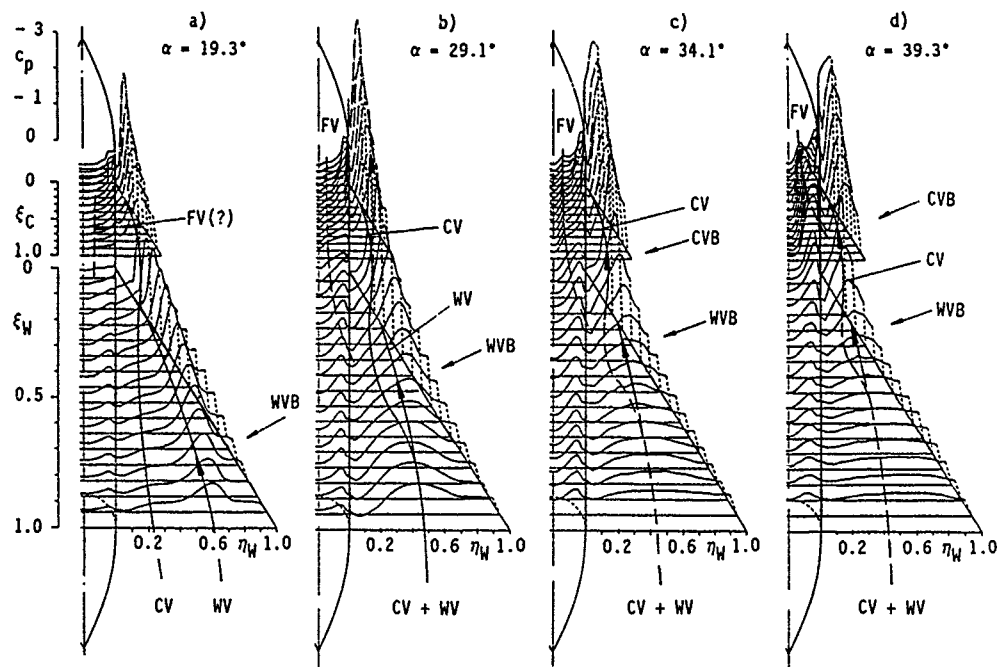


Fig. 12: Suction side pressure distributions for the canard-on configuration in symmetrical flow ( $\beta = 0^\circ$ ) for various angles of attack  $\alpha$ ,  $Re = 1.4 \cdot 10^6$  (WV Wing vortex, FV Fuselage vortex, CV Canard vortex, B Breakdown)

of the trailing-edge of the canard the vortices stretch considerably in radial direction and form a bubble in their center, but due to the acceleration of the flow by the wing this bubble closes again in the vicinity of the wing's leading-edge and more downstream over the wing ordinarily structured canard vortices without vortex breakdown are present. This bubble type structure of the canard vortices has been observed by H.-Chr. Oelker [21] for angles of attack  $\alpha > 14^\circ$  on the configuration with a thin fuselage and this phenomenon is also present within the canard vortices on the present configuration.

For  $\alpha > 17^\circ$  vortex breakdown takes place in the wing vortices over the wing, but the effects on lift and pitching moment remain relatively small due to the slow upstream movement of the breakdown position with increasing angle of attack. At  $\alpha \approx 32^\circ$  the maximum lift coefficient is reached for the canard-on configuration, and its value is much larger than for the canard-off configuration according to Fig. 5. The flow structure in this region is characterized by wing vortex breakdown at  $\xi_W = 0.4$  and by a vortex-type flow at the canard. For even larger angles of attack the destruction of the merged vortex system over the wing continues. The pressure distributions in the rear part of the wing indicate considerable reductions of suction, which might be due to changes in the flow structure of the canard vortices downstream of the bubble region. This leads at first to a loss of lift on the wing and to a corresponding increase of the nose-up pitching moment according to Fig. 5. The pressure distributions measured at the canard for  $\alpha = 34.1^\circ$  and  $39.1^\circ$  show still very high suction generated by a vortex-type flow there, but the favourable interference from the wing vortices is no longer able to avoid vortex breakdown at the

canard. The bubble within the canard vortices is no longer closed at its rear end and this means that a final breakdown of the canard vortices takes place. The breakdown position moves upstream over the canard and causes reductions of the suction which are clearly indicated in Fig. 12. This means that at very large angles of attack the lift loss is also extended to the canard and this leads to additional nose-down pitching moments, see Fig. 5.

The change of the flow structure from a vortex-type to a deadwater-type flow at high angles of attack on the present configuration is very complicated in detail. Therefore much more investigations are necessary to understand the bubble phenomenon, its relation to vortex breakdown and its contribution to the decay of vortical flow.

### 3.2.3 FLOW STRUCTURE IN UNSYMMETRICAL FLOW

A sequence of pressure distributions measured on the suction side of the canard-on configuration for an angle of attack of  $\alpha = 24.2^\circ$  and various angles of sideslip is shown in Fig. 13. In symmetrical flow  $\beta = 0^\circ$  vortex breakdown takes place in the wing vortices over the rear part of the configuration. In unsymmetrical flow within the wing vortex system vortex breakdown moves upstream on the windward side and downstream on the leeward side. The tendency towards merging between the vortex systems of canard and wing decreases on the windward side and increases on the leeward side of the configuration. At  $\beta = 10^\circ$  on the windward side the wing vortex (with vortex breakdown) is separate from the canard vortex. On the leeward side vortex breakdown has disappeared and

merging of the canard vortex into the wing vortex takes place. At  $\beta = 20^\circ$  the merging process of the two vortices on the leeward side has further developed and in this case the wing vortex may be regarded as the continuation of the canard vortex close to the leeward leading-edge. On the windward side of the configuration, however, the flow structure has completely changed. Vortex breakdown within the wing vortex takes place far upstream and only a small portion of the wing vortex close to the wing apex has the ordinary structure without vortex breakdown. This wing vortex which is destroyed to a large extent by vortex breakdown is no longer able to avoid vortex breakdown within the canard vortex by means of favourable induced velocities. This means that with increasing angle of sideslip  $\beta$  vortex breakdown suddenly occurs within the canard's vortex system on the windward side. Details of the destruction of the bubble-type canard vortex flow and the abrupt occurrence of vortex breakdown within the canard vortices over the canard are not known at present. The vortex breakdown position moves upstream very rapidly and already at  $\beta = 20^\circ$  the canard vortex is completely destroyed by vortex breakdown and a deadwater-type flow is present over the windward side of the canard. The corresponding changes in the pressure distribution lead to sudden losses of lift, of nose-up pitching moment and of negative rolling moment which are clearly indicated in the results of the six-component measurements according to Fig. 11.

The sudden changes of the aerodynamic characteristics at high angles of attack for the canard-off and the canard-on configuration according to Figs. 6 and 11 are closely related to the collapse of vortical flow on the windward side of the configuration. For the canard-off configuration this collapse is caused by the facts that the breakdown position in the windward wing vortex reaches the apex of the wing and that a vortex-type flow separation at the wing leading-edge no longer takes place. For the canard-on configuration the situation is much more complicated due to the interference between wing and

canard. In this case the collapse of a vortical flow on the windward side of the canard is caused by the sudden loss of favourable interference effects from the wing by which a vortical flow without vortex breakdown at the canard had been established so far. After the collapse of the windward canard flow a deadwater region generated by the canard interferes with the vortex-type flow (with vortex breakdown) over the windward side of the wing. The final collapse of vortical flow on the windward side of the configuration takes place when the vortex breakdown position with the windward wing vortex reaches the apex of the wing.

The system of fuselage vortices on the canard-on configuration is difficult to detect from the pressure distributions according to Fig. 13 as well as from the flow visualizations. In symmetrical flow  $\beta = 0^\circ$  some suction in the pressure distribution on the fuselage in the region of the canard indicates the existence of fuselage vortices. They are much weaker than at the canard-off configuration according to Fig. 9 since for the canard-on configuration the free floating nose of the fuselage is considerably shorter. With increasing angle of sideslip the fuselage vortices increase in strength due to reduced screening of the fuselage nose by the canard. The trace of the windward fuselage vortex for  $\beta = 10^\circ$  and  $\beta = 20^\circ$  is clearly indicated by local suction. This vortex passes separately over the leeward parts of fuselage and wing. In this case a favourable influence of the fuselage vortex on the flow over the windward side of the wing does no longer exist and since also the interference between the canard vortex and the wing vortex on the windward side of the wing is reduced with increasing angle of sideslip, the wing vortex is rapidly destroyed there by means of vortex breakdown. The leeward fuselage vortex merges quickly into the canard-wing vortex system with increasing angle of sideslip.

The flow structure at the canard-on configuration for different angles of attack and various angles of sideslip is documented in Fig. 14 for the right-hand

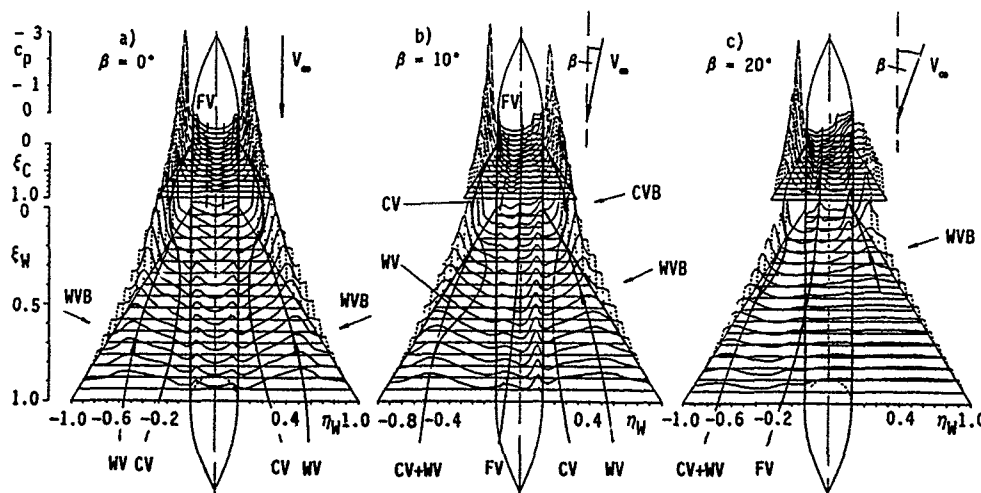


Fig. 13: Suction side pressure distributions for the canard-on configuration at angle of attack  $\alpha = 24.2^\circ$  and different angles of sideslip  $\beta$ ,  $Re = 1.4 \cdot 10^6$  (WV Wing vortex, FV Fuselage vortex, CV Canard vortex; B Breakdown)

half of the configuration. The lower border marks the occurrence of vortex breakdown within the wing vortices at the trailing-edge of the wing. In comparison with the flow states at the canard-off configuration according to Fig. 10 this border has been generally shifted towards higher angles of attack due to the favourable effects of the canard on the wing. This shift is small on the windward side and large on the leeward side since the favourable merging process takes place mainly on the leeward side. This lower border is again not distinctly marked in the results of the six-component measurements since the nonlinear effects are small. At large angles of attack a second border indicates the occurrence of vortex breakdown within the canard vortices at the trailing-edge of the canard. The contribution of the bubble-type canard vortex flow to this process needs further investigations. The second border is well documented by the six-component measurements, the pressure distribution measurements as well as by the flow visualizations up to an angle of attack of  $\alpha = 27.5^\circ$ . For even larger angles of attack all lines in the diagram are dashed and they are still subject to some discussion. The second border should pass to the leeward side of the configuration at very high angles of attack since the favourable interference effects should get lost on this side also. After crossing the second border at large angles of sideslip the vortex-type flow collapses abruptly and a deadwater-type flow is present over the canard. For small angles of sideslip in the vicinity of the symmetrical case  $\beta = 0^\circ$ , however, a small corridor exists in which a vortex-type flow is present over the canard which has been documented by Fig. 12 up to very large angles of attack. At high angles of attack  $\alpha$  and large angles of sideslip  $\beta$  a third border should occur which marks the final collapse of a vortex-type flow close to the apex of the wing. That part of Fig. 14 which is given in dashed lines needs further investigations.

#### 4. CONCLUSIONS

A close-coupled canard-wing-body combination has been investigated both in symmetrical and unsymmetrical flow. The coplanar mid-wing configuration consisted of a delta canard and a delta wing of aspect ratios  $A_C = A_W = 2.31$  and a body of revolution as fuselage. Six-component and surface pressure distribution measurements as well as laser-lightsheet flow visualizations have been carried out at Reynoldsnumbers  $Re = (1.1)1.4 \cdot 10^6$  for the canard-off and the canard-on configuration.

On the canard-off configuration a system of wing vortices has been found for all angles of attack whereas fuselage vortices could be detected for larger angles of attack and/or sideslip only. In symmetrical flow,  $\beta = 0^\circ$ , vortex breakdown is present in the wing vortices for  $\alpha > 10^\circ$ . With increasing angle of attack the fuselage vortices merge into the wing vortices and this leads to a delay in the upstream movement of the vortex breakdown position within the wing vortices. At  $\alpha > 34^\circ$  vortex breakdown reaches the apex of the wing and a collapse of the vortex-type flow into a deadwater-type flow over the wing takes place. Correspondingly lift is reduced and a certain increase of the nose-down pitching moment is observed. In unsymmetrical flow,  $\beta \neq 0^\circ$ , unsymmetrical vortex breakdown occurs within the wing

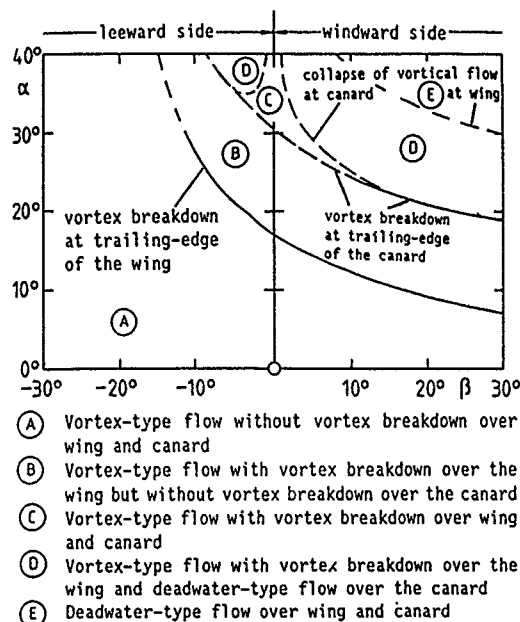


Fig. 14: Flow structure on the canard-on configuration for different angles of attack  $\alpha$  and various angles of sideslip  $\beta$  (Flow state is documented for the right-hand half of the configuration)

vortices. The tendency towards merging the fuselage vortices into the wing vortices increases on the leeward side and decreases on the windward side of the configuration. The collapse of the vortex-type flow takes place at first on the windward side. This causes losses of lift and of negative rolling moments as well as an increase of nose-down pitching moments. With increasing angle of attack the sudden change of the flow structure takes place at a lower angle of sideslip and the abruptness of the corresponding changes in the aerodynamic coefficients is reduced due to the increasing interference effects from the merging fuselage vortices.

On the canard-on configuration a vortex formation has been observed on the wing and on the canard. Fuselage vortices could be detected for large angles of attack and/or sideslip only, and these vortices were much weaker than those for the canard-off configuration due to the shorter free floating front part of the fuselage. In symmetrical flow,  $\beta = 0^\circ$ , at first all three vortex systems developed separate from each other, but the tendency towards merging the canard vortices into the wing vortices and the fuselage vortices into the canard-wing vortices increased with increasing angle of attack. Between canard and wing a very strong interference is present. The lift gain at the canard is compensated by a lift loss at the wing due to the downwash effects caused by the canard. At larger angles of attack a delay of vortex breakdown is observed at the wing due to the same downwash effects and also at the canard through a favourable upstream influence from the wing which causes an acceleration of the flow over the upper surface of the canard. Vortex breakdown takes place over the configuration within the wing vortices for  $\alpha > 17^\circ$  and within the canard vortices for  $\alpha >$

31°. In unsymmetrical flow the whole vortex system moves towards the leeward side of the configuration. The tendency towards merging of the vortices increases on the leeward side and decreases on the windward side. At larger angles of attack unsymmetrical vortex breakdown takes place within the wing vortices first and at even larger angles of attack also within the canard vortices. The occurrence of vortex breakdown at the canard is due to the sudden loss of favourable interference effects from the wing. At larger angles of sideslip the vortex-type flow over the windward side of the canard collapses abruptly into a deadwater-type flow and this causes sudden losses of lift and of negative rolling moment as well as an additional nose-down pitching moment. For very low angles of sideslip, however, a small corridor exists in which the interference between wing and canard still keeps a vortex-type flow with vortex breakdown at the canard up to extremely large angles of attack.

## REFERENCES

- [1] H. Behrbohm: Basic low speed aerodynamics of the short-coupled canard configuration of small aspect ratio. Saab TN 60 (1965).
- [2] D. W. Lacey, St. J. Chorney: Subsonic aerodynamic characteristics of close-coupled canards with varying area and position relative to a 50° swept wing. Naval Ship Research and Development Center, Techn. Note AL-199 (1971).
- [3] J. R. Krouse: Effects of canard planform on the subsonic aerodynamic characteristics of a 25° and a 50° swept-wing research aircraft model. Naval Ship Research and Development Center, Evaluation Report AL-91 (1972).
- [4] J. Ottensooser: Wind tunnel data on the transonic aerodynamic characteristics of close coupled canards with varying planform position and deflection relative to a 50° swept wing. Naval Ship Research and Development Center, Test Report AL-88 (1972).
- [5] D. W. Lacey: Transonic characteristics of close-coupled canard and horizontal tail installed on a 50 degree sweep research aircraft model. Naval Ship Research and Development Center, Evaluation-Report AL-81 (1972).
- [6] B. B. Gloss, L. W. McKinney: Canard-wing lift interference related to manoeuvring aircraft at subsonic speeds. NASA TM X-2897 (1973).
- [7] B. B. Gloss: Effect of canard location and size on canard-wing interference and aerodynamic-center shift related to manoeuvring aircraft at transonic speeds. NASA TN D-7505 (1974).
- [8] W. P. Henderson: The effect of canard and vertical tails on the aerodynamic characteristics of a model with a 59° sweptback wing at a Mach number of 0.30. NASA TM X-3088 (1974).
- [9] B. B. Gloss: The effect of canard leading-edge sweep and dihedral angle on the longitudinal and lateral aerodynamic characteristics of a close-coupled canard-wing configuration. NASA TN D-7814 (1974).
- [10] B. B. Gloss: Effect of wing planform and canard location and geometry on the longitudinal aerodynamic characteristics of a close-coupled canard wing model at subsonic speeds. NASA TN D-7910 (1975).
- [11] R. P. Boyden: Subsonic dynamic stability characteristics of two close-coupled canard-wing configurations. NASA TP-1291 (1978).
- [12] B. B. Gloss: Effect of camber on the trimmed lift capability of a close-coupled canard-wing configuration. NASA TM 78686 (1978).
- [13] B. B. Gloss, E. J. Rav, K. E. Washburn: Effect of canard vertical location, size and deflection on canard-wing interference at subsonic speeds. NASA TM 78790 (1978).
- [14] R. B. Eberle, R. T. Stancil, W. C. Fowler: A critical review of canard relative to aft horizontal tail based on low- and high-speed tunnel tests of a fighter/attack configuration. AIAA-Paper No. 71-8 (1971).
- [15] S. E. Goldstein, C. P. Combs: Trimmed drag and maximum flight efficiency of aft tail and canard configurations. AIAA-Paper No. 74-69 (1974).
- [16] H. John, W. Kraus: High angle of attack characteristics of different fighter configurations. AGARD-CP-247 (1978), 2-1 to 2-12.
- [17] W. Kraus: Delta canard configuration at high angle of attack. Z. Flugwiss. Weltraumforsch. Z (1983), 41 - 46.
- [18] J. Er-El, A. Seginer: Vortex trajectories and breakdown on wing-canard configurations. J. Aircraft 22 (1985), 641 - 648.
- [19] G. Drougge: The international vortex flow experiment for computer code validation. ICAS-Proceedings 1988, Vol. 1, XXXV - XLI.
- [20] A. Elsenaar, L. Hjeltnberg, K. Bütetisch, W. J. Bannink: The international vortex flow experiment. AGARD-CP-437 (1988), 9-1 to 9-23.
- [21] H.-Chr. Oelker: Aerodynamische Untersuchungen an kurzgekoppelten Entenkonfigurationen bei symmetrischer Anströmung. Dissertation TU Braunschweig 1990. Zentrum für Luft- und Raumfahrt-technik der TU Braunschweig, Forschungsbericht 90-01 (1990).
- [22] D. Hummel, H.-Chr. Oelker: Vortex interference effects on close-coupled canard configurations in incompressible flow. Proceedings of the Symposium on the International Vortex Flow Experiment on Euler Code Validation, Stockholm, October 1 - 3, 1986, Flygtekniska Forsöksanstalten, Bromma, Schweden. (1986), 47 - 61.
- [23] H.-Chr. Oelker, D. Hummel: Experimentelle Untersuchungen an Entenkonfigurationen. DGLR-Bericht 86-03 (1986), 172 - 191.
- [24] D. Hummel: Documentation of separated flows for computational fluid dynamics validation. AGARD-CP-437 (1988), Vol. 2, P 15-1 to P 15-24.
- [25] H.-Chr. Oelker, D. Hummel: Investigations on the vorticity sheets of a close-coupled delta-canard configuration. ICAS-Proceedings 1988, Vol. 1, 649 - 662. See also J. Aircraft 26 (1989), 657 - 666.
- [26] D. Hummel, H.-Chr. Oelker: Effects of canard position on the aerodynamic characteristics of a close-coupled canard configuration at low speed. AGARD-CP-465 (1989), 7-1 to 7-18.
- [27] D. Hummel: On the vortex formation over a slender wing at large angles of incidence. AGARD-CP-247 (1978), 15-1 to 15-17.
- [28] D. Hummel, G. Redeker: Über den Einfluß des Aufplatzens der Wirbel auf die aerodynamischen Beiwerte von Deltaflügeln mit kleinem Seitenverhältnis beim Schiebeflug. Jb. 1967 der WGLR, 232 - 240.

# AN EXPERIMENTAL STUDY OF THE FLOW OVER A SHARP-EDGED DELTA WING AT SUBSONIC AND TRANSONIC SPEEDS<sup>\*)</sup>

by

A. Eisenaar and H.W.M. Hoeijmakers  
National Aerospace Laboratory NLR  
Amsterdam, The Netherlands

## SUMMARY

The flow about a sharp-edged cropped delta wing is investigated experimentally. The experiment comprised detailed surface pressure measurements at low-subsonic, transonic and low-supersonic free-stream Mach numbers for angles of attack up to 27 deg. The major part of the measurements were carried out at a Reynolds number of 9 million, but some data was also obtained at lower and at higher Reynolds numbers. The investigation included continuous schlieren flow-field visualization as well as surface-flow visualizations at a limited number of free-stream conditions. The analysis of the measured data embraced flow-field phenomena such as primary separation and the formation of the leading-edge vortex, secondary separation and the formation of the secondary vortex, shock waves and the onset of vortex breakdown. Considered are the influence of Mach number, incidence and Reynolds number on these flow features.

## 1. INTRODUCTION

The vortical flow over highly swept delta wings has raised the interest of the aerodynamic community since more than forty years. The introduction of leading edge sweep postponed the adverse effects of compressibility to higher Mach numbers, thus allowing more efficient flight at greater speeds. At high angles of attack the vortex that is formed due to flow separation at the leading edge interacts with the flow over the wing upper surface, resulting in a lift increase and hence improving the take-off and landing performance. This vortex induced lift increment is also beneficial at transonic and supersonic speed where it contributes to the manoeuvring capabilities of fighter aircraft.

The vortical flow on delta wings has been studied extensively in the past though mainly at subsonic (e.g. Refs. 1, 2, 3, 4, 5, 6 and 7) or supersonic (e.g. Refs. 8, 9 and 10) and not as much at transonic speeds (e.g. Refs. 11 and 12). The prediction of the aerodynamic characteristics of configurations with vortical type of flow could for a long time only be done with semi-empirical methods or with methods requiring an a priori knowledge on the (simple) topology of the vortical-flow structures. However, the improvements in computing power over the last decade have enabled numerical simulation of these complicated flows by solving the Euler or (Reynolds-averaged) Navier Stokes equations. These new capabilities stimulated the interest of the CFD community in vortical flows and numerous papers have been published over the last 5 years that show impressively the degree of sophistication that has been achieved today in the simulation of this type of flow.

The latter type of computational methods provide the detailed flow field quantities as an integral part of the numerical solution. This gives the researcher the opportunity to investigate in detail the structure of the flow field and to unravel the flow features that determine the surface pressure

distribution and with that the aerodynamic forces and moments experienced by the aircraft.

To validate and further improve these computational tools there continues to be a strong need for detailed experimental data especially in the transonic flow regime. With this in mind, a joint experimental and theoretical program was carried out between 1983 and 1987, known as the "The International Vortex Flow Experiment on Euler Code Validation" (see Ref. 13). The parties involved in this rather successful international cooperation were FFA, NLR, AFAL, DLR, MBB, DORNIER and the Technical Universities of Delft and Braunschweig. Experimentally the program concentrated on a 65-deg cropped delta wing with a sharp, round or a drooped leading edge, although other configurations (55-deg cropped delta wing, addition of a canard) were tested as well. At NLR wind-tunnel tests were carried out on a model with interchangeable leading edge (the "AFAL model") for Mach numbers between 0.4 and 4.0. The experimental data obtained include surface pressure distributions, surface flow visualisations as well as flow-field surveys. Also DLR, FFA and the two universities contributed to the experimental part of the program. Ref. 13 describes all experimental work as well as the application of computational methods to numerically simulate the flow. A review of this cooperative effort, including a list of recommended test cases can be found in Ref. 14.

The analysis of the experimental data carried out within the framework of the international program, concentrated primarily on the round leading edge configuration. A round leading edge is of greater practical interest but the flow about a round-edged configuration is also more complicated as far as its flow physics is concerned. The part-span flow separation at the wing leading edge, which governs the build-up and strength of the leading-edge vortex is a complex phenomenon, that strongly depends on the leading-edge radius in combination with the Mach number, Reynolds number and incidence. The situation is considerably less complex in the case of a sharp-edged configuration for which flow separation will take place all along the leading edge and a full-span leading-edge vortex will be formed for a wide range of Mach number, Reynolds number and incidence. For both round-edged and sharp-edged configurations the flow field at transonic conditions becomes even more complex due to the occurrence of shock waves and their interaction with the vortical flow and flow separations.

Sharp-edged configurations are the preferred choice for comparing experimental results with theoretical results. For inviscid-flow methods, i.e. potential-flow and Euler methods, in which viscous effects such as separation and the mechanism behind the generation of flow-field vorticity are to be modeled explicitly, at least the location of the primary separation is known. However, the smooth-surface secondary separation occurring on the upper surface underneath the leading-edge vor-

<sup>\*)</sup>This investigation has been carried out under contract with the Netherlands Agency for Aerospace Programs (NIVR) for the Netherlands Ministry of Defence



tex is a viscous-flow dominated flow feature not easily captured in inviscid-flow methods. For Navier-Stokes methods the sharp-edged configuration is also the preferred first choice since one can then focus on the secondary separation rather than having to deal with capturing both smooth-surface primary and secondary separation.

For these reasons the sharp-edged 65-deg cropped delta wing configuration was selected as a test case in another joint program (e.g. Ref. 15) aimed at the development and validation of Euler and Navier-Stokes methods for configurations exploiting vortex flow. It was deemed necessary to extend and enlarge the original experimental data set, especially in the transonic speed regime. At NLR a new model was built similar to the sharp-edged one tested in the "International Vortex Flow Experiment" but with three times as many pressure taps. At the present stage in the program pressure measurements and flow visualizations have been completed while flow-field surveys will be carried out in the near future. The present paper describes and analyzes these new results.

## 2. DESCRIPTION OF THE EXPERIMENT

### 2.1. The model

The model is a 65-deg cropped delta wing mounted on an under-wing fuselage, see Fig. 1. The wing has a root chord of 0.6 m and a semi-span of 0.238 m. The wing has a fixed sharp leading edge and neither camber nor twist. It has a chordwise airfoil section consisting of: the NACA 64A005 section from the point of maximum thickness (40%) to 75% chord; a straight line from 75 to 100% chord; a circular arc, at 40% chord fitting slope-continuous to the NACA section and at the (straight) leading edge fitting slope-continuous to a circle of radius 0.00013 m. This leading edge radius is small enough that the edge can be considered aerodynamically sharp.

Due to the choice of nominally similar chordwise sections the spanwise sections (see Fig. 1) are not conically similar, the wing thickness in terms of local semi-span decreases in chordwise direction rather than being constant as is the case for conical similarity. Furthermore, on the forward part of the wing the cross-flow-plane leading-edge wedge angle becomes rather large. This implies that compared to a flat-plate delta wing the separation at the leading edge will start at a higher incidence.

The straight-line wing tip is rounded with a radius equal to the local semi-thickness of the airfoil section. The straight-line trailing edge is also rounded with a radius of 0.00013 m.

The under-wing fuselage consists of a cylindrical body, with a cross-section build-up out of a semi-circle and vertical tangent lines, and an ogival shaped fairing as nose. The apex of the wing extends a short distance (2.1% root chord) in front of the nose of the fuselage, yielding a sharp and well-defined wing apex (Fig. 1). Also note that the fuselage does not intersect the upper wing surface. The fuselage accommodates three duplex scani-valves for pressure measurements but no balance for force measurements and is attached to a slender sting.

The model has nominally the same scale and geometry as the (sharp-edged) configuration used in the "International Vortex Flow Experiment". The main differences are the more slender sting, the different wing tip, the different apex area and the fuselage not protruding the upper wing surface (in the "AFWAL model" this could not be avoided due to the balance housing). The most important improvement as compared with the previous model is the large number of pressure taps, specifically on the upper surface of the wing. A total number of 269

pressure holes were present, 230 on the upper wing surface and 39 on the lower wing surface arranged in spanwise and chordwise rows as indicated in Fig. 2. The dense distribution of pressure holes allows a much more detailed analysis of the pressure distribution than possible with the AFWAL model which features only three spanwise rows of pressure orifices.

### 2.2. The wind tunnel and the test program

The model has been tested in the high speed wind tunnel (HST) at NLR. The tunnel with test section dimension  $1.6 \times 2.0 \text{ m}^2$  has closed side walls and slotted top and bottom walls. The tunnel can be pressurized to vary the Reynolds number. A photograph of the model installed in the wind tunnel is shown in Fig. 3. In the tests with the AFWAL model, in the plane of symmetry top and bottom wall pressures have been measured to assess the wall interference. From the results of these tests and from comparisons with results produced in other wind tunnels with the same or a smaller model (Ref. 14) it can be concluded that wall interference effects are negligible. Based on the experience during the previous free-transition tests, which showed predominantly turbulent boundary layers, it was not considered necessary to impose boundary-layer tripping.

Pressure measurements were taken at a Mach number ( $M_\infty$ ) of 0.15, 0.2, 0.4, 0.5, 0.7, 0.8, 0.85, 0.9, 0.95 and 1.2, for incidences between  $-3$  and  $27$  deg with increments of  $1$  degree, but for zero side-slip conditions only. The major part of the test program was carried out at a Reynolds number ( $Re_\infty$ ), based on root chord, of  $9 \times 10^6$ . At  $M_\infty = 0.2$  tests were also carried out at an additional Reynolds number of  $2.7 \times 10^6$ . At  $M_\infty = 0.85$  measurements were taken at the additional Reynolds numbers of  $4.5 \times 10^6$  and  $12 \times 10^6$ , but this over a limited range of incidence only. The measurements at the lowest speed took place at  $Re_\infty = 2 \times 10^6$ . In addition to the pressure measurements schlieren visualization has been recorded continuously while surface oil flow pictures have been taken at a number of selected characteristic flow conditions.

## 3. DISCUSSION OF TEST RESULTS

### 3.1. A general description of the flow field

The isobar plots in Fig. 4, the spanwise (Fig. 5a) and chordwise (Fig. 5b) surface pressure distributions for  $\alpha = 5, 10, 15$  and  $20$  deg, for one subsonic and for one transonic flow condition, are illustrative for the results obtained during the present pressure measurements.

Due to the sharp leading edge flow separation all along the leading edge starts already at relatively small values of the incidence  $\alpha$ . This separation is the source of the vorticity in the shear layer emanating from the leading edge. The shear layer rolls up to form the leading-edge vortex that dominates the flow field above the wing. As seen in Figs. 4 and 5a the presence of this primary vortex is reflected in the upper surface pressure distribution: underneath the vortex a pronounced suction peak with large spanwise pressure gradients is observed. For a given Mach number and at a given station  $x/c_x = \text{constant}$  the suction peak induced by the leading-edge vortex increases in height with increasing incidence, broadening in the process.

Just outboard of the suction peak the adverse pressure gradient causes the flow to separate, resulting in a secondary vortex system. In oil-flow pictures like the ones presented in Fig. 6, again for one subsonic and one transonic condition, secondary separation is identified as a region where oil accumulates and moves in downstream direction along a ray through the apex.

Fig. 6 presents two oil-flow pictures, one taken while the tunnel was still running, the other one



after the tunnel had been stopped. This may lead to an appreciation of the difficulties encountered in the interpretation of this type of flow visualization.

In the pressure distribution secondary separation is characterized by a plateau-like region between the location of secondary separation and the leading edge, as can be seen from Figs. 4 and 5. Under some conditions the secondary vortex is so strong that it produces a detectable suction peak within the plateau region.

On the upper surface between the plane of symmetry and the suction peak and on the lower surface away from the leading edge the pressure distribution is relatively flat. A local maximum in these areas indicates the location of a (re-)attachment point. The isobar pattern (Fig. 4) as well as flow visualization (Fig. 6) suggest that the flow is more or less conical. This is often the case for slender configurations like the present one, though this can be only approximately so due to the non-conical geometry of the wind-tunnel model. Furthermore, one should realize that even in case of a conical configuration in supersonic flow truly conical flow is not possible because of viscous effects. More importantly, at subsonic flow conditions conical flow is not possible since the presence of the apex will be felt in upstream direction while also near the downstream end of the model the flow has to return to free stream conditions in some continuous fashion (e.g. see Fig 5b). The apex and the trailing-edge effects cause the pressure to vary in chordwise direction, the chordwise gradients decreasing in magnitude with increasing Mach number. In this respect the flow may possess a geometrical structure resembling the one of a conical flow but flow quantities like velocity and pressure will inevitably vary along rays from the apex of the configuration rather than being constant like in conical flow.

Three different phenomena prompt deviations from the description given above.

#### (i) Part-span separation

At low incidences ( $\alpha < 5$  deg) and specifically on the forward part of the configuration the presence of the fuselage affects the local flow direction near the wing leading edge. The forward part of the configuration may be considered to have a negative chordwise camber. At low incidence (up to about 3 deg) this causes the flow to separate at the leading edge on the forward part but not yet on the aft part, this in spite of the circumstance that the above mentioned with increasing  $x/c_x$  decreasing leading-edge wedge angle tends to increase the susceptibility to separation.

The resulting vortex trails over the upper surface of the configuration at a rather inboard location and is discernable as a bump in the spanwise pressure distributions at the downstream stations where the flow is still attached. At incidences approaching 5 deg the flow also separates along the aft part of the leading edge and it appears that two vortices are formed, which at about 5 deg incidence start to merge into one leading-edge vortex. This "part-span" vortex formation is rather different from the part-span separation encountered on round-edged configurations where the vortex formation starts near the wing tip and moves forward with increasing incidence. However, the present fuselage induced effects are no longer easily detectable for incidences above 5 deg for which the flow separates all along the leading edge. Comparison of results of calculations for the isolated wing with measured data for the complete configuration have indicated (Ref. 14) that for incidences of 10 deg and higher the influence of the fuselage on the upper surface pressure distribution is rather small.

#### (ii) Compressibility

Compressibility effects constitute another cause of deviations from the above sketched general flow pattern. Compressibility causes the  $C_p$ -distribution to become more constant in chordwise direction, as can be seen from Figs. 4 and 5. The pressure coefficient increases considerably in the apex region and decreases somewhat on the rear part of the configuration. However, the effects of compressibility are most prominent when shock waves are formed in the flow field, which is discussed in the next section.

#### (iii) Vortex breakdown

Finally, vortex breakdown occurring at incidences exceeding 20 deg has a very large effect on the overall flow field. At a given station  $x/c_x = \text{constant}$  the suction peak underneath the leading-edge vortex increases gradually in height with increasing incidence, until vortex breakdown reaches the station. Above this critical incidence the vortex loses its well-ordered compact structure resulting in the suction peak becoming lower and broader, see section 3.3.

#### 3.2. The occurrence of shock waves

In Ref. 16 a discussion is presented on shock wave formation in the flow above a delta wing at moderate to high incidence. Due to the overall circulation and the vortex induced flow field, the local flow velocities become already supersonic at moderate free-stream Mach numbers. In a three-dimensional flow field this is a necessary but not a sufficient condition for the formation of shock waves. In Ref. 16 it is conjectured that shock waves might be formed in a decelerating flow when the Mach number component in a direction perpendicular to the local isobar surface exceeds 1.0. Based on this hypothesis, shock waves might be formed at two locations, both on the upper surface (see Fig. 7):

- (i) underneath the primary vortex, at a about constant percentage local semi-span, just outboard of the suction peak induced by the primary vortex: this shock is termed the cross-flow shock
- (ii) on the aft part of the wing near and perpendicular to the plane of symmetry at about constant  $x/c_x$ : this shock is termed the rear (or terminating) shock.

The formation of these two shocks will be discussed next, primarily by considering at fixed incidence the development with Mach number of the surface pressure distribution (see Fig. 8), but also by considering at fixed transonic Mach number the development with incidence (Figs. 4 and 5).

##### 3.2.1 The cross-flow shock

Fig. 8 presents for  $\alpha = 15$  deg the development with Mach number of the spanwise pressure distribution on the upper wing surface at the stations  $x/c_x = 0.3, 0.6$  and  $0.8$ . At the two most forward stations, due to the effects of compressibility, the peak in the  $C_p$ -distribution reduces in height and shifts inboard with increasing  $M_\infty$ . On the aft part of the wing the height of the suction peak remains about constant but the inboard shift still occurs. Near the plane of symmetry increasing  $M_\infty$  results in a  $C_p$ -distribution which is almost constant in chordwise direction. On the lower surface the  $C_p$ -distribution is almost invariant under changes in the free-stream Mach number.

Secondary separation causes the plateau region between the peak and the wing leading edge, while the presence of the secondary vortex is indicated by a small suction peak in this same plateau region. Note that as  $M_\infty$  increases the secondary separation line moves inboard just like the suction peak due to the leading-edge vortex. The latter indicates that presumably also the leading-edge vortex moves inboard with increasing  $M_\infty$ . Although the pressure distributions of Fig. 8 do not clear-

ly reveal the presence of a cross-flow shock wave underneath the vortex, it is seen that at  $M_\infty = 0.85$  there is a disruption of the gradual change with Mach number of the  $C_p$ -distribution. A similar break in the development of the pressure distribution is seen in Figs. 4 and 5a, but now for varying incidence at fixed Mach number.

The possibility of the appearance of the cross-flow shock wave, at least on the surface of the wing, can be established on the basis of theoretical reasoning. As indicated schematically in Fig. 9, it is required to determine the component of the velocity in the direction perpendicular to the isobar. This can easily be done when the flow is conical, in an approximate fashion only otherwise. In the conical case the isobars are simply rays from the apex, which in the region inboard of the suction peak is indeed more or less the case, e.g. see Fig. 4. From the pressure coefficient the local Mach number is derived using the isentropic relations, which presumably may be applied outside the boundary layer and upstream of the cross-flow shock. The direction of the velocity along the surface is deduced from an integration of the (conical) Euler equations employing the spanwise  $C_p$ -distribution. The integration starts from the attachment line. At the attachment line, which manifests itself as a local maximum in the pressure, the flow direction is known, i.e. here the flow is directed along the ray through the apex. The approximate analysis has been carried out for a number of flow conditions, using the spanwise surface pressure distributions as shown in Fig. 5a.

Results for the case  $M_\infty = 0.85$ ,  $Re_\infty = 9 \times 10^5$  are presented in Fig. 10 as a function of incidence, for one representative station ( $x/c_R = 0.6$ ). Shown is the Mach number at the location of the peak in the  $C_p$ -distribution, the latter is upstream and usually close to the position where secondary separation occurs and more readily identified in the measured  $C_p$ -distributions. It indicates that the local Mach number in the peak ( $M_{max}$ ) exceeds one for incidences above 5 deg and increases steadily with increasing incidence up to a certain level of 1.85 at  $\alpha \approx 16$  deg. The flow angle  $\phi(M_{max})$ , measured relative to the direction of the ray, at the same spanwise location also increases with increasing incidence. It shows that the relative flow angle can reach values as high as 45 deg. The break in this curve is associated with the rapid inboard shift of the secondary separation position and therefore with the first occurrence of vortex-induced separation.

The local mach number and the local flow direction yield  $M_{conical}(M_{max})$ , the component of the Mach number normal to the isobar. Fig. 10 shows that the surface flow Mach number perpendicular to the isobar exceeds 1.0 already for  $\alpha \approx 10^\circ$ . Since outboard of the suction peak the flow has to decelerate and the pressure has to return to the higher values in the plateau region an (oblique) shock wave might be required to realize this. The shock will also help to turn the flow into chordwise direction again. At locally sub-critical conditions secondary separation is due to separation of the boundary layer in an adverse pressure gradient. At sufficiently high  $M_\infty$ - $\alpha$  combinations the cross-flow shock wave will start to form. The adverse pressure gradient will become even more adverse and secondary separation will occur earlier, i.e. at a more inboard location. For a given  $\alpha$  the suction peak will be lowered in the process, though the height of the peak in the  $C_p$ -distribution still continues to increase with incidence until the maximum is attained (see Fig. 10). The switch from pressure-gradient to shock-induced boundary-layer separation results in the break in the curves shown in Fig. 10. For the station considered the switch from one type of boundary-layer

separation to another occurs at  $\alpha \approx 14.5$  deg.

Figs. 4 and 5, which include the  $C_p$ -distributions for the present case, indeed show that at 10 deg incidence there is no cross-flow shock wave present while at 15 deg a weak and at 20 deg apparently a stronger cross-flow shock has formed, causing secondary separation at a much more inboard location. Furthermore, it is noted that the break in the curves of Fig. 10 occurs at a conical Mach number close to 1.4. This is a value representative for shock-induced separation in other (primarily two-dimensional) situations as well, e.g. Ref. 17, which tends to support this explanation of the formation of the cross-flow shock.

The surface oil flow patterns for  $M_\infty = 0.85$ ,  $\alpha = 20$  deg, as shown in Fig. 6 (photographed during and after the run), indicates a very sharp line and change in the direction of the oil streak lines at the location of the secondary separation, strongly suggesting the presence of the cross-flow shock. It should be noted that the occurrence of a cross-flow shock has been suggested by others (Refs 18, 19 and 20) although a clear experimental confirmation through flow-field measurements and or flow-field visualization has not been reported thus far. To map out such a shock wave the flow field has to be probed with a very high resolution, while flow-field visualization through for instance schlieren requires special arrangement of the experimental set up. As reported in Ref. 13 and more recently in Ref. 21 there is some theoretical support for the occurrence of a cross-flow shock, i.e. computational simulations of the flow using Euler methods have shown the formation of a cross-flow shock. However, in the Euler methods smooth-surface separation is not simulated and the cross-flow shock is not associated with secondary separation, rather is required in the numerical solution primarily in order to turn the flow in chordwise direction again.

### 3.2.2. The rear terminating shock

From Fig. 8 it is also clear that with increasing  $M_\infty$  on the rear part of the wing upper surface, in addition to secondary separation and the cross-flow shock, yet another flow feature comes into play. This flow feature, which causes the distribution for  $M_\infty = 0.95$  at  $x/c_R = 0.8$  to be different in character from the ones for lower free-stream Mach numbers. Also for the development of the  $C_p$ -distribution with incidence this same flow feature is of importance for the flow on the aft part of the configuration, e.g. see Fig. 5

Fig. 11 shows for  $\alpha = 15$  deg the development with  $M_\infty$  of the chordwise pressure distribution on the upper surface in the plane of symmetry. At low free-stream Mach numbers a pressure peak is observed at the wing apex and the pressure increases all along the chordwise section. Increasing  $M_\infty$  reduces the height of the peak at the apex and over the central part of the section a pressure plateau develops, followed again over the aft part of the wing by a region with an adverse pressure gradient. When the free stream Mach number is increased the pressure peak at the apex disappears completely and a favourable pressure gradient is observed over the first part of the wing.

This is very similar to the flow development with increasing Mach number of the flow over two-dimensional airfoils, a phenomenon due to compressibility effects known as "Mach freeze".

For Mach numbers exceeding  $M_\infty = 0.7$  the pressure distribution on the rear of the wing becomes steeper, indicative of the onset of shock wave formation. For  $M_\infty = 0.85$  and  $0.95$  the pressure coefficient over the central part of the wing is below the critical value  $C_p^*(M_\infty)$ , as follows from the list of values in Fig. 11, and the flow is supersonic. This is more clearly indicated in Fig. 12

where for a number of free-stream Mach numbers the distribution of the local Mach number has been plotted rather than the pressure coefficient. From Fig. 12 it is evident that for the chosen incidence of 15 deg the flow over the central part of the wing becomes supersonic at a free stream Mach number between 0.8 and 0.85. Since, in order to return to free stream conditions, the flow has to decelerate near the trailing edge, and since the local isobars are perpendicular to the plane of symmetry a shock wave will be formed that terminates the region with supersonic flow. This "rear" shock wave moves downstream with increasing Mach number, as is seen in Figs. 11 and 12.

Very similar to the development of the rear shock observed in Fig. 11, where for fixed  $\alpha$  the free-stream Mach number is varied, is the development seen in Fig. 5b, where for a fixed  $M_\infty$  of 0.85 the incidence is varied and in the first two chordwise sections the rear shock appears between 15 and 20 deg.

Contrary to the cross-flow shock, the rear shock can actually be observed employing schlieren flow visualization, as already noted by Elle (Ref. 22) in 1960. For the condition  $M_\infty = 0.85$ ,  $\alpha = 20$  deg,  $Re_\infty = 9 \times 10^6$  this is illustrated for the present configuration in Fig. 13. In this picture the rear shock shows up rather clearly as a discontinuity, more or less normal to the wing surface, with also some wavelets visible further away from the surface. Upstream of the rear shock the axis of the core of the leading-edge vortex can be identified as the sharp nearly horizontal interface between the lighter and a darker area. Downstream of the rear shock the look-through image of the highly three-dimensional flow field provided by the schlieren technique can not be used directly to single out specific flow features.

As far as the surface oil-flow visualization is concerned, unlike the cross-flow shock, the rear shock hardly leaves any imprint on the surface oil pattern (see Fig. 6). Most likely the shock is too weak (the Mach number upstream of the shock is 1.16) to affect the boundary layer. Although the extent of the shock in vertical direction is clearly visible from the schlieren pictures, the extent in spanwise direction is still open to speculation. Away from the plane of symmetry the flow turns rapidly towards the leading edge of the wing, whereas the isobars (at least on the wing surface) curve from the direction normal to the plane of symmetry into chordwise direction, i.e. towards the wing trailing edge (see Fig. 4). This suggests that the component of the Mach number normal to the isobar will decrease away from the plane of symmetry, unless the local Mach number increases rapidly which however is only the case underneath the leading-edge vortex.

Ref. 23, which describes a detailed investigation of the flow field above a sharp-edged pure 65-deg delta wing, includes some discussion on whether or not and if so how the rear and the cross-flow shock might be connected. This uncertainty in the process of attempting to reconstruct the flow structure is illustrative for the highly complex nature of this three-dimensional vortical flow field. It is hoped that the future flow-field measurements will shed more light on the flow structure.

### 3.3. Vortex breakdown

#### 3.3.1. Background

Vortex breakdown can be described as a sudden increase of the cross-sectional area of the vortex core, in many cases accompanied by the onset of unsteadiness and turbulence in the vortical flow region. Downstream of the point where vortex

breakdown occurs the vortex core seems to have lost some of its coherent structure, though the global strong circulatory flow pattern does persist. Also, upstream of the vortex breakdown point the flow is hardly affected at all, another indication of the slender type of flow one is dealing with. Although vortex breakdown has been studied extensively in the past (see e.g. Refs. 24, 25, 26, 22 and 27) as well as more recently (Refs. 28, 29 and 30), the understanding of this phenomenon still appears to be incomplete.

At least two types of vortex breakdown are distinguished, i.e. the spiral and the bubble type of vortex breakdown. The spiral type of vortex breakdown is thought to be initiated by a hydrodynamic instability of the swirling flow. The bubble type of vortex breakdown is usually associated with the occurrence of reversed flow in the vortex core. In the latter case, in analogy with the separation of a boundary layer, it is conjectured that the flow in the vortex core, which has suffered total-pressure losses due to viscous effects, can no longer negotiate the external adverse pressure gradient and stagnates.

It should be noted here that this latter explanation is also used to explain why Euler calculations (e.g. Ref. 31) seem to describe vortex breakdown reasonably well. It is argued that, similar to the real viscosity, the numerical viscosity introduces total pressure losses that (fortuitously?) appear to have the same order of magnitude as the actually observed total-pressure losses (Ref. 32).

Direct experimental evidence of vortex breakdown can only be obtained by studying the vortex itself. Bütchsch (see Ref. 16) has actually measured the increase in cross-sectional area of the vortex core due to vortex breakdown for the rounded version of the present 65-deg cropped delta wing configuration at  $M_\infty = 0.85$  employing Laser Doppler Anemometry (LDA).

#### 3.3.2. Vortex breakdown in subsonic flow

An example of the vortex breakdown phenomena that became manifest during the present experiment, is given in Fig. 14. Presented are for the case of  $M_\infty = 0.2$ ,  $Re_\infty = 9 \times 10^6$  the schlieren picture before ( $\alpha = 20$  deg) and the one after ( $\alpha = 24$  deg) vortex breakdown. This figure shows that, at this entirely sub-critical condition, the axis of the vortex core again corresponds with the marked interface between the lighter and the darker area above the model. At  $\alpha = 20$  deg this axis can be followed all along the length of the model and into the near-wake region. For  $\alpha = 24$  deg vortex breakdown has occurred and downstream of the breakdown point the axis of the vortex core can no longer be identified, also due to some unsteadiness of the flow.

The effect of vortex breakdown on the pressure distribution on the wing surface is only small for this condition. Fig. 15 shows, for a number of incidences before and after vortex breakdown, the surface pressure distributions along the chordwise section in the plane of symmetry. The more than proportional increment in the  $C_p$ -distribution on the aft part of the wing when increasing  $\alpha$  from 22 to 24 deg is the only quantitative effect. This corresponds with the observation that the point of vortex breakdown along the vortex core moves gradually upstream with increasing incidence. This relatively small and gradual effect on the wing pressure distribution is also evident from the isobar pattern before and after vortex breakdown (Fig. 16), which have the same general appearance.

### 3.3.3 Vortex breakdown in transonic flow

At transonic conditions ( $M_\infty = 0.85$ ,  $Re_\infty = 9 \times 10^6$ ) vortex breakdown is a much more dramatic event. Now it becomes apparent in the surface pressure distribution and the isobar pattern changes rather drastically upon the occurrence of vortex breakdown. This is demonstrated in Fig. 17 which shows the isobar pattern just before ( $\alpha = 22$  deg) and just after ( $\alpha = 24$  deg) the onset of vortex breakdown. The region with an approximately conical flow structure, which extends up to 80% root chord before vortex breakdown (e.g. see Fig. 4), is significantly reduced after vortex breakdown. The most important change that occurs is that the rear shock shifts upstream from about 80% to about 50% root chord, while also the flow pattern downstream of the rear shock is completely different. In the latter region the cross-flow shock is absent, but in addition to the forward shifted rear shock a second shock normal to the plane of symmetry forms at about 90% root chord.

The corresponding schlieren pictures (Fig. 18) confirm the very pronounced change in the position of the rear shock and the presence of the second shock further downstream. It was also observed in the experiment that the change in the flow structure occurs rather abruptly and is accompanied by more unsteadiness than at lower Mach numbers. The change in the position of the rear shock is also clearly reflected in the pressure distribution along the section in the plane of symmetry (Fig. 19). The single rear shock system before vortex breakdown has changed into a two-shock system after vortex breakdown. This shock system persists up to the highest incidence considered in the present investigation ( $\alpha = 27$  deg). Similar changes from a one- to a two-shock system have been reported in Ref. 33 for a pure 65-deg swept sharp-edged delta wing for which the vortex breakdown occurs at a somewhat lower incidence ( $\alpha = 17$  deg).

The question can be posed whether the rear shock provokes vortex breakdown or vortex breakdown causes the branching to the second type of shock system. A possible explanation that supports the second possibility is given below.

Fig. 20 presents, as a function of the free-stream Mach number, the incidence at which vortex breakdown occurs above the configuration. The critical value of  $\alpha$  has been derived from the break in the development with incidence, for fixed  $M_\infty$ , of the spanwise pressure distribution at  $x/c_R = 0.8$ . Also information has been deduced from the continuous schlieren visualization recorded during the experiment. Fig. 20 suggests a rather weak effect of compressibility on the onset of vortex breakdown. For free-stream Mach numbers up to values of 0.7 the onset of vortex breakdown is delayed somewhat, presumably due to the diminishing upstream influence.

For higher Mach numbers, but still below  $M_\infty = 0.85$ , the flow becomes supersonic over most of the wing and the cross-flow shock forms. Close to the trailing edge the flow returns to subsonic, eventually through the rear shock. In this range of Mach numbers the onset of vortex breakdown occurs somewhat sooner the higher  $M_\infty$ . For Mach numbers near and above 0.85 the more dramatic type of vortex breakdown with the switch from one shock pattern to another takes place. At  $M_\infty = 0.9$  the dip of the vortex-breakdown-onset boundary drawn in Fig. 20 is reached. For this flow condition vortex breakdown occurs at  $\alpha = 19$  deg.

The gradual variation for  $M_\infty < 0.85$  suggests that the same phenomenon, i.e. a change in structure of the vortex core itself, might be responsible for the observed flow development on the wing surface. The increase in the cross-sectional area of the

vortex core causes an acceleration of the flow and an decrease of the pressure on the rear part of the wing. This effect is small at  $M_\infty = 0.2$ , see Figs. 15 and 16. However, at the higher Mach numbers this effect changes the downstream condition of the rear shock terminating the region with supersonic flow. Since the rear shock is rather weak (see Fig. 19) even a small change in the downstream condition will be sufficient to frustrate the necessity for the existence of the shock at that location. A somewhat similar situation occurs in the development of the transonic flow on an airfoil. Sinnott (Ref. 34) has shown that the shock location in transonic flow results from a precise and susceptible match between the supersonic upstream and subsonic downstream conditions. For airfoils a sudden upstream shift of the shock is associated with a change in the pressure at the trailing edge.

For the present three-dimensional flow it is conjectured that the change in the pressure downstream of the rear shock, caused by the breakdown of the vortex core, forces the rear shock to jump to a new equilibrium position further upstream. Downstream of this shock the flow seems to expand rapidly to supersonic conditions again. Since the flow eventually has to return to the subsonic conditions the second shock is required. For still higher Mach numbers the rear shock becomes stronger and is located closer to the trailing edge, which results in a delay of vortex breakdown and the branching from the one-shock to the two-shock system.

It should be stressed here that the above hypothetical view is based on aerodynamic reasoning, rather than on direct experimental evidence. Clearly more detailed experiments are needed to substantiate this explanation.

Finally it is of interest to have some insight into the level of unsteadiness of the flow for conditions with vortex breakdown. To this aim unsteady pressure and velocity distributions should be measured rather than their mean values as was pursued in the present experimental investigation. However, the mean pressure measurements, taken with a filtering time of order 0.1s, appear to be satisfactorily reproducible. This is illustrated in Fig. 21 which shows a comparison of the isobar patterns obtained from two measurements taken at different times for the same post-critical transonic flow condition. The largest deviations are observed underneath the burst vortex, suggesting that the two-shock system itself is reasonably steady.

### 3.4. The effect of Reynolds number

To investigate the effect of the Reynolds number on the development of the flow a limited Reynolds number variation has been made at  $M_\infty = 0.2$  and 0.85. For the flow over a delta wing the Reynolds number can have an effect on amongst others the following:

- (i) primary separation and associated with it the strength of the leading-edge vortex;
- (ii) the development of the boundary layer starting at the attachment line on the wing upper and lower surface;
- (iii) secondary separation;
- (iv) the development of the flow near the center of the vortex;
- (v) vortex breakdown.

Most of these will be discussed subsequently.

#### 3.4.1. Primary separation

Since the formation of the leading-edge vortex is related to the (primary) separation of the boundary layer at the wing leading edge, a variation in Reynolds number will have an effect for the configuration with a round leading edge. The Reynolds number effect in this case has been discussed to some extent in Ref. 14. The configuration con-

sidered here has a sharp leading edge, so that separation is fixed entirely by the geometry and Reynolds number effects are absent.

### 3.4.2. Upper-surface boundary layer

In the flow field induced by the leading-edge vortex the flow is forced around the vortex and reattaches on the upper wing surface at an attachment line which is approximately aligned with a ray through the apex. At higher incidences the attachment line moves inboard until it lies in the plane of symmetry. The boundary layer flow starting at the attachment line can be laminar or turbulent, depending on the Reynolds number and the local pressure distribution. Even in case the boundary layer flow at the attachment line is laminar, transition might occur further downstream due to Tollmien-Schlichting or cross-flow instabilities. In Ref. 35 a discussion is presented on the development of the boundary layer on the upper surface of a 65-deg delta wing in incompressible flow. It is shown on theoretical grounds that the boundary layer is most likely turbulent for a Reynolds number (based on root chord) of  $9 \times 10^6$ . This has been substantiated in the present experimental investigation by acenaphtene tests. However, it should be borne in mind that part of the boundary layer can be laminar at the lower Reynolds numbers employed. This is especially the case near the apex of the wing. The difference in the displacement thickness due to a laminar or a turbulent boundary layer will hardly have any effect on the pressure distribution near the plane of symmetry. Also, for a given type of boundary layer, the effect of a different Reynolds number will be small.

For the Reynolds numbers used in the present experimental investigation this is indicated in Figs. 22 and 23 for  $M_\infty = 0.2$  and  $0.85$ , respectively. Considered in these figures is the development with incidence of the surface pressure distribution along the section in the plane of symmetry. For the subsonic condition there are some minor differences between the results for different Reynolds numbers and that in the apex region of the wing only. For the transonic flow condition differences between results obtained for  $Re_\infty = 9 \times 10^6$  and  $12 \times 10^6$  are negligible. At the higher incidences there are small differences between these results and the results obtained for  $Re_\infty = 4.5 \times 10^6$ , specifically around the rear shock.

### 3.4.3. Lower wing surface

On the lower wing surface the attachment line shifts gradually with increasing incidence from a location very close to the leading edge in inboard direction towards the plane of symmetry (e.g. see Fig. 5a). The flow on the lower wing surface is an accelerating flow and Reynolds-number effects are small, as might have been expected. This is illustrated in Figs. 24 and 25 for a subsonic ( $M_\infty = 0.2$ ) and a transonic ( $M_\infty = 0.85$ ) flow condition. Shown in these two figures are the spanwise surface pressure distributions at  $x/c_a = 0.3, 0.6$  and  $0.8$  for  $\alpha = 0, 5, 10, 15$  and  $20$  deg for the Reynolds numbers considered in the present investigation. The differences in the pressure distributions on the lower surface measured for different Reynolds numbers are small indeed.

### 3.4.4. Secondary separation

The most pronounced effect of the boundary layer being laminar or turbulent is its effect on the location of the secondary separation. Starting at the attachment line the boundary layer on the wing upper surface first accelerates, this until the peak in the  $C_p$ -distribution underneath the leading-edge vortex is reached. Subsequently the boundary layer, still flowing in the direction of the leading edge, encounters an adverse pressure gradient and therefore decelerates. The pressure gradient is such that the boundary layer will

always separate and usually the free shear layer thus formed rolls up into the secondary vortex. Underneath the shear layer, i.e. at the downstream side of the secondary separation line, the velocity is directed along the separation line which approximately runs along a ray through the apex. This can be recognized on the oil-flow pictures presented in Fig. 6.

Secondary separation is intrinsically coupled to primary separation. However, the location and the extent of the region affected by the secondary separation is strongly influenced by the state of the boundary layer (laminar or turbulent) and, but to a lesser degree, by the Reynolds number. A laminar secondary separation will be located more inboard, whereas a turbulent secondary separation will take place at a location further outboard. The latter will result in a smaller and weaker secondary vortex system than is the case for laminar secondary separation. In the present experimental investigation the boundary layer was turbulent with the possible exception of the region close to the apex, where for the lower incidences the boundary layer might have been laminar.

Fig. 24 displays the spanwise pressure distributions for  $M_\infty = 0.2$  and for the two Reynolds numbers considered in the present experiment, namely  $Re_\infty = 2.7 \times 10^6$  and  $9 \times 10^6$ . This figure shows that, judging from the position of the secondary separation line relative to the position of the peak associated with the primary vortex, the boundary layer was turbulent at the secondary separation line, and this for both Reynolds numbers. Here we used, as a practical way of determining the location of the secondary separation line, the most inboard point of the plateau region as the point where secondary separation takes place.

At the lower incidences increasing the Reynolds number from  $2.7$  to  $9$  million shifts the secondary separation location in outboard direction, which results in a higher primary suction peak. In the plateau region outboard of the secondary separation position the peak associated with the secondary vortex system is detectable for  $Re_\infty = 9 \times 10^6$  only. The explanation for this is that at the higher Reynolds number the boundary layers and the free shear layers are thinner so that the secondary vortex can develop into a compact vortical flow region rather than being (partly) embedded within a region with viscosity-dominated flow. At  $\alpha = 15$  and  $20$  deg the difference in the location of secondary separation due to the difference in the Reynolds number becomes small at  $x/c_a = 0.3$ , but larger at the stations further downstream. Here we see for the higher Reynolds number a shift of the location of both the secondary separation and the primary suction peak in inboard direction, i.e. contrary to what one would expect. This is thought to be connected with above mentioned effect that for the higher Reynolds number the secondary vortex system is less diffuse and stands distinctly clear from the viscous layers. Such a secondary vortex system will have a stronger interaction with the primary vortex, apparently resulting in an inboard shift of the secondary separation position as Reynolds number is increased.

At  $M_\infty = 0.85$  (see Fig. 25) the flow is presumably turbulent as well. The suction peak underneath the primary vortex appears to be affected only slightly by increasing the Reynolds number from  $4.5$  to  $9$  and  $12$  million. Especially the results for  $9$  and those for  $12$  million are almost identical. As far as the results for  $4.5$  and  $9$  million is concerned it is noted that for the lower incidences the differences are negligible. For the higher incidences, where the cross-flow shock develops, differences become more significant. It is again hypothesized that at the higher Reynolds number the

secondary vortex is more distinctly developed, as indicated by the more pronounced suction peak in the plateau region, which results in a stronger interaction with the primary vortex. In the transonic case this will lead to a somewhat earlier formation of the cross-flow shock which shifts the location of the secondary separation further inboard.

That the secondary vortex itself and its effect on the pressure distribution is more pronounced at a higher Reynolds numbers due to thinner free and wall shear layer has also been suggested by J. H. B. Smith in the technical evaluation report of Ref. 13. However, it should be added that the interaction of the secondary vortex with the primary vortex and the rest of the flow field might shift the location of secondary separation, promote or delay the formation of the cross-flow shock, etc., weakening or strengthening the Reynolds-number effect. Nevertheless, the effects seem to be relatively small.

#### 3.4.5. Vortex breakdown

It has been suggested in the literature (Ref. 36) that the Reynolds number effect on vortex breakdown is small. This is in line with the notion that the development of free shear layers (viscous losses in the absence of a wall) depends only on their initial conditions and not on the Reynolds number. Only their thickness and internal structure depends on the Reynolds number (Ref. 37).

The present experimental results also show in general a very small (of the order of 1 deg) variation with Reynolds number of the onset of vortex breakdown. However, such a weak dependence might still result in large changes in the pressure distribution when near the boundary for the onset of vortex bursting, at a fixed ( $M_\infty, \alpha$ ) combination, the Reynolds number is varied. This is demonstrated in Fig. 26 for the transonic case ( $M_\infty = 0.85$ ). Here it is shown that for  $\alpha = 22$  deg a doubling of the Reynolds number from 4.5 to 9 million has little effect, while for  $\alpha = 23$  deg the same increase in Reynolds number changes the flow from pre- to post-breakdown structure. However, such a comparison does not identify a large influence of Reynolds number on the flow. It rather indicates the occurrence of a discontinuity (branching) in the development of the flow with some other parameter ( $\alpha$  or  $M_\infty$ ), while the way in which the development itself takes place depends weakly on the Reynolds number.

#### 4. CONCLUDING REMARKS

The transonic flow over a 65-deg cropped delta wing with a sharp leading edge is strongly influenced by compressibility effects. This is summarized in Fig. 27 which shows in the ( $M_\infty, \alpha$ ) plane the various boundaries signifying the appearance of the flow features discussed. Already at  $M_\infty = 0.5$  the flow becomes supersonic at the higher incidences. Above approximately  $M_\infty = 0.6$  shocks are formed in the flow field above the configuration, which change the overall characteristics of the flow.

The shocks formed are the cross-flow shock, located approximately along a ray from the apex, and on the aft part of the configuration, approximately normal to the plane of symmetry, the rear shock. The (oblique) cross-flow shock shifts secondary separation inboard. The rear shock terminates on the central part of the wing the region with supersonic flow. The rear shock is a weak normal shock and it does not provoke any strong boundary-layer/shock-wave interaction.

The local Mach numbers in the flow field upstream of the cross-flow shock can well exceed a value of 2. Though over the shock the increase in static pressure is only modest, and of the same order of magnitude as the one over the rear shock, the high value of the Mach number upstream of the oblique cross-flow shock will result in very significant total-pressure losses across the shock. The interaction of the cross-flow shock with the boundary layer changes the type of the secondary separation from pressure-gradient induced to shock-induced separation.

The onset of vortex breakdown is only weakly influenced by the free stream Mach number. The effect of the occurrence of vortex breakdown on the surface pressure distribution is relatively small for sub-critical flow conditions. However, for transonic flow conditions the effect on the  $C_p$ -distribution is dramatically large. The rear shock shifts abruptly to a much more forward location that lies upstream of the breakdown location. Downstream of this location the rear shock has associated with it an re-expansion to supersonic flow terminated by a second (normal) shock.

In general Reynolds number effects appear to be small for the present sharp-edged configuration with predominantly turbulent flow. The secondary vortex is more pronounced at the higher Reynolds numbers, which also leads to a somewhat stronger interaction with the rest of the flow field. However, it should be mentioned that even for the present case of the high-Reynolds-number flow about a sharp-edged configuration viscous effects are instrumental in the separation at the leading and the trailing edge, in the occurrence of the smooth-surface secondary separation and in the formation of the leading-edge vortex core as a compact region with distributed vorticity.

#### ACKNOWLEDGEMENTS

The authors like to thank S.J. Boersen and B. Rohne who prepared and carried out the wind-tunnel tests. Thanks are also due to R. Abdulgani who did some of the analysis of the pressure distributions and W.M. van der Poel who did the calculations for the cross-flow Mach number with a computer program developed by E.M. Houtman of the Delft University of Technology.

#### REFERENCES

1. Earnshaw, P.B.: An Experimental Investigation of the Structure of a Leading-Edge Vortex. ARC R&M No. 3281 (1962).
2. Wentz, W.H., McMahon, M.C.: An Experimental Investigation of the Flow Fields about Delta and Double-Delta Wings at Low Speeds. NASA CR 521 (1966).
3. Hummel, D.: On the Vortex Formation Over a Slender Wing at Large Incidence. AGARD CP-247, Paper 15 (1979).
4. Verhaagen, N.G.: An Experimental Investigation of the Vortex Flow over Delta and Double-Delta Wings at Low Speeds. AGARD CP-342, Paper 7 (1983).
5. Verhaagen, N.G., Naarding, S.H.J.: Experimental and Numerical Investigation of the Vortex Flow Over a Yawed Delta Wing. AIAA Paper 88-2563 (1988). See also J. of Aircraft, Vol. 26, No. 11, pp. 971-978 (1989).
6. Kjelgaard, S.O., Sellers III, W.L., Weston, R.P.: The Flow Field over a 75 Degree Swept Delta Wing at 20.5 Degrees Angle of Attack. AIAA Paper 86-1775 (1986).

7. Payne, F.M., Ng, T.T., Nelson, R.C., Schiff, L.B.: Visualization and Flow Surveys of the Leading-Edge Vortex Structure on Delta-Wing Planforms. AIAA Paper 86-0330 (1986). See also AIAA J. Vol. 26, No. 2, pp. 137-143 (1988).
8. Stanbrook, A., Squire, L.C.: Possible Types of Flow at Swept Leading Edges. Aeron. Quarterly, Vol. 15, pp. 72-82 (1964).
9. Miller, D.S., Wood, R.M.: An Investigation of Wing Leading-Edge Vortices at Supersonic Speeds. AIAA Paper 83-1816 (1983). See also J. of Aircraft Vol. 21, No. 9, pp. 680-686 (1984) and NASA TP 2430 (1985).
10. Szodrach, J., Ganzer, U.: On the Lee-Side Flow for Slender Delta Wings at High Angle of Attack. AGARD CP-247 Paper 21 (1979).
11. Houtman, E.M., Bannink, W.J.: Experimental Investigation of the Transonic Flow at the Leeward Side of a Delta Wing at High Incidence. Report LR-518, Faculty of Aerospace Engineering, Delft University of Technology (1987).
12. Schrader, K.F., Reynolds, G.A., Novak, C.J.: Effects on Mach Number and Reynolds Number on Leading-Edge Vortices at High Angles-of-Attack. AIAA Paper 88-0122 (1988).
13. Elsenaar, A., Eriksson, G. (eds.): Proceedings of the Symposium on the "International Vortex Flow Experiment on Euler Code Validation". Stockholm, October 1-3, 1986 (published by FFA).
14. Elsenaar, A., Hjelmborg, L., Bütetisch, K.A., Bannink, W.J.: The International Vortex Flow Experiment. In AGARD CP-437 (1988).
15. Williams, B.R., Kordulla, W., Borsi, M., Hoeijmakers, H.W.M.: Comparison of Solutions of Various Euler Solvers and One Navier-Stokes Solver for the Flow About a Sharp-Edged Cropped Delta Wing. This FDP Symposium, AGARD CP- , Paper 2 (1990).
16. Elsenaar, A., Bütetisch, K.A.: Experimental Study on Vortex and Shock Wave Development on a 65° Delta Wing. In: Proceedings Symposium Transonicum III, IUTAM, (1988).
17. Delery, J., Marvin, J.G.: Turbulent Shock Wave Boundary Layer Interaction. AGARDograph No. 280 (1985).
18. Brocard, Y., Schmitt, V.: Interaction Aérodynamique entre un Canard Proche et une Aile en Flèche en Écoulement Transsonique. ONERA TP 1980-34 (1980).
19. Huylaert, J.M.: Vortex Bursting on Slender Delta Wings in Transonic Flow and its Influence on Missile Aerodynamic Characteristics. Jahrestagung DGLR, Aachen, 12-14 May 1981.
20. Vorropoulos, G., Wendt, J.F.: Laser Velocimetry Study of Compressibility Effects on the Flow Field of a Delta Wing. AGARD CP-342, Paper 9 (1983).
21. Hoeijmakers, H.W.M., Jacobs, J.M.J.W., van den Berg, J.I.: Numerical Simulation of Vortical Flow over a Delta Wing at Subsonic and Transonic Speeds. ICAS Paper 90-3.3.3. Also NLR TP 90029 (1990).
22. Elle, B.J.: On the Breakdown at High Incidence of the Leading Edge Vortices on Delta Wings. J. Royal Aer. Soc., Vol. 64 (1960).
23. Bannink, W.J., Houtman, E.M.: Experiments on Transonic Flow over a Delta Wing at High Angles of Attack. In Ref. 13, (1986).
24. Peckham, D.H., Atkinson, S.A.: Preliminary Results of Low Speed Wind Tunnel Tests on a Gothic Wing of Aspect Ratio 1.0. ARC Rep. CP-508 (1957).
25. Peckham, D.H.: Low Speed Wind Tunnel Tests on a Series of Uncambered Slender Pointed Wings with Sharp Edges. ARC Rep. R&M No. 3186 (1958).
26. Elle, B.J.: An Investigation at Low Speed of the Flow Near the Apex of Thin Delta Wings with Sharp Leading Edges. ARC Rep. R&M No. 3176 (1958).
27. Lambourne, N.C., Bryer, D.W.: The Bursting of Leading-Edge Vortices - Some Observations and Discussion of the Phenomenon. ARC Rep. R&M No. 3282 (1961).
28. Kegelman, J.T., Roos, F.W.: Effects of Leading-Edge Shape and Vortex Burst on the Flowfield of a 70-degree-sweep Delta Wing. AIAA Paper 89-0086 (1989).
29. Kegelman, J.T., Roos, F.W.: The Flowfields of Bursting Vortices over Moderately Swept Delta Wings. AIAA Paper 90-0599 (1990).
30. Roos, F.W., Kegelman, J.T.: An Experimental Investigation of Sweep-Angle Influence on Delta Wing Flows. AIAA Paper 90-0383 (1990).
31. Hitzel, S.M.: Wing Vortex Flows up into Vortex Breakdown. A Numerical Simulation. AIAA Paper 88-2518 (1988).
32. Murman, E.M., Powell, K.G., Goodsell, A.M., Landahl, M.: Leading-Edge Vortex Solutions with Large Total Pressure Losses. AIAA Paper 87-0039 (1987).
33. Bannink, W.J., Houtman, E.M., Ottochian, S.P.: Investigation of the Vortex Flow Over a Sharp-Edged Delta Wing in the Transonic Speed Regime. Report LR-594, Faculty of Aerospace Engineering, Delft University of Technology (1989).
34. Sinnott, C.S., Osborne, J.: Review and Extension of Transonic Aerofoil Theory. ARC R&M 3156 (1961).
35. de Bruin, A.C., Hoeijmakers H.W.M.: Computation of the Three-Dimensional Boundary Layer Transition and Separation on a 65 Deg Swept Delta Wing at 20 Deg Angle of Attack. NLR MP 86075 (1986). Also included in Ref. 13.
36. Erickson, G.E.: Water-tunnel Studies of Leading-Edge Vortices. J. of Aircraft, Vol. 19, No. 6, pp. 442-448 (1982).
37. Townsend, A.A.: The Structure of Turbulent Shear Flow. Cambridge University Press (1956).



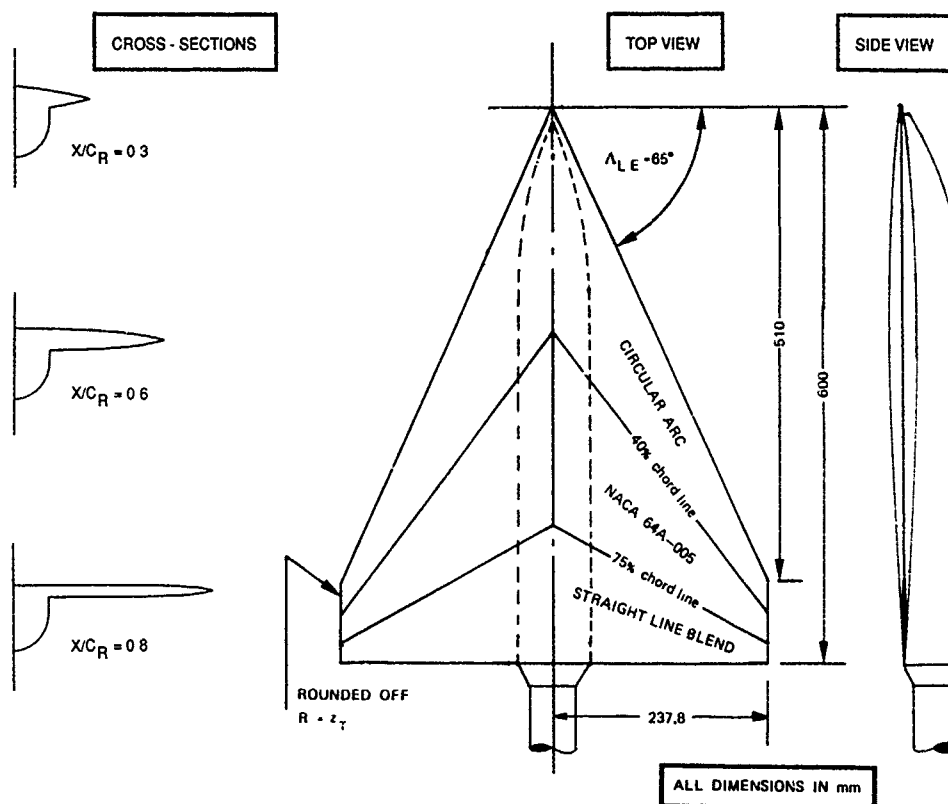


Fig. 1 Geometry of wind-tunnel model

(MODEL IS ROLLED UPSIDE DOWN)

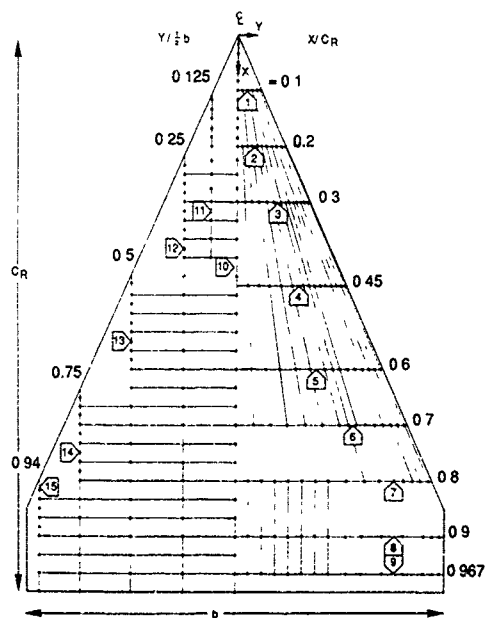


Fig. 2 Distribution of 230 pressure taps on upper wing surface. Lower wing surface has 39 pressure taps.

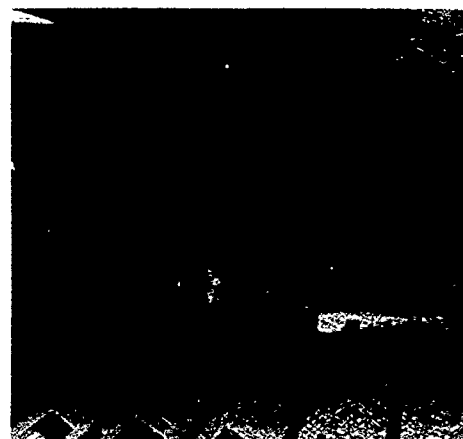


Fig. 3 Model installed in NLR High-Speed Tunnel (HST)



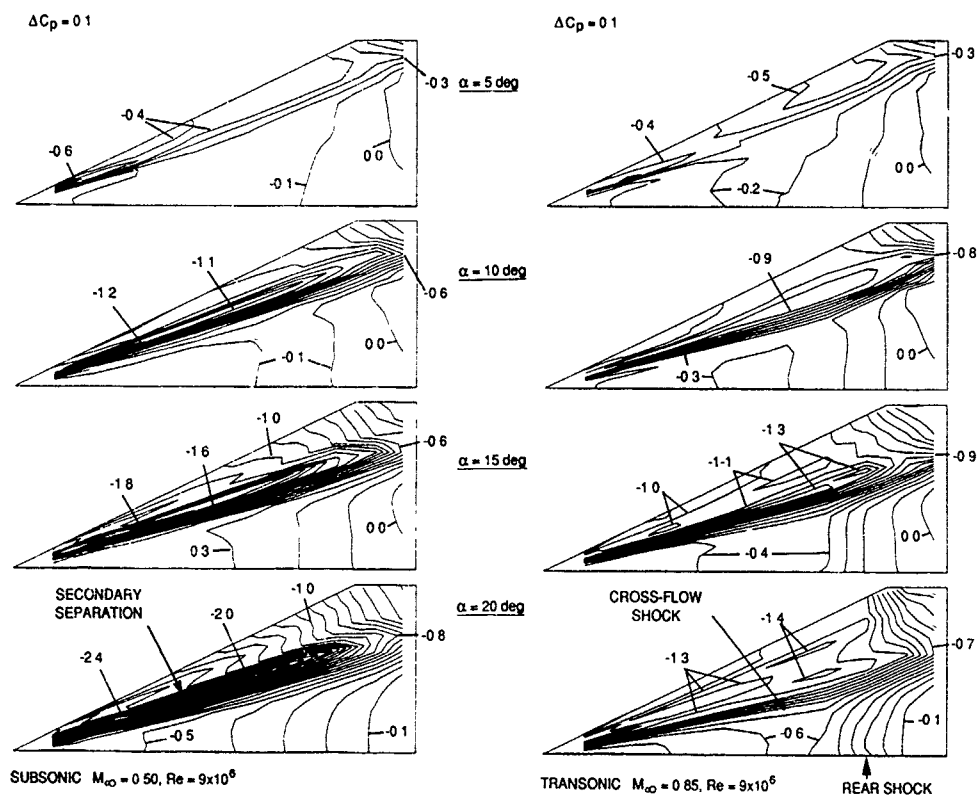


Fig. 4 Isobar pattern on the upper wing surface

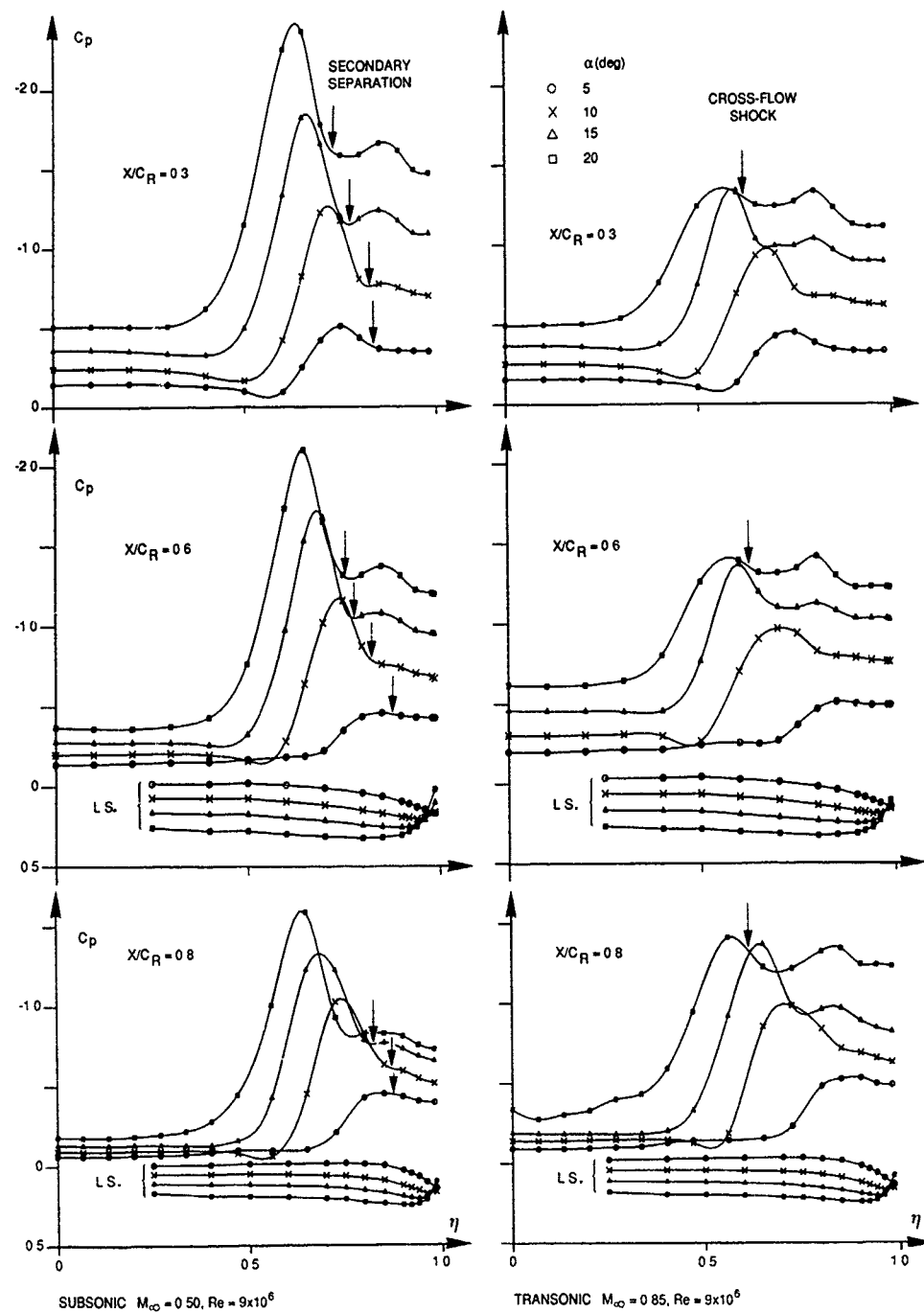


Fig. 5a Spanwise surface pressure distribution

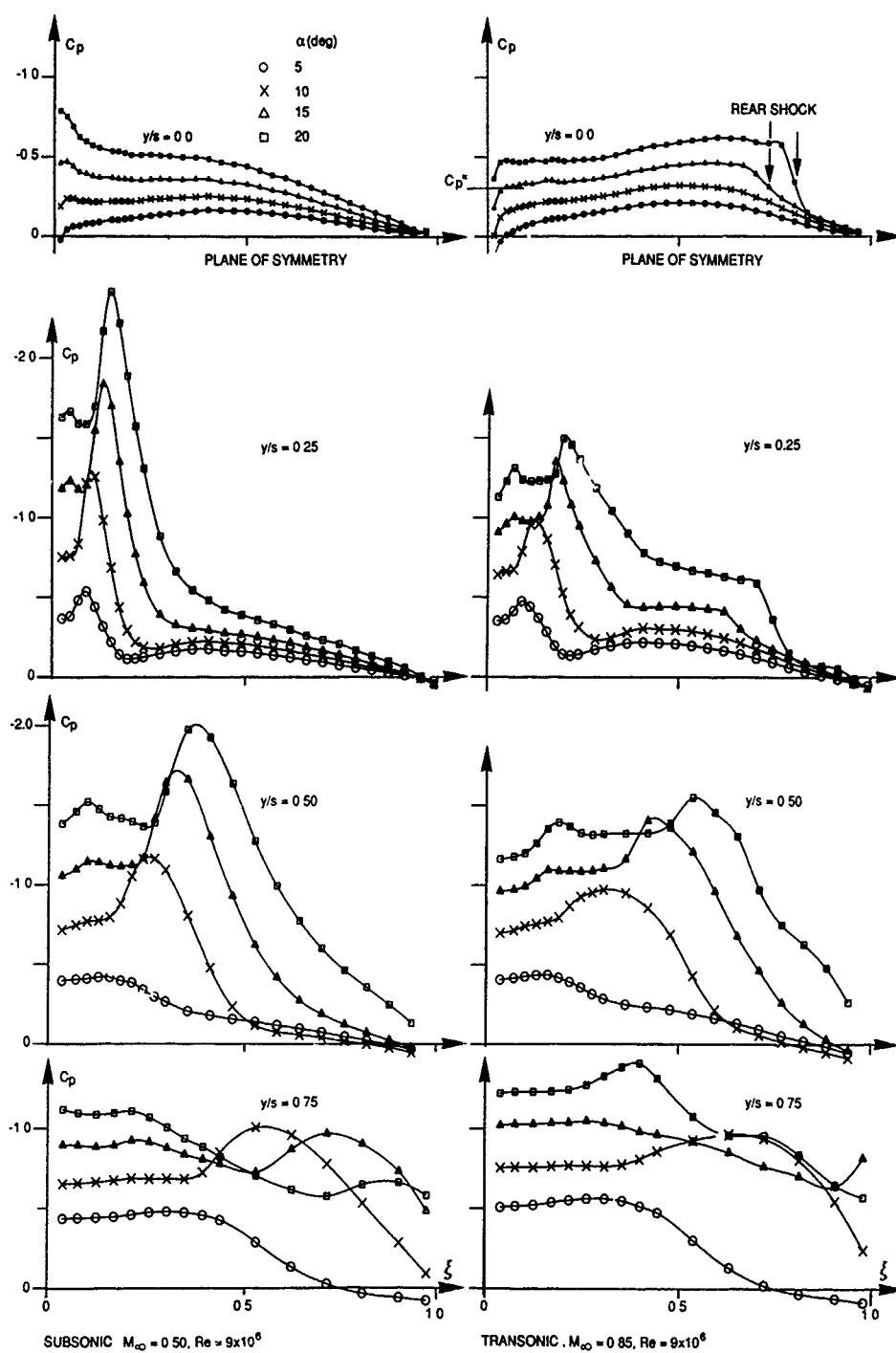
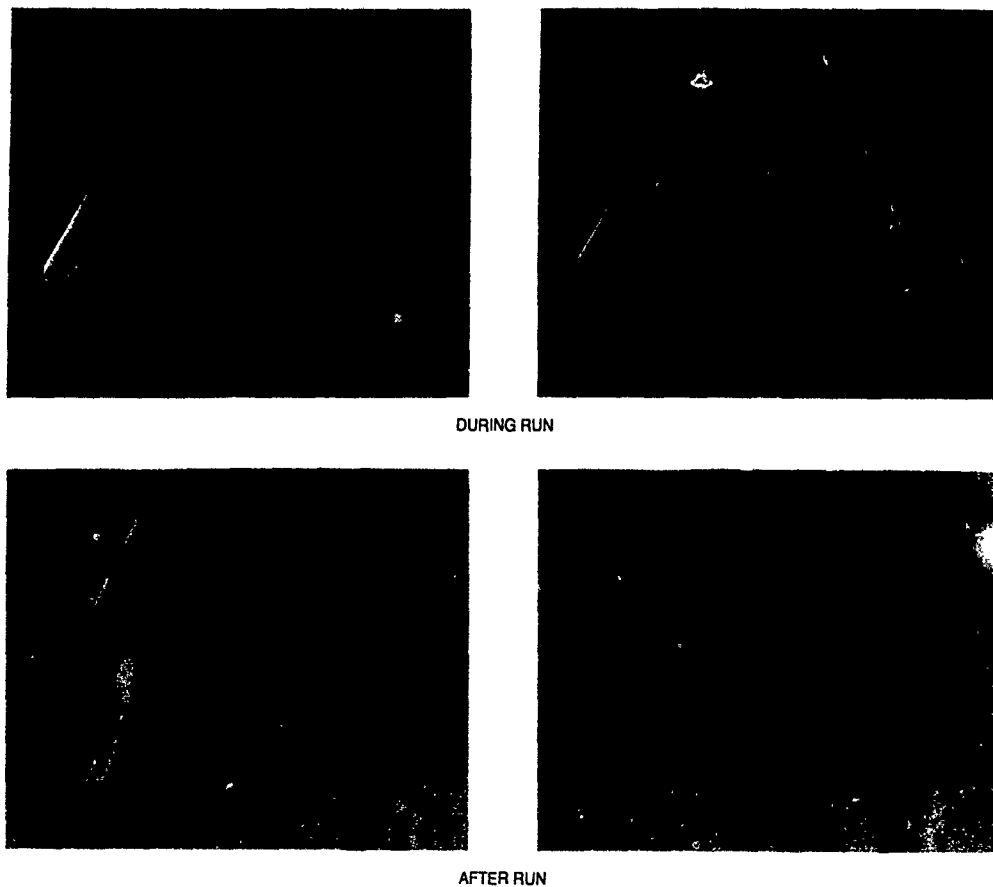


Fig. 5b Chordwise surface pressure distribution



DURING RUN

AFTER RUN

SUBSONIC ·  $M_{\infty} = 0.50$ ,  $\alpha = 20$  deg  $Re = 9 \times 10^6$ TRANSONIC ·  $M_{\infty} = 0.85$ ,  $\alpha = 20$  deg  $Re = 9 \times 10^6$ 

Fig 6 Oil-flow visualization on the upper wing surface

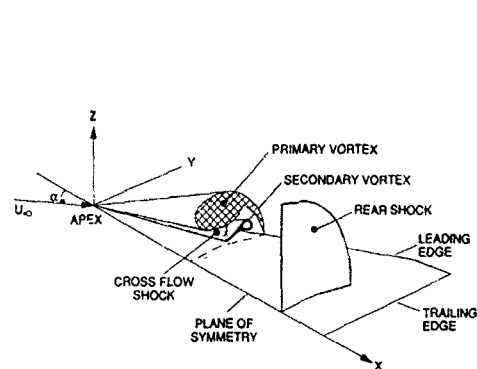


Fig 7 Formation of shock waves above a sharp-edged configuration

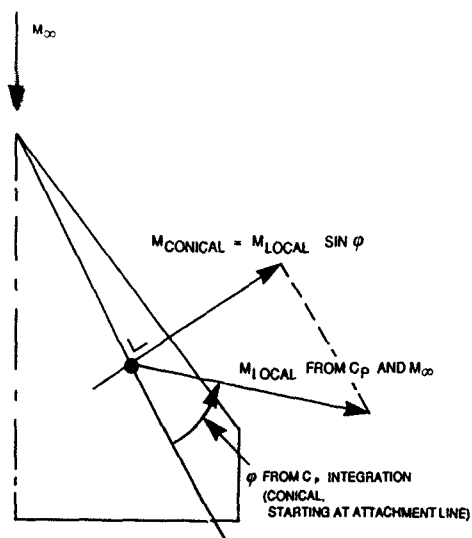


Fig. 9 Approximate analysis to determine component of Mach number normal to isobar

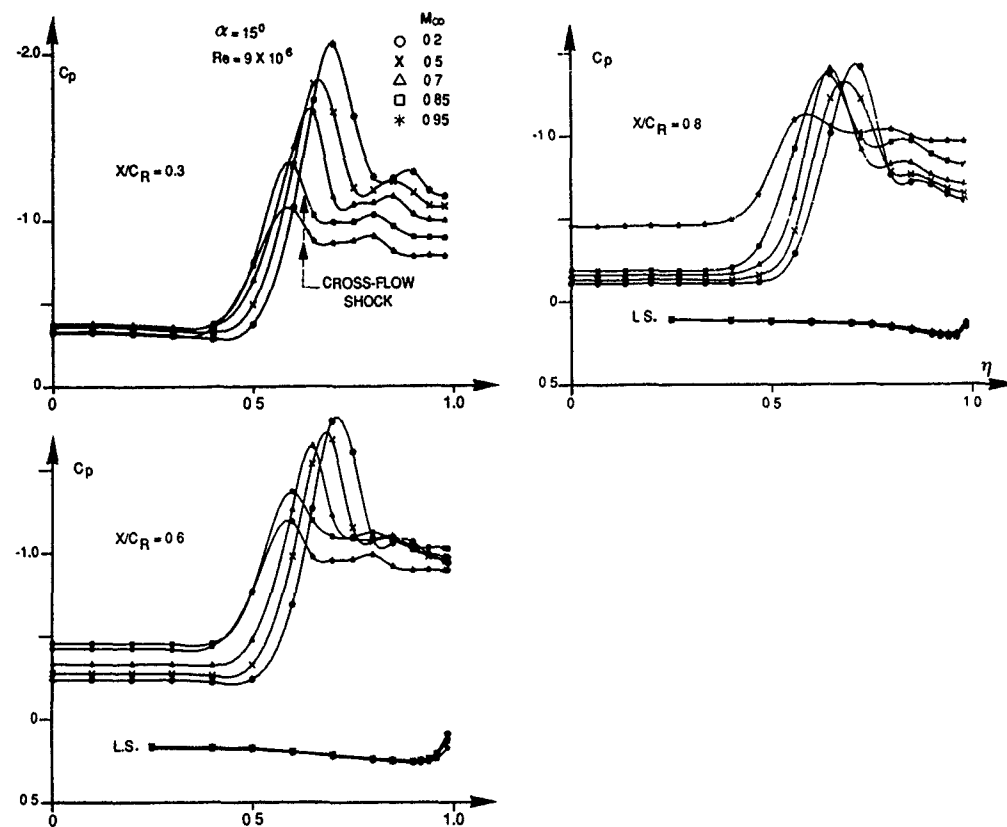


Fig. 8 Development with Mach number of spanwise surface pressure distribution,  $\alpha = 15$  deg

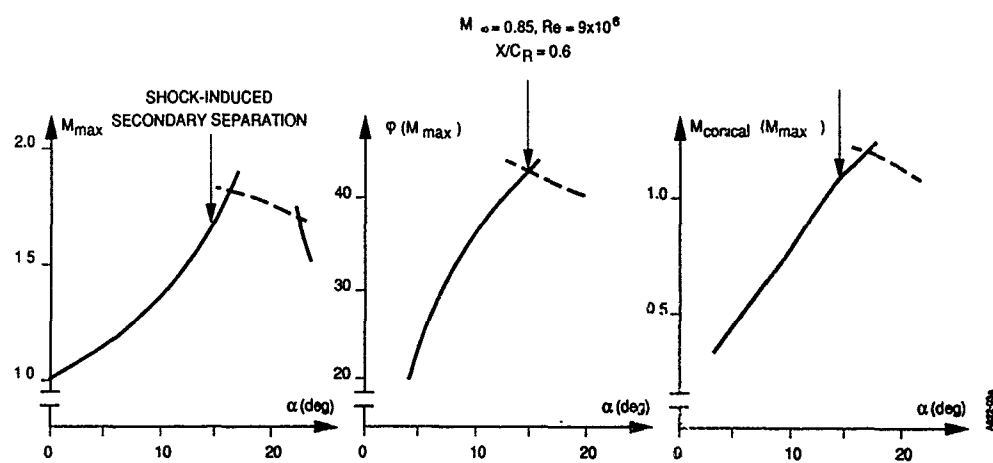


Fig. 10 Cross-flow shock induced secondary separation

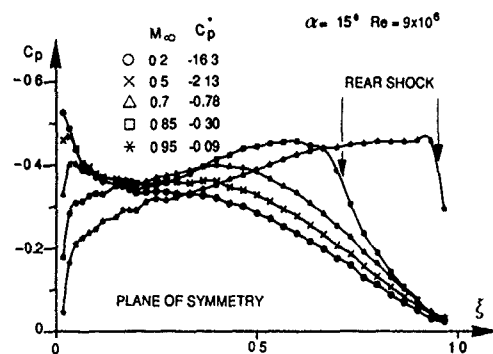


Fig. 11 Development with Mach number of chordwise surface pressure distribution,  $\alpha = 15$  deg

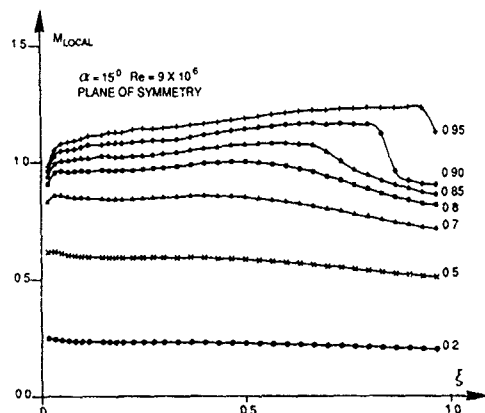


Fig. 12 Development with Mach number of chordwise local Mach number distribution,  $\alpha = 15$  deg

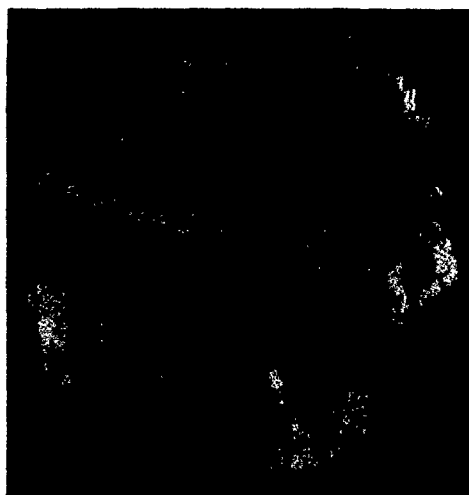
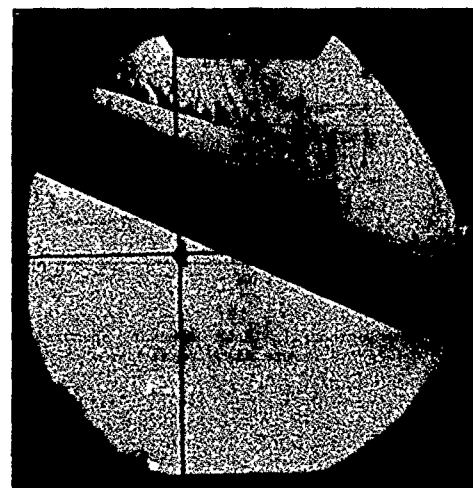


Fig. 13 Schlieren picture for transonic flow showing the rear shock



$M_\infty = 0.2$ ,  $\alpha = 20$  deg  $Re = 9 \times 10^6$



$M_\infty = 0.2$ ,  $\alpha = 24$  deg  $Re = 9 \times 10^6$

Fig. 14 Schlieren picture for subsonic flow just before and after vortex breakdown

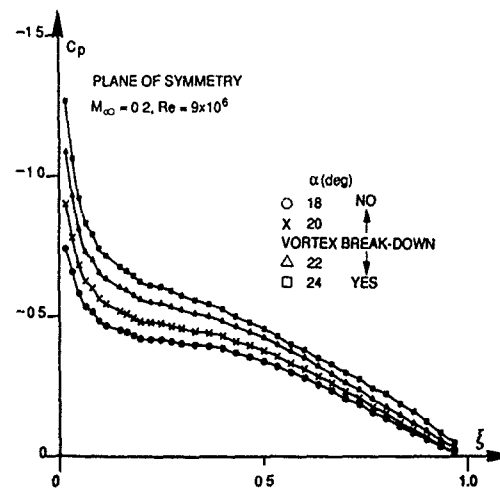


Fig. 15 Chordwise surface  $C_p$ -distribution in the plane of symmetry, before and after vortex breakdown, subsonic flow

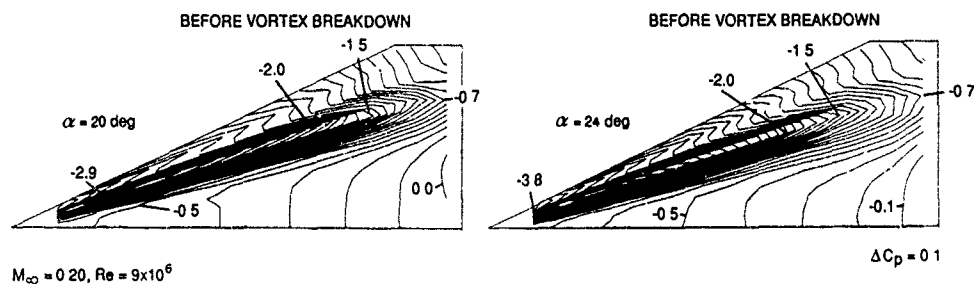


Fig. 16 Isobar pattern on upper surface before and after vortex breakdown, subsonic flow

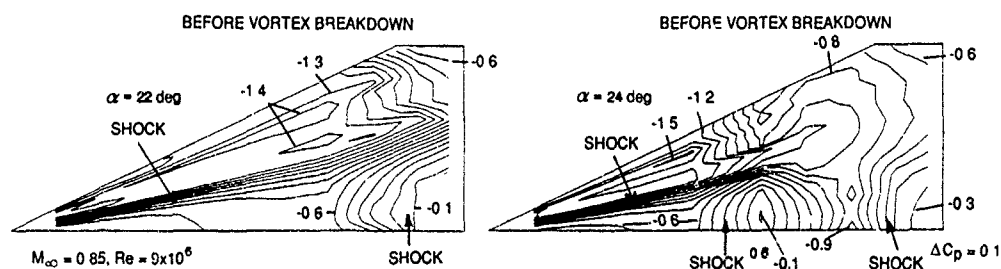
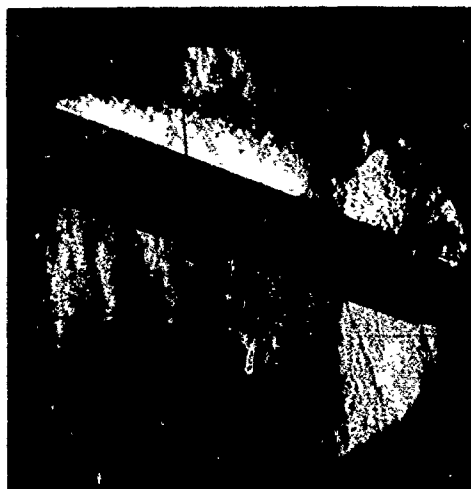


Fig. 17 Isobar pattern on upper surface before and after vortex breakdown, transonic flow



$M_\infty = 0.85, \alpha = 22 \text{ deg } Re = 9 \times 10^6$

$M_\infty = 0.85, \alpha = 24 \text{ deg } Re = 9 \times 10^6$

Fig. 18 Schlieren pictures just before and just after vortex breakdown, transonic flow

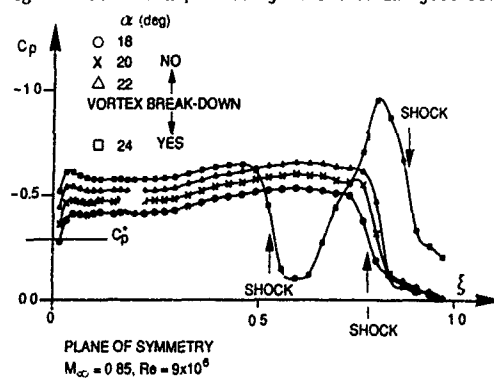


Fig. 19 Chordwise surface  $C_p$ -distribution in the plane of symmetry, before and after vortex breakdown, transonic flow

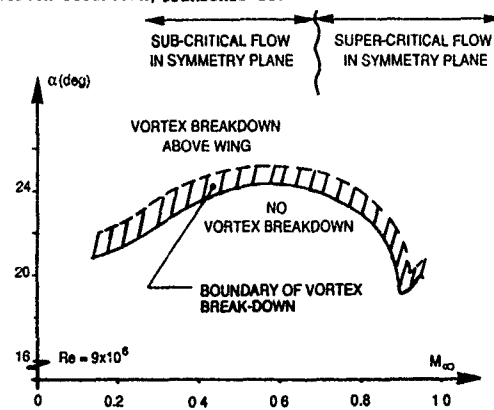


Fig. 20 Onset of vortex breakdown as a function of the free-stream Mach number

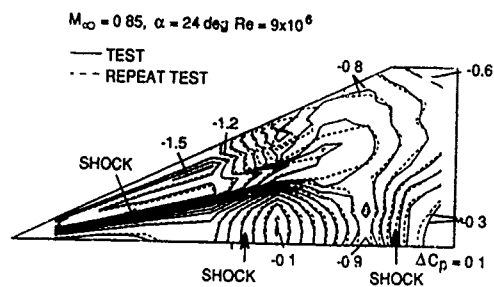


Fig. 21 Measure for unsteadiness of flow after vortex breakdown, isobar pattern at two moments in time

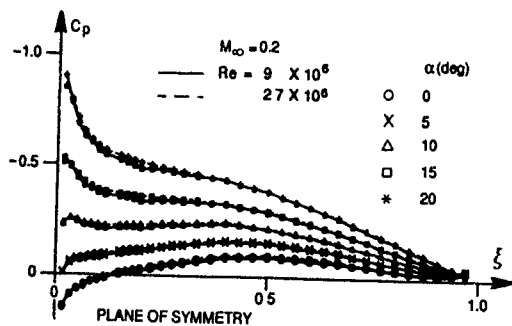


Fig. 22 Effect of Reynolds number on the chord-wise surface pressure distribution, subsonic flow

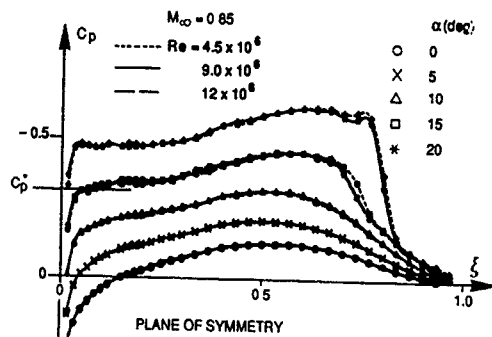


Fig. 23 Effect of Reynolds number on the chord-wise surface pressure distribution, transonic flow

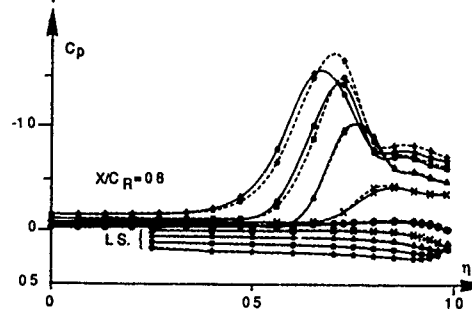
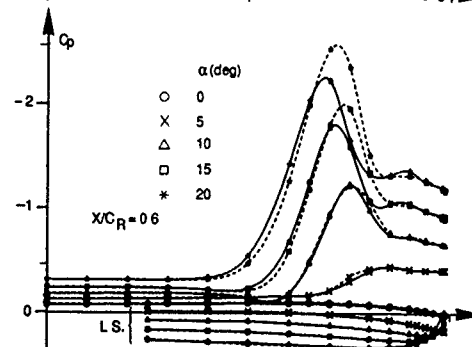
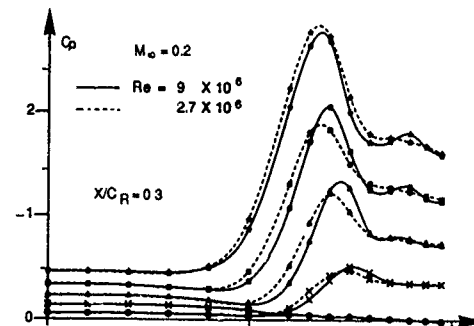


Fig. 24 Effect of Reynolds number on the span-wise surface pressure distribution, subsonic flow



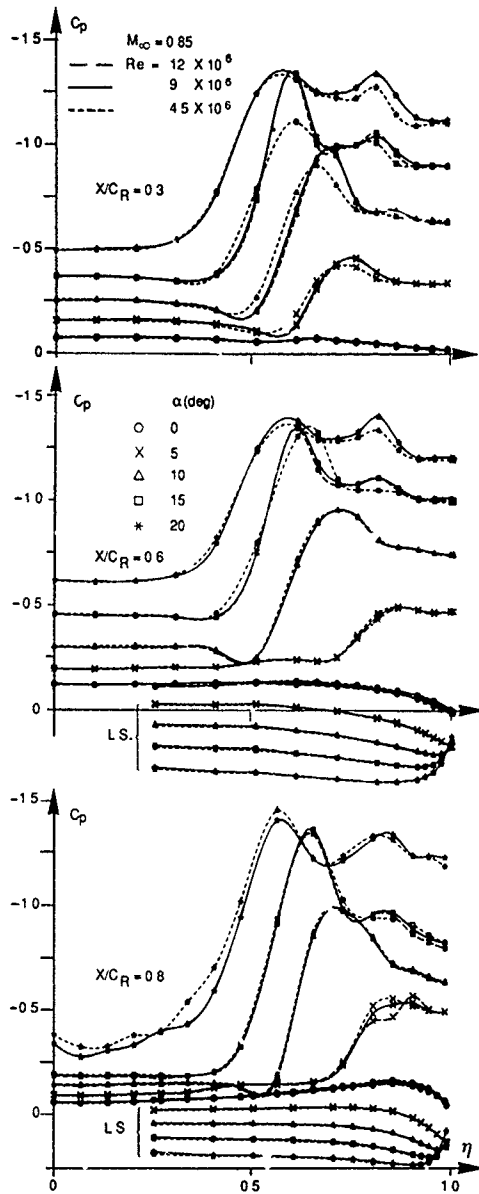


Fig. 25 Effect of Reynolds number on the spanwise surface pressure distribution, transonic flow

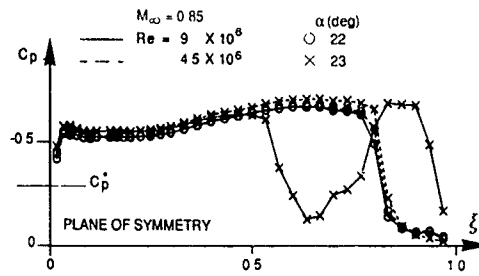


Fig. 26 Effect of Reynolds number on the chordwise surface pressure distribution, near vortex breakdown, transonic flow

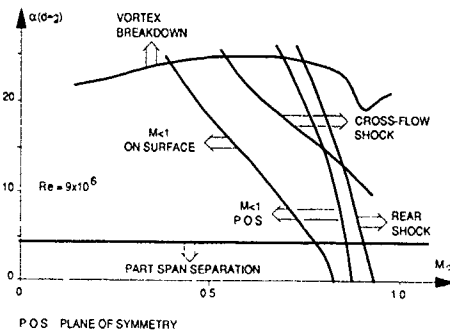


Fig. 27 Summary of flow features in  $(M_\infty, \alpha)$  plane

# CARACTERISTIQUES D'UNE COUCHE LIMITE EN AVAL D'UN TOURBILLON DE BORD D'ATTAQUE

G. PAILHAS - J. COUSTEIX

ONERA/CERT  
Département d'Aérothermodynamique  
2 avenue E. Belin - 31055 TOULOUSE CEDEX (FRANCE)

## RESUME

On étudie expérimentalement le comportement de la couche limite se développant en aval d'un tourbillon de bord d'attaque sur l'extrados d'une aile mise en flèche et en incidence.

Le profil d'aile considéré est un profil ONERA D de type peaky; l'aile est symétrique avec une épaisseur relative de 0,10 et une corde de 200 mm; elle est montée entre les deux parois haute et basse de la veine d'essais et maintenue en une position telle que l'angle de flèche soit égal à  $60^\circ$  et l'angle d'incidence à  $15^\circ$ .

Le champ de la vitesse moyenne et le champ turbulent ont été mesurés en diverses stations en aval de la ligne de recollement du tourbillon de bord d'attaque mais également en quelques stations au cœur du tourbillon à l'aide de sondes anémométriques à 1 fil et 4 fils chauds.

## SUMMARY

The boundary layer developing downstream a leading edge vortex has been investigated. This experiment is devoted to the understanding of the behaviour of such a boundary layer submitted to the effects of a leading edge vortex developing on the suction side of a swept wing.

The infinite swept wing considered for the present study is mounted between the top and the bottom walls of the test section at a sweep angle of  $60^\circ$  and at an incidence of  $15^\circ$ . The aerofoil is symmetric and has a maximum thickness ratio of .1 and a chord length of 200 mm; it is an ONERA D aerofoil, i.e. peaky-type aerofoil.

Mean and turbulent velocity profiles surveys have been carried out in various positions located downstream of the reattachment line but also for few positions in the vortex core by means of hot wire anemometry; measurements in the vortex core and in the boundary layer have been made by using respectively a four and single hot wire probe.

## 1 - INTRODUCTION

Les phénomènes aérodynamiques relatifs au cas très général de l'aile en attaque oblique constituent encore aujourd'hui, après avoir suscité un intérêt certain pendant des décennies, un des pôles essentiels de la recherche aéronautique moderne. En effet, que ce soit dans le cadre du vol dans le domaine du haut subsonique, du vol aux grandes incidences ou du vol purement dans le domaine supersonique, il importe d'approfondir davantage les connaissances et les enseignements issus des mesures ou des visualisations d'écoulements autour d'un tel type d'aile.

De ces recherches et investigations sur la structure de ces écoulements dépendent les qualités et les performances de l'avion.

Que connaissons-nous déjà, fruit de nos recherches et de nos investigations, de la structure de l'écoulement autour d'une aile en flèche?

Nous savons qu'une structure tourbillonnaire se développe à l'extrados de l'aile, lorsque celle-ci est placée avec suffisamment de flèche et d'incidence, qui régit et influence ses qualités et performances.

Le schéma d'un écoulement tourbillonnaire, alimenté par du fluide provenant de l'intrados, se décomposant en un tourbillon principal, éventuellement accompagné de tourbillons secondaires contrarotatifs (dans le cas d'une aile épaisse), est depuis longtemps acquis.

On sait que la présence tourbillonnaire pour un angle de flèche donné dépend de l'incidence de l'aile ; mais cette incidence, nécessaire à l'animation tourbillonnaire est fortement liée à la géométrie du bord d'attaque de l'aile (Réf. 1).

On sait également que le nombre de Reynolds constitue un facteur déterminant dans la présence d'un écoulement tourbillonnaire sur une aile ; d'une façon très générale, une augmentation du nombre de Reynolds conduit à une diminution sensible de son domaine d'existence.

Ainsi, dans le cas de profils de type "peaky", par exemple, caractérisés par l'existence d'une pointe de suritesse importante, c'est le nombre de Reynolds qui régit le "caractère transitionnel" de l'écoulement au bord d'attaque (notion de bulbe long ou bulbe court) et c'est précisément de ce caractère transitionnel dont dépend avant tout le comportement du tourbillon sur l'aile.

De fait, aux fortes valeurs du nombre de Reynolds, l'origine du tourbillon qui apparaît sur la partie externe de l'aile se déplace le long du bord d'attaque vers l'apex lorsque l'incidence croît (réf. 2) ; aux faibles valeurs du nombre de Reynolds, l'axe du tourbillon gardant la même origine dans la région de l'apex pivote, comme pour se rapprocher de la corde d'emplanture. Par la mesure du champ de vitesse autour du tourbillon, il est aujourd'hui aisé de déterminer avec précision à la fois sa trajectoire et son intensité.

Un tourbillon de bord d'attaque sur une aile en flèche n'est pas seulement un enroulement du fluide en cornet, bien organisé, mais aussi le signe d'une certaine instabilité.

Des expériences récentes (Réf. 3) ont montré, par le biais d'une étude spectrale, une forte contribution énergétique des fluctuations dans les basses fréquences, d'autant plus marquée que l'on se rapproche de la frontière du tourbillon ; il semblerait que des instabilités soient générées dans la région du décollement de bord d'attaque et se propagent sur la nappe tourbillonnaire jusqu'au recollement.

Il apparaît clairement que l'on définit la structure tourbillonnaire de l'écoulement autour d'une aile en flèche, en mesurant les vitesses moyennes et fluctuantes au sein de la nappe tourbillonnaire afin de préciser le comportement, la trajectoire et l'intensité du tourbillon mais aussi en définissant précisément la nature de l'écoulement dans cette région, creuset de son histoire, comprise entre le bord d'attaque de l'aile et la ligne de décollement.

Mettant à l'écart l'aspect essentiellement déterministe de l'écoulement tourbillonnaire, nous avons pensé qu'il était peut-être intéressant de s'attacher à la "qualité" de l'écoulement juste en aval du tourbillon ; que devient la couche limite d'extrados après avoir subi les effets fortement perturbateurs d'un écoulement tourbillonnaire ?

La couche limite hérite-t-elle d'une tridimensionnalité qui ne lui serait pas naturelle ? S'enrichit-elle d'une turbulence qu'à elle seule, elle ne pourrait convecter ? Garde-t-elle les "stigmates" d'un cisaillement accentué ?

Cette étude expérimentale s'inscrit dans le cadre très général de la caractérisation d'un écoulement cisailé tridimensionnel autour d'une aile en flèche. Une précédente étude avait été menée qui avait pour but de qualifier l'écoulement de coin dans une région délimitée par l'aile et le plancher de la veine d'essais (Réf. 4).

Avant de présenter les résultats essentiels relatifs à la couche limite se développant en aval du recollement, nous donnons quelques résultats de mesures effectuées au sein du tourbillon.

## 2 - MONTAGE EXPERIMENTAL

Le montage expérimental est constitué d'un profil d'aile (il s'agit d'un profil ONERA "D" de type Peak de 200 mm de corde et d'épaisseur relative égale à 0,10) placé avec une flèche de 60° et une incidence normale de 15°, dans la veine d'essai de la soufflerie. En fait, l'aile traverse la veine d'essai de part en part, au niveau du plancher et du plafond. La maquette est équipée de 5 rangées de prises de pression et grâce à un mécanisme (fig. 1) assurant sa translation, il est possible de définir très finement la répartition de la pression sur l'aile.

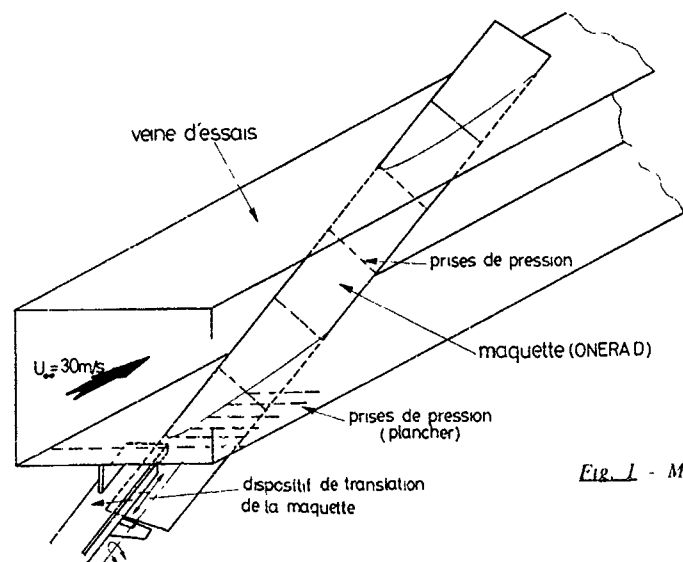


Fig. 1 - Montage expérimental

### 3 - CONDITIONS D'ESSAIS ET TECHNIQUES DE MESURE

Lors de ces essais, la vitesse de référence dans la veine a été fixée à  $30 \text{ ms}^{-1}$  correspondant à un nombre de Reynolds de corde de  $4 \cdot 10^5$ .

Le système d'exploration (fig. 2), entièrement automatisé, comporte 5 motorisations "attachées" à 5 degrés de liberté : trois translations et deux rotations.

Ce dispositif permet donc de déplacer une sonde dans des plans perpendiculaires à l'axe veine en alignant celle-ci dans une direction privilégiée, la direction de la ligne de courant locale par exemple, et en assurant sa translation suivant une normale en tout point au profil. Cet explorateur est relié à un ordinateur qui assure son pilotage permettant le déplacement de la sonde et son positionnement automatique au point de mesure.

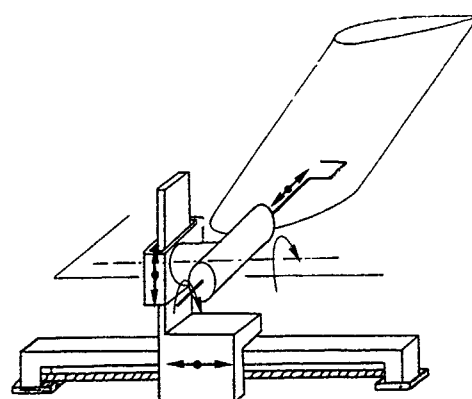


Fig. 2 - Schéma du dispositif d'exploration

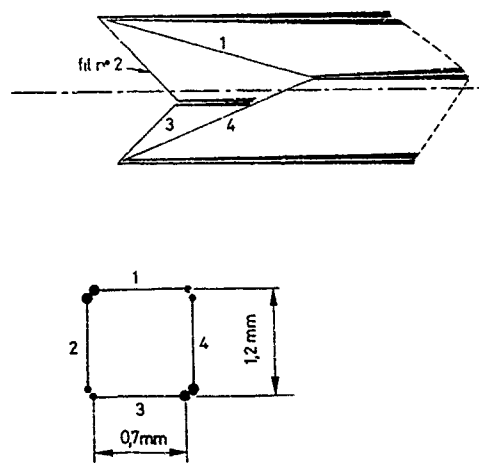


Fig. 3 - Schéma de la sonde à quatre fils chauds

Les mesures effectuées sont essentiellement des mesures par anémométrie fil chaud ; deux types de sondes ont été utilisées :

- sonde à quatre fils chauds (fig. 3) pour la détermination à la fois du champ moyen et du champ turbulent dans des plans perpendiculaires à l'axe veine ; chaque plan constitue un maillage de 30 points de mesure (suivant la direction OY) par 35 points (suivant la direction OZ) ; les points les plus rapprochés du profil se trouvent environ à 1 mm de celui-ci ;
- sonde miniature à 1 fil spécialement adaptée à la mesure de la vitesse moyenne et de sa composante fluctuante dans la direction longitudinale de l'écoulement, au sein d'une couche limite de faible épaisseur.

### 3.1. Méthode de mesure avec la sonde à quatre fils

La sonde à quatre fils (fig. 3) est conçue de telle sorte que les fils forment un ensemble de deux sondes en X. Si l'on suppose que l'angle  $\gamma$  entre un fil et l'axe de la sonde est le même pour tous les fils et que la vitesse effective Ueff est la vitesse normale au fil, on peut écrire pour une sonde idéale :

$$U_{eff1}^2 = (U \sin \gamma - W \cos \gamma)^2 + V^2$$

$$U_{eff3}^2 = (U \sin \gamma - W \cos \gamma)^2 + V^2$$

$$U_{eff2}^2 = (U \sin \gamma - V \cos \gamma)^2 + W^2$$

$$U_{eff4}^2 = (U \sin \gamma - V \cos \gamma)^2 + W^2$$

où U, V, W sont les composantes de la vitesse dans un repère cartésien lié à la sonde.

La mesure des tensions  $E_1, E_2, E_3$  et  $E_4$  fournit les valeurs de  $U_{eff1}, U_{eff2}, U_{eff3}, U_{eff4}$  d'après lesquelles on doit calculer les composantes de la vitesse.

Le principe de la méthode mise en oeuvre consiste à déterminer trois fonctions des vitesses effectives qui donnent directement la valeur de la vitesse en module et direction.

Le vecteur vitesse est repéré par rapport à la sonde à l'aide de deux angles  $\theta$  et  $\varphi$  (fig. 4) et l'on forme les quantités :

$$f = \text{Arctg} \frac{U_{eff2}^2 - U_{eff4}^2}{U_{eff1}^2 - U_{eff3}^2} \quad g = \frac{[(U_{eff1}^2 - U_{eff3}^2)^2 - (U_{eff2}^2 - U_{eff4}^2)^2]^{1/2}}{\sum U_{effi}^2} \quad h = \sum U_{effi}^2$$

On a :

$$U_{eff1}^2 - U_{eff3}^2 = -4 UW \sin \gamma \cos \gamma$$

$$U_{eff2}^2 - U_{eff4}^2 = -4 UV \sin \gamma \cos \gamma$$

d'où :

$$f = \varphi \quad g = \frac{\sin 2\gamma \tan \theta}{2 \sin^2 \gamma + \tan^2 \theta (1 + \cos 2\gamma)} \quad h = [U]^2 [4 \sin^2 \gamma + 2 \tan^2 \theta (1 + \cos 2\gamma)]$$

Ces formules permettent donc de déterminer directement les angles  $\varphi$  et  $\theta$  et le module de la vitesse.

La solution est unique si l'on admet que  $\theta$  est inférieur à une valeur  $\theta_m$  pour laquelle la fonction  $g$  possède un maximum  $g_m$  ; l'expression de  $g$  montre que  $\theta_m$  et  $g_m$  sont fonctions de l'angle  $\gamma$ .

En fait, les formules données ci-dessus sont théoriques et un étalonnage est nécessaire. Il consiste essentiellement à mesurer les vitesses effectives en fonction des angles  $\theta$  et  $\varphi$  pour une valeur fixée du module de la vitesse.

L'étalonnage est réalisé pour les valeurs de  $\varphi$  comprises entre  $-180^\circ$  et  $+180^\circ$  par pas de  $15^\circ$  et pour les valeurs de  $\theta$  comprises entre  $0$  et  $45^\circ$  par pas de  $5^\circ$ ; la vitesse de la soufflerie est donc fixée et la sonde est déplacée par rapport au vecteur vitesse.

Pour chaque valeur de  $\theta$  et  $\varphi$ , on relève la tension  $E$  et l'on en déduit la vitesse effective  $U_{eff}$ .

En fonction de  $\theta$  et  $\varphi$ , on détermine alors les variations des fonctions  $F$ ,  $G$ ,  $H$  définies par :

$$F = \text{Arctg} \frac{U_{eff2}^2 - U_{eff4}^2}{U_{eff1}^2 - U_{eff3}^2} \quad G = \frac{(|U_{eff1} - U_{eff3}| + |U_{eff2} - U_{eff4}|)}{\sum U_{effi}} \quad H = \frac{\sum U_{effi}^2}{\sum U_{effi}^2(\theta=0)}$$

La fonction  $F$  est identique à la fonction  $f$  définie précédemment, mais les fonctions  $G$  et  $H$  sont différentes de  $g$  et  $h$ ; la forme de  $G$  a été préférée à celle de  $g$  car il a été observé qu'elle permet d'étendre légèrement le domaine de mesure en  $\theta$  et la forme de  $H$  est simplement égale  $h/h(\theta=0)$ , ce qui permet d'éliminer l'influence du module de la vitesse.

Les fonctions  $F$ ,  $G$  et  $H$  déterminées expérimentalement sont représentées sur les figures 5a, b, c. On observe que  $F$  n'est pas fonction de  $\theta$ ;  $F$  est fonction seulement de  $\varphi$ ; notons que pour une sonde idéale, on aurait  $F = \varphi$ .

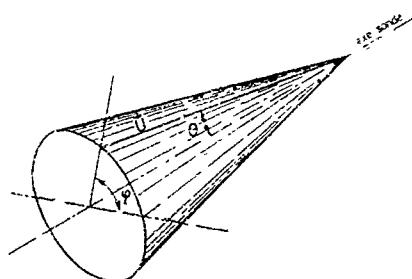


Fig. 4 - Définitions

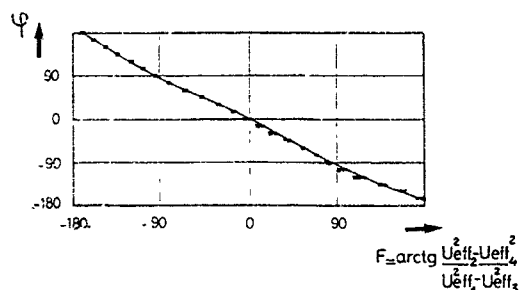


Fig. 5a - Etalonnage angulaire : évolution de  $F$

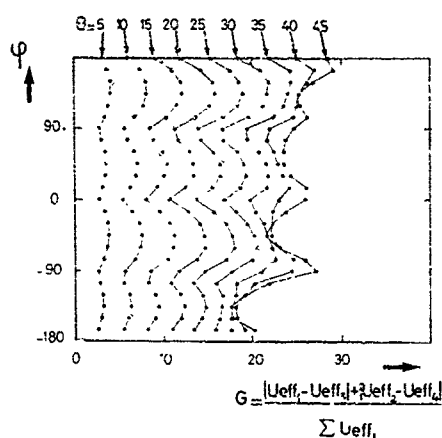


Fig. 5b - Etalonnage angulaire : évolution de  $G$

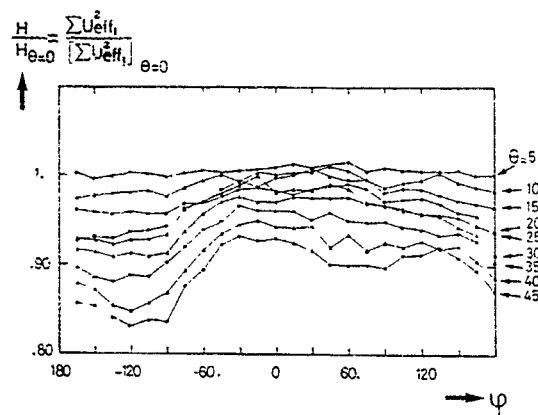


Fig. 5c - Etalonnage angulaire : évolution de  $H$

La fonction  $G$ , fonction théoriquement de  $\theta$  seulement, dépend en fait de  $\theta$  et  $\varphi$ ; la fonction  $H$  dépend peu de  $\varphi$  aux faibles valeurs de  $\theta$ , mais ses variations s'accroissent lorsque  $\theta$  augmente. Dans une expérience, la direction du vecteur vitesse par rapport à la sonde n'est pas connue. En un point de l'écoulement, la mesure consiste à relever les tensions  $E_1, E_2, E_3, E_4$  appliquées à chaque fil. A partir de ces tensions  $E_i$ , on calcule les vitesses effectives  $U_{effi}$  et on forme la fonction  $F$ . On en déduit la valeur de l'angle  $\varphi$ ; on forme ensuite la fonction  $G$ , ce qui fournit la valeur de l'angle  $\theta$ . Enfin, connaissant  $\theta$

et  $\varphi$ , on détermine la valeur de la fonction  $H = \Sigma U_{eff,i}^2 / \Sigma U_{eff,i}^2_{\theta=0}$  ; or, d'après les mesures, on connaît la quantité  $\Sigma U_{eff,i}^2$  ; on obtient donc la valeur de  $\Sigma U_{eff,i}^2_{\theta=0}$  qui, par définition, est égale à  $4 |U|^2 \sin^2 \gamma$  ; d'où la valeur du module de la vitesse  $|U|$ .

De cette façon, on calcule finalement les composantes de la vitesse instantanée ; ces mesures sont répétées un grand nombre de fois, de manière à réaliser un échantillonnage convenable.

Les composantes de la vitesse moyenne ainsi que les tensions de Reynolds sont alors calculées par traitement statistique.

### 3.2. Méthode de mesure avec la sonde miniature à un fil

Une sonde "miniature" à un fil de longueur 0,6 mm a été réalisée de telle sorte que soit minimisé son encombrement lors des mesures au sein de la couche limite en aval du tourbillon. Rappelons que la sonde est montée sur un support motorisé qui autorise notamment une translation suivant un axe normal à la paroi du profil et une rotation autour de ce même axe.

Le principe de la mesure consiste à faire tourner la sonde autour de son axe et à enregistrer la tension délivrée par l'anémomètre pour différentes inclinaisons du fil par rapport à l'écoulement. Ainsi, la direction de la vitesse correspond à l'angle d'inclinaison du fil pour lequel la tension à ses bornes est maximum. La position du maximum est obtenue par la méthode indiquée sur la figure 6 : la courbe formée par les points de mesure est coupée par différentes droites  $E = \text{cste}$  et la position du maximum est déterminée en extrapolant le lieu des milieux des segments formés par les points d'intersection des différentes droites  $E = \text{cste}$ .

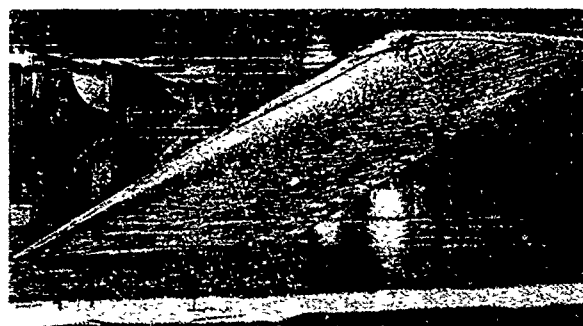
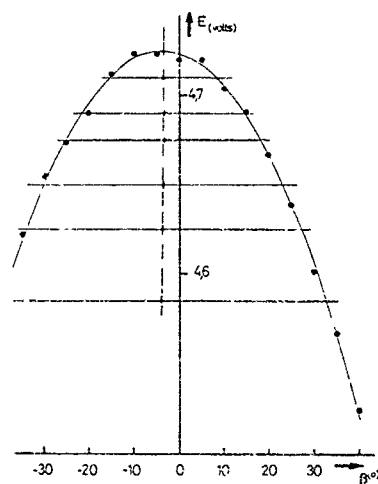


Fig. 7 - Visualisation pariétale

Fig. 6 - Méthode de mesure avec la sonde à un fil

La direction de la vitesse locale étant ainsi déterminée, la sonde est alignée dans cette direction privilégiée et l'acquisition de la tension délivrée par le fil est alors déclenchée.

## 4 - VISUALISATIONS ET REPARTITIONS DE PRESSION

### 4.1. Visualisations pariétales

Les visualisations pariétales ne fournissent, certes, qu'une vue d'ensemble et figée de l'écoulement mais donnent de ce dernier, dans le cas plus particulier des écoulements à structure tourbillonnaire, une première et indispensable caractérisation.

L'aile est entièrement recouverte d'un enduit, composé de phtalate de butyle et de noir de fumée, dont la viscosité nécessite d'être finement adaptée au cas de l'essai.

Compte tenu de l'incidence et de la flèche du profil, l'écoulement d'intrados contourne le bord d'attaque et décolle sous l'effet d'un gradient de pression positif intense; l'écoulement s'organise alors en formant un tourbillon en cornet qui s'amplifie au fur et à mesure que l'on s'éloigne de l'emplanture. Le tourbillon imprime très nettement sur l'enduit visqueux ce que nous appelons abusivement sa trace et qui correspond en fait à une ligne de recollement (R) du fluide; très schématiquement, on peut dire que la région comprise entre le bord d'attaque et cette ligne (R) correspond à la région tourbillonnaire (figure 7). Cette ligne de recollement est aussi bien souvent appelée ligne de partage, car c'est à partir de cette dernière que le fluide tente de se rétablir en une couche limite stable sur l'extrados du profil.

On note aussi que, vers le bord de fuite, les lignes tracées sur l'enduit visqueux sont moins bien fermées: signe que l'enduit est moins entraîné et donc que le frottement est plus faible.

Ce schéma de l'écoulement tourbillonnaire sur l'extrados du profil semble être parfaitement validé par nos résultats expérimentaux; sur la figure 8, nous avons retracé la ligne de recollement telle que nous l'avons obtenue d'après les sondages de couche limite sur le profil et nous l'avons comparée à son dessin issu de la visualisation pariétale; l'axe du tourbillon déduit des courbes de pression, en considérant le  $C_p$  tourbillonnaire minimum, est également représenté; la cohérence des résultats de mesures et de visualisation est tout à fait satisfaisante.

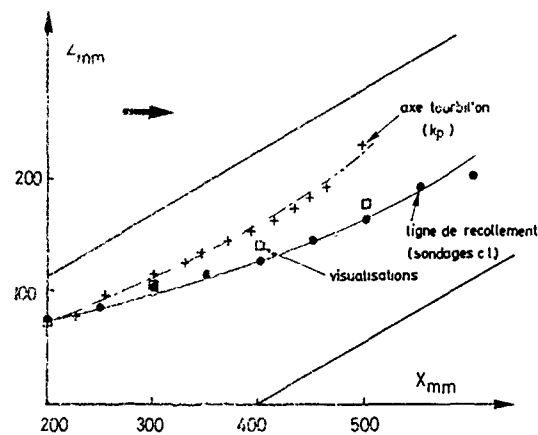


Fig. 8 - Schématisation de l'écoulement tourbillonnaire sur l'aile

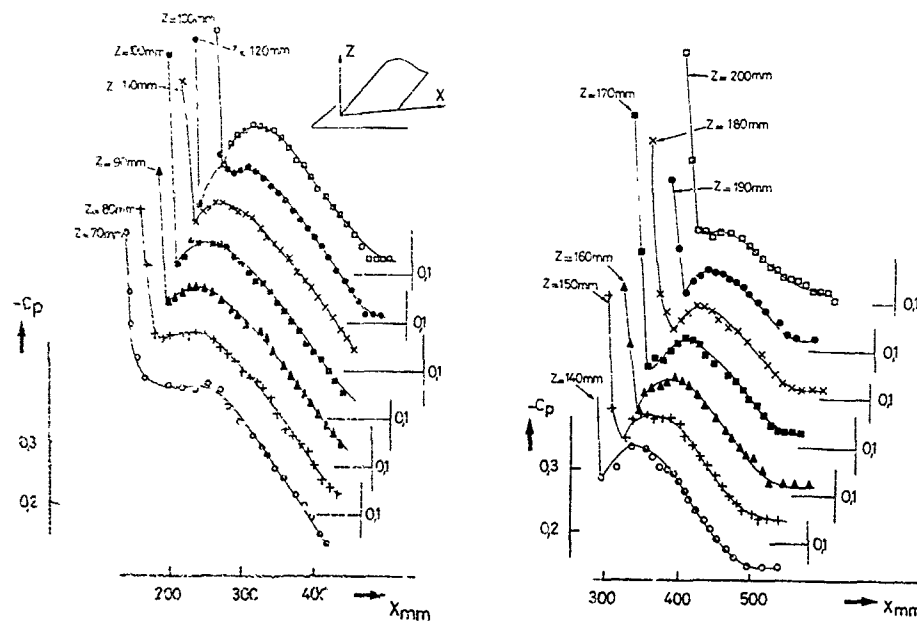


Fig. 9a, b - Répartition de pression sur l'aile



#### 4.2. Répartitions de pression

Grâce aux prises de pression dont est équipé le profil et au degré de liberté de translation dont il est doté, on peut définir assez précisément les répartitions des pressions sur toute sa surface d'extrados.

Les figures 9a, b donnent l'évolution du coefficient de pression ( $C_p = p - p_0 / \frac{1}{2} \rho U_0^2$ ) sur l'aile en différentes lignes  $Z = \text{cste}$  parallèles à la ligne d'intersection entre le profil et le plancher de la veine et formant l'axe  $OX'$ , l'origine  $O$  étant située à l'intersection du bord d'attaque et du plancher.

Un pic de survitesse (non représenté sur les figures) apparaît dans la région du bord d'attaque et décroît progressivement lorsqu'on se rapproche de la jonction aile-plancher. La poche de dépression apparaissant après le pic de survitesse est caractéristique de la présence du tourbillon de bord d'attaque; on peut observer sur cette distribution de pression que la forme de "cloche" est plus prononcée dans la première moitié de l'aile (côté emplanture) que dans sa région extérieure.

Quelle que soit la station en  $Z$  considérée, cette poche de dépression est toujours suivie d'une forte recompression jusqu'au bord de fuite du profil.

La détermination de l'axe tourbillonnaire, comme il a été signalé au paragraphe précédent, peut être déduite de façon approximative à partir de la localisation, en diverses sections de l'aile, du  $C_p$  tourbillonnaire minimum.

#### 5 - MESURES AU SEIN DU TOURBILLON ET DANS LA REGION EXTRADOS DELIMITEE PAR L'AILE ET LE PLANCHER DE LA VEINE

La localisation des plans  $YOZ$  perpendiculaires à l'axe veine où ont été effectuées des mesures à l'aide de la sonde anémométrique à quatre fils est donnée sur la figure 10; ces mesures ne concernent pas seulement la région tourbillonnaire sur l'extrados de l'aile mais tout un plan perpendiculaire à la direction de l'écoulement amont et délimité par l'aile et le plancher de la veine; les sondages ont été effectués en divers plans  $YOZ$  situés à  $X = -75 \text{ mm}$ ,  $50 \text{ mm}$ ,  $150 \text{ mm}$ ,  $250 \text{ mm}$ ,  $350 \text{ mm}$ . Nous ne présenterons que les résultats relatifs à deux plans de mesures:  $X = 150 \text{ mm}$  et  $X = 250 \text{ mm}$ .

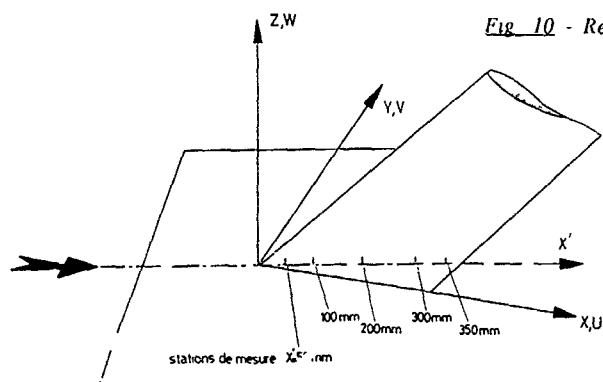


Fig 10 - Repère de projection - Stations de mesure

##### 5.1. Champ des vitesses secondaires ( $V$ , $W$ ) (fig. 11a, b)

Précisons, tout d'abord, que l'importance relative de la composante transversale de la vitesse  $V$  suivant la direction  $Y$  est due au repère de projection  $XYZ$  considéré; en effet, par rapport à la direction de la vitesse à l'infini amont, le plan  $(OX, OZ)$  est incliné de  $7,5^\circ$ , ce qui entraîne une répercussion sur le module de la composante  $V$  de la vitesse.

Dans la région proche du coin, à la station  $X = 150 \text{ mm}$  par exemple, on peut noter que les vitesses secondaires sont faibles; cependant, près du profil, la composante transversale  $W$  est relativement forte; il en est de même à la station  $X = 250 \text{ mm}$ .

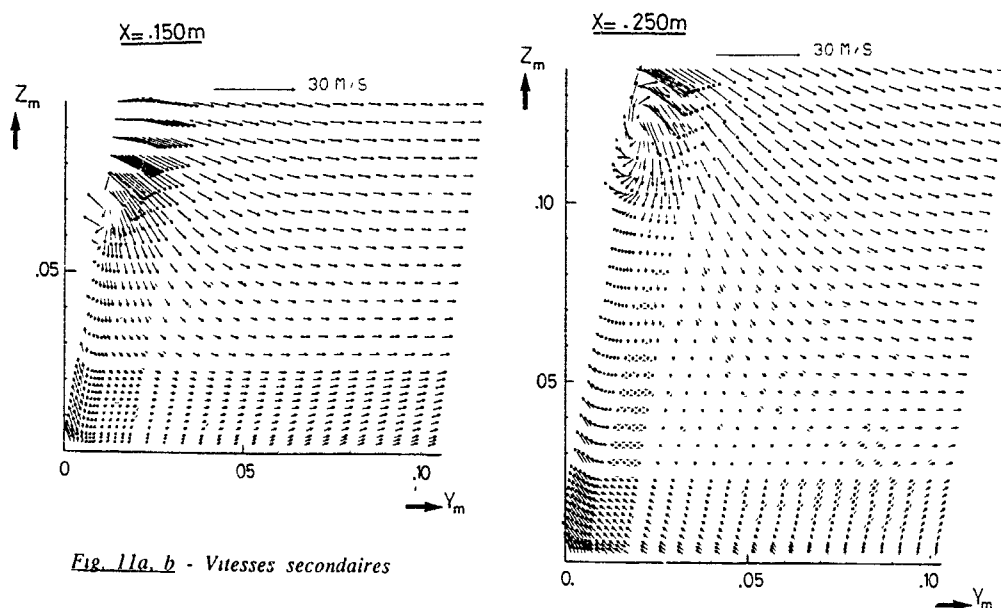


Fig. 11a, b - Vitesses secondaires

La structure tourbillonnaire du fluide contournant le bord d'attaque du profil est bien mise en évidence dans cette représentation; l'amplification de la zone tourbillonnaire est déjà décelable en considérant ces deux stations de mesure.

De même, l'inclinaison de l'axe du tourbillon par rapport au bord d'attaque du profil ainsi que son écartement progressif de la paroi peuvent être vérifiés.

## 5.2. Champ turbulent

Les figures 12a, b donnent une représentation sous la forme de lignes de niveau de la fluctuation longitudinale de la vitesse aux deux stations de mesure considérées. On peut bien sûr noter l'accroissement du  $u'$  lorsque l'on se rapproche de l'axe du tourbillon; les niveaux de la fluctuation de vitesse varient très peu d'une station de mesure à l'autre. Par contre, cette représentation met bien en évidence l'expansion de la zone tourbillonnaire lorsque l'on se rapproche de l'extrémité de l'aile.

Notons aussi que dans la région confinée du coin, on n'observe pas de mouvement caractéristique des lignes iso- $u'$  traduisant, comme l'a montré par exemple SHABAKA (Réf. 5), la présence d'un tourbillon de type fer à cheval dans le cas d'une aile droite.

L'utilisation de la sonde à quatre fils chauds nous a permis d'obtenir les six composantes du tenseur de Reynolds dans la région du plan YOZ intéressant le tourbillon.

Les corrélations  $\overline{u'v'}$ ,  $\overline{v'w'}$ ,  $\overline{u'w'}$  sont données sur la figure 13; nous pouvons remarquer que les trois composantes du frottement turbulent à l'intérieur du tourbillon sont du même ordre de grandeur. D'autre part, les termes  $\overline{u'v'}$  et  $\overline{v'w'}$  présentent un changement de signal franchement marqué au tiers environ de la hauteur du tourbillon suivant Z. L'évolution de ces deux quantités, qui représentent les composantes du frottement turbulent dans le plan XOZ, est à rapprocher de celle des gradients des composantes de la vitesse moyenne  $\frac{\partial U}{\partial y}$ ,  $\frac{\partial V}{\partial x}$  pour  $\overline{u'v'}$  et  $\frac{\partial V}{\partial z}$ ,  $\frac{\partial W}{\partial y}$  pour  $\overline{v'w'}$ ; la quantité  $\overline{u'v'}$  présente un changement de signe bien que le terme gradient  $\frac{\partial V}{\partial x}$  soit faible devant le terme  $\frac{\partial U}{\partial y}$ . Le terme  $\overline{u'w'}$ , caractérisant le frottement dans le plan XOY, bien que lié principalement au terme gradient  $\frac{\partial U}{\partial z}$  ne présente pas de changement de signe.

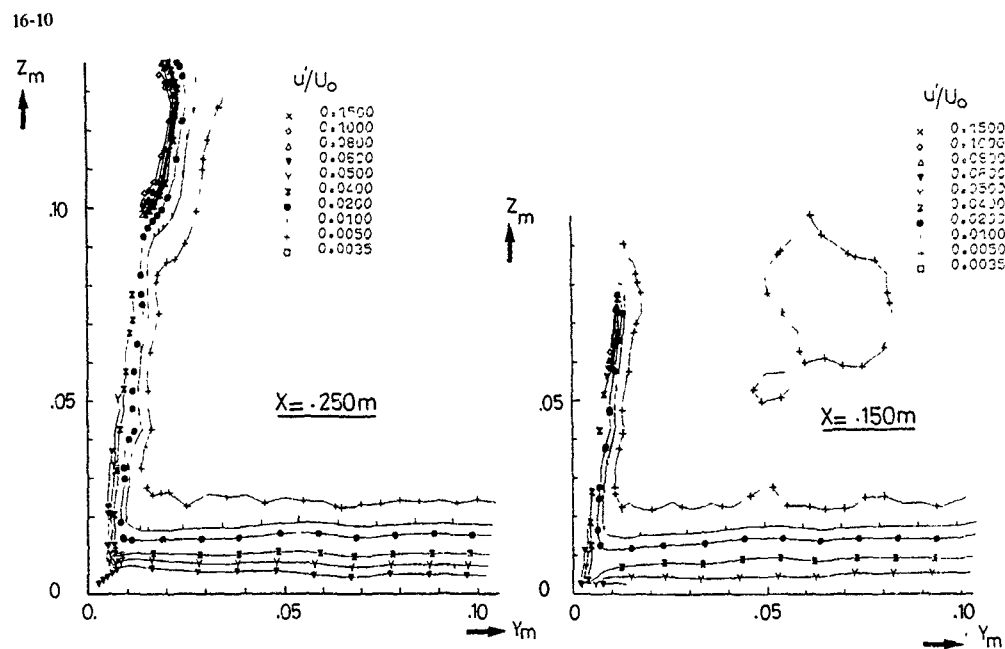


Fig. 12b - Lignes iso- $u'$  -  $X = 250 \text{ mm}$

Fig. 12a - Lignes iso- $u'$  -  $X = 150 \text{ mm}$

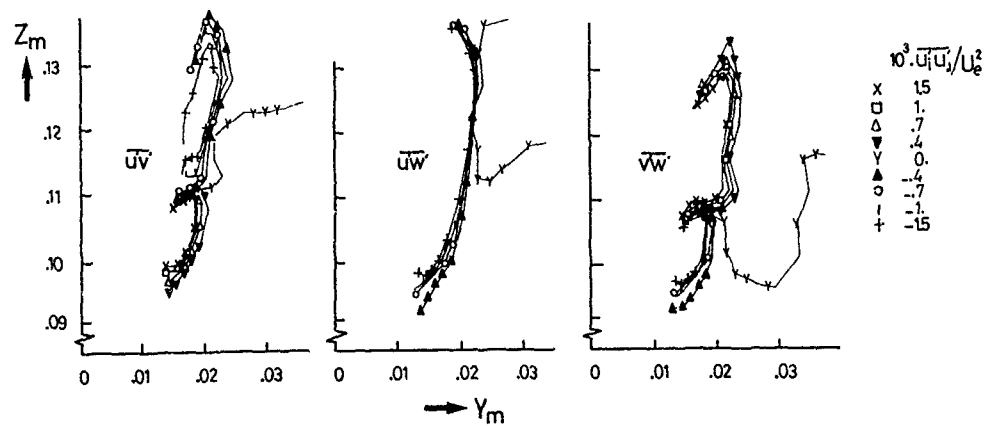


Fig. 13 - Lignes iso- $u_i u_j$  au coeur du tourbillon

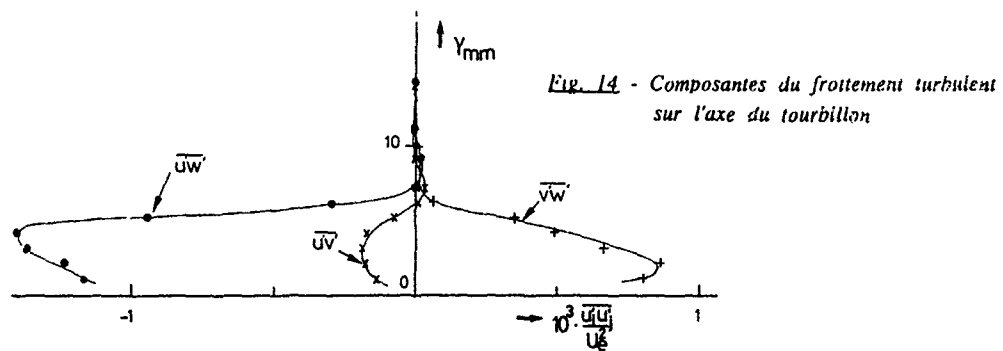


Fig. 14 - Composantes du frottement turbulent sur l'axe du tourbillon

Sur la figure 14, est représentée l'évolution des trois composantes du frottement turbulent suivant une direction  $Z = \text{cste}$  passant par l'axe du tourbillon; nous pouvons observer la faible contribution de la composante  $u'v'$ , dans la génération du frottement sur l'axe, en comparaison des deux autres composantes  $u'w'$  et  $v'w'$ .

## 6 - MESURES AU SEIN DE LA COUCHE LIMITE EN AVAL DU TOURBILLON

Afin de sonder la couche limite aussi près de la paroi que possible, le capteur utilisé est une sonde à un seul fil chaud.

Les sondages ont été effectués dans 9 plans de mesure suivant  $X$ :  $X = 200 \text{ mm}$  à  $X = 600 \text{ mm}$  (fig. 15).

La couche limite a été sondée en diverses altitudes  $Z$  pour une station  $X$  donnée en aval de la ligne de recollement, mais aussi pour quelques stations situées en amont de celle-ci, c'est-à-dire dans le tourbillon.

Les résultats sont exprimés dans un repère OXYZ (fig. 16) lié à la ligne de courant extérieure; OY est normal à la paroi du profil, OX est tangent à la ligne de courant extérieure, OZ est perpendiculaire à OX et OY.

Fig. 15 - Stations de mesure

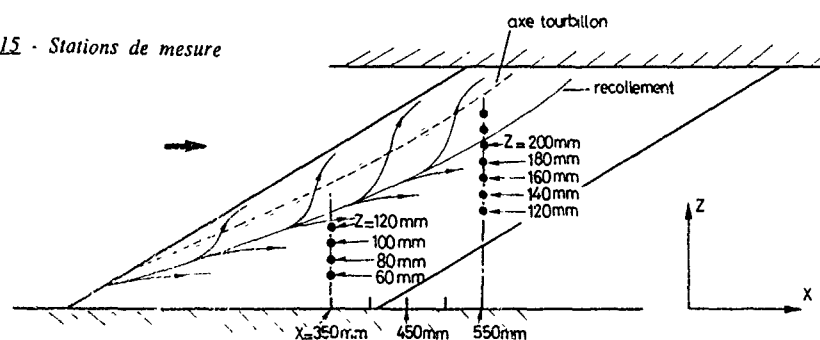
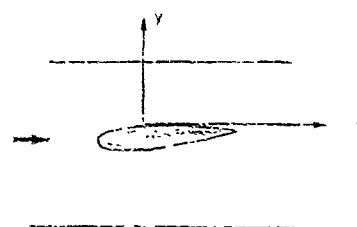
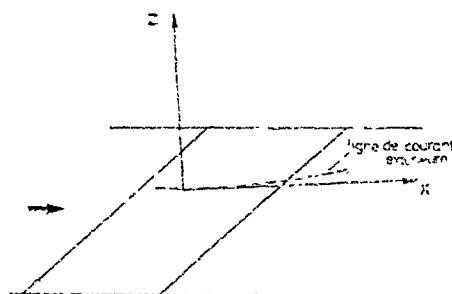


Fig. 16 - Repère de projection



### 6.1. Champ des vitesses moyennes

#### 6.1a. Vitesse longitudinale

Pour la clarté de l'exposé, nous ne présentons que les résultats relatifs à un plan de mesure, en l'occurrence  $X = 350 \text{ mm}$ .

Les profils de vitesse longitudinale dans le plan de mesure  $X = 350 \text{ mm}$  et aux diverses stations en  $Z$  sont présentés figure 17. Nous avons tracé d'une part les profils mesurés uniquement au sein de la couche limite de l'aile et d'autre part, les profils mesurés dans la couche limite et dans le tourbillon. Il est intéressant de remarquer que l'épaisseur de la couche limite diminue lorsque l'on se rapproche de la ligne de recollement, c'est-à-dire lorsque  $Z$  croît; à l'altitude  $Z = 120 \text{ mm}$ , dans une

région proche de celle du recollement (localisé à  $Z = 130$  mm), la couche limite a une épaisseur de 1 mm environ.

La zone tourbillonnaire est parfaitement détectée par un accroissement rapide de la vitesse dont le module dans la périphérie de cette zone devient supérieur à celui de la vitesse prise comme référence à l'extérieur du tourbillon, au niveau de l'axe veine. Cette observation d'une couche limite à l'épaisseur fortement diminuée près de la région de recollement du tourbillon est valable, quel que soit le plan de mesure où l'on se situe.

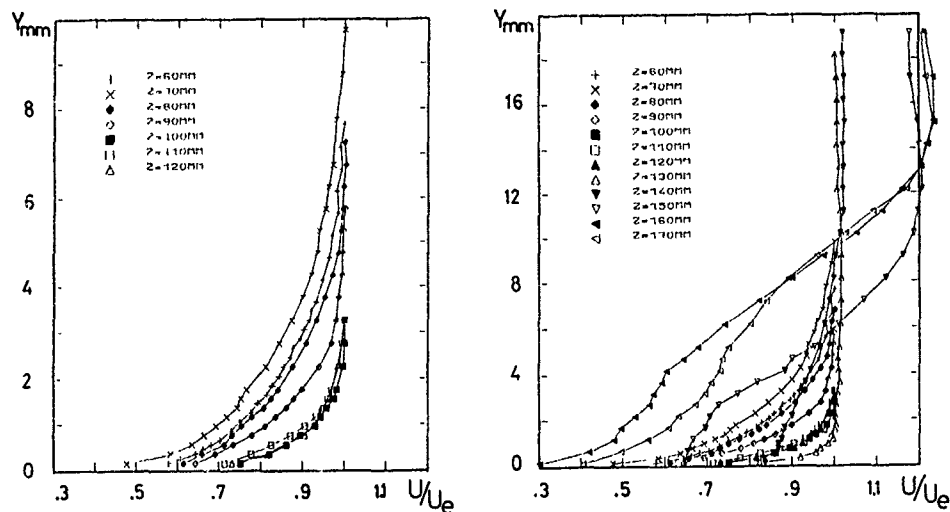


Fig. 17 - Vitesse longitudinale dans a) la couche limite  
b) la couche limite et le tourbillon

Ce phénomène-là est bien indépendant du chemin parcouru par le fluide, en d'autres termes indépendant d'un "effet Reynolds", comme en témoigne la figure 18. Sur cette figure, nous avons reporté deux grandeurs susceptibles d'être caractéristiques de l'épaisseur de la couche limite immédiatement en aval de la ligne de recollement pour les diverses stations en  $X$  :

- l'épaisseur  $\delta$  de couche limite pour laquelle la vitesse locale est égale à la vitesse extérieure ;

- l'épaisseur  $\delta_{u'}$  pour laquelle la valeur RMS de la fluctuation longitudinale de la vitesse est égale à 3 % de la vitesse extérieure.

Excepté pour la première station de mesure, on peut dire que  $\delta$  ou  $\delta_{u'}$  reste pratiquement constant quel que soit le plan  $X$  considéré et, donc, quelle que soit la distance  $\Delta X$  entre le point de mesure et le bord d'attaque de l'aile ; sur la figure 18, nous avons associé cette distance en pourcentage de corde au point de mesure considéré.

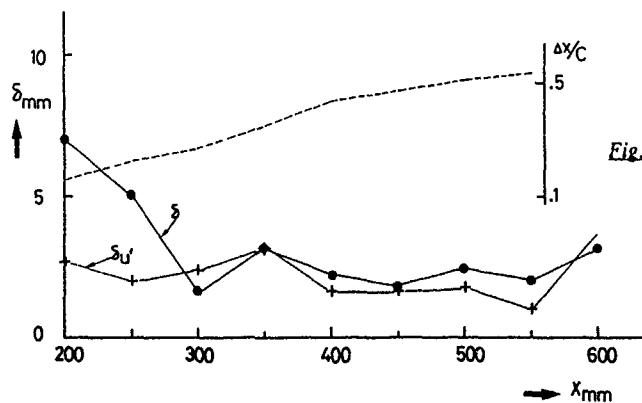


Fig. 18 - Epaisseur de la couche limite en aval du recollement

La figure 19 présente une analyse des profils de vitesse à l'aide de la loi logarithmique de paroi, à partir de laquelle nous avons déduit le coefficient de frottement. Dans la région située en aval du recollement, cette loi semble exister sur une portion appréciable de la couche limite.

La figure 20 met en évidence la décroissance du coefficient de frottement (déduit de la loi logarithmique de paroi), décroissance dans une région soumise à un gradient de pression positif. Notons également la valeur constante du coefficient de frottement à la station de mesure située immédiatement en aval du recollement dans les plans de mesure concernés :  $X = 350, 400, 450$  mm.

Le paramètre de forme (donné pour quelques stations de mesure figure 21) évolue peu ( $H \approx 1.4 - 1.5$ ) excepté dans la région comprise entre  $X = 300$  et  $350$  mm.

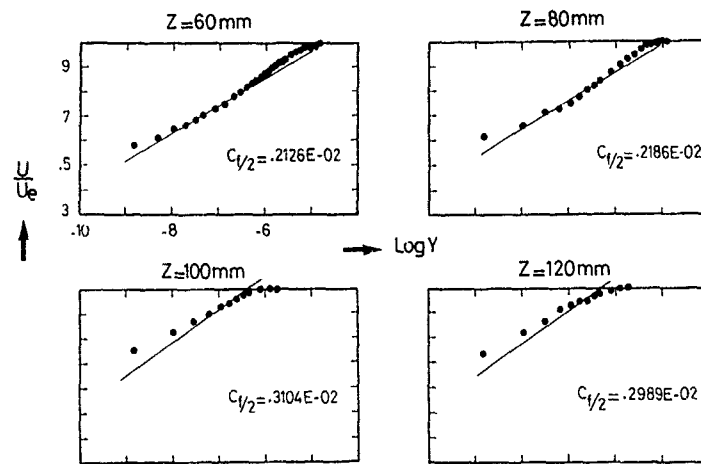


Fig. 19 - Analyse de la loi logarithmique de , aroi

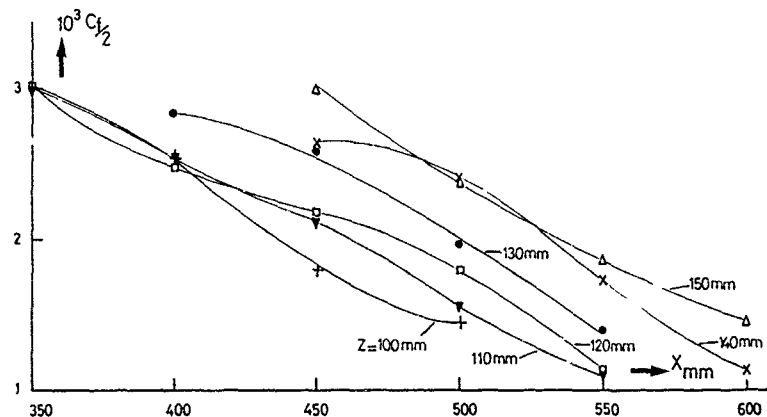


Fig. 20 - Evolution du coefficient de frottement

Il est intéressant d'observer l'évolution du paramètre de forme immédiatement à l'aval du recollement (fig. 22); dans la première région de l'aile, c'est-à-dire entre  $X = 200$  et  $300$  mm, le paramètre de forme semble croître bien que sa détermination à la station  $X = 300$  mm paraisse entachée de quelque imprécision expérimentale; tout au long de la ligne de recollement, depuis  $X = 350$  mm jusqu'à  $X = 600$  mm, il garde une valeur pratiquement constante et voisine de 1,6.

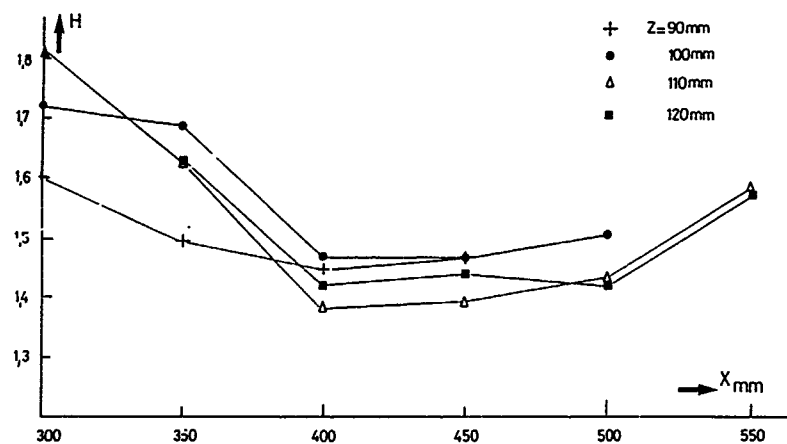


Fig. 21 - Evolution du paramètre de forme

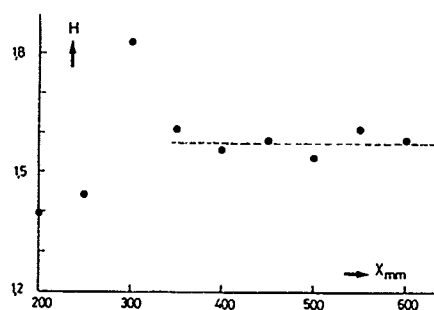
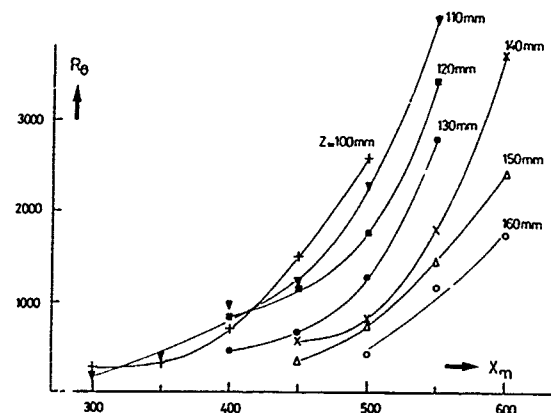


Fig. 22 - Evolution du paramètre de forme en aval de la ligne de recollement

Fig. 23 - Evolution de  $R_\theta$  suivant  $X$ 

On peut également remarquer (fig. 23) que le nombre de Reynolds  $R_\theta$  formé avec l'épaisseur de quantité de mouvement reste faible aux stations en  $X$  où il est mesuré ( $X = 300, 400, 500$  mm), eu égard au fait qu'il est censé caractériser un écoulement turbulent.

La diminution du  $R_\theta$ , lorsque  $Z$  augmente, est en accord avec une diminution du coefficient de frottement lorsque  $Z$  diminue; ceci correspond, en fait, à un "effet Reynolds", lié à la variation du trajet turbulent depuis le bord d'attaque du profil jusqu'à la station de mesure suivant la ligne  $Z = \text{cste}$  considérée.

Il est également intéressant de remarquer que les différentes courbes se regroupent assez bien par translation; ceci montre que la couche limite (par la valeur de son épaisseur de quantité de mouvement  $\theta$ ) évolue de façon identique à partir de la ligne de recollement, quelle que soit la station de mesure considérée.

#### 6.1b Vitesse transversale

Après analyse des profils de vitesse transversale (fig. 24), on constate que les effets tridimensionnels sont peu marqués à l'aval de la ligne de recollement; aux points de mesure les plus proches de la paroi, la vitesse transversale atteint environ 10 % de la vitesse extérieure.

Cette observation est d'ailleurs confirmée par la visualisation pariétale de l'écoulement qui n'indique des effets tridimensionnels importants que dans la zone confinée entre le bord d'attaque du profil et la ligne de recollement du tourbillon, ainsi que dans une région très proche du bord de fuite.

Lorsque  $Z$  est suffisamment élevé pour que l'on se situe en amont de la ligne de recollement, les vitesses transversales deviennent nettement plus importantes et leurs profils prennent la forme de ceux rencontrés dans un écoulement tourbillonnaire.

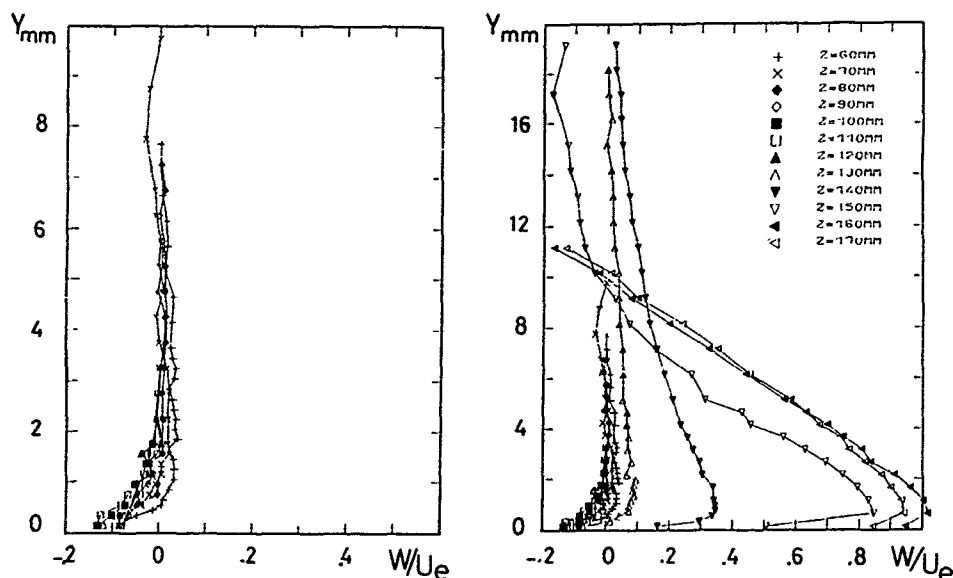


Fig. 24 - Profils de vitesse transversale

#### 6.1c Profils de vitesses en représentation polaire

L'évolution des profils de vitesses suivant  $X$  à une altitude  $Z = \text{cste}$  est également donnée sous forme polaire (fig. 25).

On peut observer un changement de signe ainsi qu'une tendance vers une déformation en "S" de ces profils lorsque  $X$  croît. Le changement de signe des vitesses transversales est lié au changement d'état négatif-positif du gradient de pression et s'effectue avec un certain retard par rapport à ce dernier. La figure 26 montre la courbure très marquée que présentent les lignes de courant extérieures.

Les profils polaires au niveau de la ligne de recollement (fig. 27) présentent un changement de signe très net à partir de la station  $X = 350 \text{ mm}$ ; l'influence du gradient de pression sensible à la distance séparant le point de mesure du bord d'attaque du profil n'est certainement pas étranger à ce fait.

#### 6.2. Champ turbulent

La faible épaisseur de la couche limite dans la région proche du recollement interdit l'intrusion au sein de celle-ci de toute sonde autre qu'une sonde anémométrique à 1 fil; de fait, une seule composante du tenseur de Reynolds peut être déterminée: la fluctuation longitudinale de la vitesse.

Les profils de la fluctuation longitudinale de la vitesse sont représentés figure 28.

Le maximum de la quantité  $\sqrt{u'^2}/U_e$  varie très peu quelle que soit la station de mesure et la ligne  $Z = \text{cste}$  considérées; ce niveau est relativement peu élevé puisque seulement voisin de 8 %.

L'incursion dans la zone tourbillonnaire est rapidement signalée par une modification du niveau des fluctuations longitudinales de la vitesse et de la forme de leurs profils associés.



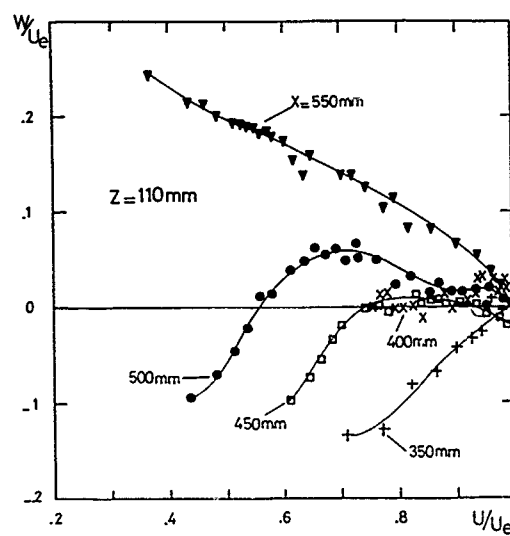


Fig. 25 - Représentation polaire des profils de vitesses

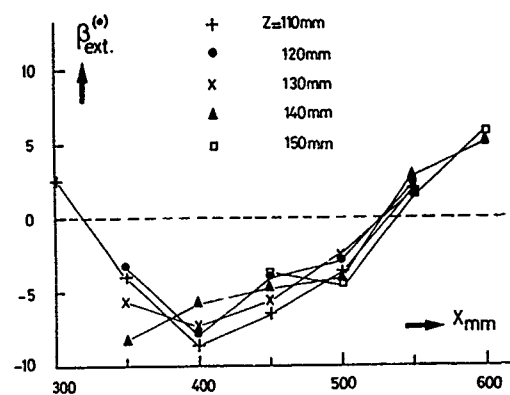


Fig. 26 - Déviation des lignes de courant extérieures

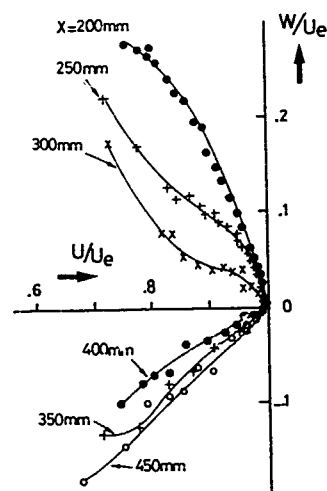
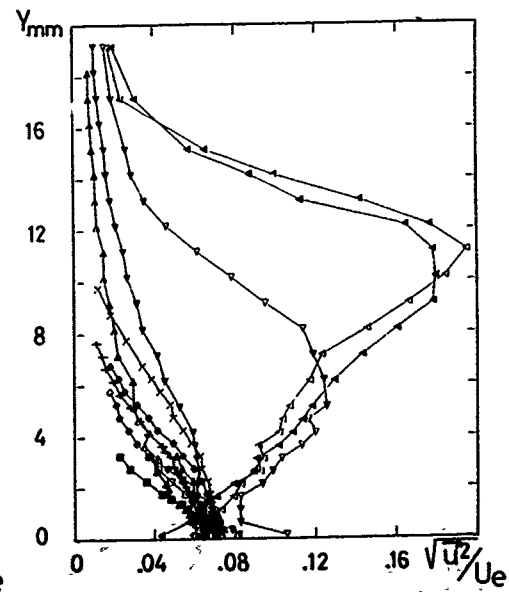
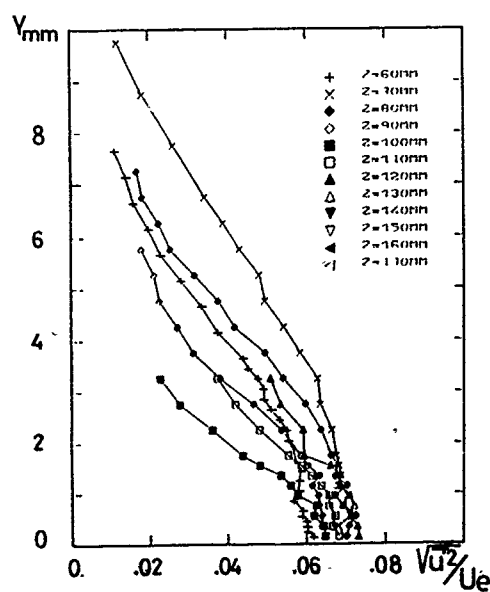


Fig. 27 - Profils polaires au niveau de la ligne de recollement

Fig. 28 - Profils de la fluctuation longitudinale de la vitesse



## 7 - CONCLUSION

La première partie de l'étude expérimentale concernant la caractérisation de l'écoulement autour d'une aile en flèche, a consisté en une analyse de l'écoulement dans la région du coin délimitée par l'aile et le plancher de la veine; nous n'avons pas observé dans cette région de phénomène particulier comme, par exemple, la présence d'un tourbillon en fer à cheval rencontré dans le cas de l'aile droite.

La seconde partie de l'étude expérimentale a eu pour but d'analyser le comportement d'une couche limite se développant en aval d'un tourbillon de bord d'attaque sur une aile en flèche et en incidence.

Des mesures de vitesses moyennes et de turbulence ont été réalisées à l'aide de l'anémométrie fil chaud dans le tourbillon ainsi que dans la couche limite immédiatement en aval de la ligne de recollement.

Nous avons présenté quelques résultats typiques et essentiels de mesures réalisées dans le tourbillon afin qu'apparaisse, de façon plus frappante, le contraste existant au niveau de la tridimensionnalité et de la turbulence de part et d'autre de la ligne de recollement.

La principale observation que nous pouvons rapporter est la faible épaisseur de la couche limite au voisinage de la ligne de recollement.

Nous avons aussi noté que la loi logarithmique de paroi existait sur une portion appréciable de la couche limite bien que les profils de vitesse soient nettement déformés dans la région proche du raccordement avec la loi  $u^+ = y^+$ .

D'autre part, les effets tridimensionnels sont peu marqués immédiatement en aval de la ligne de recollement. Lorsque l'on s'éloigne de la ligne de recollement, les profils de vitesse en représentation polaire se déforment; un changement de signe des vitesses transversales apparaît.

Nous avons également observé que la couche limite présentait des niveaux de turbulence du même ordre de grandeur que ceux d'une couche limite turbulente classique même au voisinage de la ligne de recollement.

Il semblerait donc que tridimensionnalité, turbulence, cisaillement, vorticités incontestés de l'agitation tourbillonnaire, demeurent confinés dans cette région de l'aile où naît et se développe le tourbillon de bord d'attaque, de telle sorte que la couche limite semble subir comme une régénération à partir de la ligne de recollement.

## REFERENCES

- /1/ D. POLL "On the generation and subsequent development of spiral vortex flow over a swept wing", AGARD 342
- /2/ M. MIRANDE, V. SCHMITT, H. WERLE "Système tourbillonnaire présent à l'extrados d'une aile en flèche à grande incidence", AGARD 247
- /3/ J. TENSI, P. ARDONCEAU "Instabilités d'un écoulement tourbillonnaire sur aile en flèche"
- /4/ J. COUSTEIX, G. PAILHAS "Méthode expérimentale d'étude des écoulements de coin", AAAF, ECULLY (1984)
- /5/ I. SHABAKA "Turbulent flow in a simulated wing-body junction", Thesis, Imperial College (LONDRES)
- /6/ F. MANIE, V. SCHMITT "Aile à flèche variable équipée du profil D - Analyse des essais - Etude de l'influence du nombre de Reynolds", Rapport 8/3072 AY 002 (1978)

ECOULEMENT TOURBILLONNAIRE SUR FUSELAGE DE MISSILE  
 ETUDE EXPERIMENTALE ET MODELISATION  
 par  
 P. CHAMPIGNY - D. BAUDIN  
 Office National d'Etudes et de Recherches Aéronautiques (ONERA)  
 B.P. N° 72 - 92322 CHATILLON CEDEX (France)

### RESUME

La connaissance de l'écoulement qui s'établit autour d'un fuselage en incidence est d'une importance primordiale pour la prévision des caractéristiques aérodynamiques des missiles.

Dans ce contexte, une étude expérimentale a été réalisée à la soufflerie S2MA de l'ONERA pour des nombres de Mach de 0,8 à 3,0 et des incidences allant jusqu'à 20°. Les mesures effectuées à l'aide de sondes 5 trous ont permis de restituer les caractéristiques locales de l'écoulement : vecteurs vitesse, nombre de Mach local et pression d'arrêt locale.

A partir de la banque de données ainsi constituée, une caractérisation des tourbillons qui se développent à l'extrados du fuselage a été menée (position, intensité, taille du noyau visqueux) et une modélisation du champ aérodynamique basée sur des tourbillons filament à noyau visqueux a été établie.

Les exemples d'application de cette modélisation montrent la nécessité de prendre en compte ces tourbillons dans les méthodes de prévision, si l'on veut estimer correctement les performances des missiles.

### ABSTRACT

The knowledge of vortex flowfield around body at incidence is of primordial importance for the prediction of missile aerodynamic characteristics.

In this context, an experimental study was conducted in the ONERA S2MA wind tunnel, for Mach numbers 0.8, 1.5, 2.0 and 3.0 and angles of attack up to 20°. The five hole probes measurements gave the local characteristics of the flow such as the transverse velocity vectors, the local Mach numbers and the local stagnation pressures.

From the large data base generated, the position, strength and core radius of the vortices are analysed and a modeling of the flowfield based on viscous vortices is described.

Some applications of this model to missile aerodynamics are presented. They clearly show the need to take into account the nose vortices in engineering methods for good performance predictions.

### 1 - INTRODUCTION

La connaissance de l'écoulement tourbillonnaire qui s'établit autour d'un fuselage en incidence est d'une importance primordiale pour la prévision des efforts aérodynamiques de voilures montées sur fuselage et pour la prévision des performances de prises d'air de missiles supersoniques.

De nombreuses études expérimentales relatives à ce problème ont déjà été effectuées, mais les résultats publiés [1], [2] ou [3] sont souvent limités et pas toujours cohérents entre eux, l'objectif recherché n'étant aussi pas toujours le même.

Dans le but de faire une modélisation des tourbillons, aussi simple mais réaliste que possible, et pour un grand domaine de nombres de Mach, la nécessité est apparue de constituer une large base de données.

Avec l'appui des Services Officiels français (DEN/STET), une étude expérimentale a été réalisée à la soufflerie S2MA de l'ONERA pour des nombres de Mach de 0,8 à 3,0 et des incidences allant jusqu'à 20°.

Les mesures effectuées ont permis entre autres de caractériser la position et l'intensité des tourbillons mais aussi la taille de leur noyau visqueux et les pertes de pression d'arrêt en leur coeur.

L'objet de cette communication est de présenter ces divers résultats, la modélisation du champ aérodynamique établie à partir de ces résultats, et quelques exemples d'application aux performances des missiles.

### 2 - NOTATIONS

- a : rayon du fuselage
- C<sub>w</sub> : portance d'une voilure

$D$  : diamètre du fuselage  
 $M_0$  : nombre de Mach à l'infini amont  
 $p_{10}$  : pression d'arrêt à l'infini amont  
 $p_{1\infty}$  : pression d'arrêt au coeur des tourbillons  
 $q_0$  : pression dynamique de l'écoulement à l'infini amont  
 $q_1$  : pression dynamique locale  
 $q_{\infty}$  : pression dynamique au coeur des tourbillons  
 $r$  : distance à l'axe du fuselage  
 $r_1$  : distance des tourbillons à l'axe du fuselage  
 $r_v$  : rayon du noyau visqueux des tourbillons  
 $X$  : distance depuis le nez de l'ogive  
 $X_s$  : abscisse de l'origine des tourbillons  
 $V_0$  : vitesse de l'écoulement à l'infini amont  
 $\alpha_0$  : incidence du fuselage  
 $\alpha_1$  : incidence locale de l'écoulement (voir fig. 2)  
 $\beta_1$  : dérapage local de l'écoulement (voir fig. 2)  
 $\Gamma_0$  : intensité des tourbillons (circulation)  
 $\eta_{p2}$  : rendement de la prise d'air  
 $\omega$  : rotationnel local  
 $\theta$  : position azimutale  
 $\theta_1$  : position azimutale des tourbillons.

### 3 - ETUDE EXPERIMENTALE

Les essais ont été réalisés à la soufflerie S2MA de l'ONERA sur une maquette composée d'une ogive parabolique d'allongement 3 et d'un cylindre de 12 calibres de longueur et de diamètre égal à 100 mm (figure 1).

Les mesures ont été effectuées à l'aide de 10 sondes anémoclinobaronétriques à 5 trous de diamètre 3 mm (figure 2) réparties sur un peigne à 4 branches (figure 1). Le peigne est motorisé en roulis et les acquisitions ont été faites sur 360° de roulis avec un pas de 5°, ce qui correspond à la grille de sondage présentée figure 2.



Soufflerie ONERA S2MA  
 Veine: 1,8 m x 1,8 m  
 Nombre de Mach: 0,8/1,5/2,0/3,0  
 Incidence:  $\alpha \rightarrow 20^\circ$   
 Maquette:  $\Phi = 0,1$  m

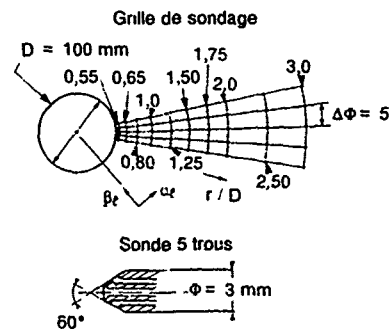


figure 1 - dispositif expérimental

figure 2 - grille de sondage et sonde 5 trous

Pour estimer plus précisément les caractéristiques des tourbillons (position, intensité, ...), les mesures expérimentales ont ensuite été interpolées sur une grille plus fine et régulière:  $\Delta\theta = 2,5^\circ$  et  $r/D = 0,05$ .

Les sondes à 5 trous ont été étudiées et étalonnées à l'ONERA dans le domaine  $0,4 < M_0 < 3$ ,  $0 < \alpha_1 < 40^\circ$ ,  $0 < \beta_1 < 40^\circ$ , suivant une technique précisée dans la référence [4].

A partir des lois d'étalonnage, il est ainsi possible de restituer l'orientation du vecteur vitesse ( $\alpha$ ,  $\beta$ ), le nombre de Mach local et la pression d'arrêt locale.

Les nombres de Mach considérés dans cette étude sont : 0,8/1,5/2,0 et 3,0 pour des nombres de Reynolds, rapportés au diamètre du fuselage, voisins de  $10^5$ . Afin d'assurer un écoulement turbulent sur toute la maquette, la transition de la couche limite a été déclenchée par des bandes de grains de carborundum placées sur la pointe de l'ogive.

#### 4 - ANALYSE DES RESULTATS

##### 4.1 - Description de l'écoulement

Aux très faibles incidences, l'écoulement incident contourne le fuselage sans décoller (exemple :  $\alpha_0 = 5^\circ$ ,  $X/D = 3$ , figure 3) et ses caractéristiques peuvent être décrites par la théorie linéarisée du potentiel.

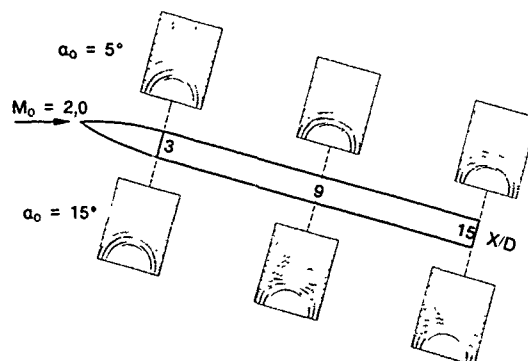


figure 3 - vecteurs vitesse transverse

Aux incidences modérées, sous l'effet des gradients de pression positifs, l'écoulement décolle à l'extrados du fuselage, pour engendrer deux tourbillons contrarotatifs (exemple  $\alpha_0 = 15^\circ$ ,  $X/D = 9$ , figure 3). Outre l'aspect rotationnel, on note dans ces zones tourbillonnaires une chute importante de la pression d'arrêt locale et de la pression dynamique locale (figure 4), qu'il est important de prendre en compte dans les programmes de modélisation, car comme on peut le voir dans l'exemple présenté, il ne reste plus que 35% de la pression d'arrêt infini amont.

Au fur et à mesure que l'incidence croît, ou que l'on s'éloigne du nez du fuselage, la zone tourbillonnaire prend de l'ampleur en espace, puis a tendance à se désorganiser à partir de  $20^\circ$  d'incidence, en particulier en supersonique (figure 5). L'aspect circulaire des tourbillons que l'on pouvait noter précédemment a disparu, et ceux-ci sont plus allongés vers l'extrados, avec des niveaux de rotationnel moins élevés, mais plus étalés (exemple du cas  $M_0 = 2$   $\alpha_0 = 20^\circ$ ).

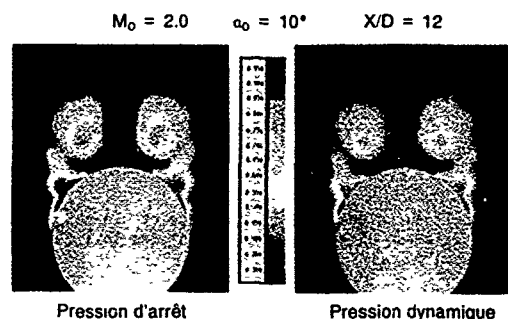


figure 4 - distributions de pressions d'arrêt et dynamique

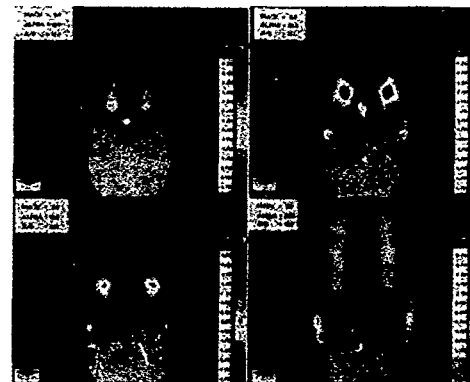


figure 5 - distributions du rotationnel

##### 4.2 - Abscisse de départ des tourbillons

Comme on le verra plus loin, les caractéristiques des tourbillons sont fonctions de la longueur de développement de la nappe, ce qui nécessite de connaître l'abscisse  $X_s$  à partir de laquelle elle s'est formée.

Pour cela deux techniques peuvent être utilisées :

- soit à partir de visualisations pariétales des lignes de courant ; dans ce cas  $X_s$  peut être considéré comme étant l'origine de la ligne de décollement ;

- soit à partir de l'examen des vecteurs vitesse dans des plans transversaux ; on suppose alors que dès que l'on observe des courants de retour dans l'écoulement transversal la nappé a pris naissance.

Il faut noter que les deux techniques conduisent à une certaine imprécision liée à l'interprétation difficile des mesures expérimentales au voisinage du décollement naissant.

En l'absence de visualisations des lignes de courant pour cette étude, la deuxième technique a été utilisée ici, et les résultats sont présentés figure 6. On note évidemment que plus l'incidence augmente, plus les tourbillons se développent tôt, mais l'abscisse de départ des tourbillons semble indépendante du nombre de Mach.

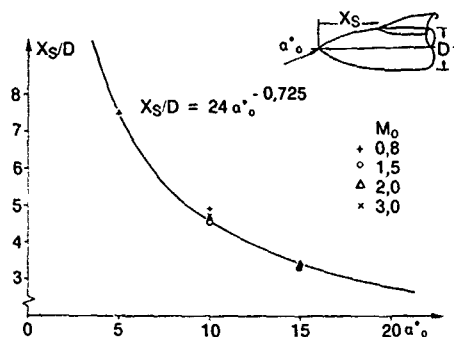


figure 6 - abscisse de départ des tourbillons

#### 4.3 - Position des tourbillons

La position des tourbillons a été déterminée comme étant le lieu où le rotationnel est maximal. Ce point correspond aussi aux minima de pression d'arrêt et de pression dynamique.

Les coordonnées des tourbillons sont présentées figures 7 et 8 en coordonnées polaires, plutôt qu'en coordonnées cartésiennes, ce qui permet d'obtenir une meilleure corrélation avec les paramètres d'essais.

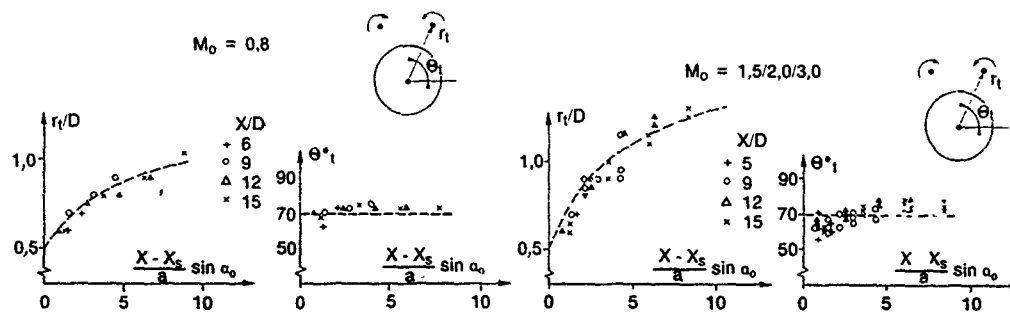


figure 7 - position des tourbillons en subsonique figure 8 - position des tourbillons en supersonique

Au fur et à mesure que  $X$  ou  $\alpha_0$  augmente, les tourbillons s'écartent du fuselage et la meilleure corrélation entre leur trajectoire et les paramètres d'essais est obtenue en considérant des lois :

$$r_t/D, \theta_t = f\left(\frac{X - X_s}{a} \sin \alpha_0\right)$$

On remarque ainsi que l'angle polaire relatif à leur position,  $\theta_t$ , reste voisin de  $70^\circ$ , et qu'il y a peu d'influence du nombre de Mach en supersonique sur leur position. Cependant, les tourbillons s'éloignent moins vite du fuselage en subsonique qu'en supersonique.

#### 4.4 - Intensité des tourbillons

Compte tenu du caractère visqueux des tourbillons, ceux-ci doivent être définis par au moins deux grandeurs caractéristiques comme leur intensité (circulation globale ou rotationnel maxi au coeur) et la taille de leur noyau visqueux.

La circulation  $\Gamma$ , peut être déterminée par intégration des vitesses sur un contour suffisamment grand autour du tourbillon. Les valeurs obtenues sont présentées figure 9 où l'on remarque que la circulation augmente régulièrement avec  $X$  ou  $\alpha_0$ , et comme pour leur position, avec des niveaux plus faibles en subsonique qu'en supersonique.

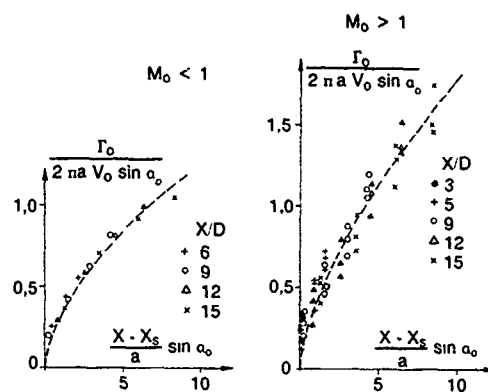


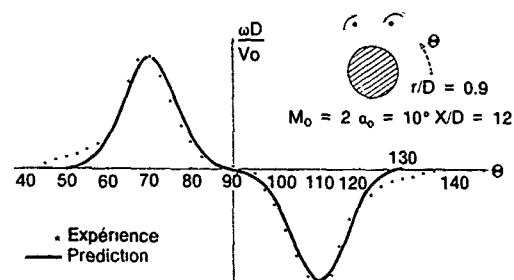
figure 9 - circulation des tourbillons

En ce qui concerne leur caractère visqueux, si l'on considère que la distribution du rotationnel est de type gaussien :

$$\omega = \omega_0 e^{-\delta^2/r^2}$$

ce qui est assez bien vérifié expérimentalement (figure 10) tant que les tourbillons restent bien organisés, alors le rayon visqueux ( $r_v$ ) est défini comme étant la distance où la vitesse induite  $V$  est maximale.

figure 10 -répartition du rotationnel



Sachant que :

$$V = \frac{\omega_0}{2r\delta^2} (1 - e^{-\delta^2/r^2}) = \frac{\Gamma_0}{2\pi r} (1 - e^{-\delta^2/r^2})$$

alors :

$$\delta^2 = \frac{1,256}{r_v^2}$$

ce qui permet de déduire le rayon visqueux des valeurs de la circulation  $\Gamma_0$  et du rotationnel  $\omega_0$  par :

$$r_v = \frac{1,256\Gamma_0}{\pi\omega_0}$$

Expérimentalement, à partir des vecteurs vitesse transverse, il est facile de calculer le rotationnel axial :

$$\omega = \frac{dw}{dy} - \frac{dv}{dx}$$

et d'en déduire le rotationnel maxi  $\omega_0$  au cœur des tourbillons.

**Nota :** On suppose ici que les tourbillons sont peu inclinés par rapport à l'axe du fuselage ; moins de  $6^\circ$  d'après les trajectoires présentées figures 7 et 8.

Les valeurs des rayons visqueux ainsi obtenues sont présentées figures 11 et 12. En fonction des différents paramètres d'essai, on observe que leur taille augmente régulièrement au fur et à mesure que les tourbillons se développent, et ce d'autant plus rapidement que  $M_0$  est grand.

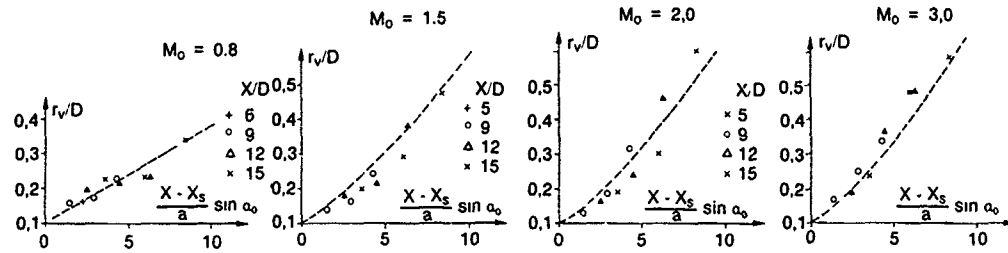


figure 11 -taille du noyau visqueux pour  $M_0 = 0,8$  et  $1,5$

figure 12 -taille du noyau visqueux pour  $M_0 = 2$  et  $3$

Comme nous l'avons vu précédemment, pour les grandes valeurs de  $X$  et  $\alpha_0$  les tourbillons sont assez allongés vers l'extrados (figure 5), aussi le calcul du rayon visqueux utilisé ici, basé sur le rotationnel maximal et la circulation globale, donne en quelque sorte une valeur moyenne dans l'espace de sa taille.

#### 4.5 - Pertes de pression

Lors de la description de l'écoulement qui s'établit autour du fuselage, nous avons observé des pertes de pressions d'arrêt et dynamique très importantes au sein des tourbillons (figure 4).

Les minima de pression relevés sont quasiment indépendants de  $X$  et  $\alpha_0$  (figure 13), autrement dit de l'intensité des tourbillons, mais sont essentiellement fonctions du nombre de Mach  $M_0$  (figure 14).

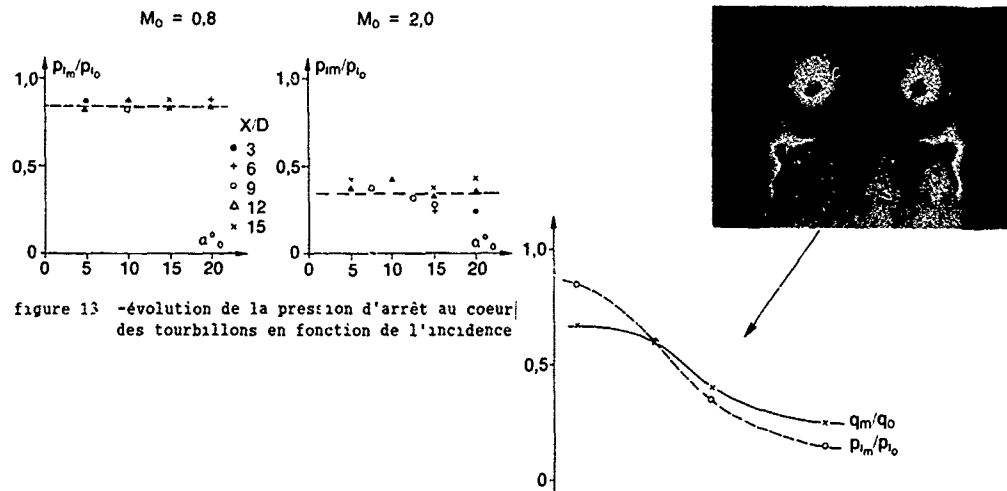


figure 13 -évolution de la pression d'arrêt au coeur des tourbillons en fonction de l'incidence

figure 14 -pressions d'arrêt et dynamique minimales

#### 5 - MODELISATION DE L'ECOULEMENT TOURBILLONNAIRE

##### 5.1. Principe

Un des buts de cette étude expérimentale étant l'amélioration des méthodes de prédiction des coefficients aérodynamiques, et plus particulièrement du programme MISSILE [5], une modélisation est proposée et quelques exemples d'application sont ensuite présentés.

Dans les méthodes de prédiction, le champ des vitesses, nécessaire au calcul de la portance d'une voilure montée sur fuselage, est défini à partir de la solution de l'écoulement potentiel, à laquelle on ajoute la contribution des tourbillons, soit d'après le schéma de la figure 15 :



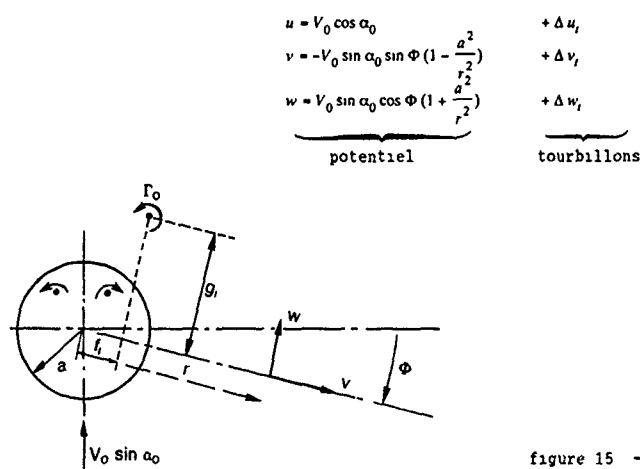


figure 15 -schéma du modèle tourbillonnaire

En assimilant les zones tourbillonnaires à des tourbillons à noyau visqueux, de longueur infinie, parallèles à l'axe du fuselage, la distribution des vitesses transversales induites est d'après la loi de Biot et Savart donnée par les relations :

$$\Delta v_i = \frac{\Gamma_0}{2\pi} \left[ 1 - e^{-\frac{g_i^2 + (f_i - r)^2}{0.796 r_v^2}} \right] \cdot \frac{g_i}{g_i^2 + (f_i - r)^2}$$

$$\Delta w_i = \frac{\Gamma_0}{2\pi} \left[ 1 - e^{-\frac{g_i^2 + (f_i - r)^2}{0.796 r_v^2}} \right] \cdot \frac{(f_i - r)}{g_i^2 + (f_i - r)^2}$$

où  $\lambda = 1,4$  est relatif aux deux tourbillons principaux et à leurs images respectives nécessaires pour respecter la condition de glissement à la paroi.

Par ailleurs, on suppose dans cette modélisation que les tourbillons n'ont pas d'influence sensible sur la vitesse longitudinale, soit  $\Delta u_i = 0$ , ce qui est assez bien vérifié expérimentalement.

A partir de la connaissance de la position et de l'intensité des tourbillons, le champ des vitesses est ainsi parfaitement défini, et donc les incidences et dérapages locaux.

Des comparaisons entre le modèle exposé ci-dessus et l'expérience sont présentées figures 16 et 17 pour l'incidence locale et le dérapage local respectivement.

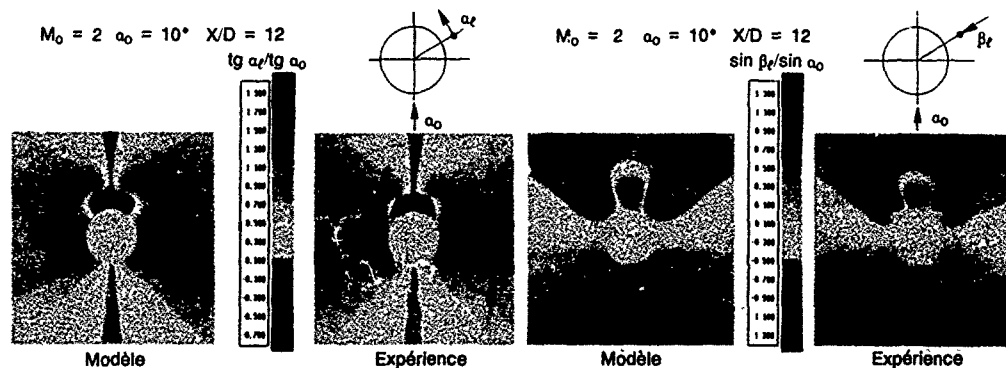


figure 16 -distribution des incidences locales

figure 17 - distribution des dérapages locaux

On remarque que le modèle proposé, avec tourbillons à noyau visqueux, représente très bien le champ des incidences et dérapages locaux.

Parmi les autres caractéristiques de l'écoulement :  $M_1$ ,  $P_{11}$ ,  $Q_1$ , seule une modélisation de la pression dynamique locale et de la pression d'arrêt locale a été effectuée.

En effet si l'on observe ces grandeurs, moyennées par exemple sur l'envergure d'une voilure de hauteur  $1D$ , on note :

- que le nombre de Mach local moyen n'évolue que de  $\pm 10\%$  ce qui compte tenu des gradients des coefficients aérodynamiques en fonction du Mach peut être considéré comme négligeable pour ces méthodes de calcul ;

- que les pressions d'arrêt et dynamique locales, moyennes, évoluent dans des proportions beaucoup plus importantes, en particulier au sein des tourbillons.

Les distributions de pression d'arrêt ou dynamique ont été prises en compte sous la forme de distribution gaussienne (comme pour le rotationnel) soit par exemple pour la pression dynamique :

$$q_1/q_0 = 1 - (1 - \frac{q_m}{q_0}) [e^{-\frac{1,256 r_1^2}{r_0^2}} + e^{-\frac{1,256 r_2^2}{r_0^2}}]$$

où  $r_1$  et  $r_2$  sont les distances du point considéré aux deux tourbillons principaux et  $q_m/q_0$  la pression minimale au coeur des tourbillons.

Cette modélisation, bien que très schématique, représente assez bien la réalité comme le montre la figure 18.

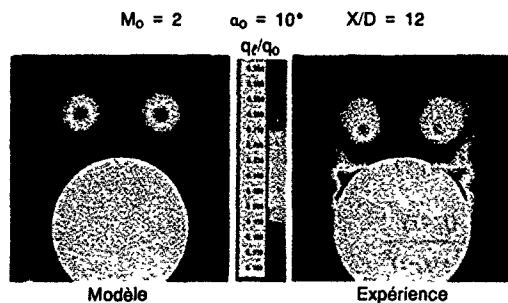


figure 18 - distribution des pressions dynamiques locales

## 5.2 - Applications

Le premier exemple d'application de cette modélisation est relatif à l'évolution de la portance d'une voilure en fonction de sa position en roulis sur le fuselage (figure 19).

Il met nettement en évidence la nécessité de prendre en compte ces tourbillons si l'on veut estimer correctement la portance de la voilure lorsque celle-ci se trouve à l'extrados du fuselage, et en particulier l'inversion de signe du  $C_x$  au voisinage des tourbillons.

Le deuxième exemple d'application est relatif au rendement d'une prise d'air supersonique montée sur un fuselage, du côté extrados.

La figure 20 montre d'une part les performances d'une prise d'air axisymétrique placée en incidence dans un champ uniforme à  $M_0 = 2$ , et d'autre part les performances de celle-ci, installée sur le fuselage.

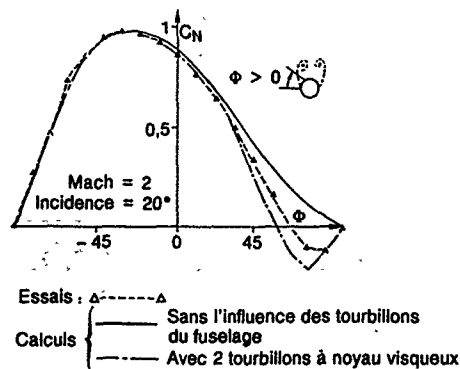


figure 19 - portance d'une aile montée sur fuselage

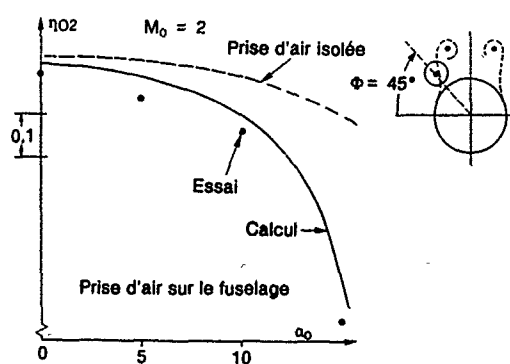


figure 20 - rendement d'une prise d'air supersonique.

L'importante chute de rendement en fonction de l'incidence que l'on note sur cette figure, peut très bien être modélisée par calcul si l'on tient compte de l'écoulement local et en particulier de la présence des tourbillons pour ce cas particulier.

## 6 - CONCLUSION

Des sondages de l'écoulement autour d'un fuselage en incidence ont été réalisés pour une large plage de nombres de Mach (0,8 à 3,0) et d'incidences (0 à 20°).

Ils ont permis de constituer une importante banque de données, à partir de laquelle un modèle décrivant le champ aérodynamique au voisinage des tourbillons a été établi.

Cette étude expérimentale a permis d'améliorer les méthodes de prédiction des performances de missiles, mais est aussi d'une grande utilité pour la validation des méthodes numériques.

Pour ces dernières, la connaissance précise de l'écoulement au voisinage des lignes de décollement est primordiale, et devrait faire l'objet d'études complémentaires, comme par exemple un sondage de couche limite, qui apporterait de précieux renseignements sur les mécanismes de formation des nappes tourbillonnaires.

## REFERENCES

- [1] M.R. MENDENHALL - J.N. NIELSEN  
Effect of Symmetrical vortex shedding on the longitudinal aerodynamic characteristics of wing-body-tail configurations.  
NASA - CR 2473 - January 1975.
- [2] A.J.C. PONTON - G.A. JOHNSON  
The analysis and modelling of body vortex flowfields around missile configuration and their interaction with lifting surfaces at subsonic and supersonic speeds.  
Royal Aeronautical Society - Londres - 1989 pp. 26-1 to 26-16.
- [3] J. LORDON - J.C. FARE - D. PAGAN  
Supersonic vortex flows around a missile body - Basic experiment and EULER numerical computation.  
AGARD/FDP 1990 on "Missile Aerodynamics".
- [4] R. GAILLARD  
Etalonnage et utilisation de sonde "cinq trous"  
ONERA TP n° 1984-2.
- [5] P. CHAMPIGNY  
Prévision de la stabilité aérodynamique des missiles.  
AGARD - CP 451 - Paper n° 1 - 1988.

## ASYMMETRIC VORTEX FLOW OVER CIRCULAR CONES

by

M. Pidd  
J. H. B. SmithAerodynamics Department  
Royal Aerospace Establishment  
Farnborough, Hampshire, GU14 6TD UK

## 1 INTRODUCTION

This paper presents an update on earlier RAE work on the formation of asymmetric vortices from slender pointed bodies at large angles of incidence. The emphasis is on theoretical and experimental work on flow over circular cones.

The theoretical work began with the generalisation of Bryson's model<sup>1</sup> for symmetrical vortex flow over bodies of revolution to flows with lateral asymmetry. We formulated the model for asymmetric vortex flow over circular cones using slender-body theory, with arbitrarily chosen, straight separation lines, and the single line-vortex model of the separated flow. We looked for conical solutions, in which the line-vortices are straight, and eventually found a family of asymmetrical solutions<sup>2</sup>. When the separation lines are placed symmetrically on either side of the incidence plane, the symmetric solutions of Bryson occur, and the asymmetric solutions then bifurcate from this symmetric branch of solutions. The solutions depend only on the angular position of the separation lines and on the incidence parameter defined as the ratio of the angle of incidence to the semi-angle of the cone. At values of the incidence parameter above that at which bifurcation occurs, a side force is predicted. This grows rapidly with the incidence parameter, reaching values comparable with the normal force, even though the separation lines are placed symmetrically. Quite large asymmetries in the positions of the separation lines, on the other hand, perturb the symmetric flow relatively little. This work pointed to an inviscid mechanism for the observed side-force on slender pointed bodies.

This early work was followed by calculations using the more realistic vortex-sheet model, developed previously for symmetric flow on wings<sup>3</sup> and bodies<sup>4</sup>. This retains the framework of slender-body theory, separation is still specified along arbitrarily chosen straight lines, and the restriction to conical flow is retained. This work confirmed the conclusions reached previously about the primary role played by bifurcation and the limited importance of asymmetry in the position of the separation lines. It also allowed favourable comparisons to be made with observations of vortex flow and with measured levels of side force<sup>5,6</sup>. The solutions are extended without difficulty to elliptic cones and it was demonstrated that a reduction in the vertical axis of the elliptic cross-section leads to an increase in the angle of incidence at which bifurcation from the symmetrical solution takes place<sup>7</sup>. Further work using this vortex-sheet method for more general shapes has been presented by Fiddes and Williams<sup>8</sup>, and Williams<sup>9</sup>.

The theoretical work in the present paper is based on the simpler line-vortex model studied initially, so it is

relevant at this point to discuss the relationship between the predictions of the two models. Fig 1 shows the star-board side of a circular cone in symmetric flow at an incidence parameter of 3. A vortex sheet solution is shown, springing from the separation line  $S_s$  at the end of the horizontal diameter of the circular cross-section, and ending at E, with its core at C joined to E by the usual 'feeding-sheet'. This separation position is typical for laminar separation. The arc identified by the figures 40° to 49° is the locus of the vortex positions in the line-vortex model for angular positions of the separation line,  $S_v$ , of between 40° and 49° above  $OS_s$ . The first point to be made is that this locus passes very close to C, indicating that the predictions of the simple model have a certain resemblance to those of the better model. The second point is that this resemblance is found for positions of the separation lines in the simpler model which lie well to leeward of the position in the better model. The reason for this is brought out by the difference in the shape of the separating stream surface. For the better model this is the vortex sheet  $S_sBE$ . For the simpler model, the separating stream surface springs from the separation line  $S_v$ , which is a typical conical flow stagnation point, so that it takes a course like that indicated by the arrow. Because the initial part of the vortex sheet,  $S_sB$ , lies relatively close to the surface of the cone, similar flows near C are generated with very different separation positions in the two models. The position of point B has been chosen so that the circulation in the sheet model about the core C and the segment BE is the same as the circulation in the line-vortex model with separation at  $S_v$ .

Before leaving this discussion of the theoretical models it is appropriate to mention the prediction of asymmetric vortex flow by more complete models. For inviscid supersonic flow over cones, conical solutions of the Euler equations governing the flow exist. Such solutions displaying lateral asymmetry have been obtained by Marconi<sup>10</sup>, who forced the occurrence of primary separation along symmetrically located separation lines. Agreement between these solutions and those of the vortex-sheet model in slender-body theory was pointed out by Fiddes and Williams<sup>8</sup>. For laminar viscous flow, as described by the Navier-Stokes equations, conical flows do not exist. However, a slightly modified equation set does display conical solutions for supersonic speeds. Asymmetric solutions of these equations for flows past circular cones have been obtained by Siclari and Marconi<sup>11</sup>. These display slight asymmetry in the position of the primary separation lines. Secondary separation also occurs, but in their overall features the flows are not markedly different from the Euler solutions of Marconi<sup>10</sup> and the vortex-sheet solutions of Fiddes and Smith<sup>5,6</sup>.

On the experimental side, it is quite impossible to review the investigations which have been carried out within the space of this introduction. A comprehensive review was provided by Hunt<sup>12</sup> in 1982. Since we are particularly interested in the flow over circular cones, we shall make extensive use of the measurements made by Fiddes, Lean and Moir<sup>13</sup> in the 5 m Wind Tunnel at RAE and briefly reported in Ref 14. Details of their wind-tunnel model are shown in Fig 2.

Fig 3 shows an example of the results obtained. The local side-force coefficient,  $C_Y$ , based on the local diameter of the cone, is plotted against the angle of roll,  $\phi$ , about the axis of the cone. The angle of incidence is  $35^\circ$ , the results are for the first station, and the tunnel pressure is only just above atmospheric, so that the boundary layer growing from the windward generator is laminar at the separation line. We see that, at about half of the selected values of roll angle, the side force takes an approximately uniform numerical value, approaching in magnitude the local normal force coefficient,  $C_N$ , shown on the upper curve. As usual, the sign of  $C_Y$  changes several times in a complete revolution about the axis. At about half the remaining values of  $\phi$ ,  $C_Y$  is small enough for us to believe that the flow is essentially symmetric. All this is consistent with the predictions of the inviscid model, that symmetric solutions and asymmetric solutions of right- and left-handed forms both occur. However, the remaining quarter of the points show values of side force which are clearly intermediate between zero and the extreme value. It is these intermediate values which provoked the work to be described below.

## 2 SOLUTIONS OF THE LINE-VORTEX MODEL FOR CONICAL FLOW OVER CIRCULAR CONES

In an attempt to explain the occurrence of the intermediate levels of side force shown in Fig 3, the solution space of the line-vortex model of Ref 2 was explored more thoroughly. The essential features of the model are illustrated in Fig 4. A pair of line-vortices  $OV_1$  and  $OV_2$  lie downstream of the pointed apex  $O$  of the body. Their circulations are  $\Gamma_1$  and  $-\Gamma_2$ . Each is joined by a feeding vortex-sheet to a separation line  $OS_1$  or  $OS_2$  on the surface of the body. These feeding sheets are surfaces of discontinuity in the velocity potential, with the magnitude of the jump depending only on the streamwise variable  $x$ , that is to say, as vortex-sheets in which the vortex-lines are transverse to the main stream. The velocity field is constructed using slender-body theory and two conditions are formulated. We require in the first place that each vortex system, comprising a line-vortex and its feeding sheet, is free of transverse forces. This is achieved by balancing the force arising from the pressure difference across the feeding sheet by a force acting on the line-vortex. The second condition expresses the occurrence of separation. It forces the velocity vector at the separation line  $OS$  to lie along  $OS$ . Both these conditions are gross simplifications of the conditions that a vortex-sheet model would satisfy, but they provide a representation of the principal kinematic and kinetic constraints on the vortex flow.

Fig 4 is drawn for conical flow over a circular cone, but it is straightforward to write the conditions for non-conical flow

and a general body of revolution. With the axes as shown, we introduce the complex variable

$$Z = y + iz$$

in the cross-flow plane, and define the vortex positions by

$$Z = Z_1(x) \text{ and } Z = Z_2(x).$$

Then, the condition of zero transverse force on the starboard vortex system can be expressed as

$$\begin{aligned} & (\bar{Z}_1 - ae^{-i\theta_1}) U \frac{d\Gamma_1}{dx} + U \Gamma_1 \frac{d\bar{Z}_1}{dx} \\ & + \Gamma_1 \left[ i\alpha U \left( 1 + \frac{a^2}{Z_1^2} \right) - \frac{aU}{Z_1} \frac{da}{dx} \right. \\ & \quad \left. + \frac{\Gamma_1 \bar{Z}_1}{2\pi i (Z_1 \bar{Z}_1 - a^2)} \right. \\ & \quad \left. + \frac{\Gamma_2}{2\pi i} \left( \frac{1}{Z_1 - Z_2} - \frac{\bar{Z}_2}{Z_1 \bar{Z}_2 - a^2} \right) \right] = 0. \end{aligned} \quad \dots (1)$$

Here  $\Gamma_1$  and  $-\Gamma_2$  are the circulations of the vortices,  $a$  is the local radius of the body and the separation line  $OS_j$  lies along  $Z = ae^{i\theta_j}$ . The first term represents the force on the feeding sheet, the second term represents the force on the line-vortex due to its inclination to the freestream, and the third term represents the force on the line-vortex due to the cross-flow. The corresponding equation for the port vortex system has the suffixes 1 and 2 interchanged. The generalised Kutta condition representing the occurrence of separation on the starboard separation line is

$$\frac{\Gamma_1 (Z_1 \bar{Z}_1 - a^2)}{2\pi |Z_1 - ae^{i\theta_1}|^2} - \frac{\Gamma_2 (Z_2 \bar{Z}_2 - a^2)}{2\pi |Z_2 - ae^{i\theta_1}|^2} = 2\alpha U \cos \theta_1 \quad \dots (2)$$

provided the angular position,  $\theta_1$ , of the separation line is independent of  $x$ . The corresponding equation for the port side is obtained on replacing  $\theta_1$  by  $\theta_2$ .

For a slender circular cone of semi-angle  $\delta$ , we have

$$a = \delta x \quad (3)$$

and we can introduce non-dimensional variables  $\zeta$  and  $\gamma$  by

$$Z_j = a\zeta_j, \quad \Gamma_j = 2\pi\delta U\gamma_j \quad j = 1, 2. \quad (4)$$

Then equation (2), and the corresponding equation for the port side, become

$$\left. \begin{aligned} \frac{\gamma_1(\zeta_1\bar{\zeta}_1 - 1)}{|\zeta_1 - e^{i\theta_1}|^2} - \frac{\gamma_2(\zeta_2\bar{\zeta}_2 - 1)}{|\zeta_2 - e^{i\theta_1}|^2} &= 2\frac{\alpha}{\delta} \cos \theta_1 \\ \frac{\gamma_1(\zeta_1\bar{\zeta}_1 - 1)}{|\zeta_1 - e^{i\theta_2}|^2} - \frac{\gamma_2(\zeta_2\bar{\zeta}_2 - 1)}{|\zeta_2 - e^{i\theta_2}|^2} &= 2\frac{\alpha}{\delta} \cos \theta_2 \end{aligned} \right\} \quad (5)$$

Introducing a non-dimensional streamwise variable  $\xi$  by

$$x = x_0 e^{\xi} \quad (6)$$

we find equation (1) becomes

$$\frac{d}{d\xi} [\gamma_1(\bar{\zeta}_1 - e^{-i\theta_1})] = \gamma_1 F(\zeta_1, \zeta_2, \gamma_1, \gamma_2, \theta_1, \frac{\alpha}{\delta}) \quad (7)$$

where

$$F(\zeta_1, \zeta_2, \gamma_1, \gamma_2, \theta_1, \frac{\alpha}{\delta}) = e^{-i\theta_1} - 2\bar{\zeta}_1 - 1 + \frac{\alpha}{\delta} \frac{\zeta_1^2 + 1}{\zeta_1} + \frac{1}{\zeta_1} + \frac{i\gamma_1\bar{\zeta}_1}{\zeta_1\bar{\zeta}_1 - 1} + \frac{i\gamma_2(\zeta_2\bar{\zeta}_2 - 1)}{(\zeta_1 - \zeta_2)(\zeta_1\bar{\zeta}_2 - 1)} \quad (8)$$

The corresponding equation for the port side becomes

$$\frac{d}{d\xi} [\gamma_1(\bar{\zeta}_1 - e^{-i\theta_1})] = \gamma_2 F(\zeta_1, \zeta_2, \gamma_1, \gamma_2, \theta_1, \frac{\alpha}{\delta}) \quad (9)$$

For conical flow, the non-dimensional variables are independent of the streamwise coordinate, so the governing equations reduce to

$$F(\zeta_1, \zeta_2, \gamma_1, \gamma_2, \theta_1, \frac{\alpha}{\delta}) = F(\zeta_2, \zeta_1, \gamma_2, \gamma_1, \theta_2, \frac{\alpha}{\delta}) = 0 \quad (10)$$

and the generalised Kutta conditions, equations (5) and (10) consist of two complex equations, equivalent to four real equations, so that we have six equations in all to determine the two coordinates of each vortex and their circulations. The parameters on which the solutions depend are the incidence parameter  $\alpha/\delta$  and the positions  $\theta_1$  and  $\theta_2$  of the separation lines.

Some solutions given in Ref 2 for symmetrically placed separation lines illustrate the generation of asymmetric solutions by bifurcation from the symmetric branch as the incidence parameter increases above a critical bifurcation value. This dependence is illustrated in Fig 5, for  $\theta_1 = \theta$  and  $\theta_2 = \pi - \theta$ . The figure represents the projection of the solution surface onto the plane of the solution parameters  $\theta$  and  $\alpha/\delta$ . The curve ABD is the projection of the edge of the surface along which the vortices reach the surface of the cone and their strength vanishes. The curve is given by

$$\alpha/\delta = 1.5 \operatorname{cosec} \theta \quad (11)$$

which is often referred to as the lower bound for solutions. In fact it is only the lower bound to the right of point B, which lies at  $\theta = \theta_c$ ,  $\approx 46.1^\circ$  where

$$\tan \theta_c = \frac{3\sqrt{3}}{13} \quad \text{and} \quad \frac{\alpha}{\delta} = \sqrt{\frac{13}{3}} \approx 2.08 \quad (12)$$

To the left of point B there are solutions for values of  $\alpha/\delta$  less than  $1.5 \operatorname{cosec} \theta$ , lying in the region between the curve BD and the curve BC. The curve BC is simply the edge of the projection of the surface, so that it represents a fold-line in the projection of the surface. Two points of the solution surface are projected onto every point of the  $(\theta, \alpha/\delta)$  plane between the curves BD and BC, so that two solutions exist for each pair of values of  $\theta$  and  $\alpha/\delta$  in this region. The significance of the remaining curve AEB appears when we consider the symmetric solutions as one branch of the set of solutions of the equations (5) and (10) with  $\theta_1 + \theta_2 = \pi$ , which govern the flow when symmetry is not assumed. The solution surface now lies in a space of even more dimensions, and it now contains a double curve, or curve of double points, along which bifurcation takes place, so that two branches of the surface intersect along the double curve. The projection of this curve onto the  $(\theta, \alpha/\delta)$  plane is the bifurcation locus shown as AEB in Fig 5. It can be shown that the determinant of the Jacobian matrix used in the solution process vanishes on the bifurcation locus, so the locus can be identified by monitoring the sign of this determinant as the symmetric branch of the solution is explored.

We now turn to the corresponding picture for the asymmetric solutions, Fig 6. The curve AEB is the bifurcation locus, the same curve as in the previous figure. Asymmetric solutions arise when  $\alpha/\delta$  is increased, at constant  $\theta$ , from points on the bifurcation locus. Once again, there are edges to the surface of solutions where one of the vortices reaches the surface of the cone. The projections of these edges are the curves BJG and AHA. Also, once again, there is a fold line FG which results from our choosing to project onto the  $(\theta, \alpha/\delta)$  space, rather than any intrinsic feature of the solution itself. There is now an extra boundary of the region of consistent solutions. The condition applied at separation, that the velocity is parallel to the separation line, is also satisfied by an attachment line. In the region labelled 'inconsistent' in Fig 6 one of the postulated separation lines is, in fact, an attachment line.

The small region of intersecting curves in Fig 6 is enlarged in Fig 7. Two curves from Fig 5 have been added, so that the figure now indicates the regions of existence of both symmetric and asymmetric solutions in this small part of the  $(\theta, \alpha/\delta)$  plane. Following up the account of the asymmetric solutions, we see them occurring above the bifurcation locus. It is easiest to trace the solution surface by moving downwards and to the left from the edge BJ of the surface where the vortex lies on the cone. Then we find either that the asymmetric solutions disappear when the lower part of the bifurcation locus, BFE, is encountered, or the solution surface folds back on itself at the fold line FG. The asymmetric solutions then extend upward and to the right in the region bounded below by the bifurcation locus BFE. Note that there is a narrow region between the fold line FG, the edge BJ and the bifurcation locus BF in which there are two pairs of asymmetric solutions for each choice of  $\theta$  and  $\alpha/\delta$ .

Our search for additional solutions has, therefore, led us into this narrow region of the parameter space. When the side forces corresponding to the different pairs of asymmetric solutions in this region are calculated, they turn out

to be quite similar, so they do not correspond to the flows with the very different levels of side force that are illustrated in Fig 3. Moreover, no further bifurcation occurs at values of  $\alpha/\delta$  up to 10. There might be other solutions which are not connected to the solution surface we have explored, but there is no simple way to search for them.

### 3 STABILITY OF CONICAL FLOWS

The situation depicted in Figs 5 to 7 is of a confusing variety of solutions of the model for conical flows over circular cones. We now put forward a stability argument which indicates which of these solutions is likely to correspond to the flows that actually occur.

The disturbances which we treat in the stability analysis are spatial rather than temporal. We suppose that a conical flow solution occurs and then, at some lengthwise station, a small disturbance is introduced into the flow, taking the form of small changes in the positions and strengths of the vortices. Since we are using slender-body theory, no upstream effect of the disturbance is possible. We investigate the initial rate of change of this disturbance in the downstream direction. If all disturbances decay, we say that the solution is stable, while if any disturbance grows, we say that the solution is unstable.

The disturbed flow is clearly non-conical, but the body shape is still a circular cone. For simplicity we assume that the separation lines are not altered by the disturbance, and that the vortex strengths are still coupled to the positions through the generalised Kutta conditions. (Some calculations with the vortex strengths unaffected by the disturbances to their positions showed stability boundaries very slightly displaced.) Then the governing equations (5) to (9), for the particular solutions with symmetric separation, are considered.

For convenience, we introduce new variables  $v_1, v_2, v_3, v_4$ , by

$$\left. \begin{aligned} v_1 + iv_2 &= \gamma_1(\bar{\zeta}_1 - e^{-i\theta_1}) \\ v_3 + iv_4 &= \gamma_2(\bar{\zeta}_2 - e^{-i\theta_2}) \end{aligned} \right\} \quad (13)$$

Since we are concerned with small disturbances about a conical solution we write each variable as the sum of a term independent of  $\xi$ , with suffix  $c$ , and a small quantity, identified by a prime, thus:

$$\left. \begin{aligned} \zeta_j(\xi) &= \zeta_{jc} + \zeta'_j(\xi), \quad \gamma_j(\xi) = \gamma_{jc} + \gamma'_j(\xi), \quad j = 1, 2 \\ v_j(\xi) &= v_{jc} + v'_j(\xi), \quad j = 1, 2, 3, 4 \end{aligned} \right\} \quad (14)$$

When these are introduced into equations (5) and (13), the resulting equations are linear and homogenous in the small quantities, so that  $\zeta'_1, \zeta'_2, \gamma'_1$  and  $\gamma'_2$  can be expressed in terms of  $v'_1, v'_2, v'_3$  and  $v'_4$ , with constant coefficients depending on the conical solution quantities with suffix  $c$ . With  $\zeta'_1, \zeta'_2, \gamma'_1$  and  $\gamma'_2$  expressed in this way, the introduction of equation (14) into equations (7) and (9) leads to four real equations which can be written in matrix form as

$$\left\{ \frac{dv'_i}{d\xi} \right\} = J_1 \{v'_j\} \quad (15)$$

where the matrix  $J_1$  is the Jacobian matrix of the real and imaginary parts of the right-hand sides of equations (7) and (9) with respect to the variable  $v'_i$ . Its elements depend on the conical solution, but not on  $\xi$ .

Now, equation (15) is a system of four first-order linear differential equations with constant coefficients. The standard treatment (theorem 8.11 of Ref 15 for example) shows that the stability of the system depends only on the real part of the eigenvalues of  $J_1$ . We have stability if the real parts are all negative and instability if any eigenvalue has a positive real part. The consequence of instability is that a disturbance with a component in the direction of the appropriate eigenvalue will grow exponentially in  $\xi$ , as long as it remains small enough for the linearised treatment to apply. In particular, if the largest real part is  $\lambda_r > 0$ , the growth is like

$$e^{\lambda_r \xi} = \left( \frac{x}{x_0} \right)^{\lambda_r}$$

by equation (6). The growth rate in  $x$  is therefore, algebraic rather than exponential, and it is more rapid the nearer to the apex the disturbance is introduced.

The solution surface described in the previous section, both symmetric and asymmetric branches, was re-explored, evaluating the eigenvalues of  $J_1$  along the way. The stability of the solutions can now be identified. For the symmetric branch the outcome is shown in Fig 5. We recall that the disturbances under consideration are not restricted to being symmetric. The only symmetric solutions stable to general disturbances are in the region ABEA, the multiple solutions are unstable. The change in stability takes place across the bifurcation locus.

For the asymmetric branch, Fig 6 shows the asymmetric solutions are generally stable. The exceptions are shown in Fig 7, where we see that the asymmetric solutions springing from the lower part of the bifurcation locus are unstable. Stable solutions only occur above and to the right of the hatched boundary and nowhere is there more than a single stable symmetric solution or a pair of asymmetric solutions. Hence, it is hydrodynamic stability that determines which of the possible solutions occurs. The figures show that a value of  $\theta$  in excess of  $30^\circ$  is required for any stable solutions at a reasonable value of  $\alpha/\delta$ . This should be taken in conjunction with the conclusion drawn from Fig 1 that the separation line in this model is well to leeward of the separation line in a more representative model.

Although the distinction between stable and unstable solutions is of theoretical importance, in a practical situation the growth rate of disturbances also plays an important part. Here we are concerned with spatial disturbances and there is only a finite length of body over which they can grow. It is therefore interesting to see the actual values of

the largest real part,  $\lambda_r$ , of the eigenvalues of the matrix  $J_1$ . For symmetric separation lines 56° beyond the mid-plane of the body, these quantities are displayed as functions of the incidence parameter in Fig 8. At small values of  $\alpha/\delta$  there is no solution. Just above 1.8, a symmetric solution becomes possible. This is initially stable and the eigenvalue is negative, though numerically very small, so that disturbances would decay very slowly, and conversely evolution towards it from a neighbouring non-conical solution would be very slow. At a value of  $\alpha/\delta$  of about 2.08, bifurcation occurs and the eigenvalue of the symmetric solution becomes positive. The eigenvalue of the asymmetric solution is negative corresponding to its stability. The eigenvalues grow numerically, but remain small for  $\alpha/\delta \leq 5$ . The kink in the curve for the asymmetric solution at  $\alpha/\delta \approx 3.8$  corresponds to the eigenvalue becoming complex at the larger values.

The small values of  $\lambda_r$  suggest that, if we are prepared to admit solutions that are not exactly conical, then approximately symmetrical and highly asymmetrical solutions may be found for the same value of  $\alpha/\delta$ , despite the outcome of the stability analysis for the conical solutions.

#### 4 MEASUREMENTS ON A 10° CONE AT AN INCIDENCE OF 35°

The experiment, using the model shown in Fig 2, was designed so as to ensure that the flow was as nearly conical as possible at the first ring of pressure holes, at the lowest total pressure available (110 kPa). The shape of the model is conical for several local diameters downstream of this station and the Reynolds number is low enough for the boundary layer to be laminar at the primary separation line. The direct evidence for the state of the boundary layer is the visualisation based on the difference in evaporation rate of methylsalicylate held in a film of china-clay, carried out by Moir<sup>16</sup>. Fig 9 is reproduced from his paper. Note that his observation is for  $\alpha = 30^\circ$ , instead of  $\alpha = 35^\circ$ , at a total pressure of 2.0 atmospheres instead of 1.1 atmospheres, and at a Mach number of 0.2 instead of 0.15. We assume that the tunnel temperatures are the same. We cannot allow for the difference in angle of incidence, but differences in total pressure and Mach number simply lead to the prediction of a different streamwise location at which transition begins to affect the separation line. Note also that the streamwise location at which the separation line first encounters a turbulent wedge depends on where the wedge originates along the transition front. Even with the wedge on the separation line, this still leaves separation laminar all along the conical part of the model for the test conditions of Fig 3.

However, when the local side-force coefficient at the first two stations are compared, it becomes clear that the flow at many roll angles is not conical. Fig 10 illustrates this. The peak levels of  $C_y$  at the two stations are slightly different, so the values at each station have been normalised with respect to the peak value of  $|C_y|$  at that station. The resulting values at the two stations are then plotted and the values at station 1 are joined to those at station 2 by arrows, so the arrow indicates the direction of the flow development. There are a number of short arrows close to the extreme states and two short arrows near the zero axis. These may well correspond to conical flow conditions.

There are also a number of longer arrows, which reach, or approach, the extreme values; these seem to correspond to flows which are evolving towards the extreme states. Certainly, the extreme values are more common at station 2. Finally, there are a number of arrows which lie away from the extreme values and often also point away from the extreme values. If these are evolving toward the extreme states, it is clear that they have a long way to go. Many of these arrows are long, indicating a marked non-conicality. It is clear that all the intermediate side force levels at station 1 have long arrows leading from them, so they must correspond to non-conical states. Many of these flows have reached, or are approaching, extreme states, which are probably conical, by station 2. Unfortunately, measurements further downstream at this angle of incidence are not available, so their further evolution cannot be traced. Pressures were measured at all stations at  $\alpha = 30^\circ$  and these results are considered in section 5.

The appearance of conical flows with extreme or zero values only is consistent with the solutions of the simple flow model and the predominance of extreme values is consistent with the stability analysis. To obtain a more complete explanation, we need to consider what happens close to the apex of the tunnel model. We note first that, since the model imperfections are finite, their size relative to the local diameter increases without limit as the notional apex is approached. Secondly, we note that such understanding of the flow as we have is based on concepts relevant at high Reynolds numbers, while the local Reynolds number tends to zero as the apex is approached. Our flow model can therefore only apply downstream of some station whose distance from the notional apex depends on the scale of the imperfections due to manufacture and handling of the tunnel model and on the unit Reynolds number of the test. At this station we must suppose that the initial conditions for the system of ordinary differential equations (7) and (9) may be quite unrelated to the symmetric or asymmetric solutions with which we are familiar. We should, therefore, not be surprised if non-conical flows are sometimes observed. It is the preponderance of approximately conical flows that requires explanation. The outcome of the stability analysis, that disturbances to stable conical solutions decay like  $(x/x_0)^{\lambda_r}$  and disturbances to unstable conical solutions grow in the same way, with  $\lambda_r = \lambda$  illustrated in Fig 8, does show that the evolution either towards or away from conical solutions may be slow, even when the flow is close to being conical.

#### 5 MEASUREMENTS ON A 10° CONE AT AN INCIDENCE OF 30°

At smaller angles of incidence, the variation of side force with roll angle is not dominated by the occurrence of extreme states. Fig 11 shows the variation of the local side force coefficient at station 1 for  $\alpha = 30^\circ$  and the same Mach and Reynolds numbers as Fig 3. The local normal force coefficient is also shown for comparison. At this lower incidence, the side force is smaller absolutely and in relation to the normal force, but it is still significant. There is no obvious correlation between the side and normal forces.

At this angle of incidence we have local side force values at all six measuring stations, of which the first four lie on the conical part of the model, see Fig 2. We shall use



values at these four stations to assess the degree of conicality of the flow. We also have values measured at three different levels of total pressure in the wind tunnel, 110 kPa, 200 kPa and 300 kPa, providing three unit Reynolds numbers at the same Mach number,  $M = 0.15$ .

Fig 12 shows the variation of the local side-force coefficient with roll angle at the first three measuring stations at atmospheric pressure. At nearly all the roll attitudes there is a significant variation in force coefficient along the length of the cone, so that conical flow concepts are not likely to be helpful.

Fig 13 shows the same quantity at the first station for the three different total pressures. Separation should be laminar for all three conditions, in accordance with the previous discussion. It is clear that Reynolds number effects are present and we can tentatively identify two of them. As the Reynolds number increases, an extra change of sign appears in the side-force variation. We can associate this with an additional feature of the nose shape becoming effective as the thickness of the boundary layer decreases. Also as the Reynolds number increases, the peak value of the side force increases. This point is pursued in Fig 14, where the numerically largest value of  $C_Y$  measured in a complete revolution in roll is plotted against Reynolds number based on the distance from the apex to the measuring station. Results are shown for all three unit Reynolds numbers and for all four measuring stations which lie on the conical part of the body. The increase in peak value shown in the previous figure now appears at the left-hand side of the picture, followed by a sharp fall and a levelling off. An attempt is made to define a band within which the measurements lie. The range of values of Reynolds number over which transition might occur at the separation line is indicated. We might guess that the reduction in peak side force is associated with turbulent reattachment since this progresses gradually in the three-dimensional flow, and obviously ends when the boundary layer is turbulent at separation.

We might hope that the consistent behaviour shown by the first five points on the left of Fig 14 would be reflected in a consistent behaviour at specific roll angles. Choosing  $\phi = 270^\circ$ , which is near a peak in  $C_Y$ , we obtain Fig 15, where values at all six measuring stations have been included to establish trends with more certainty. Concentrating on the left-hand edge of the plot, we see that an increase in  $Re_x$ , brought about by an increase in unit Reynolds number, at station 1 produces an increase in side force, while the same increase in  $Re_x$  brought about by an increase in  $x$  produces a marked decrease in side-force coefficient.

The results at many other roll angles behave in a similar way, so we conclude that although the local Reynolds number has some value in correlating the maximum value of side-force coefficient, it does not determine the flow at particular roll angles.

In Fig 16 we present the variation of local side force coefficient with lengthwise station for four roll angles. These have been chosen, not because they are typical, but because they include the variations which are most nearly constant, and so might correspond to conical flows. In Fig 16a we might think a conical flow is emerging as the unit Reynolds number increases, but in Fig 16b the nearest

approach to a constant value comes at the intermediate Reynolds number. In Fig 16c, all the variations are small, but two distinct near-constant levels appear, a near-zero value at the two higher Reynolds numbers and a non-zero value, about the same as that in Fig 16b at the lowest Reynolds number. In Fig 16d we see a change from a rising to a falling side force coefficient as the Reynolds number varies, with a near constant level in between.

## 6 CONCLUSIONS

(a) For the single line-vortex model of asymmetric conical flow over circular cones with symmetric separation lines, a thorough exploration of parameter space has revealed only insignificant regions of multiple solutions and no further bifurcation locus from which asymmetric solutions could arise.

(b) An examination of the stability of solutions of this model to small spatial disturbances has shown that stable symmetric solutions are confined to a narrow band of values of the incidence parameter, but that, with insignificant exceptions, the asymmetric solutions are stable. There is no combination of separation line position and incidence parameter for which both stable symmetric and asymmetric solutions are possible. The growth rate of disturbances to symmetric solutions is algebraic rather than exponential and the growth rates are not large.

(c) An examination of low-speed experimental data shows that asymmetric flow over a circular cone can be significantly non-conical with large variations in local side-force coefficient along the length of the cone. At an angle of incidence of  $35^\circ$  on a  $10^\circ$  cone, the approximately conical flows appear to predominate, but at  $30^\circ$  they only occur exceptionally.

(d) This behaviour may be described using ideas from the theory of systems of ordinary differential equations. Very near the apex, any real body departs significantly from an ideal circular cone, so the flow there defies rational description and provides initial values for the system which are essentially arbitrary. At the larger angles of incidence, for which a stable conical solution exists, the flow evolves towards it in the downstream direction, the solution acting as an attractor. This conical solution will be asymmetric at larger incidences and symmetric at smaller incidences. At even smaller incidences, for which no stable conical solution exists, but separation still occurs, a non-conical behaviour emerges.

## REFERENCES

- 1 Bryson, A.E. Symmetrical vortex separation on circular cylinders and cones. *J. Appl. Mech. (ASME)*, 28, pp 643-8 (1957)
- 2 Dyer, D.E., Fiddes, S.P., Smith, J.H.B. Asymmetric vortex separation from cones at incidence - a simple inviscid model. *Aeronautical Quart.*, 33, pp 293-312 (1982), also RAE Technical Report 81330 (1981)
- 3 Smith, J.H.B. Improved calculations of leading-edge separation from slender, thin delta wings. *Proc. Roy. Soc. Lond. A*, 306, pp 67-90 (1968), also RAE Technical Report 66070 (1966)
- 4 Fiddes, S.P. A theory of the separated flow past a slender elliptic cone at incidence. Paper 30 in *Computation of Viscous-Inviscid Interaction*, AGARD CP 291 (1980)

- 5 Fiddes, S.P., Smith, J.H.B. Calculations of asymmetric separated flow past circular cones at large angles of incidence. Paper 14 in *Missile Aerodynamics*, AGARD CP 336 (1982)
- 6 Smith, J.H.B. Theoretical modelling of three-dimensional vortex flows in aerodynamics. In *Aerodynamics of Vortical Type Flows in Three Dimensions*, AGARD CP 342 (1983), also *Aeronautical J.*, 88, pp 101-116 (1984)
- 7 Fiddes, S.P., Smith, J.H.B. Asymptotic separation from slender cones at incidence. In *Boundary-layer Separation*, ed. Smith, F.T. and Brown, S.N., Springer (1987)
- 8 Fiddes, S.P., Williams, A.L. Recent developments in the study of separated flows past slender bodies at incidence. Paper 31 in *The Prediction and Exploitation of Separated Flow*, Royal Aeron. Soc. Lon. (1989)
- 9 Williams, A.L. The effect of body shape on the development of vortex asymmetry in the flow past slender bodies. Univ. of Bristol Aero. Eng. Rept., 413 (1990), also 17th ICAS Conf. Stockholm (1990)
- 10 Marconi, F. Asymmetric separated flow about sharp cones in a supersonic stream. Proc. 11th Int. Conf. Num. Meth. in Fluid Dyn., *Lecture Notes in Physics*, 323, Springer (1989)
- 11 Siclari, M.J., Marconi, F. The computation of Navier-Stokes solutions exhibiting asymmetric vortices. AIAA Paper 89-1817 (1989)
- 12 Hunt, B.L. Asymmetric vortex forces and wakes on slender bodies. AIAA Paper 82-1336 (1982)
- 13 Fiddes, S.P., Lean, D.E., Moir, I.R.M. Experimental investigation of the separated flow past slender bodies in the RAE 5 metre low-speed pressurised wind tunnel. RAE to be published
- 14 Fiddes, S.P. Separated flow about cones at incidence - theory and experiment. In *Studies of Vortex Dominated Flows*, ed. Hussaini, M.Y. and Salas, M.D., Springer (1987)
- 15 Jordan, D.W., Smith, P. Non-linear ordinary differential equations. Clarendon Press, Oxford, 2nd ed. (1987)
- 16 Moir, I.R.M. Recent experiences in the RAE 5 metre wind tunnel of a china clay method for indicating boundary layer transition. *Aeronautical J.*, 90, pp 6-9 (1986)

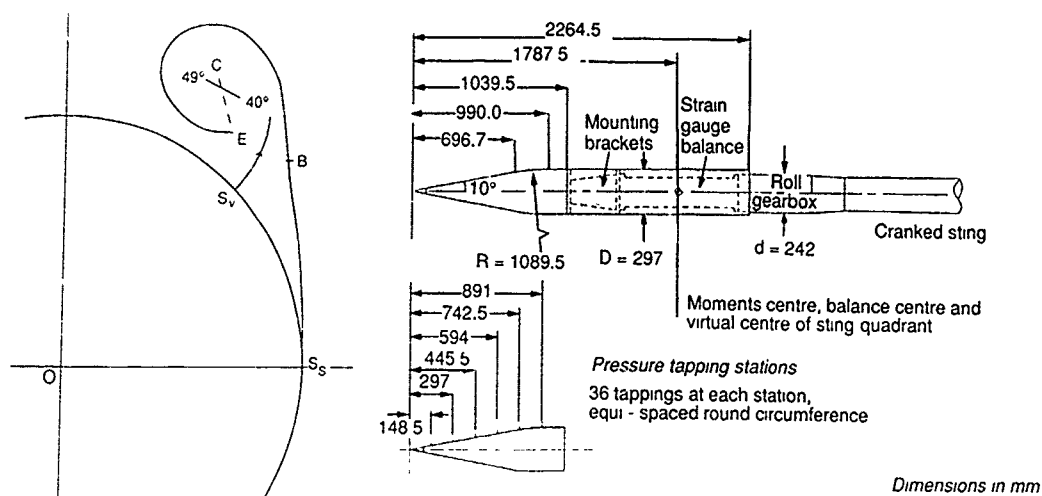


Fig 2 Details of cone-cylinder model

Fig 1 Comparison of line-vortex and sheet-vortex models for symmetrical flow past a circular cone

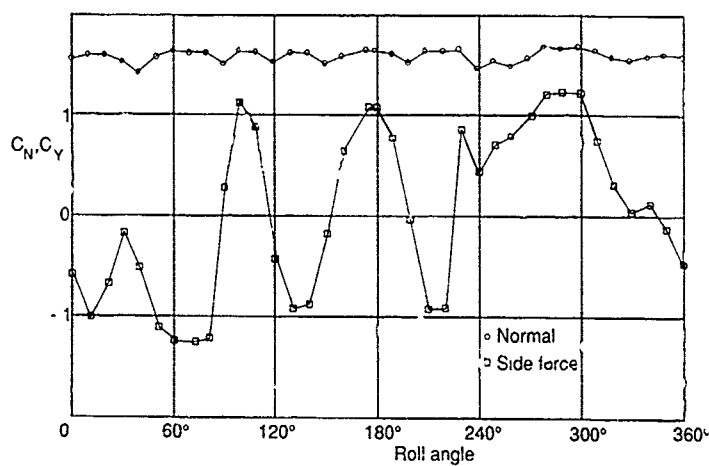
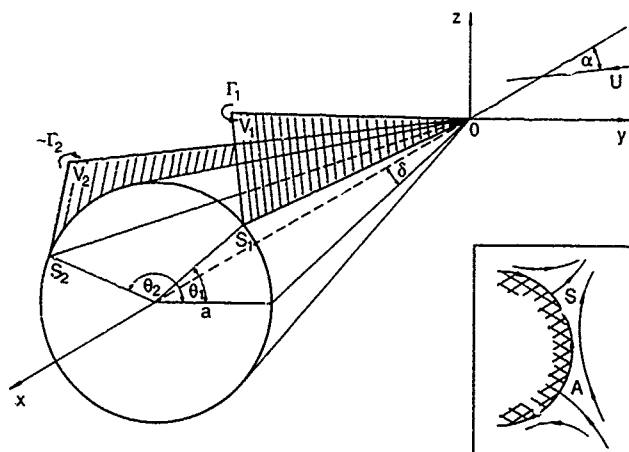
Fig 3 Variation of local side and normal force with roll angle at station 1,  $\alpha = 35^\circ$ 

Fig 4 Configuration and coordinate system (inset: flow structure)

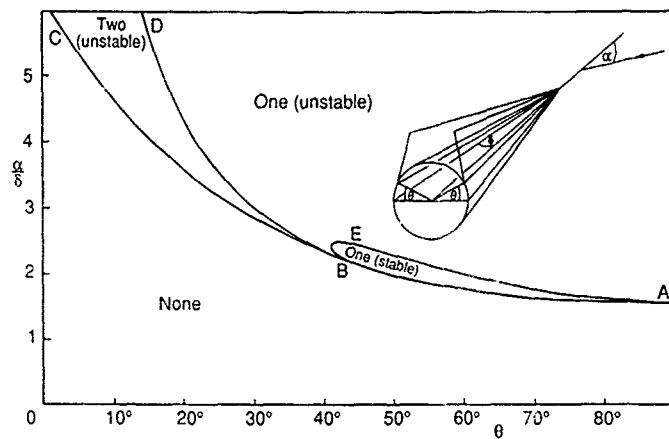


Fig 5 Range of symmetric solutions

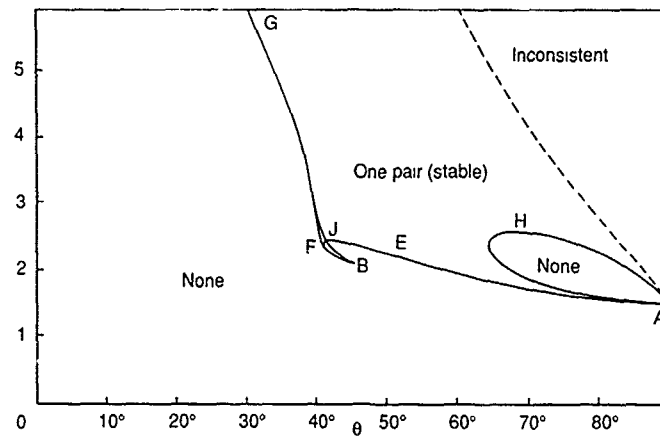


Fig 6 Range of asymmetric solutions

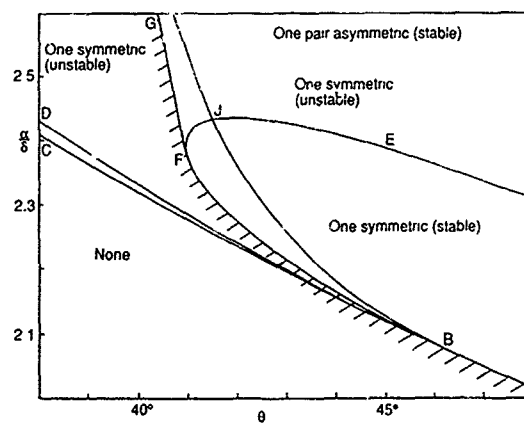
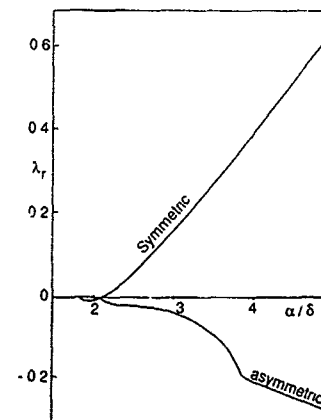
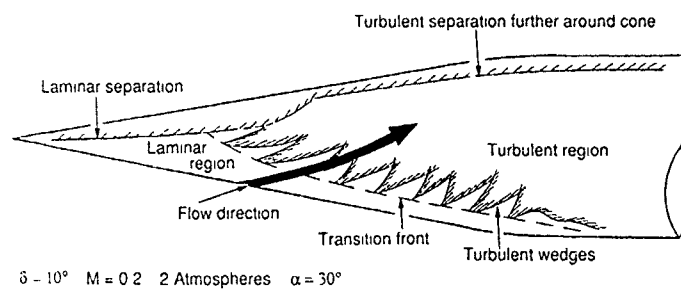


Fig 7 Range of asymmetric solutions (detail)

Fig 8 Real part of dominant eigenvalue,  $\theta = 56.0^\circ$



$\delta = 10^\circ$   $M = 0.2$  2 Atmospheres  $\alpha = 30^\circ$

Fig 9 Transition and separation on tunnel model

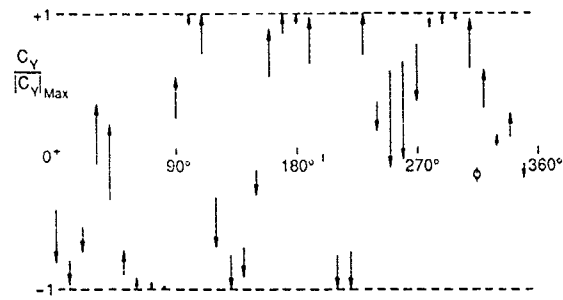


Fig 10 Shift in side-force between stations 1 and 2  
 $\alpha = 35^\circ$ ,  $Re_p = 1.0 \times 10^6$

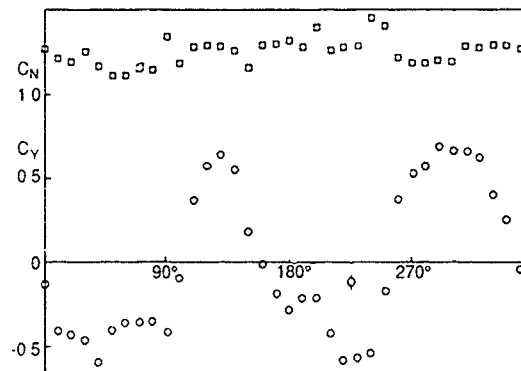


Fig 11 Local force coefficient vs roll angle  
 $\alpha = 30^\circ$ , station 1,  $P_t = 110$  kPa

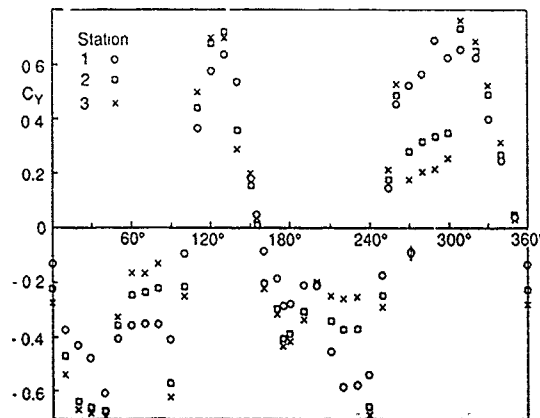


Fig 12 Local side-force coefficient vs roll angle  
 $\alpha = 30^\circ$ ,  $P_t = 110$  kPa

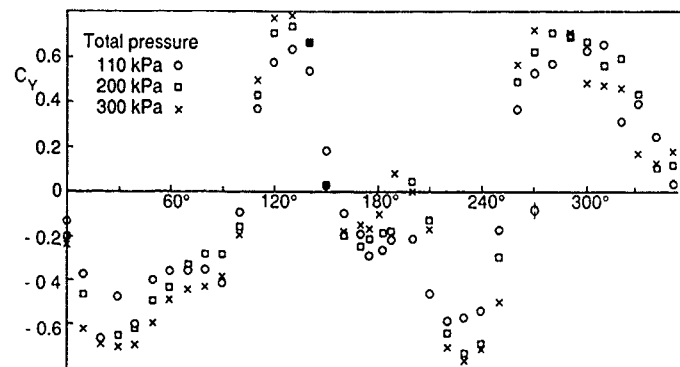


Fig 13 Local side-force coefficient vs roll angle  
 $\alpha = 30^\circ$ , station 1

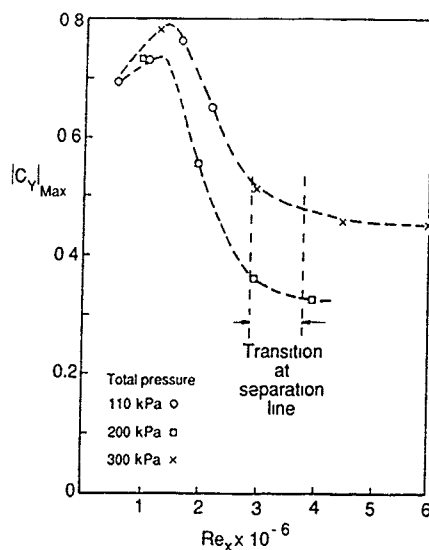


Fig 14 Peak side-force coefficient vs local  
Reynolds number  $\alpha = 30^\circ$

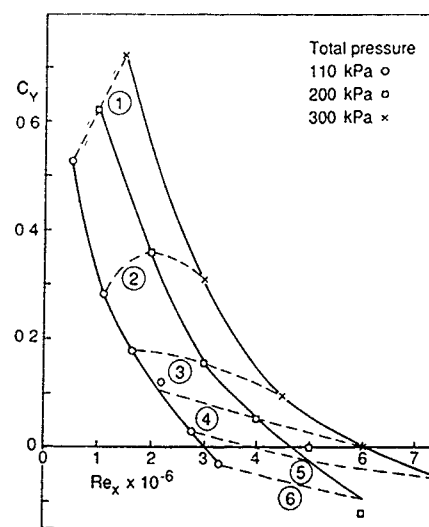


Fig 15 Side-force coefficient vs local Reynolds number  
 $\alpha = 30^\circ$ ,  $\phi = 270^\circ$

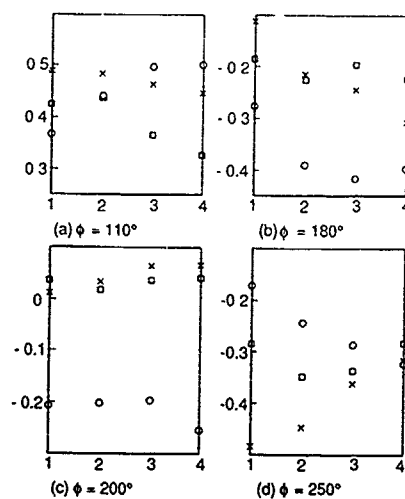


Fig 16 Variation of local side-force coefficient along cone for total  
pressure 110 (O), 200 (□) and 300 (X) kPa

# AN EXPERIMENTAL INVESTIGATION OF THE EFFECT OF FINENESS RATIO ON LATERAL FORCE ON A POINTED SLENDER BODY OF REVOLUTION

by

I.R.M. Moir

Aerodynamics Department  
Royal Aerospace Establishment  
Farnborough, Hampshire GU14 6TD, United Kingdom

## SUMMARY

Tests have been made on a slender body model in the RAE Farnborough 5 metre pressurised low-speed Wind Tunnel. Measurements of side force variation with angle of incidence and with roll angle are presented in this paper, together with an examination of the angle of incidence at which side force onset occurs and how this varies with nose apex angle, overall fineness ratio and Reynolds number. A flow visualisation technique was used to study the development of vortical asymmetry as angle of incidence was increased.

## 1 INTRODUCTION

It is well established that a pointed body of revolution, although axially symmetric, can nevertheless give rise to an asymmetric flow field at moderate angles of incidence<sup>1-5</sup>. This results from the separation of the cross flow around the body, the separated shear layers from which roll up to form vortices in the lee of the body. At first these are oriented symmetrically about the incidence plane as shown in simplified form in Fig 1a, but as the angle of incidence is increased further, one vortex of the pair moves closer to the body and usually towards the incidence plane, while the other moves away, as shown in Fig 1b. The consequence of this phenomenon is that an out-of-plane, or side force is induced on the body as a result of the asymmetric pressure distribution now occurring on the surface, as shown in the example in Fig 2.

A typical variation of side force coefficient with angle of incidence, together with the corresponding variation of normal force coefficient, is shown in Fig 3. The region of zero side force consists firstly of attached flow, followed by separated flow with symmetric vortices. The coefficient becomes non-zero as the vortices start to show asymmetry, and the angle of incidence at which this occurs is usually termed the 'onset angle'. As may also be seen from Fig 3, side force can attain similar magnitudes to normal force. It has been established by Wardlaw and Morrison<sup>6</sup>, amongst others, that the phenomenon is essentially a low-speed one; the side force decreases progressively from about  $M = 0.4$  to become virtually zero as  $M = 1$  is approached. It is however of great significance to the control of missiles and combat aircraft, both of which may be required to manoeuvre subsonically.

As the angle of incidence, (or the length of the body) is increased further, the separation of the vortices from the surface also increases, and at some point a new vortex system forms closer to the surface under the first pair, and further downstream. The effect is to generate a cellular structure along the length of the body, the side force 'cells' being of alternating sign, appearing as a stable Karman vortex street in the cross-flow plane. It is the progressive change in the distribution of positive and negative side

force that results in the change of sign of the overall side force as typified in Fig 3.

Furthermore, as fineness ratio is increased, and consequently as the first vortex pair withdraws from the afterbody, we must expect a secondary vortex cell to be formed even at low angles of incidence and independently of the nose apex angle. Intuitively, we might expect such a flow structure to be less stable. The implication is, therefore, that we should expect the variation of side force with angle of incidence to be strongly dependent upon fineness ratio.

The mechanism which causes one of the vortices in a pair to leave the surface is thought to be essentially due to the appearance, above the onset angle, of stable asymmetric states<sup>7</sup>, the choice of which state, left- or right-handed, being dictated by small imperfections in the geometry of the nose close to the apex<sup>8</sup>. The radial distribution of such imperfections usually results in the sign of the overall side force being sensitive to the roll orientation of the body, as illustrated in Fig 4. The roll angles at which the side force changes sign are often referred to as 'switching points'.

Notwithstanding the wealth of previous research on slender body configurations, the foregoing suggests that further investigation into the effects of nose apex angle and overall fineness ratio would be profitable. Furthermore, whilst flow visualisation techniques have been used to examine the flow over the nose region of slender bodies, very little such work has been carried out on cylindrical afterbodies. A research programme, based on the RAE 5 metre pressurised low-speed Wind Tunnel, has therefore been carried out and the main results are presented in this paper.

## 2 RAE TEST PROGRAMME

Experimental tests on slender body configurations at low speed has been undertaken in the RAE by a number of workers, most recently by Mundell<sup>9</sup>, and Smith<sup>10</sup>. Smith carried out some preliminary tests in the 5 metre pressurised low-speed Wind Tunnel to establish the basic principles of this type of test, and to investigate the dependence of side force on Reynolds number and Mach number. These tests were of a limited nature as only two nose shapes and one afterbody length were available. Also, the need to use an existing strain-gauge balance and mounting resulted in a model which was too large (about 300 mm diameter) to make it possible to test at the lower values of Reynolds number where transitional effects were thought to occur. However, some useful work was done in the early 1980's, which was extended to include measurement of surface pressures on the noses by Fiddes *et al*<sup>11</sup> to provide data for the CFD work of Fiddes and Smith<sup>7,12</sup>, and also the development of a device to control the side force onset by Moir, Peckham and Smith<sup>13</sup>.

In view of the known dependence of side force on Reynolds number near  $0.5 \times 10^6$  (based on model diameter)<sup>14</sup>, and of the probability, discussed in the Introduction, that side force could depend on both nose apex angle and the overall fineness ratio, a new model was manufactured. As shown in Fig 5, this is about half the diameter of the earlier model at 150 mm, and has three interchangeable nose configurations and three afterbody lengths available. The three noses are:

- (i) A cone with a  $10^\circ$  semi-apex angle, faired into the constant diameter portion via a circular arc.
- (ii) A 5:1 circular arc tangent ogive (semi-apex angle  $11.4^\circ$ ).
- (iii) A 3:1 circular arc tangent ogive (semi-apex angle  $18.9^\circ$ ).

Noses (i) and (iii) have an integral constant diameter portion to bring their overall fineness ratio to 5:1.

Together with the nose sections, the constant diameter cylindrical afterbody sections give total fineness ratios of 5.5:1, 10:1 and 15:1. No surface pressure tapings were incorporated due to the small size of the model.

The model was tested mainly on a 76 mm square strain-gauge balance, which, while not being well suited to slender body work (the normal force and side force component ranges differ substantially), has yielded useful results as will be described. The model and balance were mounted via a roll gearbox, which allowed  $360^\circ$  of roll angle variation, on the 5 metre Wind Tunnel sting rig as shown in Fig 6. This latter having a  $19^\circ$  crank angle enabled an incidence range from about  $1^\circ$  to  $38^\circ$  to be provided. Model pitch and roll attitude was measured with accelerometers which were mounted within the model.

A more accurate strain-gauge balance that was specifically designed for slender body work has now been acquired, as has also a high incidence mounting rig which allows angles of incidence of up to  $90^\circ$  to be attained; some of the data presented here were obtained with these facilities.

Forces and moments on the model were measured over the range of angle of incidence at constant roll angle, and over  $360^\circ$  of roll at various fixed angles of incidence. Visualisation of the surface flow was carried out using diesel oil mixed with a dye which fluoresced when viewed under ultra-violet light.

The tests were carried out in the RAE 5 metre Wind Tunnel mostly at  $M = 0.2$  and Reynolds numbers of 0.7, 1.3 and 2.0 million, based on model diameter. The Reynolds number range was also extended by running at  $M = 0.1$  at minimum tunnel total pressure, giving 0.35 million.

### 3 RESULTS AND DISCUSSION

#### 3.1 Variation of side force with angle of incidence

Fig 7 illustrates a typical variation of side force coefficient with angle of incidence over the range of Reynolds number tested; the model configuration chosen has a 3:1 ogive nose, and has an overall fineness ratio of 15:1. It is seen that there is some dependence on Reynolds number in that CY at 0.7 million is significantly lower than that at the

two higher Reynolds numbers. The onset angle does not however appear to be affected significantly.

Fig 8 again shows the variation of CY with angle of incidence, but in this case three nose shapes were tested each with an overall fineness ratio of 15:1. It is seen that the onset angle is virtually the same for all three configurations.

Fig 9 gives an example of the variation of CY with angle of incidence for one nose shape (the 3:1 ogive), but for the three values of overall fineness ratio. It is obvious that fineness ratio has a major influence on onset angle. While it has been suggested<sup>15</sup> that onset angle is only dependent on the semi-apex angle of the nose, it is evident from the present data that this does not appear to hold for most of the configurations tested. Fig 10a shows the onset angles from all the nine configurations tested plotted against semi-apex angle. The figure also shows the relationship of onset angle with semi-apex angle as proposed by Keener and Chapman<sup>15</sup>, amongst others:

$$\alpha_{\text{onset}} = 2 \times \theta_A \quad (1)$$

It is seen that there is quite a good correlation of the measured results with apex angle for the lowest fineness ratio, but the longer bodies show progressively worse correlation. This confirms the speculation that onset angle should also be fineness ratio dependent.

Fig 10b shows the measured values of onset angle plotted against fineness ratio. Also shown is the relationship derived by Sarpkaya<sup>16</sup> from measurements of the angle of incidence at which asymmetric flow first appears at the base of an inclined blunt nosed cylinder, relating onset angle directly to fineness ratio:

$$\alpha_{\text{onset}} = \tan^{-1} \left( \frac{4d}{T} \right) \quad (2)$$

The figure shows that there is some correlation between the experimental values of onset angle and this function of fineness ratio, at least for the higher values of fineness ratio and the larger apex angles. The figure also shows the onset angles suggested by the semi-apex angle relationship; these show that for the lower values of fineness ratio and smaller apex angles, onset angle is increasingly influenced by apex angle.

It would appear, therefore, that in general, onset angle is a function of both apex angle and fineness ratio. Making use of the admittedly approximate measured values of onset angle, Fig 10c suggests the form that this function might take. The constant onset angle 'contours' in the figure have been derived by using equations (1) and (2) to define the end points, and fitting the best possible curves through the present data points.

Reference to the work of Sarpkaya<sup>16</sup> would suggest that a slender body of sufficiently high fineness ratio behaves as a blunt nosed cylinder, irrespective of the nose apex angle. Furthermore, this might also lead to the conclusion that the flow asymmetry similarly first appears at the base of the afterbody. In an attempt to verify this supposition, flow visualisation was carried out over a range of angles of incidence, starting from below the onset of side force. Examples are shown in Fig 11 of the 3:1 ogive nose with 15:1 overall fineness ratio, the photographs being taken from the leeside of the model. At the lowest angle of incidence shown,  $12^\circ$ , vortical flow was already established over almost the full length of the body, but did not yet show



any asymmetry. The next picture is at 25° of incidence — here it can be seen that there was substantial asymmetry on the afterbody but the flow over the nose region was essentially symmetrical. The following picture is at 35°, which is less than 3° below the apex angle for this nose. Here the afterbody asymmetry had almost reached the nose region, although the nose itself retained substantially symmetrical flow. (The leeward generator has been drawn in the figure, showing that the photograph was taken from slightly off-axis.) The final picture of the set is at an angle of incidence of 42°, some 3° above the apex angle. It is seen that there was now asymmetry on the nose as well as over the entire afterbody.

It would appear, therefore, that, in this case at least, the afterbody asymmetry has reached the nose region at an angle of incidence close to a value of twice the nose semi-apex angle (37.9°) above which the flow over the nose is seen to become asymmetric. This is in agreement with the results obtained by Keener and Chapman<sup>15</sup> who established, by means of measurements on a slender nose in the presence of a decoupled afterbody, that the nose does not develop side force below an angle of incidence equal to twice the semi-apex angle, even in the presence of an afterbody.

Flow visualisation on the 5:1 ogive nose, illustrated in Fig 12, appears to show a similar trend. The nose is again shown with the 15:1 overall fineness ratio, and at angles of incidence of 17°, 21°, 22° and 23°. It is seen that there was very small asymmetry at 17°, but by 21° there was easily detectable asymmetry on the afterbody. By 22° this asymmetry was well developed, and by 23° it had moved forward to just aft of the nose region, which itself showed signs of incipient asymmetry.

On the basis of the semi-apex angle relationship, we would expect the angle of incidence for side force onset to be 22.8° whereas the onset angle for this configuration is about 15°. Therefore, it would appear that, as with the 3:1 ogive, asymmetry has again developed on the afterbody and moved forward to reach the nose region by an angle of incidence approximately equal to the apex angle of the nose. The inference to be made from these two cases is that the rate of the progression of the afterbody flow asymmetry with increasing incidence is governed by the nose apex angle; this rate of progression is such that the asymmetry reaches the nose at an incidence for which an isolated nose would be expected to reach its onset angle. Thus, while the present results would appear to agree with those of Sarpkaya<sup>16</sup> in suggesting that the angle of incidence at which asymmetry first occurs at the base of a long cylindrical body is independent of the nose shape, it also shows that the subsequent flow behaviour, as incidence is increased, is strongly dependent upon nose shape. This aspect is discussed further in the following section. Further resolution of the question posed by the foregoing, namely, the relationship between nose and afterbody flow asymmetry, is probably not possible with the data obtained from existing noses as the 5:1 ogive nose has an apex angle rather too close to the value of the onset angle for the 15:1 fineness ratio. A 4:1 ogive (apex angle 28.5°) would give more opportunity to study the progression of the afterbody flow asymmetry and its relationship to asymmetry on the nose. Also, if it were possible to measure surface pressures over the entire body, the development of flow asymmetry with increasing angle of incidence could be studied in much greater detail. Alternatively, a wake imaging technique such as a laser light sheet<sup>17</sup> could be used to study the streamwise development of the vortical structure.

### 3.2 Variation of side force with roll angle

As discussed in the Introduction, when a slender body is rolled about its axis at an angle of incidence above that for side force onset, it will, in general, exhibit a characteristic 'switching' of side force direction at certain roll angles. It is generally accepted<sup>14,18</sup> that the switching points are determined by the distribution of minute imperfections at the extreme nose apex, at least for conditions where vortical asymmetry is occurring on the nose. These switching points then appear to be characteristic of a particular nose; this view is supported by a comparison of the variation of side force coefficient with roll angle for the three nose shapes of the present tests, as seen in Fig 13. It is supposed that two noses of nominally the same axisymmetric shape would have different switching points since it would be implausible to suppose that, in general, manufacturing imperfections would be reproduced. Indeed, it has been found, during the present tests, that the switching points for one of the noses changed over a period of time; this is thought to be due to the nose being cleaned before each run, a process which eventually resulted in some of the imperfections being smoothed until they no longer affected the flow.

It became apparent during the present tests that the flow field can be highly unstable in the neighbourhood of the switching points. On a number of occasions when CY was in the process of changing sign, the model was excited into a state of severe vibration, resulting in the need to carry out an emergency shut-down of the tunnel. This phenomenon often occurred over a small range of roll angle and rolling the model in either direction by as little as 1° was sufficient to stop the vibration. The vibration was most severe when the variation of CY with roll angle was of 'square wave' form, and under these conditions it was noticed that as the side force changed sign, substantial movement of the model occurred as a result of insufficient rigidity in the model mounting. It is supposed that the movement of the model resulted in an effective change in angle of incidence or in roll angle which was sufficient to trip the flow into a further reversal and that this built up into a vibration. Evidently the amplitude of the oscillation was dependent upon the resonant frequency and stiffness of the mounting.

In many of the present configurations, significant flow asymmetries apparently occur only on the afterbody. In these cases, one might reasonably expect to re-examine the hypothesis that the switching points are related to the nose geometry rather than that of the afterbody. However, when we compare the variation of side force coefficient with roll angle for the two longer afterbodies but with the same nose (3:1 ogive in this case), Fig 14 shows that the switching points are identical. It is also interesting to examine the result of a test in which the 3:1 ogive nose section was displaced from its normal angular position relative to the afterbody by an angle of 72°. Fig 15 shows that the switching points were also displaced from those for the nose in its regular position by an angle very close to 72°.

The above example was for the model at an incidence of 27°, which as seen earlier is well below that at which flow asymmetry appears on the 3:1 ogive nose itself. From Fig 16 it is seen that the switching points remain the same whether the angle of incidence is above or below that at which the flow on the nose becomes asymmetrical. Hence it can be concluded that although the nose itself may exhibit a symmetrical flow pattern, it can nevertheless influence the behaviour of the asymmetry on the afterbody. It would appear that although the surface flow pattern on the nose is imperceptibly asymmetric nevertheless there is inherent in the flow a finite and persistent asymmetry convected with

the stream which is capable of triggering afterbody asymmetry. This mechanism appears to be another example of the influence the nose has over the afterbody flow, in addition to that of the rate of forward movement of the afterbody asymmetry.

### 3.3 Reynolds number effects

In section 3.1, reference was made to Reynolds number effect on the variation of CY with angle of incidence. Throughout the present experiments, there was evidence that at a Reynolds number of about  $0.7 \times 10^6$ , side force is smaller than at the higher values and that from about  $1.0 \times 10^6$ , the maximum CY remains virtually constant as Re is increased.

In order to obtain greater understanding of this variation, measurements have been made at the lowest practicable value of Re. This was provided when the tunnel was run at  $M = 0.1$  at atmospheric pressure, it being presupposed that compressibility effects were negligible at these Mach numbers. Unfortunately, this resulted in a deterioration of repeatability in the measured side force coefficients — a variation of up to 0.3 was seen at constant angle of incidence. This was possibly due to a mismatch of the balance to the low level of loads being measured.

Fig 17 shows the variation of CY with angle of incidence for the 3:1 ogive nose with 15:1 fineness ratio. It is seen that, as stated above, for Reynolds numbers of 2.0 and 1.3 million, the values of maximum side force coefficient are very similar, while at 0.7 million the value is more than halved. For these three values of Reynolds number side force onset occurs near the value established in section 3.1 for a fineness ratio of 15:1. At 0.35 million, however, a very different pattern emerges. Taking into account the large amount of scatter mentioned earlier, the side force appears to remain near zero until the angle of incidence approaches twice the semi-apex angle of the nose. Side force then increases rapidly, reaching a maximum value higher than at the other values of Reynolds number.

These results agree in general with the findings of Champigny<sup>14</sup>, who demonstrated that CY changes rapidly in the range of Reynolds number 0.4 to 0.6 million; this variation was found to be accompanied by changes in the longitudinal distribution of CY on a slender body. Additionally, it would appear, from this single case, that the appearance of asymmetric flow on the afterbody is strongly dependent on Reynolds number.

It may well be that the variation of CY with Reynolds number is related to flow changes in the nose apex region where flow visualisation has shown that sub-critical, trans-critical and super-critical boundary layer conditions all exist in a small area. The fact that the Reynolds number effect has been observed at angles of incidence below which asymmetric flow is seen on the nose suggests that the nose flow again influences the flow over the afterbody in a similar manner to that described earlier. Unfortunately, the flow visualisation survey that has been carried out was insufficient to provide clear evidence of these effects. Clearly, further investigations in this area are required.

## 4 CONCLUSIONS AND FUTURE WORK

Tests have been carried out on a slender body of revolution to investigate the effects of fineness ratio and

nose apex angle on the angle of incidence at which side force onset occurs, and the way in which this phenomenon is influenced by Reynolds number. The development of flow asymmetry has also been examined using flow visualisation.

It has been found that, for high values of fineness ratio and high semi-apex angle, the onset angle is dependent only on fineness ratio, while for low fineness ratio and low apex angle, the onset angle becomes purely apex angle dependent. An expression derived empirically by Sarpkaya<sup>16</sup> for blunt nosed cylinders has been found to produce a reasonable collapse of measured onset angle for configurations in the former category, while the generally accepted dependence on semi-apex angle appears to apply for configurations of the latter type.

The former case has been found to be associated with the development of vortical asymmetry on the cylindrical afterbodies of the configurations tested, and the asymmetry, having first appeared near the base of the model progresses forward, reaching the tapered nose region at an angle of incidence close to twice the semi-apex angle of the nose. Asymmetry was seen in the surface flow pattern on the nose for angles of incidence just above this value. It is concluded from this that the rate at which flow asymmetry on the afterbody moves forward with increasing angle of incidence is governed by the nose geometry. However, the question of whether the development of asymmetries on the afterbody and on the nose are two separate mechanisms, or whether they are linked is not resolved — this might be clarified by further tests with a nose of apex angle of about  $28^\circ$  to bridge the gap between the noses at present available. Measurement of surface pressures on the nose and afterbody of bodies of high fineness ratio might also assist the investigation, by providing a more precise measure of the development of asymmetry than that allowed by surface flow visualisation.

When the model was rolled at a constant angle of incidence above that for side force onset, the expected characteristic 'switching' of side force direction was seen. The roll angles at which this occurred were found to be a characteristic of the particular nose used and were unaffected by the choice of afterbody length. The switching points also remained at the same positions throughout the incidence range covered. This implies that even for angles of incidence at which vortical asymmetry existed on the afterbody only, the nose controlled the orientation of the asymmetry.

The effect of Reynolds number on side force was also investigated during the present tests. For values of 0.7 million and above this appears to have little influence on the angle of incidence for side force onset or the angle of roll at which direction switching occurs. There does, however, appear to be a sharp change in the magnitude of side force at about  $Re = 0.7 \times 10^6$ . At this value, the maximum CY measured was less than half that at higher Reynolds numbers, and the maximum CY at the highest two Re values was constant. At lower Reynolds numbers there appear to be major changes in the way in which the flow over the body develops, and the magnitude of maximum side force coefficient appears to be highest at low Reynolds number. However, further work is required in this area in order to identify the flow features which might account for the Reynolds number effects. These large scale effects highlight the need to carry out tests, such as those presented here, over a range of Reynolds number. In this respect, access to a high Reynolds number facility, such as the RAE Farnborough 5 metre Wind Tunnel, is very important.

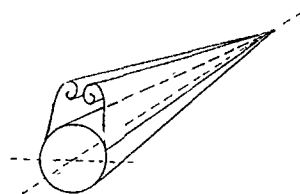
## LIST OF SYMBOLS

$\alpha$ (alpha)	angle of incidence
$\alpha_{\text{onset}}$	angle of incidence
CN	normal force coefficient
CY	side force coefficient
Cp	pressure coefficient
Re	Reynolds number
$\theta_A$ (theta)	nose semi-apex angle
l	overall length of slender body
d	body diameter
l/d	fineness ratio

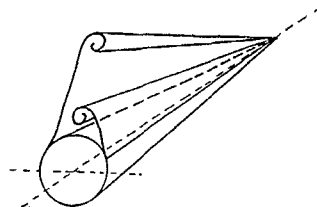
## REFERENCES

- 1 Allen, H.J., Perkins, E.W. 'Characteristics of flow over inclined bodies of revolution.' NACA RMAS0L07, March 1951
- 2 Letko, W. 'A low-speed experimental study of the directional characteristics of a sharp-nosed fuselage through a large angle-of-attack range at zero angles of sideslip.' NACA TN 2911 (1953)
- 3 Dunn, E.L. 'A low speed experimental study of yaw forces on bodies of revolution at large angles of pitch and zero sideslip.' Ballistics Division, Aerodynamics Branch, US Naval Ordnance Test Station. TM 1588, 1954
- 4 Maltby, R.L., Peckham, D.H. 'Low speed flow studies of the vortex flow patterns above inclined slender bodies using a new smoke technique.' RAE TN Aero 2482 (1956)
- 5 Spence, A., Trebble, W.G. 'Low speed tunnel tests on the flow structure behind a body of revolution of fineness ratio 16.67:1.' RAE TN Aero 2406 (1955)
- 6 Wardlaw, A.B. Jr., Morrison, A.M. 'Induced side forces at high angles of attack.' NSWC.WOLTR75-176, November 1976
- 7 Fiddes, S.P. 'Separated flow about cones at incidence — theory and experiment.' RAE TM Aero 2055 (1985)
- 8 Keener, E.R., Chapman, G.T., Cohen, L., Taleghani, J. 'Side forces on a tangent-ogive forebody with a fineness-ratio of 3.5 at high angles of attack and Mach numbers from 0.1 to 0.7.' NASA TMX3437, February 1977
- 9 Mundell, A.R.G. Unpublished RAE Tech Memo (1982)
- 10 Smith, J.S. 'Preliminary tests of slender bodies in the 5 metre pressurised low-speed Wind Tunnel.' RAE TM Aero 1973 (1983)
- 11 Fiddes, S.P., Moir, I.R.M., Dobney, D.G. 'Pressure measurements on a pointed slender body of revolution.' Unpublished RAE Tech Memo (1985)
- 12 Fiddes, S.P., Smith, J.H.B. 'Calculations of asymmetric flow past circular cones at large angles of incidence.' RAE TM Aero 1949 (1982)
- 13 Moir, I.R.M., Peckham, D.H., Smith, J.S. 'Low-speed wind tunnel tests of a device for reducing the out-of-plane force on a pointed slender body of revolution.' RAE TM Aero 1992 (1984)
- 14 Champigny, P. 'Reynolds number effects on the aerodynamic characteristics of an ogive-cylinder at high angles of attack.' AIAA Paper 84-2176, August 1984
- 15 Keener, E.R., Chapman, G.T. 'Onset of aerodynamic side force at zero sideslip on symmetric forebodies at high angles of attack.' AIAA Paper 74-770, August 1974
- 16 Sarpkaya, T. 'Separated flow about lifting bodies and impulsive flow about cylinders.' AIAA Journal Vol 4, pp 414-420, March 1966
- 17 Gaudet, L. 'A scheme for a laser-illuminated vapour screen flow visualisation technique for the 8 ft x 8 ft Wind Tunnel.' RAE TM Aero 2133 (1988)
- 18 Dexter, P.C. 'A study of asymmetric flow over high angles of attack in a low turbulence environment.' AIAA Paper 84-0505, January 1984

Copyright © Controller HMSO London 1990



a) Low Angle Of Incidence



b) High Angle of Incidence

Figure 1 Vortex Shedding from a Slender Pointed Nose

Figure 2 Local Pressure Distribution on a Slender Pointed Nose

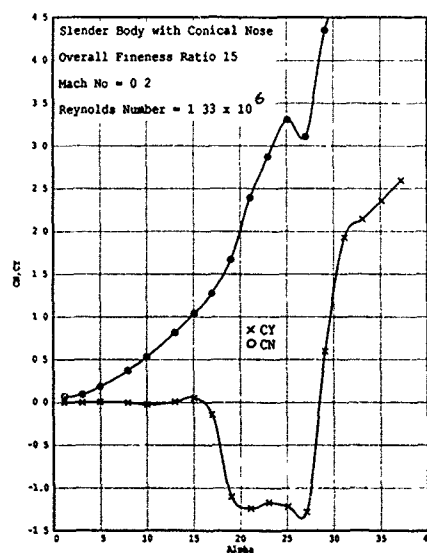
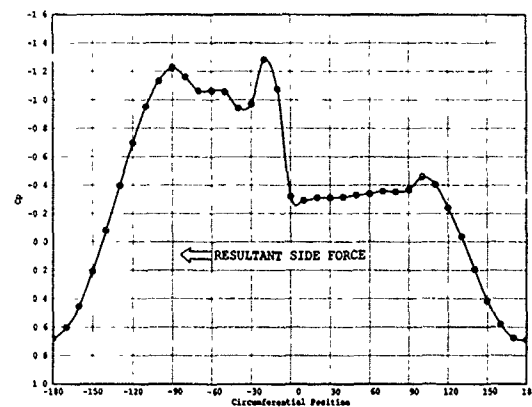


Figure 3 Example of Variation of Side Force and Normal Force Coefficients with Angle of Incidence

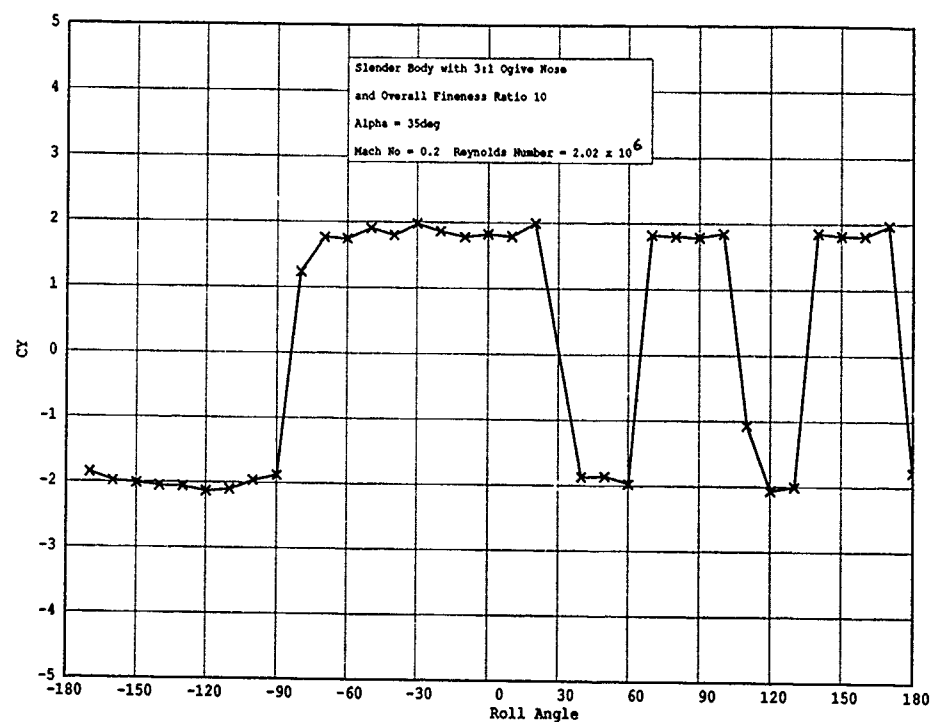


Figure 4 Example of Variation of Side Force Coefficient with Roll Angle

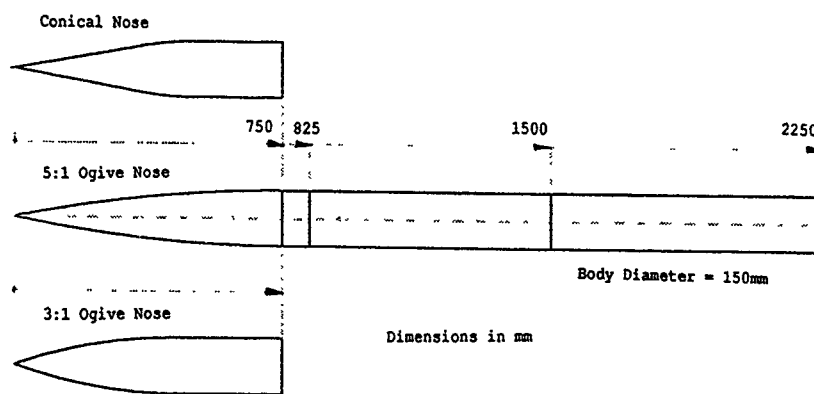


Figure 5 Slender Body Model



Figure 6 Slender Body Model in  
RAE 5 metre Wind Tunnel

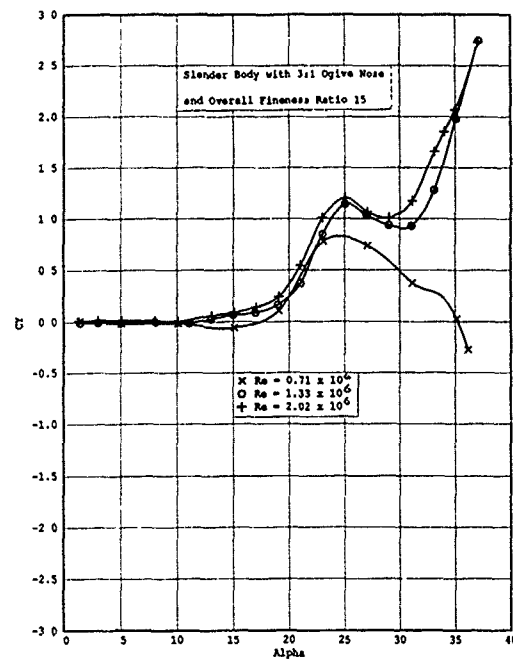


Figure 7 Variation of Side Force Coefficient  
with Angle of Incidence and Reynolds Number

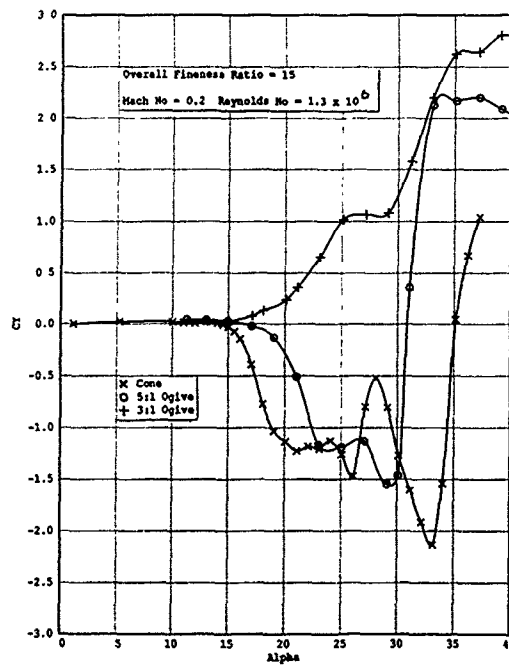


Figure 8 Variation of Side Force Coefficient  
with Angle of Incidence and Nose Shape

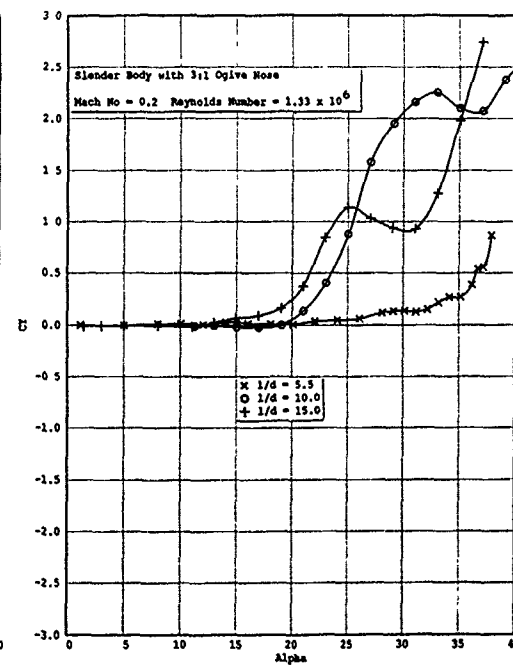


Figure 9 Variation of Side Force Coefficient  
with Alpha and Fineness Ratio

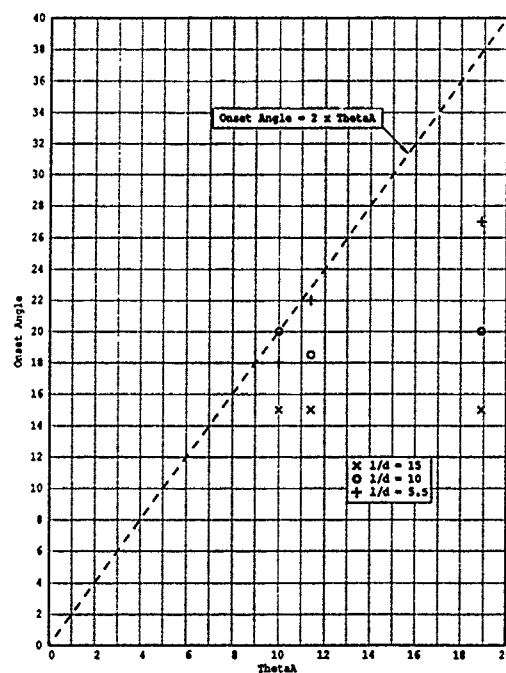


Figure 10a Variation of Onset Angle with  
Nose Semi-Apex Angle

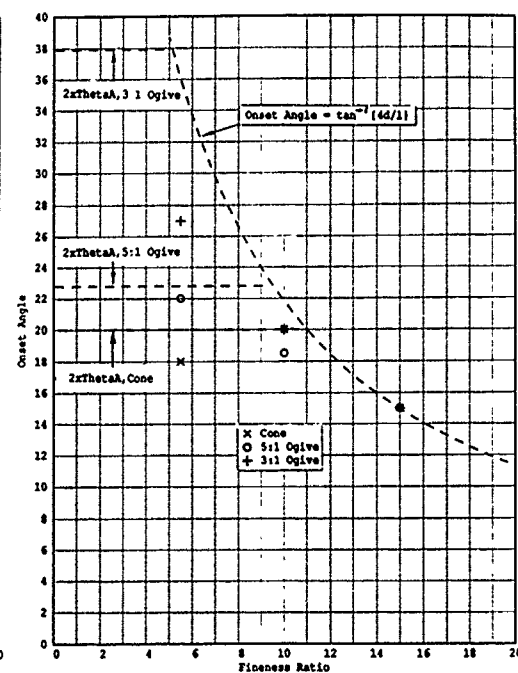


Figure 10b Variation of Onset Angle  
with Fineness Ratio

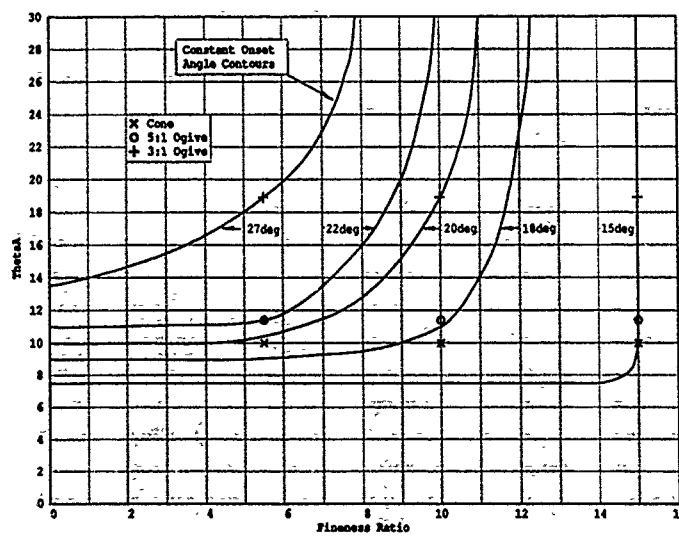


Figure 10c Variation of Onset Angle with  
Semi-Apex Angle and Fineness Ratio

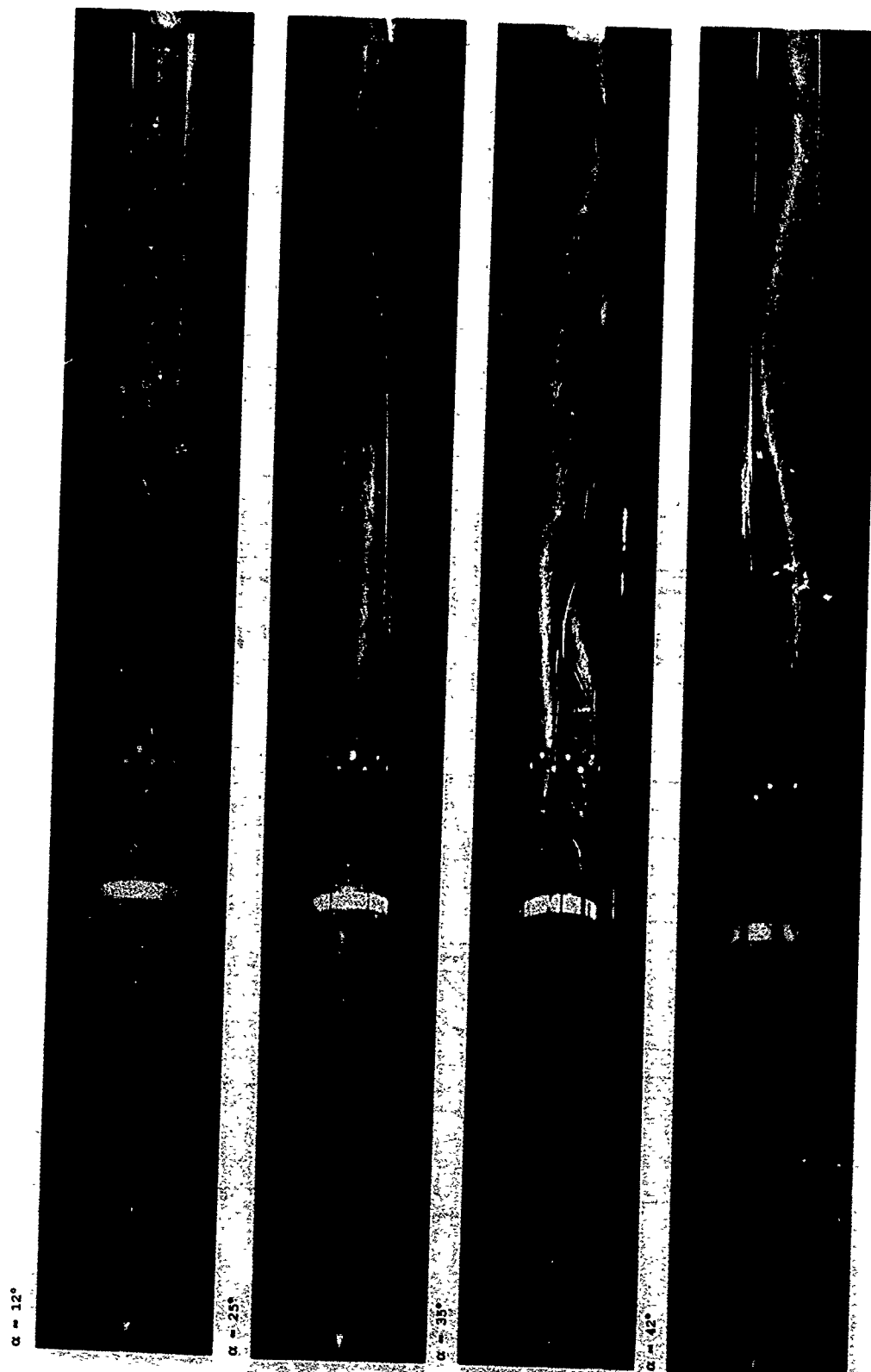


Figure 11 Flow Visualisation on 15:1 Fineness Ratio  
Slender Body with 3:1 Ogive Nose





Figure 12. Flow Visualisation on 15:1 Fineness Ratio  
Slender Body with 5:1 Ogive Nose.

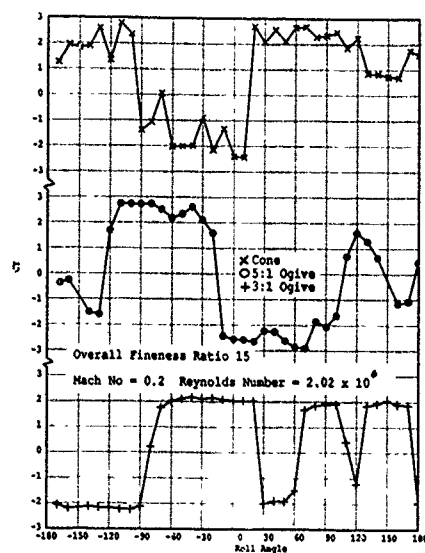


Figure 13 Variation of Side Force Coefficient with Roll Angle and Nose Shape

Figure 14 Variation of Side Force Coefficient with Roll Angle and Fineness Ratio

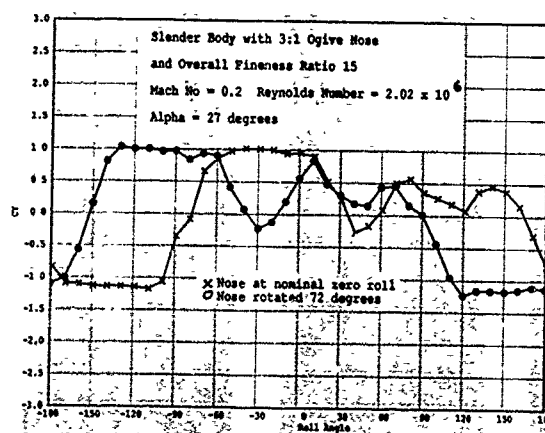
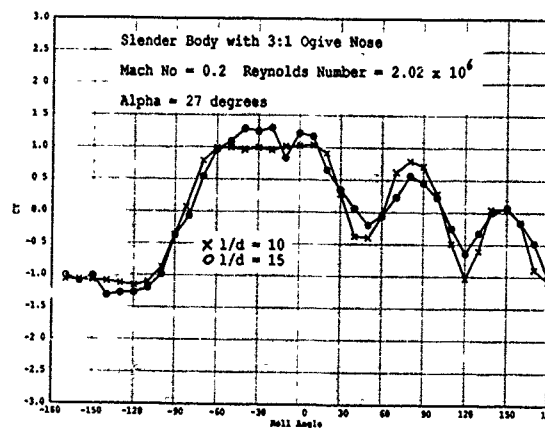


Figure 15 Variation of Side Force Coefficient with Roll Angle for Rotated Nose

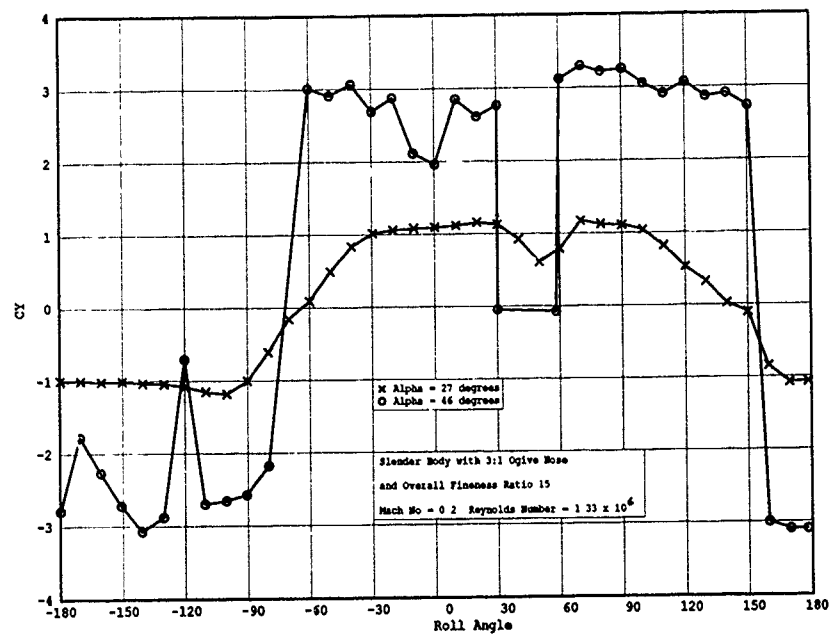


Figure 16 Variation of Side Force Coefficient with Roll Angle and Alpha

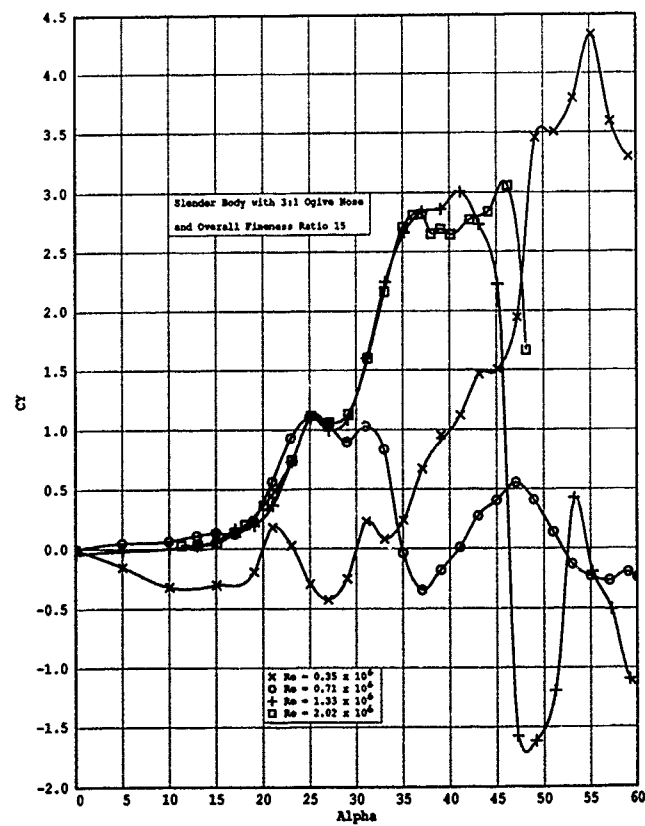


Figure 17 Variation of Side Force Coefficient with Alpha and Reynolds Number

AGARD/FDP Symposium sur "l'Aérodynamique des écoulements tourbillonnaires"  
1 - 4 Octobre 1990, Scheveningen, Pays-Bas

PHYSIQUE DES ECOULEMENTS TOURBILLONNAIRES

par

J. DELERY

Office National d'Etudes et de Recherches Aéronautiques (ONERA)

92320 - CHATILLON - France

RESUME

En écoulement tridimensionnel, le décollement conduit à la formation de structures tourbillonnaires formées par enroulement de la "nappe" de fluide visqueux qui, jusqu'alors collée à la paroi en une couche mince, surgit brusquement au sein de l'écoulement externe non dissipatif. La compréhension physique de ce phénomène doit s'appuyer sur une analyse rationnelle du champ faisant appel à la théorie des points critiques. On peut ainsi donner une interprétation correcte des spectres pariétaux, véritables empreintes du champ externe, et décrire avec précision l'organisation des enroulements tourbillonnaires. Cette démarche est appliquée à des décollements engendrés sur des corps de forme typique dont le champ a été soigneusement étudié à partir de visualisations et d'explorations par sondes multi-trous et vélocimétrie laser. Le problème de l'éclatement tourbillonnaire, si important dans de nombreuses applications, est discuté de façon plus rapide, le sujet méritant à lui seul une communication entière.

SUMMARY

In three-dimensional flows, separation leads to the formation of vortical structures resulting from the rolling up of the "sheet" of viscous flow, initially contained in a thin boundary-layer, which springs out from the obstacle surface into the outer perfect fluid flow. A clear physical understanding of this phenomenon must rely on a rational analysis of the flowfield calling upon the critical points theory. With this theory it is possible to correctly interpret the surface flow patterns which constitute the imprints of the outer flow and to give a rational description of the vortical system. This kind of analysis is applied to separated flows generated by typical bodies, the field of which has been carefully investigated by means of visualizations and surveys using multi-hole probes and laser velocimetry. The problem of vortex breakdown, so important for a large number of applications, is discussed more rapidly, the subject being worth of a full paper.

1 - INTRODUCTION

Le vol à grande incidence des avions de combat ou bien des véhicules hypersoniques lors de leur phase de rentrée et aussi des missiles tactiques confère un intérêt pratique évident à l'étude des écoulements tridimensionnels décollés. Les applications concernent également les écoulements internes, les prises d'air et les turbomachines en particulier, où la géométrie souvent complexe du canal ainsi que la présence éventuelle d'ondes de choc provoquent presque inmanquablement le décollement de la couche limite.

Or, en tridimensionnel, le décollement entraîne la formation de *structures tourbillonnaires* - appelées pour simplifier, mais improprement, *tourbillons* - formées par enroulement de la "nappe" de fluide visqueux qui, jusqu'alors collée à la paroi en une couche limite mince, surgit au sein de l'écoulement externe non dissipatif. Bien que connu depuis longtemps, le phénomène est encore incomplètement élucidé sur le plan physique et sa modélisation se heurte à des difficultés sérieuses en raison de la complexité du champ aérodynamique dont il est difficile de capturer tous les composants.

De nombreuses méthodes de prévision sont basées sur des modèles de fluide parfait, les premiers d'entre eux faisant appel au concept de nappes tourbillonnaires - en tant que surface de discontinuité du champ de vitesse - avec discrétisation suivant différents procédés (doublets, filaments tourbillonnaires, particules tourbillons, etc...). Les travaux dans ce domaine sont trop nombreux pour que nous les citions ici. Un plus grand réalisme dans la description de l'écoulement a ensuite été obtenu par la résolution directe des équations d'Euler complètes, ce qui permet - en théorie - une capture automatique des discontinuités du type nappe (Hitzel et Schmidt, 1984; Rizzi et Eriksson, 1984; Borrel et al., 1988; Siclari et Del Guidice, 1990; Lordon et al. 1990). Toutefois, les modèles de fluide parfait, dont certains donnent une bonne description des décollements autour de configurations complexes, sont incapables de prédire le phénomène de *séparation* lui-même qui est - par essence

- un processus visqueux. Ce n'est que dans des situations bien particulières (bord d'attaque ou bord de fuite aigu d'une aile, culot franc d'un projectile) que le "sens commun" ou bien la viscosité numérique du code de calcul permettent de situer l'origine de la nappe tourbillonnaire. Quand le décollement se produit sur un obstacle régulier, dont la surface a partout un rayon de courbure grand devant l'épaisseur de la couche limite locale, la ligne de séparation est une donnée du problème de fluide parfait. Elle doit être fournie, soit par des corrélations empiriques, soit par un calcul de couche limite qu'il conviendra éventuellement de coupler avec le calcul de l'écoulement extérieur.

Une solution vraiment satisfaisante au problème ne peut être apportée que par la résolution des équations de Navier-Stokes qui contiennent le phénomène dans sa globalité. Cette approche soulève, bien évidemment, de nombreux problèmes sur le plan numérique, sur celui de la modélisation de la turbulence et exige des ressources informatiques importantes. Toutefois, les résultats déjà publiés montrent que de tels calculs permettent une représentation très fidèles des phénomènes, notamment dans les régions de formation des décollements (Kordulla et al., 1986; Elsenaar et Eriksson, 1986; Rizzetta et Shang, 1986; Fuji et Schiff, 1989; Han, 1989; Thomas et Newsome, 1989; Wong et al., 1989; Chima et Yokota, 1990; Hsu et Liu, 1990; Hartwich et Hall, 1990).

Il est remarquable que ces progrès spectaculaires dans le domaine théorique aient été accompagnés, sur le plan expérimental, par une véritable percée en matière de métrologie. En effet, grâce au développement de techniques d'exploration fines par sondes de pression multi-trous et surtout par vélocimétrie laser, on est désormais en mesure de définir avec précision la structure d'écoulements complexes.

Dans cette communication, nous nous proposons d'utiliser ces renseignements expérimentaux pour donner une description des processus de décollement tridimensionnel et de formation des enroulements tourbillonnaires. Il s'agira de dégager, ou de rappeler, certaines "évidences" physiques dont la connaissance est indispensable à la bonne compréhension des écoulements décollés tridimensionnels et à l'évaluation des modélisations numériques.

On considère d'abord le problème du décollement proprement dit - ou séparation - en écoulement tridimensionnel où cette notion doit être soigneusement définie. Le passage du bidimensionnel au tridimensionnel oblige, en effet, à reconsidérer complètement la question par l'introduction de concepts plus généraux et une terminologie précise.

Le deuxième aspect examiné est celui du développement du tourbillon qui, progressivement, "décolle" de la surface de l'obstacle en croissant en intensité et en taille. Différents modes de génération des tourbillons sont étudiés en considérant des décollements sur des maquettes de forme typique. L'organisation des écoulements qui en rés-

ultent est mise en évidence, en particulier par l'analyse de situations où des structures peuvent s'organiser en plusieurs centres tourbillonnaires.

Enfin, le phénomène de l'éclatement tourbillonnaire - si important dans de nombreuses applications - est brièvement discuté, le sujet méritant à lui seul une communication entière. Il s'agit plutôt d'une introduction au problème basée sur l'examen de certains aspects expérimentaux.

## 2 - DECOLLEMENT EN ECOULEMENT TRIDIMENSIONNEL

### 2.1 - REMARQUES INTRODUCTIVES

Pour un écoulement bidimensionnel stationnaire, il est généralement admis que le décollement se produit quand le frottement pariétal  $\tau_p$  s'annule en un point D, appelé point de décollement. En aval de D, il existe une région où  $\tau_p$  est négatif, la distribution de vitesse selon une normale à la surface de l'obstacle comportant - près de la paroi - une zone où la composante longitudinale  $u$  est à contre courant de l'écoulement principal. Souvent, à une certaine distance en aval de D, l'écoulement recolle en un point R où le frottement pariétal repasse par zéro pour redevenir positif. Comme indiqué sur le schéma de la figure 1a, l'écoulement s'organise en un *bulbe de recirculation* - appelé parfois tourbillon - où les lignes de courant sont des courbes refermées sur elles-mêmes. Une ligne particulière, la ligne de courant *discriminatrice* joint le point de décollement D au point de recollement R. Elle sépare le fluide piégé dans le bulbe du fluide s'écoulant de l'infini amont vers l'infini aval.

En écoulement tridimensionnel, la définition du décollement à partir du passage par zéro du frottement pariétal est inadéquate et même inopérante. En effet, sur un obstacle tridimensionnel, il n'existe pas en général de directions privilégiées le long desquelles le signe du frottement - qui est alors un vecteur *frottement* - a une signification physique bien définie, excepté dans des situations très particulières, telles qu'un plan de symétrie ou bien une configuration d'aile en flèche d'envergure infinie. En outre, le schéma de la figure 1a ne correspond plus à la réalité, l'écoulement tridimensionnel ayant la possibilité de développer des composantes de vitesse transverses qui permettent au fluide de s'échapper latéralement. Au schéma 1a, doit être substitué le schéma 1b où - dans le plan considéré - la "ligne de courant" stagnant au point de recollement R est distincte de celle émanant du point de décollement D, le fluide qui s'écoule entre ces deux lignes s'échappant dans le tourbillon T. Mais ces notions demandent à être approfondies.

Les concepts du bidimensionnel sont en fait inutilisables en tridimensionnels où leur emploi, ainsi que celui de la terminologie associée, sont souvent sources de confusion. La première tentative pour donner une définition rationnelle et générale du décollement tridimensionnel est probablement due à Maskell (1955). Toutefois, les progrès décisifs dans ce domaine ont été apportés par les réflexions

de Legendre (1956, 1977), d'Oswatitsch (1958) et de Lighthill (1963). Ces considérations s'appliquent, notamment, aux structures parfois très complexes révélées par les visualisations pariétales par enduit visqueux, qui moyennant certaines précautions, peuvent être assimilées au spectre des lignes de frottement sur l'obstacle. Ces visualisations, qui apportent des informations capitales sur la structure des écoulements tridimensionnels, sont largement utilisées pour diagnostiquer les décollements. Mais précisons ces notions.

## 2.2 - LA THEORIE DES POINTS CRITIQUES

Les considérations qui suivent s'appliquent à un écoulement stationnaire, donc en principe laminaire. En fait, il est possible d'inclure dans la discussion les écoulements turbulents à condition de considérer un champ moyen dont les propriétés sont définies à partir de moyennes temporelles indépendantes du temps. Les représentations dites stationnaires sont fictives mais elles sont cohérentes avec une modélisation faisant appel à la notion de moyenne au sens de Reynolds et donc une approche théorique fondée sur les équations de Navier-Stokes moyennées en temps.

Comme on le sait, quand la distance  $y$  à la paroi d'un obstacle tend vers zéro, la direction du vecteur vitesse - dont le module est nul à la paroi - tend vers une limite colinéaire avec celle du vecteur frottement pariétal  $\vec{\tau}_p$ . En même temps, la ligne de courant tend vers une position limite appelée ligne de courant limite, ou encore ligne de courant pariétale. En vertu de ce qui vient d'être dit, cette ligne est également une trajectoire, ou ligne de force, du champ des vecteurs  $\vec{\tau}_p$ : pour cette raison, on l'appelle aussi ligne de frottement, concept qui nous semble plus convenable et que nous adopterons par la suite, car il est associé à une grandeur physique mesurable, à savoir le frottement.

La discussion du problème du décollement en écoulement tridimensionnel s'appuie sur la théorie des points critiques. Cette théorie, qui découle des travaux de Poincaré (1892) sur les points singuliers des systèmes différentiels, envisage dans sa généralité un espace à  $n$  dimensions. Toutefois, pour des raisons de simplicité, nous considérerons dans ce qui suit l'espace à deux dimensions constitué par la surface d'un obstacle. Les implications pour l'écoulement à trois dimensions seront utilisées par la suite dans l'examen des enroulements tourbillonnaires, mais sans justification théorique.

Soit, dans ces conditions, un système d'axes ortho-normés local  $(x, z)$  repérant la position d'un point sur la surface et désignons par  $\tau_x(x, z)$  et  $\tau_z(x, z)$  les composantes de  $\vec{\tau}_p$  selon  $x$  et  $z$  respectivement.

En écoulement stationnaire les lignes de frottement pariétales sont régies par le système différentiel autonome (indépendant du temps):

$$(1) \quad \frac{dx}{\tau_x(x, z)} = \frac{dz}{\tau_z(x, z)}$$

Ces équations définissent une infinité de courbes appelées caractéristiques ou trajectoires qui s'identifient aux lignes de frottement. En général, par chaque point de la surface passe une trajectoire et une seule. Les seuls points ne satisfaisant pas à cette règle sont les points singuliers du système (1) où le frottement s'annule, c'est-à-dire où l'on a simultanément:

$$\tau_x(x, z) = 0, \quad \tau_z(x, z) = 0$$

Pour étudier l'allure des trajectoires au voisinage d'un point singulier  $P_0(x, z)$ , recherchons une solution sous forme d'un développement de Taylor limité au premier ordre:

$$\tau_x(x, z) = \left( \frac{\partial \tau_x}{\partial x} \right)_{P_0} (x - x_0) + \left( \frac{\partial \tau_x}{\partial z} \right)_{P_0} (z - z_0)$$

$$\tau_z(x, z) = \left( \frac{\partial \tau_z}{\partial x} \right)_{P_0} (x - x_0) + \left( \frac{\partial \tau_z}{\partial z} \right)_{P_0} (z - z_0)$$

Dans ce qui suit, par commodité nous placerons l'origine au point  $P_0$  et nous supprimerons l'indice 0, d'où le système:

$$\frac{dx}{\frac{\partial \tau_x}{\partial x} x + \frac{\partial \tau_x}{\partial z} z} = \frac{dz}{\frac{\partial \tau_z}{\partial x} x + \frac{\partial \tau_z}{\partial z} z}$$

Supposant que les dérivées partielles de  $\tau_x$  et  $\tau_z$  ne sont pas simultanément nulles au point singulier et désignant par  $\lambda$  et  $\mu$  deux constantes, nous pouvons écrire:

$$(2) \quad \frac{dx}{\frac{\partial \tau_x}{\partial x} x + \frac{\partial \tau_x}{\partial z} z} = \frac{dz}{\frac{\partial \tau_z}{\partial x} x + \frac{\partial \tau_z}{\partial z} z} = \frac{\lambda dx + \mu dz}{\lambda \left( \frac{\partial \tau_x}{\partial x} x + \frac{\partial \tau_x}{\partial z} z \right) + \mu \left( \frac{\partial \tau_z}{\partial x} x + \frac{\partial \tau_z}{\partial z} z \right)}$$

Une solution est recherchée en mettant (2) sous la forme d'une dérivée logarithmique, soit:

$$\frac{d(\lambda x + \mu z)}{S(\lambda x + \mu z)} = \frac{\lambda dx + \mu dz}{\lambda \left( \frac{\partial \tau_x}{\partial x} x + \frac{\partial \tau_x}{\partial z} z \right) + \mu \left( \frac{\partial \tau_z}{\partial x} x + \frac{\partial \tau_z}{\partial z} z \right)}$$

Une telle forme est possible si les conditions suivantes sont satisfaites simultanément:

$$\left( \frac{\partial \tau_x}{\partial x} - S \right) \lambda + \frac{\partial \tau_z}{\partial x} \mu = 0$$

$$\frac{\partial \tau_x}{\partial z} \lambda + \left( \frac{\partial \tau_z}{\partial z} - S \right) \mu = 0$$

Pour que ce système homogène en  $(\lambda, \mu)$  admette des solutions non triviales, il est nécessaire que son déterminant soit nul; d'où la condition sur  $S$ :

$$(3) \quad \begin{vmatrix} \frac{\partial \tau_x}{\partial x} - S & \frac{\partial \tau_z}{\partial x} \\ \frac{\partial \tau_x}{\partial z} & \frac{\partial \tau_z}{\partial z} - S \end{vmatrix} = 0$$

Le comportement des lignes de frottement au voisinage du point singulier - ou critique -  $P_0$  est déterminé par la nature des solutions de l'équation (3), c'est à dire par le caractère réel ou imaginaire ainsi que le signe des valeurs propres  $S_1$  et  $S_2$  solutions de (3).

Introduisant la matrice jacobienne:

$$F = \begin{vmatrix} \frac{\partial \tau_x}{\partial x} & \frac{\partial \tau_z}{\partial x} \\ \frac{\partial \tau_x}{\partial z} & \frac{\partial \tau_z}{\partial z} \end{vmatrix}$$

et posant:

$p = - \text{trace de } F \text{ et } q = \text{déterminant de } F$

les valeurs propres sont données par:

$$S_{1,2} = \frac{-p \pm \sqrt{p^2 - 4q}}{2}$$

les différents types de comportement obtenus en fonction des valeurs propres sont situés dans le plan  $[p, q]$  de la figure 2 et les trajectoires au voisinage des points critiques sont dessinées Fig. 3. La représentation adoptée est la forme canonique, c'est-à-dire que les vecteurs propres sont perpendiculaires (pour le détail des calculs, voir Chanetz, 1986). Cette forme, qui peut toujours être trouvée par un changement de coordonnées approprié, correspond physiquement à des situations au voisinage de plans de symétrie. Il est à noter que le problème, tel qu'il a été posé, est indéterminé, les paramètres  $\lambda$  et  $\mu$  pouvant être choisis arbitrairement. Une solution au problème de mécanique des fluides exigerait l'insertion des développements dans les équations de Navier-Stokes.

Si les deux racines  $S_1$  et  $S_2$  sont réelles et distinctes, le point singulier est du type *noeud*. Alors, toutes les trajectoires - sauf une - ont en  $P_0$  une tangente commune (voir Fig. 3a). Dans le cas où les deux valeurs propres sont égales (points situés sur la parabole II d'équation  $q = p^2 / 4$ ), les trajectoires ont toutes des pentes différentes en  $P_0$ . Le noeud est alors dit *isotrope* (voir Fig. 3b).

Si les valeurs propres sont réelles et de signes contraires (c'est-à-dire si  $q$  est négatif), le point singulier est du type *col*. Alors, seules deux courbes solutions passent par  $P_0$ , les autres l'évitent en prenant des allures en forme d'hyperbole, comme indiqué sur le schéma de la figure 3c.

Si les valeurs propres sont imaginaires conjuguées, les trajectoires aboutissent toutes au point singulier en s'enroulant autour de lui pour constituer

un *foyer* (voir Fig. 3d). Si  $p$  est nul pour  $q$  positif (zone III), le point singulier n'est pas atteint. Alors, les trajectoires sont des courbes fermées ayant une allure d'ellipse (Fig 3e). Le point singulier est appelé un *centre*.

Si  $q = 0$  (région I dans le plan  $[p, q]$ ), la solution prend l'allure schématisée Fig. 3f qui peut être interprétée comme une suite infinie de noeuds ou de cols.

Selon les cas, comme indiqué sur la figure 2, les trajectoires sont parcourues soit en s'éloignant, soit en s'approchant du point singulier. D'après la terminologie mathématique habituelle, le point critique est alors dit stable ou instable. En mécanique des fluides, où les trajectoires sont interprétées comme des lignes de courant ou de frottement, le point singulier sera dit:

- d'*attachement* si l'écoulement s'en éloigne,

- de *séparation* s'il s'en rapproche.

Comme nous le verrons dans ce qui suit, les cols et foyers sont étroitement liés au phénomène de décollement.

Les noeuds et les foyers sont en fait topologiquement équivalents: ce sont des "sources" ou des "puits" de lignes de frottement. Compte tenu de cette remarque, on établit la relation suivante entre la somme des noeuds/foyers et la somme des cols pour un corps isolé simplement connexe:

$$\sum \text{noeuds} - \sum \text{cols} = 2$$

Cette relation peut être utilisée pour s'assurer de la cohérence de la description d'un écoulement tridimensionnel en termes de points critiques. Il faut toutefois bien garder présent à l'esprit le fait qu'elle s'applique à un obstacle *complet*.

Les deux trajectoires passant par un *col* sont appelées *séparatrices* ou lignes *séparatrices*. Nous verrons qu'elles jouent un rôle spécial et important dans la topologie d'un champ.

Bien que relativement ancienne pour son application à la mécanique des fluides, la théorie des points critiques connaît un regain d'intérêt suscité par le besoin, déjà mentionné, de disposer d'un cadre rationnel pour appréhender les écoulements tridimensionnels complexes (Perry et Fairlie, 1974; Wang, 1975; Tobak et Peake, 1978; Dallmann, 1983; Hornung et Perry, 1984; Perry et Chong, 1987). En outre, cette théorie constitue un outil précieux pour interpréter et analyser les masses de résultats produits par les moyens modernes de mesure et de calcul appliqués à l'étude et à la prévision des écoulements tridimensionnels (Kaynak et al., 1986; Mehta et Lim, 1986; Doerffer et Dallmann, 1989a et b).

### 2.3 - SEPARATION ET ATTACHEMENT

La situation la plus simple est celle d'un corps

fuselé à incidence nulle, ou très faible, dont le spectre pariétal comporte un noeud d'attachement au point d'arrêt et un noeud de décollement à l'arrière. Les lignes de frottement enveloppant l'obstacle ont pour origine le noeud d'attachement. Elles se terminent toutes au noeud de décollement, comme le montre la figure 4a.

On dira que l'écoulement sur un tel corps est *décollé* - suite à un accroissement de l'incidence par exemple - si son champ pariétal contient plus de deux noeuds. Puisque les lignes de frottement passant par des noeuds de même nature ne peuvent se croiser, un point critique - obligatoirement du type col - doit être placé quelque part entre ces deux noeuds (voir Fig. 4b). On en conclut que tout écoulement tridimensionnel décollé possède au moins un col par où passent deux lignes de frottement particulières - les séparatrices - dont l'une est appelée la *ligne de séparation*. Une telle ligne définit deux domaines dans l'écoulement de surface. Les lignes de frottement appartenant à ces domaines ont des origines distinctes, c'est-à-dire proviennent de noeuds différents.

Les lignes de frottement de chacune des deux familles longent la ligne de séparation sans qu'il soit possible souvent de déterminer sur un spectre quelle est la séparatrice qui - hormis le fait qu'elle passe par un col - ne se distingue pas des autres lignes de frottement.

Toutefois, sous l'action d'un gradient de pression, il tend à se produire une *convergence* des lignes de frottement voisines vers la ligne de séparation qui devient alors bien distincte, ce phénomène pouvant se produire loin en aval du col origine de la ligne de séparation. Or, comme l'a montré très simplement Lighthill (1963), une telle convergence a une profonde répercussion sur l'écoulement extérieur.

En effet, se référant à la figure 5, considérons un tube de courant de section rectangulaire, infiniment délié, limité par deux lignes de courant ( $l_1$ ) et ( $l_2$ ) et deux lignes de frottement ( $f_1$ ) et ( $f_2$ ). Le débit massique traversant la section nh de ce tube de courant est:

$$q_m = \rho n h \bar{V}$$

où  $\bar{V}$  est la valeur moyenne de la vitesse  $\bar{V}$ , supposée rester parallèle à elle-même et varier linéairement sur la distance h normale localement à la paroi.

Alors nous avons:

$$h = \frac{q_m}{\rho n \bar{V}}$$

relation qui montre que la convergence des lignes de frottement en direction d'une ligne de séparation ( $n \rightarrow 0$ ) entraîne une croissance de h. Autrement dit, les lignes de courant les plus voisines de l'obstacle tendent, près d'une ligne de séparation, à s'éloigner de la surface. Il en résulte une dilatation des régions dissipatives.

Ce "décollement" des lignes de courant est d'autant plus brusque que la convergence des lignes de courant est plus rapide. Il peut conduire - comme le montreront les résultats qui suivent - à un véritable "surgissement" au sein de l'écoulement extérieur non dissipatif du fluide visqueux initialement contenu dans la couche limite. Ce phénomène est certainement la caractéristique la plus typique et la plus spectaculaire du décollement en écoulement tridimensionnel.

Le comportement local des lignes de frottement au voisinage d'une ligne de séparation (S) a fait l'objet de certaines discussions, les visualisations pariétales manquant souvent de finesse pour bien distinguer ce qui se passe. D'après le schéma original de Maskell (1955), il y avait contact entre (S) et les lignes voisines, la ligne de séparation apparaissant alors comme un lieu de points de rebroussement. Cette interprétation a été mise en doute par Legendre (1956), puis par Lighthill (1963), qui ont avancé qu'une telle concentration de singularités était hautement improbable. En fait, la convergence des lignes de frottement vers la ligne séparatrice - quand elle se produit - se fait sans contact.

En d'autres termes, ce que l'on pourrait appeler le décollement *effectif*, en tant que phénomène caractérisé par un épaississement rapide des régions dissipatives, jusqu'à l'envahissement du champ de fluide parfait, est à associer - non pas à la naissance de la ligne de séparation - mais à la convergence rapide des lignes de frottement.

Ainsi que nous l'avons déjà souligné, cette convergence peut survenir assez loin en aval du col, cause réelle de la séparation au sens stricte. Cette distinction, en fait purement quantitative mais ne portant pas sur l'essence du phénomène, est à l'origine de bien des confusions et des polémiques, celle concernant notamment les concepts de séparation *ouverte* ou *fermée* (Wang, 1983). Pour résumer:

- nous dirons qu'il y a séparation si une ligne séparatrice existe dans le spectre des lignes de frottement pariétales. La présence de cette ligne est obligatoirement liée à la présence d'un col.

- la séparation effective, que l'on pourra alors appeler décollement véritable, a lieu quand il y a convergence des lignes de frottement en direction de la ligne de séparation.

Le processus symétrique de *recollement* ou d'*attachement* peut se définir - mutatis mutandis - dans des termes analogues, à cette différence près que, maintenant, il y a divergence des lignes de frottement de part et d'autre de la séparatrice qui prend le nom de ligne d'attachement. Dans ce cas, l'écoulement "plonge" en direction de la paroi. La figure 6 montre la différence entre une ligne de séparation et une ligne d'attachement.

La notion de séparatrice s'attache aussi bien à une séparation effective - ou décollement - qu'à un at-



tachement - ou recollement. De ce fait, le terme ligne de séparation est parfois utilisé au sens générique de ligne séparatrice sans que les notions physiques de décollement et de recollement soit distinguées. Cette absence de rigueur dans le langage amène à une certaine confusion contribuant à obscurcir un peu plus la notion de décollement en écoulement tridimensionnel. Pour éviter ce travers, dans ce qui suit nous ferons une distinction nette entre séparatrice, ligne de séparation et ligne d'attachement, bien que ces concepts soient identiques au sens mathématique.

#### 2.4 - CAS DE L'ÉCOULEMENT BIDIMENSIONNEL DECOLLE

Le décollement bidimensionnel - plan ou axisymétrique - apparaît comme un cas bien particulier de la définition générale tridimensionnelle. En effet, dans le cadre de l'analyse qui précède, une ligne de décollement (ou de recollement) bidimensionnelle est constituée par une suite *infinie* de cols répartis sur une droite perpendiculaire au plan contenant l'écoulement (région I du diagramme de la figure 2). On conçoit intuitivement qu'une telle situation est hautement improbable sur le plan physique. L'étude expérimentale des écoulements décollés dits plans montre, qu'en fait, l'influence - inévitable - des bords latéraux du montage conduit toujours à une situation tridimensionnelle. Même quand des précautions particulières sont prises, on observe que l'écoulement pariétal tend à s'organiser en structures plus ou moins régulières (Ginoux, 1958; Settles et al., 1978). Sur les configurations de révolution - en principe libres de tout effet de bord - l'écoulement prend aussi une structure tridimensionnelle. Au recollement, notamment, les visualisations pariétales mettent clairement en évidence une structure fine où la ligne de recollement porte une succession de noeuds et de cols (Roshko et Thomke, 1966). Ainsi, la figure 7a montre une visualisation du recollement turbulent sur une jupe à un nombre de Mach de 5 (Joulot, 1990). Le schéma interprétatif de la figure 7b montre que la ligne de recollement porte une succession, en nombre fini, de noeuds et de cols traduisant l'existence dans l'écoulement de structures analogues aux tourbillons de Görtler (Inger, 1977).

#### 2.5 - SURFACE DE SEPARATION ET NAPPE TOURBILLONNAIRE

Les notions qui précèdent se généralisent aux lignes de courant de l'écoulement à trois dimensions entourant l'obstacle puisqu'elles s'appliquent à tout champ de vecteurs continu et permanent. Le formalisme mathématique devenant toutefois nettement plus complexe, nous nous limiterons dans ce qui suit à énoncer un certain nombre de propriétés.

Egalement, si l'on considère l'écoulement dans un plan de coupe (P) - opération souvent pratiquée pour décrire les champs tridimensionnels - il est possible de construire les trajectoires, ou lignes de force, du champ de vecteurs constitué des projections de la vitesse dans (P). L'ensemble de ces "pseudo" lignes de courant se prête aussi à une

description en termes de points critiques et de lignes séparatrices. C'est ce qui est fait dans le schéma de la figure 1b qui montre une situation où la vitesse a en réalité une composante perpendiculaire au plan du des.in. Il convient toutefois de garder présent à l'esprit le fait qu'une telle image du champ n'est pas objective, puisqu'elle est fonction du plan de coupe, ou du point de vue, adopté. Sauf situation particulière, un plan de symétrie par exemple, les lignes de force d'un champ en coupe ne sont donc pas des lignes de courant. Pour éviter toute confusion, nous les appellerons *trajectoires*.

La ligne de séparation est la trace sur l'obstacle d'une surface de courant de l'écoulement tridimensionnel qui joue aussi un rôle particulier. Elle fait en effet office de barrière entre les lignes de courant ayant "décollé" de la surface d'un des côtés de la ligne de séparation de celles qui ont "décollé" de l'autre côté. La figure 8 représente schématiquement une telle surface de séparation ( $\Sigma$ ) passant par le col C, origine de la ligne de séparation (S). L'existence d'une surface de courant telle que ( $\Sigma$ ) prenant appui sur le corps n'est possible qu'en raison de la nature d'une séparatrice. Les lignes de courant constituant ( $\Sigma$ ) ont pour origine le point C qui - sur ( $\Sigma$ ) - prend le caractère d'un noeud (en fait un demi-noeud).

La surface de séparation ( $\Sigma$ ) peut être assimilée à ce que l'on nomme une *nappe de décollement*, bien que le concept de nappe - définie comme surface de discontinuité pour le champ de vitesse - soit attaché au modèle de fluide parfait. Dans la réalité, en fluide visqueux, les champs de vitesse et de rotationnel sont continus, si bien qu'il est souvent difficile de définir avec précision de telles nappes à partir de l'examen des résultats expérimentaux.

De par son origine, la surface de séparation est située dans la région du champ où le rotationnel tend à se concentrer et les *structures tourbillonnaires*, caractéristiques des écoulements tridimensionnels décollés, peuvent être interprétées comme un enroulement de la surface de séparation. En règle générale, une ligne de séparation (S) se termine en un foyer autour duquel elle s'enroule en spirale. Ce foyer est la trace sur l'obstacle du tourbillon provenant de l'enroulement de la surface de séparation portée par (S). Une telle situation, avec deux foyers  $F_1$  et  $F_2$  de part et d'autre du col C est représentée sur la figure 9a. Elle correspond à ce que l'on nomme un *tourbillon trombe*. Le foyer "portant" le tourbillon peut être situé dans un plan de symétrie, comme nous le verrons dans les exemples qui suivent; on parle alors de tourbillon *en fer à cheval* (voir Fig. 9b).

Du fait de l'enroulement de la surface de séparation, le rotationnel né dans la couche limite et ayant migré dans l'écoulement externe va avoir tendance à se concentrer fortement au coeur de l'enroulement. Ainsi, loin des parois, le champ est constitué de régions isolées où le rotationnel se trouve concentré. Cette propriété, bien connue et

mise à profit par les modèles théoriques de fluide parfait, peut aussi être utilisée pour décrire l'écoulement décollé à partir d'un "squelette" de tourbillons (Hornung, 1983; Perry et Hornung, 1984).

### 3 - ANALYSES DE FORMATIONS TOURBILLONNAIRES TYPIQUES

#### 3.1 - REMARQUES INTRODUCTIVES

Les notions de point critique, de ligne séparatrice et de surface de séparation s'appliquent à tout champ de vecteurs continu et stationnaire. Elles ne sont pas attachées à une théorie des écoulements tridimensionnels décollés avec valeur prédictive. Plutôt, ces concepts constituent une "grammaire" permettant de décrire des écoulements complexes de façon rationnelle et avec une terminologie rigoureuse (Peake et Tobak, 1980). Leur emploi se révèle vite indispensable quand il faut interpréter des visualisations ou des mesures de champ afin d'en donner une représentation cohérente (Werlé, 1975).

Ces notions sont donc largement utilisées dans les paragraphes qui suivent où l'on se propose de décrire des écoulements tourbillonnaires observés au cours d'expériences, effectuées pour la plupart à l'ONERA. La démarche adoptée va consister à démontrer d'abord l'intérêt de la théorie des points critiques pour interpréter des spectres pariétaux dans des cas particulièrement complexes. Ces spectres sont l'empreinte sur l'obstacle du champ externe et une bonne interprétation de l'information qu'ils contiennent est indispensable à toute compréhension de l'écoulement. Ensuite, sont examinés des décollements sur différents corps en envisageant successivement des situations où la séparation est imposée par une ligne singulière, puis celle où c'est l'origine des lignes de séparation qui est fixée; enfin celle du décollement entièrement "libre" est envisagée.

#### 3.2 - SPECTRES PARIETAUX ATTACHES A DES DECOLLEMENTS MULTIPLES

##### 3.2.1 - CANAL TRANSSONIQUE

Le premier cas examiné est celui d'un canal transsonique tridimensionnel dont la géométrie est précisée sur la figure 10. Une bosse, dont le ligne de crête présente une flèche de 30° relativement à la direction de la vitesse amont, est montée sur la paroi inférieure du canal dont les trois autres faces sont planes. L'envergure de la veine d'essai est de 0,120 m et sa hauteur, dans la section d'entrée, de 0,100 m. L'écoulement, subsonique à l'entrée du canal, s'accélère dans la partie convergente de la veine pour atteindre l'état sonique au voisinage du sommet de la bosse qui constitue un col. En aval, l'écoulement passe en supersonique; puis, en raison de l'effet de blocage produit par un second col, il se ralentit au travers d'ondes de choc interagissant fortement avec les couches limites turbulentes des quatre faces de la veine.

L'objectif principal de ces expériences était de produire, à partir d'une géométrie simple, un écoulement fortement tridimensionnel afin de constituer un cas test pour valider les méthodes de calcul (Cambier et Escande, 1989). Cet écoulement a donc été soigneusement étudié au moyen de visualisations pariétales, de mesures de pression et de sondages du champ par vélocimétrie laser à trois composantes (Benay et al., 1986). Dans ce qui suit, nous porterons uniquement notre attention sur l'examen des spectres pariétaux, notre propos étant d'illustrer l'intérêt de la théorie des points critiques pour décrire un écoulement complexe.

Les figures 11a à 11d montrent des photographies des visualisations par enduit visqueux pratiquées sur les quatre parois du canal. Les schémas préétablis, dessinés sur la figure 12, ont été établis d'après ces photographies et une observation directe des visualisations en cours d'essai qui révèle des informations perdues lors de la prise de vue, notamment le sens d'écoulement de l'enduit. Ces schémas, bien qu'ayant valeur qualitative, respectent fidèlement les proportions de la réalité.

L'examen de l'écoulement sur la bosse (Figs. 11a et 12a) montre l'existence de deux foyers  $F_1$  et  $F_2$  bien visibles dans la moitié gauche du canal. La séparatrice ( $S_1$ ) passant par le col  $C_1$  et s'enroulant autour de  $F_1$  et  $F_2$ , constitue une barrière située approximativement au pied de l'onde de choc oblique du système en  $\lambda$  engendré par l'interaction.

Les lignes de frottement venant de l'amont et contenues dans le domaine limité par la séparatrice ( $S_2$ ) passant par le col  $C_2$  vont s'enrouler autour, soit de  $F_1$ , soit de  $F_2$ , selon qu'elles sont situées d'un côté ou de l'autre de la séparatrice ( $S_3$ ) portant les cols  $C_1$  et  $C_2$ . Une partie de ces lignes contourne la barrière ( $S_1$ ) en s'incurvant rapidement à son approche. La structure constituée par ( $S_1$ ), ( $S_2$ ) et les foyers  $F_1$  et  $F_2$  est classiquement observée dans les interactions onde de choc - couche limite en canal avec effets tridimensionnels (Green, 1969; Reda et Murthy, 1972; Schofield, 1985).

Dans la situation présente, ( $S_1$ ) peut être associée sans ambiguïté à une séparation et ( $S_2$ ) à un attachement. Ainsi,  $C_1$  et  $C_2$  sont respectivement des cols de séparation et d'attachement. Les enroulements autour des foyers  $F_1$  et  $F_2$  sont les empreintes sur la paroi des tourbillons s'échappant dans l'écoulement extérieur, la ligne ( $S_1$ ) étant la trace de la surface de séparation qui s'enroule autour des axes des structures tourbillonnaires, conformément au schéma de la figure 9a.

Revenant à la figure 12a, on observe que les lignes de frottement en provenance de l'amont se partagent en deux familles; les unes, proches de la face B, s'écoulent continuellement de l'amont vers l'aval.

Les autres, voisines de A, se séparent à leur tour en deux sous ensembles:

- celles comprises entre ( $S_2$ ) et la séparatrice ( $S_4$ ), aboutissant au demi-col  $C_3$ , poursuivent leur chemin vers l'aval;

- celles situées entre la paroi A et ( $S_4$ ) vont s'enrouler autour d'un troisième foyer  $F_3$  pour former un "tourbillon" délimité par la séparatrice ( $S_5$ ) issue du demi-col  $C_4$ .

Une description semblable peut être appliquée aux spectres observés sur les trois autres faces du canal. Mais nous arrêtons là cette discussion, de peur de lasser le lecteur. Remarquons simplement la complexité du spectre relevé sur la face A où un noeud  $N_1$  et un demi-noeud  $N_2$ , situé à la jonction avec la face supérieure du canal, sont les origines des lignes de frottement de la partie aval de l'écoulement pariétal, celles en provenance de l'amont disparaissant dans le foyer  $F_4$ .

Réunissant en un seul point les demi-noeuds et les demi-cols en correspondance et sachant qu'un foyer est topologiquement équivalent à un noeud (voir § 2.2 ci-dessus), le dénombrement des points critiques conduit à la relation:

$$\sum \text{noeuds} - \sum \text{cols} = 14 - 12 = 2$$

où, dans le décompte des noeuds, nous avons ajouté deux noeuds fictifs à l'infini amont et à l'infini aval, source et aboutissement des lignes de frottement.

Des discussions très approfondies de ce genre, appliquées au même type d'écoulement, ont permis de mettre en évidence les modifications du spectre survenant quand un paramètre varie, le nombre de Reynolds ou le nombre de Mach, par exemple (Dallmann et Schewe, 1987; Doerffer et Dallmann, 1989a; Doerffer et Dallmann, 1989b). En effet, l'expérience montre, que dans le cas de l'écoulement de canal envisagé ici, une variation légère des conditions d'essai peut entraîner un changement notable dans la disposition et le nombre des points critiques. Toutefois - sauf altération profonde de la situation expérimentale - les traits les plus "forts" de l'écoulement, tels que les foyers tourbillonnaires  $F_1$  et  $F_2$ , ainsi que les séparatrices attachées, demeurent présents.

### 3.2.2 - PREMIER ETAGE DE LANCEUR SPATIAL

Dans certaines situations particulièrement complexes, le dessin d'un écoulement pariétal topologiquement cohérent requiert des renseignements sur la structure du champ externe. En effet, les visualisations par enduit visqueux sont souvent d'une finesse insuffisante pour mettre en évidence tous les points critiques et toutes les séparatrices de l'écoulement de paroi. C'est en assurant la concordance entre les champs externe et surfacique que l'on parvient à définir l'écoulement correctement.

Pour illustrer ce point, nous considérerons un exemple fourni par une étude de l'écoulement autour d'une maquette à l'échelle 1/100 de l'arrière-corps

du futur lanceur européen ARIANE 5. Comme le montre la figure 13, ces expériences ont été exécutées sur un montage à corps central, à un nombre de Mach de 4, les jets des deux propulseurs d'appoint latéraux et du moteur central étant simulés par de l'air comprimé. En plus des visualisations pariétales, le champ a été exploré par vélocimétrie laser ce qui a permis de définir l'organisation de l'écoulement dans l'espace inter-tuyères (Reijasse et Détery, 1989).

Sur la figure 14 est reproduite une visualisation strioscopique mettant en évidence les jets issus des différents moteurs. Compte tenu de l'altitude simulée, ces jets éclatent et interagissent fortement entre eux, ce qui d'une part est la cause d'un courant de reflux intense en direction du culot du moteur central, d'autre part peut induire un décollement de l'écoulement externe en amont de l'extrémité des fuselages. La figure 15 représente l'interprétation du spectre pariétal observé. Considérant d'abord le fuselage du moteur central, on y voit une séparatrice ( $S_1$ ) issue du col  $C_1$  situé en amont de la pièce de jonction entre le propulseur d'appoint et le moteur central. La ligne ( $S_1$ ) se rapproche d'abord du plan de symétrie perpendiculaire à la figure pour devenir très voisine de la séparatrice ( $A_1$ ) - une ligne d'attachement - contenue dans ce plan. Puis, elle s'écarte progressivement de ( $A_1$ ) et, près du culot, ( $S_1$ ) s'incurve brusquement pour se diriger vers le noeud de décollement  $N_2$  en suivant pratiquement l'arête du culot. En aval du col  $C_1$ , il existe au pied de la pièce de jonction, un noeud d'attachement  $N_1$  d'où part une famille de lignes de frottement ( $f_1$ ). La ligne de séparation ( $S_1$ ) discrimine ainsi la famille ( $f_1$ ) de la famille ( $f_2$ ) formée des lignes de frottement venant de l'amont, depuis un point de type noeud non accessible aux visualisations.

Une deuxième ligne de séparation ( $S_2$ ) prend naissance au col ( $C_2$ ). Elle sépare la famille ( $f_1$ ) de la famille ( $f_3$ ) des lignes de frottement ayant pour origine le noeud  $N_3$ . Les trois familles ( $f_1$ ), ( $f_2$ ) et ( $f_3$ ) aboutissent au noeud de décollement  $N_2$ . La description de cette partie de l'écoulement doit être complétée par l'introduction de la ligne de séparation ( $S_3$ ) passant par le col  $C_3$  et confondue avec l'arête du culot.

La séparation principale attachée à ( $S_1$ ) est certainement provoquée par l'impact sur le fuselage central de l'onde de choc se formant au nez du propulseur d'appoint. Quant à la séparation le long de ( $S_2$ ), elle résulte probablement de la perturbation prenant naissance à l'extrémité de la pièce de jonction. Elle peut aussi être due à l'éclatement des jets.

Considérons maintenant ce qui se passe sur un des propulseurs d'appoint. Un noeud d'attachement  $N_4$  - du type isotrope - doit exister au nez de l'ogive. Les visualisations montrent distinctement la séparatrice ( $S_4$ ), provenant du col  $C_4$  situé près de l'épaule de l'ogive, ainsi que la séparatrice ( $S_5$ ) issue d'un col  $C_5$  placé au pied de la pièce de jonction. Le décollement dont ( $S_4$ ) est la trace

doit résulter de la réflexion sur le moteur central du choc se formant devant le propulseur d'appoint. On distingue également les noeuds d'attachement  $N_5$  et  $N_6$ . Toutes les lignes de frottement du propulseur d'appoint aboutissent au noeud de décollement  $N_7$  situé sur l'arête du culot, l'organisation de l'écoulement dans cette région étant voisine de celle observée sur le moteur central. Sur la figure 15, on a également dessiné le spectre sur la partie du propulseur d'appoint opposée au moteur central où se voit très bien le mouvement de convergence de toutes les lignes de frottement pariétal vers le noeud  $N_7$ . La figure 16 donne une vue de l'ensemble du spectre.

Il n'est pas possible dans cet exemple d'appliquer la relation (4) puisque seule une partie de l'obstacle est accessible à l'observation, notamment les culots ne sont pas visibles.

Ainsi que nous l'avons souligné, la cohérence d'un tel dessin est assurée en examinant en même temps l'organisation du champ externe. Pour cela, reportons nous à la figure 17 où sont tracées les lignes de courant de l'écoulement de la zone inter-tuyère situées dans le plan de symétrie contenant les axes des tuyères. Ce tracé met en évidence un premier foyer  $F_6$  autour duquel s'enroulent les lignes de courant "piégées" dans le courant de recirculation. Ces lignes appartiennent à une famille délimitée par la séparatrice ( $S_7$ ) venant de l'amont et aboutissant à la lèvre de sortie de la tuyère. Ainsi, les lignes de courant s'écoulant entre le fuselage et ( $S_7$ ) disparaissent dans  $F_6$ . Une des lignes s'enroulant autour de  $F_6$  prend naissance au culot, au niveau du noeud  $N_2$  de l'écoulement pariétal. Comme nous l'avons vu plus haut, il existe à l'origine de la jupe du propulseur d'appoint un noeud d'attachement  $N_8$  où aboutit une ligne séparatrice ( $S_8$ ). Les lignes situées - sur le schéma - au dessus de ( $S_8$ ) refluent vers l'amont et celles comprises entre ( $S_7$ ) et ( $S_8$ ) s'écoulent vers l'aval. Certaines de ces lignes s'infléchissent pour contourner le courant de retour, puis elles tournent brusquement en direction de l'aval sous l'action de l'entraînement produit par le jet du moteur central.

### 3.3 - DECOLLEMENT AVEC LIGNE DE SEPARATION FIXEE

#### 3.3.1 - AILE DELTA A BORD D'ATTAQUE AIGU

L'aile delta à bord d'attaque aigu placée en incidence a depuis longtemps suscité l'intérêt des chercheurs en raison de la "force" des tourbillons qui se forment sur son extrados - ce qui les rend facilement détectables - et aussi de son caractère conceptuellement simple, en premier examen. Dans une telle situation, le raisonnement intuitif, guidé par des observations expérimentales, permet en effet de fixer le long du bord d'attaque la ligne de séparation origine de la nappe dont l'enroulement va constituer la structure tourbillonnaire. Une partie du problème trouve ainsi une solution immédiate. De ce fait, cette configuration se prête à des modélisations simplifiées et très tôt - bien avant l'apparition des moyens informatiques -

des résultats théoriques extrêmement instructifs ont été obtenus grâce à l'emploi de méthodes analytiques (Legendre, 1952). Il n'est pas de notre propos de faire ici un historique des études nombreuses consacrées à l'aile delta; cela nous entraînerait beaucoup trop loin. Soulignons simplement que, si les renseignements sur les propriétés pariétales de l'écoulement sont abondantes, en revanche des mesures de champ permettant de définir avec précision les organisations tourbillonnaires ne sont apparues que relativement tard (Hummel, 1976; Hoeijmakers et al., 1983; Taylor et al., 1987; Elsenaar et Bütetisch, 1988; Narayan et Hartmann, 1988; Kegelmann et Roos, 1990).

Les tourbillons d'aile delta forment une famille très nombreuse si l'on considère la flèche de l'aile, la forme de son bord d'attaque, le nombre de Mach de l'écoulement amont, le nombre de Reynolds, etc... Dans ce qui suit, nous limiterons notre propos à une description de l'écoulement incompressible s'établissant sur une aile à bord d'attaque aigu, de flèche égale à  $75^\circ$  (voir Fig. 18). Pour cela, nous utiliserons des résultats récents comportant des mesures de champ par sonde de pression à cinq trous et vélocimétrie laser (Pagan et Solignac, 1985; Molton, 1986; Solignac et al., 1989).

L'existence, dans ces conditions, de tourbillons d'extrados vigoureux est attestée par la photographie de la figure 19 qui montre une visualisation par plan laser du champ d'extrados d'une aile placée sous une incidence de  $20^\circ$ . Le traceur, en l'occurrence de la fumée, tend à se concentrer dans les régions rotationnelles, mettant ainsi en évidence ce que l'on appelle le tourbillon. La figure 20a montre une visualisation obtenue pour une incidence  $\alpha$  de  $7,5^\circ$  et à une vitesse  $V_\infty$  de 40 m/s. Compte tenu de la taille de l'aile (corde  $C = 1,45$  m, d'où un nombre de Reynolds:  $Re_c = 4 \cdot 10^6$ ) la couche limite était turbulente sur la plus grande partie de l'extrados. Il apparaît clairement que les lignes de frottement pariétales sont parallèles à la corde de l'aile dans la partie médiane de cette dernière. Puis, se dirigeant vers le bord d'attaque, une première séparatrice ( $A_1$ ), ayant le caractère de ligne d'attachement, est visible. Le spectre révèle ensuite une deuxième séparatrice ( $S_2$ ), correspondant à ce que l'on nomme le décollement - ou séparation - secondaire, la ligne de séparation primaire ( $S_1$ ) étant confondue avec le bord d'attaque. La figure 20b montre un schéma interprétatif de ce spectre ainsi que le système tourbillonnaire dont il est la trace. La déflexion des séparatrices visible peu après la pointe est due à la transition laminaire-turbulent de la couche limite.

La figure 21 montre le spectre observé quand l'incidence est de  $20^\circ$ , le champ étudié ne couvrant que la partie arrière gauche de l'aile pour que les détails soient plus visibles. Maintenant, trois lignes de séparation ( $S_1$ ) - le long du bord d'attaque - ( $S_2$ ) et ( $S_3$ ) sont présentes et la ligne d'attachement "primaire" ( $A_1$ ) est située dans la plan de symétrie. Un examen attentif des visualisations permet de détecter les lignes d'attachement

(A<sub>2</sub>) et (A<sub>3</sub>) devant exister entre les lignes de séparation.

Il est à noter que l'organisation générale de ce type d'écoulement est assez peu sensible au nombre de Reynolds quand l'incidence est élevée. On peut donc compléter la description qui précède par l'examen de résultats obtenus à  $V_{\infty} = 20$  m/s sur une maquette de dimensions notablement inférieures (corde  $C$  égale à 0,5 m, nombre de Reynolds  $Re_c = 0,7 \cdot 10^6$ ) pour laquelle des mesures très fines ont été exécutées. Ainsi, la figure 22a donne le champ de vitesse projeté dans un plan vertical situé à l'abscisse réduite  $X/C = 0,58$ , l'incidence étant égale à  $20^\circ$ . Une trajectographie dans ce champ, associée à l'examen du spectre pariétal, permet d'établir le schéma de la figure 22b qui montre l'existence des points critiques suivants situés sur l'aile:

- demi-cols  $C_1$ ,  $C_2$  et  $C_3$  correspondant aux séparatrices du spectre pariétal ( $S_1$ ), ( $S_2$ ) et ( $S_3$ );

- demi-cols  $C_4$ ,  $C_5$  et  $C_6$  correspondant aux séparatrices ( $A_1$ ), ( $A_2$ ) et ( $A_3$ );

En dehors de l'aile, on observe:

- une première séparatrice ( $S_1$ ), issue du demi-col  $C_1$  placé au bord d'attaque, s'enroule autour du foyer  $F_1$  constituant le centre du tourbillon primaire;

- une deuxième séparatrice ( $S_2$ ) aboutit au demi-col d'attachement ( $C_4$ );

- la séparatrice ( $S_3$ ) issue de  $C_2$  s'enroule autour du foyer  $F_2$ , centre du tourbillon secondaire;

- une quatrième séparatrice ( $S_4$ ) aboutit au demi-col  $C_5$ ;

- une cinquième séparatrice ( $S_5$ ) s'enroule autour du foyer  $F_3$ , centre du tourbillon "tertiaire";

- enfin, la séparatrice ( $S_6$ ) "stagne" au point critique  $C_7$  placé dans le plan de symétrie de l'aile.

Sur la figure 23 est dessinée l'organisation dans l'espace des différentes nappes de séparation.

La définition du champ tourbillonnaire sur la même aile est complétée par une représentation dans des plans verticaux de grandeurs déduites des explorations. Ainsi, la figure 24 montre les répartitions dans trois plans de coupe de  $\Omega_x$ , composante selon l'axe horizontal  $X$  du rotationnel, quantité mesurant la "force" du mouvement de rotation. La figure 25 donne une représentation en perspective des lignes d'égale valeur de la pression d'arrêt dont la répartition est proche de celle du rotationnel. De tels tracés mettent bien en évidence le mode de constitution de la structure tourbillonnaire principale par enroulement de la nappe issue du bord d'attaque dans laquelle s'est transféré le rotationnel initialement contenu dans les couches limi-

tes d'extrados et d'intrados. Egalement, ces tracés montrent la concentration de ce rotationnel au centre de ce qui constitue le tourbillon primaire, de loin le plus intense. Le tourbillon secondaire se manifeste sur ces tracés par la présence d'une seconde région à rotationnel de signe contraire mais d'intensité bien moindre. Quant au tourbillon tertiaire, il est pratiquement indiscernable.

Il est à noter que seule la séparation donnant naissance au tourbillon primaire est fixée par la singularité de surface au bord d'attaque de l'aile. Les autres structures tourbillonnaires - dont l'effet sur la répartition de pression pariétale est appréciable - naissent sur la surface plane de l'aile. De ce fait, elles ne peuvent pas être représentées par les modèles de fluide parfait. Enfin, si des informations déjà utiles pour valider les codes de calcul sont disponibles en subsonique et en supersonique, les explorations de champ en hypersonique font presque totalement défaut (Monnerie et Werlé, 1968).

### 3.3.2 - ECOULEMENT DE CULOT

Le deuxième exemple de configuration où le décollement principal est fixé par une discontinuité de paroi est l'arrière-corps à culot franc. Dans ce cas, l'écoulement s'écoulant le long du fuselage décolle à l'arête du culot ce qui donne lieu à la formation d'une large zone dissipative ou sillage. Nous considérerons ici un arrière-corps de révolution, d'axe  $OX$ , non propulsé (absence de jet) dont le culot est plan et perpendiculaire à  $OX$ . A incidence nulle, la structure du sillage est bien connue (voir, en particulier, Détery et Lacau, 1987). Comme le montre la figure 26a, il s'établit juste en aval du culot une zone de recirculation organisée en un tourbillon toroïdal. La topologie dans un plan méridien comporte: un demi-col  $C_1$  à l'arête  $D$ , un col  $C_2$  (le point de recollement  $R$ ) au sein de l'écoulement, sur l'axe de symétrie, et un deuxième demi-col  $C_3$  au centre du culot. La séparatrice ( $S_1$ ) joignant  $C_1$  et  $C_2$  fait office de ligne discriminatrice (voir § 2.1 ci-dessus). La ligne ( $S_2$ ) reliant les points d'arrêt  $C_1$  et  $C_3$  est également une séparatrice. Dans chacun des tourbillons, les lignes de courant sont des courbes fermées tournant autour des centres  $\mathcal{A}_1$  et  $\mathcal{A}_2$ .

La structure du sillage quand un effet tridimensionnel est introduit est moins bien connue. La description que nous allons faire résulte d'une mise sous une incidence  $\alpha$  de  $5^\circ$  d'un arrière-corps de révolution de calibre  $D = 0,030$  m, comportant un rétreint de  $6^\circ$  de longueur  $L = D$ , placé dans un écoulement subsonique de nombre de Mach égal à 0,54 (voir Fig. 27). Le nombre de Reynolds a pour valeur  $Re_D = 3,56 \cdot 10^5$ . Cette configuration - qui est la situation tridimensionnelle la plus simple pouvant être imaginée à partir du cas de révolution - a été étudiée par l'Institut Franco-Allemand de Recherches de Saint-Louis (ISL) qui a procédé à des explorations de champ très fines au moyen d'un vélocimètre laser tridirectionnel (Bernier, 1989; Bernier et Dupéroux, 1990).

Il est à noter que cette configuration présente un plan de symétrie formé par l'axe de la maquette et le vecteur vitesse à l'amont. La figure 28 représente le champ de la composante de vitesse dans quatre plans longitudinaux situés à des distances  $Z$  différentes du plan de symétrie vertical  $Z = 0$ , ce qui donne une bonne image de la zone de culot, encore dite *proche sillage*. Comme le montre la figure 29, l'organisation tourbillonnaire dans le *sillage lointain* est mise en évidence par les champs de la composante de vitesse dans des plans transversaux situés à des distances  $X$  croissantes du culot. Pour aider à la compréhension de l'écoulement, on a tracé en superposition sur les figures 28 et 29, les trajectoires de ces champs. La figure 30 donne une interprétation topologique du champ transversal valable pour des plans situés à une certaine distance en aval du culot. On y distingue un col  $C_1$  par où passe la séparatrice ( $S_1$ ) qui sépare les trajectoires joignant les infinis bas et haut de celles qui vont disparaître dans les foyers  $F_1$  et  $F_2$ . Une deuxième séparatrice ( $S_2$ ), passant par le col  $C_2$ , fait office de barrière entre les trajectoires montantes et descendantes de la zone de formation des foyers. Examinons maintenant l'écoulement dans le plan de symétrie vertical du sillage proche où les trajectoires sont des lignes de courant. Comme l'indique la figure 31, la séparatrice ( $S_1$ ) issue de l'épaulement A s'enroule autour du foyer  $F_1$  et une deuxième séparatrice ( $S_2$ ) aboutit au point d'arrêt - ou demi-col -  $C_2$  situé sur le culot. Enfin, une troisième séparatrice ( $S_3$ ) naissant au col  $C_3$ , confondu avec l'épaulement inférieur B, sépare l'écoulement venant de l'"extrados" de celui en provenance de l'"intrados".

Il existe une grande différence entre les situations 26a et 26c où l'on est passé d'une topologie à 4 cols et 2 foyers à une situation à 3 cols et un seul foyer. La "bifurcation" de a vers c est sans doute précédée - pour des incidences très faibles - par la structure b où les centres  $\mathcal{A}_1$  et  $\mathcal{A}_2$  sont remplacés par des foyers  $F_1$  et  $F_2$ .

Faute de visualisations pariétales, le spectre des lignes de frottement dessiné Fig. 32 est en grande partie conjectural. Sur la partie fuselage (voir Fig. 32a), le spectre comporte deux points critiques, à savoir: un demi-noeud  $N_1$  situé à l'épaulement supérieur A du culot et un demi-col  $C_1$  à la position symétrique B. Toutes les lignes de frottement du corps sont "aspirées" par le noeud de décollement  $N_1$ . La situation sur le culot est représentée Fig. 32b. Au point B est placé un demi-col  $C_2$  (complémentaire de  $C_1$ ) et en A un demi-noeud  $N_2$  (complémentaire de  $N_1$ ). Le noeud  $N_2$  sur la face du culot coïncide avec l'impact de la séparatrice ( $S_2$ ): il alimente l'écoulement de surface qui disparaît dans le noeud  $N_2$ . Dans le cadre de cette description, une séparatrice ( $S_2$ ) court le long de l'arête entre le col  $C_1 + C_2$  et le noeud  $N_1 + N_2$ . La figure 32c montre le spectre dans le cas de révolution "pur" (incidence nulle). Là, un noeud isotrope est placé au centre du culot dont l'arête porte une suite infinie de cols.

Les éléments précédents permettent d'exécuter le

dessin de la figure 33 représentant la surface de séparation portée par la séparatrice  $S_1$ . Dans un mouvement assez complexe, cette surface s'enroule sur elle-même en un "ourlet" qui se distend en deux branches se courbant vers l'aval. La coupe de cette surface par un plan transversal donne les deux foyers représentés sur la figure 30. Il s'agit d'un seul tourbillon en fer à cheval analogue à celui se formant devant un obstacle arrondi.

### 3.4 - CORPS ELANCE A OGIVE POINTUE

La configuration examinée ici est celle de l'obstacle fuselé, à nez pointu, placé en incidence. Une telle géométrie correspond à un corps de missile ou bien à la partie avant d'un fuselage d'avion supersonique. Dans ce cas, la position des lignes séparatrices ne peut pas être "devinée" à l'avance, mais il peut sembler évident que l'origine de ces lignes doit se trouver à l'extrémité pointue de l'obstacle. En raison de son intérêt pratique, cette forme a fait l'objet d'un très grand nombre d'expériences, la plupart consistant en des relevés de pression pariétale et en des mesures de coefficients aérodynamiques. En revanche, les études fines incluant des explorations du système tourbillonnaire engendré par un tel corps sont relativement rares (Jorgensen et Perkins, 1955; Fidler et al., 1977; Yanta et Wardlaw, 1981, 1982; Ponton et Johnson, 1989; Champigny et Baudin, 1990; voir aussi: pour une étude topologique à partir de visualisations par plan de lumière, voir Ward et Katz, 1989).

Nous analyserons ici les résultats obtenus avec une maquette de révolution constituée d'une partie cylindrique, de diamètre  $D = 0,030$  m, précédée d'une ogive circulaire de longueur égale à trois calibres (voir Fig. 34). Les expériences ont été exécutées en supersonique à un nombre de Mach  $M_\infty = 2$  et à une pression génératrice de  $5 \cdot 10^4$  Pa, ce qui conduit à un nombre de Reynolds ayant la valeur:  $Re_0 = 1,61 \cdot 10^5$ . Dans ces conditions, la couche limite - avant séparation - est laminaire.

L'écoulement a été étudié pour des incidences  $\alpha$  variant de  $5^\circ$  à  $20^\circ$ ; chaque fois le spectre pariétal a été défini avec soin par des visualisations; les pressions à la paroi ont été mesurées et le champ a été exploré au moyen d'une sonde de pression à cinq trous dans plusieurs plans perpendiculaires à l'axe  $X$  de la maquette (Pagan et Molton, 1990). Dans ce qui suit, nous ne retiendrons que les résultats obtenus pour  $\alpha = 5^\circ$  et  $20^\circ$ . Pour ces incidences, et compte tenu du nombre de Mach de l'écoulement, il n'y a pas de risque d'établissement d'un régime à structures tourbillonnaires dissymétriques.

Les vues de dessus et de côté de la visualisation pariétale réalisée à  $5^\circ$  d'incidence sont reproduites Figs. 35a et 35b, avec les schémas interprétatifs correspondants. Les lignes de frottement provenant de l'apex, et situées d'un côté de la ligne d'attachement ( $A_1$ ) située dans le plan de symétrie vertical à l'intrados, convergent progressivement vers une ligne de séparation primaire ( $S_1$ ) claire-



ment identifiable à partir de l'abscisse  $X \approx 4 D$ . En avant de cette position, il est impossible de déterminer quelle ligne de frottement est la ligne de séparation.

Dans le plan de symétrie, côté extrados, existe une deuxième ligne d'attachement ( $A_2$ ), les lignes de frottement en provenance de ( $A_2$ ) se dirigeant vers la ligne de séparation secondaire ( $S_2$ ). De même que pour ( $S_1$ ), le mouvement de convergence vers ( $S_2$ ) n'est vraiment visible qu'à partir de la station  $X \approx 5 D$ . Entre ( $S_1$ ) et ( $S_2$ ), le frottement est trop faible pour entraîner l'écoulement visqueux; cependant, il doit exister une ligne d'attachement ( $A_3$ ), placée approximativement sur la vue de côté de la figure 35b.

En fait, comme le montreront les résultats analysés § 3.6, ce spectre pariétal est topologiquement très proche de ce qui est observé sur un corps à nez arrondi. A la différence que, dans le cas présent, le système de noeuds et de cols, à introduire pour compléter l'interprétation, est indiscernable de l'extrémité de l'ogive.

A partir de ce spectre pariétal, il est possible de concevoir différents champs dans des plans transversaux, perpendiculaires à l'axe  $OX$  de la maquette. Le premier (voir Fig. 36a), constitué d'un tourbillon primaire de foyer  $F_1$  et d'un tourbillon secondaire de foyer  $F_2$  rappelle la structure observée sur les ailes delta (voir § 3.3.1 ci-dessus). Le second (voir Fig. 36b), contient un col  $C_2$  au sein de l'écoulement. Enfin, le troisième (voir Fig. 36c), fait correspondre aux séparatrices ( $S_1$ ) et ( $S_2$ ) des tourbillons de faible amplitude et associe le tourbillon principal à un col  $C_2$  situé dans l'écoulement. A l'incidence de  $5^\circ$ , le système tourbillonnaire est trop près de la paroi pour pouvoir être sondé avec précision. Il n'est donc pas possible de décider quelle est la structure qui se réalise effectivement. Toutefois, l'analogie avec des écoulements connus (l'aile delta par exemple) et la fait - intuitif - que la configuration la plus simple est celle qui a le plus de chance de se réaliser, amenant à penser que le bon schéma est celui de la figure 36a. Les enroulements tourbillonnaires correspondants sont représentés en perspective Fig. 37 où les proportions de la réalité ne sont pas respectées, les tourbillons réels étant beaucoup plus proches de la paroi.

La visualisation obtenue pour  $\alpha = 20^\circ$  est reproduite Fig. 38. Maintenant, le départ des séparatrices au nez de la maquette est bien visible. Comme le montrent les schémas interprétatifs, on identifie quatre lignes de séparation (seules dessinées) et cinq lignes d'attachement. Pour plus de clarté, le spectre est développé sur la figure 39 en conservant approximativement les distances longitudinales et circonférentielles. La ligne d'attachement ( $A_1$ ), située dans le plan méridien à l'intrados, est au milieu de la figure. La ligne d'attachement ( $A_2$ ) de l'extrados, dédoublée, se retrouve sur les bords du schéma. Les lignes de séparation ( $S_2$ ) et ( $S_3$ ) sont reportées sur la figure, en revanche la ligne située très près de ( $S_2$ ) et appelée

( $S_4$ ) sur la figure 38 est ignorée par souci de clarté. En effet, le tourbillon engendré par la séparation se produisant le long de ( $S_4$ ) est d'une dimension trop faible pour affecter notablement l'écoulement transversal.

Dans ce cas, le système tourbillonnaire se détache nettement de la paroi, ce qui permet, grâce aux sondages, d'en donner une représentation plus quantitative. La figure 40a montre le champ de vitesse projeté dans le plan transversal situé à l'abscisse réduite  $X/D = 8$  où apparaît très distinctement le gros tourbillon primaire attaché à la séparation ( $S_1$ ). En revanche, en raison de la petitesse du champ, les structures engendrées par les autres séparations sont peu visibles. Néanmoins, par une trajectographie dans ce champ de vecteurs et en s'appuyant sur les visualisations pariétales, il est possible d'exécuter le dessin de la figure 40b où les proportions de la réalité sont respectées.

Le tracé de la répartition spatiale de la pression génératrice  $p_i$  donne aussi une image parlante du système tourbillonnaire. La figure 41 montre deux résultats obtenus dans les plans situés à  $X/D = 4$  et  $X/D = 8$ . On y voit nettement les régions fortement rotationnelles - au cœur du tourbillon principal et dans la zone des tourbillons secondaires - marquées par un déficit prononcé de  $p_i$ . L'accroissement selon  $X$  du domaine tourbillonnaire - par déferlement continu des couches limites - apparaît de manière frappante sur la représentation en perspective de la figure 42.

### 3.5 - CORPS A NEZ ARRONDI

Considérons maintenant une situation où le décollement a lieu sur un corps à nez arrondi dont le rayon de courbure est partout grand devant l'épaisseur de la couche limite. Ce genre d'écoulement est encore plus difficile à modéliser dans la mesure où la position et l'origine de la - ou des - ligne(s) de séparation ne peuvent être déterminées que par une prévision fidèle du comportement de la couche limite dans son évolution vers la séparation.

La plupart des expériences exécutées pour contribuer à la compréhension de ce type de décollement ont envisagé des corps en forme d'ellipsoïde. Après les premiers travaux d'Eichelbrenner et Oudard (1955), de nombreuses études ont suivi, généralement limitées à des mesures de pression ou à des visualisations pariétales. Ce n'est que depuis une date relativement récente que l'on dispose de renseignements quantitatifs sur la structure de l'écoulement externe (Vollmers et al., 1983; Meier et al., 1984; Costis et al., 1987; Hoang et al., 1990).

Nous retiendrons ici une étude effectuée sur une maquette constituée d'un demi-ellipsoïde aplati prolongé par une portion cylindrique que termine un culot franc (voir Fig. 43). La maquette, d'une longueur  $L$  de 1,83 m, a été essayée à une vitesse de 50 m/s pour des angles d'incidence  $\alpha$  allant de  $0^\circ$  à  $40^\circ$ . Le nombre de Reynolds  $Re_L$  variant  $6,4 \cdot 10^6$ , la transition se produit dans la région du nez. La

couche limite est donc turbulente dans la zone où les enroulements tourbillonnaires se développent pleinement (Werlé, 1985; Chanetz, 1986; Chanetz et Détery, 1988).

Les visualisations par enduit visqueux obtenues pour  $\alpha = 10^\circ$ ,  $20^\circ$  et  $30^\circ$  sont présentées Fig. 44. Chaque figure donne une vue de l'extrados et une vue de côté. Quand l'incidence est de  $10^\circ$  (voir Fig. 44a), le noeud d'attachement au nez de la maquette est légèrement déplacé vers l'intrados et le spectre pariétal est remarquablement symétrique, avec convergence très progressive des lignes de frottement en direction du plan de symétrie vertical. A cette incidence, aucune ligne de séparation caractérisée n'est détectée (la région du culot étant exclue de cette analyse). Cette absence de séparation est confirmée par un calcul de couche limite (Barberis, 1986).

Quand  $\alpha$  devient égale à  $20^\circ$  (voir Fig. 44b), on observe sur le dernier tiers de la maquette, dans une région voisine des bords latéraux, un infléchissement rapide des lignes de frottement qui convergent vers une ligne de séparation bien distincte. Dans le cas présent, comme pour l'écoulement autour du corps fuselé à incidence modérée (voir § 3.4 ci-dessus), le col par où doit passer la ligne de séparation n'est pas clairement identifiable sur le spectre pariétal, ce qui tendrait à conforter le concept de décollement ouvert introduit par Wang (1983). En fait, comme nous allons le voir, la construction de l'écoulement autour du corps oblige à introduire un, ou plusieurs, cols dont l'existence est nécessaire à l'établissement d'un schéma topologiquement cohérent, même si certains points critiques ne sont pas détectables par l'expérience.

Pour l'incidence  $\alpha = 30^\circ$  (voir Fig. 44c), les lignes de frottement divergent rapidement depuis le plan de symétrie vertical qui contient la ligne d'attachement ( $A_1$ ) et convergent en direction d'une ligne de séparation ( $S_2$ ). En outre, les lignes de frottement en provenance de l'intrados tendent vers une autre ligne de séparation située près du bord latéral de la maquette. Cette ligne ( $S_1$ ) est associée au décollement primaire qui donne naissance au tourbillon le plus vigoureux. La ligne de séparation secondaire ( $S_2$ ) correspond au décollement du fluide qui, près de la paroi, s'écoule depuis le plan de symétrie extrados en direction du bord de la maquette. Ainsi ( $S_2$ ) est à l'origine d'un tourbillon secondaire situé au dessous du tourbillon primaire. Entre les deux lignes de séparation ( $S_1$ ) et ( $S_2$ ), existe une ligne d'attachement ( $A_2$ ), peu visible sur les photographies reproduites ici, mais parfaitement observables lors des essais.

Sur les figures 45a et 45b sont dessinés les schémas interprétatifs des spectres pariétaux observés aux incidences  $\alpha = 20^\circ$  et  $30^\circ$  pour lesquelles il y a décollement. Sur ces schémas, les proportions de la réalité sont respectées pour les vues de dessus et de côté; le dessin du spectre sur l'intrados, exécuté en effectuant un pseudo développement, est approximatif.

Si l'on fait abstraction de la région du culot, le spectre observé pour  $\alpha = 20^\circ$  contient trois séparatrices, à savoir (voir Fig. 45a):

- deux lignes d'attachement ( $A_1$ ) et ( $A_2$ ), situées respectivement côtés extrados et intrados, dans le plan de symétrie vertical de l'écoulement;
- une ligne de séparation ( $S_1$ ) bien visible sur la partie arrière de la maquette, près de ses bords latéraux.

Une construction topologiquement cohérente de ce spectre oblige à introduire au moins trois points critiques dans la région du nez de l'obstacle. Il s'agit d'un noeud d'attachement  $N_1$ , du col  $C_1$  - par où passe la ligne de séparation ( $S_1$ ) et les deux lignes d'attachement ( $A_1$ ) et ( $A_2$ ) - un second noeud d'attachement  $N_2$  devant exister en aval de  $C_1$ . Seul le noeud  $N_1$  est en fait clairement mis en évidence par la visualisation; il se confond avec le point d'arrêt au sens usuel du terme. Ainsi,  $N_1$  et  $N_2$  sont les lieux de naissance de deux ensembles distincts de lignes de frottement séparés par ( $S_1$ ).

Les schémas correspondant à  $\alpha = 30^\circ$  sont dessinés sur la figure 45b. Ainsi que nous l'avons déjà signalé, dans ce cas, deux lignes de séparation ( $S_1$ ) et ( $S_2$ ) sont identifiables, surtout sur la partie arrière de la maquette. Egalement, trois lignes d'attachement sont présentes: les deux lignes ( $A_1$ ) et ( $A_2$ ) devant exister, comme pour la configuration précédente, dans le plan de symétrie vertical, et la ligne ( $A_3$ ) située entre ( $S_1$ ) et ( $S_2$ ). On est donc conduit à introduire les points critiques suivants dans la région du nez:

- noeuds d'attachement  $N_1$ ,  $N_2$ ,  $N_3$  ( $N_1$  étant le point d'arrêt);
- cols  $C_1$  et  $C_2$  origines des lignes de séparation ( $S_1$ ) et ( $S_2$ ).

Il est à noter que seul  $N_1$  est bien mis en évidence par les visualisations pariétales, mais l'existence de  $C_1$  est confirmée par les calculs de couche limite (Barberis, 1986).

Comme dans le cas du corps fuselé à faible incidence, les séparatrices effectuent un long parcours depuis leur origine en demeurant indifférenciées des lignes de frottement voisines. Ce n'est qu'après la jonction ellipsoïde - cylindre que ces cernières lignes amorcent le mouvement de convergence vers les lignes de séparation ou bien de divergence depuis les lignes d'attachement.

Dans l'examen de l'organisation tourbillonnaire résultant du décollement, nous considérerons la configuration obtenue à  $\alpha = 30^\circ$  qui a fait l'objet d'une étude approfondie avec mesures de champ par sondes multi-trous et vélocimétrie laser.

La figure 46 montre le champ de la composante de vitesse dans quatre plans perpendiculaires à l'axe OX de la maquette pour un secteur limité par les



positions angulaires:  $\theta = 19^\circ$  et  $90^\circ$ . Les abscisses de ces plans ( $X = 0,88 - 0,92 - 0,96$  et  $1,00$  m) correspondent à la région où les enroulements tourbillonnaires deviennent bien distincts.

La structure de l'écoulement dans cette région peut aussi être visualisée en considérant les lignes d'égale valeur de la composante  $\tilde{\Omega}_x$  du rotationnel (voir Fig. 47). Elles mettent en évidence l'existence d'une "couche" de faible épaisseur, où  $\tilde{\Omega}_x$  augmente très rapidement, pouvant être assimilée à la nappe de décollement.

Comme le montre la figure 48, où sont représentés les champs de vitesse dans quatre plans transversaux plus en aval, les structures tourbillonnaires se détachent nettement de la paroi, ce qui permet de mieux définir l'organisation de l'écoulement.

Ainsi, à partir de trajectographies dans les champs de vitesse et en s'appuyant sur les visualisations pariétales qui donnent avec précision les positions des lignes de séparation et d'attachement, il est possible de tracer les trajectoires de l'écoulement transversal (voir Fig. 49). Les points critiques révélés par ces tracés sont:

- les deux foyers  $\mathcal{F}_1$  et  $\mathcal{F}_2$ ;
- les demi-cols  $C_3$  et  $C_4$  traces des lignes de séparation ( $S_1$ ) et ( $S_2$ );
- le demi-col  $C_5$  correspondant à la ligne d'attachement ( $A_3$ );
- le col  $C_2$  et le demi-col  $C_1$  situés dans le plan de symétrie.

Les résultats obtenus sur cette maquette à  $\alpha = 30^\circ$  révèlent une organisation bien définie du système tourbillonnaire. Jusqu'à une abscisse un peu supérieure à  $1,12$  m, les tourbillons primaires et secondaires sont contenus dans une couche mince au contact de la paroi, la structure de l'écoulement dissipatif étant alors peu différente de celle d'une couche limite classique. Ce n'est qu'à partir de  $X = 1,12$  m que les deux tourbillons se détachent réellement de la paroi pour constituer un système tourbillonnaire bien organisé associé à un décollement franc. A cette évolution correspond un changement net du spectre pariétal, les lignes de séparation et d'attachement devenant identifiables.

Les schémas qui vont maintenant être proposés pour l'écoulement autour de la maquette placée à une incidence de  $30^\circ$  sont qualitatifs en raison de la quasi-impossibilité de représenter les choses en respectant les proportions de la réalité.

Ainsi qu'il est dessiné sur la figure 50, une configuration plausible peut être construite en introduisant cinq lignes séparatrices et cinq points critiques. Pour raccorder ce spectre à ce qui se passe à l'extérieur, dans le plan de symétrie, il faut faire correspondre aux trois noeuds  $N_1$ ,  $N_2$  et  $N_3$  les demi-cols  $C_7$ ,  $C_8$  et  $C_9$  par où passent trois séparatrices. Aux cols  $C_1$  et  $C_2$  sont associés les

demi-cols  $C_{10}$  et  $C_{11}$  d'où émergent les séparatrices ( $S_3$ ) et ( $S_4$ ) s'enroulant autour des foyers  $\mathcal{F}_2$  et  $\mathcal{F}_3$ .

Les écoulements sur la surface et dans le plan de symétrie sont les traces du système à deux tourbillons en fer à cheval dessiné sur la figure 51. Une première surface de séparation ( $\Sigma_1$ ), ayant pour trace sur l'obstacle la ligne de séparation primaire ( $S_1$ ), s'enroule autour d'un "axe" passant par le foyer  $\mathcal{F}_3$  dans le plan de symétrie. Toutes les lignes de courant définissant ( $\Sigma_1$ ) ont pour origine le noeud  $N_1$  coïncidant avec le demi-col  $C_{10}$  dans le plan de symétrie et le col  $C_1$  sur la surface du corps. D'une manière analogue, une deuxième surface de séparation ( $\Sigma_2$ ) naît de la ligne de séparation ( $S_2$ ), ses lignes de courant provenant du noeud  $N_2$  en coïncidence avec  $C_{11}$  et  $C_2$ .

Une autre organisation peut être imaginée, elle-aussi topologiquement correcte et en accord avec les observations expérimentales (voir Fig. 52). Si nous considérons d'abord le spectre pariétal, aux cinq séparatrices ( $A_1$ ), ( $A_2$ ), ( $A_3$ ), ( $S_1$ ) et ( $S_2$ ) - dont l'existence est prouvée de manière indiscutable par les visualisations - s'ajoute une troisième séparatrice ( $S_3$ ) issue du col  $C_2$  qui va s'enrouler autour du foyer  $\mathcal{F}_1$ . Maintenant, la ligne de séparation ( $S_2$ ) s'enroule, elle-aussi, autour de  $\mathcal{F}_1$  qui va être l'empreinte sur la surface de l'enroulement secondaire. La cohérence du schéma impose l'existence d'un troisième col  $C_3$ , situé en dehors du plan de symétrie, par où doit précisément passer la séparatrice ( $S_2$ ).

Les surfaces de séparation compatibles avec la présente interprétation sont dessinées sur la figure 53. On a d'abord représenté (voir Fig. 53a), la nappe primaire ( $\Sigma_1$ ) dont la trace sur l'obstacle est la ligne de séparation ( $S_1$ ) et l'intersection par le plan de symétrie la séparatrice ( $S_2$ ) spiralant autour du foyer ( $\mathcal{F}_3$ ). Son enroulement forme un tourbillon en fer à cheval. L'organisation du tourbillon secondaire est cette fois plus complexe. Nous distinguons d'abord (voir Fig. 53b) une première surface ( $\Sigma_2$ ) ayant pour trace la ligne de séparation ( $S_2$ ) et pour empreinte le foyer  $\mathcal{F}_1$ . Une deuxième nappe ( $\Sigma_3$ ), qui s'enroule à l'intérieur de ( $\Sigma_2$ ), a également pour empreinte  $\mathcal{F}_1$  (voir Fig. 53c), l'ensemble ( $\Sigma_2$ ) + ( $\Sigma_3$ ) s'organisant en un tourbillon trombe. Les lignes de courant définissant ( $\Sigma_1$ ) et ( $\Sigma_2$ ) partent des demi-noeuds  $N_3$  et  $N_2$ , en coïncidence avec les cols  $C_3$  et  $C_2$  sur la maquette. La figure 53d montre l'assemblage des trois surfaces ( $\Sigma_1$ ), ( $\Sigma_2$ ) et ( $\Sigma_3$ ) formant les enroulements primaire et secondaire.

Pour clore cette discussion, examinons brièvement l'évolution de la structure de l'écoulement quand - à nombre de Reynolds fixé - on augmente l'incidence  $\alpha$  en considérant ce qui se passe dans le plan de symétrie au voisinage du nez de la maquette. Comme le montre la figure 54a, tant que  $\alpha$  ne dépasse pas  $10^\circ$ , le champ ne contient qu'un point critique, à savoir un demi-col auquel correspond le noeud d'attachement principal, ou point d'arrêt. Dans ce domaine d'incidence, une variation de  $\alpha$  entraîne

une déformation continue du champ, le point critique se déplaçant progressivement vers l'extrados si  $\alpha$  augmente (voir Fig. 54b).

En revanche, pour  $\alpha \approx 20^\circ$  (voir Fig. 54c), le champ externe contient quatre points critiques, à savoir: trois demi-cols et un foyer. Quand l'incidence est portée à  $30^\circ$  (voir Fig. 54d), sept points critiques sont présents dans l'écoulement, soit: cinq demi-cols et deux foyers (on n'a retenue que la première interprétation).

Ainsi, par variation continue d'un paramètre - en l'occurrence l'incidence - l'écoulement tridimensionnel subit des changements discontinus de structure se traduisant par une augmentation du nombre des points critiques du spectre des lignes de courant ou de frottement. Un tel comportement - également noté à propos des écoulements de culot (voir § 3.3.2) - s'apparente à un phénomène de bifurcation. En réalité, le passage d'une organisation à l'autre doit se faire par une phase instationnaire à laquelle la description précédente ne peut pas s'appliquer. Cet aspect très important et particulièrement intéressant des écoulements tridimensionnels décollés ne sera pas discuté ici (voir, Tobak et Peake, 1982; Dallmann, 1986).

#### 4 - ECLATEMENT TOURBILLONNAIRE

##### 4.1 - REMARQUES GENERALES

Dans certaines circonstances, encore assez mal élucidées, une structure tourbillonnaire enroulée est susceptible de subir une désorganisation brutale connue sous le nom d'*éclatement*.

Ce phénomène peut affecter, par exemple, les tourbillons intenses se formant au-dessus de la voilure à forte flèche d'un avion évoluant à grande incidence. L'éclatement modifie alors sensiblement le champ de pression sur l'aile ce qui conduit à une chute de portance, le plus souvent dissymétrique, l'éclatement ne se produisant pas au même endroit sur chacune des ailes; d'où l'apparition d'un moment de roulis pouvant rendre le contrôle de l'appareil délicat.

La figure 55 montre une visualisation au tunnel hydrodynamique de l'éclatement des tourbillons au-dessus d'une aile delta dont le bord d'attaque aigu a une flèche de  $65^\circ$  (Werlé, 1960). Le phénomène se traduit par une dilatation de la structure - dont le noyau est auparavant très concentré - avec l'apparition de fluctuations à grande échelle génératrices d'une forte turbulence. Comme le décollement d'une couche limite, processus avec lequel il présente une parenté, l'éclatement entraîne une croissance spectaculaire de la place occupée par les zones dissipatives au sein de l'écoulement. Il en résulte:

- une augmentation de l'effet de déplacement visqueux, ce qui influe fortement sur l'ensemble du champ aérodynamique;
- une aggravation des pertes d'efficacité et un ac-

croissement de la traînée par intensification des effets dissipatifs;

- l'apparition de vibrations engendrées par les mouvements fluctuants auxquels l'éclatement donne naissance.

Préjudiciable à l'aérodynamique des avions, l'éclatement tourbillonnaire peut en revanche être bénéfique dans certaines applications. Par exemple, il constitue un moyen permettant d'améliorer le mélange carburant-comburant dans une chambre de combustion ou bien de hâter la dissipation des tourbillons émanant des extrémités d'aile des avions gros porteurs.

Le problème de l'éclatement se rencontre en supersonique sous la forme d'une interaction onde de choc / tourbillon, pendant du phénomène plus familier d'interaction onde de choc / couche limite. Comme le montre la figure 56, une telle interaction peut se produire sur un avion évoluant à grande incidence et en transsonique élevé ou bien quand un tourbillon engendré par une surface portante est avalé par une prise d'air placée en aval. Si le choc est assez intense, il est à même de provoquer l'éclatement de la structure tourbillonnaire qui le traverse selon une direction sensiblement normale; d'où, là aussi, des conséquences néfastes. Des situations similaires sont imaginables sur un véhicule hypersonique où coexistent des ondes de choc intenses et des tourbillons dont l'interaction peut être à l'origine de flux de chaleur locaux élevés sur certaines parties du fuselage.

##### 4.2 - ECLATEMENT EN ECOULEMENT INCOMPRESSIBLE

Etant donnée son importance pratique, l'éclatement tourbillonnaire a fait l'objet de très nombreux travaux et est encore activement étudié (pour une revue récente, voir Escudier, 1988). Il n'est pas question dans le cadre restreint de cette communication d'entrer dans le détail de la physique de l'éclatement à propos duquel nous disposons d'un assez grand nombre de renseignements en *incompressible*. Nous nous contenterons ici de qualifier le phénomène à partir de résultats expérimentaux obtenus dans l'air (Pagan et Solignac, 1986; Détery et al., 1987; Pagan, 1989).

Dans l'étude considérée, un tourbillon engendré par une aile delta placée en incidence est soumis, assez loin en aval du bord de fuite de l'aile, à un gradient de pression adverse créé par des volets mobiles. Ce dispositif permet d'étudier le phénomène hors du champ de pression engendré par l'aile et autorise une variation des principaux paramètres d'influence, à savoir:

- la force du tourbillon que l'on commande en faisant varier l'incidence de l'aile;
- l'intensité du gradient de pression qui joue le rôle de la perturbation provoquant l'éclatement.

Le tourbillon créé est sensiblement de révolution autour d'un axe X, Y et Z désignant les axes trans-

versaux. Sur la figure 57 sont tracées les composantes axiales  $V_x$  et tangentielles  $V_t$  du vecteur vitesse moyenne dans le plan méridien vertical. Ces résultats ont été obtenus grâce à l'emploi d'un vélocimètre laser à trois composantes. L'examen de ces champs montre que le tourbillon éclaté est organisé en un "bulbe" où la composante axiale de vitesse est dirigée à contre courant de l'écoulement principal. En même temps, le mouvement de rotation s'effondre, conséquence de la dilatation de la structure. Sur la figure 58 sont dessinées les trajectoires du mouvement méridien qui mettent en évidence les propriétés suivantes:

- en amont de l'éclatement, les trajectoires sont pratiquement rectilignes et parallèles, preuve que l'écoulement tourbillonnaire initial et quasi cylindrique;
- à partir du point d'éclatement - placé au col  $C_1$  - les trajectoires venant de l'amont divergent pour contourner le bulbe de recirculation dont la frontière est matérialisée par la séparatrice ( $S_1$ );
- à l'intérieur du bulbe, l'écoulement moyen semble s'organiser en plusieurs centres.

Les vues précédentes sont relatives à une description du champ en termes de moyennes temporelles, comme dans l'étude classique des couches limites turbulentes. Une telle approche, parfaitement légitime, peut masquer certains aspects du phénomène qui est en fait affecté par une assez grande *instationnarité*.

Les aspects fortement fluctuants de l'éclatement peuvent être caractérisés en construisant les histogrammes des composantes  $V_x$  et  $V_z$  de la vitesse instantanée. Rappelons que de tels histogrammes sont une approximation de la densité de probabilité croisée des deux variables aléatoires  $V_x$  et  $V_z$ . Trois de ces histogrammes sont représentés sur la figure 59 où est portée la répartition selon  $X$  de la composante moyenne  $\bar{V}_x$  sur l'axe  $X$  afin de situer les endroits concernés. En amont et en aval du point moyen d'éclatement  $\bar{E}$ , les histogrammes ont une forme classique présentant un pic unique avec, autour, un étalement plus ou moins grand résultant principalement de ce que l'on considère comme étant de la turbulence. En revanche, au voisinage du point où  $\bar{V}_x$  passe par zéro, les histogrammes comportent deux pics bien distincts, indices d'une forte *intermittence* affectant l'origine  $E$  de l'éclatement instantané. En d'autres termes,  $E$  oscille fortement autour de la position moyenne  $\bar{E}$ .

L'oscillation longitudinale de l'origine de l'éclatement est aussi révélée par la visualisation à court temps d'exposition présentée Fig. 60. La partie centrale sombre des photographies correspond au cœur du tourbillon d'où les particules de traceur sont éjectées par la force centrifuge. On remarque le rapide élargissement de la structure tourbillonnaire lors de l'éclatement ainsi que la variation importante de la position de l'origine du phénomène sur des photographies prises à des instants différents.

#### 4.3 - INTERACTION ONDE DE CHOC - TOURBILLON

L'interaction entre une onde de choc et une structure tourbillonnaire a été très peu étudiée, bien que la question présente un grand intérêt, sur les plans pratiques et fondamentaux (Horowitz, 1984; Détery et al., 1984; Metwally et al., 1989; Copening et Anderson, 1989). Nous illustrerons ce problème en présentant les résultats d'une étude où le tourbillon engendré par une demi-aile delta placée dans le collecteur d'une veine supersonique traverse une onde de choc droite formée au sein de l'écoulement supersonique uniforme par un dispositif fonctionnant en prise d'air (voir Fig. 61). Un des objectifs des expériences était de rechercher les conditions limites d'éclatement sous l'effet du choc en fonction:

- de l'intensité du choc caractérisée par le nombre de Mach amont  $M_\infty$ ;
- de la force du tourbillon mesurée par le rapport  $\tau$  de la vitesse tangentielle maximale  $V_{t_m}$  à la composante axiale  $V_{x_E}$  à la frontière extérieure de la structure.

La limite ainsi obtenue dans le plan  $[M_\infty, \tau]$  est tracée Fig. 62. L'allure générale de la courbe confirme le fait intuitif que le saut de pression nécessaire pour faire éclater le tourbillon est d'autant plus élevé que le taux de rotation est plus faible. On retrouve la tendance bien confirmée en incompressible.

#### 5 - CONCLUSION

La théorie des points critiques est maintenant reconnue comme étant une base indispensable à toute description cohérente d'un champ tridimensionnel décollé. Elle constitue, en effet, un outil logique, doté d'une terminologie précise, pour interpréter aussi bien les résultats des simulations numériques que les données expérimentales. Ainsi, la théorie des points critiques permet une définition précise des spectres des lignes de frottement pariétales obtenus par visualisation. C'est le décodage attentif de ces spectres qui révèle la présence de points critiques et de séparatrices indicateurs de l'existence de décollements. Les spectres pariétaux sont véritablement l'empreinte sur le corps du champ tourbillonnaire externe et leur considération est un préalable à toute analyse de l'écoulement.

Les explorations au moyen de sondes multi-trous, ou bien par vélocimétrie laser à trois composantes, permettent d'étendre l'investigation au champ externe. Par le couplage des visualisations et des sondages, il est possible de décrire avec finesse et réalisme des écoulements tourbillonnaires résultant de décollements sur des obstacles de formes variées. Dans le cas où la surface du corps comporte une arête (vive ou arrondie), une ligne de séparation est généralement confondue avec la singularité. Cette ligne est l'origine d'une surface de séparation dont l'enroulement constitue un tourbillon primaire intense. Cette circonstance favori-

se la modélisation dans le cadre d'une approche fluide parfait puisqu'alors l'origine de la nappe est évidente. Toutefois, il se forme aussi dans ce cas des tourbillons dits secondaires, attachés à aucune particularité de la paroi, dont l'influence sur le champ est notable.

Sur un obstacle arrondi, dont le rayon de courbure est grand devant l'épaisseur de la couche limite locale, rien ne permet de fixer à priori la position de la, ou des, séparation(s). Si le corps comporte un nez pointu, les expériences tendent à montrer que - même à incidence modérée - les différentes séparatrices ont pour origine la pointe où s'accumulent les points critiques. Un tel degré de singularité est peu crédible physiquement. Il est probable que les cols ou noeuds origines des séparatrices sont en fait distincts et contenus dans un petit domaine au voisinage de la pointe qui, à une échelle suffisamment petite, est forcément arrondie.

Quand le corps présente un fort émoussement, les points critiques n'ont plus de raison de se placer en un point singulier de la surface. Toutefois, pour le corps considéré, qui est proche de nombreuses configurations pratiques, ceux-ci sont tous situés dans la région du nez, seul le noeud d'attachement "principal" étant clairement détecté par les visualisations. Le procédé de l'enduit visqueux - dont l'effet perturbateur est en outre non négligeable dans les régions où la couche limite a une épaisseur comparable à celle du film d'huile - manque de finesse pour résoudre le spectre réel et mettre en évidence les autres points critiques dont l'existence est nécessaire pour assurer la cohérence topologique de l'ensemble.

Sauf à de très grandes incidences, la convergence des lignes de frottement vers la (ou les) séparatrice(s) ne se produit qu'à une certaine distance en aval du nez ou de la pointe de la maquette. Auparavant, rien ne distingue la ligne de séparation des autres lignes de frottement. Tout au long de ce parcours amont, les structures tourbillonnaires, qui naissent *obligatoirement* dans la région des points critiques, sont immergées au sein de la couche limite et comportent une faible concentration de rotationnel. Ce n'est que lorsque la convergence a lieu que ces structures quittent la paroi en emportant avec elles du rotationnel pour former des tourbillons bien identifiables. On peut alors véritablement parler de *décollement* au sens commun du terme.

La représentation des phénomènes très fins à l'origine des séparatrices exige une grande précision de calcul avec l'emploi de maillages extrêmement raffinés. Il est probable qu'une telle qualité du calcul n'est pas indispensable pour la grande majorité des applications. Ainsi, des méthodes capables de définir les lignes de séparation seulement à partir du moment où celles-ci deviennent bien caractérisées sont certainement suffisantes comme moyen de prévision du décollement, même si la cohérence topologique du champ calculé n'est pas assurée. Les structures fines gommées par le manque de raffine-

ment de la discrétisation influent alors peu sur la qualité finale du résultat. Il en va bien sûr autrement pour la compréhension physique profonde du phénomène ainsi que pour les applications où l'échelle de ces structures est comparable à celle du dispositif, comme c'est le cas des écoulements de canal.

Enfin, sous l'action d'un gradient de pression adverse, ou d'une onde choc, il est fréquent que les tourbillons à fort taux de rotation se désorganisent brusquement. Cet éclatement de la structure tourbillonnaire demeure un phénomène encore mal élucidé, surtout sur le plan théorique, et à ce titre il mérite des études approfondies.

#### REMERCIEMENTS

L'étude sur l'arrière-corps ARIANE 5 a été financée par le Centre National d'Etudes Spatiales et les études sur les enroulements tourbillonnaires ont bénéficié du soutien financier de la Direction des Recherches Etudes et Techniques ainsi que du Service Technique des Programmes Aéronautiques du Ministère de la Défense. L'auteur remercie C. Berner de l'ISL pour lui avoir permis de présenter les résultats sur l'arrière-corps en incidence. Enfin, il exprime sa gratitude à C. Quelin pour sa contribution à la confection des figures illustrant cet exposé.

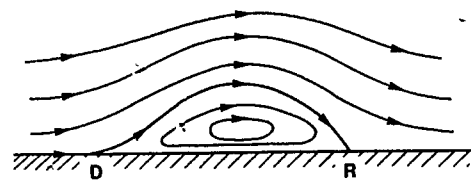
#### 6 - REFERENCES

- BARBERIS, D. (1986) "Calcul de la couche limite tridimensionnelle en modes direct ou inverse sur des obstacles quelconques". La Recherche Aérospatiale, N° 1986-3 (Mai-Juin 1986)
- BENAY, R.; DELERY, J. et POT, T. "Analyse expérimentale de l'écoulement dans un canal transsonique tridimensionnel". La Recherche Aérospatiale, N° 1986-6, pp. 399-414 (Novembre-Décembre 1986)
- BERNER, C. (1989) "Measurements and Interpretation of 3-D High Speed Flows". Proceedings of the 3rd International Conference on Laser Anemometry, Swansea, Royaume-Uni, 26-29 Septembre 1989 et ISL-Report CO 242/89
- BERNER, C. et DUPEROUX, J. P. (1990) "Mesures simultanées des trois composantes du vecteur vitesse dans le sillage d'arrière-corps à symétrie de révolution et en incidence". ISL Report (en cours de publication)
- BORREL, M.; MONTAGNE, J.-L.; DIET, J.; GUILLEN, Ph. et LORDON, J. (1988) "Méthode de calcul d'écoulements autour de missiles tactiques à l'aide d'un schéma décentré". La Recherche Aérospatiale, N° 1988-2
- CAMBIER, L. et ESCANDE, B. (1989) "Navier-Stokes Simulation of a Shock-Wave / Turbulent Boundary - Layer Interaction in a Three-Dimensional Channel". AIAA Paper N° 89-1851 (Juin 1989)

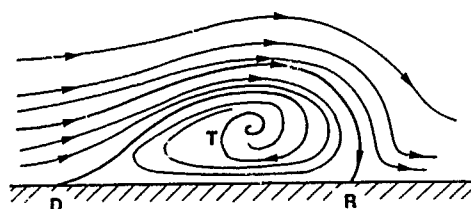
- CHAMPIGNY, P. et BAUDIN, D. (1990) "Ecoulement tourbillonnaire sur fuselage de missile. Etude expérimentale et modélisation". Symposium AGARD/FDP sur L'aérodynamique des écoulements tourbillonnaires, Scheveningen, Pays-Bas, 1-4 Octobre 1990
- CHANETZ, B. (1986) "Contribution à l'étude du décollement tridimensionnel en écoulement turbulent incompressible". Thèse de Doctorat, Université Claude Bernard de Lyon (Septembre 1986)
- CHANETZ, B. et DELERY, J. (1988) "Etude expérimentale du décollement turbulent sur un ellipsoïde - cylindre aplati". La Recherche Aérospatiale, N° 1988-3, pp. 59-77 (Mai-Juin 1988)
- CHIMA, R. V. et YOKOTA, J. W. (1990) "Numerical Analysis of Three-Dimensional Viscous Internal Flows". AIAA Journal, Vol. 28, N° 5, pp. 798-806 (Mai 1990)
- COPENING, G. et ANDERSON, J. (1989) "Numerical Solutions to Three-Dimensional Shock-Wave / Vortex Interactions at Hypersonic Speeds". AIAA Paper N° 89-0674 (Janvier 1989)
- COSTIS, C. E.; POLEN, D. M.; HOANG, N. T. et TELIONIS, D. P. (1987) "Laminar Separating Flow over a Prolate Spheroid". AIAA Paper N° 87-1212 (Juin 1987)
- DALLMANN, U. (1983) "Topological Structures of Three-Dimensional Flow Separation". DFVLR-IB N° 221-82
- DALLMANN, U. (1986) "On the Formation of Three - Dimensional Vortex Flow Structures". DFVLR-IB N° 221-85-A13
- DALLMANN, U. et SCHEWE, G. (1987) "On Topological Changes of Separating Flow Structures at Transition Reynolds Numbers". AIAA Paper N° 87-1266 (Juin 1987)
- DELERY, J. et LACAUX, R. G. (1987) "Prediction of Base-Flows". *Special Course on Missile Aerodynamics*, AGARD Report N° 754
- DELERY, J.; PAGAN, D. et SOLIGNAC, J.-L. (1987) "On the Breakdown of the Vortex Induced by a Delta Wing". Proceedings du Colloque *Vortex Control and Breakdown Behavior*, Gaden, Suisse, 6-7 Avril 1987
- DELERY, J.; HOROWITZ, E.; LEUCHTER, O. et SOLIGNAC, J.-L. (1984) "Etudes fondamentales sur les écoulements tourbillonnaires". La Recherche Aérospatiale, N° 1984-2, pp. 81-104 (Mars-Avril 1984)
- DOERFFER, P. et DALLMANN, U. (1989a) "Reynolds Number Effect on Separation Structures at Normal Shock-Wave / Turbulent Boundary-Layer Interaction". AIAA Journal, Vol. 27, N° 9, pp. 1206-1212 (Septembre 1989)
- DOERFFER, P. et DALLMANN, U. (1989b) "Mach Number Dependence of Flow Separation Induced by Normal Shock-Wave / Turbulent Boundary-Layer Interaction at a Curved Wall". AIAA Paper N° 89-0353 (Janvier 1989)
- EICHELERENNER, E. A. et OUDARD, A. (1955) "Méthode de calcul de la couche limite tridimensionnelle". ONERA Publication N° 76
- ELSENAAR, A. et ERIKSSON, G. (1986) Proceedings of the Symposium on the *International Vortex Flow Experiment on Euler Code Validation*, Stockholm, 1-3 Octobre 1986, NLR MP-84078U
- ELSENAAR, A. et BUTEFISCH, K. A. (1988) "Experimental Study on Vortex and Shock-Wave Development on a 65° Delta Wing". *Symposium Transsonicum III*, Eds. J. Zierep et H. Oertels, Springer-Verlag
- ESCUDIER, M. (1988) "Vortex Breakdown: Observations and Explanations". *Progress in Aerospace Sciences*, Vol. 25, N° 2, pp. 189-229
- FIDLER, J. E.; NIELSEN, J. N. et SCHWIND, R. G. (1977) "An Investigation of Slender-Body Wake Vortices". AIAA Paper N° 77-7 (Janvier 1977)
- FUJII, K. et SCHIFF, L. B. (1989) "Numerical Simulation of Vortical Flows over a Strake-Delta Wing". AIAA Journal, Vol. 27, N° 9, pp. 1153-1162 (Septembre 1989)
- GINOUX, J. (1958) "Experimental Evidence of Three - Dimensional Perturbations in the Reattachment of a Two-Dimensional Laminar Boundary-Layer". VKI TN-1
- GREEN, J. E. (1970) "Interactions Between Shock - Waves and Turbulent Boundary-Layers". *Progress in Aerospace Sciences*, Vol. 11, Ed. D. Küchemann et al., Pergamon Press, Oxford
- HAN, T. (1989) "Computational Analysis of Three - Dimensional Turbulent Flow around a Bluff Body in Ground Proximity". AIAA Journal, Vol. 27, N° 9, pp. 1213-1219 (Septembre 1989)
- HARTWICH, P. M. et HALL, R. M. (1990) "Navier - Stokes Solutions for Vortical Flows over a Tangent - Ogive Cylinder". AIAA Journal, Vol. 28, N° 7, pp. 1171-1179 (Juillet 1990)
- HITZEL, S. M. et SCHMIDT, W. (1984) "Slender Wings with Leading-Edge Vortex Separation: a Challenge for Panel Methods and Euler Solvers". *Journal of Aircraft*, Vol. 21, N° 10, pp. 751-759 (Octobre 1984)
- HOANG, N. T.; TELIONIS, D. T. et JONES, G. S. (1990) "The Hemisphere - Cylinder at an Angle of Attack". AIAA Paper N° 90-0050 (Janvier 1990)
- HOEIJMAKERS, H. W. M.; VAATSTRA, W. et VERHAAGEN, N. G. (1983) "Vortex Flow over Delta and Double - Delta Wings". *Journal of Aircraft*, Vol. 20, N° 9, pp. 825-832 (Septembre 1983)
- HORNUNG, H. (1983) "The Vortex Skeleton Model for Three-Dimensional Steady Flows". AGARD CP N° 342

- HORNUNG, H. et PERRY, A. E. (1984) "Some Aspects of Three Dimensional Separation. Part I: Streamsurface Bifurcations". Z. Flugwiss. Weltraumforsch. 8, Heft 2, pp. 77-87
- HOROWITZ, E. (1984) "Contribution à l'étude de l'éclatement tourbillonnaire en écoulement compressible. Interaction onde de choc - tourbillon". Thèse de Docteur Ingénieur, Université Pierre et Marie Curie, Paris (Décembre 1984)
- HSU, C. H. et LIU, C. H. (1990) "Navier-Stokes Computation of Flow around a Round-Edge Double-Delta Wing". AIAA Journal, Vol. 28, N° 6, pp. 961-970 (Juin 1990)
- HUMMEL, D. (1976) "On Vortex Formation over a Slender Wing at Large Angles of Incidence". AGARD CP N° 247 (Janvier 1976)
- INGER, G. R. (1977) "Three-Dimensional Heat- and Mass Transfer Effects across High-Speed Reattaching Flows". AIAA Journal, Vol. 15, N° 3, pp. 383-389 (Mars 1977)
- JORGENSEN, L. H. et PERKINS, E. W. (1955) "Investigation of Some Wake Vortex Characteristics of an Inclined Ogive-Cylinder Body at Mach Number 1.98". NACA RM-A55E31 (Août 1955)
- JOULOT, A. (1990) Communication privée
- KAYNAK, U.; CANTWELL, B. J.; HOLST, T. L. et SORENSEN, R. L. (1986) "Numerical Simulation of Transonic Separated Flows over Low Aspect Ratio Wings". AIAA Paper N° 86-0508 (Janvier 1986)
- KEGELMAN, J. T. et ROOS, F. W. (1990) "The Flowfields of Bursting Vortices over Moderately Swept Delta Wings". AIAA Paper N° 90-0599 (Janvier 1990)
- KORDULLA, W.; VOLLMERS, H. et DALLMANN, U. (1986) "Simulation of Three-Dimensional Transonic Flow with Separation past a Hemisphere-Cylinder Configuration". AGARD CP N° 412
- LEGENBRE, R. (1952) "Ecoulement au voisinage de la pointe avant d'une aile à forte flèche aux incidences moyennes". La Recherche Aéronautique, N° 30, pp. 3-8
- LEGENBRE, R. (1956) "Séparation de l'écoulement laminaire tridimensionnel". La Recherche Aéronautique, N° 51 (Novembre-Décembre 1956)
- LEGENBRE, R. (1965) "Lignes de courant d'un écoulement continu". La Recherche Aérospatiale N° 105, pp. 3 - 9 (Mars-Avril 1965)
- LEGENBRE, R. (1977) "Lignes de courant d'un écoulement permanent. Décollement et séparation". La Recherche Aérospatiale, N° 197-6, pp. 327-335 (Novembre-Décembre 1977)
- LIGHTHILL, J. M. (1963) "Attachment and Separation in Three Dimensional Flow". In *Laminar Boundary Layer Theory*, Section II, 2-6, pp. 72-82, Ed. L. Rosenhead, Oxford University Press
- LORDON, J.; FARE, J.C. et PAGAN, D. (1990) "Supersonic Vortex Flows around a Missile Body. Basic Experiment and Euler Numerical Modélisation". AGARD/FDP Symposium sur l'Aérodynamique des missiles, Friedrichshafen, R.F.A., 23-26 Avril 1990
- MASKELL, E. C. (1955) "Flow Separation in Three Dimensions". RAE Aero Report N° 2565 (Novembre 1955)
- MEHTA, R. D. et LIM, T. T. (1986) "Flow Visualization Study of a Vortex / Wing Interaction". NASA TM-86 656
- MEIER, H. U.; KREPLIN, H. P.; LANDHAUSER, A. et BAUMGARTEN, D. (1984) "Mean Velocity Distribution in Three-Dimensional Boundary-Layers Developing on a 1:6 Prolate Spheroid with Artificial Transition". DFVLR-IB N° 222-24-A11
- METWALLY, O.; SETTLES, G. S. et HORSTMAN, C. (1989) "An Experimental Study of Shock-Wave / Vortex Interaction". AIAA Paper N° 89-0082 (Janvier 1989)
- MOLTON, P. (1986) "Aile delta en écoulement incompressible. Etude expérimentale à F2". ONERA RT N° 36/1147 AN (Décembre 1986)
- MONNERIE, B. et MERLE, H. (1968) "Etude de l'écoulement supersonique et hypersonique autour d'une aile élançée en flèche". AGARD CP N° 30
- NARAYAN, K. Y. et HARTMANN, K. (1988) "Transonic and Supersonic Flow past a 65° Delta Wing with Rounded Leading Edges. Analysis of Experimental Data". DFVLR-FB N° 88-44
- OSWATITSCH, K. (1958) "Die Ablösungsbedingung von Grenzschichten". In *Grenzschichtforschung*, ed. H. Görtler, pp. 357-367, Springer-Verlag
- PAGAN, D. (1989) "Contribution à l'étude expérimentale et théorique de l'éclatement tourbillonnaire en air incompressible". Thèse de Doctorat, Université Pierre et Marie Curie, Paris (Novembre 1989)
- PAGAN, D. et SOLIGNAC, J.-L. (1985) "Etude expérimentale de la formation des nappes tourbillonnaires sur une aile delta en écoulement incompressible". ONERA RTS N° 34/1147 AY (Avril 1985)
- PAGAN, D. et SOLIGNAC, J.-L. (1986) "Etude expérimentale de l'éclatement d'un tourbillon engendré par une aile delta". La Recherche Aérospatiale, N° 1986-3, pp. 197-219 (Mai-Juin 1986)
- PAGAN, D. et MOLTON, P. (1990) "Etude expérimentale du système tourbillonnaire engendré par un fuselage de missile en incidence. Première partie: couche limite laminaire". ONERA RT N° 40/1147AY (Janvier 1990)
- PEAKE, D. J. et TOBAK, M. (1980) "Three-Dimensional Interactions and Vortical Flows with Emphasis on High Speed". AGARDograph N° 252 (Mars 1980)

- PERRY, A. E. et HORNUNG, H. (1984) "Some Aspects of Three-Dimensional Separation. Part II: Vortex Skeleton". Z. Flugwiss. Weltraumforsch. 8, Heft 3, pp. 155-160
- PERRY, A. E. et FAIRLIE, B. D. (1974) "Critical Points in Flow Patterns". Adv. in Geophysics, B-18, pp. 299-315
- PERRY, A. E. et CHONG, M. S. (1987) "A Description of Eddy Motions and Flow Patterns Using Critical Point Concepts". Ann. Rev. of Fluid Mech., Vol. 19, pp. 125-155
- POINCARÉ, H. (1892) "Les points singuliers des équations différentielles". C. R. Académie des Sciences de Paris, 13-2-1892 et Oeuvres Complètes, Vol. 1
- PONTON, A. J. C. et JOHNSON, G. A. (1989) "The Analysis and Modelling of Body Vortex Flowfields around Missile Configurations and their Interaction with Lifting Surfaces at Subsonic and Supersonic Speeds". *The Prediction and Exploitation of Separated Flows*, The Royal Aeronautical Society, Paper N° 26
- REDA, D. C. et MURTHY, J. D. (1972) "Shock-Wave / Turbulent Boundary-Layer Interactions in Rectangular Channels". AIAA Paper N° 72-715
- REIJASSE, Ph. et DELERY, J. (1989) "Analyse expérimentale de l'écoulement au culot de l'arrière-corps du lanceur ARIANE 5. Exploitation des résultats". ONERA Rapport Final N° 6/4362AY (Novembre 1989)
- RIZZETTA, D. P. et SHANG, J. S. (1986) "Numerical Simulation of Leading Edge Vortex Flows". AIAA Journal, Vol. 24, N° 2, pp. 237-245 (Février 1986)
- RIZZI, A. W. et ERIKSSON, L. E. (1984) "Computation of Flow around Wings Based on the Euler Equations". Journal of Fluid Mechanics, Vol. 148, pp. 45-71
- ROSHKO, A. et THOMKE, G. J. (1966) "Observations of Turbulent Reattachment behind an Axisymmetric Downstream Facing Step in Supersonic Flow". AIAA Journal, Vol. 4, N° 6, pp. 975-980 (Juin 1966)
- SCHOFIELD, W. H. (1985) "Turbulent Boundary-Layer Development in an Adverse Pressure Gradient after an Interaction with a Normal Shock-Wave". J. Of Fluid Mech., Vol. 154
- SETTLES, G. S.; FITZPATRICK, T. J. and BOGDONOFF, S. M. (1979) "A Detailed Study of Attached and Separated Compression Corner Flowfields in High Reynolds Number Supersonic Flow". AIAA Journal, Vol. 17, N° 6, pp. 579-585 (Juin 1979)
- SICLARI, M. J. et DEL GUIDICE, P. (1990) "Hybrid Finite Volume Approach to Euler Solutions for Supersonic Flows". AIAA Journal, Vol. 28, N° 1, pp. 66-74 (Janvier 1990)
- SOLIGNAC, J.-L.; PAGAN, D. et MOLTON, P. (1989) "Etude expérimentale de l'écoulement à l'extrados d'une aile delta en régime incompressible". La Recherche Aéronautique, N° 1989-6, pp. 47-65 (Novembre-Décembre 1989)
- TAYLOR, S. L.; KJELGAARD, S. O.; WESTON, R. P.; THOMAS, J. L. et SELLERS III, W. L. "Experimental and Computational Study of the Subsonic Flow about a 75° Swept Delta-Wing". AIAA Paper N° 87-2425 (Août 1987)
- THOMAS, J. L. et NEWSOME, R. W. (1989) "Navier - Stokes Computations of Lee-Side Flows over Delta Wings". AIAA Journal, Vol. 27, N° 12, pp. 1673-1679 (Décembre 1989)
- TOBAK, M. et PEAKE, D. J. (1978) "Topology of Three - Dimensional Separated Flows". Ann. Rev. of Fluid Mech., Vol. 14, pp. 61-85
- VOLLMERS, H.; KREPLIN, H. P. et MEIER, H. U. (1983) "Separation and Vortical-Type Flow Around a Prolate Spheroid. Evaluation of Relevant Parameters". AGARD CP-342
- WANG, K. C. (1975) "Boundary-Layer over a Blunt Body at Low Incidence with Circumferential Reversed Flow". J. Fluid Mech., Vol. 72, Part 1, pp. 49-65
- WANG, K. C. (1983) "On the Dispute about Open Separation". AIAA Paper N° 83-0292 (Janvier 1983)
- WARD, K. C. et KATZ, J. (1989) "Topology of the Flow Structures Behind an Inclined Projectile: Parts A and B". J. of Aircraft, Vol. 26, N° 11, pp. 1016-1031 (Novembre 1989)
- WERLE, H. (1960) "Sur l'éclatement des tourbillons d'apex d'une aile delta aux faibles vitesses". La Recherche Aéronautique, N° 74, pp. 23-30
- WERLE, H. (1975) "Ecoulements décollés. Etude phénoménologique à partir de visualisations hydrodynamiques". ONERA TP N° 1975-14
- WERLE, H. (1985) "Principaux types de décollements libres observés sur maquettes ellipsoïdales". ONERA Note Technique N° 1985-7
- WONG, T. C.; KANDIL, O. A. et LIU, C. H. (1989) "Navier - Stokes Computations of Separated Vortical Flows past Prolate Spheroid at Incidence". AIAA Paper N° 89-0553 (Janvier 1989)
- YANTA, W. J. et WARDLAW Jr., A. B. (1981) "Flow-field about and Forces on Slender Bodies at High Angles of Attack". AIAA Journal, Vol. 19, N° 3, pp. 296-302 (Mars 1981)
- YANTA, W. J. et WARDLAW Jr., A. B. (1982) "The Secondary Separation Region on a Body at High Angles of Attack". AIAA Paper N° 82-0343 (Janvier 1982)



a - Ecoulement bidimensionnel



b - Ecoulement tridimensionnel

Fig. 1 - Conceptions simples du décollement

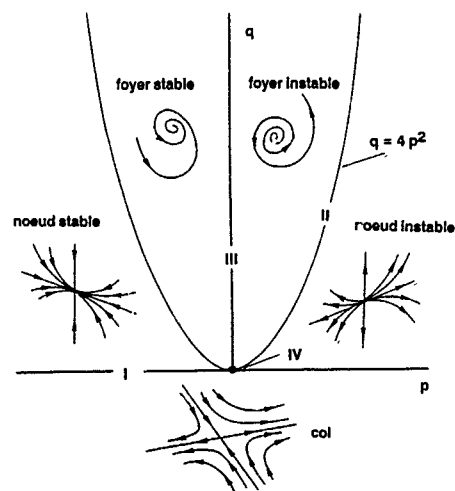
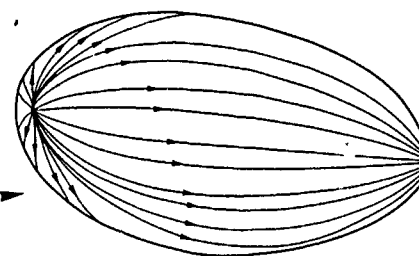
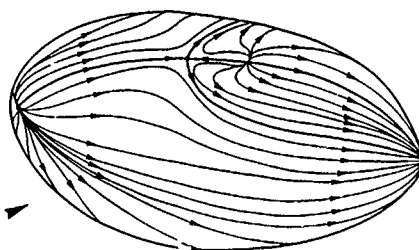


Fig. 2 - Classification des points critiques



a - Ecoulement non décollé



b - Ecoulement décollé

Fig. 4 - Décollement sur une obstacle tridimensionnel

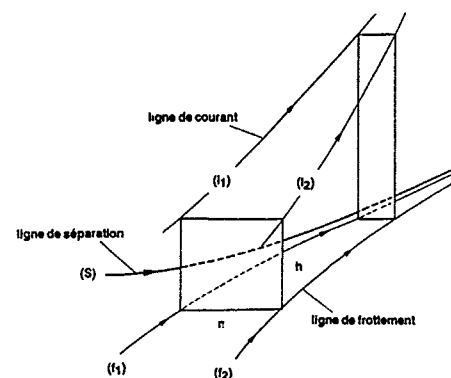
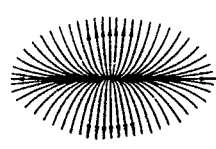
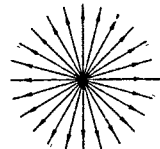


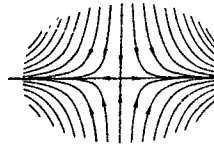
Fig. 5 - Ecoulement au voisinage d'une ligne de séparation



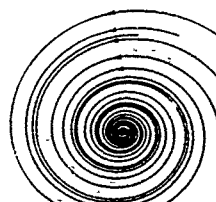
a - Noeud d'attachement



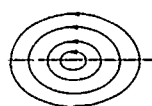
b - Noeud isotrope



c - Col



d - Foyer



e - Centre (région III)



f - Noeud-col (région I)

Fig. 3 - Trajectoires au voisinage d'un point critique



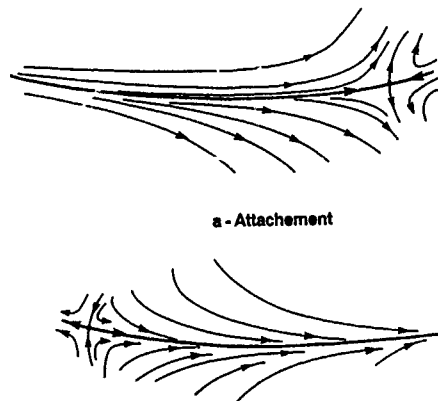


Fig. 6 - Lignes séparatrices

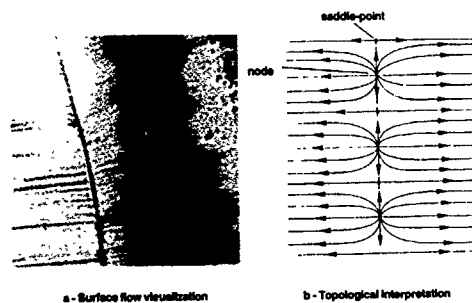


Fig. 7 - Recollement en écoulement bidimensionnel

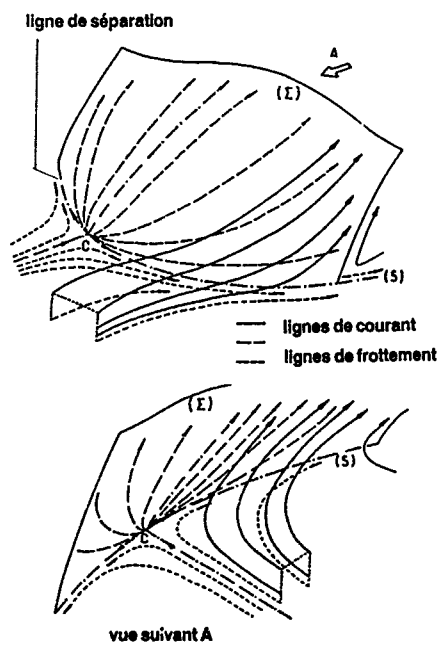


Fig. 8 - Surface de séparation

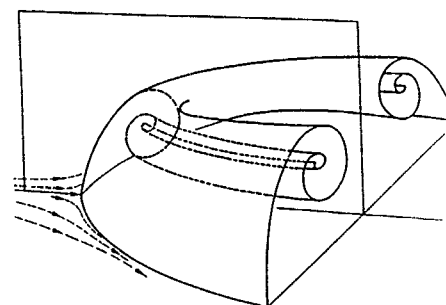
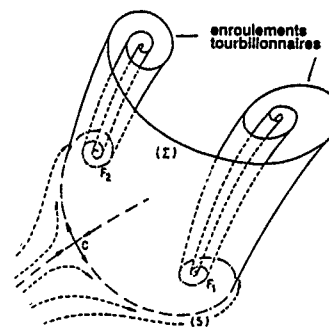


Fig. 9 - Formation des tourbillons

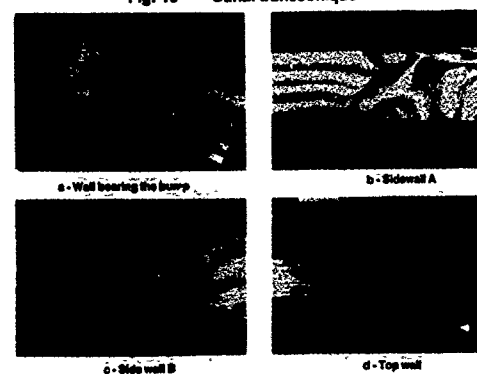
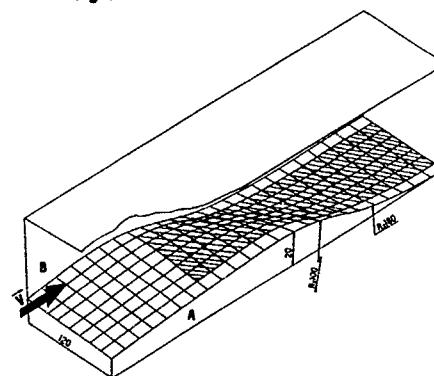


Fig. 11 - Canal transsonique. Visualisations pariétales

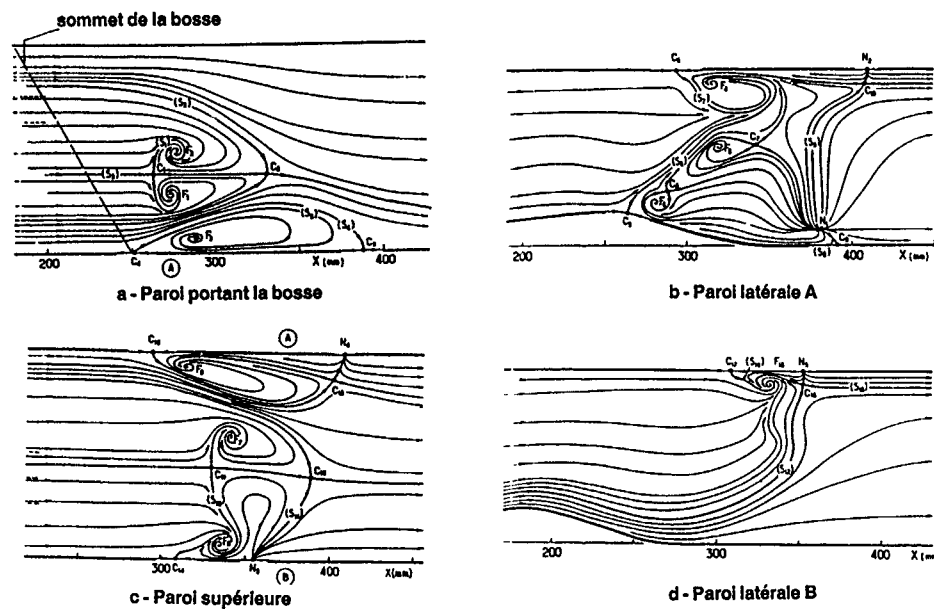


Fig. 12 - Canal transsonique. Interprétation des spectres pariétaux

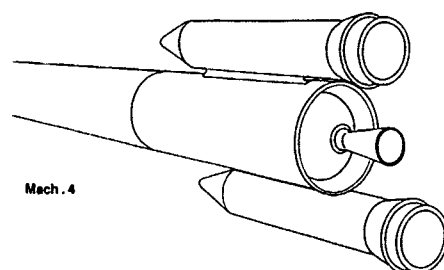


Fig. 13 - Arrière-corps du lanceur ARIANE 5



Fig. 14 - Arrière-corps ARIANE 5. Visualisations striescopiques

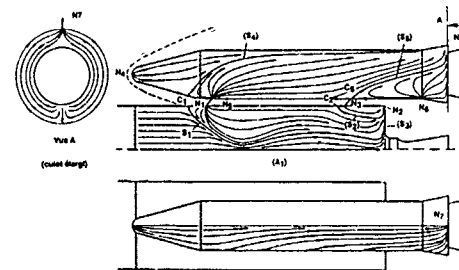


Fig. 15 - Arrière-corps ARIANE 5. Interprétation du spectre pariétal

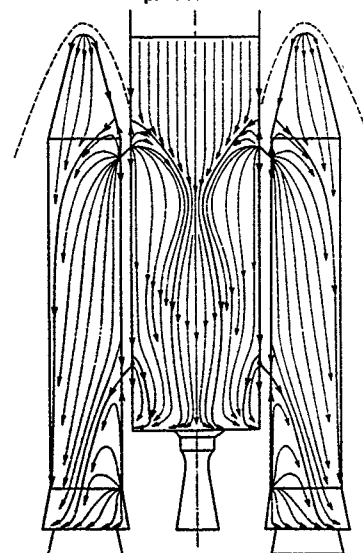


Fig. 16 - Arrière-corps ARIANE 5. Ensemble du spectre pariétal

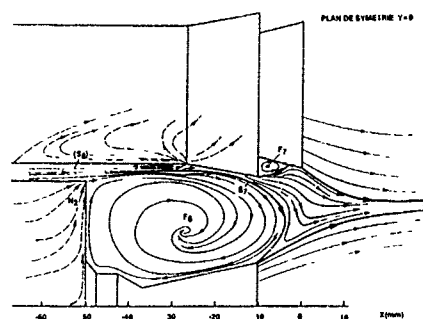


Fig. 17 - Arrière-corps ARIANE 5.  
Ecoulement dans un plan  
de symétrie

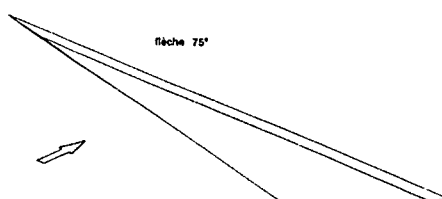


Fig. 18 - Aile delta à bord d'attaque aigu

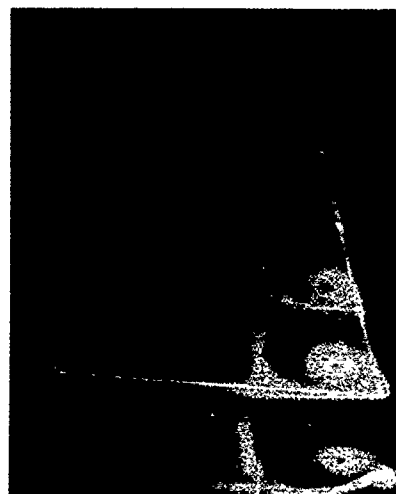


Fig. 19 - Aile delta à bord d'attaque aigu.  
Visualisation par plan laser

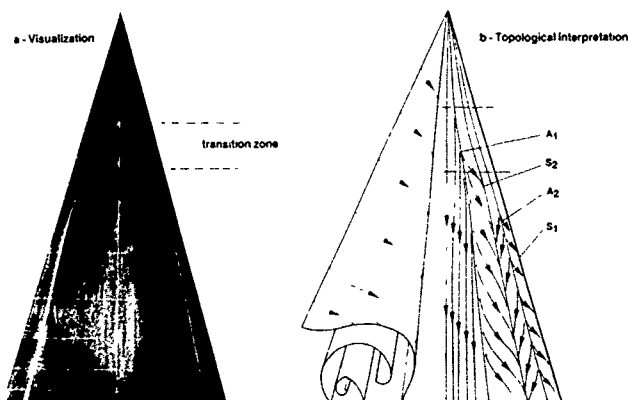


Fig. 20 - Aile delta à bord d'attaque aigu.  
Spectre pariétal. Incidence: 7,5°

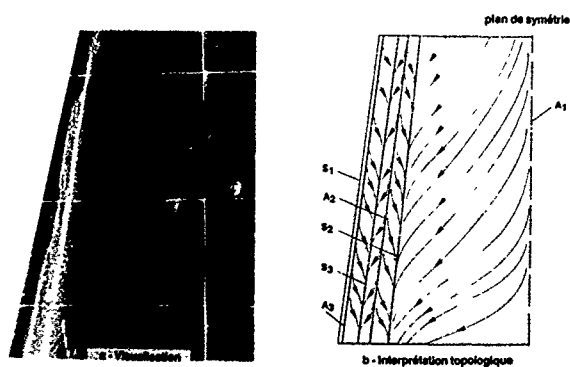


Fig. 21 - Aile delta à bord d'attaque aigu.  
Spectre pariétal. Incidence: 20°

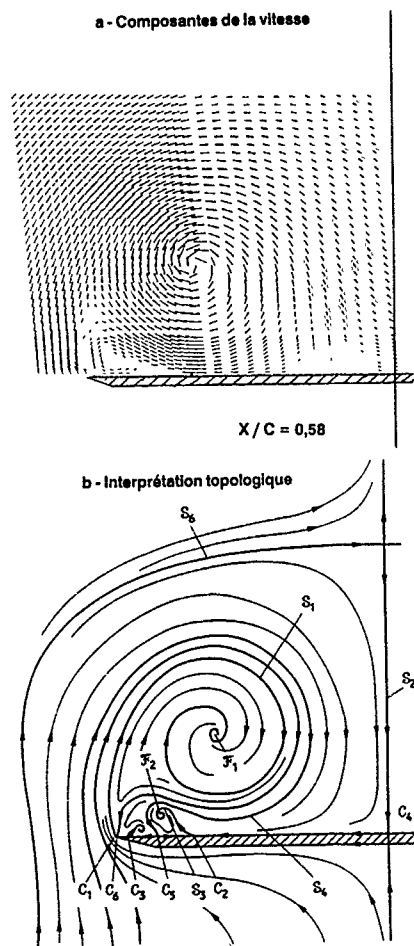


Fig. 22 - Aile delta à bord d'attaque aigu.  
Champ transversal. Incidence:  $20^\circ$

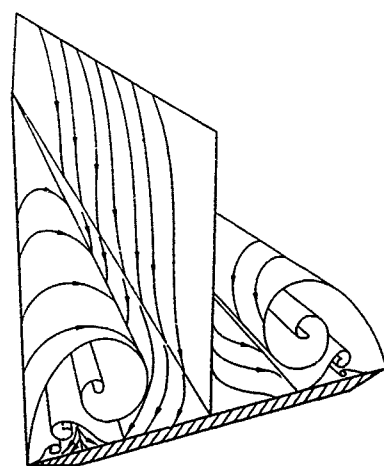
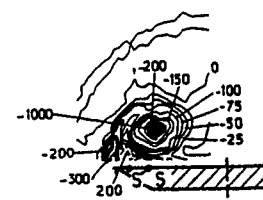
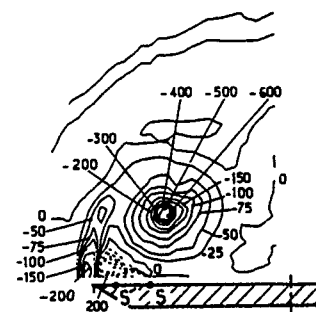


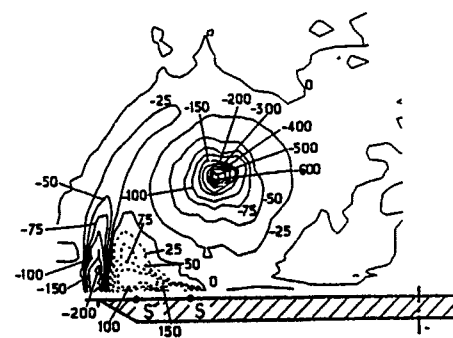
Fig. 23 - Aile delta à bord d'attaque aigu.  
Organisation de l'écoulement. Incidence:  $20^\circ$



$X / C = 0,20$



$X / C = 0,36$



$X / C = 0,58$

Fig. 24 - Aile delta à bord d'attaque aigu.  
Rotationnel dans des plans transversaux

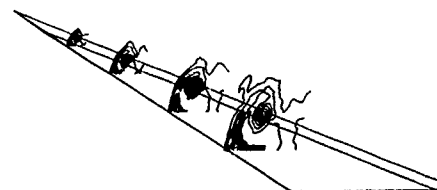


Fig. 25 - Aile delta à bord d'attaque aigu.  
Répartitions de pression d'arrêt

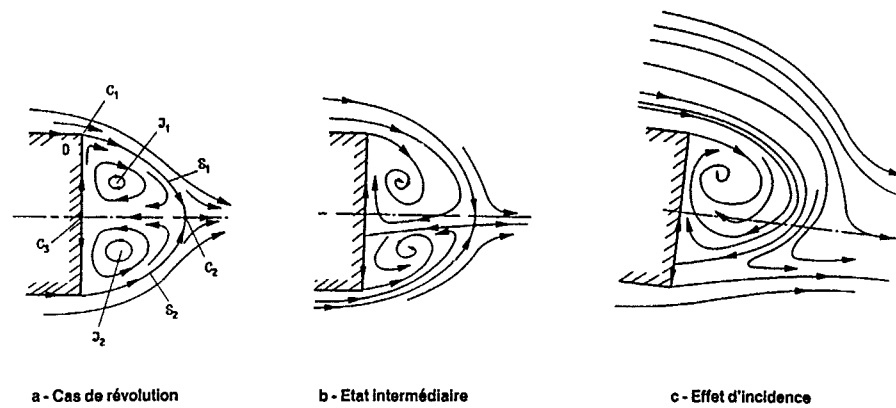


Fig. 26 - Ecoulement au culot d'un arrière-corps

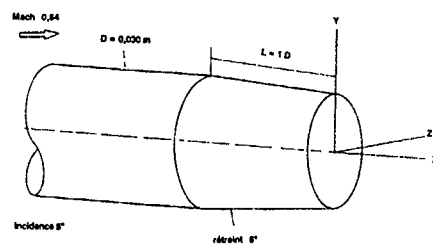
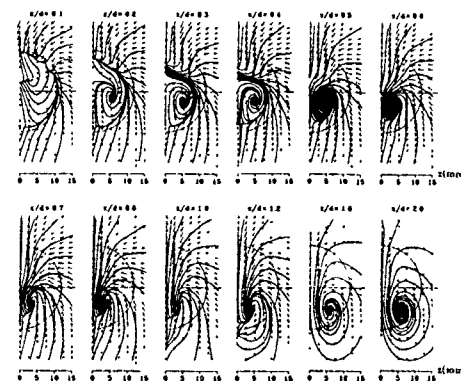
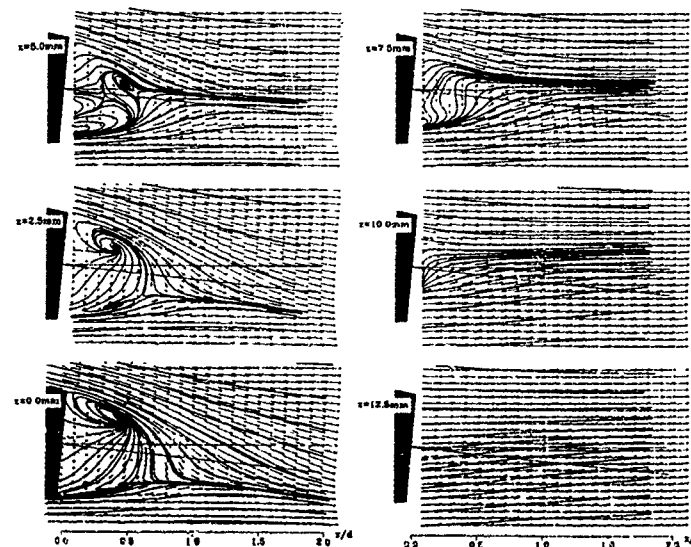


Fig. 27 - Arrière-corps de révolution (étude ISL)

Fig. 29 - Arrière-corps de révolution.  
Champs de vitesse transversauxFig. 28 - Arrière-corps de révolution.  
Champs de vitesse longitudinaux

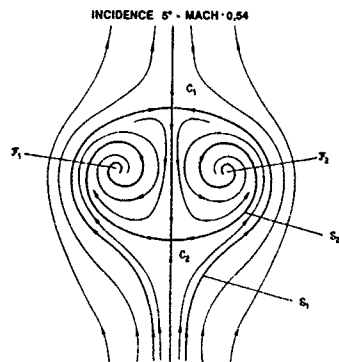


Fig. 30 - Arrière-corps de révolution.  
Topologie du champ transversal.  
Sillage lointain

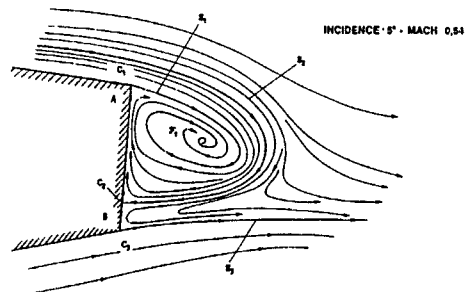


Fig. 31 - Arrière-corps de révolution.  
Topologie du champ longitudinal.  
Sillage proche

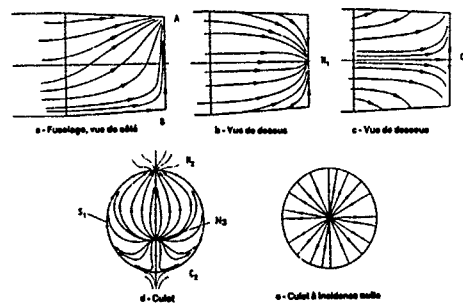


Fig. 32 - Arrière-corps de révolution.  
Spectre des lignes de frottement  
pariétales

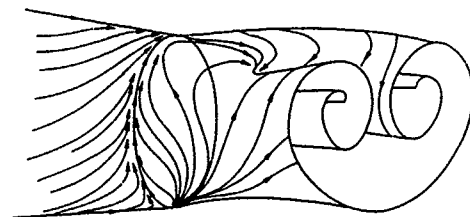


Fig. 33 - Arrière-corps de révolution.  
Surface de séparation principale

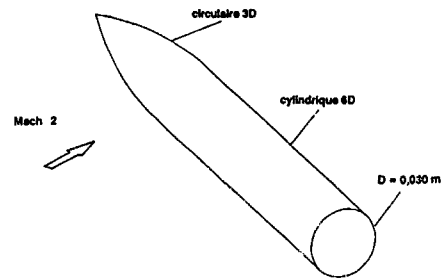


Fig. 34 - Corps élancé à nez pointu

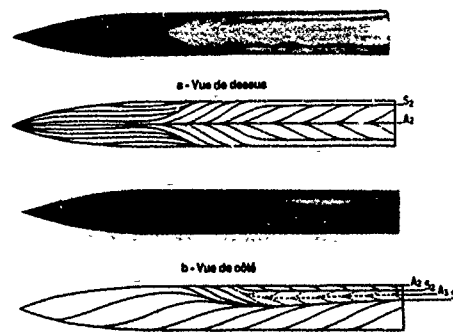


Fig. 35 - Corps élancé à nez pointu.  
Spectre pariétal. Incidence: 5°

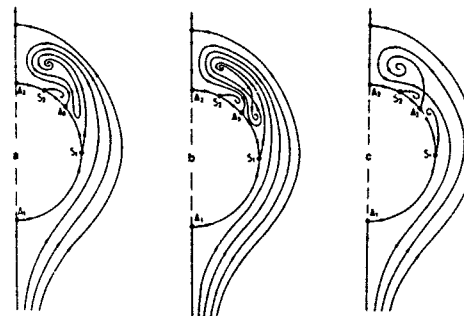


Fig. 36 - Corps élancé en incidence.  
Topologies possibles du champ  
transversal. Incidence 5°

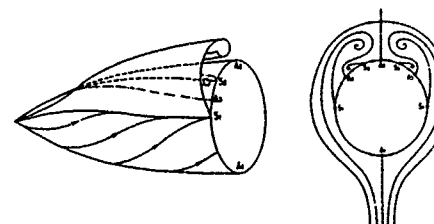


Fig. 37 - Corps élancé à nez pointu.  
Schéma des enroulements  
tourbillonnaires. Incidence: 5°

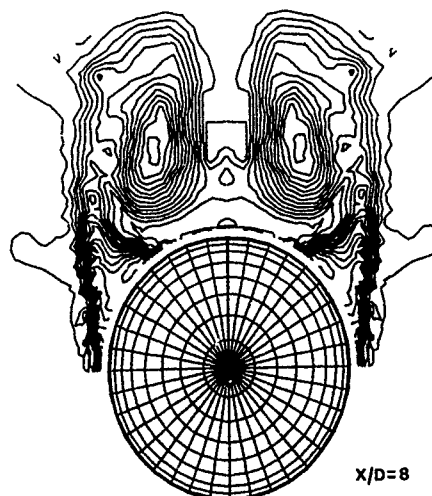
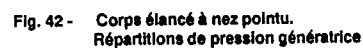
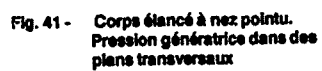
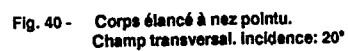
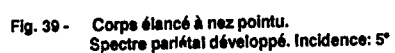




Fig. 44 - Ellipsoïde-cylindre aplati.  
Visualisations pariétales

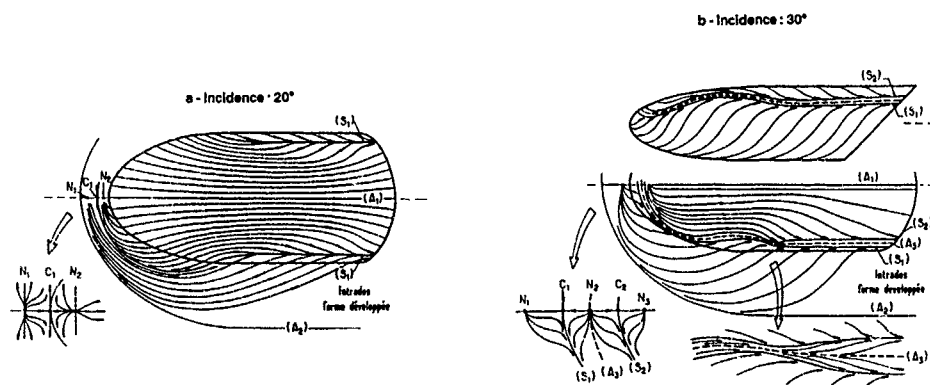


Fig. 45 - Ellipsoïde-cylindre aplati.  
Interprétation des spectres  
pariétaux

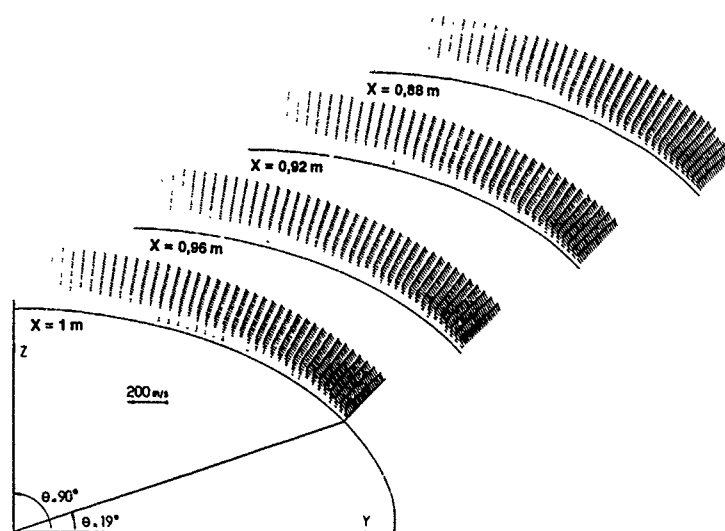


Fig. 46 - Ellipsoïde-cylindre aplati.  
Champ transversal amont. Incidence: 30°



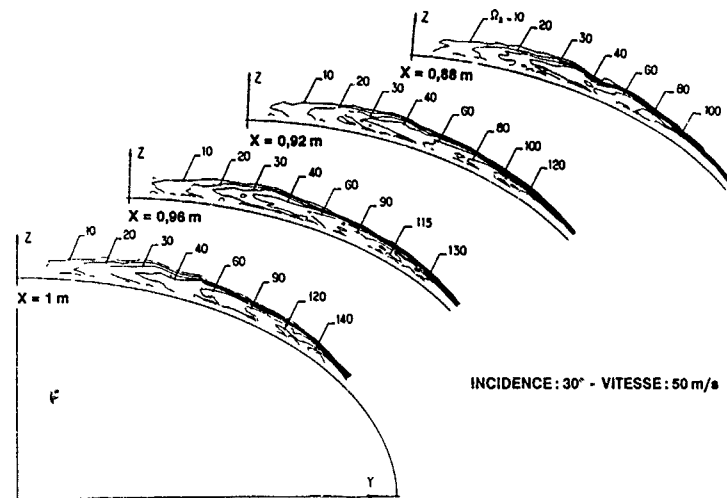


Fig. 47 - Ellipsoïde-cylindre aplati.  
Rotationnel axial dans des  
plans transversaux

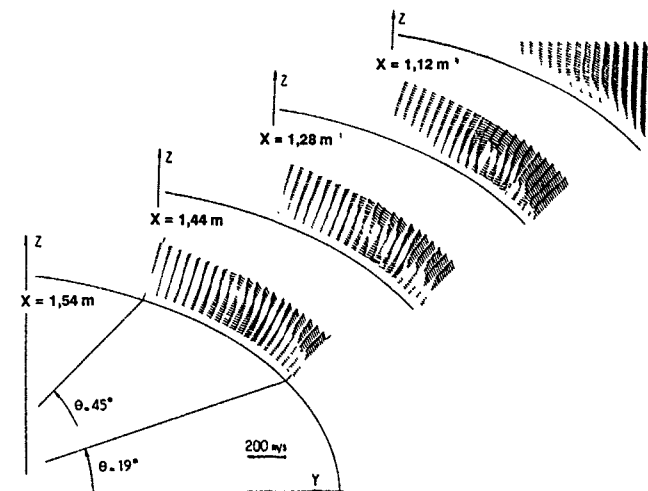


Fig. 48 - Ellipsoïde-cylindre aplati.  
Champ transversal aval. Incidence: 30°

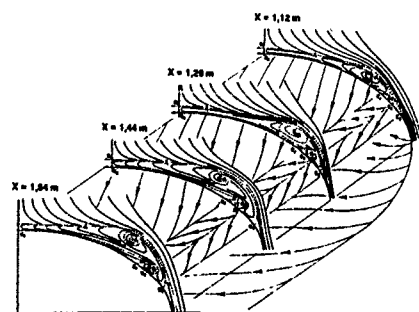


Fig. 49 - Ellipsoïde-cylindre aplati.  
Topologie du champ transversal.  
Incidence: 30°

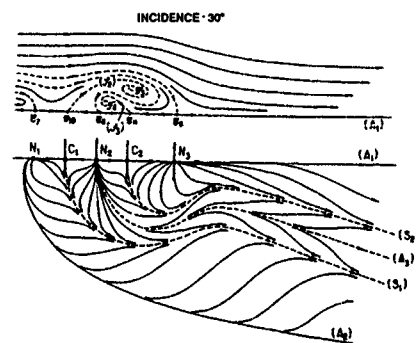


Fig. 50 - Ellipsoïde-cylindre aplati.  
Organisation de l'écoulement.  
Première interprétation

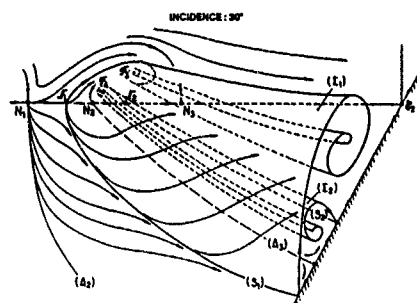


Fig. 51 - Ellipsoïde-Cylindre aplati.  
Surfaces de séparation.  
Première interprétation

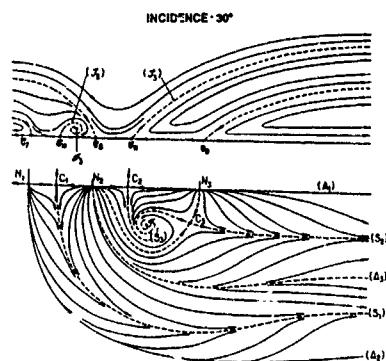


Fig. 52 - Ellipsoïde-cylindre aplati.  
Organisation de l'écoulement.  
Deuxième interprétation

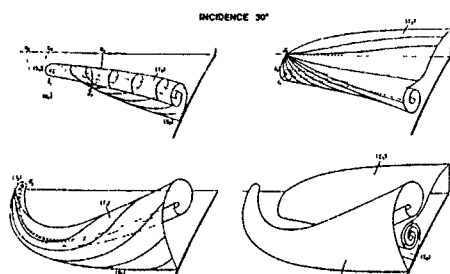


Fig. 53 - Ellipsoïde-Cylindre aplati.  
Surfaces de séparation.  
Deuxième interprétation

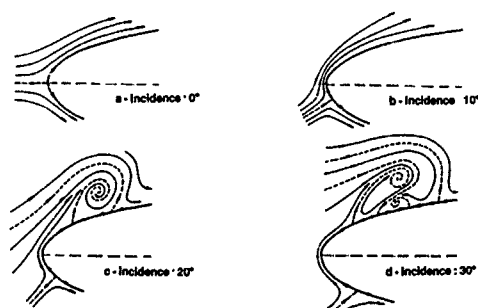


Fig. 54 - Bifurcations de l'écoulement  
dans le plan de symétrie

Sweep angle : 75°



Fig. 55 - Eclatement tourbillonnaire

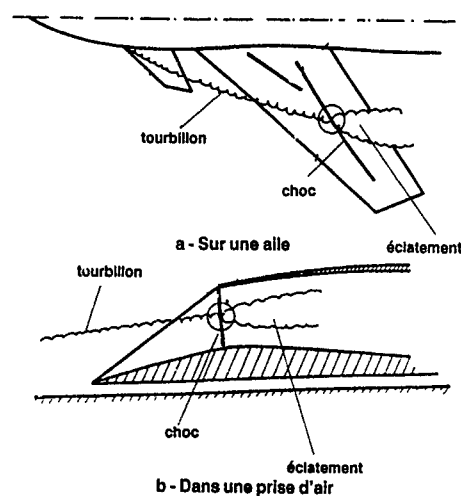


Fig. 56 - Interaction onde choc / tourbillon

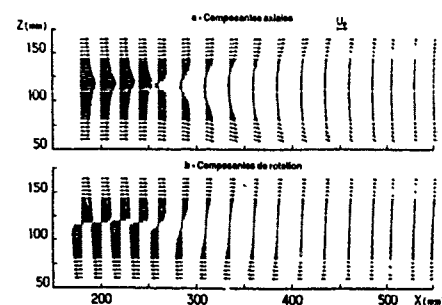


Fig. 57 - Eclatement tourbillonnaire.  
Champs de vitesse moyenne

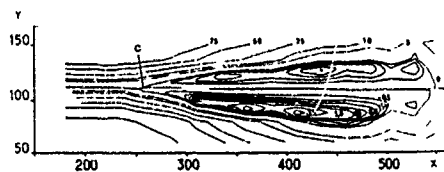


Fig. 58 - Eclatement tourbillonnaire.  
Organisation du champ moyen

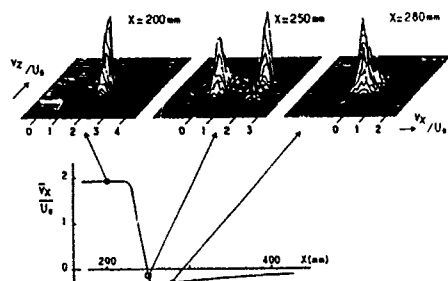


Fig. 59 - Aspects instationnaires de l'éclatement.  
Histogrammes de vitesse instantanée



Fig. 60 - Aspects instationnaires de l'éclatement.  
Visualisations instantanées.

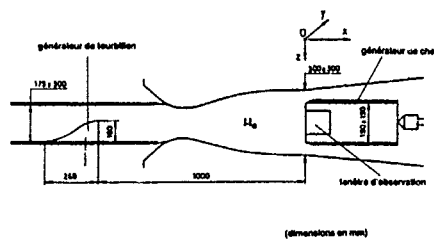


Fig. 61 - Interaction onde choc / tourbillon.  
Montage expérimental.

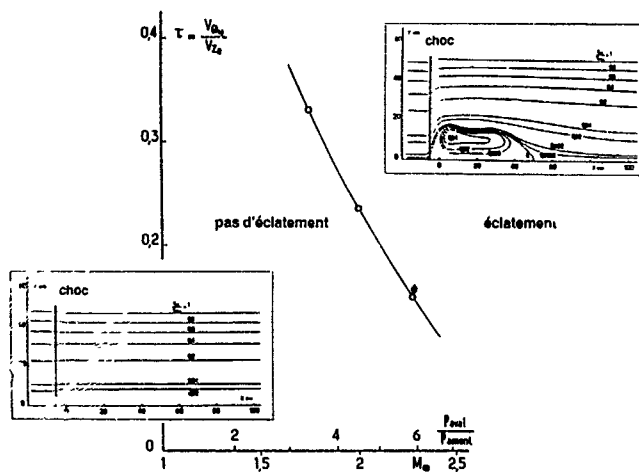


Fig. 62 - Interaction onde choc / tourbillon.  
Limite d'éclatement

# Breaking Down The Delta Wing Vortex

## The Role of Vorticity in the Breakdown Process

R. C. Nelson and K. D. Visser

Department of Aerospace and Mechanical Engineering  
University of Notre Dame  
Notre Dame, Indiana 46556  
The United States of America

### Abstract

Experimental x-wire measurements of the flowfield above a 70° and 75° flat plate delta wing were performed at a Reynolds number of 250,000. Grids were taken normal to the wing at various chordwise locations for angles of attack of 20° and 30°. Axial and azimuthal vorticity distributions were derived from the velocity fields. The dependence of circulation on distance from the vortex core and on chordwise location was also examined. The effects of nondimensionalization in comparison with other experimental data is made. The results indicate that the circulation distribution scales with the local semispan and grows in a nearly linear fashion in the chordwise direction. The spanwise distribution of axial vorticity is severely altered through the breakdown region and the amount of vorticity present appears to reach a maximum immediately preceding breakdown. The axial vorticity components with a negative sense, such as that found in the secondary vortex, seem to remain unaffected by changes in wing sweep or angle of attack, in direct contrast to the positive components. In addition, the inclusion of the local wing geometry into a previously derived correlation parameter allows the circulation of growing leading edge vortex flows to be reduced into a single curve.

### Nomenclature

$c$	chord
$r$	radial direction
$r_c$	vortex core radius
$P$	pressure
$Re$	Reynolds number
$s$	semi span
$s^*$	local semi span
$U_\infty$	freestream velocity
$V_i$	velocity in the $i$ direction
$x$	chordwise direction
$y$	spanwise direction
$z$	direction normal to wing surface
$\alpha$	angle of attack
$\epsilon$	apex half angle
$\Gamma$	circulation
$\Lambda$	sweep angle
$\phi$	angular direction
$\Omega_i$	vorticity in the $i$ direction

### Introduction

The underlying physics of the vortex structure above a delta wing planform, and more particularly the process by which the flowfield undergoes the rapid transition referred to as vortex breakdown, has been a topic of concern for many years in the aerospace field. At high angles of attack, the boundary layer on the lower surface of the delta wing flows outboard. The fluid separates at the sharp leading edge, forming a free shear layer which curves upward and rolls into a core of high vorticity on the top side of the wing. Each of the two counter-rotating vortices also contain axial flow components in the central core regions, around and along which the fluid spirals. This axial flow can attain velocities up to three times the freestream value.

Additional spanwise outflow is induced on the upper surface beneath the coiled vortex sheet. The fluid separates from the surface as it approaches the leading edge to form the so called "secondary vortices". The main effect of the secondary vortex is to displace the primary vortex upwards and inwards. The size and strength of the primary vortex increases with angle of incidence. It becomes the dominant steady flow feature through a wide range of practical flight attitudes. The acceleration of the flow in these vortices results in an incremental lift termed the "vortex" or "nonlinear" lift. As much as 30% of the total wing lift is attributable to the pressure distribution created on the wing surface by these leading edge vortices.

Delta wing performance is limited, however, by a phenomenon known as vortex breakdown. Breakdown, or "bursting" as it is sometimes referred to, is characterized by an increase in vortex diameter followed by large scale turbulent dissipation, and a decrease in the core's axial and circumferential velocity. This leads to a loss of lift and a reduction in the magnitude of the nose down pitching moment. Experimental, theoretical, and numerical investigations have been carried out in an effort to not only understand what is occurring, but to predict the onset of this drastic change in the flowfield. Efforts have included variation of all manner of possible parameters, including wing geometry, angle of attack, and Reynolds numbers.

Most investigators approach the study of delta wing vortical flows, however, by asking such questions as: "Why does vortex breakdown occur?" and "What factors influence breakdown?" A different perspective on the problem can be gained by posing the inverse question: "Why does the vortex manage to maintain a cohesive flow structure upstream of the transition/breakdown region?" In other words, with core velocities measured at over three times that of the freestream velocity and corresponding circumferential velocities approaching 2.5 times of freestream: "Why does it stay together for as long as it does, instead of breaking down immediately?" This was the motivation for the current investigation.

### Background

Many factors can influence vortex breakdown. Lambourne and Bryer [1] suggest the total pressure in the core and the adverse pressure gradient along the axis are essential factors in causing breakdown to occur. Harvey [2] observed that variation of the swirl of the flow in tube vortices indicated breakdown to be an intermediate stage between two types of flow: those that exhibit axial velocity reversal and those that do not.

Erickson [3] discusses in detail the effect of Reynolds number on vortex flow development. From experiments it appears that large scale vortex structures are determined primarily by convective transport mechanisms, implying an independence of Reynolds number. Erickson concludes that the majority of the phenomena observed in the delta wing flow field is dominated by potential flow effects associated with the external field, i.e. the pressure gradient.

An extensive literature review by Payne [4] on the factors which can influence breakdown is summarized below. Increasing the sweep angle or decreasing the angle of attack causes the location of the breakdown to move aft. The breakdown position will move forward during flow acceleration and remain so until the steady speed condition is reached whereupon it returns to its normal breakdown position [1]. The reverse is true for deceleration. The actual position of this breakdown is a strong function of the pressure gradient along the vortex, the initial axial core velocity, and the angle of sideslip, or yaw angle. An increase in the swirl of the flow or a larger adverse pressure gradient tends to promote the onset of breakdown. Thicker wings, rounded leading edges, lower Reynolds numbers, and of course more complex geometries can also substantially influence the location of breakdown. Kegelmann and Roos [5] investigated leading edge geometries, ranging from blunt rounded edges to leeward and windward bevels, and found the breakdown location to be strongly affected by these geometric variations. In addition, the maximum value of the lift curve was found to be significantly affected by this variation in leading edge shape.

Payne has also listed factors examined by other investigators in the literature which have been found

to have little or no influence on the breakdown position. Effects due to changes in the Reynolds number are small at high Reynolds numbers. This applies to sharp edged, thin delta wings at moderate angles of attack. The breakdown position seems to be independent of the turbulent breakdown of the shear layer near the leading edge. Attempts at altering the leading edge by Lambourne and Bryer [1], including a trip wire on the upper surface had no significant effect. Weitz [6] observed that variation of the trailing edge geometry of 70° sweep delta, diamond and arrow planforms, had a negligible effect on vortex breakdown location. Wentz also found [7] that the vortex breakdown region crossed the trailing edge at the same angle of attack for all these trailing edge configurations.

The complexities of this vortical flow are such that a complete analytical solution is difficult to obtain. Theories do exist that partially predict the occurrence of certain flow phenomena, such as vortex breakdown in which the vortex behavior changes dramatically, and to indicate the sensitivity of the breakdown region to the severity of axial pressure gradients. Several pertinent breakdown theories are summarized below, and a more extensive discussion can be found in Wedemeyer [8]:

Ludweig [9] has suggested that the spiral form of breakdown results from hydrodynamic instabilities in the flow due to upstream spiral disturbances. A similar view of breakdown was developed by Jones [10]. It has been proposed by Squire [11] that breakdown is a standing wave phenomenon. Once the flow is capable of supporting infinitesimal standing waves, downstream disturbances can propagate upstream and therefore disrupt the flow. Randall & Leibovich [12] contend that this is in fact a finite amplitude wave.

Another hypothesis is the view taken by Benjamin [13]. He suggests that breakdown is a finite transition (subcritical to supercritical) between conjugate flow states analogous to the hydraulic jump in open channel flows. While Squire postulated that the existence of waves leads to breakdown, Benjamin claims that the leading wave is the breakdown. Escudier [14] goes a step further by proposing a two stage (supercritical-supercritical supercritical-subcritical) transition. The first stage is isentropic while the latter is not. In addition, his analysis suggests breakdown occurs for a unique swirl number  $\Gamma / \pi r_c U_\infty$  which is equal to 1.414 for a Rankine vortex with an infinitesimally small core radius,  $r_c$ . In a theory analogous to boundary layer separation, Gartshore [15] concluded that breakdown occurred because of a diffusion of vorticity from the core of the vortex.

Several theories rely on the supposition that breakdown is predicted by the failure of the quasicylindrical approximations of the equations of motion. Hall [16], in 1966, suggested that breakdown is associated with some change in the flowfield outside the core, such as the rate of feeding of vorticity or the pressure. Bossel [17] used the ideas of Hall to estimate that a swirl angle, defined as  $\tan^{-1}(V_z / V_x)$ ,

of  $54.8^\circ$  anywhere in the vortex would cause flow stagnation. Mager [18] associated a singularity in the incompressible quasicylindrical momentum-integral solution with breakdown. Wilson [19] approached the problem in a similar manner to obtain a swirl parameter for thin delta wings in subsonic flow.

Grabowski and Berger [20], using solutions of the full, steady, axisymmetric Navier-Stokes equations, concurred with Hall [21] in that breakdown is the result of a critical retardation of the flow. As well, his results also showed that a vortex with sufficient swirl can be reduced to the critical breakdown state by diffusion of vorticity, flow divergence and pressure forces.

A recent hypothesis has been proposed by Brown and Lopez [22] on the physical mechanism governing vortex breakdown which occurs in confined cylindrical flows. Variation of the problem parameters has resulted in an axial flow deceleration great enough to sustain a stagnant flow region containing recirculating fluid. This phenomena is very similar to that seen in cylindrical tubes and over delta wings. Their basic argument is that the physical mechanisms involved in the breakdown process rely on the production of negative azimuthal vorticity, that is

$$\Omega_\theta = \frac{\partial V_r}{\partial x} - \frac{\partial V_x}{\partial r}$$

which results from a tilting and stretching of the predominantly axial vorticity vector as seen in Figure 1. They then address the question of why the strong vortical core diverges by considering the Euler equation of the radial momentum and comment on how this type of mechanism would apply to a delta wing flowfield. Their analysis eventually leads to the following inequality

$$\frac{V_\theta^2}{r} - \frac{1}{\rho} \frac{\partial P}{\partial r} > 0$$

which would then initiate breakdown. Brown and Lopez hypothesize that vorticity diffusion leads to a radial redistribution of the circulation and a stretching and tilting of vortex lines due to a local increase of the tangential velocity,  $V_\theta$ . This is followed by a reduction in the initially positive azimuthal component of vorticity with axial distance and the subsequent beginning of an 'inviscid breakdown' process.

As of yet, none of these ideas are sufficient to accurately predict vortex breakdown. Recent work by O'Neil, Barnett, and Louie [23] and Ekaterinaris and Schiff [24] using Euler and Navier-Stokes codes respectively have demonstrated a vortex breakdown in their results for certain conditions. These computational results do correspond to experimental data. However, no theory exists which can yield the flow detail in the breakdown zone nor universally predict breakdown locations which consistently compare with experimental results. Because of this, it is essential that the flowfield be examined

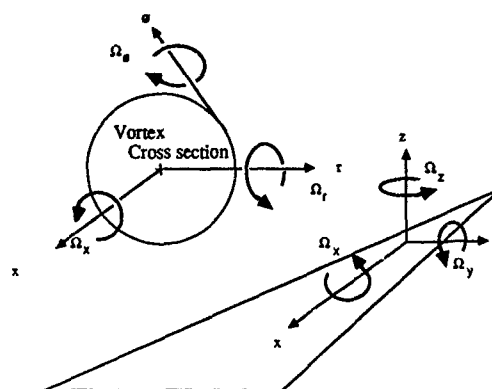


Figure 1. Delta Wing Vortex Geometry

experimentally in an effort to uncover information which may shed light on this problem.

The vortex flowfield can be regarded as a transition from one flow state to another which may occur as a result of a combination of certain flow parameters reaching a critical or unstable state. One can attempt to quantify such critical breakdown parameters in two forms: as a function of either the independent or the dependent variables. The former would involve factors such as angle of attack, sweep angle of the wing, and sideslip. An indication parameter involving dependent variables would be based upon flow conditions which result from the geometry of the problem. Items such as local vorticity and chordwise pressure gradient fall into this category.

The determination of such breakdown indication parameters could be based on several forms:

- a. A local balance between the generation and convection of vorticity.
- b. A local balance of the pressure forces with the acceleration of the fluid.
- c. The size of the local length scale compared to the wing geometry.
- d. An empirical fit parameter based on wing geometry, angle of attack, etc.

The aspects of the vorticity field would seem to be of utmost importance in gaining a better understanding of the flowfield behavior. Both the generation of vorticity, which is transported into the vortex, and the convection rate downstream of this vorticity could play a crucial role in determining where the breakdown of the primary vortex occurs as suggested by Lee and Ho [25]. The complete role of the secondary vortex, which is a direct result of the viscous nature of the flow, is also not well understood. Its presence, illustrated in Figure 2 via a titanium tetrachloride vapor method for marking vortical flows [26], is known to displace the primary vortex inwards and upwards. Questions still remain, however, as to the effect of the secondary vortices on the reduction of the primary vortex pressure peaks as compared to an Euler type solution, or on even more nebulous concepts such as the effect on the vorticity distribution above the wing surface.

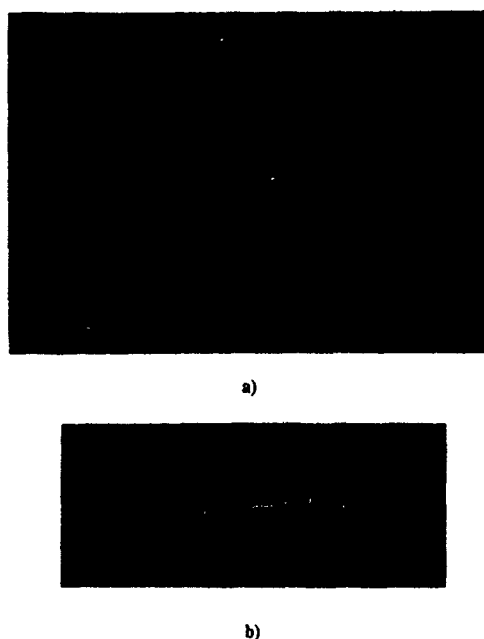


Figure 2. Flow Visualization of Primary and Secondary Vortices a) three quarter view, b) side view

Although the data base of delta wing flowfield information is growing, most experimenters are constrained to a specific configuration at a fixed angle of attack or chord location. This information, helpful for the sake of comparison, provides little or no information on the changing flow field state in the chordwise direction. Aspects such as rate of vorticity generation or circulation distribution in the streamwise direction are impossible to address.

In addition, there are other subtler reasons which make comparison difficult. Data compiled from several different investigators [27 - 30] is compared in Table 1. Both the sweep angles and the angles of attack are roughly the same. The values of vorticity presented are the maximum values found in the flow field and coincide with the core axis. Typically, investigators use the model chord,  $c$ , and the freestream velocity,  $U_\infty$ , as nondimensionalizing scales for the flow. The results are seen to vary quite substantially. The local semispan,  $s^*$ , could also be considered a viable length scale, since flow visualization indicates the vortex structures to scale with the wing geometry. Use of the local semispan would account for local geometric changes due to sweep angle and allow for comparison of data taken at different chord stations. The data of Kjølgaard and Sellers [27], for example, indicates a lower value of vorticity than that of Payne for a location 20% farther from the apex. If  $s^*$  is used as a scaling factor, the magnitude of the axial vorticity component is seen to exceed that of Payne. It is also noted that identical geometries, such as that of Payne and the current investigation, have produced different values of the axial vorticity component. These differences indicate there are other factors which have not been taken into

account. A closer examination of the grid resolution of each investigation provides some insight. As indicated in Table 1, the highest derived vorticity values correspond to the finest grid resolution and vice versa. Since vorticity is a measure of the smallest scales of the flow, it would only make sense that a finer measurement grid would be able to 'capture' the high gradients of velocity present in the field. These differences in flowfield measurement add to the difficulty in obtaining a clear picture of the physics involved.

Table 1. Maximum Axial Vorticity Data

Investigator	Angle of Attack ( $^\circ$ )	Sweep Angle ( $^\circ$ )	Chord (mm)	Freestream Velocity $U_\infty$ (m/s)	Chordwise Station $x/c$	Maximum Vorticity $\Omega_x$ (1/s)	$\Omega_x c$ $U_\infty$	$\Omega_x s^*$ $U_\infty$	Measurement Grid Resolution (mm)
Payne	20.0	75	406.4	10	0.5	8,383	341	46	0.04166
Kjølgaard and Sellers	20.5	75	568.8	12.8	0.7	7,113	316	59	0.0323
Visser and Nelson	20.0	75	406.4	9.7	0.5	12,340	517	69	0.030
	20.0	75	406.4	10.0	0.5	22,774	925	124	0.015
Verhaeghe	20.4	76	2220.0	25	0.5	17,400	1545	193	0.0145
Carcillet	20.0	75	500	20.3	0.6	23,061	568	91	♦
	20.0	75	500	119	0.6	114,144	480	77	♦
	20.0	75	1450	40	0.8	11,034	400	86	♦
Payne and Solgnaac	19.3	75	560	14.5	1.4 (wake)	6,732	260	70	♦

♦ Value unavailable

For the reasons stated above, a study was undertaken to measure the delta wing flowfield at various chordwise locations over delta wings. Models with different sweep angles at different angles of attack were used in an attempt to determine if the flow reaches some measurable critical state, particularly involving aspects of the vorticity components, that would then initiate a flow transition to the post breakdown state.

#### Experimental procedures

All experiments were carried out in the University of Notre Dame subsonic wind tunnel facilities. The tunnel is powered by an 18.6 kw AC induction motor which drives an 8 bladed 1.2 meter (4 foot) fan located in the diffuser outlet (Figure 3). The four degree of freedom, computer controlled, probe traversing test section is preceded by a 24:1 contraction inlet. The minimum step sizes possible in the streamwise, spanwise, and normal directions were 0.0064mm, 0.0254mm, and 0.0208 mm respectively. The section dimensions were 610 mm by 610 mm by 1820 mm (24 by 24 by 76 inch). The models used were flat plate delta wings having a windward  $25^\circ$  bevelled edge, a root chord of 406.4 mm (16 inches) and a thickness of 6.35 mm (0.25 inches). The minimum distance between the wing surface and the probe was 3.0 mm due to probe geometry.

A TSI IFA 100 constant temperature anemometer system was used to acquire the data in conjunction with a Macintosh II computer which also maneuvered

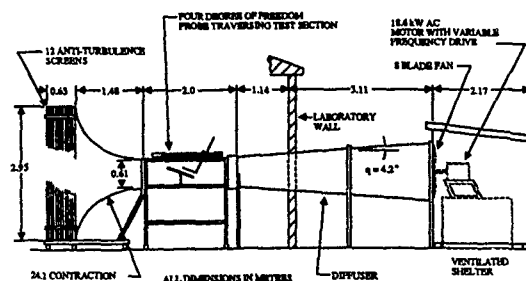


Figure 3. Notre Dame Subsonic Wind Tunnel Facility

the x-wire probe in the test section. The probes utilized five micrometer diameter tungsten wires giving an length/diameter ratio of 250. Overheat ratios were set to 1.8. The wires were calibrated for every test to reduce the possible errors associated with property changes of the wires. In addition, this procedure eliminated the need for temperature compensation as the ambient temperature did not vary by more than  $\pm 1^\circ \text{C}$  over the course of any individual test.

The technique of Sherif and Pletcher [31] was employed to determine the magnitudes of the velocity components. This is based on the effective velocity measurement method. The wire senses a velocity composed of vectors normal and tangential to the wire which cool the wire at different rates,  $k_1$  and  $k_2$ . Jørgensen [32] has expressed the most general form of this equation as:

$$U_{\text{eff}}^2 = U_N^2 + k_1^2 U_T^2 + k_2^2 U_B^2$$

for an X-wire lying in the NT plane (Figure 4a). The effective velocities were obtained using a least squares fit based on the calibration and then the method of Sherif and Pletcher [31] to determine the magnitudes of the velocity components.

In order to fully determine the three velocity components and their associated directions, however, it was necessary to take four normal grid sweeps above the wing at each chordwise location. Two x-wire probe configurations were utilized and are shown in Figure 4b. Probe 1, a DISA 55P62, had wires lying in a plane perpendicular to the probe axis, while the wires of probe 2, a DISA 55P61, were lying in a plane parallel to the probe axis, as shown by the accompanying schematic. The initial two grid sweeps used probe 1 with wire 1 at the reference of zero degrees and wire 2 at negative 90 degrees using the geometry in Figure 4b and in accordance with that of Sherif and Pletcher [31]. The probe was then rotated  $45^\circ$  about its axis and a second sweep initiated. This provided enough information for the velocity magnitudes to be determined. The second probe was used to take two sweeps with the plane of the wires parallel to the wing and perpendicular to it respectively. This second set of sweeps determined the direction of the transverse (v) and normal (w) velocity components. It was assumed that the direction of u was always in the positive direction as the probe was kept in the flow forward of the breakdown

region.

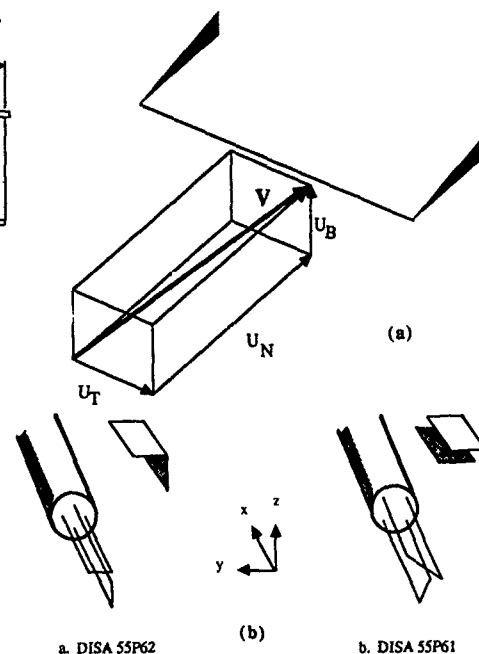


Figure 4. Hot Wire Probe Geometries and Configuration  
a) Effective Velocity Coordinates of Jørgensen,  
b) X-wire probes

## Results and Discussion

The majority of data was accumulated over a  $75^\circ$  sweep delta wing at  $20^\circ$  angle of attack. Measurements were made at various chordwise stations in grid planes normal to the upper surface. The angle of attack was then increased to  $30^\circ$  and chordwise stations were measured upstream of the probe induced breakdown of approximately  $x/c = 0.5$ . Experiments by Payne, Ng, and Nelson [33] comparing LDV and seven hole probe data have shown that the effect of introducing a probe into the flowfield does not greatly distort the flowfield provided the measurements are taken upstream of the breakdown zone. Finally, a  $70^\circ$  sweep configuration was utilized at  $20^\circ$  angle of attack in an effort to observe the effect of sweep. All tests were conducted at a Reynolds number of 250,000.

Typical flowfield distributions are shown in Figure 5. The axial velocity  $u/U_\infty$  is actually the velocity normal to the measurement plane at the chordwise station. The jetting core structure of the vortex is seen to be quite well defined, with the majority of the measured field maintaining a velocity above the freestream velocity. Measurements encompassed a  $z/s$  of 0 to approximately 1 and were taken from the chord centerline out to a  $y/s$  of 1.2 on the right side of the wing. Using this grid, the details of the primary, secondary, and the shear layer can be captured. Grid increments were set to a  $y/s$  and  $z/s$  of 0.03 at each station. The transverse and normal



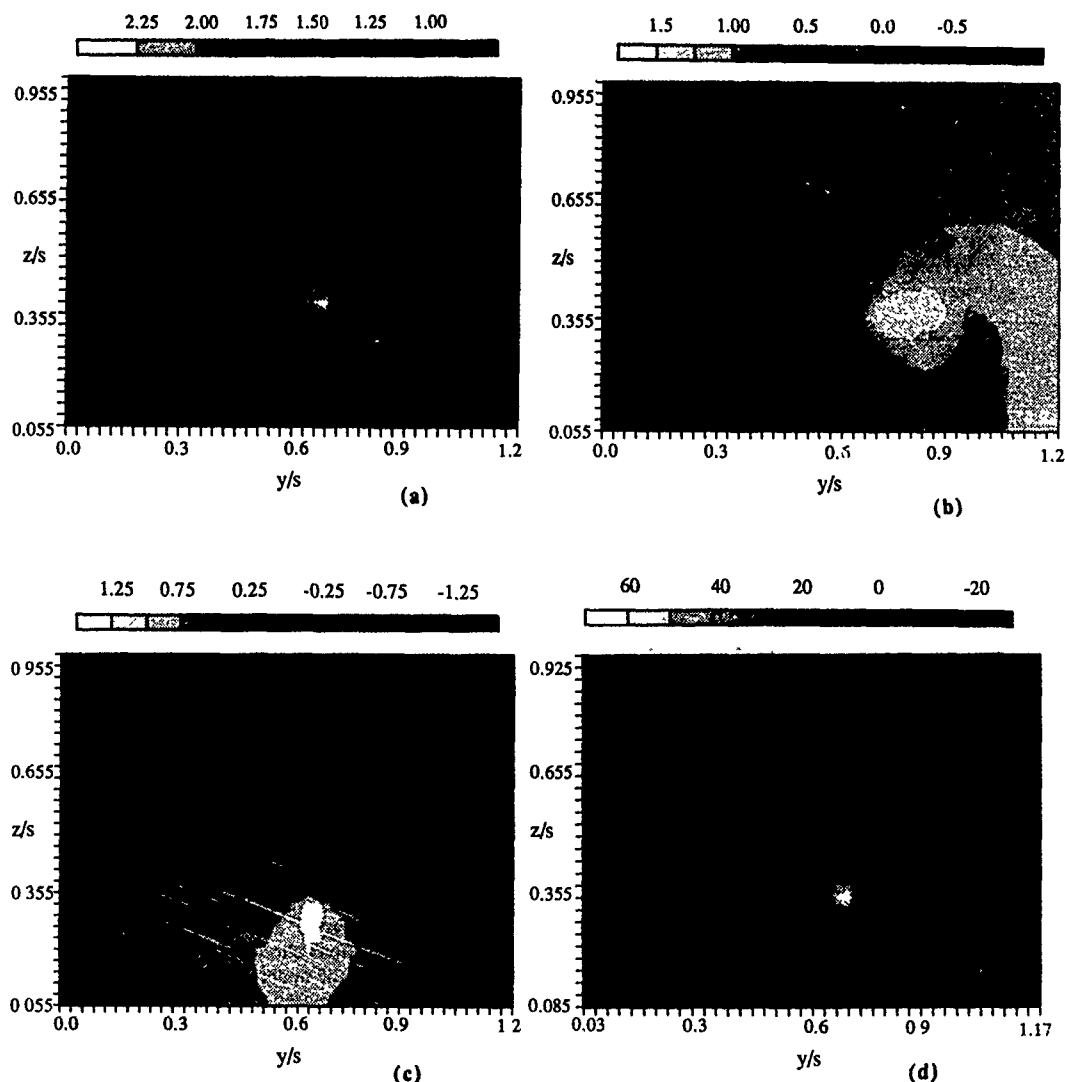


Figure 5. Chord Station Flowfield Maps for Sweep = 75°, Angle of Attack = 20°,  $x/c = 0.50$   
a)  $u/U_\infty$ , b)  $v/U_\infty$ , c)  $w/U_\infty$ , d)  $\Omega_x$

velocity components,  $v/U_\infty$  and  $w/U_\infty$  respectively, are depicted in Figures 5b and 5c. These data were then centrally differenced spatially to obtain the axial vorticity component,

$$\Omega_x = \frac{\partial w}{\partial y} - \frac{\partial v}{\partial z}$$

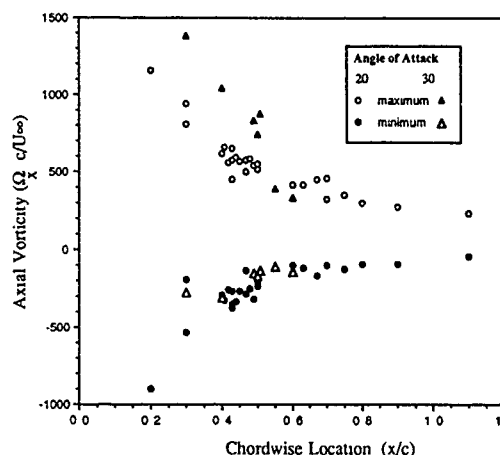
shown in Figure 5d.

Since the role of vorticity, including the effects incurred by the secondary vortex on the primary, was the motivation for this investigation, the local magnitudes and chordwise distributions were the logical places to begin. An initial proposition was that the vortex structure may be unable to exist in the cohesive, pre-breakdown nature if a maximum local value of vorticity in the vortex, say  $\Omega_{x_{max}}$ , is

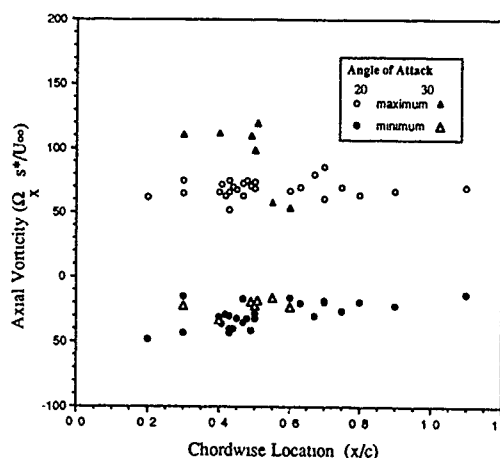
reached. Conventionally, investigators such as Kjølgaard and Sellers [27] have multiplied the calculated vorticity by the ratio of the root chord to the freestream velocity providing an overall view of the absolute vorticity in the entire flowfield. As mentioned previously, the use of the local spanwise distance provides a means to scale each cross-sectional flow plane in order to examine the effect of the local geometry on the flow characteristics. The local semispan was used to scale the current data in addition to using the chord.

The maximum value of vorticity was obtained at each station as well as the minimum. These values are presented in Figure 6 for the 75° sweep wing at 20° and 30° angle of attack. The vorticity data is nondimensionalized using the two conventions mentioned above. From Figure 6a, in which the

vorticity is multiplied by the ratio of the root chord to the freestream velocity, it appears that the magnitudes of both the positive and negative maximum values are decreasing with increasing distance from the apex. No breakdown existed over the wing for the 20° angle of attack case. The 30° case was seen to have a breakdown occurring between the 0.50 and 0.55 x/c location. The positive values of vorticity show a slight drop at this station, however the negative values show no change at all.



(a)



(b)

Figure 6. Chordwise Comparison of Maximum and Minimum Vorticity for 75° Sweep Nondimensionalized Using a) chord, b) local semispan

If the vorticity is now nondimensionalized by the local semispan,  $s^*$ , as shown in Figure 6b, the data appears to indicate a constant value in the chordwise direction for both the positive and negative values. The drop in the positive value for the 30° case is more evident, however a large scatter in the data is still seen to exist.

This scatter in the data can be attributed to several factors. The vorticity is a measure of the smallest scales of the flow. Details of the velocity gradients

will be lost if the grid is not sufficiently fine. In addition, these values of vorticity were obtained by differentiating discrete data which has the effect of increasing the error associated with such measurements. Therefore simply examining the maximum value of the vorticity is not enough to make a definitive statement of the vortex status at that chord station.

The leading edge sheet continually feeds vorticity into the vortex flowfield along the entire length of the delta wing. An interesting possibility is that the vortex can only 'hold' or contain a certain amount of vorticity before it must revert to a more stable configuration in order to contain or transport this increase in vorticity. Extending this further, suppose that the breakdown position maintains an average mean location because the generated vorticity is balanced by the vorticity being convected downstream for some given set of fixed conditions (i.e. sweep and  $\alpha$ ) as suggested by Lee and Ho [25]. The flow conditions are then in some way altered, so as to add more vorticity upstream of the breakdown without a corresponding increase in the convection rate downstream. If the breakdown is seen to move upstream, this would indicate some critical condition based on a maximum vorticity distribution may exist above which the initial vortex structure will transition to the post breakdown state. An increase in  $\alpha$  or a decrease in sweep angle would also then imply that, momentarily, the relative vorticity generation rate becomes higher than the convective rate and the transition/breakdown point changes until a stable situation is again reached.

The distribution of vorticity throughout the vortex was therefore examined for possible maximum amounts of vorticity per unit area or volume at a chordwise location. The integration of discrete data has the effect of smoothing errors associated with the data. In order to evaluate the reliability of differentiating the discrete velocity field, the circulation,  $\Gamma$ , was also calculated and compared to the integration of the vorticity field over the area normal to it:

$$\Gamma = \int_V \mathbf{V} \cdot d\mathbf{r} = \int_A (\nabla \times \mathbf{V}) \cdot d\mathbf{A} = \int_A \Omega_x dA$$

The vorticity field distribution was spatially integrated and is presented with the equivalent line integral of the velocity field, for the  $\Lambda = 75^\circ$ ,  $\alpha = 20^\circ$  case, in Figure 7. The values are plotted outward from the core center ( $r = 0$ ) where the radial distance has been nondimensionalized by the local semispan. Each curve represents a chordwise location and the circulation is seen to grow in a chordwise manner. This is what one would expect, as the feeding sheet is continually being wrapped into the vortex. The circulation and integrated vorticity values are seen to correspond quite well, which would indicate that differentiating the velocity fields does not increase the error substantially.

The circulation values were then scaled by the local semispan,  $s^*$ , and plotted in Figure 8. It appears that

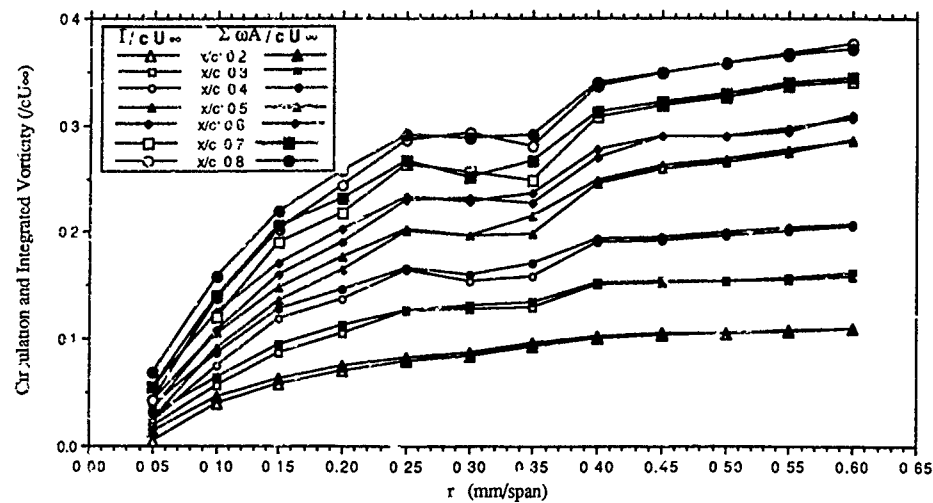


Figure 7 Radial Distribution of Circulation and Integrated Vorticity, Sweep = 75°, Angle of Attack = 20

this has the effect of causing the curves to fall quite closely onto each other. The data taken for  $\Lambda = 75^\circ$ ,  $\alpha = 30^\circ$  is also shown for comparison. If scaled by the chord,  $\alpha = 30^\circ$  has a distribution similar to that of  $\alpha = 20^\circ$  in Figure 7. The data in Figure 8 would seem to imply that the chordwise development of circulation at a constant angle of attack grows in a linear manner, indicative of a conical type of flowfield.

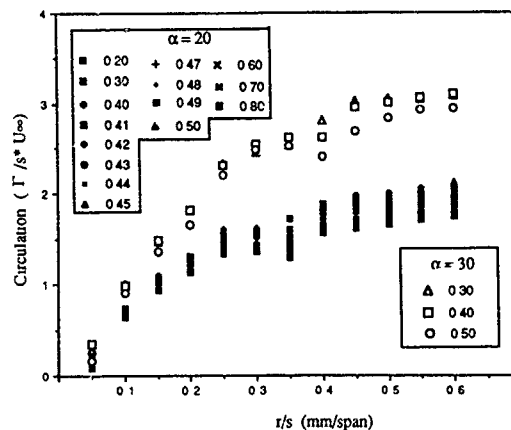


Figure 8. The Effect of Angle of Attack on the Radial Circulation Distribution Nondimensionalized by Local Semispan for Sweep = 75°

A possible way to account for the angle of attack effect would be to further incorporate some function of  $\alpha$  as a scaling parameter. If the circulation values are divided through by, say,  $\sin(\alpha)$  the results in Figure 9 are obtained. The data for  $\Lambda = 70^\circ$ ,  $\alpha = 20^\circ$  has also been added for comparison.

Each of the curves shown previously in Figure 7 illustrates the distribution of the circulation in the radial direction. Each curve is seen to increase to an  $r/s$  of approximately 0.25, which represents the extent of the primary vortex. A further increase in the curve profile is also observed corresponding to the

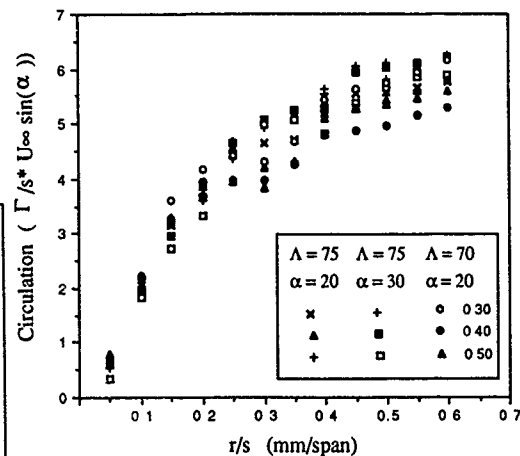
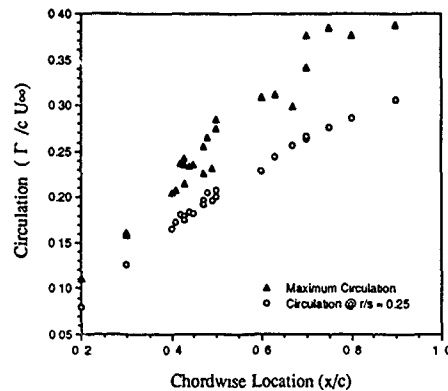


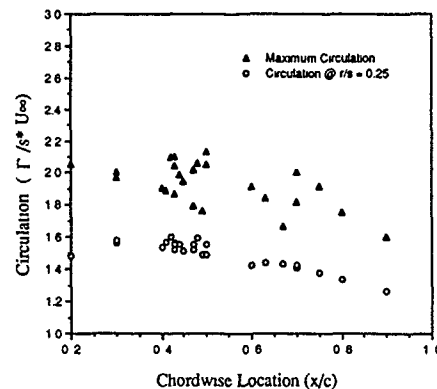
Figure 9 Radial Circulation Distribution Nondimensionalized by Local Semispan and Angle of Attack

shear layer of fluid which has separated from the leading edge. If the maximum value of the circulation scaled by the chord is plotted for each chord station, the curve shown in Figure 10a results. Although the data corresponding to the maximum radius of integration,  $r/s = 0.6$ , appears to be following a somewhat linear trend, there is widespread scatter in the data. Since the core is located at a  $z/s$  of about 0.37 to 0.40, the lower integration path is bounded by the upper surface of the wing for any  $r/s$  values greater than this. Depending on the proximity of the probe to the wing surface, velocity components contributing to a negative vorticity component will have a varied effect on the resulting integration. A better representation is obtained if the circulation values corresponding to the initial leveling off of the curves in Figure 7 is used. The values for this radial distance of  $r/s = 0.25$  are also plotted in Figure 10a. A much smaller scatter is present in the data. The

values tend to follow a near linear distribution, except near the aft of the wing surface, whereupon a leveling off is observed.



(a)



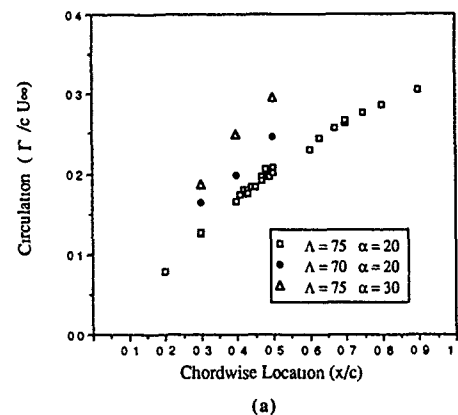
(b)

Figure 10. Chordwise Comparison of Circulation for sweep = 75°, Angle of Attack = 20°, nondimensionalized using a) chord, b) local semispan.

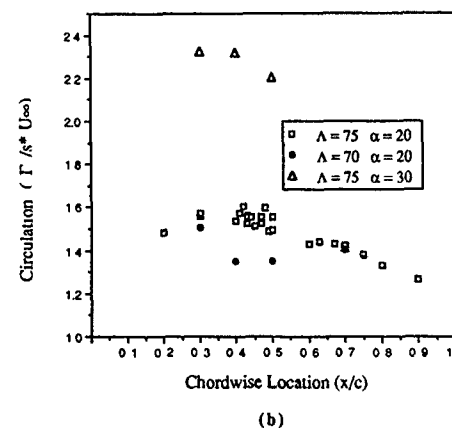
Scaling the values in Figure 10a by  $s^*$  instead of  $c$  produces the distributions of Figure 10b. Both the  $r/s = 0.6$  and  $r/s = 0.25$  cases indicate values which are dropping slightly in the axial direction. The scatter in the maximum values appears to be even greater than in Figure 10a. It should be remembered however, that nondimensionalization of data can introduce other subtleties. The chord used to scale the data is a constant for all the cases presented here and simply multiplies the data by approximately 2.5, while maintaining the same relative distance between curves. On the otherhand, if the values in Figure 10a are multiplied by  $c/s^*$  in order to scale by the local semispan, that is equivalent to multiplying by  $\tan(\Lambda)/(x/c)$ . In effect, any differences are magnified (local chord)<sup>-1</sup>.

The data from the other wing configurations is presented in Figure 11a, along with that of Figure 10, for  $r/s = 0.25$ . For the 75 degree sweep case, the circulation at 30° angle of attack case is seen to be greater than  $\alpha = 20^\circ$ , as one would expect. The  $\Lambda =$

70°,  $\alpha = 20^\circ$  case is also seen to lie above the data of Figure 10, indicating the vortex over the 70° sweep wing to be stronger than that of 75° for the same angle of attack. This is in accordance with the idea that a stronger vortex causes breakdown to occur sooner; that is, sweeping a wing forward at a constant angle of attack causes breakdown to occur closer to the apex due to increased vortex strength. An interesting observation is made of the data if  $s^*$  is again used as the scaling parameter in Figure 11b. The data for  $\Lambda = 70^\circ$  is seen to fall below that of  $\Lambda = 75^\circ$  for  $\alpha = 20^\circ$ . This would seem to imply that there is a lower total amount of distributed vorticity over the 70° wing per unit span than the 75° wing, even though the absolute values are larger. The spanwise distribution of vorticity will be examined in more detail using core traverse data later in this paper.



(a)



(b)

Figure 11. The Effect of Angle of Attack and Sweep on the Chordwise Circulation Distribution at  $r/s = 0.25$  Nondimensionalized using a) chord, b) local semispan.

The close agreement of the integrated vorticity with the circulation can be exploited to examine the separate changes in the total positive and total negative vorticity which is not evident from the circulation alone. Integrating the positive and negative values of vorticity separately over their respective areas leads to the results shown in Figure 12. From Figure 12a, it appears that the amount of negative vorticity present above the wing is relatively similar for all three configurations, the  $\Lambda = 70^\circ$ ,  $\alpha = 20^\circ$  case

having the largest magnitude at each respective chord location. The positive values, however, show a marked difference. The 70° swept wing at 20° angle of attack is seen to approach the values associated with the 75° sweep at an angle of attack of 30°. Scaling by  $s^*$  causes the positively integrated values to remain relatively constant or slightly decrease with increasing chord location. In addition, the  $\Lambda = 70^\circ, \alpha = 20^\circ$  case is seen to fall in the same region as  $\Lambda = 75^\circ, \alpha = 20^\circ$ . The negative vorticity values remain together at approximately a constant value for all three cases.

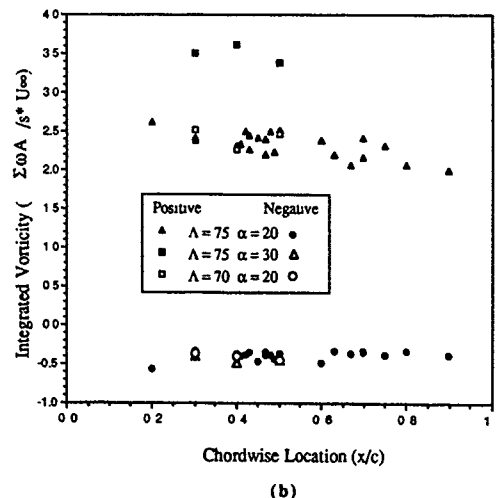
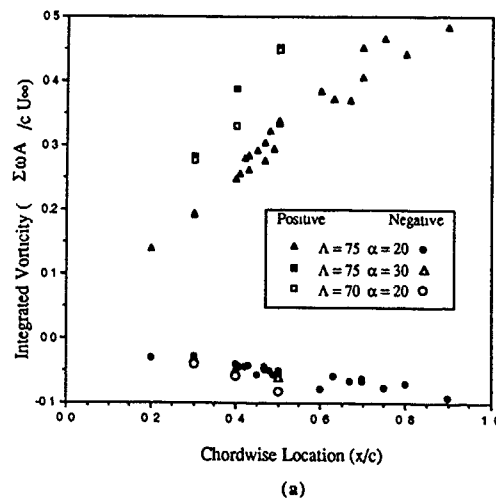


Figure 12. Chordwise Variation of Integrated Vorticity Nondimensionalized using a) chord, b) local semispan.

A similarity relationship proposed by Hemsch and Luckring [34] for the vortex circulation as a function of the apex half angle,  $\epsilon$ , angle of attack, chord and freestream velocity. It has the form:

$$g = \frac{\Gamma}{U_\infty c \tan^2 \epsilon \cos \alpha} = AK^n \quad \text{where } K = \frac{\tan \alpha}{\tan \epsilon}$$

for some value  $n$ . Hemsch and Luckring found that if  $g$  and  $K$  are plotted in a log-log format, a fit of the

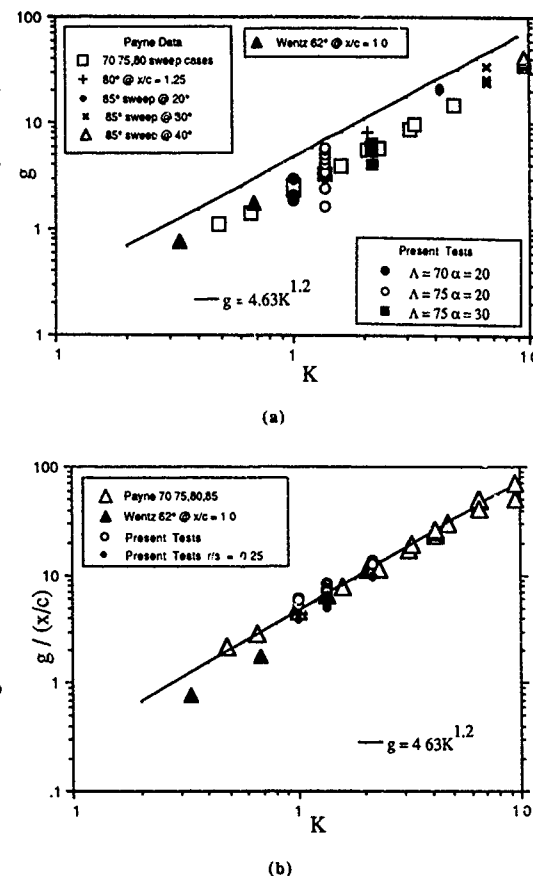


Figure 13. Correlation of Hemsch and Luckring a)  $g$  vs  $K$ , b)  $g/(x/c)$  vs  $K$ .

form  $g = AK^{1.2}$  was seen for data obtained from Wentz and MacMahon [35],  $\Lambda = 62^\circ$  and Delery, Pagan, and Solignac [36], ranging from  $g$  of 0.5 to 10.0 and  $K$  of 0.2 to 2.0. Theory by Smith [37] resulted in the form  $g = 4.63K^{1.2}$ . For comparison, seven hole probe data from Payne [4,33] is plotted in Figure 13a with that of Wentz and MacMahon and the curve of Smith for  $n = 1.2$ . Payne's data represents sweep angles of 70°, 75°, 80°, and 85° at various chord locations. It is seen to follow the line of Smith to a  $g$  of 100 and a  $K$  of 10.

The data from this investigation, representing three  $K$  values, was also plotted in Figure 13a and the expected collapse of data was not immediately evident. Hemsch and Luckring used data that was acquired in the wake of the models. Since the present tests were conducted at locations above the wing surface, a further scaling of  $g$  by the local chord ratio,  $x/c$ , was found to bring the data into line with that of Smith as shown in Figure 13b. This same scaling was used on the data of Payne and is shown in Figure 13b also. Manipulation of the above expression of Hemsch and Luckring to include the ratio  $x/c$  and expressing it in terms of  $s^*$  leads to the following:

$$g = \frac{\Gamma}{U_{\infty} s^* \tan \epsilon \cos \alpha}$$

If  $g$  is further divided through by  $K$ :

$$g = \frac{\Gamma(\tan \epsilon \cos \alpha)^{n-1}}{U_{\infty} s^* (\sin \alpha)^n}$$

or

$$g = \frac{\Gamma(\tan \epsilon \cos \alpha)^{0.2}}{U_{\infty} s^* (\sin \alpha)^{1.2}} \quad \text{for } n = 1.2$$

where  $g$  is now simply equal to a constant. It is interesting to see how closely this corresponds to the function used in Figure 9 and that if  $n = 1$ , they would be exactly identical.

The characterization of the circulation shown above leads to an overall view of the flowfield for each wing configuration and is helpful in evaluating gross properties, such as the lift, at a particular set of test conditions. Unfortunately, the mechanism for the breakdown process is not elucidated and a more detailed look at the chordwise vorticity distributions was undertaken. In an effort to examine the validity of the theoretical ideas proposed by Brown and Lopez [22] as well as investigate what appears to be unexpected spanwise vorticity density results of Figure 11b above, values of  $\Omega_{\theta}$  and  $\Omega_x$  were calculated based on the grid traverse through the core center utilizing polar coordinates. Under the assumption that the radial velocity and its gradient were negligible compared to the other terms along the traverse through the core:

$$\Omega_{\theta} = -\frac{\partial V_x}{\partial r} = -\frac{\partial u}{\partial r}$$

and

$$\Omega_x = \frac{V_{\theta}}{r} + \frac{\partial V_{\theta}}{\partial r} = \frac{w}{r} + \frac{\partial w}{\partial r}$$

The velocities based on the traverse through the core, and corresponding to the  $\Lambda = 75^\circ$ ,  $\alpha = 20^\circ$ ,  $x/c = 0.50$  data in Figure 5, are plotted in Figure 14a against distance from the core center. The  $z/s$  location for the traverse was based on the maximum value of  $u/U_{\infty}$ . As can be seen, the radial velocity,  $v = V_r$  along the traverse can be regarded as negligible compared to the respective values of  $u$  and  $w$ , or  $V_x$  and  $V_{\theta}$ . The nondimensional calculated values of  $\Omega_x$  and  $\Omega_{\theta}$  are given in Figures 14b and 14c. The axial vorticity is seen to increase to a maximum at the center of the core. The earlier maximum, presented in Figure 6b, based on the spatial derivative in Cartesian coordinates shows a comparable value. In a similar manner,  $\Omega_{\theta}$  also increases as it nears the core centerline, however it drops to a value of zero at  $r/s = 0$ . Since  $\partial u/\partial r$  is always negative with increasing distance from the core, as indicated in Figure 14a,  $\Omega_{\theta}$  is always positive except at  $r/s = 0$  where  $u$  is a maximum and the gradient becomes zero.

The majority of the axial vorticity component appears to be confined to 10% of the span on either side of the core center location,  $r/s = \pm 0.1$ . A slight rise also occurs at  $r/s = 0.30$ , probably due to the shear layer in the feeding sheet. The azimuthal vorticity is seen to have a wider, more erratic distribution. It also appears to have a rise at  $r/s = 0.30$  due to the feeding sheet.

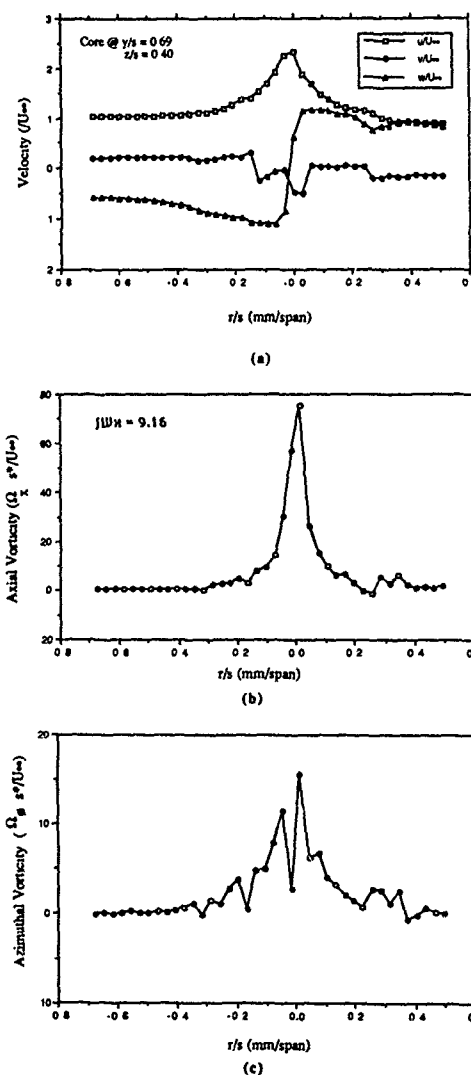


Figure 14. Core Flowfield Profiles for Sweep =  $75^\circ$ , Angle of Attack =  $20^\circ$ ,  $x/c = 0.50$  a) Velocity Components, b) Axial Vorticity,  $\Omega_x$ , c) Azimuthal Vorticity,  $\Omega_{\theta}$

If the axial vorticity profiles are now overlaid for each of the measured  $x/c$  locations, Figure 15a, similar profiles are seen to exist at each station. In light of the fact that no breakdown is occurring over the wing, this would seem to be acceptable. Both  $\Lambda = 75^\circ$ ,  $\alpha = 30^\circ$  and  $\Lambda = 70^\circ$ ,  $\alpha = 20^\circ$  exhibited similar features. It was hoped that some indication of the imminent breakdown, especially with the  $\Lambda = 75^\circ$ ,  $\alpha = 30^\circ$  case, would be evident from these distributions. This premise was based on results derived using an

earlier investigators' velocity data. Axial vorticity was calculated from LDA velocity data acquired by Iwanski [38] over a one inch thick,  $70^\circ$  sweep, flat plate delta at  $\alpha = 30^\circ$ . The different chord stations are presented in Figure 15b. The axial vorticity profile distribution is seen to increase in magnitude and narrow in width in the downstream direction, up to  $x/c = .411$ . The peak then broadens and a reduction in the values is seen further downstream as the breakdown region is entered.

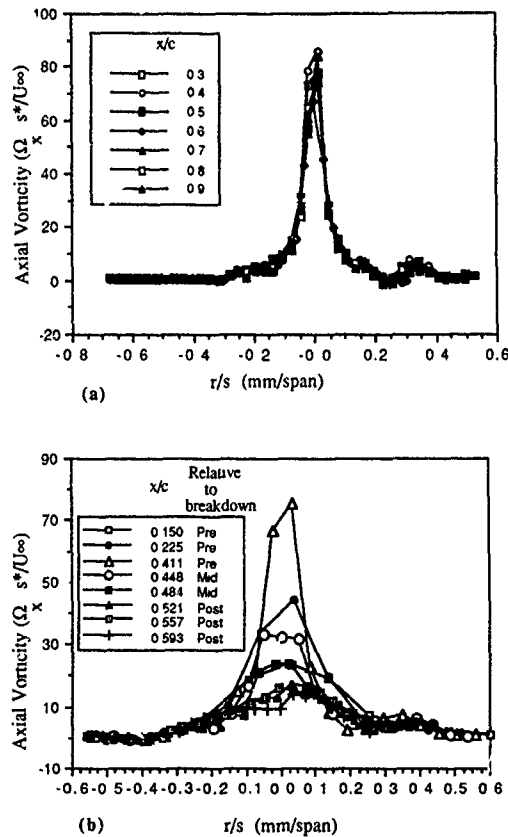


Figure 15. Axial Vorticity Distributions a) Present Tests  
b) Iwanski data

These calculated axial vorticity values of Iwanski were then nondimensionally integrated along each respective semispan to derive a set of values indicative of the local vorticity density distribution which are plotted against their chord locations in Figure 16a. Also included are the values of the axial component of helicity, obtained by taking the dot product of the vorticity field with the velocity field. Both the integrated vorticity and the helicity components appear to reach a maximum at a distance of about 10 to 15% of the chord upstream of the breakdown region. Whether this indicates that the vortex reaches a saturated or critical condition is still open to question, due to the scarcity of data. This is then followed by a rapid decline through the breakdown region and beyond. Figure 16b depicts the integrated results for the present tests. No trend is seen for  $\Lambda = 75^\circ$ ,  $\alpha = 20^\circ$ . The data for the  $\Lambda = 75^\circ$ ,  $\alpha = 30^\circ$

configuration does not give any indication of the upcoming flow transition, however the probe was still upstream of breakdown and the  $x/c$  increment was not nearly as fine as that used by Iwanski.

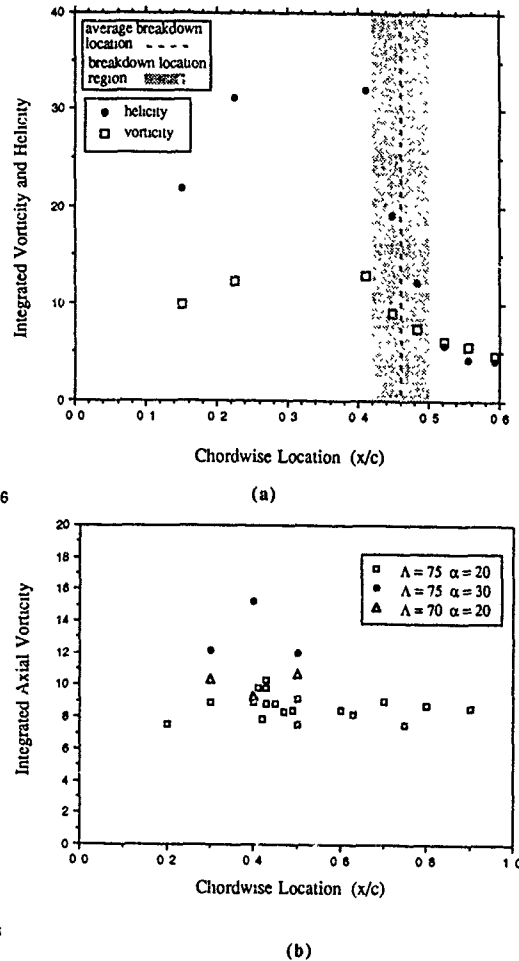


Figure 16. Chordwise Distributions of Integrated Properties Nondimensioned by the Local Semispan  
a) Iwanski data, b) Present Tests

Azimuthal vorticity values derived from Iwanski's data are presented in Figure 17a. This component of vorticity becomes negative at certain spanwise locations as soon as the breakdown region is entered, supporting the ideas of Brown and Lopez [22]. The azimuthal component appears to reach a maximum negative value, however as this data represents time averaged values of a highly fluctuating region, care should be taken when drawing conclusions. It should be noted that there may be a non-negligible radial velocity component in the expansion region of the breakdown region, which would act to provide a positive contribution to  $\Omega_\theta$ , which is not considered in the evaluation of Iwanski's data due to a lack of sufficient information. Pagan and Solignac [30] also determined that the value of  $\Omega_\theta$  becomes negative as the breakdown region is encountered. Their spatial results indicate local minimums shortly after the

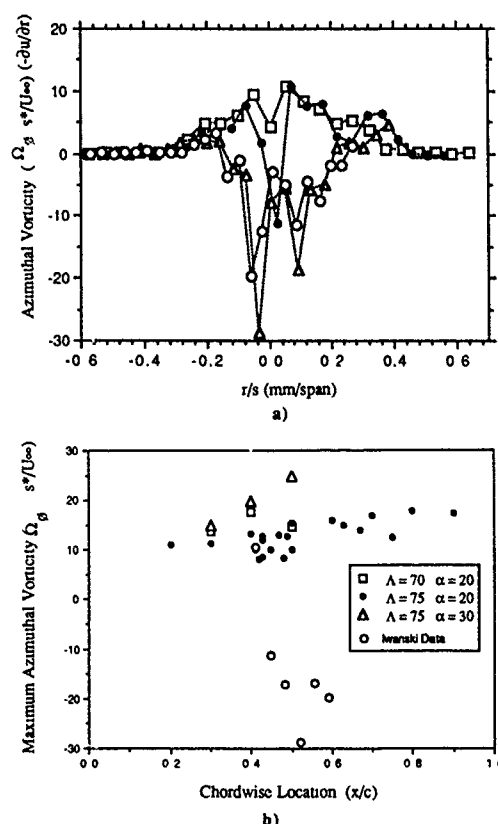


Figure 17 Azimuthal vorticity Distributions a) Iwanski Data  
b) Maximum Azimuthal Vorticity

breakdown. They conclude that the vorticity vector,  $\Omega$ , rotates from an essentially longitudinal direction to a generally tangential one in the breakdown zone as Brown and Lopez's analytical hypothesis surmise.

Since there is no sense physically in integrating the azimuthal vorticity distributions, the maximum values of  $\Omega_\theta$  were plotted instead in Figure 17b. These values represent the maximum gradient of the axial velocity and are increasing slightly in the axial direction for the present tests. The data of Iwanski reflects the change from a positive to a negative sense. It should be noted that unless there is a local axial velocity deficit,  $-\partial u/\partial r$  will always be positive. Other investigators have shown this to occur in the breakdown region, but the present method was found to be inaccurate for regions of the flow where  $u$  is much less than  $v$  or  $w$  and the low axial velocity regions present at breakdown gave results which could not be considered reliable. In addition negative values of  $u$  could not be measured using this method.

Flow visualization at the University of Notre Dame has indicated an additionally interesting phenomena that while the outer flow region of the vortex seems to scale with the local geometry of the wing, the subcore appears to maintain a more or less constant diameter. The nature of the data in Figure 14 leads to the possibility of two core size definitions: a jet effect core due to the presence of the axial velocity component and a much smaller core based on the

distance between the maximum and minimum values of  $w$  or  $V_\theta$ , usually referred to as the subcore. If a minimum value of  $u/U_\infty$ , say 1.5, is used to set a threshold cutoff, a jet core can be defined and the growth rate compared to that of the subcore defined above.

The evaluated core diameters are presented in Figure 18, both in absolute units and scaled by the local semispan of the wing. The grid resolution of 0.03  $y/s$  leads to more scatter in the determination of the size of the subcore than the jet core, however Figure 18a does indicate that the jet core is growing at a faster rate than the subcore, albeit both are in a linear fashion. Scaling by the semispan shows that both cores are scaling by the local geometry. Closer inspection, though, reveals that the jet core may appear to be slightly shrinking in size relative to the local span and that the subcore is growing. These could be the effects of diffusion acting on the subcore region and/or the jet. Two finer grid resolution (0.015  $y/s$ ) stations are also included in Figure 18 and would seem to indicate a more constant core diameter on the absolute scale. The scatter of the data makes interpretation difficult and more data will be required at a finer grid resolution before any definitive statements can be made.

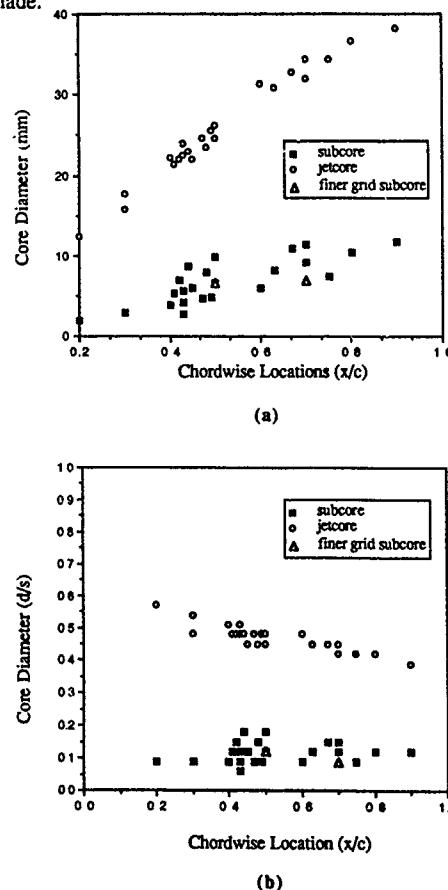


Figure 18. Jet core and Subcore Diameters a) millimetres, and b) scaled by local span



Other investigators have also looked into this aspect of the subcore growth. Verhaagen and van Ransbeeck [28] have measured a more or less constant subcore diameter from  $x/c = 0.1$  to  $0.7$  on a  $2.22$  m,  $76^\circ$  swept delta wing, indicating a cylindrical rather than conical flow. Data obtained from Hawk, Barnett, and O'Neil [39], however, points to a linear type of core growth with chordwise distance over a  $762$  mm chord,  $70^\circ$  swept wing. These discrepancies again indicate that due to such factors as grid resolution, which is usually not compared between experimental data sets, differing statements concerning observable properties can exist between investigators and comparisons should be examined in light of these factors.

### Conclusions

Scaling of the radial circulation distribution or the vorticity by the local semispan indicates the distributions to be similar at each chordwise location for regions of pre-breakdown vortex flow. This is a good indication that the local semispan is a variable which should be incorporated into any nondimensionalization scheme used to examine flows generated by swept leading edge geometries. This is further substantiated by the results obtained using the correlation of Hemsch and Luckring. Incorporating the factor  $x/c$  appears to correlate circulation distributions in regions where the vortex size and strength are increasing, such as over a delta wing. The circulation at a given radius from the core center is also seen to grow in a nearly linear fashion in the chordwise direction.

Spanwise vorticity distributions based on a single traverse through the core of the vortex also scale with the local geometry in the pre-breakdown state. The vorticity distribution is severely altered as the breakdown region is encountered and appears to indicate there is some maximum type of vorticity distribution that may occur in the region just preceding breakdown. The maximum azimuthal vorticity also maintains a more or less constant value in the vortex upstream of breakdown, but is observed to become negative upon entering the breakdown zone.

The majority of the axial vorticity appears to be confined to the subcore region of the vortex, at least with respect to the pre-breakdown vortex state. The use of the maximum value of axial vorticity can be deceptive, however, in determining the local strength of the vortex structure. Factors such as grid resolution should be accounted for when comparisons of data are made.

The distributions of negative axial vorticity are similar for the different configurations investigated here, despite geometric and angle of attack differences. Adjustment of the flowfield to changing test conditions seems to occur for the most part in the positive axial vorticity regions. Whether this indicates that the secondary vortex structure is a relatively constant influence or perhaps solely a function of the Reynolds number remains to be seen.

The jet core and subcore growth rates both appear to be functions of the local semispan, although they are growing at different rates. Relative to the local geometry, the subcore appears to be constant and the jet core shrinking in size in the axial direction. Finer grid data and flow visualization indicate that the subcore decreases in size relative to the local geometry; that is, it maintains a constant diameter.

### Acknowledgements

The authors gratefully acknowledge the support of the NASA Langley Research Center, grant NAG-1-1156, and the University of Notre Dame for this research effort. In addition they wish to thank Isabelle Maillot and Florence Pipelier of the B.R.I. École Polytechnique Féminine for their computational assistance.

### References

- [1] Lambourne, N. C., and Bryer, D. W., "The Bursting of Leading Edge Vortices-Some Observations and Discussion of the Phenomena," Aeronautical Research Council Reports and Memoranda, No. 3282, April 1961.
- [2] Harvey, J. K., "Some Observations of the Vortex Breakdown Phenomenon" Journal of Fluid Mechanics Vol. 14 pp. 585-592, 1962.
- [3] Erickson, Gary E., "Vortex Flow Correlation", Technical Report AFWAL-TR-80-3143 Flight Dynamics Laboratory, Wright Patterson Air Force Base, January 1981.
- [4] Payne, F. M. "The Structure of Leading Edge Vortex Flows Including Vortex Breakdown" PhD Dissertation, University of Notre Dame, May 1987.
- [5] Kegelman, J.T. and Roos, F.W. "Effects of Leading Edge shape and Vortex Burst on the Flowfield of a 70-Degree-Sweep Delta Wing" AIAA Paper 89-0086 Jan 9-12, 1989 Reno, NA.
- [6] Wentz, W.H. and Kohlman D.L. "Vortex Breakdown on Slender Sharp Edged Wings." Journal of Aircraft Vol.8 #3. March 1971 (AIAA Paper 69-778 July 14-16, 1969).
- [7] Wentz, W.H. and Kohlman D.L. "Wind Tunnel Investigations of Vortex Breakdown on Slender Sharp Edged Wings" NASA CR-98737, 1969.
- [8] Wedemeyer, E. "Vortex Breakdown", No.9, AGARD-LS-121, December 1982.
- [9] Jones, J.P. "The breakdown of vortices in separated flow", Dept of Aer and Astro, Univ. of Southampton, Rep. No. 140, 1960.
- [10] Squire, H.B. Imperial College, London, Dep. of Aero. Report. No. 102, 1960.

- [11] Ludweig, H. "Contribution to the Explanation of the Instability of Vortex Cores Above Lifting Delta Wings", Aero. Versuchsanstalt, Gottingen, Rep. AVA/61 A01, 1961.
- [12] Randall, J.D. and Leibovich, S., "The Critical State: A Trapped Wave Model of Vortex Breakdown", J. Fluid Mech., Vol.58, 1973.
- [13] Benjamin, T.B. "Theory of Vortex Breakdown Phenomena" J. Fluid Mech., Vol.14, June 1962.
- [14] Escudier, M.P. and Keller J.J. "Vortex Breakdown: A Two Stage Transition" AGARD-CP-342, No. 25, April 1983.
- [15] Gartshore, I. S., "Recent Work In Swirling Incompressible Flow", NRL (Canada), LR-343, June 1962.
- [16] Hall, M.G. "The Structure of Concentrated Vortex Cores", Progress in Aeronautical Science (Ed. D. Kucheman), Vol 7, 1966.
- [17] Bossel, H.H. "Vortex Breakdown Flowfield", Phys. of Fluids, Vol. 12, No. 3, March 1969.
- [18] Mager, A. "Dissipation and Breakdown of a Wingtip Vortex" J. Fluid Mech., Vol.55 1972.
- [19] Wilson, J.D. "Calculations of Vortex Breakdown Locations for Flow Over Delta Wings", J. Aircraft, Vol. 145, No. 10, Oct 1977.
- [20] Grabowski, W.J. and Berger, S.A. "Solutions of the Navier Stokes Equations for Vortex Breakdown." J. Fluid Mech., Vol.75, 1976.
- [21] Hall, M.G. "Vortex Breakdown", Ann. Review of Fluid Mech., Vol. 4, 1972.
- [22] Brown, G.L. and Lopez, J.M. "Axisymmetric Vortex Breakdown Part II: Physical Mechanisms" Aeronautical Research Laboratories, P.O. Box 4331, Melbourne, Vic., 3001, Australia. A.R.L. Aero. Rep. 173, AR-004-572 (1988).
- [23] O'Neil, P.J., Barnett, R.M., and Louie, C.M., "Numerical Simulation of Leading Edge Vortex Breakdown Using an Euler Code" 89-2189-CP.
- [24] Ekaterinaris, J. and Schiff, L.B., "Vortical Flows over Delta Wings and Numerical Prediction of Vortex Breakdown" AIAA 90-0102 January 8-11, 1990 Reno, Nevada.
- [25] Lee, M. and Ho, C-M. "Vortex Dynamics of Delta Wings" Frontiers in Experimental Fluid Mechanics" Lecture Notes in Engineering Vol. 46 © 1989 Springer-Verlag, Berlin.
- [26] Visser, K.D., Nelson, R.C., and Ng, T.T., "Method of Cold Smoke Generation for Vortex Core Tagging" AIAA Journal of Aircraft Vol.25, No.11 November 1988.
- [27] Kjelgaard, S.O. and Sellers, W.L. III, "Detailed Flowfield Measurements over a 75° Swept Delta Wing for Code Validation" AGARD Symposium on Validation of Computational Fluid Dynamics, Lisbon, Portugal, May 2-5, 1988.
- [28] Verhaagen, N. and van Ransbeeck, P. "Experimental and Numerical Investigation of the Flow in the Core of the Leading Edge Vortex" 28th AIAA Aerospace Sciences Meeting, AIAA 90-0384 January 8-11, 1990 Reno, Nevada.
- [29] Carcaillet, R., Manie, F., Pagan, D. and Solignac, J.L. "Leading Edge Vortex Flow Over a 75 Degree-Sweep Delta Wing- Experimental and Computational Results." ICAS 86.
- [30] Pagan, D. and Solignac, J.L. "Experimental Study of the Breakdown of a Vortex Generated By a Delta Wing" La Recherche Aéropatiale, No 3, May-June 1986.
- [31] Sherif, S.A. and Pletcher, R.H. "A Normal-Sensor Hot Wire/Film Probe Method for the Analysis of Highly Three Dimensional Flows" ASME Applied Mechanics Biomechanical and Fluid Engineering FED Vol 49, p19-22, Cincinnati, OH, 1987
- [32] Jørgensen, F.E. "Directional Sensitivity of Wire and Fiber-film Probes *An Experimental Study*" DISA Information No.11 May 1971.
- [33] Payne, F.M., Ng, T.T., and Nelson, R.C. "Experimental Study of the Velocity field on a Delta Wing" 19th AIAA Fluid Dynamics, Plasma Dynamics, and Laser Conference, AIAA-87-1231, Honolulu, Hawaii, June 8-10, 1987.
- [34] Hemsch, M. J. and Luckring, J. M. "Connection between Leading Edge Sweep, Vortex Lift and Vortex Strength for Delta Wings" AIAA Journal of Aircraft Vol.27, No.5 May 1990.
- [35] Wentz, W.H. and MacMahon, M.C., "Further Experimental Investigations of Delta and Double Delta Flowfields at Low Speeds", NASA CR-714, Feb 1967.
- [36] Delery, J., Pagan, D. and Solignac, J.L., "On the Breakdown of the Vortex Induced by a Delta Wing" Colloquium on Vortex Control and Breakdown Behavior, Baden, Switzerland, ONERA TP 1987-105, April 6-7, 1987.
- [37] Smith, J.H.B. "Calculations of the Flow over Thick, Conical, Slender Wings with Leading Edge Separation" ARC R&M 3694, March 1971
- [38] Iwanski, Kenneth P. "An Investigation of the Vortex Flow Over a Delta Wing with and without External Jet Blowing" Masters Thesis, University of Notre Dame, April 1988.
- [39] Hawk, J., Barnett, R., and O'Neil, P. "Investigation of High Angle of Attack Vortical Flow Over Delta Wings" 28th AIAA Aerospace Sciences Meeting, AIAA 90-0101 January 8-11, 1990 Reno, Nevada.

DETERMINATION DE CRITERES D'ECLATEMENT TOURBILLONNAIRE  
PAR RESOLUTION DES EQUATIONS D'EULER ET DE NAVIER STOKES  
par

T.H. LE\*, PH. MEGE\*, Y. MORCHOISNE\*\*

\* Office National d'Etudes et de Recherches Aérospatiales (ONERA)  
B.P. N° 72 - 92322 CHATILLON CEDEX (France)

\*\* Office National d'Etudes et de Recherches Aérospatiale (ONERA) et  
L.A.N., Université Paris VI, 75230 PARIS Cedex 05, France

RESUME

Le phénomène de l'éclatement tourbillonnaire joue un rôle important dans l'aérodynamique des avions de combat ou des missiles aux grandes incidences. Malgré de nombreux travaux, la connaissance précise de l'éclatement tourbillonnaire reste imparfaite et en particulier il n'existe pas de critère fiable pour caractériser ce phénomène.

Au moyen de simulations numériques, basées sur la résolution des équations d'Euler et de Navier-Stokes, une étude paramétrique sur le cas d'un tourbillon isolé soumis à une perturbation initiale a été réalisée.

Les résultats de cette étude permettent de préciser le domaine de validité d'un critère basé sur le nombre de Rossby pour déterminer l'état éclaté ou non éclaté du tourbillon.

ABSTRACT

The vortex breakdown plays a key role in aerodynamics, especially on fighter aircraft or missile at high angles of attack. In spite of many studies, the knowledge of vortex bursting phenomenon is not complete and no reliable criterion is available to characterize it.

Based upon numerical simulations which solve the Euler of the Navier-Stokes equations, a parametric study is carried out on the configuration of an isolated vortex subjected to an initial perturbation.

Results obtained from this study allow to specify a criterion based upon an appropriately defined local Rossby number in order to determine the region where breakdown occurs.

1 ■ INTRODUCTION

Le phénomène de l'éclatement tourbillonnaire joue un rôle important dans l'aérodynamique des configurations aux grandes incidences. Ce phénomène, qui se produit sur le véhicule aérodynamique, conduit à une perte de stabilité et par conséquent à un contrôle délicat de celui-ci. Ces instabilités induisent un moment de roulis qu'il est important d'évaluer de façon correcte afin éventuellement de la corriger pour les besoins du pilotage. Une meilleure compréhension de ces phénomènes permettrait de prévoir et de maîtriser les écoulements tourbillonnaires, par exemple lors des manoeuvres de sustentation demandées au décollage et à l'atterrissage.

De nombreuses études théoriques [1-8] et expérimentales [9-15] lui ont été consacrées, tant à l'ONERA que dans d'autres laboratoires en France et à l'étranger. Malgré ces travaux, la connaissance précise de l'éclatement tourbillonnaire reste imparfaite et en particulier il n'existe pas de critère fiable pour caractériser ce phénomène.

Le but du présent article est de déterminer, à l'aide d'une étude des paramètres définissant le tourbillon initial, les conditions de l'éclatement de ce tourbillon. Cette étude est réalisée au moyen de simulations numériques, basées sur la résolution des équations d'Euler [16, 17] et de Navier-Stokes tridimensionnelles en instationnaire pour un écoulement de fluide incompressible. Le cas traité est celui d'un tourbillon isolé soumis à une perturbation initiale.

2 - FORMULATION MATHÉMATIQUE2.1. Problème continu

Le problème consiste à résoudre les équations de Navier-Stokes, en variables primitives, pour un écoulement tridimensionnel, instationnaire, de fluide incompressible, dans le domaine  $\Omega = [-a, a] \times [-b, b] \times [c, d]$ , de frontière  $\Gamma$ .

En variables adimensionnées à l'aide d'une longueur de référence  $L$  et d'une vitesse de référence  $U_r$ , le problème s'écrit :

$$(1) \quad \frac{\partial U}{\partial t} + (\nabla \wedge U) \wedge U + \nabla(P + \frac{1}{2}U^2) = \frac{1}{Re} \Delta U$$

$$(2) \quad \nabla \cdot U = 0$$

où  $U$  est la vitesse,  $P$  la pression et  $Re = \frac{U_r L}{\nu}$  le nombre de Reynolds. Les équations d'Euler sont obtenues en prenant la viscosité égale à 0.

À ces équations, sont associées des conditions initiales et des conditions aux limites portant sur la vitesse :

conditions initiales

. dans tout le domaine

$$U(x, t=0) = U_0(x)$$

conditions aux limites

. sur les frontières latérales, des conditions de Dirichlet,

$$U(-a, x_2, x_3, t) = e(x_2, x_3)$$

$$.. U(a, x_2, x_3, t) = -e(x_2, x_3)$$

$$. U(x_1, -b, x_3, t) = f(x_1, x_3)$$

$$.. U(x_1, b, x_3, t) = -f(x_1, x_3)$$

. sur la frontière amont, des conditions de Dirichlet,

$$.. U(x_1, x_2, c, t) = g(x_1, x_2)$$

. sur la frontière aval, des conditions de Neumann,

$$.. \frac{\partial U}{\partial n}(x_1, x_2, d) = 0$$

avec  $x = (x_1, x_2, x_3)$  et  $n$  la normale extérieure à la frontière  $\Gamma$ .

Ces conditions aux limites permettent, pour un domaine de calcul suffisamment grand, d'étudier l'évolution d'un tourbillon isolé jusqu'à son éclatement sans que les frontières ne viennent perturber de façon notable la solution.

La prise en compte de l'équation de continuité (équation (2)) est obtenue par minimisation d'une norme de la divergence de la vitesse à l'aide d'un algorithme itératif, la pression totale étant considérée comme un multiplicateur de Lagrange associé. L'équation pour le calcul de la pression est obtenue en appliquant l'opérateur divergence à l'équation (1), puis en écrivant que la divergence de la vitesse est nulle, équation (2).

## 2.2. Problème discret

L'approximation discrète se fait à l'aide de schémas aux différences finies en temps et en espace développés initialement pour la simulation directe de la turbulence [18].

### 2.2.1. Schéma en temps

Le schéma en temps utilisé est un schéma explicite d'Adams-Bashforth précis à l'ordre 2, l'approximation discrète des équations étant évaluée au temps  $n + \frac{1}{2}$ .

Les équations semi-discrètes s'écrivent alors :

$$(3) \quad \frac{U^{n+1} - U^n}{\Delta t} + (\nabla \wedge U^*) \wedge U^* + \nabla Q^{n+\frac{1}{2}} = \frac{1}{Re} \nabla^2 U^*$$

$$(4) \quad \nabla \cdot U^{n+1} = 0$$

avec  $U^* = 1,5U^n - 0,5U^{n-1}$  et  $Q = P + \frac{1}{2}U^2$  la pression totale.

### 2.2.2. Schéma en espace

La discrétisation en espace se fait à l'aide de formules aux différences finies, précises à l'ordre 4, centrées pour les points courants et décentrées au "voisinage" des frontières du domaine. Le système d'équations linéaires associé s'écrit :

$$(5) \quad A(U^{n+1} - U^n) + \Delta t G Q^{n+\frac{1}{2}} = \Delta t K(U^n, U^{n-1})$$

$$(6) \quad D \cdot U^{n+1} = 0$$

où  $U$  est un vecteur contenant la valeur de la vitesse aux points du maillage et où  $Q$  est un vecteur contenant la valeur de la pression aux mêmes points.

Les matrices  $G$ ,  $D$  et  $K$  représentent respectivement, les matrices associées aux opérateurs gradient et divergence et la partie explicite du schéma (convection + diffusion). La matrice  $A$  représente un opérateur implicite de lissage ( $A$ ) des termes de convection et de diffusion. Les conditions aux limites, portant sur la vitesse, sont prises en compte par l'intermédiaire de cet opérateur. Cet opérateur est factorisé sous la forme  $A = A_1 A_2 A_3$ , avec

$$A_1 = 1 - \eta \frac{\partial^2}{\partial x_1^2} \quad \text{et} \quad \eta = O(\Delta t^2)$$

et des expressions analogues pour  $A_2$  et  $A_3$ .

L'opérateur  $A$  fait intervenir une dérivée seconde discrétisée par un schéma de différences finies d'ordre 2. Il permet d'étendre le domaine de stabilité tout en conservant un schéma précis à l'ordre 2 en temps lorsque  $\eta = O(\Delta t^2)$ .

### 2.2.3 Calcul de la pression

En appliquant l'opérateur divergence discrétisé  $D \cdot$  à l'équation (5), la pression totale  $Q$  vérifie l'équation de Poisson suivante :

$$-D \cdot A^{-1} G Q^{n+\frac{1}{2}} = \frac{D \cdot U^{n+1}}{\Delta t} - \frac{D \cdot U^n}{\Delta t} - D \cdot A^{-1} K(U^n, U^{n-1})$$

Le principe du calcul de la pression est basé sur la minimisation de la norme discrète de  $D \cdot U^{n+1}$ . Le système linéaire associé est rendu régulier par élimination des modes parasites [19] et résolu de façon itérative par la méthode Multigradient [20].

Les opérateurs  $A_1$ ,  $A_2$  et  $A_3$  sont factorisés sous la forme L.U., la résolution des systèmes linéaires associés se réduit alors à une simple descente-remontée à chaque pas de temps.

### 3 APPLICATION

#### 3.1. Description du cas test

L'étude effectuée est celle de l'évolution, dans un repère  $(0, x, y, z)$ , d'un tourbillon isolé d'axe Oz dont les caractéristiques dans l'état initial non perturbé sont données par le champ de vitesse axisymétrique suivant :

$$V_r = 0$$

$$V_\theta = \Gamma \left( 1 - \exp\left(-\frac{r^2}{\delta^2}\right) \right) / r$$

$$V_z = V_o + (V_{axe} - V_o) \exp\left(-\frac{r^2}{\delta^2}\right)$$

$$\text{avec } \sqrt{x^2 + y^2} = r$$

ou  $V_r$ ,  $V_\theta$  et  $V_z$  représentent respectivement les composantes radiale, tangentielle et axiale de la vitesse. Les vitesses  $V_o$  et  $V_{axe}$  correspondant respectivement à l'écoulement potentiel et à la vitesse sur l'axe. La longueur caractéristique  $L$  est prise égale à  $\delta$ , la vitesse de référence  $U_r$  est prise égale à  $V_o$ . Les profils de vitesse imposés sont ceux décrits par Batchelor [21]. Les valeurs de  $V_{axe}$  supérieures à  $V_o$  correspondent à une survitesse axiale représentative des tourbillons d'ailes delta [15]. La composante azimutale du champ de vitesse correspond au tourbillon bidimensionnel de Burgers.

De façon à obtenir un éclatement tridimensionnel, on introduit une perturbation au champ initial de vitesse azimutale [16].

#### 3.2. Maillage

Compte tenu du champ de vitesse initial, le tourbillon est concentré dans le voisinage de l'axe z. Le maillage retenu est cartésien, régulier suivant la direction z et présente dans la direction radiale un resserrement au voisinage de l'axe. Dans ce but, les coordonnées des points de maillage seront définies par  $x$ ,  $y$  :

$$x = f(\xi_1)$$

$$y = f(\xi_2)$$

$$\text{avec } f(\xi_l) = \frac{\alpha_l (\xi_l - \beta_l)}{1 - \gamma_l (\xi_l - \beta_l)^2} \quad l = 1, 2$$

La coordonnée  $z$  est donnée par la formule suivante :

$$z = \xi_3$$

$(\xi_1, \xi_2, \xi_3)$  sont les coordonnées dans l'espace de calcul où les pas de discrétisation sont constants. Le maillage dans un plan  $xy$  est composé de  $33 \times 33$  points de discrétisation. On considérera 403 points équirépartis dans la direction  $z$ .

Les dimensions du domaine de calcul sont  $[-8,8] \times [-8,8] \times [-10,30]$ .

Pour ce maillage les constantes  $\alpha_l$ ,  $\beta_l$ ,  $\gamma_l$  valent :

$$\alpha_1 = 0,048$$

$$\beta_1 = 17$$

$$\gamma_1 = 3,53 \cdot 10^{-3}$$

Ces valeurs donnent les tailles de maille minimales et maximales suivantes :

$$\Delta x_{\min} = \Delta y_{\min} = 0,048; \Delta z_{\min} = 0,1$$

$$\Delta x_{\max} = \Delta y_{\max} = 4,5; \Delta z_{\max} = 0,1$$

Les calculs sont effectués sur CRAY 2. Le coût de calcul est de  $9 \cdot 10^{-6}$  secondes par point et par pas de temps, avec un nombre moyen de 6 itérations par pas de temps pour le calcul de la pression. Le coût total d'un calcul est compris entre 30 minutes et 45 minutes suivant les configurations étudiées.

#### 4 - CARACTERISATION DE L'ECLATEMENT

Il est admis, selon [22], que l'éclatement tourbillonnaire est caractérisé par la présence d'un point d'arrêt sur l'axe pour ce qui concerne les simulations numériques et les expériences en milieu confiné. Pour les études expérimentales en milieu non confiné, l'éclatement est défini comme une rapide expansion du noyau tourbillonnaire, associé à une décélération brutale de la vitesse axiale. De plus, les résultats numériques de certains auteurs [23] mettent en évidence un éclatement tourbillonnaire sans présence de point d'arrêt sur l'axe.

La caractérisation de l'éclatement sera déterminée dans cet article suivant les développements récents d'une théorie de la caractérisation de la stabilité hydrodynamique au sein d'écoulements [24]. Le principe de cette théorie consiste à introduire, à l'instant  $t = 0$  et à un endroit quelconque du fluide, une perturbation, puis d'étudier la réponse donnée par l'écoulement.

L'étude des profils de vitesse d'un tourbillon isolé, en fonction de son taux de rotation donne différents types de réponses possibles (figure 1) :

- pour un taux de rotation suffisamment faible l'écoulement est stable, la perturbation n'est pas amplifiée ; une représentation schématisée est donnée par la figure 1a,
- lorsque le taux de rotation augmente l'écoulement devient convectivement instable, un paquet d'onde apparaît et se déplace à partir du point source vers l'aval du domaine ; l'amplitude de la perturbation commence par croître exponentiellement, puis décroître vers zéro lorsque  $t$  tend vers l'infini. La présence de deux fronts d'onde se convectant vers l'aval est représentée sur la figure 1b,
- pour un certain seuil du taux de rotation, le fluide est proche de la transition supercritique-subcritique au sens de Benjamin (analogie au ressaut hydraulique), l'écoulement devient de type instable absolu ; l'état instable absolu est défini comme un état où l'amplitude des perturbations est non bornée dans le temps, la vitesse du groupe du paquet d'onde associé tendant vers zéro (état critique, figure 1c),
- pour des valeurs supérieures de ce taux de rotation, le fluide devient fortement subcritique, l'écoulement, absolument instable, est le siège de perturbations se propageant, à la fois vers l'amont et vers l'aval, il apparaît au sein du fluide une zone de recirculation qui a tendance à se déplacer vers l'amont.

#### 5 - ETUDE PARAMETRIQUE

##### 5.1 Nombre de Rossby, nombre de Reynolds

On étudie l'influence des paramètres qui définissent le profil de vitesse initiale sur l'apparition de l'éclatement tourbillonnaire. Ces paramètres peuvent se ramener à une grandeur caractéristique adimensionnée, le nombre de Rossby.

Pour les profils de vitesse considérés, le nombre de Rossby s'exprime sous la forme :

$$R_o = \frac{(V_{axe} - V_o) \delta}{\Gamma}$$

Le second nombre sans dimension caractéristique des écoulements visqueux est le nombre de Reynolds donné par la relation :

$$R_e = \frac{V_o \delta}{\nu}$$

La variation de la viscosité  $\nu$ ,  $\delta$  étant constant, permet d'étudier l'influence du nombre de Reynolds.

### 5.2. Description de l'étude paramétrique

Une première partie des résultats a été obtenue en faisant varier la circulation  $\Gamma$ , ce qui revient à faire varier le nombre de Rossby, les autres paramètres étant fixés.

La seconde partie de l'étude consiste à faire varier le nombre de Reynolds, à nombre de Rossby fixé.

La troisième partie de l'étude paramétrique concerne l'influence du rayon visqueux  $\delta$ , de la circulation et de la viscosité, ces paramètres variant de façon à ce que les nombres de Rossby et de Reynolds restent constants.

### 5.3. Influence du nombre de Rossby

L'étude de l'influence du nombre de Rossby est effectuée pour un nombre de Reynolds fixé égal à  $4 \cdot 10^4$ . Cette étude porte sur quatre valeurs de la circulation (0,1 ; 0,3 ; 0,5 ; 0,8) auxquelles correspondent quatre valeurs du nombre de Rossby (3,76 ; 1,25 ; 0,62 ; 0,47). Les profils initiaux de vitesse correspondant sont donnés sur la figure 2. Pour ces quatre valeurs de la circulation, les profils de vitesse axiale sont identiques, en ce qui concerne les profils de vitesse azimutale le rayon du tourbillon reste constant.

La figure 3 montre l'évolution de la vitesse axiale au cours du temps en fonction du nombre de Rossby. Les quatre diagrammes associés représentent les quatre types de configurations décrites au paragraphe 4.

Pour  $Ro = 3,76$ , l'écoulement est stable, du moins jusqu'au temps  $t = 50$ , temps final du calcul. Lorsque le nombre de Rossby diminue ( $Ro = 1,25$ ), la perturbation initiale s'amplifie tout en étant convectée vers l'avant à la vitesse de l'écoulement potentiel ( $V_0$ ). L'état est convectivement instable.

On atteint le seuil critique pour un nombre de Rossby égal à 0,62. L'écoulement franchit alors le stade d'un état absolument instable. Cette configuration correspond exactement au seuil à partir duquel l'éclatement est observé.

Pour un nombre de Rossby inférieur, égal à 0,47, il apparaît, en plus du front se convectant vers l'avant, une zone de recirculation qui se propage vers l'amont du domaine. Ce cas correspond à un état où le fluide est fortement subcritique.

L'accroissement du taux de rotation, équivalent d'une diminution du nombre de Rossby, entraîne donc une évolution de l'écoulement vers un état éclaté.

### 5.4. Influence du nombre de Reynolds

La seconde partie de l'étude paramétrique porte sur l'influence du nombre de Reynolds, à nombre de Rossby fixé.

La figure 4 montre l'évolution de la vitesse axiale sur l'axe pour des calculs effectués à différents nombres de Reynolds, pour un nombre de Rossby de 0,62 correspondant au seuil critique obtenu précédemment.

Les résultats obtenus pour des nombres de Reynolds supérieurs à 400 mettent en évidence deux minima, le premier étant situé au voisinage de la position où la perturbation initiale a été introduite.

Aux nombres de Reynolds inférieurs, le profil de vitesse axial ne présente plus de gradient brusque, la vitesse axiale étant constante pour un nombre de Reynolds de 100. Pour ces cas l'éclatement tourbillonnaire n'a pas lieu. Les calculs effectués pour un nombre de Rossby égal à 0,7, au mêmes nombres de Reynolds que précédemment révèlent des états non éclatés.

Cependant on remarque une chute de vitesse axiale localisée près de la frontière amont, d'autant plus importantes que le nombre de Reynolds est faible. Le profil de vitesse initiale imposé au cours du temps sur cette frontière vérifie les équations d'Euler. Pour un calcul effectué à partir des équations de Navier-Stokes, cette condition n'est plus adaptée. Un autre type de condition amont semble donc nécessaire pour résoudre ce problème [25].

### 5.5. Influence du rayon visqueux à $Ro$ et $R_e$ fixés

Cette étude est effectuée en se fixant les nombres de Reynolds et de Rossby, les paramètres  $\delta$ ,  $\nu$  et  $\Gamma$  variant de façon simultanée.

La configuration étudiée concerne un cas Euler ( $\nu = 0$ ), et un nombre de Rossby de 0,26. Pour cette valeur du nombre de Rossby deux calculs ont été effectués avec les doublets ( $\delta = 0,34$  ;  $\Gamma = 1,47$ ) et ( $\delta = 0,19$  ;  $\Gamma = 0,85$ ). Les profils initiaux de vitesse sont représentés sur la figure 5 ainsi que les résultats correspondants. Les courbes de vitesse axiale présentent les mêmes caractéristiques d'évolution, à savoir la présence, dans les deux cas, de deux minima mettant en évidence l'apparition d'un éclatement tourbillonnaire. Aux grands nombres de Reynolds il apparaît donc une totale indépendance du phénomène de l'éclatement vis à vis du paramètre  $\delta$ .



### 5.6. Critère d'éclatement

Un balayage systématique des paramètres a été effectué et a permis de préciser un seuil d'éclatement. Les résultats obtenus par les présentes simulations, ainsi que l'ensemble des résultats connus [22], sont donnés sur la figure 7 sous la forme d'un diagramme Rossby-Reynolds, les symboles représentant les cas traités. Ces symboles sont pleins (resp. vides) pour les états éclatés (resp. non éclatés).

Pour les nombres de Reynolds supérieurs à 400, l'ensemble des résultats obtenus par l'étude paramétrique est en bon accord qualitatif avec les résultats expérimentaux existants. Pour ces valeurs, l'éclatement se produit pour un nombre de Rossby égal à 0,62, légèrement inférieur à celui donné par les expériences (entre 0,64 et 0,7). Pour des nombres de Reynolds inférieurs à 400, la validité de tous les résultats numériques de cette figure est fortement sujette à caution compte tenu de la remarque du paragraphe 5.4. Par ailleurs il n'existe pas à notre connaissance, pour de tels nombres de Reynolds, de données expérimentales permettant d'initialiser le calcul.

### 6. CONCLUSION

Le but de cette étude était double : d'une part la mise au point d'un code de calcul permettant une description détaillée de l'éclatement d'un tourbillon isolé, d'autre part, à l'aide d'une étude paramétrique, une meilleure compréhension du phénomène et donc de sa prédiction.

Les caractéristiques essentielles de l'éclatement tourbillonnaire obtenues dans le cas présent permettent de tirer les conclusions suivantes :

- l'apparition du phénomène est brutale,
- il est de nature tridimensionnelle et instationnaire,
- il met en évidence une structure spirale, confinée, suivie de l'apparition en aval d'un bulbe de recirculation étendu,
- un régime turbulent caractérisé par de petites structures s'établit dès l'instant  $t = 25$ .

L'étude paramétrique réalisée, loin d'être exhaustive, permet cependant de tirer plusieurs enseignements quant à la stabilité d'écoulement de type jet rotatif. L'augmentation du taux de rotation fait évoluer l'écoulement d'un état convectivement instable à un état absolument instable. Ces résultats corroborent les travaux théoriques, effectués dans le cadre d'une gamme d'écoulements plus variés, de P.Huerre et P.A. Monkevitz [24].

Les représentations physiques du phénomène pourraient être améliorées par la mise en place d'un modèle de sous-maille permettant l'étude précise des petites structures tourbillonnaires qui apparaissent après l'éclatement.

La prise en compte de la proximité d'une paroi serait également nécessaire pour la simulation des configurations d'éclatements réalistes, par exemple celles se produisant au-dessus d'une voilure.

\* Cette étude a bénéficié du soutien financier de la Délégation Générale de l'Armement (DGA/DRET).

### REFERENCES

- [1] Hall M.G.  
"A new approach to vortex breakdown". Proc. Heat Trans. Fluid Mech. Inst., University California, 319-340, 1967.
- [2] Bossel W.M.  
Proceedings of Int. Conf. Numer. Methods Fluid Dyn. 2nd, pp. 365-370, 1971.
- [3] Ludwig H.  
"Zur Erklärung der Instabilität der überangestellten Deltaflügeln abretenden freien Wirbelkerne". Z.Flugwiss. Band 10 p. 242-249 1962.
- [4] Squire H.B.  
"Analysis of the vortex breakdown phenomenon, Part 1". Imperial College of Science and Technology, Aeronautics Department, Report n° 102, 1960.
- [5] Leibovich S., Stewartson K.  
"A sufficient condition for the instability of columnar vortices". J.F.M. Vol. 125, pp. 335-356, 1983.
- [6] Benjamin T.B.  
"Theory of the vortex breakdown phenomenon". J.F.M., Vol. 14, pp. 593-629, 1962.
- [7] Hasimoto H.  
"A soliton on a vortex filament". J.F.M. Vol. 51, pp. 477-485, 1972.
- [8] Leibovich S., Ma H.Y.  
"Soliton propagation on vortex cores and the Hasimoto soliton". Phys. Fluids, Vol. 26, pp. 3173-3179, 1983.

- [9] Werlé H.  
"Quelques résultats expérimentaux sur les ailes en flèche, aux faibles vitesses, obtenus en tunnel hydrodynamique". La Recherche Aéronautique n° 41, 1954.
- [10] Peckham D.H., Atkinson S.A.  
"Preliminary results of low-speed wind-tunnel tests on a gothic wing of aspect ratio 1.0.". Aeronautical research council CP-508, 1957.
- [11] Lambourne N.C., Bryer D.W.  
"The bursting of leading-edge vortices. Some observations and discussion of the phenomenon". Aeronautical research council R.M 3282, 1961.
- [12] Sarpkaya T.  
"Effect of the adverse pressure gradient on vortex breakdown". AIAA Journal, Vol. 12, n°5, May 1974.
- [13] Faler J.H., Leibovich S.  
"An experimental map of the internal structure of a vortex breakdown". J.F.M., Vol. 86, pp.313-335, 1978.
- [14] Uchida S., Nakamura Y., Ohsawa M.  
"Experiments on the axisymmetric vortex breakdown in a swirling air flow". Transaction of the Japan society for aeronautical and space sciences. Vol 27, n° 78, p.206-216, 1985.
- [15] Pagan D., Solignac J.L.  
"Etude expérimentale de l'éclatement d'un tourbillon engendré par une aile delta". La Recherche Aérospatiale n° 1986-3.
- [16] Lê T.H., Mège Ph., Morchoisne Y.  
"Simulation numérique de l'éclatement tourbillonnaire par résolution des équations d'Euler en fluide incompressible". La Recherche Aérospatiale, Année 1989 n° 5 (Septembre Octobre), p. 35 à 49.
- [17] Mège Ph., Lê T.H., Morchoisne Y.  
"Numerical simulation of vortex breakdown via 3-D Euler equations". Actes du Congrès Turbulence 89, Grenoble, France, 18-21 Septembre 1989. T.P.ONERA n° 1989-211.
- [18] Deschamps V., Loisel P., Morchoisne Y.  
"Recent developments in inhomogeneous turbulence numerical simulation". 7ème Colloque International sur les Méthodes de Calcul Scientifique et Technique, Versailles, 9-13 décembre 1985. T.P. ONERA n° 1985-169.
- [19] Lê T.H., Morchoisne Y.  
"Traitement de la pression en incompressible visqueux". Méthodes numériques appliquées à la mécanique, à paraître, C.R.A.S. 1990.
- [20] Ryan J., Lê T.H., Morchoisne Y.  
"Panel code solvers". Proceedings of the 7th GAMM, Louvain (Belgique), 9-11 Septembre 1987. T.P.ONERA n° 1987-139.
- [21] Batchelor G.K.  
"Axial flow in trailing line vortices" J.F.M. Vol. 20, pp.645, 1964.
- [22] Spall R.E., Gatski T.B., Grosch C.E.  
"On a criterion for vortex breakdown". ICASE Report n° 87-3.
- [23] Liu C., Menne S.  
"Simulation of a three-dimensional vortex breakdown". AIAA Paper 89-1806, 20 th Fluid Dynamics, Plasma Dynamics and Laser Conference, Buffalo, N.Y., June 12-14, 1989.
- [24] Huerie F., Monkewitz P.A.  
"Local and global instabilities in spatially developing flows". Annu. Rev. Fluid Mech., vol. 22 pp. 473, 537, 1990.
- [25] Mège Ph.  
"Simulation numérique de l'éclatement tourbillonnaire par résolution des équations de Navier-Stokes en fluide incompressible". Thèse de doctorat de l'Université PARIS VI, Novembre 1990 (à paraître).

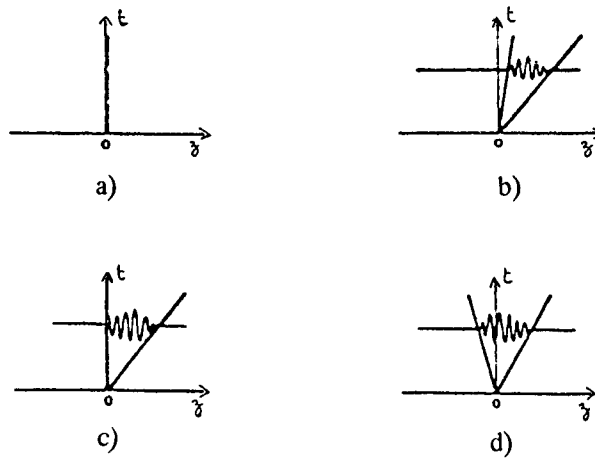


Figure 1 : Diagramme de stabilité

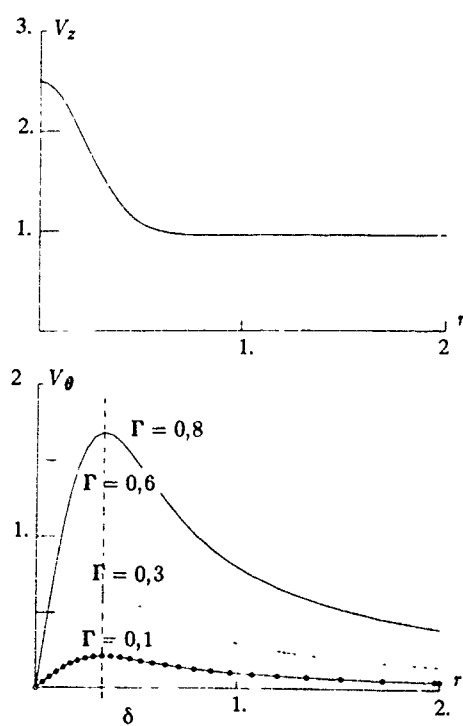


Figure 2 : Profils initiaux de vitesse

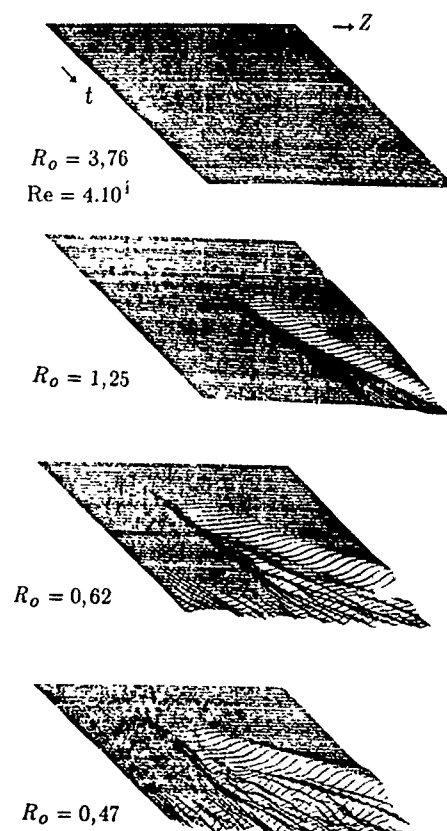


Figure 3 : Evolution de la vitesse axiale

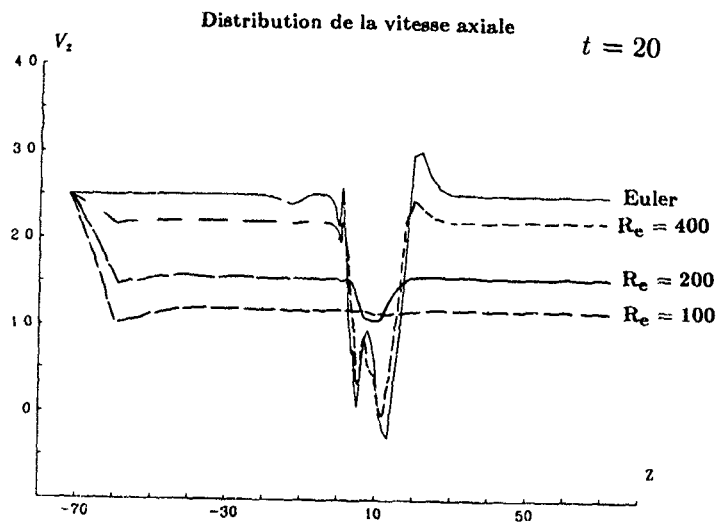


Figure 4 : Influence du nombre de Reynolds

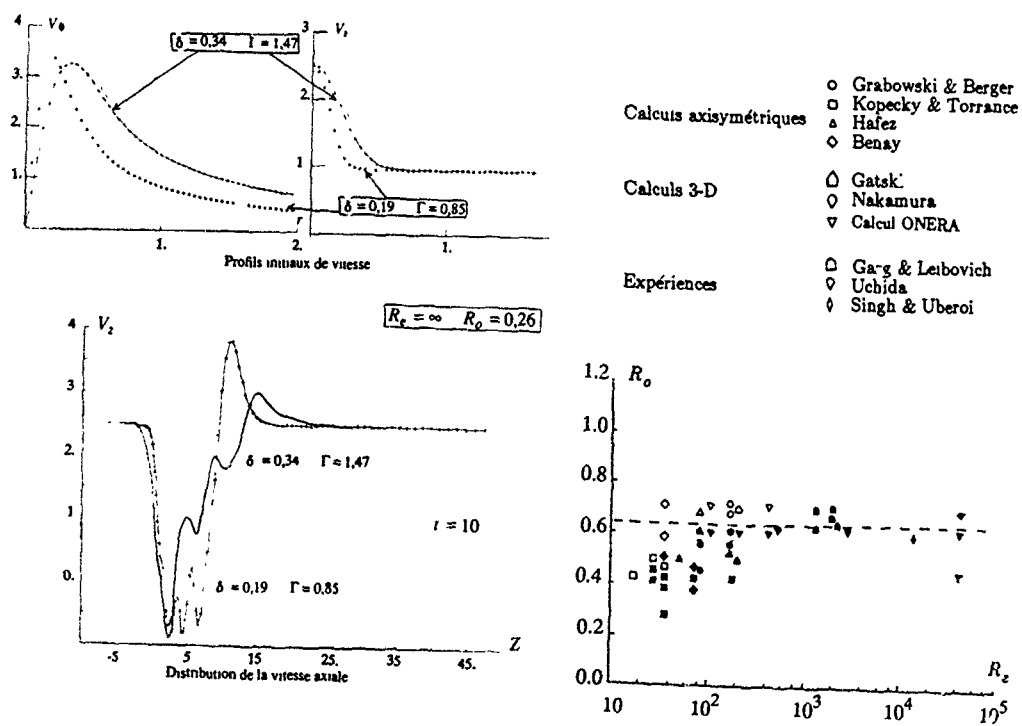


Figure 5 : Influence du profil initial de vitesse

Figure 6 . Diagramme Reynolds-Rosby

# ETUDES FONDAMENTALES SUR L'ECLATEMENT TOURBILLONNAIRE ET SON CONTROLE

D. Pagan<sup>\*</sup> et P. Molton

ONERA

Office National d'Etudes et de Recherches Aéronautiques  
Châtillon-sous-Bagneux  
BP 72 - 92322 Châtillon Cedex FRANCE

## RESUME

Une étude expérimentale et théorique des conditions d'apparition de l'éclatement d'un tourbillon soumis à un gradient de pression a été réalisée. Le but de cette étude est de mettre en évidence l'effet d'un soufflage sur l'axe du tourbillon comme moyen de contrôle de l'éclatement. Sur le plan expérimental, le tourbillon est engendré par un système composé de deux ailettes placées à des incidences opposées. Les mesures par vélocimétrie laser ont permis de caractériser l'organisation de l'écoulement et de déterminer les conditions d'apparition de l'éclatement. Sur le plan théorique, différentes méthodes de calcul ont été expérimentées, basées soit sur la résolution des équations de Navier-Stokes laminares pour un écoulement de révolution, soit sur l'approximation quasi-cylindrique de ces équations. Cette dernière formulation permet de bien représenter l'évolution du tourbillon jusqu'au point d'éclatement. Les résultats montrent un bon accord entre l'expérience et le calcul en ce qui concerne la limite d'apparition de l'éclatement.

## NOTATIONS

A: Section d'entrée de la prise d'air.  
A<sub>c</sub>: Section de sortie de la prise d'air.  
C<sub>μ</sub>: Coefficient de débit de quantité de mouvement.  
D<sub>j</sub>: Diamètre du jet.  
K<sub>p</sub>: Coefficient de pression  $K_p = 2(p-p_0)/\rho V_0^2$ .  
Oxθ: Repère cylindrique associé au repère Oxyz.  
Oxyz: Repère cartésien:  
Ox suivant l'axe de la veine, sens du vent,  
Oy horizontal, perpendiculaire à Ox, droite pilote,  
Oz vertical ascendant,  
Origine 0 prise à l'extrémité de l'ogive.  
p: Pression.  
p<sub>0</sub>: Pression de référence prise en amont du montage.  
q<sub>m</sub>: Débit massique.  
r<sub>c</sub>: Rayon du noyau visqueux du tourbillon.  
R<sub>c</sub>: Nombre de Reynolds basé sur r<sub>c</sub>,  $V_0 r_c / \nu$ .  
Ro: Nombre de Rossby  $r_c U_{axe} / \Gamma_0$ .  
S<sub>ref</sub>: Surface de référence pour le calcul de C<sub>μ</sub>.  
U<sub>axe</sub>: Composante U mesurée sur l'axe du tourbillon.  
UVW: Composantes de la vitesse moyenne dans le repère Oxyz.  
UV<sub>r</sub> V<sub>θ</sub>: Composantes de la vitesse moyenne dans le repère Oxθ.  
u'v'w': Ecart-type des fluctuations de vitesse.  
V<sub>0</sub>: Vitesse de l'écoulement amont non perturbé.  
V<sub>j</sub>: Vitesse moyenne du jet.  
Γ<sub>i</sub>: Circulation divisée par 2π.  
Γ<sub>0</sub>: Circulation extérieure du tourbillon sur 2π.  
ν: Viscosité cinématique de l'air.  
T: Taux de rotation  $T = \text{Ro}^{-1}$ .

ρ: Masse volumique.  
ψ: Fonction de courant de l'écoulement méridien.  
ω: Composante du rotationnel normale au plan méridien.

## 1. INTRODUCTION

En Aérodynamique, le phénomène d'éclatement tourbillonnaire affecte principalement les tourbillons qui se forment à l'extrados des ailes en flèche et sur les fuselages lors du vol à grande incidence. L'éclatement est un processus essentiellement commandé par les propriétés dynamiques locales (champ de vitesse) du tourbillon et l'intensité de la perturbation (champ de pression externe). En fait, le champ de vitesse tourbillonnaire local résulte du développement antérieur du tourbillon. La connaissance des profils de vitesse initiaux et de leur évolution sous l'influence du champ de pression externe et de la viscosité est donc capitale.

A ce jour, il n'existe pas de théorie prédictive de l'éclatement. Cependant, les simulations numériques directes les plus récentes [1] donnent des résultats très encourageants quant à la phénoménologie prise en compte dans des configurations simples. Les études paramétriques réalisées au moyen de ces simulations doivent permettre d'améliorer les moyens de prédiction de l'éclatement et de faire progresser notre connaissance physique de ce phénomène. Cependant, elle ne peuvent pour l'instant représenter l'évolution complète d'un tourbillon placé dans un champ aérodynamique complexe, et doivent être validées par des comparaisons avec les expériences.

Par ailleurs, diverses études théoriques ont, dans le passé, été consacrées à la prédiction de l'apparition de l'éclatement d'un tourbillon soumis à un gradient de pression adverse. Ces études sont basées soit sur l'utilisation des équations de Navier-Stokes moyennées en temps [2,3,4], soit sur l'approximation quasi-cylindrique de ces équations [5]. Ces approches, plus simples de mise en oeuvre que la simulation directe, peuvent être directement confrontées à l'expérience.

Le but de la présente étude est d'analyser l'évolution puis l'éclatement d'un tourbillon isolé soumis à un gradient de pression, et de tester l'effet d'un soufflage sur l'axe comme moyen de contrôle de son éclatement. Les mesures sont réalisées en soufflerie au moyen de la vélocimétrie laser tridirectionnelle. Les calculs reposent sur l'utilisation des équations de Navier-Stokes complètes ou dans le cadre de leur approximation quasi-cylindrique.

## 2. ETUDE EXPERIMENTALE

### 2.1 Montage expérimental

Les essais ont été réalisés dans la soufflerie de

(\*) Présentement à l'Aéronautique, Division des Engins  
Tactiques, 2, rue Béranger, 92320 Châtillon.

type Eiffel S2L de Chalais-Meudon. La veine d'essais de cette soufflerie subsonique a un diamètre de 1 m. Le tourbillon est engendré au moyen d'un système composé de deux ailettes, placées à des incidences opposées, et installées verticalement dans la veine (Figs. 1 et 2). Ces ailettes sont des profils NACA 0012 de 150 mm de corde placés à une incidence de  $10,5^\circ$ . Ils prennent appui d'un côté sur la paroi de la soufflerie, et de l'autre sur un tube cylindrique haubanné, de 40 mm de diamètre, placé sur l'axe de la soufflerie. Ce tube est hémisphérique à son extrémité amont et se termine en aval par une ogive dont la méridienne est ellipsoïdale (grand axe égal à 200 mm). Comme le montre la figure 3, l'extrémité aval de l'ogive est équipée d'orifices permettant d'injecter de l'air au cœur du tourbillon pour moduler le profil de vitesse axial indépendamment du profil de vitesse tangentielle. Trois ogives ont été réalisées, les diamètres  $D_j$  des orifices étant de 1, 2 et 4 mm.

Le champ de pression imposé au tourbillon qui se développe en aval de ce montage est ajustable au moyen d'un dispositif en forme d'entrée d'air (Figs. 1 et 2). Ce dispositif est constitué de deux plaques planes traversant horizontalement la soufflerie. Ces plaques sont équipées dans leur partie aval de volets qui permettent de faire varier le rapport entre le débit d'air capté et débit d'air passant à l'extérieur. Ainsi, la répartition de pression en amont du dispositif peut-elle être ajustée. Chaque répartition de pression est identifiée par le rapport  $A_c/A$  des sections de sortie et d'entrée de la prise d'air. Les essais ont été réalisés dans les conditions suivantes:

- vitesse à l'infini amont:  $V_0 = 15$  m/s,
- nombre de Reynolds  $R_c$  basé sur le rayon  $r_c$  du noyau visqueux:  $R_c \approx 5.10^3$ .

## 2.2 Configuration sans soufflage

Certaines configurations éclatées ont été systématiquement sondées au moyen de la vélocimétrie laser tridirectionnelle [6] afin de tracer des cartographies détaillées des champs de vitesse moyenne et de turbulence. Ces cartographies aident à la compréhension des phénomènes physiques et permettent de constituer des bases de données expérimentales aptes à servir de référence pour la validation des codes de calcul.

Dans le but de qualifier l'écoulement en l'absence de soufflage, une configuration particulière d'éclatement a été étudiée. Elle a été obtenue en fixant le rapport  $A_c/A$  à une valeur de 0,363. Dans ces conditions, l'éclatement se produit à environ 175 mm en aval de l'extrémité de l'ogive. Ceci peut être constaté sur les figures 4, 5 et 6 qui présentent respectivement les lignes iso-valeurs de la composante axiale de la vitesse moyenne  $U$ , de la composante transversale de la vitesse moyenne  $V$  et de l'écart-type des fluctuations de vitesse axiale  $u'$ . Ces résultats obtenus grâce à la vélocimétrie laser à trois composantes sont relatifs à un plan vertical passant approximativement par l'axe du tourbillon. La structure de cet éclatement est très proche de celle de l'éclatement d'un tourbillon d'aile delta [7] et a été décrite plus en détail par ailleurs [8,9]. En amont de l'éclatement, la vitesse axiale présente un extremum sur l'axe ( $U/U_0 \approx 1,2$ ). Au cours de l'éclatement, la valeur de  $U$  mesurée sur l'axe diminue rapidement et devient négative, la circulation diffuse radialement et les valeurs de  $u'/U_0$  atteignent 0,45. Ces valeurs très élevées indiquent que l'origine de l'éclatement est le siège de fluctuations à grande échelle [8].

## 2.3 Conditions d'apparition de l'éclatement

L'effet du soufflage sur l'éclatement a été mis en évidence de deux manières. D'abord en effectuant la mesure de  $U_{axe}$ , composante axiale de la vitesse mesurée sur l'axe du tourbillon, ensuite en réalisant, par visualisation, une étude systématique des conditions d'apparition de l'éclatement en fonction des paramètres d'influence.

Les mesures par vélocimétrie laser ont été exécutées pour différentes intensités de soufflage et différentes ogives mais pour une répartition de pression fixée ( $A_c/A = 0,363$ ). Pour chaque cas, l'évolution de  $U_{axe}(x)$  a été tracée sur la figure 7. Dans le cas sans soufflage,  $U_{axe}$  décroît régulièrement, avant de s'annuler au début de la zone de recirculation. D'autre part, on remarque que l'éclatement se produit d'autant plus en aval que la valeur de  $U_{axe}$  mesurée dans la section la plus en amont est grande. L'efficacité du soufflage augmente donc avec la survitesse axiale qu'il engendre.

Ensuite ont été déterminées les conditions d'apparition de l'éclatement en fonction des caractéristiques des profils de vitesse moyenne mesurés dans la section  $x = 120$  mm et de la répartition de pression imposée au tourbillon. Pour cela, l'éclatement est visualisé au moyen de fumées de sulfite d'ammonium créées par le mélange des gaz ammoniac et anhydride sulfureux émis par deux orifices situés comme indiqués sur la figure 3. Les visualisations ont été réalisées pour différents débits d'injection, c'est-à-dire pour différentes formes du profil de vitesse axiale. Le débit massique  $q_m$  injecté était mesuré au moyen d'un débitmètre à col sonique. Les valeurs de  $q_m$  ont été fixées à 0,1, 0,15, 0,20, 0,25 et 0,3 g/s.

La perte de charge entre le débitmètre et l'orifice étant inconnue, le débit de quantité de mouvement axiale  $q_m V_j$  du jet a été évalué à partir de profils de vitesse axiale mesurés dans la section  $x = 120$  mm (présentés sur la figure 8 et décrits ci-dessous), par intégration sur un disque de 30 mm de rayon. L'intensité du soufflage est caractérisée par le coefficient de débit de quantité de mouvement:

$$(1) \quad C_\mu = 2q_m V_j / (\rho V_0^2 S_{ref}),$$

où la surface de référence choisie,  $S_{ref}$ , est le maître-couple du cylindre central du montage expérimental. Le tableau suivant donne les valeurs de  $C_\mu$  calculées pour les différentes ogives et les différents débits massiques.

$q_m$ (g/s)	0,1	0,15	0,2	0,25	0,3
$D_j$ (mm)					
1	0,13	0,35	0,52		
2	0,09	0,05	0,15	0,35	0,41
4	0,01	0,01	0,02	0,04	0,07

Tableau I: Valeurs de  $C_\mu$

Sur les figures 8 et 9 ont été tracés les profils de  $U$  et  $V$  mesurés dans la section  $x = 120$  mm, pour les trois ogives utilisées et les différentes valeurs de  $q_m$ . Sur ces mêmes figures ont été portées les courbes obtenues par les formules suivantes:

$$(2) \quad U(r) = U_0 + U_1 \exp(-r^2/r_1^2) + U_2 \exp(-r^2/r_2^2)$$

$$(3) \quad Vg(r) = \Gamma_0/r [1 - \exp(-r^2/r_3^2)],$$

dont les paramètres  $U_0, U_1, U_2, r_1, r_2, \Gamma_0$  et  $r_3$  ont été déterminés par la méthode des moindres carrés. Ces courbes sont très proches des mesures expérimentales et leur utilisation permet d'obtenir de manière systématique les paramètres représentatifs des profils de  $U$  et  $V$ . D'autre part, les formules (2) et (3) fournissent des conditions amont lissées, plus exploitables que les données expérimentales brutes par les codes de calcul.

On observe que pour des valeurs de  $C_\mu$  inférieures à 0,05, le soufflage ne modifie pas de manière sensible le profil de vitesse axiale. Pour les valeurs de  $C_\mu$  les plus fortes ( $C_\mu \geq 0,4$ ), l'accroissement de la valeur de  $U$  mesurée sur l'axe,  $U_{axe}$ , peut atteindre 12%. En revanche, le soufflage affecte peu les profils de  $V$ .

De la même façon sur la figure 10 ont été tracées les répartitions de pression mesurées à la paroi de la veine, dans le plan horizontal passant par l'axe du tourbillon, pour différentes valeurs du rapport  $A_c/A$ . La formule choisie pour représenter les mesures est:

$$(4) \quad Kp(x) - Kp(-\infty) = c_1 [th(c_2(x-x_0)) + 1].$$

Les notations suivantes s'introduisent naturellement:

$$(5) \quad c_1 = \Delta Kp/2 \text{ et } c_2 = (dKp/dx)_{max}/c_1,$$

où:

$$\Delta Kp = Kp(+\infty) - Kp(-\infty).$$

Les valeurs de  $c_1$  et  $c_2$  sont déterminées par la méthode des moindres carrés. On observe là aussi un excellent accord entre ces formules et les mesures expérimentales.

Les conditions d'apparition de l'éclatement sont représentées sur la figure 11 par des points de différentes natures sur un diagramme donnant le taux de rotation  $\tau = \Gamma_0/(r_c U_{axe})$  - qui n'est autre que l'inverse d'un nombre de Rossby  $R_0 = \tau^{-1}$  - en fonction de la recompression imposée au tourbillon  $Kp(+\infty) - Kp(x=120 \text{ mm})$ . Il apparaît que les points expérimentaux se regroupent sur une courbe unique. Etant donné que le taux de rotation fait intervenir  $U_{axe}$ , le soufflage permet donc de stabiliser le tourbillon, en ce sens qu'une plus forte recompression est nécessaire pour déstabiliser un tourbillon possédant une forte survitesse sur son axe.

### 3. ETUDE THEORIQUE

Sur le plan théorique deux méthodes de calculs ont été expérimentées. Elles sont basées sur la résolution des équations de Navier-Stokes en écoulement de révolution:

- la forme complète des équations de Navier-Stokes laminaires (NS) et,

- l'approximation quasi-cylindrique (QC) des équations de Navier-Stokes.

#### 3.1 Equations de Navier-Stokes en écoulement laminaire de révolution

Un code numérique résolvant les équations de Navier-Stokes en écoulement laminaire de révolution a été développé pour traiter le phénomène de l'éclatement. Ce code prévu initialement pour calculer l'éclatement à l'intérieur d'une conduite cylindrique [3] a été étendu par la suite au cas d'un tourbillon placé en atmosphère illimitée et soumis à un gradient de pression adverse [10]. Cette dernière version a été utilisée ici dans le but de déterminer les conditions d'apparition de l'éclatement pour des tourbillons semblables à ceux décrits au § 2.

Ce code résout les équations de Navier-Stokes instationnaires écrites en variables rotationnel  $\omega$ , fonction de courant  $\psi$  et circulation  $\Gamma$  au moyen d'un schéma implicite, au différences finies et décentré dans le sens de la vitesse. La précision est du premier ordre en temps et en espace. Une précision convenable peut cependant être obtenue par l'utilisation de maillages resserrés.

Le calcul est effectué dans un domaine rectangulaire comportant une section d'entrée, une section de sortie, une frontière extérieure et un axe de symétrie (voir figure 12). Dans la section d'entrée sont imposés les profils de vitesse axiale  $U(r)$  et tangentielle  $Vg(r)$  en utilisant les formules (2) et (3) du § 2, avec  $U_2 = 0$  et  $r_1 = r_3 = 0,945r_c$ . Pour ce qui concerne la vitesse radiale  $V_r$ , la dérivée  $\partial V_r / \partial x$  est supposée nulle. Dans la section de sortie, on suppose l'invariance axiale des trois variables de calcul  $\Gamma, \psi$  et  $\omega$ . Sur la frontière extérieure, on se donne l'évolution de  $U = f(x)$  et on suppose que la circulation reste radialement constante. Sur cette frontière, les formules utilisées pour  $\omega$  et  $\psi$  sont:

$$(6) \quad \partial \psi / \partial r = r f(x),$$

$$(7) \quad \partial(r\omega) / \partial r = - \partial^2(rf) / \partial z^2.$$

Par l'intermédiaire de la loi de Bernoulli appliquée le long de la frontière extérieure, la loi  $U = f(x)$  peut-être obtenue à partir d'une répartition de pression  $Kp(x)$ . En pratique c'est l'expression donnée par les formules (4) et (5) du § 2 qui a été utilisée.

Quand une solution éclatée stationnaire est obtenue, ce qui est le cas pour de faibles nombres de Reynolds ( $R_e \leq 200$ ), les lignes iso- $\psi$  prennent l'allure du tracé de la figure 13. Sur cette figure on distingue une zone de recirculation typique d'un éclatement de type bulbe. Pour des nombres de Reynolds plus élevés on obtient des solutions instationnaires.

Ce code a été exploité pour déterminer les conditions d'apparition de l'éclatement. Ainsi, il a été possible de relier entre eux les différents paramètres d'influence:  $U_{axe}/V_0, \Gamma_0, R_0, \Delta Kp$  et  $r_c(dKp/dx)_{max}$ .

Les courbes de la figure 14 présentent l'influence du nombre de Reynolds  $R_e$  sur la valeur  $\tau_{lim}$  que prend  $\tau$  pour les conditions d'apparition de l'éclatement. Ces courbes sont données pour  $\Delta Kp = 0,4, (dKp/dx)_{max} = 0,2$  et  $U_{axe}/V_0 = 0,5, 1,0$  et  $1,5$ . On observe que l'effet du nombre de Reynolds n'est sensible que pour des valeurs inférieures à 100. Une diminution de  $R_e$  entraîne une stabilisation du tourbillon, en ce sens que le taux de rotation  $\tau_{lim}$  nécessaire pour provoquer l'éclatement doit être plus élevé. Pour les valeurs de  $R_e$  plus grandes, la valeur de  $\tau_{lim}$  reste sensiblement constante et indépendante de  $U_{axe}/V_0$  lorsque ce paramètre varie.

entre 1 et 1,5. Pour une valeur de 0,5, le tourbillon apparaît plus instable.

La courbe limite d'éclatement déterminée pour les conditions expérimentales du § 2 a été reportée en trait continu sur la figure 11, où l'on observe un excellent accord avec les résultats expérimentaux. On constate que cette approche permet de prévoir convenablement les conditions d'éclatement d'un tourbillon. En fait, l'accord avec l'expérience reste bon tant que le gradient de pression imposé au tourbillon s'applique sur une distance pas trop grande devant  $r_c$  [ $(r_c/\Delta Kp) \cdot (dKp/dx)_{\max} \geq 10^{-2}$ ]. Pour des gradients s'appliquant sur des distances plus grandes [ $(r_c/\Delta Kp) \cdot (dKp/dx)_{\max} \leq 10^{-2}$ ] il est indispensable de tenir compte de l'influence de la turbulence qui modifie les profils de vitesse moyenne.

### 3.2 Equation de Navier-Stokes en approximation quasi-cylindrique

On appelle approximation quasi-cylindrique des équations de Navier Stokes, l'approximation qui consiste à supposer que l'échelle des évolutions radiales des grandeurs est petite devant celle des évolutions axiales. On obtient ainsi un système parabolique, semblable aux équations de la couche limite dans le cadre de l'approximation du 1<sup>er</sup> ordre, qui peut être résolu par une méthode de marche en espace. Cette approximation peut être considérée comme valable dans le cas des tourbillons étudiés ici. Elle permet de bien représenter l'évolution du tourbillon en amont de l'éclatement. D'autre part, elle indique la position de l'éclatement sous la forme de l'apparition d'une singularité, du même type que la singularité de Goldstein [11], rencontrée au point de décollement d'une couche limite laminaire.

Sur la figure 15 ont été portées les évolutions de  $U_{axe}$  déterminées par le code Navier-Stokes et le code quasi-cylindrique pour les mêmes profils initiaux et le même champ de pression extérieur dans le cas d'un écoulement laminaire. Dans le cas sans éclatement (nombre de Reynolds faible), les deux codes donnent des résultats extrêmement proches. Pour un nombre de Reynolds plus élevé conduisant à l'éclatement, la prédiction de la position du point d'éclatement fournie par le code quasi-cylindrique est proche du point d'arrêt calculé par le code Navier-Stokes.

La figure 16 présente une évolution de  $U_{axe}$  en fonction de  $x$ , pour 4 cas de soufflage, pour la répartition de pression  $A_c/A = 0,363$ . Dans la partie amont, le calcul recoupe assez bien les résultats expérimentaux, mais au fur et à mesure que  $x$  augmente, la courbe obtenue par le calcul s'éloigne de l'expérience. En particulier, le point d'éclatement est beaucoup plus en aval.

### 4. CONCLUSION

Sur le plan expérimental, le but de l'étude était de préciser l'importance des distributions de vitesse axiale sur l'éclatement. Ainsi, les mesures de champ réalisées grâce à la vélocimétrie laser ont permis de constituer une importante base de donnée pouvant servir à la validation des simulations numériques. La détermination des conditions d'apparition de l'éclatement a mis en évidence le rôle important joué par le taux de rotation  $\Gamma = \Gamma_0/r_c U_{axe}$  calculé à l'aide de la circulation  $\Gamma_0$ , du rayon visqueux  $r_c$  et de la vitesse  $U_{axe}$ , lors de l'éclatement en présence d'une recompression. En particulier, il

apparaît qu'un accroissement de  $U_{axe}$ , obtenu dans l'expérience par un soufflage sur l'axe, stabilise le tourbillon et repousse l'éclatement vers l'aval.

Sur le plan théorique, la résolution des équations de Navier-Stokes laminares a montré que l'on pouvait obtenir un bon accord avec l'expérience pour la détermination des conditions d'éclatement. Cependant, ce modèle laminaire ne permet pas d'obtenir de bon résultats lorsqu'il s'agit de déterminer l'évolution des profils de vitesse au coeur du tourbillon sur de grandes distances en amont de l'éclatement. Le même défaut se retrouve dans l'approximation quasi-cylindrique. Une prise en compte de la turbulence est alors nécessaire.

Cette étude a été réalisée avec le soutien financier du Service Technique des Programmes Aéronautiques du Ministère de la Défense.

### REFERENCES

- [1] Lê T.H., Mège P. et Morchoisne Y., 'Simulation numérique de l'éclatement tourbillonnaire par résolution des équations d'Euler en fluide incompressible.', La Recherche Aéronautique n° 1989-5, (1989).
- [2] Grabowski W.J., 'Solutions of the Navier-Stokes equations for vortex breakdown', Coll. Eng. Univ. California, Rep. n° FM-74-6, (1974).
- [3] Benay R., 'Modélisation numérique de l'éclatement d'un tourbillon en écoulement laminaire de révolution', La Recherche Aéronautique n° 1984-4, (1984).
- [4] Menne S., 'Simulation of vortex breakdowns in tubes', AIAA 88-3575, First Nat. Fluid Dyn. Conf. July 25-28, Cincinnati Ohio, (1988).
- [5] Krause E., 'A contribution to the problem of vortex breakdown', AGARD CP n° 342, 26, (1983).
- [6] Boutier A., d'Humières C. et Soulevant D., 'Three dimensional laser velocimetry: a review', 2<sup>nd</sup> Int. Symp. on Applications of Laser Anemometry to Fluid Mechanics, Lisbonne (1984) et ONERA TP 1984-4.
- [7] Pagan D., Solignac J.-L., 'Etude expérimentale de l'éclatement d'un tourbillon engendré par une aile delta', La Recherche Aéronautique n° 1986-3, (1986).
- [8] Pagan D., 'Contribution à l'étude expérimentale et théorique de l'éclatement tourbillonnaire en air incompressible', Thèse de l'Université Pierre et Marie Curie (Paris VI), (1989).
- [9] Pagan D., Molon P. et Solignac J.-L., 'Etude expérimentale et simulation numérique de l'éclatement d'un tourbillon d'ailettes', ONERA RT 38/1147 AY, (1988).
- [10] Pagan D., Benay R., 'Etude numérique de l'éclatement de tourbillons soumis à des gradients de pression', La Recherche Aéronautique n° 1988-1, (1988).
- [11] Goldstein S., 'On laminar boundary layer flow near a position of separation', Quat. J. Mech. Appl. Math., Vol 1, Part 1, (March 1948).



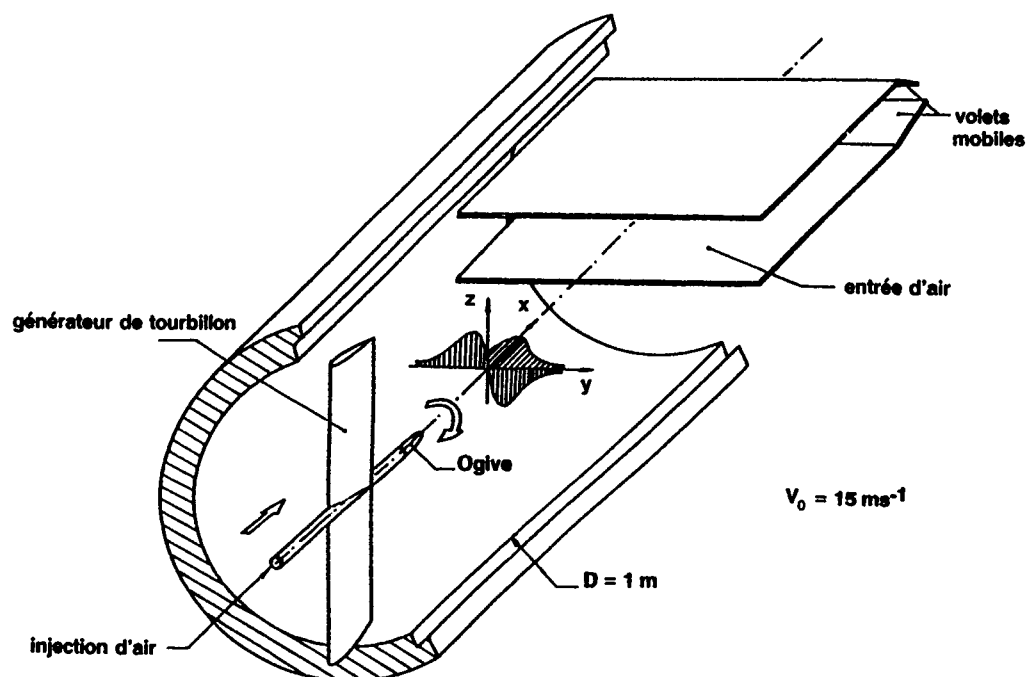


**Fig.1 - Vue d'ensemble du dispositif expérimental**

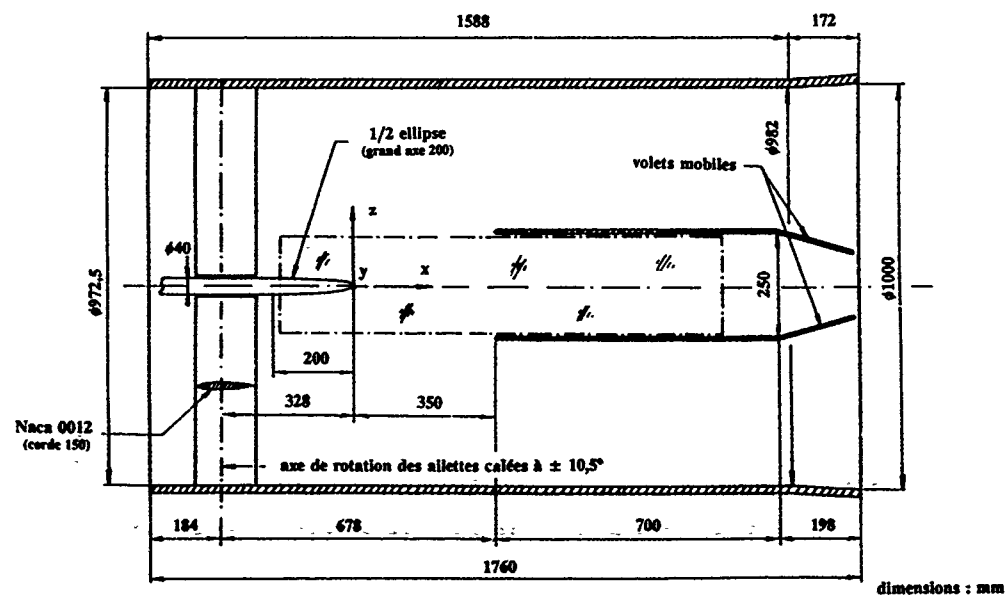


**Fig.2 - Dimensions principales du montage**

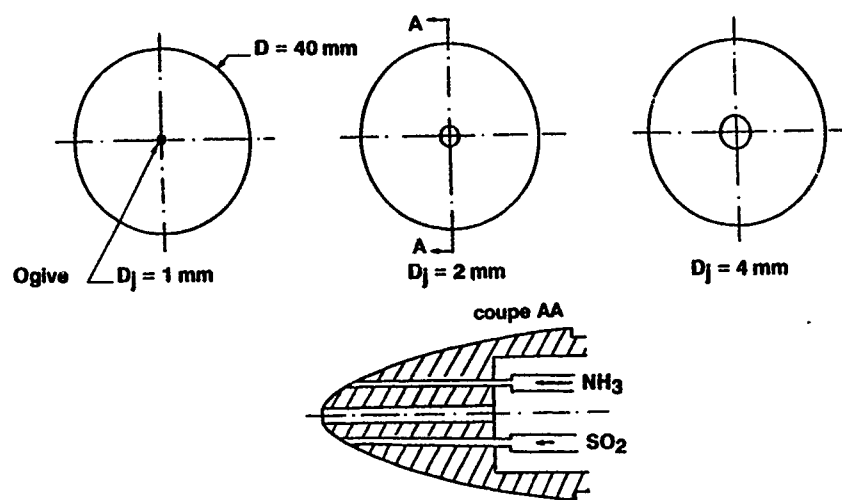


Fig.3 - Schéma des ogives utilisées

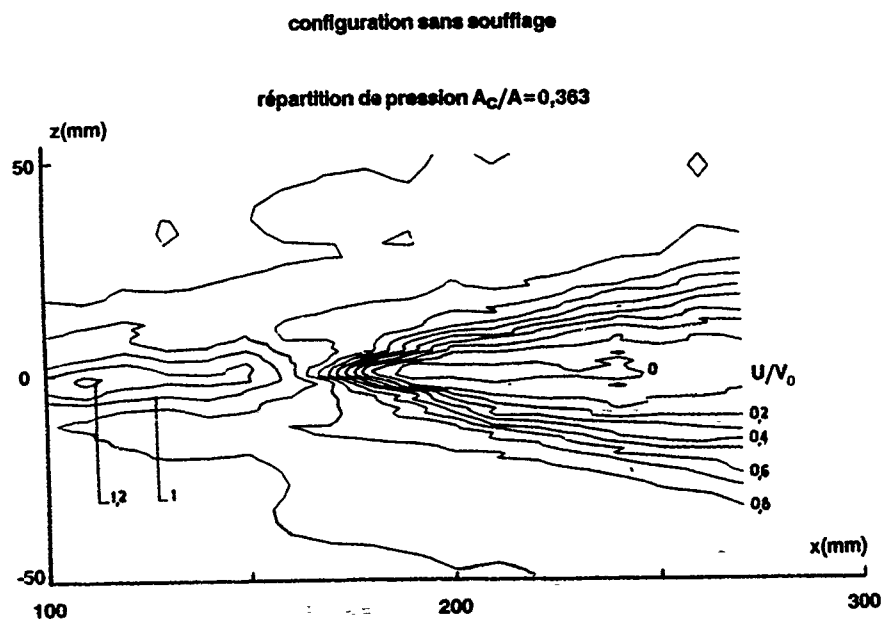


Fig.4 - Champ de la composante U de la vitesse moyenne dans un plan méridien

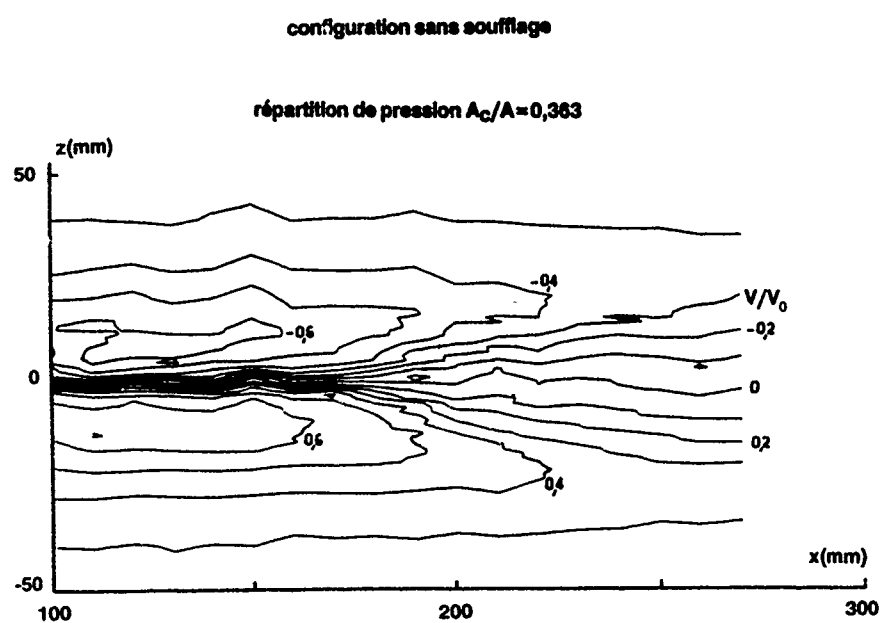


Fig.5 - Champ de la composante V de la vitesse moyenne dans un plan méridien

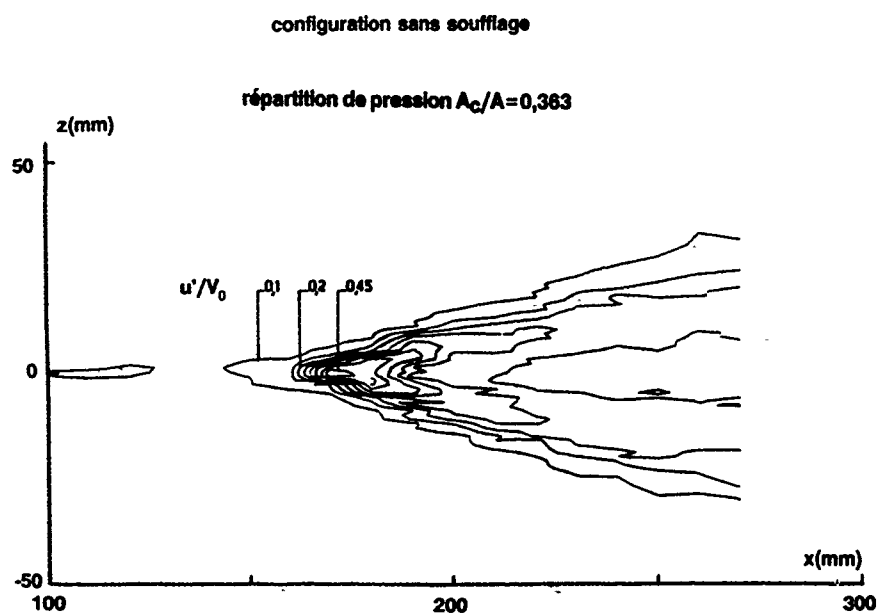
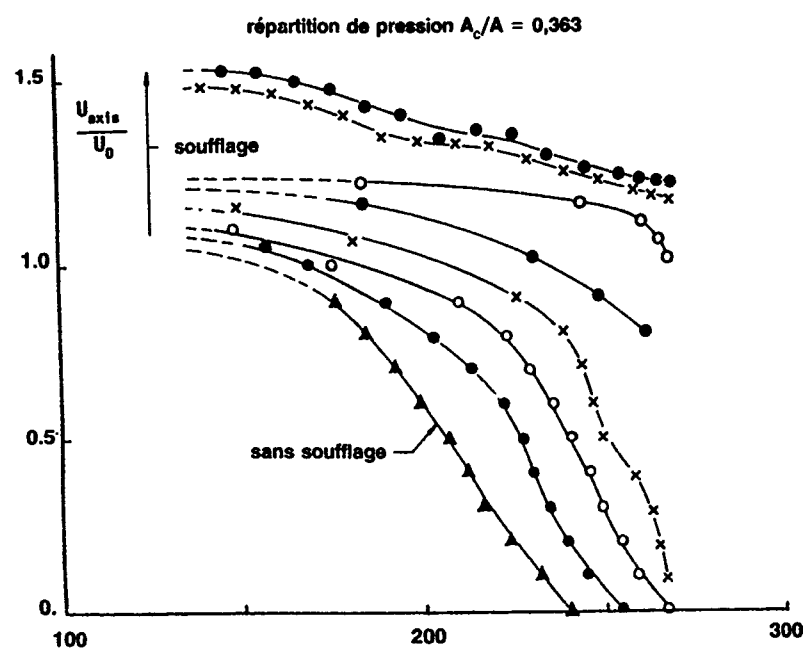
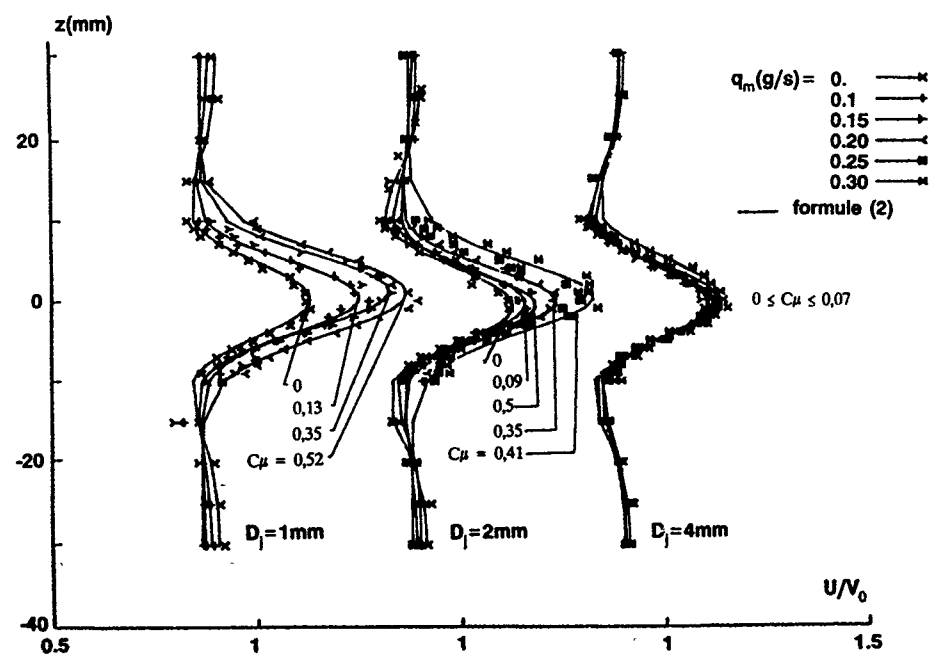


Fig.6 - Ecart-type des fluctuations de la composante U de la vitesse dans un plan méridien

Fig.7 - Evolution de  $U_{axis}$  composante de vitesse axiale mesurée sur l'axe du tourbillonFig.8 - Distribution de la composante axiale de la vitesse à  $x=120$  mm

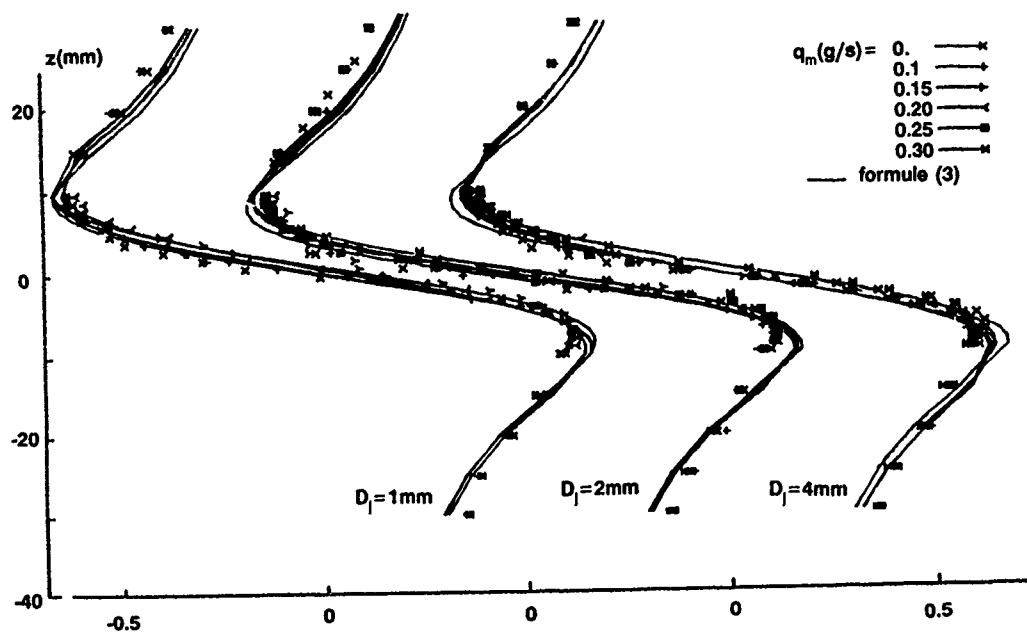


Fig.9 - Distribution de la composante V de la vitesse moyenne mesurée à  $x=120$  mm

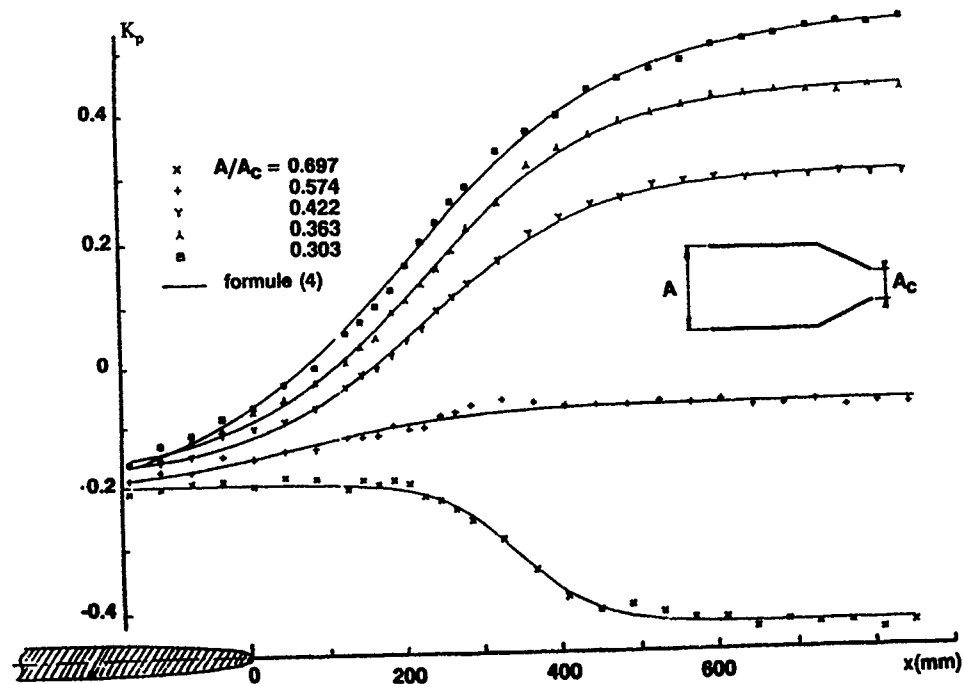


Fig.10 - Répartition de pression mesurée à la paroi de la soufflerie

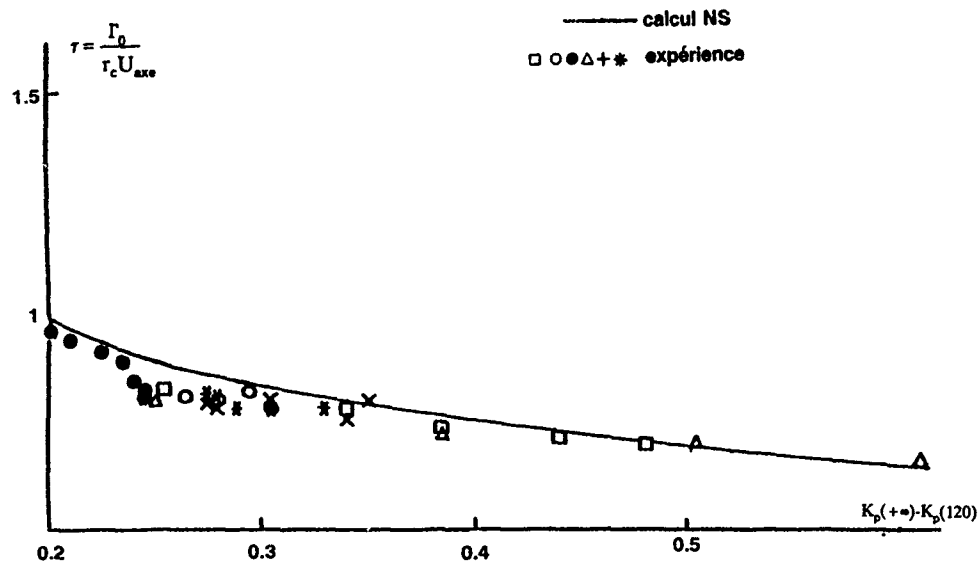


Fig.11 - Comparaison calcul - expérience des conditions d'éclatement naissant

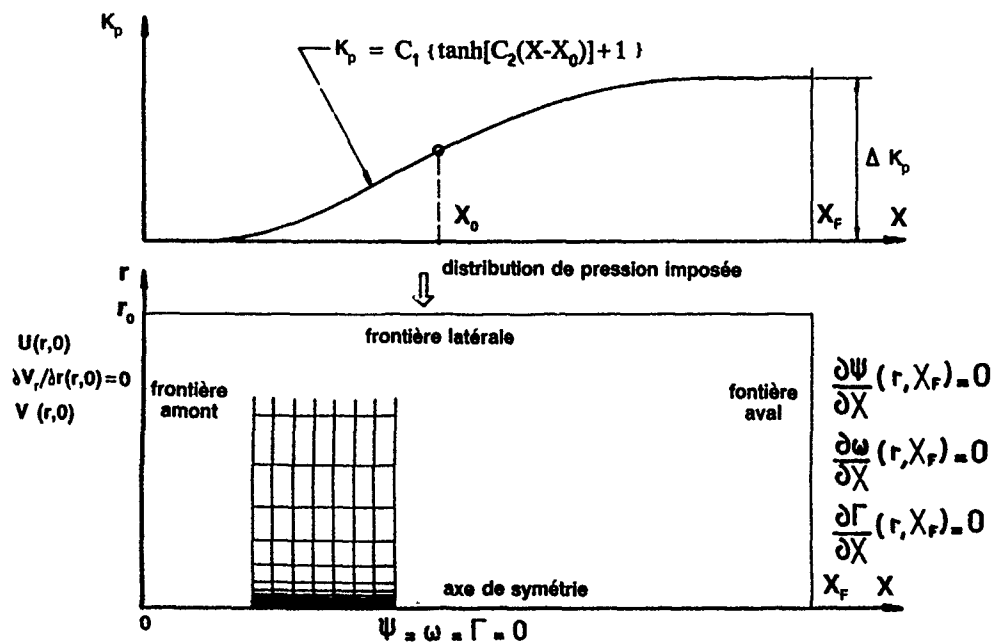
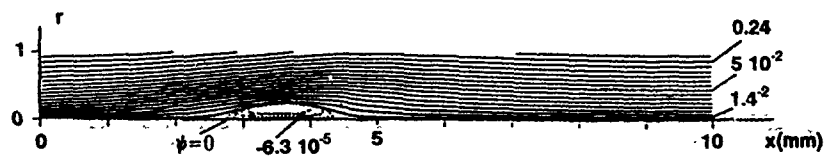


Fig.12 - Domaine de calcul et conditions aux limites (NS)

Fig.13 - Calcul NS : tracé des lignes iso-\$\gamma\$ du plan méridien pour \$\Delta K\_p = 0.45\$, \$r\_c(dK\_p/dX) = 5.8 \cdot 10^{-2}\$  
\$\Gamma\_0/r\_c U\_{axe} = 1.03\$

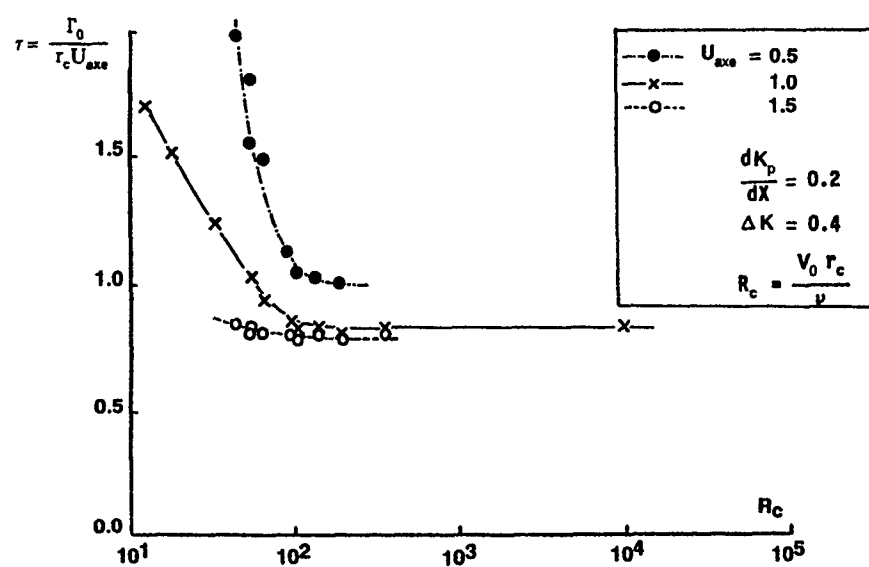
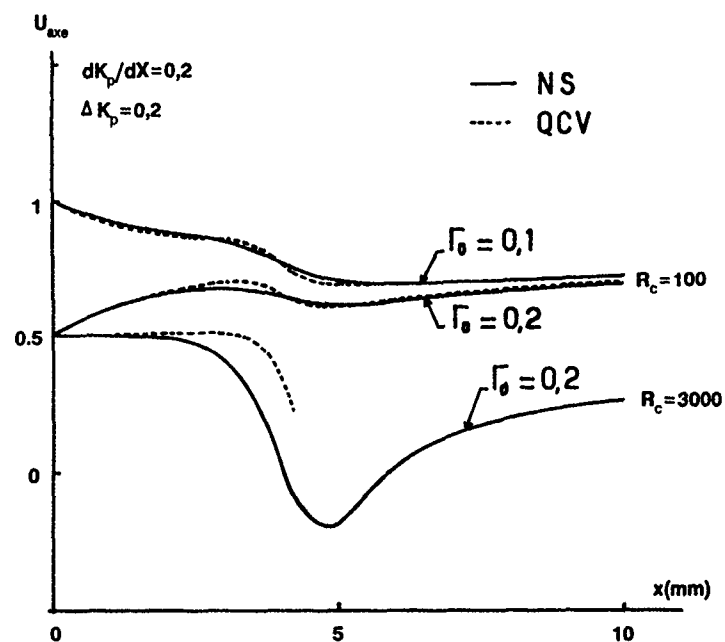


Fig.14 - Evolution de la courbe limite d'éclatement en fonction du nombre de Reynolds

Fig.15 - Evolution de  $U_{axe}$  : Comparaison entre le calcul Navier-Stokes (NS) et l'approximation quasi-cylindrique (QCV)

23-12

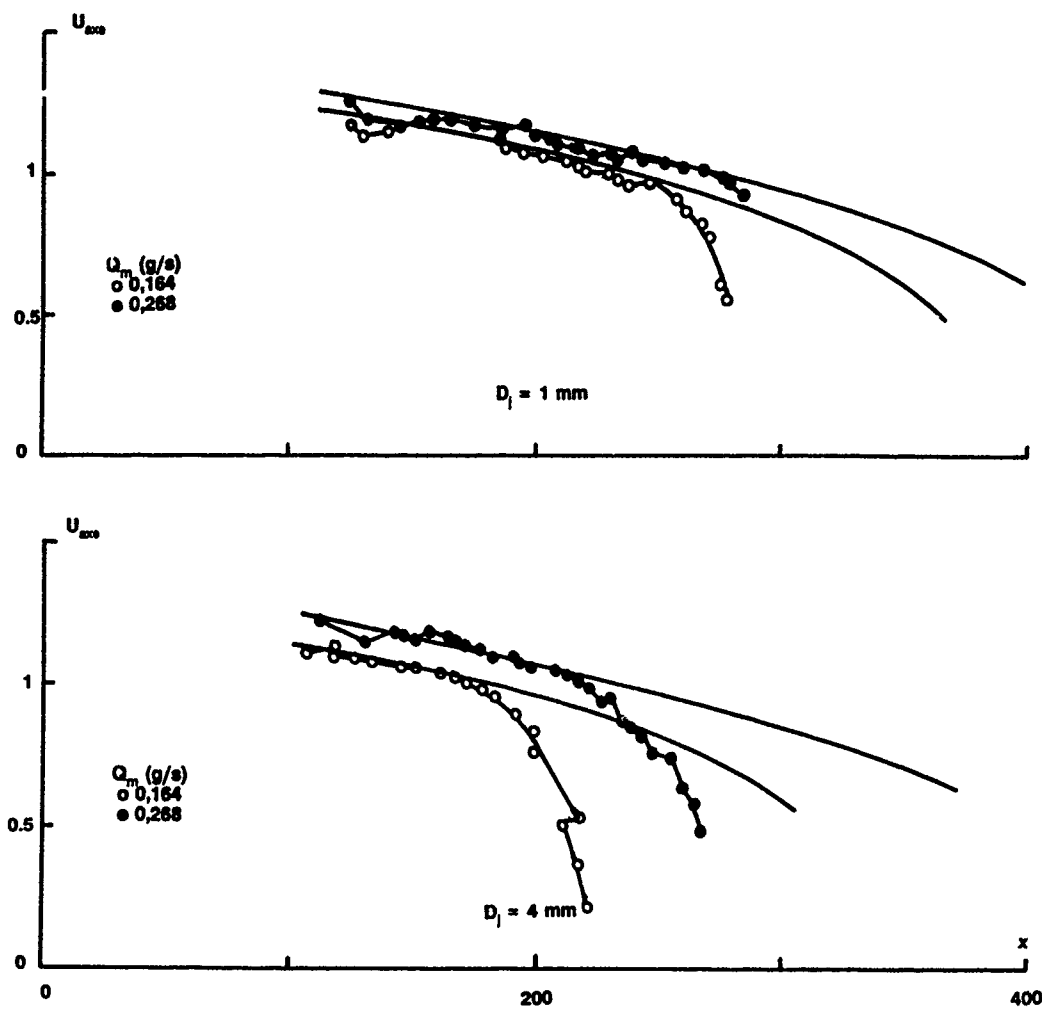


Fig.16 - Evolution de  $U_{200}$  : Comparaison entre le calcul QCV et l'expérience



# INVESTIGATION OF VORTEX BREAKDOWN ON A DELTA WING USING EULER AND NAVIER-STOKES EQUATIONS

S. Agrawal  
R. M. Barnett  
B. A. Robinson

Aerodynamics Department  
McDonnell Aircraft Company  
McDonnell Douglas Corporation  
P.O. Box 516  
St. Louis, Missouri 63166  
USA

## SUMMARY

A numerical investigation of leading-edge vortex breakdown on a delta wing at high angles of attack is presented. The analysis has been restricted to low speed flows on a flat plate wing with sharp leading edges. Both Euler and Navier-Stokes (assuming fully laminar and fully turbulent flows) equations have been used in this study and the results are compared against experimental data. Predictions of vortex breakdown progression with angle of attack with both Euler and Navier-Stokes equations are shown to be consistent with the experimental data. However, the Navier-Stokes predictions show significant improvements in breakdown location at angles of attack where the vortex breakdown approaches the wing apex.

The location of the primary vortex and the level of vorticity in the pre-breakdown regions in these flowfield solutions are affected very little by the viscous effects, even though the Navier-Stokes solutions exhibit viscous phenomena such as secondary and tertiary vortices which are not present in the Euler solutions. In the post-breakdown regions, however, the levels of vorticity in the primary vortex have increased differences between the Euler and Navier-Stokes solutions at comparable locations. Navier-Stokes indicates the presence of a secondary vortex even after the primary vortex is burst. The predicted trajectories of the primary vortex are in very good agreement with the test data, the laminar solutions providing the overall best comparison. The Euler shows a small displacement of the primary vortex, relative to experiment, due to the lack of secondary vortices. The turbulent Navier-Stokes, in general, fall between the Euler and laminar solutions. These findings are based on solutions from meshes that are not usually considered fine enough for resolving vortical flows. To further understand the vortex breakdown phenomenon and the fine details of the vortical flow structure, further calculations with the finer meshes and improved turbulence models are necessary.

## 1. INTRODUCTION

The accurate calculation of vortical flows is a very important yet challenging task in the design of modern fighter aircraft which are required to maneuver at high angles of attack. A flat plate delta wing with sharp leading edges presents a simple configuration for the study of vortical flows. At sufficiently high angles of incidence the dominant feature of flows over such wings is a pair of counter-rotating vortices (the so-called primary or leading-edge vortices). These vortices form over the upper surface of the

wing as a result of the roll-up of the vortex sheet shed from the leading edges. The flow induced by these primary vortices can separate near the wing surface due to the adverse pressure gradient the flow encounters in the spanwise direction (Reference 1). This separated flow may then form an oppositely rotating secondary vortex which tends to move the primary vortex inboard and away from the wing upper surface. These secondary vortices can also form tertiary vortices by the same process. The formation of these vortices over delta wings has been successfully demonstrated in a number of numerical solutions of the Navier-Stokes equations (e.g., References 2-7).

The leading-edge vortices at high angles of incidence can experience a phenomenon called breakdown or "burst". The vortex breakdown is characterized by a sudden deceleration of the axial flow in the vortex core, and a decrease in the circumferential velocity associated with the rapid expansion of the vortex core (References 8-13). Typically, this process occurs over a distance on the order of the vortex core size and results in the vortex core transitioning from a well-defined vortical structure before burst to a more diffuse structure with milder velocity gradients and higher levels of turbulence after the burst. The location of burst on a delta wing is seen to move forward toward the wing apex in a smooth fashion with increasing angle of attack. The bursting of the vortex on a flying aircraft may result in several adverse effects, e.g., abrupt change in pitching moment, loss in lift, buffet, etc., and can be a strict limitation of its maneuverability. Effects of the bursting may be felt not only by the individual aerodynamic surfaces on which the bursting occurs, but also on those in their close proximity. Realistic flow calculation about an aircraft at high angles of attack, therefore, requires an accurate prediction of vortex breakdown. While the leading-edge vortex and the effects produced by the presence of such a vortex have been studied extensively by researchers, there is currently no universally accepted theory on the mechanism of vortex breakdown. Analytical efforts have been restricted to only simplified vortex models without including the presence of the wing (References 14 and 15).

Numerical solutions obtained using Euler equations have recently been shown to be qualitatively, and somewhat quantitatively, realistic for sharp-edged delta wings (e.g., References 8-10, 16). It is also concluded in References 9 and 10 that the leading-edge vortex breakdown is governed primarily by inviscid effects and that the viscous effects are only secondary. However, one would expect that the viscous effects would strongly affect the inviscid results if the pressure gradients in the vortex core due to the burst are large. Also, the effects of secondary and

tertiary vortices, as observed in the Navier-Stokes solutions, are absent in the Euler results. Such details of the vortical flowfield can only be obtained from the Navier-Stokes equations.

The intent of the present study is to analyze in detail the differences between Euler and Navier-Stokes solutions on a delta wing at high angles of attack, with a particular emphasis on predicting flowfields before and after the occurrence of vortex breakdown. Differences between the inviscid and viscous solutions are addressed in order to determine which set of equations best predicts the flow in the pre- and post-breakdown regions. The geometry chosen for this study is a flat plate semispan delta wing with a leading-edge sweep of  $70^\circ$  and a  $25^\circ$  bevel on the lower surface along the leading and trailing edges as shown in Figure 1. An extensive experimental database exists for this configuration (References 17 and 18). The database consists of flow visualization, force and moment, surface pressures, three component Laser Doppler Velocimetry (LDV) and seven-hole probe flowfield surveys. These data were obtained by McDonnell Aircraft Company (MCAIR) in conjunction with McDonnell Douglas Research Laboratories (MDRL) as part of a United States Navy funded investigation of leading-edge vortex behavior on delta wings.

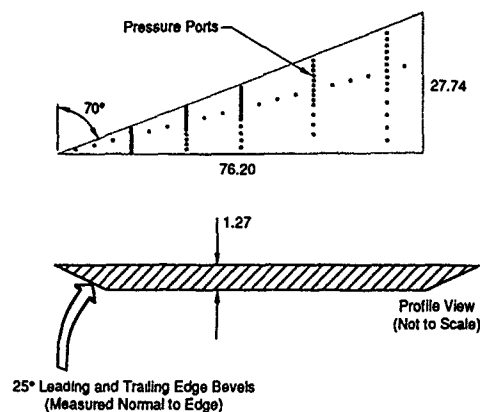


Figure 1. Flat Plate Semispan Delta Wing Model

The results for this analysis were computed using an Euler/Navier-Stokes code, CFL3D (Reference 2), briefly described in the next section. The computational mesh topology and results are discussed in sections 3 and 4, respectively. The conclusions drawn from this study are summarized in section 5.

## 2. NUMERICAL METHOD

The computational algorithm in CFL3D is based on a thin-layer approximation of the three-dimensional, time-dependent, conservation law form of the compressible Navier-Stokes equations. The code solves the discretized flow equations implicitly using an upwind-biased spatial differencing scheme with either flux difference splitting or flux vector splitting for the convective and pressure terms, and central differencing for the shear stress and heat transfer terms. In this study the Roe-averaged flux difference splitting scheme was applied for the spatial differencing. This scheme does not require the addition of artificial dissipation terms which can adversely affect the solution. Flux limiting is also used

to alleviate oscillations near high gradient regions such as shock waves. The Baldwin-Lomax turbulence model is used to calculate the turbulent viscosity. This code is used extensively in the aerospace industry and has been verified for numerous geometries and flow conditions.

## 3. MESH TOPOLOGY

An H-O type mesh topology for a half plane model of the delta wing was used in this study. The half plane wing was used to provide the best mesh resolution around the wing for a given number of points. The delta wing mesh was constructed by successive generation of two-dimensional meshes normal to the wing centerline. These were generated using a computer program which solves an elliptic system of partial differential equations. This program is based on the method described in Reference 19. It automatically sections the cross-plane domain into a number of simpler domains based on singular points on the surface geometry, such as the wing leading edge. High quality meshes are first generated on these simpler domains and then matched smoothly at their common boundaries. This procedure results in a highly orthogonal mesh near difficult areas, such as the sharp leading edges of the wing, as shown in Figure 2a. The surface mesh along with the symmetry plane and a crossflow plane is shown in Figure 2b. The mesh dimensions are 61 (axial), 65 (radial), and 89 (circumferential). These dimensions were used for most of the analyses, and will be referred to as the medium mesh. A mesh embedding technique was also utilized to refine the medium mesh around the leading edge and the upper side of the wing from the apex to the trailing edge. The extent of embedding in the normal direction was just far enough to include the region where most of the vortical flow phenomenon is observed. Such a refinement of the medium mesh yielded an embedded region with dimensions 81 (axial), 87 (radial), and 133 (circumferential). Figure 3 shows a partial view of the embedded region in a crossflow plane. In addition, a few calculations were performed on a mesh of dimensions  $61 \times 33 \times 89$ , to be referred to as the coarse mesh in this paper.

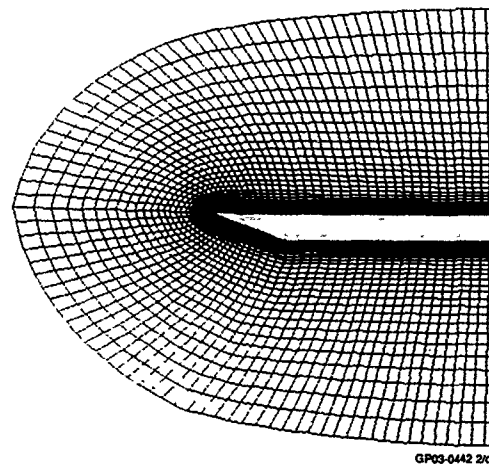
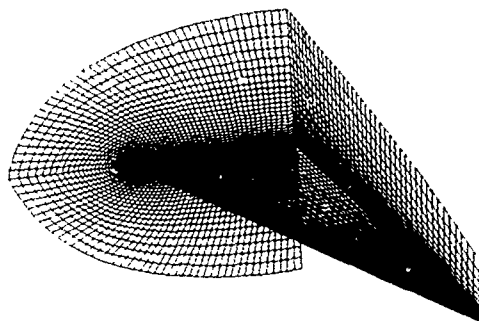
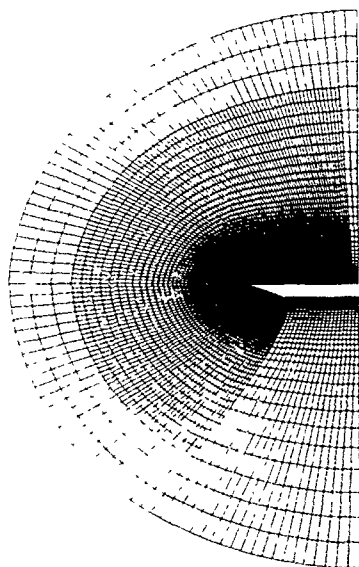


Figure 2a. Cross-Section View of the Medium Computational Mesh  
Mesh Dimensions: 61 (Axial) x 65 (Radial) x 89 (Circumferential)



GP03 0442 3/cjg

Figure 2b. Partial View of the Computational Mesh for Delta Wing  
Medium Mesh 61 (Axial) x 65 (Radial) x 89 (Circumferential)



GP03 0442 4/dxt

Figure 3. Cross-Section View of the Embedded Medium Mesh  
Mesh Dimensions in the Embedded Region 81 x 87 x 133

#### 4. RESULTS

The numerical results presented here have been obtained using the CFL3D code. Calculations were performed at a free stream Mach number,  $M_\infty = 0.3$  and several angles of attack ( $\alpha$ ). The Reynolds number based on the root chord ( $Re_c$ ) was one million. While only steady-state solutions were sought, there were indications of unsteadiness in the flow solutions at the higher angles of attack. The level of unsteadiness, however, appeared to be quite small as the fluctuations in lift, drag and pitching moment coefficients at the assumed steady-state conditions were less than 1% for most calculations. Solution convergence on the medium mesh was achieved in approximately three CPU hours on the Cray-2 computer at the National Aerodynamic Simulation (NAS) facility. On the coarse mesh, runs were executed on a Cray-XMP, and convergence was reached in a CPU time equivalent to one hour of CPU on the Cray-2. The average residuals were reduced by approximately two to three orders of

magnitude in 1000 to 2000 iterations, depending on the mesh size and angle of attack. At the higher angles of attack, where vortex breakdown is observed over the wing, the solution convergence was slower although it was always possible to achieve convergence of integrated forces and moments. Figure 4 shows typical residual and lift convergence histories for an angle of attack where vortex breakdown is observed. Navier-Stokes solutions were obtained using either a fully laminar or a fully turbulent flow model. Results from these calculations are shown in Figures 5 through 19.

The location or trajectory of the leading-edge vortex from the Euler and Navier-Stokes solutions, for several angles of attack, using the medium mesh are shown in Figures 5a through 5c. Three orthogonal views of the wing are given in this figure to completely define the primary vortex location relative to the wing. Available flow visualization data are also shown. The vortex location from the computed solutions was identified by locating the points of minimum total pressure in the primary vortex at each axial station. The computational solutions, in general, show excellent agreement with each other and the experimental data before vortex breakdown occurs (as indicated on the plots). A closer inspection of the planform views in Figures 5a-5c indicates that the vortex locations from the Euler solutions are slightly outboard of the other data. The leading-edge vortices in the laminar and turbulent solutions are further inboard which gives somewhat better agreement with the experimental data. Such a trend in these solutions is not too surprising as the secondary and tertiary vortices usually outboard of the primary ones are absent in the Euler solutions. The secondary vortex is formed by the separation of the spanwise flow under the primary vortex due to viscous effects. This secondary vortex displaces the primary vortex inboard and slightly upward. Another point worth noting here is that although the laminar and turbulent results are very similar and, in some cases, almost identical (e.g., for  $\alpha = 20^\circ$ , Figure 5a), the laminar solutions overall provide the best comparison with the test data. In general, the turbulent solutions fall between the Euler and laminar solutions.

The various views shown in Figures 5a-5c also indicate that the vortex follows an almost linear path in the pre-breakdown regions, whereas they become jagged beyond the breakdown. After vortex breakdown has occurred the point of minimum total pressure, which was used to define the vortex center, can be seen to enter a swirling type motion as it moves downstream. This swirling of the vortex center is consistent with the behavior observed experimentally in what is referred to as a spiral type vortex breakdown (Reference 11). The experimental data shown is from flow visualization of the leading-edge vortex using smoke and a thin laser light sheet. A video image of the flow visualization was digitized and the approximate location of the vortex center selected by visual inspection (Reference 18). Since the video images of the vortex after breakdown show only a large diffuse vortex core area, the center was selected and therefore no spiraling motion is observed in the experimental data.

The vortex sheet or shear layer shed from the leading edge of the delta wing rolls up above the wing to form the primary vortex. It is possible to trace the location of this sheet by plotting the locus of maximum swirl in an axial plane. These plots are created by performing radial surveys outward from the vortex center. The point of maximum swirl along these lines is determined by linear interpolation of the available data. By

plotting the maximum swirl points along the different radial lines the sheet position can be determined. Shown in Figure 6 is a comparison of the shear layers determined by this method for the CFL3D solutions and the Laser Doppler experimental data. The trend in vortex locations shown in this

figure is similar to that shown in Figures 5a-5c for vortex centers. Again, the Euler solution shows the most outboard location of the primary vortex and the laminar solution the most inboard. Some jaggedness is apparent in the shape of these curves due to the linear interpolation and a relatively coarse mesh size.

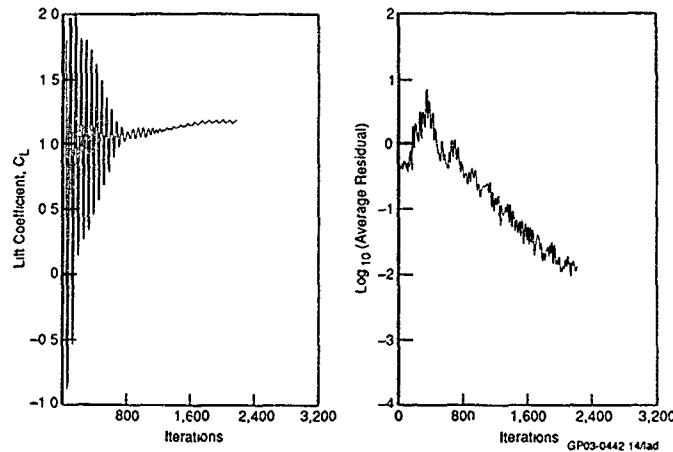


Figure 4. Lift and Residual Histories for CFL3D Euler Solutions  
Medium Mesh,  $M_\infty = 0.30$ ,  $\alpha = 30^\circ$

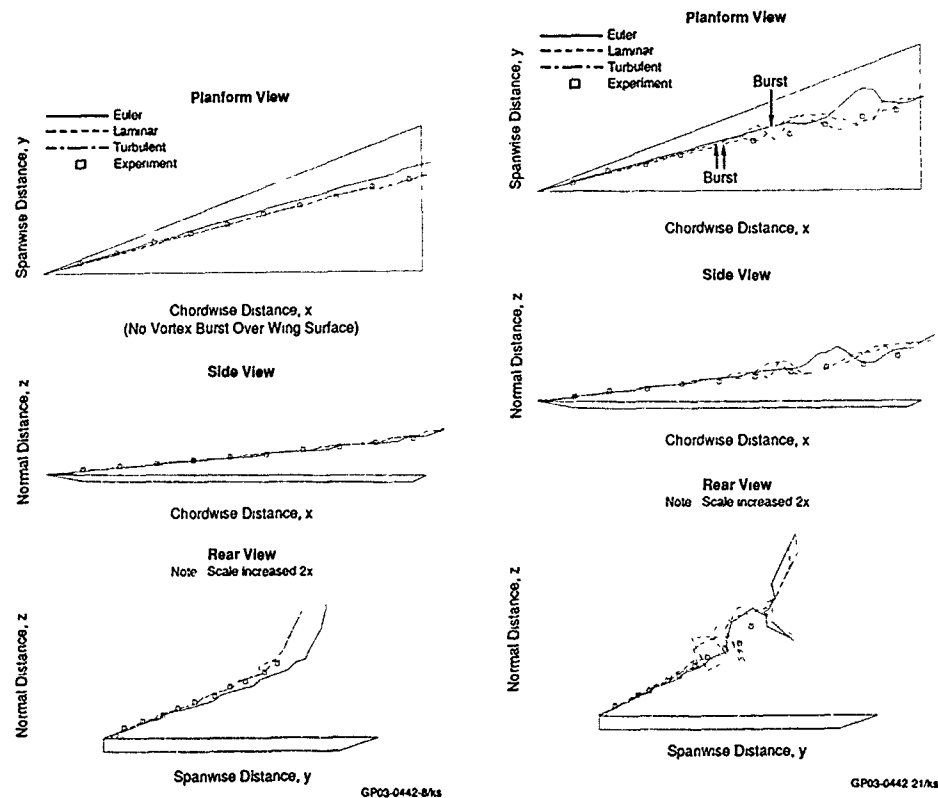


Figure 5a. Comparison of Predicted Vortex Location with Test Data  
Medium Mesh,  $M_\infty = 0.30$ ,  $Re_c = 1 \times 10^6$ ,  $\alpha = 20^\circ$

Figure 5b. Comparison of Predicted Vortex Location with Test Data  
Medium Mesh,  $M_\infty = 0.30$ ,  $Re_c = 1 \times 10^6$ ,  $\alpha = 30^\circ$

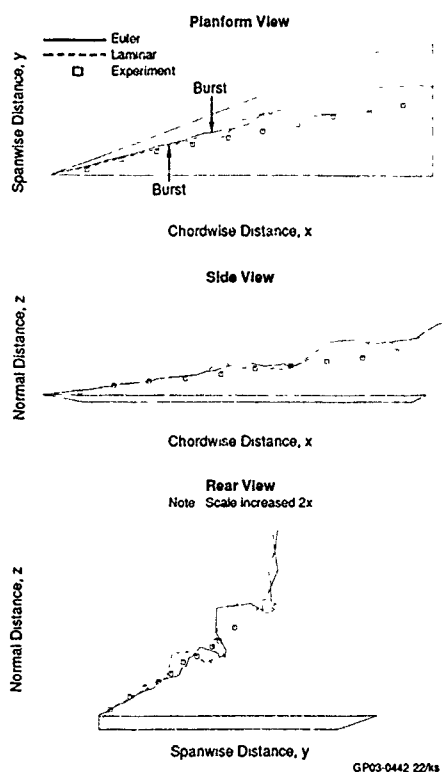


Figure 5c. Comparison of Predicted Vortex Location with Test Data  
Medium Mesh,  $M_\infty = 0.30$ ,  $Re_c = 1 \times 10^6$ ,  $\alpha = 35^\circ$

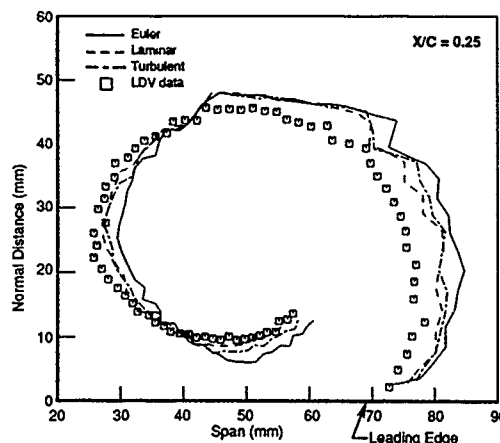


Figure 6a. Comparison of Shear Layers Defined by the Locus of Maximum Swirl  
Medium Mesh,  $M_\infty = 0.30$ ,  $\alpha = 30^\circ$ ,  $Re_c = 1 \times 10^6$

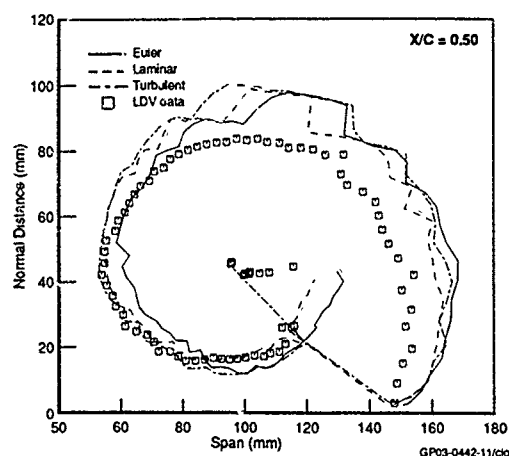


Figure 6b. Comparison of Shear Layers Defined by the Locus of Maximum Swirl

Medium Mesh,  $M_\infty = 0.30$ ,  $\alpha = 30^\circ$ ,  $Re_c = 1 \times 10^6$

The lift coefficients obtained from the CFL3D solutions are shown in Figure 7. The predicted values of lift are in fair agreement with the experimental data. However, the experimental values can be seen to be offset from the computational results. The negative camber produced by the lower surface bevel on the delta wing produces a shift in the point of zero lift predicted by the computational codes. The experimental data shows less effects from this negative camber due to flow separation on the trailing edge level. The predictions of pitching moment (not shown here) suffer from the same problem as the lift. It appears that the separation on the beveled surfaces is not being modeled with the medium mesh used for most of the analysis. Increasing the mesh density along the axial direction is expected to improve the predictions of this separation and thereby the lift.

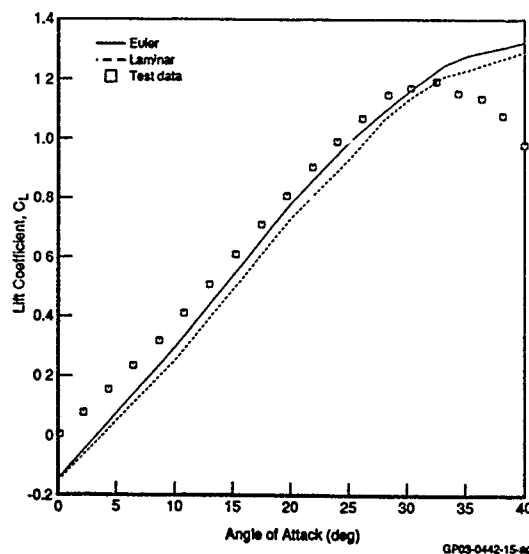


Figure 7. Comparison of Predicted Lift with Test Data  
Medium Mesh,  $M_\infty = 0.30$ ,  $\alpha = 30^\circ$ ,  $Re_c = 1 \times 10^6$

A comparison of the surface pressures on the upper surface of the delta wing at 50% of the root chord is shown in Figure 8, for  $\alpha = 30^\circ$ . The pressure distribution shown at this station can be seen to agree with the trends shown in Figures 5a-5c. The peak suction pressures occur underneath the primary vortex, which again indicates that in the Euler solutions the primary vortex is further outboard than either of the Navier-Stokes solutions or the experimental data. These peak pressures for the experimental data are shown to be higher than any of the computational results. The Euler solution shows the best agreement with these peak values followed by the turbulent and laminar solutions, respectively. The peak suction pressures on the upper surface of the wing at each axial station are shown in Figure 9. The experimental data from the row of pressure taps along the 65% local span stations, which also corresponded to the peak suction pressures, are shown for comparison with this data. The Euler solutions are again seen to predict higher peak suction pressures on the wing than the Navier-Stokes solutions (Figures 8 and 9). The pressure contours on the entire upper surface of the wing at  $\alpha = 30^\circ$  are shown in Figure 10. The breakdown locations, which correspond to those marked in Figure 5b, are also indicated.

The experimental surface pressures were obtained in the wind tunnel with blockages approaching 10% at the highest angle of attack tested ( $40^\circ$ ). The effects of this blockage on the vortex location and burst characteristics were found to be negligible when compared with wings with half the calculated blockage in the same facility. Therefore, the comparison of these surface pressures with the computational results, which do not account for the presence of these walls and the resulting blockage effects, may be misleading. The comparison of these pressures with computational solutions on meshes which model the wind tunnel walls is a possible solution. However, attempts to obtain solutions on such a mesh have shown poor convergence for the  $70^\circ$  delta wing with vortex breakdown occurring over the wing. Further efforts are required to obtain such solutions.

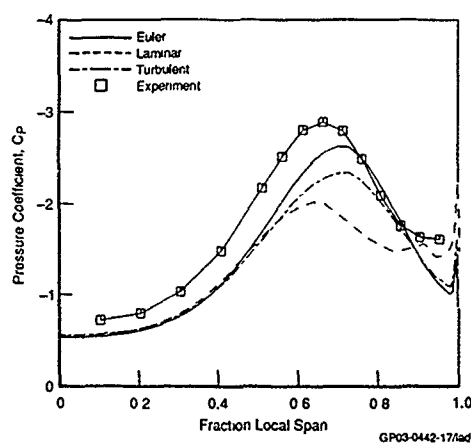


Figure 8. Comparison of Predicted Upper Surface Pressure with Test Data  
Medium Mesh,  $M_\infty = 0.30$ ,  $\alpha = 30^\circ$ ,  $Re_c = 1 \times 10^6$ ,  $x/c = 0.50$

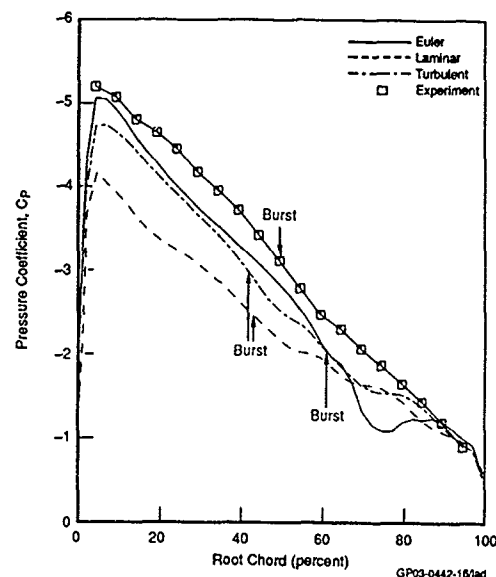


Figure 9. Maximum Negative Surface Pressure Coefficients  
Medium Mesh,  $M_\infty = 0.30$ ,  $\alpha = 30^\circ$ ,  $Re_c = 1 \times 10^6$

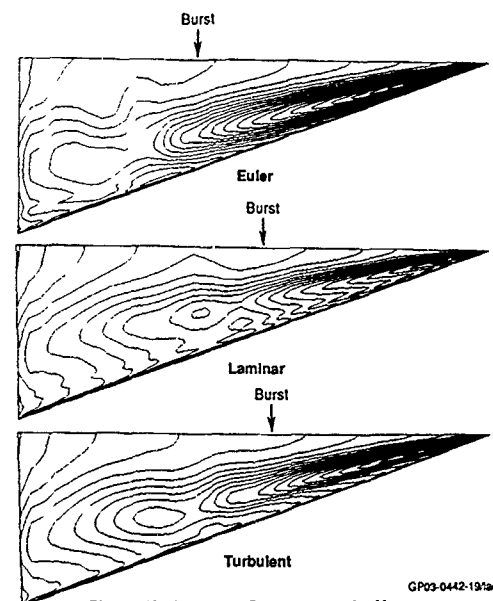


Figure 10. Pressure Contours on the Upper Surface of Delta Wing  
Medium Mesh,  $M_\infty = 0.30$ ,  $\alpha = 30^\circ$ ,  $Re_c = 1 \times 10^6$

Figure 11 shows the particle traces from the Euler and laminar solutions on the coarse mesh, at several angles of attack. This gives a qualitative picture of the flowfields in the leading-edge vortex. The abrupt change in the traces from a regular, ordered structure is an indication of the vortex breakdown occurring in the flowfield, which is clearly illustrated in this figure. Figure 11

also illustrates that the apparent location of the vortex breakdown, as in experimental investigations, moves toward the apex with increasing angle of attack. These plots were generated using a postprocessor, PLOT3D (Reference 20), developed at the NASA Ames Research Center. The breakdown location was identified by inspection of the streamwise component of velocity on each axial mesh plane using PLOT3D. A rapid decrease in this velocity component and increase in vortex core size are observed at the onset of vortex breakdown.

For comparison purposes, the particle traces from the Euler, laminar and turbulent solutions obtained on the medium mesh are shown in Figure 12 for  $\alpha = 25^\circ$ ,  $28^\circ$  and  $30^\circ$ . This mesh relative to the coarse mesh, had twice the number of points in the direction normal to the surface. This figure shows behavior which appears quite similar to that shown for the coarse mesh in Figure 11. The location of the burst regions indicated by the particle traces appears qualitatively similar to that of the coarse mesh solutions. Also, it appears that at a fixed angle of attack the

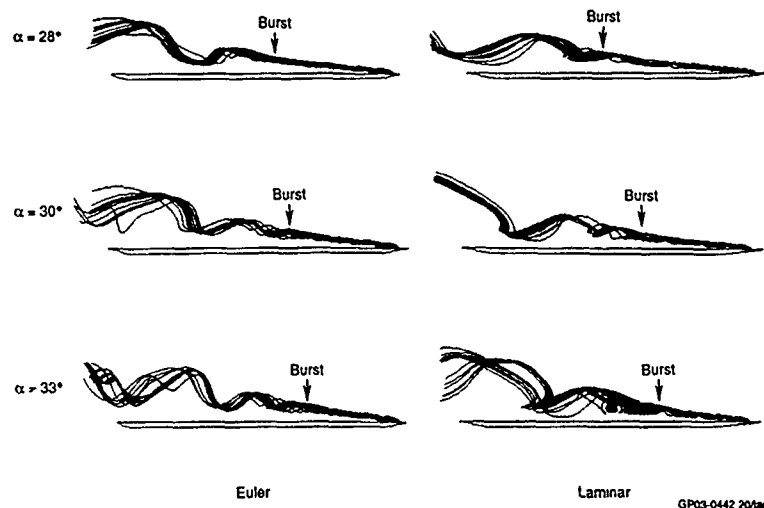


Figure 11. Vortex Breakdown Regions Indicated with Particle Traces from Euler and Navier-Stokes (Laminar) Solutions  
Coarse Mesh,  $M_\infty = 0.30$ ,  $Re_c = 1 \times 10^6$

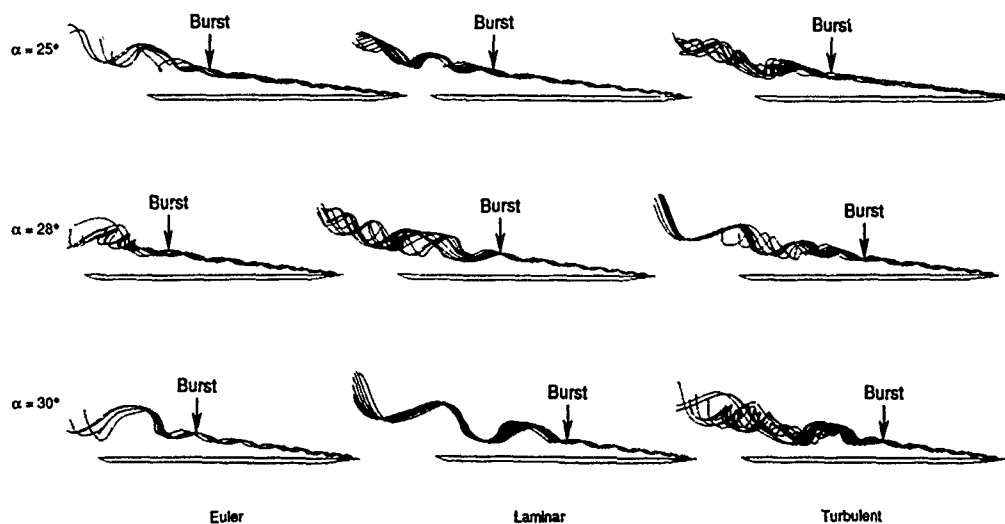


Figure 12. Vortex Breakdown Regions Indicated with Particle Traces from Euler and Navier-Stokes Solutions  
Medium Mesh,  $M_\infty = 0.30$ ,  $Re_c = 1 \times 10^6$

breakdown moves aft if the viscous effects are not included. On the other hand, comparison of the laminar and turbulent traces indicate that the breakdown occurs slightly downstream for the laminar case. Although it appears that increasing the mesh dimensions in the normal direction does not significantly alter the particle traces, a closer inspection of the flowfield (presented later in this section) indicates that for properly resolving the flowfield gradients in the boundary layer and in the vortex core, mesh dimensions need to be increased even further.

At this point, a more refined criterion to determine the burst location is in order. While PLOT3D gives a reasonably good idea of the breakdown regions, the precise location of the onset of vortex breakdown from the computational results was determined by inspecting the axial velocity distribution in the leading-edge vortex. To accomplish this, the location of the center of the vortex core was determined using the point of minimum total pressure in each axial plane. These vortex center locations were then used to determine an average angular orientation, in the region before burst, of the vortex relative to the wing centerline and the upper surface of the wing. The vortex trajectory was then approximated as being a straight line originating at the apex of the wing and the velocities were transformed to this new coordinate system. After such a transformation, the axial velocities were inspected using contour plots as shown in Figure 13. The nature of the distribution of axial velocities can be seen to alter after the onset of vortex breakdown. Before breakdown, the axial velocity is shown to increase to a single peak value at the vortex center. With the onset of vortex breakdown the axial velocity at the core of the vortex begins stagnating and shows significant asymmetry. The burst point was thus determined by locating the axial station where this transformation in the axial velocities was first observed.

The progression of the vortex breakdown location with increasing angle of attack was determined from the Euler, laminar and turbulent solutions for the medium mesh. The sensitivity of the flowfields to mesh refinement is evaluated by comparison of coarse mesh breakdown locations (Figure 14) with those of the medium mesh (Figure 15). These figures show the quantitative predictions of the breakdown locations for various angles of attack along with the experimental data. The breakdown locations shown here also correlate with those shown in Figures 11 and 12.

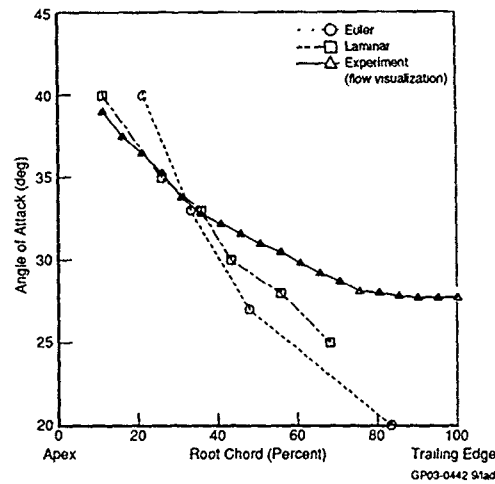


Figure 14. Vortex Breakdown Progression with Angle of Attack  
Coarse Mesh,  $M_\infty = 0.30$ ,  $Re_c = 1 \times 10^6$

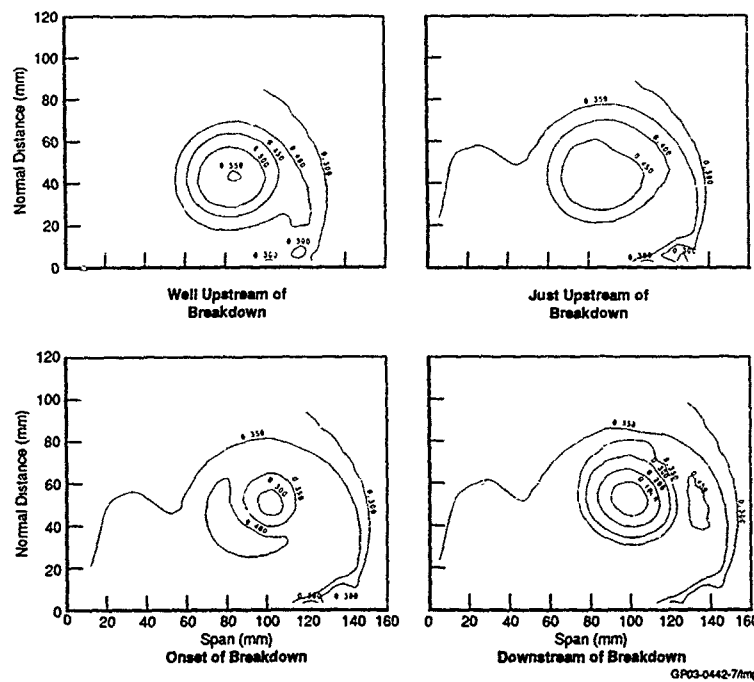


Figure 13. Identifying Vortex Breakdown from Axial Velocity Contours  
Medium Mesh,  $M_\infty = 0.30$ ,  $\alpha = 30^\circ$ ,  $Re_c = 1 \times 10^6$ , Laminar Solution



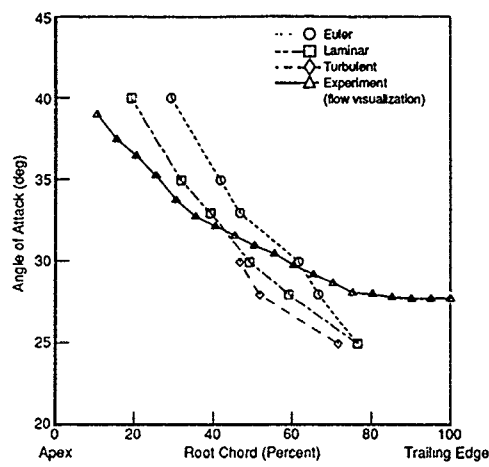


Figure 15. Vortex Breakdown Progression with Angle of Attack  
Medium Mesh,  $M_\infty = 0.30$ ,  $Re_c = 1 \times 10^6$

It should be noted that both the location and the rate at which the vortex breakdown progresses with the angle of attack are different for the Euler and Navier-Stokes solutions (Figures 14 and 15). These figures also show that the breakdown location predicted from the laminar solutions better matches experiment than the Euler solutions. This is particularly evident when the angles of attack are above  $30^\circ$ , which corresponds to the maximum lift from experiment. This is believed to be due to the viscous effects which play an important role when the primary vortex is burst, but the secondary vortex may still exist. Similar conclusions for the turbulent case can not be drawn as yet due to insufficient data points for comparison, although results from the turbulent solutions are found to be similar to the laminar results.

Figures 16 and 17 show the streamwise vorticity contours in the pre- and post-breakdown regions, as determined from the Euler and Navier-Stokes solutions at  $\alpha = 30^\circ$  on the medium mesh. The experimental data and the embedded mesh solution for the laminar case are also included. The experimental data shown in these figures is from an LDV survey of 4912 points with the survey point spacing near the vortex center being about 0.8 millimeters for  $x/c = 0.25$ . For  $x/c = 0.70$ , the number of points in the LDV survey was 5007 with the spacing near the vortex center being about 2.2 millimeters. The experimental data was interpolated, where necessary, to obtain a square matrix of velocity data for use in PLOT3D. The velocities were non-dimensionalized by the freestream value in both experimental and computational data while the physical dimensions are in dimensional units.

Comparison of experimental and computational vorticity levels shows that the computed results have lower maximum values of vorticity in the primary vortex and a slight spreading of the vortical flow relative to the experimental data (Figure 16). The predicted contour levels in the primary vortex core are very similar, although the maximum value of vorticity in the vortex core is nearly five times greater in the LDV data than in any of the computed solutions. Navier-Stokes solutions and the experimental data indicate the presence of a secondary vortex, shown by the negative magnitudes of the vorticity. The laminar solution shows a much larger secondary vortex than

the turbulent solution which is consistent with the observations from previous experiments. Presence of a tertiary vortex having positive vorticity is also seen in the laminar solution with mesh embedding. The Euler solution, as expected, shows no indication of a secondary or a tertiary vortex. The increased resolution with mesh embedding results in more pronounced vortices, as also shown by several researchers (e.g., References 21-22). For example, the vorticity level in the primary vortex core is significantly higher with the embedded mesh than without it. This also results in a closer match with the experimental data as seen from the figure. The level of vorticity in the secondary vortex, on the other hand, is predicted quite well from the Navier-Stokes solutions, even without the mesh embedding. Only laminar calculations were performed with the embedded mesh. It is again noted here that the predicted location of the primary vortex is slightly outboard and above, as compared against the test data.

Figure 17 shows the vorticity contours at a location where the primary vortex is burst. The vorticity levels in the primary vortex are now found to be much smaller than in the pre-breakdown region. Another observation is that the secondary vortex is present in the Navier-Stokes solutions even after the primary vortex is burst, but the level of vorticity in the secondary vortex core after burst is lower than that found in the pre-breakdown region. The decrease in vorticity level after breakdown is consistent with the experimental data. Figure 17 also shows that the predicted vorticity distribution in the primary vortex after burst is asymmetric. This asymmetric pattern is not exhibited in the LDV data. One possible explanation for this discrepancy is the inability of the CFD method to properly model the increase in the level of turbulence in the burst vortex region, exhibited in the LDV data. In spite of the complex flowfield in the burst vortex region, the overall agreement with experiment is considered to be fair.

The velocity data obtained with the LDV surveys can provide further insight into the reasons for the apparent differences between the computed solutions and the wind tunnel data. A survey of the velocity data along a line parallel to the upper surface of the wing was used to compare the predicted solutions with the LDV data. This line was selected to coincide with the maximum chordwise velocity in the LDV data which should be near the center of the primary vortex. The computed solutions were interpolated on this line and are compared with the test data in Figure 18, which shows the non-dimensional chordwise velocity distribution. It is readily seen that the computed results do not match either the peak value or the shape of the velocity distribution obtained from the experiment. The medium mesh size apparently does not have sufficient resolution in the center of the vortex to capture this detail. However, the mesh embedding does improve the predictions at and outboard of the vortex center locations. From this plot, it can be anticipated that further refinement of the mesh near the vortex core is needed to better resolve the sharp gradients occurring in the primary vortex.

To further understand the breakdown phenomenon, it is helpful to examine the pressure distribution in the vortex core. Figure 19 shows such a plot of pressure coefficients versus the distance from the wing apex for the computed solutions at  $\alpha = 30^\circ$ . The pressures shown are at the same location as the minimum total pressure in the primary vortex. It is readily observed that the suction (negative pressure coefficient) at the

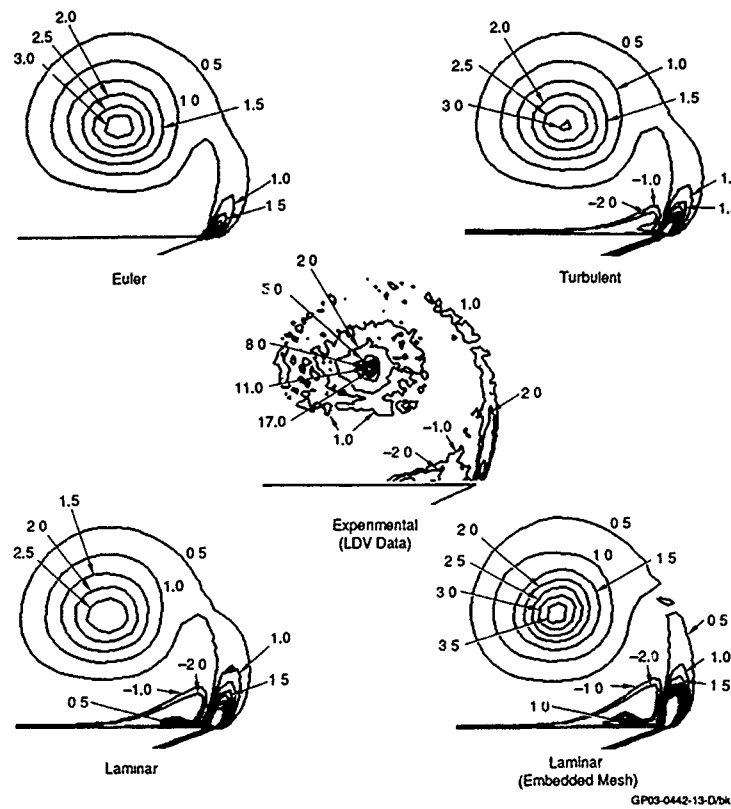


Figure 16. Comparison of Predicted Vorticity Levels (x-Direction) from Euler and Navier-Stokes Solutions, Before Burst,  $M_\infty = 0.30$ ,  $\alpha = 30^\circ$ ,  $Re_c = 1 \times 10^6$ ,  $x/c = 0.25$

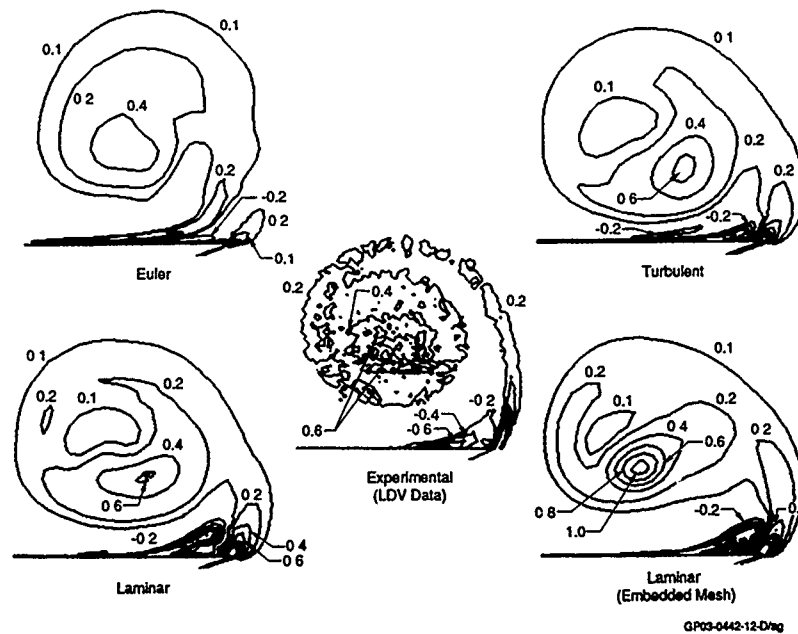


Figure 17. Comparison of Predicted Vorticity Levels (x-Direction) from Euler and Navier-Stokes Solutions, After Burst,  $M_\infty = 0.30$ ,  $\alpha = 30^\circ$ ,  $Re_c = 1 \times 10^6$ ,  $x/c = 0.70$

center of the vortex increases rapidly as the leading-edge vortex develops above the delta wing. After reaching a peak value near the wing apex this suction begins to decrease fairly rapidly. The slopes of the three solutions in this area are very close to each other. The adverse pressure gradient is encountered as the axial flow in the vortex core begins to slow. The breakdown occurs as this pressure gradient becomes large, or as the pressure increases rapidly for a fairly short distance. The locations of vortex burst determined through the inspection of the axial velocity contours are also shown on this figure. Vortex burst is shown to fall approximately in the center of the region where the pressure is increasing most rapidly. This is consistent with the changes in axial velocity in the vortex core in this region. The Euler and Navier-Stokes solutions in the figure show fairly similar trends in pressure in the vortex core. The Euler solution, however, shows a stronger vortex before breakdown which is consistent with the other comparisons made in previous figures. The relative locations of vortex breakdown are also evident from this figure.

The findings from this study are based on solutions from meshes that are not usually considered fine enough for resolving flowfields in the primary vortex regions. Further study is required to properly understand the breakdown phenomenon and the complex flowfield structure in the primary vortex. Effort is under way to resolve the flowfield gradients in the vortex core with much finer meshes obtained with a higher level of mesh embedding. Recently, a two level embedding on a delta wing was shown to improve predictions significantly (Reference 23). Several areas of further research have been identified in the course of this study. For example, an adaptive mesh embedding technique would be very useful in reducing the high cost of computing, suggested by several researchers (e.g., Reference 24). The standard Baldwin-Lomax turbulence model is not adequate at large angles of attack (Reference 25). Therefore, future research should also consider improved turbulence models, non-equilibrium turbulence models, transition models, etc., on the vortex breakdown prediction. Finally, the effects of wind tunnel walls which may be significant at higher angles of attack, should be included.

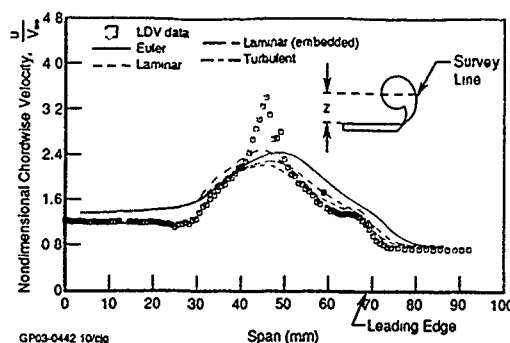


Figure 18. Comparison of Chordwise Velocity Along a Line Parallel to the Wing  
 $M_\infty = 0.30$ ,  $Re_c = 1 \times 10^6$ ,  $\alpha = 30^\circ$ ,  $x/c = 0.25$ ,  $z = 24.91$  mm

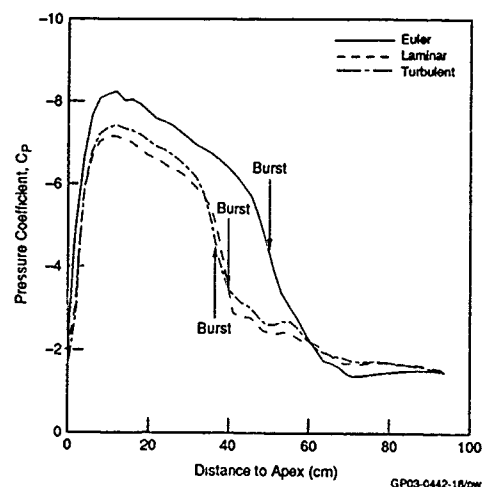


Figure 19. Pressure Coefficients Along the Vortex Core  
 Medium Mesh,  $M_\infty = 0.30$ ,  $\alpha = 30^\circ$ ,  $Re_c = 1 \times 10^6$

## 5. CONCLUSIONS

A numerical investigation of leading-edge vortex breakdown at high angles of attack was conducted on a flat plate delta wing with sharp leading and trailing edges. Predicted solutions of Euler, laminar and turbulent Navier-Stokes equations were compared against an extensive experimental database. The vortex breakdown progression with angle of attack with both Euler and Navier-Stokes equations was found to be consistent with the experimental data. The Navier-Stokes solutions, however, showed significant improvements in breakdown location at angles of attack where the vortex breakdown approached the wing apex.

The locations of the primary vortex predicted by the solutions were in very good agreement with the test data, particularly in the pre-breakdown region. The laminar solutions provided the overall best comparison. Relative to experiment, the Euler solutions showed a small displacement of the primary vortex due to the lack of secondary or tertiary vortices in these solutions. The turbulent Navier-Stokes solutions, in general, fell between the Euler and laminar solutions.

The location of the primary vortex and the level of vorticity in the pre-breakdown regions in these flowfield solutions were affected very little by the viscous effects, even though the Navier-Stokes solutions exhibited viscous phenomena such as secondary and tertiary vortices. The tertiary vortex was only observed in the laminar solution on an embedded mesh. In the post-breakdown regions, however, the levels of vorticity in the primary vortex had increased differences between the Euler and Navier-Stokes solutions at comparable locations. The predicted vorticity distribution in the primary vortex after burst was found to be asymmetric. Also, the Navier-Stokes solutions indicated the presence of a secondary vortex even after the primary vortex was burst, but the level of vorticity in the secondary vortex core after burst was lower than that found in the pre-breakdown region.

Analysis of the pressure distribution in the vortex core indicated that the breakdown occurs as the adverse pressure gradient in the core becomes very large or as the pressure increases very rapidly for a fairly short distance. The Euler and Navier-Stokes solutions showed similar trends in pressure near the vortex core.

These findings are based on solutions from meshes that are not usually considered fine enough for resolving vortical flows. To further understand the vortex breakdown phenomenon and the fine details of the vortical flow structure, further studies are necessary.

#### REFERENCES

1. Hummel, D., "On the Vortex Formation Over a Slender Wing at Large Angles of Incidence," AGARD-FDP Symposium, Sandefjord 1978, AGARD-CP-247, High Angle of Attack Aerodynamics, October 1978, pp. 15.1-15.17.
2. Thomas, J.L., Taylor, S.L., and Anderson, W.K., "Navier-Stokes Computations of Vortical Flows Over Low Aspect Ratio Wings," AIAA-87-0207, January 1987.
3. McMillin, S.N., Thomas, J.L., and Murman, E.M., "Euler and Navier-Stokes Solutions for the Leeward Flow Over Delta Wings at Supersonic Speeds," AIAA-87-2270, August 1987.
4. Rizzi, A., Muller, B., and Purcell, C.J., "Comparison of Euler and Navier-Stokes Solutions for Vortex Flow Over a Delta Wing," AIAA-87-2347, August 1987.
5. Fujii, K., and Schiff, L. B., "Numerical Simulation of Vortical Flows over a Strake-Delta Wing," AIAA Journal, Vol. 27, September 1989, pp. 1153-1162.
6. Ekaterinaris, J.A., and Schiff, L.B., "Vortical Flows over Delta Wings and Numerical Prediction of Vortex Breakdown," AIAA-90-0102, January 1990.
7. Vadyak, J., and Schuster, D.M., "Navier-Stokes Simulation of Burst Vortex Flowfields for Fighter Aircraft at High Incidence," AIAA-89-2190-CP, July 1989, pp. 227-237.
8. Hitzel, S.M., and Schmidt, W., "Slender Wings with Leading-Edge Vortex Separation: A Challenge for Panel Methods and Euler Solvers," Journal of Aircraft, Vol. 21, No. 10, October 1984, pp. 751-759.
9. Hitzel, S.M., "Wing Vortex Flows Up Into Vortex-Breakdown, A Numerical Simulation," AIAA-88-2518-CP, June 1988, pp. 73-83.
10. O'Neil, P.J., Barnett, R.M., and Louie, C.M., "Numerical Solution of Leading-Edge Vortex Breakdown Using an Euler Code," AIAA-89-2189, July 1989.
11. Lambourne, N.C., and Bryer, D.W., "The Bursting of Leading-Edge Vortices - Some Observations and Discussion of the Phenomenon," A.R.C., R. & M No. 3282, April 1961.
12. McKernan, J.F., and Nelson, R.C., "An Investigation of the Breakdown of the Leading-Edge Vortices on a Delta Wing at High Angles of Attack," AIAA-83-2114, August 1983.
13. Hartwich, P.M., Hsu, C.H., Luckring, J.M., and Liu, C.H., "Numerical Study of the Vortex Burst Phenomenon for Delta Wings," AIAA-88-0505, January 1988.
14. Berger, M.S., "Remarks on Vortex Breakdown," Proceedings of the Workshop on Mathematical Aspects of Vortex Dynamics, Edited by Russell E. Caflisch, April 1988, pp. 171-182.
15. Hoeijmakers, H.W.M., "Numerical Simulation of Vortical Flows," NLR-MP-86032-U, Notes of lectures presented during Lecture Series "Introduction to Vortex Dynamics", Von Karman Institute for Fluid Dynamics, Rhode-Saint-Genese, Belgium, May 1986.
16. Raj, P., Sikora, J.S., and Keen, J.M., "Free-Vortex Flow Simulation Using a Three-Dimensional Euler Aerodynamic Method," Journal of Aircraft, Vol. 25, No. 2, February 1988, pp. 128-134.
17. Investigation of Flow Characteristics of a Developed Vortex, Final Report (to appear), NADC Contract N62269-86-C-0284, 1990.
18. Kegelman, J.T., and Roos, F.W., "Effects of Leading-Edge Shape and Vortex Burst on the Flowfield of a 70-degree-Sweep Delta Wing," AIAA-89-0086, January 1989.
19. Thompson, J.F., Thames, F.C., and Mastin, C.W., "Automatic Numerical Generation of Body-Fitted Curvilinear Coordinate System for Field Containing Any Number of Arbitrary Two-Dimensional Bodies," Journal of Computational Physics, Vol. 15, No. 3, July 1974, pp. 299-319.
20. Buning, G.P., and Steger, J.L., "Graphics and Flow Visualization in Computational Fluid Dynamics," AIAA-85-1507, July 1985.
21. Fujii, K., "A Method to increase the Accuracy of Vortical Flow Simulations," AIAA-88-2562-CP, June 1988, pp. 321-328.
22. Ekaterinaris, J.A., and Schiff, L.B., "Numerical Simulation of the Effects of Variation of Angle of Attack and Sweep Angle on Vortex Breakdown over Delta Wings," AIAA-90-3000-CP, August 1990, pp. 59-67.
23. Krist, S.L., Thomas, J.L., Sellers, W.L., and Kjølgaard, S.O., "An Embedded Grid Formulation Applied to a Delta Wing," AIAA-90-0429, January 1990.
24. Powell, K.G., Beer, M.A., and Law, G.W., "An Adaptive Embedded Mesh Procedure for Leading-Edge Vortex Flows," AIAA-89-0080, January 1989.
25. Degani, D., Schiff, L.B., and Levy, Y., "Physical Considerations Governing Computation of Turbulent Flows Over Bodies at Large Incidence," AIAA-90-0096, January 1990.

#### ACKNOWLEDGEMENTS

This study was supported by the McDonnell Douglas Independent Research and Development program. Computer resources for this work were provided by the National Aerodynamic Simulation Facility at the NASA Ames Research Center. The authors would also like to express their sincere thanks to Dr. James L. Thomas and Ms. Sherrie Krist of the NASA Langley Research Center for providing assistance in executing the latest version of the CFL3D code used in this study.

# VORTEX CONTROL — FURTHER ENCOUNTERS

by

Dhanvada M. Rao  
ViGYAN, Inc.  
30 Research Drive, Hampton VA 23666  
United States

## Abstract

This paper updates the progress, of continuing investigations on vortex control techniques pursued by the author and his associates. The following topics are briefly discussed and salient results of exploratory low-speed wind tunnel experiments presented: 1) Vortex flaps adapted for high-alpha control; 2) Alleviation of LEX vortex induced twin-tail buffet; 3) Controlled de-coupling of interactive forebody chine and wing vortices; 4) Forebody vortex manipulation by mechanical and pneumatic techniques; and 5) Stall-departure alleviation of high aspect-ratio wings. The investigations, primarily aimed at concept validation, were performed on generic configurations utilizing flow visualizations and pressure and balance measurements. Selected results included in this paper illustrate the efficacy and potential for development of specific vortex control concepts for improved high-alpha configuration aerodynamics.

## 1. Introduction

Aerodynamics technology is historically rooted in the principle of avoiding or reducing the dissipative and largely unpredictable flow phenomena associated with separation, turbulence and vortices, by shape design as well as angle-of-attack restrictions to ensure efficient and safe operation of flight vehicles. Of relatively recent origin is the idea of promoting and manipulating dominant vortical flow structures, to enhance aerodynamic control of vehicles at the limits of lift and into the post-stall regime. This approach has been spurred by the need for supermaneuverability and agility across a virtually unlimited angle of attack range, of the new generation of combat aircraft within the configurational constraints as dictated by low observables.

During the past decade of this research, a host of vortex manipulation principles and devices have been conceived and tested, and exploration continues for vortex management techniques of increasing sophistication. While the initial attempts were essentially intuitive and experiment-based, impressive progress is being made in the numerical modelling and prediction of naturally-generated as well as architected vortical flows of high technological potential.

The intent of this paper is to update (following a 1987 review, ref. 1) the progress of an on-going research program concerning vortex control techniques being pursued by the author and his associates. The topics selected for this update are: 1) Adaptation of vortex flaps for high-alpha control; 2) Alleviation of vortex engendered twin-tail buffet; 3) Controlled de-coupling of chine/wing vortex interactions; 4) Chine-forebody vortex manipulation by mechanical and pneumatic techniques; and 5) Stall-departure alleviation of high aspect-ratio wings.

The reported studies were primarily aimed at concept validation on generic configurations, employing standard low-speed wind tunnel test techniques and at relatively low Reynolds numbers. Some justification for this approach is provided by the growing literature and experience supporting the technological value of small-scale laboratory explorations of vortex flows and vortex modification techniques utilizing water facilities (refs. 2, 3), usually at Reynolds numbers much less than those obtaining in these wind tunnel tests (about 500,000). Unlike the majority of water tunnel investigations which are

limited to qualitative studies however, the present experiments consistently attempt to obtain quantitative evaluations for the purpose of identifying key parameters requiring further research and testing in large-scale facilities.

## 2. Vortex Flaps for High-Alpha Control

The vortex flap (ref. 1) was conceived originally as a means of drag reduction of slender supersonic wings, whose thin and highly swept wings are prone to separation and vortex formation at relatively low angles of attack. The down-deflected leading-edge flaps confine the vortex suction to their upper surfaces and thus create an aerodynamic thrust component. Conversely, up deflection of the flaps extends the vortex suction foot-print across the hinge line to the wings while generating a drag component from the aft-inclined flap normal force. Whereas the aerodynamics of vortex flaps in the moderate incidence range are now well understood, their post-stall characteristics are inadequately known. Preliminary balance data were therefore acquired on a 60 deg. flat-plate delta wing/body configuration with symmetrically deflected full-span leading edge flaps at angles of attack to 50 deg (ref. 4). The axial force data (fig. 1) provide a sensitive measure of the flap thrust and drag characteristics, which are found to be approximately linear with flap angle and also to remain effective well beyond the maximum lift. As indicated in fig. 2, flap deflection of  $\pm 45$  deg. provides nearly equal and opposite flap thrust/drag and wing lift increments in the post-stall regime.

The above high-alpha vortex flap characteristics formed the basis of a proposed arrangement of segmented flaps disposed in pairs forward and aft of the aircraft center of gravity, each segment being independently actuated to positive or negative angles (fig. 3). By selecting appropriate differential settings of the flap segments, their thrust and drag forces were intended to generate control moments compensating for the declining effectiveness of conventional trailing-edge surfaces in post-stall flight. The flap segments of course may still be deployed in the conventional vortex flap sense for drag reduction. Typical test results with 45 deg. deflected flap segments on the 60 deg. delta wing model provide a preliminary assessment of their control potential. For yaw control, the forward aft flap pairs were set differentially and in opposition; this flap configuration was compared with the conventional rudder at 15 deg.

deflection. As seen in fig. 4, the rudder effectiveness drops rapidly above  $\alpha=30$  deg. whereas the differential flaps maintain yaw control (at a level equal to the low-alpha rudder power) up to the maximum angle of attack. Also noteworthy is that the induced rolling moment in the post-stall range remains proverse when differential flaps are employed for yaw control.

When the forward and aft flap pairs are deflected differentially but in a like sense (i.e., both segments down on one side and up on the other), the unbalanced lift on the wing panels generates a rolling moment directed towards the side of up-deflected flaps (as may be expected from the incremental lift characteristics already seen in fig. 2). When the flaps are coordinated with elevon deflection, the combined rolling moment capability above  $\alpha=30$  deg. is nearly twice that provided by elevons alone. The induced yawing moment with flap-elevon combination remains proverse.

When considered for use as control surfaces, the flap hinge moment should be minimized in order to facilitate rapid actuation. In this respect, the hinged flap may pose a limitation. An alternate design, called the 'pivoted' flap, was proposed where both mass and aerodynamic balance help to reduce the actuator power requirements. A preliminary aerodynamic assessment was performed to compare the pivoted and hinged flaps of equal area on the same 60 deg delta model. As before, the incremental axial force at constant flap angle provides a relative assessment of the flap thrust characteristics (fig. 6). As seen, the pivoted flap produces significantly higher thrust force in the high alpha region, particularly at 45 deg. deflection. This is consistent with flow visualizations (not presented here) which showed the vortex to persist on the pivoted flap at high angles of attack when the hinged-flap vortex had migrated inboard to the wing (see sketches in fig. 6). Comparative yaw control measurements (fig. 7) corroborate the advantage of the pivoted flap design, including a significant alleviation of the induced rolling moment (which still is proverse). Further tests are needed to determine the hinge-moment characteristics and also the drag reduction capability of pivoted flap in comparison with hinged vortex flap.

### 3. Twin Vertical Tail Buffet Alleviation

Highly swept strakes integrally affixed to the leading edge/fuselage junction (or LEX's) were historically the first usage of custom-generated large scale vortices for augmenting the maximum lift capability of trapezoidal wings, as employed on the F-16 and F-18 fighters (ref. 5). The twin vertical stabilizer configuration of F-18, combined with its unrestricted alpha capability however revealed an unanticipated consequence of the LEX vortex breakdown in the vicinity of the vertical tails (fig. 8), leading to intense tail buffet and diminished fatigue life of the tail structure. Although industry-developed fixes, e.g., the LEX fence, have contained the tail buffet problem on in-service aircraft, this experience underscores the need to understand the causative flow phenomena and to develop alternate buffet alleviation techniques, for the benefit of future fighter configurations which are likely to feature forward vortex-generating components such as nose chines, canards etc., together with twin tails (ref. 6).

Detailed LDV surveys in a cross-plane located immediately upstream of the vertical tails (ref. 7) have identified regions of vortical concentration and high level of velocity fluctuations surrounding the tail region, which are traceable to LEX vortices (fig. 9). The results at  $\alpha=15$  deg show the LEX vortex located close to the wing upper surface and somewhat outboard of the vertical tail which lies in a relatively undisturbed flow. At  $\alpha=25$  deg. however, the vortical region expands greatly and envelops the entire tail. RMS contours show that the expanded vortical flow contains high levels of lateral fluctuations which can be expected to generate considerable dynamic loading on the tail. The mean velocity surveys at  $\alpha=25$  deg. indicate a considerable rotation of the vortical mass as well as a strong outflow across the tail root. These measurements are indicative of a fundamental change in the tail flow environment between  $\alpha=15$  deg. and 25 deg., which flow visualizations show to be associated with LEX vortex breakdown moving upstream of the tails.

Two alternate approaches to tail buffet alleviation recently explored (ref. 8) consisted of: 1) passive dorsal extensions of the tail roots, and 2) controllable, longitudinally-hinged edge section of the LEX, (fig. 10). The dorsal extension was intended to create a new longitudinal vortex from the strong outflow induced in the tail-root region (see fig. 9), rotating counter to the corresponding LEX vortex and intended to re-structure and diffuse the vortical flow at the tail. The dorsal additionally could serve to stiffen the tail attachment thereby relieving the dynamic stresses associated with buffet. The controllable LEX was intended to directly influence the vortex-production mechanism and thus its interaction with the wing and tail flowfields including the breakdown characteristics. The individually up-rotated edge section could also serve to unload the LEX surfaces on either side, symmetrically or non-symmetrically, as a potential means of improving the post-stall handling characteristics.

Smoke flow visualizations and tail vibration measurements were performed on a semi-span generic model representing a LEX/twin-tail configuration to evaluate the above tail buffet alleviation concepts. Tracings of vortex patterns in a cross flow plane immediately upstream of the tail at increasing angles of attack, with and without the dorsal extension, are compared in fig. 11. The baseline case shows a well-formed LEX vortex just outboard of the tail at  $\alpha=15$  deg, which moves inboard with increasing alpha until at  $\alpha=25$  deg. it is positioned directly on the tail, when it also was observed to become quite unsteady as a result of breakdown. With the dorsal attached, the vortex cross-section expands and assumes a S-shaped structure, with the counter-rotating dorsal vortex clearly discernible below the primary LEX vortex at all four angles of attack shown. The tail vibration (first-order bending mode) measurements in the baseline case show the typical rapid increase of RMS after crossing  $\alpha=20$  deg. and reaching a peak at  $\alpha=40$  deg.; with dorsal attached (without touching the vertical tail), the vibration characteristics are seen to be considerably alleviated.

Similar tail vibration measurements made with a 45 deg. up LEX (fig. 12) show a reduction of the tail vibration RMS in the entire high-alpha range. The

data also indicate that addition of dorsal extension to the LEX up-deflected configuration produced further small improvements in the tail RMS characteristics. The tail-buffet alleviation capability of the dorsal extension and deflected-LEX concepts were verified in NASA Langley tests on a complete-span generic model of a twin-tail/LEX configuration. It should be emphasized that in none of these tests was the tail structurally modeled as required for a standard aero-elastic investigation; the purpose of the experiments was essentially to validate the effectiveness of proposed vortex-modification concepts in reducing the dynamic energy of the tail flow environment.

The effects of LEX deflection on the high-alpha aerodynamic characteristics were measured in NASA Langley tests of the complete-span generic model. As shown in fig. 13, the partial unloading of the 45° up-deflected LEX only marginally reduces the maximum lift, but provides a measure of pitch-up relief and also improves the lateral instability characteristics. By deflecting more of the LEX area and also to a greater angle than 45 deg., these high-alpha stability improvements may be further enhanced (ref. 9).

#### 4. Forebody-Chine/Delta Wing Vortex Decoupling

Closely-coupled configurations such as forebody chines blending with sharp, highly swept leading edges are well known to promote strong vortex interactions which lead to unique high-alpha aerodynamic characteristics. While the maximum lift capability of such configurations is enhanced by the interacting vortices, several adverse effects are manifested at post-stall angles of attack, e.g., pitch up, zero-beta asymmetry, reduced roll and yaw damping, and dynamic excitation of the vertical stabilizers. Controlled de-coupling of the forebody and wing vortex systems was proposed in order to selectively prevent their interaction in the post-stall range, to avoid the above mentioned difficulties.

Two alternate de-coupling means considered for preliminary investigations, viz. a passive modification and an active control, are illustrated in fig. 14. The passive modification consisted simply of disconnecting the chine from the wing apex, thus allowing the chine vortices to break away before being 'captured' by the downwash field contained between the wing vortices. In the active technique, part-span inboard leading-edge flaps are employed primarily to suppress the wing vortices in the critical apex region, and also to disconnect the chine to force a shedding of the forebody vortices, as an effective means of preventing vortex interaction.

Initial flow visualizations and wing upper-surface pressure measurements were performed to investigate the feasibility of the proposed techniques on a 60 deg. flat plate delta wing in combination with a chined forebody (ref. 12). Vortex patterns were visualized in a cross-flow plane passing through the wing centroid which also contained a spanwise row of upper-surface pressure orifices. A typical result presented in fig. 15 indicated the effectiveness of the modified chine in de-coupling the forebody and wing vortex pairs; also shown is the corresponding effect on spanwise pressure distributions, where the asymmetry of the baseline configuration is removed by the modification. Comparable results

were obtained with the inboard leading edge flaps, as shown in fig. 16; in this case, the chine vortices were observed to lift away freely with little spanwise migration during their downstream convection, attesting to a total liberation from the wing pressure field.

The effects of chine modification on the wing characteristics at sideslip and  $\alpha=30$  deg. are shown in fig. 17. On the baseline configuration, the windward leading edge vortex breakdown occurs sooner while being delayed on the leeward wing, resulting in the characteristic unstable roll as suggested by the asymmetric spanwise  $C_p$  distributions. The modified chines de-couple the leeward vortex interaction thus reducing the associated suction peak; at the same time the windward suction level is augmented, thus creating a stabilizing roll potential.

Six-component balance measurements on the chine/delta configuration (incorporating a central vertical tail) provide corroborating evidence of the vortex de-coupling benefits in the directional/lateral characteristics. The yawing and rolling moment as a function of sideslip angle at  $\alpha=30$  deg. compared for the baseline and de-coupling configurations are presented in fig. 18. In the range  $\beta=\pm 5$  deg. a remarkable improvement in both the directional and lateral stability is produced by vortex de-coupling.

Forebody/wing vortex interactions and breakdown generate a high-energy dynamic environment at the vertical stabilizer locations, as already discussed in Sec 3. Vortex de-coupling can play a beneficial role by alleviating the unsteadiness and vortical concentration causing tail buffet. Preliminary measurements on a wing mounted twin-tail arrangement show significant reduction of the tail vibration RMS at high angles of attack, as shown in fig. 19.

#### 5. Chine Forebody Vortex Control

The feasibility and attendant benefits of forebody/wing vortex de-coupling discussed in the foregoing section suggests that direct control of the forebody chine vortices, and their interaction with the lifting and empennage surfaces, may be worth investigating as a means of enhancing the high-alpha controllability of such configurations. Modification of chine vortex development requires controlling the vorticity production over a substantial length of the chines, for which mechanical or pneumatic techniques may be viable. An exploratory study was performed on a generic chine forebody/55 deg. delta wing configuration. This initial study was limited to flow visualizations and wing upper-surface pressure measurements in order to obtain a preliminary evaluation of the proposed chine control concepts (fig. 20).

A mechanically controlled chine concept that combines simplicity, robustness and ease of integration is the longitudinally hinged chine that may be rotated to a variable anhedral or dihedral angle. This hinged chine idea has a basis in prior investigations of the articulated LEX (ref. 9) and deflectable forebody strakes (ref. 13). For pneumatic control of chine vortices, spanwise blowing via narrow slots coincident with the chine edges was proposed. Controlled injection of fluid momentum



directly at the site of vorticity production has been demonstrated previously on thin, highly-swept delta wings to strongly influence the roll-up characteristics of the vortex layer as well as displace the vortex core trajectory (ref. 14).

The 'hinged' chines were simulated on the test model by means of flat-plate chines inserted in the horizontal meridian plane of the ogive forebody, bent at 45 deg. up or down to represent dihedral/anedral configurations. An alternate forebody incorporating a plenum chamber with wedge-shape chine attachments containing blowing slots was provided for pneumatic testing.

The effect of chine deflection on the forebody vortex positions in a cross-plane passing through the wing apex, as determined by smoke visualizations in shown in fig. 21 at increasing angles of attack. The examples presented depict the effects of symmetric chine configurations. In comparison with the baseline (i.e., undeflected chines), dihedral draws the vortices inwards and elevates them at all angles of attack. The anti-symmetric chines produce a corresponding spatial anti-symmetry in the forebody vortex pair, which also persists through the angle of attack range. The effect of vortex manipulation due to chine deflection on the wing pressures at  $\alpha=30$  deg. is shown in figs. 22 and 23, for the symmetric and anti-symmetric cases respectively. Dihedral and anedral have opposite effects on the wing suction levels, which translate into increased or decreased normal force  $C_n$  respectively in the post-stall alpha range as shown in fig. 23. Similarly, the opposite suction levels induced on the two wing panels by anti-symmetric chines generate a potential for rolling moment. This effect is also produced by non-symmetrical (i.e., one sided) chine configurations; the three test cases and their rolling moment ( $C_{RM}$ ) characteristics are compared in fig. 25. A significant post-stall roll control capability is indicated by these data.

Turning next to pneumatic chines, the case of symmetrical (i.e., both chines) blowing will be first considered. The  $C_p$  distributions at  $\alpha=30$  deg. (fig. 26) show that symmetric blowing tends to eliminate the pronounced asymmetry prevailing on the baseline (i.e., unblown) configuration at this alpha. Alleviation of zero-beta asymmetry during approach to maximum lift is thus a potential advantage of pneumatic chine control.

The effect of non-symmetric blowing is to augment the suction levels on the blown side of the wing, as shown in fig. 27 for the case of left chine blowing at  $\alpha=30$  deg. This allows a controllable lift asymmetry to be introduced between the wing panels, generating a rolling moment potential in the post-stall alpha range, as depicted in fig. 28, for both left and right blowing. The local rolling moment coefficient (based on intragaited upper-surface  $C_p$  distributions) in either direction is found to increase linearly with blowing momentum up to  $C_{\mu}=.015$  approximately (fig. 29). The constructional limitations of the test model precluded any definitive attempts at slot optimization (e.g., varying slot width and length, tapered slots, etc.), which is believed to have potential for improving the pneumatic efficiency of the blown chine concept.

The preliminary results presented in this section have indicated substantial lateral control potential in the post-stall regime via differential lift characteristics generated by either mechanically or pneumatically controlled chine vortices. A forebody side force accompanying non-symmetrical chine activation (fig. 30) should produce a coordinated yawing moment in order for the roll control to be useful for maneuvering. This aspect requires further investigation of the six-component aerodynamics of the controlled chine/wing configurations at high angles of attack.

## 6. Stall Departure Alleviation of High Aspect Ratio Wings

In this last example of applying vortex control techniques to enhance high-alpha aerodynamics, we turn from highly-swept and vortex dominated configurations considered in the foregoing sections to the case of unswept wings of high aspect ratio such as commonly employed on general aviation and sport aircraft. Such wings are well known to have abrupt stall and uncontrollable departure characteristics. The stall onset is preceded by the appearance of 'stall cells', i.e., localized regions of reversed flow spaced along the wing span, producing a distinctive three-dimensional breakdown pattern. The stall cells develop non-symmetrically resulting in powerful rolling moments as  $C_{LMAX}$  is approached.

These observations suggested that the post-stall behavior of high aspect ratio wings might be controlled by forcing the stall pockets to grow symmetrically, and also by striving to maintain attached flow in the tip regions even past  $C_{LMAX}$  in order to improve post-stall roll damping and aileron effectiveness. An approach to this end developed by NASA Langley is the use of part-span leading edge droop, which has been proven in wind tunnel and flight tests to be an effective departure alleviator. However, a potential cruise-drag penalty as well as aesthetic considerations have reportedly inhibited the adoption of this technique by aircraft manufacturers.

An alternative proposal for 'fixing' the stall cells on a high aspect ratio wing was to cut narrow vertical notches or slots in the leading edge at selected span locations. These slots, penetrating to less than 5 percent of the local chord, each generate a contra-rotating vortex pair on the wing upper surface from the cross-jets created by the leading-edge pressure differential (fig. 31). Interaction with the upper-surface bounding layer initiates local wedge-shaped flow shear regions between these vortex pairs, which ultimately develop into stall cells. This postulated flow mechanism was verified in smoke and oil flow visualization tests on a generic high aspect ratio, semi-span wing model, (fig. 32) typical results obtained with a pressure instrumented wing at a stalled angle of attack (fig. 33) show that the vortex slots restore the upper-surface suction peaks at the alternate span stations lying between the slot-generated stall cells. The modified stall behavior due to the vortex slots is evident in the balance data (ref. 18) presented in fig. 34. The resulting lift curve has a flat top feature with considerably reduced negative slope after  $C_{LMAX}$  in comparison with the basic wing, which is the key to stall departure alleviation. Also shown for comparison is the effect of a typical NASA part-span droop addition, which produces a stall modification



similar to the vortex slots. While the droop improves  $C_{L,MAX}$  as expected, it also creates significant drag penalty at cruise lift coefficient over and above that caused by vortex slots.

A unique arrangement of the NASA part-span droop and vortex slot was developed for application to a general aviation design, the 'Questair Venture'. This involved the use of a moderate degree of droop combined with a vortex slot at its inner end plus a second slot provided further inboard on the undrooped leading edge (fig. 35) NASA Langley wind tunnel tests (ref. 19) of the tuft-visualized stall patterns indicate the progressive improvements due to the part-span droop alone and then in combination with the vortex slots. These stall improvements are reflected in the corresponding lift curves, which show that addition of slots to the droop essentially removes the negative lift-slope feature. In addition, the combined modification provides a significant increase in the post-stall aileron control due to the trip regions retaining attached flow.

## 7. Conclusions

Selected results of recent low-speed wind tunnel tests of several vortex-control concepts have been presented to illustrate their potential in five specific applications:

- 1) Adaptation of the vortex flap concept in a unique segmented leading edge arrangement for lateral/directional control at post-stall angle of attack;
- 2) Twin-tail buffet alleviation via LEX vortex manipulation;
- 3) Controlled de-coupling of interactive forebody-chine and delta wing vortices;
- 4) Mechanical and pneumatic manipulation of forebody chine vortices; and
- 5) Leading edge slot vortex generators to alleviate stall departure of high aspect ratio wings

The above examples presented in this review are illustrative of the scope of problem areas concerning high-alpha aerodynamics of flight vehicles under continuing study, with emphasis on vortex control techniques.

## Acknowledgements

A large part of the experimental work described in this paper was performed in VIGYAN 3x4 ft. low speed diagnostics wind tunnel, whose personnel contributed greatly to the outcome. The encouragement and support of NASA Langley Research Center and Air Force Wright Aeronautical Laboratory is gratefully acknowledged.

## References

- 1) Rao, D. M. And Campbell, J. F., (1987); Vortical Flow Management Techniques Prog. Aerospace Sci. Vol. 24, No. 3, pp. 173-244.
- 2) Erickson, G. E., (1982); Vortex Flow Correlation ICAS 13th Congress, Paper No. 82-6.6.1.
- 3) Erickson, G. E., et al (1986); Water Facilities in Retrospect and Prospect - an Illuminating Tool for Vehicle Design, NASA TM 899409.
- 4) Rao, D. M., (1990); Potential of Segmented Vortex Flaps for Post-Stall Controllability NASA High-Angle-of-Attack Technology Conference (to be presented).
- 5) Polhamus, E. C., (1983); Application of Slender Wing Benefits to Military Aircraft AIAA-83-2566.
- 6) Scott, W. B., (1990); YF-23A Preview: Design Features of Future Fighters. Aviation Week and Space Technology, July 2, pp. 16-21.
- 7) Sellers, W. L., III, Meyers, J. F., and Timothy, E. H., (1988); LDV Surveys Over a Fighter Model at Moderate to High Angles of Attack. SAE Tech. Paper 881448.
- 8) Rao, D. M., and Puram, C. K., and Shah, G. H., (1989); Vortex Control for Tail Buffet Alleviation on a Twin-Tail Fighter Configuration. SAE Tech. Paper 892221.
- 9) Rao, D. M., and Huffman, J. K., (1982), Hinged Strakes for Enhanced Maneuverability at High Angles of Attack. J. Aircraft, Vol. 19, No. 4
- 10) Erickson, G. E. and Brandon, J. M., (1985); Low-Speed Experimental Study of the Vortex Flow Effects of a Fighter Forebody Having Unconventional Cross-Section. AIAA Paper 85-1798-CP.
- 11) Erickson, G. E. and Brandon, J. M., (1987); On the Non-Linear Aerodynamic and Stability Characteristics of a Generic Chine-Forebody Slender-Wing Fighter Configuration. NASA TM 89447.
- 12) Rao, D. M., (1989); Feasibility Study of Vortex Interaction Control a Chine Forebody/Delta Wing Configuration at High Angle of Attack. Paper No. 89-3350. AIAA Atmospheric Flight Mechanics Conference, 1989.
- 13) Rao, D. M., Moskovitz, C. and Murri, D. G., (1986); Forebody Vortex Management for Yaw Control at High Angles of Attack ICAS-86-2.5.2.
- 14) Kuchemann, D.; The Aerodynamic Design of Aircraft. Pergamon, 1978. pp. 387.
- 15) Rao, D. M. and Puram, C. K., (1990); Low-Speed Wind Tunnel Investigations of Mechanically and Pneumatically Controlled Forebody Chine Concepts. (to be issued as AFWAL report)
- 16) Winkleman, A. E. and Barlow, J. B., (1980); Flowfield Model for a Rectangular Planform Wing Beyond Stall. Journal AIAA, Vol. 18, No. 8, pp. 1006-1007.

- 17) Staff of Langley Research Center (1979); Exploratory Study of the Effects of Wing Leading-Edge Modifications on the Stall/Spin Behavior of a Light General Aviation Airplane, NASA TP-1589.
- 18) Meyer, H. F., (NASA Langley Research Center); Private Communication, 1989.
- 19) Meyer, H. F.; et al (1989); Experimental Investigation of the High Angle of Attack Characteristics of a High Performance General Aviation Aircraft. AIAA 89-2237-CP.

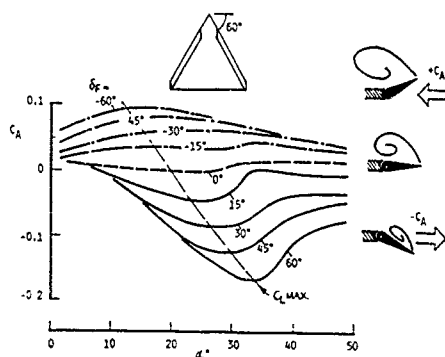


Fig. 1 Axial force characteristics versus angle of attack for symmetric flap deflections

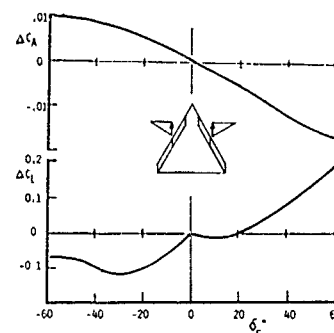


Fig. 2 Incremental axial force and lift coefficients versus symmetric flap deflection angle at  $C_{L \text{ MAX}}$

Fig. 3 Segmented vortex flap arrangement in typical differential configuration

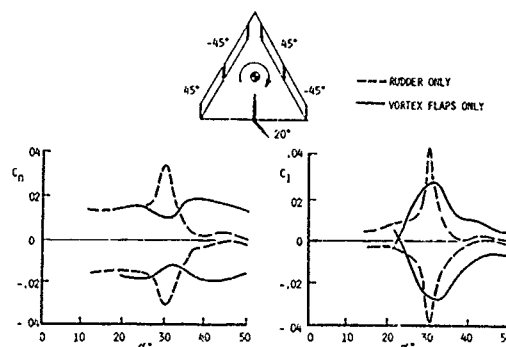
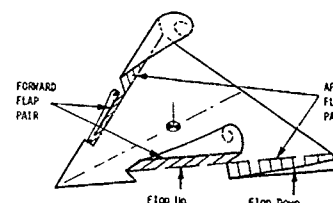


Fig. 4 Yawing moment and associated rolling moment versus angle of attack with differential flaps.

Fig. 5 Rolling moment and associated yawing moment versus angle of attack with differential flaps in combination with elevons.

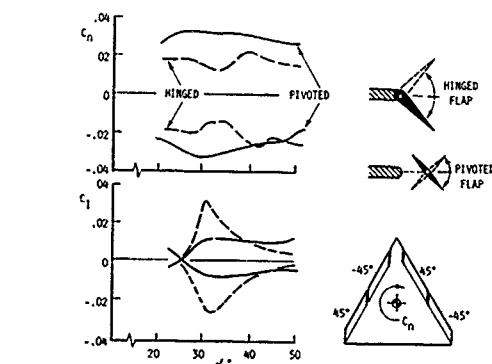


Fig. 6 Incremental axial force versus angle of attack at three flap deflection angles, comparing hinged and pivoted flaps.

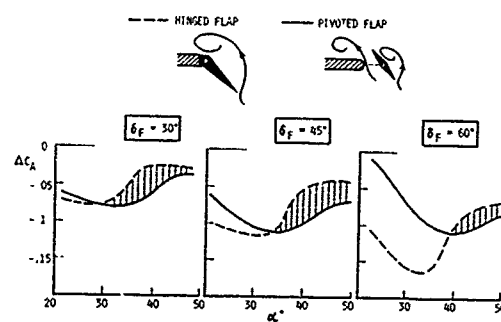


Fig. 7 Yawing moment and associated rolling moment versus angle of attack, comparing hinged and pivoted flaps.

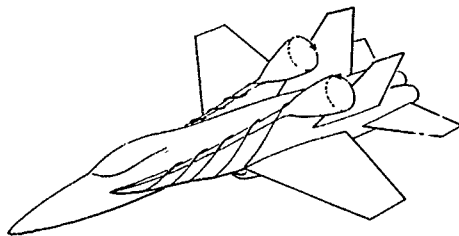


Fig. 8 LEX vortex breakdown as a source of vertical tail dynamic excitation.

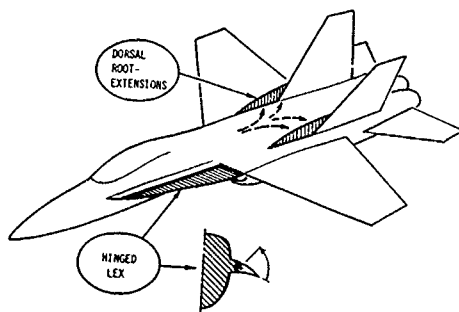


Fig. 10 Passive and active control concepts for vertical tail buffet alleviation vertical.

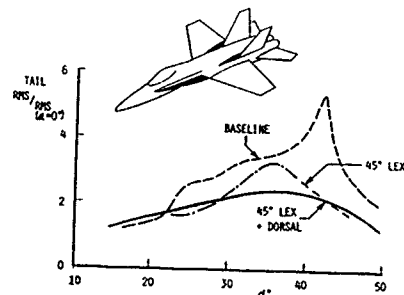


Fig. 12 Vertical tail vibration characteristics versus angle of attack with and without LEX deflection and dorsal combination.

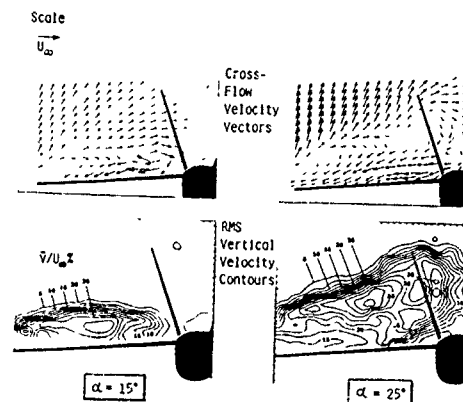


Fig. 9 LDV flow surveys in a vertical tail entry crossplane (taken from ref. 7).

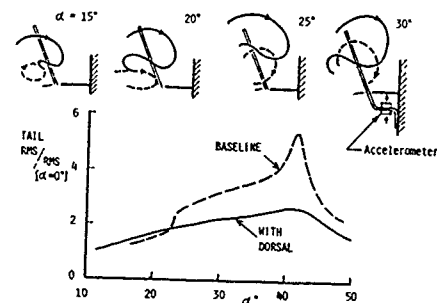


Fig. 11 Vertical tail vibration characteristics versus angle of attack with and without dorsal extension

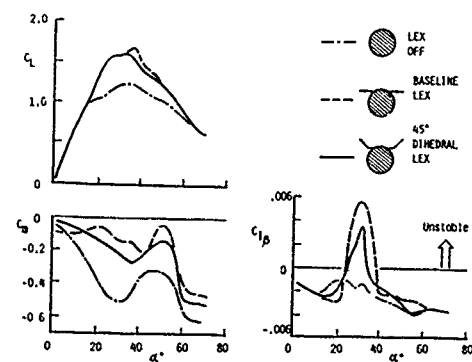


Fig. 13 Lift, pitching moment and lateral stability characteristics versus angle of attack with and without basic and dihedral LEX.

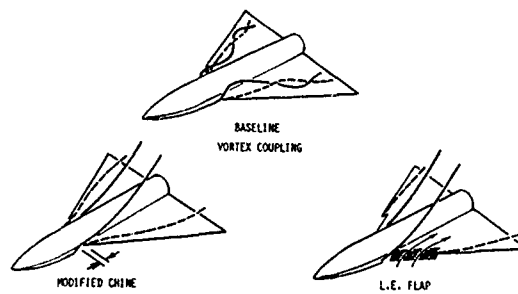


Fig. 14 Chine/delta wing vortex coupling, and passive and active de-coupling concepts.

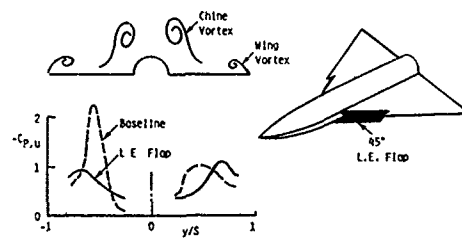


Fig. 16 Vortex de-coupling via inboard leading edge flaps; flow visualizations and pressure measurements at  $\alpha = 25$  deg.

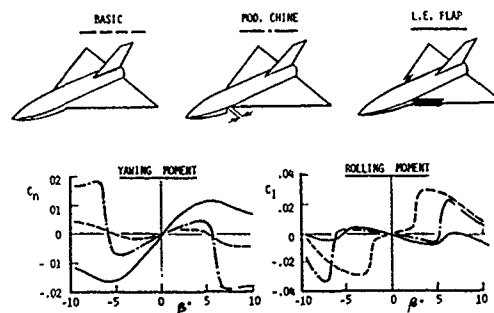


Fig. 18 Directional and lateral stability characteristics of chine/delta wing configuration, with and without, modified chines and leading-edge flaps at  $\alpha = 30$  deg.

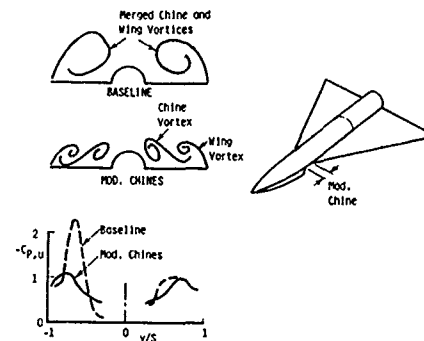


Fig. 15 Vortex de-coupling via modified chines; flow visualizations and pressure measurements at  $\alpha = 25$  deg.

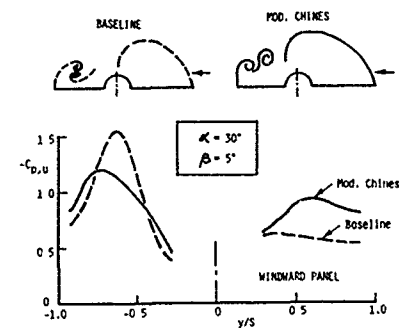


Fig. 17 Vortex de-coupling via modified chines at  $\alpha = 30$  deg. and  $\beta = 5$  deg.

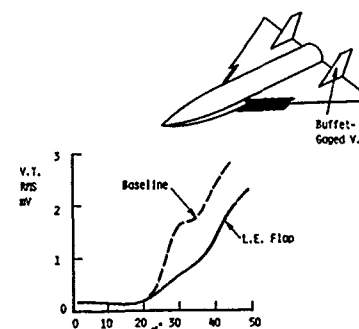


Fig. 19 Twin vertical tail vibration characteristics versus angle of attack on a chine/delta wing configuration with and without leading edge flaps.

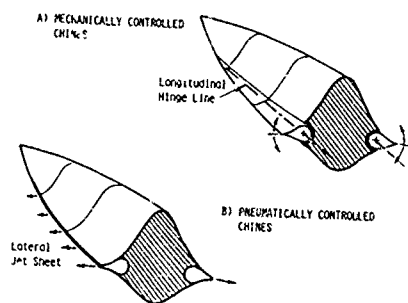


Fig. 20 Forebody chine vortex control concepts mechanical and pneumatic.

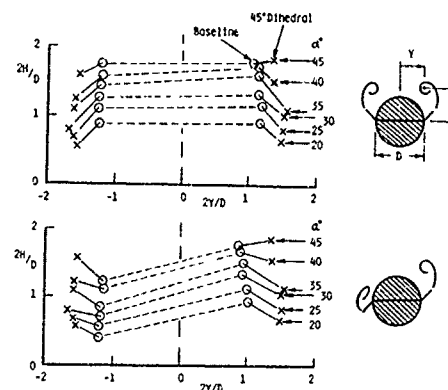


Fig. 21 Chine vortex manipulation by symmetric and anti-symmetric 45 deg. chine deflections.

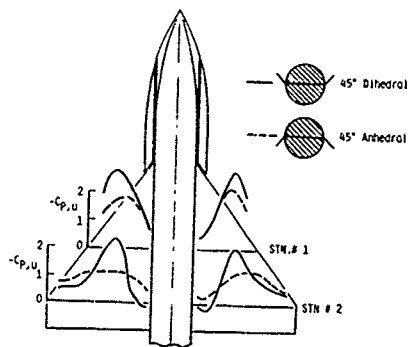


Fig. 22 Delta wing pressure distributions due to 45 deg. symmetric dihedral and anhedral chine deflection at  $\alpha=30$  deg.

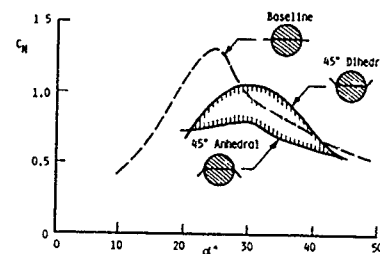


Fig. 23 Pressure-integrated local normal force characteristics versus angle of attack as modified by symmetric dihedral and anhedral chine deflection.

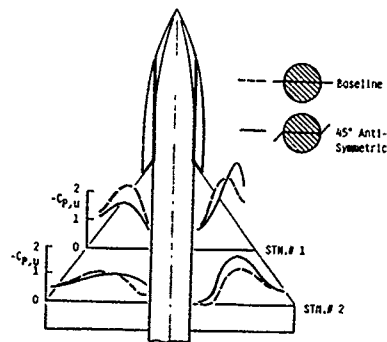


Fig. 24 Delta wing pressure distributions due to 45 deg. anti-symmetric chine deflection at  $\alpha=30$  deg.

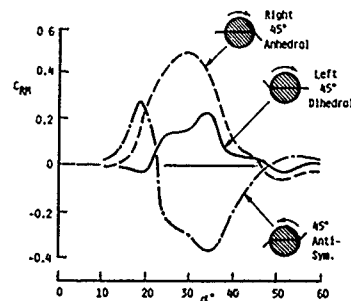


Fig. 25 Pressure-integrated local rolling moment characteristics versus angle of attack with three types of non-symmetric chine deflection.

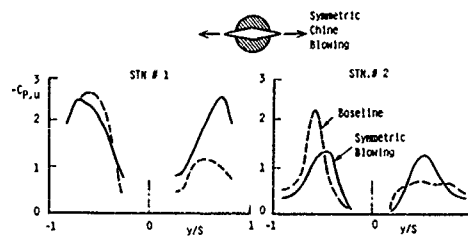


Fig. 26 Delta wing pressure distributions as modified by symmetric chine blowing at  $\alpha=30$  deg.

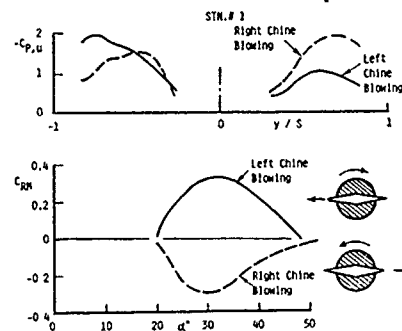


Fig. 28 Delta wing pressure distributions at  $\alpha=30$  deg, and local rolling moment characteristics versus angle of attack due to one left-side and right-side chine blowing.

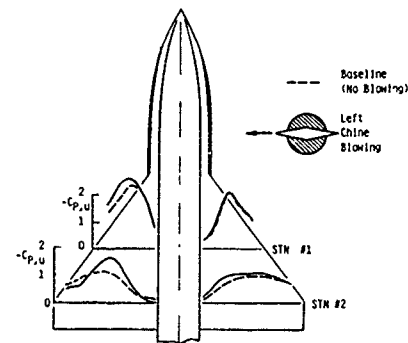


Fig. 27 Delta wing pressure distributions as modified by left-side chine blowing at  $\alpha=30$  deg.

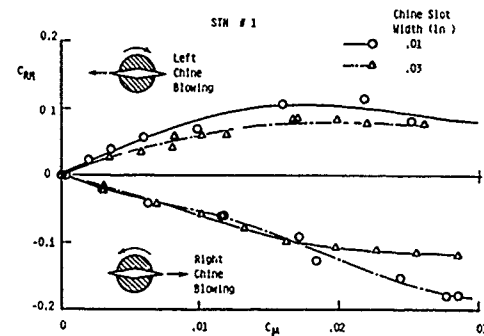


Fig. 29 Local rolling moment characteristics versus momentum coefficient with left-side and right-side chine blowing at  $\alpha=30$  deg.

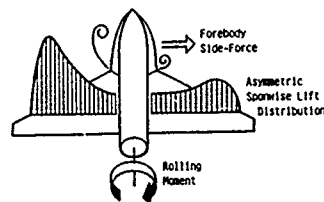


Fig. 30 Non-symmetric chine vortex manipulation for co-ordinated directional/lateral control.

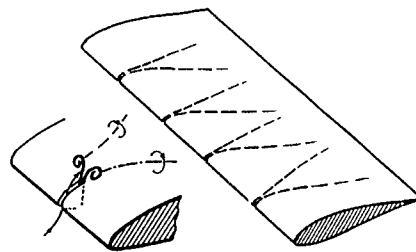


Fig. 31 Leading-edge slot vortex generator.

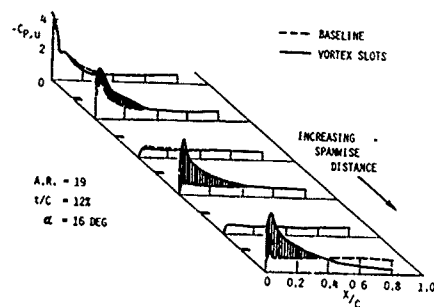


Fig. 32 Upper-surface pressure distributions on a high aspect ratio unswept wing at post-stall angle of attack, with and without vortex slots.

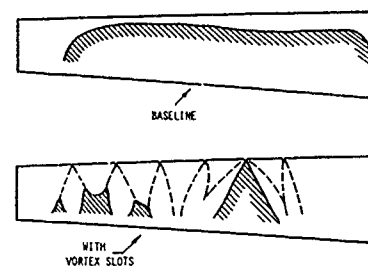


Fig. 33 Effect of vortex slots on stall pattern of high aspect ratio wing.

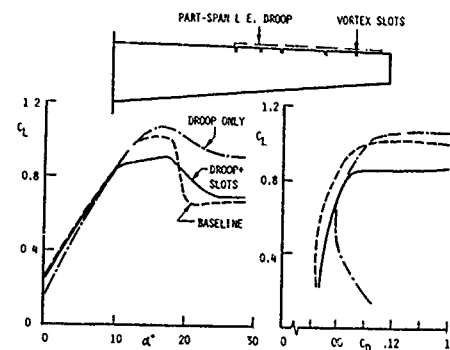


Fig. 34 Lift and drag characteristics of high aspect ratio wing with and without vortex slots and part-span droop.

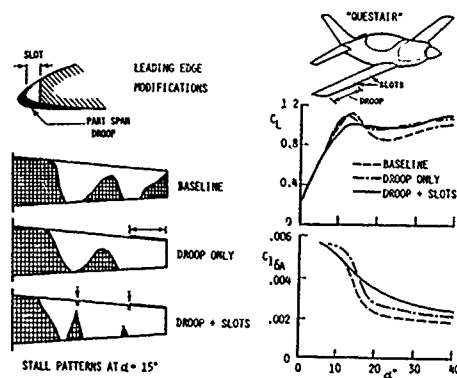


Fig. 35 Combination of vortex slots and part-span droop on 'Questair'.



## On Aircraft Wake Properties and Some Methods for Stimulating Decay and Breakdown of Tip Vortices

by

R. Staufenbiel and T. Vitting  
Department of Aerospace Engineering  
Aachen, University of Technology  
D 5100 Aachen

### SUMMARY

In the first part of this paper, investigations on the formation and structure of wing tip vortices are presented. A computational method for the time-dependent roll-up process is derived, which is based on the Biot-Savart approach with a particular technique of amalgamation which preserves energy, center of vorticity and the second moment of vorticity distribution. The results are compared with LDV measurements performed in a water tunnel.

In the second part of the paper the influence of lift distribution on maximum circumferential velocity of trailing vortices is investigated. Moreover, some special devices for vortex wake alleviation were experimentally investigated in order to reveal the potential of three methods for vortex wake alleviation:

- artificially destabilizing the vortex,
- inducing breakdown of the vortex core and
- spreading and splitting the vorticity of trailing vortices.

### INTRODUCTION

Trailing vortices generated by larger aircraft can present severe hazard to other aircraft which inadvertently encounter the vortices. This topic is of growing interest because of the increasing air traffic density and the airport congestion. Runway capacity could be enlarged if the vortex problem will have been alleviated.

During this study it became obvious that a successful control of vortices depends largely upon the understanding of the basic fluid motions involved in the formation of trailing vortices. For controlling the roll-up of wing vortex sheet or imposing disturbances on the core of a concentrated vortex, a detailed knowledge of the birth process and the structure of trailing vortices is mandatory.

After a short overview on methods for wake hazard reduction, the paper is concerned with two main topics

- the formation of trailing vortices
- methods for reducing the strength of trailing vortices

### WAKE HAZARD REDUCTION

The hazards, imposed by trailing vortices, can be reduced if the vorticity in the trailing vortex sheet is prevented from becoming concentrated or if concentrated vorticity is dissipated fast enough.

In principle, two ways for reducing the wake hazard are possible, which can be distinguished as prenatal and postnatal methods (Fig. 1).

*Prenatal* methods should prevent the development of strong trailing vortices. Two ways look promising:

1. The design of a wing configuration with a favourable lift distribution which implies that the vorticity after roll-up is less concentrated,
2. Methods of disturbing or disordering the roll-up process which could, in the most favourable case, lead to a chaotic and widespread vorticity distribution.

The *postnatal* vortex alleviation intends to disturb the already concentrated vortex core by one of the following methods

3. Destabilizing the vortex
4. Stimulating vortex break-down
5. Splitting the tip vortex in sub-vortices of lower strength
6. Controlled meandering for stimulating selfdestruction of vortices
7. Methods to magnify the ageing process

In general, all active methods should apply devices which put limited penalties on aircraft empty weight and drag.

In this paper the methods (1), (3), (4) and (5) are considered in more detail.

### THE FORMATION OF TRAILING VORTICES

In this section, some fundamentals of the roll-up process will be treated first. Then, LDV measurements of velocity components in trailing vortices will be presented. A main subject is the introduction of a new, simple numerical method for calculating the roll-up process. Finally, theoretical results will be compared with experiments.

### Fundamentals of the roll-up process

In the following diagrams, the streamwise, spanwise and wing normal coordinates are denoted by  $x$ ,  $y$ ,  $z$ , respectively.  $V_c$  is the circumferential velocity, induced by the vorticity in the crossflow plane.

Fig. 2 illustrates the two main effects which a wing imposes on passing air flow. It shows the wake of a wing of rectangular planform shortly behind the trailing edge measured in a water tunnel by an LDV. Velocity components in spanwise and streamwise direction were measured along a line normal to the wing planform at three span stations.

The spanwise component reveals the shear layer of the vortex sheet and shows a large maximum circumferential velocity near the wing tip caused by a high concentration of vorticity - already half a chord length behind the trailing edge.

The streamwise velocity component indicates the momentum loss in the boundary layer which is related to the profile drag. The deficit of the streamwise velocity component is reduced towards the wing tip and even a jet-type profile is obtained at the location of the vortex center because of the reduced static pressure in the vortex core.

Following Spreiter and Sacks [1], the rate of formation of circumferential energy in the wake, induced by the trailing vortices, is directly related to the induced drag (Fig. 3)

$$(1) \quad D_i = \frac{1}{L} \iint_V \frac{1}{2} \rho V_c^2 dV = \iint_{CP} \frac{1}{2} \rho V_c^2 dA$$

where the integral must be performed over an infinite sheet of thickness 1 normal to the flight direction  $c$  in the crossflow plane ( $=CP$ ).

### LDV measurements

Fig. 4 shows axial and circumferential velocity profiles - in units of freestream velocity - measured at three different downstream stations behind a wing with rectangular planform and an aspect ratio of  $AR=4$ . Surprising is the rapid decrease of the axial velocity turning a jet-type into a wake-type profile ( $V_x/V_\infty \approx 1.3 > 0.7$ ). Also the maximum circumferential velocity decreases with downstream distance, but at a much smaller rate. The results of an inviscid numerical approach, a modified line vortex method presented later on, show similar tendencies so that no ageing process is to be assumed as the reason for this behaviour.

In Fig. 5 the axial velocity at the vortex center and the maximum circumferential velocity are shown as a function of downstream positions. Both values are reduced with increasing downstream distance. About five

half span behind the wing trailing edge, the vortex structure becomes practically constant which means that the roll-up process is practically finished. The advantage of the rectangular planform, used in these experiments, is the fast roll-up process which is already terminated within the test section of the water tunnel.

Fig. 6 shows the core radius as function of the downstream distance. The core radius increases with distance and a saturation can be observed with a value of about 2.5% of the halfspan. The final value depends on the lift distribution, that is, on wing planform and aspect ratio.

### A numerical method for calculating the roll-up process

To understand the experimental results better, a numerical method is presented which is based on a modified point vortex approximation. This simple method was developed as a design tool suitable to perform parametric studies for investigating basic influences.

Multi-discrete-vortex models have been used for a long time to simulate the evolution of vortex sheets emanating from the trailing edges of lifting surfaces, see, e.g., the survey given in Ref. [2]. In the point-vortex approach (better rectilinear line-vortex approach), the three-dimensional steady vortex sheet is considered to be two-dimensional and unsteady. The lift distribution of the wing defines the initial distribution of the array of potential vortices with the strength of  $\gamma_i$ . The motion of the line vortices and, thus, the roll-up process can be calculated by solving a system of first order ordinary differential equations, the Biot-Savart equations:

$$(2) \quad \begin{aligned} \frac{dy_i}{dt} &= - \sum_{j \neq i} \frac{1}{2\pi} \gamma_j \frac{z_i - z_j}{(y_i - y_j)^2 + (z_i - z_j)^2} \\ \frac{dz_i}{dt} &= \sum_{j \neq i} \frac{1}{2\pi} \gamma_j \frac{y_i - y_j}{(y_i - y_j)^2 + (z_i - z_j)^2} \end{aligned}$$

Every multi-discrete-vortex model leads to the difficulty that the vortex filaments are singularities and create large velocities in their neighborhood. Instability and sheet crossings during roll-up seem unavoidably and turn the array of the line vortices into chaos.

Fig. 7 shows the result of the classical point vortex approximation for a wing with an elliptical lift distribution at a non-dimensional time  $\tau=2.5$  ( $\tau=tU_0/s^2$ ). Even if the roll-up of the vortex sheet looks quite promising, the line vortex methods are not suitable for a comparison with experiments describing the roll-up process. This statement is valid for the two-dimensional point vortex as well as for three-dimensional vortex-lattice methods. Particularly, the most interesting velocity profile of the circumferential velocity can not be obtained from discrete-vortex model simulations. The reason is that the local values of the circumferential

velocity are unsteady, with high peak values near the concentrated singularities of the chaotically moving line vortices.

In spite of the irregular, chaotic motion, the Biot-Savart approach meets some important conservation laws, as can easily be derived from the shown differential equations [3]. In particular, the so-called Kirchhoff-Routh function

$$(3) \quad K = \frac{1}{2\pi} \sum_{i < j} \gamma_i \gamma_j \ln(r_{ij} / s)$$

is time-invariant. Moreover, the spanwise position of the center of vorticity (for each half wing), and the second moment of vorticity distribution (for likesign vorticity) are conserved.

It is a very interesting fact that the K.-R. function is directly related to the induced drag

$$(4) \quad -K \rightarrow D_i / \rho$$

if a sufficiently high number of vortices represent the vortex sheet shed by the wing [4]. Thus, the time-invariance of the K.-R. function is equivalent to the conservation of the rotational energy in the cross-flow plane during roll-up. It is remarkable that in the K.-R. function the singularities of the line vortices are eliminated so that a finite rotational energy is obtained corresponding to the finite value of the induced drag. Moreover, the K.-R. function can be very easily evaluated. One only must know the circulation of the line vortices and the relative distances between all line vortex pairs  $r_{ij}$ , a knowledge obtained by solving the Biot-Savart equations. No difficult integration process is necessary, as would be the case if Eq. (1) must be evaluated.

The two statements:

- results of the point vortex method have no relationship to experimental results (because of singularities and chaos) and
- the time-invariant K.-R. function, which is calculated by the point vortex approach, is directly related to induced drag

look controversial. This discrepancy can be solved if we consider the derivation of the relation between rotational energy and K.-R. function. It is not valid in any case. First, it is applicable only if the vorticity, distributed with positive and negative sign, sums up to zero so that the circulation at large distances from the vorticity center is zero. Otherwise the rotational energy would be infinite. This condition is fulfilled for vorticity generated by lifting surfaces. Moreover, the stated relationship requires that the vorticity is distributed along a continuous vortex sheet which is represented by point vortices as finite elements. As soon as a self-crossing of the vortex sheet occurs or the sheet is destroyed - as is

the case in the chaotic region - this representation is going lost.

For restoring the relationship between rotational energy and K.-R. function, the prevention of chaos or the reconstruction of an ordered vortex sheet in the chaotic region is necessary.

Until now, the prevention of chaos was not successful in spite of the many proposed modifications of the classical line vortex methods: Velocity cutoff schemes, use of vortices with a core, amalgamation of a number of vortices into a single vortex, use of subvortices, re-discretization of the sheet, and other filtering and smoothing techniques [2]. In any case, these "surgical" techniques mean a manipulation of the Biot-Savart equations with uncertain influences on the vortex structure.

In this paper, a special way of reconstruction of a vortex sheet in the core region is described. It is based on a special amalgamation process embedded in the point vortex method. Vortices which are turning into chaos are amalgamated into a concentrated vortex. The proposed modification of the point vortex approximation can be described in the following way:

- 1) The amalgamation process is initiated every time when a self-crossing of the vortex sheet occurs.
- 2) The amalgamated vorticity is distributed homogeneously, in accordance with a modified Lamb-Oseen model [5], across a concentrated region around the already amalgamated vorticity center.
- 3) The parameters of the model are updated - at every amalgamation step - by the conditions that
  - the K.-R. function is conserved
  - the second moment of vorticity is not changed over an amalgamation step and
  - the total circulation is conserved
  - the center of amalgamated vorticity is kept constant

In this way, the relevance of the conservation of rotational energy is brought back into the simple line vortex method.

Three time-dependent parameters are incorporated in the modified Lamb-Oseen model

$$(5) \quad \Gamma = \Gamma_{am} [A + (1 - A) r / R_o] \left\{ 1 - e^{-(r/R_i)^2} \right\}$$

$\Gamma_{am}$ ,  $R_o$  and  $R_i$ . The parameter  $A$  has a smaller influence on the results and was chosen as constant,  $A=0.7$ . The term in the second bracket describes the well-known Lamb-Oseen model. By adapting, at each amalgamation step, the "inner radius"  $R_i$  - which is approximately equal to the core radius  $R_c$  - it is possible to conserve the energy, given by the Kirchhoff-Routh function. The term in the first bracket permits to conserve the second moment of vorticity distribution by adapting the "outer radius"  $R_o$ .  $\Gamma_{am}$  is the time-

dependent circulation determined by the already amalgamated vorticity. Fig. 8 shows circulation, vorticity distribution and circumferential velocity profile for the amalgamated vortex after a non-dimensional roll-up time of  $\tau=2.5$  for an elliptic lift distribution. Details of the modified point vortex method are presented in [6].

As a first result, Fig. 9 shows the ordered roll-up and the prevention of chaos by using the special amalgamation process for the same case as displayed in Fig. 7 obtained by the classical point vortex method.

The proposed method has the advantage that important conservation laws are met, particularly the energy conservation, by suppressing the chaos with the consequence that

- a viscous-like vortex core with finite circumferential velocity is obtained and
- a time-dependent, analytical model of the vortex core can be evaluated for a comparison with experiments.

The conservation of rotational energy is of paramount importance for any numerical algorithm which is going to describe the roll-up process and the final vortex structure. Fig. 10 shows the strong influence of the Kirchhoff-Routh function on core radius and maximum circumferential velocity. An error of only 10% in energy provides a deviation of 60% from the true values of core radius and maximum circumferential velocity.

In this respect, Euler and Navier-Stokes codes are expected to suffer from the limited resolution in spatial and time coordinates, which lead to core radii which are too large and maximum circumferential velocities which are too low. Numerical viscosity acts in the same sense. It seems that, at this time, it is almost hopeless that three-dimensional schemes can cope with the necessary spatial resolution (required by the high concentration of vorticity in the core region) and the integration over a long distance (10 to 100 halfspan, depending on lift distribution) without "loosing" too much energy.

#### Theoretical results

Fig. 11 shows a comparison of simulation and LDV measurements for the vortex core radius as a function of distance behind the trailing edge. The wing has a rectangular planform of aspect ratio  $AR=4$ . The basic tendency of a growing core radius, as found in experiments, is reproduced by the proposed theoretical approach. Also the final value of the core radius ( $R_f > 0.034 \cdot s$ ) is in good agreement with the experiments, even if the measurement could not be extended above a distance of ten halfspans. But, the measurements show larger core radii directly behind the trailing edge. As the main reason for this deviation, a pre-concentration of vorticity is considered which occurs already over the wing along the wing tip. Such an effect is not included in the theory.

Fig. 12 shows the calculated maximum circumferential velocity. If, again, the pre-concentration phase is excluded, a smooth decrease of the maximum circumferential velocity is reproduced, similar as shown in the experimental results of Fig. 5. For comparison purpose, also the simulation result for an elliptical lift distribution is plotted. The higher density of vorticity in case of the rectangular wing leads to final values of the circumferential velocity which are considerably higher than for the elliptical distribution.

As an interesting experimental result, the decrease of the maximum axial velocity at the vortex center was found. Also this effect can be derived, at least qualitatively, using the proposed numerical method.

Considering the balance between pressure and centrifugal forces, the static pressure at the vortex center is related to the circulation of the amalgamated vortex as

$$(6) \quad \frac{p_0 - p_\infty}{\rho} = - \frac{1}{(2\pi)^2} \int_0^\infty \frac{\Gamma^2}{r^3} dr$$

The integral and, therefore,  $p_0$  can be evaluated because the circulation is known as function of the radial distance and time (or downstream distance) from the vortex center. Because the integral decreases - due to a widening of the core, the static pressure in the core region increases as long as the roll-up process has not been terminated, thereby reducing the axial velocity in the vortex core. In Fig. 13, the axial velocity at the vortex center is shown as function of downstream position for an elliptical lift distribution. The simulation is evaluated for three values of the parameter  $AR/C_L$ . In this evaluation, the initial value of the axial velocity, which is related to the total pressure at the vortex center, must be given. In Fig. 13 an initial value of  $V_x/V_\infty=1.4$  was chosen.

#### METHOD FOR REDUCING THE STRENGTH OF TRAILING VORTICES

In the second part of the paper, the following effects and methods for reducing vortex strength will be considered:

- Influence of lift distribution
- Destabilizing vortex cores
- Breakdown of cores
- Splitting vorticity and generating subvortices

#### Effect of lift distribution on maximum circumferential velocity

The amalgamation method permits investigations of the roll-up process for arbitrary lift distributions. Fig. 14 shows the maximum circumferential velocity, related to the free-stream velocity and the lift coefficient, for three circulation distributions: for an elliptical and a parabolic distribution as well as for rectangular planforms of

various aspect ratios. The lift distribution has a considerable influence on the vortex structure. The maximum circumferential velocity differs by a factor of about 4 between the parabolic distribution and the rectangular planform. A smaller reduction of circumferential speed is observed for all distributions if the aspect ratio increases.

Fig. 15 should help to understand the considerable influence of the lift distribution. This diagram presents four different circulation distributions: a rectangular wing case with an aspect ratio of 8, the elliptical, the parabolic lift distribution and a special configuration: an Ogee-type wing tip. The last wing has a circulation distribution which is in-between the elliptical and parabolic case. All distributions provide the same lift. The values of the induced drag of the parabolic distribution and the rectangular cases are almost equal and differ by about 10% from the elliptical case. The plot indicates, that the values of the circulation at midspan (the maximum value) are remarkably different from each other, where the parabolic distribution has the largest value (30% above the rectangular case). It seems surprising that just the distribution with the highest midspan circulation gives the lowest maximum circumferential speed

This effect can be easily understood if it is noticed that the induced drag varies only little among the four cases. An increase of the midspan circulation by a factor  $\omega$  leads to an induced drag proportional to  $\omega^2$  if the core radius would be held constant. Thus, a stretching of the vortex cores is mandatory to compensate for the increased rotational energy in the outer field. Fig. 16 shows quantitatively the large influence of midspan circulation on the maximum circumferential velocity. The 30% higher value of the midspan circulation of a parabolic distribution reduces the maximum circumferential velocity by a factor of about 7 compared to the rectangular planforms. A variation of induced drag is of minor importance on this strong influence, as shown by the plots in the figure.

For proving this large effect, a wing with an Ogee-tip was investigated. The chosen wing configuration is shown in Fig. 17. The tip vortex structure of the Ogee configuration was investigated by LDV measurements of axial and circumferential velocity profiles as shown Fig. 18. The axial velocity reveals a widely spread wake for the Ogee configuration compared to the strong and very concentrated wake of a rectangular planform. As a consequence, the vortex core is considerably larger and the maximum circumferential velocity for the Ogee tip is reduced by an order of magnitude compared to the rectangular reference case.

#### Hydrodynamic instability of vortices

One method of controlling tip vortices might be the stimulation of hydrodynamic instability which could possibly lead to vortex breakdown.

An instability criterion, developed by Leibovich and Stewartson [7], was used for guiding experiments. For assessing vortex stability, the measured circumferential and axial velocity profiles were approximated analytically. For this purpose, the circumferential velocity profiles near the vortex center can be described by the Lamb-Oseen model

$$(7) \quad \frac{V_c(r)}{V_\infty} = \frac{C}{r} \left( 1 - e^{-\lambda r^2} \right),$$

while the axial velocity profiles are assumed to be of Gaussian type

$$(8) \quad \frac{V_a(r)}{V_\infty} = 1 - \delta e^{-\mu r^2}$$

By inserting these analytical models in the Leibovich-Stewartson theory, a sufficient condition for vortex instability can be derived, where parameters of the vortex structure are combined to a stability measure  $S$

$$(9) \quad S = \frac{V_{c,max}}{\sigma \cdot |\delta| \cdot V_\infty} < 0.9, \quad \text{with } \sigma = \lambda / \mu.$$

For instability,  $S$  must be less than 0.9. Most important for the following considerations is the fact, that instability is particularly fostered by increasing the axial velocity defect  $\delta$ .

#### Experiments with spoilers

To increase the wake defect, an experiment was carried out in which a small spoiler has been installed near the wing tip at such a position that the additional wake of the spoiler penetrated the center of the trailing vortex. The spoiler was placed on the wing tip in a part where a high concentration of vorticity is to be expected. Its position turned out to be very sensitive for destabilizing the vortex. The final spoiler position is shown in Fig. 19. Results are presented for a rectangular wing planform of aspect ratio  $AR=4$ .

Fig. 20 shows the velocity profiles of the axial and circumferential velocity components for three different downstream positions. The axial velocity profiles change significantly over a short length in streamwise direction. From  $x/s=0.5$  to  $0.6$ , the axial velocity defect increases rapidly, from  $0.1 V_\infty$  to about  $0.5 V_\infty$ , but changes only slightly over the following distance, between  $0.6$  s and  $2$  s. Within the investigated range the circumferential velocity is only slightly reduced.

A flow visualization experiment revealed that the sudden change in the axial velocity coincides with a widening of the core region where the straight vortex center winds up to a helix with a diameter in the order of the vortex core, Fig. 21. Downstream of that position (see arrow), the

flow character does not change any more as the photo illustrates.

Evaluating the stability parameter at a downstream position of  $x/s=0.6$  gives  $S=1.03$ , a value which comes close to the stability boundary of 0.9. Further downstream, at  $x/s=2$ , the vortex is considered as slightly unstable, corresponding to  $S=0.84$ . Thus, it can be concluded that the change in the flow behavior, observed in the photo, is caused by a destabilizing mechanism induced by the additional wake of the spoiler. Even though  $S$  falls a little below the stability boundary, vortex breakdown does not appear.

A comparison of the time-averaged velocity profiles at  $x/s=2$ , with and without a spoiler, is given in Fig. 22. Beside the large difference in the axial velocity — the defect grows up from about 0 to about  $0.5 \cdot V_\infty$ , also the core radius and the maximum circumferential velocities differ. But, the most interesting maximum circumferential velocity is only slightly reduced, by about 20%.

#### Breakdown of cores

Yet another configuration was investigated which directly stimulates breakdown.

As is well known from delta-wings at high angle of attack, leading edge vortices can breakdown very closely behind or even above the wing. In general, this type of vortex breakdown is combined with a drastic change of the flow pattern. Now, the question arose whether it is possible to stimulate also tip vortices of more conventional wing planforms to breakdown. For this purpose, a specially shaped wing with a half-delta tip was designed and investigated in the water tunnel.

Top and front views of the half-delta configuration are shown in Fig. 23, in addition to a reference wing tip. In both cases the wing has a rectangular planform of aspect ratio  $AR=5$  with a Clark-Y airfoil. The half-delta is a sharp edged plate which extends the flat lower side of the wing profile. In addition, a reference configuration with the same span width was tested. In this case, the airfoil of the inner wing is continued to the tip and tapered with the same chord distribution as the half-delta; leading and trailing edges are equally swept rearward and forward by the same angle.

It was found, that the chosen half-delta configuration generates a leading edge vortex as a regular delta wing does. But, at the same angle of attack, the leading edge vortex is stronger at the half-delta and breaks down earlier than leading edge vortices of delta wings because lift coefficient and circulation are larger at a given angle of attack. Fig. 24 indicates, that, at an angle of attack of  $\alpha=13$  degree, a concentrated leading edge vortex breaks down at approximately the half chord position. Corresponding velocity profiles are given in the Fig. 25.

At the half-delta configuration, core radius and velocity profiles are remarkably different from the reference case.

The reference wing generates an axial velocity profile with a narrow and deep defect revealing a small core radius. For the half-delta, the core radius grows by a factor of almost three while the maximum circumferential velocity is reduced by about 35%, related to the reference case. Since the angle of attack was kept constant in this experiment, the reduction of the maximum circumferential velocity would amount to about 45% at equal lift.

#### Stator located in a tip vortex

The last example for alleviating trailing vortex strength is addressed to the splitting of the concentrated tip vortex into several subvortices. For this purpose a stator was investigated which was located in the tip vortex center behind the wing. The stator consisted of four blades.

The redistribution of wing vorticity by a stator may be described as follows. The vorticity in the wing wake is assumed to be highly concentrated so that the inflow to the stator has a strong rotational component. If the stator, with hub and blades, is properly designed for working in a rotational flow field, vorticity is transferred from the wing tip vortex to the blade tip vortices, as visualized in Fig. 26. The strength of these vortices depends on the blade design and the number of blades.

Results of this effect, obtained by LDV measurements, are shown in Fig. 27. Here, the flow fields behind the clean configuration and downstream of a four-bladed stator with a radius of 40% of wing chord are compared. In the latter case, axial and circumferential velocity components were measured along two different lines. The largest values of maximum circumferential velocity are obtained along a line which cuts two of the blade tip vortices (marked as 0 degree) while a smoothed profile is measured along the 45-degree line. In the clean configuration, the maximum circumferential velocity is about five times as high as it is downstream of the stator. The scattering of the measurements of the axial velocity indicates that the level of turbulence is raised by the presence of the stator which may, in addition, lead to a faster ageing process.

In addition to the velocity profiles, forces and pitching momentum were measured in the water tunnel, using a five-component strain gage balance, to investigate the performance of different configurations. For the configuration described above, the total drag is reduced by about 7% at the same lift. In principle, a stator in a vortex field redistribute the vorticity concentrated in the tip vortices. Behind a wing tip, the flow can be deviated in such a way that some of the rotational energy of the tip-vortex is recovered. The change in flow direction leads to a reaction force on the blades which can reduce the resultant induced drag. A simple model illustrates this effect where it is assumed that the vorticity, concentrated in the wing tip vortex, is transferred to the tip vortices of stator blades and spread over a cylindrical ring with the radius of the blades - as would be the case for a large number of stator blades. Then, the induced drag can easily

be calculated using the Kirchhoff-Routh function. The result of this calculation is summarized in Fig. 28 showing a considerable reduction of the induced drag with increasing values of the ring radius  $a$ .

For radii of the blades of 10% of the half-span, about 20% of induced drag can be saved as a benefit offered in addition to the mainly intended considerable reduction of maximum circumferential velocity.

## CONCLUSIONS

Experiments which investigated the roll-up process of a vortex sheet behind lifting surfaces of rectangular planform provided the results that

- the core radius grows,
- the maximum circumferential velocity decreases even though the circulation in the vortex grows,
- the axial velocity at the center of the vortex is considerably reduced.

These characteristics were reproduced by a computational method for the time-dependent roll-up process, developed as a design tool, which is based on the Biot-Savart approach with a particular technique of amalgamation. The results agree well with LDV measurements performed in a water tunnel.

The theoretical results, presented in the second part of the paper, showed a large influence of the lift distribution on maximum circumferential velocity. The special devices for vortex wake alleviation, even if not optimized, provided a remarkable reduction of the maximum circumferential velocity. As particularly promising, a stator configuration was found which not only reduces the vortex strength considerably but also leads to a decrease in the total drag of the wing-stator combination.

## ACKNOWLEDGMENT

The research was supported by the "Deutsche Forschungsgemeinschaft (DFG)" within the frame of the Sonderforschungsbereich 25 (SFB 25) which is directed to research on Vortex Flow in Aeronautics. The authors are grateful to Dr.-Ing. D. Coors for valuable discussions and to Dipl.-Ing. S. Fell who was helpful at performing some numerical calculations.

## LITERATURE

- [1] Spreiter, J.R. and Sacks, A.H.: The rolling up of the trailing vortex sheet and its effect on the downwash behind wings, *J. Aeron. Sci.* 18, 1951, pp. 21-32
- [2] Sarpkaya, T.: Computational Methods with Vortices - The 1988 Freeman Scholar Lecture, *Journ. of Fluids Engineering*, Vol. 111, March 1989, pp. 5-52

[3] Kochin, N.E., Kibel I.A. and Roze, N.V.: *Theoretical Hydrodynamics*, Interscience Publisher 1964, pp. 198-202

[4] Staufenberg, R.: Ein Modell zur analytischen Beschreibung von Randwirbeln, *Z. Flugwiss. u. Weltraumforsch.*, (ZFW), 1985, Nr. 9, Heft 5

[5] Staufenberg, R.: Structure of Lift-Generated Rolled-up Vortices, *Journal of Aircraft*, Vol. 21, 1984, pp. 737-744

[6] Staufenberg, R. and Scherer, Th.: Ein modifiziertes Punktwirbelverfahren zur Beschreibung des Aufrollvorgangs bei Randwirbeln, submitted to *Z. Flugwiss. u. Weltraumforsch. (ZFW)*, 1989.

[7] Leibovich, S. and Stewardson, K.: A Sufficient Condition for the Instability of Columnar Vortices, *J. Fluid Mechanics*, Vol. 126, 1983, pp. 335-356

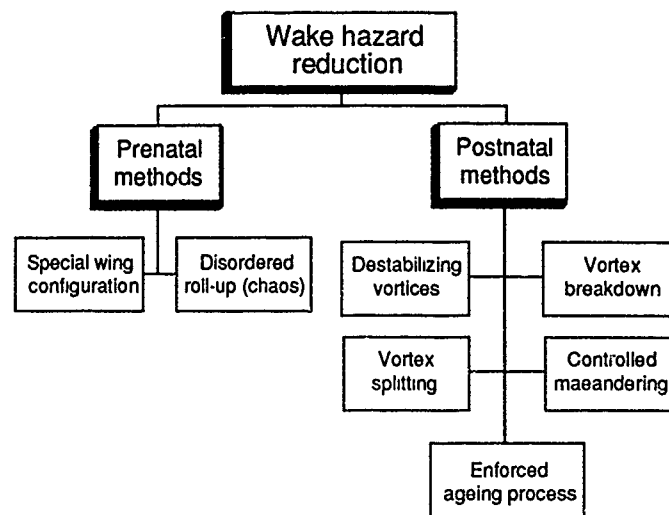


Fig. 1 Methods of wake hazard reduction

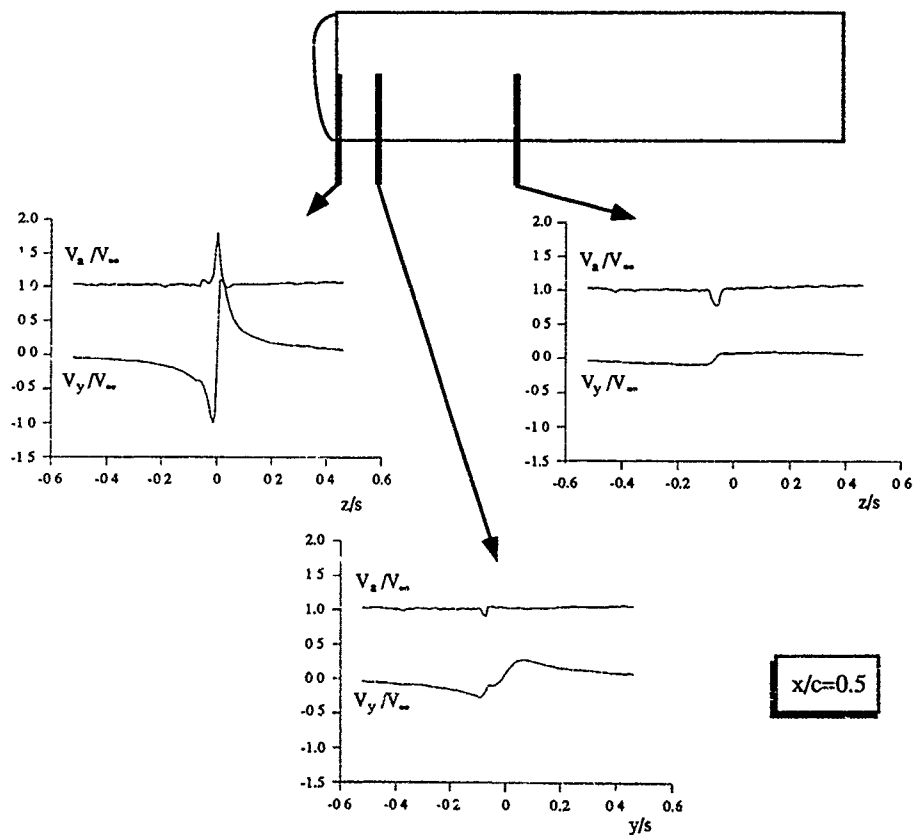


Fig. 2 LDV measurements of the wake behind a wing with rectangular planform



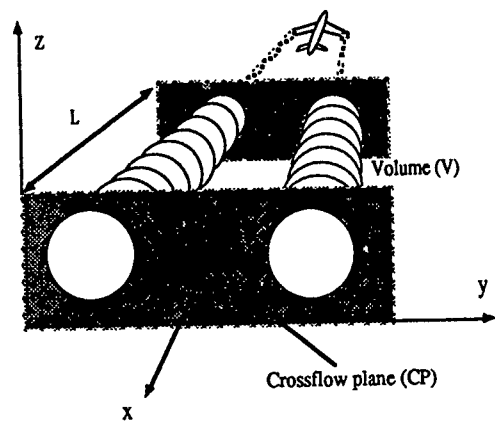


Fig. 3 Coordinate system

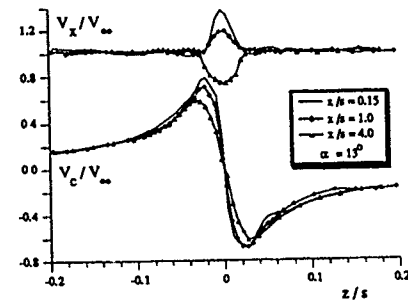


Fig. 4 Axial and circumferential velocity components at three streamwise positions

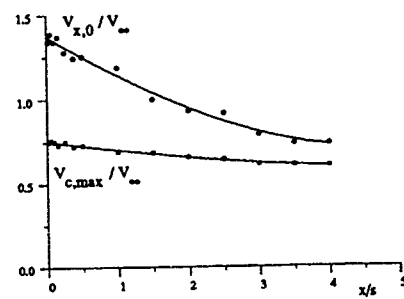


Fig. 5 Maximum circumferential velocity and axial velocity at the vortex center as function of downstream position

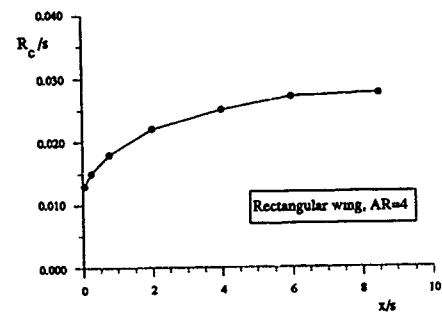


Fig. 6 Core radius as function of downstream position

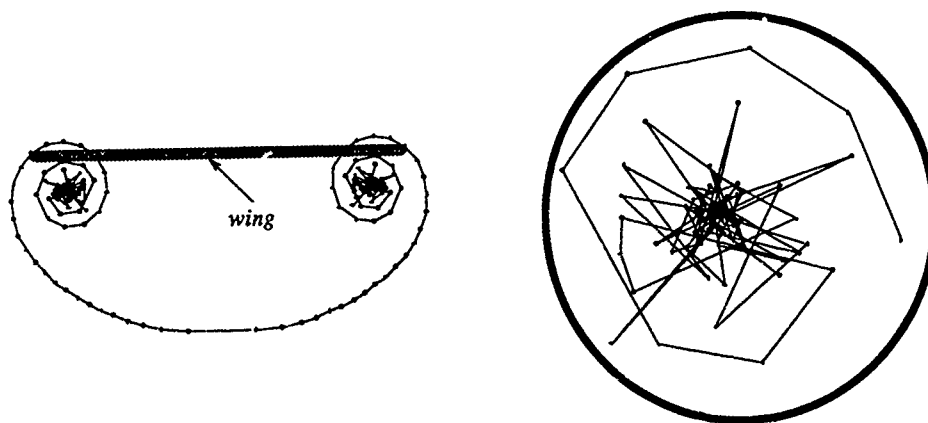


Fig. 7 Point vortex simulation (Biot-Savart)

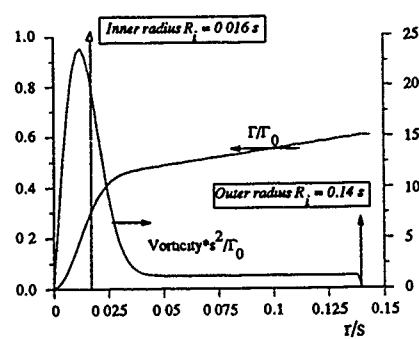


Fig. 8a Circulation and vorticity distribution of the amalgamated vortex

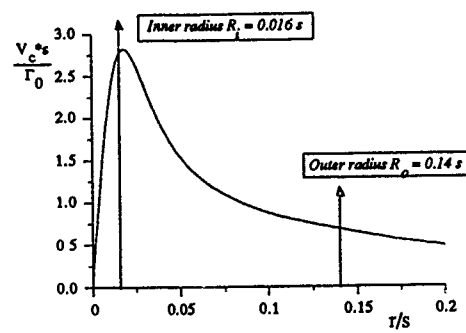


Fig. 8a Circumferential velocity profile of the amalgamated vortex

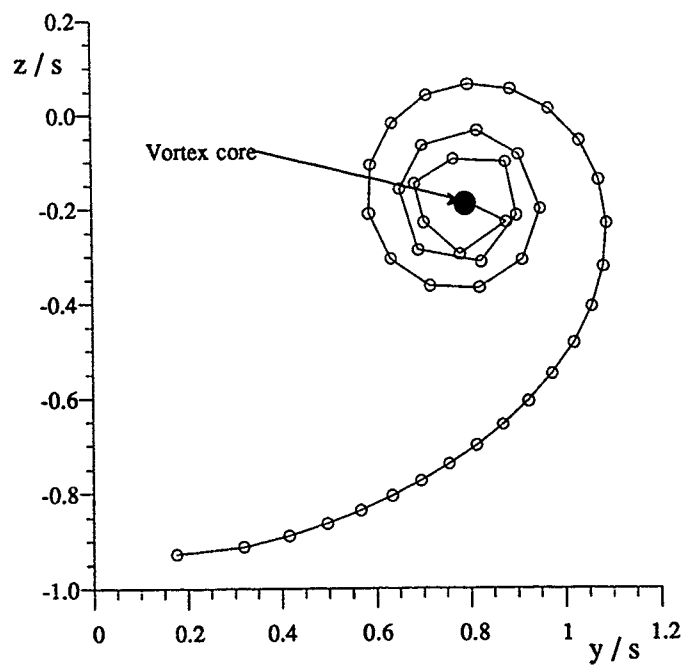


Fig. 9 Simulation results obtained by the modified point vortex method with amalgamation

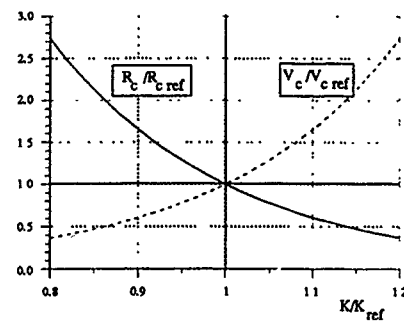


Fig. 10 The dependence of vortex structure on rotational energy (K-R. Function)

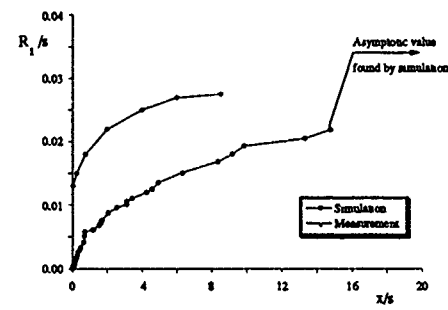


Fig. 11 Comparison of measured core radius with simulation results

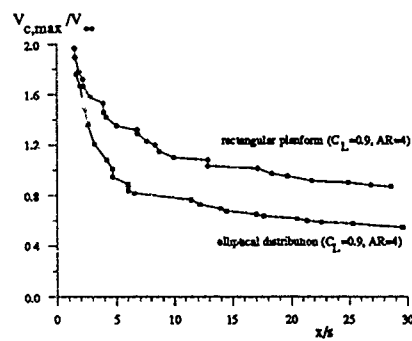


Fig. 12 Maximum circumferential velocities depending on downstream position

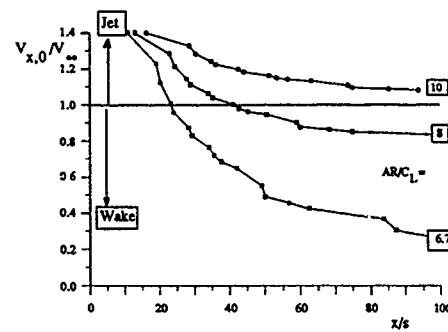


Fig. 13 Axial velocity at the vortex center

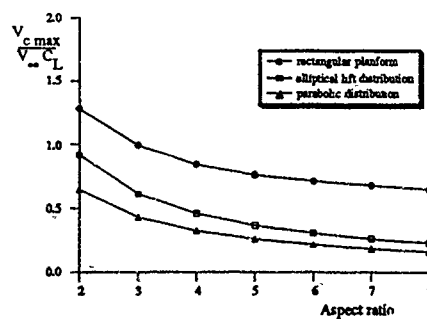


Fig. 14 Effect of lift distribution on maximum circumferential velocity

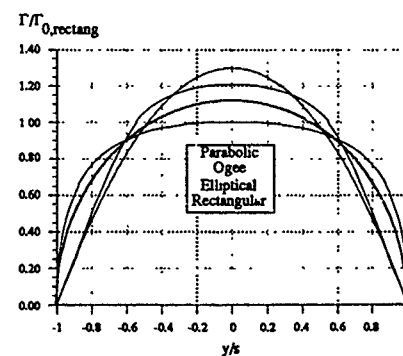


Fig. 15 The investigated lift distributions

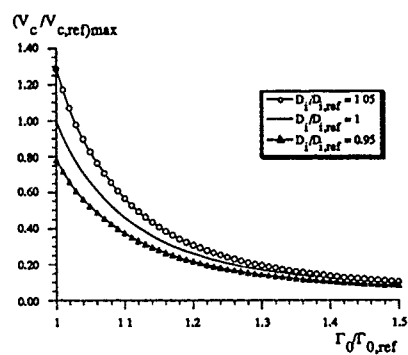


Fig. 16 Influence of midspan circulation on maximum circumferential velocity

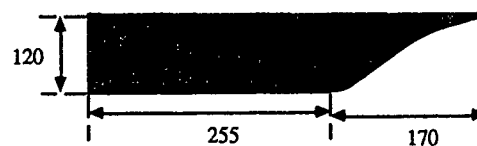


Fig. 17 An Ogee-type wing configuration

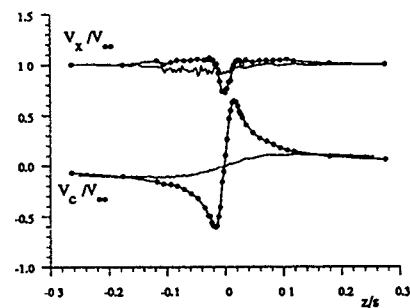


Fig. 18 Measured velocity profiles behind an Ogee-tip configuration

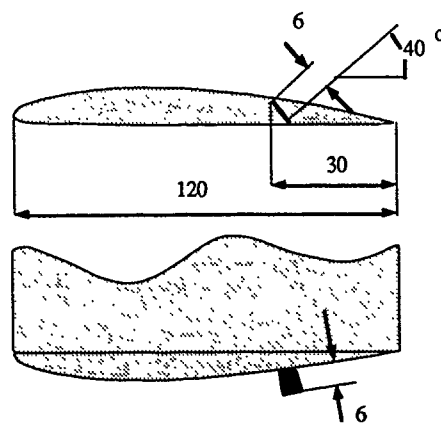


Fig. 19 Configuration with spoiler

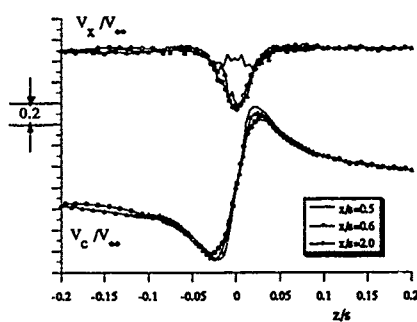


Fig. 20 Velocity profiles behind spoiler configuration

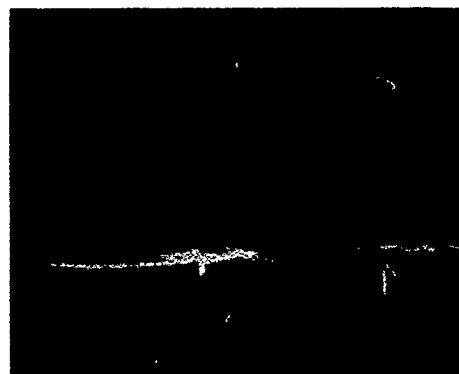


Fig. 21 Flow visualization behind spoiler configuration

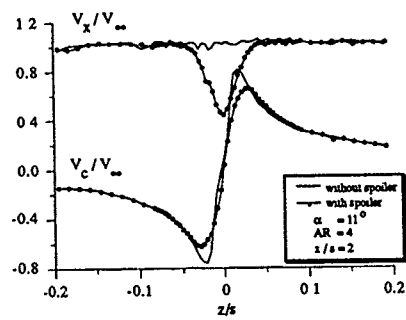


Fig. 22 Comparison of velocity profiles with and without spoiler

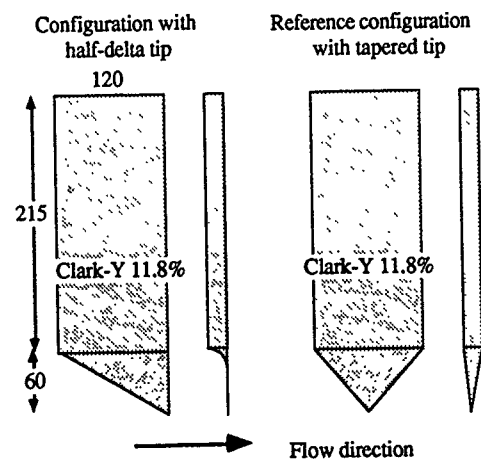


Fig. 23 Configuration with half-delta wing tip

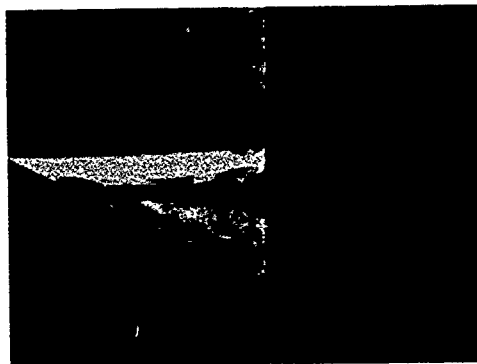


Fig. 24 Visualized flow over and behind half-delta wing tip

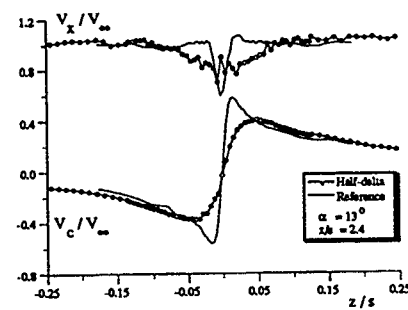


Fig. 25 Velocity profiles behind half-delta configuration

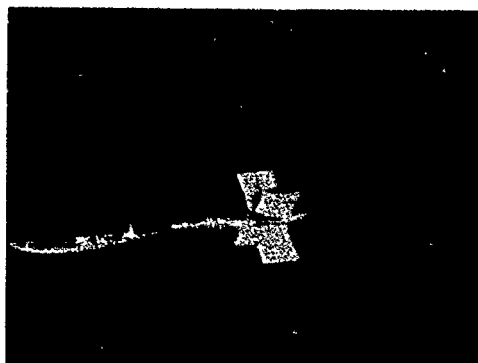


Fig. 26 Stator located in a tip vortex

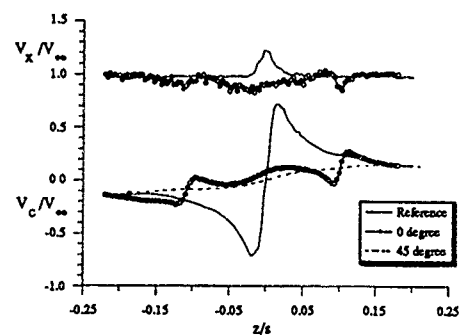


Fig. 27 Effect of stator on velocity profiles

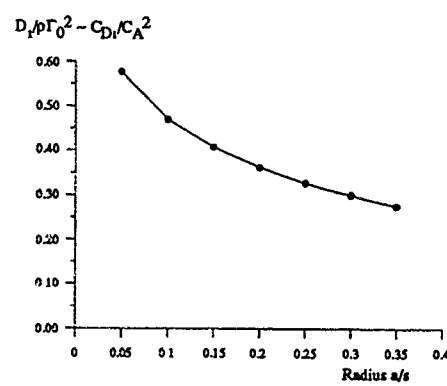


Fig. 28 Reduction of induced drag by spreading vorticity

# CONTROL OF FOREBODY VORTICES BY SUCTION AT THE NOSE OF THE RAE HIGH INCIDENCE RESEARCH MODEL

by

A. Jean Ross  
E. B. Jefferies  
Geraldine F. Edwards

Aerodynamics Department  
Royal Aerospace Establishment  
Farnborough, Hampshire GU14 6TD, United Kingdom

## SUMMARY

The concept of applying suction at the nose of forebodies at high angle of attack to control the vortex flow has been applied in static and dynamic wind-tunnel tests on the RAE High Incidence Research Model. The first series of static tests showed that sideforce and yawing moment varied near-linearly with flow rate (or mass flow) coefficient, rather than momentum coefficient, up to a maximum, but the maximum control powers available were small on the original drooped forebody. The results for suction on a large ogival forebody give yawing moment equivalent to about 25° of rudder at an angle of attack of 30°, and significantly higher for higher angles. They also show some dependence on whether separation is laminar or turbulent, and parameters defining the variation with flow rates are compared. Dynamic experiments on a free-to-yaw rig, with active control of flow rates, were inconclusive and further experiments are being conducted.

## 1 INTRODUCTION

It is well known that the vortices shed by the forebody of an aircraft tend to become asymmetric at high angles of attack, even at zero sideslip angle, causing large sideforce and yawing moment (see the summary in Ref 1). Relative to their symmetric positions, one of the vortices moves away from the surface, and the other moves closer, but which of the two moves in a given direction appears to be arbitrary. Thus the sign of the sideforce is also arbitrary, and may change as angle of attack is increased. However, for a given configuration at particular angle of attack, the magnitude of the sideforce is bounded<sup>2</sup>. Such asymmetries in the sideforce, yawing and possibly rolling moments cause aircraft to depart from symmetric flight conditions, and may lead to departure from controlled flight.

Several experiments<sup>2,3</sup> have been conducted using small jets of air very close to the nose to control the positions of the vortices, but most experiments reported have been static tests in wind tunnels. Heydan<sup>4</sup> showed that it is possible to control a simple missile configuration mounted on a free-to-yaw rig by applying suction differentially at the port and starboard holes, the amount of suction being actively controlled using the angle of sideslip as feedback.

The investigations reported here are the first stages of a continuing research programme to investigate the possibility of controlling an aircraft at high angle of attack using suction to influence the asymmetric development of the nose vortices. Section 2 describes the models used, whilst sections 3 and 4 cover respectively the static and dynamic wind-tunnel tests. The conclusions of these tests and plans for further work are discussed in section 5. Each of these aspects of the research programme is also summarised briefly below.

A lightweight model of the RAE High Incidence Research Model (HIRM1) had been made for experiments on the Whirling Arm at Cranfield Institute of Technology, and was modified to have a sharp nose with two suction holes. It was also possible to fit a suction control system inside the fuselage, and to make provision for mounting the model on the free-to-yaw rig.

Definitive static tests using a conventional sting and strain-gauge balance in the 13 × 9 ft wind tunnel at RAE Bedford were conducted first, to give data on forces and moments over ranges of angles of attack and sideslip, for varying suction rates. The investigation by Heydan<sup>4</sup> appeared to show that the effectiveness depended on momentum of the flow through the holes, so the sharp nose was made with smaller diameter holes than the original nose tip used on the missile. However, the results from the first series of static tests showed that effectiveness depends on mass flow (or flow rate), and the suction levels needed to achieve the required mass flow through the smaller holes were too high to be practicable.

The static tests were repeated, with the holes enlarged and with flow meters to measure flow rates directly. Results at nominal angles of attack near 30° and 33° are as expected, with sideforce, yawing and rolling moments varying near-linearly with mass flow up to a maximum effect, beyond which increasing mass flow does not change the force or moments. At angles of attack above about 35°, the variation with mass flow is not so definitive, possibly due to the induced effects of the vortices on the canard/wing/tail/fin. Flow visualisation using a laser light sheet with smoke showed the movement of the vortices as flow rates were varied.

The results for yawing moment at  $\alpha = 30^\circ$  were used to design control laws for controlling the model on the free-to-yaw rig. A ventral fin had to be added to the model, to improve directional stability at high angles of attack. It was just possible to hold the model at a demanded small or zero angle of sideslip, but it was very unsteady on the rig, with large amplitude oscillations in both pitch and yaw.

Several longer forebodies, without droop, have been tested, in order to obtain greater control powers from the stronger vortices for angles of attack near 30°. A selection of the results for the largest of these forebodies is described, in particular to show the increased magnitudes of sideforce and yawing moment due to flow rate, and the effects of transition on the forebody.

## 2 DESCRIPTION OF MODEL AND TEST CONDITIONS

The lightweight Model 2206 is a 4/9-scale version of the free-flight model known as HIRM1 (High Incidence Research Model), and has canard and tailplane surfaces which can be set to various angles. The original model had

the long nose probe as used in the free-flight tests<sup>5</sup>, but for the work reported here this was replaced initially by a sharp nose on the drooped forebody\*, and later by the same sharp nose on a longer undrooped ogival forebody. Both configurations are shown in Fig 1, and the geometric details of the model are given in Table 1. The sting mounting in the 13 x 9 tunnel was compatible with the model, so a strain gauge balance could be used for the static tests. It was also possible to provide a mounting from underneath the fuselage at the reference centerline, so that the model could be tested on the free-flight rig for the dynamic tests.

The sharp nose, of 27° included angle, has two holes about 4 mm back from the apex, situated circumferentially at 30° down from the top, which had been found<sup>2</sup> to be the optimum position for affecting the forebody vortices by blowing. An enlarged sketch of the nose tip is shown on Fig 2, together with the systems for applying the suction. Each hole is connected to a plenum chamber, in which the suction levels are controlled to give varying flow rates through the holes. For the static wind-tunnel tests, the constant suction levels were applied using suction equipment outside the working section, and were monitored with flow meters and/or pressure gauges. For the dynamic experiments, the flow rates through the two holes were controlled by needle valves housed in the fuselage (see Fig 2), the positions of the needle valves being changed according to the chosen control laws. The varying pressures were recorded, but it was not possible to obtain continuous records of flow rates from the flow meters.

The original nose used by Heydari had holes of nominal diameter of 1 mm, but it had been suggested that smaller holes might be beneficial, so the new nose made for Model 2206 had holes of 0.5 mm. These holes did not give sufficient flow through, since high suction levels, up to 6 psi instead of 1 psi, had to be used to change the sideforce from one extreme to the other. The original nose was re-fitted to Model 2206 for part of the first series of tests, and the new nose was modified to have holes of 0.75 mm diameter, the maximum diameter possible for this nose design, for later tests. The nose cones also fit on to the ogival forebody, which was designed to blend with the lines of the original fuselage near the cockpit apex.

A laser light sheet was used to visualise the vortices as part of the static experiments, with smoke introduced upstream of the model at about the height of the nose. Video records were taken of the positions and movement of the forebody vortices as flow rates were varied<sup>7</sup>. Oil flows were also photographed, most attention being paid to the separation and re-attachment lines on the forebody<sup>8</sup>.

Tests have been made with control settings to give zero pitching moment near  $\alpha = 30^\circ$ , the canard either zero or  $-10^\circ$ , and tailplane  $-20^\circ$ . Tunnel speed had to be restricted to 33 m/s with  $\alpha < 37^\circ$ , and to 20 m/s for higher angles of attack, because of model strength considerations. Comparisons made by Ormerod<sup>6</sup> with results obtained at higher speeds (40 m/s and 70 m/s) on Model 2130, of identical geometry and size, showed some small changes in lift and pitching moment at wing stall, but these had to be

accepted as it is necessary to use the lightweight model on the free-flight yaw rig.

### 3 STATIC WIND TUNNEL TESTS

#### 3.1 Initial results for drooped forebody

The variations of the control powers available in sideforce and yawing moment due to suction on either port or starboard side are shown in Fig 3, for  $\alpha = 30.9^\circ$ . The asymmetry in the vortex flow at zero section is indicated by the non-zero values of  $C_y$  and  $C_n$ , for this test series being negative. Suction on the starboard side causes a positive increment, and zero values of  $C_y$  and  $C_n$  are reached at the highest suction applied. Suction on the port side (shown on the left-hand side of the graphs with suction increasing in the negative direction), causes a negative increment, and a limit appears to be reached at the highest suction levels. However, the control powers do vary smoothly as suction changes, and are approximately additive, as shown by the results for constant suction on one side and varying suction on the other. These results are typical for angles of attack up to about  $36^\circ$ , and the maximum control powers available increase with angle of attack in this range.

The variation of sideforce (or yawing moment) with suction is presented in Fig 3 in terms of flow rate (or mass flow), although the previous results on the missile configuration had been presented in terms of momentum coefficient<sup>4</sup>, following the usage for experiments with blowing. The two coefficients are defined as

$$C_Q = \frac{m}{\rho V S_{REF}} = \frac{(\text{flow rate})}{V S_{REF}} \text{ assuming incompressible flow} \quad (1)$$

$$C_\mu = \frac{m U_H}{\frac{1}{2} \rho V^2 S_{REF}}, \text{ where} \quad (2)$$

$$m = \text{mass flow} = \rho U_H A_H = \rho U_H A_H \quad (3)$$

$$A_H = \text{area of hole}$$

$$U_H = \text{velocity of air through hole}$$

$$S_{REF} = \text{wing area } (0.4073 \text{ m}^2)^{**}.$$

It may be shown<sup>7</sup> that the assumption of incompressible flow is acceptable for the low levels of suction applied, less than 1 psi, the maximum value of  $U_H$  being less than 100 m/s.

It was found that the results measured for the two noses with different hole sizes did not collapse using  $C_\mu$  as parameter, as shown in Fig 4a. The sideforce measured at  $\alpha = 35^\circ$ , with suction applied through the nose with 0.5 mm diameter holes at two tunnel speeds, are plotted with the corresponding results for suction applied through the original nose (used on the missile model<sup>4</sup>) with larger holes. Different levels of asymmetry were present at zero suction for these three tests, and analysis of later results<sup>8</sup> (described in section 3.2) showed that comparisons should

\* The 'nose' is defined here as the nose tip shown in Fig 1, which is the same external geometry for all tests, and the 'forebody' is the fuselage between the nose tip and the cockpit.

\*\* Wing area has been used for this report, but recent tests in the RAE 5m tunnel on the free-flight model indicate that  $S_{REF}$  should refer to hole geometry in some manner.



be made by considering incremental suction relative to that for symmetric flow (ie zero sideforce and yawing moment). The data are thus plotted against  $\Delta C_{\mu}$ , although a similar result<sup>7</sup> is obtained if  $\Delta C_Y$  versus  $C_{\mu}$  is used, taking the incremental sideforce from that at zero suction. The change in sideforce with momentum coefficient is much smaller for the nose with smaller holes, compared with results for the nose with larger holes. The maximum effect had not been reached at  $V = 20$  m/s for suction on the starboard side. A few results at  $V = 34$  m/s gave consistent results. In contrast, tests with the original nose at  $V = 34$  m/s showed that the maximum effects on  $C_Y$  could be achieved with suction through port or starboard holes, and the initial variation of  $C_Y$  with  $C_{\mu}$  is much steeper.

The alternative parameter, flow rate (or mass flow) is more acceptable from a physical point of view, since suction should be represented by a sink. This does not introduce a region of flow in the mainstream with different total pressure, in contrast to jets blown in the stream. The two holes in the original nose were found to be of slightly different diameters, so that same suction level gives different flow rates. The slopes of  $C_Y$  with  $\Delta C_Q$  are the same for the port and starboard holes on both noses, and for the two speeds, as shown in Fig 4b. The collapse of the results on to a mean line is remarkably good, as the model was unsteady on the sting, leading to scattered data. Repeat readings were taken, to indicate the magnitude of the unsteadiness, and these are shown in Fig 4 for one of the tests at  $V = 20$  m/s.

### 3.2 Control powers with the large forebody

The tests with the original forebody (without nose probe) showed that the sideforce and yawing moments generated by suction through one of the holes near the apex were near their maximum values with flow rate coefficients of  $C_Q = 2.5 \times 10^{-6}$ . The results for these flow rates applied to the original and large forebodies are shown in Fig 5. It may be seen that significant control powers are present for  $\alpha > 25^\circ$  for the large forebody, and that there is a factor of about 10 between maximum powers for the two different forebodies at  $\alpha = 30^\circ$ . The results for flow rates through port and starboard holes are also symmetric for the large forebody, indicating that the vortex flows from the forebody are mirror-images of each other for large equal flow rates through port or starboard holes, despite the random asymmetry at zero flow rates.

The yawing moment due to  $10^\circ$  of rudder is also shown in Fig 5; the rudder is still effective at  $\alpha = 30^\circ$ , and the small control power available with the original forebody is obvious. However, the maximum yawing moment on the large ogival forebody is equivalent to about  $25^\circ$  of rudder at  $\alpha = 30^\circ$ , and at higher angles of attack the rudder loses effectiveness while suction at the nose causes increasing yawing moment, up to the highest angle of attack tested,  $41^\circ$ .

The variations of sideforce, yawing, rolling and pitching moments with varying flow rates are shown in Fig 6a-d, for angles of attack between  $25^\circ$  and  $37^\circ$ . Results for flow rates through the port holes are shown on the left of each graph, increasing flow rate being plotted in the negative direction, with conventional increasing flow rate through the starboard hole shown on the right.

The shape of the variations of  $C_Y$  and  $C_n$  with  $C_{QP}$  and  $C_{QS}$  (Fig 6a&b) are similar to those obtained with the original forebody, but the maximum positive and negative values are almost symmetric, even though sideforce and yawing moments are not zero at zero flow rate. The results were analysed to see if a suitable approximate formula could represent the variation adequately, based on empirical data. It was found that the same form could be chosen for  $C_Y$  and  $C_n$  for variation between the maximum positive and negative levels, ie

$$\frac{C_Y}{C_{YL}} = \gamma(3 - 2|\gamma|^{1/2}) \quad (4)$$

where  $\gamma = (Q - Q_0)/Q_L$ , and  $Q$  is flow rate,  $Q_0$  is the value at which  $C_Y$  is zero,  $[Q_L + Q_0]$  and  $[-Q_L + Q_0]$  are the values at which the maximum  $\pm C_{YL}$  are attained. For flow rates greater than these, sideforce and yawing moment remain at the maximum positive and negative values for flow rates on starboard and port sides respectively.  $Q$  is here taken to be positive for flow rate through starboard hole, and negative through port hole. The values of  $C_{YL}$ ,  $Q_0$  and  $Q_L$  were chosen to obtain a good fit to the experimental data, by the method described in the Appendix. A corresponding expression for  $C_n$  was used, with different values of  $Q_0$  and  $Q_L$  at given angle of attack. (Note that the coefficient form of flow rate could be used, but it is not necessary to denote this in the equations because only ratios are needed.)

The variation of these parameters with angle of attack is discussed in the section 3.3, where further comparisons are made. The mean curves obtained from these empirical formulae are shown in Fig 6a&b, and are seen to be acceptable representations of the variations with flow rate. It was also found<sup>7</sup> that the formulae could be used using differential flow rate, as indicated by the earlier results shown in Fig 3.

It has not been thought worthwhile to find approximate formulae for rolling and pitching moments, although it may be possible to derive nonlinear forms. The variation of rolling moment with flow rates is shown in Fig 6c, and is seen to be irregular for angle of attack greater than  $31^\circ$ , having a large effect for small flow rates, but then decreasing as flow rate increases further. Such characteristics would be difficult to use in a flight control system. Pitching moments (Fig 6d) are also affected, particularly at the higher angles of attack and small flow rates, but these may possibly be alleviated if the flight control system includes a control law to maintain constant angle of attack.

### 3.3 Effect of transition strips on forebody

During the first series of tests (October 1989) with the large forebody, D G. Mabey suggested that the position of the change from laminar to turbulent separation on the forebody could affect the control powers, although previous work by Mundell<sup>2</sup> using small geometric asymmetry to trip the vortex asymmetry had shown no effect on sideforce and yawing moment due to changing Reynolds number, and tests<sup>7</sup> at the two wind speeds of 20 m/s and 33 m/s on the original forebody had not shown any definite trends. Transition strips of gritted paper were stuck on the forebody at about  $80^\circ$  radial position, ie below the expected laminar separation line, and some measurements were made with the model on the strain-gauge balance and sting. These showed appreciable changes in the maximum magnitude of the control forces, but later experiments (January 1990) with flow visualisation using oil flows showed that the

transition had not been complete. Repeat force measurements were undertaken in January 1990, using longer transition strips on the large forebody, from near the junction of the nose apex and the forebody to the cockpit position, as shown in Fig 7.

Although the same nose cone and same large forebody were used for the two test series, the sign of the asymmetries was reversed, as shown by the results for yawing moment with zero suction in Fig 7. The addition of the transition strips did not change the sign of the basic asymmetry in vortex flow, although there are small changes in the magnitude of  $C_N$ . However, with flow rate coefficients of  $2.5 \times 10^{-6}$ , the results for maximum yawing moments for the two series of tests are similar when transition is free, as shown in Fig 7, any differences between the two sets of results for free transition being much smaller than the difference at zero flow rate.

The results in Fig 7 also show that the transition strips, which cause the separation to be turbulent along the forebody, cause a loss in maximum effects of flow rates, the loss increasing as angle of attack increases, i.e. there is less control power available if the boundary layer is turbulent. However, at angle of attack below the onset of asymmetry with zero suction, which occurs at about  $\alpha = 29^\circ$  (Fig 7), the control powers are nominally unaffected by transition.

Analysis of the results for varying flow rate showed that the same form of variation of  $C_Y$  and  $C_N$  could be used, with different values of the parameters at a given angle of attack. An example is shown in Fig 8a, for yawing moment at  $\alpha = 30.9^\circ$ . The two important parameters are  $C_{N_L}$ , the maximum control power shown in Fig 7, and  $C_{Q_L}$ , the range of effectiveness of flow rate. It was found that fixing transition also reduced this range (see Fig 8b), as well as reducing the maximum control power, but there is a progressive change in yawing moment with flow rates. Also shown on Fig 8b is the pressure difference required to give these levels of flow rate for a full-scale aircraft flying at  $M = 0.3$  at 20K ft assuming that  $S_{REF}$  (Eq.(1)) refers to hole geometry. For values of  $\Delta p < 2$  psi, the internal flow can be assumed to be incompressible, so such flow rates are achievable without choking.

As mentioned above, the maximum yawing moments shown in Fig 7 give the parameter  $C_{N_L}$ , and the value of  $C_{Y_L}$  may also be obtained. These values have been used to derive the moment arm of the maximum asymmetric sideforce. When the position is plotted relative to the model geometry ahead of the centre of moments (shown in Fig 9), it is obvious that forebody effects dominate over those of the fin, with sideforce acting near the front of the cockpit. The effects of transition state are seen to be small, so it is the magnitude of maximum sideforce which is changed by the change from laminar to turbulent separation, rather than its axial location.

### 3.4 Effect of sideslip

Results are available<sup>8</sup> for angles of sideslip between  $-4^\circ$  and  $+4^\circ$ , over the range of angle of attack and flow rates. The values of derivatives for the model with the original forebody were not significantly dependent on flow rates, but the data for the large ogival forebody were very nonlinear. The derivatives, evaluated for  $\beta = \pm 1^\circ$ , showed significant changes for small flow rates, but are not discussed here.

## 4 DYNAMIC TESTS WITH ORIGINAL FOREBODY

For the dynamic tests the model was mounted on a spindle with bearings, so that it was free to yaw about the body axis, and the vertical support was braced with wires, as may be seen in Fig 10. Initial tests were with the model tied to load cells mounted at the side of the tunnel, to check that steady flow rate gave similar effects to previous results from the static tests. For the actual dynamic tests, the wires attaching the model to the load cells were lengthened, to restrain the model to a maximum sideslip angle of  $|\beta| = 3.9^\circ$ . The model could be fixed at angles of attack of  $30^\circ$  and  $35^\circ$  (plus higher angles not investigated), and was found to be rather unsteady in pitch. The directional stability in yaw is unstable for  $\alpha > 22^\circ$ , so a ventral fin was added (a spare canard surface), and tests showed that stability was about neutral at  $\alpha = 30^\circ$ .

The needle valves and actuators were mounted in the model, but the analogue computer with the control laws was outside the tunnel, as were the flow meters indicating the changes in flow rates. (It was not possible to record flow rates, but analogue records were taken of pressures in the nose cavities, and of signals in the analogue computer.) The computer controlled the flow rates to starboard and port holes via the needle valves, changing the rates differentially in response to the angle of sideslip. The aim of the control law was to hold a steady demanded angle of sideslip, usually zero, so a proportional plus integral feedback of the error in sideslip (or yaw) angle was used.

The model was very unsteady in both pitch and yaw at  $\alpha = 35^\circ$ , but some results were achieved with the model at  $30^\circ$  and two examples are discussed here. The mean yaw angle of the model (i.e. sideslip angle) could be changed using the demand system, but the unsteady oscillation was of similar amplitude to the changes which could be made before maximum flow rate was reached, so quantitative measurements of lags or response to varying gains could not be made. The changes in  $\beta$ -demand are indicated on Fig 11 by the number of turns on the potentiometer determining the offset level on the input amplifier.

For the first 50 seconds of the record, shown on the left-hand side of Fig 11a, the model was being held at a positive sideslip angle of about  $2^\circ$  with flow rates just above half that available (Fig 11c), indicated by the positions of the servos controlling the needle valves. Note that the sign of the port servo is opposite to that of the starboard, so that records appear to be parallel rather than mirror images in Fig 11c. The mean value of the error signal is zero (Fig 11a), shown by the dashed line. As the demand is changed to a smaller angle, in the approximate time interval between about 55 seconds and 65 seconds, the needle valves controlling the flow rate move to very near their limiting position (maximum flow rate on starboard and zero on port), while the model moves to a near-zero sideslip angle. However, the error signal is not zero, and a limiting position is reached, but the model does not diverge completely because of limiting imposed in the control laws. The records on the right-hand side show that the model moves back to near its original positive sideslip angle when the demand is changed back again. The amplitude of the oscillatory disturbance appears to be greater when the flow rates are near the limits.

Experiments were made to investigate the effects of changing the relative gains on the proportional and integral terms, and a differential term was also added. There were

differences in the responses, but it was not possible to determine an optimum control law, although the responses shown in Fig 11 are typical of the best achieved.

The model with the large forebody was also tested on the free-to-yaw rig, but the increased control powers available meant that the needle valves were only working over a small part of their range. The model was controlled for short intervals, but a divergent oscillation occurred, of high frequency. Experiments are continuing to investigate whether this instability is due to aerodynamic or servo characteristics.

## 5 CONCLUSIONS

The static tests have shown that the force and moments due to the asymmetry in forebody vortices on HIRM1, at angles of attack greater than 28°, can be affected by suction applied through two small holes very near the nose apex. The effectiveness appears to depend on flow rate, rather than momentum coefficient used for blowing tests, so most results are presented in terms of flow rate coefficient.

The control powers available in sideforce and yawing moment are highly dependent on the forebody length at a given angle of attack, as they depend on the strength of the forebody vortices. Results for suction applied at the nose of the large forebody also showed that the maximum control powers are also dependent on the position of the change from laminar to turbulent separation on the forebody, so future tests will be with transition fixed by strips along the 80° generator. Further series of static and dynamic tests in wind tunnels are being undertaken, with a selection of undrooped forebodies of various fineness ratios.

Dynamic tests with the model mounted on a free-to-yaw rig were not conclusive, due mainly to the unsteadiness of the rig and model in pitch and yaw. A simple proportional + integral control law was derived to minimise the error between actual and demanded sideslip angle, using sideslip angle as feedback, and needle valves to control flow rates to the port and starboard holes individually. It was just possible to maintain the model with the drooped forebody at zero sideslip or at demanded positive sideslip angle, with angle of attack at 30°.

Plans are being made to incorporate the active control of flow rates on a free-flight model of HIRM1, to be tested at RAE Larkhill. The original drooped forebody will be replaced by a longer ogival forebody, probably using one of the nose tips from the wind-tunnel models, and the needle valves can also be used. Suction will be provided by an electric pump. The existing Departure Prevention System will be used to give stabilised flight, but it is unlikely that angles of attack greater than about 33° will be controllable, because the rudder becomes ineffective for  $\alpha > 35^\circ$ .

### Appendix Evaluation of parameters in empirical formula

The parameters defining the maximum control power and the range of control effectiveness are used in the empirical formula for  $C_Y$  and  $C_N$  as functions of flow rate given in Eq.(4) in the main text, *i.e.* for yawing moment,

$$\frac{C_N}{C_{N_L}} = \gamma (3 - 2|\gamma|)^{1/2}, \quad (A-1)$$

where  $\gamma = (Q - Q_0)/Q_L$ . These parameters are shown in Fig 8a, for yawing moment, together with the parameter

$C_{Q_0}$ , which may have a random value depending on the amount of asymmetry in the vortex flow at zero suction in a particular test.

The value of  $C_{N_L}$  is given directly by the experimental data, as shown in Fig 8a, where a mean value is chosen if there is a difference in positive and negative levels. The flow rates at which half the maximum positive and negative  $C_{N_L}$  are obtained may be interpolated from the experimental data, and Eq.(4) gives that

$$C_N = \pm \frac{C_{N_L}}{2} \text{ when } \gamma = \pm 0.25. \quad (A-2)$$

These values of flow rates through port and starboard holes are designated  $-Q_{P1}$  and  $Q_{S1}$  respectively, and are used to give

$$Q_L = 2(Q_{S1} + Q_{P1}) \quad (A-3)$$

$$Q_0 = \frac{Q_{S1} - Q_{P1}}{2}. \quad (A-4)$$

It should be noted that analysis of  $C_Y$  and  $C_N$  at a given angle of attack usually gives different values of  $Q_L$  and  $Q_0$ .

Table 1 Geometric details of Model 2206

Wing	area	S = 0.40731 m <sup>2</sup> (gross)	
	span	b = 1.1572 m	
	chord	c = 0.38575 m (aerodynamic mean)	
	LE sweep	42°	
	TE sweep	14°	
	LE droop	20°	
Forebody		Original	Large
	droop	4°	0°
	length, m	0.42	0.79 (from canard/body junction)
	max dia, m	0.156	0.156
	nose	27°	27° (cone angle)
Canard deflection		-10° or 0°	
Tail deflection		-20°	
Centre of moments		0.125 c (0.84965 m behind original nose apex)	

## REFERENCES

- 1 Fiddes, S.P.; 'Separated flow about cones at incidence - Theory and experiment'. RAE Technical Memorandum Aero 2055 (1985)
- 2 Mundell, A.R.G.; 'Low-speed wind tunnel tests on the use of air jets to control asymmetric forces and moments occurring on aircraft at the high incidences'. RAE Technical Memorandum Aero 1984 (1984)
- 3 Skow, A.M.; 'Forebody vortex blowing - a novel control concept to enhance departure/spin recovery characteristics of fighter and trainer aircraft'. AGARD CP 262, Paper 24 (1979)
- 4 Heydari, F.; 'Active yaw control of a generalised missile body at high angles of attack by means of nose suction'. RAE Technical Memorandum Aero 2140 (1988)

- 5 Ross, A. Jean and Edwards, Geraldine F.; 'Correlation of predicted and free-flight responses near departure conditions of a High Incidence Research Model'. AGARD CP 386, Paper 31 (1985)
- 6 Ormerod, A.O.; Unpublished report. College of Aeronautics, Cranfield Institute of Technology.
- 7 Ross, A. Jean, Jefferies, E.B. and Edwards, Geraldine F.; 'Control of forebody vortices by suction at the nose of RAE High Incidence Research Model: Wind tunnel tests'. RAE Technical Memorandum Aero 2172 (1990)
- 8 Ross, A. Jean, Jefferies, E.B. and Edwards, Geraldine F.; 'RAE High Incidence Research Model with a large forebody'. With an Appendix by D.G. Mabey (to be published)

Copyright ©, Controller HMSO, London, 1990

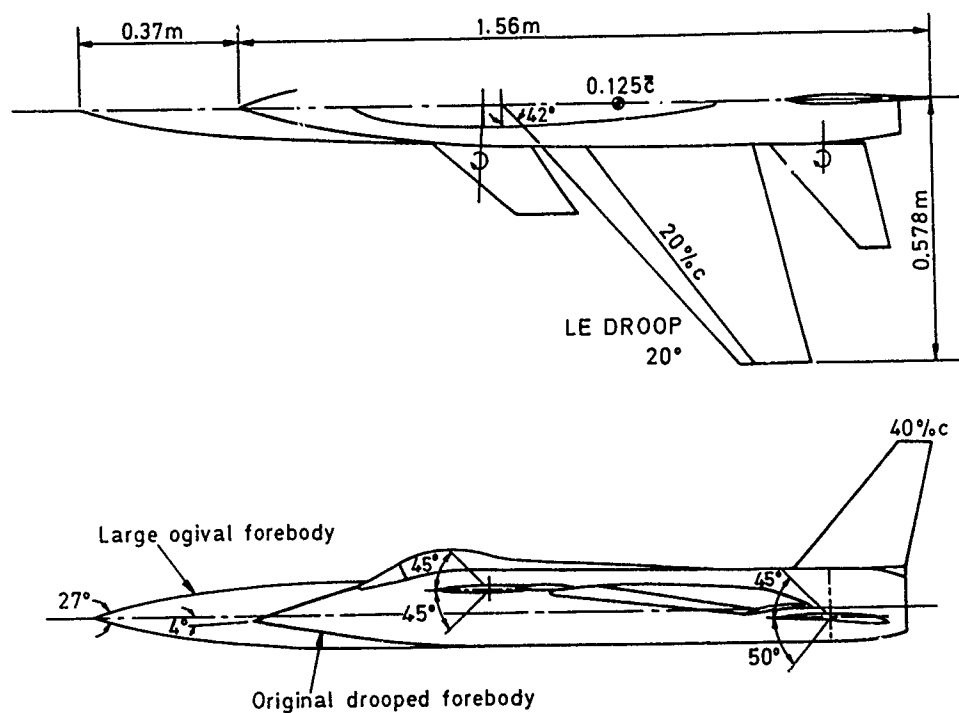


Fig 1 GAs of High Incidence Research Model with alternative forebodies

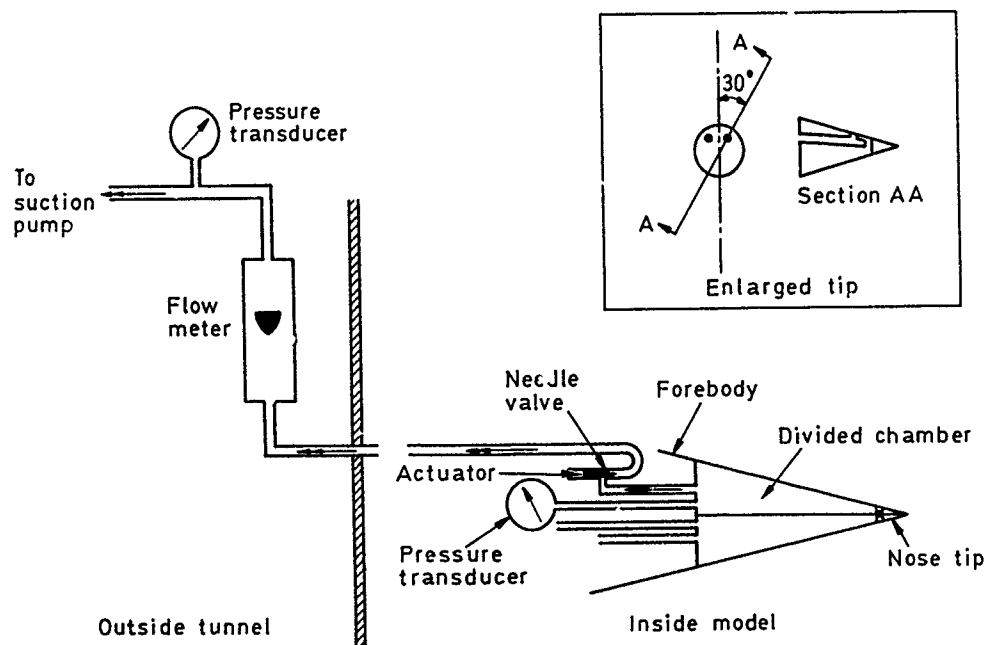


Fig 2 Sketch of suction system (port side only)

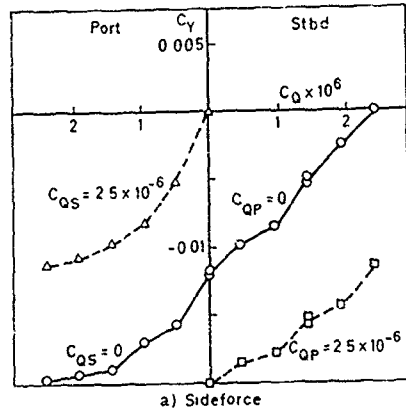


Fig 3 Sideforce and yawing moment due to suction.  
Original forebody,  $\alpha = 30.8^\circ$ ,  $V = 33$  m/s

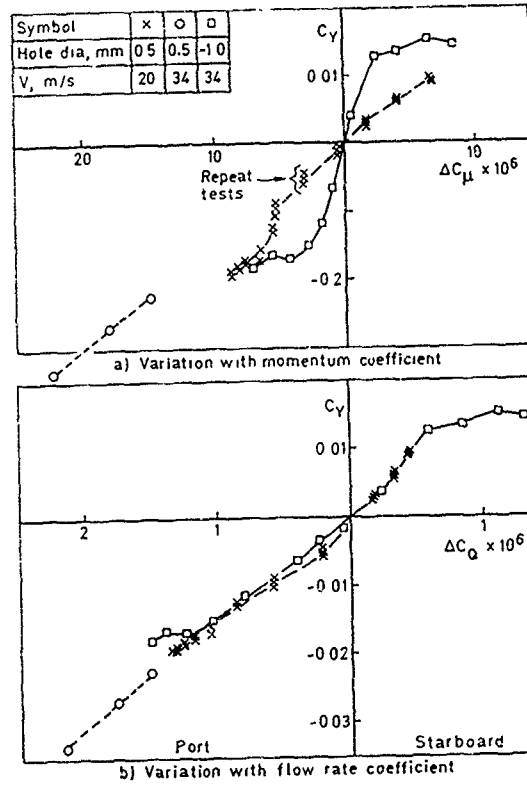


Fig 4 Side force due to suction through different holes.  
Original forebody,  $\alpha = 35^\circ$

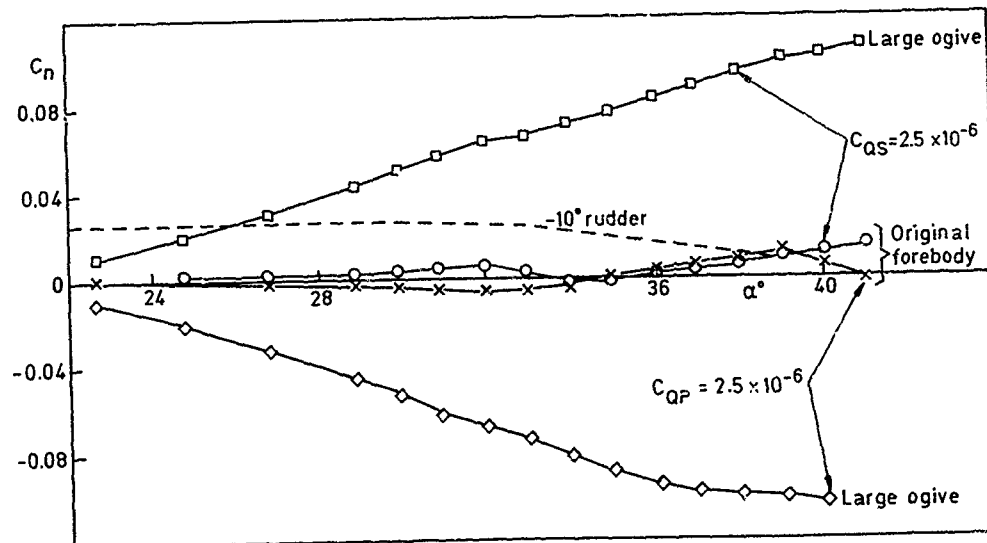


Fig 5 Comparison of yawing moments due to maximum flow rates.  
Original and large ogival forebody

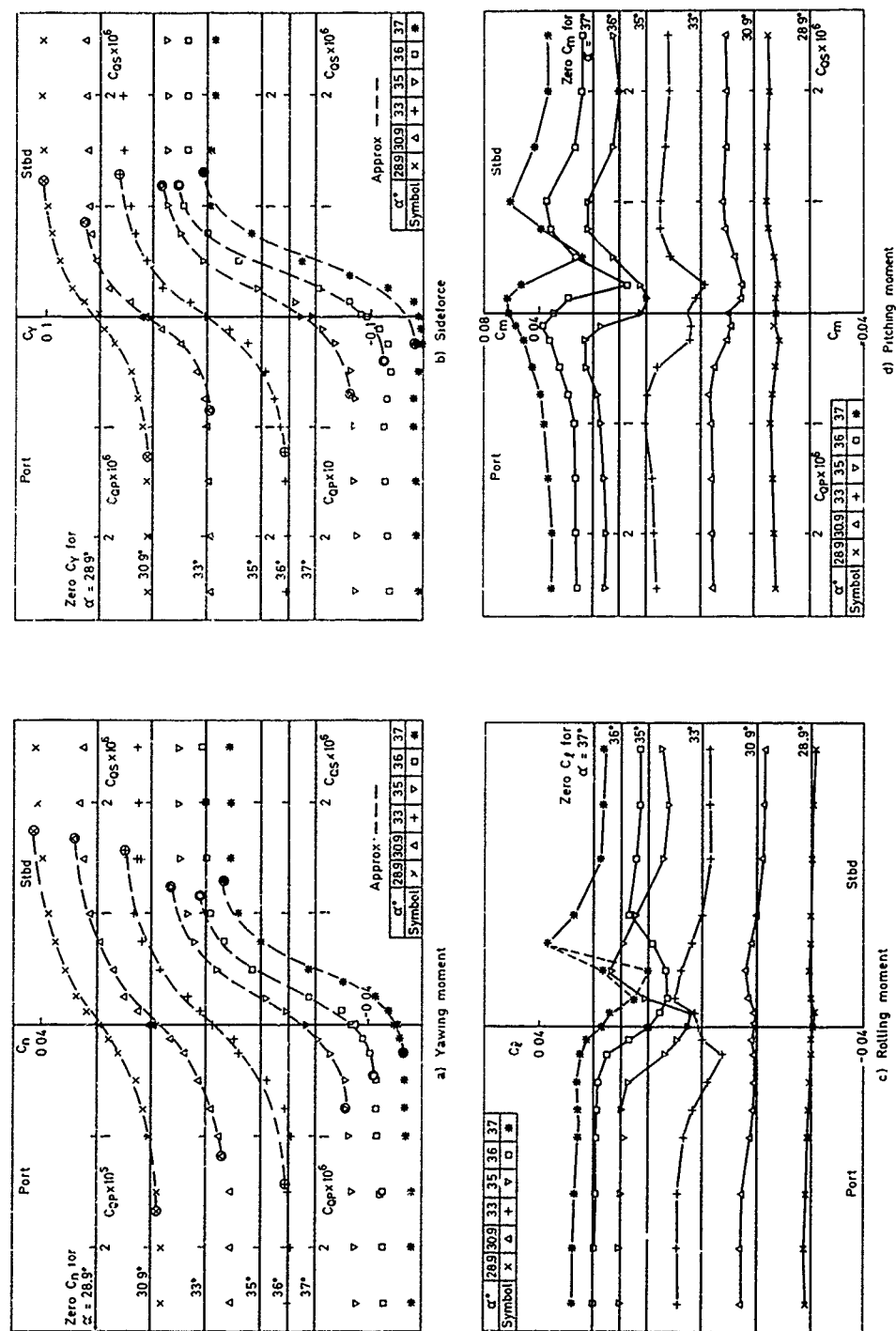


Fig 6 Variation with flow rate, transition fixed

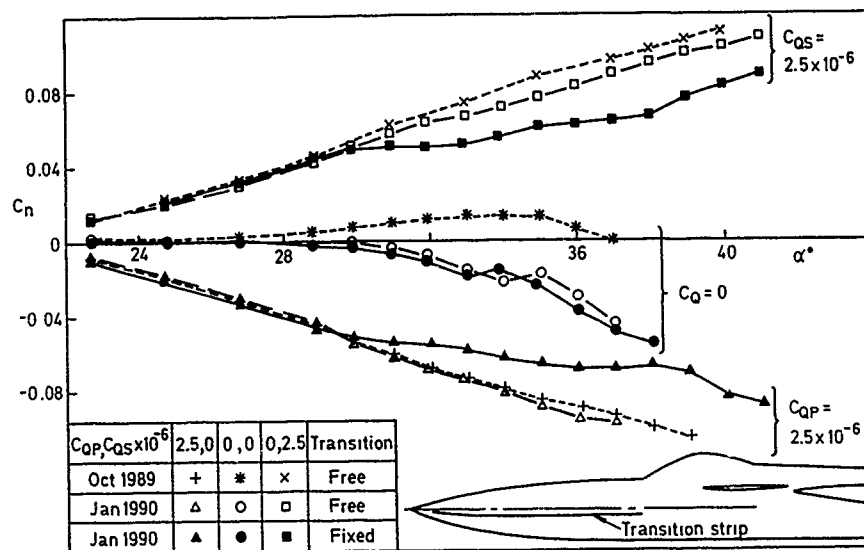
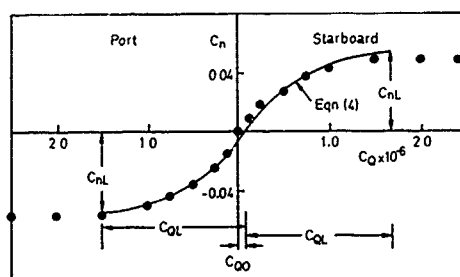


Fig 7 Comparison of yawing moments due to zero and maximum flow rates. Free and fixed transition on large forebody



a) Example of curve fit to control effectiveness  $\alpha = 30.9^\circ$ , transition fixed

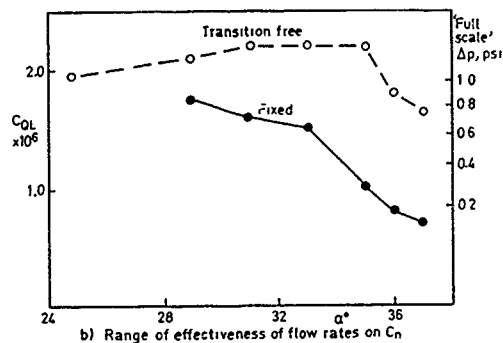


Fig 8 Definition and comparison of range of effective flow rates. Free and fixed transition on large forebody

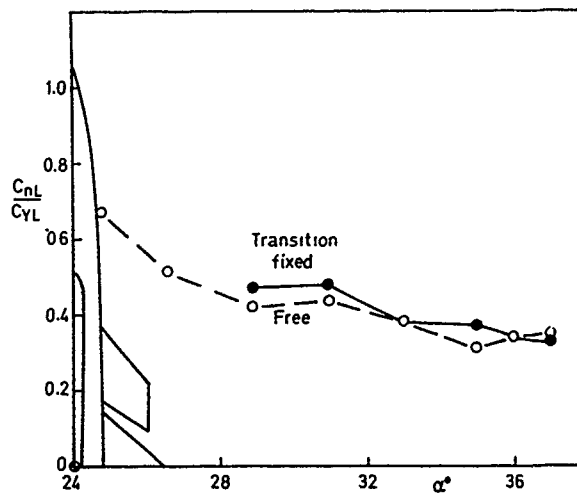


Fig 9 Moment arm of maximum sideforce, large forebody



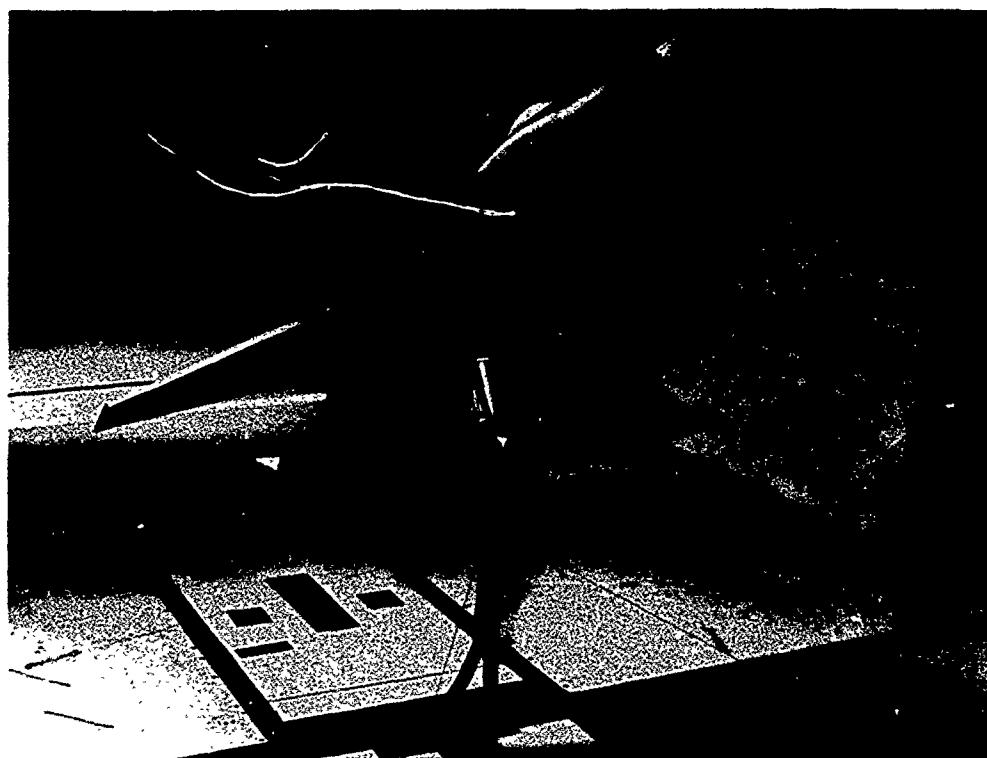


Fig 10 Model on free-to-yaw rig, showing support wires, load cell and ventral fin

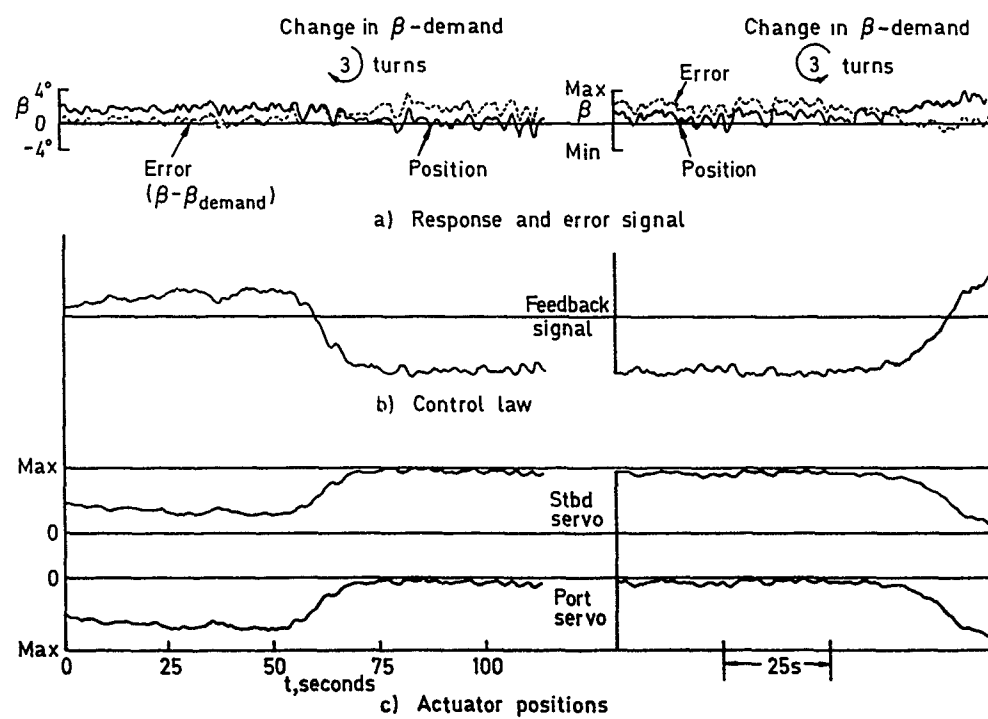


Fig 11 Responses to  $\beta$ -demand, free-to-yaw rig,  $\alpha = 30^\circ$ ,  $V = 33$  m/s

# AN EXPERIMENTAL INVESTIGATION OF VORTEX FLAPS ON A CANARD COMBAT-AIRCRAFT CONFIGURATION

by

D. A. Lovell  
Royal Aerospace Establishment  
Farnborough, Hampshire GU14 6TD, England

## SUMMARY

A low-speed wind-tunnel investigation of two vortex-flap configurations fitted to a canard-delta combat-aircraft research model having a 53° sweep wing is reported. The effect of foreplane interference and vortex-flap geometry on the aerodynamic performance of the vortex flaps is determined. It is concluded that vortex flaps can generate large gains in trimmed lift and lift to drag ratio, particularly when used in conjunction with trailing-edge flaps.

## 1 INTRODUCTION

For an effective combat aircraft, high aerodynamic efficiency needs to be maintained up to high angles of incidence, on configurations for which the wing shape is largely determined by transonic and supersonic performance requirements. Variable-camber leading-edge and trailing-edge devices have commonly been used to provide good sustained-turn performance at moderate values of lift coefficient. At higher angles of incidence, appropriate to instantaneous-turn performance and combat agility, the flow on combat-aircraft wings with round leading edges becomes less ordered, leading to a large increase in drag and a reduction in controllability of the aircraft. Vortex flaps (Fig 1) have been investigated extensively as a potential means of providing a controlled vortex flow at high angles of incidence, and more efficient lift generation. The pioneering work by Rao<sup>1</sup> at NASA Langley, and the subsequent work at Langley reviewed by Rao and Campbell<sup>2</sup>, has shown that a sharp-edged, flat plate, extending from the leading edge of wings with sweeps in the range 60° to 74°, can produce significant gains in lift to drag ratio at moderate to high angles of incidence. This work led to the successful flight test of a fixed, leading-edge vortex flap on an F106 aircraft.

The aim of the research on vortex flaps at Aerodynamics Department, RAE, is to investigate the potential gains in aerodynamic performance from the use of a vortex-control device that could be incorporated as a variable geometry device on the wing of a canard-delta combat aircraft. The cavity-flap arrangement proposed by Rao<sup>3</sup> (Fig 1) has been chosen as being more acceptable structurally than the leading-edge vortex flap. With a cavity flap it is envisaged that by fixing the flap on the wing lower surface (typically at 5% chord aft of the nose) a vortex shed from the sharp leading edge may be contained within the cavity formed between the top surface of the flap and the undersurface of the basic wing leading edge. The cavity flap has been investigated at RAE using a canard-delta research model having a wing of 53° sweep (Fig 2) to determine the effect of a foreplane on the aerodynamic performance of a vortex flap, and whether the device remains effective on wings of lower sweep than those tested at Langley. The combat-aircraft research model has been used previously for extensive investigations of canard configurations<sup>4</sup>. This paper presents results from low speed wind-tunnel tests of two vortex-flap planforms (Fig 3), constant chord and constant percentage chord, covering a range of flap chords and deflection angles. Measurements of longitudinal forces and moments have been made up to an angle of incidence of 47°, for a range of

foreplane deflection angles, and without a foreplane. The effect of deflecting trailing-edge flaps in conjunction with vortex flaps has been examined, and a comparison has been made between the vortex flaps and the conventional leading-edge flaps fitted to the model. These data have been used to assess the trimmed lift and drag performance of the canard configuration for several arrangements of wing high-lift devices.

## 2 DESCRIPTION OF THE MODEL

A general arrangement of the RAE canard research model is shown in Fig 2, and the principal dimensions are given in Table 1. The general characteristics of the model have been investigated<sup>5</sup> for three wing sweep settings (48°, 53° and 58°). The model features a low aspect-ratio wing design<sup>6</sup> having a camber and twist distribution chosen to meet a design point of  $C_L = 0.45$  at  $M = 0.9$ , for the 58° sweep setting. Two alternative camber shapes were incorporated by means of full-span deflection of leading-edge and trailing-edge sections of the wing, to meet manoeuvre conditions at  $M = 0.8$  ( $C_L = 0.6$ ), and  $M = 0.7$  ( $C_L = 0.7$ ). The wing design for the 58° sweep setting has also been tested in an extensive high-incidence research programme, including free-flight and wind-tunnel measurements<sup>7</sup>. The fuselage has a basically rectangular cross-section with rounded corners, an axisymmetric nose and a faired canopy. Fig 3 shows a photograph of the basic model. Two types of planform were tested for the vortex flaps, constant chord and constant percentage chord (ie linearly tapered), and these are sketched in Fig 4. Table 2 lists the range of values of the geometric parameters tested. All the flaps extend over the full wing span, and have streamwise edges. Fig 5 shows a photograph of the model fitted with the constant-chord vortex flaps. Foreplane deflection angles covering a range from 0° to -25°, and wing trailing-edge flap deflections of 5° and 10° were tested. To provide a comparison with a conventional leading-edge device, the basic wing leading-edge flap was drooped to 10°, as shown in Fig 1.

## 3 DESCRIPTION OF TESTS

The tests were made in the 3.5m x 2.6m Low-speed Atmospheric Wind Tunnel at RAE Farnborough, at a wind-speed of 85 m/s. Reynolds number based on aerodynamic mean chord was 2.2 million. A transition-fixing band was attached to the body 60 mm aft of the nose, but transition was allowed to occur naturally on the wings and foreplanes. The model was mounted on an internal 6-component strain-gauge balance, which was connected to a 20° cranked sting. With this mounting arrangement an angle of incidence range from 13° to 47° was covered in 2° increments. Corrections were applied to the model angle of incidence to allow for the bending of the model sting under load. Because of the small size of the model; wing area is 3% of the tunnel cross-sectional area, no corrections were applied for the constraint effects of the wind-tunnel walls. All of the results are referred to a moments reference centre at 0.2413c.

## 4 RESULTS AND DISCUSSION

### 4.1 Effects of leading-edge devices

Fig 6 shows the variation with angle of incidence of the lift performance of the model, starting from the basic wing-body combination and adding various high-lift devices. While the foreplane produces only a moderate increment in lift at low angles of incidence it has major effect at high incidence, where a large increment in lift is produced. The close-coupled foreplane functions in a similar manner to a wing leading-edge slat by reducing the loading on the inboard section of the wing, and hence allowing attached flow to be maintained to a higher angle of incidence. At the higher angles of incidence the vortex flow generated by the foreplane interacts with the wing flow to stabilise the separation of the wing flow, in a similar manner to a leading-edge root extension. Drooping the leading-edge section of the wing produces a further small increment in lift coefficient (0.035). Adding a vortex flap to the basic wing profile gives a large increment in lift at the higher angles of incidence tested. The fractional gains in lift are typically up to 30% higher than the fractional increases in projected area obtained by deploying the vortex flaps. The constant-percentage-chord vortex flap (15% of local chord) produces a decrement in lift, relative to the basic wing, at the lower angles of incidence. This may be due to the effect of the large-chord inboard section of the flap on the effective incidence of the wing in the root region, combined with the effect of the downwash flow from the foreplane. In contrast the constant-chord vortex flap (40% of tip chord) produces a gain in lift over the whole incidence range. Some previous measurements of forces and moments for angles of incidence in the range  $-5^\circ$  to  $20^\circ$  had shown that separated flow existed on the underside of the vortex flap up to angles of incidence greater than  $10^\circ$ .

Fig 7 shows the variation of axial force coefficient with angle of incidence for the same set of model configurations. For all of these configurations negative values of axial force (i.e. a thrust force along the body axis) are obtained. The effect of adding the foreplane to the basic wing-body combination is to delay the loss of thrust by  $10^\circ$  incidence, and to maintain some significant thrust component up to the highest angle of incidence tested. Drooping the leading edge produces an increment in thrust of about  $-C_A = 0.03$  over most of the incidence range tested. Adding vortex flaps to the basic wing produces a very large increase in thrust, with a maximum increment of  $-C_A = 0.13$ . Comparison of the changes in projected vertical area for the wing with the drooped leading edge and with the vortex flaps fitted indicates that a greater mean suction is acting on the upper surface of the vortex flap. The thrust produced at lower angles of incidence by the constant-percentage-chord vortex flap is lower than that from the constant-chord flap, presumably because the former has a larger proportion of the flap area inboard on the wing, which is subjected to the downwash field from the foreplane. Fig 8 shows the variation of  $L/D$  with lift coefficient for the set of high-lift devices. Combining the benefits of increased lift and reduced drag, the foreplane produces a very large gain in  $L/D$  performance when added to the basic wing-body combination. The further gains from drooping the leading edge become small above  $C_L = 1.2$ , but this device matches the performance of the constant-percentage-chord vortex flap for  $C_L < 1.0$ . At values of lift coefficient greater than 1.0 the vortex flaps produce considerable gains, with the constant-chord vortex flap being consistently better than the constant-percentage-chord flap, up to the maximum  $C_L$  attained.

### 4.2 Effect of vortex-flap geometry

Fig 9 shows the effect of vortex flap size for the constant-percentage-chord flap, plotted as  $L/D$  versus lift coefficient. The 5% chord flap gives similar gains to those obtained with the drooped leading edge. It should be noted that the 5% flap produces no increase in planform area, because the hinge line is at 5% chord, and that the increase in projected vertical area is similar to that produced by the drooped leading edge. Doubling the size of the flap to 10% of the local chord gives a large gain in  $L/D$  for  $C_L > 0.9$ . A further increase in the size of the flap to 15% of the local chord has a negligible effect on  $L/D$ , and in fact produces inferior performance for  $1.0 < C_L < 1.4$ . Fig 10 shows the corresponding effects of vortex flap size for the constant-chord flap, again plotted as  $L/D$  versus lift coefficient. Increasing the flap size from 20% to 40% of the wing tip chord produces progressive gains in performance at high  $C_L$ , but for  $C_L < 1.2$  the 30% tip-chord flap is the most effective.

Fig 11 shows the effect of varying the deflection angle of the constant-chord vortex flap on the variation of  $L/D$  with  $C_L$ . There are gains in aerodynamic performance as flap deflection is increased from  $30^\circ$  to  $40^\circ$ , but these are small when compared with those obtained in deflecting the flap to  $30^\circ$ . From these figures it is evident that the improved  $L/D$  performance obtained with vortex flaps on this canard configuration changes in a nonlinear manner with variation of geometry, and varies considerably with lift coefficient.

### 4.3 Flow development

The surface flow on the wing and vortex flap was examined using a fluorescent powder suspension in paraffin, which was painted on the wing and the oil evaporated at the 85 m/s test windspeed. Figs 12, 13 and 14 show some photographs of the resulting flow visualisation, for angles of incidence of  $25^\circ$ ,  $35^\circ$  and  $45^\circ$  respectively. The wing was fitted with a constant-chord vortex flap (40% of tip chord), deflected  $40^\circ$ . At  $25^\circ$  incidence, Fig 12, a slender-wing type of vortex flow develops from the apex of the vortex flap at the wing root. This vortex grows in an approximately conical manner over the inner 20% of the flap span. A kink then occurs in the separation line under the leading-edge vortex, possibly due to transition having occurred in the flow approaching separation. The vortex then runs parallel to the flap leading edge until about 60% span when it has grown sufficiently to spill over the leading edge of the basic wing. In the photograph of the wing upper surface there is evidence of the vortex leaving the upper surface of the wing outboard of 60% span, and possibly merging with the vortex springing from the highly-swept wing tip. Superimposed on this flow is the effect of the vortex flow generated by the lifting foreplane, which causes the general outflow on the wing upper surface. With increase in the angle of incidence to  $35^\circ$  (Fig 13) the vortex formed at the wing apex grows more quickly and is swept aft more rapidly. There is again evidence of a change in direction of the secondary separation line, but this occurs close to the leading edge of the basic wing which may be influencing the vortex growth. The vortex from the flap leading edge spills over onto the top surface of the wing at about 30% span. At this angle of incidence the upper-surface flow on the wing appears to be dominated by the foreplane interference effect. At an angle of incidence of  $45^\circ$  (Fig 14) the vortex from the flap leading edge spills over onto the top surface of the wing at about 20% span, and interacts with the foreplane-body flow to produce a strong recirculating region inboard on the wing upper surface. Thus in general, and

contrary to the simple two-dimensional model for the flow, the vortex from the leading edge of the vortex flap does not remain trapped in the cavity between the flap upper surface and the wing nose undersurface, for the 53° sweep wing. Relating the flow visualisation results on this and other vortex flap configurations to the measurements of model axial force it appears that maximum thrust is produced when the vortex spills over the basic wing leading edge at about mid semi span.

#### 4.4 Effect of varying foreplane and wing trailing-edge deflection angles

Fig 15 shows the effect on  $L/D$  versus lift coefficient of varying the foreplane deflection angle over the range  $-25^\circ$  to  $0^\circ$ , for the wing with a constant-percentage-chord vortex flap (15% of local chord), deflected  $30^\circ$ . Decreasing the foreplane deflection angle to more negative angles than  $-10^\circ$  produces considerable reduction in the maximum lift. Two mechanisms related to the flow development on the foreplane are likely to contribute to this effect. At moderate values of  $C_L$  the more negative setting angles for the foreplane will lead to a higher loading on the inboard section of the wing, so that local flow separation on the wing will occur at a lower angle of incidence. At the higher values of  $C_L$  the vortex flow generated by the foreplane will be far weaker with the more negative foreplane setting angles, so this flow will not be able to influence the development of the wing upper-surface flow to the same extent, and hence this flow will breakdown completely at a lower angle of incidence. Note that even with a foreplane deflection angle of  $-25^\circ$  useful benefits in  $L/D$  and  $C_L$  remain, relative to the performance of the basic wing-body combination. However to maximise the aerodynamic performance of a canard configuration at high lift it is obviously worthwhile examining means of maintaining foreplane angle in the range of settings  $-10^\circ$  to  $0^\circ$ . Fig 16 shows the effect on  $L/D$  versus lift coefficient of varying the deflection angle of the full-span flap on the wing trailing edge, for the wing fitted with a constant-chord vortex flap (40% of tip chord) deflected  $40^\circ$ , and with the foreplane deflected  $-5^\circ$ . Deflecting the trailing-edge flap downwards  $5^\circ$  produces increments in  $C_L$  and  $L/D$  that decrease with increasing incidence, reaching  $\Delta L/D = 0.2$  at  $C_L = 1.7$ . Further deflection of the flap to  $10^\circ$  is of no benefit below  $C_L = 1.2$ , but at  $C_L = 1.7$  an additional gain of 0.2 in  $L/D$  is obtained, and there is an associated gain in maximum lift.

#### 4.5 Pitching moment characteristics and longitudinal trim

Fig 17 shows the pitching-moment behaviour for the range of high-lift configuration considered in section 4.1 above. The basic wing-body combination has small positive stability with the centre of gravity at 24%  $\bar{c}$ ,  $\frac{dC_m}{dC_L} = -0.015$ .

Addition of the foreplane produces an unstable configuration for which  $\frac{dC_m}{dC_L} = 0.13$ . Drooping the wing leading edge to  $10^\circ$  has a negligible effect on stability but adding either type of vortex flap (constant-percentage-chord, 10% of local chord, or constant chord, 40% of tip chord) to the basic wing produces a slight increase in the overall slope of the  $C_m$  versus  $C_L$  curve ( $\frac{dC_m}{dC_L} = 0.15$ ).

However the curves are more nonlinear, and there are areas where the local instability is much higher. The pitch up that occurs at the stall on the basic wing and on the

wing with the drooped leading edge becomes less severe when the vortex flaps are added. From this figure it is evident that decrements in pitching-moment coefficient in the range 0.05 to 0.15 are necessary to trim the configuration at moderate to high values of lift coefficient.

Fig 18 shows the effect on pitching-moment coefficient of variation in the deflection angles for the foreplane and the wing trailing-edge flap. At values of lift coefficient up to 1.4 the effectiveness of the foreplane and the wing trailing-edge flap remains approximately constant, with the flap typically 30% more effective than the foreplane

$$\left( \frac{dC_m}{d\eta_F} = -0.010 \text{ and } \frac{dC_m}{d\eta_c} = -0.007 \text{ respectively at} \right.$$

constant lift coefficient). At the higher values of lift coefficient the foreplane effectiveness is reduced by up to 50% for the range of deflection angles tested ( $-25^\circ$  to  $0^\circ$ ), but the effectiveness of the trailing-edge flap is only slightly reduced. With the cg at 24% of the aerodynamic mean chord (corresponding to a low-incidence instability of 15%  $\bar{c}$ ) Fig 18 shows that the canard configuration may be trimmed in pitch, using foreplane and flap deflections within the ranges tested, for values of lift coefficient up to 1.54, albeit with a greatly increased level of instability at the highest value of  $C_L$ . A reduction in the instability of the configuration (eg by the choice of a more forward cg), or the use of larger ranges of deflection angles for the foreplane and the wing trailing-edge flap, would allow trimmed conditions to be obtained at higher values of lift coefficient.

Fig 19 shows a comparison of the trimmed aerodynamic performance, as trimmed  $L/D$  versus trimmed lift coefficient, for six wing configurations with the cg at 24%  $\bar{c}$ . The trim curves were obtained by varying foreplane deflection angle over the range  $-25^\circ$  to  $-5^\circ$ . All of the leading-edge high-lift devices produce gains in  $L/D$  and  $C_L$  relative to the performance of the wing with the basic leading edge. For the configurations with undeflected trailing-edge flaps those with vortex flaps become superior to that with the drooped leading edge for  $C_L > 1.0$ , eg comparing the latter with the constant-percentage-chord vortex flap, deflected  $30^\circ$ . The constant-chord vortex flap gives consistently better trimmed  $L/D$  and  $C_L$  than the constant-percentage-chord vortex flap, as can be seen by comparing the curves for the two vortex-flap planforms in conjunction with  $5^\circ$  deflection of the trailing-edge flap. Deflection of the trailing-edge flap to  $10^\circ$ , in conjunction with the constant-chord vortex flap, produces the highest trimmed  $C_L$  and substantial benefits in  $L/D$  at the higher values of  $C_L$ . The results for this configuration indicate that further gains in aerodynamic performance should be possible by the use of larger deflection angles for the wing flap.

To interpret these findings in the context of improved manoeuvre performance for a combat aircraft, it should be noted that for a constant drag of  $C_D = 0.2$  these results show that the vortex flap provides a gain in trimmed lift of approximately 15%. For a combat aircraft with high thrust-to-weight ratio this may be translated directly into increased sustained turning performance at subsonic Mach numbers. Similarly for a constant drag of  $C_D = 0.4$ , appropriate to instantaneous turning performance, gains of over 30% in trimmed lift may be expected. As an alternative to increasing turn rate these gains in aerodynamic performance may be used to reduce the energy loss for a given level of turning performance.

## 5 CONCLUSIONS

Low-speed wind-tunnel measurements of the longitudinal force and moment characteristics of a canard combat-aircraft research model having a 53° sweep wing fitted with two planforms of vortex flaps have shown:

- (1) At moderate angles of incidence the deployment of a vortex flap from the wing lower surface produces comparable values of lift-to-drag ratio to those obtained with a conventional, drooped leading-edge, high-lift device.
- (2) At high values of lift coefficient the vortex flaps produce considerable gains in L/D relative to the drooped leading edge.
- (3) A constant-chord vortex flap produces a greater increase in L/D than a constant-percentage-chord (ie linearly tapered) vortex flap.

- (4) Variation of foreplane deflection angle produces a large change in the L/D obtained with the vortex-flap configurations.
- (5) Wing trailing-edge flaps remain effective up to an angle of incidence of 47° when used in conjunction with the vortex flaps.

Overall the gains in trimmed L/D and trimmed lift generated by the vortex flaps offer the prospect of greatly enhanced manoeuvrability for canard combat-aircraft configurations.

## 6 ACKNOWLEDGMENT

The author wishes to thank Mr I.A. Cheema who carried out the experimental investigation of the constant-percentage-chord vortex flap.

Table 1  
Principal dimensions of model

Wing area (S)	0.2918 m <sup>2</sup>
Wing span (b)	0.8940 m
Wing aerodynamic mean chord ( $\bar{c}$ )	0.3817 m
Wing leading-edge sweep	53°
Distance of moments reference centre aft of wing leading edge (equivalent to 0.2413 $\bar{c}$ )	0.3185 m
Overall length of body	1.230 m
Foreplane net area	0.0497 m <sup>2</sup>
Foreplane gross span	0.4484 m
Foreplane leading-edge sweep	58°
Distance of foreplane pivot forward of moment reference centre	0.3170 m

Table 2

### Geometry of vortex flaps

Constant percentage chord VF	
Flap hinge line	5% of local chord
Flap chord	5%, 10%, 15% of local chord
Deflection angle	30°
Constant chord VF	
Flap hinge line	5% of tip chord
Flap chord	20%, 30%, 40% of tip chord
Deflection angle	30°, 40°

## REFERENCES

- 1 Rao, D.M., "Leading-edge vortex-flap experiments on a 74° delta wing", NASA CR-159161 (1979)
- 2 Rao, D.M. and Campbell, J.F., "Vortical flow management techniques", Progress in Aerospace Sciences, 24, 173-224 (1987)
- 3 Rao, D.M., "Towards an advanced vortex flap system - the 'cavity flap'", NASA CP2416, 1, 219-230 (1985)
- 4 Lovell, D.A., "Some recent experimental investigations into aerodynamic aspects of controls for canard combat aircraft layouts", AGARD CP465, Paper 6 (1989)
- 5 Howarth, R.N.L. and Lee, P., "Transonic wind-tunnel tests on a combat aircraft research model having a variable sweep wing (48°, 53° and 58°)", RAE Technical Memorandum Aero 2156 (1989)
- 6 Wilson, K.H., "The aerodynamic design of a wing of 58° leading-edge sweep for a combat aircraft research model", RAE Technical Memorandum Aero 2074 (1986)
- 7 O'Leary, C.O. and Rowthorn, E.N., "Low speed dynamic tests on a canard configured High Incidence Research Model (HIRM 2)", RAE Technical Report 82024 (1988)

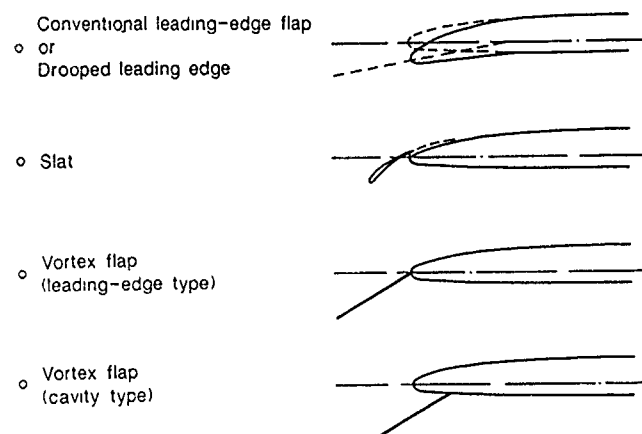


Fig 1 High-lift devices for the leading edge of a wing

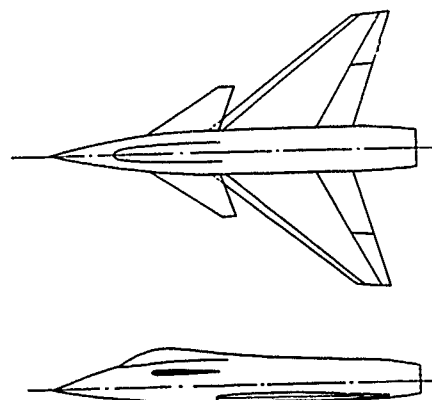


Fig 2 53° Sweep Combat-Aircraft Research Model

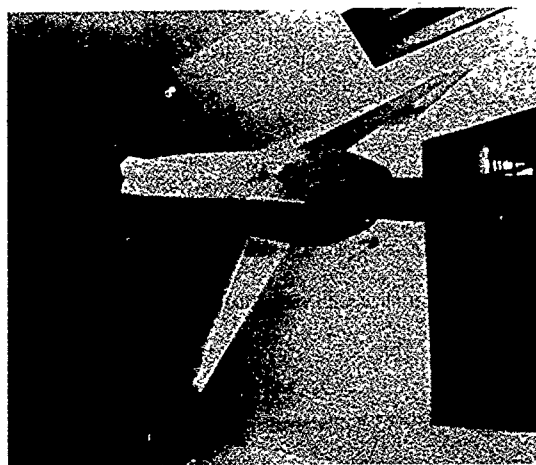


Fig 3 Combat aircraft research model in 3.5m x 2.6m wind tunnel

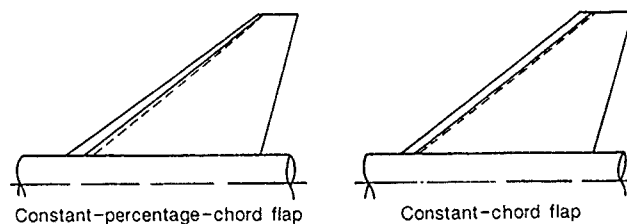
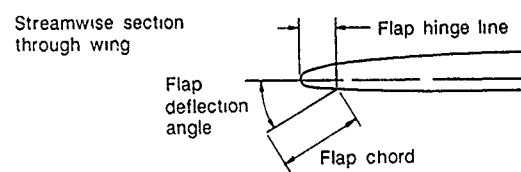


Fig 4 Definition of geometry of vortex flaps

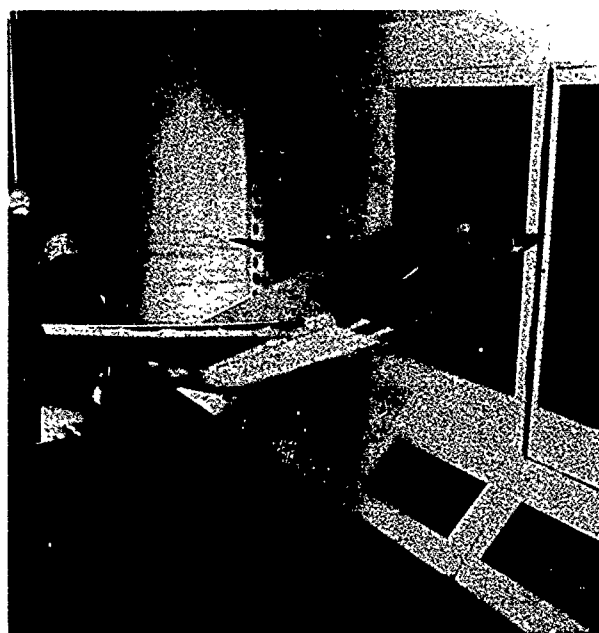


Fig 5 Combat aircraft research model fitted with vortex flaps

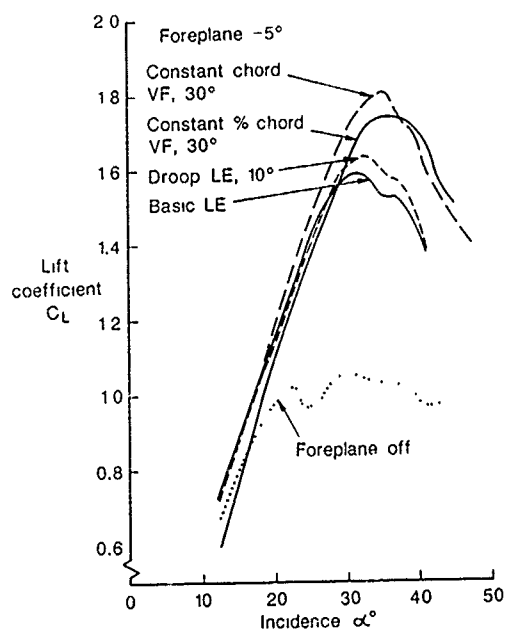


Fig 6 Effect of leading-edge high-lift devices on lift coefficient

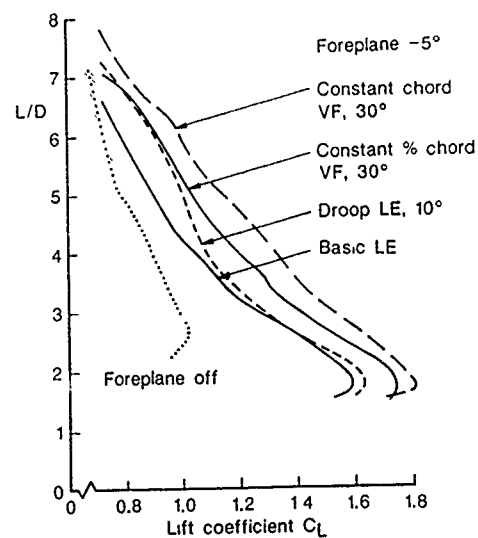


Fig 8 Effect of leading-edge high-lift devices on L/D

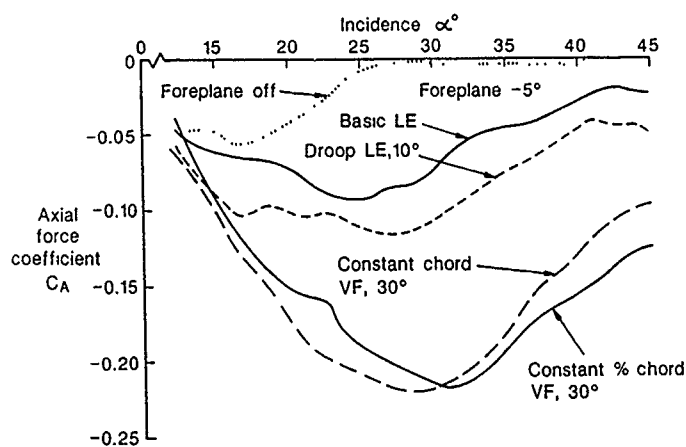


Fig 7 Effect of leading-edge high-lift devices on axial force coefficient



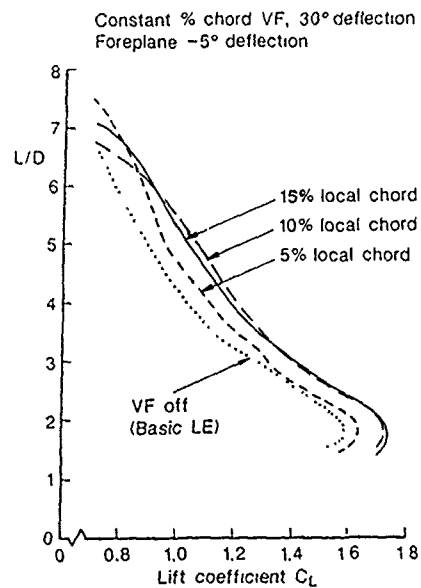


Fig 9 Effect of size of constant % chord vortex flaps on L/D

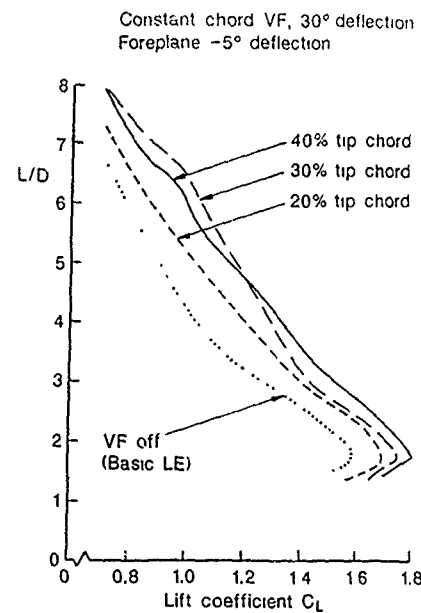


Fig 10 Effect of size of constant chord vortex flaps on L/D

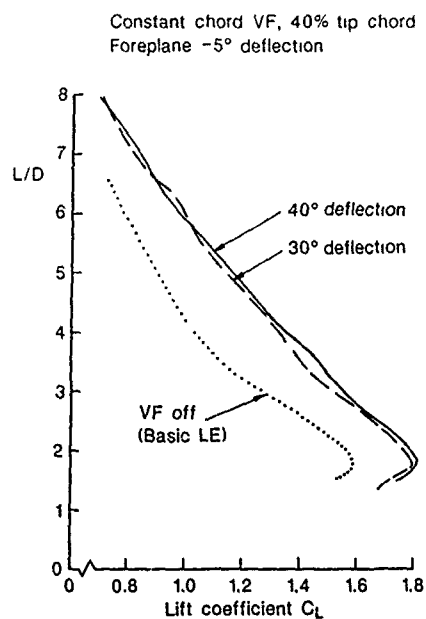
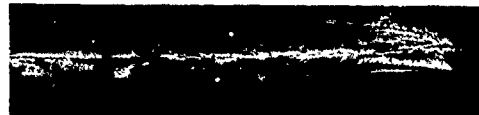


Fig 11 Effect of deflection angle of constant-chord vortex flap on L/D



Constant chord VF, 40% tip chord, 40° deflection

Foreplane - 5° deflection

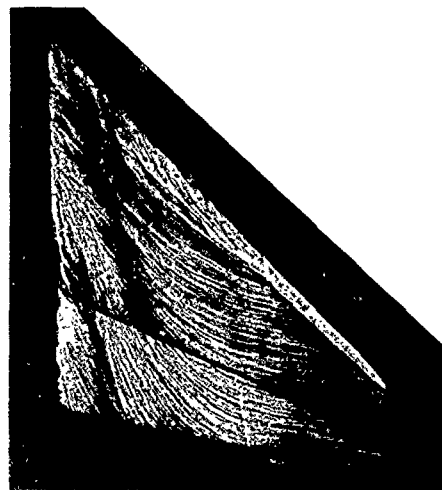


Fig 12 Surface flow pattern at 25° incidence



Constant chord VF, 40% tip chord, 40° deflection

Foreplane - 5° deflection

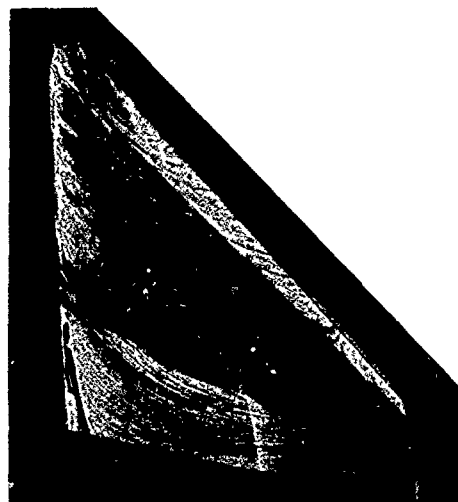
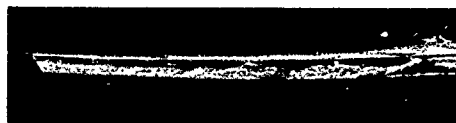


Fig 13 Surface flow pattern at 35° incidence



Constant chord VF, 40% tip chord, 40° deflection  
Foreplane - 5° deflection



Fig 14 Surface flow pattern at 45° incidence

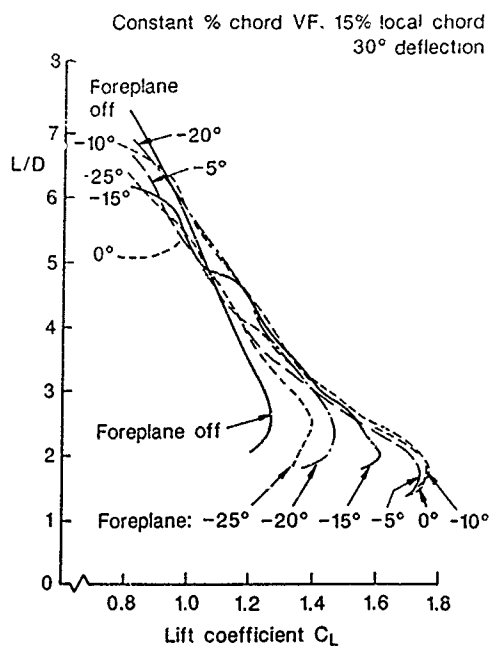


Fig 15 Effect of foreplane deflection angle on L/D

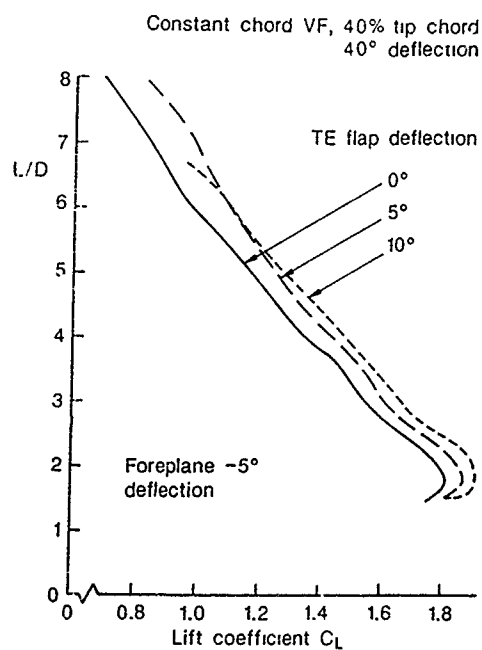


Fig 16 Effect of trailing-edge flap deflection angle on L/D

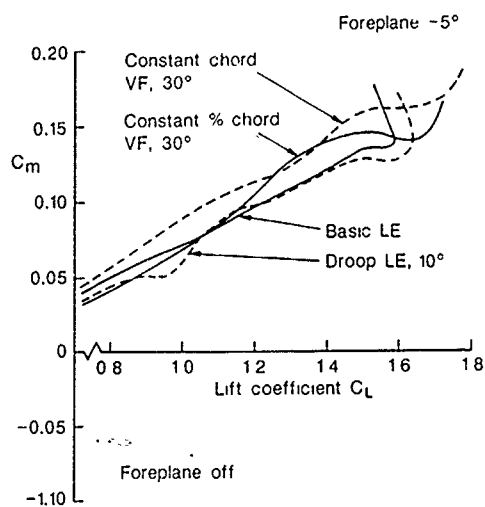


Fig 17 Effect of leading-edge high-lift devices on pitching moment coefficient

Constant chord VF, 40% tip chord,  
40° deflection

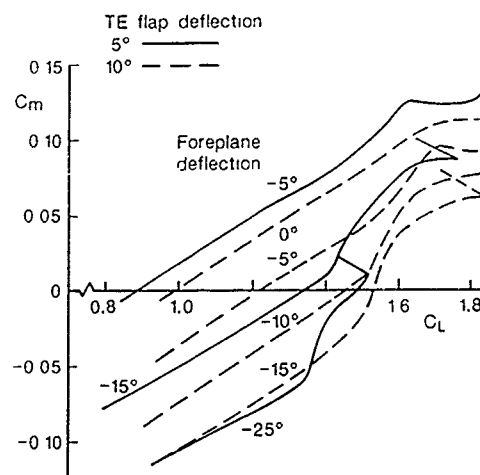


Fig 18 Effect of foreplane and wing trailing-edge flap deflection on pitching moment coefficient

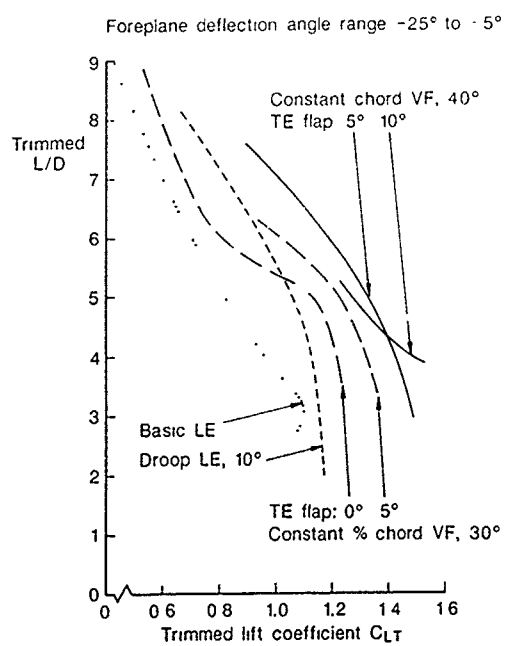


Fig 19 Trimmed L/D for vortex flap configurations

# STEADY AND UNSTEADY AERODYNAMICS OF A PITCHING STRAKED WING MODEL AT HIGH ANGLES OF ATTACK

by

A.M. Cunningham, Jr.  
General Dynamics, Fort Worth, Texas

R.G. den Boer  
National Aerospace Laboratory (NLR)  
P.O. Box 90502, Anthony Fokkerweg 2, 1006 BM Amsterdam, The Netherlands

## SUMMARY

Results are presented and discussed for the low speed test of a straked wing model oscillating in pitch that was conducted during 1986 at the National Aerospace Laboratory of The Netherlands in cooperation with General Dynamics. The model was oscillated about mean angles of attack ranging from -4 deg to 48 deg with amplitudes varying from 2 deg to 18 deg for a maximum incidence range of -8 deg to 50 deg. It was also oscillated in pitch at side slip angles of +5 deg and -5 deg. Force, pressure and flow-visualization data were recorded, processed and documented in a final report as well as digital and analog magnetic tapes. This paper presents a description of the model, test program, steady aerodynamic characteristics and unsteady aerodynamic characteristics. These results are used to provide a better understanding of the unsteady forces experienced by rapidly pitching wings at low speed conditions ranging from zero incidence to fully stalled flows. Dynamic rolling moments for the pitching model at steady side-slip are also discussed to illustrate asymmetric aerodynamic hysteresis effects. Finally, implications for aircraft flight dynamics modeling are discussed with particular emphasis on non-linear time dependency effects.

## 1.0 INTRODUCTION

Post stall maneuvering capability requirements for fighter aircraft are becoming a distinct possibility as emphasized in recent research programs being conducted by NASA, U.S. Air Force, U.S. Navy and DARPA. Two basic classes of hi- $\alpha$  maneuvers have evolved: (1) a low-speed rapid turn with high decelerations going into the turn and high accelerations coming out of the turn;<sup>1</sup> and (2) a rapid pitch-point fire maneuver at higher speeds.<sup>2,3</sup> The first type of maneuver is akin to a "hammerhead" stall where as the second is a pitch-doublet similar to that demonstrated by Pougachev in a Russian Su-27 at the Paris Air Show in 1989, nicknamed the "Cobra" maneuver.

Although aerodynamic loads encountered in low speed rapid turns would be small, those produced during rapid pointing maneuvers at higher speeds would be significant and highly dynamic. Moreover, the dynamic aerodynamic loads in the latter case would be quite different from sustained maneuver loads in both magnitude and character. Hysteresis effects in forces and moments as well as dynamic overshoots of steady maximum forces are typical of the differences. Many of the current fighter aircraft which have the potential to perform such maneuvers are straked wing configurations as

exemplified by the F-16, F-18, MiG-29, and Su-27. Thus, the unsteady aerodynamic loads would be produced by vortex flows peculiar to straked wing planforms, subject to bursting and stalled conditions at high incidences and high pitch rates.

In order to better understand the development of unsteady air loads for these fighters maneuvering beyond stall, a low speed wind tunnel test of an oscillating straked wing model was performed during 1986 in a cooperative program between General Dynamics and the National Aerospace Laboratory (NLR) of The Netherlands.<sup>4</sup> The testing was funded by the Air Force Wright Research and Development Center using the model that was designed and built at NLR with funds provided by General Dynamics and NLR.

This paper will present steady and unsteady force and moment results from the 1986 test of the straked wing model pitching at large amplitudes and varying frequencies up to maximum incidences of 50 deg. The discussions will represent an extension of those already given in References 5, 6, and 7 through the addition of (1) dynamic pitching moment and axial force characteristics for pitching motions at zero side-slip as well as (2) steady and unsteady normal force, pitching moment and rolling moment results for the model pitching with fixed values of side-slip angle. Pressure and flow-visualization data will be used to provide insight as to how the flow fields interact with the model to produce the observed force and moment characteristics. Implications for aircraft flight dynamics modeling will be discussed with particular emphasis on non-linear time history effects.

## 2.0 MODEL AND TEST PROGRAM

The full-span model shown in Figure 1 was instrumented with a six-component balance, 42 in-situ pressure transducers, nine vertical accelerometers and an angle-of-attack sensor. Boundary layer transition was not fixed on the model. The model was mounted on the dynamic support system also shown in Figure 1 with the capability of maximum amplitudes of + 18 deg (36 deg peak-to-peak) and maximum frequencies of 16 hz (limited to + 2 deg amplitude). The total incidence range was from -8 deg to 50 deg with the capability of statically yawing the model and support system as indicated in Figure 1. Flow-visualization of the vortex structure was accomplished with smoke injection from the model nose with laser light sheet illumination. For unsteady flows, the laser sheet was pulsed in phase with model motion to provide illumination at a fixed model incidence during the cycle.

Force, pressure and flow-visualization data were obtained for a wide variety of static and dynamic conditions at incidences up to 50 deg. An extensive data base was

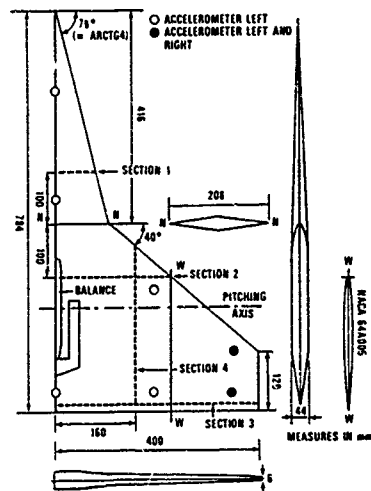


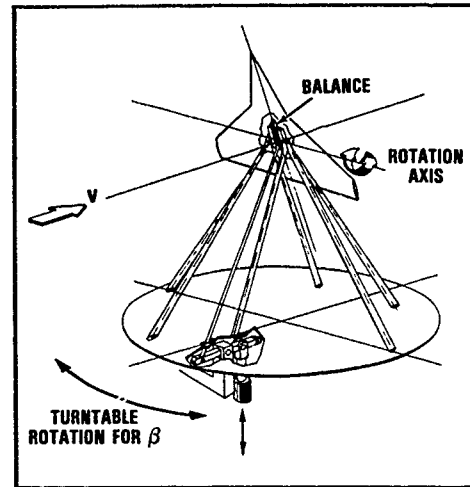
Figure 1 Straked Wing Model, Instrumentation, and Dynamic Support System

developed from over 1200 test points and 3600 flow-visualization photos and is fully documented in References 4 and 5. In order to minimize any significant transonic effects, the test speeds were limited to about  $M = 0.2$  utilizing the NLR 2.25 x 3.00m<sup>2</sup> Low Speed Tunnel.

The tests were conducted using a matrix of mean incidence, amplitude and frequency so that the effects of pitch rate, amplitude and incidence range could be systematically separated. Time histories as well as harmonic component results were recorded for forces, moments and pressures. Results were also obtained for the model pitching at fixed yaw angles of  $\pm 5$  deg. Flow-visualization data were recorded at dynamically similar conditions selected from the larger test matrix. Sign conventions for the forces, moments, and angles are shown in Figure 2.

### 3.0 SYMMETRIC FLOW

The key to understanding the unsteady aerodynamics is to first understand the steady aerodynamics. The combination of force, pressure and flow-visualization data available from this test makes it possible to break down the angle of attack range of  $-8$  deg to  $50$  deg into definable flow regimes separated by smaller transition regimes.



### 3.1 Symmetric Steady Aerodynamic Characteristics

The variations of steady normal force,  $C_N$ , pitching moment,  $C_m$ , and axial force,  $C_T$ , with angle of attack,  $\alpha$ , are shown in Figure 3 for zero side-slip. Important flow field characteristics and transitions are also denoted where the "sections" referred to in those notations are the pressure transducer rows shown in Figure 1. Corresponding steady pressure data for all four sections are shown in Figure 4 for  $\alpha = 10$  deg,  $19$  deg,  $22.4$  deg,  $36$  deg and  $42.3$  deg. The pressure data were chosen to highlight various flow regimes and transitions.

The "Linear" range of aerodynamic force development is clearly evident in Figure 3 in both the  $C_N$  and  $C_m$  data from  $\alpha = -8$  deg to  $8$  deg. Maximum  $C_T$  is noted at  $\alpha = 0$  deg and development of leading edge suction is evident in the linear range. Beyond  $8$  deg, the  $C_N$  and  $C_m$  curves show an upward change in slope that is indicative of the development of vortex flows over both the wing and strake. This is illustrated by the pressure data in Figure 4 at  $\alpha = 10$  deg for pressure section 2. The small peak at  $2y/b = 0.45$  is produced by the strake vortex and the stronger peak at  $2y/b = 0.8$  by the wing vortex. The vortex structure is also illustrated by the

$$\begin{aligned}
 C_N &= \frac{N}{SQ} & c_r &= \text{ROOT CHORD} \\
 C_m &= \frac{m}{SQc_r} & b &= \text{SPAN} \\
 C_T &= \frac{T}{SQ} & Q &= \text{DYNAMIC PRESSURE} \\
 C_l &= \frac{l}{SQb} & S &= \text{SURFACE AREA} \\
 f &= \text{FREQ, Hz} \\
 k &= \frac{2\pi f c_r}{2V} \\
 V &= \text{FREE STREAM VELOCITY}
 \end{aligned}$$

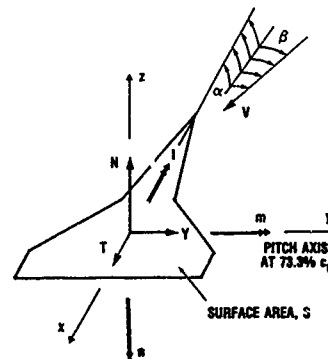


Figure 2 Coordinate System and Term Definitions

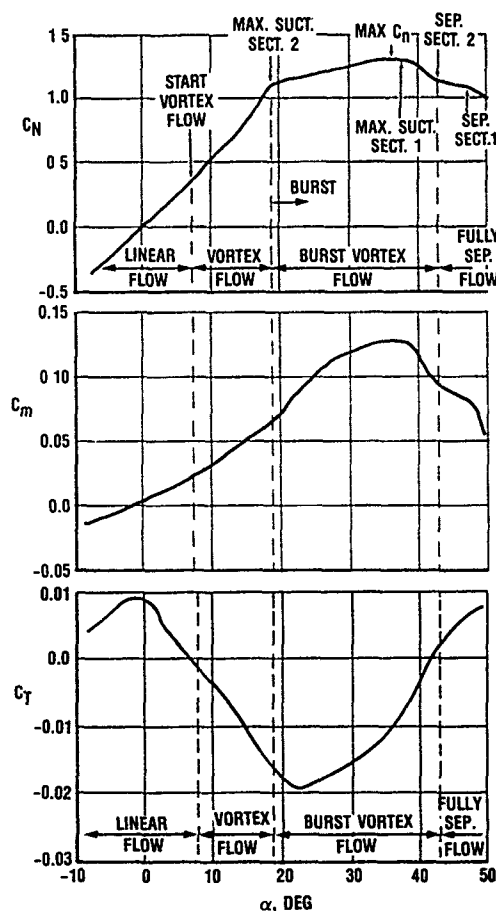


Figure 3 Steady Force and Moment Results for Symmetric Flow

accompanying sketch in Figure 4. A similar development in  $C_T$ , indicating increased suction slope change with incidence, does not appear in Figure 3 until about 12 deg.

The vortex flow range continues to develop until  $\alpha = 18$  deg to 19 deg where a distinct break occurs in the  $C_N$ ,  $C_m$ , and  $C_T$  data. This break signals the onset of vortex burst which represents the limit of vortex strength that can be maintained by the flow fields. Bursting tends to occur simultaneously for the wing and strake vortices when the two merge as discussed in References 6 and 7 with the flow-visualization results. The pressure data for  $\alpha = 19$  deg in Figure 4 show well developed vortices at both the forward pressure sections (1 and 2) but a deterioration of pressure recovery on the outboard half of the trailing edge section (3). The burst vortex structure is also illustrated in the sketch for  $\alpha = 19$  deg in Figure 4.

For increasing  $\alpha$  in the burst vortex regime, the strake vortex strength increases but the burst point continues to move forward. These opposing trends result in a much lower slope in the  $C_N$  curve as shown in Figure 3, however, the slope is almost constant from  $\alpha = 19$  deg to about 34 deg. The gain in lift forward due to strake vortex strength increase and the loss in lift aft due to vortex burst forward movement produces a pitch-up in the  $C_m$  curve as shown in Figure 3. Minimum  $C_T$  at about 22 deg is indicated by the  $C_T$  curve in Figure 3 after which leading edge suction deteriorates with the further development of vortex bursting. The pressure data in Figure 4 for  $\alpha = 19$  deg, 22.4 deg, and 36 deg show the deterioration of the wing vortex strength at section 2 and the continued increase of the strake vortex strength up to 36 deg at section 1. These characteristics are illustrated in the sketches for  $\alpha = 19$  deg, 22.4 deg and 36 deg.

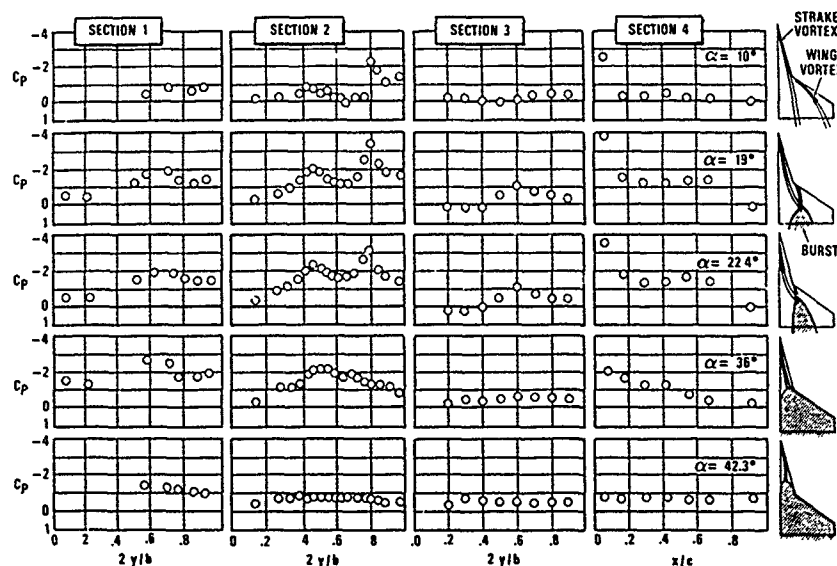


Figure 4 Variation of Steady Pressure Distributions with Alpha

Beyond the maximum value of  $C_N$  at  $\alpha = 36$  deg the flow over the entire wing and strake rapidly collapses to completely separated or flat plate flow. Under these conditions for increasing  $\alpha$  the normal force is falling off and the center of pressure is moving toward the geometric centroid of the planform as indicated by a rapid decrease in pitching moment. Axial force is increasing with incidence and crosses zero at about 42 deg near the beginning of fully separated flow. The pressure data at  $\alpha = 42.3$  deg in Figure 4 show that the pressure distributions are nearly flat at about the same level for all sections except section 1 on the strake. At this angle, the strake vortex burst has progressed forward of section 1 as shown in the sketch for  $\alpha = 42.3$  deg.

### 3.2 Symmetric Unsteady Aerodynamic Characteristics

The symmetric unsteady flow fields associated with the pitching straked wing model at zero side-slip and their effect on the dynamic normal force characteristics were discussed in References 6 and 7. An extension to that discussion will be presented here that includes the unsteady flow field effects on pitching moment and axial force. These results are shown in Figures 5, 6, and 7 at low frequency at the three important incidence ranges: (1) low incidence,  $\alpha = 4$  deg to 24 deg, linear/vortex flow; (2) medium incidence,  $\alpha = 8$  deg to 38 deg, vortex/burst vortex flow; and (3) high incidence,  $\alpha = 22$  deg to 50 deg, vortex burst/stalled flow. The effect of a constant starting angle,  $\alpha_{min}$ , and constant peak angle,  $\alpha_{max}$ , is also illustrated in each of these figures. In all cases, the pitch direction on the dynamic hysteresis loops is denoted by solid lines for pitch-up and dashed lines for pitch-down. Arrows are added where possible. The steady mean characteristics are shown in each dynamic plot as dash-dot-dash lines for reference.

The hysteresis effects in the three components and incidence ranges are quite different for various amplitudes depending on whether the minimum angles or maximum angles are fixed. These differences are related to how the max and min angles are positioned relative to the important flow field transition points such as vortex burst (about 18 deg) and total flow separation (about 42 deg). The effect of pitch rate is to introduce a change in the incidence at which a given transition takes place relative to the static angle. Since a finite time is required for a transition to occur, the apparent incidence delay in flow breakdown or re-establishment tends to increase with higher pitch rates. This delay is also affected by the types of flow fields encountered during the pitch excursion.

Results shown in Figure 5 for  $\alpha = 4$  deg to 24 deg emphasize the second order effects of pitching motion where the flow fields are dominated by linear and/or unburst vortex flows. Since the transition from attached to vortex flow is benign, the potential for generating significant hysteresis effects is very small. The primary effect of pitch rate seen in Figure 5 is to retard vortex flow on pitch-up and promote it on pitch-down. This results in lower normal force, a less nose-up pitching moment and higher axial force (reduced leading-edge suction) for positive pitch rate. The opposite is true for negative pitch rate. The influence of amplitude with either constant  $\alpha_{min}$  or  $\alpha_{max}$ , is likewise quite small and is almost lost in the plots.

The enclosure of vortex burst at  $\alpha = 18$  deg within the pitch excursions leads to more pronounced dynamic effects in the mid-incidence range of  $\alpha = 8$  deg to 38 deg as shown in Figure 6. The  $C_N$  loops are more dynamic if the burst angle,  $\alpha_{burst}$ , is enclosed within the pitch excursion, that is  $\alpha_{max} > \alpha_{burst}$  and  $\alpha_{min} < \alpha_{burst}$ . For the results shown in Figure 6, the maximum center of pressure hysteresis is on

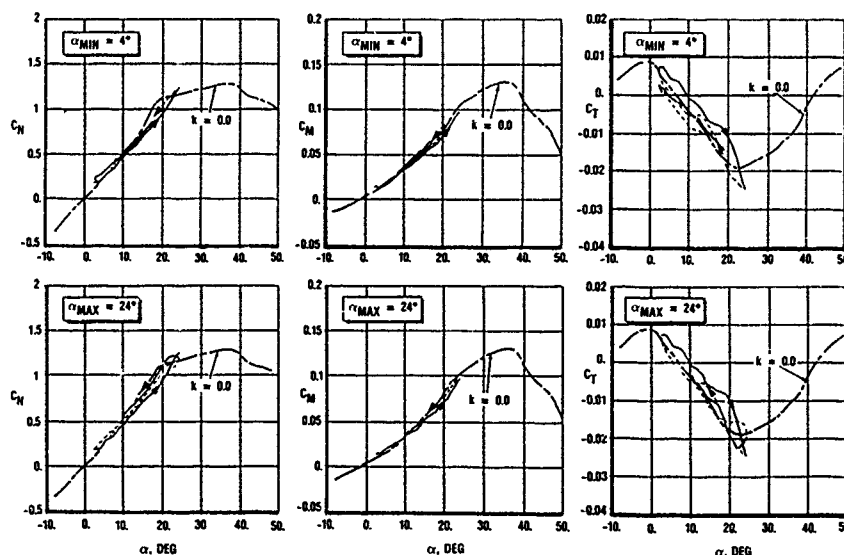


Figure 5 Effect of  $\alpha_{min}$  and  $\alpha_{max}$  on Symmetric Force/Moment Characteristics at  $k = 0.09$  and Low Incidence  $\alpha = 4$  deg to 24 deg



the order of 2% - 3% of the wing root chord,  $C_r$ . The effect of positive pitch rate is to delay vortex burst and produce less pitch-up in  $C_m$ . Negative pitch rate has the opposite effect by prolonging the existence of vortex burst to lower angles and promoting pitch-up in  $C_m$ .

Dynamic effects of model pitching motion on axial force,  $C_T$ , as shown in Figure 6 are much more pronounced. This is due to the reversal of trends with  $\alpha$  at vortex burst as well as the low level of forces involved which shows greater sensitivity to changes in the flow fields. With the onset of vortex burst, the development of increased leading-edge suction with  $\alpha$  is reversed at a slightly higher angle, to decreasing leading-edge suction with in-

creasing  $\alpha$ . Thus, the delay of vortex burst with positive pitch rate is clearly evident where the dynamic  $C_T$  loop shows reversal at angles higher than that for steady flow. For the maximum amplitude, this reversal is delayed from 22 deg statically to about 26 deg dynamically. With negative pitch rate the persistence of burst vortex flow is indicated by a lower angle at which the leading edge suction reversal occurs. This angle is reduced from the static value of 22 deg to a dynamic value of about 15 deg. Asymmetry of the dynamic lag for suction reversal is a result of the time required for vortex bursting ( $\Delta\alpha = 4$  deg, pitch-up) being much less than for re-establishing unburst vortex flow ( $\Delta\alpha = -7$  deg, pitch-down).

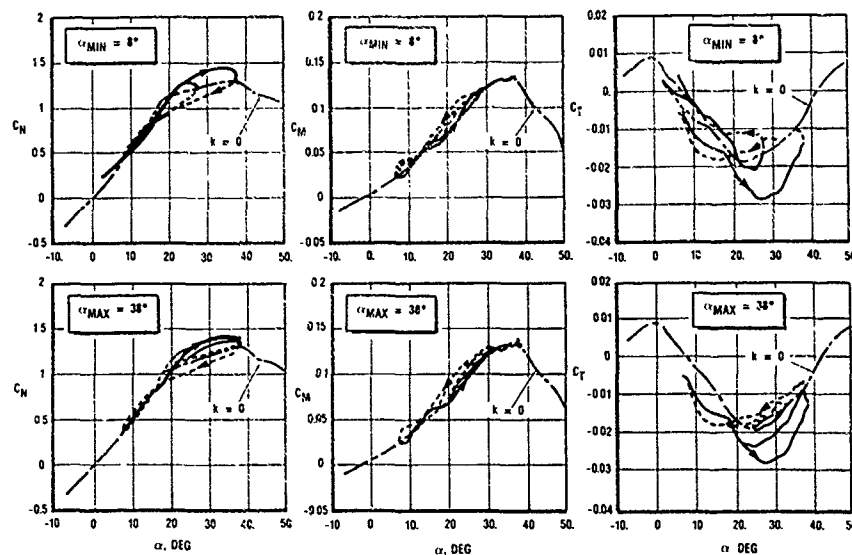


Figure 6 Effect of  $\alpha_{min}$  and  $\alpha_{max}$  on Symmetric Force/Moment Characteristics at  $k = 0.09$  and Mid-Incidence  $\alpha = 8$  deg to 38 deg

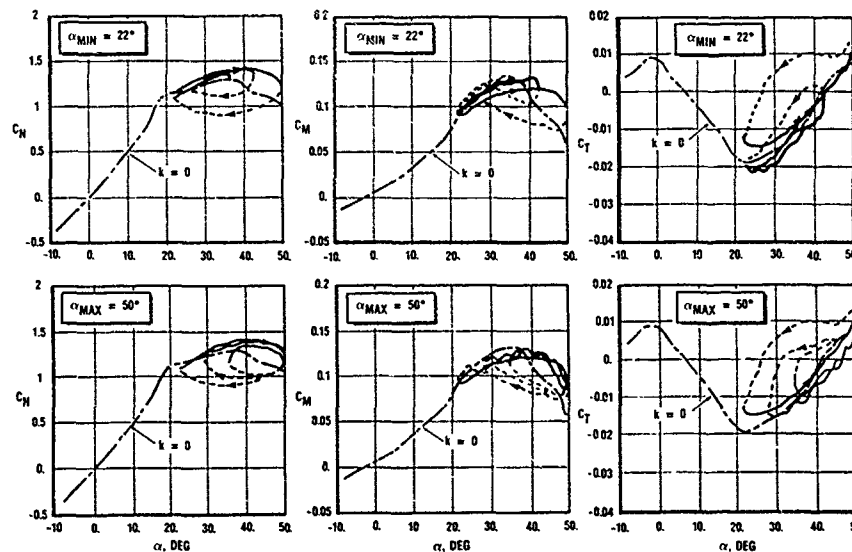


Figure 7 Effect of  $\alpha_{min}$  and  $\alpha_{max}$  on Symmetric Force/Moment Characteristics at  $k = 0.09$  and High Incidence  $\alpha = 22$  deg to 50 deg

Stalling of the flow fields in the high incidence range of 22 deg to 50 deg is a more chaotic transition than vortex bursting, and thus leads to even more pronounced dynamic effects as shown in Figure 7. The influence of  $\alpha_{min}$  and  $\alpha_{max}$  relative to the stall angle,  $\alpha_{stall}$ , at about 42 deg is also more evident. For constant  $\alpha_{min}$  and  $\alpha_{max} < \alpha_{stall}$ , the  $C_N$ ,  $C_m$ , and  $C_T$  results in Figure 7 show very little dynamic effects since, for  $\alpha_{min} > \alpha_{burst}$ , no major flow transition points occur within the pitch excursion. As soon as  $\alpha_{max}$  exceeds  $\alpha_{stall}$ , dynamic effects are much more pronounced. The extension of burst vortex flow characteristics to higher angles with positive pitch rate is seen in  $C_N$ ,  $C_m$ , and  $C_T$  for all values of  $\alpha_{min}$  in Figure 7. (This is not the case for  $\alpha_{min} > \alpha_{stall}$  as shown by smaller amplitude data in Reference 4.) Likewise, the extension of stalled flow characteristics to angles lower than static  $\alpha_{stall}$  with negative pitch rate is also seen in Figure 7. For fixed  $\alpha_{min}$  results, negative pitch rate effects are quite sensitive to  $\alpha_{max}$ . However, for  $\alpha_{max}$  fixed well above  $\alpha_{stall}$ , negative pitch rate effects are not as sensitive to  $\alpha_{min}$ .

The previous discussions on dynamic axial force characteristics in the mid-incidence range are equally applicable to the high-incidence range results in Figure 7. Since  $\alpha_{min}$  is equal to or greater than the leading edge suction reversal angle,  $\alpha_{SR} = 22$  deg, the persistence of burst vortex flow characteristics is dominant with positive pitch rate. This persistence is almost unaffected by  $\alpha_{min}$  or  $\alpha_{max}$  and the dynamic trends tend to follow the static curve.

For negative pitch rate with  $\alpha_{max} > \alpha_{stall}$ , the dynamic  $C_T$  characteristics reflect a similar persistence of the stalled flow. These characteristics take the form of a tendency to maintain a constant level of  $C_T$  that is about the same as the peak value reached at  $\alpha_{max}$ . This is illustrated in Figure 7 for the maximum amplitude

where the initial reduction of  $C_T$  begins at about 36 deg. This point is at an angle greater than that for re-establishment of burst vortex flow from stalled flow. This angle is indicated by the corresponding  $C_m$  loop to be about 25 deg on pitch-down (where the stalled flow  $C_m$  characteristic rejoins the static  $C_m$  curve). A change in the  $C_T$  curve slope is also noted at about 27 deg on pitch-down which may be a more sensitive indication of re-established burst vortex flow. The reduction of  $C_T$  between 36 deg and 27 deg is attributed to (1) the build up of higher pressure on the upper surface aft of the pitch axis and (2) increased leading-edge suction due to higher vertical velocities normal to the leading edge. Each of these two effects is a direct result of negative pitch rate. Once burst vortex flow is re-established the transition toward the static curve is quite abrupt as is also shown for the other amplitudes where  $\alpha_{max}$  is fixed at 50 deg.

The effect of frequency on  $C_N$  for the three incidence ranges is shown in Figure 8 for fixed  $\alpha_{min}$  and  $\alpha_{max}$ . As expected, not much effect is seen in the lower incidence range. At the mid-incidence range of 8 deg to 38 deg, the dynamic loops are simply higher and the effects of amplitude for fixed  $\alpha_{min}$  or  $\alpha_{max}$  are similar to those seen in Figures 5, 6, and 7. The same observation is seen at the higher incidence range of 22 deg to 50 deg with exception that an apparent displacement of the loop end points at  $\alpha_{min}$  or  $\alpha_{max}$  from the static curve is more pronounced at the higher frequency.

#### 4.0 ASYMMETRIC FLOW WITH SIDE-SLIP

The important flow transitions discussed above for symmetric flows are equally important for asymmetric flows with side-slip. The principle difference is that side-slip affects where and how these transitions occur and it causes them to occur differently on the windward and leeward wings. This is best understood by first examining the steady aerodynamics as

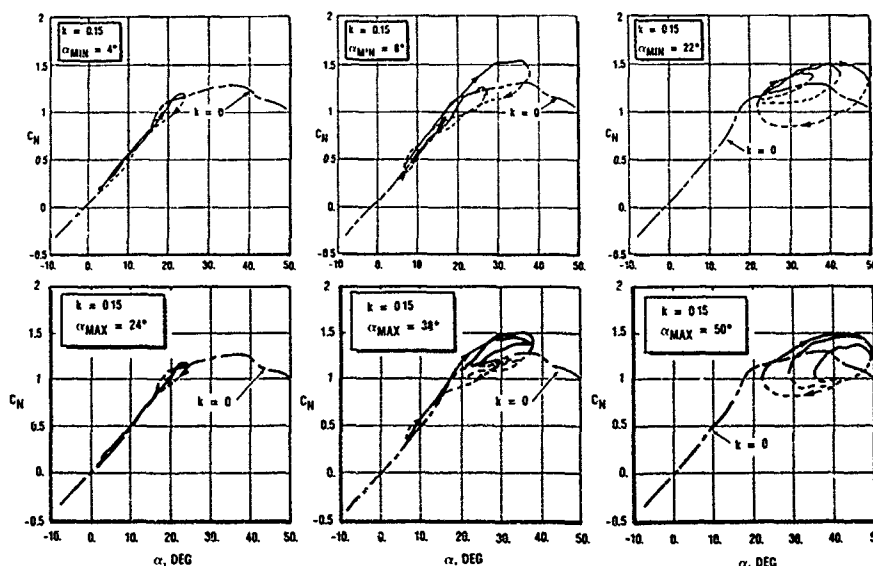


Figure 8 Effect of  $\alpha_{min}$  and  $\alpha_{max}$  on Symmetric  $C_N$  Characteristics at  $k = 0.15$  and All Incidence Ranges

was done above for symmetric flows. The unsteady aerodynamics are then developed by considering the effects of dynamic lag on the steady aerodynamics.

#### 4.1 Steady Aerodynamic Characteristics with Side-Slip

Measurements were made with the model placed at  $\pm 5$  deg side-slip by rotating the turn table as shown in Figure 1. Steady normal force,  $C_N$ , pitching moment,  $C_m$ , and rolling moment,  $C_l$ , variations with  $\alpha$  are shown in Figure 9 for side-slip of  $\beta = -5$  deg. These curves were constructed from mean values of forces and moments taken from low amplitude and/or low frequency unsteady data since no steady side-slip data were recording during the test. For reference, corresponding results for symmetric flow,  $\beta = 0$  deg, are also shown in Figure 9 as dashed lines.

Similar to the symmetric data, the "linear" range in Figure 9 is evident in the  $C_N$  and  $C_m$  data from  $-8$  deg to  $8$  deg. Beyond  $8$  deg the development of vortex flow is also seen in Figure 9 but the effect of side-slip is indicated by an earlier (1 deg) pitch-up in the  $C_m$  curve at about  $17$  deg. This is a result of earlier vortex bursting on the windward wing which is also indicated by a corresponding but less discernable break in the  $C_N$  curve. Above vortex burst, the developments of  $C_N$  and  $C_m$  follow trends similar to those shown for symmetric flow in Figure 3. The lower levels for either quantity are due to earlier development of vortex bursting as precipitated by the lower sweep of the windward wing. It is also clear in the  $C_m$  curve that fully separated flow occurs earlier with side-slip. Pressure data in Reference 4 support this observation where fully separated flow exists on the windward wing well below  $\alpha = 36$  deg as a result of lower sweep.

The more interesting result shown in Figure 9 is rolling moment,  $C_l$ , variation with  $\alpha$ . For the sign conventions shown in Figure 2,  $\beta = -5$  deg places the nose right and positive  $C_l$  is for windward wing to roll up. Positive  $C_l$  is therefore stabilizing for negative  $\beta$  since it tends to reduce  $\beta$ . Thus, in the linear range up to  $\alpha = 8$  deg, the development of  $C_l$  with  $\beta$  is stabilizing as a result of the windward wing with lower sweep experiencing higher lift than the leeward wing.

The development of vortex flows, beginning at about  $8$  deg to  $10$  deg, signals the onset of a destabilizing trend in  $C_l$ . Under these flow conditions the windward wing rolling moment increase with  $\alpha$  is less than that of the leeward wing. This is attributed to (1) a more rapid growth of the strake vortex induced lift inboard on the windward wing and (2) slower growth of the wing vortex induced lift outboard on the windward wing. These two effects result in an inboard movement of the spanwise center of pressure (CP) on the windward wing. Since the opposite process is occurring on the leeward wing with increasing  $\alpha$ , the net result is a deterioration of  $C_l$  with side-slip.

Unlike simple, highly swept, delta wings which experience stabilizing  $C_l$  trends with side-slip in vortex flows, the straked wing acts just the opposite. The

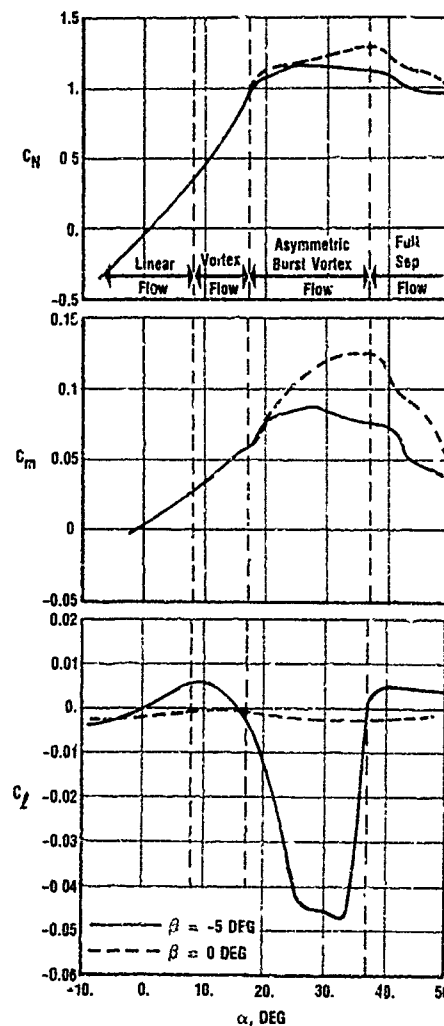


Figure 9 Steady Force and Moment Results for Asymmetric Flow

strake flow fields, however, do act like a simple delta wing in that lift on the windward strake increases with incidence over that on the leeward strake. The slower growth of wing vortex induced lift on the outboard windward wing is believed to be caused by displacement of that vortex through influence of a stronger strake vortex. This is evidenced in pressure data in Reference 4 where the suction peak under the wing vortex is displaced inboard. The peak is also weakened and flattened which is indicative of displacement away from the wing surface. Both of these displacements would be expected as a result of mutual influence of the wing and strake vortices on the windward wing. Finally, because of the larger moment arm for the decreasing wing vortex induced lift, this loss in rolling moment tends to override the gain from the strake vortex induced lift.

The destabilizing trend in  $C_l$  that began with onset of vortex flows is greatly intensified with vortex bursting. This trend is consistent with highly swept delta wings where burst is initiated on the wind-

ward wing because of the lower sweep. Burst development and consequent loss of lift on the windward wing precedes that on the leeward wing and, thus, maintains a destabilizing tendency to roll the leeward wing up and increase side-slip. Burst onset is noted in the  $C_l$  curve in Figure 9 at about 17 deg where a change in slope with respect to  $\alpha$  is seen. This downward slope continues until about 25 deg where it abruptly changes to a nearly flat "bottom" or "bucket". The occurrence of this "bucket" also coincides with static  $C_{Nmax}$  and  $C_{mmax}$  as noted in the other curves shown in Figure 9. Based on the pressure data in Reference 4, it is postulated that the windward wing vortex is fully burst at about 25 deg.

Within the "bucket", the windward wing remains essentially unchanged from its fully separated condition and contributes very little to the development of  $C_N$ ,  $C_m$ , and  $C_l$  with  $\alpha$ , which, in fact, is true up to the maximum tested incidence of 50 deg. Since  $C_N$ ,  $C_m$ , and  $C_l$  are nearly constant over the  $\alpha$  range of the "bucket", about 25 deg to 33 deg, the development of vortex burst over the leeward wing apparently has little effect on lift. It is highly probable that the stalled flow field over the windward wing is partly responsible for this behavior.

The destabilizing "bucket" is abruptly terminated starting at about 33 deg where the  $C_l$  curve becomes stabilizing at 37 deg. This is attributed to the stalling process on the leeward wing which happens very quickly as has been observed in various flow visualization tests.<sup>8</sup> Once both wings are stalled, the influence of side-slip through changes in leading edge sweep is no longer important. The stabilizing level of  $C_l$  remains nearly constant from about 40 deg up to 90 deg as has been shown in other tests of the subject straked wing planform.<sup>9</sup> This characteristic is quite persistent once the wing is totally stalled as will be demonstrated later in unsteady flow.

#### 4.2 Unsteady Aerodynamic Characteristics with Side-Slip

The asymmetric unsteady flow fields associated with the pitching straked wing model with side-slip and their effect on dynamic normal force, pitching moment and rolling moment are presented in this section. These results were obtained with the model dynamically pitching at turntable positions of 5 deg and -5 deg relative to the freestream direction. Thus, the dynamic aerodynamic characteristics are representative of an airplane pitching in a plane that is yawed relative to the flight path. These results are shown in Figures 10, 11, and 12 for different frequencies and amplitudes in the same three incidence ranges covered in Figures 5, 6, and 7 for symmetric flow. The primary difference is that  $C_N$ ,  $C_m$ , and  $C_l$  are presented for side-slip. Again, line symbols are the same as were used for symmetric flow.

The hysteresis effects in the three components are quite different for different incidence ranges depending on the relationship between  $\alpha_{min}$  and  $\alpha_{max}$  and major flow transition points. The distinction between symmetric and asymmetric flows is that the major flow transitions occur at different angles; and, as discussed for steady flow, a transition may not occur on the windward and leeward wing at the same angle. As just discussed above for steady asymmetric flow, wing stall was suspected to occur at about 25 deg to 27 deg on the windward wing but at about 33 deg to 37 deg on the leeward wing.

The effect of pitch rate is to introduce a change in the angle at which a given transition may take place relative to the static angle. This is due to the finite time required for a transition to occur which is similar to symmetric flow. A distinction between symmetric and asymmetric flows, however, is that an additional time lag is introduced for the development of asymmetric flows. This results in a tendency for transitions to occur more

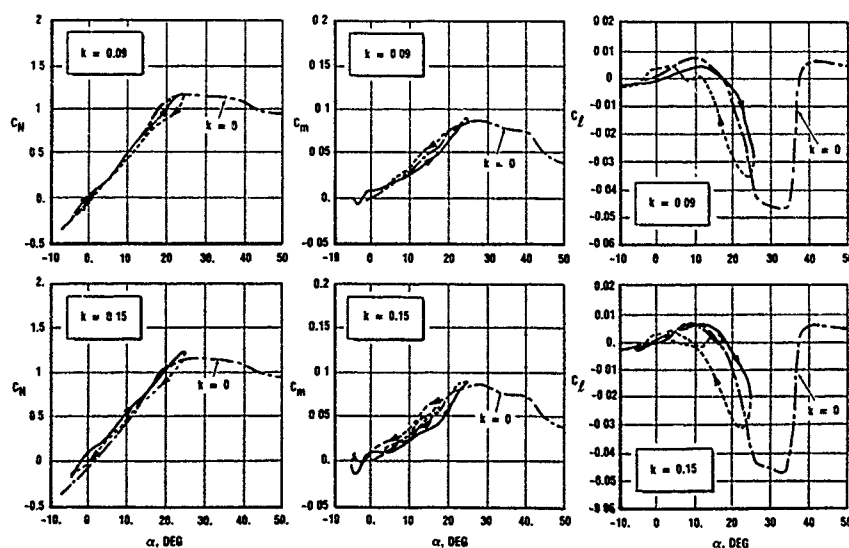


Figure 10 Effect of Frequency and Amplitude on Asymmetric  $C_N$ ,  $C_m$  and  $C_l$  at Low Incidence,  $\alpha = -4$  deg to 24 deg,  $\beta = -5$  deg

nearly simultaneously on both wings, even with wide-slip, and to initially minimize asymmetric effects. With sufficient pitch rate it is possible to almost entirely eliminate asymmetric effects under certain conditions.<sup>9</sup>

The results shown in Figure 10 for  $\alpha = -4$  deg to 24 deg emphasize the similarity with symmetric  $C_N$  and  $C_m$  results as shown in Figure 5. These dynamic effects are again second order where the flow fields are dominated by linear and/or unburst vortex flows. The dynamic effects on  $C_l$  are quite pronounced, however, and show considerable hysteresis in the vicinity of the lower side of the destabilizing "bucket". This hysteresis appears as a simple lag in the development of vortex and

burst vortex flows on pitch-up and reestablishment of flows on pitch-down. The effect of higher frequency is to widen the hysteresis loop width but not significantly alter the slopes. Loop height for the reduced amplitude is also remarkably similar to that for the large amplitude loop at the high frequency.

The mid-incidence range for  $\alpha = 8$  deg to 38 deg encloses both vortex burst and stalled flows on the windward and leeward wings. Burst occurs at 17 deg and stall at about 25 deg to 27 deg on the windward wing in steady flow, where as these transitions occur at about 25 deg and 37 deg respectively on the leeward wing. As a result of enclosing both burst and stall points, the dynamic effects for maximum amplitude in

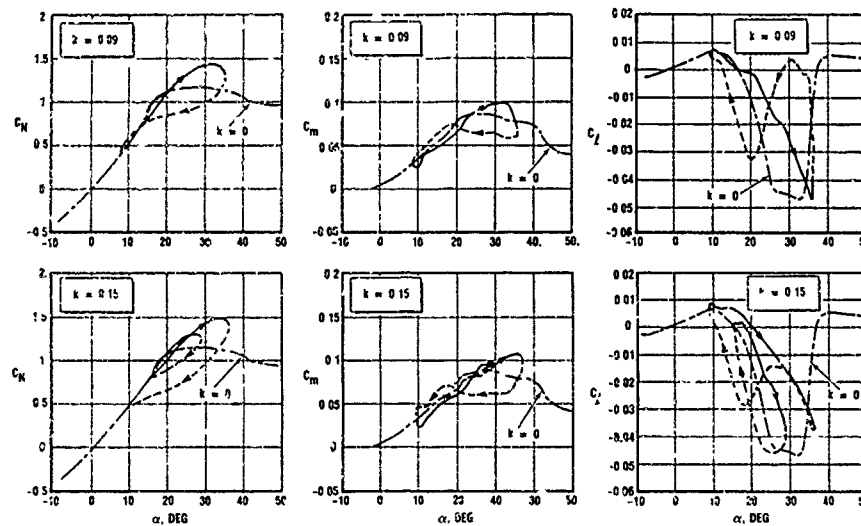


Figure 11 Effect of Frequency and Amplitude on Asymmetric  $C_N$ ,  $C_m$  and  $C_l$  at Mid-Incidence,  $\alpha = 8$  deg to 38 deg,  $\beta = -5$  deg

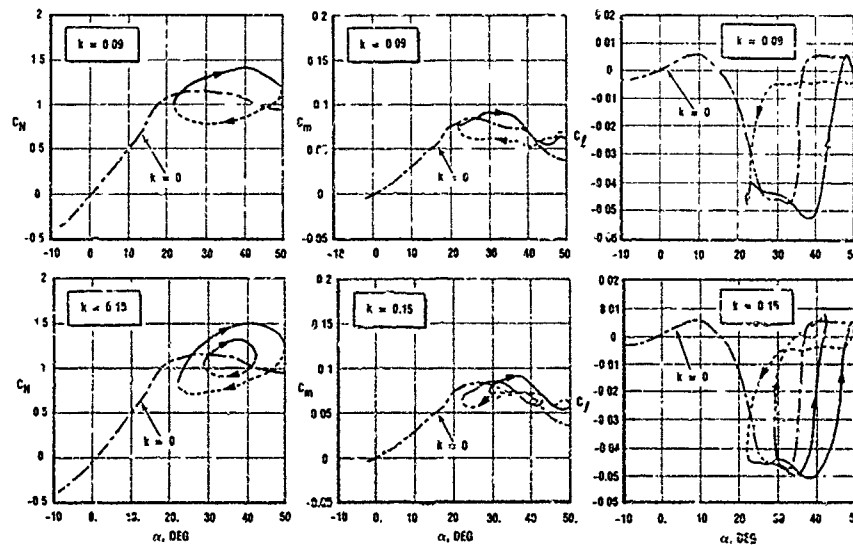


Figure 12 Effect of Frequency and Amplitude on Asymmetric  $C_N$ ,  $C_m$  and  $C_l$  at High Incidence,  $\alpha = 22$  deg to 50 deg,  $\beta = -5$  deg

this incidence range are much more pronounced with side-slip as shown by the results in Figure 11. Comparing  $C_N$  and  $C_m$  results in Figure 11 with those for symmetric flow in Figure 6 indicates that the hysteresis loops have amplitude excursions that are more like those seen in symmetric flow at the higher incidence in Figure 7. This is attributed to the enclosure of the stall point within the pitching motion which emphasizes importance of flow transition similarity on affecting dynamic characteristics as opposed to incidence similarity. The peculiar dynamic loops for  $C_l$  are directly tied to inclusion of the two major flow transition points and will be more easily understood after discussing dynamic effects in the high incidence range.

The results shown in Figure 12 cover the incidence range of 22 deg to 50 deg which encloses vortex burst on the leeward wing and stall transition on both wings. Because the flow field characteristics for maximum amplitude motion are more similar between symmetric and asymmetric flows, the dynamic  $C_N$  and  $C_m$  loops are also similar as can be seen by comparing Figures 7 and 12. The dynamic mechanism is essentially a flip-flop between vortex burst flow and stalled flow on the leeward wing while the windward wing is essentially stalled during the pitching motion. Time lag in the transition to or from stalled flow on the leeward wing produces the hysteresis loops shown in Figure 12. Dynamic loops for  $C_l$  results particularly emphasize the flip-flop characteristics with simple lag. The effects of frequency and amplitude on the dynamic  $C_l$  loops are minimal as long as the leeward wing stall transition is enclosed in the pitching motion. This suggests that there exists a limit pitch rate above which the dynamic  $C_l$  loops are essentially unchanged at higher rates.

Returning to the dynamic  $C_l$  loops in Figure 11 at the mid-incidence range, it is now evident how the shape of the loops for maximum amplitude is tied to the two flow transition points. The "Figure 8" characteristic at  $k = 0.09$  in Figure 11 is an almost quasi-steady distortion with simple lag of the "bucket". The rapidity of transition to stalled flow, as indicated by a very rapid rise in  $C_l$  at  $\alpha_{max}$ , is quite remarkable and is in agreement with earlier observations on how quickly flow fields can stall.<sup>8</sup> Increasing frequency to  $k = 0.15$  for the maximum amplitude, however, does not allow enough time for stall transition to occur and the  $C_l$  curve on pitch-down tends to retrace its path generated on pitch-up. This retracing implies that perhaps vortex bursting was not encountered on the leeward wing until about 30 deg, sometime after pitch-down had started; otherwise, hysteresis would be present similar to that also shown in Figure 11 for the lower amplitude and  $k = 0.15$ . The lower negative slope of  $C_l$  versus  $\alpha$  on pitch-up for maximum amplitude and  $k = 0.15$  (which is similar to the static slope for unburst vortex flow between  $\alpha = 12$  deg and 17 deg) is further evidence supporting this contention.

#### 5.0 IMPLICATIONS FOR FLIGHT DYNAMICS MODELING

The non-linearities and time history (or path dependency) effects in the aerodynamic forces and moments discussed in

this paper must be accounted for in the accurate modeling of flight path characteristics associated with dynamic maneuvering at post stall conditions. The influences of pitch rate and the incidence range encountered during such maneuvers are dominant in driving the aerodynamic characteristics along one branch or another depending on previous developments of the flow field time history. Results that have been discussed in this paper are directly applicable to full-scale post-stall maneuvering where the maximum incidence is 50 deg or higher. Maximum pitch rates scale to about 25 deg/sec for full-scale flight for a root chord of 30 ft and velocity of 300 FPS. The following discussions will cover two basic classes of non-linear behavior that have been illustrated in this paper.

The first type of aerodynamic non-linear behavior will be referred to as "state non-linearity". This type refers to characteristics that can be described on the basis of current state variables such as Mach,  $\alpha$ ,  $\dot{\alpha}$ ,  $\beta$ ,  $\dot{\beta}$ , etc. As an example, consider dynamic  $C_N$  variation in Figure 7 for fixed  $\alpha_{max}$ . For positive  $\dot{\alpha}$ , the  $C_N$  increase over static values can be fairly well defined on the basis of  $\alpha$  and  $\dot{\alpha}$ . For negative  $\dot{\alpha}$ , the  $C_N$  decrease from static values also can be defined as a function of  $\alpha$  and  $\dot{\alpha}$ , however, the coefficients will not be the same as for  $\dot{\alpha} > 0$ . As can be seen in Figure 7, the  $C_N$  reduction for  $\dot{\alpha} < 0$  is much greater than the  $C_N$  increase for  $\dot{\alpha} > 0$ . In this case the incremental changes from static curves due to dynamic effects are dependent on  $\alpha$  and  $\dot{\alpha}$ . This first type of non-linearity is applicable to dynamic conditions in which the aircraft encounters similar flow fields and flow field transitions within a given maneuver range. The incidence range for linear attached flow and vortex flow up to burst is a good example of flow regimes to which state non-linearity is applicable. It can also be used to define aerodynamic characteristics where vortex and burst vortex flows or stalled flows are encountered without transition occurring.

The second type of aerodynamic non-linear behavior will be referred to as "path dependent non-linearity". This type exhibits bifurcations that are controlled by the time history development of the flow fields resulting from model or aircraft motions. As an example, the dynamic variation of  $C_N$  in Figure 7 for fixed  $\alpha_{min}$  shows a noticeable sensitivity to  $\alpha_{max}$  depending on whether  $\alpha_{max}$  is greater than or less than the stall angle. The loop for  $\alpha_{max} = 36$  deg does not enclose stall and is not very dynamic. However, when  $\alpha_{max}$  is increased to 43 deg and does enclose stall, the loop is much more dynamic and shows a strong similarity to the loop for  $\alpha_{max} = 50$  deg. This example illustrates the importance of inclusion or exclusion of major flow transitions within the model or aircraft motion.

A more disturbing example of path dependent non-linearity is shown in Figure 11 for dynamic  $C_l$  variation with frequency. At the low frequency,  $k = 0.09$ , the dynamic  $C_l$  loop had the appearance of a lag distorted "bucket". This was a result of encountering both asymmetric vortex burst and total stall within the range of the pitch excursion. At the higher frequency,  $k = 0.15$ , the dynamic  $C_l$  loop appearance changed

significantly and no longer reflected the occurrence of leeward wing stall at  $\alpha_{max}$ . In fact, the data indicated that vortex burst did not even occur on the leeward wing during pitch-up. Thus, the stalled flow branch taken at the lower pitch rate was not taken at the higher pitch rate since sufficient time was not available for the leeward wing to stall in the latter case. In this example, bifurcation was driven by pitch rate rather than incidence range, however,  $\alpha_{min}$  and  $\alpha_{max}$  had to be within certain ranges for this phenomenon to occur.

Clearly, state parameter values are not sufficient to define dynamic aerodynamic characteristics where path dependency is dominant. In the cases of large amplitude aircraft maneuvers where several flow field types are encountered ranging from linear attached flow to post stall, an integration approach is necessary for this definition. The integration technique must have the intelligence to select the appropriate paths when encountering aerodynamic bifurcation points. It must also be able to perform these functions without prior knowledge of what state parameter values will be encountered. This capability is necessary for non-linear flight path modeling where the aerodynamic forces that drive the aircraft are determined by feedback from the aircraft past and current dynamic state.

#### 6.0 CONCLUSIONS

This paper has presented a discussion of force and moment data results from the low speed wind tunnel test of an oscillating straked wing model. The model was oscillated in pitch in symmetric flow and in a yawed plane in asymmetric flow. Normal force, pitching moment and axial force results were analyzed for symmetric steady and unsteady flow where as normal force, pitching moment and rolling moment results were analyzed for the asymmetric conditions. Pressure and flow-visualization data also obtained in that test were used to interpret flow field characteristics associated with static and dynamic force and moment trends.

Four basic flow regimes were identified in steady symmetric flow as (1) linear, (2) vortex flow, (3) burst vortex flow and (4) fully separated or stalled flow. The relationships between the flow regimes and the development of normal force, pitching moment and axial force were discussed. These relationships formed the basis for discussing the unsteady aerodynamic characteristics.

Unsteady symmetric flow results were presented for three incidence ranges: (1) low incidence with linear and vortex flows, (2) mid-incidence with vortex and burst vortex flows, and (3) high incidence with burst vortex and stalled flows. Hysteresis effects in unsteady flows were shown to be more significant for the more chaotic flow fields associated with increasing incidence. These effects also increased with frequency of oscillation and with the inclusion of flow transition points in the pitch excursion. As an example, very little hysteresis was observed for model oscillation between the vortex burst and stall angles without enclosing either point within the oscillation range. Enclosing either vortex burst or stall angle within

the oscillation range produced a significant increase in hysteresis effects. This was true for all three components of force and moment that were discussed.

The four basic flow regimes identified in symmetric flow were also identified in asymmetric flow. The effect of side-slip was to shift the flow field transitions to higher angles or lower angles on the leeward or windward wings respectively. Influence on normal force and pitching moment were not large for a  $\pm 5$  deg or  $\pm 5$  deg yawing of the pitch plane. Stabilizing rolling moments were developed in the linear flow regime which were reduced with the onset of vortex flow. Destabilizing rolling moments were produced with asymmetric vortex burst and were returned to a stable condition with total wing stall.

Unsteady asymmetric flow results in the three incidence ranges revealed some very interesting characteristics. The effects of side-slip on dynamic normal force and pitching moment were noticeable due primarily to the existence of stalled flow on the windward and leeward wings within the mid-incidence range. Thus, characteristics typical of the high incidence range in symmetric flow were seen in the mid-range in asymmetric flow. Dynamic rolling moments were very much affected by frequency and pitch amplitude in the mid-incidence range. At a low frequency and maximum amplitude, the dynamic rolling moment loop showed the characteristics of vortex, burst vortex and stalled flows. At a higher frequency and same amplitude, stalled flow was not achieved on the leeward wing which resulted in completely different dynamic loop characteristics. In the high incidence range, a persistent flip-flop characteristic was seen in the rolling moment dynamic loops that was attributed to the leeward wing being unstalled on pitch up and stalled on pitch down.

The non-linear and path dependent effects on unsteady aerodynamic forces and moments presented in this paper were then discussed with regard to accurate modeling of flight path characteristics associated with dynamic maneuvering at post stall conditions. Two types of non-linear behavior were presented and referred to as "state non-linearity" and "path dependent non-linearity". It was demonstrated that state parameters were insufficient to define the dynamic aerodynamics where path dependency and bifurcation processes are dominant. A time integration technique was considered necessary which has the intelligence to select the correct aerodynamic path when encountering a bifurcation point.

#### REFERENCES

1. Herost, W.B.: "Future Fighter Technologies", *Journal of Aircraft*, Vol. 17, August 1980, pp. 561-566.
2. Cunningham, A.H., Jr.: Invited Presentation, U.S. Government sponsored "Workshop on Supermaneuverability", Air Force Wright Research and Development Center, 5-7 June 1984.
3. Lang, J. and Francis, H.S.: "Unsteady Aerodynamics and Dynamic Aircraft Maneuverability", AGARD-CP-386, May 1985.

4. Cunningham, A.M., Jr., den Boer, R.G., et al: Unsteady Low-Speed Wind Tunnel Test of a Straked Delta Wing Oscillating in Pitch, AFWAL-TR-87-3098 (Parts I through VI), April 1988.
5. den Boer, R.G. and Cunningham, A.M., Jr.: "Low Speed Unsteady Aerodynamics of a Pitching Straked Wing at High Incidence - Part I: Test Program", Journal of Aircraft, Vol. 27, January 1990, pp. 23-30.
6. Cunningham, A.M., Jr., and den Boer, R.G.: "Low Speed Unsteady Aerodynamics of a Pitching Straked Wing at High Incidence - Part II: Harmonic Analysis", Journal of Aircraft, Vol. 27, January 1990, pp. 31-41.
7. Cunningham, A.M., Jr.: "A Critique of the Experimental Aerodynamic Data Base for an Oscillating Straked Wing at High Angles", Proceedings Fourth Symposium on Numerical and Physical Aspects of Aerodynamic Flows, California State University, Long Beach, California, 16-19 January 1989.
8. Cunningham, A.M. Jr.: "Vortex Flow Hysteresis", Paper 11, NASA CP 2416, Vol. I, 1986.
9. Cunningham, A.M., Jr. and Bushlow, T.: "Steady and Unsteady Force Testing of Fighter Aircraft Models in a Water Tunnel", AIAA Paper No. 90-2815, August 1990.



## SOME CHARACTERISTICS AND EFFECTS OF THE F/A-18 LEX VORTICES

by

D. Brown, B.H.K. Lee and F.C. Tang  
Institute for Aerospace Research  
National Research Council  
Ottawa, Ontario K1A 0R6, Canada

**SUMMARY**

The first phase of a wind tunnel programme to measure mean and unsteady forces and moments and pressure distributions on the forward fuselage, leading-edge extension, fins and in the LEX vortex wake of a 6% rigid model of the F/A-18 aircraft has been accomplished. The effect of compressibility up to  $M=0.8$  has been studied. The mean chord Reynolds number range was 1.2 to 3.8  $\times 10^6$ .

Mean pressures were measured at 84 orifices distributed between canopy, forward fuselage and the LEX. Unsteady and mean pressure measurements were made at four points on the LEX and at 24 points on each side of the fin. The vortex wake measurements were made with a 49 tube total pressure rake of which 13 tubes were capable of acquiring unsteady as well as mean pressures.

The effects of the LEX fences, that have been retroactively fitted to CF-18 aircraft in service, have been assessed. The influence on aircraft lift and pitching moment is small. The data shows their local effect on LEX pressures, reduction in fin mean and unsteady loading that they cause and their effect on the stagnation pressure distribution in the vortex wake.

**Symbols**

$A_F$	fin area
$A_j$	area of $j$ th panel on fin
$\bar{c}$	wing aerodynamic mean chord
$c_l$	fin local chord
$\bar{c}_f$	fin mean aerodynamic chord
$C_M$	mean pitching moment about reference point (23.79 inches behind nose)
$C_M'$	rms value of unsteady pitching moment
$C_L$	lift coefficient
$C_N'$	rms value of unsteady normal force coefficient
$C_{N1}$	fin mean normal force coefficient
$C_{N1}'$	rms value of unsteady normal force on fin inner surface
$C_{N0}'$	rms value of unsteady normal force on fin outer surface
$C_p$	mean pressure coefficient
$C_p'$	rms value of unsteady pressure coefficient
$f$	frequency (Hz)
$F_1$	time function of pressure at point 1
$F_2$	time function of pressure at point 2
$k$	non-dimensional frequency ( $fc/U$ )
$M$	freestream Mach number
$p_i$	mean pressure on fin inner surface
$p_o$	mean pressure on fin outer surface
$p_i \text{ rms}$	rms value of unsteady pressure on fin inner surface at $j$ th panel
$p_o \text{ rms}$	rms value of unsteady pressure on fin outer surface at $j$ th panel
$q$	freestream dynamic pressure
$Re_{\bar{c}}$	Reynolds number based on $\bar{c}$
$R_{1,2}(\tau)$	cross correlation function of $F_1$ and $F_2$
$t$	time
$U$	freestream velocity
$x, y, z$	aircraft model co-ordinate system with origin at nose

$x, y, z$ , fin co-ordinate system with origin at intersection of leading edge and fuselage

$\alpha$  angle of incidence (degrees)  
 $\tau$  time delay

**INTRODUCTION**

The high degree of manoeuvrability of modern fighter aircraft at subsonic flight speeds is largely due to the ability of the wing planform to generate vortical flows that produce useable lift coefficients at high angles-of-attack that are substantially higher than possible with earlier planforms.

The F/A-18 by virtue of its high lift devices, optimized fin and stabilator arrangement, an advanced digital control system and effective engine air induction system is capable of controlled flight at angles-of-attack up to more than 50°.

Among the wings' high lift devices i.e. leading-edge extension (LEX), full span leading and trailing-edge flaps (flap/aileron outboard), the LEX has been credited with effecting a 22% increase in maximal lift coefficient and with increasing the angle of attack for max.  $C_L$  by 10°, compared with a LEX off configuration (Reference 1).

As is well known the lift enhancement arises from the rolling-up of separated flows at the highly swept leading edges of the LEX into a pair of intense vortices that trail rearwards. These induce a low pressure field over the LEX, upper surface of the fuselage and inner regions of the wings. At high angles of attack a strong outflow is apparent over much of the wing upper surface.

Ultimately the vortices burst and they degenerate into strongly turbulent flow. Interaction of the burst region with aircraft structure results in vibration which can be damaging. Peak accelerations up to 450g close to the tip of the vertical fin have been reported from flight tests at the Aeronautical Engineering Test Establishment at Cold Lake (Reference 2). The same reference demonstrates the efficacy of the standard LEX fences in reducing the peak acceleration to 200g.

Flow visualization work at small scale (1/72) in water tunnels, supported by wind tunnel investigations with a 6% model and full scale flight measurements have established an approximately linear relation between the aircraft angle-of-attack and the axial position of vortex burst (Reference 2). Since the vortex originates at a sharp edge the axial position is insensitive to Reynolds number - the measurements cited in Reference 2 cover three orders of magnitude. Also the variation of burst position appears to be insensitive to Mach number up to 0.4 at least.

The relation between burst position and angle-of-attack indicates that below 15° the burst occurs sufficiently to the rear to have little adverse effect on the fins. Above  $\alpha=15^\circ$  the burst position is sufficiently far forward for the turbulent regions to subject the fins to increasingly severe random loading as  $\alpha$  increases.

This paper describes the measurements and gives data from a wind tunnel investigation on a 6% scale rigid model of the F/A-18, with and without LEX fences. The measurements were performed in the 5ft X 5ft blowdown wind tunnel of the High Speed Aerodynamics Laboratory.

Data are presented for mean and unsteady force and moments on the model, LEX and fin pressures (mean and unsteady) and stagnation pressure measurements in the vortex wake behind the fin. The investigation was made at Mach numbers 0.19, 0.246, 0.6 and 0.8 and the angle-of-attack range was from  $0^\circ$  to  $35^\circ$ .

### MODEL AND INSTRUMENTATION

#### 1. Model

This is a 6% scale F/A-18 shown in Figure 1. It consists of 3 major pieces, namely an aluminum alloy forebody with integral strakes (equipped with removable fences) and a single place canopy; a stainless steel centre-fuselage with integral wings; and a stainless steel rear fuselage. These parts are made with close tolerance spigotted joints and are dowelled and bolted together. The centre fuselage is bored to accept a 1.5 inch diameter sting balance.

Leading- and trailing-edge flaps are fastened to the wings by simple bolted lap joints. For these measurements the flap deflections were  $35^\circ$  (L.E.F.) and  $0^\circ$  (T.E.F.).

The vertical fins are bolted to the rear fuselage which also carries adjustable angle stabilizers. These were set at  $-9^\circ$  for the measurements.

The wing tips carried models of the AIM9 missile and launcher rail but the underwing pylons were not fitted. Transition trips were placed on upper and lower surfaces of the LEX, wings, fins and stabilizers at approximately 0.4 inches from the leading edge. Trips were also placed around the forebody and along the lower generator in a manner similar to that described in Ref. 4.

#### 2. Model Support

Figure 2 illustrates the sting mounting arrangement of the model in the transonic test-section of the 5 ft X 5 ft blowdown wind tunnel at the Institute for Aerospace Research. A cranked sting was used to obtain a wind-off angle-of-attack range of  $0-33^\circ$ . Under aerodynamic loading an increment of  $2^\circ$ , due to sting bending is typically obtained.

#### 3. Instrumentation of Model

The forebody was instrumented with 84 pressure orifices located on the canopy, starboard fuselage side and upper and lower surface of the starboard LEX. Orifice pressures were measured on 5 electronically scanned pressure modules that were located in a cavity under the canopy. The LEX upper surface also contained 4 surface mounted Endevco 8515B (50 psia) absolute pressure transducers for dynamic pressure measurement. The locations of orifices and dynamic pressure transducers are indicated in Figure 3 and defined in Tables 1 and 2 respectively.

For these measurements the standard starboard fin was replaced by an extensively instrumented version containing 48 (24 per side) Endevco 8515B (50 psia) absolute transducers. These are embedded a short distance under the surface to give high dynamic response. The fin was also instrumented with root strain gauges and contained an accelerometer near the tip (3/4 span, 1/3 local chord).

Pressure calibration of the transducers was effected by fitting a pressure tight 'glove' over the entire fin, mounted on the model, thus subjecting each transducer to a common pressure from a nitrogen supply. The fin pressure transducer locations are indicated in Figure 4. Table 3 gives the locations of the transducers.

#### 4. Vortex Rake

Stagnation pressure in a 6-inch square cross-section behind the starboard fin was measured by the 49 tube rake depicted in Figure 5. This was mounted on the sting. Thirteen of the 45 active tubes (the corner tubes

were not connected) contained 1/16 inch diameter Kulite 25 psi differential pressure transducers for high frequency response. The reference side of these transducers were connected to an external pressure source.

Internal chamfers of  $40^\circ$  included angle were machined in the ends of the dynamic and the mean pressure tubes so as to reduce the directional sensitivity of the rake since it was required to operate over a  $35^\circ$  angle-of-attack range. The rake was aligned with the freestream direction when the model was at  $20^\circ$  angle-of-attack.

### RESULTS AND DISCUSSION

#### 1. Balance Data

The variations of lift coefficient  $C_L$  and pitching moment  $C_M$  at  $M=0.8$  and  $Re_\infty=3.8 \times 10^6$  are shown in Figures 6(a) and 6(b). These figures demonstrate that the effect of the LEX fences, especially on  $C_L$ , is small. The effect on  $C_M$  is mixed, an increase (decreased nose down value) is noted for  $C_L > 1.3$  with a decrease for  $0.7 < C_L < 1.3$  and a slight increase for low and negative lift. These data were obtained with the vortex rake in place. As shown in Figures 7(a) and 7(b), the presence of the rake causes a noticeable and even significant interference on the measured aerodynamic characteristics. The results shown in Figures 7(a) and 7(b) were obtained at  $M=0.6$  (the only Mach number for which we have rake on and off comparisons). It is seen, Figure 7(a), that there is a slight decrease in  $C_L$  due to the presence of the rake, the discrepancy becoming greater as  $C_L$  increases up to about 1.6 and then diminishing. The greater interference may be seen in  $C_M$ , Figure 7(b). For values of  $C_L < 1.5$ , the discrepancy amounts to about 13% of the total range in  $C_M$ , the effect being an increase in the moment.

However the effect of the LEX fences is not obscured by the presence of the vortex rake. The minimal effect of the fences on  $C_L$  is apparent in Figure 7(a) while the decrease in  $C_M$  due to the fences, seen in Figure 7(b), is similar for vortex rake on and off. This being the case the changes in  $C_L$  and  $C_M$  already noted at  $M=0.8$  in Figures 6(a) and 6(b) are held to be valid within the limitations of experimental errors. The loop is more pronounced ( $0.5 < C_L < 1.3$ ) for  $M=0.6$  than for  $M=0.8$  ( $0.7 < C_L < 1.3$ ).

The variation of unsteady normal force and pitching moment coefficients (rms values) is shown in Figures 8(a) and (b) for  $M=0.8$ . Some results at  $M=0.19$  and  $M=0.246$  are also included. Both quantities indicate a sharp rise in unsteadiness in the  $\alpha$ -range of  $25^\circ-27.5^\circ$ . The effect of the fences is to effect some delay in the rise. Normal force rather than lift coefficient was chosen to illustrate the variation of unsteadiness for the sake of simplicity, it being possible to record the rms value of the balance output directly. Similar characteristics occur for  $M=0.6$ , as shown in Figures 9(a) and (b). These curves show that the onset of the sharp increases in  $C_N'$  and  $C_M'$  occurs between  $2^\circ$  and  $5^\circ$  earlier than at  $M=0.8$  but approximately the same values of  $C_N'$  and  $C_M'$  are attained for  $\alpha \geq 30^\circ$ .

Our data at the low Mach numbers of 0.19 and 0.246 are limited to  $\alpha=30^\circ$  and  $24.5^\circ$  respectively. The unsteady force and moment coefficients for these conditions are also included in Figures 8(a) and (b). These results indicate slightly higher values of unsteady force and moment coefficients. However there are insufficient data to reach a conclusion regarding Mach number effects.

#### 2. Forward fuselage and LEX pressure distribution

##### (a) Canopy centre-line

Pressure coefficient distributions along the canopy centre-line are shown from  $\alpha=0^\circ$  to  $35^\circ$  at  $M=0.8$ ,

$Re_c = 3.8 \times 10^6$  in Figure 10. The critical value  $C_p^*$ , assuming isentropic flow, is marked at the appropriate level for each curve. Each curve is characterized by a compression-expansion-compression-expansion followed by a region of more uniform pressure prior to compression and expansion on the fuselage behind the canopy. Even at  $\alpha = 0^\circ$  there is a small zone of supersonic flow in the vicinity of the orifice at  $x/\bar{c} = 1.319$ . This region grows in extent and local Mach numbers increase such that at  $\alpha = 35^\circ$  supersonic flow is indicated from  $x/\bar{c} = 1.228$  to 1.798 with the peak Mach number of 1.33.

It should however be noted that it may be inappropriate to ascribe isentropic external flow over the canopy at some of the higher angles of incidence, due to the presence of vortical flow emanating from the forebody of the model with consequent loss of total pressure. However total pressure losses due to vortices shed from the forebody are expected to be small so that assuming isentropic flow for the canopy region would not be a serious error.

#### (b) Upper fuselage side

The development of the  $C_p$  distribution along this line of pressure orifices (17-28 in Figure 3) is shown at  $M = 0.8$ , in Figure 11, from  $\alpha = 0^\circ$  to  $35^\circ$ . The formation of forebody vortices is believed to commence at some  $\alpha$  slightly greater than  $15^\circ$  since at this angle the pressure is almost constant from  $x/\bar{c} = 1.336$  to 1.728. Peak suction occurs near  $x/\bar{c} = 1.728$  for all angles up to  $35^\circ$ , which was the highest angle in this experiment.

At all values of  $\alpha$  there is a short zone near  $x/\bar{c} = 1.06$  where near freestream velocities occur but upstream of this point local velocities rise rapidly with  $\alpha$ . Up to  $\alpha = 25^\circ$  the values of  $C_p$  at  $x/\bar{c} = 0.965$  are lower than at the downstream suction peak but beyond this angle the lowest pressures are seen at the downstream peak. The difference is largest at  $\alpha = 30^\circ$ . The peak suction is obtained with  $\alpha = 32.5^\circ$  at  $x/\bar{c} = 1.728$ .

The large adverse velocity gradients to be seen near  $x/\bar{c} = 1$ , and also 1.75, exhibit similar shapes for  $C_p$  distribution to those where shock-wave termination of supersonic flow occurs.

The above results apply to the LEX fences off case but closely similar pressure distributions were also obtained with the fences on.

Mach number effects on the fuselage pressure distribution are exemplified in Figure 12 where  $C_p$  distribution curves are shown for the fences off case at  $\alpha = 30^\circ$  for  $M = 0.19, 0.6$  and  $0.8$ .

#### (c) Upper surface of LEX

The development of the LEX upper surface pressure distributions along the two lines of orifices ( $y/\bar{c} = 0.253$  and  $0.355$ ) are shown for  $M = 0.8$  for the fences off case in Figures 13(a) and 13(b). The inner row distributions indicate the incipience of the vortex near  $\alpha = 5^\circ$ , when a reduction of pressure at the first orifice ( $x/\bar{c} = 1.662$ ), brought on by separation at the sharp leading edge, is seen. Subsequent increases in  $\alpha$  to  $10^\circ$  and  $15^\circ$  bring on extensive zones of low  $C_p$  with the peak suction point moving back to  $x/\bar{c} = 1.993$ . A further increase in  $\alpha$  to  $20^\circ$  causes a wholesale shift of the pressure profile to lower  $C_p$  values and a slight backward shift of the peak to  $x/\bar{c} = 2.060$ .

The minimum  $C_p$  that we could discern occurred near  $\alpha = 22.5^\circ$ . Further increases in  $\alpha$  cause a fundamental change in the pressure profile in that the suction peak near  $x/\bar{c} = 2$  collapses but the pressure from  $x/\bar{c} = 1.927$  forward goes on decreasing monotonically with  $\alpha$  to form a broad forward peak as indicated in the  $\alpha = 35^\circ$  curve.

This figure also shows the values of  $C_p$  deduced from a fixed pressure transducer at  $x/\bar{c} = 1.894$ ,  $y/\bar{c} = 0.263$ . Values of  $C_p$  indicated by this instrumentation are usually close to the data from the pressure orifices, although a large discrepancy can be seen at  $\alpha = 10^\circ$ . Since

this transducer is at a different lateral position from the line of orifices a difference in  $C_p$  may be indicative of lateral pressure gradients.

The positions of vortex bursts as determined in water tunnel tests (Reference 2) are marked. It will be noted that the position at  $\alpha = 30^\circ$  roughly coincides with the collapse of the pressure peak. At  $\alpha = 25^\circ$  there is an abrupt flattening of the  $C_p$  profile a short distance forward of the marked burst point. These effects may be related.

Unlike the  $C_p$  profiles for the upper fuselage side these LEX pressure profiles do not exhibit precipitous increases in pressure. It seems that there are extensive areas of supersonic flow at all angles above  $10^\circ$  (precise limits cannot be set) but relatively gradual diffusion of the flow rather than deceleration through shock waves appears to predominate. The positive peak pressures behind the diffusion zone move rearwards with  $\alpha$  increasing.

Pressure distributions at the outer row are shown in Figure 13(b). The suction peak that is established at  $\alpha = 15^\circ$  increases sharply to  $C_p = -1.25$  and moves back to  $x/\bar{c} = 2.425$  for  $\alpha = 20^\circ$ . The lowest value of  $C_p$  was found to be  $-1.3$  occurring at  $x/\bar{c} = 2.36$  for  $\alpha = 22.5^\circ$  but a subsequent increase in  $\alpha$  to  $25^\circ$  effected a forward shift of the peak to  $x/\bar{c} = 2.292$  and an increase in  $C_p$  to  $-1.17$ . Complete collapse of the peak followed increases of  $\alpha$  to  $30^\circ$  and  $35^\circ$  and unlike the inner row profile the low pressures do not appear to have been re-established at  $\alpha = 35^\circ$ .

Values of  $C_p$  from two fixed pressure transducers, at  $x/\bar{c} = 2.392$  and  $2.59$ , are shown in Figure 13(b). The data from these agree well in some cases but poorly in others. Again their lateral positions were not quite the same as that of the line of orifices.

The positions of the vortex bursts are in qualitative agreement with the collapse of the pressure peaks for  $\alpha > 25^\circ$ . Diffusion from the peak low pressures occurs fairly gradually, as at the inner row.

Profiles of  $C_p$  for the 'fences on' case at  $M = 0.8$  are shown in Figure 14(a). The development of the vortical flow follows that with fences off, with similar collapse of the suction peak (near  $x/\bar{c} = 2$ ) at  $\alpha = 30^\circ$  and establishment of a broad peak, located forward, at  $\alpha = 35^\circ$ . At  $\alpha = 15^\circ$  to  $30^\circ$  inclusive the effect of the fence is to cause a very abrupt rise in pressure very close to the fence leading edge. Figure 14(b) shows  $C_p$  profiles for the outer row of orifices in the presence of the fence. The local effect of the fence is exhibited in this figure through the sharply peaked profiles that are produced. These commencing at  $\alpha = 10^\circ$  reach higher suction peaks than the fence off case, with the highest occurrence at  $\alpha = 25^\circ$ . Unlike the inner row the suction peak is maintained to  $\alpha = 30^\circ$  but at  $35^\circ$  it collapses.

Some direct comparisons between fence on and fence off  $C_p$  profiles are shown in Figure 15(a). For clarity symbols are omitted and the origins are staggered. It is seen that at all angles of incidence, forward regions of the profiles are virtually unaffected by the presence of the fence but for  $\alpha = 35^\circ$  the entire profile is unaffected. Possibly this is because the vortex has burst well forward of the fence and there is no organised vortical flow to act on it. Similar results for  $M = 0.6$  are reported in Reference 2 but the pressure gradients seen with fences on are less acute at this lower Mach number.

Comparisons for the outer LEX  $C_p$  profiles are shown in Figure 15(b). They demonstrate a large effect of the fence over the entire range of  $x/\bar{c}$  with the exception of data at  $\alpha = 35^\circ$  where again it can be seen that the fence has virtually no effect due to vortex bursting well ahead of the fence (at  $x/\bar{c} = 1.66$ ). However if the burst position at  $\alpha = 30^\circ$  with fences on is close to that 'fence off' ( $x/\bar{c} = 2.13$ ) it would appear that the fence is effective in promoting the high peak suction in spite of being immersed in turbulent flow.

Mach number effects at  $M = 0.19, 0.6$  and  $0.8$  on the inner and outer row of LEX orifices at  $\alpha = 30^\circ$  are shown in

Figure 16(a) (fences off) and Figure 16(b) (fences on). It will be noted that the Mach number effect is large - the peak suction being approximately halved between  $M=0.19$  and  $0.8$ . It is also noticeable that whereas the addition of LEX fences has little effect on the forward part of the inner pressure distribution ( $y/c=0.253$ ) at  $M=0.6$  and  $0.8$ , this is not the case at  $M=0.19$  since  $C_p$  is increased from  $-2.8$  to  $-2.55$  with the fences. Figures 17(a) and 17(b) show effects at  $\alpha=25^\circ$  and  $M=0.246, 0.6$  and  $0.8$  at the inner row of orifices only.

The foregoing pressure data was obtained with the vortex rake mounted since results at  $M=0.19, 0.246$  and  $0.8$  were obtained with this configuration only. Comparative data for vortex rake on and off is shown at  $M=0.6$  in Figure 18 for a fence off condition. At  $\alpha=15^\circ$  the rake interference is quite small but at  $\alpha=30^\circ$  it is obviously a matter for some concern, if absolute accuracy is required. However the relative performance comparisons that have been made are considered to be valid.

In Figure 19 unsteady pressure effects at  $M=0.8$  on the LEX upper surface are shown as plots of the rms values of  $C_p$ , measured at the four surface pressure transducers, versus  $\alpha$ . The data is presented for fence off and on configurations. The first transducer indicates a sharp rise in  $C_p$  between  $32.5^\circ$  and  $35^\circ$ , the presence of the fence having a small but beneficial effect in reducing the unsteadiness. Transducer 2 which is almost in-line with the fence and ahead by  $0.175$  in  $x/c$  shows a large reduction in  $C_p$  for  $\alpha>25^\circ$ . Transducer 3 which is adjacent to the fence and just outside indicates a sharp upturn in  $C_p$  at  $\alpha=22.5^\circ$  with fences off and  $5^\circ$  later with fences on. In the interval from  $\alpha=30^\circ$  to  $35^\circ$  the improvement is reduced. The fourth transducer which is downstream of the fence and well outside its line shows the greatest effect of the fence for  $22.5^\circ \leq \alpha \leq 32.5^\circ$ .

Similar results are given in References 2 and 3 for  $M=0.6$ .

At low speeds we tabulate  $C_p$  at  $\alpha=24.5^\circ$  and  $30^\circ$  as follows:

M	$\alpha^\circ$	Configuration	$C_{p1}$	$C_{p2}$	$C_{p3}$	$C_{p4}$
0.19	30	fences off	0.047	0.096	0.073	0.085
0.19	30	fences on	0.039	0.086	0.50	0.264
0.246	24.5	fences off	0.032	0.058	0.045	0.053
0.246	24.5	fences on	0.03	0.053	0.52	0.225

The 'fences off' values of  $C_p$  at each transducer generally agree with values shown in Figure 19, as do the 'fences on' values at the first two transducers. The very high values of  $C_p$  'fences on' at transducers 3 and 4 are noted but we cannot suggest reasons for them. We have no reason to fault the instrumentation. These values exceed the comparable data at  $M=0.6$  and  $0.8$  by up to a factor of 5.

### 3. Surface Flow Visualization

Figure 20 displays surface streamlines on the upper surface of the wing and part or whole of the LEX for 'fence off' and 'fence on' configurations. The display was obtained by 'dotting' the surface with an oil and lamp-black mixture then performing a 10 second wind tunnel run at a fixed angle-of-incidence. The streamlines show features of the surface flow for  $M=0.6$  at  $\alpha=30^\circ$ . The influence of the LEX fence is seen to be local, the surface flow on the leading-edge flap, wing and fuselage fillet being virtually the same in each case. This conclusion is supported by the small changes that have been seen in  $C_L$  and  $C_M$  from 'fences off' to 'fences on'.

### 4. Fin Pressure Distribution

Examples of the fin steady  $C_p$  distributions on each side of the fin at  $M=0.8, 0.6$  and  $0.19$  at  $\alpha=30^\circ$ , fences on

and off, are shown in Figures 21, 22 and 23 respectively. The locations of the rows of pressure transducers are indicated in Figure 4 and given in Table 3. For clarity each set of curves is displaced upwards, the position of the baseline being indicated in the figures with the row number in parentheses.

At  $M=0.8$  (Figure 21) the effect of the fence is quite substantial on each surface, unlike the results for  $M=0.6$  (Figure 22) where the effect of the fences on the outboard surface is small but quite large on the inboard. At  $M=0.8$  the fences consistently increase  $C_p$  along each row of transducers on the outboard surface. On the inboard surface the effect is to increase  $C_p$  along rows 1 and 2 (near the fin root) but the opposite holds for the four outer rows. At  $M=0.6$  (Figure 22) the effect of the fences is to decrease  $C_p$  substantially at all measurement points on the inboard surface. The shape of the pressure distributions is generally the same at  $M=0.8$  and  $0.6$  but this does not hold at  $M=0.19$ .

Figure 23 indicates a mixed effect of the fences at  $M=0.19$ . The effects are roughly similar on each surface but with the exception of rows 2 and 5 on the inboard and rows 4, 5 and 6 on the outboard surface there is no clear effect of the fence at this low speed. On these rows the effect of the fences is to increase  $C_p$ . Unlike the results at the high speeds some of the greatest increases in  $C_p$  now occur towards the tip of the fin.

As may be expected the  $C_p$  profiles are affected by the presence of the vortex rake.

Figures 24, 25 and 26 show the variation of the normal force coefficient acting on the fin. These were computed from the measured pressure distributions by the equation

$$C_{Nf} = \sum_{j=1}^{24} (p_{ij} - p_{oj}) A_j / q A_F$$

and is positive in the outward direction. The areas  $A_j$  for each panel are indicated in Figure 4. It is assumed that the pressure is constant over each panel.

Figures 24 and 25 show the variation of  $C_{Nf}$  with  $\alpha$  at  $M=0.8$  and  $0.6$  respectively with the vortex rake mounted while Figure 26 gives  $C_{Nf}$  at  $M=0.6$  with the vortex rake removed. At each Mach number a reduction in  $C_{Nf}$  is effected by the LEX fences (starting at about  $15^\circ$  in  $\alpha$ ) but the decrement is larger at  $M=0.6$  and extends to  $\alpha=35^\circ$  compared with  $25^\circ$  at  $M=0.8$ . The peak values are about the same. The change in  $C_{Nf}$  between  $\alpha=15^\circ$  and  $27.5^\circ$  indicates a large change in the effective angle-of-attack of the fin.

The pressure data on which  $C_{Nf}$  is based was found to be extremely repeatable - at  $M=0.6$  data from two runs at  $\alpha=30^\circ$  and three runs at  $35^\circ$  gave a variation in  $C_{Nf}$  of only 0.001 while at  $M=0.8$  repeated multiple incidence runs also showed variations of only 0.001 at all angles above  $20^\circ$  and 0.002 below this.

Comparison of Figures 25 and 26 illustrates the influence of the vortex rake on the fin steady force. It will be noted that aside from increases in peak values of about 12% on the positive side the removal of the rake does not materially change any conclusions to be drawn regarding the fence effects.

Unsteady pressures on the fins are shown in Figures 27, 28 and 29 relating to  $M=0.8, 0.6$  and  $0.19$  respectively at  $\alpha=30^\circ$ . The curves are displaced for clarity. It is clear that the fences confer distinct improvements in reducing the unsteady pressure coefficients on the fin inboard surface at each Mach number, the reductions becoming greater as the Mach number is reduced. On the outboard surface consistent reductions in unsteady pressure coefficients along each row are seen only at  $M=0.19$ . They are generally smaller than on the inboard surface. At  $M=0.8$  and  $0.6$ , for the

rows nearer the fin root the effect is mixed.

The unsteady forces on each side of the fin were derived by integration of the unsteady pressure coefficients by a scheme similar to that for derivation of the fin steady force. The unsteady normal force coefficient on the inboard surface is given by:

$$C'_{Ni} = \sum_{j=1}^{24} p_{i \text{ rms } j} A_j / q A_F$$

and the coefficient for the outboard surface is found by replacing  $p_{i \text{ rms}}$  by  $p_{o \text{ rms}}$ . The inboard and outboard sides were summed separately as we had no information on phasing of signals from inboard and outboard transducers at the time of the data reduction.

This formulation assumes that the rms pressures are constant over each panel of the fin and that the fluctuations are correlated on the panel but uncorrelated between adjacent panels.

Figure 30 shows the variation of  $C'_{Ni}$  and  $C'_{No}$  with  $\alpha$  at  $M=0.8$ . On the inboard surface small reductions in  $C'_{Ni}$  due to the LEX fences are noted between  $\alpha=15^\circ$  and  $22.5^\circ$  but become large in the interval  $22.5^\circ$  to  $30^\circ$  - up to 40% of the 'fence off' value is seen at  $\alpha=27.5^\circ$ . Reductions in  $C'_{No}$  on the outboard surface commence at  $\alpha=15^\circ$  and remain fairly constant at about 16% of the 'fence off' level up to  $\alpha=30^\circ$ . A rapid rise in  $C'_{No}$  (regardless of fences) commences between  $\alpha=5^\circ$  and  $10^\circ$  compared with about  $22.5^\circ$  for the inboard surface.

Figure 31 shows the variation of  $C'_{Ni}$  and  $C'_{No}$  with  $\alpha$  at  $M=0.3$ . The general shape of the curves is different and the values achieved fence on and off are considerably more than at  $M=0.8$ . The effectiveness of the fences in reducing the unsteady force coefficients is rather less than at  $M=0.8$  e.g. at  $\alpha=27.5^\circ$  a reduction of 33% in  $C'_{Ni}$  is achieved.

The results displayed in Figures 30 and 31 were obtained with the vortex rake in place.

At low speed we have the following results:

M	$\alpha^\circ$	Fences off		Fences on	
		$C'_{Ni}$	$C'_{No}$	$C'_{Ni}$	$C'_{No}$
0.19	30	0.168	0.178	0.102	0.148
0.246	24.5	0.104	0.158	0.061	0.121

The reductions in unsteady force coefficient are close to those at  $M=0.8$  for the inner surface and rather higher on the outer surfaces.

## 5. Analysis of Unsteady Signals

### (a) LEX Pressure transducer signals

Figures 32 and 33 show the power spectral density of the unsteady signals from the first and third pressure transducers, that are fixed in the LEX surface (Figure 3), at  $M=0.6$ .

In figure 32 the P.S.D. is plotted against the non-dimensional frequency  $k$  at  $\alpha=30^\circ$ , fences off and on while Figure 33 gives results at  $\alpha=35^\circ$ .

It will be seen that the effect of the fences is generally to lower the level at each transducer for  $\alpha=30^\circ$  whereas at  $\alpha=35^\circ$  the level at transducer 1 is lowered but increased at transducer 3.

There is a difference in level of the signal at transducer 1 between  $\alpha=30^\circ$  and  $35^\circ$ . The low speed water tunnel data (Reference 2) suggests that the vortex bursting takes place behind this transducer at  $\alpha=30^\circ$  but ahead of it at  $35^\circ$ . The higher level of  $C_p$  at transducer 1 for  $\alpha=35^\circ$  would be caused by the high turbulence in the bursting vortex.

### (b) Fin pressure transducer signals

Figures 34 to 37 show broadband cross-correlation functions on the inboard and outboard surfaces of the fin, in which the first transducer in the second row (transducer 6) is used as the reference.

The cross-correlation, defined as

$$R_{12}(\tau) = \lim_{T \rightarrow \infty} \frac{1}{T} \int_{-T}^T F_1(t) F_2(t+\tau) dt$$

was obtained by processing digitized FM tape recordings of the unsteady signals using the IEEE CCSE routine (Reference 5). The sampling frequency and FFT length for each case were 80,000 Hz and 8192 samples respectively. The test conditions were  $M=0.6$ ,  $\alpha=30^\circ$  with LEX fences on and the vortex rake off. Figure 34 shows that the unsteady pressure field on the inboard surface is well correlated in the chordwise direction along the second row. The average broadband eddy convection velocity, computed from the distance between the reference transducer and those following and the time displacements of the peak correlation function is 490 ft/second i.e.  $0.72U$ .

Figure 35 shows the results of cross-correlation in the spanwise direction from transducer 6 along transducers 11, 16 and 20. The correlation becomes poor rapidly towards the tip of the fin as indicated by the curves labelled  $R(6, 16, \tau)$  and  $R(6, 20, \tau)$ .

On the outboard surface we see the opposite to these effects. Figure 36 shows a poor correlation in the chordwise direction, considering transducer 6 (outboard) as the reference, whereas Figure 37 demonstrates the unsteady pressure field out towards the tip from transducer 6 to be well correlated. The average broadband eddy convection velocity is found to be about 600 ft/second ( $0.88U$ ).

Good spanwise correlation is also seen beyond the fin mid-chord line. Figure 38 shows the correlation curves for transducer 4 (the reference) and transducers 9, 14, 19 and 22 on the outboard surface. An eddy convection velocity of about 300 ft/second ( $0.44U$ ) is estimated. The reason for the large correlation distance along the line of these transducers is believed to be that they lie close to the surface streamlines on the fin surface (Reference 2, Figure 13(b)).

## 6. Vortex Wake

Stagnation pressure coefficient contours at  $M=0.19$  and  $\alpha=30^\circ$ , in the vortical flow immediately behind the vertical fin, are shown for 'fences off' and 'fences on' configurations respectively in Figures 39 and 40. At this low Mach number the freestream value of  $C_p$  is 1.009 so it is clear that in each case the entire cross-section of the flow shown in each figure is below freestream stagnation pressure. The effect of the LEX fence appears to be an elongation and a flattening of the low pressure region that straddles the fin, e.g. the  $C_p=0$  contour and the occurrence of cells of low  $C_p$  on each side of the fin. Also the mean value of  $C_p$  inside the  $C_p=0$  contour appears to be higher with the fences on.

Unsteady pressure coefficients are given in the following tables which show the value of  $C_p$  along the vertical and horizontal centre-lines of the vortex wake.

Point	H1	H2	H3	V4	H4	H5	H6
$C_p$ (fences off)	0.341	0.262	0.181	0.208	0.275	0.300	0.394
$C_p$ (fences on)	0.262	0.236	0.156	0.176	0.270	0.195	0.330
Point	V1	V2	V3	V4	V5	V6	V7
$C_p$ (fences off)	0.392	0.221	0.158	0.208	0.316	0.433	0.417
$C_p$ (fences on)	0.374	0.252	0.161	0.176	0.248	0.351	0.391

At all horizontal points the fences bring about a reduction in  $C_p$ . The effect is mixed in the vertical direction but the majority show a reduction.

Figures 41 and 42 give contours of  $C_p$  at  $M=0.8$  and  $\alpha=30^\circ$ , fences off and on respectively. At the high speed condition the freestream value of  $C_p$  is 1.17. It may be inferred that the region of vortical flow is larger than in the low speed case, by a comparison of the areas inside the contours e.g. the  $C_p=0$  and  $-0.24$  contours enclose considerably larger areas at high speed. Also regions of lower  $C_p$  are seen at  $M=0.8$  than at 0.19.

With the fences on, the shape of the vortical region changes to a more elongated region but contrary to the low speed case the lowest pressure regions are now seen with fences on.

The lobe on the inside of the fin, Figure 42, with fences on is very similar in shape to that observed at low speed, Figure 40. This appears to be a region influenced by the LEX fence tip vortex.

Values of  $C_p$  measured at the rake's dynamic transducers are as follows:

Point	H1	H2	H3	V4	H4	H5	H6
$C_p$ (fences off)	0.255	0.216	0.15	0.123	0.210	0.280	0.453
$C_p$ (fences on)	0.111	0.093	0.096	0.139	0.242	0.282	0.435

Point	V1	V2	V3	V4	V5	V6	V7
$C_p$ (fences off)	0.311	0.204	0.145	0.123	0.191	0.373	0.536
$C_p$ (fences on)	0.215	0.136	0.119	0.139	0.221	0.379	0.519

At  $M=0.8$  these data indicate that the fences promote a reduction in unsteadiness outboard and towards the tip of the fin but an increase inside the fin and towards the root.

### CONCLUSIONS

The following conclusions are drawn from the wind tunnel investigation:

The measurements generally exhibited good repeatability and gave us confidence in the data. The interference effects of the vortex rake were established at  $M=0.6$ . The interference did not obscure the incremental effects (mean or unsteady) that occur when the LEX fences were mounted.

The aircraft mean force and moment characteristics were only marginally changed by the addition of the LEX fences either at  $M=0.6$  or  $0.8$  (or at the low Mach numbers of 0.19 and 0.246 for which data were limited to single angles). However the unsteady values of  $C_N$  and  $C_M$  were quite distinctly reduced by the presence of the fences.

Pressure distributions in the neighbourhood of and on the LEX show large changes over the angle-of-attack range. The upper fuselage side pressure distribution appears to be influenced by the forebody vortices in its forward regions. LEX pressure distributions indicate the formation of the LEX vortex at a quite low angle-of-attack, near  $5^\circ$ . Very high suction peaks were measured on the LEX and very rapid recompressions with LEX fences on. Mach number influence on LEX pressure distributions are strong especially at  $\alpha=30^\circ$ . For this angle the pressure peak at  $M=0.8$  collapses. The effect of the vortex rake on mean pressure distribution on the LEX is significant at  $\alpha=30^\circ$  but quite small at  $\alpha=15^\circ$ . Incremental effects however are hardly affected. Rapidly rising unsteady pressures were recorded on the LEX at angles-of-attack in excess of about  $22.5^\circ$ , depending on location of the monitored point, at  $M=0.8$ , similar to some earlier reported results at  $M=0.6$ . The LEX fences delay the rise in unsteady pressures. At the lowest Mach numbers some very high values of the unsteady pressure coefficients were noted at two locations near the LEX fence. Further investigation is required to validate these data.

The mean value of aerodynamic force coefficients on the fins was reduced by the presence of the

LEX fences at  $M=0.8$  over most of the range of  $\alpha$ , but the reductions were not as large as those for  $M=0.6$ . Significant reductions were also observed at low speed.

At the higher values of  $\alpha$  unsteady force coefficients computed from pressures on the fin surfaces indicate that reductions due to the fences are relatively insensitive to Mach number on the inboard surface but on the outboard surface larger reductions are to be seen at low Mach number.

Processing of 'fence on' unsteady pressure signals at  $\alpha=30^\circ$  for  $M=0.6$  at various points on the fin revealed sharply differing correlations in chordwise and spanwise directions from the inboard and outboard surfaces respectively. Other Mach numbers and model attitudes may exhibit different behaviour.

The vortex wake measurements of stagnation pressure demonstrate a low pressure region with lateral and vertical directions considerably larger than fin height. The LEX fences cause large changes in the shape of the pressure contours and the signature of the fence vortex is clearly seen. At low Mach number, for  $\alpha=30^\circ$ , the fence has the effect of raising the stagnation pressure across the vortex field but the opposite hold at  $M=0.8$ .

At the high angles-of-attack that are of interest the measurements on the model and in the vortex wake indicate a very complicated flowfield. Considerable work is further required to achieve more understanding of the phenomena.

### ACKNOWLEDGEMENTS

The wind tunnel programme was supported in part by the Department of National Defence. We are grateful to them and to the National Research Council for the use of facilities and permission to publish.

We are indebted to colleagues in the High Speed Aerodynamics Laboratory for their work on the instrumentation of the model, data acquisition system and ongoing data reduction.

### REFERENCES

1. Frazier, F. Alan, "F-18 Hornet - LEX fence flight test results" Society of Experimental Test Pilots' Symposium, Beverley Hills, California, October 1988.
2. Lee, B.H.K. et al, "Wind tunnel investigation and flight tests of tail buffet on the CF18 aircraft" Paper No. 1, AGARD Specialists Meeting on Aircraft Dynamic Loads, Structures and Materials Panel, Sorrento, Italy, 1-6 April 1990.
3. Lee, B.H.K. and Brown, D., "Wind tunnel studies of F/A-18 tail buffet." AIAA 16th Aerodynamic Ground Testing Conference, Seattle, Washington, June 18-20, 1990.
4. Erickson, G.E. et al, "Experimental investigation of the F/A-18 vortex flows at subsonic through transonic speeds." AIAA-89-2222 (Invited paper), AIAA 7th Applied Aerodynamics Conference, Seattle, Washington, July 31-August 2, 1989.
5. Carter, G.C. and Ferrie, J.F., "A Coherence and Cross Spectral Estimation Program." Chapter 2.3 in "Programs for digital signal processing". IEEE Press, 1979, Institute of Electrical and Electronics Engineers, New York.

**Table 1. Pressure Orifice Locations on LEX**

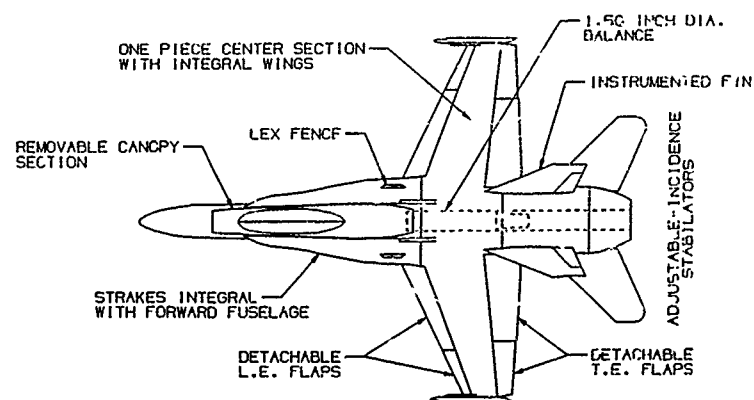
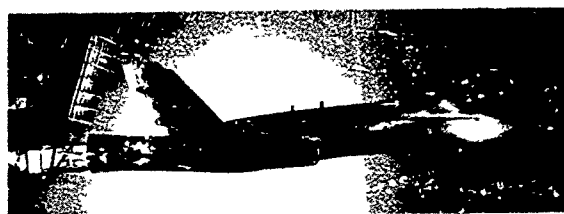
Orifice No. (Fig. 3)	x/c	y/c	Orifice No. (Fig. 3)	x/c	y/c
29	1.662	0.253	41	2.458	0.253
30	1.728	0.253	42	2.524	0.253
31	1.794	0.253	43	2.590	0.253
32	1.861	0.253	44	2.657	0.253
33	1.927	0.253	45	2.160	0.355
34	1.993	0.253	46	2.226	0.355
35	2.060	0.253	47	2.292	0.355
36	2.126	0.253	48	2.358	0.355
37	2.192	0.253	49	2.425	0.355
38	2.259	0.253	50	2.491	0.355
39	2.325	0.253	51	2.557	0.355
40	2.391	0.253	52	2.623	0.355

**Table 2. Pressure Transducer Locations on LEX  
(Figure 3)**

Transducer No.	x/c	y/c
1	1.894	0.263
2	2.126	0.297
3	2.392	0.335
4	2.590	0.364

**Table 3. Pressure Transducer Locations on Vertical Fin**

Transducer No. (Fig. 4)	x <sub>f</sub> /c <sub>f</sub>	y <sub>f</sub> /c <sub>f</sub>	Transducer No. (Fig. 4)	x <sub>f</sub> /c <sub>f</sub>	y <sub>f</sub> /c <sub>f</sub>
1	0.252	0.141	13	0.924	0.578
2	0.453	0.141	14	1.061	0.578
3	0.653	0.141	15	1.197	0.578
4	0.853	0.141	16	0.888	0.816
5	1.053	0.141	17	0.971	0.816
6	0.434	0.339	18	1.072	0.816
7	0.605	0.339	19	1.174	0.816
8	0.776	0.339	20	1.100	0.985
9	0.947	0.339	21	1.177	0.985
10	1.119	0.339	22	1.236	0.985
11	0.651	0.578	23	1.180	1.035
12	0.788	0.578	24	1.230	1.035

**Fig. 1 F/A-18 model features**

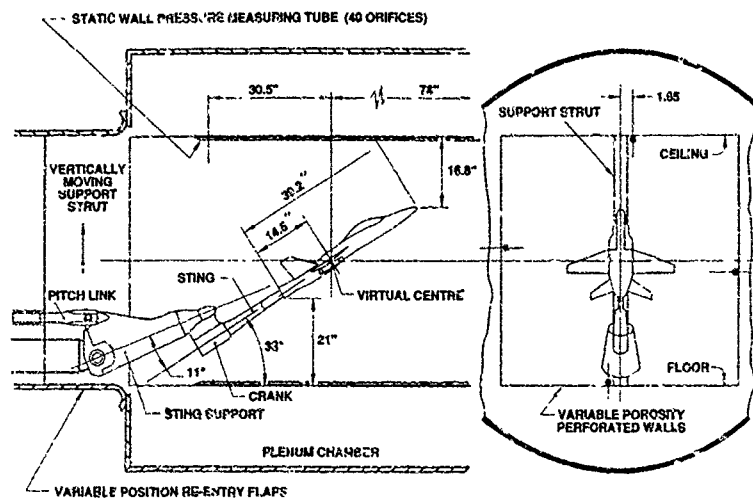


Fig. 2 Model support in transonic test-section

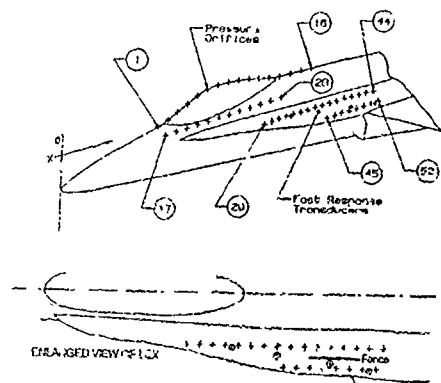


Fig. 3 Forward fuselage and LEX pressure measurement locations

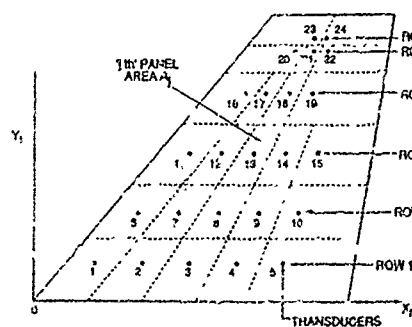


Fig. 4 Fin pressure transducer locations

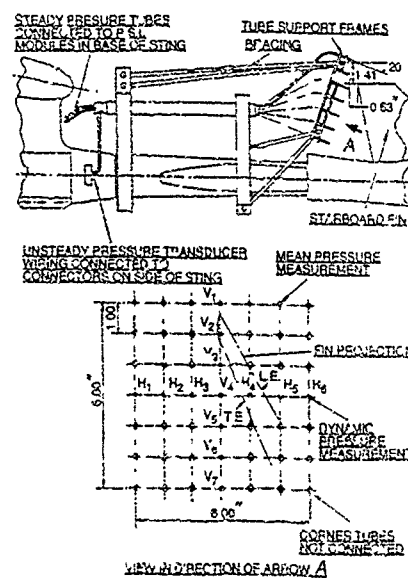
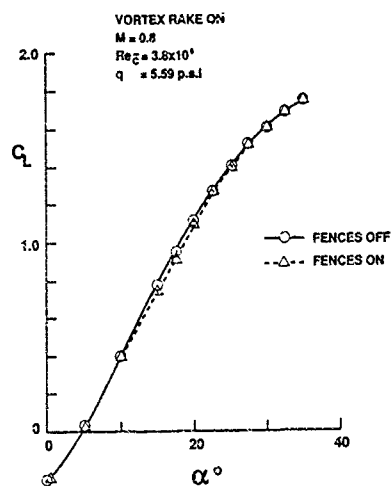
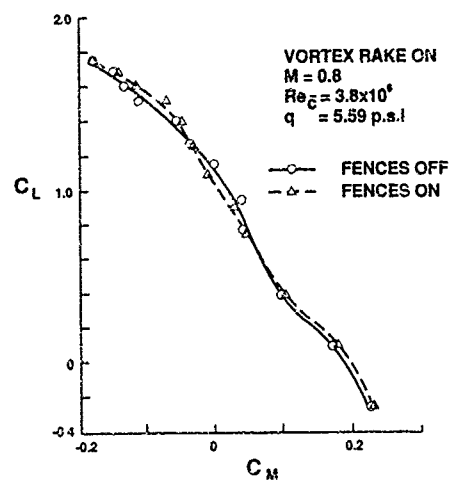
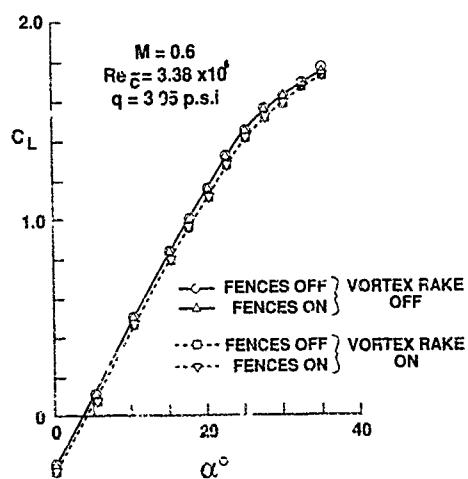
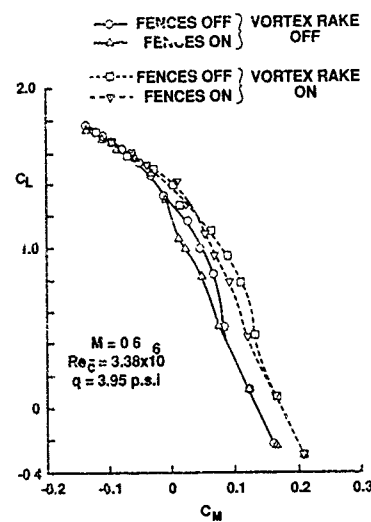
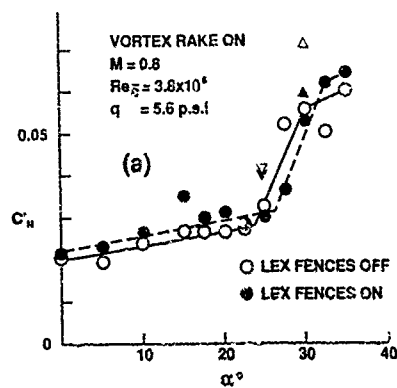
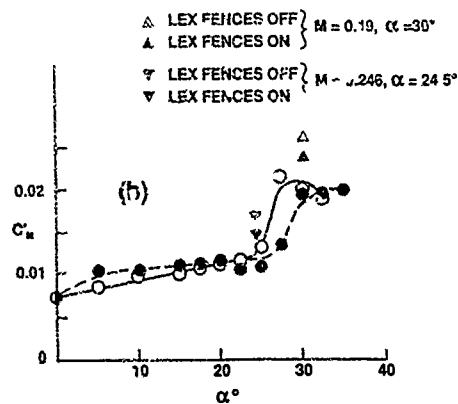
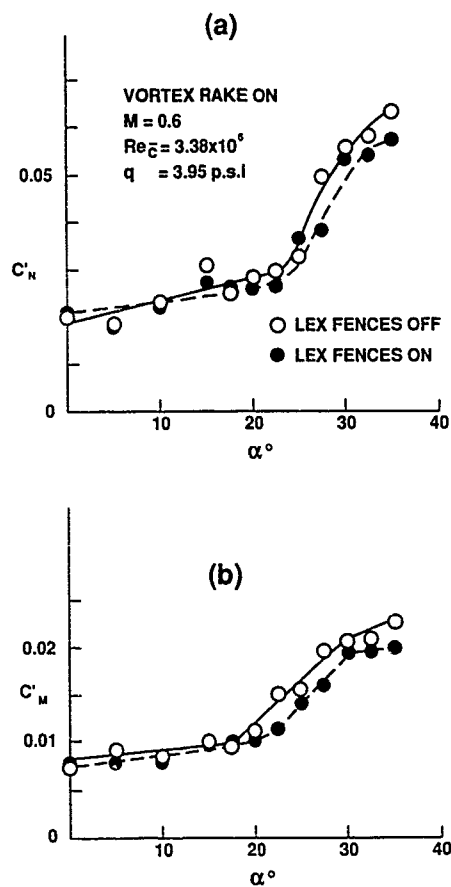
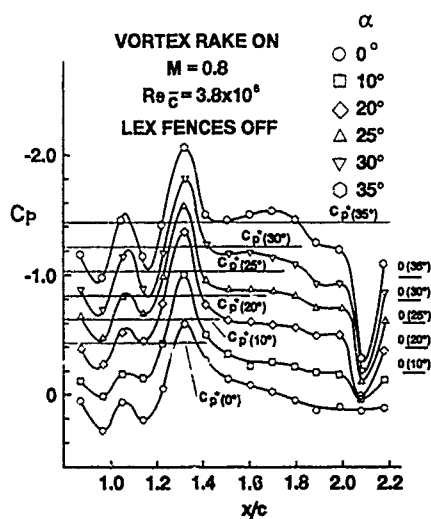
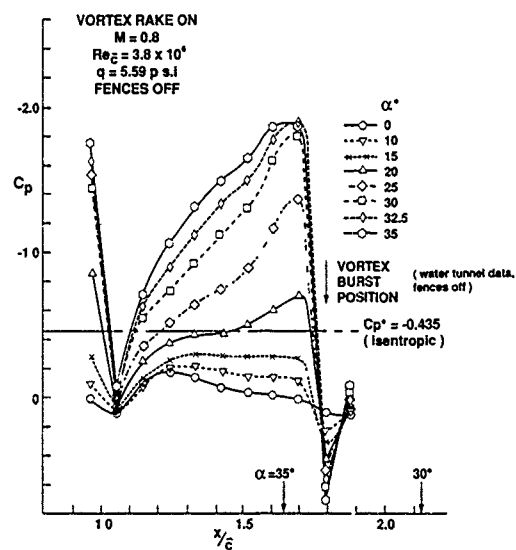
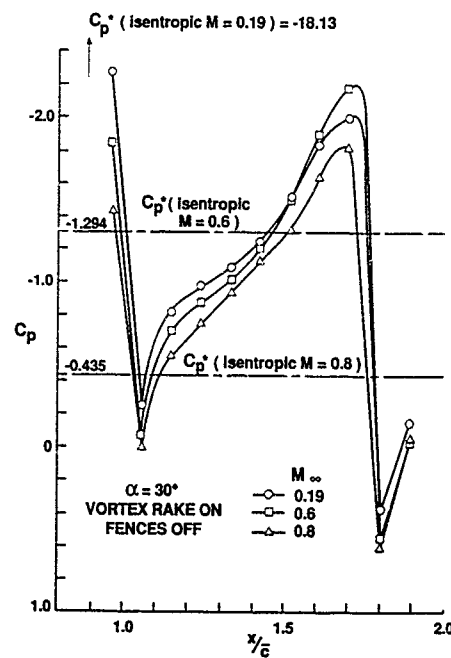
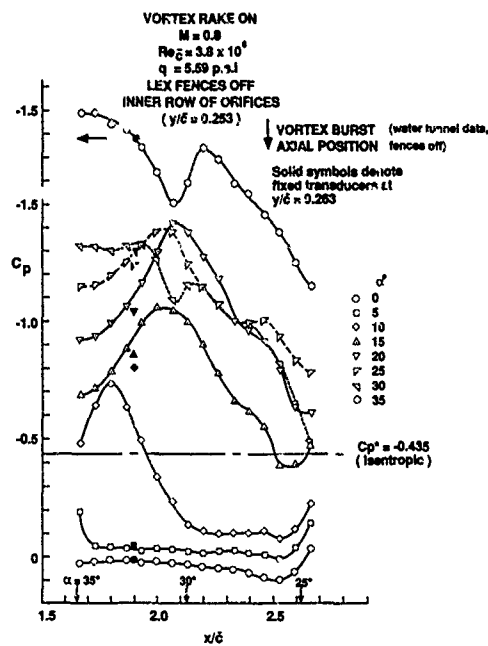
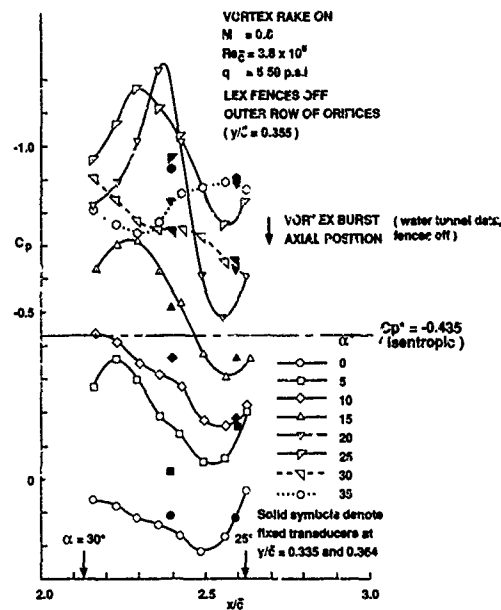
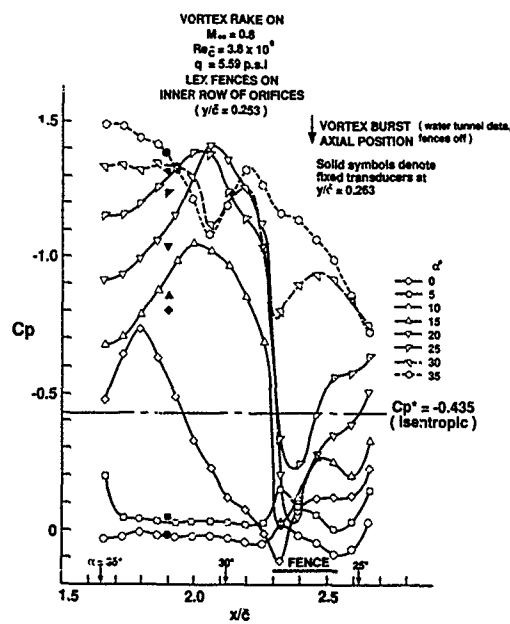
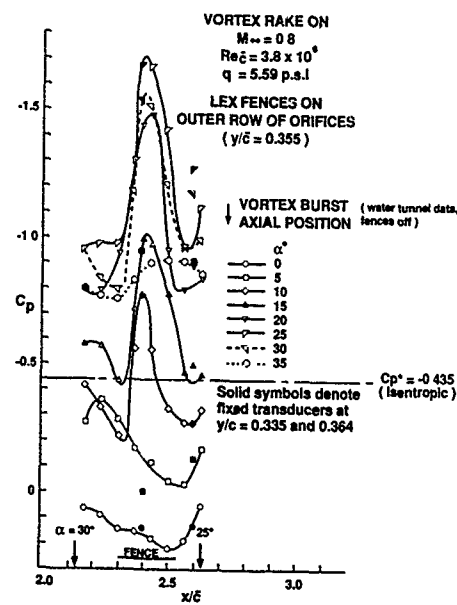


Fig. 5 Vertex rake



Fig. 6(a) Lift coefficient versus  $\alpha$ Fig. 6(b) Pitching moment coefficient versus  $\alpha$ Fig. 7(a) Vortex rake interference on  $C_L$  at  $M=0.6$ Fig. 7(b) Vortex rake interference on  $C_M$  at  $M=0.6$ Fig. 8  $C_N$  and  $C_M$  versus  $\alpha$  at  $M=0.8$ 

Fig. 9  $C'_N$  and  $C'_M$  versus  $\alpha$  at  $M=0.6$ Fig. 10 Canopy centre line  $C_p$  distributionFig. 11 Fuselage side  $C_p$  distributionFig. 12 Mach number effect on fuselage side  $C_p$

Fig. 13(a) Inner LEX  $C_p$  distribution, fences offFig. 13(b) Outer LEX  $C_p$  distribution, fences offFig. 14(a) Inner LEX  $C_p$  distribution, fences onFig. 14(b) Outer LEX  $C_p$  distribution, fences on

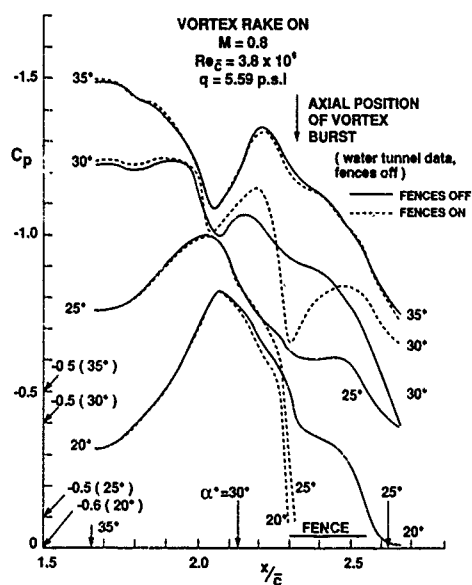


Fig. 15(a) Fences off, fences on comparisons, inner LEX

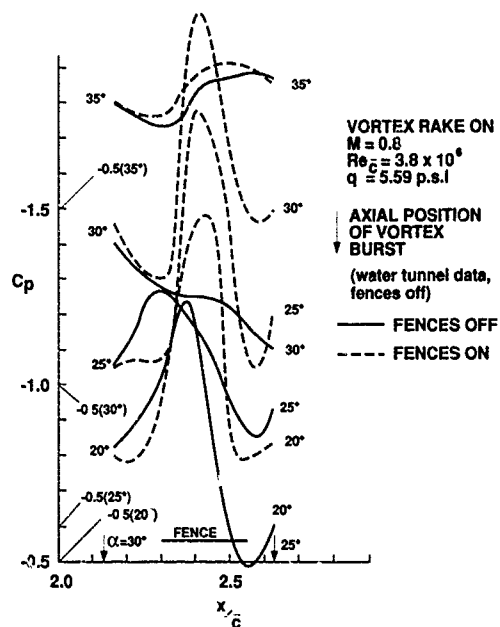
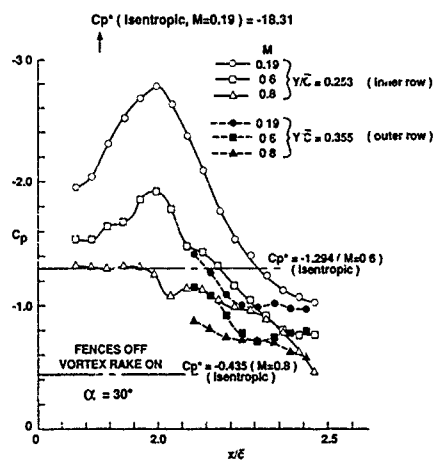
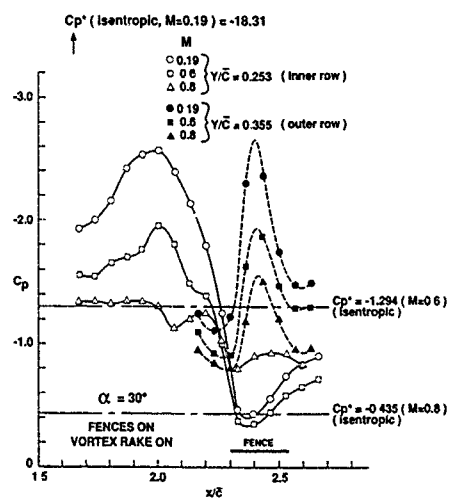
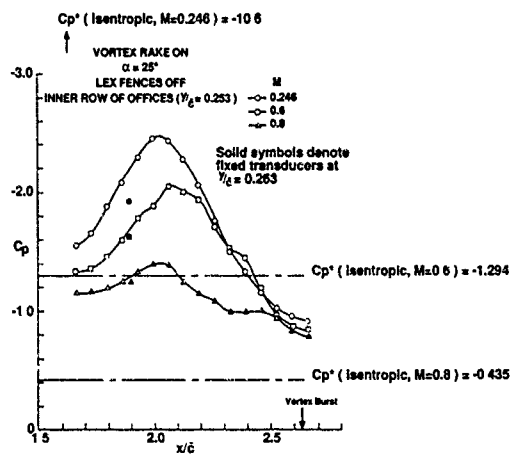
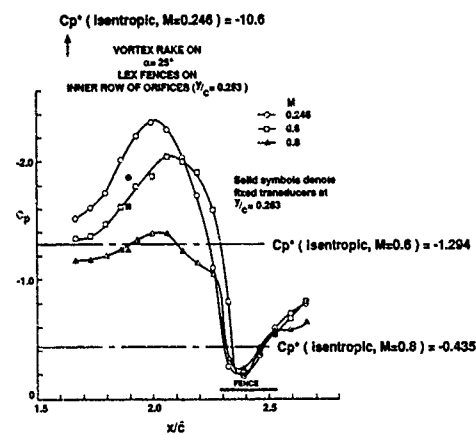
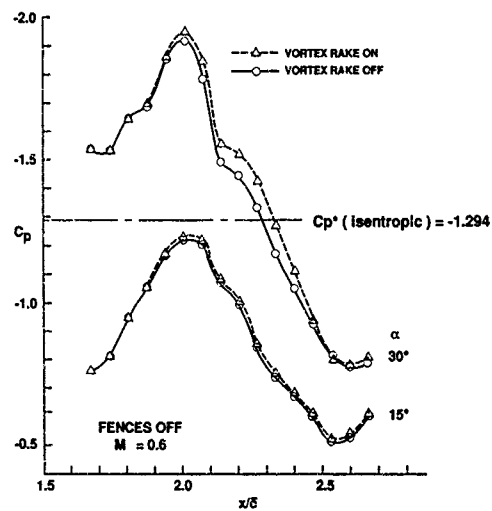
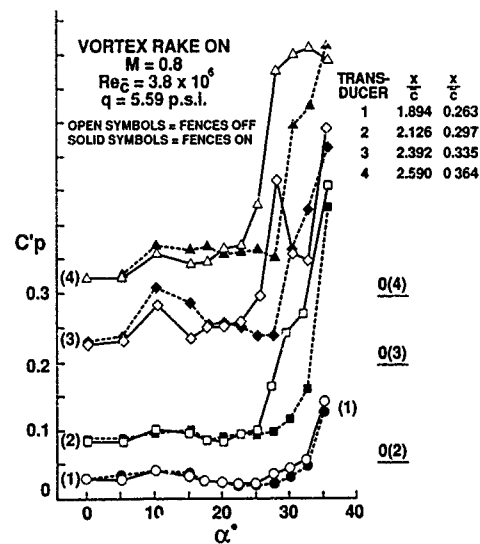


Fig. 15(b) Fences off, fences on comparisons, outer LEX

Fig. 16(a) Mach number effect on LEX  $C_p$  fences offFig. 16(b) Mach number effect on LEX  $C_p$  fences on

Fig. 17(a) Mach number effect on LEX  $C_p$ , fences offFig. 17(b) Mach number effect on LEX  $C_p$ , fences onFig. 18 Vortex rake interference on LEX  $C_p$ Fig. 19 LEX unsteady  $C_p$  versus  $\alpha$

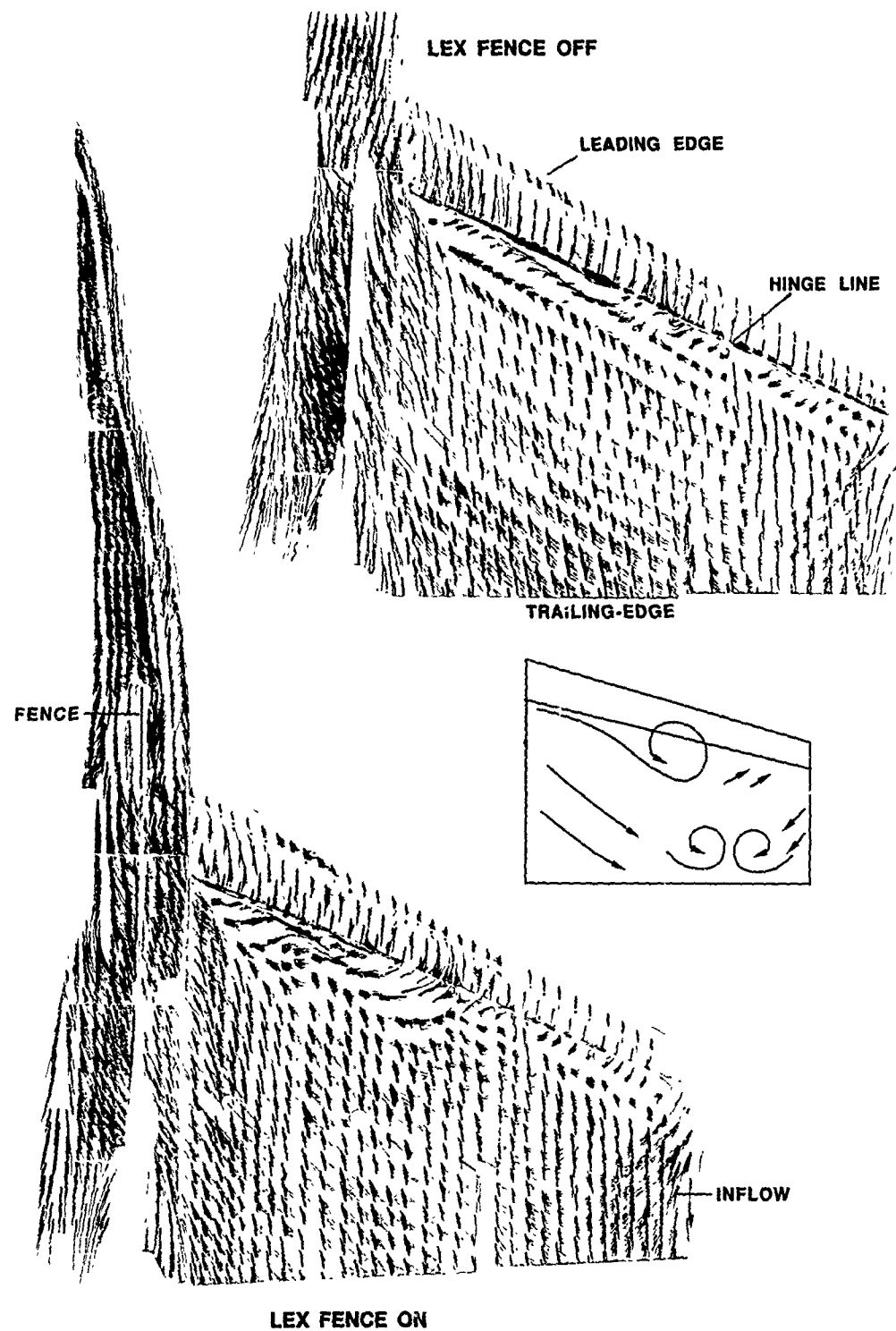
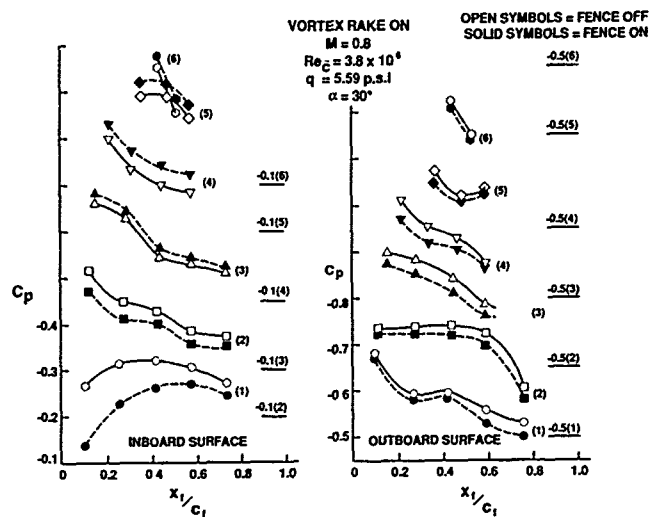
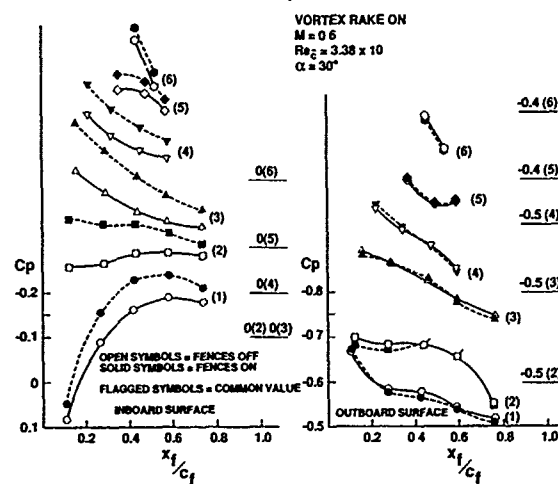
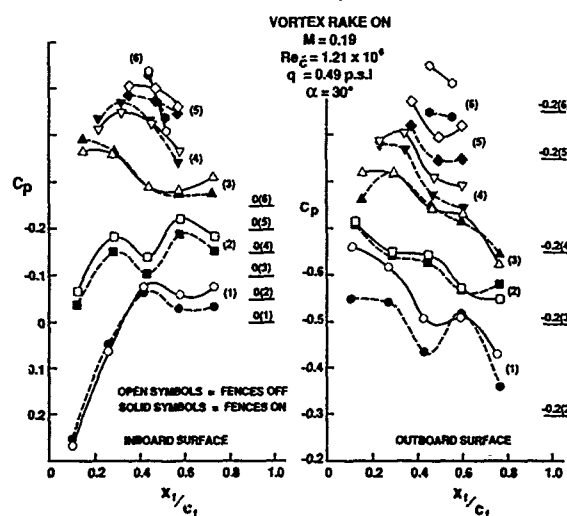
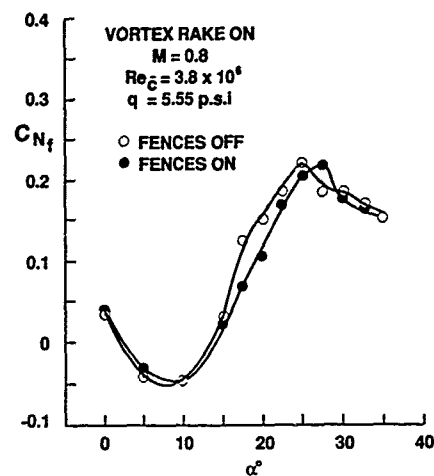
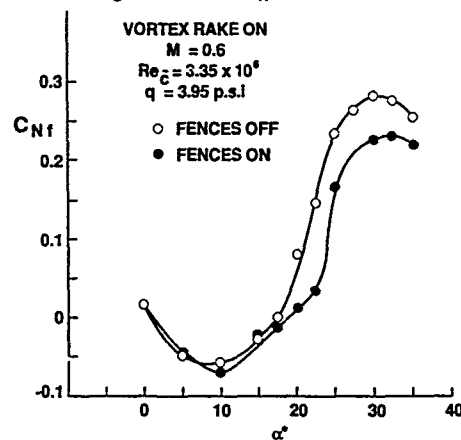
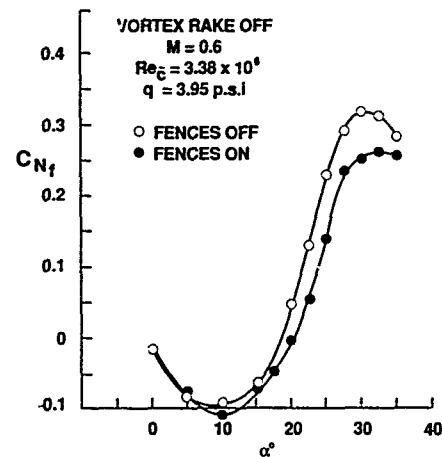
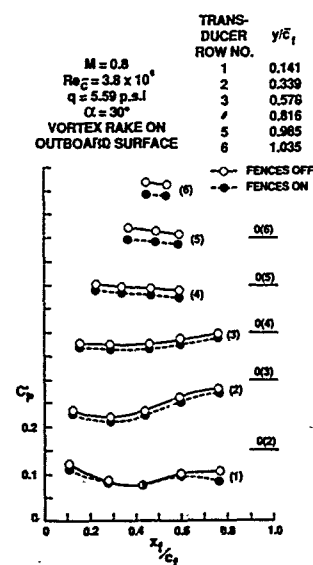
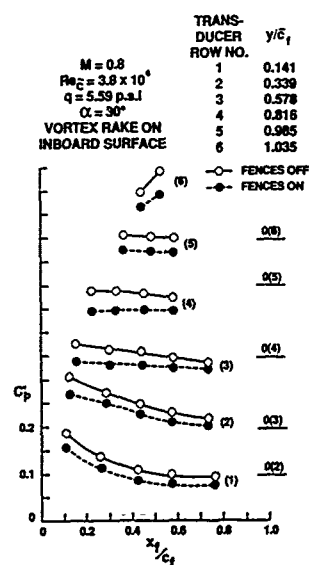
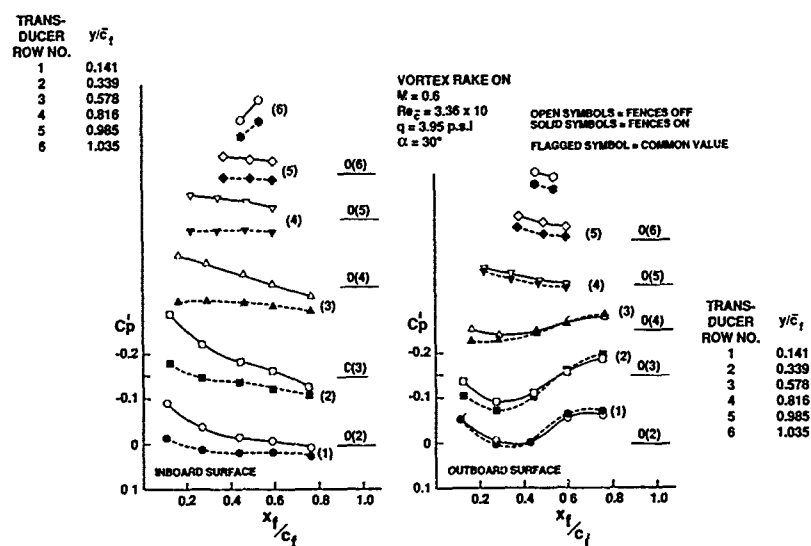
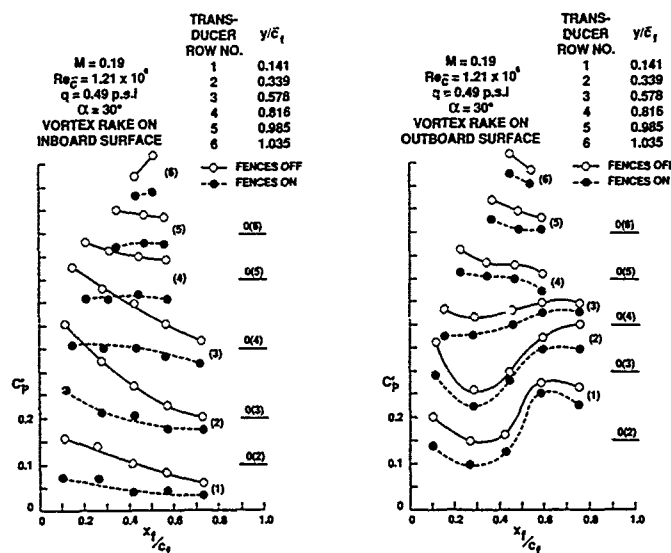


FIG. 20: LEX AND WING UPPER SURFACE FLOW VISUALIZATION,  
 $M = 0.6$ ,  $\alpha = 30^\circ$ , L.E. FLAP DROOP  $= 35^\circ$

Fig. 21 Fin  $C_p$  distributionFig. 22 Fin  $C_p$  distributionFig. 23 Fin  $C_p$  distribution

Fig. 24 Fin  $C_N$  versus  $\alpha$ Fig. 25 Fin  $C_N$  versus  $\alpha$ Fig. 26 Fin  $C_N$  versus  $\alpha$ Fig. 27 Fin unsteady  $C_p$



Fig. 28 Fin unsteady  $C_p$ Fig. 29 Fin unsteady  $C_p$

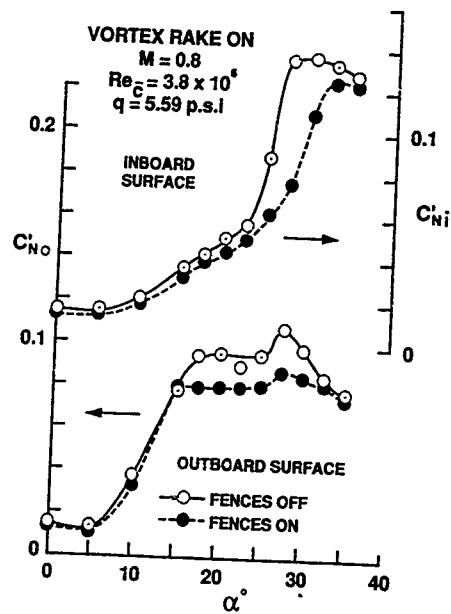
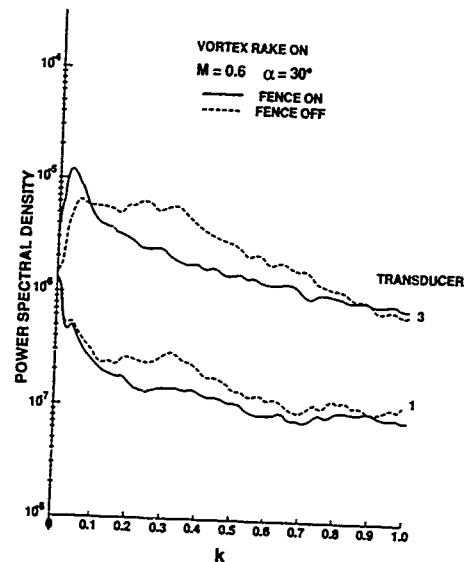
Fig. 30 Fin unsteady  $C_N$  versus  $\alpha$ 

Fig. 32 Power spectral density for LEX unsteady pressure signals

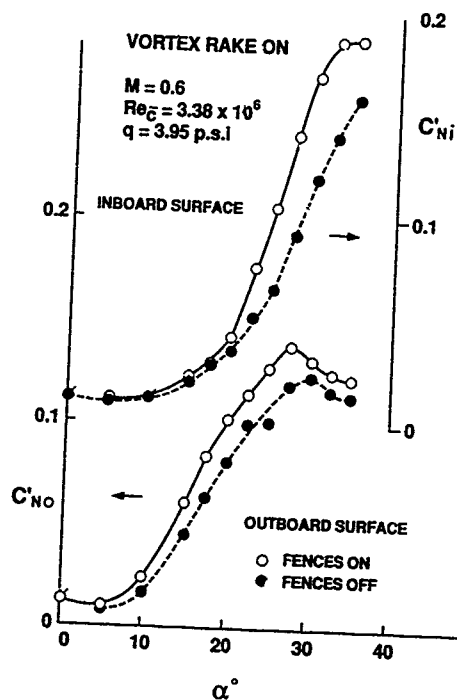
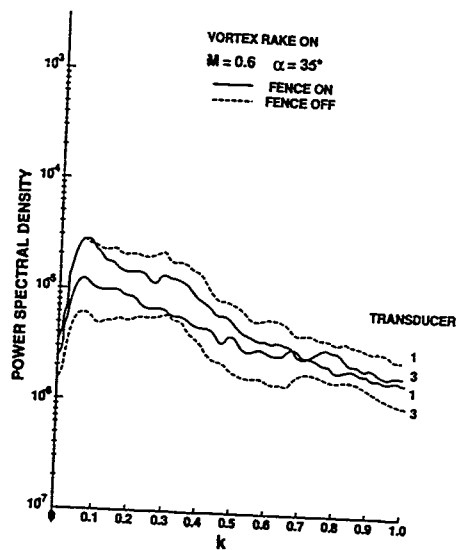
Fig. 31 Fin unsteady  $C_N$  versus  $\alpha$ 

Fig. 33 Power spectral density for LEX unsteady pressure signals

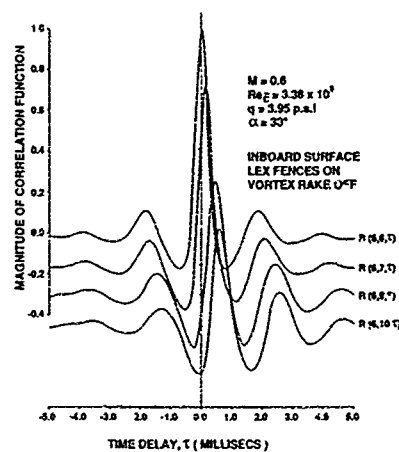


Fig. 34 Chordwise cross-correlations for fin unsteady pressure signals

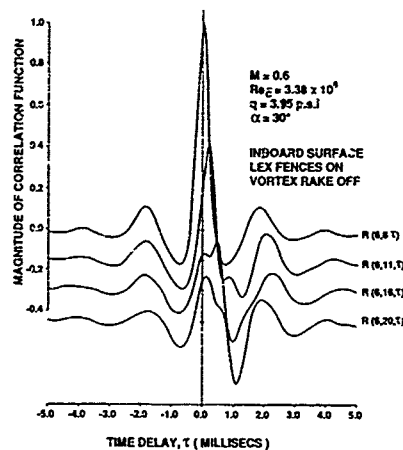


Fig. 35 Spanwise cross-correlations for fin unsteady pressure signals

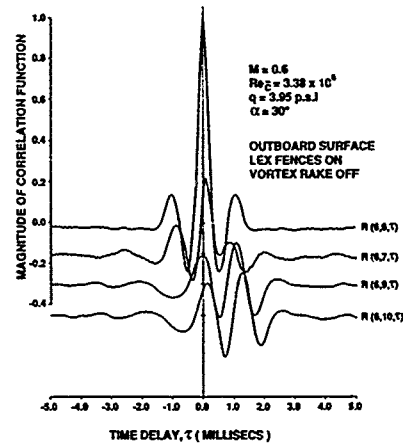


Fig. 36 Chordwise cross-correlations for fin unsteady pressure signals

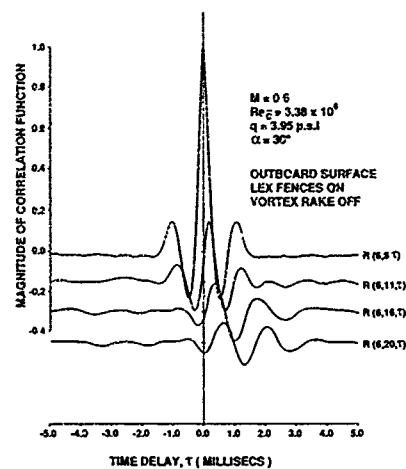


Fig. 37 Spanwise cross-correlations for fin unsteady pressure signals

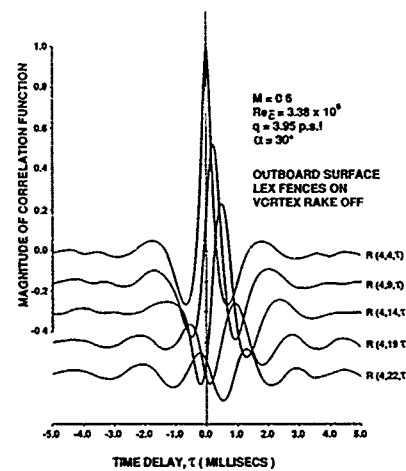


Fig. 38 Spanwise cross-correlations for fin unsteady pressure signals

$M = 0.19$   
 $Re_{\bar{c}} = 1.21 \times 10^6$   
 $\alpha = 30^\circ$

LEX FENCES OFF

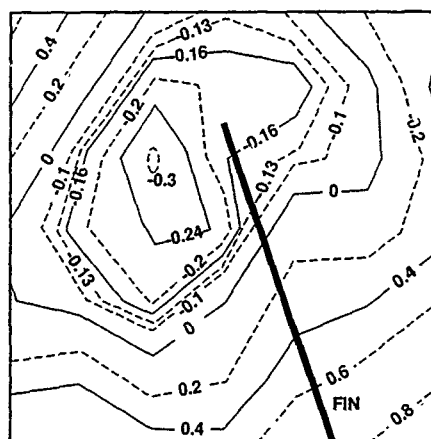


Fig. 39 Vortex wake  $C_p$  contours

$M = 0.8$   
 $Re_{\bar{c}} = 3.8 \times 10^6$   
 $\alpha = 30^\circ$

LEX FENCES OFF

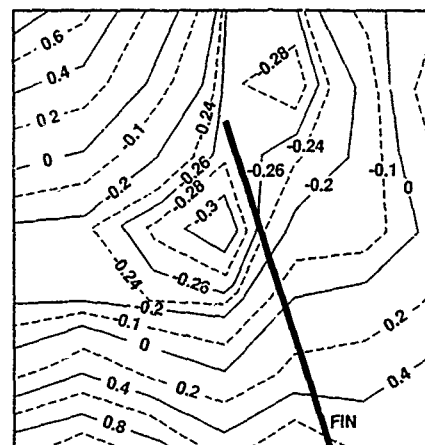


Fig. 41 Vortex wake  $C_p$  contours

$M = 0.19$   
 $Re_{\bar{c}} = 1.21 \times 10^6$   
 $\alpha = 30^\circ$

LEX FENCES ON

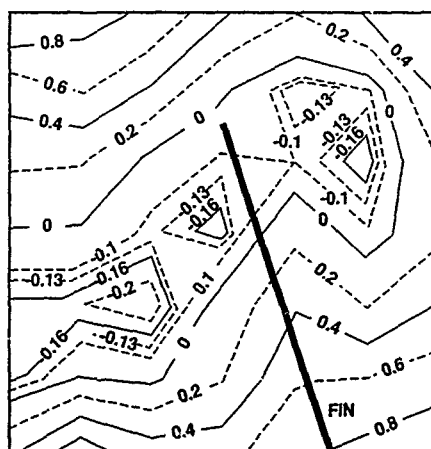


Fig. 40 Vortex wake  $C_p$  contours

$M = 0.8$   
 $Re_{\bar{c}} = 3.8 \times 10^6$   
 $\alpha = 30^\circ$

LEX FENCES ON

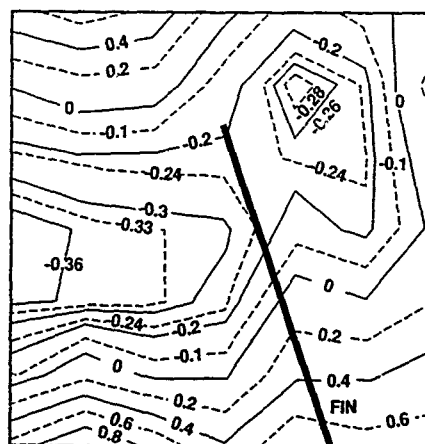


Fig. 42 Vortex wake  $C_p$  contours

# MULTIPLE ROLL ATTRACTORS OF A DELTA WING AT HIGH INCIDENCE\*

by

E.S. Hanff†

Institute for Aerospace Research††  
Ottawa, Ontario, Canada

L.E. Ericsson†††

Lockheed Missiles & Space Company, Inc.  
Sunnyvale, CA 94089-3504, United States

## Abstract

A comprehensive roll oscillation test program on a 65° delta wing has been conducted at the IAR (formerly NAE) 2m / 3m low-speed wind tunnel. The principal objectives of the program were to obtain a better insight of the vortex dynamics associated with large-amplitude and high-rate roll oscillations and to validate the hypersurface representation of aerodynamic loads as a means of improving prediction of aircraft dynamics in the non-linear regime. Although some of the observed unusual roll response characteristics can be qualitatively explained in terms of existing knowledge regarding unsteady aerodynamic effects of separated flow, further tests and data analyses will be needed to reach the in-depth understanding of the flow phenomena which is required for the successful design of future high-agility aircraft.

## Nomenclature

- b    Wingspan
- $\bar{c}$     Mean aerodynamic chord
- $C_L$     Rolling moment coefficient =  $\frac{L}{qSb}$
- $C_{L\dot{\phi}}$     Aerodynamic roll stiffness =  $\frac{\partial C_L}{\partial \dot{\phi}}$
- $C_{L\ddot{\phi}}$     Aerodynamic roll damping =  $\frac{\partial C_L}{\partial \ddot{\phi}}$
- f    Oscillation frequency
- k    Reduced frequency =  $\frac{\omega b}{2U_\infty}$
- L    Rolling moment
- q    Dynamic Pressure
- S    Model planform area
- t    Time
- $U_\infty$     Freestream velocity
- $\alpha$     Angle of attack
- $\Delta\phi$     Roll oscillation amplitude
- $\sigma$     Pitch angle (of body-fixed model axis)
- $\phi$     Roll angle
- $\phi_0$     Mean roll angle
- $\dot{\phi}$     Reduced roll rate =  $\frac{b}{2U_\infty} \frac{\partial \phi}{\partial t}$
- $\ddot{\phi}$     Reduced roll acceleration =  $\frac{b}{2U_\infty} \frac{\partial^2 \phi}{\partial t^2}$
- $\Lambda$     Leading-edge sweep angle
- $\omega$     Angular frequency =  $2\pi f$

\* Work conducted under Joint Research Program of U.S. Air Force Office for Scientific Research and Wright Research and Development Center Flight Dynamics Lab., Institute for Aerospace Research and Canadian Dept. of National Defence.

† Senior Research Officer

†† Formerly National Aeronautical Establishment

††† Senior Consulting Engineer

### Introduction

The evolution of high-performance aircraft requires ever-increasing maneuverability and agility capabilities, including flight at high angle of attack and motions involving large amplitudes and high angular rates, where unsteady separated flow conditions prevail. Under these conditions, the flow physics needs to be better understood and new, more effective aerodynamic models have to be used to account for the highly non-linear, time dependent loads that may be present. The latter requirement arises from the inability of fully or partially linear mathematical models, implicit in the stability derivative formulation, to handle the loads at hand<sup>1,2,3,4</sup>.

Consequently, a different approach to represent aerodynamic reactions, that does not rely on assumptions of linearity, and can thus be used for simulations in the non-linear flight regime, has been proposed<sup>5</sup>. The simulations are based on the utilization of the instantaneous values of the pertinent aerodynamic loads as forcing functions in the equations of motion. Special wind-tunnel testing techniques are required to provide the information on the airloads as a function of the motion variables. One such technique, which permits efficient measurement of instantaneous values of aerodynamic reactions in terms of the corresponding instantaneous values of the pertinent motion variables, has been described in Ref.6. The measured reactions are stored as a function of the motion variables in look-up tables that can be used directly in simulations. In a topological sense, the look-up tables that describe the reactions as functions of  $n$  motion variables, correspond to reaction hypersurfaces in  $n+1$  dimensions.

It bears mentioning that the measurement technique and load representation, in addition to improving flight mechanics prediction capabilities, also provide, by virtue of the detailed information they generate, a means to increase the understanding of flows in the non-linear regime.

### Experimental program

A 65° delta wing model (Fig 1) was tested statically and under forced roll-oscillation conditions in a program that comprised steady and unsteady force and pressure measurements as well as high-speed laser-sheet and surface-oil flow visualization. Moreover, free-to-roll tests were also conducted. The test matrix for the complete program is shown in Table I. A single degree of freedom motion in roll was selected for the dynamic tests because of its relevance to wing rock problems and its relatively simple mechanical implementation. Details on the wind-tunnel rig have been described in Ref. 7.

The force tests provided the data base required to conduct single degree-of-freedom (roll) simulations that could then be validated through a comparison with actual motions obtained in the free-to-roll tests. Flow visualization and pressure tests were conducted to complement the global load data by providing a better insight of the physical mechanisms underlying the measured loads. The substantial number of force tests, involving a variety of oscillation amplitudes, frequencies and roll offset angles shown in Table I, were required to generate an adequately populated data base for the instantaneous aerodynamic reactions as functions of the instantaneous values of  $\phi$ ,  $\dot{\phi}$  and  $\ddot{\phi}$ . The various offset angles are needed to independently control these quantities.

Inasmuch as each run entailed the acquisition of data for 20-40 seconds, most of the noise was eliminated from the signals by an ensemble averaging process, resulting in very good repeatability. Tare measurements were done in air due to the impossibility of evacuating the wind tunnel. Moreover, no support or wall interference corrections were attempted. A similar test program, to be conducted shortly at another wind tunnel, is expected to shed some light on the possible impact of interference effects.

The free-to-roll tests, intended to validate the aerodynamic load representation by comparing single DOF motion predictions, based on force data, with actual motions obtained under free-to-roll conditions, were conducted by releasing the model from any desired roll angle at zero initial roll rate. In spite of the removal of all bearing seals and use of light oil for lubrication in these tests, some friction still remained that needs to be accounted for in the simulations.

### Experimental results

A large body of data was acquired in the test program, much of it not having been fully analyzed to date. Experimental results obtained from the forced-oscillation and free-to-roll tests conducted in 1989 at a roll axis inclination of  $\sigma = 30^\circ$  have been previously described<sup>8</sup>. The most important findings are summarized in this section, complemented with data for the same case obtained in a subsequent test series (1990). In the following section an attempt to qualitatively explain the physical mechanisms underlying the observed characteristics is presented. Although the forced-oscillation data were obtained as functions of  $\phi$ ,  $\dot{\phi}$  and  $\ddot{\phi}$ , the dependence on  $\ddot{\phi}$  has not yet been utilized. It should be pointed out that the requirement for higher time derivatives depends on the flow conditions at hand and the specific goals of the analysis<sup>9</sup>.

Reaction surfaces corresponding to the rolling moment coefficient in terms of  $\phi$  and  $\dot{\phi}$  are shown in Fig.2 (a) and 2(b) for oscillations about  $\phi_0 = 0$  and  $28^\circ$  respectively. The surfaces were obtained on the basis of the fundamental frequency component as well as five harmonics of the rolling moment. The trajectories on the  $\phi$ - $\dot{\phi}$  phase planes correspond to oscillations with  $\Delta\phi = 5, 12, 19, 26, 33$  and  $40$  degrees at  $k = 0.14$ . They are not exactly elliptical due to slight distortions of the motion. Note that the surfaces have been offset by  $\Delta C_L = 0.1$  in order to facilitate viewing and that they use the same axes and perspective.

It has been shown<sup>5</sup> that in this representation the static and dynamic stability derivatives are related to the orientation of the surface relative to the axes at the point of interest, specifically, they are equal to the direction numbers (with

respect to  $\phi$  and  $\dot{\phi}$  respectively) of the normal to the surface at that point. Moreover, a stable attractor (trim condition) is present wherever the  $\phi$  axis penetrates the reaction surface at a location exhibiting static and dynamic stability.

Figures 3(a) - 3(d) show the intersections of the reaction surfaces with planes at different values of  $\phi$ . The figures reveal that the surface for  $\phi_0 = 0$  is quite distinct from the others, which, in fact, tend to coalesce into one; except for the region of  $\phi > 10^\circ$  and positive  $\dot{\phi}$ , where the surface corresponding to  $\phi_0 = 14^\circ$  is somewhat displaced toward the one for  $\phi_0 = 0^\circ$ .  $C_L \dot{\phi}$  is represented in Fig. 3 by the slopes of the curves, indicating that the damping associated with the  $\phi_0 = 0$  surface is generally considerably higher than those for the other surfaces.

The intersection of the reaction surfaces with the plane  $\dot{\phi} = 0$  is shown on Fig. 4, where the static information has been superimposed. Here again the above mentioned clustering of the reaction surfaces can be observed up to the largest roll angles encountered, with the exception of the points for the case of  $\phi_0 = 7^\circ$  and  $\phi > 0$  which gradually approach those for  $\phi_0 = 0$  with increasing  $\phi$ . The statically measured rolling moment coefficient (diamonds and solid triangles) for  $\phi > 7^\circ$  agree quite well with the corresponding points on the reaction surfaces for  $\phi_0 > 7^\circ$ , indicating a negligible rolling acceleration effect. For  $3^\circ < |\phi| < 7^\circ$  the static and dynamic data are quite different, with the former exhibiting static instability. On the other hand for  $-3^\circ < \phi < 3^\circ$  the static data agrees well with the dynamic one for  $\phi_0 = 0$ . Finally, for  $\phi < -7^\circ$ , the static data agrees with the antisymmetric dynamic data obtained for negative values of  $\phi_0$  (not shown). The figure shows that the stiffness associated with the  $\phi_0 = 0$  reaction surface is higher than for  $\phi_0 \neq 0$  and that  $C_L$  is 0 at the statically stable points  $\phi = 0$  and  $\phi = 21^\circ$ , which Fig 3 (a) and (c) show to be also dynamically stable. Keeping in mind the antisymmetry of the reaction surfaces, it follows that there are stable attractors at  $\phi = 0$  and  $\phi = \pm 21^\circ$ .

The characteristics of the reaction surfaces seem to reflect the existence of three flow regimes, depending on the mean roll angle of the oscillation, where two such regimes were described above and the third one is represented by the reaction surfaces for negative mean roll angles. Additional testing and a detailed analysis of the flow visualization and pressure data is expected to yield an explanation for the observed characteristics.

Free-to-roll experiments were conducted using a variety of initial roll angles. As mentioned before, the initial roll rate was always zero due to characteristics of the experimental set-up. In all cases the model behaved in a stable fashion, trimming at  $\phi = 0^\circ$  or  $\phi = \pm 21^\circ$  depending on the initial roll angle. If the model was released from  $-2^\circ < \phi < -60^\circ$  the trim angle was  $21^\circ$  on the same side as the initial roll angle, whereas, if the initial roll angle was outside the above range the model trimmed at  $\phi = 0^\circ$ . Interestingly, multiple attractors were also observed at other angles of attack as well as in the case of an  $80^\circ/65^\circ$  double delta configuration<sup>8</sup> (Table II).

Simulations were conducted using both the locally linearized method based on the measured static rolling moment coefficient  $C_L(\phi)$  and damping derivative  $C_{L\dot{\phi}}(\phi_0)$ , as well as the non-linear method described in Ref. 10. Various free-to-roll motion histories with increasing initial roll angle  $\phi(0)$  are depicted in Fig. 5. Simulations are superimposed on Fig. 5(a) and 5(d). A complete discussion on these results can be found in Ref. 8. It is clear that the non-linear simulations agree considerably better with the observed motions than the traditional, locally linearized, simulations. However, the possibility that the good agreement is fortuitous cannot be ruled out at this stage. There is obviously a need to understand better the underlying physics of the observed unusual characteristics.

To this end, high-speed laser sheet flow visualization videos were taken, which are still being analyzed, and unsteady surface pressures were obtained on the leeward side of the model at the locations indicated on Fig. 1. Carpet and isobar plots of the pressures obtained under static conditions for  $-42^\circ < \phi < 42^\circ$  and  $\sigma = 30^\circ$  are shown in Fig. 6(a), where they are displayed as if they were due to a slow oscillation about  $\phi_0 = 0$  with  $\Delta\phi = 42^\circ$ . The measurements were taken on the port wing which is to leeward of the model centerline for  $\phi > 0^\circ$  and its downstroke corresponds to  $0 < \omega t < 180^\circ$ . Fig. 6(b) shows the pressures for an oscillation about  $\phi_0 = 0^\circ$  with  $\Delta\phi = 40^\circ$  and  $k=0.14$ , and Fig. 6(c) for the same conditions but with  $\phi_0 = 28^\circ$ . A plot of the pressures on the starboard wing (obtained on the port wing when using  $\phi_0 = -28^\circ$ ) for the last case is given in Fig. 6(d). Likewise, Figs. 6(e) and 6(f) depict the pressures on the port and starboard wings respectively for  $\phi_0 = 28^\circ$ ,  $\Delta\phi = 26^\circ$  and  $k = 0.14$ . Note that to time-correlate the pressures of both wings, roll angles of equal magnitude and opposite sign must be aligned. The importance of the dynamic effects is clearly underscored by the differences among the various figures. As can be observed, there are, in addition to large time lags, important changes in the flow structure that result in quite different pressure fields.

#### Fluid mechanics considerations

The observed phenomena are clearly the result of complex fluid mechanics processes that make it difficult to provide a detailed explanation of the observations on the basis of the information available at this point. Here an attempt is made to provide a qualitative explanation pending additional experiments and data analysis. We start by identifying the mechanisms that define the observed static characteristics (Fig. 4). Fig. 7 shows the experimentally determined boundaries for breakdown of delta-wing leading edge vortices<sup>11</sup>. Breakdown occurs over the trailing edge of the wing when the angle of attack reaches the boundary and progresses forward as the angle of attack is increased further<sup>12</sup> (Fig. 8).

At an arbitrary roll angle  $\phi$ , the angle of attack and effective leading edge sweep of the delta wing are given by:

$$\alpha(\phi) = \tan^{-1}(\tan \sigma \cos \phi) \quad (1)$$

$$\Lambda(\phi) = \Lambda \pm \tan^{-1}(\tan \sigma \sin \phi) \quad (2)$$

where the effective sweep of the wing half that rolls up (leeward wing half) increases and that of the other decreases, resulting in an aft and forward motion, respectively, of the corresponding leading edge vortex breakdown locations. These motions lead to an increase of vortex-induced lift on the leeward wing half and a decrease on the windward wing half, both contributing to a statically destabilizing rolling moment.

It can be seen in Fig. 8 that for  $\sigma = 30^\circ$  and  $\Lambda = 65^\circ$ , small changes in effective sweep (say  $< 2^\circ$ ), corresponding to  $|\phi| < 3.5^\circ$  according to Eq. 2, result in rather small shifts in the position of the breakdown points ( $< 10\%$ ). The corresponding statically destabilizing effect is insignificant compared to the increase in roll stability due to the crossflow-induced changes of the loads generated by attached flow and by the (intact) leading edge vortices upstream of the breakdown locations<sup>13</sup>. As the roll angle is increased further, the position of the breakdown point on the leeward wing half moves very rapidly aft, in fact reaching a discontinuity as it jumps from about 50% centerline chord to the trailing edge. Figure 7 shows that for  $\sigma = 30^\circ$  this occurs at  $\Lambda = 69^\circ$ , which according to Eq. (2) requires a roll angle of  $7^\circ$  (note rapid change in pressure in Fig. 6(a) at the appropriate range of  $\phi$ ). This large shift of the breakdown point due to small roll angle variations leads to significant changes in the vortex-induced lift, which thus becomes the dominant mechanism producing the local static roll instability observed experimentally. It should be noted that the change in angle of attack under the above conditions is insignificant ( $0.2^\circ$ ).

For  $|\phi| > 7^\circ$ , the fully attached vortex on the leeward wing-half has a stabilizing effect, whereas the statically destabilizing effect of the vortex breakdown on the windward wing half becomes more and more insignificant because of the slow forward progression of the breakdown location (Fig. 8). This leads to the off-zero trim angles observed at  $\phi = \pm 21^\circ$ . Thus, the static characteristics depicted in Fig. 4 can be explained in a straightforward manner.

Explaining the dynamic characteristics shown in Figs. 2 through 6 presents more difficulties than the previously discussed static characteristics. The non-linear aerodynamics under consideration and the limited success of the locally linearized model in predicting the free-to-roll motions suggest that the dynamics in the latter must be explained in terms of phenomena that occur under realistic motion amplitudes and rates. An indication of this need can be found from a comparison of the pressure plots in Fig. 6 which dramatically demonstrate the effect of the motion parameters on the flow field. Of particular interest is the very large time lag in the position of the vortex breakdown point under oscillatory conditions and the significant changes in the magnitude and location of the suction peak as a function of these conditions.

Unlike the case of fully attached vortices, where changes in the vortices (e.g. due to a step in angle of attack) propagate downstream from the apex at close to the freestream velocity<sup>14</sup>, resulting in relatively small phase lags, here we are concerned with the motion of the breakdown points themselves. In this case flow inertia effects limit the propagation speed to values considerably lower than the freestream velocity, yielding the observed very large time lags. As can be expected, under dynamic conditions involving substantial angular rates, such as those encountered in the free-to-roll tests, these time lags have a profound effect on the rolling moment as a function of the roll angle. Therefore a fairly detailed knowledge of the flow field as a function of time is required to explain the free-to-roll histories. It is expected that the analysis of the high-speed flow visualization videos, currently in progress, will contribute significantly to such knowledge. In the meantime, we will attempt to explain some of the free-to-roll observations in terms of the available pressure data. To this end, pressure data, obtained for an oscillation waveform and frequency that approximately correspond to the first half cycle of the free-to-roll motion history, is used to provide some insight of the observed behavior. Of course care has to be exercised in utilizing pressure data obtained under oscillatory conditions to interpret the transient free-to-roll motions, as the flow initial conditions are quite different. Therefore it is necessary to limit the discussion to sections of the motion histories sufficiently removed from the starting point, where it is probably realistic to assume the transient pressure field adequately approximates the oscillatory one for the purpose at hand.

The motion history shown in Fig. 5(a) barely reaches the discontinuity observed statically at  $\phi = 7^\circ$  and thus is expected to converge on the  $\phi = 21^\circ$  attractor. The fact that the locally linearized simulation reasonably predicts the motion history, indicates that the non-linear effects are of relatively little importance in this case. The release depicted in Fig. 5(b), however, is more interesting as the model stopped virtually exactly at the  $\phi = 0^\circ$  attractor and rather than remain there, returned to settle at  $\phi = 21^\circ$ . Inasmuch as the kinetic energy is zero at the first overshoot peak, the subsequent motion is due to the aerodynamic moment produced by the time-delayed flow field. In fact, Fig. 6(e) indicates that at the end of the downstroke ( $\phi = 0^\circ$ ) the port wing leading edge vortex was attached at least up to 75% centerline chord (pressure measurement station), whereas Fig. 6(f) shows very little suction on the starboard wing, thus providing the necessary restoring moment to force the model away from the zero attractor. The importance of the dynamic effects is underscored by the dramatic difference between this situation and a static one where for  $\phi = 0^\circ$  the suction on both wings is the same. In Fig. 5(c) the model is released from close to the maximum initial roll angle that converges on the  $\phi = 21^\circ$  trim angle. Here the first overshoot peak is close to the  $\phi = -21^\circ$  attractor where, according to the static data, the model should trim. Clearly the same time delay effects cause the model to reverse its motion and eventually converge on the  $\phi = 21^\circ$  attractor. It is interesting to note the presence of the first undershoot which indicates a tendency to return to the zero trim point. As expected, time lag effects extend this tendency to much higher values of the roll angle ( $0^\circ < \phi < 14^\circ$ ) than those predicted from the static data ( $0^\circ < \phi < 3^\circ$ ). Finally, Fig. 5(d) shows a release from  $\phi \sim 66^\circ$  where the first overshoot peak is exactly at the  $\phi = -21^\circ$  attractor and then continues on to the



zero attractor. Fig. 6(c) shows that at the first overshoot peak the suction is approximately at its maximum (vortex probably fully attached) and occurs on the windward half-wing ( $\phi < 0$  for port wing), whereas the corresponding suction on the starboard wing is considerably lower (Fig. 6(d)), thus providing the restoring moment that prevents the model from remaining at the attractor located there.

The motion history plots show that larger initial roll angles lead to larger damping during the first cycle. Comparing Figs. 5(a) and 5(d) one finds that in the latter the amplitude is reduced from  $\Delta\phi \sim 66^\circ$  to  $\Delta\phi \sim 12^\circ$  after one cycle, whereas in the former the reduction is only from  $\Delta\phi \sim 19^\circ$  to  $\Delta\phi \sim 8^\circ$ . The enormous increase in damping for the case of the larger release angle is the result of catching the discontinuity in the vortex breakdown location. However the flow mechanism that determines the eventual trim point is not yet understood. Some evidence indicates that the maximum rate achieved during the free-to-roll motion influences this process<sup>8</sup>. In any case it is clear that kinetic energy and time lag plays an important role. It is possible that in addition to the history effects already discussed, accelerated flow and moving wall effects<sup>15,16</sup> may also be of significance, especially in the case of wings with rounded edges. Additional testing and analysis is required before the highly non-linear vehicle dynamics of the  $65^\circ$  delta wing at high incidence can be fully understood.

### Conclusions

Wind-tunnel rolling tests conducted on a  $65^\circ$  delta wing at  $30^\circ$  inclination of the roll axis have revealed the presence of severe aerodynamic non-linearities that are not amenable to treatment by a locally linearized mathematical model. Of particular interest is the existence of multiple roll attractors (trim angles). An explanation for the observed static characteristics has been given in terms of existing knowledge of aerodynamics of delta wings. A tentative explanation of the dynamic characteristics, which have not been observed before, has been presented on the basis of unsteady surface pressure measurements. The measured data clearly demonstrates the different characteristics of the flow under large-amplitude and high-rate oscillation, from those under static or more benign dynamic situations, such as those usually encountered in conventional dynamic stability testing or less demanding flight maneuvers.

Aerodynamic non-linearities as well as attractor multiplicity could be handled well by simulations utilizing the hypersurface representation of aerodynamic loads, suggesting that this approach can provide considerable improvements for the prediction of aircraft behavior in the non-linear regime.

### Acknowledgements

The authors wish to thank Dr. K. Orlik-Rückemann for his support and valuable suggestions for the preparation of the manuscript. The software development work carried out by Mr. S. Jenkins is also gratefully acknowledged.

### References

1. Beyers, M.E., "Free-Flight Investigation of High-Maneuverability Missile Dynamics", AIAA J. of Spacecraft and Rockets, Vol.14, April 1977.
2. Tobak, M., Schiff, L., "Aerodynamic Mathematical Modeling-Basic Concepts", AGARD Lecture Series LS-114, 1981.
3. Kalviste, J., "Use of Rotary Balance and Forced Oscillation Test Data in a Six Degrees of Freedom Simulation", AIAA Paper 82-1364, Aug. 1982.
4. Orlik-Rückemann, K.J., "Aerodynamic Aspects of Aircraft Dynamics at High Angles of Attack", AIAA J. of Aircraft, Vol.20, Sept. 1983.
5. Hanff, E.S., "Dynamic Non-Linear Airloads - Representation and Measurement", AGARD Symposium on Unsteady Aerodynamics - Fundamentals and Applications to Aircraft Dynamics", AGARD CP-386 Göttingen, May 1985.
6. Hanff, E.S., "Determination of Non-Linear Loads on Oscillating Models in Wind Tunnels", IEEE Int. Con. on Instrumentation in Aerospace Simulation Facilities, ICIAF'83 Record, Sept. 1983.
7. Hanff, E.S., Kapoor, K., Anstey, C.R., Prini, A., "Large-Amplitude High-Rate Roll Oscillation System for the Measurement of Non-Linear Loads", AIAA Paper 90-1426, June 1990.
8. Hanff, E.S., Jenkins, S.B., "Large-Amplitude High-Rate Roll Experiments on a Delta and Double Delta Wing", AIAA Paper 90-0224, Jan. 1990.
9. Jenkins, J.E., Hanff, E.S., "Non-Linear Airload Hypersurface Representation - A Time Domain Perspective" To be presented at AGARD FDP Specialists' Mtg. on Maneuvering Aerodynamics, Toulouse, May, 1991.
10. Hanff, E.S., Jenkins, S.B., "A Method for Non-linear Flight Mechanics Simulations" Presented at IEEE Int. Con. on Instrumentation in Aerospace Simulation Facilities, Göttingen, Sept., 1989.
11. Polhamus, E.C., "Prediction of Vortex-Lift Characteristics by a Leading-Edge-Suction Analogy", J. of Aircraft, Vol.8, April 1971.
12. Wentz, W.H., Kohlman, D.L., "Vortex Breakdown on Slender Sharp-Edged Delta Wings", AIAA Paper 69-778, July 1979.

13. Ericsson, L.E., King, H.H.C., "Rapid Prediction of Slender-Wing Aircraft Stability Characteristics", AIAA Paper 90-0301, Jan. 1990.
14. Lambourne, N.C., Bryer, D.W., Maybrey, J.F.M., "The Behaviour of the Leading Edge Vortices over a Delta Wing Following a Sudden Change of Incidence", Aer. Res. Council, Great Britain, R&M No.3645, March 1969.
15. Ericsson, L.E., Reding, J.P., "Fluid Dynamics of Unsteady Separated Flow, Part II, Lifting Surfaces", Progress Aerospace Sci., Vol. 24, 1987.
16. Ericsson, L.E., "Moving Wall Effects in Unsteady Flow", Journal of Aircraft, Vol. 25, Nov. 1988.

TABLE I  
IAR ROLL EXPERIMENTS TEST MATRIX (1989/90)

TEST	$\sigma$ (deg)	$\phi_0$ (deg)	$\Delta\phi$ (deg)	k	$Re_{\bar{c}}$ (millions)
Static force	30, 35, 40	$\pm(42, 28, 14, 7, 6, 5, 4, 3, 2, 1, 0)$	N/A	N/A	2.4
Dynamic force	30, 35, 40	42, 28, 14, (7), 0	5, 12, 19, 26, 33, 40	0.08, 0.14, 0.2	2.4
Free-to-roll	20, 25, 30, 35, 40	-65 to 65	N/A	N/A	2.4
Static surface pressure	30, 35	$\pm(42, 28, 14, 11, 9, 7, 6, 5, 4, 3, 2, 1, 0)$	N/A	N/A	2.4
Dynamic surface pressure	30, 35	$\pm(42, 28, 14, 7, 0)$	5, 12, 19, 26, 33, 40	0.08, 0.14	2.4
Laser sheet flow visualization	30, 40	42, 28, 14, 0	5, 12, 19, 26, 33, 40	0.11, 0.2	1.7
Surface oil flow visualization	30, 35	42, 28, 14, 7, 0	N/A	N/A	2.4

TABLE II  
ROLL ATTRACTOR LOCATIONS

$\sigma$	MODEL NOSE	
	65°	80°
20°	0°	0°
25°	$\pm 1.5^\circ$	0°
30°	0, $\pm 21^\circ$	0, $\pm 16^\circ$
35°	$\pm 11^\circ$	$\pm 14^\circ$
40°	0°	0°

\* Data is insufficient to exclude the possibility of an attractor at 0°

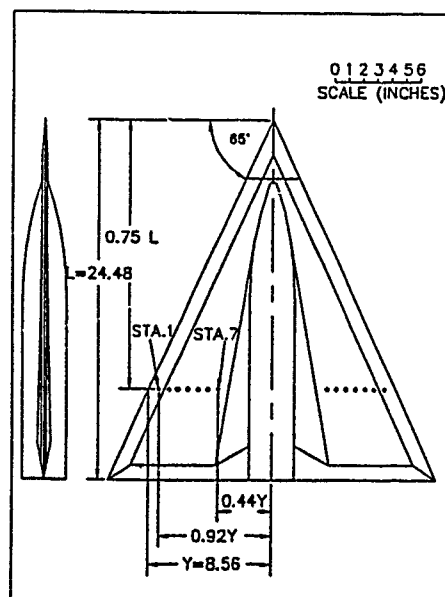
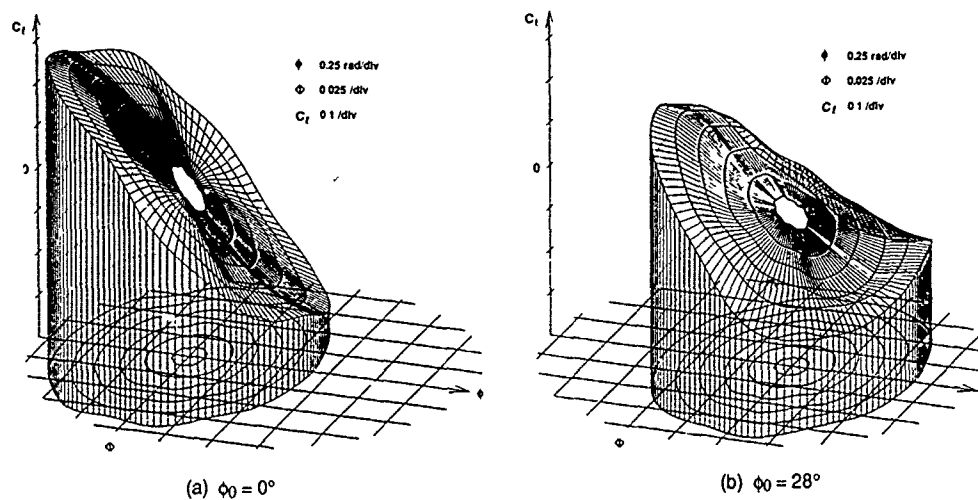
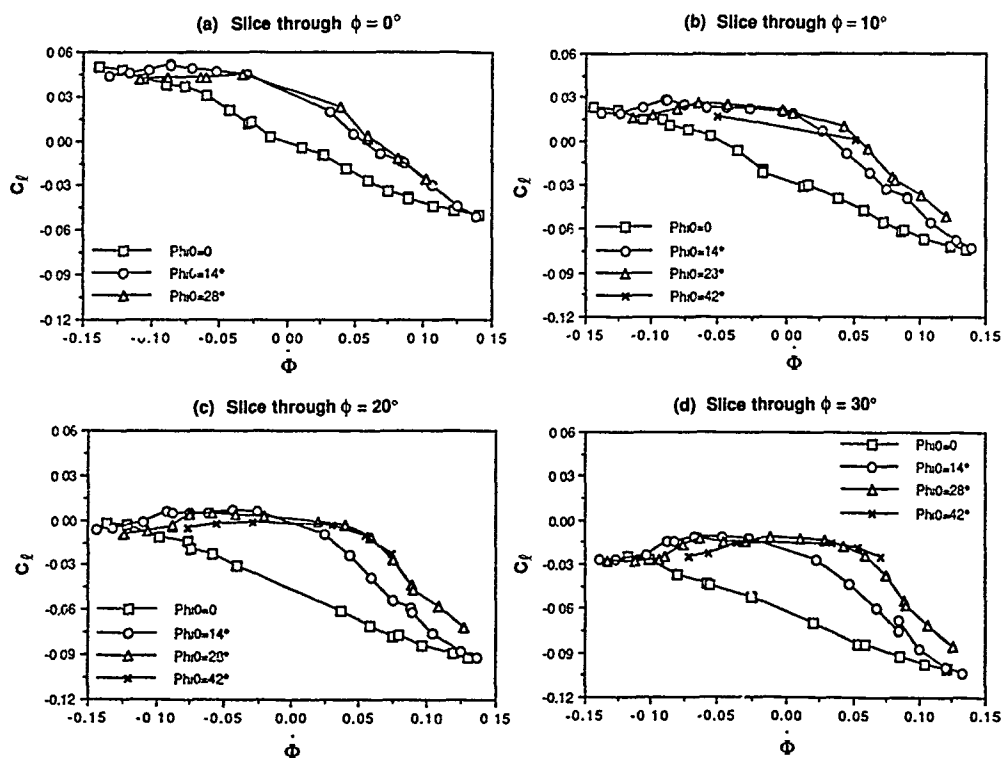


Fig.1 Delta wing model

Fig 2 Reaction surfaces for  $\sigma = 30^\circ$  at  $k = 0.14$ Fig.3 Intersection of reaction surfaces with fixed  $\phi$  planes.

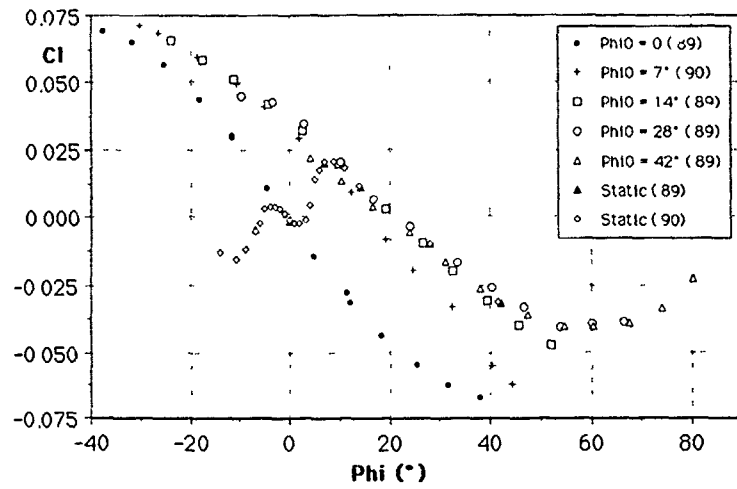
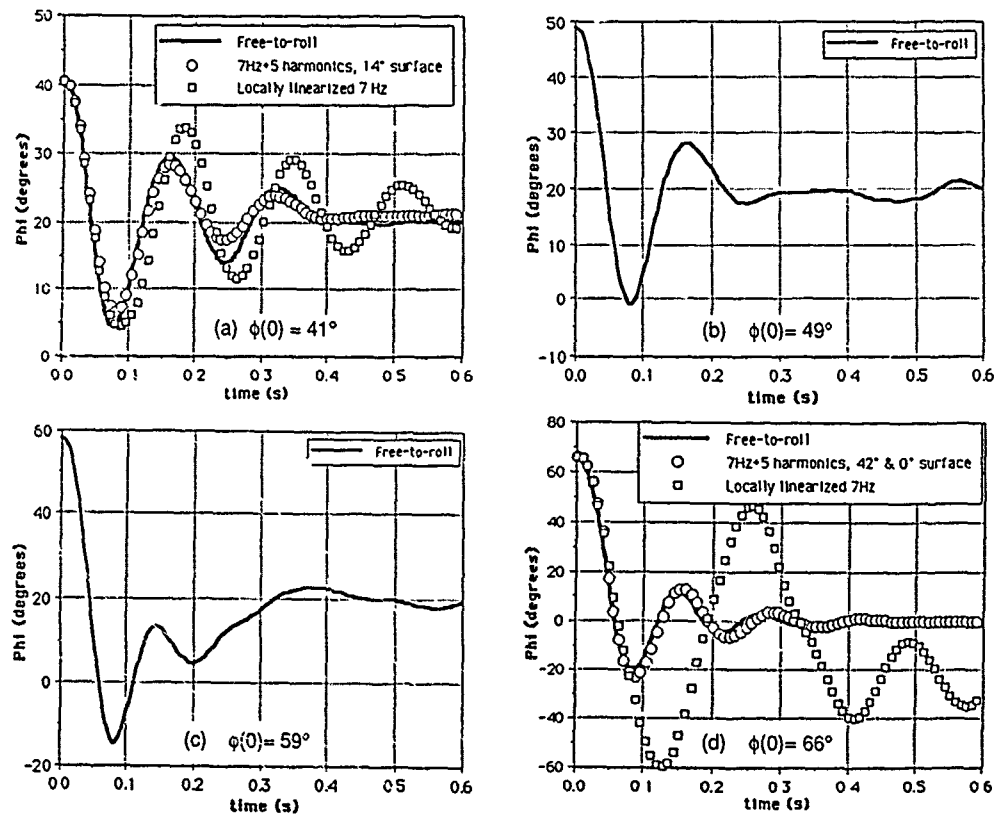
Fig 4 Intersection of reaction surfaces with  $\Phi = 0$  plane

Fig.5 Free-to-roll motion histories.

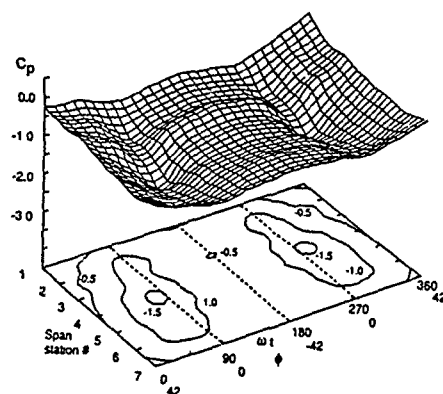
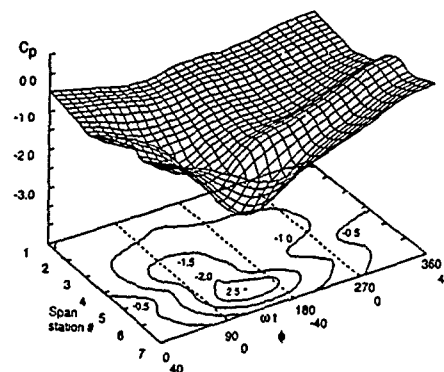
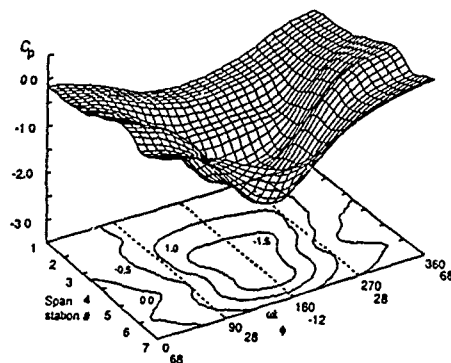
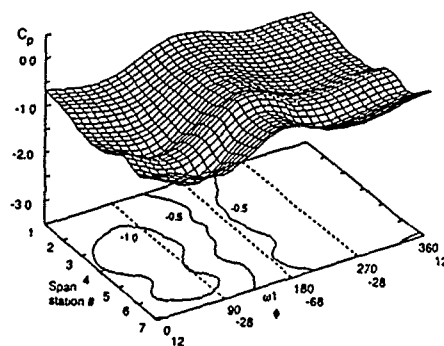
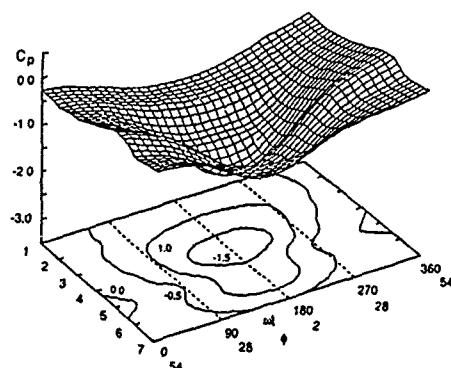
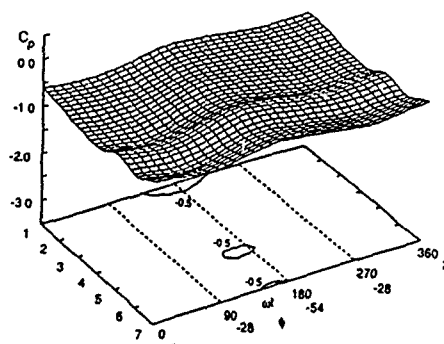
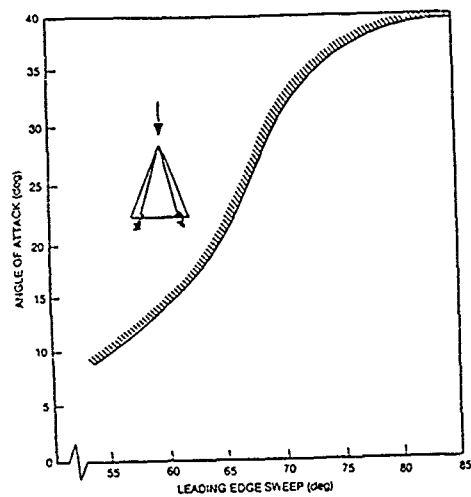
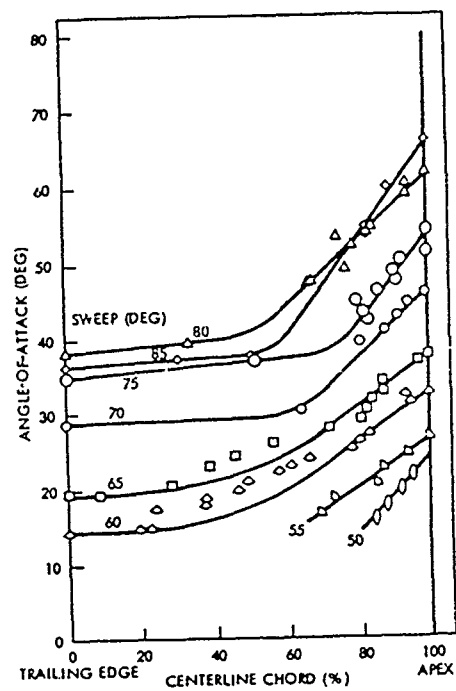
(a)  $\phi_0 = 0^\circ; \Delta\phi = 42^\circ; k=0$ (b)  $\phi_0 = 0^\circ; \Delta\phi = 40^\circ; k=0.14$ (c)  $\phi_0 = 28^\circ; \Delta\phi = 40^\circ; k=0.14$ (d)  $\phi_0 = -28^\circ; \Delta\phi = 40^\circ; k=0.14$ (e)  $\phi_0 = 28^\circ; \Delta\phi = 26^\circ; k=0.14$ (f)  $\phi_0 = -28^\circ; \Delta\phi = 26^\circ; k=0.14$ 

Fig.6 Pressure coefficient carpet and contour plots.

Fig.7 Boundary for vortex breakdown<sup>11</sup>.Fig.8 Vortex breakdown position on sharp delta wings<sup>12</sup>.

## NUMERICAL SIMULATION OF VORTEX STREET-EDGE INTERACTION

by

M.O. Kaya, C.R. Kaykayoglu and K.C. Bayar  
Faculty of Aeronautics and Astronautics  
Istanbul Technical University  
Maslak 80626 Istanbul  
Turkey

J.M.R. Graham  
Imperial College of Science and Technology  
Aeronautical Engineering Department  
Prince Consort Road, London SW7 2BY  
United Kingdom

## ABSTRACT

Preliminary results and computational method reviews are presented for the simulation of a vortex street impinging on three different leading edge geometries of sharp, blunt and elliptic type, making use of Lagrangian and mixed Lagrangian-Eulerian vortex methods. Two new computer codes have been developed to capture the essential features of the interaction mechanisms near the edge surface. The first method utilizes Discrete Vorticity Method (DVM) where a fixed Eulerian mesh system is needed to move the vortices through the flow domain. A more advanced computer model of the full Navier Stokes equations of motion combines the Lagrangian convection and Eulerian diffusion schemes and is called Hybrid Moving Vortex Diffusive Method (HMVDM). An unsteady shear layer flow arising from boundary layer separation at a bluff trailing edge creates the downstream vortex street. The models simulate most features of the impingement including the secondary vortex shedding as a truly self-generated phenomenon arising from impingement of the large-scale incident disturbances. The approaching vortex street is effected by the diverging flow around the elliptic edge. Vortex impingement on a blunt edge causes the most complex features of the interaction. The unsteady pressure distributions agree with the common observations.

## 1. INTRODUCTION

Several different computational approaches to making time accurate simulations of unsteady shear layers are currently of great interest [1,2,3]. Solutions produced by various computational models could provide cheap and effective alternatives to experimental testing.

However, accurate and practical numerical methods do not yet exist to compute unsteady shear layers which are highly vortical. Although various Eulerian Method formulations in the form of finite difference and finite element methods are available, such methods become extremely costly at moderate or high Reynolds numbers. On the other hand, Lagrangian Vortex Methods provide an alternative for high Reynolds number, vorticity dominated, unsteady flows. The capabilities of the Vortex Methods are very well reviewed in references [3,4].

The vorticity formulation is appropriate in the study of unsteady shear layers

since the role of vorticity in the dynamics of the problem is very important. A number of Lagrangian schemes have been designed to provide a more natural and efficient description of the vortical structures. These schemes have been evolved from the inviscid Discrete Vorticity Method (DVM). DVM represents the vorticity field as the sum of large numbers of discrete vortex blobs. Dynamically, these points follow the fluid, like particles. Representation of the shear layer and its convection by discrete vortices constitute the essentials of the Lagrangian description [3]. Viscous diffusion can be taken into account by allowing the blobs to increase in size with time. Alternatively, addition of a random walk to the discrete vortices can be used to represent the effects of viscosity [5]. Although the Lagrangian Vortex Methods turn out to be more stable than most Eulerian Methods, they are very costly. The DVM in its Cloud-in-Cell (CIC) formulation copes with this difficulty by speeding up the computation of the velocity fields. The simulation of various types of flows by CIC Methods are very well documented in reference [4].

Lagrangian schemes are economical for flows with a strong convection of vorticity. However they are less successful to the representation of viscous diffusion in the fluid. In these situations, Eulerian Methods work without difficulty.

A detailed survey of Eulerian finite difference solutions of the Navier Stokes (N-S) Equations may be found in Roache [6]. In the Eulerian mesh methods, the 2-dimensional N-S equations are often solved in their vorticity-transport form. The finite difference approximation on a fixed Eulerian mesh system is capable of treating two-dimensional flows with large separation, at Reynolds numbers of at least  $10^3$ . The difficulty increases with increase of Reynolds number since the requirement of small grid size near the body surface is crucial so as to model boundary layers accurately.

It appears that presently neither the Lagrangian Methods nor the Eulerian Methods alone can treat high Reynolds number flows. A combination of Lagrangian convection and Eulerian diffusion schemes could therefore eliminate many of the problems of both methods. A mixed Lagrangian-Eulerian method the so called Hybrid Moving Vortex Diffusive Method (HMVDM) is an alternative method to obtain solutions for the N-S vorticity transport equations. The HMVDM

was employed to extend the DVM in its C-I-C formulation to study vortex shedding from flat-bottomed barges with various bilge geometries [ 7 ]. This was the first study in which the HMVDM was used to simulate vortex shedding. No previous research in this area was met in the literature. In an extension of this study Kaykayoglu and Graham [ 8 ] adopted the method to study vortex interaction with a sharp edge.

Regions of fluctuating organized vorticity are inherent to all self sustained oscillations of unsteady shear layers that impinge on a downstream edge. In most situations they result from natural instability of the shear layer separating from a body; continued growth of the instability leads to formation of vortices, whose concentration of the vorticity varies with time and spatial position in accordance with the feedback mechanism generated [ 9 ]. Figure 1a shows the basic explanation of the vortex impingement mechanism. A central aspect of the interaction is the classification of the flow patterns at the edge. These interaction patterns are highly repeatable and set the stage for a complex unsteady boundary layer development downstream of the edge. The fact that an unsteady vortex street aft of a bluff trailing edge involves well-defined vortical structures is chosen as a basis of testing the efficiency of the numerical methods developed. The schematic of the problem under investigation is depicted in Figure 1b.

This paper concerns the application of the DVM and HMVDM described above to the problem of 2-D vortex street development and its subsequent interaction with a downstream leading edge having various geometries. Three different edge types are considered a sharp edge with an including edge angle of  $30^\circ$ , a blunt edge and an elliptic edge (see Figure 2).

An understanding of the interactions of regions of vorticity, or vortex-like structures, with leading edges or bluff two dimensional bodies is of fundamental importance in a number of applications. Such interactions occur at the leading edges of wings, helicopter blades, turbine blades, heat exchangers, bridge decks, turbulence attenuators and weapon bays as well as at a variety of flap, cavity, tube bundle and valve / gate configurations [ 10 ].

Most of the attention has been focussed on the experimental investigations of the vorticity field - edge interactions and important developments have been achieved [11,12,13,14]. Practical numerical methods are not available to compute vorticity dominated unsteady flows and their consequent interaction with impinging surfaces. Although several categories of simulation methods have been tried for vortex-body interactions [ 15,16,17,18,19 ] there is still a demand for more elaborate and more exact methods. Figures 3a through 3j shows the previously investigated configurations of point vortex-edge boundary interactions.

Concerning the category of impinging shear flow experiments, Rockwell et.al. [ 20,21, 22,23,24 ] has conducted the primary

research in this area. Interaction of a mixing layer vortex with a sharp edge has been examined with the objectives of studying the unsteady flow mechanism and induced unsteady pressure fields. Figure 4a shows the important features of the interaction mechanism [ 12,21 ]. The secondary vortex shedding at the tip is the result of the impinging large scale coherent incident vortex. Another category is shown in Figure 4b where a planar jet is impinging on a sharp edge [ 14,22 ]. The vortex induced boundary layer separation creates a secondary vortex. This vortex pairs with the primary jet vortex and convects downstream along the edge surface. The interaction of a vortex with a sharp corner is shown in Figure 4c [ 13 ]. While some share of the vortex passes above the corner, a fraction of the incident vorticity is swept along the front face causing secondary separation. The incident vorticity field is spread out by diverging flow near the elliptic leading edge in Figures 4d and 4e [ 23,24 ].

A number of challenging aspects of vorticity field-leading edge interaction pose interesting numerical research possibilities. Some of these aspects are reviewed in Figure 5. In a general sense, unresolved predictions are: to simulate secondary shedding due to the nature of the edge (Fig. 5a), the vortex induced boundary layer separation (Fig. 5b), incident vortex edge boundary layer interaction ( Fig. 5c). Another real challenge is the phasing of the interaction between the incident vorticity and the edge separation as depicted in Figure 5d.

Clearly the most important deficiency of the presently available numerical methods is the inability to accommodate the details of the deformation of the incident vortical field at the edge and the generation and shedding of vorticity of opposite sense at the leading edge. There is also a strong need for an improved numerical model to simulate the redistribution and possible severing of regions of concentrated vorticity at the impingement surface. The structure of the incident vortices will depend on how they are generated, i.e. their upstream history. Generation of the vortex-edge interaction mechanism without specific knowledge of the degree of vorticity concentration upstream is inappropriate. Experimental observations indicate that one must accommodate an arbitrary distribution of vorticity in the incident vortex and a means of accounting for viscous effects at the edge.

The present work on numerical simulation of a vortex street represents several major innovative contributions. First, the Discrete Vortex Method (DVM) has been developed to predict the vortex shedding from a bluff trailing edge and simulate impingement on a downstream body of arbitrary geometry via a specially prepared inverse transformation technique. Thus, upstream history and means of generation of vorticity for an upstream body is well simulated for the first time. Secondly, the inviscid discrete vortex method coupled with the viscous diffusion is a new innovative method. HMVDM, is applied to study bluff trailing edge wake flows ( see Figure 6 ). Trailing edge vortex



shedding mechanisms were investigated with extensive numerical experimentation. The basic fundamentals of vortex street leading edge interactions were revealed. Finally, we may also note that both methods are able to simulate the details of the incident vorticity field. An accurate modelling of the detailed structure of the incident vortices is a real challenge to the predictor in the simulation of vortex impingement upon a surface.

## II. DISCRETE VORTICITY MODEL (DVM) OF IMPINGING VORTEX STREET

Organized vortices have been observed within the self-sustained oscillations of an impinging vortex street [9,24]. These vortices are generated by the instability of the shear layer separating from the upstream body. Using discrete vortices an attempt is made to simulate self-sustained oscillations. Although various models have been applied, this is the first work which includes the simulation of the "feedback" event to the best of the authors' knowledge. The process of feedback and disturbance amplification in the shear layer is accommodated. Conlisk and Rockwell [16] use experimentally determined locations and strength of vortices to simulate the vortex-corner interactions. Similarly, Panaras [17,18] represents impinging vortices by a vortex sheet of finite thickness composed of four rows of discrete vortices. Neither Panaras work nor Conlisk and Rockwell study were able to simulate the upstream flow details.

The modelling of vortex street-edge interaction described herein involves formulation of the irrotational flow past a bluff trailing edge, with discrete vortices originated from the fixed separation points of the edge. The modelling is considered in several phases. These steps are investigated below at various levels.

### Numerical Solution of Schwartz-Christoffel Transformation

Investigation of the unsteady vortex street-edge interaction involves generation of trailing edge wake flow impinging on a downstream edge. Due to its higher accuracy in representing the boundary conditions on the body a numerical Schwartz Christoffel transformation was employed to obtain the desired set up in the present study. This transformation algorithm enables the bluff trailing edge and the leading edge of arbitrary geometries (physical plane) to be transformed to a straight line segment (intermediate plane) as depicted in Figure 7. In the application of the HMVDM the computations are performed on rectangular grids (transformed plane). The appropriate general transformation can be shown to have the form:

$$\frac{dz}{d\zeta} = M \prod_{k=1}^n (\zeta - a_k)^{\alpha_k / \pi} \quad (2.1)$$

where the symbols are defined in the Figure 7. A grid system which will be used later by both numerical methods is successfully set up using the rectangular mesh system in the transformed plane. The full integration of Equation (2.1) is handled

with a numerical algorithm based on the technique discussed by Davis [25]. The general numerical Schwartz-Christoffel transformation algorithm based on Davis's approach has been developed by Cozens [7]. In this study this routine was modified and used to generate grids including the generation of the trailing edge and the impingement edge geometries. The details of the grid structures used, both for free and impinging vortex streets, are shown in Figure 8.

### Basis of the DVM and the Numerical set up

The oldest and most simple vortex method is the DVM in which the vortices are represented by Dirac distributions. Then the vorticity field is represented by:

$$\omega(\vec{x}, t) = \sum_{k=1}^N \Gamma_k \cdot \delta(\vec{x} - \vec{x}_k(t)) \quad (2.2)$$

in which  $\vec{x}_k(t)$  is the instantaneous position of the point vortex with index  $k$  and circulation  $\Gamma_k$  and  $\delta$  is the Dirac distribution.

To satisfy the 2-D inviscid vorticity transport equation

$$\frac{\partial \omega}{\partial t} + (\vec{u} \cdot \nabla) \omega = 0 \quad (2.3)$$

the velocity of each vortex has the value of the velocity field at its present location

$$\frac{d\vec{x}_k(t)}{dt} = \vec{u}(\vec{x}_k, t) \quad (2.4)$$

This local fluid velocity  $\vec{u}(\vec{x}_k, t)$  is induced by all other vortices, except the vortex itself, together with an additional potential velocity representing the free stream potential flow past the body. Figure 9 shows the appropriate planes with the potential flow models. A uniform flow-doublet combination transforms into the potential flow past the trailing and leading edge combination in the physical plane as is shown in Figure 9c. Hence, the mean flow chosen for this study is given by

$$W_m(\zeta) = -iu\zeta + u/\zeta \quad (2.5)$$

The basis of the DVM consists in the representation of the shear layer from a bluff trailing edge by a series of point discrete vortices (see Figure 10). In general, the form of the vortex system and its image in the intermediate plane are known. In the intermediate plane, the complex potential,  $W(\zeta)$ , for a set of discrete vortices superposed on a mean flow is given by

$$W(\zeta) = W_m(\zeta) + \sum_{j=1}^N \frac{i\Gamma_{ju}}{2\pi} \log(\zeta - \zeta_{ju}) - \sum_{j=1}^N \frac{i\Gamma_{ju}}{2\pi} \log(\zeta - \bar{\zeta}_{ju}) - \sum_{j=1}^N \frac{i\Gamma_{jl}}{2\pi} \log(\zeta - \zeta_{jl}) + \sum_{j=1}^N \frac{i\Gamma_{jl}}{2\pi} \log(\zeta - \bar{\zeta}_{jl}) \quad (2.6)$$

where in equation (2.6),  $N$  is the number of vortices released into the mean flow from the upper and lower separation points of the trailing edge,  $\Gamma_{uk}$  and  $\Gamma_{lk}$  are the strength of the separating vortices from the upper and lower separation points,  $\zeta_{uk}$  and  $\zeta_{lk}$  are their respective positions.

The equation of motion of the vortices can be written in the physical plane at each point  $z$  of the vortex sheet with Routh's correction,

$$\frac{dz_k}{dt} = \frac{\partial W}{\partial z_k} = \left\{ iU + \frac{1}{\zeta_k} + \frac{1}{2\pi m} \sum_{m \neq k} \Gamma_{um} \left( \frac{1}{(\zeta_{uk} - \zeta_{um})} - \frac{1}{(\zeta_{uk} - \bar{\zeta}_{um})} \right) + \frac{1}{2\pi} \Gamma_{uk} \left( -\frac{1}{(\zeta_{uk} - \bar{\zeta}_{uk})} \right) - \frac{1}{2\pi} \sum_{m \neq k} \Gamma_{lm} \left( \frac{1}{(\zeta_{lk} - \zeta_{lm})} - \frac{1}{(\zeta_{lk} - \bar{\zeta}_{lm})} \right) - \frac{1}{2\pi} \Gamma_{lk} \left( -\frac{1}{(\zeta_{lk} - \bar{\zeta}_{lk})} \right) \right\} \frac{\partial \zeta_k}{\partial z_k} - \frac{\Gamma_{uk}}{4\pi} (f''(z_{uk})/f'(z_{uk})) - \frac{\Gamma_{lk}}{4\pi} (f''(z_{lk})/f'(z_{lk})) \quad (2.7)$$

The vortices are shed from the points corresponding to the edges into the shear layers as a result of the separation of the boundary layers along the upper and lower faces of the trailing edge.

Among the various critical aspects of the method, particularly the problem of advancing the vortices, deserves more attention due to the complexity of the transformations between the physical and intermediate planes. For this reason, "Scan Line Algorithm" has been developed to obtain the corresponding position of the vortex in the computational space (intermediate plane). On the other hand, the transformation  $z=f(\zeta)$  is carried out with the numerical integration of the Schwartz Christoffel transformation. Given each vortex position in the physical plane, the new vortex positions are computed by a system of first order differential equations of motion with one step Euler integration. The corresponding position of the vortex in the intermediate plane is required for the next advancement and this task is carried out with numerical inverse transformation. This inversion task is accomplished with the use of the grid structures in the two successive planes.

### III. HYBRID MOVING VORTEX DIFFUSIVE METHOD (HMVDM) MODEL OF IMPINGING VORTEX STREET

This new simulation model based on a mixed Lagrangian-Eulerian Vortex Method for the simulation of two dimensional separated flow from a trailing edge and its consequent impingement on the downstream leading edge, will be presented in this section. The fluid is incompressible and the Reynolds number is high. This numerical method combines the Lagrangian convection and Eulerian diffusion schemes thereby eliminating the disadvantages of the purely Lagrangian inviscid model using discrete vortices of the previous section. This new vortex method represents a new approach to the solution of the Navier Stokes equations and is called the Hybrid Moving Vortex Diffusive Method (HMVDM) [7].

The method solves, subject to the

elliptic Vorticity-Stream function Poisson equation, the Navier-Stokes vorticity transport equation. The computations are performed in the transformed plane where the computational grids are set up (see figure 8d). Viscous diffusion is carried out in a standard way by finite differences on a fixed grid. But the convection terms in the vorticity transport equation are simulated by convecting point vortices as in the inviscid method through the grid. A split time step approach is used to separate diffusion and convection.

The flow field is transformed as before into rectangular domain with the solid boundaries along the top and bottom walls. The 2-D unsteady Navier Stokes equations in vorticity stream function form in the computational plane (transformed plane) are

$$\nabla^2 \psi = -J^{-1} \omega \quad (2.8)$$

$$J \frac{\partial \omega}{\partial t} + \tilde{u} \cdot \nabla \omega = \nu \nabla^2 \omega \quad (2.9)$$

where  $J$  is the Jacobian of the transformation. For convection purposes the vorticity field is represented by a distribution of discrete vortex points.

The details of the method are given in Cozens [7]. Here the main steps of the HMVDM will be given.

1. Perform the general Schwartz-Christoffel transformation to obtain the mesh network in accordance with the arrangement presented in Figure 2.
2. Distribute the point vorticity onto the mesh system by bi-linear weighting.
3. Solve the Poisson's Equation (2.8) on the mesh and obtain mesh values of the stream function. This is done by Fast Fourier Transform and Gaussian elimination of the resulting tridiagonal set of equations.
4. Perform diffusion by finite differences on the meshes subject to the vorticity boundary condition on the solid walls.
5. Repeat step 3 using the values of mesh vorticity computed in step 4.
6. Project the new mesh vorticity back onto the system of point vortices.
7. Compute mesh velocities from the stream function using a finite difference approximation.
8. Compute convection velocities at the point vortices from the known mesh velocities and convect the vortices according to their respective convection velocities.

The HMVDM is in general similar to finite difference Navier Stokes methods but with Lagrangian Convection.

### IV. RESULTS

The flow structure in the leading edge region involves different mechanisms for each edge type. The structures will be illustrated through the use of computed vortex distributions, instantaneous

streamlines and velocity vectors in moving and fixed reference planes, and instantaneous vorticity contours.

In this section the results of the simulation models will be presented. Concerning the modelling of the impinging vortex street on sharp and blunt leading edges, DVM applications and the results will be discussed. The instantaneous vortex distribution and the streamlines in a reference frame moving with  $-U_\infty$  accompanied by velocity vectors. The time dependent pressure fluctuations, that are induced on a point of the interaction surface, will be related to the deformations of the incident vortical structures.

An extensive numerical experimentation with the viscous HMVDM showed that the interaction of vortices with a leading edge produces different interaction patterns depending upon the Reynolds number and the edge geometry. The corresponding Reynolds number chosen in the present numerical simulation, based on the thickness of the trailing edge, is  $Re=1800$ , ( $Re=U_b/\nu$ ).

#### Numerical Simulation of a Free Shear Layer

The trailing edge wake flow was computed as a test case by the two new computer codes. Vortex shedding and the formation of the vortex street behind the bluff trailing edge have been simulated and presented in Figures 11 and 12.

The instantaneous vortex distribution and streamlines in a reference frame moving with  $-U_\infty$  accompanied by instantaneous velocity vectors are shown in Figures 11a through 11c. Vortices of alternate sign are formed which convect from the trailing edge under their mutually induced velocity field and the main free stream. Both the streamline contours and the velocity vectors represent the nature of vortical structures.

Figures 12 a - c show the nature of the unsteady viscous flow from left to right past the bluff trailing edge obtained via HMVDM. The Reynolds number based on the trailing edge thickness is 1800. Figure 12a shows that the development of the vortex street is purely laminar and shows some signs of instability downstream. The numerical experiments showed that this instability may be removed with more fine mesh structure which crowds the points in the downstream area. However, the cost of computing becomes really high due to the increase of mesh points. The instantaneous streamlines on a fixed reference frame represents the wavy character of the vortex sheet. The developing vortical regions of the flow are depicted in Figure 14c with the help of instantaneous velocity vectors at a reference frame moving with  $-0.7 U_\infty$ . The careful screen by screen study of the evolution of the free shear showed that the vortices are convecting with an approximate velocity of  $0.7 U_\infty$ .

#### Numerical Simulation of an Impinging Shear Layer

Concerning the simulation of an impinging vortex street, the DVM computer code has been applied for flow past sharp and blunt leading edge geometries. Figure 13 shows an overview of the vortex-street sharp edge

interaction patterns at three instants of time. The distribution of point vortices at the corresponding times are given in the left column. The flow past the trailing edge produces a vortex street with the main features of a wake flow at high Reynolds number. When the vortex distributions are studied at successive times it is realized that alternating sign vortices are subjected to rapid distortion near the edge. The vortical structures are split in two and some portion of the vorticity is swept along the other side of the sharp edge surface depending on the character of the approaching vorticity. Similar to the planar jet-edge interactions [14,22] unsteady flow distortion on both sides of the edge causes periodic interaction patterns. Contours of the constant streamlines constructed after superposing  $-U_\infty$  on the entire flow field are shown in the middle column (See Fig. 13). The flow field shows closed streamlines having an appearance similar to the pattern of classical vortex-street. The splitting of the incident vorticity field into two portions are very well simulated in these figures. The computed instantaneous velocity vectors are shown on the right column.

The computed interaction mechanisms for vortex street blunt edge interactions are presented in Figure 14. It is important to note that the wavelength of the vortex street is much higher than that of the case in Figure 13. This is due to different geometric properties of the impingement set up (different impingement length and edge thickness). The partial clipping of the incident vortical structure on the edge boundary is then followed by severe distortion along the surface. The splitting mechanism of the incident vorticity field is different than the distortions observed in the sharp edge case.

Figure 15 shows the corresponding unsteady pressure coefficient variation obtained during the impingement process. The pressure traces are obtained with the unsteady Bernoulli's Equation. For direct comparison two points are chosen on two opposite sides of the edges. It is clear that pressures are periodic and repeatable with small scale noise components on each trace. This is due to the chaotic behaviour of the discrete vortices near the surface under the influence of their images inside the body. Furthermore there is almost  $180^\circ$  phase difference between the fluctuating pressure signals.

Although the method has a very good computational efficiency and is able to simulate the distortion of the vortical structures at the edge, possible generation of secondary vortex or vortex induced boundary layer separation requires separate modelling. This is why the second viscous computer code has been developed.

The nature of the organized vortices within the oscillating vortex street that impinge on leading edges are very well simulated with the viscous vortex method, HMVDM, in the present study. Figure 16 shows an overview of the computed interaction mechanisms at six successive times for each leading edge type. The vortical regions are characterized with a high density of point vortex distributions. The dense cloud of point vortices is distorted at the sharp

edge. The impingement scenario for each case starts at the same elapsed computation time. There is a distinct phase lag between the appearance of the events near the edge. This is the clear evidence of the "feedback" from the downstream edge. The upstream moving perturbation excites the separation point and shedding occurs in accord with the downstream flow fluctuations near the edge surface. As the bluntness of the downstream leading edge increases, both the wavelength and the size of the vortical structures decrease. The distorted incident vorticity field conserves its identity further downstream of the sharp leading edge whereas the incident vorticity field loses coherence during the interaction with elliptic and blunt edges.

In order to examine in detail the effect of the impingement edge on the flow field the instantaneous vorticity contours are studied at successive times. It is realized that the vortices are subjected to rapid distortion near the edge, deforming into elongated structures. In Figure 17, regions of negative vorticity (shaded areas) and positive vorticity (open areas) at six successive times during the period are shown in the left column. Contours of constant dimensionless vorticity at the corresponding times are given in the right column. The vortical structures are split in two and some portion of the negative vorticity is swept along the lower surface of the edge (see Figure 17a). The major part of the incident vortex with negative vorticity interacts with the edge boundary layer. The vorticity within the incident vortices convected by the mean flow is small compared to the large vorticity in the edge wall layer. Numerical simulations show that the vortex Reynolds number  $Re = U/\nu$  is around 5000. Similar mechanisms are responsible for the lower surface flow activity. The nature of the edge boundary layer deserves special attention. The sign of the vorticity fluctuation changes around the stagnation point. The vorticity within the vortical structures is redistributed during the sweep along the surface of the edge (see Figure 17).

Figures 18 and 19 present the cases for the blunt and elliptic edge interactions. In the case of vortex-street impingement on an elliptic edge, important features of the laboratory observations [24] were revealed by the viscous computer code. The passing of the primary vortices do not induce strong boundary layer separation. The edge boundary layer is attached most of the time.

The viscous numerical model predicts the rapid distortion of vortex structures near the blunt edge. Furthermore a sharp blunt edge corner causes the flow to separate and leads to the formation and shedding of small scale vortices. An extensive numerical study is underway to investigate the coupling of these vortices with the primary vortices of the vortex-street. Inspection of sequences of the vortex impingement shows that approaching vortex is split into two unequal parts. A major part of the vortex continues to roll up over the edge surface while the other portion ceases on the other side. The split and arrival of the vortices affects also temporal development of vorticity near the front surface of the blunt edge.

## REFERENCES

- [1] Claus, R.W., Huang, P.G. and MacInnes, J.M., Time-Accurate Simulations of a Shear Layer Forced at a Single Frequency, *AIAA J.*, Vol.28, No.2, 1990, 267-275.
- [2] Sarpkaya, T., Computational Methods with Vortices, The 1988 Freeman Scholar Lecture, *J. Fluid Eng.*, Vol.111, No.5, 1989, 5-52.
- [3] Spalart, P.R., Leonard, A. and Baganoff, D., Numerical Simulation of Separated Flows, NASA TM-84328, 1983.
- [4] Round Table Discussion on Modelling of Time-Variant Flows Using Vortex Dynamics, Agard Advisory Report No.239, 1987.
- [5] Chorin, A.J., Numerical Study of Slightly Viscous Flow, *J. Fluid Mech.*, Vol. 57, 1973, 785-796.
- [6] Roache, P.J., Computational Fluid Dynamics, Hermosa, New York, 1972.
- [7] Cozens, P., Computation of Separated Flows Using a Viscous Vortex Method, Ph.D. Thesis, Imperial Coll., 1988.
- [8] Kaykayoglu, C.R. and Graham, J.M.R., Vortex Sharp Edge Interactions, *Imp. Coll. Aero. Rep. TM 89-01*, 1989.
- [9] Rockwell, D.O., Oscillations of Impinging Shear Layers, *AIAA J.* Vol 21, 1983, 645-664.
- [10] Rockwell, D.O. and Naudascher, F., Self Sustained Oscillations of Impinging Free Shear Layers, *Ann. Rev. Fluid Mech.*, Vol.11, 1979, 67-94.
- [11] Rockwell, D.O. and Knisely, G., The organized nature of Flow Impingement upon a Corner, *J. Fluid Mech.*, Vol.93, 1979, 413-432.
- [12] Ziada, S. and Rockwell, D.O., Vortex Leading Interaction, *J. Fluid Mech.*, Vol. 118, 1982, 79-107.
- [13] Tang, Y.-P. and Rockwell, D.O., Instantaneous Pressure Fields at a corner Associated with Vortex Impingement, *J. Fluid Mech.*, Vol.126, 1983, 187-204.
- [14] Kaykayoglu, C.R. and Rockwell, D.O., Unstable Jet-Edge Interaction Part I: Instantaneous Pressure Fields at a Single Frequency, *J. Fluid Mech.*, Vol.169, 1986, 125-149.
- [15] Rogler, H., The Interaction Between Vortex-Array Representation of Free Stream Turbulence and Semi-Infinite Flat Plates, *J. Fluid Mech.*, Vol.87, 1978, 583-606.
- [16] Conlisk, A.T. and Rockwell, D.O., Modelling of Vortex-Corner Interaction Using Point Vortices, *Physics of Fluid*, Vol.24, 1981, 2133.
- [17] Panaras, A.G., Pressure Pulses Generated by the Interaction of a Discrete Vortex with an Edge, *J. Fluid Mech.*, Vol. 154, 1985, 445-461.
- [18] Panaras, A.G., Numerical Modelling of the Vortex/Airfoil Interaction, *AIAA J.*, Vol. 25, 1987, 5-11.
- [19] Kaykayoglu, C.R., Numerical Simulations of Vorticity field 2-dimensional Body Interactions, *Proceedings of 20th Midwestern Mechanics Conf., Develop. in Mech.*, Vol.14(b), 1987, 543-548.
- [20] Rockwell, D.O., Kaykayoglu, C.R., Sohn, D. and Kuo, C.H., An Assessment of Some Vorticity Field-Leading Edge Interactions, *Shear Flow-Structure Phenomena*, Edited by A. Akay and M. Reischman, ASME NCA Vol.1, 1985, 79-88.
- [21] Kaykayoglu, C.R. and Rockwell, D.O., Vortices Incident Upon a Leading Edge: Instantaneous Pressure Fields, *J.*

- Fluid Mech., Vol. 156, 1985, 439-461.
- [22] Kaykayoglu, C.R. and Rockwell, D.O., Unstable Jet-Edge Interaction Part II: Multiple Frequency Pressure Fields, J. Fluid Mech., Vol. 169, 1986, 151-172.
- [23] Sohn, D.Y., Vortex-Interaction with a Leading-Edge of Finite-Thickness, M.S. Thesis, Lehigh University, 1985.
- [24] Gursul, I., Interaction of Karman VortexStreet with an Elliptical Leading Edge, Ph.D. Thesis, Lehigh University, 1988.
- [25] Davis, R.T., Numerical Methods for Coordinate Generation Based on Schwartz-Christoffel Transformations, AIAA Paper 79-143, Williamsburg, Virginia, 1979.
- [26] Harrington, S., Computer Graphics, McGraw Hill Book Company, New York, 1977.

## ACKNOWLEDGEMENT

The support of NATO under research grant number 373/87 is acknowledged.

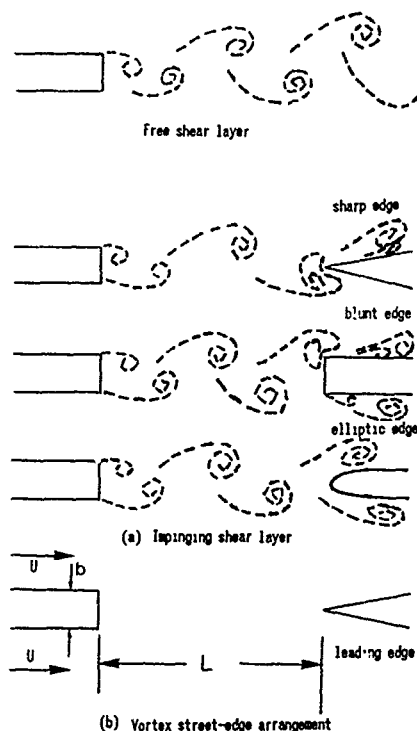


Figure 2.

Inviscid and viscous simulations of vortex street-edge interaction arrangements.

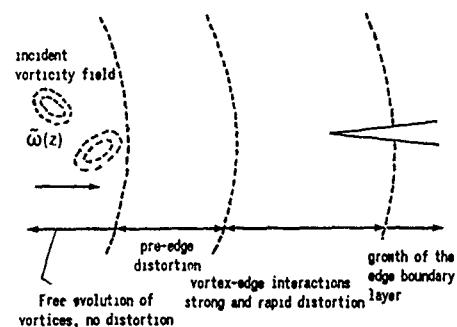


Figure 1a. Fundamentals of Vortex-Edge Interaction.

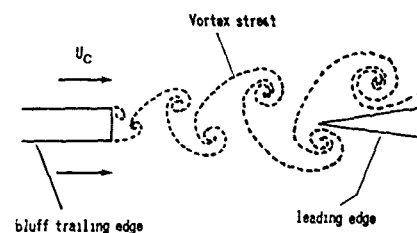


Figure 1b. Schematics of vortex street-edge interaction.

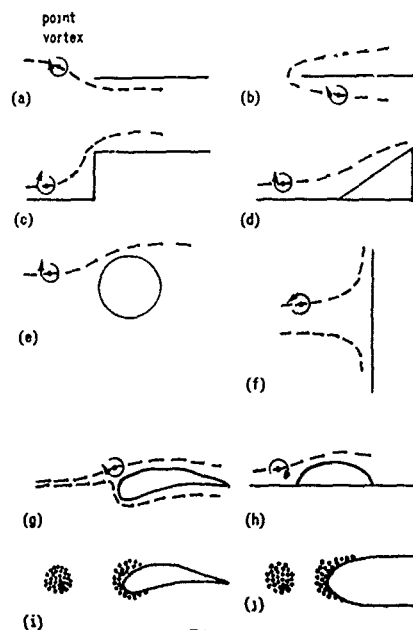


Figure 3.

Previously investigated linear, inviscid, point vortex simulations of vortex-edge interactions.

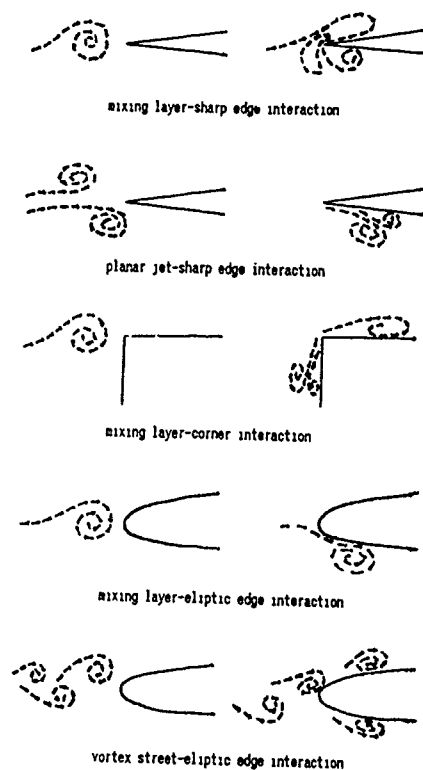


Figure 4. Experimentally investigated vorticity field-leading edge interactions.

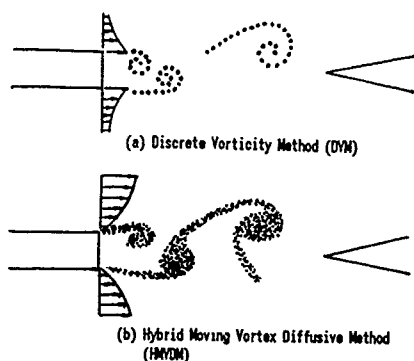


Figure 6. Models of the present numerical simulation.

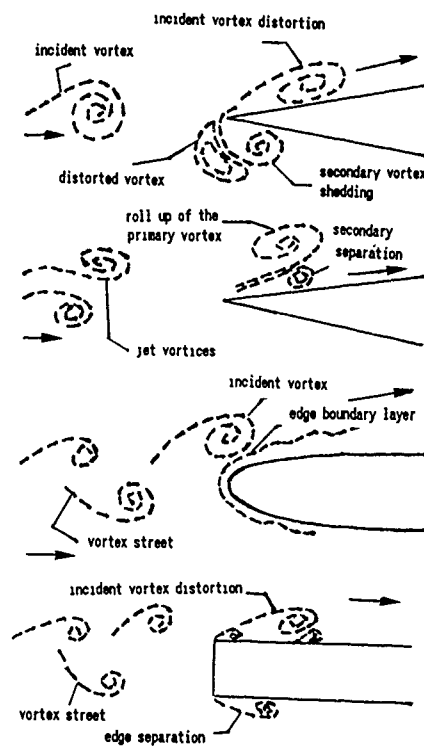


Figure 5

Challenging aspects of vorticity field-edge interactions posing interesting numerical simulation possibilities.

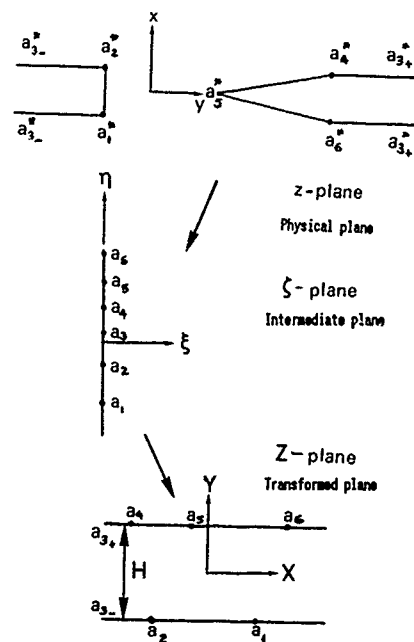


Figure 7. Transformation planes.

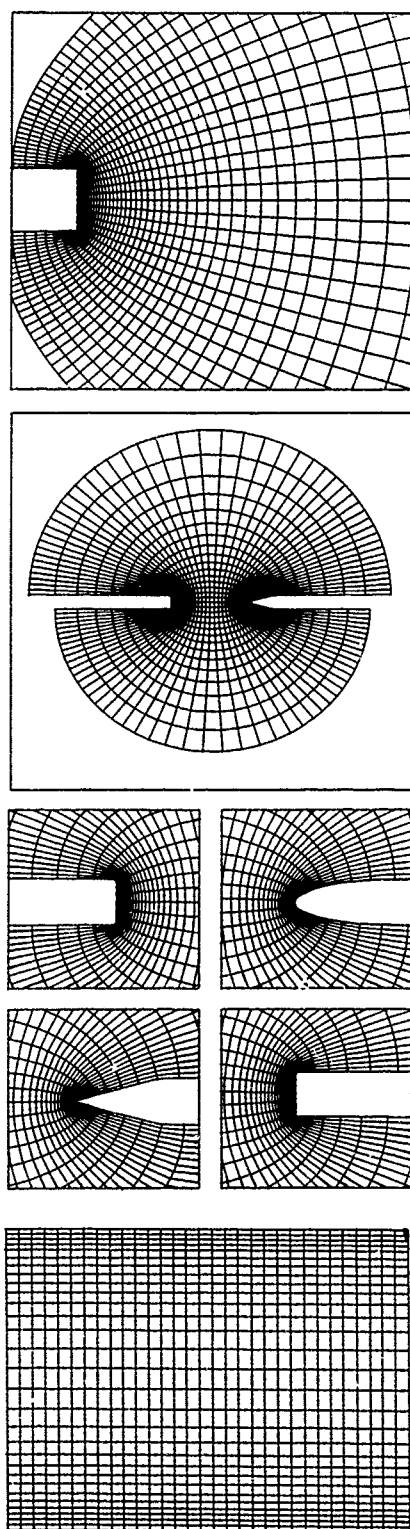
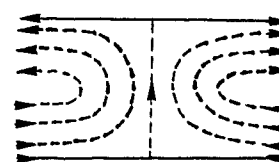


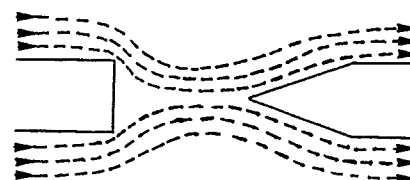
Figure 8. Details of the grid structures.



(a) Transformed plane



(b) Intermediate plane



(c) Physical plane

Figure 9. Potential flow models in different planes.

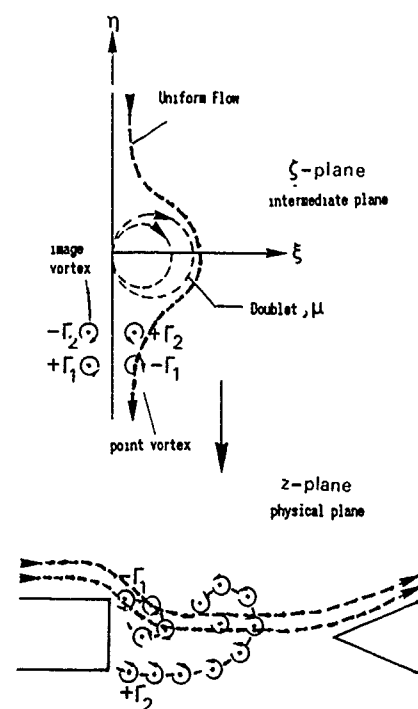


Figure 10. Essentials of the Discrete Vorticity Method (DVM) simulation

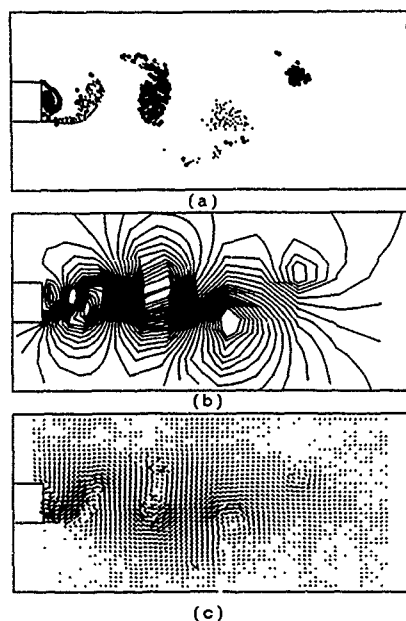


Figure 11. Discrete Vorticity Method (DVM) simulation of the free shear layer exhibited by  
 (a) discrete vortices,  
 (b) streamlines at a moving reference plane,  
 (c) instantaneous velocity vectors.

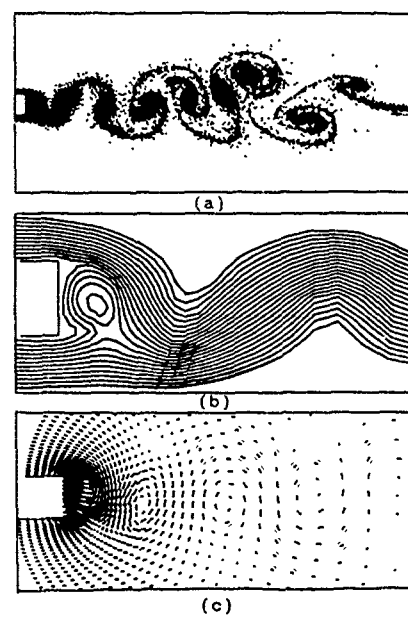


Figure 12. Hybrid Moving Vortex Diffusive Method (HMVDM) simulation of the free shear layer exhibited by  
 (a) discrete vortices,  
 (b) streamlines at a fixed reference plane,  
 (c) instantaneous velocity vectors.

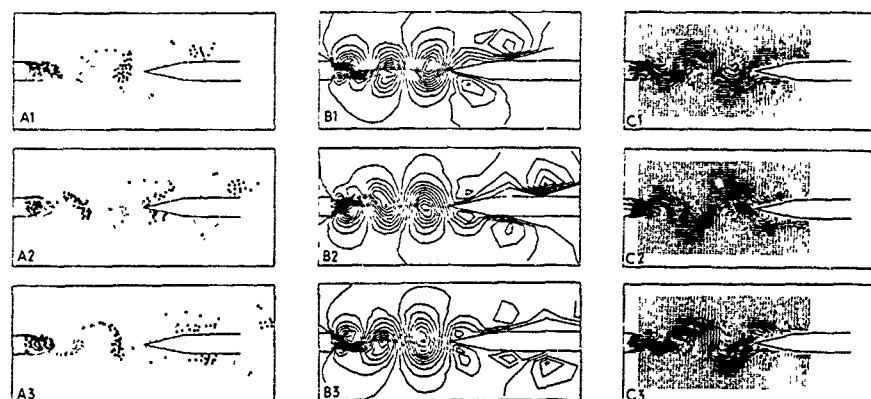


Figure 13. Discrete Vorticity Method (DVM) simulation of the vortex street sharp edge interaction exhibited by  
 (a) discrete vortices,  
 (b) streamlines at a moving reference plane,  
 (c) instantaneous velocity vectors at a moving reference plane.



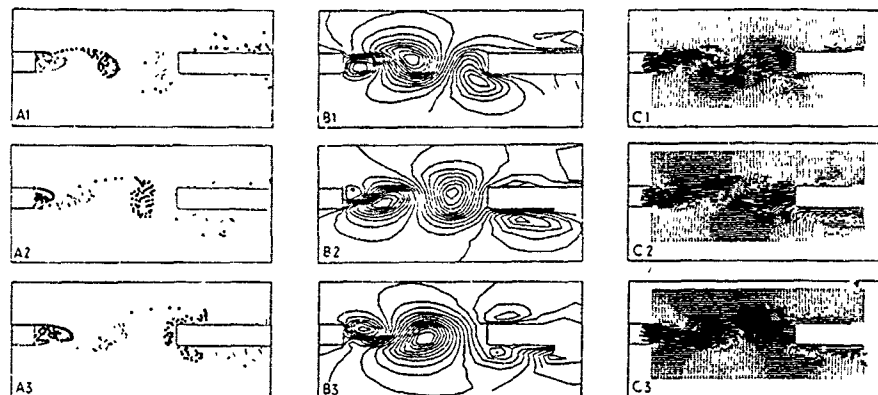


Figure 14. Discrete Vorticity Method (DVM) simulation of the vortex street blunt edge interaction exhibited by  
 (a) discrete vortices,  
 (b) streamlines at a moving reference plane,  
 (c) instantaneous velocity vectors at a moving reference plane.

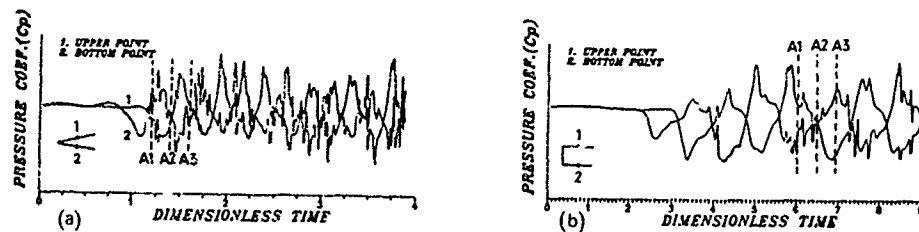


Figure 15. Unsteady pressure fluctuations on the edge surface induced by an incident vortex street  
 (a) sharp edge (b) blunt edge

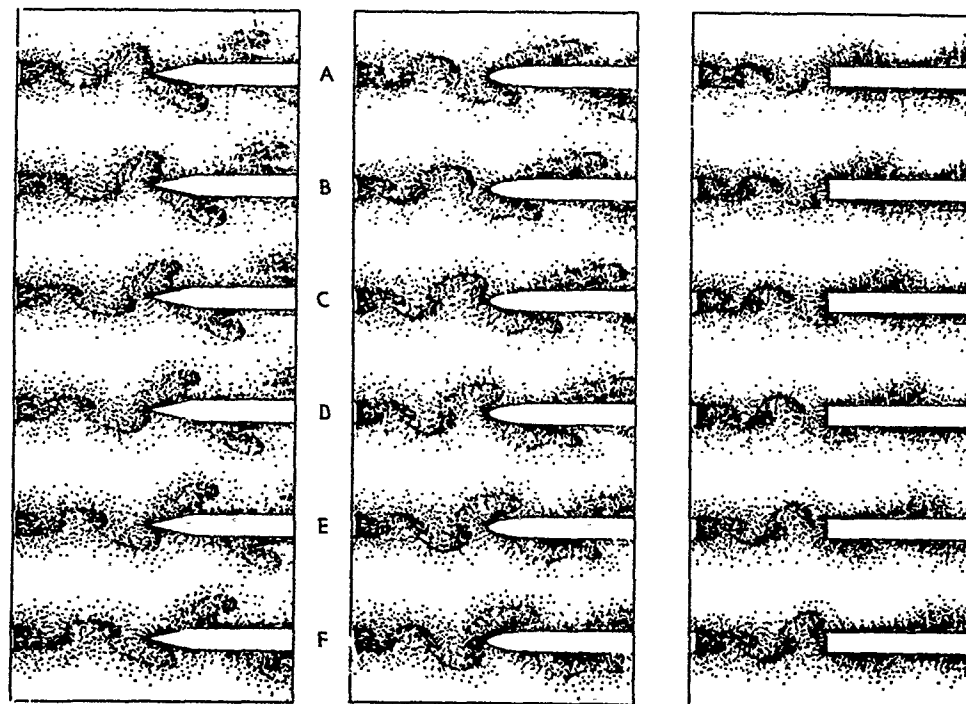


Figure 18. Overview of the vortex street edge interaction exhibited by instantaneous vortex distributions obtained by HMVDM simulation.

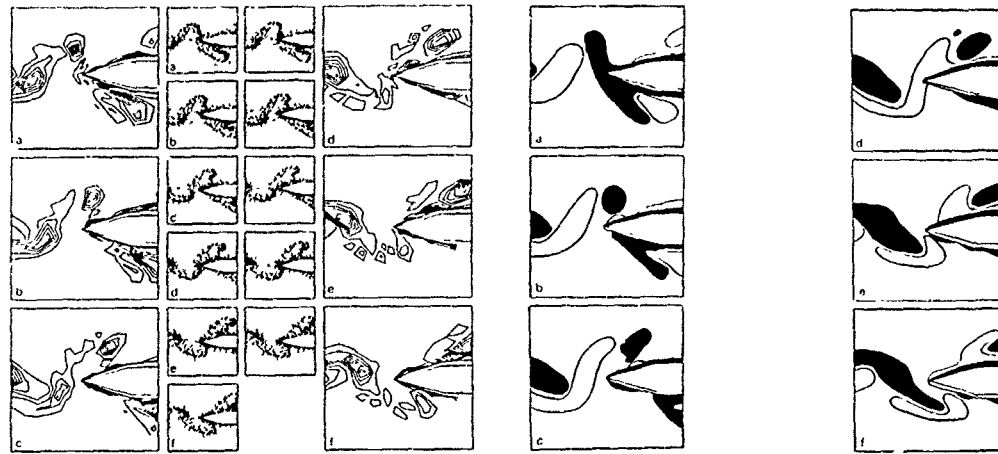


Figure 17. Overview of the contours of constant vorticity at corresponding time and regions of negative vorticity (shaded areas) and positive vorticity (open areas) for sharp edge interaction.

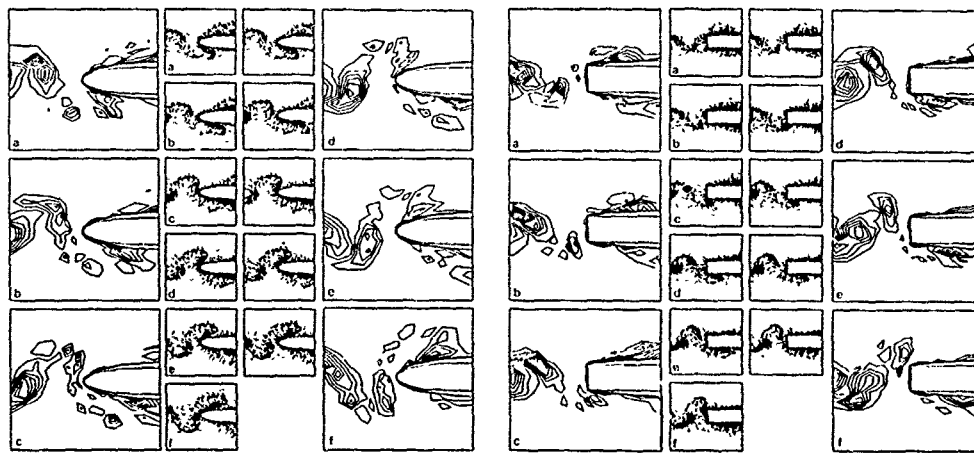


Figure 18. Overview of the contours of constant vorticity at corresponding time for elliptic edge interactions.

Figure 19. Overview of the contours of constant vorticity at corresponding time for blunt edge interactions.

# NUMERICAL SIMULATION OF VORTEX FLOWS PAST IMPULSIVELY STARTED WINGS

A. Baron, M. Boffadossi(\*), S. De Ponte

Politecnico di Milano  
Dipartimento di Ingegneria Aerospaziale  
Via C. Golgi, 40 - 20133 Milano - Italy

(\*) Fellow, Fondazione Ing. P. Foresio, Milano

## Summary

A non linear unsteady vortex lattice method is used to predict the geometry of the wakes and the distribution of aerodynamic loads on impulsively started wings.

Wings are assumed to have negligible thickness, arbitrary aspect ratio and planform. They can undergo a general unsteady motion. Multi-wing configurations can be treated.

Wakes can be released in the flowfield from any of the sharp edges of the lifting surfaces, depending on planform, aspect ratio and attitude of the wings.

Particular emphasis is placed on the simulation of vortex core diffusion which is regarded as a prominent factor in a correct development of unsteady wakes. A vortex core diffusion model is proposed which seems to be able to deal even with the severe roll-up of the shear layers past highly swept multi wing configurations with leading edge separation.

The prediction capabilities of the method are verified by comparison of the numerical results with experimental data published by various Authors.

## List of symbols.

AR	aspect ratio	T	dimensionless time $T=tU/C$
b	shear layer thickness	u, v, w	components of the absolute velocity V in the local frame of reference
C	wing root chord	U	characteristic velocity (of the body)
CL	lift coefficient	V	velocity (absolute frame of reference)
CM	pitching moment coefficient	X, Y, Z	local cartesian frame of reference
CN	normal force coefficient	X, Y, Z	absolute cartesian frame of reference
e	unit vector in Biot-Savart law (see Fig.1)	$\alpha$	angle of attack
K	constant in the turbulent diffusion model	$\phi$	velocity potential
h	distance of a generic point from a vortex segment in the Biot-Savart law (see Fig.1)	$\vec{\Gamma}$	linear vortex density vector
l	spanwise dimension of the elementary portion of shear layer	$\Gamma$	circulation
m	number of vortex segments on the lifting surfaces	$\Lambda$	sweep angle
M	number of vortex segments released in the wake	$\mu$	doublet strength distribution
n	local unit vector normal to the body surface	$\vartheta$	angle (see Fig.1)
N	number of panels laying on the lifting surfaces	suffixes	
r	vortex core radius	B	body
R	absolute position vector	D	turbulent diffusion
s	line delimiting surface S	L	lower
S	surface of the cross section of an elementary portion of shear layer, surface of the cross section of the vortex core	ST	stretching (transversal)
t	time	Sb	body surface
		Sw	wake surface
		u	upper
		o	initial value (time $t=0$ )
		ss	steady state

## 1 - Introduction.

Modern fighter aircraft operation at high angle of attack, during take-off, landing and unsteady maneuvering, is dominated by the interaction of vortical type flows and lifting surfaces.

In such flight conditions, unsteadiness and flow separation can produce nonlinear aerodynamic effects which significantly influence the instantaneous load distribution on the lifting surfaces and the controllability of the aircraft.

Numerical simulation of unsteady aerodynamics and the consequent wake dynamics is therefore much needed in flight dynamics and for structural load analysis.

Unfortunately, detailed solution of the complete time dependent fluid dynamic equations (Navier-Stokes equations) requires storage capabilities and computing times which are still unacceptable. However, when high Reynolds numbers are involved and flow separation is induced by sharp edges, Prandtl's hypotheses apply and simplified fluid dynamic equations can be used. While retaining three dimensionality and unsteadiness, the flowfield can be assumed to be irrotational and vorticity is only confined in shear layers of negligible thickness.

A wide family of formulations for the velocity potential, based on these assumptions, has been developed during the past years. They involve the solution of a Laplace's equation. An additional advantage of potential formulations lies in the use of Green's theorem. This results in an integral equation which is then solved on the body's boundary only, rather than over a complex grid spanning the whole fluid volume.

Starting from initial work by Belotzerkowskii (1967), Hess and Smith (1967), Woodward (1968), Labruyere et al. (1970) and others, related to steady flow problems, in which wakes were assigned and their geometries were assumed to be rigid, various extensions in simulation capability have been introduced.

Potential methods were extended to include small harmonic wing oscillations about small angles of attack by Morino and Kuo (1974).

Limitations on the angle of attack were removed, in steady flow conditions, by introducing nonlinear effects, such as tip and leading edge separation, by Belotzerkowskii (1969), Rehbach (1973), Weber et al. (1976), Kandil et al. (1977) and Hoeijmakers and Bennekers (1978). Wakes are determined as a part of the solution of the problem by the use of iterative techniques relaying on a first guess and successive corrections of the configuration of the wakes.

Finally, potential schemes have been formulated capable to cope with fully unsteady and highly nonlinear phenomena.

Following a two-dimensional scheme formulated by Giesing in 1968, wakes and flowfield are determined simultaneously, starting from an initial state of rest. Wings are impulsively started and wakes are generated with a Lagrangian process during which, at each time step, the vorticity present on the edges of the wings is convected in the field (Belotzerkowskii, 1977; Kandil et al., 1977; Mook, 1988; Konstantinopoulos et al., 1985; Katz and Maskew, 1988).

With time dependent approaches, aerodynamic loads and geometries of the wakes during unsteady maneuvers can be easily simulated considering the actual time dependent boundary conditions which represent, at each time step, the instantaneous velocity and flight attitude of the aircraft. Moreover, a Lagrangian generation does not require a first guess of the shape of the vortical sheets, which can be critical when multi-wing configurations of low aspect ratio have to be treated.

In all of these methods the vorticity of the wakes is discretized into a lattice of vortex filaments.

Vortex filaments are extremely efficient from a computational point of view and their use is in practice compulsory when iterative or time marching schemes have to be used. Nevertheless, a discrete vortex representation for continuous vortex sheets can turn out to be a too crude approximation when rapidly stretching and rolling-up wakes are involved (Hoeijmakers, 1983). As a result, difficulties can arise, mainly in the simulation of the flow past delta wings, such that no converged solution can be obtained.

Many numerical techniques have been developed in the attempt of overcoming this problem, such as the vortex filament/feeding sheet model, suggested by Smith (1978) and Hoeijmakers (1989), or the replacement of the system of discrete vortex lines with a single concentrated core (Kandil, 1985), or the "hybrid" method proposed by Jepps (1978). None of these techniques, however, can be applied to the simulation of unsteady three-dimensional flow fields, because of the simultaneous presence of both streamwise and spanwise time dependent components of the vorticity vector.

The use of a numerical method developed by Baron and Boffadossi (1989) for the simulation of the unsteady nonlinear three-dimensional flow past multi wing configurations confirmed once more that vortex modelling is a crucial aspect in the numerical simulation of vortical flows.

While the use of Rankine vortices together with viscous core diffusion has been successful in treating impulsively started wings (regardless of their planform, aspect ratio and angle of attack), provided leading edge separation was absent, numerical solution of the flow around delta wings with leading edge separation, on the contrary, proved to be extremely sensitive to the value of the artificial viscosity coefficient used to produce viscous core diffusion.

In the present work a physically consistent and numerically efficient viscous core

diffusion mechanism is proposed, capable to cope with the rapid roll-up process of unsteady wakes, whatever wing geometries, discretization and angle of attack. Even multiple delta wing configurations can be analyzed and reliable predictions of both geometries of the wakes and aerodynamic load coefficients are obtained.

## 2 - The computational method.

On the basis of a formulation first introduced by Belotzerkowskii (1977) and Kandil et al. (1977), a nonlinear vortex lattice scheme has been developed (Baron and Boffadossi, 1989) to model the unsteady incompressible flow past thin wings of arbitrary planform. The basic assumptions, relationships and limitations of the method are briefly summarized in the following, for the sake of completeness.

Wings are assumed to have a negligible thickness and are simulated as rigid or flexible, plane or cambered surfaces. They can undergo general motion. Geometry of the wakes and distribution of aerodynamic loads are predicted, as a function of time, starting from an initial state of rest. Wakes can be released in the flowfield from any of the sharp edges of the wings, depending on planform, aspect ratio and attitude of the wings. The code can treat general planforms, whatever their aspect ratio and number of edges, and multi-wing configurations, provided the lines along which separation takes place (regardless of their number) are prescribed.

The unsteady flow of an incompressible ideal fluid is irrotational in the region outside of the lifting surfaces and the separated vortex sheets. It is therefore governed by the Laplace's equation:

$$\nabla^2 \phi(R, t) = 0 \quad (2.1)$$

where  $\phi$  is the velocity potential, at time  $t$ , expressed in terms of the absolute position vector  $R$ .

The second order, linear differential equation (2.1) can be solved once appropriate boundary conditions are prescribed at any time  $t$ . These express the far field condition ( $\nabla \phi = 0$ ,  $R \rightarrow \infty$ ) and the no-penetration condition on the material surfaces  $S_s$ :

$$[\nabla \phi(R, t) - V_s(R, t)] \cdot n(R, t) = 0 \quad \text{on } S_s \quad (2.2)$$

where  $V_s(R, t)$  is the local body velocity vector and  $n(R, t)$  is the local unit vector normal to the surface, both at time  $t$ .

Using Green's theorem according to Hunt (1980), the velocity at the generic point  $P$ , at time  $t$ , can be written in the usual integral form:

$$V_P = \nabla_P \phi = \frac{1}{4\pi} \iint_{S_s} \Delta \phi_Q \nabla_P \left[ \frac{1}{|P-Q|} \right] \cdot n_Q dS_Q + \frac{1}{4\pi} \iint_{S_w} \Delta \phi_Q \nabla_P \left[ \frac{1}{|P-Q|} \right] \cdot n_Q dS_Q \quad (2.3)$$

where  $\nabla_P$  and  $\nabla_Q$  denote the gradient operators evaluated in  $P$  and  $Q$ ,  $|P-Q|$  is the distance between point  $P$  and the generic point  $Q$  laying on the lifting surfaces  $S_s$  or on the vortex sheets  $S_w$  across which the jump in the velocity potential  $\phi$  is  $\Delta \phi_Q$ .

For the solution of equation (2.3) wings and wakes are discretized into a finite number of surface panels with constant doublet strength  $\mu = \Delta \phi$ . Due to the equivalence between doublet and vorticity distributions (Hoeijmakers 1989), each panel is therefore made up of straight vortex segments lying on its perimeter, forming a closed loop of circulation  $\Gamma = \Delta \phi$  (Mook 1988). Note that closed loop vortices are more convenient than usual horseshoe vortices for representing both streamwise and spanwise vorticity components present in time dependent flows.

Once vorticity has been discretized and Biot-Savart law is applied, equation (2.3) reduces to:

$$V(R, t) = V_{S_s}(R, t) + V_{S_w}(R, t) = \frac{1}{4\pi} \sum_{i=1}^m \left[ \frac{\cos \theta_A(R, t) - \cos \theta_B(R, t)}{h(R, t)} \Gamma(t) \right] e_i(R, t) + \frac{1}{4\pi} \sum_{j=1}^{N(t)} \left[ \frac{\cos \theta_A(R, t) - \cos \theta_B(R, t)}{h(R, t)} \Gamma(t) \right] e_j(R, t) \quad (2.4)$$

where  $m$  and  $M$  are the number of vortex segments laying on the lifting surfaces and on the free wakes respectively. The terms in equation (2.4) are identified in Fig.1. Note that when velocity is computed in a point laying on the lifting surfaces, one has to account for the self-induced tangential velocity due to the local strength of the vortex sheet.

The unknown values of the  $N$  circulations  $\Gamma(t)_i$  on the lifting surface panels are

determined, at each time step, imposing the zero normal velocity condition (2.2) on the panel control points. Velocities are evaluated at control points through equation (2.4). A linear system of  $N$  algebraic equations is obtained, to be solved at each time  $t$ :

$$\sum_{i=1}^N A(t)_{ij} \Gamma(t)_j = \left[ v_b(t) \cdot n(t) \right]_i - \left[ v_{sw}(t-\Delta t) \cdot n(t) \right]_i \quad (i=1, N) \quad (2.5)$$

where:

$A(t)_{ij} = (v_{sb} \cdot n)_i$  is the normal component of the velocity induced, at time  $t$ , in the control point of the  $i$ -th panel by a unit circulation lying on the  $j$ -th panel;

$\Gamma(t)_j$  circulation present, at time  $t$ , on the  $j$ -th panel;

$v_b(t)_i$  velocity of the control point of the  $i$ -th panel ensuing from unsteady motion of the lifting surface;

$v_{sw}(t-\Delta t)_i$  velocity induced by the wakes on the control point of the  $i$ -th panel at time  $(t-\Delta t)$ , which, at time  $t=0$ , is assumed equal to zero, consistently with the hypothesis of impulsive start;

$n(t)_i$  unit vector normal to the  $i$ -th panel, at time  $t$ .

Equation (2.5) is more conveniently formulated in a body fixed reference frame in which, when rigid lifting surfaces are involved,  $A(t)_{ij}$  and  $n(t)_i$  become independent on time.

Starting from the rest, wakes are generated in a Lagrangian process, by releasing in the field the vorticity present on the edge panels. At the instant motion begins no vorticity has been convected. No wakes exist but a starting vortex forms along the sharp edges and is subsequently shed in the field. In order to obtain this, from the edges along which vorticity is shed, panels are "moved" in the field and form a first row of wake panels. At next time steps, each node of the existing wake is convected to a new position and a new row of panels is added to the wakes.

The instantaneous local velocity is computed and used to displace the nodes in order to produce force free vortical sheets. Displacement can be obtained by integration of velocity according to a first order Euler formula:

$$R(t+\Delta t) = R(t) + V(R, t) \Delta t \quad (2.6)$$

Iterative techniques similar to those used in steady flow problems, are suggested by Kandil (1985) and Mook (1988) to account for the error introduced by equation (2.6). Nevertheless much longer computing times are the counterpart for increased accuracy.

In the present method, a second order Adams-Bashforth integration formula is used instead of (2.6):

$$R(t+\Delta t) = R(t) + \left[ \frac{3}{2} V(t) - \frac{1}{2} V(t-\Delta t) \right] \Delta t \quad (2.6)$$

which proved to give more accurate results, without influencing at all computing times.

In the Lagrangian process, vorticity is conserved and circulation around each vortex segment in the wakes remains constant, according to Kelvin's theorem.

The distribution of the net pressure coefficient on the lifting surfaces is calculated by using Bernoulli's unsteady equation written in a body fixed reference frame (Kandil 1985). The total load coefficients are obtained by integration of pressure.

### 3 - Vortex core modelling.

The discretization of vorticity into vortex filaments (point vortices in plane flows), although computationally attractive, introduces in the flowfield lines along which the induced velocity, according to the Biot-Savart law, tends to infinity. This situation is not only unrealistic from a physical point of view, but can also turn out to be numerically inadequate to simulate flows in which regions of high vorticity content are present (typically the roll-up region of three dimensional wakes). The singular behavior of vortex filaments can be such to produce numerical instabilities and may cause the solution to diverge (Baron and Boffadossi, 1989).

In principle, the problem can be easily eliminated by preventing the induced

velocity, in points close to the vortex axes, from increasing above a certain value. This can be done in a variety of ways and basically consists in introducing what is called a vortex, or vortex core, model.

Some authors overcome numerical instabilities by adopting an "appropriate" cut-off radius below which the velocity induced by vortex filaments is assumed to be equal to zero. Satisfactory results are reported, even in unsteady flow simulation, by Mook (1988). Solutions, however, depend significantly on the assigned value of the cut-off radius which must therefore be carefully tuned in order to deal with each particular application (i.e. wing aspect ratio, angle of attack, geometrical discretization, etc.)

Rankine vortices, having a viscous core in solid body rotation, have been also used by many authors involved in the numerical simulation of vortical three-dimensional steady flows (Rusak et al., 1985; Buresti and Lombardi, 1989). Although Rankine vortices approximate to a larger extent the physical behaviour of real vortices, the same problem arises when the radius of their viscous core must be assigned (Rusak et al., 1985).

Artificial diffusion of the vortex cores (Bloom and Jen, 1974) can further improve the simulation capabilities of vortex lattice schemes provided, once again, a suitable diffusion law is prescribed.

Nevertheless, none of the above mentioned techniques proved to be fully successful, in author's experience, in the simulation of unsteady vortical flows past highly swept delta wings with leading edge separation (Baron and Boffadossi, 1989).

An attempt is made in the present work to extend the applicability of the simple Rankine vortex model, while avoiding recourse to any form of tuning. In order to do this, the diffusion process of turbulent shear layers is followed and a turbulent diffusion law for the vortex core radius is derived.

#### 4 - Vortex core turbulent diffusion

At trailing edges of finite span wings, at angle of attack, vorticity is shed in the flowfield due to a difference in direction of the flow on the upper and lower surfaces. If Reynolds number is large, convection dominates diffusion and vorticity remains confined within thin free shear layers. Due to self induction, shear layers tend to roll up into vortex cores in which vorticity is continuously fed. As a consequence, a continuous stretching is applied to the shear layers in spanwise direction and vortex core radii progressively grow with time. At this stage, diffusion, either viscous or turbulent, begins to play a dominant role in the physical roll-up process.

Unfortunately most of the discrete vortex methods, and vortex lattice among them, are only consistent with the vorticity convection equation but completely neglect diffusion. Therefore, when diffusion becomes a prevailing phenomenon, it must be accounted for by explicit modelling. A physically consistent diffusion mechanism can significantly extend the simulation capability of vortex lattice schemes, while retaining their intrinsic simplicity. In the following, a turbulent diffusion model is derived in which vortex cores spread according to the turbulent diffusion rules of continuous shear layers.

Consider an elementary portion of a continuous shear layer small enough as to assume its curvature to be negligible and vortex strength  $\gamma = \mathbf{V}_u - \mathbf{V}_l$  to be uniformly distributed on its surface (Fig.2) and select a cartesian local frame of reference with  $y$  axis normal to the shear layer and  $x$  parallel to the local direction of vector  $\gamma$ .

A conventional shear layer thickness  $b$  is defined (Fig.3), at each time  $t$ , according to Oster and Wygnanski (1982):

$$b = y_{0.1} - y_{0.95} \quad (4.1)$$

with:  $y_{0.1}$  corresponding to the location at which  $u = u_L + 0.1 \Delta u$

$y_{0.95}$  corresponding to the location at which  $u = u_L + .95 \Delta u$ .

The shear layer thickness  $b$  varies in time owing to two phenomena, namely turbulent diffusion and stretching in planes normal to vector  $\gamma$  (transversal stretching). As a matter of fact, a stretching in planes parallel to vector  $\gamma$  (longitudinal stretching) also exists. However, its effect is negligible with respect to the transversal one and to turbulent diffusion. This is true in both the initial stage of the shear layer roll-up (starting vortex) and in the downstream roll-up process in which, as formerly mentioned, diffusion becomes dominant. Therefore, the rate of change of thickness  $b$  of a shear layer can be expressed as:

$$\frac{db}{dt} = \left( \frac{db}{dt} \right)_D + \left( \frac{db}{dt} \right)_{ST} \quad (4.2)$$

namely, as the sum of the contributions due to turbulent diffusion (suffix  $D$ ) and transversal stretching (suffix  $ST$ ).

Let us examine the two contributions separately. The term due to turbulent diffusion is roughly independent on Reynolds number and, according to Prandtl's mixing length approximation, is proportional to velocity fluctuations which, in turn, can be

considered to be proportional to the velocity jump  $\Delta u$  across the layer. Therefore:

$$\left( \frac{db}{dt} \right)_D = K \Delta u = K \gamma \quad (4.3)$$

These assumptions are supported by a large number of experiments (Liepmann and Laufer 1947; Brown and Roshko, 1974; Lesieur 1987). In particular, a work by Oster and Wygnanski (1982), in which an exhaustive review of experimental results on forced and unforced shear layers is reported, allows to define a value for the universal diffusion constant  $K$  equal to 0.095.

Examine now the second contribution in equation (4.2), related to transversal stretching. Consider the cross section of an elementary portion of shear layer (Fig.4), having spanwise dimension  $\ell$ , thickness  $b$  and cross sectional area  $S$ . Circulation of velocity along line  $\Delta$  delimiting surface  $S$  is conserved in the stretching process. The area of  $S$  remains also unchanged, provided the fluid behaves as incompressible and longitudinal stretching is negligible. One can therefore write:

$$\left( \frac{dS}{dt} \right)_{ST} = \left( \frac{d}{dt} (b\ell) \right)_{ST} = \left( \frac{db}{dt} \right)_{ST} \ell + \left( \frac{d\ell}{dt} \right)_{ST} b = 0 \quad (4.4)$$

which turns into:

$$\left( \frac{db}{dt} \right)_{ST} = - \frac{b}{\ell} \frac{d\ell}{dt} \quad (4.5)$$

Coming back to equation (4.2), the time rate of change of thickness  $b$  is given by:

$$\frac{db}{dt} = K \gamma - \frac{b}{\ell} \frac{d\ell}{dt} \quad (4.6)$$

Once the evolutive behavior of a continuous shear layer has been expressed, discretization into Rankine vortices is carried out. Each discrete vortex is assumed to behave in the same way as the portion of continuous shear layer it replaces. Equivalence must be intended in terms of circulation  $\Gamma$ , diffusion and stretching (fig 5). In other words, the "equivalent" Rankine vortices are assumed to spread in a way such that their cross sectional area  $S$  and circulation  $\Gamma = \gamma \ell$  are equal, at each time, to spreading and circulation of a continuous shear layer containing the same vorticity. This brings to the relation:

$$\frac{dS}{dt} = \frac{d}{dt} (b\ell) = \frac{db}{dt} \ell + \frac{d\ell}{dt} b = 2 \pi r \frac{dr}{dt} \quad (4.7)$$

which implies a rate of change of their radius  $r$ :

$$\frac{dr}{dt} = \frac{1}{2\pi r} \left[ \left( K \frac{\Gamma}{\ell} - \frac{b}{\ell} \frac{d\ell}{dt} \right) \ell + \frac{d\ell}{dt} b \right] = \frac{K \Gamma}{2\pi r} \quad (4.8)$$

Equation (4.8) is therefore used to model the core diffusion process of each Rankine vortex in the vortex lattice scheme.

It states that vortex core diffusion is:

- proportional to the circulation  $\Gamma$  of the vortex,
- inversely proportional to its radius,
- independent on transversal stretching, namely on the rate of change of the distance between the axes of the vortices.

Integration of (4.8) brings to:

$$r(t) = \sqrt{\frac{K \Gamma}{\pi} (t - t_0) + r_0^2} \quad (4.9)$$

where  $r_0$  is the core radius at the initial time  $t=t_0$ .

Forms analogous to (4.8) are also proposed by Squire (1965), Govindaraju and Saffman (1971) and Leonard (1980) for the turbulent diffusion of single line vortices, however they involve empirical constants the value of which can not be defined in a general form. The present approach brings to a diffusion model consistent with the behavior of continuous turbulent shear layers and, in addition, information of experimental nature is introduced in a fully general way.

A final observation can be done on the vortex core diffusion model. Other techniques, as mentioned above, turn out to be strongly dependent on the number of vortex filaments used to discretize the continuous distribution of vorticity in the flowfield (Rusak et al., 1985). The present approach, on the contrary, is virtually independent on discretization, being turbulent diffusion explicitly related to the circulation of each



vortex filament and, therefore, to the number of vortices. This brings to a kind of "self adaptation" of the model and explains why, in a variety of applications (see next paragraph), no tuning is necessary for a correct simulation of vortex core diffusion.

## 5 - Numerical results.

Some applications of the unsteady vortex lattice scheme are presented with the purpose of comparing numerical predictions obtained with the present method with experimental, theoretical or numerical data published by various Authors. Although the present method can treat either impulsive starts or general unsteady motion of wings, in most cases comparative data, both experimental and numerical, are only available for the steady state. This implies that transient computations can often be only analyzed in a qualitative way.

Vortex core diffusion is modelled according to equation (4.9) without any form of tuning of the numerical parameters. An integration time step equal to one dimensionless panel chord is used for time discretization, which brings to nearly uniform vortex elements on wakes and lifting surfaces.

### 5.1 - Rectangular wings.

Numerical results concerning two rectangular wings of  $AR=6$  and  $AR=1$  are presented in Figures 6 to 11.

The above mentioned difficulties relative to vortex modelling and diffusion are not critical for this type of wings for which leading edge separation is absent and the roll-up of the wake is not so intense. Nevertheless, many experimental and theoretical studies are available in the literature for wings of this type, which makes it possible to verify some of the prediction capabilities of the present method.

For rectangular wings of relatively high aspect ratio (6 in the present case) an extension to finite span wings of the two dimensional potential theory of airfoils in nonuniform motion (Jones, 1940) can be used to verify the time evolution of the lift coefficient consequent to an impulsive start.

A comparison between theoretical and numerical predictions is shown in Figure 6 for an angle of attack of 12 degrees. Results are reported in dimensionless form due to the fact that theory predicts an asymptotic lift coefficient slightly higher than the real one (the computed value of the steady state lift coefficient is .91, which agrees with experiments, while the extension of the two dimensional potential theory brings to .97). The comparison is limited to a dimensionless time interval from  $T=0$  to  $T=6$ . The predicted behaviour of the transient lift coefficient closely matches the theoretical one.

For the same wing and angle of attack, the time dependent development of the wake is shown in Figure 7, at three different stages (.5, 1 and 2 chords). Solid lines in the wake represent longitudinal and transversal vortex filaments. A starting vortex forms first, along the wing tip and trailing edge during the impulsive start and is then convected downstream. Steady state configuration of the near wake is reached for a dimensionless time  $T$  approximately equal to 6.

The spanwise load distribution is reported in Figure 8, as a function of time. It is interesting to note how, despite of the relatively high aspect ratio, and according with experimental observations, a suction peak appears close to the wing tip, produced by a correct simulation of the tip separation.

Three dimensional features obviously become more evident in the flow past rectangular wings of lower aspect ratio. The time evolution of the wake configuration and that of normal force and moment coefficients are shown in Figures 9 and 10, for a wing of unit aspect ratio at an angle of attack of 14.5 degrees. Dotted lines represent longitudinal vortex filaments, transversal ones are omitted and solid lines show cross sections of the wake in planes normal to the wing. Steady state aerodynamic characteristics are in good agreement with experimental data by Belotzerkowskii (1969).

The spanwise load distribution, at the same angle of attack, is reported, as a function of time, in Figure 11. A peak in the load distribution again appears near the wing tip, grows and progressively tends toward the tip as lift increases with time. When steady state is approximated, load distribution closely matches measurements by Scholz (1949).

### 5.2 - Delta wing of unit aspect ratio.

Numerical results relative to a delta wing of unit aspect ratio, at an angle of attack of 20.5 degrees, are presented in Figures 12 to 14. This test case has been chosen as an example of flow involving both leading edge and severe roll-up of the wake, phenomena for the simulation of which vortex core modelling and diffusion are believed to play a determinant role. Furthermore, exhaustive experimental information is available for this wing planform.

The time dependent development of the wake is shown in Figure 12 at four different

stages (.25, .5, 1 and 2 root chords). Again dotted lines represent longitudinal vortex filaments, transversal ones are omitted and solid lines show cross sections of the wake in planes normal to the wing.

A starting vortex forms first, along the sharp edges, during the impulsive start, which rapidly rolls-up and is then convected downstream. Steady state configuration of the near wake is approximately reached for a dimensionless time  $T$  equal to 3.

A correct roll-up of the wake (Fig.13) is obtained despite of the limited number of vortex panels used in this example (8 by 16 panels in chordwise and spanwise directions, respectively). The effect of the counter-rotating vorticity shed at the trailing edge is also captured and, compatibly with discretization, vorticity distribution across the wake is quite well approximated. In Figure 13 a comparison is made with measured total pressure contours (Hummel, 1979) and numerical results (Hoeijmakers, 1989) in a plane normal to the free stream direction, 0.133 root chords downstream the trailing edge (equivalent to 0.533 half spans). Solid circles in Figure 13 have radii proportional to the circulation of each vortex filament. Being comparative data, both experimental and numerical, relative to the steady state condition, computation has been carried on until almost invariant loads and near wake configuration are reached.

The evolution in time of the aerodynamic loads acting on the wing (lift coefficient and longitudinal location of the centre of pressure) is reported in Figure 14. A good agreement with steady state measurements by Peckham (1958) is again observed. Oscillations in the time evolution of the loads appear during the initial stage of generation of the wake. This is due to the fact that leading edge vortices require a time interval approximately equal to one chord before they reach the trailing edge and their influence is exerted on the entire wing.

Note that, when intense roll-up of the wake is involved, vortex filaments may sometimes tend to cross the lifting surface being the no-penetration condition imposed only on a limited number of panel control points. To avoid this, a minimum distance of the vortex filaments from the solid surface can be imposed. However, wake body distance cannot be arbitrarily selected as it significantly influences induction of the vortices on panel control points and, consequently, both loads distribution and development of the wake. In the present method, consistently with physics, a local minimum distance is considered equal to the local core radius of each vortex, the time evolution of which is computed according equation 4.9.

### 5.3 - Double delta wing-canard configuration.

A time dependent generation of the wakes is particularly suitable for treating multiple wing configurations, even if a steady state condition has to be simulated. This is due to the fact that a time dependent scheme does not require a first guess of the shape of the vortical sheets which, as mentioned above, can become crucial mainly when planform, attitude and relative position of the wings are such to produce closely interfering wakes.

As a counterpart, a time dependent scheme is computationally more expensive than a relaxation method as a greater number of terms is involved (the circulations of transversal vortical filaments, which are virtually absent at steady state). In addition, longer computing times are necessary in order to develop the wakes for a sufficient length.

However, a significant time saving can be obtained if, after reaching a certain stage of development of the wakes, only the mutual induction of wakes and wings is accounted for, while self induction of the vortex filaments is neglected. As a matter of fact, self induction produced in the far wake proves only to increase roll-up and stretching, without changing at all the influence of the wake on load distribution.

It turns out that, for practical purposes, in most cases, vorticity in the wake can be simply convected, starting from a distance of the order of a couple of chords downstream the trailing edge. Being the number of vortices shed in the wakes proportional to the length of the wake, this procedure enormously speeds up the computations.

Numerical results are presented in Figures 16 to 17 for a double delta wing-canard configuration (Fig.15) for which wind tunnel tests were carried on in co-operation with Aermacchi S.p.A. (Trabucchi and Travostino, thesis work; 1988).

Wing and canard have the same planform, the canard is scaled 1:2.58 with respect to the wing and is located 0.09 wing chords above the wing and 0.09 wing chords upstream. The aspect ratio of both is 2.5.

The development of the wake is shown in Figure 16 for an angle of attack, of both wing and canard, of 12 degrees. Due to the relatively high aspect ratio and to the presence of rounded leading edges, separation of the vortical sheets is only observed at the tips and trailing edges of the lifting surfaces. The same condition is imposed to the numerical scheme.

Time evolution of the lift coefficient is presented in Figure 17, where a comparison is made with steady state measurements. The lift coefficients of wing alone, interfering wing and complete configuration are referred to the area of the wing, while the lift coefficient of the canard is referred to its own area.

The lift growth of the wing-canard combination differs somewhat from the monotonic lift increase of the wing alone. The starting vortex released by the canard induces on the wing a lift higher than that of the wing alone, during the initial stage of the impulsive start, until it reaches a downstream location of approximately one quarter of the wing root chord. After, its influence is such to reduce the wing's lift as long as it passes

over the wing ( $T=1$ ). Finally wing's lift begins to increase slowly and reaches a steady state value which, as known, is significantly lower than that of the wing alone. This is due to the canard induced downwash while an upwash effect is produced by the wing with the result of an increase in the canard's lift.

#### 6 - Conclusions.

A nonlinear vortex lattice scheme, capable to treat a general unsteady motion of multiple lifting surfaces, is used for the simulation of the flow past impulsively started wings.

The comparison of numerical results with data available in the literature indicates that reliable predictions can be obtained for a variety of wing planforms and attitudes, even when leading edge separation is present and lifting surfaces are subject to strong mutual interference.

The satisfactory behaviour of the code, in highly unsteady flow conditions, as are impulsive starts, is probably ascribable to the use of a physically consistent vortex core diffusion model to the formulation and validation of which most of the present work is devoted.

#### References

- BARON A., BOFFADOSI M. (1989), "Simulazione numerica di scie vorticosi non stazionarie tridimensionali", Proceedings of the X Convegno Nazionale di Aeronautica e Astronautica, Pisa.
- BURESTI G., LOMBARDI G., PETAGNA P. (1989), "Analisi dell'interazione fra superfici portanti mediante un modello potenziale", Proceedings of the X Convegno Nazionale di Aeronautica e Astronautica, Pisa.
- BELOTZERKOWSKII S.M. (1967), "The theory of thin wings in subsonic flow", Plenum Press, New York.
- BELOTZERKOWSKII S.M. (1969), "Calculation of the flow around wings of arbitrary planform in a wide range of angles of attack", NASA TT F-12,291.
- BELOTZERKOWSKII S.M. (1977), "A study of unsteady aerodynamics of lifting surfaces using the computer", Ann.Rev.Fl.Mech., Vol.9, pp. 469-494.
- BLOOM A.M., JEN H. (1974), "Roll-up of aircraft trailing vortices using artificial viscosity", J. of Aircraft, Vol.11, No.11, pp. 714-716.
- BROWN G.L., ROSHKO A. (1974), "On density effects and large structure in turbulent mixing layers", J.Fl.Mech., Vol.64, pp. 775-816.
- HESS J.L., SMITH A.M.O. (1967), "Calculation of potential flow about arbitrary bodies", "Progress in Aeron. Sciences", Vol.8, Pergamon Press, pp. 1-138.
- HOEIJMAKERS H.W.M., BENNEKERS B. (1978), "A computational model for the calculation of the flow about wings with leading edge vortices", AGARD-CP-247.
- HOEIJMAKERS H.W.M. (1983), "Computational aerodynamics of ordered vortex flows", NLR TR 88088.
- HOEIJMAKERS H.W.M. (1989), "Computational vortex flows aerodynamics", AGARD CP 342.
- HUMMEL D. (1979), "On the vortex formation over a slender wing at large incidence", AGARD CP 247.
- HUNT B. (1980), "The mathematical basis and numerical principles of the boundary integral method for incompressible potential flow over aerodynamic configuration", in "Numerical Method Applied in Fluid Dynamics", Ed. by B.Hunt, Academic Press, London, pp. 49-135.
- GIESING J.P. (1968), "Nonlinear two-dimensional unsteady potential flow with lift", J. of Aircraft, Vol.5, No.2, pp 135-143.
- GOVINDARAJU S.P., SAFFMAN P.G. (1971), "Flow in a turbulent trailing vortex", The Physics of Fluids, Vol.14, No.10, pp. 2074-2080.
- JEPPE S.A. (1978), "The computation of vortex flows by panel methods", VKI L.S. 1978-4 on "Computational Fluid Dynamics".
- JONES R.T. (1940), "The unsteady lift of a wing of finite aspect ratio", NACA Report No.681, pp.193-202.
- KANDIL O.A., ATTA E.H., NAYFEH A.H. (1977), "A three dimensional steady and unsteady asymmetric flow past wings of arbitrary plan forms", AGARD-CP-227.
- KANDIL, O.A. (1985), "Steady and unsteady incompressible free-wake analysis", in "Computational Methods in Potential Aerodynamics", Ed. by Morino, Springer-Verlag.
- KATZ J., MASKEW B. (1988), "Unsteady low speed aerodynamics model for complete aircraft configurations", J. of Aircraft, Vol.25, No.4, pp 302-310.
- KONSTANDINOPOULOS P., MOOK D.T., NAYFEH A.H., WATSON L. (1985), "A vortex lattice method for general, unsteady aerodynamics", J. of Aircraft, Vol.22, No.1, pp 43-49.
- LABRUYERE Th.E., LOEWE W., SLOOF J.M. (1970), "An approximate method for the calculation of the pressure distribution on wing-body combination at subcritical speed", AGARD-CP-71.
- LESIEUR M. (1987), "Turbulence in fluids, stochastic and numerical modelling", Martinus Nijhoff Publishers, Dordrecht.
- LEONARD A. (1980), "Vortex method for flow simulation", J. of Comp. Physics, Vol.37, pp. 289-335.
- LIEPMANN H.W., LAUFER J. (1947), "Investigation of free turbulent mixing", NACA TN 1257.

- MOOK D.T. (1988), "Unsteady aerodynamics", VKI L.S. 1988-07 on "Unsteady Aerodynamics".
- MORINO L., KUO C.C. (1974), "Subsonic potential aerodynamics for complex configurations: a general theory", AIAA J., Vol.12, No.2, pp. 191-197.
- OSTER D., WYGNANSKI I. (1982), "The forced mixing layer between parallel streams", J.Fl. Mech., Vol.23, pp. 91-130.
- PECKHAM D.H. (1958), "Low-speed wind-tunnel tests on a series of uncambered slender pointed wings with sharp edges", Ministry of Supply Reports and Memoranda No.3186.
- REHBACH C. (1973), "Calculation of flows around zero thickness wings with evolutive vortex sheets", NASA TT F-15,183.
- RUSAK Z., SEGNER A., WASSERSTROM E. (1985), "Convergence characteristic of a vortex-lattice method for nonlinear configuration aerodynamics", J. of Aircraft, Vol.22, No.9, pp. 743-749.
- SCHOLZ N. (1949), "Force and pressure distribution measurements over small aspect ratio lifting surfaces", Forschung Ing.Wes., Vol.3, No.16, pp.85-91.
- SMITH J.H.B. (1978), "Inviscid fluid models, based on rolled-up vortex sheets, for three-dimensional separation at high Reynolds number", AGARD-LS-94.
- SQUIRE H.B. (1965), "The growth of a vortex in turbulent flow", The Aeron. Quarterly, Vol.16, pp. 302-306.
- TRABUCCHI P., TRAVOSTINO G. (1988), "Effetto del posizionamento orizzontale e verticale di un pianetto canard a delta sulle caratteristiche portanti di un'ala a delta", Thesis, Politecnico di Milano, Dipartimento di Ing.Aerospaziale.
- WEBER J.A., BRUNE G.W., JOHNSON F.T., LU P., RUBBERT P.E. (1976), "Three-dimensional solution of flows over wings with leading-edge vortex separation", AIAA J., Vol.14, No.4, pp.519-515.
- WITTENBERG K.R., KAO T.J., TINOCO E.N. (1987), "CFD wake and flowfield predictions", AIAA Paper 87-2618.
- WOODWARD F.A. (1968), "Analysis and design of wing-body combinations at subsonic and supersonic speeds", J. of Aircraft, Vol.5, No.6, pp. 528-534.

#### Acknowledgments

The authors wish to thank Ing.G.Gibertini for his valuable suggestions in the development of the turbulent diffusion model.

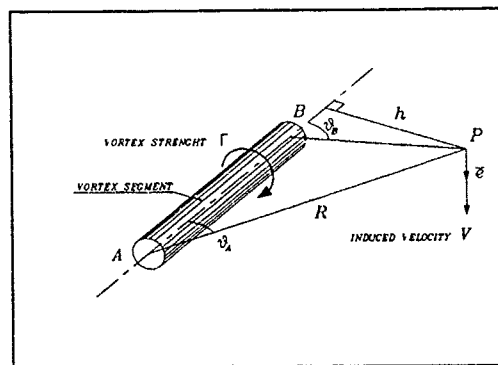


Fig.1- Velocity induced by a vortex segment: definition of the terms appearing in the Biot-Savart law.

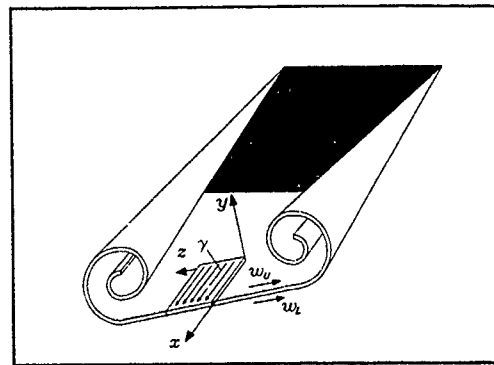


Fig.2 - Elementary portion of shear layer.

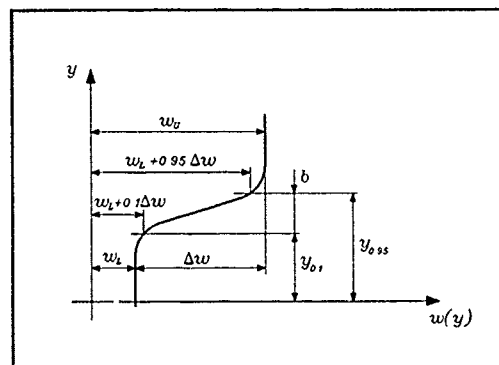


Fig.3 - Velocity distribution across the elementary portion of shear layer and definition of the conventional shear layer thickness  $\delta$ .

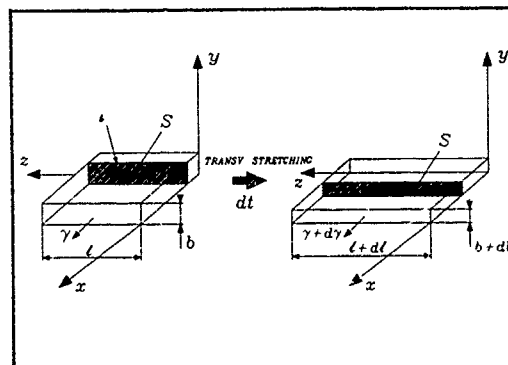


Fig.4 - Effect of transverse stretching on an elementary portion of shear layer.

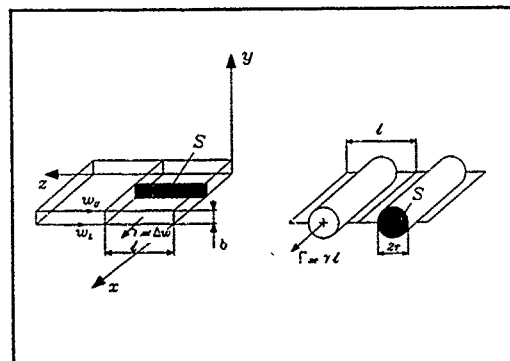


Fig.5 - Equivalence between a continuous shear layer and discrete vortices.

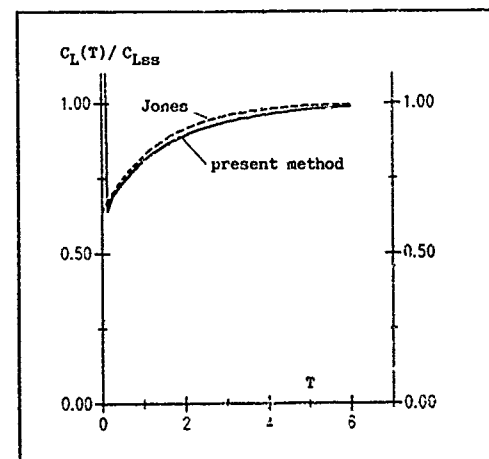


Fig.6 - Time evolution of lift consequent to an impulsive start of a rectangular wing ( $AR=6$ ,  $\alpha=12^\circ$ ). Theoretical prediction by Jones (1940).

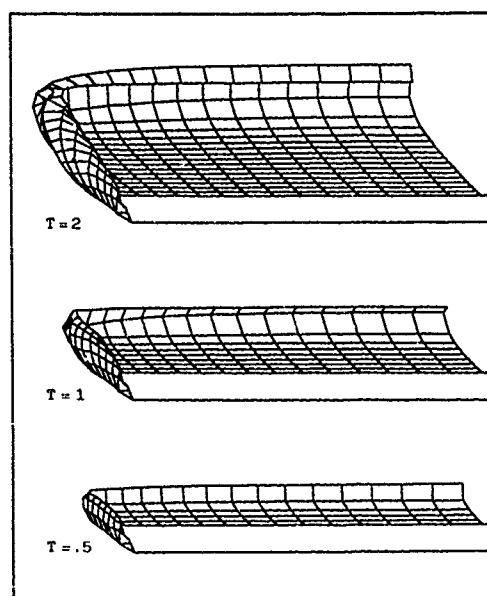


Fig.7 - Time dependent development of the wake past a rectangular wing ( $AR=6$ ,  $\alpha=12^\circ$ ).

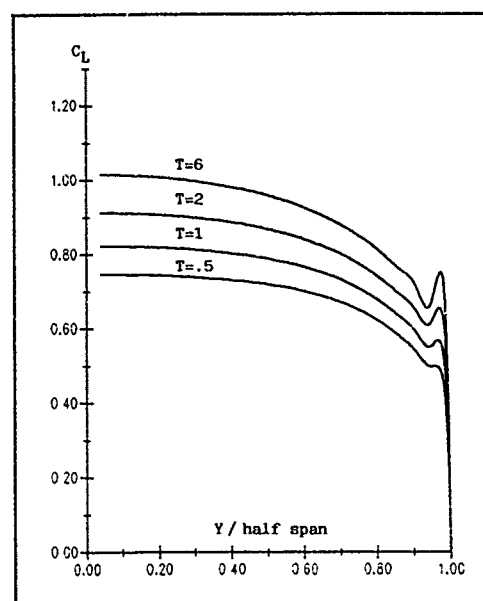


Fig.8 - Spanwise load distribution as a function of time for a rectangular wing ( $AR=6$ ,  $\alpha=12^\circ$ ).

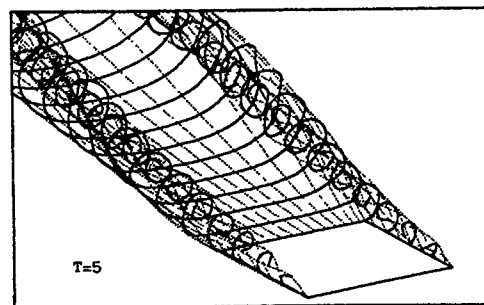
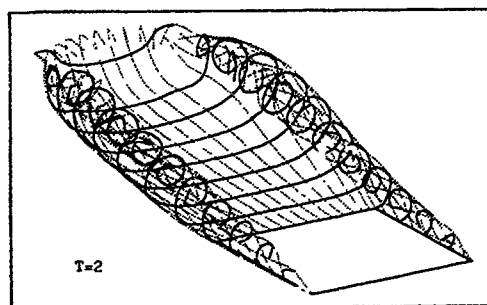
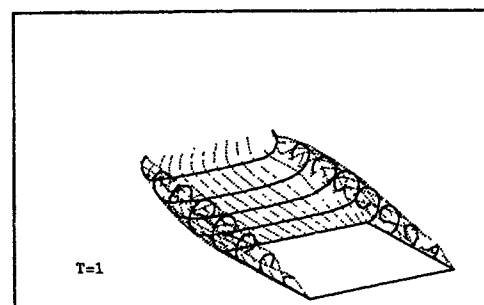
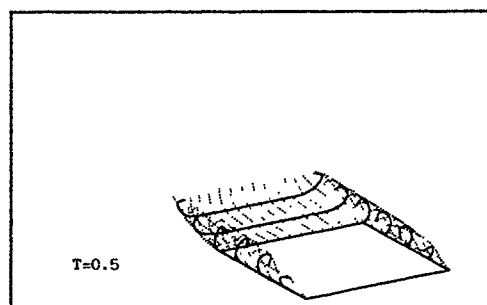


Fig.9 - Time evolution of the wake past a rectangular wing of unit aspect ratio ( $\alpha=14.5^\circ$ ).

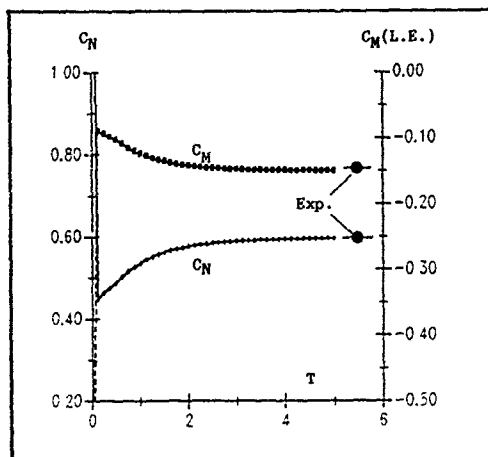


Fig. 10 - Time evolution of normal force and moment coefficients for a rectangular wing of unit aspect ratio ( $\alpha=14.5^\circ$ ). Steady state data by Belotzerkowskii (1969).

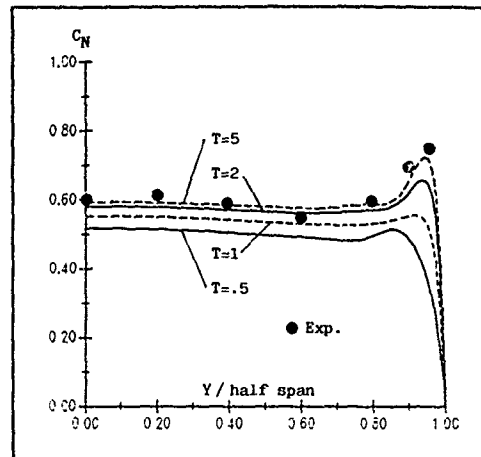


Fig. 11 - Time evolution of spanwise load distribution for a rectangular wing of unit aspect ratio ( $\alpha=14.5^\circ$ ). Steady state measurements by Scholz (1949).

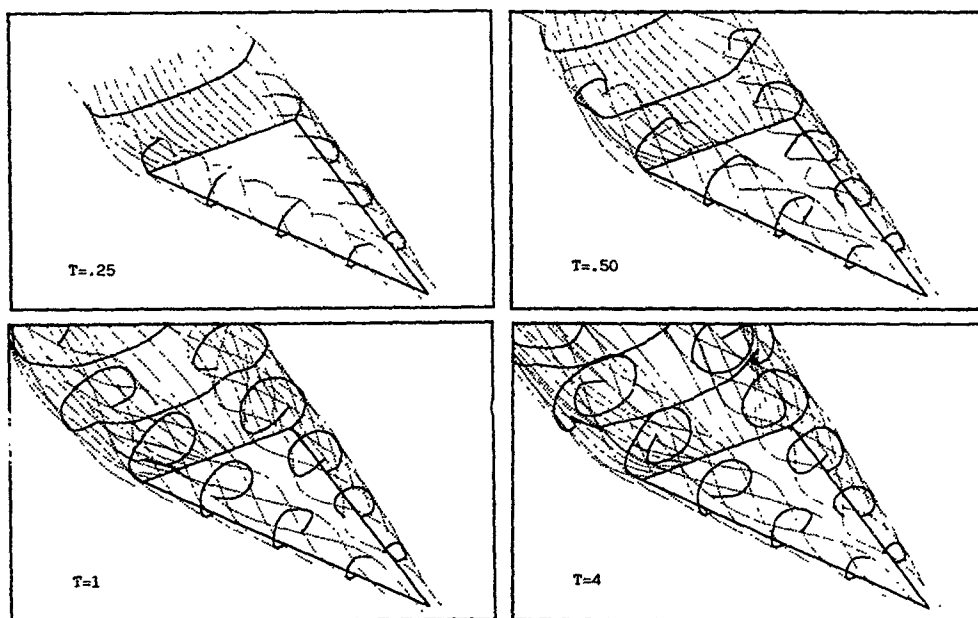


Fig. 12 - Time evolution of the wake past a delta wing of unit aspect ratio ( $\alpha=20.5^\circ$ ).

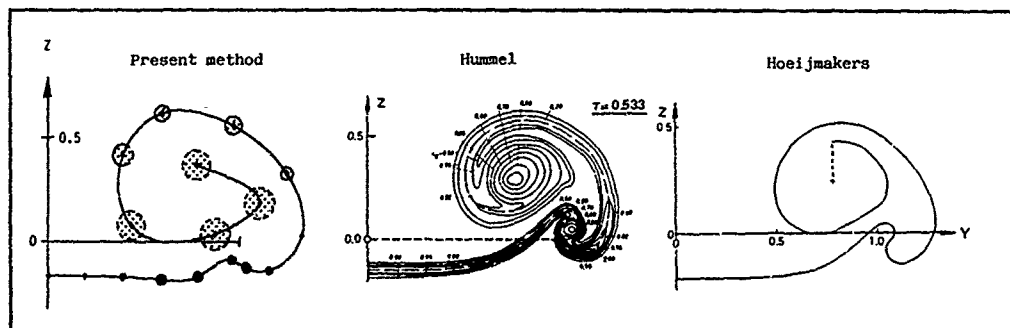


Fig. 13 - Comparison of computational results with measured total pressure contours (Hummel, 1979) and numerical results (Hoeijmakers, 1989) in a plane normal to the free stream direction ( $X/C=0.133$   $AR=1$   $\alpha=20.5^\circ$ ).

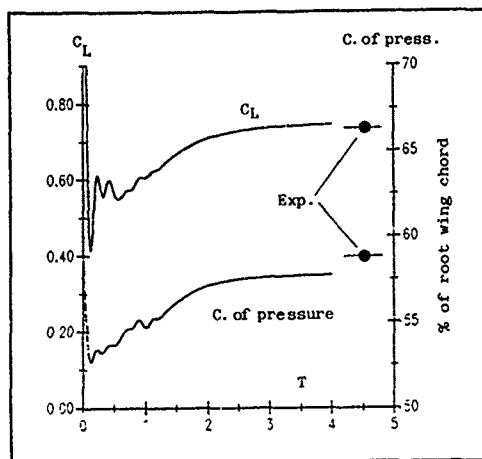


Fig. 14 - Time evolution of lift coefficient and location of the centre of pressure for a delta wing of unit aspect ratio ( $\alpha=20.5^\circ$ ).

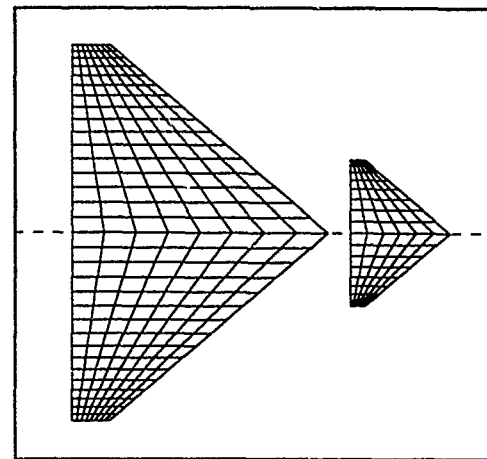


Fig. 15 - Plan view and panel distribution for the double delta wing-canard configuration ( $AR=2.5$ ,  $A=50^\circ$ ).

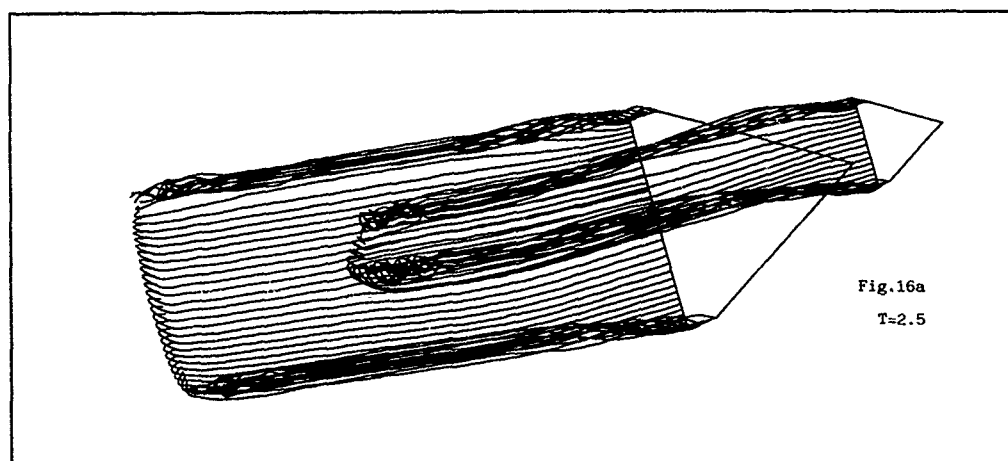


Fig. 16a  
 $T=2.5$

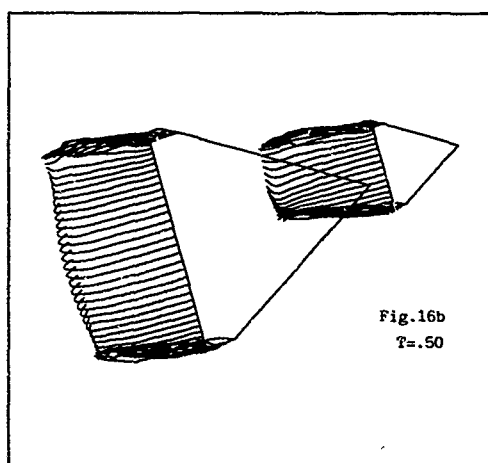


Fig. 16b  
 $T=5.0$

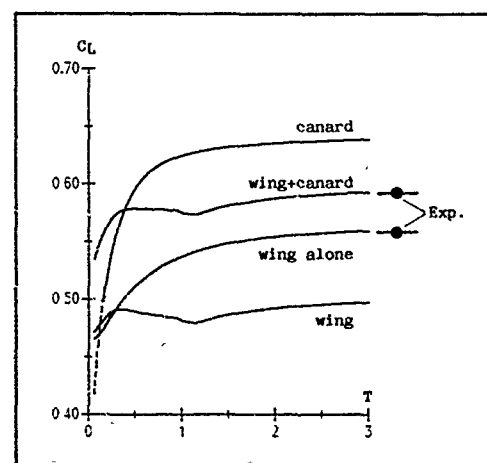


Fig. 16 - Geometry of the wake for a double delta wing-canard configuration ( $AR=2.5$ ,  $A=50^\circ$ ,  $\alpha=12^\circ$ ).

Fig. 17 - Time evolution of the lift coefficient for the double delta wing-canard configuration ( $AR=2.5$ ,  $A=50^\circ$ ,  $\alpha=12^\circ$ ). Steady state measurements by Trabucchi and Travostino (1988).



## ROUND TABLE DISCUSSION

Mr. J.H.B. Smith

The first point to make is that these are, as it says in the programme, the remarks of the Technical Evaluator. They are certainly not a preview of his report, which he will have a little longer to think about. Then I should like to express my regret at the absence of Jim Campbell and Jim Luckring from this meeting. It was Jim Campbell who arranged for me to act as Technical Evaluator, and I understand he was responsible for most of the planning. That contribution would have been completed by his presence here. We shall miss him in the discussion which follows. We have already missed Jim Luckring's review of computational techniques. This would, I am sure, have concentrated on Navier-Stokes methods and U.S. work. It would have complemented Harry Hoelmakers excellent review, with its concentration on inviscid approximations and European work.

This was the first of our invited papers, and it set a standard. I am happy to say that the other invited papers lived up to that standard. We have been treated to a set of authoritative and well-presented accounts of a range of important topics. However, it is perhaps invidious to single out the invited papers because all the papers at this meeting have been interesting. The quality of the presentation has been high. The interest the papers generated has been demonstrated by the keen discussions which have followed the papers. It is a tribute to the abilities of our chairmen and the self-discipline of our speakers that time has been found for these discussions. I should say that I wrote that last night! Time alone is not enough, we also need papers that are full of ideas and we need an informed audience, and we have clearly had both.

Of course, there is always room for improvement. This time I would like to pick on slide quality. Why is it that when we become authors we forget the frustrations that we have suffered as viewers of slides on which the lines are too thin and the symbols are too small? Let us remember when we make our slides that some unfortunate person has got to try and read them from the back of the room.

I have been going to conferences on vortex flows for many years and it is very easy to comment that the same unsolved problems turn up every five years or so, from one meeting to another. However, it is also very easy to see that real progress is being made. I think that this has been the case across the whole field that has been treated at this conference. We have seen steady progress in computational techniques and in the associated validating experiments, particularly now at transonic speeds. There is now a large body of experimental data, at least on one configuration. If anybody ever does make an aircraft with a 65 degree swept wing, we should be in a good position. Much of this, of course, has come from the International Vortex Flow Experiment and the IEPC exercise which followed it. It may be that there is a message here for the AGARD FDP in coordinating international efforts on particular problems on a rather wider scale.

We also saw rather dramatic progress in the simulation of vortex breakdown. At the AGARD Rotterdam meeting in 1983 we were impressed by the calculation of the breakdown of a single vortex by an Euler code. The discussion there was still dominated by the rival theories of stability and finite transition. Yesterday we were all, I imagine, impressed by Dr. Agrawal's calculation of the whole flow field of a wing with vortex breakdown. Let us remember that what we were looking at were contours of vorticity derived from experiment and derived from three different calculation models and we were comparing the labels on those vorticity contours. Now, this seems to me to represent a real advance in predictive capability. Of course, he shouldn't just have dismissed those experimental results on the right-hand side of his picture when they didn't agree with his calculations, but nonetheless this represented a substantial achievement. Although the concentration was on breakdown prediction, one of the interesting features was that even with that extremely dense grid of points with his imbedded grid, he was not able to reproduce the circumferential velocity component near the vortex core. You will remember that that was the chief difficulty when we were concerned with inviscid solutions of similar flows. We were very bothered that total pressure losses occurred in the core vortices. There was a great deal of speculation about where these came from, whether they were convected from the leading edge, and so on. I believe it is now accepted that those losses are local discretization errors which arise in the region of the vortex core. At that time, we believed that when we went to the Navier-Stokes equations we would be expecting total pressure losses and these would no doubt be calculated correctly. What we now see is that there are still residual errors in the region of the vortex core in the Navier-Stokes solution, we are still not agreeing with experiment. It may be that turbulence has something to do with it, but I suspect that it is much more the difficulty of constructing a mesh which will adequately reflect the structure of the flow in the neighborhood of the vortex core, whether it is supposed to be inviscid or viscous.

The study of Dr. Agrawal was of course a very expensive study. A much less expensive study, but I thought an equally impressive one was the work at Braunschweig presented by Mr. Oelker. We shall remember that pocket of dye sitting behind the trailing edge of the canard and above the apex of the wing in his water tunnel. Of course, this was a laminar flow, and no doubt a turbulent flow behaves differently. But, how differently? We will wait to find out; somebody should try and tell us. I think that sheds a whole new light on the account of how the canard vortices interact with the wing. Of course, the other significant thing in his paper was the dramatic changes in the aerodynamic characteristics which arose when vortex breakdown reached the apex of the wing. For a long time we have worried about when vortex breakdown reached the trailing edge of the wing; it is now clear that the really dramatic change is when vortex breakdown reaches the apex.

Something else we should remember is the sight of the tail of the F-18 bending to and fro in front of our eyes. We need a lot more progress of some sort, certainly if we are going to predict that with Navier-Stokes solutions. Of course, one might say that you don't actually need CFD techniques to tell you not to put a tail plane in a vortex. Before I realized how the time was going I was going to challenge Dennis Mabey to explain to us just why he believed there was no feedback mechanism between the vortex and the fin. There may not be time, Dennis, but prepare yourself.

RTD-2

This is not the only example of how far our understanding and predictive capability is from the real world even in this central area of fighter wing design, which has been the main subject of the meeting. The vortex flap that David Lovell was describing was conceived in terms of capturing a vortex along its whole length. It worked quite well with the vortex spilling over the trailing edge of it quite early. The problems all apparently arise in asymmetric flow, not in symmetric flow at all. How many CFD codes can provide for asymmetric calculations?

We had some good news about turbulence modelling. That is sufficiently unusual to be worth a celebration. Dr. Kaynak and his colleagues from Turkey showed that changing to the Johnson-King model made very little difference to the position of a swept separation line. Now we know that this change is very important for unswept separation lines. This suggests that turbulence modelling, which is the limiting consideration in the calculation of unswept separations, may not be a problem in highly 3-d situations. This is an advance which we really need to pursue and attempt to exploit.

Another piece of fundamental work which seemed at the time to have a rather negative outcome was the study by Mr. Pailhas from ONERA who looked at the flow downstream of an attachment line and found that it was in fact not very exciting. I believe that this is because the vortex that he used was rather large so that the flow which was attaching, not re-attaching, behind the vortex was coming essentially from the free stream. It would be very useful to repeat the exercise for smaller vortices in which the turbulence of the vortex is contaminating the flow which is attaching further downstream (or further inboard, depending on what geometry you are thinking of).. It seems that we have two difficulties between French and English. One is that there are two words for separation in French, one of which you can define and the other one means something physical. The other difficulty is that there are two words in English: 'attachment line' and 're-attachment line'. Although we tend to use them in a confusing way, they are available with distinct meanings so that we could keep 're-attachment line' for a line along which fluid which has already left the surface arrives back on the surface, that is re-attachment. In the other circumstances we can call it an attachment line. Now when you think of turbulence the distinction is not so clear of course, but there is a significant difference there which we would do well to bear in mind.

Well, we are getting a little bit abstract now aren't we. I should mention the papers that reminded us of very different vortex flows, Professor Staufenbiel's trailing vortices certainly had some of us wondering about the fundamentals of our subject again, and if you did destroy the trailing vortices, what kept the wing up was what was passing through my mind. Seriously, I think that one does have to worry about what happens very much further downstream than you can examine in a windtunnel. It seems possible that the fragmented structures which you can produce on the scale of a span or two may well look on the scale of an aircraft separation distance really rather similar. It is very difficult, of course, to do anything either experimentally or theoretically on this. It does seem to me there is a danger of recombination of vortices.

Professor Rizzi reminded us that heat transfer is sometimes more important than pressure. He didn't say very much about transition, and of course, neither did most of the other calculators. The person that did say a lot about transition, of course, was Dennis Mabey again. I am a little worried about this. It is not enough to stick some roughness grains here and there and say that we have fixed transition. How do you know you fixed transition? It is not too bad with a wing so long as it is not too highly swept. We know more or less what to do. But when the flow is going to leave the surface and come back on again at some other position, then we need to be fixing transition where it comes back on. And when we are dealing with forebodies where there is a strong expansion of the flow along the lower surface attachment line, then fixing transition is by no means straightforward. I detected, I thought, a somewhat cavalier attitude to this question. A lot of results were claimed to be with transition fixed when it was by no means clear to me that they necessarily were.

For myself I have to admit to being fascinated by the paradoxes of the side force on slender bodies at incidence. Ian Moir's discovery that the hand of the asymmetry at the rear of the body is determined by the nose, even when the nose flow is apparently symmetric is something that calls for a deal of explanation. Jean Ross's success in obtaining a proportional control out of vortex asymmetry, when the standard form of vortex asymmetry is a step-function variation with roll angle is something else which needs explaining. I should like to think that the work on non-conical flows like Mike Pidd described on our behalf may help with that. The very multiplicity of flows which can arise on a circular cone with the same incidence, Mach number and Reynolds number is quite a challenge to aerodynamics.

Today I was certainly impressed by the reaction to Professor Baron's presentation. When he started I thought, more old stuff, but in fact this was a very convincing account and the interest which it generated among people who wish to use it shows that there is life in these approaches yet. Of course, Dr. Cunningham's paper was also of great interest. I don't know how he imagines that he is ever going to take all that data into his head and produce an intelligible account of it, but it is a splendid ambition. It was nice to see the applications of dynamical systems in the paper on the role of the delta wing also.

I think it has been a very worthwhile conference, a very successful conference, but then, vortex flow conferences always are.

Prof. A.D. Young

Well, our time is getting short, but what I would like to do at this stage is to invite the chairmen of the different sessions to make any points that they would like to make, very briefly please - a minute or two, arising from the sessions which they chaired in addition to what Jeremy has just covered in his excellent survey. Dr. Bonnet, do you have any points that you want to raise at this stage?

If past practice still applies, I think that this discussion will be recorded, so if anyone speaks, would they give their name and affiliation before they start their address.

Prof. A. Bonnet

In fact the main purpose of the first session was comparison. I have noted three points of comparison:  
Point A: Comparison of Euler codes together but:

A1 either keeping the same algorithm and using structured or unstructured grids.  
Mr. Selmin's paper shows clearly the advantages or the drawbacks of both approaches.

A2 or keeping the same mapping techniques and using various algorithms.

Point B: Comparison of Euler codes with a Navier-Stokes one

Point C: Comparison of numerical codes (Euler or Navier-Stokes) with experimental results.

If I start with the point A2, that is to say the comparison of Euler codes together with various algorithms, we can say that we have to make a distinction between the either global or local point of view. For the global point of view, I mean, for example, the determination of aerodynamic coefficients like the lift, the pitching moment or the drag, apparently all the methods are very close together. On the other hand, the local point of view, the pressure coefficient  $C_p$  distribution for example, it seems that good agreement appears except for the trailing edge, coming certainly from a mistreatment of this zone. In the same spirit, a great difference appears in the calculation of the loss of total pressure due certainly to artificial or numerical viscosity, I think. On the point B, that is to say the comparison of Euler codes and Navier-Stokes code, or on the point C, that is to say comparison with experimental results, the most interesting thing is what has been called secondary separation, but Mr. Delery showed that there exists also tertiary separation. This secondary separation appears in the experiments and is predicted by the Navier-Stokes code but not by the Euler codes. The effect is that the high  $C_p$  peak which arises in Euler code simulations disappears and consequently the lift coefficient in Navier-Stokes is less than this in Euler codes, and appears close to experimental measurements.

Dr. R.G. Bradley, General Dynamics

Actually, Mr. Smith did an excellent job in commenting on the second session. He made comments on several of the papers. The only thing I would like to add is that it is quite obvious from the results presented in my session, and other sessions, that we are really talking about two classes of experiments here. We have analogue experimentation (wind tunnel) for which we take data, and we have numerical experimentation (CFD) for which we generate flow field data. There are still a number of questions in both areas concerning the data that result. We continually talk about things such as transition and turbulence models in CFD. We should also talk about grids in CFD and scales of flow in both types of experimentation when considering accuracy.

Prof. Young

Could we open up now for a general discussion on the first two sessions dealing with vortex computation techniques. Does anyone want to make a particular point from their reactions to the discussions and papers presented, additional to the ones that have already been raised.

Dr. U. Kaynak, TUSAS

I would like to be controversial on the Euler vs Navier-Stokes computations. The impression that I got from this conference and from similar and earlier symposia, there is always a controversy between Euler and Navier-Stokes. Let me give you some numbers which are generally accepted. For example, if you have an isolated wing Euler computation, people tend to use about 300,000 grid points. For Navier-Stokes there are different numbers starting from 300,000, 600,000, to one million, sometimes two million grid points. But the fact is that you don't have to go as high as one million or two million, but 200,000 to 500,000 grid points is just fine. In fact 300,000 grid points could be, for example, enough for both computations, Euler and Navier-Stokes. Another fact is that Euler equations are unable to capture, of course, the secondary separation. Furthermore, the overhead of Navier-Stokes computation against Euler using the same grid is maybe 30 or 40%. So if you can use the same grid with only 30 or 40% increase in the computational cost, I wonder if anybody wants to do Euler computation for the isolated wing from now on anymore.

Prof. Young

It is a challenge. Anybody wish to take up the challenge?

Dr. S. Agrawal, McDonnell Douglas

I just want to make a comment on the remarks that Mr. Kaynak just made regarding the grid sizes. The number of grid points concerned really depends on what you are looking for, what exactly you are after. If you are looking for the pressure distribution, I think that is a reasonably good number, but if somebody wants to look at skin friction, for example, then that is not good enough and you do have to use a higher number of grid points, because you want to resolve the boundary layer accurately. I think that also applies on his second comment about whether Euler calculations should be sufficient or whether somebody should really do the Navier-Stokes calculations because it adds only a 20 or 30% additional cost. For somebody on a project, the cost is an issue, i.e., even though you are adding only 30% to the cost, still you are adding, so why do Navier-Stokes calculations?

RTD-4

Mr. S. Hitzel, Dornier

A few of the questions you were raising here already are answered by our colleagues from McDonnell Douglas. We now have quite a lot of experience with Euler calculations and also made up some numerical experiments in order to find out what is necessary to obtain a good Euler solution with regard to experiments. Our experience is that for an isolated wing, a mesh of about 200,000 to 300,000 grid points is quite sufficient in case you are aware what you are doing with Euler and you are remembering all the restrictions. If you would do the same wing with Navier-Stokes, e.g., on a laminar case, I would guess you have to triple or have even four times the number of grid points, but you also have to keep in mind that with the usual meshes used you are only resolving the area around the surface, thus you only get a quite good resolution in the secondary separation and in the boundary layer. With all the Navier-Stokes results I saw in recent months and years, I saw that nobody really cared about the vortex core and about the vortex sheet. At Dornier we investigated a delta wing configuration by an Euler-simulation in an adaptive block structural mesh in the vortex area. The mesh provided an equivalent of 6 million gridpoints at the expense of 1.4 million points. The final outcome provided a distinct vortex-sheet rolling up more than 360 degrees into a vortex core. For the first time we experienced the flow on the wing's upper surface to be almost free of total-pressure losses, indicating that the numerical dissipation or the artificial viscosity was falling to zero there, as it should be. This shows the need of very dense meshes in this vortex sheet and core area and this again multiplies the number of grid points mentioned earlier. You are ending up with 5 or 8 or 10 million grid points and you never can afford this regularly. Thus the only way to go with that is to have an adaptive grid somehow. This may be achieved by an adaptive block-structured approach, adaptive grid-techniques or their combination or you may have to go to unstructured grids which may add grid points in the area where you are interested in. All the Navier-Stokes results we see with 300,000 or 500,000 equally distributed grid points are just insufficient. For the flow considered, nobody compared the relative size of the artificial viscosity so to name with the real viscosity that is coming out of the equations. I think it would be a worthwhile effort to show whether the Navier-Stokes results really are Navier-Stokes solutions rather than modified Euler solutions. This would provide knowledge to push Navier-Stokes simulations to become superior to Euler solutions with regard to experiments.

Dr. W.J. McCroskey

I don't want to prolong this particular part of the discussion, but for the benefit of those who were not at our last symposium in Friedrichshafen on Missile Aerodynamics, I would like to make an observation about discussions along these lines that we had there at that time. The basic controversy might be summarized by someone saying the discussion was about CFD, fact or fiction. The Euler community said that Euler was fact and Navier-Stokes was fiction because of all the problems with turbulence modelling and lack of resolution, etc. Of course, the Navier-Stokes community was saying that Euler is fiction and Navier-Stokes is fact. From the point of view of stimulating creative thinking about what to do as we try to improve our codes to get better ultimate utility and accuracy, I think that it is healthy that this discussion continue.

Prof. Young

One more comment on this point and then we will have to move on to the other sessions.

Dr. A.N. Cunningham, General Dynamics

With regard to unsteady aerodynamics, I would like to point out that most of these solutions use local time stepping, and if you are doing an unsteady solution you have to use global time stepping. The resulting unsteady computations end up with much more than a 30% increase in cost, and more realistically, orders of magnitude increase. This point was made by John Edwards in Sorrento this Spring, that we are looking at hundreds to thousands of hours on a CRAY II to do a real-time buffet simulation for one data point.

Prof. Young

Perhaps we should move on from there. These are problems, obviously, that we are going to discuss time and time again, but it is useful to have them aired at this stage. Session 3 was Measurements and Visualization and Prof. Onorato was the Chairman.

Prof. M. Onorato

Starting from the invited paper, we have to be grateful to the Program Committee of this Symposium for inviting Mr. Mabey to review the meeting of the AGARD Structures and Material Panel. It has been very comfortable to sit here and to have a condensed version of all aerodynamic aspects that were discussed in that meeting. From this lecture we get suggestions that much greater attention should be given to establishing the magnitudes of the possible scale effect and also much attention to predict buffeting. The message to the experimental aerodynamicists is then to make use of the cryogenic windtunnel, if you have one of course, and to assess and remove any unsteady effects from your tunnel that are not genuine. I think that this work is going on in many windtunnels. Going to the four contributed papers, two of them deal with complete configurations and they give in a complementary way a satisfactory and complete picture of vortical flow around the configurations at low Mach number. The first Del Frate paper is characterized by showing the correlations between flight test and ground test and personally as a windtunnel worker, I was happy to learn that these correlations were in general good. The second Eckler paper is characterized by showing canard effect on the system of vortices and on the relative breakdown and by showing the results also in the case of non-symmetrical flow.

The paper of Elsenaar, coming from an international cooperation, extended the physical picture of the vortex system at transonic and supersonic speed. In my opinion, the very complex flow structure of vortices and shock waves on a delta wing was clearly interpreted, and I think that when the program flow field measurements will be completed we will have a very good reference experiment for looking at the physics of such flows and we will have a useful database for the validation of numerical methods. The only wrong thing in the paper of Elsenaar was that the written version of the paper was not available at the time of this meeting. Finally, a mention to Pailha's paper, they showed that complex measurements, turbulent flow, may be done in complex boundary layer and they show that this is possible. I think that if they will go ahead applying this methodology, maybe to most realistic flow, we will have data that may give some confidence to the users of 3-d boundary layer numerical methods. Concluding, I was happy to chair this session, both for the high quality of the papers and for the exciting discussion that came from the audience.

Prof. Young

Would anybody like to raise any points associated with that session?

Dr. L.E. Ericsson, Lockheed

I would like to make two comments. One is in regard to structural response to separated flow. In the AGARD SMP meeting in Sorrento earlier this year there was one paper presented on three types of structural response to separated flow. It is reference number 17 in Mr. Mabey's review at this meeting. Being a review-type paper, he probably thought it outside of the scope of his review. In it was shown that the simplest problem is that of buffet response, where the interaction with the structural response does not change the aerodynamics. In this case I think it is alright to have, as we have had in industry, separate departments for the determination of structural response and definition of the aerodynamics. However, I don't think this works now when we are flying in the separated flow region, where you get two other types of much more complicated structural responses. You can no longer have this isolation of the two groups. They have to interact much more. The second type of response is what I call self-excited response. In that case the interaction between the structural response and the aerodynamics causes a change of the aerodynamics, which can produce negative aerodynamic damping (or undamping, if you will), that surpasses the structural damping. The result can be a catastrophic increase of the response amplitude, leading to structural failure. In contrast, in the case of buffet, the structural damping available often guarantees a limited response. Furthermore, because the buffet response usually is associated with a critical frequency, one can, at least in principle, avoid the problem by changing the structural stiffness or the flight condition. It is easy in principle, maybe not in practice. In the case of the self-excited response, it occurs over a wide frequency range. Finally, the most complicated case of all is when the interaction of the structural response with the aerodynamics changes the aerodynamic forcing function itself. One example of that is the transitory response of a circular cylinder to Karman vortex shedding. There is a frequency window in which this interaction will result in lock-on of the vortices. In this case, the maximum response amplitude does not occur at the critical frequency, but at 20% lower frequency, and can be three to four times as large as the resonant response. In the Sorrento meeting I suggested that we need to have something like the interaction that has taken place between the Flight Dynamics and Fluid Dynamics Panels in the case of rigid body dynamics. An initial meeting in 1978 in Athens and a later meeting in Göttingen in 1985 have proved to be very fruitful. Professor Forshing, when summing up the meeting, expressed similar sentiments; it really may be time to have joint meetings with the Fluid Dynamics Panel.

My second comment is much shorter. It is in regard to scaling, a subject that was also touched upon by Mr. Mabey in his review paper. He suggested that we use tripping devices to fix boundary layer transition. I will expand on Professor Smith's comments earlier, that this requires that you know exactly what you are doing. Unless the full scale flight vehicle is flying with such fixed boundary layer transition, you cannot use fixed transition in your windtunnel experiment and hope to get dynamic simulation. There is a very strong interaction between vehicle motion and boundary layer transition. One example of it is the bending wing response published by Maybe et al (J. Aircraft, Vol 24, July 1984), where you can see that the structural response was of the self-excited type and could have led to structural failure. Both Maybe and I agree that transition is the mechanism that drives that bending oscillation. What we can't agree upon, as readers of the Journal of Aircraft know, is the flow mechanism behind that interaction. The problem is that to guarantee dynamic simulation in the subscale tests, you have to have free transition if you have it in full scale, and you have to test at the full-scale Reynolds number. That is a big problem. You usually cannot test at the full-scale Reynolds number. In a recent issue of Progress in Aerospace Sciences (Vol. 27, 1990, pp. 121-144) this problem of dynamic simulation is addressed, and it is suggested that one possible solution, while we are all waiting for ready access to the cryogenic windtunnel, is to do subscale testing and use what I call analytic extrapolation to predict the full-scale vehicle dynamics.

Prof. Young

I don't want to get involved in what is really another topic for a big symposium, modelling dynamic phenomena generally. But I feel that Dennis Mabey must have an opportunity to respond to that briefly.

Dennis Mabey

Both the questions that have been addressed are, of course, very serious. First of all I have been accused of treating the difficulties of fixing transition in a cavalier fashion. When you have a three day meeting summarized in thirty minutes, you have to ride like a cavalier. I think the difficulties of fixing transition have to be considered seriously, but equally they are often over-emphasized. Those of you who want to follow this controversy more fully should look at the paper that I presented to ICAS in September 1990 (ICAS 90-3.4.1) which is the first half of a monumental tome on "A review of scale effects in unsteady flows".

RTD-6

Most of the flows that we have been considering here are, in fact, unsteady. Whether or not they are steady in your mathematical solutions, in reality they are highly unsteady flows. Transition is a phenomenon unsteady both in space and time. If you are going to get that mixed up with the other unsteadiness in the flow, then you are going to be in trouble. If you want to hear the second half of that tome, hopefully that will be given at an AGARD SMP meeting in San Diego in October 1991.

I would like to move on to the Mini-lectures that Lars gave us on the different aeroelastic phenomena, with which most of us are familiar. All three phenomena, carefully delineated, are illustrated in a paper on model response at high angles of incidence (ICAS, 90-3-8R). With respect to the important question of what is the precise motion on the F-18 fin, I will call two independent witnesses to prove that the phenomena is buffeting and not single degree of freedom flutter. The first witness is Marty Fetman from McDonnell Douglas. In paper 2 of AGARD CP-483, he showed that starting from pressure fluctuation measurements on a rigid model, you can predict the same motion that he measured on a correctly scaled dynamic model.

The second witness is my own unpublished work. Generally, in a buffeting test, the frequency parameter is varied simply by changing the velocity with a fixed modal frequency. It is essential, if you want to establish the type of phenomenon, to vary the frequency parameter by changing either the stiffness (which is generally difficult) or the generalized mass. This is very easy on a fin, by putting on tip pods. If you do an experiment like that you can calculate the buffet excitation parameter as a range of frequency parameter for a whole range of different F-18 type configurations. For every configuration a unique buffet excitation parameter is found as a function of frequency parameter, despite the enormous variation in the amplitude of the model motion.

Therefore, ladies and gentlemen, in this particular problem there is no aerodynamic feedback. Despite the very large accelerations measured, which are astronomically high (as much as 600 or 800 g), this really is buffeting!

Prof. Young

Perhaps we had better pass on from there quickly. Otherwise we will be talking about the F-18 even more than we have during the course of this Symposium. Let's go on to the slender body vortex flows. I wonder whether Professor Gersten would like to say something.

Prof. Gersten

One of the main aspects in the slender body session was asymmetry of the flow. I, in particular, enjoyed the paper by Mr. Pidd and Mr. Smith where they showed that with inviscid theory you can predict things quite nicely. The only drawback is that you have to assume something about the separation line. This could perhaps be avoided by adding boundary layer calculations in order to get the separation line. Maybe there is a possibility to get certain information about the separation line by the inviscid theory only, e.g., a certain kind of extended Kutta condition. For example, the proper solutions of the inviscid flow case may be those with no singularity at the separation line, like in the two-dimensional free-streamline theory. So, there might be criteria for the separation line even without a boundary layer calculation. I wonder why the results are so good without any further precise prediction of the separation line. So, I believe, there is still space for the good old boundary layer theory or even for something simpler which comes out of inviscid theory as criterion for the separation line.

Prof. Young

Are there any other comments on that session? I wasn't quite clear, Klaus, whether you were arguing in favor of boundary layer theory coupled with some inviscid model or dispensing with boundary layer theory?

Prof. Gersten

Sometimes I wonder why people go all the way into Navier-Stokes before they try the boundary layer theory. I am very much in favor of the boundary layer theory, but in this particular case, obviously Mr. Pidd and Mr. Smith did a good job even without the boundary layer theory. I wonder if this is so, or is there something behind it?

J. Smith

I think the answer to that is fairly simple. In fact the separation line positions in the cases that we were looking at are not very different, whether the vortex motion is symmetric or asymmetric, the difference in separation line position is relatively small. It is there and, of course, it does affect the actual forces that come out. If we move the separation line position, then we certainly get different forces. We were not really trying to predict the magnitudes of the forces. We were trying to demonstrate the structure of the flow. I think that if you want to go beyond the question of the mechanisms that are operative, if you want to know what the actual forces were, then you have a very much more difficult task. You would certainly need a much more elaborate flow model than the slender body model that we used. Well, I don't really see how you are going to do it at all, actually, because I think to do it you have to resolve a very small-scale flow at the apex of the body. I don't think there is any way that the Navier-Stokes people can do this. I think that the only way that we are going to get predictable results is by not talking about pointed bodies, but admitting that all bodies must have finite radii of curvature.

Prof. Young

The next session was devoted to Vortex Development and Breakdown. Dr. Elsenaar was the Chairman.



Dr. Elsenaar

Just a few remarks. One is that I am a bit afraid about Euler/Navier-Stokes calculations that they smear out a lot of the details and a lot of the physics of the flow. The message of Delery and others is that you really should look to the physics of the flow as well and the surface topology that Delery described is a good example of how you can do that. There were more examples in the conference. But if you look at a paper like Riley, about the coupling of boundary layers, going on with the remark that Klaus made, the coupling of boundary layer and inviscid flow, the detail of physics that is in that coupling is very important and you should look into this in your Euler/Navier-Stokes calculations as well. The same applies if you look at the vortex breakdown phenomena. I was happy to have in my session a very fundamental study of vortex breakdown from Navier-Stokes, an almost empirical study of experimental study of vortex breakdown and an overall Euler/Navier-Stokes view of vortex breakdown. It would be very interesting in the future, I think, to see those three different approaches combined in the unified view what vortex breakdown really is, because although the comparison with experiment was very well for the paper of Agrawal, I still don't understand the reasons why.

Prof. Young

Are there any other comments on vortex breakdown, how it should be treated?

Dr. D. Woodward, RAE

I was particularly struck in Mr. Agrawal's paper by the good agreement he showed between the vortex positions calculated by Euler and Navier-Stokes. This contrasts quite markedly with the large differences that I was showing in the paper that I presented. His wing is  $75^\circ$  leading edge sweep and the IEPG wing is, as we have heard,  $65^\circ$ . Mr. Agrawal went on to say, if I remember correctly, that he felt that the secondary separation was having a major effect on the vortex breakdown. If that is true, then perhaps one ought to be looking more seriously at vortex breakdown at lower sweeps, where the secondary separation influences the flow development more severely.

Dr. A. Cunningham, General Dynamics

I would like to also point out that vortex breakdown can be significantly influenced by downstream blockages, sting interference, leading edge shapes, and undersurface interference. There is also an influence due to velocity, which I don't know if it is velocity or Reynolds number, but in our test of a straked delta wing we saw a  $2^\circ$  difference in vortex burst characteristics depending on whether we were testing at 30 meters per second or 80 meters per second. I would like to caution about these points, particularly the support interference.

S. Hitzel, Dornier

I just would like to give a short comment on what Dr. Woodward was stating on the paper from McDonnell Douglas. We had this discussion before with the mesh densities. It was a typical example of mesh density problems. This was a mesh quite suitable for some Euler investigations, keeping in mind that you have a tremendous amount of numerical viscosity in there. He used as far as I understood, exactly the same meshes for the Navier-Stokes calculations and thus he probably never revealed the natural viscosity in the proper manner. This is probably the reason why you got almost the same vortex paths and also a very good agreement with some experimental results. So, I would suggest to invest a little more in meshes and try again with the Navier-Stokes solution and compare it again. This also may give some ideas on the vortex breakdown phenomenon you calculated.

S. Agrawal, McDonnell Douglas

The mesh density is certainly a critical issue. We have not resolved that. We are resolving that right now with mesh embedding, higher level of mesh embedding, and I think that ought to make the comparison a little bit better between the numerical and experimental data. I wanted to go back to the comment that was made about the effect of the secondary vortex on the breakdown. I think what is going on here is that the pressure distribution in the vortex core is being modified by the presence of the secondary and tertiary vortices that we may have there and it is the pressure distribution that is responsible for breakdown. As far as how much of an effect it has on the breakdown, it depends on the Reynolds number, depends on the size of the secondary vortex which should be analyzed further. I think we are going to do some of that later on for some additional test cases. A very quick comment on the sweep angle that you mentioned. The sweep angle was  $70^\circ$  rather than  $75^\circ$ . One more comment on Mr. Hitzel's remarks about the mesh density, the same mesh being used for the Euler and Navier-Stokes calculations. That is what I showed yesterday, same mesh for both calculations. However, we had also used a smaller mesh, smaller in the normal direction, for the Euler calculations. We got more or less the same solution. So the Euler calculations were done on two different meshes, with no shift in the vortex positions. However, the breakdown locations were different.

Prof. Young

Perhaps we should pass on. The next session was one which I chaired on Vortex Control. I will be very brief. There were a number of interesting papers about different devices which can be used in various ways to produce control. Jeremy Smith referred to the interesting control system that Jean Ross has been working on using suction at the nose of a body. I would also endorse Jeremy Smith's query to Prof. Staufenbiel as to whether, if you use devices to break up tip vortices in a way that at first sign looks very promising, what happens further downstream may not go against your initial optimism; an aircraft following in the wake of another one, might still be subject to quite large vertical velocities because the vortices may by then reassemble and resume the strength that they had without the device.

RID-8

The vortex flap clearly is a device of considerable importance and effectiveness and it is perhaps the only one of the devices talked about for which we have some kind of physical understanding of what is happening. I would like to see more work done on the other devices to see what the physics of the processes that they induce is. I will offer no further comments. I don't know whether Prof. Staufenbiel would like to react to the points that I have just made or which Jeremy Smith made earlier.

Would anybody else like to make a comment on that particular session on vortex control.

We will come now to the last session on unsteady effects for which Dr. Orlik-Rückemann was chairman. Have you any points you want to make on that session?

Dr. K. Orlik-Rückemann, Canada

I would like to comment briefly on the three papers on the unsteady windtunnel experiments that were presented this morning in my session. If there was any common denominator in these papers, and in particular in papers by Dr. Cunningham and Dr. Haniff, it is that at rapid manoeuvres at high angles of attack the old linear approach is no longer adequate. It is mandatory to develop prediction methods that are non-linear and that take into account the path and rate dependency of the aerodynamic reactions, and this should include time lags and time histories. We need to present our data in a way that could make this possible, by introducing new methods of representing aerodynamic loads such as perhaps the one presented by Dr. Haniff in the form of hypersurfaces. We also need a much better understanding of unsteady vortical flows around manoeuvring configurations and we need non-linear and unsteady CFD codes to calculate such flows. The Fluid Dynamics Panel is organizing a Specialists' Meeting next Spring, where these matters will be discussed in more detail.

Prof. Young

Well I suspect that the last comment would be enough material for a symposium or two. There is room for one more comment and then we must close the proceedings.

B. Masure, France

It is a general remark. The scope and title of this meeting was Vortex Flow Aerodynamics. In my mind when you speak of vortex flow you think first of vortex flow around a propeller; second, vortex flow around helicopter rotor; third, vortex flow around missiles; and fourth, and only fourth, vortex flow around wing and aircraft. It appears that almost no papers were presented on the three first topics. This is for me a surprise. I do not say that everything was not interesting, it was very interesting, but I ask the committee programmers if they tried to have papers on the two first topics, i.e., propeller and helicopter rotor, and why there were so few papers on missiles?

Prof. Young

Well, I haven't got the call for papers in front of me, but my recollection was that it was fairly general, and we had to take the papers that were submitted and select those that would offer a reasonably coherent program. I am not sure that I would agree with you about putting those first three topics before the last one. In my mind the last one is the most important.

Now perhaps we should close the proceedings. At this stage, it remains only for me to thank all the speakers, they presented papers which I found most interesting and valuable, and to also thank you, the audience, for so eagerly and energetically participating in the discussions which I think were very stimulating. Now I will hand over to Dr. McCroskey, our Chairman, who will close the proceedings.

Dr. W.J. McCroskey

Thank you Prof. Young. Now it is time to bring this 67th Meeting of the Fluid Dynamics Panel to a close. Whatever your secret emotions about vorticity and what kinds of problems it applies to, or transition fixing, or Navier-Stokes calculations, whatever, I hope that you found the Symposium both informative and stimulating and that you have enjoyed the local environment as much as I have.

Just a brief word from our sponsor, as we say in the US, here are some of the events that you will find in the AGARD "cable channel" in the near future. I would just mention in connection with the last question, that we had a meeting in Friedrichshafen last May on "Missile Aerodynamics". Anyway, we have in our 1991 program a pair of specialist meetings in Toulouse next Spring. One is on "Effects of Adverse Weather on Aerodynamics", and a second one on "Manoeuvring Aerodynamics" which might be considered in some ways an extension of the last session of this meeting. Of course, there is a lot more in that specialist's meeting as well. In the Fall, our venue changes to Texas in the US where we have a meeting on Aerodynamic Engine/Airframe Integration. Then we will sponsor two special courses to be held at von Karman Institute and other locations, as noted here, "Aircraft Dynamics at High Angles of Attack - Experiments and Modelling" and "Engineering Methods in Aerodynamic Analysis and Design of Aircraft". These are closely related to our Panel activities addressing a somewhat different audience than this one here.



RTD-9

I will skip the next half hour of my address in the interest of time and just say that, assuming that you found something here to cheer about, I would like on your behalf, the audience, to thank the Program Committee, and especially the co-chairmen, Dr. Campbell who could not be here, and Prof. Young who served very admirably. We appreciate your efforts very much. Of course, we thank the speakers for their contributions, the audience participation, and a special word to our technical evaluator, Mr. Jeremy Smith. Next I wish to thank our Dutch friends and hosts who kept things moving, particularly Captain Sombroek and Mrs. Van de Veen and I would particularly mention Madame Slooff and Madame Steketee, and also Mrs. Goodrich who helped to organize the spouses program. Successful meetings like this one rely heavily on the staff of AGARD. That includes our Panel Executive, Dr. Winston Goodrich, our Panel Secretary, Madame Anne-Marie Rivault and the technicians who operated the projections and audio equipment during the week, Mr. Damin and Mr. Kohler. Next to last, special thanks and compliments to our panel musicians, Prof. Bernard, Madame Bowers, Dr. Boorstel of NLR and Prof. Steketee. That was really a special event and we appreciate it. Now to mention our interpreters who worked very hard all week keeping up with our supersonic conversations, Mrs. Hertz, Mrs. Wabbe and Mr. Shir. Finally, and once again, thanks to you very much, ladies and gentlemen, have a nice lunch and a pleasant trip home, but Panel Members come back at 2:30.

REPORT DOCUMENTATION PAGE			
1. Recipient's Reference	2. Originator's Reference	3. Further Reference	4. Security Classification of Document
	AGARD-CP-494	ISBN 92-835-0623-5	UNCLASSIFIED
5. Originator	Advisory Group for Aerospace Research and Development North Atlantic Treaty Organization 7 rue Ancelle, 92200 Neuilly sur Seine, France		
6. Title	VORTEX FLOW AERODYNAMICS		
7. Presented at	the Symposium of the Fluid Dynamics Panel in Scheveningen, The Netherlands. 1st to 4th October 1990.		
8. Author(s)/Editor(s)	Various		9. Date July 1991
10. Author's/Editor's Address	Various		11. Pages 546
12. Distribution Statement	This document is distributed in accordance with AGARD policies and regulations, which are outlined on the back covers of all AGARD publications.		
13. Keywords/Descriptors			
<div style="display: flex; justify-content: space-between;"> <div>           Boundary layer separation ,            Flow visualization ,            Three dimensional flow ,            Turbulent flow ,         </div> <div>           Vortex generators ,            Vortices ,            Wings ,            Fighter aircraft ,         </div> </div>			
14. Abstract			
<p>The AGARD Fluid Dynamics Panel sponsored this Symposium to provide an update review of the aerodynamic effects of separation-induced vortex flows on the design and off-design performance of fighter aircraft. A better understanding is needed to predict and control these vortex flows throughout the flight envelope at subsonic, transonic, and supersonic speeds, and especially during high lift operations for take-offs, landings, and sustained and instantaneous maneuvers. <i>Keywords:</i></p> <p>In addition to the papers presented at the Symposium, the results of the Round Table Discussion recorded at the end of the Symposium are presented in this report.</p> <p>Papers presented and discussions held at the Symposium of the Fluid Dynamics Panel in Scheveningen, The Netherlands, 1st to 4th October 1990.</p>			

<p>AGARD Conference Proceedings 494 Advisory Group for Aerospace Research and Development, NATO VORTEX FLOW AERODYNAMICS Published July 1991 546 pages</p> <p>The AGARD Fluid Dynamics Panel sponsored this Symposium to provide an update review of the aerodynamic effects of separation-induced vortex flows on the design and off-design performance of fighter aircraft. A better understanding is needed to predict and control these vortex flows throughout the flight envelope at subsonic, transonic, and supersonic speeds, and especially during high lift operations for take-offs, landings, and sustained and instantaneous maneuvers.</p> <p>P.T.O.</p>	<p>AGARD-CP-494</p> <p>Boundary layer separation Flow visualization Three dimensional flow Turbulent flow Vortex generators Vortices Wings Fighter aircraft</p>	<p>AGARD Conference Proceedings 494 Advisory Group for Aerospace Research and Development, NATO VORTEX FLOW AERODYNAMICS Published July 1991 546 pages</p> <p>The AGARD Fluid Dynamics Panel sponsored this Symposium to provide an update review of the aerodynamic effects of separation-induced vortex flows on the design and off-design performance of fighter aircraft. A better understanding is needed to predict and control these vortex flows throughout the flight envelope at subsonic, transonic, and supersonic speeds, and especially during high lift operations for take-offs, landings, and sustained and instantaneous maneuvers.</p> <p>P.T.O.</p>	<p>AGARD-CP-494</p> <p>Boundary layer separation Flow visualization Three dimensional flow Turbulent flow Vortex generators Vortices Wings Fighter aircraft</p>
<p>AGARD Conference Proceedings 494 Advisory Group for Aerospace Research and Development, NATO VORTEX FLOW AERODYNAMICS Published July 1991 546 pages</p> <p>The AGARD Fluid Dynamics Panel sponsored this Symposium to provide an update review of the aerodynamic effects of separation-induced vortex flows on the design and off-design performance of fighter aircraft. A better understanding is needed to predict and control these vortex flows throughout the flight envelope at subsonic, transonic, and supersonic speeds, and especially during high lift operations for take-offs, landings, and sustained and instantaneous maneuvers.</p> <p>P.T.O.</p>	<p>AGARD-CP-494</p> <p>Boundary layer separation Flow visualization Three dimensional flow Turbulent flow Vortex generators Vortices Wings Fighter aircraft</p>	<p>AGARD Conference Proceedings 494 Advisory Group for Aerospace Research and Development, NATO VORTEX FLOW AERODYNAMICS Published July 1991 546 pages</p> <p>The AGARD Fluid Dynamics Panel sponsored this Symposium to provide an update review of the aerodynamic effects of separation-induced vortex flows on the design and off-design performance of fighter aircraft. A better understanding is needed to predict and control these vortex flows throughout the flight envelope at subsonic, transonic, and supersonic speeds, and especially during high lift operations for take-offs, landings, and sustained and instantaneous maneuvers.</p> <p>P.T.O.</p>	<p>AGARD-CP-494</p> <p>Boundary layer separation Flow visualization Three dimensional flow Turbulent flow Vortex generators Vortices Wings Fighter aircraft</p>

<p>In addition to the papers presented at the Symposium, the results of the Round Table Discussion recorded at the end of the Symposium are presented in this report</p> <p>Papers presented and discussions held at the Symposium of the Fluid Dynamics Panel in Scheveningen, The Netherlands, 1st to 4th October, 1990.</p> <p>ISBN 92-835-0623-5</p>	<p>In addition to the papers presented at the Symposium, the results of the Round Table Discussion recorded at the end of the Symposium are presented in this report.</p> <p>Papers presented and discussions held at the Symposium of the Fluid Dynamics Panel in Scheveningen, The Netherlands, 1st to 4th October 1990.</p> <p>ISBN 92-835-0623-5</p>
<p>In addition to the papers presented at the Symposium, the results of the Round Table Discussion recorded at the end of the Symposium are presented in this report.</p> <p>Papers presented and discussions held at the Symposium of the Fluid Dynamics Panel in Scheveningen, The Netherlands, 1st to 4th October 1990.</p> <p>ISBN 92-835-0623-5</p>	<p>In addition to the papers presented at the Symposium, the results of the Round Table Discussion recorded at the end of the Symposium are presented in this report.</p> <p>Papers presented and discussions held at the Symposium of the Fluid Dynamics Panel in Scheveningen, The Netherlands, 1st to 4th October 1990.</p> <p>ISBN 92-835-0623-5</p>

AGARD

NATO OTAN

7 RUE ANCELLE - 92200 NEUILLY-SUR-SEINE  
FRANCE

Téléphone (1)47.38.57.00 - Téléc 610 176  
Télécopie (1)47.38.57.99

DIFFUSION DES PUBLICATIONS  
AGARD NON CLASSIFIEES

L'AGARD ne détient pas de stocks de ses publications, dans un but de distribution générale à l'adresse ci-dessus. La diffusion initiale des publications de l'AGARD est effectuée auprès des pays membres de cette organisation par l'intermédiaire des Centres Nationaux de Distribution suivants. A l'exception des Etats-Unis, ces centres disposent parfois d'exemplaires additionnels; dans les cas contraire, on peut se procurer ces exemplaires sous forme de microfiches ou de microcopies auprès des Agences de Vente dont la liste suit.

CENTRES DE DIFFUSION NATIONAUX

**ALLEMAGNE**

Fachinformationszentrum,  
Karlsruhe  
D-7514 Eggenstein-Leopoldshafen 2

**BELGIQUE**

Coordonnateur AGARD-VSL  
Etat-Major de la Force Aérienne  
Quartier Reine Elisabeth  
Rue d'Evere, 1140 Bruxelles

**CANADA**

Directeur du Service des Renseignements Scientifiques  
Ministère de la Défense Nationale  
Ottawa, Ontario K1A 0K2

**DANEMARK**

Danish Defence Research Board  
Ved Idrætsparken 4  
2100 Copenhagen Ø

**ESPAGNE**

INTA (AGARD Publications)  
Pintor Rosales 34  
28008 Madrid

**ETATS-UNIS**

National Aeronautics and Space Administration  
Langley Research Center  
M/S 180  
Hampton, Virginia 23665

**FRANCE**

O.N.E.R.A. (Direction)  
29, Avenue de la Division Leclerc  
92320, Châtillon sous Bagneux

**GRECE**

Hellenic Air Force  
Air War College  
Scientific and Technical Library  
Dekelia Air Force Base  
Dekelia, Athens TGA 1010

**ISLANDE**

Director of Aviation  
c/o Flugrad  
Reykjavik

**ITALIE**

Aeronautica Militare  
Ufficio del Delegato Nazionale all'AGARD  
3 Piazzale Adenauer  
00144 Roma EUR

**L. JEMBOURG**

Voir Belgique

**NORVEGE**

Norwegian Defence Research Establishment  
Attn: Biblioteket  
P.O. Box 25  
N-2007 Kjeller

**PAYS-BAS**

Netherlands Delegation to AGARD  
National Aerospace Laboratory NLR  
Kluuyverweg 1  
2629 HS Delft

**PORTUGAL**

Portuguese National Coordinator to AGARD  
Gabinete de Estudos e Programas  
CLAFIA  
Base de Alfragide  
Alfragide  
2700 Amadora

**ROYAUME UNI**

Defence Research Information Centre  
Kentigern House  
65 Brown Street  
Glasgow G2 8EX

**TURQUIE**

Milli Savunma Bakanlığı (MSB)  
ARGE Daire Başkanlığı (ARGE)  
Ankara

LE CENTRE NATIONAL DE DISTRIBUTION DES ETATS-UNIS (NASA) NE DETIENT PAS DE STOCKS  
DES PUBLICATIONS AGARD ET LES DEMANDES D'EXEMPLAIRES DOIVENT ETRE ADRESSEES DIRECTEMENT  
AU SERVICE NATIONAL TECHNIQUE DE L'INFORMATION (NTIS) DONT L'ADRESSE SUIT.

AGENCES DE VENTE

National Technical Information Service  
(NTIS)  
5285 Port Royal Road  
Springfield, Virginia 22161  
Etats-Unis

ESA/Information Retrieval Service  
European Space Agency  
10, rue Mario Nikis  
75015 Paris  
France

The British Library  
Document Supply Division  
Boston Spa, Wetherby  
West Yorkshire LS23 7BQ  
Royaume Uni

Les demandes de microfiches ou de photocopies de documents AGARD (y compris les demandes faites auprès du NTIS) doivent comporter la dénomination AGARD, ainsi que le numéro de série de l'AGARD (par exemple AGARD-AG-315). Des informations analogues, telles que le titre et la date de publication sont souhaitables. Veuillez noter qu'il y a lieu de spécifier AGARD-R-nnn et AGARD-AR-nnn lors de la commande de rapports AGARD et des rapports consultatifs AGARD respectivement. Des références bibliographiques complètes ainsi que des résumés des publications AGARD figurent dans les journaux suivants:

Scientific and Technical Aerospace Reports (STAR)  
publié par la NASA Scientific and Technical  
Information Division  
NASA Headquarters (NTT)  
Washington D.C. 20546  
Etats-Unis

Government Reports Announcements and Index (GRA&I)  
publié par le National Technical Information Service  
Springfield  
Virginia 22161  
Etats-Unis

(accessible également en mode interactif dans la base de  
données bibliographiques en ligne du NTIS, et sur CD-ROM)



Imprimé par Specialised Printing Services Limited  
40 Chigwell Lane, Loughton, Essex IG10 3TZ